Proceedings

of

Symposium on Energy Engineering in the 21st Century (SEE2000)

Volume 2

Edited by

Ping Cheng
Mechanical Engineering Department
The Hong Kong University of Science and Technology
Clear Water Bay, Kowloon, Hong Kong

Begell House
New York, Wallingford (U.K.)

DISTRIBUTION STATEMENT A
Approved for Public Release
Distribution Unlimited

DTIC QUALITY INSPECTED 1

20000223 145

Library of Congress Cataloging-in-Publication Data

Catalog record is available from the Library of Congress.

This book represents information obtained from authentic and highly regarded sources. Reprinted material is quoted with permission, and sources are indicated. A wide variety of references are listed. Every reasonable effort has been made to give reliable data and information, but the authors and the publisher cannot assume responsibility for the validity of all materials or for the consequences of their use.

All rights reserved. This book, or any parts thereof, may not be reproduced in any form without written consent from the publisher.

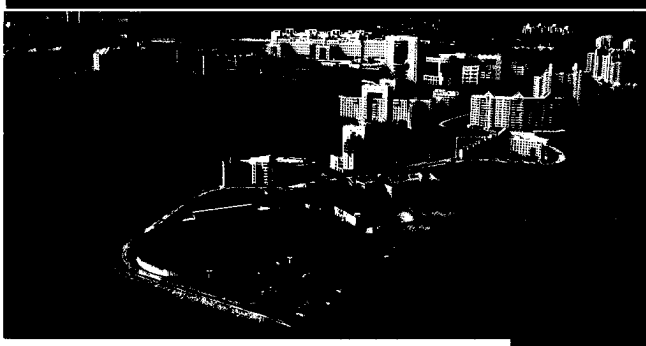
Direct all inquiries to Begell House, Inc., 79 Madison Avenue, New York, NY 10016.

© 2000 by Begell House, Inc.

ISBN 1-56700-132-7 (hard cover edition)

Printed in Hong Kong 1 2 3 4 5 6 7 8 9 0

January 9-13, 2000 Hong Kong



Proceedings of

Symposium on Energy Engineering in the 21st Century (SEE 2000)

Volume **Two**

DISTRIBUTION STATEMENT A
Approved for Public Release
Distribution Unlimited

Begell House New York, Wallingford (U.K.)

Ping Cheng Editor

REPORT DOCUMENTATION PAGE

Form Approved
OMB No. 0704-0188

The public reporting burden for this collection of information is estimated to average 1 hour per response, including the time for reviewing instructions, searching existing data sources, gathering and maintaining the data needed, and completing and reviewing the collection of information. Send comments regarding this burden estimate or any other aspect of this collection of information, including suggestions for reducing the burden, to Department of Defense, Washington Headquarters Services, Directorate for Information Operations and Reports (0704-0188), 1215 Jefferson Davis Highway, Suite 1204, Arlington, VA 22202-4302. Respondents should be aware that notwithstanding any other provision of law, no person shall be subject to any penalty for failing to comply with a collection of information if it does not display a currently valid OMB control number.
PLEASE DO NOT RETURN YOUR FORM TO THE ABOVE ADDRESS.

1. REPORT DATE *(DD-MM-YYYY)*	2. REPORT TYPE	3. DATES COVERED *(From - To)*
14-02-2000	Conference Proceedings	9-13 Jan 00

4. TITLE AND SUBTITLE

Proceedings of Symposium on Energy Engineering in the 21st Century (SEE 2000) ~~(Four Volumes)~~ Vol. 2

5a. CONTRACT NUMBER
F6256299M9146

5b. GRANT NUMBER

5c. PROGRAM ELEMENT NUMBER

6. AUTHOR(S)

Conference Committee

5d. PROJECT NUMBER

5e. TASK NUMBER

5f. WORK UNIT NUMBER

7. PERFORMING ORGANIZATION NAME(S) AND ADDRESS(ES)

Hong Kong University of S&T
Clear Water Bay
Hong Kong
Hong Kong

8. PERFORMING ORGANIZATION REPORT NUMBER

N/A

9. SPONSORING/MONITORING AGENCY NAME(S) AND ADDRESS(ES)

AOARD
UNIT 45002
APO AP 96337-5002

10. SPONSOR/MONITOR'S ACRONYM(S)

AOARD

11. SPONSOR/MONITOR'S REPORT NUMBER(S)

CSP-991002

12. DISTRIBUTUION/AVAILABILITY STATEMENT

Approved for public release; distribution is unlimited.

13 SUPPLEMENTARY NOTES

14. ABSTRACT

Volume 1, Page 1 – 406 Includes:
Keynote Papers, Forced Convection, Natural Convection, and Boiling and Condensation
Volume 2, Page 407 – 903 Includes:
Two-Phase Flow, Porous Media, Heat Pipes and Thermosyphons, Conduction and Radiation, Microscale Heat Transfer, Heat Transfer Enhancement, Solar Energy & Nuclear Energy, Thermal Storage, Melting & Solidification
Volume 3, Page 904 – 1,345 Includes:
Drying & Food Processing, Heat Exchangers, Air-Conditioning and Refrigeration, Cryogenic Engineering, Energy and Environment, Combustion and Fire
Volume 4, Page 1,346 – 1,734 Includes: Cycle Analysis, Engine Combustion, Waste Treatment by Thermal Methods, Fuel Cells, Clean Combustion Technology, Coal Combustion

15. SUBJECT TERMS

Fire Surpression

16. SECURITY CLASSIFICATION OF:			17. LIMITATION OF ABSTRACT	18. NUMBE OF PAGES	19a. NAME OF RESPONSIBLE PERSON
a. REPORT	b. ABSTRACT	c. THIS PAGE			Terence J. Lyons, M.D.
U	U	U	UU	1,734	19b. TELEPHONE NUMBER *(Include area code)* +81-3-5410-4409

FORWARD

The signing of the Montreal Protocol in 1987 and the Kyoto Protocol in 1997 by various nations serves as a reminder once again of the intimate relationship between energy and environment, which will no doubt remain one of the major issues in the 21st Century. This is particularly so in Southeast Asia, where industrial growth has taken place at such a rapid pace during the last two decades. At the same time, research in energy engineering is accelerating in this part of the world. At the Hong Kong University of Science and Technology (HKUST), the Center for Energy and Thermal Systems (CETS) was recently established for the research and development of energy efficient and environmentally benign thermal systems. Thus, it is a privilege for CETS to be able to host the Symposium on Energy Engineering in the 21st Century (SEE2000) on the HKUST campus between 9-13 January 2000, the first international energy engineering conference ever held in Hong Kong.

The aim of this Symposium is to provide a forum for technical interchange in various aspects of energy engineering. The 226 papers (including 11 keynote papers) presented in the 25 technical sessions of the Symposium are published in this proceedings which contains 4 volumes, covering a variety of topics from heat and mass transfer, various energy and thermal systems, to clean combustion technology.

It has been a great pleasure for me to work with Symposium Co-Chairmen Professor Kefa Cen of the Zhejiang University and Professor Patrick Takahashi of the University of Hawaii in the planning of this Symposium. I would like to express my sincere thanks to keynote speakers for their efforts in writing up-to-date review papers, to members of the International Advisory Committee and the Organizing Committee for their enthusiasm in promoting the Symposium, and to members of the Local Committee for their hard work in reviewing the manuscripts. Special thanks are due to Dr. H. H. Qiu (the Symposium Secretariat) and Ms. Lotta Tse for their help in making conference arrangements, as well as to Ms. Ellie Ho, Ms. Ronnie Tse and other clerical staff for their help in the typing of the manuscripts and for the preparation of the proceedings. The generous financial support from the K. C. Wong Education Foundation, U.S. Air Force Asian Office of Aerospace Research and Development, U.S. Army Research Office - Far East, U.S. Office of Naval Research - Asia, and the International Technic HVAC Company are gratefully acknowledged.

Ping Cheng
Symposium Chair

Hong Kong
January 2000

SYMPOSIUM CHAIRMAN

Professor Ping Cheng
Department of Mechanical Engineering
Hong Kong University of Science and Technology
Clear Water Bay, Kowloon, Hong Kong
Fax: (852) 2358-1543 E-mail: mepcheng@ust.hk

SYMPOSIUM CO-CHAIRMEN

Professor Kefa Cen
Institute for Thermal Power Engineering
Zhejiang University
Hangzhou 310027, China
Fax: (86) 571-595-1616
E-mail: kfcen@sun.zju.edu.cn

Professor Patrick Takahashi
Hawaii Natural Energy Institute
University of Hawaii
Honolulu, Hawaii 96822, U.S.A.
Fax: (808) 956-2336
E-mail: ptakaha@uhccmvs.uhcc.hawaii.edu

SYMPOSIUM SECRETARIAT

Dr. H. H. Qiu
Department of Mechanical Engineering
Hong Kong University of Science and Technology
Clear Water Bay, Kowloon, Hong Kong
Fax: (852) 2358-1543 E-mail: meqiu@ust.hk

INTERNATIONAL ADVISORY COMMITTEE

Tien, C. L., (Honorary Chairman), University of California, Berkeley
Bull, S. R., National Renewable Energy Laboratory, Golden
Chen, X. J., Xian Jiaotong University, Xian
Chiu, H. H., Cheng Kung University, Tainan
Cotta, R. Federal University of Rio de Janeiro, Rio de Janeir
De Vahl Davis, G., University of New South Wales, Sydney
Fang, L. J., Industrial Technology Research Institute, Hsinchu
Fletcher, "Skip" L. S., Texas A & M University, College Station
Fujita, Y., Kyushu University, Fukuoka
Goldstein, R., University of Minnesota, Minneapolis
Gori, F., University of Rome, Rome
Hahne, E., University of Stuttgart, Stuttgart
Leontiev, A. I., Moscow State University, Moscow
Martynenko, O. G., Byelorussian Academy of Sciences, Minsk
Mayinger, F., Technical University of Munich, Munich
Mujumdar, A. S., McGill University, Montreal
Ro, S. T., Seoul National University, Seoul
Shi, S. X., Tianjin University, Tianjin
Sidemann, S., Israel Institute of Technology, Haifai
Tanasawa, I., Tokyo University of Agriculture & Technology, Tokyo
Viskanta, R., Purdue University, West Lafayette
Wang, B. X., Tsinghau University, Beijing
Yang, K. T., University of Notre Dame, Notre Dame

ORGANISING COMMITTEE

Auracher, H. L., Technical University of Berlin, Berlin
Cai, R. X., Institute of Engineering Thermophysics, Beijing
Chen, T. S., University of Missouri, Rolla
Faghri, A., University of Connecticut, Storrs
Fujii, T., Kobe University, Kobe
Fukusako, S., Hokkaido University, Sapporo
Groll, M., University of Stuttgart, Stuttgart
Guo, Z. Y., Tsinghua University, Beijing
Howell J., University of Texas, Austin
Inaba, H., Okayama University, Okayama
Kakac, S., University of Miami, Miami
Kashiwagi, T., Tokyo University of Agriculture & Technology, Tokyo
Kaviany, M., University of Michigan, Ann Arbor
Kennedy, L. A., The University of Illinois at Chicago, Chicago
Kim, Jong Hyun, EPRI, Palo Alto
Kurosaki, Y., University of Electro-Communications, Tokyo
Law, C. K., Princeton University, Princeton
Lee, J. S., Seoul National University, Seoul
Lloyd, A. C., Desert Research Institute, Reno
Lou, D. Y. S., University of Nebraska, Lincoln
Minkowycz, W. J., University of Illinois at Chicago, Chicago
Nelson, R. A., Los Alamos National Laboratory, Los Alamos
Ni, M. J., Zhejiang University, Hangzhou
Nishio, S., University of Tokyo, Tokyo
Peng, X. F., Tsinghua University, Beijing
Peterson, G. P., Texas A & M University, College Station
Radebaugh, R., National Institute of Standards and Technology, Boulder
Saitoh, T. S., Tohoku University, Sendai
Serizawa, A., Kyoto University, Kyoto
Shoji, M., University of Tokyo, Tokyo
Son, J. E., Korea Institute of Energy Research, Taejon
Straub, J., Technical University of Munich, Munich
Suzuki, K., Kyoto University, Kyoto
Tong, T. W., Colorado State University, Fort Collins
Wang, C. Y., Pennsylvania State University, College Park

LOCAL COMMITTEE

Hsu, C. T, HKUST
Chao, Y. H., HKUST
Chi, Y, Zhejiang University
Kot, S. C., HKUST
Lee, H. K., HKUST
Qiu, H. H., HKUST
Zhao, T. S., HKUST.

SPONSORS

American Society of Mechanical Engineers
Japanese Society of Mechanical Engineers
Chinese Society of Power Engineering
International Center of Heat and Mass Transfer
K. C. Wong Education Foundation
U.S. Air Force Asian Office of Aerospace Research and Development
U.S. Army Research Office-Far East
U.S. Office of Navy Research-Asia

SUMMARY OF TECHNICAL SESSIONS

Volume 1

A. Keynote Papers
B. Forced Convection
C. Natural Convection
D. Boiling and Condensation

Volume 2

E. Two-Phase Flow
F. Porous Media
G. Heat Pipes and Thermosyphons
H. Conduction and Radiation
I. Microscale Heat Transfer
J. Heat Transfer Enhancement
K. Solar Energy & Nuclear Energy
L. Thermal Storage
M. Melting and Solidification

Volume 3

N. Drying and Food Processing
O. Heat Exchangers
P. Air-Conditioning and Refrigeration
Q. Cryogenic Engineering
R. Energy and Environment
S. Combustion and Fire

Volume 4

T. Cycle Analysis
U. Engine Combustion
V. Waste Treatment by Thermal Methods
W. Fuel Cells
X. Clean Combustion Technology
Y. Coal Combustion

CONTENTS OF VOLUME 2

	Forward	**iii**
E.	**Two-Phase Flow**	**407**
E1.	Critical Two-Phase Flow in a Short Converging Nozzle *A. M. C. Chan and I. G. Elphick*	408
E2.	An Investigation on the Bubble and Slug Flow Patterns and Its Transition for Gas/Oil-Water Emulsions *Y. Luo, T. K. Chen and J. Y. Cai*	416
E3.	Hydrodynamics and Dust Separation Efficiency of Two-Phase Rotating Flow *A. Khalatov, N. Syred, I. Borisov and S. Shevtsov*	422
E4.	Experimental Investigations on Evaporative Heat Transfer of Water Film in a Vertical Duct with Counter-Currently Passed Air Condition *Y. M. Kang and G. C. Park*	430
E5.	A Visual Study of Slug Bubbles in Miniaturized Channels *Q. C. Bi and T. S Zhao*	438
E6.	Flow Pattern of Pure Refrigerant HFC134a Evaporating in a Horizontal Capillary Tube *K. Kuwahara, S. Koyama, J. Yu , C. Watanabe and N. Osa*	445
E7.	Analyses of Motion and Drag Coefficient of Water Droplets in a Natural Draught Cooling Tower *B. M. Liu and M. N. A. Hawlader*	451
E8.	Numerical Analysis and Experimental Verification of Two-Phase Flow of Refrigerant Through Electronic Expansion Valve *B. F. Yu, Z. G. Wang, D. Q. Wang and X. Z. Meng*	459
F.	**Porous Media**	**465**
F1.	Experimental Study of Disordered 3D and 2D Packing of Rigid Fibres: Influence of the Aspect Ratio on the Structure *M. Novellani, R. Santini and L. Tadrist*	466
F2.	Flow Regions of Granules in Dorfan Impingo Filter for Gas Cleanup *J. T. Kuo and J. Smid and S. S. Hsiau and H. H. Tsai and C. S. Chou*	474
F3.	Effect of Homogeneous and Hetrogeneous Source Terms on the Macroscopic Description of Heat Transfer in Porous Media *M. Quintard, B. Ladevie and S. Whitaker*	482
F4.	Study on Improved Performance of Plate Heat Exchanger with Packed Beads and Mini-Longitudinal Channels on Plate Surface *B. X. Wang, J. H. Du and Z. J. Zhang*	490
F5.	Heat Transfer of a Porous Channel Heat Sink Subjected to Oscillating Flow *H. L. Fu, K. C. Leong, X.Y. Huang and C. Y. Liu*	497
F6.	Effective Thermal Conductivity of Bi-Dispersed Porous Media *Z. Q. Chen, P. Cheng and C. T. Hsu*	505
F7.	Rewetting Phenomena and Thermal Stability At Steam Generation on Surfaces with Porous Coatings *V. I. Borzenko and S. P. Malyshenko*	512
F8.	Numerical Analysis of Two-Phase Flow in Porous Media with Finite Element Method *Q. Bai, T. Hyuga and Y. Fujita*	521
F9.	Forced Convection and Flow Boiling in Mono- and Bi-Dispersed Porous Channels *Z. Q. Chen, P. Cheng and T. S. Zhao*	529
G.	**Heat Pipes and Thermosyphons**	**538**
G1.	Thermal Control of Electronic Components by Two-Phase Thermosyphons and Pulsating Heat Pipes *N. Gavotti and F. Polasek*	539

G2.	A Study on the Thermal Hydraulic Phenomena of Decay Heat Removal System Using the Closed Two-Phase Thermosiphon Loop *Y. Ahn, G. Park and M. Kim*	557
G3.	Heat Transfer Performance of a Corrugate Tube Thermosyphon *M. Hirashima and K. Negishi*	564
G4.	Miniature High Heat Flux Heat Pipes for Cooling of Electronics *Z. J. Zuo and M. T. North*	573
H.	**Conduction and Radiation**	**580**
H1.	Optimization of the Annular Fin with Base Wall Thermal Resistance *B. T. F. Chung and Z. Ma*	581
H2.	Modeling of Viscosity and Thermal Conductivity of Hydrocarbons Based on Equation of State *X. Q. Guo, C. Y. Sun, S. X. Rong, G. J. Chen and T. M. Guo*	588
H3.	Determination of the Thermal Diffusivity of Aqueous Solutions of Salts by a Laser-Induced Thermal Grating Technique *J. Wang,Z. H. Chen and M. Fiebig*	598
H4.	Experimental Evaluation of Radiation Reflection Characteristics of Real Surfaces for Heat Transfer Computation *T. Makino, H. Wakabayashi and S. Y. Okada*	604
H5.	Thermal Conductivity of Fiber Filled Aerogels *G. R. Cunnington and S. C. Lee*	613
H6.	Self-Similar Growth of a Compound Layer in Thin-Film Binary Diffusion Couples *H. Zhang and H. Wong*	621
H7.	Heat Transfer Properties and Structure of $CaCl_2$ Reactor Beds Used for Chemical Heat Pumps *K. Fujioka, K. Oido and Y. Hirata*	628
H8.	On the Use of Diamond-Coated Junctions to Enhance Thermal Contact Conductance *K. C. Chung and C. T. Chen*	636
I.	**Microscale Heat Transfer**	**642**
I1.	Two-Phase Flow Patterns in an Ultra-Small Scale Flowing Passage *Z. Feng and A. Serizawa*	643
I2.	Measurement of Friction Factors for R134A and R12 Through Microchannels *L. S. Ding, H. Sun, X. L. Sheng and B. D. Lee*	650
I3.	Characteristics of Frictional Resistance for Gas Flow in Microtubes *Z. Li, D. X. Du and Z. Guo*	658
I4.	Study on Heat Transfer for Flow Flim Condensation in Vertical Mini tube with Interfacial Waves *X. Z. Du and B. X. Wang*	665
I5.	Non-Equilibrium Mass Transfer at Liquid-Vapor Interface *T. Tsuruta and G. Nagayama*	672
I6.	Microscale Heat Transfer at Fast Time Studied by Novel Laser-Based Measurement Techniques *K. X. He, J. C. Wang, A. Chow , J. Mo and C. Holden*	680
J.	**Heat Transfer Enhancement**	**687**
J1.	Turbulent Augmented Heat Transfer from the Surface of an Immersed Tube in a Magnetofluidized Bed *S. C. Saxena and V. L. Ganzha*	688
J2.	Drag Reduction and Heat Transfer Enhancement of Water Flow in a Pipe Using New Surfactants for Environmentally Acceptable Drag Reducing Additives *K. Nobuchika, T. Nakata, K. Sato, F. Yamagishi, S. Tomiyama, H. Inaba, A. Horibe and N. Haruki*	695

J3. An Experimental Study on the Compound Enhancement of Tubeside Heat Transfer with Air Flow 701
Q. T. Zhou, Z. N. Wang, H. Zhang and F. Xiong
J4. Experimental Investigations of Enhanced Evaporation Surfaces for Cooling Systems in Motor Vehicles 708
B. Schmidt, R. Mertz and M. Groll
J5. Feasibility Study of New Heat Transportation System with Drag-Reducing Surfactant Additives 716
P. W. Li, Y. Kawaguchi and A. Yabe
J6. Flow and Heat Transfer Characteristics of Water Solution with Flow Drag Reduction Additive in Curved Tubes 723
H. Inaba, N. Haruki and A. Horibe
J7. Transient Development of Heat Transfer Enhanced by Oscillating Flows Past a Circular Cylinder 731
C. T. Hsu and M. K. Kwan

K. Solar Energy & Nuclear Energy 739

K1. Numerical Investigation of the Fluid Flow and Heat Transfer in a Solar Domestic Hot Water Store with a Mantle Heat Exchanger for the Solar Loop 740
E. Hahne, H. Mandel and H. Druck
K2. Characteristic of Solar Collector Utilizing Electro-Hydro-Dynamic Effect 748
M. Sato, H. Aoki and Y. Wako
K3. Determination of the Optimum Conditions for Maximum Solar Energy Collection of Plane Reflector-Tilted Solar Collector System 751
H. M. S. Hussien, G. E. Ahmad and M. A. Mohamad
K4. Developments and Designs of Solar Engineering Fresnel Lenses 759
R. Leutz, A. Akisawa, T. Kashiwagi and A. Suzuki
K5. Experimental Study of a Compact Solar Collector 766
E.S. Mettawee and G. M. R. Assassa
K6. Performance Improvement of a Non-Conventional Solar Water Pump 774
K. Sumathy
K7. Neutronic Performances of the (D,T) Driven Hybrid Blankets, Fueled with U3O8 and UF4 for Various Coolants to breed Fissile Fuel for LWRs 778
O. Ipek

L. Thermal Storage 787

L1. General Model of Analyzing the Thermal Performance of Latent Heat Thermal Energy Storage Systems with Various PCM Capsules 788
Y. B. Kang, Y. P. Zhang, Y. Jiang and Y. X. Zhu
L2. High Temperature Latent Heat Thermal Energy Storage System for Solar Rankine Engines 796
T. S. Saitoh and A. Hoshi
L3. Thermal Storage and Heat Transfer in Phase Change Material Inside the Spherical Capsules of a Packed Bed Thermal Storage System 804
Y. Q. Zhu, Y. B. Kang, Y. P. Zhang and Y. Jiang
L4. Heat Transfer Enhancement of Direct Contact Melting Process in Thermal Storage System by Vibration 813
M. Oka
L5. Behavior of Charge and Discharge of Thermal Energy in a Storage Type Heat Exchanger 821
H. H. Lin, G. T. Lin, B. C. Yang and S. H. Huang
L6. Solar Energy Storage, Utilizing Paraffin Wax as a Phase-Change Material 826
N. E. Chazly, N. Khattab, S. E. Deeb, A. E. Sharkawy and M.El-Kotb
L7. Mechanism of Heat and Mass Transfer During Gas Hydrate Cool Storage Process 835
L. Q. Xiao and S. P. Wang

L8. Development of Ice Thermal Storage Type Air-Conditioning and Hot Water System for the House 843
S. Aoyama, K. Machida, K. Hamada, M. Matsushita and M. Kimura
L9. Flow and Heat Transfer of Ice Water Slurry in a Straight Pipe 852
H. Inaba, A. Horibe, N. Haruki, M. Yokota and S. Aoyama
L10. Effective Additives for Preventing Recrystalizxation in Ice-Slurry Systems 860
S. S. Lu, T. Inada, A. Yabe, X. Zhang and S. Grandum
L11. Heat Recovery from Domestic Warm Water Application for Bifilar Heating Floors 866
C. D. Lazarescu, I. Olaru, C. Antohi and V. Ciocan

M. Melting and Solidification **872**

M1. Measurement of Transient Double Diffusive Convection and Crystal Growth Using Real-Time Phase Shifting Interferometer 873
S. Maruyama, K. Takahashi and A. Komiya and M. Behnia
M2. On Characteristics of a Rectangular, Annular Natural Circulation Loop with the Inner Tube Filled with a Phase Change Materials or Air Under Cyclic Pulsating Heat Load 881
C. J. Ho and G. H. Tan
M3. Heat and Mass Transport During Dissolution in a Binary Metallic System 888
A. A. Boral, F. B. Cheung amd S. W. Shiah
M4. Heat and Mass Transfer in Free Surface Flows with Solidification 896
A. V. Kuznetsov

Authors Index to Volumes 1-4 xi

E. Two-Phase Flow

CRITICAL TWO-PHASE FLOW IN A SHORT CONVERGING NOZZLE

A.M.C. Chan and I.G. Elphick
Department of Mechanical Engineering, McMaster University
Hamilton, Ontario, CANADA
Email: albert.chan@oht.hydro.on.ca Fax: (416) 207-6004

Keywords: critical discharge, two-phase flow, blowdown, converging nozzle, critical discharge models

ABSTRACT. Experiments on high-enthalpy water blowdown through a short converging nozzle were preformed to measure the critical discharge flowrate under different stagnation conditions. Two-phase critical flow models were reviewed and three of the simple predictive models were described. The test results were compared with the simple predictive models. It was found that the Henry-Fauske Model provided the best overall agreement with the experimental data. Photographic studies of the two-phase flashing jet revealed the presence of three distinct regions in the jet. These regions are consistent with the jet geometry proposed in previous studies.

1. INTRODUCTION

When a pressurized high-enthalpy liquid in a reservoir is discharged through a small opening, a vapor-liquid two-phase jet will emerge. This physical system can be found in the combustion of pressurized liquid fuels, and in the event of a pipe rupture in a chemical or nuclear power plant. In the latter cases, hazardous radioactive or otherwise toxic gases and aerosols may escape into the plant air environment. The release of fission products into the containment building in a nuclear power plant during a loss-of-coolant accident (LOCA) is of particular concern for safety reasons. It is important to know how the fission products are transported through containment so that releases from containment to the environment can be properly assessed. There are many pathways for the transport and depletion of fission products in containment. All these pathways are linked to the coolant system by the critical discharge of the high enthalpy coolant through the pipe break and its subsequent dispersion as an unbounded two-phase jet.

The characteristics of a flashing jet were investigated using a small-scale pressurized blowdown test facility in the present study. The jet was formed by discharging high-pressure water at slightly subcooled conditions from a pressure vessel into ambient atmosphere through a small converging nozzle. Due to the large and rapid drop in pressure, the fluid flashed and the flow became choked (critical) at the nozzle exit. The flow then expanded very rapidly due to flashing forming a two-phase jet downstream. The problem can thus be divided into two: the upstream flow up to the opening or nozzle exit and the downstream unbounded two-phase jet flow.

Since the flow is choked (critical) at the nozzle exit, the downstream ambient conditions have very little influence on the flow upstream. The geometry of the two-phase jet downstream, on the other hand, is determined largely by the upstream stagnant conditions. Healzer and Singh [1] divided the jet into three regions as shown in Figure 1: Region 1 extends from the break to the end of a jet core; Region 2 extends from the end of the jet core to an asymptotic plane and Region 3 starts at the asymptotic plane and is assumed to expand at a half angle of ten degrees. The length of the cone-shaped jet core was found to be a function the jet subcooling at the break plane. The distance from the break plane to the asymptotic plane depends on the critical mass flux and the stagnation pressure upstream. Some limited information on the geometry of the two-phase jet was obtained in the present study using photography. This will be shown later when the test results are presented.

Critical or choked flow in a pipe or nozzle is the maximum flow rate achievable for given upstream conditions. In a pressurized flow system, the flow rate will increase when the downstream pressure is reduced until a maximum value is reached after which the flow will remain constant even if the downstream pressure is further reduced. This maximum flow rate is generally referred to as the critical or choked flow. Critical two-phase flow is important in the nuclear industry in the event of a loss-of-coolant accident as discussed above. In addition, the rate of coolant discharged through a pipe rupture has a first order effect on the coolant inventory in the primary heat transport system and directly affects the heat transfer rate in the reactor core. It is also important in the sizing of emergency relief systems in the chemical and process industries.

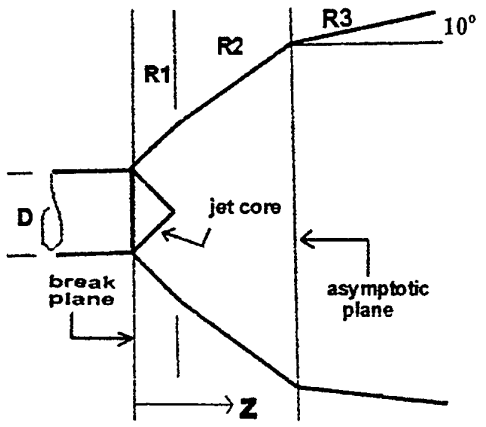


Figure 1: Geometry of flashing two-phase jet

A large amount of work on critical two-phase flows exists. Predictive models of different levels of sophistication are available. It ranged from the simple homogeneous equilibrium model (HEM) which is essentially a pseudo single-phase flow model to the complicated two-fluid models incorporating all the major non-equilibrium interfacial transport phenomena [2-4]. In between are a large number of models treating one or more of the non-equilibrium effects mechanistically. This included models by Henry and Fauske [5], Kroeger [6], Stuhmiller [7], Reocreux [8], Ardron [9] and Alamgir and Lienhard [10] and many others. An excellent overview on the various analytical approaches to two-phase critical flow modeling was given by Wallis [11]. Wallis [11] concluded that: "The appropriate analytical approach should be consistent with our understanding of the physical phenomena and the precision with which they can be defined". This suggests that the use of the full two-fluid model may still be premature today because proper modeling of the many interfacial transfer terms under realistic blowdown conditions is still lacking.

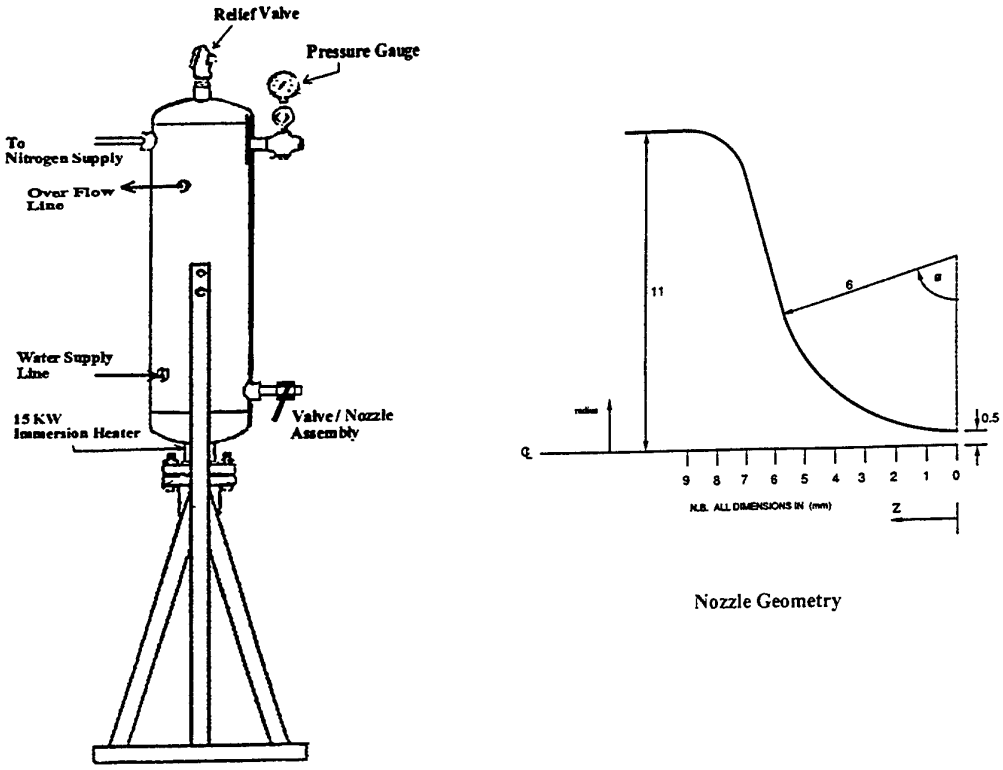
2. EXPERIMENTS

Test Setup

A schematic diagram of the Small-Scale Blowdown Test Facility used in the present study is shown in Figure 2. It consists of a pressure vessel, a shut-off valve and nozzle assembly, a nitrogen cover gas system and a digital weight scale. The pressure vessel was fabricated from type 316 stainless steel and was rated at 3.5 MPa and 250°C. It had a dimension of 10" (254 mm) in diameter and 42.5" (1080 mm) in overall length and a volume of 50 liters. It was fitted with a 15-kW electric immersion heater. The vessel was insulated to reduce heat losses during heat up. The nitrogen cover gas system was used to obtain and maintain a subcooled condition in the vessel when needed. The water temperature and back pressure in the vessel were controlled by the respective controllers. The pressure vessel was mounted on a Fisher 0-200 kg Electromatic weight scale used to measure the discharge rate during blowdown. The total discharge could be measured to ±0.05 kg. Blowdown through the jet nozzle was initiated by opening the stainless steel ball valve.

Valve and Nozzle Assembly

The valve and nozzle assembly consists of a short length (76 mm) of stainless tube (25.4 mm dia.), a stainless steel shut-off ball valve and a custom brass nozzle. The diameter of the components of the assembly was uniform at 22 mm. The nozzle had a short transition length. Its diameter was reduced from 22 mm to 1 mm at the exit over a distance of 9 mm. The geometry of the nozzle is shown in the insert of Figure 2. The assembly was connected to the pressure vessel through a 25.4 mm half coupling about 200 mm from the bottom of the vessel. A short nozzle with a small throat area was used to minimize the pressure drop from the vessel to the nozzle so that flashing would not occur upstream of the nozzle exit.



Nozzle Geometry

Figure 2: Small-scale blowdown test facility schematics

Instrumentation

In addition to the total weight of the vessel, three water-temperature and two pressure measurements were acquired during the blowdown transients. Water temperatures were measured using ground junction stainless steel sheathed type-K thermocouples (uncertainty: ±1 °C) in three locations: at the top of the vessel (T_R); inside the vessel close to the entrance to the valve assembly (T_u) and immediate upstream of the nozzle (T_o). The fluid pressures were measured using strain-gauge type transducers (full scale: 5 MPa; uncertainty: ±15 kPa) at the top of the vessel (P_R) and immediate upstream of the nozzle (P_o). Data were acquired during the blowdown using a computer controlled data acquisition system at 1 hz. Photographs of the two-phase jet were also taken during the blowdown using both flash and back lighting.

Test Procedure and Test Conditions

A simple test procedure was followed in the present experiment:

1. In preparation for the test, all the water in the pressure vessel was first drained and the weigh scale reset to zero.
2. The vessel was then filled with de-ionized water and heaters were turned on until boiling occurred. Steam was allowed to vent from a vent line at the top of the vessel for a few minutes.
3. The vent line was closed and the vessel was pressurized with nitrogen gas. The vessel pressure was set and controlled by a pressure controller connected to the nitrogen gas supply system.
4. The water temperature in the vessel was allowed to rise to the desired blowdown temperature.
5. The heaters were then turned off and the data acquisition system activated. The mass shown on the weigh scale was recorded. The shut-off valve was opened to initiate the test.
6. The test was terminated after approximately 5 minutes by closing the shut-off valve. The final mass shown on the weigh scale was recorded.

Blowdown tests were performed with vessel pressures ranged from 1.0 MPa to 3.0 MPa and water subcoolings from 6 °C to 50 °C.

3. RESULTS AND DISCUSSIONS

Test Results

The transient pressure and temperature measurements during the blowdown test with the smallest subcooling (P_R=3 MPa; ΔT_{sub}=6 °C) were shown in Figure 3. The pressure measurements confirmed that the pressure drop between the vessel and the nozzle was indeed very small. A slow decay in vessel pressure was observed in the duration of the test (about 5%). However, the nozzle temperature remained below the saturation temperature throughout the test. Flashing thus occurred downstream at the nozzle exit at all times. The discharge rate or critical flow rate was calculated from the weight scale readings recorded before and after the test. An average value over the duration of the blowdown was thus obtained. This can be compared with predictions using various existing models.

Critical Discharge Models

As discussed in the Introduction, there are a large number of predictive models available. However, the two-fluid models are not recommended at present due to our incomplete understanding of the non-equilibrium interfacial transfer phenomena involved. It will be more appropriate and much easier to use the simple mechanistic models. Three simple models were chosen in the present study for comparison purposes. They are the Homogeneous Equilibrium Model [12], the Henry-Fauske Model [5] and the Pressure Undershoot Correlation [10].

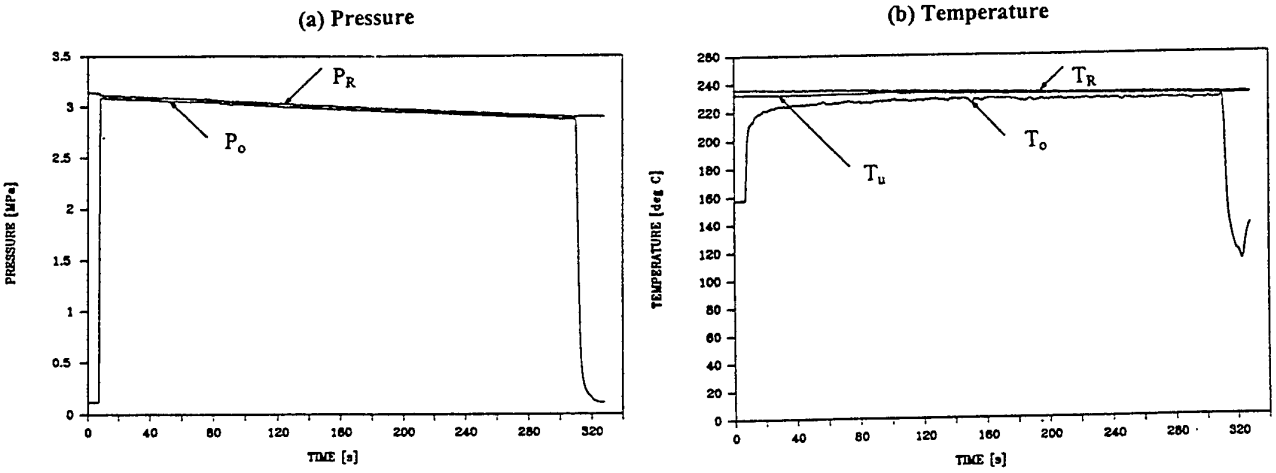


Figure 3: Transient pressure and temperature measurements in typical blowdown test (P_R=3 MPa; ΔT_{sub}=6^{0}C)

The Homogeneous Equilibrium Model (HEM) is a simple extension of the single-phase flow model. It treats the two-phase mixture as a pseudo-fluid with equal velocities and temperatures. It provides a base model against which the non-equilibrium effects for given two-phase flow processes can be assessed. The mass flowrate is given by:

$$G_{HEM} = \{2[h_o - (1-x_E)h_{fE} - x_E h_{gE}]\}^{1/2} / [(1-x_E)v_{fE} + x_E v_{gE}] \quad (1)$$

The critical mass flowrate (G^c_{HEM}) was obtained from Eqn (1) by lowering the downstream pressure successively until a maximum mass flowrate was achieved.

The Henry-Fauske Model also assumes equal phase velocities (mechanical equilibrium), however, it allows for thermal non-equilibrium by introducing a coefficient, N, which accounts for partial phase change (i.e., vapor generation) at the throat. N was correlated as a function of throat equilibrium quality, x_{tE}:

$$N = x_{tE}/0.14 \quad \text{for } x_{tE} < 0.14$$

$$= 1 \quad \text{for } x_{tE} > 0.14 \tag{2}$$

For subcooled blowdown conditions, the mass flowrate can be simplified to:

$$G_{HF} = \{[(v_{gE} - v_{fo})/(s_{gE} - s_{fE})]\, N(ds_{fE}/dP)\}^{-1/2} \tag{3}$$

Since no vapor is formed until the throat, it is assumed that the critical pressure ratio can be calculated from the single phase momentum equation and is given by:

$$\eta = P_t/P_o = 1 - (v_{fo}G^2/2P_o) \tag{4}$$

Eqn (3) and (4) can be combined to give a transcendental expression for the critical pressure ratio. The critical mass flowrate can then be calculated.

When high-temperature, high-pressure water is suddenly depressurized, it passes from a subcooled to a superheated state. It can reach a pressure (p_n) far below its saturated pressure (p_{sat}) that it flashes into steam explosively. This pressure difference (p_{sat} - p_n) was termed the pressure undershoot by Alamgir and Lienhard [10]. A correlation for the pressure undershoot was devised based on the classical nucleation theory and was found to depend on the initial water temperature and the depressurization rate. Since the correlation can be used to determine the initial conditions in a blowdown, it can thus be used in predicting the two-phase flowrate following a rapid depressurization. The Pressure Undershoot Correlation takes the form:

$$p_{sat} - p_n = 0.252[\sigma^{3/2}\, Tr^{13.73}(1+14\Sigma^{0.8})^{0.5} / [(kT_c)^{0.5}(1-(v_f/v_g)] \tag{5}$$

The depressurization rate, Σ could be written in the Eulerean frame experienced by a particle of fluid flowing in a nozzle [13]:

$$\Sigma = (\partial p/\partial t)_z + v(\partial p/\partial z)_t \tag{6}$$

In the case of steady flow in the nozzle, only the convective term is important and Eqn (6) can be simplified to [13]:

$$\Sigma = (m_t^3/\rho^2 A^4)(dA/dz) \tag{7}$$

To calculate the critical flowrate, the throat pressure (p_n) was obtained from Eqn (5) assuming maximum depressurization rate, Σ. Σ was maximum when (dA/dz) in Eqn (7) was maximized. This required that the detailed geometry of the nozzle be known.

Experimental Comparisons

The test results on critical discharge were compared with critical flowrates calculated using the three simple models described above. This is shown in Figure 4. Figure 4 plotted the critical discharge of initially subcooled water against the fluid enthalpy. Results at vessel pressures of 1.0 and 3.0 MPa were given. It can be seen that the Homogeneous Equilibrium Model provided the worst overall predictions. It under-predicted the critical mass fluxes significantly, especially at low subcoolings. This is to be expected because no non-equilibrium effects were considered in the HEM. The Pressure Overshoot Correlation, on the other hand, over-predicted the critical mass fluxes in general. However, it did very well in predicting the test results for the lower pressure (P_o=1.0 MPa) tests at low subcoolings. The Henry-Fauske Model gave the best overall agreement with the test data. It appears to work best for large subcoolings. At low subcoolings, the model also under-predicted the critical mass fluxes. Figure 5 compared directly the mass fluxes as predicted by the three models with the measured values for all the blowdown tests, including tests with 1.0<P_o<3.0 MPa. This confirms that the Henry-Fauske Model is the most appropriate model to use under the present test conditions.

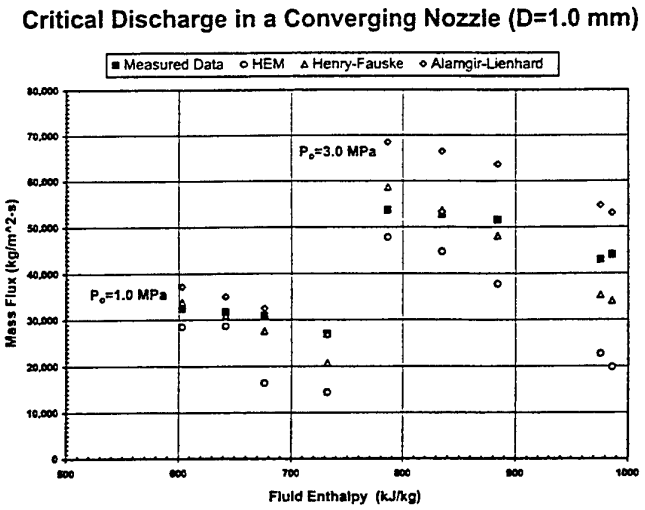


Figure 4: Comparison of experimental results and model predictions

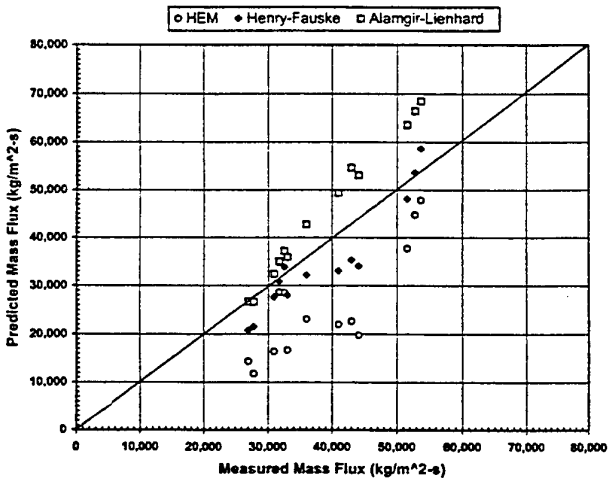


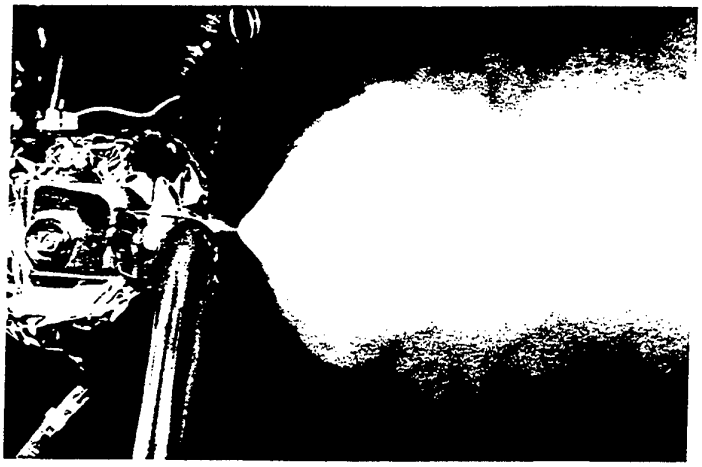
Figure 5: Predicted vs measured mass fluxes - critical discharge in a nozzle

Photographic Study of the Flashing Two-Phase Jet

The flashing two-phase jet was photographed to identify regions in the jet and to measure the major geometric parameters. Two sets of pictures were taken for each test conditions. The first set was obtained with front lighting using a flash and the other set was made with back lighting using an overhead projector lamp. Typical pictures taken with front and back illuminations are shown in Figure 6a and 6b respectively. Front illumination was useful to outline the overall shape of the jet. Back lighting revealed some information on the structures within the jet. Regions of different densities in the jet were shown in Figure 6b. Because of light refraction, the jet shown in Figure 5b appeared to be bigger than that in Figure 6a.

From Figure 6, it can be seen that the jet expanded initially at approximately 50° and then tapered down to a much smaller angle of about 13°. Three regions can be identified: (1) a high density cone; (2) a region of lower density with the same expansion angle; and (3) a high turbulent region with a smaller expansion angle. Using smoke as a tracer, it was found that air entrainment was important in the latter two regions. It should be noted that the regions identified are consistent with the jet geometry shown in Figure 1.

(a) Front Lighting



(b) Back Lighting



Figure 6: Pictures of flashing two-phase jet (P_R=3 MPa; ΔT_{sub}=6^{0}C)

4. CONCLUSIONS

A series of experiment was conducted using a short converging nozzle at reservoir pressures ranging from 1.0 to 3.0 MPa and at different water subcoolings. The discharge flowrates were measured and compared with predictions from different critical discharge models. Three models were described. They are the Homogeneous Equilibrium Model, the Henry-Fauske Model and the Pressure Undershoot Correlation. It was found that the Pressure Undershoot Correlation over-predicted, whereas, the HEM under-predicted the present set of test data. The Henry-Fauske Model, on the other hand, gave the best overall agreement with the test data and worked best for large subcoolings. The two-phase flashing jet from the nozzle was also photographed to study its flashing and dispersion characteristics. Three regions were identified: a high density cone with a large expansion angle which extends only a short distance downstream from the nozzle; a lower density region behind the high density cone which has essentially the same large expansion angle and a dispersion region further downstream with a much smaller expansion angle.

ACKNOWLEDGEMENTS

The experiments were performed in the Thermo-Fluids Laboratory in Ontario Hydro Research Division.

REFERENCES

1. J.M. Healzer and A. Singh, "A Simplified Model for Jet Expansion and Impingement Loads", EPRI Report: NP-4418 (1986).
2 H.J. Richter, "Separated Two-Phase Flow Model: Application to Critical Two-Phase Flow", Int. J. Multiphase Flow, Vol. 9, pp. 511-530 (1983).
3. F. Dobran, "Non-Equilibrium Modeling of Two-Phase Critical Flow in Tubes" ASME J. of Heat Transfer, Vol. 109, pp. 731-738 (1987).
4. C.F. Schwellnus and M. Shoukri, "A Two-Fluid Model for Non-Equilibrium Two-Phase Critical Discharge", Can. J. of Chemical Engineering, Vol. 69, pp. 188-197 (1991).
5. R.E. Henry and H.K. Fauske, "The Two-Phase Critical Flow of One-Component Mixtures in Nozzles, Orifices and Short Tubes", ASME J. Heat Transfer, Vol. 95, pp. 179-187 (1971).
6. P.G. Kroeger, "Application of a Non-Equilibrium Drift Flux Model to Two-Phase Blowdown Experiments", Proc. of the CSNI Specialist Meeting, AECL, Vol. 1, pp. 112-152 (1976).
7. J.W. Stuhmiller, "The Application of Two-Phase Flow Modeling", EPRI Report: NP-349 (1977).
8. M. Reocreux, "Experimental Study of Steam-Water Choked Flow", Proc. of the CSNI Specialist Meeting, AECL, Vol. 2, pp. 637-669 (1976).
9. K.H. Ardron, "A Two-Fluid Model for Critical Vapor-Liquid Flow", Int. J. Multiphase Flow, Vol. 4, pp. 323-337 (1978).
10. Md. Alamgir And J.H. Lienhard, "Correlation of Pressure Undershoot During Hot-Water Depressuization", ASME J. Heat Transfer, Vol. 103, pp. 52-55 (1981).
11. G.B. Wallis, "Critical Two-Phase Flow", Int. J. Multiphase Flow, Vol. 6, pp. 97-112 (1980).
12. E.S. Starkman, V.E. Schrock, K.F. Neusen and D.J. Maneely, "Expansion of a Very Low Quality Two-Phase Fluid Through a Convergent-Divergent Nozzle", ASME J. Basic Engineering, Series D, Vol. 86, pp. 247-256 (1964).
13. N. Abuaf, O.C., Jr. Jones and B.J.C. Wu, "Critical Flashing Flows in Nozzles with Subcooled Inlet Conditions", ASME J. Heat Transfer, Vol. 105, pp. 379-383 (1983).

NOMENCLATURE

A	nozzle flow area
D	nozzle diameter
G	mass flux
h	enthalpy
m	mass flow rate
N	phase change coefficient
p, P	pressure
s	entropy
t	time
T	temperature
v	velocity
x	quality
z	axial coordinate
Σ	depressurization rate
ν	specific volume
ρ	fluid density
σ	surface tension

Subscripts

c	critical
E	thermodynamic equilibrium
f	liquid phase
g	gas phase
n	minimum
o	stagnation or reservoir conditions
r	reduced
R	reservoir
sat	saturation conditions
sub	subcooling
t	nozzle throat
u	upstream

AN INVESTIGATION ON THE BUBBLE AND SLUG FLOW PATTERNS AND ITS TRANSITION FOR GAS/OIL-WATER EMULSIONS

Yushan Luo Tingkuan Chen Jiyong Cai
State Key Laboratory of Multiphase Flow in Power Engineering
Xi'an Jiaotong University, Xi'an, Shaanxi, 710049, China
E-mail: yshluo@xjtu.edu.cn; Fax: (86)-29-2668789

Keywords: gas/oil-water emulsions, flow pattern transition, vertical upward pipe

ABSTRACT. The experimental investigation on flow pattern and its transition for gas/oil-water emulsions in vertical upward pipe has been undertaken. In the test series the input water fraction in oil-water emulsion was varied between 0% (pure oil) and 100% (pure water). The test section was a steel tube with inner diameter of 44mm and length of 1.5m. The pressure conditions for test section were varied between 0.1 MPa and 0.5 MPa, the temperatures were varied from 10 to 40 °C, gas superficial velocity V_{SG} = 0.1 ~26m/s, oil-water emulsion superficial velocity V_{SL} = 0~2.5m/s. The test oil was 46# machine tool oil. In this paper, the flow pattern characteristics of bubble and slug regime at w/o (water in oil) and o/w (oil in water) are described. The phase inversion point between w/o and o/w is obtained through used the Yeh method and the pressure drop of test section. The water fraction at the phase inversion point is 0.56. There are certain relations between flow patterns, frequency and amplitude of pressure drop pulsation. In the experiments a group of data which determine flow pattern by pressure drop pulsation has been obtained for vertical upward pipes. The predictable model for flow pattern transition is established. The predictable model is in good agreement with experimental results.

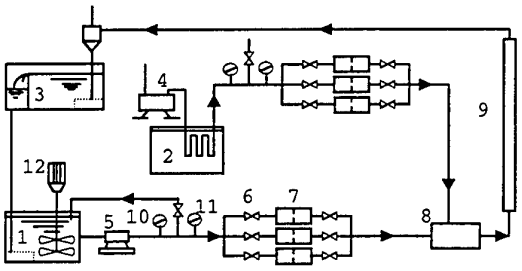
1. INTRODUCTION

When gas, oil and water flow in pipe in general, because of stirring by gas and valve, bends in pipelines the oil and water form emulsion and half emulsion. In this case the superficial viscosity of oil-water mixture changes substantially, and it will greatly affect on the description of oil-water two-phase flow. Besides the oil-water emulsions will form two structures of w/o (water in oil) and o/w (oil in water) with change of water fraction. There are differences on the flow characteristics at w/o and o/w types. So it is important to know the flow characteristics of gas/oil-water emulsions, such as flow pattern and pressure drop. It is often occurs in petroleum industry where oil-gas-water three-phase flow in vertical upward pipe, such as production of crude oil and natural gas in wells and transportation in pipeline. Up to now most studies for oil-gas-water three-phase flow was in which the oil-water was no emulsive. In this paper the flow pattern characteristics and transition of three-phase flow were studied for gas/oil-water emulsions in vertical upward pipe.

2. EXPERIMENTAL SET-UP

The experimental data were obtained in the oil-gas-water three-phase flow test loop of State Key Laboratory of Multiphase Flow in Power Engineering of Xi'an Jiaotong University. The test loop is shown in Fig.1. The oil-water emulsion with certain ration of oil and water was prepared in advance in the storage by using an electrical stirrer and pumped to the loop by a pump. The emulsion was mixed with air coming from the air compressor to form the three-phase mixture. The three-phase mixture flow via the test section and after the test section entered into the separator, the oil-water emulsion was recalculated. The air was vented from the top of the separator. The flowrates of the oil-water emulsion and air were separately measured by orifices. The fluid temperature was measured by thermocouples, the pressure was measured using pressure transducer. All experimental signals were automatically acquired and stored by the computer. Stainless steel pipe with diameter of 51*3.5 mm and length of 1.5 m was used as the test section, 46# machine tool oil, water and air are used as the fluid in test. The experimental conditions were:

Oil-water emulsion superficial velocity V_{SL}:	0~2.5 m/s.		
Pressure p:	0.1~0.5 MPa	Water fraction ε_w:	0.0~1.0
Temperature T:	1 0~40 °C	Air superficial velocity V_{SG}:	0.1~26 m/s



1. oil tank
2. water tank
3. separator
4. air compressor
5. oil pump
6. valve
7. orifice
8. gas-liquid mixer
9. test section
10. thermocouple
11. pressure meter
12. electrical stirrer

Fig. 1. The experimental set-up

3. FLOW PATTERN AND EMULSION STRUCTURE

There are four basic flow patterns for oil-gas-water three-phase flow in vertical upward pipe: bubble, slug, churn and annular flow. Based on the structure of oil-water interface, there are two emulsion structures, they are water-in-oil (w/o) and oil-in-water (o/w). Their characteristics are: in the case of water-in-oil (w/o) the water droplets are dispersed in a continuous oil phase and occurs in lower water fraction; in the case of oil-in-water (o/w) the oil droplets are dispersed in a continuous water phase and occurs in higher water fraction.

In this paper, the water fraction of oil-water emulsion in phase inversion point between o/w and w/o cases was determined by the Yeh method [1] and the change of pressure drop in test section. The emulsion structure was obtained as follows:

(1) w/o: for $\varepsilon_w < 0.56$
(2) o/w: for $\varepsilon_w > 0.56$
(3) w/o: for $\varepsilon_w = 0.56$ at $u<0.9$ m/s
o/w: for $\varepsilon_w = 0.56$ at $u>0.97$ m/s
w/o or o/w: Unstable, for $\varepsilon_w = 0.56$ at $u=0.9\sim0.97$ m/s

When o/w emulsion transfer to w/o, the pressure drop of oil-water emulsion in pipe greatly increased due to increase of the viscosity of oil-water emulsion, as shown in Figure 2. Because of the difference of oil-water interface, the characteristics of w/o type are different than o/w type at both of bubble and slug flow. In bubble flow, because of the superficial viscosity of w/o emulsion is larger than o/w type, so the pressure drop of w/o emulsion is greater than that of o/w type, whether the surface tension between gas bubble and oil-water emulsion in w/o type is greater than that in o/w type.

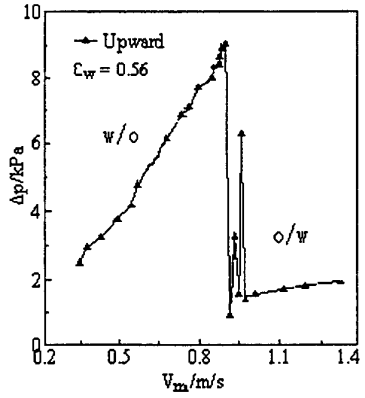


Fig.2. The pressure drop changing at the phase inversion point of oil-water emulsion in vertical upward pipe

In slug flow, the liquid phase which contacting inner wall of pipe is oil in the w/o type and that is water in the o/w type. In the experiments it was observed that liquid film thickness between Taylor gas bubble and inner wall of pipe was different, the thickness at w/o is thicker than that at o/w, the numbers of gas bubble in liquid slug between two Taylor gas bubble at w/o are more than that at o/w.

4. DETERMINING THE FLOW PATTERNS BY PRESSURE DROP PULSATION METHOD

The transition of flow patterns will occur with change of flow velocity and void fraction when gas/oil-water

emulsions flow in pipe, and pressure drop pulsation will change at same time. So there are certain relation between flow patterns and frequency, amplitude of pressure drop pulsation. Pressure drop pulsation oscillogram in the test section may present out different pulsation locus diagram for different flow patterns. Thus pressure drop pulsation method may be used to analysis and determine the flow patterns.

In the flow of gas/oil-water emulsions in vertical upward pipe the various flow patterns present out different pressure drop pulsation. The analysis results from pressure drop pulsation for flow patterns of gas/oil-water emulsions three-phase flow in vertical upward pipe are shown in table 1. According to the frequency f and amplitude ratio R of pressure drop pulsation, flow patterns may be determined.

Table 1. Determining Flow Pattern by Pressure Drop Pulsation

Amplitude ratio R Frequency f (1/s)		Flow pattern		Suitable range on three-phase flow of gas/oil-water emulsions in vertical upward pipe	
				Superficial liquid velocity V_{SL} (m/s)	Superficial air velocity V_{SG} (m/s)
1	24<R<48, f>150	W/O	Annular	$0.01<V_{SL}<2.4$	$V_{SG}>12.7$
	25<R<48, 120<f<150	O/W		$0.01<V_{SL}<2.4$	$V_{SG}>12.4$
2	1<R<1.35	W/O	Slug	$0.01<V_{SL}<1$	$0.07<V_{SG}<1.6$
	1.35<R<2.6	O/W		$0.01<V_{SL}<0.55$	$0.11<V_{SG}<1.1$
3	1<R<1.35, 4<f<7	W/O	Churn	$0.01<V_{SL}<2.4$	$1.6<V_{SG}<12.7$
	1<R<1.35, f<4	O/W		$0.01<V_{SL}<2.4$	$1.1<V_{SG}<12.4$
4	6<R<12	W/O	Bubble	$0.01<V_{SL}<2.4$	$0.01<V_{SG}<0.07$
	R>12	O/W		$0.01<V_{SL}<2.4$	$0.01<V_{SG}<0.37$
Note: When $V_{SL}=1$, $V_{SG}=1$, $\varepsilon_w=0.54$, the amplitude is $V_{standard}$, in the table $R = V_{standard}/V_i$					

5. THE PREDICTING MODEL OF FLOW PATTERNS TRANSITION FROM BUBBLE FLOW TO SLUG FLOW

Through analysis to pressure drop pulsation it is shown that superficial viscosity of oil-water emulsion greatly affected flow pattern transition from bubble flow to slug flow. When flow pattern transition from bubble flow to slug flow occurs the value of void fraction is not same at different water fraction in gas/oil-water emulsions. This means that the transition void fraction is changed with changing superficial viscosity of oil-water emulsion. Then formula of transition void fraction can be given. From the literatures the void fraction of bubble flow is lower than 0.35 [2,3]. So transition void fraction from bubble flow to slug flow may be expressed as follows:

$$\alpha_c = 0.35(\mu_e/\mu_c)^m \tag{1}$$

Based on the experimental results in our test, the transition void fraction from bubble flow to slug flow can be given as follows:

$$\text{At w/o: } \alpha_c = 0.35(\mu_e/\mu_c)^{-0.082} \tag{2}$$

$$\text{At o/w: } \alpha_c = 0.35(\mu_e/\mu_c)^{-0.076} \tag{3}$$

where μ_e and μ_c are the superficial viscosity of oil-water emulsion and continuous phase viscosity at w/o and o/w respectively.

When velocity of oil-water emulsion is lower, the upward velocity V_∞ of gas bubble in liquid phase can be estimated as follows:

$$V_\infty = 1.53\alpha\sqrt{1-\alpha}/V_{SL} \cdot \left[g\sigma(\rho_L-\rho_G)/\rho_L^2\right]^{0.25} \tag{4}$$

The correlation between gas phase velocity V_G in bubble flow and average velocity V_L in oil-water emulsion is expressed as follows:

$$V_G = V_L + V_\infty \tag{5}$$

$$\text{namely, } V_G = V_L + 1.53\alpha\sqrt{1-\alpha}/V_{SL}\cdot\left[g\sigma(\rho_L-\rho_G)/\rho_L^2\right]^{0.25} \tag{6}$$

If the gas phase is an incompressible flow, then continuous equation for bubble flow can be written as follows:

$$V_G\alpha + V_L(1-\alpha) = V_m \tag{7}$$

because of $V_G=V_{SG}/\alpha$ and $V_L=V_{SL}/(1-\alpha)$, so the following equation can be obtained from equations (6) and (7):

$$V_{SG}/V_{SL} = \alpha/(1-\alpha)+1.53\alpha\sqrt{1-\alpha}/V_{SL}\cdot\left[g\sigma(\rho_L-\rho_G)/\rho_L^2\right]^{0.25} \tag{8}$$

Then, replaced of α in equation (8) with transition void fraction in equations (2) and (3) at transition from bubble flow to slug flow, the equation of transitions between bubble flow and slug flow in w/o and o/w type is established:

$$V_{SG}/V_{SL} = \alpha_c/(1-\alpha_c)+1.53\alpha_c\sqrt{1-\alpha_c}/V_{SL}\cdot\left[g\sigma(\rho_L-\rho_G)/\rho_L^2\right]^{0.25} \tag{9}$$

When fluid property is given, equation (9) gives the value of transitions between bubble flow and slug flow in w/o and o/w type can be calculated.

In Figure 3 the pattern transition between bubble flow and slug flow at different water fraction in w/o type is shown. From the figure we can see that under same superficial velocity of oil-water emulsions the pattern transition from bubble flow to slug flow occurs at lower superficial air velocity with increase of water fraction.

In Figure 4 the pattern transition between bubble flow and slug flow at different water fraction in o/w type is shown. Under same superficial velocity of oil-water emulsions the pattern transition from bubble flow to slug flow occurs at higher superficial air velocity with increase of water fraction.

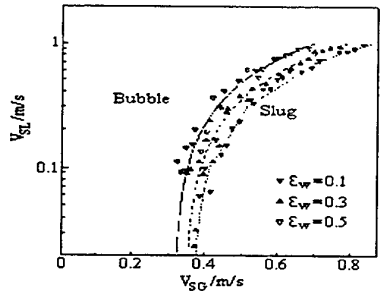


Fig.3. The pattern transition from bubble flow to slug flow at different water fraction in w/o type

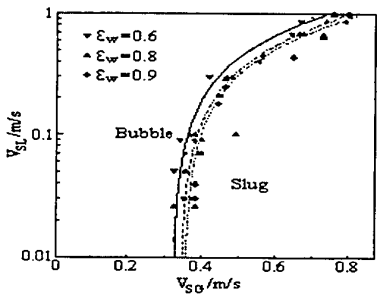


Fig.4. The pattern transition from bubble flow to slug flow at different water fraction on o/w type

In Figures 5 and 6, the compared results by the experimental data with equation (9), Taitel-Dukler's [3], Chen's [4], Kabir & Hasan's [5] predicting models in w/o and o/w types are presented.

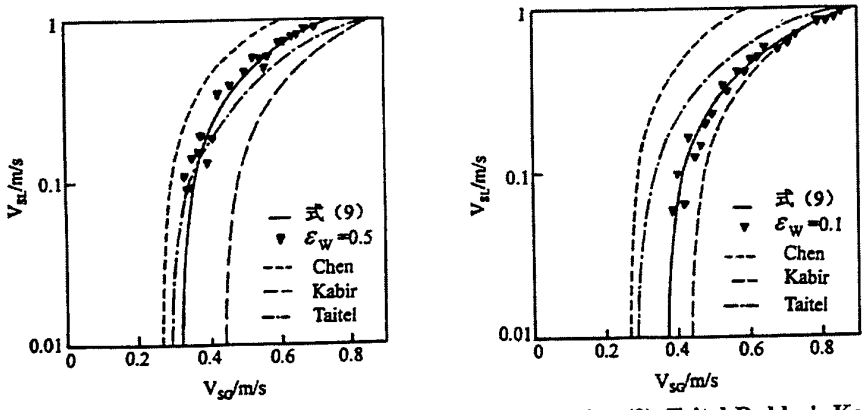


Fig. 5. The compared results by the experimental data with equation (9), Taitel-Dukler's Kabir & Hasan's, Chen's predicting models when flow pattern transition from bubble flow to slug flow in w/o type

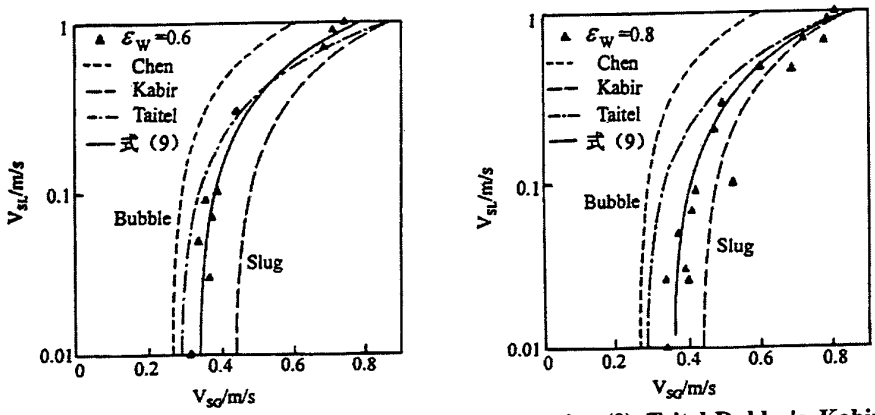


Fig. 6. The compared results by the experimental data with equation (9), Taitel-Dukler's, Kabir & Hasan's, Chen's predicting models when flow pattern transition from bubble flow to slug flow in o/w type

From these figures it is shown that author's predicting model is in good agreement with experimental data; and under lower water fraction in w/o type the experimental data is in better agreement with the Taitel-Dukler's and Kabir & Hasan's predicting models, but there is greater difference with Chen's predicting model; with gradual increase of water fraction, the experimental data is in better agreement with the Chen's predicting model [4], but there is greater difference with Kabir & Hasan's model [5]. In o/w type, with increase of water fraction the experimental data is in better agreement with Taitel-Dukler's and Kabir & Hasan's predicting models[5], but is in poor agreement with Chen's model [4] in over all. The main reason for this difference is that transition void fraction of pattern transition between bubble and slug flow determined by different researcher is not same, at the same time in their tests they didn't consider the effect of the experimental fluid viscosity.

6. CONCLUSIONS

Based on the experimental results, the following conclusions may be obtained:

1. The water fraction in oil-water emulsion has strong effect on the pattern transition from bubble flow to slug flow in air /oil-water emulsions. In w/o type the transition from bubble flow to slug flow is easier to occur with increase of water fraction, namely: superficial air velocity when transition occurred is lower; but in o/w type that is just reverse, the transition is occurred at higher superficial air velocity with increase of water fraction, namely: the transition is more difficult than the w/o type.

2. According to the frequency f and amplitude ratio R of pressure drop pulsation the three-phase flow patterns of gas/oil-water emulsions can be determined by pressure drop pulsation method. In the experiments a group of data is given to determine the flow pattern of gas/oil-water emulsions in vertical upward pipe by pressure drop pulsation.

3. In this paper the predicting model for flow pattern transition from bubble flow to slug flow is established, and effect of superficial viscosity of oil-water emulsion on flow pattern transition is considered in this model. The predicting model is in good agreement with the experimental results and is suitable to gas/oil-water emulsions three-phase flow.

4. When oil-water emulsion flows in vertical upward pipe, the water fraction at phase inversion point between w/o and o/w is 0.56.

REFERENCES

1. G.C. Yeh., AIChE J. v.10, pp.260-265 (1964).
2. P. Griffith & G.B. Wallis, ASME J.Heat Transfer v. 83(3), pp.307-320 (1961).
3. Y. Taiter, D. Barnea & A.E. Dukler, AIChE J. v. 26(3), pp.345-354 (1980).
4. X.Z. Chen, et al., Journal of Xi'an Jiaotong University v. 26(11), pp.53-62 (1992).
5. A.R. Hasan & C.S. Kabir, SPE Production Engineering pp.263-272 (1988).

HYDRODYNAMICS AND DUST SEPARATION EFFICIENCY OF TWO-PHASE ROTATING FLOW

A Khalatov, N Syred
School of Engineering, Cardiff University,
Cardiff, United Kingdom
Email: khalatov@cardiff.ac.uk

I Borisov, S Shevtsov
Institute of Engineering Thermophysics, National Academy of Sciences,
Kiev, Ukraine
Email:borisov@ittfnan.kiev.ua

Keywords: two-phase, rotating flow, vortex chamber, hydrodynamics, dust separation.

ABSTRACT. The broad experimental study of hydrodynamics and the dust separation efficiency in two-phase rotating flow has been carried out by a joint team under the project funded by the Royal Society (UK). It was found that within the rotating two-phase flow the specific interphase surface between air and water reaches up to 1000 m^2/m^3 being two times as much as high than that in traditional equipment based on the concept of two-phase flow. Total pressure losses, pressure drop within rotating two-phase flow were measured and components of pressure drop were assessed. The experimental correlations for the average rotating velocity of air-water flow, average bubble diameter have been obtained as a result of the experimental study. The fine dust separation efficiency within rotating two-phase flow has been studied and the experimental and theoretical correlations for the fractional efficiency has been developed. It was shown that the dust separation efficiency exceeds results available for the other equipment currently used in separation technology in terms of the total clean-up efficiency and the minimal 'cut-off' diameter of separated particles.

1. INTRODUCTION

The idea of the vortex bubble chamber (VBC) is based on creation of a vortex bubble flow (VBF) within stationary vortex chamber. Gas (air) comes into a chamber through few tangential slots while a liquid (water) supplies into a chamber from a top to bottom. Swirled gas flow picks up a water involving it in rotation promoting thereby formation of the rotating gas-liquid flow over the inner chamber's surface. Since the average bubble diameter is inversely proportional to the centrifugal acceleration, the rotating flow has a highly developed interface between gas and liquid and approximately uniform bubble diameter throughout a flow. Due to variations in the centrifugal acceleration the average bubble diameter and interface can be varied in a wide range without loss of a flow stability. The previous studies of VBF include limited data on rotational velocity, interphase surface, void fraction and pressure drop [1-3]. However, some very important parameters of VBF still unknown, while the other ones need to be further clarified. For example, the correlations describing rotational velocity do not take into account effect of a liquid phase, no direct measurements of a bubble diameter; some available data are controversial, no studies towards dust collection within two-phase rotating flow. Some novel scientific results extending available fundamental basis in the field are presented in this study.

2. EXPERIMENTAL RIG

An experimental programme was performed in the experimental rig (Figure 1) the major component of which was the stationary vortex bubble chamber. The swirl generator had a form of a circular ring with an inner diameter D_c = 180 mm and height h_c=29 mm in which 15 tangential slots of 1 mm in width and 14,5 mm in depth were evenly arranged in staggered manner around perimeter on it's top and bottom. The non-dimensional free cross section of slots was S = 2,65%, it's angle of slope to the chamber radius was 70 degrees. The air-water flow thickness was maintained constant by means of limited ring 7 (Figure 2) it's thickness was 10; 15; 20; 25 and 30 mm. The following parameters were measured in the experimental programme: the average rotating velocity of air-water flow; average bubble diameter as a function of the centripetal acceleration; total pressure drop within a chamber, pressure drop in rotating two-phase flow; dust separation efficiency.

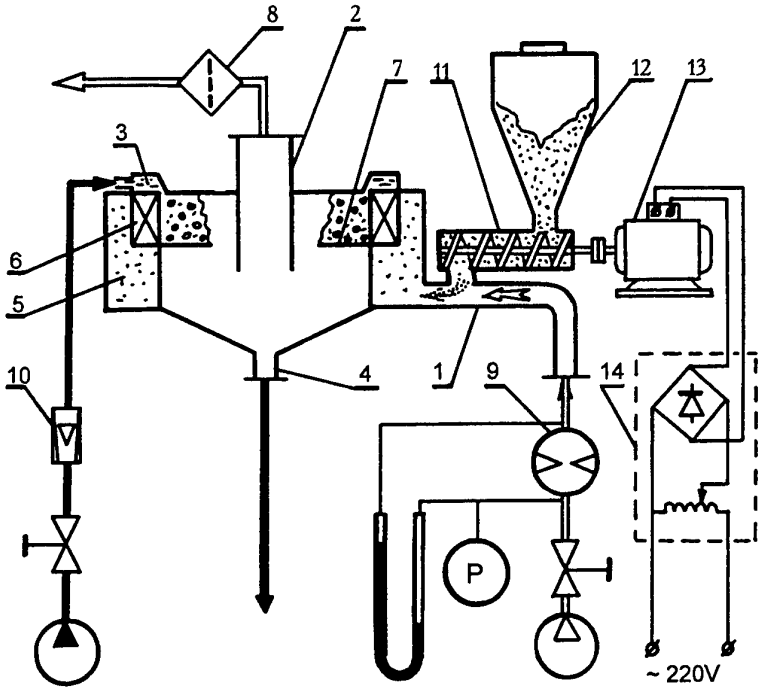


Fig. 1. Scheme of experimental facility
(1 - air inlet. 2 - air outlet. 3 - water inlet. 4 - dust/liquid Suspense outlet. 5 - gas header. 6 - swirl generator. 7 - limited ring. 8 - filter. 9, 10 - flow Mmter. 11 - dcrew geeder. 12 - dust bunker. 13 - electric motor. 14 - rectifier.)

The rotating velocity of air-water flow was measured by means of the anemometer which consists of few blades fixed on a vertical axis and placed into rotating flow. It was shown [3] that the local rotating velocity depends slightly on the radius, therefore only an averaged velocity would be enough to characterise rotating velocity of air-water flow. The average bubble diameter was registered by means of the experimental technique based on registration of electrical signal coming from sensitive element of the hot-wire anemometer. That signal is due to periodic passing of bubbles through the control volume around the sensitive element. The diameter and length of element are 5 micron and 0.8 mm respectively, it's holders were electrically insulated from air-water flow. To study the dust separation efficiency the feed system to supply dust into an air flow was included in the experimental circuit. The dust feed was supplied from the bunker by the screw feeder. Nonseparated dust fraction was accumulated in the cloth filter placed at the outlet. Dust concentration in air was registered by weighting of a dust in the bunker and filter before and after experiment. A dust with hydrophilic properties and the density of 2300 g/m^3 was used in experiments. The fractional dust composition was measured by the laser analyser PRO-7000.

The following range of the basic parameters was studied in the experimental programme: air mass flow rate was 25 - 45 g/s, water mass flow rate was 25 - 75 g/s, inlet air temperature was 15 °C, inlet dust-in-air concentration was from 10 to 20 g/m^3.

3. RESULTS AND DISCUSSION

3.1. Hydrodynamics

The main parameters of the rotating air-water flow are as follows: the rotating velocity of a gas-liquid flow w_L; average bubble diameter d_B; interphase surface between gas and liquid and pressure losses. First two parameters related closely, since the velocity w_L determines the centripetal acceleration $g^* = w_L^2/R_c$ (R_c is vortex chamber radius).

3.1.1. Rotating velocity of VBF. Experimental data show the rotating velocity of two-phase rotating flow (VBF) w_L is a liner function of the air velocity w_0 at the inlet of swirl generator. Figure 2 presents the non-dimensional velocity ($\overline{w} = w_L/w_0$) versus the thickness H_L.of rotating flow. These data locate below results

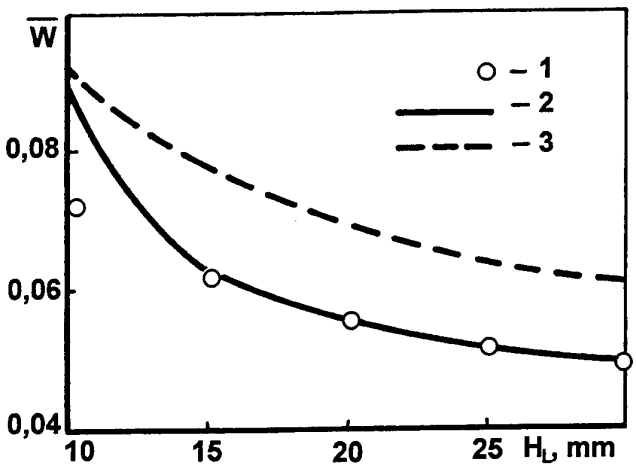


Fig. 2. Nondimensional rotating velocity of VBL
(G_g = 30 g/s; G_g/G_{liq} = 1.0. 1-Experiments of Authors Data. 2-Correlation (1). 3-Data of [3].)

obtained in [3] for the case without liquid overflow (no limited ring). In the processing of experimental data the swirling flow nature was taken into consideration in the equation of the angular momentum conservation. In addition, it was assumed that the liquid film exists at the bottom of VBL, so that the liquid volumetric content in this area is 1.0. The final correlation describing quite well all experimental data has the following form:

$$\overline{w} = \frac{-\xi(1+\beta)+\sqrt{\xi^2(1+\beta)^2+4A(1-\xi^3)}}{2A(1-\xi^3)} \qquad (1)$$

where $\xi = \frac{R_c - H_L}{R_c}$; $\beta = \frac{G_{liq}}{G_g}$; $A = \frac{2\pi R_c \sin\theta \cdot C_f \varepsilon \rho_{liq}/\rho_g}{3\eta Nb}$; θ is the angle between slot direction and chamber radius; ρ_g is the gas density; $\eta = \frac{h_c}{R_c}$; N is number of slots; b is a slot width; G_g and G_{liq} is the gas and liquid flow rate; R_1 is the external radius of VBL; C_f is the friction coefficient (≅0,025 according to [3]); ε is the volume liquid content near the butt ends; ρ_{liq} is the liquid density.

3.1.2 Bubble diameter. Interphase surface. Figure 3 highlights the results of direct measurements of air bubble diameter undertaken in this research and it's comparison with data of [1,4] where the bubble diameter was calculated from the equation (2) and the specific interphase measurements by indirect method:

$$a = \frac{6\varphi}{d_B} \qquad (2)$$

Here a is the specific interphase surface, m^2/m^3. As follows, given in [1] the absolute magnitude of d_B is substantially higher than that obtained in the present research. The results obtained in [1] depend more appreciably from the centripetal acceleration ($d_B \sim \overline{g}^{-0,95}$, where $\overline{g}$ =g*/g is the nondimensional centripetal acceleration) than data of [4] which are closer to the commonly-used assessment $d_B \sim l_c$ where

$l_c = \sqrt{\frac{\sigma}{(\rho_{liq} - \rho_g)g^*}}$ is the capillary constant. The following correlation has been obtained in this research as a result of experimental data processing ($6 < \bar{g} < 13$):

$$d_B = 7{,}85 \cdot 10^{-3} (\bar{g})^{-0.3}, \text{ m} \qquad (3)$$

The specific interphase surface between gas and liquid is the major parameter which determines the efficiency of heat and mass transfer processes. Relation between the interface and average flow velocity for different type of two-phase flow equipment is presented in Figure 4. It is seen the absolute value of interface a obtained in the present study (1000 m^2/m^3) exceeds considerably all traditional types of equipment (400 m^2/m^3) [5] being comparable with a cyclone foam equipment [6].

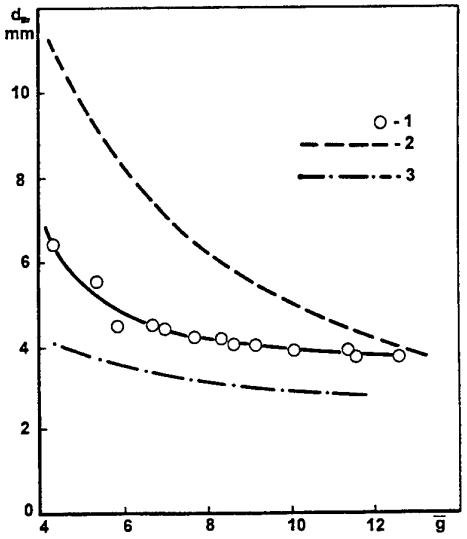


Fig. 3. Average bubble diameter as a function of nondimensional centripetal acceleration
(1-Experiments of Authors. 2; 3 - Data of [1; 4].)

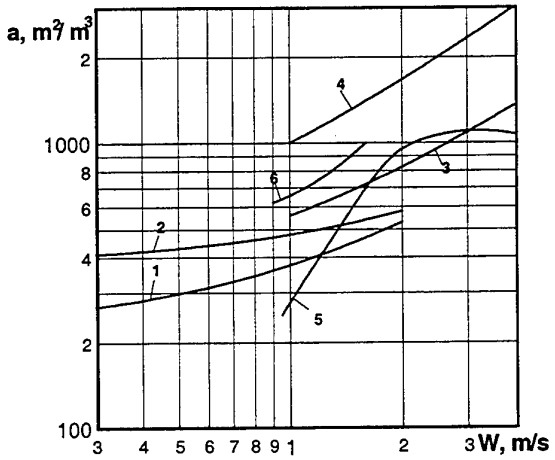


Fig. 4. Specific interphase surface for different types of equipment
(1; 2-sieve and perforated tray [5]. 3; 4-rotating vortex chamber; n=200 and 350 rpm respectively [1]. 5-cyclone foam equipment [6]. 6 - author's results: stationary vortex chamber.)

3.1.3. Pressure drop. The pressure drop within VBC can be presented as a sum of three different components: inlet pressure losses in front of rotating air-water flow including pipe, gas header and swirl generator (1); pressure losses within VBF (2) and outlet pressure drop after VBF (3). Since the air tangential velocity beyond VBF is very small the third term is quite negligible compared to the first and second terms. Figure 5 presents the pressure drop behaviour against the inlet gas mass flow rate W; for comparison the pressure drop in one-phase equipment is also shown in this figure. It is seen the hydraulic losses in VBC gradually increase at the gas flow rate growth; however these losses always remain less than in one-phase equipment. The later is due to the fairly low outlet flow velocity in two-phase flow equipment. The same effect is occurred in a vortex chamber with particles under a high concentration conditions.

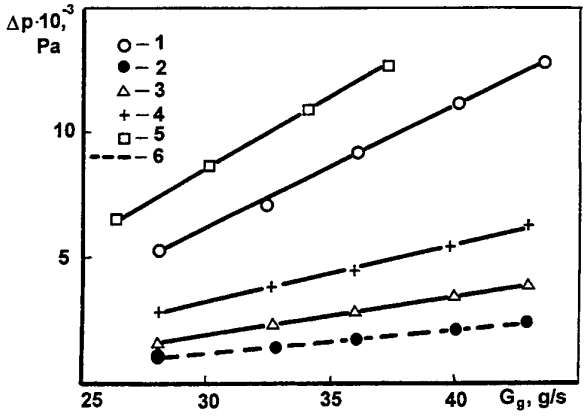


Fig. 5. Pressure drops in VBC; H_L=20 mm
(1-total pressure drop (VBC). 2-radial pressure drop (VBF). 3-kinetic energy losses (VBF). 4-total pressure (VBF). 5-one-phase (gas) vortex chamber. 6-equation (4).)

The pressure drop inside of the vortex bubble flow (VBF) in turn is a sum of the kinetic energy losses within the two-phase rotating flow ($\Delta P_k = \rho_g w_0^2/2$; reductions in the tangential velocity) and radial pressure losses. The value of ΔP_R is a slight function of G_g and H_L; this parameter defines the "work" of in-coming air breakdown, bubble formation and surface friction between bubble and surrounding liquid while it's moving through the gas-liquid flow:

$$\Delta p_R = \frac{6\sigma}{d_B} + \frac{1}{128}\rho_{liq}\left(\frac{w}{\varphi}\right)^2 C_D, \qquad (4)$$

The equation (4) is presented in Figure 5 with the dotted line and it compares with experimental data on pressure drop. As follows from measurements and theory at any two-phase rotating flow thickness the whole inlet kinetic energy is actually lost within vortex bubble flow. This is the reason why the pressure losses in a vortex chamber do not depend on the absolute thickness of VBF.

The main way to reduce the total pressure drop within VBC is to reduce the inlet pressure drop ΔP_{in}. Installation of guide vanes in swirl generator instead tangential slots promotes remarkable reductions in the total pressure rate within VBC (up to 2.5 - 3.0 kPa).

3.2 Dust Separation Efficiency

In experiments on dust separation efficiency the gas-liquid flow thickness was constant (20 mm), it's rotating velocity was 2.6 - 3.2 m/s, the centripetal acceleration was varied from 70 to 110 m/s^2. The average bubble (air) diameter was calculated from the equation (3). The value of d_B was varied from 3.8 to 4.3 mm. Altogether 12 sets of experiments were performed in the experimental programme.

The composition of inlet dust and dust detained in a cloth filter is presented in the Figure 6. The particles having a diameter more than three micron are virtually absent in the dust coming through the gas-liquid flow. A total rate of the cleaning efficiency defines as $\eta = \frac{M_1 - M_2}{M_1}$ reaches 99.5% in the range of operating parameters; here: M_1 is a total amount of dust coming in the gas-liquid flow, M_2 is amount of detained dust.

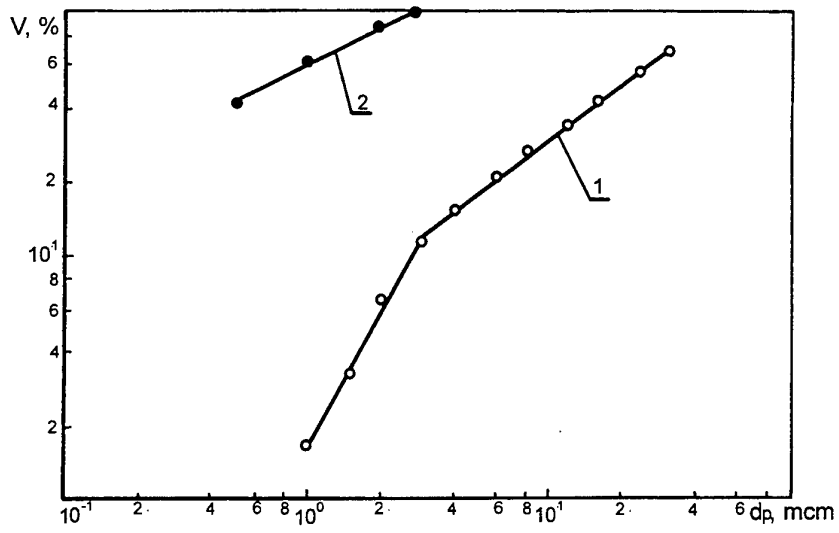


Fig. 6. Dispersed composition of dust (V is the particles distribution according to it's volume)
(1-inlet. 2-dust collected in a cloth filter.)

In experiments the least registered particle diameter was 0.5 micron; the fractional composition of particles having diameter less than 0.5 micron was predicted under assumption of it's normal distribution. The fractional separation efficiency of VBC is presented in the Fig.7 along with data for the other types of dust collectors [7]. As follows from this figure, the dust separation efficiency of VBC exceeds the other types of separation equipment. This important result is explained by a breakage of air flow in the field of centrifugal force and creation of a highly developed interphase surface. Due to this reason the 'cut off' diameter d_{50} within VBA reaches up to 0.2 micron.

Two basic mechanisms of a dust sedimentation were analysed in this research: due to rotational motion of bubble together with the whole gas-liquid flow (1) and due to air circulation inside a bubble (2). In the first case the sedimentation rate of particles can be found from the correlation [8]:

$$v_\omega = \frac{d_p^2 \rho_p}{18\mu_g} \frac{w_L^2}{R_c} = \tau_r \frac{w_L^2}{R_c} \tag{5}$$

where d_p is particles diameter: μ_g is the gas dynamic viscosity; $\tau_r = \frac{d_p^2 \rho_p}{18\mu_g} \frac{w_L^2}{R_c}$ is the relaxation time. The rate of dust concentration was predicted under assumption that sedimentation process occurs in the radial direction only within hemisphere's area $F = \frac{1}{4}\pi d_b^2$.

The rate of the dust concentration is:

$$\frac{dn}{d\tau} = -\frac{3}{2}\frac{v_\omega n}{d_b} \tag{6}$$

where n is a concentration of dust particles of a certain diameter, m^{-3}.

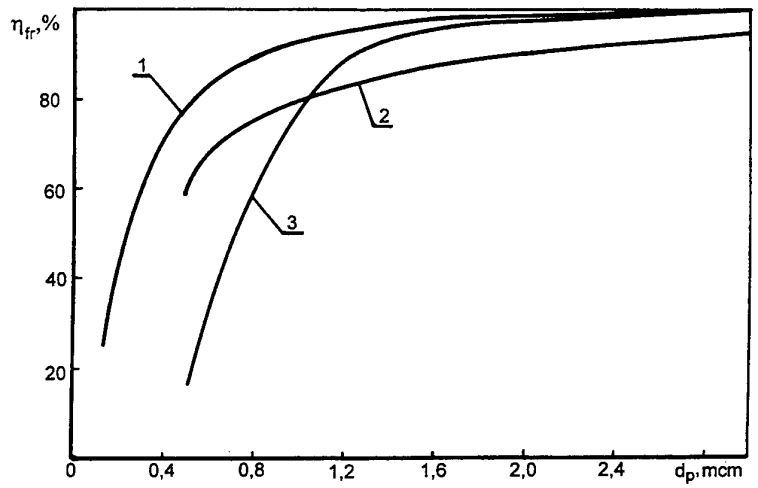


Fig. 7. Comparison of the fractional efficiency of dust collectors: various types of equipment
(1-Vortex Bubble Chamber. 2-Foam Dust Collector [7]: w=2.6 m/s. 3-Inertial Dust Collector [7].)

The sedimentation rate of particles due to circulation mechanism can be found from the correlation [8]:

$$v_V = \frac{9}{2}\frac{w_b \tau_r \sin\theta}{d_b} \tag{7}$$

where θ is an angle between the radius-vector and bubble's motion direction; w_b is the bubble floating velocity.

The rate of the dust concentration in this case is as follows:

$$\frac{dn}{d\tau} = -18 w_b^2 \tau_p \frac{1}{d_b^2} n. \tag{8}$$

To analyse each mechanism of the separation the method of two characteristic time comparison was used: the bubble residence time in a flow $\tau_{res} = \frac{H_L}{w_b}$ and the sedimentation time (2) by means of each (i) mechanism following from the equation:

$$\tau_i = \left| \frac{n}{dn/d\tau} \right| \tag{9}$$

For each mechanism of sedimentation the following correlations have been obtained:

$$\tau_\omega = \frac{2}{3}\frac{d_b}{v_\omega} = \frac{2}{3}\frac{d_b R_c}{\tau_r w_L^2}$$
$$\tau_v = \frac{d_b^2}{18(K w_b)^2 \tau_r} \tag{10}$$

The coefficient K in (10) takes into account the fact that according to the circulation mechanism a motion of particles starts with a 'zero velocity'.

Comparison of the characteristic times shows that $\tau_V << \tau_\omega$ i.e. the circulating mechanism of sedimentation prevails in the rotating air-water flow. Thus, this method allows us to assess various mechanisms of

sedimentation in terms of the separation efficiency and to define processes prevailing within VBF. Based on the assumption of the circulation mechanism of sedimentation the following theoretical correlation describing the fractional efficiency of dust separation has been obtained after integration the equation (8) between $\tau = 0$ and $\tau_{res} = \tau_V$:

$$\eta_f = \frac{n_0 - n_e}{n_0} = 1 - \exp\left(-A \cdot Stk \frac{H_L}{d_b}\right) \qquad (11)$$

Here n_0 and n_e is the initial and final concentration of dust inside of a bubble; $Stk = \tau_r \frac{w_b}{r_b}$ is Stokes number; A = 200. Comparison shows that experimental data are located around the theoretical correlation (11) with scattering ±7% at A = 270. Apparently, some additional peculiarities of the separation process should be taken into account at the initial moment of bubbles formation.

REFERENCES

1. A.P. Burdukov, M.A. Goldshtik, V.I. Kazakov, and T.V. Li , 'Heat and Mass Transfer in Vortex Bubble Layer'. Calculation of Heat and Mass Transfer in Energy-Chemical Processes' (in Russian), Novosibirsk, Inst. of Thermophysics, pp. 37-58 (1981).
2. A.P.Burdukov and V.I. Kazakov, 'Hydrodynamics of Rotating Bubble Layer'. Investigations of Disperse Systems in Energy-Chemical Processes' (in Russian), Novosibirsk, Inst. of Thermophysics, pp. 20-27 (1982).
3. M.A.Goldshtik, T.V.Li, N.P.Khanin, and N.P.Smirnov, 'Concerning Rotating Velocity of Gas-Liquid Flow in a Vortex Chamber'. Transfer Processes in Energy-Chemical Multiphase Systems (in Russian), Novosibirsk, Inst. of Thermophysics, pp. 93-99 (1983).
4. A.P.Burdukov et al, 'Structure of Liquid Flow and Heat-Mass Transfer in Vortex Equipment of Barbotage Type'. Wall-Jet Flows (in Russian), Inst. of Thermophysics, pp.30-32 (1984).
5. V.M.Ramm, *Absorption of Gases* (in Russian), Moscow, Khimia (1966).
6. S.A.Bogatych, *Cyclone Foam Apparatuses* (in Russian), Leningrad, Mashinostroenie (1978).
7. O.S.Balabekov, L.S. Baltabayev, *Gas Cleaning in Chemical Industry. Processes and Apparatuses* (in Russian), Moscow, Khimia (1991).
8. V.N.Uzhov et al. *Cleaning of Industrial Gases from Dust* (in Russian), Moscow, Khimia (1981).

EXPERIMENTAL INVESTIGATIONS ON EVAPORATIVE HEAT TRANSFER OF WATER FILM IN A VERTICAL DUCT WITH COUNTER-CURRENTLY PASSED AIR CONDITION

Y.M.Kang and G.C.Park
Department of Nuclear Engineering
University of Seoul national University
Shilimdong, Kwanakgu, Seoul, Korea 151-742
Email: kangym@nanum.kaeri.re.kr, parkgc@snu.ac.kr, Fax: 82- 02-889-2688

Keywords: evaporation, forced convection, vertical duct, counter-current air flow, PCCS

ABSTRACT. After TMI and Chernobyl accidents, many efforts have been made to enhance the nuclear safety with passive features. Among such passive features, the PCCS(passive containment cooling system) has been suggested by Westinghouse in the AP600 plant. The containment with PCCS is a dual containment, and consists of a stainless steel vessel and a concrete wall. In the gap between these structures, air and water can counter-currently pass and cool the steel surface. In this study, the water cooling test was performed to obtain the evaporative heat transfer coefficients in a vertical duct with one-sided heated plate. Air-steam mixture temperature and velocity, relative humidity and wall heat flux are measured to obtain the evaporative heat transfer. The measured evaporative heat transfer coefficients are compared to an analytical model which use a mass transfer coefficients. From the comparison, the predicted coefficients show good agreement with experimental data, however, some discrepancies exist when the effect of wave motion is not considered. Also, a new correlation for mass transfer coefficient is proposed.

1. INTRODUCTION

In recent years, as a consequence of TMI and Chernobyl accidents, many efforts have been made in the nuclear industry to enhance nuclear safety with passive features that are activated and operated by natural forces during accidents. Among such passive features, the PCCS(Passive Containment Cooling System) has been suggested by Westinghouse in the AP600 next generation nuclear plant to remove heat in the containment by evaporative heat transfer during postulated accidents. The containment in the AP600 plant is a dual containment, and consists of a stainless steel vessel and a concrete wall. In the gap between these two structures, air and water can counter-currently pass and cool the steel surface. Fig. 1 shows the schematic diagram of the PCCS and its cooling mechanism; natural convection of air and evaporation. For an analysis of the PCCS cooling capability, it is important to know the evaporative heat transfer coefficient under counter-current flow conditions in closed ducts. Peters[1] and Ambrosini[2] investigated evaporative heat transfer coefficients under conditions of counter-current, forced convective air flows for water films; Peters performed the integrated cooling tests with air and water for the PCCS, and the local phenomenological studies such as air flow resistance and water distribution on a heated plate. In these experiments, heat transfer rates were measured with condensation rates inside the steel vessel. The water film was formed by the cold water sprayed at the top of the plate. Based on their studies, Peters, et. al. proposed that the Colburn's correlation on mass transfer could be used to predict the evaporative heat transfer. Also, Ambrosini, et al.[2] performed experimental studies on air and water cooling with a 2m long vertical duct. In their study, the evaporation heat flux was obtained from a simple energy balance considering the applied electrical power, the sensible heat transfer used to heat up the water film, the convective heat transfer from the water film surface to bulk air, and the heat loss to the environment. Their experimental results were compared to the semi-empirical correlations obtained by Kreith[3] for a short duct. The number of data points in the Ambrosini, et al. experiments are too few and parametric effects such as evaporative heat and mass transfer for the film flow rate, film temperature, air flow rate and gap size were not sufficiently quantified. In this study, the water cooling test was performed to obtain the evaporative heat transfer coefficients in a vertical duct. In experiments, air-steam mixture temperatures, velocity, relative humidity and wall heat flux are measured at three points according to the vertical plate. And, the local heat transfer coefficients are calculated and averaged through the vertical plate of the facility from the measured data. For the evaluation of the measured heat transfer coefficients and physically understanding of the phenomena, a simple analytical model for the local evaporative heat transfer is also established. The analytical evaporation model is based on the heat and mass transfer analogy. Also the effects of the complex phenomena such as interfacial shear caused by count-current flow, wavy effect of water film are evaluated in the analytical model. From the comparison, the

predicted coefficients show good agreement at low water film temperature even some discrepancies at high water film temperature.

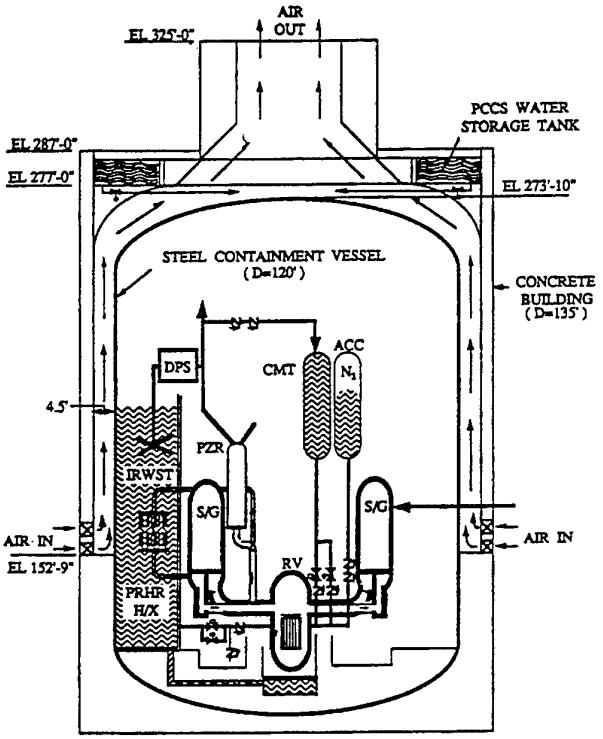


Fig. 1 Schematic diagram of PCCS in AP600 nuclear plant

2. EXPERIMENTAL APPARATUS AND CONDITIONS

The experimental facility used in the presented investigation is shown schematically in Fig. 2. The facility consists of a stainless steel plate, an air baffle, electrical heaters, an air blower system, a liquid film flow rate regulator, and a liquid film preheating system. The test channel consists of a heated plate and an air baffle. The

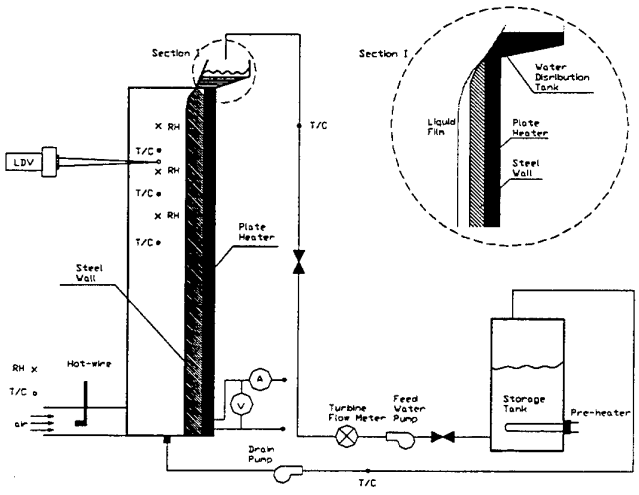


Fig. 2 Schematic diagram of experimental facility and measuring equipment.

stainless steel heated plate is 2m long, 0.5m wide and 10mm thick, and has plate heaters on its back side. The movable air baffle, consisting of a 12mm thick acrilan plate, can be located 5 - 20 cm away from the heated plate surface, where the liquid film flows. The distance between the air baffle and the heated plate surface can be adjusted for different experimental conditions. At the left side of the test channel, 6 visual windows are installed to measure the air-steam mixture velocities by a LDV(Laser Doppler Velocimeter) made by DANTEC. The visual windows are made of a 10mm thick reinforced glass, and were located at uniform distances along the vertical height. At the bottom of the steel plate, a water drain line is installed to capture the downward flowing water. The plate type electrical heaters are attached grouped in 10 heating blocks, with total power of up to 30kw. Each heating block consists of a temperature sensor, a temperature controller, and a thyristor power regulator. The maximum power of each heater is 3kW. Except for the test surface, all other surfaces are insulated with a ceramic fiber, which has a low thermal conductivity. The electrical power is controlled with a thyristor to keep the wall heat flux at a constant value. An air blower is installed to investigate the effect of air mass flow rates on the evaporative heat transfer, and the blower is controlled by a thyristor with a digital voltmeter. The air duct that is connected to the test channel is made with an acrilan plate. Preheaters are used to increase the film temperature of incoming water, in order to achieve sufficient evaporation in the test channel. In the preheating system, the K-type thermocouple is used to measure the temperature of water in the storage tank and this temperature value was transmitted to the temperature controller. The water temperature in the storage tank is controlled within a 1 - fluctuation from the adjusted value. The liquid film flow rate induced in the test channel is measured by a turbine flowmeter, and controlled by valves. The film flow rate in this experiment ranges from a maximum of 0.53kg/m-sec to a minimum film flow rate required for full surface wetting. To measure the temperatures of air-vapor gas mixture, 15 thermocouples are inserted in the test channel at three different locations along the vertical axis. At each vertical location, a total of 5 thermocouples are arranged to cover the whole width of the channel. In order to obtain the evaporative heat transfer coefficients, temperatures of water film at inlet and outlet, and temperatures of air-steam mixture in the test channel, the film flow rate, and the air flow rate were measured by 18 thermocouples, turbine flow meters and LDV, respectively. To reduce the detector errors, the thermocouples and the turbine flow meter are carefully calibrated by an isothermal vessel and a digital electronic balance. All the measured data are stored in personal computers by on-line data acquisition systems.

In order to estimate the evaporative heat transfer rate, the air-steam mixture temperatures, and the relative humidity in the channel, the air inlet velocity and the temperature difference between the film inlet and the outlet of the heated plate were measured. In these experiments, the electrical power was carefully controlled in order to obtain the evaporative heat transfer coefficients. The air mass flow rates and the water inlet temperatures were varied during the experiments. The air velocity ranged up to a maximum value of 8.5 m/sec. This velocity range corresponds to an air Reynolds number value of up to 80,000. The range of air velocity is restricted to prevent significant entrainment of drops from film surface. The gap size was used as the characteristic length in the definition of the Reynolds number. The film flow rate was also changed in the experiments, over the range of 0.3 - 0.53 kg/m-sec, in order to investigate the effect of film Reynolds number on the evaporative heat transfer. In these experiments, the entire heating surface was wetted. The water film temperature in the test section was changed from 35 - 75°C, in order to investigate the effect of water temperature on the evaporative heat transfer. The experimental conditions used in the investigation reported here are summarized in Table 1. Comparisons with other experiments by Westinghouse and Ambrosini, are also indicated in this table.

Table 1. Comparisons of Experimental Conditions Between Presented and Other Studies

	L/D_h	Heat Flux (kW/m^2)	Film Flowrate (kg/m-sec)	Air Velocity (m/sec)	Air Temperature (°C)	Relative Humidity	Water Temperature (°C)
Westinghouse	18	5-28	0.02-0.083	Up to 12	Up to 40	Up to 60	
Ambrosini	11.67	Up to30	0.013-0.17	Up to 10	25-50	45-85	
Presented Study	5.5-23	15-30	Up to 0.5	Up to 8.5	16-25	Up to 80	35-75

3. EXPERIMENTAL PROCEDURES

When the condensation or evaporation heat transfer occurs on a vertical plate, the separated flow model of a liquid film and gas layer can be used to obtain the heat transfer coefficient. The heat transfer model involves two heat transfer resistances. The first resistance represents energy transfer through the liquid film layer, while the second resistance represents through the gas layer. Among these two resistances, the heat resistance of the liquid film layer can be neglected because the film layer is very thin and the conduction heat transfer is large. Thus, the heat transfer through the gas layer is of main interest in condensation or evaporation heat transfer.

The heat transfer through the gas layer consists of three mechanisms; convective heat transfer, radiation heat transfer and evaporative heat transfer. In the case of simultaneous heat and mass transfer, the heat transfer by evaporation is much larger than the combined mechanisms of radiation and convective heat transfer. The evaporative heat transfer coefficient is defined as follows, using the evaporative heat transfer rate and the liquid film interface temperature;

$$h_{evap} = \frac{\dot{q}''_{evap}}{(T_i - T_b)} \tag{1}$$

Thus, in order to obtain the evaporative heat transfer coefficients, the evaporative heat transfer rate, the air-steam mixture temperature, and the film surface temperature in the test channel should be measured.

The evaporative heat transfer rates were obtained from the balance of energy through the entire surface of the test section, just as was done in the investigations of Peters, et. al.[1] and Ambrosini, et. al.[2]. The total evaporative heat transfer rate in test section can be obtained from the applied electrical power, the sensible heat transfer to the liquid film, and the heat loss to the environment, including convection heat transfer from the film surface to the bulk air-steam mixture. Considering these three parameters, the overall evaporative heat transfer coefficient is defined as follows,

$$\dot{q}_{evap} = \dot{q}_t - \dot{q}_s - \dot{q}_{loss} \tag{2}$$

Using the evaporative heat flux in Eq. (2), the averaged evaporative heat transfer coefficient is defined as follows,

$$\bar{h}_{evap} = \frac{\dot{q}_{evap}}{(T_i - T_\infty)A} \tag{3}$$

where, T_i and T_∞ are the liquid film surface temperature and the ambient air temperature, respectively.

In order to obtain the averaged evaporative heat transfer coefficients from Eqs. (2) and (3), the applied electrical power, the film flow rate and its temperature difference between inlet and outlet, and the ambient air temperature are measured. Because the water film is very thin and its surface is not rigid, the film surface temperature cannot be measured. Thus, the film surface temperature in this investigation is assumed to equal the averaged value of film temperatures in the test section.

Table 2. Error Range of Controlled Values and Measured Temperatures

Error Term	Water flow rate (Controlled)	Gas Temperature	Water Temperature	Gas Velocity (Controlled)
Maximum Deviation	0.01 kg/sec	.7°C	1.0°C	0.7m/sec
Ratio of deviations to adjusted values	less than 4%	-	-	less than 10%

In the estimation of $\bar{h}_{evap}$ from Eq. (3), the uncertainty analysis was also performed based on the error of measured and controlled variables. The Table 2 shows the error range of measured and controlled values. The magnitude of error for resultant heat transfer coefficient is less than 20%.

4. EXPERIMENTAL RESULTS

Under conditions of counter-current flow, convective heat and mass transfer occurs in a PCCS channel. The air induced into the bottom of the channel rises by the buoyancy force to the top of the gap but the film flows down by the gravitational force. In these experiments, the evaporative heat transfer coefficients were measured in a PCCS channel, with the variations of air mass flow rate, liquid film flow rates, liquid film temperatures and hydraulic diameters.

Figs. 3 and 4 show the experimental results for averaged evaporative heat transfer coefficient for each gap size. As can be seen from these figures, the heat transfer coefficients increase as the water film temperature and the air mass flow rate increases, but the water flow rate has negligible effect on the evaporative heat transfer. Because the film heat resitance is very small in comparison with that of the gas mixture layer, the film flow rate has little effect on the heat transfer rate. However, if the film flow rate increase very substantially, the heat transfer rate is affected by the surface wavy motion. But the change in the film flow rate is small enough to neglect this effect. As the air velocity increases, so does the mass transfer coefficient, inspite of differences in experimental conditions. As the momentum shear and vapor removal capability increases, the evaporative heat transfer rate increases with increasing air velocity. The correlations of Colburn and Kreith[3] show that the convective mass transfer rate is proportional to the air Reynolds number with a power of 0.8.

In the present study, the measured evaporative heat and mass transfer coefficients are also presented in terms of the Sherwood number, which is defined in terms of measured experimental data as follows;

$$Sh_{evap} = \frac{D_h \dot{m}''_{evap}}{D_v (C_{v,i} - C_{v,\infty})} \tag{4}$$

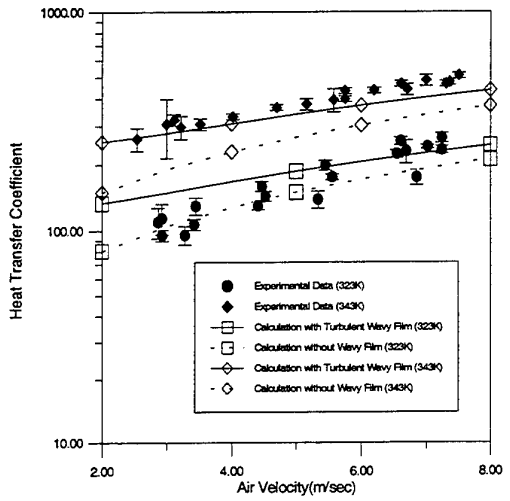


Fig. 3 Comparison of experimental data and computed results (5cm gap).

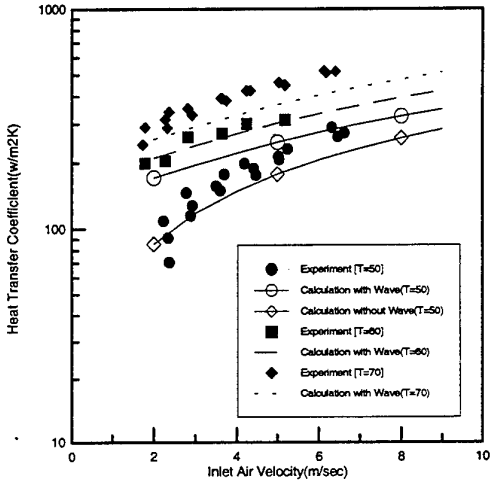


Fig. 4 Comparison of experimental data and computed results (10 cm gap).

Fig. 5 showed the experimental data obtained for different gap sizes. Measured Sherwood numbers increase as the channel width increases. However, as the channel width increases further, the rate of increase becomes small. For flow in the PCCS channel, the thermal boundary layer thickness reaches the baffle, and thus, the duct effects on heat and mass transfer appear. The vapor evaporated from the film surface transfers to the air and

mixes. For the smaller gap width, the amount of vapor that mixes with the air is larger than that in a wide channel. Thus, the vapor concentration difference between the film surface and the bulk gas is larger in a wide channel. However, although the channel width increases, concentration gradient does not change and the evaporative heat transfer rate is not affected as the concentration boundary layer thickness does not reach the baffle. Thus, the increase in the rate of heat transfer coefficient reduces as the channel width increases.

With the experimental data of averaged evaporative heat and mass transfer coefficients, a new correlation was obtained. For the evaporative mass transfer rate, Sherwood number was correlated as a function of air Reynolds number, geometrical ratio, and vapor concentration on the film surface. The constants were determined based on a least-squares best fit, and the final equation is given as follow,

$$Sh = 0.015\left[1 + (D_h / L)^{0.4}\right] Re_g^{0.8} \left(\frac{1}{1 - W_i}\right)^3 \tag{5}$$

where, $Re_g = u_\infty D_h / \nu_g$ and $W_i = P_{sat} / P_t$. The above correlation is valid in the film temperature range of 40°C to 70°C and ratios of hydraulic diameter to channel length of between 0.1 and 0.5, and air Reynolds number range of up to 65,000. The correlated values are agreed well with the experimental data, within an error of 25%, as shown in Fig. 6.

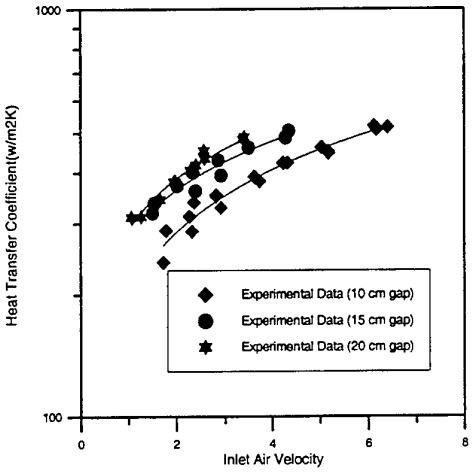


Fig. 5 Comparison of experimental data and calculation results for different gap size experimental data

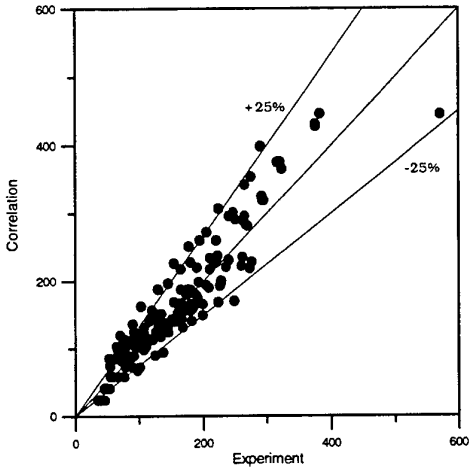


Fig. 6. Comparisons of correlation and (65°C of water film temperature)

5. SIMPLE MODEL OF EVAPORATIVE HEAT TRANSFER

In this study, a simple model of evaporative heat transfer was also developed to evaluate the experimental results. This model does not consider the heat transfer through the liquid film but considers the film flow by a zeroth order turbulent equation model to calculate the interfacial velocity. Also, homogeneous and saturated gas mixture conditions are assumed. For turbulent flow over a vertical plate, the mass transfer rate can be determined by the following correlation;

$$\frac{h_p}{h_g} = \frac{f}{2} Sc_t^{-1} \tag{6}$$

where, $f/2 = 0.0296 Re_g^{-0.2}$ and $Sc_t = Sc^{-3/2}$.

This model does not include the interfacial shear effect due to counter-current flow and due to wavy effect on the liquid film surface. To account for this factor, McAdams and Zazuli[4] suggested the wave multiplication factors. Thus, the interfacial shear by wave motion should be considered. Considering the increase of shear by wavy motion, the friction coefficients can be rewritten as follow,

$$\tau = \frac{f}{2}\rho u^2 + \tau_{i,w} = \frac{f'}{2}\rho u^2 \tag{7}$$

For the vertical plate, H.C.Kang[5] measured the interfacial shear by wave motion on the liquid film interface for different air flow velocities. In the figure, the increasing of the air velocity and film Re number proportionally increases the interfacial shear by wave motion. In this paper, the effect of wave motion was simply introduced by linear interpolation of the air velocity for simple applications, though the experimental data slightly show nonlinearity. With the mass transfer coefficient calculated from equation (19), the evaporation mass flux is calculated by the multiplication of the vapor partial pressure difference between the water film surface and the bulk vapor as follow,

$$\dot{m}''_{evap} = h_D(\rho_{v,i} - \rho_{v,b}) \tag{8}$$

Subsequently, the evaporation heat transfer coefficient is determined from the definition of heat transfer coefficient.

In Fig. 3, good agreement is obtained between the experimental data and the calculation results that do not include the wave effect at low air inlet velocity. But, the calculation results without wave effect underestimate the experimental data at high air inlet velocity. In Fig. 4, the same trend was observed at 50°C film temperature. However, for higher film temperature, the calculation results without wave effect considerably underestimate the experimental data over the entire range of air inlet velocities, as shown in Fig. 8. Although discrepancy exists between the experimental data and calculations, the trends of the experimental data with respect to the air Reynolds number are essentially similar. These discrepancies are caused by the fact that the magnitude of wave effect increases in air inlet velocity or film temperature increases. However, as the air inlet velocity increases, the wave effect becomes relatively small compared with the increase in convective heat and mass transfer, though it increases in magnitude. The increase in film temperature reduces the viscosity and surface tension of water film and thus, the magnitude of wave effect increases. For the counter-current flow situation, the generation mechanism and the magnitude of waves are related to the film Reynolds number or the Weber number and the gas velocity on the interface.

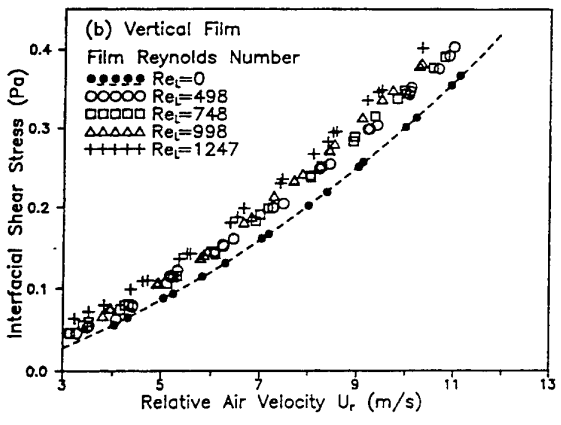


Fig. 7 Interfacial shear stress for vertical films (Ref. [5])

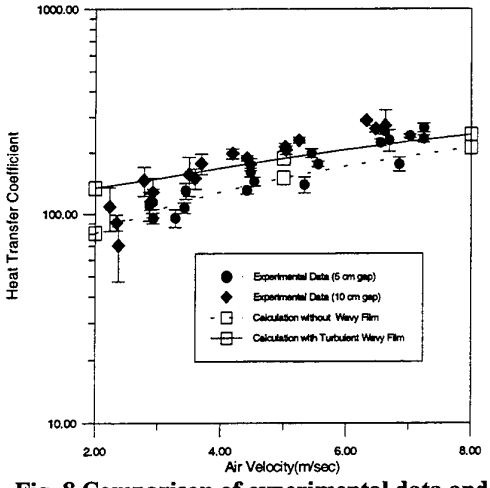


Fig. 8 Comparison of experimental data and calculation results at different gap size

6. CONCLUSIONS

In this study, the water cooling test was performed to obtain the evaporative heat transfer coefficients in a vertical duct with one-sided heated plate. Air-steam mixture temperature and velocity, relative humidity and wall heat flux are measured to obtain the evaporative heat transfer. The measured evaporative heat transfer coefficients are compared to an analytical model which use a mass transfer coefficients. From the comparison, the predicted coefficients show good agreement with experimental data, however, some discrepancies exist when the effect of wave motion is not considered. Also, a new correlation for mass transfer coefficient is proposed.

ACKNOWLEDGMENTS

This study thanks to an organization of Korean Government, Center of Advanced Reactor Research, for their sponsorship.

REFERENCES

1. F.E. Peters, et al., "Advanced PWR Passive Containment Cooling Experimental Program", Proceeding of International Conference on New Trends in Nuclear Thermohydraulics, PISA, 1994.
2. W.Ambrosini, et al., "Heat Transfer from a Plate Cooled by a Water film with Count-current Air Flow", Proceeding of International Conference on New Trends in Nuclear Thermohydraulics, PISA, 1994.
3. F.Kreith, "Principles of Heat Transfer", Harper & Row, 1986.
4. K.R.Chun and R.A.Seban, "Heat Transfer to Evaporating Liquid Films", Journal of Heat Transfer. 1971.
5. H.C.Kang, and M.H.Kim, "The Relation between the Interfacial Shear Stress and the Wave Motion in a Stratified Flow", Int. J. Multiphase Flow, Vol. 19, No.1, 1993.
6. J.P.Holman, "Heat Transfer", 7th edition, Mc.Graw-Hill, 1992.

A VISUAL STUDY OF SLUG BUBBLES IN MINIATURIZED CHANNELS

Q. C. Bi and T. S. Zhao*
Department of Mechanical Engineering
The Hong Kong University of Science and Technology
*Email: metzhao@ust.hk; Fax: (852)-2358-1543

Keywords: bubble behavior, miniaturized channel, stagnant water, drift velocity.

ABSTRACT. This paper deals with the bubble rising behaviors in vertical miniaturized channels closed at the bottom and filled with a stagnant liquid. Our theoretical analysis shows that the drag on a bubble increases significantly as the circular tube diameter decreases and approaches the bubble's diameter. As a result, the up-motion of the gas bubble is slowed down, and ceases completely when the circular tube size is sufficiently small. This bubble rising behaviors is experimentally verified and it is found that the critical tube diameter is 2.9 mm for a given gas nozzle, which equals to the bubble departure diameter in the pool with the same nozzle. More importantly, the results of the experimental investigation show that for the noncircular tubes the elongated bubble always rises upward even though the hydraulic diameter is as small as 0.866 mm. This peculiar phenomenon is of importance for the study of two-phase flow and boiling heat transfer in miniaturized channels.

1. INTRODUCTION

Two-phase flow and boiling heat transfer in a confined space or micro-sized geometry has attracted a great deal of attention in the past few years because of its applications in the cooling of high-density multi-chip modules in supercomputers and other high-heat-flux modular electronics, high-powered X-ray and other diagnostic devices, and high-flux heat exchangers in aerospace systems and cryogenic cooling systems in satellites, and so on. One of the important aspects associated with two-phase flows in microchannels is to study the bubble behaviors. In this work, the motion of slug bubbles formed in miniature channels filled with stagnant liquids is investigated.

Drift-flux model is widely used for the analysis of gas-liquid two-phase flow, primarily because it is applicable to various flow patterns and a wide range of void fractions. According to the theory [1], the velocity of the gas phase in a tube is given by

$$v_g = j_g/\alpha = C_0\, j + V_b \tag{1}$$

where α is the void fraction, C_0 is distribution parameter, and $j=(j_l+j_g)$ represents the mixture volumetric flux with j_l and j_g being the superficial velocities of liquid and gas phase. The last term V_b in Eq. (1) is the so-called drift velocity, which is defined as the velocity of the penetration of a bubble into a stagnant liquid column [2]. Generally, the drift velocity is influenced by various forces exerted on the bubble such as the local interfacial drag, the buoyancy force, and the surface tension.

Previous studies [3-5] have shown that the bubble rising velocity in vertical tubes with large-diameters is proportional to $\sqrt{gd}$, where g is the local gravitational acceleration and d is the tube diameter. It has also been shown that when the tube size becomes sufficiently small, the bubble rising velocity diminishes faster than $\sqrt{d}$, and for tubes of small enough diameter, bubble motion in the stagnant water ceases completely.

It should be noted, however, the above conclusions concerning the drift velocity were drawn based on the experiments in circular tubes. Recently, a new type of ultracompact condenser consisting of a number of parallel, multiport miniaturized non-circular channels with hydraulic diameter of 0.3~2.0 mm has been developed [6]. Although this ultracompact condenser appears to be a promising heat exchanger for a wide variety of engineering applications, there is virtually no research work performed on two-phase flows in these miniaturized non-circular

tubes. For instance, the bubble rising behaviors in miniaturized triangular or rectangular tubes remain unclear. Motivated by this need, we have experimentally investigated the elongated bubble behaviors in miniature noncircular channels. The experiments show that for the triangular and rectangular channels, elongated bubbles always rose upward even though the hydraulic diameter of the tube was as small as 0.866 mm. This unique phenomenon is reported for the first time in this paper.

2. THEORETICAL ANALYSIS

Consider a physical problem illustrated in Fig. 1, where a single air bubble departs from a nozzle ($2R_0$ in diameter) and plunges into a circular tube (D in diameter) filled with stagnant water. First, we consider the case in which the ratio of the tube diameter to the nozzle diameter $D/2R_0$ is sufficiently large such that the tube wall does not influence the departure behavior. Under this situation, before the bubble departure the major forces exerted on the bubble include buoyancy F_b, gravity W, and surface tension between the bubble and the nozzle F_s. Assuming that the bubble is sphere in shape and the diameter is d, these forces can be represented, respectively, by

$$F_b = \rho_l V g = \frac{1}{6}\pi d^3 \rho_l g \tag{2}$$

$$W = \rho_g V g = \frac{1}{6}\pi d^3 \rho_g g \tag{3}$$

$$F_s = 2\pi R_0 \sigma \tag{4}$$

Where σ is the surface tension of water, R_0 is the radius of the gas nozzle, ρ_l and ρ_g represent the densities of water and air, respectively.

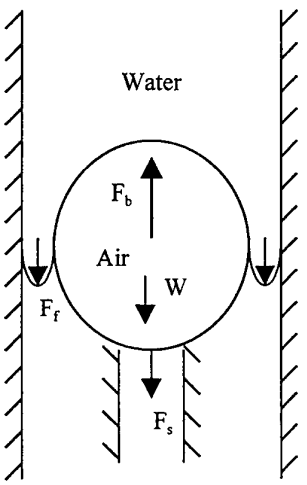


Fig. 1. Forces exerted on a bubble

As the bubble grows, the buoyancy force becomes larger than the sum of the gravity and the surface tension. As a result, the bubble tends to departure from the nozzle. In this case, the balance of these three forces will yield the bubble departure diameter d_b as follows:

$$d_b = \left[\frac{12\sigma \cdot R_o}{g \cdot (\rho_l - \rho_g)}\right]^{1/3} \tag{5}$$

Equation (5) indicates that the bubble departure diameter depends on the nozzle size only for given fluids. As will be shown by the results of the visual study, for the tubes tested in the present work, the tube wall had no influence on the bubble departure diameter. After the departure, the bubble rising velocity is determine by the buoyancy, gravity, and stokes force exerted on the bubble.

We now consider the case in which the tube become smaller and approaches the bubble departure diameter such that the tube wall will affect the bubble behavior inside the tube. As illustrated in Fig. 1, under this situation, the bubble departure and its rising behavior is also influenced by the wall stress F_f, in addition to the aforementioned forces such as buoyancy F_b, gravity W, and surface tension between the bubble and the nozzle F_w. Note that the upward motion of the bubble will cause downward motion of liquid between the bubble and the wall. Based on this observation, the liquid flow may be assumed as an annulus flow between the tube wall and the bubble such that the wall stress force F_f can be obtained from [7]

$$F_f = 2f\frac{G^2}{\rho_l}A = 2\frac{c}{Re}\frac{G^2}{\rho_l}\pi(D-d)L = 2\frac{c\mu}{G(D-d)}\frac{G^2}{\rho_l}\cdot\pi(D-d)L = 2\pi c\mu L\frac{G}{\rho_l} \tag{6}$$

where G is the mass flow rate of the liquid, D and d are diameter of tube and bubble, c is a constant between 16 to 24 varying with the ratio of D to d, and L is the contact length between bubble and liquid. As the bubble rises up at a velocity u_b, the liquid will move downward at a velocity u. Based on the mass balance, the volume evacuated by the bubble will be occupied by the liquid such that

$$\frac{\pi}{4}d^2u_b = \frac{\pi}{4}\left(D^2 - d^2\right)u \tag{7}$$

The liquid flow rate G can readily be obtained from Eq. (7) as

$$G = \rho_l u = \frac{\rho_l u_b}{\left(\frac{D}{d}\right)^2 - 1} \tag{8}$$

Substituting Eq. (8) into (6), we obtain

$$F_f = 2\pi c\mu L \frac{u_b}{\left(\frac{D}{d}\right)^2 - 1} \tag{9}$$

Equation (9) is plotted in Fig. 2, where it is seen that as the tube size becomes smaller, the wall stress increases rapidly. Therefore, we can conclude that the wall stress becomes a predominant force for small tubes and due to this force, the upward motion of the bubble is slowed down and even completely ceased.

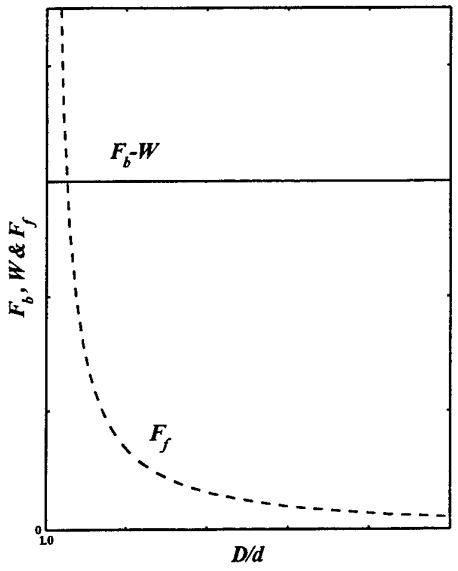


Fig. 2. Forces F_b, W and F_f vary with the characteristic size *D-d*.

3. EXPERIMENTAL APPARATUS

The experiments were carried out in a number of the test sections including eleven circular tubes, three triangular channels, two square channels, and one rectangular channel. The three circular test sections with large diameters (6.35, 4.36, and 3.18 mm) were made from Tygon® tubing, whereas the others having diameters of 2.89, 2.78, 2.70, 2.58, 2.50, 2.32, 2.17, and 1.89 mm were fabricated using Lucite glass block. As shown in Fig. 3a, the three larger circular tubes were tested by inserting them in a slender water container with a rectangular cross section so that the influence of the light refraction from the round surface of the tubes on the results of flow visualization could be minimized. All the noncircular channels were made from Lucite glass. The side lengths of the three triangular channels (shown in Fig. 3b) were 5.0, 2.5, and 1.5 mm, which are equivalent to 2.886, 1.443, and 0.866 mm in hydraulic diameter. The two square channels had side lengths of 1.5 and 1.0 mm (1.5 and 1.0 mm in hydraulic diameter), whereas the rectangular channel had a cross-section of 1.5x0.75 mm^2 (1.0 mm in hydraulic diameters). Air bubbles were injected into the test sections by a gas nozzle (a capillary glass pipette with an inner diameter of 0.556 mm), which was located at the bottom of test sections and connected to a vibrating orifice aerosol generator (TSI Model 3450) through Tygon® tubing. One of the most important features of this aerosol generator (used to inject air into water) is that the air injector can be pushed at an extremely slow speed ranging from $0.1\text{x}10^{-3}$ to $9.9\text{x}10^{-2}$ mm/s. In the present experiment, an injector having a cross-sectional area of $5.5\text{x}10^{2}$ mm^2 was used. In order to minimize the influence of the injector on the bubble departure behaviors, the injecting speed was set at as slow as $0.5\text{x}10^{-2}$ mm/s.

A high-speed motion analyzer (Kodak Ekapro-1000) was employed to visualize the bubble behaviors in the test sections. The bubble behaviors were observed by analyzing the images taken at a speed of 1000 pictures per second for full screen or up to 12000 pictures per second for split screen and replayed at a speed as slow as one picture per second afterwards. In addition, a digital handy video camera (Sony DCR-TRV900E) was also used in the test. A Nikon 105 mm telephoto lens and Nikon bellows PB-6 were used for micro shooting.

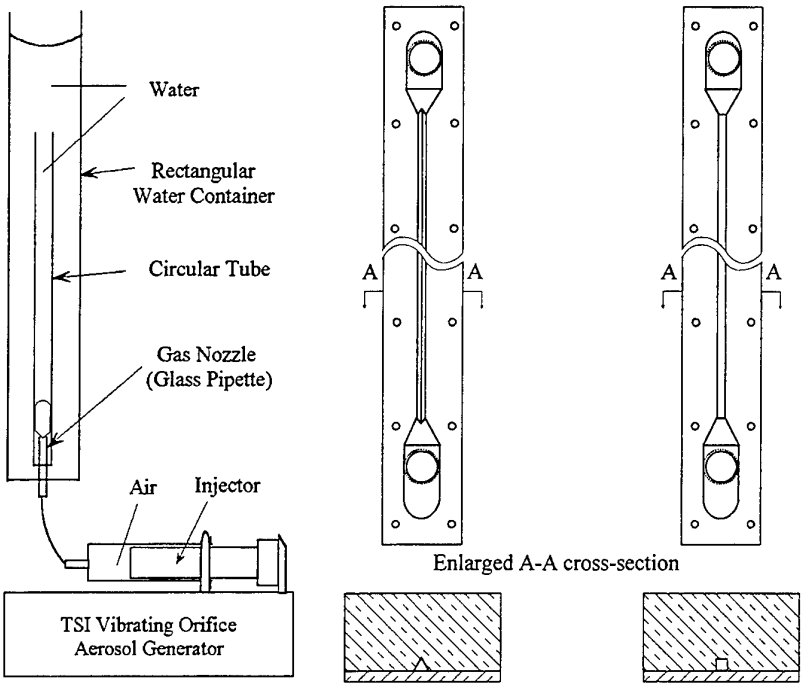


Fig. 3. Schematic diagram of the test sections

4. VISUALIZATION RESULTS AND DISCUSSION

First, we observed the bubble departure characteristics in an open water pool in which air were injected from the nozzle located under water. It was seen from Fig.4a that as the air pressure in the nozzle became sufficiently high, a tiny air bubble appeared (see the second image), taking the shape of a nearly perfect sphere. As seen from the third to the sixth image, once formed, the air bubble grew up and was elongated in the vertical direction due to the effect of the buoyancy force. As the size of the bubble became large enough, the neck linking the bubble to the nozzle became extremely thin. Immediately following this instant, the bubble departed from the nozzle and rose up. As indicated in the seventh image of Fig. 4a, at the instant of bubble departure, its diameter was 2.67 mm, which was measured along the horizontal direction (departure diameter is 2.84 mm, which is the volume-equivalent sphere diameter). The bubble horizontal diameter was increased to 2.73, 2.99 and 3.17 mm afterwards because of its deformation. Empirically, the following equation can predict the departure diameter of a bubble in an open water pool when gas is injected through an orifice with more accuracy than Eq. (5) [8].

$$d_b = 2\left[\frac{\sigma \cdot R_o}{g \cdot (\rho_l - \rho_g)}\right]^{1/3} \tag{10}$$

Based on Eq. (10), the bubble departure diameter is 2.9 mm under the condition of 25 °C and 1 bar. Apparently, this value is in reasonable agreement with the present experimental data (d_b=2.84 mm).

We now present the results of the visual study on the bubble behaviors in the circular tubes closed at the bottom. Figure 4b shows the bubble behaviors in the tube of d=3.18 mm. It is seen that at the instant of bubble departure (the fifth image in Fig. 4b) the bubble horizontal diameter was 2.70 mm (the volume-equivalent sphere diameter d_b=2.78 mm), which is rather close to the value predicated by Eq. (10) for the case of the open

water pool discussed above, implying the tube wall having no effect on the bubble departure diameter. This is because at the instant of bubble departure the smaller bubble was not relatively far away the large-diameter tube wall and its departure was mainly influenced by the buoyancy force and the adhesive force between the bubble and the nozzle. However, it was observed that once bubble departed from the nozzle, the tube wall had influence on the bubble behavior, reflected by the slower rising velocity as compared with the case of the open pool, even though the bubble kept rising in the tube. The experimental results for the large-diameter tubes (d=6.35 and 4.36 mm) also indicate that the bubble departure diameter in the tubes was not affected by the tube wall, but the rising velocities in the large-diameter tubes became higher as compared with the tube of d=3.18 mm.

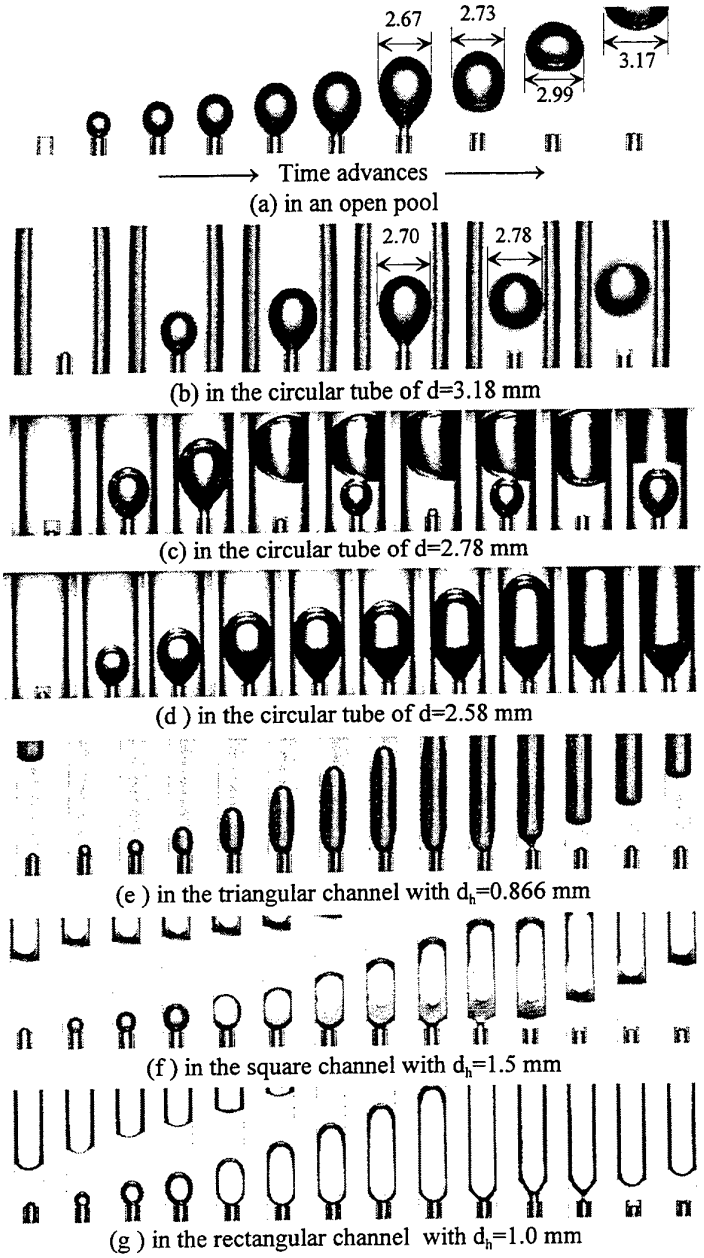


Fig. 4. The images of the bubble behaviors as time advanced.

However, as the diameter of the tube became smaller, the air bubble in the tube behaved differently. First of all, the drift velocity was found to become smaller with the decrease of the tube diameters. It was further observed that the up-motion of gas slugs ceased completely when the diameter of the circular tubes was reduced to a value less than the bubble departure diameter predicted by Eq. (10), i.e.: d_b=2.9 mm. In the tubes with diameters d=2.89 mm and d=2.78 mm, the gas plug formed and this can be evident from the consecutive snapshots of the bubble behaviors in the tube of d=2.78 mm presented in Fig. 4c. As seen from the figure, bubbles usually departed from the nozzle and rose up in the tube with the critical diameter. However, since the departed bubble was deformed during its rising along a spiral path, it adhered to the tube wall at a certain elevation due to relatively large surface tension for a small-diameter tube. The bubble adhered to the tube wall grew up due to the collision and coalesce with the subsequent departed bubbles. As a result, a gas plug formed within the tube. Since the gas plug separated the liquid column in the tube and the liquid phase became discontinuous, the buoyancy force played no role in assisting the air plug rising and its motion ceased completely, meaning that the drift velocity was zero.

When the tube diameter was smaller than 2.78 mm, it was found that the bubble never departed from the nozzle. Typical situations are shown in Fig. 4d for the tube of d=2.58 mm. The second to the fourth images in Fig. 4d indicate that the initially air bubble grew up by pushing the surrounding water. The further bubble growth was restricted by the tube wall (see the fifth image of Fig. 4d). The subsequent addition of air caused the growth of the gas slug in the vertical direction only. As a result, a gas plug formed (see the last image of Fig. 4d). As mentioned earlier, once a gas plug formed, the liquid column became discontinuous and the buoyancy force vanished. Thus the gas plug never departed from the nozzle and rose in the tube. Similar situations were observed for the circular tubes with diameter less than 2.58 mm.

Next, we turn our attention to Fig. 4e, where the gas bubble behaviors in a vertical capillary triangular channels (d_h=0.866 mm) closed at the bottom are presented. Continuous scan from the second to the ninth images presented in Fig. 4e shows that bubble growth led to the formation of a gas slug. This is rather similar to the situation presented in Fig. 4d. However, it is clearly seen from the remaining images (starting from the 10^{th}) in Fig. 4e that this gas slug rose up when it became large enough. The recorded movies show that this translation of the gas slugs within the triangular channel was periodic. The peculiar behavior can be explained as follows. For triangular channels, the liquid phase is always occupied the channel corners owing to the capillary force or the Gregorig effect [9], implying that the liquid phase can be maintained to be continuous although the gas phase occupies the majority of the cross section of the channel. Thus, the buoyancy force always exists and it becomes stronger with the growth of the gas slug. Consequently, the up-motion of the elongated bubble in miniature triangular can be maintained, i.e., the drift velocity is not zero for a miniature triangular channel. The bubble behaviors for the other three miniature triangular channels were generally similar to the scenario displayed in Fig. 4e. It was found, however, that as the channels size was reduced, the gas slugs in the triangular channels became longer and the rising velocity became smaller.

The bubble behaviors in the miniature square and rectangular channels are presented in Figs. 4f and 4g. It is seen that the scenario of the bubble behaviors in these miniature channels are generally similar to those in the miniature triangular channel, i.e., the drift velocity is not zero even though the elongated bubble seems larger than in the triangular channel.

5. CONCLUDING REMARKS

The bubble behaviors in vertical miniature circular and noncircular (triangular, square and rectangular) tubes closed at the bottom and filled with stagnant water have been investigated both theoretically and experimentally. The theoretical analysis shows that the drag on a bubble increases significantly as the circular tube diameter decreases and approaches the bubble's diameter. As a result, the up-motion of the gas bubble is slowed down, and ceases completely when the circular tube size is sufficiently small.

The experimental results show that for large circular tubes (d>2.9 mm), bubbles rose up periodically. As the diameter of the circular tubes became smaller, the up-motion of the gas slugs was slowed down, and ceased

completely when the tube size was sufficiently reduced (d<2.9 mm). For the miniature triangular channels, however, it is found that the gas slug always rose upward even though the hydraulic diameter was as small as 0.866 mm. Similarly, it has been found that the drift velocity in the other two kinds of polygonal (square and rectangular) channels is not zero. One of the most important implications of the unusual behavior is that when a polygonal-cross-sectional channel and a circular tube are filled with a stagnant liquid and subjected to a heating load, the critical heat flux for the former one will be higher than that for the latter one. This is simply because the generated bubble in the polygonal channel can be automatically move up due to the existence of the buoyancy force. However, for the miniature circular tube, the growth of the bubbles generated in the tube would cause the liquid phase to be discontinuous and as a result, the buoyancy force vanishes, leading to partial dryout within the channel.

ACKNOWLEDGEMENT

Support of this work by Hong Kong Research Grant Council Grant (No. HKUST6045/97E) is gratefully acknowledged.

REFERENCES

1. G. B. Wallis, *One dimensional two-phase flow*, McGraw-Hill (1969).
2. T. B. Benjamin, Gravity currents and related phenomena, Journal of Fluid Mechanics, vol. 31, part 2, pp. 209-248 (1968).
3. E. E. Zukoski, Influence of viscosity, surface tension, and inclination angle on motion of long bubbles in closed tubes, J. Fluid M Journal of Fluid Mechanics, vol. 25, part 4, pp. 821-837 (1966).
4. K. W. Tung and J. Y. Parlange, Note on the motion of long bubbles in closed tube-influence of surface tension, Acta Mechanica, vol. 24, pp. 313-317 (1976).
5. Y. Kataoka, H. Suzuki and M. Murase, Drift-flux parameters for upward gas flow in stagnant liquid, Journal of Nuclear Science & Technology, vol. 24, pp. 580-586 (1987).
6. Leon A. Guntly and Norman F. Costello, Condenser with small hydraulic diameter flow path, *US Patent* 4998580, March 12 (1991).
7. W. M. Kays, and M. E. Crawford, *Convective Heat and Mass Transfer*, McGraw-Hill (1980).
8. S. S. Kutateladze and M. A. Styrikovich, Hydraulics of gas-liquid systems, Wright Field Trans. F-TS-9814/V (1958).
9. V. P. Carey, *Liquid-vapor phase-change phenomena*, Hemisphere (1992).

FLOW PATTERN OF PURE REFRIGERANT HFC134a EVAPORATING IN A HORIZONTAL CAPILLARY TUBE

Ken Kuwahara, Shigeru Koyama, Jian Yu
Institute of Advanced Material Study
Kyushu University
Email: kenk@cm.kyushu-u.ac.jp; Fax:(81)-92583-7833
Email: koyama@cm.kyushu-u.ac.jp; Fax:(81)-92583-7833
Email: jianyu@cm.kyushu-u.ac.jp; Fax:(81)-92583-7833

Choyu Watanabe, Noburo Osa
Electrotechnology Applications R & D Center
Chubu Electric Power CO., INC.
Email: twatanab@rdbgw.rd.chuden.co.jp; Fax:(81)-52624-9234
Email: osa@rdbgw.rd.chuden.co.jp; Fax:(81)-52624-9234

Keywords: capillary tube, evaporating, flow pattern, experiment

ABSTRACT. In the present study, the characteristics of flow pattern are investigated experimentally for evaporation of pure refrigerant HFC134a in a capillary tube of 1.2mm I.D. The capillary tube consists of a heating-copper tube section and a glass-tube section, which is located at the right after the outlet of the heating section. The flow pattern is observed through the glass tube section in the ranges of mass velocity of G=80~1260 kg/(m^2 s) and vapor quality of x=0.008~0.975 at a constant pressure of 920 kPa. The flow patterns observed are the bubble, the plug, the slug, the wavy-annular and the annular flow. These flow patterns are typical for a relatively large diameter tube used as the heat transfer tube in commercial refrigeration and air-conditioning systems. However the transition points between each flow pattern are different from the modified Baker map and the Taitel-Dukler map, which are proposed for a relatively large diameter.

1. INTRODUCTION

Environmental or energy problems are becoming serious caused by too much economical and social activities, for example, increasing global energy consumption, climate change, acid rain and destruction of ozone layer. From this point of view, the use of new refrigerants harmless to environment and heightening the performance will be necessary in the refrigerator and air-conditioning fields. And so, decreasing diameter of heat transfer tube or multi-pass tube, which hydraulic diameter is of about 1mm, are trying to improve the performance of heat exchanger in industry.

Large amount of studies about heat transfer or flow visualization in a capillary tube are carried out for water-air system, and those are mainly focused on critical heat flux or void fraction and flow observation. Some of those are about heat transfer or two phase flow observation on a hydrated fluorocarbons. Wambsganss et. al.[1] carried out experiments about boiling heat transfer of R113 in a horizontal tube of 2.92mm I.D. Fukano et. al. [2] carried out experiments about pressure drop and flow observation in a horizontal tube, 1.0, 2.4 and 4.9mm in inside diameter, and proposed a correlation of Lockhart-Martinelli's parameter in small diameter tubes. Aoki et. al.[3,4] carried out experiments about boiling heat transfer of R134a and flow observation in a horizontal tube, 1.0 and 2.0mm in inside diameter. Heat transfer characteristics and flow pattern, however, are not clarified caused by instability of two phase flow in a small diameter channel and difficulty of measurement of heat transfer rate.

In this paper, flow observation of pure refrigerant HFC134a evaporating in the horizontal capillary tube of 1.2mm I.D. is carried out as a first step of clarifying phase change heat transfer process in a small diameter channel.

2. EXPERIMENTAL APPARATUS AND MEASUREMENT

Experimental Apparatus

Figure 1 shows the schematic view of test loop. The refrigerant liquid discharged from a gear pump (1) flows

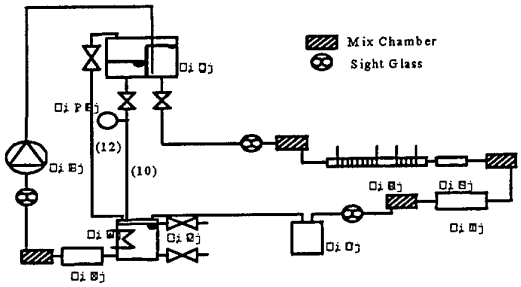
into a header tank (2) eliminating for pulsatory motion. In the header tank, refrigerant head is a kept constant and branches into test and overflow loops. In the test loop, the refrigerant controlled the flow rate flows into a evaporator (3) through an inlet mixing chamber and a glass tube for observation which has almost the same inner diameter as the evaporator; in the evaporator the refrigerant is heated and vapor quality at the outlet of evaporator is controlled. Then, the flow pattern is observed in the glass tube. And then, the refrigerant flows into a condenser (5) through an outlet mixing chamber. The refrigerant condensed in the condenser is returned to the pump through a mass flow meter (6), a liquid receiver (7) and a sub-cooler (9). Vapor spaces of the header tank and the liquid receiver are joined by pressure equalizing tube, then the refrigerant flows due to head difference. Table 1 shows the specifications of the heat transfer tube for the evaporator and the Pyrex glass tube for flow observation.

Table 1. Specification of Capillary Tubes

	Material	I.D. [mm]	O.D. [mm]
Tube for evaporator	Oxygen free copper	1.20	1.99
Tube for Visualizing	Pyrex glass	1.20	7.00

Table 2. Experimental Range

Mass velocity G (kg/m^{2}s)	Vapor quality x (-)	Pressure P (kPa)
80	0.119~0.975	920
180	0.042~0.835	
290	0.038~0.814	
430	0.015~0.781	
1060	0.008~0.170	
1260	0.010~0.103	



(1) Pump
(2) Header Tank
(3) Evaporator
(4) Glass Tube
(5) Condenser
(6) Mass Flow Meter
(7) Liquid Receiver
*(3)+(4) Capillary Part
(8) Heater
(9) Sub-Cooler
(10) Bypass
(11) Pressure Equalizing Tube
(12) Pressure Guage

Figure 1. Schematic view of experimental apparatus

Measurement

Table 2 shows experimental ranges. Experiments were carried out about several vapor qualities in each mass velocity. Flow pattern is recorded by a high speed digital video camera (shutter speed: 1/12000, number of frame : 1000 frames/s). Refrigerant temperatures are measured by K-type thermocouples at the mixing chambers located at the inlet of evaporator and the outlet of glass tube (inlet and outlet of capillary part). Absolute pressure at the inlet of capillary part and pressure drop between inlet and outlet of capillary part are measured by an absolute pressure transducer and a differential-pressure transducer, respectively. The mass flow rate is measured by the mass flow meter at the outlet of condenser.

Experimental data were gotten three times and averaged when the system is steady state. Whether the state is steady or not is judged from mean deviation of temperature, pressure and flow rate. If those values are within the following values, the state is judged to be steady and the measurement is started; deviation of ΔP (pressure drop of capillary part) is within±0.1[kPa], P_{in} (absolute pressure at the inlet of evaporator) is within ±0.5[kPa], W (refrigerant mass flow rate) is within ±0.03[kg/h], T_{in} (refrigerant temperature at the inlet of evaporator) is within ±0.01[K] and T_{out} (refrigerant temperature at the outlet of evaporator) is within ±0.01 [K].

3. CALCULATION PROCEDURE OF REFRIGERANT PRESSURE AND QUALITY AT THE INLET OF GLASS TUBE

In this study, for calculating vapor quality at the inlet of glass tube for visualization, pressure distribution along the flow direction has to be estimated from measured pressure and temperature at the inlet and the outlet of capillary part and heat transfer rate. Because measuring points of temperature and pressure are only located at those points. Then, vapor quality and pressure distributions are estimated by using calculation model as shown in Fig. 2.

Pressure drop of liquid single-phase flow region from the inlet of capillary part to starting point of evaporation is mainly caused by friction in the capillary tube. Then, this pressure drop is calculated by the following equation.

$$\Delta P_L = 4f \frac{\Delta z_{ent}}{d} \frac{G^2}{2\rho_L} \tag{1}$$

Where ΔP_L is the pressure drop of liquid single-phase flow [Pa], Δz_{ent} is the distance from the inlet of capillary part to starting point of vaporization [m], d is the inner diameter of the test tube [m], ρ_L is the density of HFC134a [kg/m^3] and f is the friction factor [--]. In the case of laminar flow, f =16/Re. In the case of turbulent flow, f value is calculated by the following equation from the experimental result shown in Fig. 3.

$$f = \frac{0.068}{Re^{0.2}} \tag{2}$$

In this case, f is higher than usual. This reason is caused by measurement error of inner diameter of the tube.

Frictional pressure drop gradient of two-phase flow region, $(dP/dz)_F$, is calculated by the following equation.

$$\left(\frac{dP}{dz}\right)_F = \left(\frac{dP}{dz}\right)_L \Phi_L^2 \tag{3}$$

where

$$\left(\frac{dP}{dz}\right)_L = \frac{2f_L[G(1-x)]^2}{d\rho_L} \tag{4}$$

ϕ_L is Lockhart-Martinelli's parameter calculated by correlation of Fukano et. al.[5] proposed for two phase flow in a horizontal capillary tube as shown in Tables 3 and 4. In those tables, name of region, for example (VVI) or (VTI), denotes the following states of flow. First character denotes laminar or turbulent flow of superficial liquid flow, second character denotes laminar or turbulent flow of liquid slug in two-phase flow and third character denotes intermittent or continuous flow. And, "V" denotes laminar flow, "T" denotes turbulent flow, "I" denotes intermittent flow and "N" denotes continuous flow.

Refrigerant state at the inlet of evaporator is sub-cooled in this case. And so, refrigerant specific enthalpy at the inlet of evaporator, h_{LEin}, is calculated from measured temperature and pressure. From the inlet of the evaporator to the starting point of evaporation, assuming distance between those points, Δz_{ent}, the pressure at the starting point is calculated by using eq.(1). By Substituting calculated pressure for an equation of state, saturation specific enthalpy at the starting point of evaporation, h_{Lsat}, will be obtained. Above calculation process will be

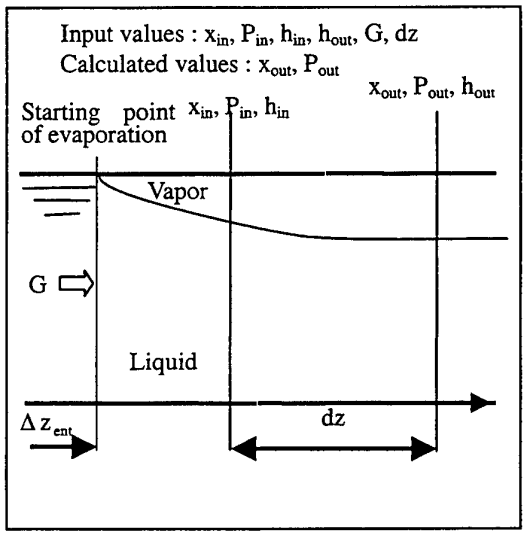


Fig. 2. Calculation model

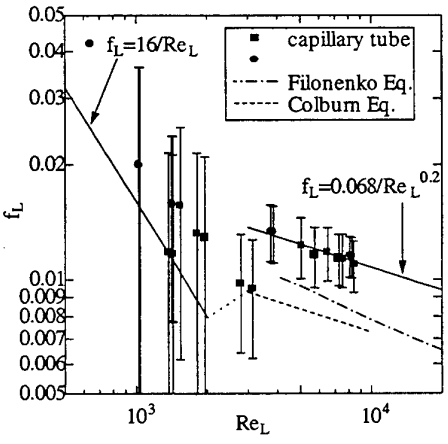


Fig. 3. Friction factor

continued as Δz_{ent} will be modified until measured heat transfer rate of this region, Q_{ent}, will coincide with calculated heat transfer rate of this region, $(h_{Lsat} - h_{LEin})A \cdot G$. Q_{ent} is calculated by the following equation.

$$Q_{ent} = I_h \times E_h \times \frac{\Delta z_{ent}}{L} \quad (5)$$

where, I_h is electric current [A] throw into the heater, E_h is voltage [V] between both end of the heater and L is a heating length [m].

In the two phase region, assuming vapor quality at the outlet of calculating sub-section, x_{out}, the pressure is calculated by substituting x_{out} for an equation as shown in Tables 3 or 4. Above calculation process will be continued as x_{out} will be modified until the measured specific enthalpy at the outlet of this sub-section, h_{out}, will coincide with calculated specific enthalpy at the outlet of this section, h_{cal}. In the case of high heat flux, heat loss becomes high and was not able to be estimated accurately, then, there is a possibility that the calculated vapor quality at the inlet of glass tube shows relatively high value.

4. RESULTS AND DISCUSSIONS

Observation of Flow Pattern

Figures 4 and 5 show photographs about flow pattern with high mass velocities of 1260 and 1060 (kg/m^{2}s), respectively. In these cases, annular flow appears from vapor quality is below 0.2. This reason is that shear stress is high at the liquid-vapor interface caused by high vapor velocity. In the case of large mass velocity, however, judgement of flow pattern is very difficult between annular and slug flow. Because, disturbance of liquid-vapor interface is large and line velocity of refrigerant is high. Figures 6(a) to (d) show photographs about flow pattern when mass velocity is 430 (kg/m^{2}s). In this case, flow pattern is almost the same as that in a relatively large diameter tubes. Figures 7(a) to (d) show photographs about flow pattern when mass velocity is 80 (kg/m^{2}s). In this case, wavy-annular flow still appears when vapor quality is around 0.9. This reason is due to effect of surface tension though shear stress is low at the liquid-vapor interface. During whole experiments, separated flow was not observed.

Table 3. Correlation for Φ_L ($Re_L < 2400$)

(VVI)region

$$\Phi_L^2 = 3.5U_L^{-0.269} \quad (L1)$$

(VTI) region

-for slug flow

$$\Phi_L^2 = 0.007\left(\frac{U_V + U_L}{U_L}\right)^{0.85} Re_L^{3/4} \quad (L2)$$

-for disturbing wave region of annular flow

$$\Phi_L^2 = 0.0011\left(\frac{U_V + U_L}{U_L}\right)^{1.2} Re_L^{3/4} \quad (L3)$$

(VVN) region

-for plug flow

$$\Phi_L^2 = 0.0038\left(\frac{U_V + U_L}{U_L}\right)^{3.5} Re_L^{3/4} \quad (L4)$$

Boundary of above equations

-Boundary between equation(L1) and (L2)

$$\left(\frac{U_V + U_L}{U_L}\right)^{0.85} Re_L^{3/4} U_L^{0.27} \cong 500 \quad (LB1)$$

-Boundary between equation(L2) and (L4)

$$\frac{U_V + U_L}{U_L} \cong 200 \quad (LB2)$$

-Boundary between equation(L1) and (L4)

$$\left(\frac{U_V + U_L}{U_L}\right)^{3.5} Re_L^{3/4} U_L^{0.27} \cong 920 \quad (LB3)$$

Table 4. Correlation for Φ_L ($Re_L > 2400$)

(TTI) region

-for bubble flow close to plug flow

$$\Phi_L^2 = 1.6\left(\frac{U_V + U_L}{U_L}\right)^{3/4} \quad (T1)$$

(TTN) region

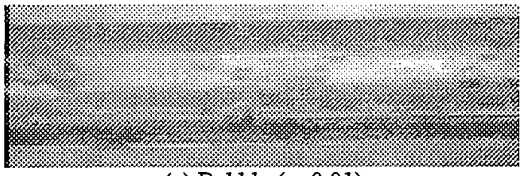
-for bubble flow

$$\Phi_L^2 = \left(\frac{U_V + U_L}{U_L}\right)^{4/7} \quad (T2)$$

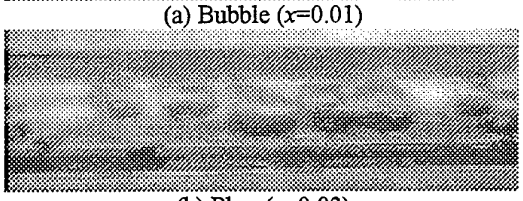
Boundary of above equations

-Boundary between equation(T1) and (T2)

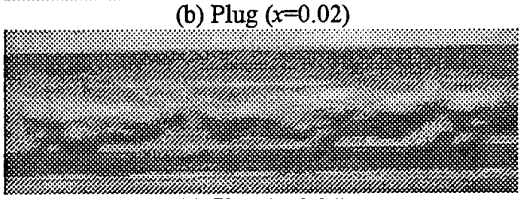
$$\frac{U_V + U_L}{U_L} = 1.6 \quad (TB1)$$



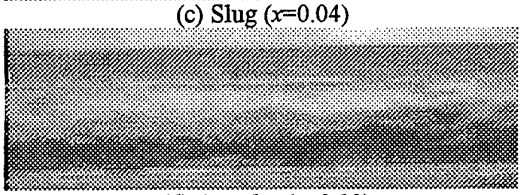
(a) Bubble (x=0.01)



(b) Plug (x=0.02)

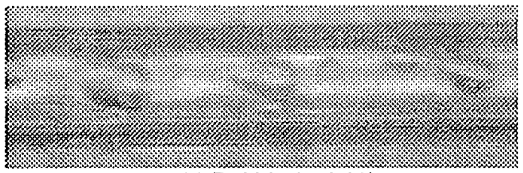


(c) Slug (x=0.04)

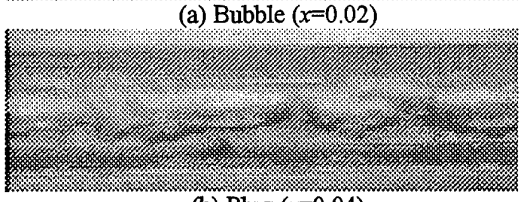


(d) Annular (x=0.10)

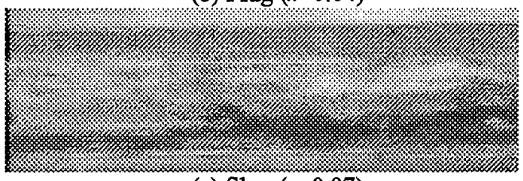
Fig. 1. Flow visualization (G=1260 kg/(m^{2}s))



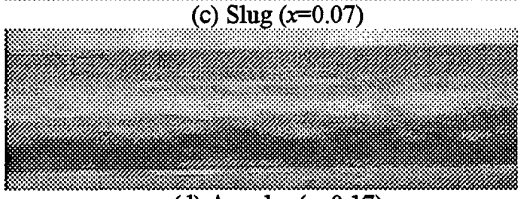
(a) Bubble (x=0.02)



(b) Plug (x=0.04)

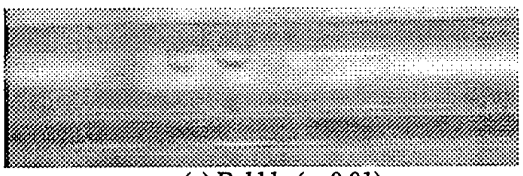


(c) Slug (x=0.07)

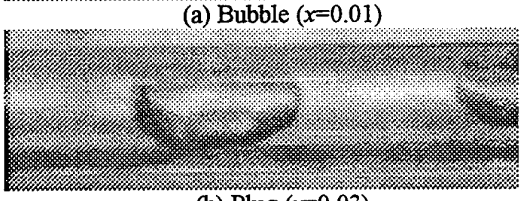


(d) Annular (x=0.17)

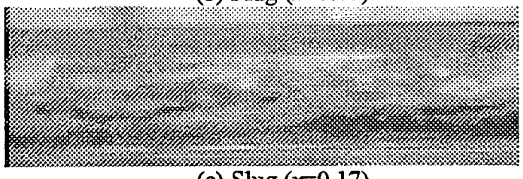
Fig. 2. Flow visualization (G=1060 kg/(m^{2}s))



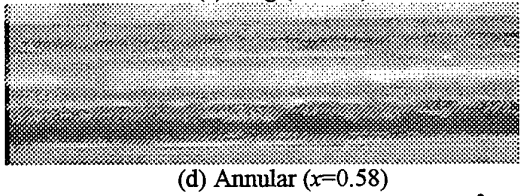
(a) Bubble (x=0.01)



(b) Plug (x=0.03)

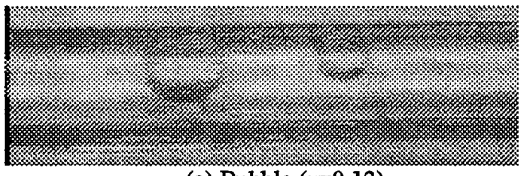


(c) Slug (x=0.17)



(d) Annular (x=0.58)

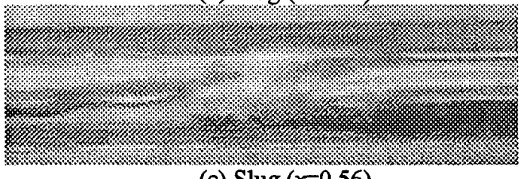
Fig. 3. Flow visualization (G=430 kg/(m^{2}s))



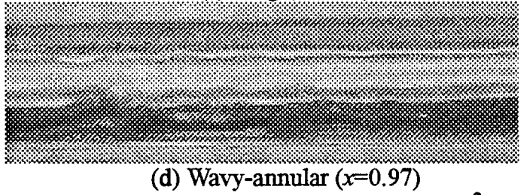
(a) Bubble (x=0.12)



(b) Plug (x=0.17)



(c) Slug (x=0.56)



(d) Wavy-annular (x=0.97)

Fig. 4. Flow visualization (G=80 kg/(m^{2}s))

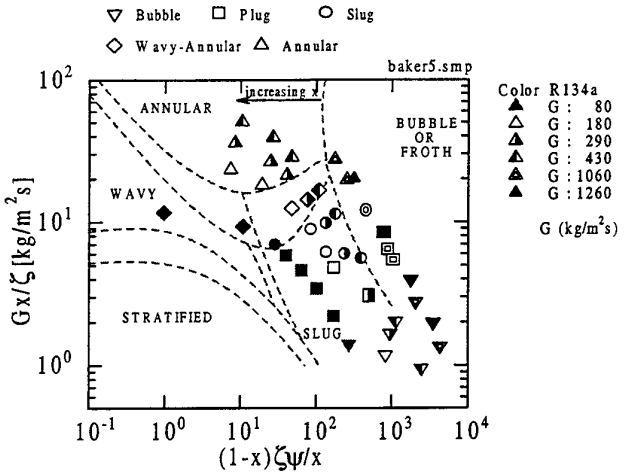


Fig. 8. Modified Baker's flow pattern map

Flow Pattern Map

Figure 8 shows observation results which plotted on modified Baker's flow pattern map. Symbols Δ, ◊, O, and ∇ denote annular, wavy-annular, slug, plug and bubble flow, respectively. In this study, wavy-annular flow appears in the region of wavy, and annular, slug and plug flow patterns appear in the region of bubble or froth. This reason is that Baker's map takes no account of influence of tube diameter. From this result, in the case of capillary tubes, it is inferred that these boundary lines of flow patterns move low vapor quality direction. Experimental results were also compared with Taitel-Dukler's flow pattern map, but most of all data didn't match with their map.

5. CONCLUSIONS

Flow patterns are experimentally investigated on in-tube evaporation of pure refrigerant HFC134a on a horizontal capillary tube. The conclusions are as follows:

Flow Pattern

(a)Separated flow was not observed in a capillary tube without depending on mass velocity.
(b)In the case of large mass velocity, annular flow appears from vapor quality is below 0.2.
(c)In the case of small mass velocity, wavy-annular flow still appears when vapor quality is around 0.9.

Compared with Modified Baker's Flow Pattern Map

(a)Wavy-annular flow appears in the region of wavy.
(b)Annular, slug and plug flow appears in the region of bubble or froth.
(c)It is inferred that boundary lines of flow patterns move low vapor quality direction.

REFERENCES

1. M. W. Wambsganss, D. M. France, J. A. Jendrzejczyk and T. N. Tran, ""Boiling Heat Transfer in a Horizontal Small-Diameter Tube", *Trans. ASME, J. Heat Transfer*, v. 115, pp. 963-972, edited by ASME, U.S.A. (1993).
2. T. Fukano, A. Kariyasaki and M. Kagawa, "Flow Patterns and Pressure Drop in Isothermal Gas-Liquid Concurrent Flow in a Horizontal Capillary Tube", *Trans. JSME(series B)*, v. 56, no. 528, pp. 174-182, edited by JSME, Japan (1990).
3. Y. Aoki, M. Taniguchi, S. Sakashita and Y. Watanabe, "Boiling Heat Transfer (1st Report: Visualization of Flow Pattern)", *Proc. of 36th National Heat Transfer Symposium of Japan*, v. 1, pp. 15-16, Japan (1999).
4. Y. Aoki, M. Taniguchi, S. Sakashita and Y. Watanabe, "Boiling Heat Transfer (2nd Report: Heat Transfer Coefficient and Pressure Drop)", *Proc. of 36th National Heat Transfer Symposium of Japan*, v. 1, pp. 17-18, Japan (1999).

ANALYSES OF MOTION AND DRAG COEFFICIENT OF WATER DROPLETS IN A NATURAL DRAUGHT COOLING TOWER

Liu Baomin and **M. N. A. Hawlader***
Department Mechanical & Production Engineering
National University of Singapore, 10 Kent Ridge Crescent, Singapore 119260
Email: mpehawla@nus.edu.sg

Keywords: water drop, drag coefficient, cooling tower, and numerical simulation.

ABSTRACT. Cooling towers have been widely used in power plants and space air conditioning systems. The rain region plays an important role in the operation of cooling towers. In this paper, four different models have been investigated that describe the motion of water droplets in the rain region of a cooling tower. Due to the non-uniformity of the flow, heat and mass transfer processes inside the cooling tower, the velocity field of water droplets is, at least, two-dimensional. Therefore, these models were tested with a numerical simulation program that accounts for the non-uniform flow. The velocity fields of water droplets, the variations of the drag coefficient with the relative velocity of water droplets have been predicted. The effect of drag and buoyancy force on the motion of water droplets were also studied numerically. The model based on Dreyer and Erens's correlation has been found to represent the actual situation reasonably well and is recommended for the modelling of water droplets motion in cooling towers.

1. INTRODUCTION

In order to get the reasonable result of a practical system by numerical simulation, one needs to develop and adopt correct mathematical and physical models. However, this is very difficult to be accomplished because a real industrial process is often complicated. As to cooling towers and other exchange equipment, there exist rain areas where water drops interacts with air stream. The water drops motion in the air is quiet different from solid spherical particles due to the internal circulation, mechanical palpation, irregular vortex shedding, and the interaction between the drops (collision and disintegration). Water drops falling freely under gravity through air remain very nearly spherical for $E_o = gd_e^2\Delta\rho/\sigma < 0.4$. Because of the large viscosity ratio $k = \mu_p/\mu$, internal circulation tends to be very slow, and the drag on such spherical drops follows closely to the standard drag curve for rigid spheres [1, 2]. If E_0 increase above 0.4 as in the case of cooling towers, some distortion from the spherical shape can be detected. Flattening occurs primarily at the leading (lower) surface, so that the shape then lacks fore- and- aft symmetry. Drops accelerating in air streams may split up and it was found that the disintegration occurs for $We = \rho d_e u^2/\sigma \geq 6.5$ [1]. For the condition of cooling tower, the maximum d_e allowed is larger than 10mm. For certain size of water drops, the drag coefficients tend to be larger than that of rigid spheres under accelerating conditions, due to the shape deformations. Wang [3] presented the procedures for predicting the acceleration of water drops under gravity. They found the instantaneous drag coefficients were based on those for water drops under terminal setting conditions. Beard [4] introduced a correction for shape distortion determined from a balance of static forces. Distances required for freely falling drops to reach 99% of their terminal velocities are of the order of 5.4m for d_e=1.0mm, 12.6m for d_e=2.0mm, and 18.1m for d_e=6.0mm [1]. These distances are so large that much of the early data obtained in the laboratory must be treated with considerable caution.

Although there are some empirical formulae that appear to be applied directly to the analysis of the water drop motion in the rain zone, almost no publications have been found to investigate, compare these models and confirm the fitness to the practical situation in cooling towers. Actually, only very few publications mentioned the solution of the water drop motion and the its drag coefficient model in detail. Majumdar et al. [5,6] express the total resistance of water drops to the air stream as $N \cdot \frac{1}{2}\rho u^2 \Delta V$, where N is total velocity head lost in the specific area. The velocity head lost in the rain zone can also be calculated by an empirical formula, $N = 0.526(Zp[m] + 1.22)(\dot{m}_l/\dot{m}_g)^{1.32}$ [7, 8]. This empirical formula was developed originally to calculate the total air pressure drop in the whole rain region in which the drop velocity changes greatly from the top to the bottom. Principally, it can be used to calculate the local resistance term of governing equation of the vertical air

velocity component if the applicable range of Zp of the empirical formula is large enough [5, 6]. But for determination of the single water drop drag force, this formula is hardly of any help. Other researchers did not mention the water drop drag force at all in their publications [9-12]. Therefore, it can be concluded that there is a need to propose a proper water drop drag coefficient model for the study of cooling towers and other similar equipment.

In this paper, we will present the equation of motion of water drops in air stream and investigate the influence of four models representing the drag coefficient. The governing equations of water drops motion, together with other equations controlling the air and water flow, heat, and mass transfer in cooling towers, are then solved with different models of drop drag coefficient. The two-dimensional velocity field of the water drops predicted by numerical method is presented. The effect of different drag coefficients on the water drop motion is also demonstrated and discussed in detail.

2. MOTION EQUATION OF WATER DROPS IN AIR STREAM

As mentioned earlier, the water drops in the rain region below the packing in a cooling tower is no longer spherical in shape. However, we can use an equivalent diameter, d_e, to express its volume as $V_d = \frac{1}{6}\pi d_e^3$ and mass as $M_d = \frac{1}{6}\pi d_e^3 \rho_w$. In addition, it is assumed that the water drops fall vertically in one dimension, and the transient problem of modelling accelerating drops may be approximated as a succession of steady states [13]. The forces exerted on a water drop falling in the air stream are gravity, G_d, buoyancy from the air, F_d, resistance from the air, R_d, as shown in the following Fig.1. The two-dimensional cylindrical coordinates system (x, r) is also defined in Fig. 1.

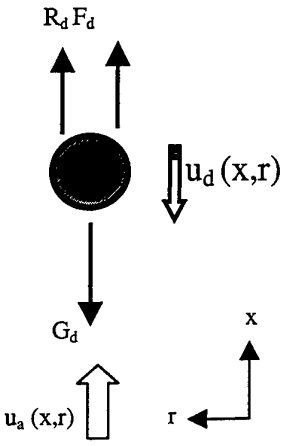


Fig. 1. Forces exerted on a water drop

Thus its gravity and the buoyancy of the air stream are $G_d = \frac{1}{6}\pi d_e^3 \rho_w g$, and $F_d = \frac{1}{6}\pi d_e^3 \rho\, g$, respectively. The resistance force R_d from the air is very complicated to deal with. Practically, a drag coefficient, C_d, is introduced, which is defined as [14],

$$C_d = \frac{R_d}{0.5\rho(u_r)^2 \cdot \frac{1}{4}\pi d_e^2} \tag{1}$$

where, $u_r = u_a + u_d$, is the relative velocity between air and water drop in vertical direction. Thus

$$R_d = \frac{\pi}{8} C_d \rho (u_a + u_d)^2 d_e^2 \tag{2}$$

The computation of C_d by different models of the drag coefficient will be presented in the following section. Based on the Newton's second law, the equation of water drop motion in counter-flow air stream can be expressed as

$$M_d \frac{du_d}{dt} = G_d - F_d - R_d \tag{3}$$

where, t stands for time here. According to the definition of u_d, $u_d = -\frac{dx}{dt}$, we get

$$dt = -\frac{dx}{u_d} \tag{4}$$

Substitute the expression of dt into the equation (3) and rearrange it

$$-\frac{u_d d(u_d)}{dx} = g(1-\frac{\rho}{\rho_w}) - \frac{3}{4}\frac{\rho}{\rho_w}\frac{C_d}{d_e}(u_a + u_d)^2 \tag{5}$$

where, both the vertical air velocity, u, and the water drop velocity, u_d, are the functions of x and r.

Equation (5) is solved numerically by iteration with the sets of Navier-Stokes equations governing the flow, heat, and mass transfer inside the cooling tower. The numerical solution is based on the finite difference method [5, 6].

3. THE WATER DROP DRAG COEFFICIENT MODELS

3.1 Model A — Water Droplets Represented by Solid Particles

Compared to the study of liquid drops, much more consideration has been paid to the determination of the terminal velocity and drag coefficient for falling rigid spheres. Clift [15] made a comprehensive review of the available correlation and presented a set of equations to predict the drag coefficient of solid spheres moving in different speed. Turton[16] improved Clift's correlation and obtained the following equation:

$$C_{ds} = \frac{24}{Re}(1 + 0.173Re^{0.657}) + \frac{0.413}{1 + 16300Re^{-1.09}}, \text{ for } 1<Re<2\times10^5 \tag{6}$$

where, $Re = \rho d_s u_t / \mu$. Originally, d_s is the diameter of the spherical particles, and u_t is the terminal velocity. When this equation is adopted here, the values of d_s and u_t equal the water drop equivalent diameter, d_e, and the relative velocity between the water drop and the air stream u_d.

3.2 Model B And C — Two Empirical Formulations for Drops and Bubbles

Due to the complexity, the calculation of liquid drop drag coefficient is mainly based on empirical formulations. Grace and Webber [1] reviewed the available studies on drops and bubbles. Some other empirical formulae are also available in the literature [17, 3]. In the present study, an empirical formula is adopted that introduces the ratio of the drop liquid viscosity to the air stream viscosity, μ_w/μ, to account for the deformation of the liquid drop [18]. And the water drop drag coefficient, C_d, is expressed as

$$C_d = \frac{32}{Re}(1 + \frac{2\mu_w}{\mu} - \frac{0.314(1 + 4\mu_w/\mu)}{Re^{0.5}}) \tag{7}$$

Abe et al. [19] analyzed the equations of droplet drag and interfacial shear stress for three-field model. In their study, the following equation was adopted to calculate the drag force on the droplet:

$$C_d = a / Re^n \tag{8}$$

where a=24, n=1 if Re<2; a=17.54, n=0.5473 if 1000 ≥Re ≥ 2 and a=0.4, n=0 if Re>1000.
Equation (7) and (8) are represented as model B and model C, respectively.

3.3 Model D — Dreyer and Erens's Correlation

Based on the experimental study, Dreyer and Erens [20] developed a set of equations to calculate the drag experienced by deformed water drops during acceleration in the air stream under the conditions of cooling towers. By using the drop terminal velocity data of Gunn [21], the drop deformation data of Beard [22] and solid sphere drag coefficient of Turton [16], they obtained the following correlation for the drag at terminal velocity:

$$\frac{C_d}{C_s} = 1 - 0.172(1-E) + 6.692(1-E)^2 - 6.605(1-E)^3 \tag{9}$$

where, E is the drop deformation effect and can be calculated as,

$$E = 1 - (\frac{u_d}{u_{dt}})^2 (1 - E_t), \text{ if } E > 0.4 \tag{10}$$

u_{dt} and E_t are the drop terminal velocity and its deformation effect as described by the following equation:

$$u_{dt} = \left(\frac{4}{3} \frac{(\rho_w - \rho) g d}{C_d \rho} \right)^{0.5} \tag{11}$$

$$E_t = \frac{1}{(1 + 0.148 E_o^{0.85})}, \text{ if } E_o > 0 \tag{12}$$

E_o is called Eotvos number and defined as

$$E_o = \frac{g d^2 (\rho_w - \rho)}{\sigma_w} \tag{13}$$

where, σ_w is the surface tension of water drops. The drag coefficient of solid spheres, C_s, is calculated by equation (6) developed by Turton [16].

Equations (9-13) are coupled and should be solved by iteration method. It can be seen that model D, which is based on Dreyer and Erens' correlation, is more complicated to be solved than the other three models.

4. RESULTS AND DISCUSSIONS

In order to investigate the influence of different models of drag coefficient on the falling water drops, an industrial natural draft counter flow cooling tower has been studied numerically. Its rain region has a height of 8.16m from the bottom of the packing to the cold water basin (or the pool) surface. The typical water drop equivalent diameter is assumed as 6.0mm [20]. Property parameters in these models, such as σ and μ, are calculated by the equations developed from the data given by Rohsenow et al. [23].

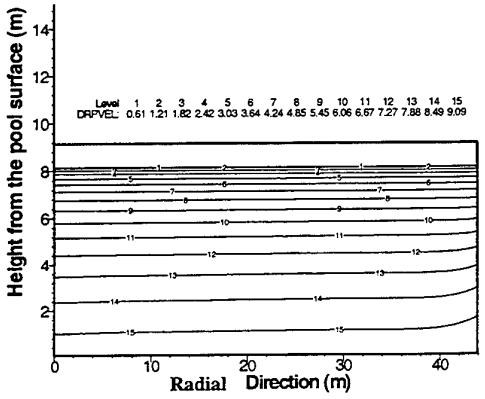


Fig. 2. 2D water drop velocity field in the rain region

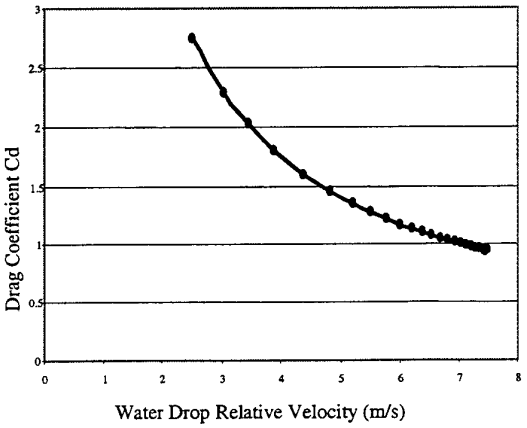


Fig. 3 Water drop drag coefficient predicted by Model B

Practically, the water drop velocity varies both horizontally and vertically due to the non-uniformity of the airflow in the rain region. The present numerically predicted 2D water drop velocity profile in the rain region is shown in Fig. 2.

It can be seen from the contour plot in Fig. 2 that the water drop velocity is larger near the entrance than the inner area of the same height. This is caused by the distribution of airflow that changes its direction from horizontal to vertical as the air enters the tower. The relative velocity between air and water drop is larger in the inner of the tower than in the outer part. High relative velocity produces larger drag force, thus lower drop velocity near the entrance. Following discussion will be focused on the predictions of drag coefficient C_d and the vertical distribution of water drop velocity on the center axis of the tower.

4.1 The Drag Coefficient C_d

The values of C_d at different relative velocity have been predicted using the four different models described in section 3 as shown in Fig.3 and 4. It is interesting to find out that the prediction of model B is 5 to 6 times larger than that of other three models, shown in Fig.3, with the relative velocity ranging from 2.5 to 7.5m/s and C_d from 2.74 to 0.95. Whereas, as seen in Fig. 4, model A which is originally correlated for solid sphere particles, unexpectedly give closer prediction of C_d to those of models C and D used recently by Abe and Dryer [19, 13].

Figures 3 and 4 also show the different trends of the C_d values obtained from different models. Compared to the increase of the prediction of model D, the values of C_d predicted by models A and B decrease as the relative velocity increases. Model C's prediction lies between those of model A and D. Firstly, it decreases from 0.47 to 0.4 as the relative velocity increases from 3.17(m/s) to about 4.2m/s, and then remains constant to a value of 0.4 when the relative velocity is above 4.2 (m/s). At a relative velocity of about 7(m/s), models A, D and C predict almost the same drag coefficients. Below this relative velocity, the prediction of model D is lower than that of models A and C. Above this velocity, model D predicts larger drag coefficient than models A and C, which gives very close predictions.

As mentioned in the last section, Dreyer and Erens's [13] correlation was obtained only a few years ago based on model A and the water drop deformation information discussed by Erens et al. [20]. It was then examined while investigating the motion of water drops and their interaction with air stream [13]. Therefore, it is more reliable for the case of cooling tower than other three models.

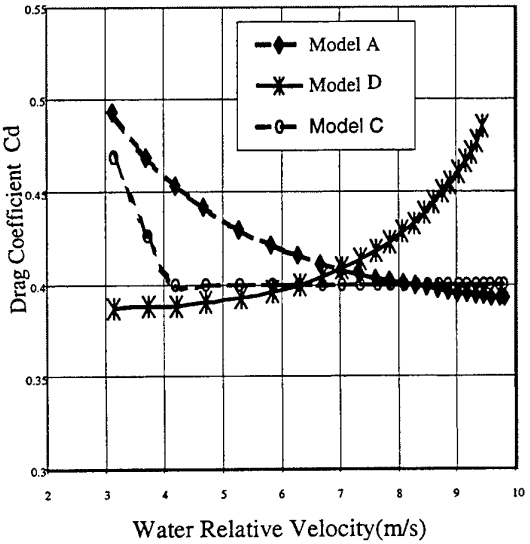


Fig. 4 Water drop drag coefficient predict by Model A, C and D.

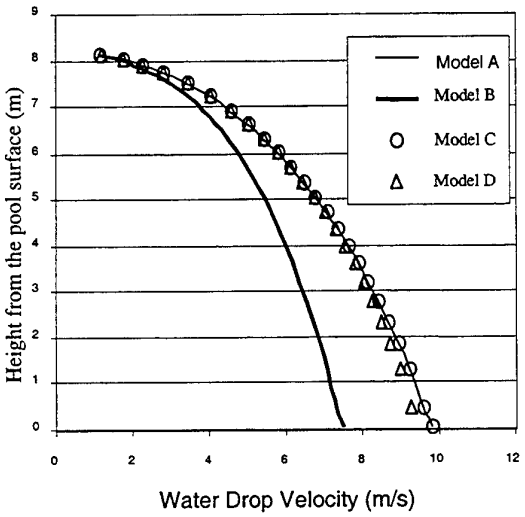


Fig 5 Water drop velocity predicted by models at different height on the central axis

Comparison of the predictions of models A and D shows that the correction of the deformation of the shape on the drag coefficient makes the model's prediction completely different in trends. To some extent, the faster a water drop moves in the air, the more severely it deforms from spherical shape. Consequently, the resistance increases and as a reflection of this fact, the drag coefficient increases with the relative velocity. From this point of view, model A has no correction of the deformation but model C includes some correction but does not truly represent real sitiuation.

4.2 Water Drop Velocity and Vertical Air Velocity on the Tower Central Axis

The velocity of water drop and the vertical velocity of air at different height have also been computed under the four different drag coefficient models and presented in Figures 5 and 6. Model B predicts much lower water drops velocity and air velocity than other three models. This is in accordance with its larger predictions of the drag coefficient. Small difference can be observed between the prediction of model D and those of model A and C that give almost the same water drop velocities. Whereas, the difference among the predictions of air velocity of model A, C and D is too small to be observed on Fig. 6. This is because that the total resistance to the air stream from water drops is very small compared to the driven force. Thus the variation of the resistance cannot affect the air velocity as much as it affects the drop velocity. However, the difference is large enough to be seen among the predictions of the relative velocity from models A, C, and D, as illustrated in Fig. 7.

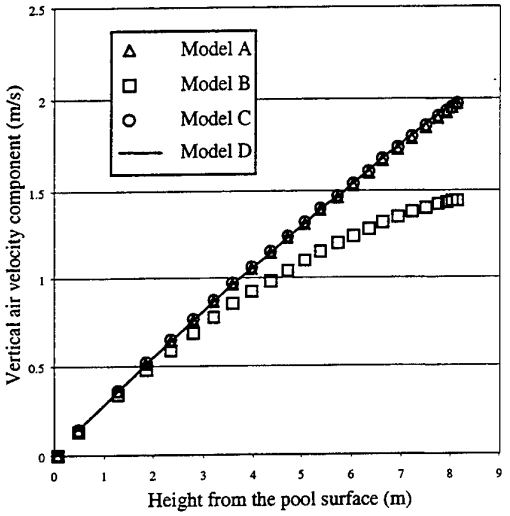


Fig. 6 Vertical component of air velocity on the central axis

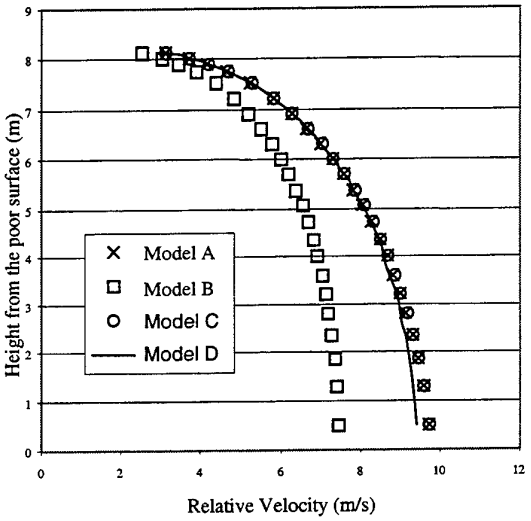


Fig. 7 Relative velocity between water drops and air stream

Figures 5 and 7 also shows that the difference among the predictions of the velocity of water drops and the relative velocity obtained from different models increases as the water drops approaches the water basin. As mentioned earlier, the distance required for freely falling drops of 6.0mm diameter to reach their terminal velocities is longer than 18.1m. However, in the present case, the rain region is only 8.16m and water drops fall at a speed much smaller than their terminal velocity and the drag force does not reach its maximum value.

4.3 Comparison of Vertical Air Velocity, Water Drop Velocity with/without Drag and Buoyancy Effect

In order to investigate the influence of the combined effect of the drag and buoyancy, we have computed the free falling velocity of water drops, u_{df}. If the buoyancy and drag forces are omitted, the governing equation of water drops becomes,

$$-\frac{u_{df}\,du_{df}}{dx} = g \tag{14}$$

This equation was solved in the same way as that of equation (2.6) to obtain the free falling water drop velocity at the exact positions of the solved real falling water drop velocity. All the four models have been tested and the

result of model D is presented here in Fig. 8. Without buoyancy and drag forces, water drops fall at a faster speed. As seen from Fig. 8, the final speed is 12.3m/s compared to 9.3m/s obtained model D that considers both drag and buoyancy effects. This difference increases as the falling distance increases. The vertical air velocity (with drag force considered) increases as it flows up. This is because the main flow direction turns vertically from horizontal direction as the air goes into the cooling tower through the inlet. This changing trend of the vertical air velocity makes the relative velocity different from the water drop velocity. If the air is stagnant, there will be no difference between the relative velocity and the velocity of water drop.

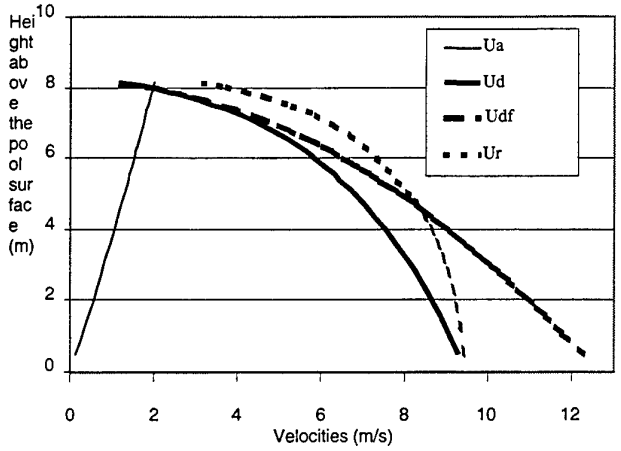


Fig 8. Air vertical velocity, relative velocity and water drop velocity with/without drag and buoyancy effect

5. CONCLUSIONS

Four typical models have been investigated for the analysis of the motion of water droplets in the rain zone of a natural-draught cooling tower. With the use of a numerical simulation program that accounts for the non-uniformity of flow and transport properties, the 2D water drop velocity field is obtained. The predicted drag coefficient by these models are presented and discussed. Model D that is based on Dreyer and Erens's correlation [20], is recommended for the calculation of the deformed water drop drag coefficient for the case of cooling towers and other similar applications. The water drop falling velocity with/without drag and buoyancy effects together with the vertical component of air velocity in the rain region are also compared.

NOMENCLATURE

C_d	Drag coefficient, see eq. (2.1)
d_e	Equivalent diameter of water drop, m
d_s	Diameter of spherical particle, m/s
E	Drop deformation effect, see eq. (3.4).
E_o	Eotvos number, see eq.(3.4.4).
F_d	Buoyancy of water drop, N
N	Total velocity head.
g	Gravity acceleration rate, 9.81m/s^2
G_d	Gravity of water drop, N
M_d	Mass of the water drop, kg
R_d	Resistance of water drop, see eq. (2.2).
Re	Reynolds Number.
t	Time, s
u_a	Air stream vertical velocity, m/s
u_d	Water drop's velocity, m/s
u_r	Relative velocity of water drop to air, m/s.
u_{df}	Free falling velocity of water drop, m/s
u_t	Terminal velocity, m/s
V_d	Volume of water drop, m^3
x, r	Vertical and horizontal co-ordinates of the cylindrical co-ordinates system

Greek Symbols

ρ	Density of air, kg/m^3
ρ_w	Density of water, kg/m^3
σ_w	Surface tension of water, N/m
μ	Viscosity of air, kg/(ms)
μ_w	Viscosity of water, kg/(ms)

Subscripts

a	moist air
e	equivalent

w	water	r	relative
s	sphere		
df	free falling of drops		

REFERENCES

1. Gad Hetsroni (editor), *Handbook of Multiphase Systems*, Hemisphere Publishing Corporation, pp. 1.204-1.223 (1982).
2. Nicholas P. Cheremisinoff, Ramesh Gupta (editors), *Handbook of Fluids in Motion*, Ann Arbor Science Publishers, pp. 1003-1025 (1983).
3. P. K.Wang, H. R. Pruppacher, "Acceleration to Terminal Velocity of Cloud and Rain Drops", Journal of Applied Meteorology, Vol. 16, pp. 275-280 (1977).
4. K. V. Beard, "On the Acceleration of Large Water Drops to Terminal Velocity", Journal of Applied Meteorology, Vol. 16, pp. 1068-1071 (1977).
5. A.K. Majumdar, A.K. Singhal, and D.B. Spalding, "Numerical Modelling of Wet Cooling Towers; Part 1: Mathematical & Physical Models", ASME Journal of Heat Transfer, No. 11, Vol. 105, No. 4, pp. 728-735 (1983).
6. A.K. Majumdar, A.K. Singhal, and D.B. Spalding,, "Numerical Modelling of Wet Cooling Towers; Part 2: Applications to Natural and Mechanical Draft Towers", ASME Journal of Heat Transfer, No. 11, Vol. 105, No. 4, pp. 736-743 (1983).
7. J.R. Sinham, Natural Draft Towers, *Hemisphere Handbook of Heat exchanger Design* (editor: Hewitt, G. F.), Hemisphere Publishing Corporation (1990).
8. F. Mills, *Basic Heat and Mass Transfer*, Chicago: Irwin, pp. 779-805 (1995).
9. D. J. Benton, W. R. Waldrop, "Computer Simulation of Transport Phenomena in Evaporation Cooling Towers", ASME Journal of Engineering for Gas Turbines and Power, No. 4, Vol. 110, pp. 190-196 (1988).
10. K. Ralvi, S.M. Varma, P. Nithiarasu & K. N. Seetharamu, "Design of Cooling Towers by the Finite Element Method", *Natural Draught Cooling Towers*, Wittek & Kratzig (eds), Balkema, pp. 361-367 (1996).
11. E. Razafindrakoto, J. L. Grange, L. Fabre, H.Delabriere, S. Delaroff, "3D Numerical Simulation of a Natural Draught Cooling Tower Flow", *Notes on Numerical Fluid Mechanics,* Vol. 53, *Proceedings of the IMACS-Cost Conference on Computational Fluid Dynamics*, Lausanne, pp. 248-255 (1995).
12. Yun-Yu, Liu, H.E. Hesketh, "Simultaneous Heat and Mass Transfer in a Catenary Cooling Tower", ASME: Journal of Engineering for Gas Turbines and Power, Vol. 109, No. 7, pp. 245-248 (1987).
13. A. A. Dreyer, P. J. Erens, "Modelling of Cooling Tower Splash Pack", Int. J. Heat Mass Transfer, Vol. 39, No. 1, pp. 109-123 (1996).
14. Keiohi Gotoh, et al, *Powder Technology Handbook*, Marcel Dekker Inc., pp. 99-116 (1977).
15. R. Clift, J. R. Grace and M. E. Weber, *Bubbles, Drops and Particles*, Academic Press, New York (1978).
16. R. Turton and O. Levenspiel, "A Short Note on the Drag Correction for Spheres", *Powder Technology*, Vol. 47, pp. 83-86 (1986).
17. X.B. Edwin, R.P. Maarten, "Equations for Calculating the Terminal Velocities of Water Drops", Journal of Applied Meteorology, Vol. 13, pp. 108-113 (1974).
18. X.L. Fei, *Advanced Flow Mechanics*, Xi'an Jiaotong University Publishing House (1989).
19. Y. Abe, A. Tomiyama and I. Kataoka, "Study on Closure Equations of Droplet Drag and Interfacial Shear Stress for Three-Field Model", *Advances in Multiphase Flow 1995*, Elsevier Science, 1995.
20. P. J. Erens, J.H. Mercker, A.A. Dreyer, "Evaporation from a accelerating droplets", *Proceedings of the 10th International Heat Transfer Conference*,Vol. 7, pp. 305-310 (1994).
21. R. Gunm, G. D. Kinzer, "The Terminal Velocity of Fall for Water Droplets in Stagnant Air", Journal of Meterology, Vol. 6, pp. 243-248 (1949).
22. K. V. Beard, C. Chuang, "A New Model for the Equilibrium Shape of Raindrops", Journal of Atmospheric Science, Vol. 44, No.11, pp. 243-248 (1987).
23. Warren M. Rohsenow, James P. Hartnett, Ejup N. Ganic, *Handbook of Heat Transfer: Applications*, McGraw-Hill, pp. 10.1-10.48 (1985).

NUMERICAL ANALYSIS AND EXPERIMENTAL VERIFICATION OF TWO-PHASE FLOW OF REFRIGERANT THROUGH ELECTRONIC EXPANSION VALVE

Yu Bingfeng Wang Zhigang Wang Dongqing Meng Xiangzhao
School of Energy and Power Engineering
Xi'an Jiaotong University
Xi'an 710049, P.R.China

Keywords: electronic expansion valve, two-phase flow, two-fluid model

ABSTRACT. In this paper, the physical model of the refrigerant two-phase flow through electronic Expansion valve(EEV) was established and numerically solved applying the two-fluid model. The velocity field of vapor and liquid, the distribution of void fraction, and the pressure field of the refrigerant during the throttling were obtained. The curves describing the relationship between the mass flow rate and the pressure difference of the refrigerant were achieved. The computing results agree with the experimental data very well. The mass flow rate- pressure difference relationship of the refrigerant based on these models in this paper can be used in the design of EEV, the research on the match and control of the refrigerating system.

INTRODUCTION

The inverter-driven air conditioners apply electronic expansion valves(EEV) to be the throttling device at most cases. However, the research on the refrigerant flow characteristics through EEV has not been penetrating and the pervious research has shown that the relationships between the mass flow rate and pressure difference, also mass flow rate and openings of EEV were usually obtained by the experimental method. Moreover, the most experiments and computation only focus on the single-phase flow and were not involved in the phase change procedure so that their experimental curves can not be used directly. Understanding the characteristics of the refrigerant two-phase flow through EEV precisely and thoroughly is of great significance for the design of EEV, match and control of the refrigerating system. No such research had been reported on the characteristics of refrigerant two-phase flow through EEV previously. In this paper, the EEV with different openings is treated as the equivalent serious of orifice-plate with varying hole diameters and the flow model of EEV at the certain operating condition is established on the basis of orifice-plate in the light of the difficulties of testing. The numerical simulation is carried out for the fields of velocity, pressure and void fraction of the refrigerant vapor and liquid phases through LAM type EEV with the capacity of 1-ton using two-fluid model and SIMPLEST algorithm. The characteristic curves of the mass flow rate versus pressure difference and mass flow rate versus openings of EEV have been obtained and provided. The comparison between the experimental data and numerical results has shown that the physical model of the equivalent orifice-plate and the mathematical model of the two-fluid model for EEV are reliable and efficient

PHYSICAL MODEL OF EEV

The electronic expansion valve is the throttling device with the variable local resistance. The refrigerant flow rate through EEV at the given lift is directly proportional to the square root of the pressure difference between before-and-after throttling, which is the same as the general throttling devices such as the orifice-plate. The flow rate coefficient and throttling area would vary with the different hole diameters and the EEV flow model at the certain operating conditions is set up based on the orifice-plates. The schematic structure of LAM type EEV is shown in Fig. 1.

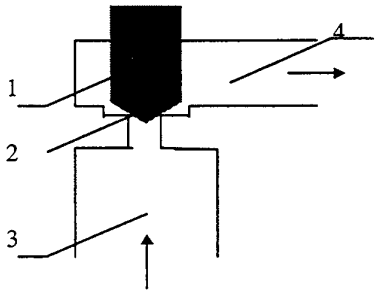


Fig. 1. Schematic of the structure of LAM type EEV (1. Valve rod, 2. Valve needle, 3. Entrance, 4. exit

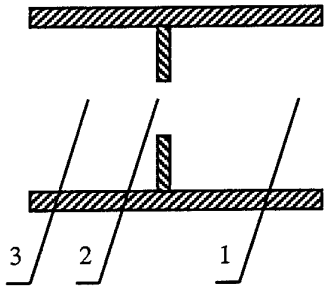


Fig.2. Schematic of equivalent orifice- plate (1. entrance 2. throttling hole 3. Exit)

MATHEMATICAL MODEL

The refrigerant flow through EEV could be treated as the two-dimensional, two-phase, adiabatic, and phase-changing flow. The two-fluid model is applied in this investigation, that is, both vapor phase fluid and liquid phase fluid are studied which fill in the flow field simultaneously and are interactive.

Governing Equations

The equations of the two-fluid model are as follows:

The continuity equation is

$$\frac{\partial(\alpha_k\rho_k)}{\partial t}+\nabla\cdot(\alpha_k\rho_k\vec{U}_k)=\Gamma_k \tag{1}$$

where Γ_k represents the mass flow rate of entering the phase through the phase surface in the unit volume mixture which is given by

$$\Gamma_k=-V^{-1}\int_{A_k}\rho_k(\vec{U}_k-\vec{U}_{sk})\cdot\vec{n}_k dA$$

The momentum equation is

$$\frac{\partial(\alpha_k\rho_k\vec{U}_k)}{\partial t}+\nabla\cdot(\alpha_k\rho_k\vec{U}_k\vec{U}_k)=-\nabla(\alpha_k P_k)+\nabla(\alpha_k\tau_k)+\alpha_k\vec{f}_k+\vec{M}_k \tag{2}$$

where $\vec{f}_k$ is the volume force on the unit mass phase *k* of the mixture, and

$$\vec{M}_k=-V^{-1}\int_{A_k}[\rho_k\vec{U}_k(\vec{U}_k-\vec{U}_{sk})+P_k I-\tau_k]\cdot\vec{n}_k dA$$

which consists of the two parts: $-V^{-1}\int_{A_k}\rho_k\vec{U}_k(\vec{U}_k-\vec{U}_{sk})\cdot\vec{n}_k dA$ indicates the momentum of entering the phase k in the unit time because of the mass exchange between two phases, $-V^{-1}\int_{A_k}(P_k I-\tau_k)\cdot\vec{n}_k dA$ stands for the force of the other phase upon the phase k through the interface of the two phases.

The total conservation equation is given by

$$\alpha_l+\alpha_v=1 \tag{3}$$

The subscript k in equations (1), (2), (3) indicates the phase, k =l for liquid phase, k =v for vapor phase.

The transport equation of the turbulent current kinetic energy k and its dissipation rate ε is :

$$\nabla\cdot(\rho_k k\overline{U}_k)=\nabla^2(\Gamma_{kk}k)+P_{kk}-\rho_k\varepsilon_k+\overline{\overline{F_k}\cdot\overline{U}_k} \tag{4}$$

$$\nabla\cdot(\rho_k\varepsilon\overline{U}_k)=\nabla^2(\Gamma_{\varepsilon k}\varepsilon)+\frac{\varepsilon}{k}(C_{\varepsilon1}P_{kk}-C_{\varepsilon2}\rho_k\varepsilon_k+C_{\varepsilon3}\overline{\overline{F_k}\cdot\overline{U}_k}) \tag{5}$$

where Γ_{kk} and $\Gamma_{\varepsilon k}$ are the exchange coefficients of turbulent current kinetic energy k and its dissipation rate of the phase k individually. $\overline{F_k}$ represents the force on the phase k by the other phase through the two-phase interface, that is, the second item of $\bar{M}_k$. $\overline{U_k}$ is the impulsion vector of k item. $\overline{\overline{F_k}\cdot\overline{U_k}}$ in k equation (4) indicates the influence on the turbulent current kinetic energy of the other phase by the phase. $C_{\varepsilon3}\frac{\varepsilon}{k}\overline{\overline{F_k}\cdot\overline{U_k}}$ in ε equation (5) stands for the effect of the turbulent current kinetic energy dissipation rate upon the other phase because the phase exists.

The equation of state in the vapor phase region is

$$Pv=ZRT \tag{6}$$

where the compression factor Z is given as follows

$$Z=1+\sum_{i=1}^{r}\left(\sum b_{ij}\Big/T_r^j\right)\rho^i \tag{7}$$

The saturated vapor pressure equation is given by

$$p_s=p_c\exp[Ri\ln T_r+(Ri-4+p_\alpha)\psi(T_r)] \tag{8}$$

where $\psi(T_r)=4[(T_r-1)/T_r]+S(T_r)-5.3\ln T_r$;

$$S(T_r)=(T_r-1)\left[0.2(T_r+1)^2+0.5\right];$$

The saturated liquid density equation is

$$\rho'=\rho_c\exp\left[a_1(1-T_r)^{1/3}+a_2S(T_r)\right] \tag{9}$$

The equation of constant-volume specific heat at the ideal gas state

$$c_{v0}=\sum_{i=0}^{4}d_iT_r^i \tag{10}$$

The heat balance equation gives

$$\Gamma_k\cdot(h_l-h_v)=C_1(h_l-h_{sl})+C_2(h_v-h_{sv}) \tag{11}$$

Boundary Conditions

The refrigerant in this investigation is R12 which is in saturated state, subcooling state, or two-phase state respectively at the entrance of EEV with the velocity, turbulent current kinetic energy k and its dissipation rate ε of the entrance refrigerant are given. The viscosity coefficient at additional source item is applied to the first grid of the fluid close to the wall face at the interface of liquid and solid, that is, the velocity at the wall face is zero, the velocity of the first grid is computed with the logorithmatic distribution characteristics close to the wall face,

the concentration at the wallface is impermeable, and the turbulent current kinetic energy and its dissipation rate is considered to be zero.

COMPUTING METHOD, RESULTS AND ITS ANALYSIS

Based on the physical model and the mathematical model described above, the grid arrangement of the computing region is shown in Fig.3. After the boundary conditions of the valve body are determined and a serious of computation for the different openings of the valve hole, the varied flow characteristics of EEV can be achieved. The following analysis of the flow field is described in the condition of the saturated state of the entrance refrigerant and the certain opening of EEV.

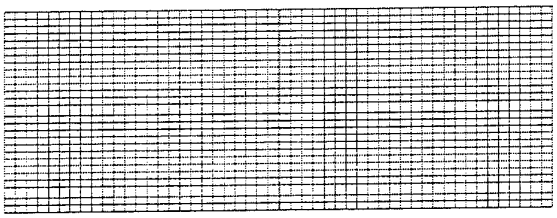


Fig.3. Grid arrangement of the computing region (orifice throttling area 0.706mm^2)

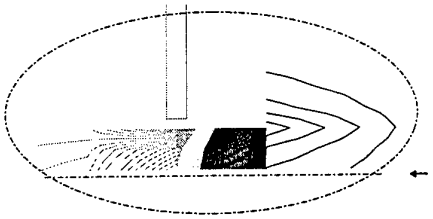


Fig. 4. Schematic of isopressure before-and-after throttling

According to the object properties determined by the analysis of the model, the finite volume difference method is used for divergence and the pressure correction algorithm is applied in the solving process. The computing results are shown in Figs.4-7 .

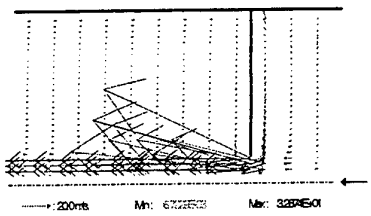


Fig.5. Schematic of velocity vector distribution of liquid phase and vapor phase

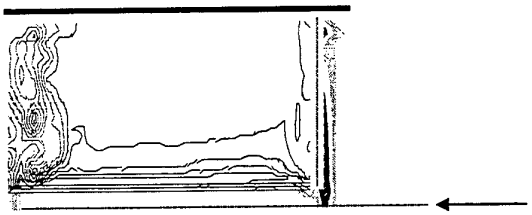


Fig. 6. Schematic of volume isoconcentration of vapor phase

Fig.4 shows the isopressure before-and-after the throttling hole. The entrance pressure of the refrigerant at the boundary of the computing region is 6.6×10^5Pa, and the pressure difference between the entrance and exit of EEV is 7.04×10^5Pa. It can be seen from Fig.4 that the isopressure line are more intensive, the pressure changes are larger and pressure fields are more non-uniform. Fig.5 is the schematic of velocity vector distribution of liquid phase and vapor phase, in which the unit arrow represents the velocity value 20m/s and the director of the vector indicates that of flow. From Fig.5, it can be known that the velocity of vapor and liquid phases flow is very big at the smallest sector of the valve and the inverse flow occurs at the beginning of exit port of the valve so that the small local eddy is formed. It could be seen that the fluid flow rate is rather uniform in the big entrance room from Fig.4 and Fig.5. Fig.6 is the schematic of the volume isoconcentration of vapor phase which shows that bulk lash vapor is produced when the fluid flows through the throttling hole and the flashes vapor ejects towards the downstream at a high speed of 100m/s along with the throttling hole. Fig. 7 is the schematic of streamline from which the eddy behind the throttling hole can be observed distinctly.

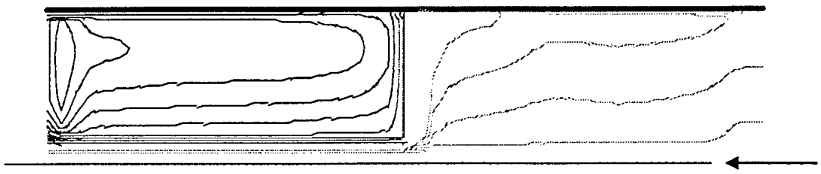


Fig. 7. Schematic of streamline

EXPERIMENTAL VERIFICATION

The experiments for EEV were carried out in a standard rig of air conditioner performance. The test environment temperatures are: for indoor, 27C (DB), 19C (WB), for outdoor, 35C (DB), 24C (WB). The sensors and the flowmeters for measuring temperatures and pressures are installed at the entrance and exit locations of refrigerating system parts, and also at the air side. After the testing conditions are fixed, the experimental system implements the data collection, communication, computation, and control output automatically. Fig.8, Fig.9 and Fig.10 show the computation results based on the experimental data. Fig.8 is the curve of relationship between the flow rate coefficient $\alpha \cdot \varepsilon$ and the driving impulse number. Fig.9 describes the relationship between the flow rate coefficient $\alpha \cdot \varepsilon$ and the refrigerant quality x. From Fig. 8 and Fig.9, it is obvious that, for the EEV investigated in this paper, its flow rate coefficient $\alpha \cdot \varepsilon$ is relative to the values of pressure change before-and-after throttling, instead of the factors such as ratio of the hole cross –section area to the pipe cross section area m , Re. Applying the least square regression method, the following expression could be obtained from the curve shown in Fig.9:

$$\alpha \cdot \varepsilon = 0.75 - 0.1407x \tag{12}$$

Fig. 10 shows the test curves of the relationship between refrigerant mass flow rate and pressure difference before-and-after throttling.

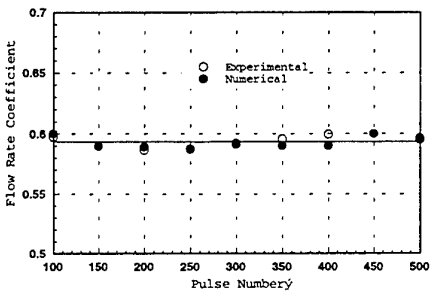


Fig.8. relationship between the flow rate $\alpha \cdot \varepsilon$ and the driving impulse number

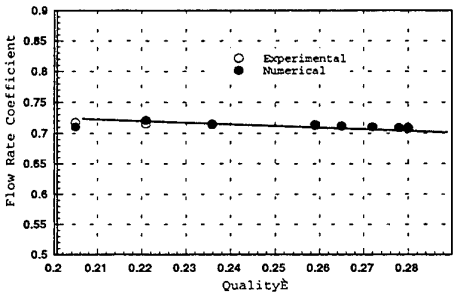


Fig.9. relationship between the flow coefficient $\alpha \cdot \varepsilon$ and refrigerant quality x

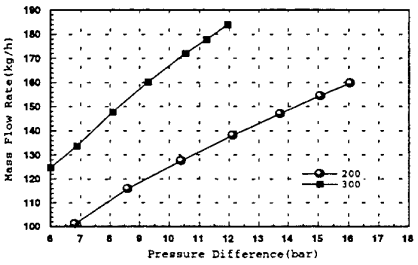


Fig.10. The test curves of the relationship between refrigerant mass flow rate and pressure difference before-and-after throttling

CONCLUSIONS

1. It is the very effective method of investigating the refrigerant flow characteristics through the electronic expansion valve that the physical model of EEV with different opening is established using the orifice-plate with varying hole diameters.
2. Applying the two-fluid model, the two-phase flow characteristics of the refrigerant through the electronic expansion valve can be described precisely. The velocity field, pressure field and the detailed distribution of the void fraction are obtained, and the formula expressing the relation between the mass flow coefficient $\alpha \cdot \varepsilon$ of EEV and the quality x of the refrigerant is provided.
3. The curves representing the relationship between the mass flow rate and the pressure difference of the refrigerant are given with the numerical method. The comparison between the computing values and the experimental data shows that the model in this paper is reliable and correct, which could be used in the design of EEV, the refrigerating system match and control for the inverter-driven air conditioner.

REFERENCES

1. W. Q. Tao, *Numerical Heat Transfer,* Xi'an Jiaotong University Press.(1988)
2. Z. G. Liu, *Computer Program of the Thermophysical Properties of Working Fluids and Its Application,* Science Press.(1992)
3 D. Y. Liu, *Two-phase Hydrodynamics*, Higher Education Press.(1993)

NOMENCLATURE

ρ_C	Critical density (g/cm^3)	x	Quality of refrigerant at exit of EEV
T_C ,T_r	Critical and reference temperature (K)	C_1, C_2	Transmission coefficient between phases
ρ	Density (g/cm^3)	h_{sl}, h_{sv}	Saturated enthalpy of liquid and vapor phase Cv0
b_{ij}	Property constant	c_{vo}	Constant-volume Specific heat of ideal gos (kJ/kg.K)
P_c	Critical pressure (10^5Pa)		
P_s	Saturated pressure (10^5Pa)	d_i	Material constant
Ri, P_α	Criteria number	a_1, a_2	Material constant

T_r Reference temperature (K0

Γ_k Mass flow rate across phases interface of unit volume mixture

$\bar{M}_k$ Momentum exchange between two phases of unit volume mixture

PK Generation rate of K of unit volume

$\Gamma_K \Gamma_\varepsilon$ Exchange coefficients of turbulent kinetic energy and its dissipation rate

α_l α_v Void fraction of liquid and vapor phases

ε Expansion coefficient; kinetic energy dissipation rate

F. Porous Media

EXPERIMENTAL STUDY OF DISORDERED 3D AND 2D PACKING OF RIGID FIBRES: INFLUENCE OF THE ASPECT RATIO ON THE STRUCTURE

M. Novellani, R. Santini, L. Tadrist
Institut Universitaire des Systèmes Thermiques Industriels - CNRS (UMR 6595)
Université de Provence - Technopôle de Château Gombert - 5, rue Enrico Fermi
13453 Marseille cedex 13, FRANCE
E-mail: novel@iusti.univ-mrs.fr; Tél: + 33 (0) 4 91 10 68 68; Fax: + 33 (0) 4 91 10 69 69

Keywords: fibres packing, aspect ratio, porosity, defects

ABSTRACT. The aim of this work is to study the structure of three-dimensional and two-dimensional loose packing of stiff cylindrical fibres, with a particular attention for the 2D structures, according to their aspect ratio. First, we have carried out an experimental study of the porosity for 3D and 2D packing. In this last case, the Elementary Representative Surfaces have been determined. Then, an attempt of interpretation of the porosity variations for 2D stacks has been realized on the basis of the Excluded Volume theory and a variation law has been proposed. We have also studied the relevance of a simplified packing model based on a single geometry of the defects. Then, some local properties of 2D stacks such as the densities and the sizes of the defects or the orientations of the fibres have been determined.

1. INTRODUCTION

Porous media present many different characteristics of structure. There is also a great diversity in the material which compose them. We find them in our natural environment (beds of sand, of gravel, wood, foams, chalky soil, ...) as well as in manufactured goods (building materials, paper, insulators, catalysts, ...). Moreover a large number of industrial products such as glass wool, filters, reticulate ceramics, new composite materials, are composed of fibres. The present study concerns the characterisation of random stacks of rigid fibres. Because of the complexity of these systems, the experimental approach is a good tool to study their structural characteristics (porosity, permeability, arrangement, etc.).

Many works concerning ordered and random stacks of spheres having one or several radii have been carried out since the thirties and literature is full of results in this field. Yet, the first experimental results concerning the random packing of fibres appeared in the seventies. Milewski [1-3] studied mixtures of fibres and glass beads to reduce the amount of resin used in making reinforced plastics. He made measurements on stacks of wooden fibres having a diameter of 2.1 mm and an aspect ratio r=L/d (fraction length over the diameter of the fibre) between 4 and 72. He determined a law of variation for the density of the stack as a function of the aspect ratio of the fibre. He obtained the same law of variation for fibreglass having a diameter equal to 13µm and has extended his study to the combinations of fibres with different aspect ratios. Nardin [4] worked on stacks of particles of different natures (glass, steel, PMMA...) and of various shapes (spheres, discs, fibres, revolution ellipsoids). Rahli [5] studied loose and close packing of Nylon or metal (copper, bronze) fibres. He, moreover, proposed a model based on the Excluded Volume determined by Onsager [6]. With this model, the variations of porosity can be described according to the aspect ratio. Parkhouse and Kelly [7] studied the packing of spaghetti having a diameter of 1.8 mm and an aspect ratio between 6 and 140. Thanks to a half-empirical model, these authors proposed an analytic expression of the law of porosity as a function of the aspect ratio.

The major results acquired on the random packing of rigid fibres are the following:
- the existence of a single variation curve of the porosity according to the aspect ratio for loose packing, whatever the nature or the size of the fibres.
- the existence of two models of variation of the porosity.

All these works concern three-dimensional stacks of rigid fibres.

The subject of the present work is the study of the loose packing of cylindrical fibres made of plastic, having a diameter equal to 5 mm and an aspect ratio between 1.2 and 50.5, for three-dimensional and two-dimensional stacks, with particular attention to the 2D structures. In this last case, the width of the packing cell is equal to the diameter of a fibre. These two-dimensional structures present many advantages in experiments as well as in

theory. In this configuration, it is possible to study the structure of the stack. In this work, the variation laws of the porosity according to the aspect ratio are determined experimentally for 2D and 3D stacks. For 2D stacks, a variation law of the porosity is proposed. The local properties of 2D stacks such as the densities and the sizes of the pores or the orientations of the fibres are studied.

2. MATERIALS AND METHODS

2.1 Fibres and Packing Cells

The fibres used are cylinders in white delrin (plastic) having a diameter of 5 mm. Their aspect ratios are contained between 1.2 and 50.5.

For 2D stacks, 3 different-sized glass cells, adapted to the lengths of the fibres, are used. The dimensions of the cells (Width W and Height H) and the aspect ratios of the fibres which can be studied are the following:

- cell 1: W = 18.6 cm H=50 cm r = 1.2 - 1.5 - 3.0
- cell 2: W = 38 cm H=50 cm r = 3.0 - 5.0 - 7.1 - 10.1 - 12.1
- cell 3: W = 100 cm H=100 cm r = 12.1 - 20.2 - 30.3 - 50.5

To obtain stacks in 2D cells we use a funnel in the shape of a triangular prism whose rectangular outlet is equal to the aperture of the cell. So, fibres are simply poured into the funnel and then drop into the cell. The packing is made without any vibration, so the stacks obtained are loose. Two examples of 2D stacks are presented in Photos 1 and 2.

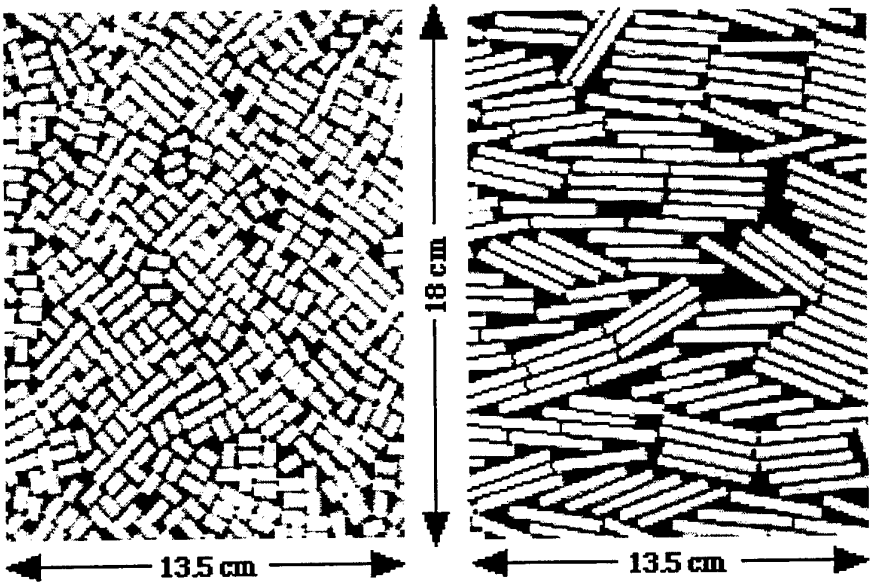


Photo 1. 2D packing for r=1.5

Photo 2. 2D packing for r=7.1

2.2 Analysis Tools

2.2.1. Determining the porosity of 2D and 3D stacks by weighing. The method of measuring the porosity by weighing is very simple but it enables only the mean porosity of all the stack to be ascertained. In particular, it integrates the possible local variation of porosity due to the effects of the sides of the cell. The 2D porosities have been obtained by averaging the values found for 3 different stacks for each aspect ratio. The deviations from the mean value are smaller than 0.5%.

2.2.2. Determining the porosity and the local properties of 2D stacks by image processing. Image processing enables the local porosity of the system on a defined surface to be studied and then the problems due to the boundaries of the stack to be minimised. The images are processed and the two-dimensional porosity of the stack is given by the fraction number of black pixels over the total number of pixels of the complete image.

To obtain a porosity in a volume, it is necessary to apply a conversion factor to the result because fibres are cylinders and not parallelepipeds. We have assessed the porosities of the stacks in central rectangular windows of increasing sizes. As can be seen in Figure 1 and Figure 2, the curves which represent the variations of the porosity according to the size of the window have two distinct parts:

- a first part where the porosity varies noticeably.
- a second part where the porosity fluctuates around a mean value; the range of these fluctuations decreases when the area of the observation window increases.

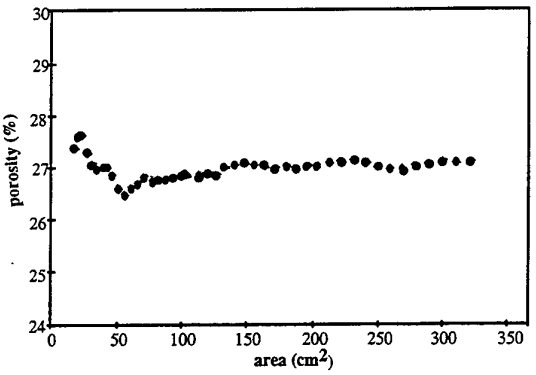


Fig. 1. Porosity for 2D packing versus the area of the observation window for r=1.5

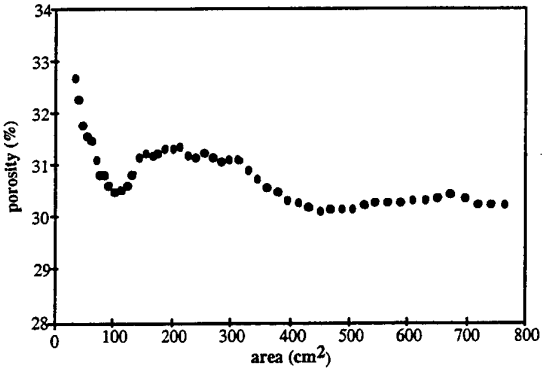


Fig. 2. Porosity for 2D packing versus the area of the observation window for r=5.0

So, we define the Elementary Representative Surface (ERS) as the smallest area for which the porosity becomes almost constant. In practice, the ERS is taken as the area after which the maximum deviation between two extreme values of porosity is less than one percent of the average of these values. Then, the mean porosity found by image analysis is defined as the average of the measured porosities for areas larger than the ERS. The dimensionless ERS (ERS^d) is defined as the fraction ERS over the apparent area of a fibre S_f (S_f = L x d). The ERS^d found for r=1.5, 3.0, 5.0, 7.1 and 10.1 is almost constant. For the studied range of aspect ratio, the ERS is equal to $300 \times S_f$.

$$ERS^d = \frac{ERS}{S_f} \approx 300 \qquad (1)$$

2.2.3. Comparison of the two methods. We have compared the two measuring methods through the values of porosity obtained by image processing and by weighing (Table 1).

Table 1. Comparison of the Porosities obtained by Image Processing and by Weighing

Aspect Ratio	Packing Area (cm^2)	Porosity by Weighting (%)	ERS (cm^2)	Porosity by Imag. Proc. (%)
1.5	800	27.3	120	27.05
3.0	810	28.6	180	27.6
5.0	1730	31.5	380	30.3
7.1	1730	34.0	490	33.6
10.1	1700	37.2	710	37.0

It can be seen that there is a good agreement. This seems to show that the cells used are large enough for the boundaries not to have a noticeable effect on the porosity determined by weighing. In these experiments, the total areas of packing are at least 2.4 times larger than the ERS.

3. EXPERIMENTAL POROSITIES

The values of the 2D porosities found by weighing and by image processing are represented in Figure 3. All these experimental points correspond to a single curve. 2D porosity is an increasing function of the aspect ratio. For an aspect ratio equal to 1.2, the porosity of the stack is equal to 26.5%. This stack can be considered as

dense. Indeed, for comparison, the lowest porosity for a compact packing of cylinders in 2D would be 21.5%. For high aspect ratios (r close to 50), the porosity is almost 50%.

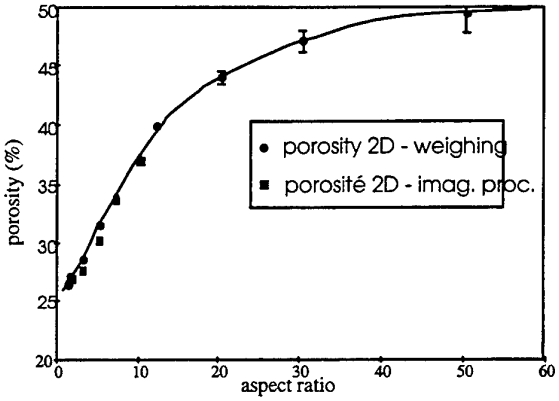


Fig. 3. 2D porosities (weighing and image processing)

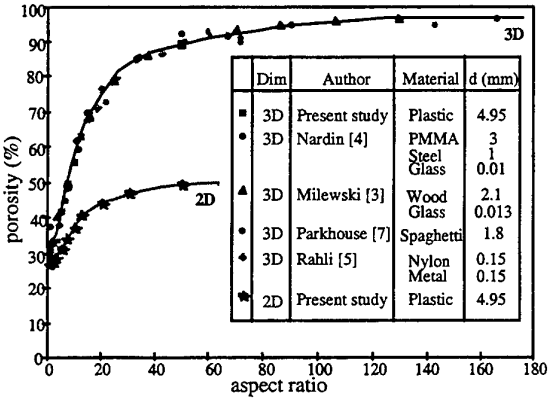


Fig. 4. 2D and 3D porosities

In the absence of a similar system to compare the variation law of the porosity found, we have established a parallel between 2D and 3D random packing of fibres. In Figure 4, the laws of variations are shown for the two types of stacks. We have also mentioned the results of the porosity measurements of 3D stacks found by Milewski [3], Nardin [4], Rahli [5] and Parkhouse [7] and we have specified the nature and the characteristics of the fibres used. It can be noted that for 3D stacks, our experimental plots are very close to the single curve found by the other authors.

The porosity variation laws for 2D and 3D structures are similar. Two behaviours can be observed:
- a noticeably linear variation with a high increase for aspect ratios lower than around 16.
- a zone where the increase is limited with an asymptotic trend for high values of r.

It can be seen that the porosity of 2D packing is lower than 3D packing. The deviation between the two curves increases with the aspect ratio.

4. ANALYSIS AND INTERPRETATION

There exists no theoretical porosity prediction model of a random packing of fibres. For 3D stacks, two semi-empirical models have been proposed by Parkhouse and Kelly and by Rahli.

The model of Parkhouse and Kelly [5], based on a statistical approach to the distribution of the pores in the stacks, leads to the following porosity law:

$$V_f \approx 2 \times \ln(r)/r \rightarrow \varepsilon \approx 1 - 2 \times \ln(r)/r \qquad (2)$$

Because of the assumptions made in this model, it is limited to 3D packing and cannot be applied to 2D stacks.

Rahli [6] proposes a porosity variation law based on the Excluded Volume model elaborated by Onsager [7]. This volume is defined as the mean portion of the space which one fibre excludes to the centre of the surrounding fibres. By dividing this volume by the volume of a fibre, the dimensionless Excluded Volume obtained can be written as following:

$$V_{excl}^{f} = \frac{\pi}{2r} + 6 + 2r \qquad (3)$$

Rahli proposes the following porosity law:

$$\varepsilon = 1 - \frac{n}{V_{excl}^{f}} = 1 - \frac{n}{\frac{\pi}{2r} + 6 + 2r} \tag{4}$$

where n is the equivalent number of fibres contained in the Excluded Volume. For 3D stacks, Rahli [6] finds that n is noticeably constant and almost equal to 11 for aspect ratios higher than 7 (Figure 5).

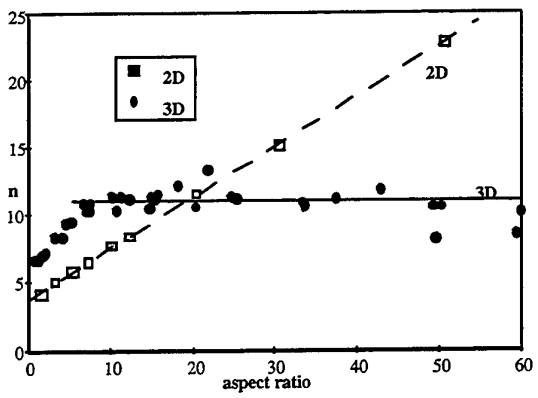


Fig. 5. number n of fibres in the excluded volume for 2D and 3D packing

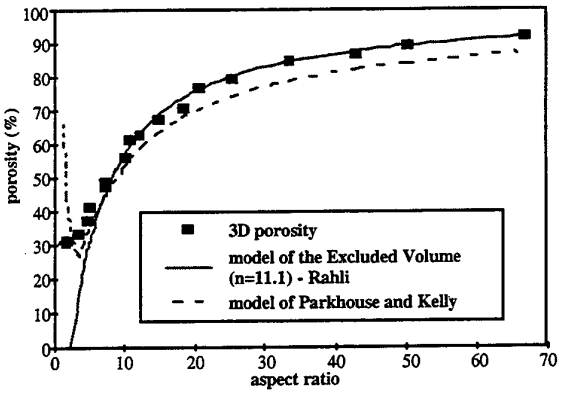


Fig. 6. 2 models of variations of porosity for 3D packing

The comparison between these two models and the experimental results shows a good qualitative concordance (Figure 6). Rahli's model gives correct results for aspect ratios higher than 7.

On the basis of these results, we have tried to apply the model of the Excluded Volume to random 2D packing. Thus, the porosity obtained for 2D stacks is:

$$\varepsilon = 1 - \frac{n}{V_{excl}^{f}} = 1 - n \times \left[\frac{8}{\pi} + \frac{16}{\pi^2} + \frac{8}{\pi^2} \times \left(r + \frac{1}{r} \right) \right]^{-1} \tag{5}$$

where n represents the equivalent number of fibres contained in the Excluded Volume. It would appear worthwhile to study the behaviour of n for 2D packing. Thus, from the experimental data of porosity we calculate the different values of n (Figure 5).

For the studied aspect ratio range, contrary to 3D packing, the parameter n is noticeably proportional to the aspect ratio.

Using the law found for n, the porosity variation according to the aspect ratio can be written as follows:

$$\varepsilon = 1 - \frac{n}{V_{excl}^{f}} = 1 - [0.376r + 3.861] \times \left[\frac{8}{\pi} + \frac{16}{\pi^2} + \frac{8}{\pi^2} \times \left(r + \frac{1}{r} \right) \right]^{-1} \tag{6}$$

In Figure 7, a good agreement can be noted between the measured values of the porosity and the values calculated with this equation. For values of r lower than 3, a small deviation appears. From this equation, we notice a limit of the porosity equal to 53.6% when the aspect ratio of the fibres tends to infinity. According to our experimental results, this limit seems reasonable. If this limit works really for high aspect ratio, it would differ significantly from the limit obtained for 3D packing which is equal to 100%.

The mechanisms of random fibres packing in 3D as well as in 2D cannot be understood from the different models which have been proposed. In Photos 1 and 2, we observe the existence of dense areas induced by

compact stacks and of loose zones due to faulty packing. The compact area is composed of a succession of fibres ordered in the form of bundles while the loose zone is characterised by faulty packing of one or several fibres. Porosity depends on two parameters: the size and the number of the pores. An observation of the stacks does not show up a characteristic pore for a given aspect ratio.

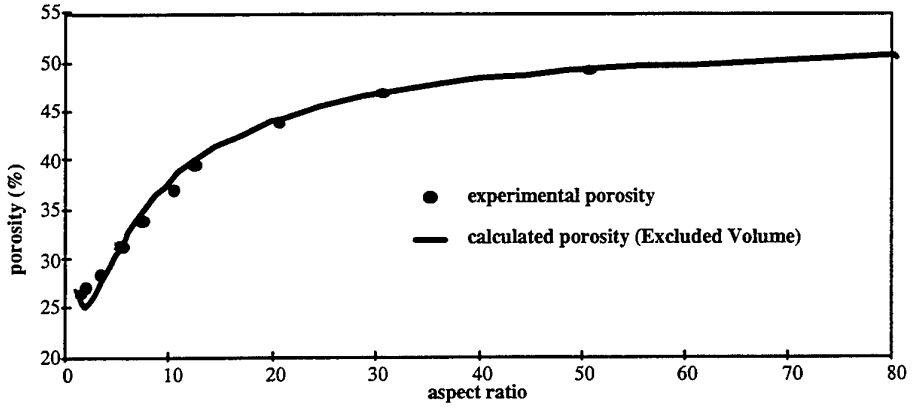


Fig. 7. Comparison of the experimental porosities and the porosities calculated with the excluded volume model for 2D packing

To estimate the influence of the size of the pores on the porosity according to the aspect ratio, a model defect formed by 4 fibres (Figure 8) was first considered. The elementary cell defined in this way occupies a volume equal to $(L+d)^2 \times d$.

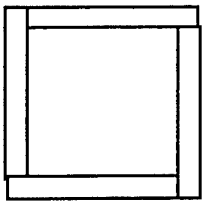


Fig. 8. Square elementary cell

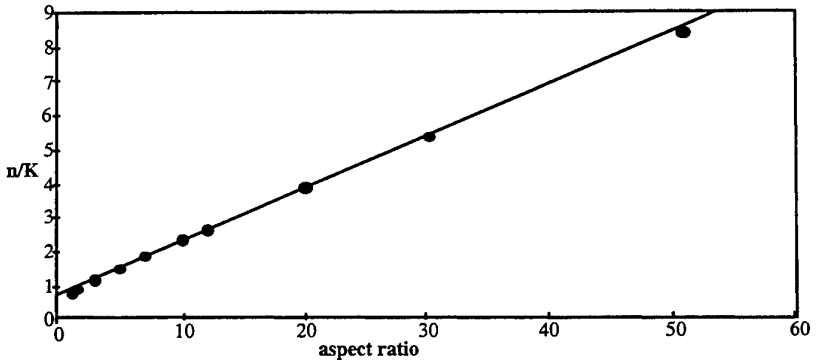


Fig. 9. Variation of n/K with the aspect ratio

To attempt to generalise this approach, the system is now divided into elementary cells whose shape is not defined precisely and whose volume is $K \times (L+d)^2 \times d$ (where K depends on the geometry of the system). Each of these cells contains a number n of fibres which includes among others the fibres ordered in bundles around the defect. The porosity evaluated in these elementary cells is:

$$\varepsilon = 1 - \pi \times \frac{n}{K} \times \frac{r}{(r+1)^2} \qquad (7)$$

Figure 9 shows that the values of n/K determined from our experimental porosities increase with the aspect ratio. So, it is essential to increase n and/or to decrease K. Indeed, according to Photos 1 and 2, it seems obvious that the geometry of the defects and thus the parameter K depend significantly on the aspect ratio of the fibres. So, it is very difficult to describe the system with only one geometry of the pores without taking into account the variation of the shape of the defects with the aspect ratio. An approach including the shapes, the sizes and the

number of the pores is necessary to uncorrelate the parameters K and n and then to predict the experimental porosity better.

5. LOCAL STRUCTURE OF 2D STACKS

To try to understand in a better way the local structure of 2D stacks, we have studied by image processing the densities and the sizes of the defects and the fibres orientations. So, the variations of the mean densities and of the mean sizes of the pores according to the aspect ratio of the fibres are shown in Figure 10 and Figure 11 and the corresponding fitting laws are given.

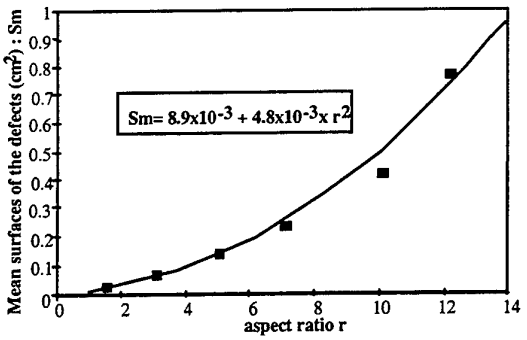


Fig. 10. Variation of the defects mean size with r

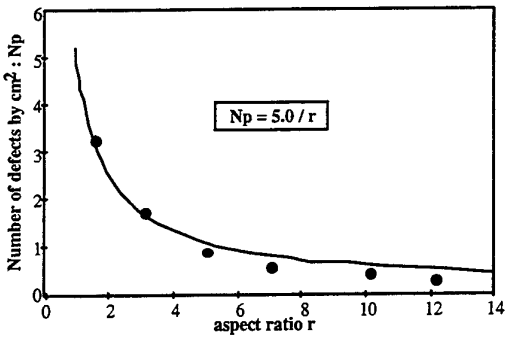


Fig. 11. Variation of the defects mean density with r

These laws show that the increase of porosity with the aspect ratio is due to the increase of the defects surface which is more important than the decrease of the defects density. However, these laws have been obtained experimentally for aspect ratios lower than 12 and the upper validity limit of these expressions is unknown.

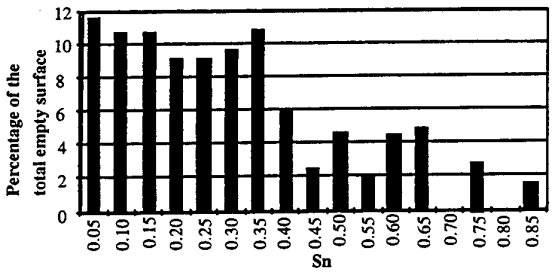


Fig. 12. Defects sizes distributions for r=1.5

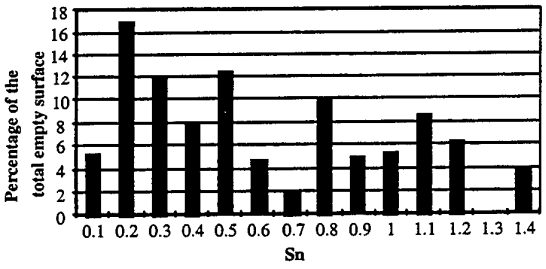


Fig. 13. Defects sizes distributions for r=10.1

An other way to characterise the defects consists in determining the pores sizes distributions. In Figure 12 and Figure 13, the percentage of the total empty surface is plotted versus the surface of the defects normalised by the surface of a fibre (Sn) for r=1.5 and r=10.1. From these histograms, we are not able to distinguish a main range of size of the defects.

Now, it would be interesting to evaluate the limit normalised size of the defects which contribute significantly to the porosity. So, we have defined the normalised surface Sn90 as follows:

The sum of the areas of all the defects having a size lower than Sn90 represents 90% of the total empty surface. The calculated values of Sn90 are given in Table 2.

Table 2. Variation of Sn90 with r

r	12.1	10.1	7.1	5.0	3.0	1.5
Sn90	1.8	1.1	1.0	1.0	0.9	0.6
Error on Sn90	0.2	0.1	0.2	0.1	0.1	0.1

From Table 2, we notice that Sn90 increases with the aspect ratio which means that when r increases, the normalised limit size of the pores which contribute to the porosity increases too.

These results on the variations of the densities and the sizes of the defects versus the aspect ratio show that it is very difficult to find a main class of defects.

Moreover, Photos 1 and 2 shows that 2D stacks are highly anisotropic, especially for the longer fibres. So, we have studied the distributions of the fibres orientations (0° corresponds to the horizontal axis). Three examples of distributions are shown in Figures 14, 15 and 16.

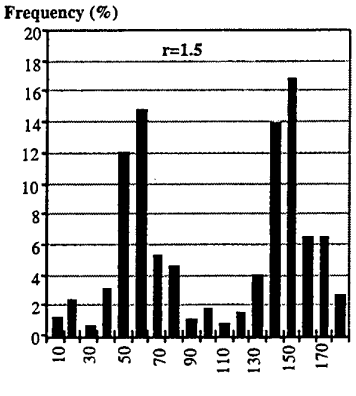


Fig. 14. Fibres orientations for r=1.5

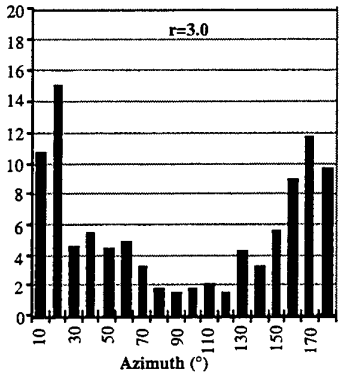


Fig. 15. Fibres orientations for r=3.0

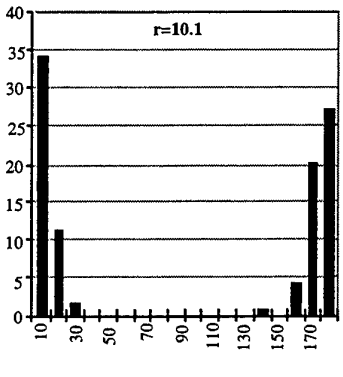


Fig. 16. Fibres orientations for r=10.1

From these figures, we notice that the mean orientation of the fibres decreases hardly with the aspect ratio: 47° for r=1.2, 31° for r=3, 9° for r=10. The standard deviation of the orientations decreases also with r. This behaviour is surely correlated to the variation of the defects geometry with the aspect ratio.

6. CONCLUSIONS AND PERSPECTIVES

The Elementary Representative Surface (ERS) for 2D stacks of fibres has been determined. We have shown that the dimensionless ERS does not depend on the aspect ratio. We have established an experimental law of porosity as a function of the aspect ratio of the fibres for 2D packing. This variation law is similar to the one corresponding to 3D packing. However, for the same aspect ratio, the 2D stack is more compact. The Excluded Volume model for 3D packing has been extended to 2D stacks. We have determined the variation law of the porosity versus r. The results obtained show that the behaviour of a 3D stack is different from that of a 2D stack. This approach predicts an asymptotic porosity limit equal to 53.6% unlike the 3D case where this limit was equal to 100%. On the basis of the simplified model developed, it seems that the variations of porosity according to the aspect ratio depend on the variation of the size and the shape of the defects which has been proved by our local analysis. However, these approaches do not help us to understand the fundamental mechanisms of fibres packing. In order to do this, a 2D fibres packing simulator is under construction. It corresponds to a next step of this work.

REFERENCES

1. J.V. Milewski, 28th Annual Technical Conference, Reinforced Plastics/Composites Institute, The Society of the Plastics Industry, Inc. (1973).
2. J.V. Milewski, Ind. Eng. Chem. Prod. Res. Dev., v. 17, 4, 363 (1978).
3. J.V. Milewski, Advanced Ceramic Materials, v. 1, 1, 36 (1986).
4. M. Nardin, E. Papirer, J. Schultz, Powder Technology, v. 44, 131 (1984).
5. O. Rahli, Ph.D. thesis, University of Provence, 1997.
6. L. Onsager, Annals New York, Academy of Sciences, 627 (1948).
7. J.G. Parkhouse, A. Kelly: The Random Packing of Fibres in Three Dimensions-Proc. R. Soc. Lond. A v. 451, 737 (1995).

FLOW REGIONS OF GRANULES IN DORFAN IMPINGO FILTER FOR GAS CLEANUP

Jing-T. Kuo, Jiri Smid
Department of Mechanical Engineering
National Taiwan University
Taipei, Taiwan 10617, R.O.C.
Email: jtkuo@w3.me.ntu.edu.tw; FAX: (886) 2-2363-1755

Shu-San Hsiau, Hsien-Hsin Tsai
Department of Mechanical Engineering
National Central University
Chung-Li, Taiwan 32054, R.O.C.
Email: sshsiau@cc.ncu.edu.tw; FAX: (886) 3-426-7341

Chuen-Shii Chou
Department of Mechanical Engineering
National Pingtung University of Science and Technology
Ping-Tung, Taiwan 91207, R.O.C.
Email: cschou@mail.npust.edu.tw; FAX: (886) 8-774-0142

Keywords: Flue gas cleanup, moving bed filter, granular flow

ABSTRACT. Inside a two-dimensional model of the louvered Dorfan Impingo panel with transparent front and rear walls, the flow regions of filter granules without gas cross flow were observed. The white PE beads with diameter of 6 mm were used as filter granules. The red colored PE beads were used as tracers. The filter bed was filled with beads continuously and gently levelled above. Then the layer of colored beads was poured on the horizontal top surface. Filter granules were discharged and circulated to the bed. The flow rate of granules was controlled by the belt conveyer. The image processing system including a frame grabber and a JVC videocamera was used to record the granular flow. Every image of motion was digitized and stored in a computer file. Four different flow regions in moving granular bed were observed: a) a quasi-stagnant zone adjacent to the louver wall; b) a transition region - a shear zone in which large velocity changes occurred at each horizontal level; c) a central flowing core of near uniform velocity distribution with a plug flow pattern; and d) the left and right free surface regions where gas flows in and out. The velocity field of filter granules was evaluated and analyzed. The velocity profiles of the vertical and horizontal velocity components were investigated.

1. INTRODUCTION

In recent years, the development of new approaches to generation of electric power from coal – notably by combined cycle processes using pressurised fluidised bed combustion or gasification – has reawakened interest in the problems of cleaning gases at high temperatures. In these processes, the gases obtained from the coal must be expanded through a gas turbine. Therefore they must be cleaned, so as to reduce problems of erosion, fouling and hot corrosion in the turbine, and this cleanup must be carried out without cooling the gases so that the cycle efficiency is not impaired. Conventional technology cannot provide the solution. Thus gas cleaning at high temperatures has emerged as a new technological process in energy engineering. The requirements for coal–based power plant have led the developments, because they represent generally the most difficult process conditions and the tightest limits on gas cleanliness. However, there are many other industries where there is an incentive to extend the range of process conditions under which gas cleaning can be carried out; obvious examples are manufacture of cement and building products and metallurgical industries. Beds of granular solids have been employed for dust collection for many years [1], but the subject has gained recent prominence as a possible means of simultaneously removing fly ash and sulfur dioxide from powerplant flue gases at temperatures in excess of 400°C.

The Dorfan Impingo filter [2, 3] was offered commercially as a dust collector in the 1950's. This filter was described in its old advertising literature as being used, for example, for the collection of asbestos dust during

drying at several Canadian installations, for collecting dust, fumes and steam arising from coking operations, and for collecting fumes arising from steel production in an electric furnace. The device was a vertical panel filter using rocks of 1.3 cm to 3.8 cm as filter media, -see Fig. 1. The filter media continuously fell through two narrow panels where they were contacted by a cross flow stream of dust-laden gas. These panels had constantly increasing cross-sectional area. The tapering construction acted to prevent hangs-up caused by increasing size of filter media as the dust builds up on them. Also, the collected dust particles increase the cohesion between filter media, thus the tapered filter channel is helpful for the ease of gravity flow of moving bed in the louvered panel. The average panel thickness was 30 cm.

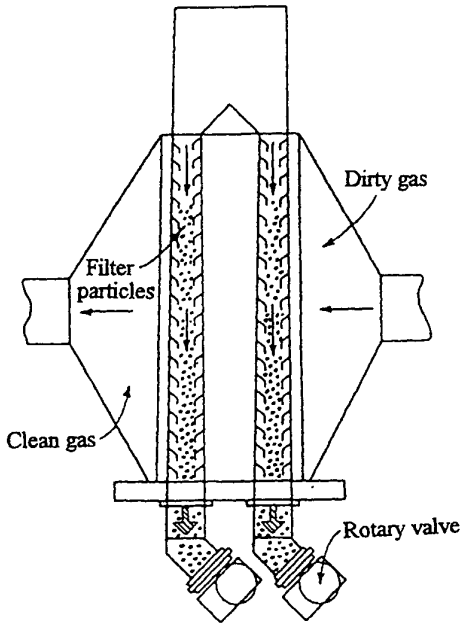


Fig. 1. The Dorfan Impingo cross-flow moving bed filter (Perry and Chilton, 1973)

The filter media flow rate was controlled by the setting of a rotary valve located near the bottom of the shaft. The dusts were then separated from the filter rocks by screening or other means. Two separate filtering louvered shafts in series were used in device. The inventor [4] stated that the efficiency was 98% for 2 to 10 μm dust particles carried by the flue gas at a superficial velocity of 1.8 m/s. Apparently, the shape and configuration of the louvers are design features that need special attention. Louvers properly designed can prevent a dense cake from forming on the panel face which may cause plugging, arching and stoppage of filter media flow [5]. These problems could cause excessive pressure drops and hampering the continuous filter operation. Moving granular bed filtration requires a filter design that puts no restrictions to the flow of filter media between the louvered walls. For the cross flow moving bed Dorfan Impingo filter, this implies that the filter media should be discharged at a continuous rate from short convergent-straight channel formed by the pair of louvers.

There are also many filters other than the Dorfan design operated on a similar concept but with different system configurations and louver designs. One notable example is the earlier model of Combustion Power Company's moving granular bed filter [6-8]. In a previous work [9] we have studied the flow patterns of filter granules between walls formed by several pairs of louvers with various configurations. A main finding of the previous work is that stagnant and quasi-stagnant zones could exist in regions adjacent to the louvers. The forming of stagnant zones is considered negative to the filter operation as far as plugging is concerned.

This paper presents the result of a study of the flow patterns in a 2-D cross flow moving bed of noncohesive granular solids flowing under steady state conditions between two vertical louvered walls of the Dorfan Impingo filter with no interstitial fluid flow relative to the solids. The objective of this study is to investigate the flow

patterns and velocity field of filter granules in Dorfan Impingo moving bed filter.

2. EXPERIMENTAL APPARATUS AND PROCEDURES

For the observation of the flow patterns occurring as the granular bed flows continuously, an experimental technique with differentially colored granules has been used. The model of the experimental moving bed is two-dimensional. It consists of a narrow layer of particulate material sandwiched between two transparent panels with louver-like side walls. The configuration of the louvers can be changed (louver spacing, louver angle and length etc.). The experimental apparatus is schematically shown in Fig. 2.

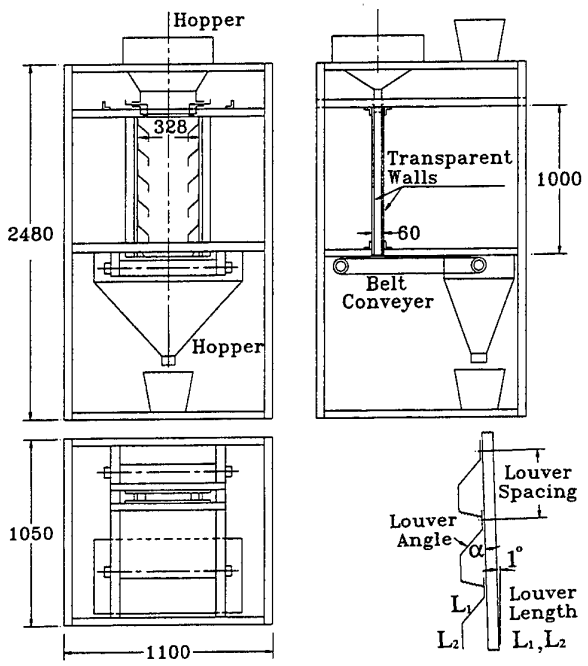


Fig. 2. The schematic drawing of the experimental apparatus

The flow of granular solids is induced and controlled by a moving belt underneath the granular bed. Granules are fed into the vertical channel from a top hopper which has a rectangular discharge slot of the same cross-section as the vertical channel. The height of the channel is fixed (1000 mm) but the width is adjustable (maximum width is 400 mm). The channel width in the experiment mentioned in this work is 328 mm at the upper part and the louvered walls are tapered with wall inclination 1° -see Fig. 3. For the experiments we have selected 6 mm diameter PE spheres with density of 964 kg/m^3 as granular solids. Packing of the spheres was characterized by the bulk density measurements. Two bulk densities were measured: a poured bulk density of 582 kg/m^3 (porosity 0.396) and a tapped bulk density of 600.5 kg/m^3 (porosity 0.377). Both densities were measured in a graduated glass cylinder. The mass flow rate measurements were made by continuous collection of the discharged granules in a tarred bucket. Weighing of full buckets was made with an electronic balance. The mass flow rate of 3.52 g/s was used in this study.

Figure 3 shows the louver geometry of the test conditions in Dorfan Impingo model filter. The louver angle of Dorfan Impingo filter was not found in the literatures, but according to the pictures it was guessed to be around 50 degrees. This is the reason why 50-degree louver angle was used in our test model. Also, after some recalculations of dimensions in different schematic drawings, the increase of filter channel width B is determined to be about 1° in slope.

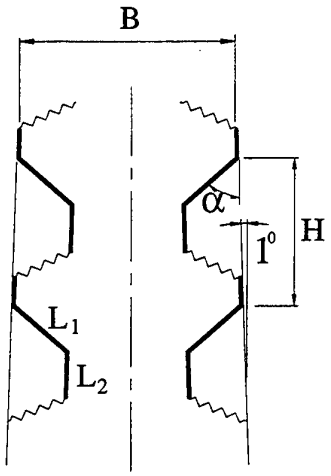


Fig. 3. The louver geometry for the test conditions

$B = 328$ mm, $L_1 = 96$ mm, $L_2 = 65$ mm, $H = 200$ mm, $\alpha = 50^0$

During filling the granular bed, the colored granules were filled in one louver section as shown in Fig. 4. In the course of the experiment, the filter channel was filled from a top hopper, which always contained an inventory of filter granules to ensure continuous supply during the experiment. Filter granules were circulated for approximately two hours to make certain that the flow has reached steady state conditions (meaning steady state bulk density distribution, flow patterns etc.). A JVC video camera was used to record the development of the flow of colored granules until the colored particles left the granular bed completely. The camera was supported on a sturdy tripod and activated several seconds before the flow of granules was started. A Dipix P360F power grabber was used to grab flow images from the recorded tape.

For the velocity measurements, a volume of 20% differentially colored granules uniformly dispersed in the moving bed were used as tracers. The steady flow of the colored granules was recorded by the video camera for about one hour. By identifying the positions of every tracer in the consecutive images, the granule displacements could be measured. Dividing the displacements by the time between two images, the individual granule velocities could be found. The flow region was divided into approximate 500 to 600 subregions depending on the louver configurations. The mean velocity in each subregion was calculated from averaging the whole tracer velocities found within the subregion. Hence the velocity field of the granular flow could be plotted.

3. FLOW REGIONS OF FILTER GRANULES

Figure 4 shows the flow history of the colored granules in eighteen frames under the test conditions. Frame 1 shows the beginning of the experiment. The time interval for frames 1 to 13 is 120 seconds. The frames following frame 13 have progressively longer time intervals. Four different flow regions were found between convergent part of the louver section:

(1) A quasi-stagnant zone adjacent to the louvered wall. The development of this zone became clear when the granular bed is circulated for about 6 minutes (see Fig. 4 frames 3 and 4). Afterwards, see Fig. 4, frames 4 to 17, the quasi-stagnant zone diminishes gradually when the model filter is operated for a long time. A new bed structure and porosity is developing in this zone as filter granules flow out from upper pair of louvers filling the underneath louver sections. Frame 18 shows that even after circulating the bed granules for almost 11 hours, the trace of this zone is still visible.

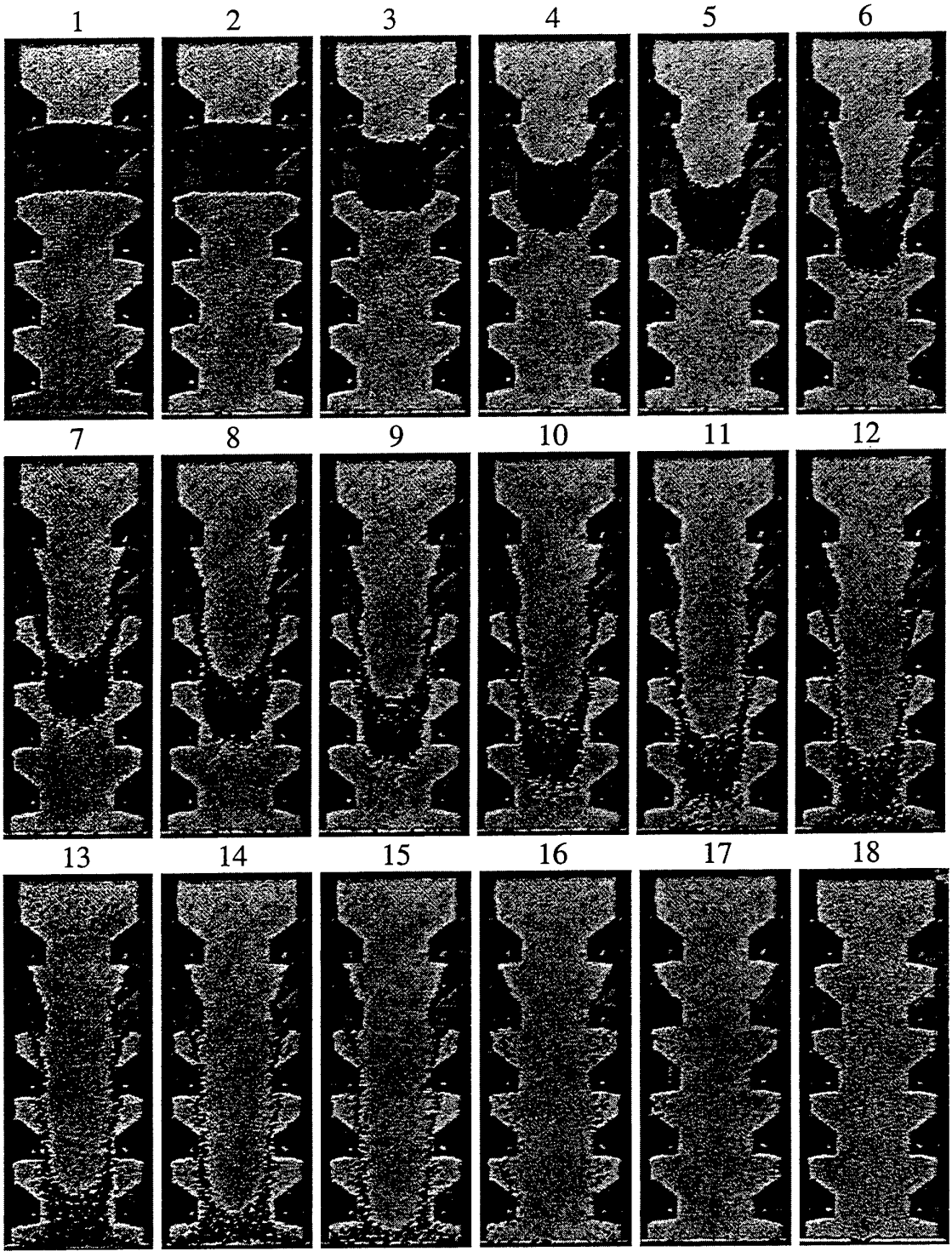


Fig. 4. Flow patterns of granules in the tapered channel of Dorfan Impingo filter. Frames 1-15, time interval 2min; frame 16, time 90 min; frame 17, time 270 min; frame 18, time 643 min

(2) A transition region between the quasi-stagnant zone and a central flowing core. In Fig. 4, the development of this region is clearly seen in frames 5 and after. Actually this region started to develop once the granules

began flowing. This is a shear zone with movement of filter granules one next to another and with significant velocity changes from point to point over a small horizontal distance. The distribution of inter-granular friction forces cause the granules to move in such a way that the boundary between the quasi-stagnant zone and this region slowly dispersing toward the walls. Taking the third pair of louvers for example, the influence of the moved granules eventually reached the granules adjacent to the walls. The movements of the granules in frames 5 to 13 indicate that granules are moving predominantly in vertical direction with relatively small horizontal dispersion. It is shown clearly in these frames that there is a cascading granular transport in the transition regions at different louver sections of the granular bed from top to bottom. Granules flow from upper transition region into the underneath transition region.

(3) A central flowing core with a plug flow. There are small velocity fluctuations about the average plug velocity [10]. The boundary between the central flowing core of filter granules and the transition region is slightly curved outwards.

(4) Left and right free surface regions. These free surfaces are not characterized by a unique angle of repose, but by a minimum angle of repose and an angle of maximum free surface stability. The angle of free surface of filter granules oscillates between these angles. It leads to avalanches of filter granules over the free surfaces. When the angle of free surface drops below the minimum angle of repose, the new filter granules will roll down the slope of free surface until the angle of maximum stability is restored.

The flow of granules between the short straight part of the louver section exhibited plug flow pattern with very thin wall layer of lower velocities. This straight part has very little overall effect on the movement of granules.

4. VELOCITY FIELD IN MOVING BED

Figure 5 show the velocity field of granules during the steady state flow period of velocity measurements. The symbols of X and Y represent the horizontal and vertical coordinates. The regions adjacent to the louver walls in Fig. 5 where no velocity vectors are shown indicate that the granule velocities in these areas are negligible as mentioned in the above section. The quasi-stagnant zones exist close to the louver walls.

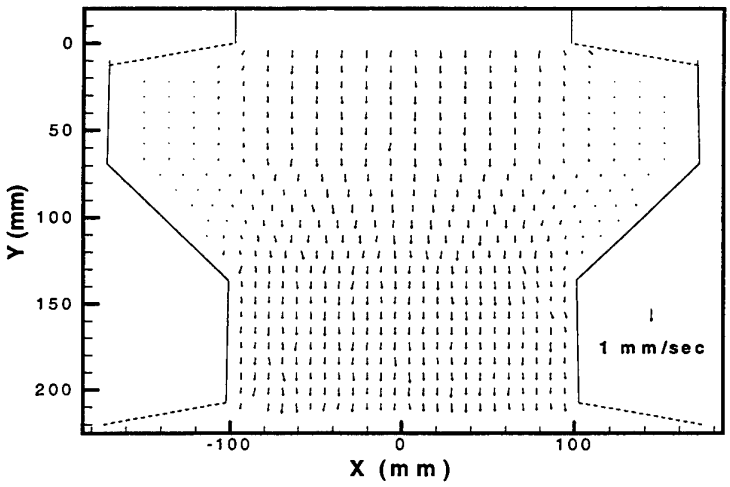


Fig. 5. Velocity vectors of granules in the louvered channel of Dorfan Impingo filter, wall inclination 1°

From Fig. 5, the quasi-stagnant zones are symmetric in the test because the louver configuration in this system is symmetric. The central plug flow zone has uniform granule velocities, which are substantially higher than the granule velocities in quasi-stagnant zones. The width of the central plug flow zone is approximately equal to the width of the straight channel between pair of louvers. The quasi-stagnant zone does not exist along the louver wall of straight channel. Nevertheless the granule velocities along the straight louver walls are less than the plug flow velocity.

For the filter operation, the sufficiently large free surface of filter granules is very important, because it is the effective area of contacts between dust particles and filter granules. Also, to avoid the plugging problems, it is necessary that the filter granules in free surface region have to be moved in order to transport the adhered dust particles out of the filter bed. Unfortunately in Dorfan Impingo filter, the free surface is just located in the quasi-stagnant zone, so the dust particles cannot be transported efficiently which may results in serious plugging problems. The flow regions described in Fig. 5 indicate that only the filter granules in the central flowing core can be moved and circulated but without efficient contacts with dust particles. So the plugging problem and the inefficient circulation of filter granules seem to be the major drawbacks of this Dorfan Impingo filter design. The dirty filter granules are removed from the moving bed to be cleaned. Then they can be used again. This circulation process is called refreshing of filter granules. For the moving bed filter operation, the granules refreshing rate is an important design parameter. The granules refreshing rate can be determined by the time required to completely replace the whole moving granular bed with a new batch of circulated particles.

5. VELOCITY PROFILES IN MOVING BED

Figures 6 and 7 show the vertical and horizontal velocity distributions at five different horizontal levels in a louver section. The curves in Figs. 6 are fitted by the second order polynomials from the original data extracted from Fig. 5. Each error bar indicates the root of the mean square deviation of the original data from the corresponding fitted curve for every 5 data points. The levels 'a' and 'e' denote the inlet and outlet of the louver section. It means the curve of level 'a' is evaluated from the velocity vectors underneath the line 'a.' On the other hand, the curve of level 'e' is evaluated based on the data above of the horizontal line 'e.'

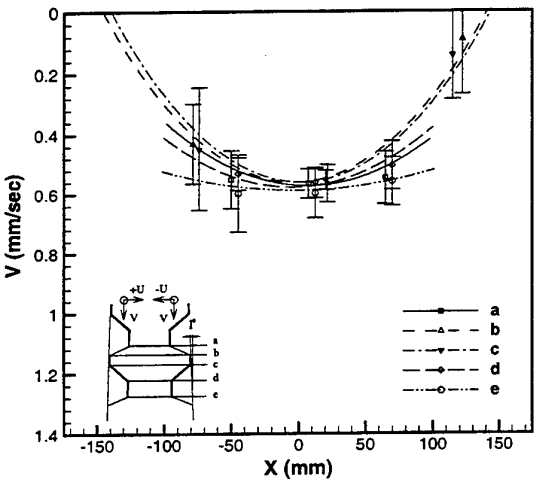


Fig. 6. The five vertical velocity profiles of granules in the louvered channel of Dorfan Impingo filter

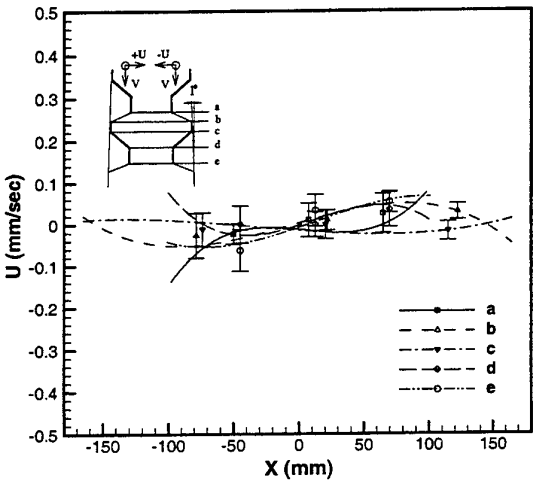


Fig. 7. The five horizontal velocity profiles of granules in the louvered channel of Dorfan Impingo filter

The horizontal velocity distributions shown in Fig. 7 are fitted by the third order polynomials from the original data extracted from Fig. 5. The error bars have the same meaning as those in Fig. 6. The curves in Fig. 7 are horizontally S shaped. This shape indicates the convergent/divergent streamlines of the filter granules. The S shapes are diverging flow type for levels 'a' and 'c.' In levels 'd' and 'e,' the opposite S shaped curves indicate clearly the converging flow. The horizontal velocity distribution in level 'b' is relatively flat.

6. CONCLUSIONS

The typical Dorfan Impingo louver configuration with tapered filter channel was tested in this study. The flow patterns and the velocity field show that the larger quasi-stagnant zones exist close to the louvers. Only central stream of filter granules is in uniform motion. But the central granular stream is almost isolated from the coming flue gas by the quasi-stagnant zones. These zones between the louvers and the central flowing core look similar

to the pockets of static granules or dead zones.

From the point of view of the mechanics of granular flows, this Dorfan Impingo filter has a too large louver angle resulting in the large quasi-stagnant zones. The very low velocity of filter granules in the quasi-stagnant zones causes the accumulation of dust coming with hot flue gases along the free surface of filter granules. When the layer of dust gathered above the free surface in the gas inlets is thick enough, the plugging will increase the pressure drop in the moving bed filter and the process of the filtration has to be stopped. For an efficient design of filter channel, the flow properties of filter granules, the wall friction and the louver angle are important parameters. In a real design of moving bed filters with louvered channel, the flow properties of mixture of filter granules with dust (fly ash) should be considered.

ACKNOWLEGEMENTS

The authors gratefully acknowledge the financial support from the National Science Council of the R.O.C. for this work through project NSC 87-2211-E-008-016. Special financial support from National Science Council of the R.O.C. for one of the author (J. Smid, Czech Republic) is also appreciated.

REFERENCES

1. J. T. Kuo, J. Smid, S. S. Hsiau and C. S. Chou, Proc. Natl. Sci.. Counc. ROC(A) v.22, pp. 17-34 (1998).
2. Avco Co., *Final Report. Contract No. PH-86-67-51, Phase III, AVATD-0107-67-RR.* pp. 8-9, 48, 67-68, U.S. Department of Commerce, Publication PB 185561, June 1969. Submitted by Advanced Chemical Process Section, Avco Applied Technology Divison, Lowell, Massachusetts 01851, USA (1969).
3. R. H. Perry, and C. H. Chilton, (Eds.), *Chemical Engineers' Handbook*, 5th ed., McGraw-Hill Book Co., New York, pp. 20-87 (1973).
4. M. I. Dorfan, M. I., "Method and Apparatus for Suppressing Steam and Dust Rising from Coke Being Quenched," U. S. Patent 2,604,187 (1952).
5. A. M. Presser and J. C. Alexander, *Symposium on Transfer and Utilization of Particulate Control Technology*, Vol. IV, Atypical Application, EPA-600/9-82-005d, pp.26-35 (1982).
6. R. G. Reese, Tappi (Journal of the Technical Association of the Pulp and Paper Industry) v. 60, pp. 109-111 (1977).
7. S. C. Saxena, R. F. Henry and W. F. Podolski, Prog. Energy Combust. Sci., v. 11, pp. 193-251 (1985).
8. J. L. Guillory, F. M. Placer and D. S. Grace, Environment International v. 6, pp. 387-395 (1981).
9. J. T. Kuo, J. Smid, S. S. Hsiau, C. Y. Wang and C. S. Chou, Filtration and Separation v. 35, pp. 529-534 (1998).
10. S. S. Hsiau, J. Smid, C. Y. Wang, J. T. Kuo, and C. S. Chou, Chemical Engineering Science, v. 53, pp. 293-301 (1998).

EFFECT OF HOMOGENEOUS AND HETEROGENEOUS SOURCE TERMS ON THE MACROSCOPIC DESCRIPTION OF HEAT TRANSFER IN POROUS MEDIA

Michel Quintard
Institut de Mécanique des Fluides de Toulouse
Allée du Professeur Camille Soula, 31400 TOULOUSE – France
Email: quintard@imft.fr; Fax: +33 5 61 28 58 78

Bruno Ladevie
Ecole des Mines d'Albi Carmaux
Centre Energétique Environnement, Campus Jarlard, 81000 Albi - France
Email: ladevie@enstimac.fr, Fax: +33 5 63 49 30 99

Stephen Whitaker
Department of Chemical Engineering
University of California at Davis, Davis, CA 95616 - U.S.A
Email: swhitaker@ucdavis.edu, Fax: +1 916 752 10 31

Keywords: porous medium, heat transfer, heat sources, averaging

ABSTRACT. Heat transfer in a porous medium subjected to the effect of internal heat sources is considered. Macroscopic equations are obtained from the method of volume averaging. Both local equilibrium and non-local equilibrium conditions are considered. It is shown that homogeneous sources can simply be taken into account by introducing averaged values in the macroscopic equations. The heterogeneous source term corresponding to heat sources at the interface between the two phases requires a different treatment. The average source is distributed in the two macroscopic equations of the local non-equilibrium model through a distribution coefficient, which is given by a local "closure problem". This closure problem is solved numerically for different representative unit cells, and for different values of the thermal conductivity ratio and Péclet number. Numerical experiments are performed to test the theory, and results show a good agreement between theoretical and "experimental" predictions.

1. INTRODUCTION

In this paper, heat transfer in a porous medium, or a two-phase system, is considered with internal homogeneous and heterogeneous sources. The system under consideration is illustrated in Fig. 1. Fluid and solid properties are assumed to be constant.

The pore-scale governing equations are the following

$$\nabla \cdot \mathbf{v}_\beta = 0, \quad \text{in the } \beta\text{ - phase} \tag{1}$$

$$(\rho c_p)_\beta \frac{\partial T_\beta}{\partial t} + (\rho c_p)_\beta \mathbf{v}_\beta \cdot \nabla T_\beta = \nabla \cdot \left(k_\beta \nabla T_\beta\right), \quad \text{in the } \beta\text{ - phase} \tag{2}$$

B.C.1 $$T_\beta = T_\sigma, \text{ at } A_{\beta\sigma} \tag{3}$$

B.C.2 $$\mathbf{n}_{\beta\sigma} \cdot k_\beta \nabla T_\beta = \mathbf{n}_{\beta\sigma} \cdot k_\sigma \nabla T_\sigma + \Omega, \text{ at } A_{\beta\sigma} \tag{4}$$

$$(\rho c_p)_\sigma \frac{\partial T_\sigma}{\partial t} = \nabla \cdot \left(k_\sigma \nabla T_\sigma\right) + \Phi_\sigma, \text{ in the } \sigma\text{ - phase} \tag{5}$$

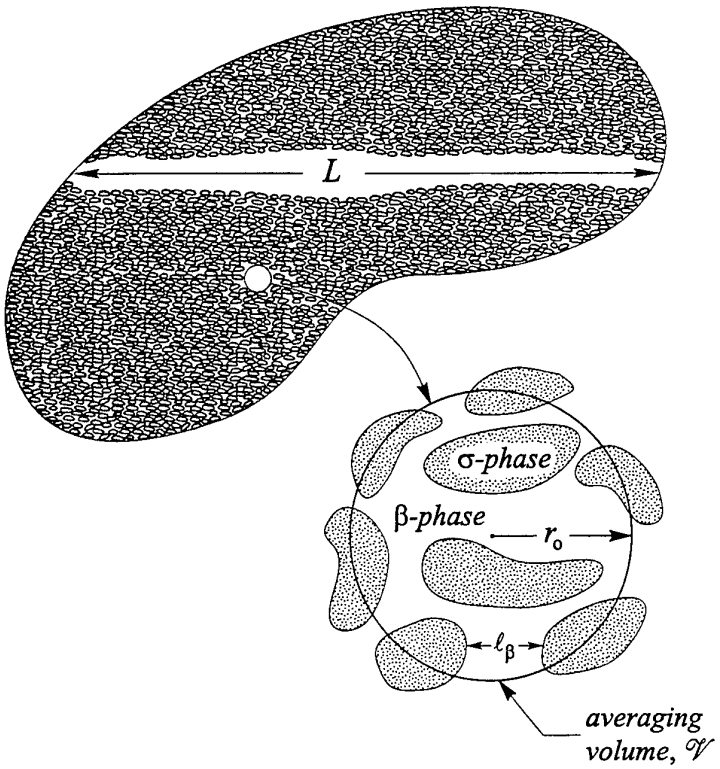


Fig. 1. Averaging volume in a porous medium

$$\rho_\beta \frac{\partial \mathbf{v}_\beta}{\partial t} + \rho_\beta \mathbf{v}_\beta \cdot \nabla \cdot \mathbf{v}_\beta = -\nabla p_\beta + \rho_\beta \mathbf{g} + \mu_\beta \nabla^2 \mathbf{v}_\beta, \text{in the } \beta\text{-phase} \tag{6}$$

B.C.3 $$\mathbf{v}_\beta = 0, \text{at } A_{\beta\sigma} \tag{7}$$

In these equations, $\mathbf{v}_\alpha$, T_α , p_α , $(\rho c_p)_\alpha$, k_α are the velocity, the temperature, the pressure, the heat capacity and the thermal conductivity of the α-phase respectively. The homogeneous source term is Φ_σ, and the heterogeneous source term is characterized by Ω. No source term is included in the β-phase, but this would not pose any additional difficulties. In these equations, $A_{\beta\sigma}$ represents the area of the interface between the two phases.

The momentum equations can be solved independently, and this would lead to the introduction of Darcy's law at the macroscopic level as discussed from the point of view of the volume averaging technique in [1]. In the sequel of the paper, $\mathbf{v}_\beta$ is assumed to be a known field. The problem of describing macroscopically heat transfer in such systems has been discussed in many papers [2,3,4,5,6]. Several questions have been addressed comprehensively such as the problem of local and non-local equilibrium, and the calculation of the effective properties found in the macroscopic equations.

The problem of the impact of the heat source terms has received less attention, and this is the subject of this paper, following ideas that have been presented in [7]. First we review the introduction of macroscopic equations from the point of view of the method of volume averaging. Then, we show how the heat source terms are included in the equations, and how the associated effective properties can be calculated. In the last section, we present some numerical results for the distribution coefficient that appears in the two-equation model associated with the heterogeneous heat sources.

2. AVERAGED EQUATIONS

In this paper, we adopt the point of view of the method of volume averaging, and averages are defined according to

$$\langle \psi_\beta \rangle = \frac{1}{V}\int_{V_\beta} \psi_\beta dV = \frac{V_\beta}{V}\frac{1}{V_\beta}\int_{V_\beta} \psi_\beta dV = \varepsilon_\beta \langle \psi_\beta \rangle^\beta \tag{8}$$

where ε_β is the β-phase volume fraction.

The pore-scale temperature fields are obtained by introducing the following decomposition

$$\psi_\beta = \langle \psi_\beta \rangle^\beta + \tilde{\psi}_\beta \tag{9}$$

From the pore-scale equations we obtain after some mathematical manipulations the two averaged equations that are given below

$$\underbrace{\varepsilon_\beta (\rho c_p)_\beta \frac{\partial \langle T_\beta \rangle^\beta}{\partial t}}_{\text{accumulation}} + \underbrace{\varepsilon_\beta (\rho c_p)_\beta \langle v_\beta \rangle^\beta \cdot \nabla \langle T_\beta \rangle^\beta}_{\text{concection}}$$
$$= \underbrace{\nabla \cdot \left[k_\beta \left(\varepsilon_\beta \nabla \langle T_\beta \rangle^\beta + \frac{1}{V}\int_{A_{\beta\sigma}} \mathbf{n}_{\beta\sigma} \tilde{T}_\beta dA \right) \right]}_{\text{conduction}} - \underbrace{(\rho c_p)_\beta \nabla \cdot \langle \tilde{v}_\beta \tilde{T}_\beta \rangle}_{\text{dispersion}} + \underbrace{\frac{1}{V}\int_{A_{\beta\sigma}} \mathbf{n}_{\beta\sigma} \cdot k_\beta \nabla T_\beta dA}_{\text{interfacial flux}} \tag{10}$$

for the β-phase, and

$$\underbrace{\varepsilon_\sigma (\rho c_p)_\sigma \frac{\partial \langle T_\sigma \rangle^\sigma}{\partial t}}_{\text{accumulation}} = \underbrace{\nabla \cdot \left[k_\sigma \left(\varepsilon_\sigma \nabla \langle T_\sigma \rangle^\sigma + \frac{1}{V}\int_{A_{\sigma\beta}} \mathbf{n}_{\sigma\beta} \tilde{T}_\sigma dA \right) \right]}_{\text{conduction}}$$
$$+ \underbrace{\frac{1}{V}\int_{A_{\sigma\beta}} \mathbf{n}_{\sigma\beta} \cdot k_\sigma \nabla T_\sigma dA}_{\text{interfacial flux}} + \underbrace{\varepsilon_\sigma \langle \Phi_\sigma \rangle^\sigma}_{\substack{\text{homogenous} \\ \text{thermal source}}} \tag{11}$$

for the σ-phase.

From these equations we see a major difference between the two types of heat sources. The homogeneous heat source appears as a simple averaged value, while the heterogeneous source will have a complicated impact on the interfacial fluxes. While the amount of energy produced by this heterogeneous source is also a simple averaged value, the way it is distributed between the two phases is the problem to be solved if one wants to obtain macroscopic equations.

Since the temperature deviations appear in the averaged equations, we need governing equations for these pore-scale fields. They are obtained by introducing the temperature deviations into the pore-scale equations and boundary conditions. We do not list the whole system of equations (indications on how to deal with such problems can be found in [7]). To illustrate the problem to be solved, we give the equation associated with the σ-phase

$$(\rho c_p)_\sigma \frac{\partial \tilde{T}_\sigma}{\partial t} = \nabla \cdot \left[k_\sigma \nabla \tilde{T}_\sigma\right] - \nabla \cdot \left[k_\sigma \left(\frac{1}{V_\beta} \int_{A_{\sigma\beta}} \mathbf{n}_{\sigma\beta} \tilde{T}_\sigma dA\right)\right]$$
$$-\frac{1}{V_\beta} \int_{A_{\sigma\beta}} \mathbf{n}_{\sigma\beta} \cdot k_\sigma \nabla \tilde{T}_\sigma dA - \frac{1}{V_\beta} \int_{A_{\sigma\beta}} \mathbf{n}_{\sigma\beta} \cdot k_\sigma \nabla \langle T_\sigma \rangle^\sigma dA + \tilde{\Phi}_\sigma \tag{12}$$

In this equation, we see different source terms involving the gradient of the averaged temperature, the deviation of the homogeneous source term. This last term is zero if the source term is constant, or it will be negligible for sufficiently small non-linearities within the averaging volume. Therefore, the closure problem, which represents an approximate solution of the coupled equations for the averaged temperatures and deviations, *will not depend on the homogeneous source term.* The induced effective properties will not be influenced either. The developments presented in this paper will show that the treatment of the heterogeneous source term is more complicated.

One-equation Model

In the case of local equilibrium, i.e., $\langle T_\beta \rangle^\beta = \langle T_\sigma \rangle^\sigma = \langle T \rangle$, an approximate solution is obtained by introducing the following mapping relations

$$\tilde{T}_\beta = \mathbf{b}_\beta \cdot \nabla \langle T \rangle, \qquad \tilde{T}_\sigma = \mathbf{b}_\sigma \cdot \nabla \langle T \rangle \tag{13}$$

in which the mapping variables are given by a "closure problem" which can be found in [5]. The averaged equations can be added to obtain the following local-equilibrium one-equation model

$$\langle \rho \rangle C_p \frac{\partial \langle T \rangle}{\partial t} + \varepsilon_\beta (\rho c_p)_\beta \langle v_\beta \rangle^\beta \cdot \nabla \langle T \rangle = \nabla \cdot \left(\mathbf{K}^* \cdot \nabla \langle T \rangle\right) + a_v \langle \Omega \rangle_{\beta\sigma} + \varepsilon_\sigma \langle \Phi_\sigma \rangle^\sigma \tag{14}$$

where a_v is the specific area and $\langle \Omega \rangle_{\beta\sigma}$ is the area averaged value of the heterogeneous thermal source. Here the heat capacity per unit volume is given by

$$\langle \rho \rangle C_p = \varepsilon_\beta (\rho c_p)_\beta + \varepsilon_\sigma (\rho c_p)_\sigma \tag{15}$$

and the effective thermal diffusion tensor $\mathbf{K}^*$ is given explicitly in terms of the mapping variables (see [5]). In the local-equilibrium model, the heterogeneous source is included in a simple manner as an average value in the macroscopic equation.

Two-equation model

In many cases, the assumption of local equilibrium does not hold, and non-equilibrium models have been proposed under the form of two-equation models. In [7] we present a formulation of the two-equation model that incorporates the effect of heterogeneous sources. The proposed mapping between averaged temperatures and deviations is the following

$$\tilde{T}_\beta = \mathbf{b}_{\beta\beta} \cdot \nabla \langle T_\beta \rangle^\beta + \mathbf{b}_{\beta\sigma} \cdot \nabla \langle T_\sigma \rangle^\sigma - s_\beta \left(\langle T_\beta \rangle^\beta - \langle T_\sigma \rangle^\sigma\right) + r_\beta \Omega \tag{16a}$$

$$\tilde{T}_\sigma = \mathbf{b}_{\sigma\beta} \cdot \nabla \langle T_\beta \rangle^\beta + \mathbf{b}_{\sigma\sigma} \cdot \nabla \langle T_\sigma \rangle^\sigma + s_\sigma \left(\langle T_\sigma \rangle^\sigma - \langle T_\beta \rangle^\beta\right) + r_\sigma \Omega \tag{16b}$$

Several closure problems are available that defines the mapping fields. Using these representations, the averaged equation for the β-phase becomes

$$\varepsilon_\beta(\rho c_p)_\beta \frac{\partial\langle T_\beta\rangle^\beta}{\partial t} + \varepsilon_\beta(\rho c_p)_\beta\langle \mathbf{v}_\beta\rangle^\beta - \mathbf{u}_{\beta\beta}\cdot\nabla\langle T_\beta\rangle^\beta - \mathbf{u}_{\beta\sigma}\cdot\nabla\langle T_\sigma\rangle^\sigma$$
$$= \nabla\cdot\left(\mathbf{K}^*_{\beta\beta}\cdot\nabla\langle T_\beta\rangle^\beta + \mathbf{K}^*_{\beta\sigma}\cdot\nabla\langle T_\sigma\rangle^\sigma\right) - a_v h\left(\langle T_\beta\rangle^\beta - \langle T_\sigma\rangle^\sigma\right) + a_v\xi\Omega \tag{17}$$

while the equation for the σ-phase is

$$\varepsilon_\sigma(\rho c_p)_\sigma \frac{\partial\langle T_\sigma\rangle^\sigma}{\partial t} + \mathbf{u}_{\sigma\beta}\cdot\nabla\langle \mathbf{v}_\beta\rangle^\beta - \mathbf{u}_{\sigma\sigma}\cdot\nabla\langle T_\sigma\rangle^\sigma$$
$$= \nabla\cdot\left(\mathbf{K}_{\sigma\beta}\cdot\nabla\langle T_\beta\rangle^\beta + \mathbf{K}_{\sigma\sigma}\cdot\nabla\langle T_\sigma\rangle^\sigma\right) - a_v h\left(\langle T_\sigma\rangle^\sigma - \langle T_\beta\rangle^\beta\right) + \varepsilon_\sigma\langle\Phi_\sigma\rangle^\sigma + a_v(1-\xi)\Omega \tag{18}$$

All effective properties are defined in terms of the mapping fields found in Eqs. 16. In this paper we focus our attention on the exchange terms, which are given by

$$a_v h = \frac{1}{V}\int_{A\beta\sigma}\mathbf{n}_{\beta\sigma}\cdot k_\beta\nabla s_\beta dA \qquad ; \; a_v\xi = \frac{1}{V}\int_{A\beta\sigma}\mathbf{n}_{\beta\sigma}\cdot k_\beta\nabla r_\beta dA \tag{19}$$

The first one describes the rate of exchange of heat between the two phases, while ξ, called the distribution coefficient, represents the way the heat generated on the surface is distributed between the two phases. We do not list all the closure problems that have been proposed. Given the scope of the paper, we give below the fourth closure problem for the mapping scalar fields r_β and r_σ.

$$(\rho c_p)_\beta v_\beta\cdot\nabla r_\beta = k_\beta\nabla^2 r_\beta - a_v\varepsilon_\beta^{-1}\xi, \quad \text{in the } \beta\text{-phase} \tag{20a}$$

B.C.1 $$\mathbf{n}_{\beta\sigma}\cdot k_\beta\nabla r_\beta = \mathbf{n}_{\beta\sigma}\cdot k_\sigma\nabla r_\sigma + 1, \text{ at } A_{\beta\sigma} \tag{20b}$$

B.C.2 $$r_\beta = r_\sigma, \text{ at } A_{\beta\sigma} \tag{20c}$$

$$0 = k_\sigma\nabla^2 r_\sigma - a_v\varepsilon_\sigma^{-1}(1-\xi), \quad \text{in the } \sigma\text{-phase} \tag{20d}$$

Periodicity: $$r_\beta(\mathbf{r}+\ell_i) = r_\beta(\mathbf{r}), \quad r_\sigma(\mathbf{r}+\ell_i) = r_\sigma(\mathbf{r}), \quad i = 1,2,3 \tag{20e}$$

Average: $$\langle r_\beta\rangle^\beta = 0, \quad \langle r_\sigma\rangle^\sigma = 0 \tag{20f}$$

Examples of solutions of this closure problem are given in the next section.

3. THE DISTRIBUTION COEFFICIENT

The closure problem introduced in the previous section has been solved numerically for different periodic unit cells using a volume element technique. Results are presented in Fig. 2 and Fig. 3 in terms of the distribution coefficient versus the cell Péclet number, for different values of the thermal conductivity ratio.
The cell Péclet number is defined as

$$Pe_{cell} = (\rho c_p)_\beta\langle v_\beta\rangle^\beta \ell_\beta / k_\beta \tag{21}$$

where l_b is some unit cell characteristic length-scale.

The results show that the distribution coefficient is very sensitive to the thermal conductivity ratio, and less sensitive to the Péclet number for the studied geometry.

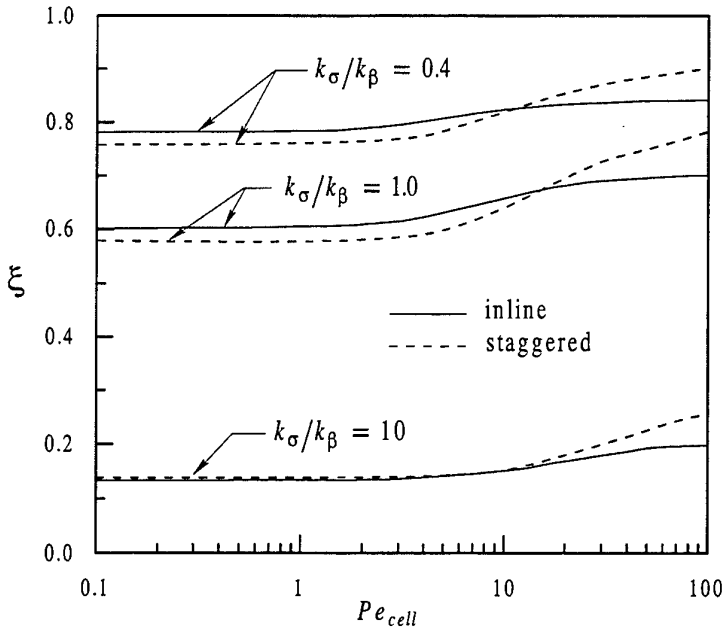


Fig. 2. Distribution coefficient for two-dimensional arrays of cylinders (ε_β = 0.38)

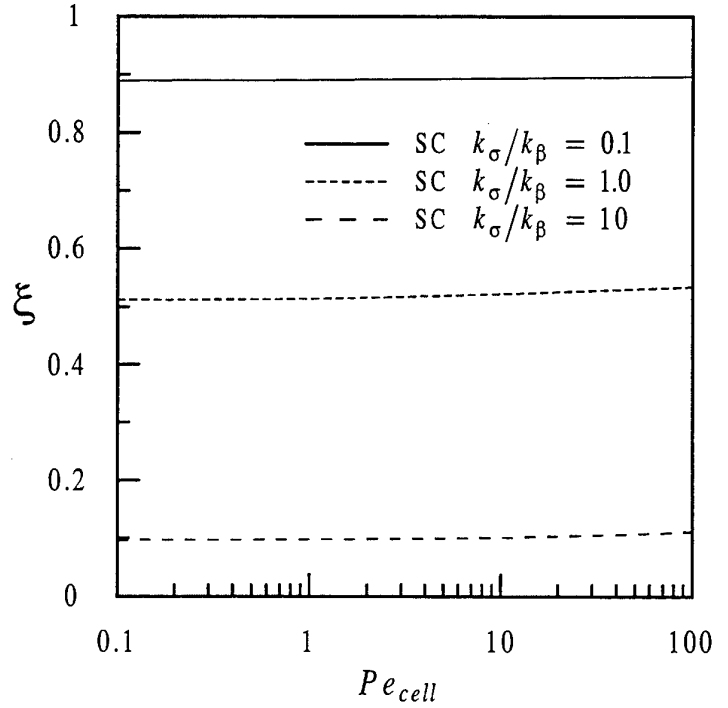


Fig. 3. Distribution coefficient for a simple cubic packing of spheres (ε_β = 0.47)

4. NUMERICAL EXPERIMENTS

In this section we present a comparison between averaged temperatures computed from direct solution of the pore-scale equations and theoretical predictions based on the solution of the averaged equations with the appropriate effective parameters obtained from the closure problems presented above. This has been done for the simple unit cell shown in Fig. 4. The initial condition corresponds to a constant temperature taken to be zero in this calculation. The system is infinite in all directions so there is no gradient of the averaged temperatures. With the above conditions, the averaged equations simplify to

$$\varepsilon_\beta (\rho c_p)_\beta \frac{\partial \langle T_\beta \rangle^\beta}{\partial t} = -a_v h \left(\langle T_\beta \rangle^\beta - \langle T_\sigma \rangle^\sigma \right) + a_v \xi \Omega \tag{22}$$

$$\varepsilon_\sigma (\rho c_p)_\sigma \frac{\partial \langle T_\sigma \rangle^\sigma}{\partial t} = -a_v h \left(\langle T_\sigma \rangle^\sigma - \langle T_\beta \rangle^\beta \right) + a_v (1-\xi) \Omega \tag{23}$$

For the unit cell under consideration, the closure problems can be solved analytically to obtain

$$\xi = \frac{\varepsilon_\sigma k_\beta}{\varepsilon_\beta k_\sigma + \varepsilon_\sigma k_\beta} \quad ; \quad \frac{a_v h (l_\beta + l_\sigma)}{k_\beta} = \frac{12 (k_\sigma / k_\beta)}{\varepsilon_\sigma + \varepsilon_\beta (k_\sigma / k_\beta)} \tag{24}$$

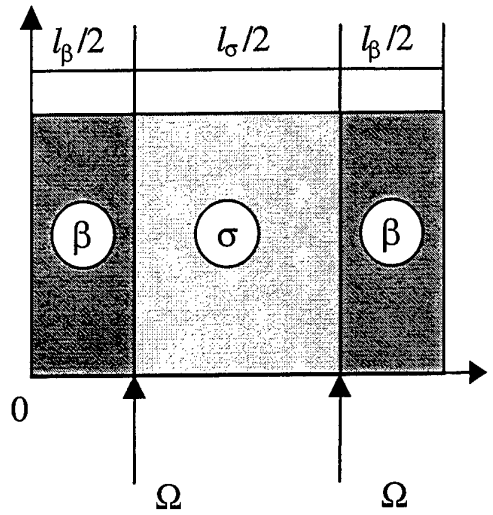


Fig. 4. Unit cell for the stratified system

The direct solution of the pore-scale equations has been obtained numerically, while the solution of the averaged equations was obtained analytically. The pore-scale temperature fields have been averaged to provide "experimental" values that can be compare to theoretical predictions obtained from the averaged equations.

An example of such a comparison is shown in Fig. 5, for which the values of the different parameters were taken to be

Ω=500 W/m^2 ; l_β=l_σ=0.01 m ; $(\rho c_p)_\beta$=10^6 J/m^3 K ; $(\rho c_p)_\sigma$=10^4 J/m^3 K ; k_β=100 W/m K ; k_σ=0.1 W/m K

The results show that, even for this chosen important contrast of properties, the agreement between theoretical predictions and actual data is very good. This confirms that the proposed solution of the coupled pore-scale and averaged equations is a good approximation and can be used in practical applications.

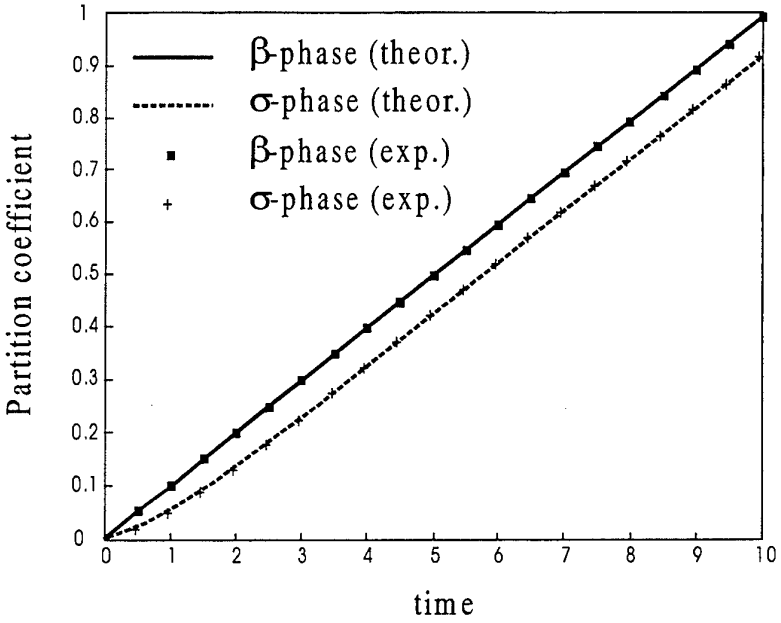


Fig. 5. Comparison between theoretical results and numerical experiments.

5. CONCLUSION

Based on the theory of volume averaging, we discussed the introduction of heat sources in the macroscopic equations describing heat transfer in porous media. The homogeneous sources are taken into account in a simple manner in both the two-equation and the one-equation models. On the contrary, the heterogeneous source requires the introduction of an additional closure problem, and leads to terms in the macroscopic two-equation model involving a distribution coefficient. This coefficient describes how the heat is distributed between the two phases.

This distribution coefficient has been calculated numerically for 2D/3D simple unit cells. Results show that this parameter is very sensitive to the thermal conductivity ratio. For a simple unit cell, the comparison between theoretical predictions and numerical experiments showed a good agreement, which emphasizes the practical interest of the proposed theory.

REFERENCES

1. S. Whitaker, Transport in Porous Media, v. 1, pp. 3-35 (1986).
2. R. G. Carbonell and S. Whitaker, in *Fundamentals of Transport Phenomena in Porous Media*, pp. 121-198, ed. by J. Bear and M. Y. Corapcioglu, Martinus Nijhof Publ., 1984.
3. F. Zanotti and R. G. Carbonell, Chem Eng Sci, v.39, pp. 263-278 (1984).
4. I. Nozad, R. G. Carbonell and S. Whitaker, Chem Eng Sci, v. 40, pp. 843-855 (1985).
5. M. Quintard and S. Whitaker, in *Advances in Heat Transfer*, pp. 369-464, Academic Press, New York (1993).
6. M. Quintard, M. Kaviany and S. Whitaker, Advances in Water Resources, v. 20 (2-3), pp. 77-94 (1997).
7. M. Quintard and S. Whitaker, in *Handbook of Heat Transfer in Porous Media*, edited by H. Hadim and K. Vafai, Marcel Decker, Inc., New York (1999).

STUDY ON IMPROVED PERFORMANCE OF PLATE HEAT EXCHANGER WITH PACKED BEADS AND MINI-LONGITUDINAL CHANNELS ON PLATE SURFACE

B.X. Wang, J.H. Du and Z.J. Zhang
Thermal Engineering Department
Tsinghua University, Beijing 100084, China
Email: bxwang@mail.tsinghua.edu.cn

Keywords: porous media, heat exchanger, mini-channels

ABSTRACT. Experiments were conducted on the fluid flow and heat transfer for packed glass beads between plates with longitudinally mini-channeled surface. The measured results were reported for different configuration combinations. Remarkable improvement in performance of pressure drop and heat transfer can be obtained. Optimum aspect ratio-channeled configuration would exist, which was found to be varied with Reynolds number.

I. INTRODUCTION

The plate heat exchangers are widely used in engineering, such as for papermaking process, chemical unit operation and refrigeration, due to its higher heat transfer coefficient. Other applications can be found in food, pharmaceutical, and hygienic industries for its convenience for cleaning. The flow maldistribution should be avoided, the cross-chevron of plates gives lattice support points against internal pressure and a complex flow channel shape for heat transfer enhancement. Further improvement is expected for reduction of volume and material cost consideration for given duty. Many forms of the corrugated surfaces can be found in commercial plate heat exchangers and more complex plate surfaces are emerging in practice[1].

Many passive and active techniques available for augumentation of heat transfer [2,3]. Insertion of some voritce devices is one of the simplest agumentation techniques, which can intensify heat transfer due to the fluid mixing induced the insertions. The micro packed beads of higher thermal conductivity has been used recently in micro-heat exchangers for cooling of electronic components, beads acting also as the extended surface for heat transfer. However, the micro-beads packing can not be employed for the conventional heat transfer equipment duo to its high pumping-power consumption. Higher porosity insertions are introduced for the tube and plate heat exchangers and low aspect ratio setting is desired from the considerations of geometry of plate heat exchangers. This practice can intensify heat transfer of the plate exchangers and also ensure the mechanical strength. With consideration of high degradation of metals due to corrosion, erosion and oxidation, solid matrix such as glass and nylon may be used for packed beads as usual. In such situations, the local thermal equilibrium between solid and fluid is usually assumed and the mechanical dispersion is dominant in heat transfer enhancement due to the continuous change of the flow direction forced by the packing. Although the higher porosity in the wall region leads to the greater velocity than in the central region and tends to enhance heat transfer, the wall effect normally abate the fluid mixing and hence decrease the overall performance of heat exchanger. A new technique to decrease the wall effect was proposed here in which mini-longitudinal channels are provided on the heated plate surface. This can reduce the flow resistance of hot water and meantime to intensify heat transfer. Since the pesuo-continumm assumption is invalid and no existing model can be applied for the theoretical analysis for such proposed combination, we conduct experimental investigation on the fluid flow and heat transfer with glass-beads packing between longitudinally mini-channeled surface plates, so as to investigate the effect of mini-channel bed surface on the pressure drop and heat transfer.

In this article, we report the measured results of the pressure drop and heat transfer with flow rate for different aspect ratio and different mini-longitudinal channels on the plate surface. The remarkable improvement in performance can be obtained with suitable combination of channeled-surface configuration.

II. EXPERIMENTAL SETUP

The experiments were performed in an experimental facility as shown in Fig.1 schematically. The system is mainly composed of a heating fluid loop, a cold fluid loop and the test section. Water was taken as testing fluids.

The water tank, pump and connecting tube make up the hot water loop. The regular valves control the flow rate. The heater in the tank, which was regulated by the applied electric voltage, maintains the temperature of water at the inlet of the experimental section. Tap water serves as the cool fluid, which directly drain away after passing through the test section.

Figure 2 shows the structure of the test section in detail. The heat exchange element is an aluminum plate assembled into a frame with sealing washer. The distance between the plate and the frame was changed by different gasket. A 120mm×300mm rectangular plate for heat transfer section is designed to ensure heat transfer to be one-dimensional approximately. At both ends of flow passage, headers serve also static mixers. The fluids flow along both sides of the plate in counter direction. Glass beads of uniform diameter, d_p, are chosen as packed medium. Stainless steel screen with a flow distributor is placed in each static mixer to hold the packed beads in place. Special opening is machined on the frame plates for convenience of packing. The lump porosity of the packing can be obtained from the weight of the packed beads and the packing volume. As the high scatter of the bed porosity for the packed channel of low aspect-diameter ratio, the bed porosity must be determined after several repackings.

The pressure drop across the test section was measured by U tube mercury manometer. Two rotameters were used to indicate the approximate flow rate, and actual flow rate were measured by the standard weight method. Teflon coated copper-constantan thermocouples were used to measure the temperature difference between the inlet and outlet of the test section. The measurement generally proceeds by maintaining the required flow rates of both hot water and cold water and the input power of heater. The steady state must be established until the data of the flow rates, the temperature and pressure difference between the inlet and outlet of the channels are recorded. It is noted that the pressure difference must be measured twice before and after packing in order to eliminate the effect of screens and the distributors. Fifteen thermocouples are placed at equally spaced locations on the plate in order to obtain the averaged mean temperature, which were calculated as:

$$\bar{t}_{bm} = \sum_{i=1}^{n} t_{bi} \Big/ n \tag{1}$$

here t_{bi} is the measured temperature at the plate and n is the number of thermocouples for the plate. If the bulk temperature of the hot fluid in the test section is taken as the arithmetic mean temperature at the inlet and the outlet, the averaged mean temperature difference between the plate and the test fluid is

$$\Delta\bar{t}_m = \frac{\left(t_1^{''}\right)}{2} - \bar{t}_{bm} \tag{2}$$

here $t_1^{'}$ and $t_1^{''}$ are the temperature of the hot fluid at the inlet and outlet of the channel. The quantity of heat transfer from the hot fluid to the coolant was obtained from the energy balance eqaution:

$$\dot{Q} = m_1\left(h_1^{'} - h_1^{''}\right) = m_1 c_p\left(T_1^{'} - T_1^{''}\right) \tag{3}$$

The heat transfer coefficient was hence evaluated as:

$$\bar{h} = \frac{\dot{Q}}{F\Delta\bar{t}_m} \tag{4}$$

where F is the effective heat transfer area of the plate. The corresponding Nusselt number, based on the space between plates, δ, can be obtained thereby:

$$Nu = \frac{h\delta}{k} \tag{5}$$

The estimated maximum deviation of pressure drop is less than 4.0%, While the relative deviation of the flow rate is less than 0.5%. The thermal balance between the hot and cold fluids was checked by the temperature differences and the flow rates. It was found to be less than 5%. The maximum relative deviation of the convective heat transfer coefficient is 13.1% and the corresponding standard square-root deviation is 11.2%. The main sources of the deviation are the errors of the heat transfer rate between the hot and the cold fluids and the temperature difference between the inlet and outlet of the fluids, which are estimated to be less than 11% and 1.5% respectively.

III. RESULTS AND DISCUSSIONS

In order to identify the effects of the mini-longitudinal channeled plate surface on flow resistance and heat transfer, different channeled plate surfaces have been investigated experimentally. The configuration of the channeled plate surface was demonstrated in figure 3. The dimension of the mini-channels are listed below:

	Plate A	Plate B	Plate C
W(mm)	0.5.	0.5	1.0
E(mm)	0.5	0.5	1.0
B(mm)	0.5	1.0	1.0
Extended surface ratio	1.178	1.356	1.356

(w+b) really represent the pitch of longitudinal channels.

Figure 4 shows the variation of Nusselt number with Reynolds number for different plates without packing. It is seen from Fig.4, the mini-longitudinal channels on the plate surface almost have no obvious effects on heat transfer in these situations. This may be explained as that, the fluid will bypass the mini-channels and flows through main passage with a lower flow resistance, the resulting low flow in the channeled region may actually result in no change in heat transfer rate on the plate. This is similar to the situation studied early by Kadle and Sparrow[4] for the effect of tip to shroud clearance on the resulting heat transfer. It can be deduced, therefor. that the mini-longitudinal channels will show no obvious effect on the pressure drop.

Figure 5 shows the typical pressure drops of hot water though the test section with packed beads of d_p =2.0mm and 5.4mm for δ =10.5mm. The corresponding variation of friction factor with Reynolds number was given in Fig.6. It demonstrates that the pressure drop decreases with the increase in the dimension of the mini-channel. Such variations of the pressure drop reflect the redistribution of flow in the channels and packed regions. It will bring about the changes in heat transfer.

Figure 7 shows the measured results for heat transfer with different packed glass beads for δ=10.5mm. It is clear that the mini-channels on the plate intensify heat transfer, the plate A and B show almost same heat transfer characteristics, while the plate C enhances heat transfer further more. The enhancement of heat transfer depends on the Reynolds number, geometrical configuraton and $\frac{\delta}{d_p}$. It would be clear that, in addition to reduce the pressure drop, the mini-channeled plate surface can also intensify heat transfer. This shows potential advantages over the packed simply. Figure 8 shows similar tendency for the case δ = 21.0mm with different packing beads. It is worthy to note from Fig.7©, with d_p = 5.45mm , the mini-channels have almost no effect on heat transfer for both the plate A and B, and get augments the heat transfer very prominently for plate C. This reminds us of the existence of optical combination of bead packing and the longitudinal mini-channels on the plate surface.

It makes sure that, the packing in parallel plates with proper diameter ratio can provide better performance than the commerical plate heat exchangers. The mini-channels on the plate surface further improved performance of plate heat exchanger with packed beads, as shown in Fig.9. With suitable configuration combination, the mini-longitudinal channels on plate surface can even provide better performance than existing heat exchangers of chervon forms.

IV. CONCLUDING REMARKS

Experiments were conducted to evaluate the pressure drop and heat transfer for the plate heat transfer element with packed beads and the mini-longitudinal channels on plate surface. The improvement in reduced flow resistance and enhanced heat transfer was obtained with such combination. An optimum $\frac{\delta}{d_p}$-channeled configuraton exists, which varies with range of Reynolds number accordingly. Since flow and heat transfer in this configuration is very complicated, many underlying fundamentals are still poorly understood. Much experimental works should continue to be conducted to identify the key factors to influencing the process. Some theoretical analysis should also need to provide guidance for the experiments.

Acknowledgment—The project in financially supported by the National Natural Science Foundation of China.

REFERENCES

1. W.M. Kays, and A.L. London, Compact Heat Exchangers, 3rh edition, McGraw-Hill, New York(1984).
2. A.E. Bergles, Some perspectives on enhanced heat Transfer-Second Generation Heat Transfer Technology, J. Heat Transfer 110:1082-1096(1988).
3. R.W. Webbs, Principles of enhanced heat transfer, A Wiley-interscience pub., New York(1994).
4. D.S. Kadle, and Sparrow, E. M., Numerical and experimental study of turbulent heat transfer and fluid flow in longitudinal fin arrays, Tran. ASME, J. Heat Transfer 108:16-23(1986).

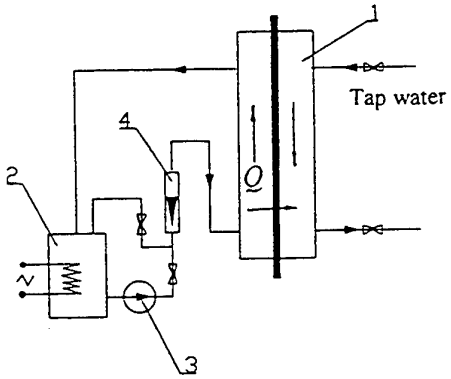


Fig.1. Experimental System
1—test section, 2—hot water tank, 3—pump, 4—rotameter

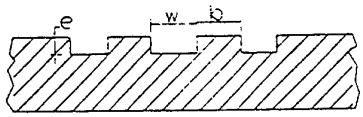


Fig.3 The Geometry of the Longitudinal Mini-channels on the Plate Surface

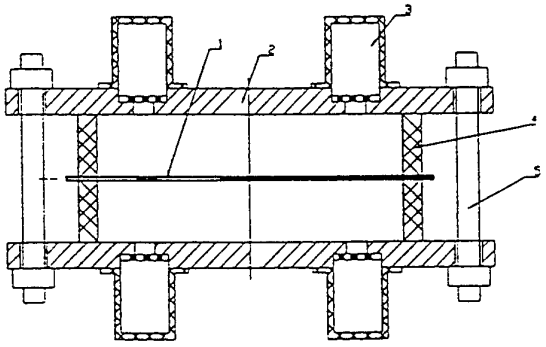


Fig.2 Test Section
1—aluminum plate, 2—frame plate, 3—header, 4—seakubg washer, 5—bolt

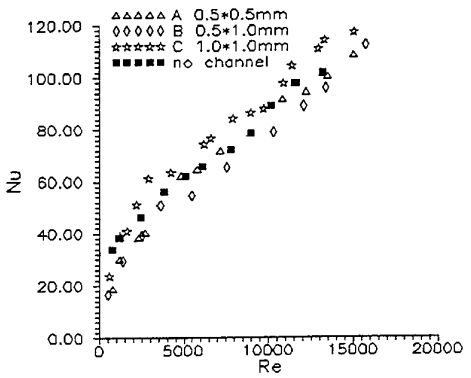
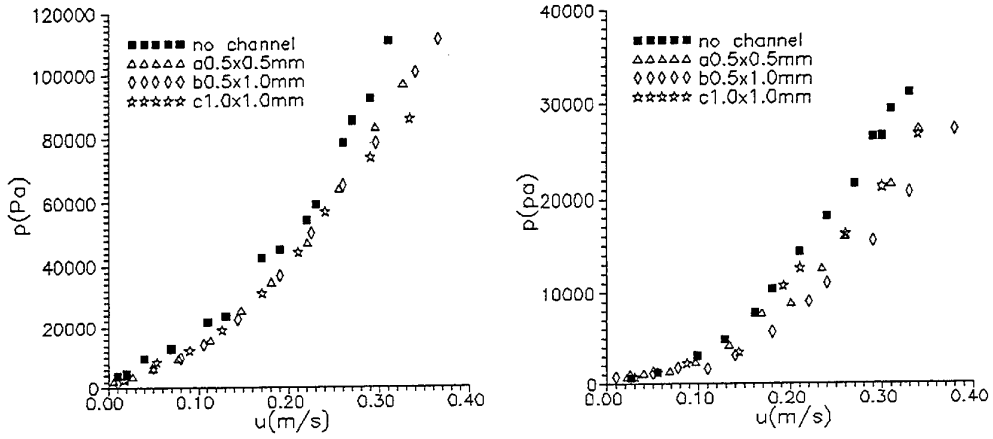
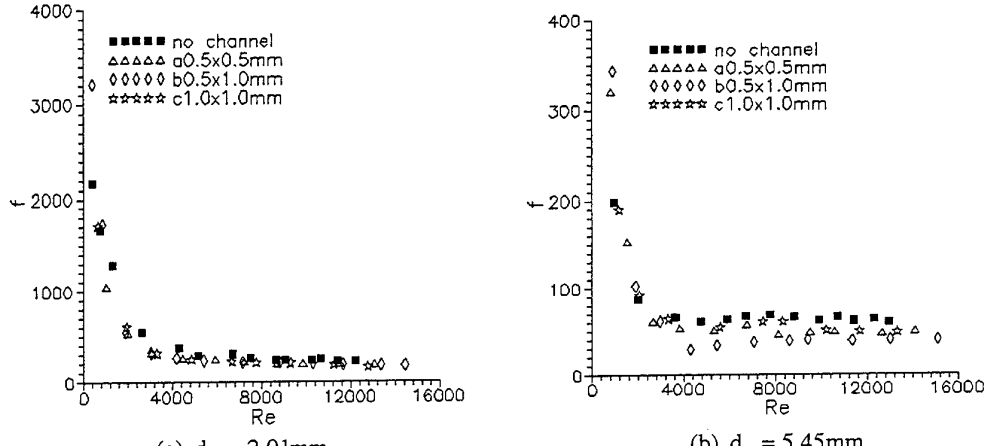


Fig.4 Nu vs. Re for different configuration without packing (δ=10.5mm)



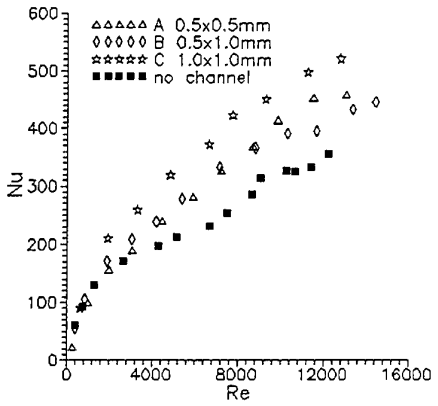
(a) d_p = 2.01mm (b) d_p = 5.45mm

Fig.5 The pressure drops of hot water through the test section packed with glass beads for δ =10.5mm.

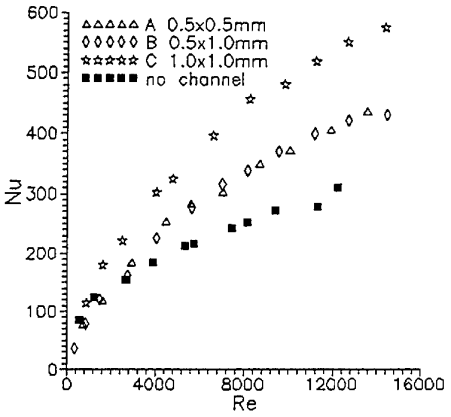


(a) d_p = 2.01mm (b) d_p = 5.45mm

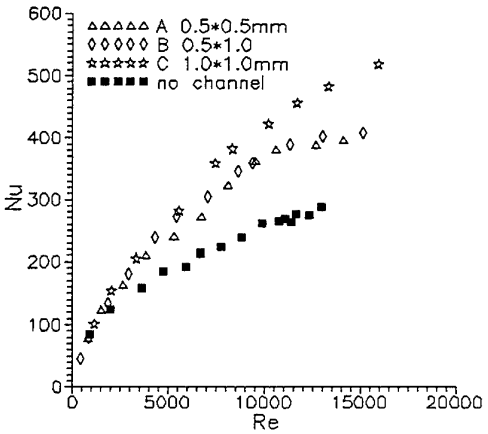
Fig.6. f vs. Re for different aspect ratios with packed glass beads for δ =10.5mm



(a) $d_p = 2.01$mm

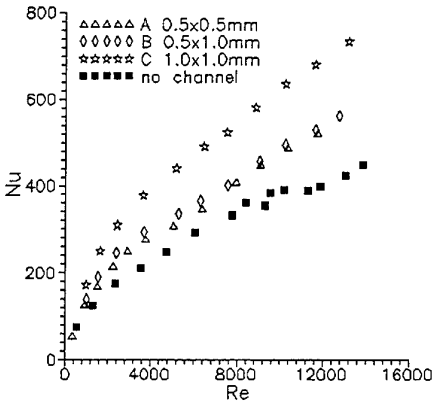


(b) $d_p = 3.45$mm

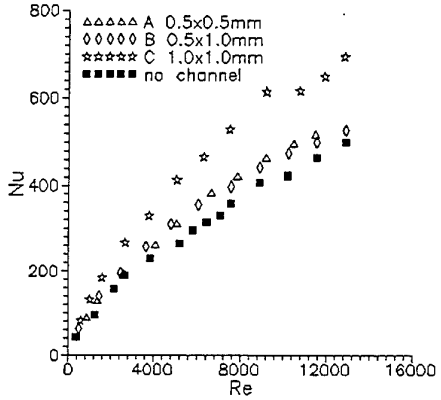


(c) $d_p = 5.45$mm

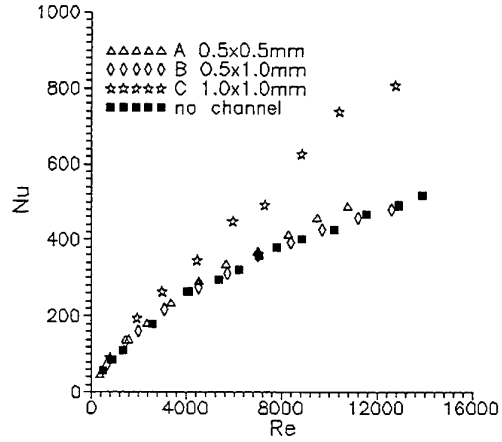
Fig.7 Nu vs. Re for different aspect ratio with packed beads for δ =10.5mm



(a) $d_p = 2.01$mm

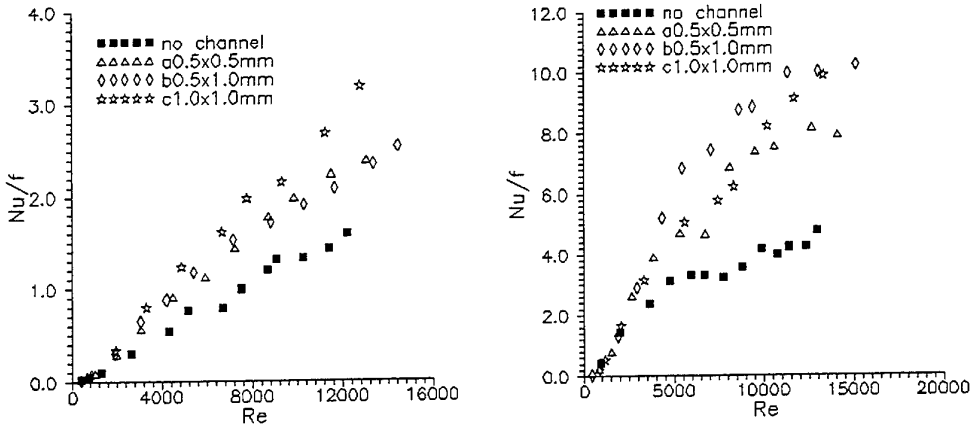


(b) $d_p = 3.45$mm



(c) $d_p = 5.45$mm

Fig.8 Nu vs. Re for different aspect ratio with packed beads for δ =21.01mm



(a) $d_p = 2.01$mm (b) $d_p = 5.45$mm

Fig.9 Nu/f vs. Re for δ =10.51mm

HEAT TRANSFER OF A POROUS CHANNEL HEAT SINK SUBJECTED TO OSCILLATING FLOW

Huili Fu, Kai Choong Leong, Xiaoyang Huang, Chang Yu Liu
School of Mechanical and Production Engineering, Nanyang Technological University
50 Nanyang Avenue, Singapore 639798
Email: mhlfu@ntu.edu.sg; Fax: (65)7924062

Keywords: porous media, heat transfer, electronic cooling, oscillating flow

ABSTRACT. In this paper, experiments have been conducted to study the heat transfer of a porous channel heat sink subjected to oscillating flow. The surface temperature distributions for both steady and oscillating flows were measured. The local and length-averaged Nusselt numbers were measured and analyzed. The experimental results revealed that the surface temperature distribution for oscillating flow is more uniform than that for steady flow. Due to the reversing flow direction, there are two thermal entrance regions for oscillating flow. The length-averaged Nusselt number for oscillating flow is much higher than that for steady flow. The porous channel heat sink subjected to oscillating flow can be considered as an effective method for cooling high-speed electronic devices.

1. INTRODUCTION

The rapid development in the design of electronic package for modern high-speed computers has led to the demand for new and reliable methods of chip cooling. As reported by Mahalingam and Berg [1], and Burd [2], the averaged dissipating heat flux can be up to 25 W/cm^2 for high-speed electronic components. However, the conventional natural or forced convection cooling methods are only capable of removing small heat fluxes per unit temperature difference, about 0.001 W/cm^2.°C by natural convection to air, 0.01 W/cm^2.°C by forced convection to air, and 0.1 W/cm^2.°C by forced convection to liquid [3]. Therefore, it is imperative to look for new methods of cooling the modern high-speed electronic components. One of these methods is to implement a channel filled with high conductivity porous media.

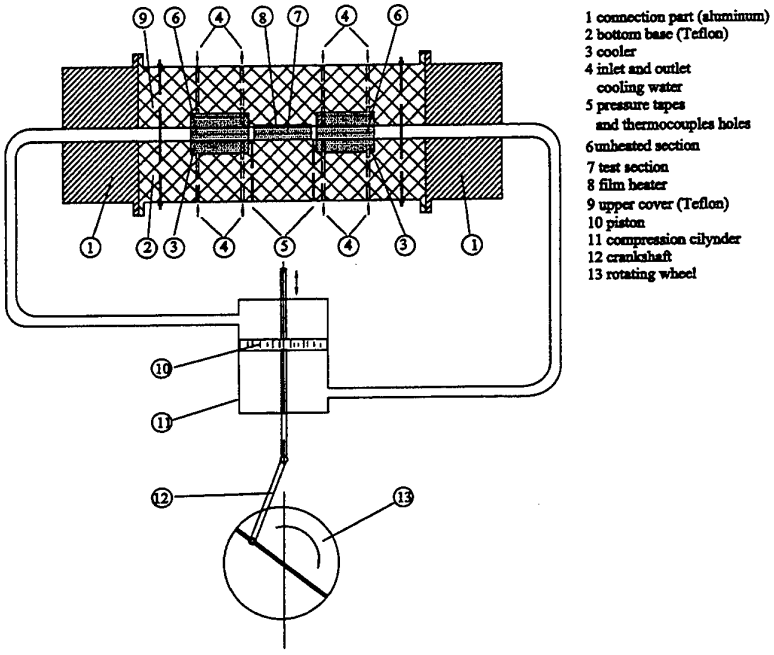
Extensive investigations have been conducted on the flow and heat transfer of a channel filled with porous media. The early works related to heat dissipation are those by Cheng et al. [4], Kaviany [5] and Hunt and Tien [6]. Cheng at al. [4] studied the forced convection in a packed channel with asymmetric heating. Hunt and Tien [6] studied the heat transfer augmentation in a duct filled with foam material. More recently, due to increased applications in electronic cooling, many researchers have studied the heat transfer enhancement of a channel filled with porous media. Tong et al. [7], Huang and Vafai [8], Hadim and Bethancourt [9], and Sozen [10] numerically studied the heat transfer enhancement of a channel (or duct) filled fully or partially with porous media subjected to steady flow. Fedorov and Viskanta [11] studied the conjugate heat transfer of a porous channel with discrete heat sources numerically. Relative little experimental work has been performed on electronic cooling with porous channel as heat sinks. Hwang and Chao [12] studied the heat transfer of sintered bronze bead channels with uniform heat flux of up to 3.2 W/cm^2. Local surface temperature distributions and local Nusselt numbers were measured. In the above literature, steady flow through the porous channel was investigated. However, as observed by Hwang and Chao [12], the local temperature of the substrate surface is more important than the averaged surface temperature in the application of electronic cooling. A temperature difference of more than 50 °C between the inlet and the hottest location of the channel was measured in the case of q = 3.2 W/cm^2 in their experiments. This indicates that steady flow through a porous channel heat sink still yield a relative high local surface temperature. In the present investigation, a facility was set up to study the heat transfer of a porous channel subjected to both steady and oscillating flows. Local surface temperature distributions were measured. The local Nusselt numbers were calculated. The surface temperature distribution and heat transfer of steady and oscillating flows were compared.

2. EXPERIMENTAL APPARATUS AND PROCEDURE

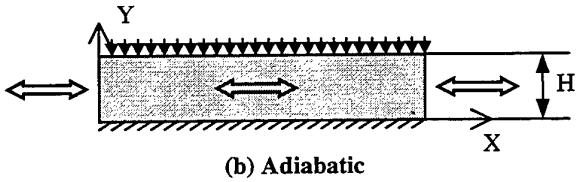
2.1 Test Section and Facility

The schematic diagram of the experimental facility is depicted in Fig. 1a. The facility consists of an oscillating flow generator, a test section, two unheated sections, and four coolers. The oscillating flow generator is a

mechanism that generates a sinusoidal oscillating flow. The mechanism consists of a compression cylinder, a piston and a crankshaft with adjustable stroke lengths. The piston was connected to the crankshaft. The crankshaft was driven by a motor to move the piston forward and backward sinusoidally. By adjusting the motor speed and the stroke length, oscillating flows with different amplitudes and frequencies were generated. A 1 mm copper plate was attached on the top. This copper plate was cut with many narrow slots to reduce the heat conduction along the flow direction. A film heater was firmly mounted on the surface of the cooper plate to supply a constant heat flux. By adjusting the supply voltage to the heater, the power input can be adjusted. The two unheated sections were the same porous material as the test section with the same dimension. They were installed adjacent (but separated) to the two ends of the test section. The two unheated sections built up a uniform velocity profile for flow through the test section. The heat carried by the flow is also transferred to the surface of coolers through the unheated porous material. The four coolers are channels filled with porous media. Cooling water was forced through the four coolers to remove the heat generated by the film heater. As shown in figure, the test section, the film heater, the two unheated sections and the four coolers were tightly fitted in a channel made by teflon material. The schematic of the test section is shown in Fig. 1b. The test section is an aluminum porous foam (ERG foam material, 40 PPI—pores per linear inch) with a dimension of 50x50x10mm. The bottom wall of the channel is adiabatic while the upper wall is subjected to a constant heat flux.



(a) Constant heat flux



(b) Adiabatic

Figure 1. The schematic of test section and experimental facility
(a) Experimental setup, (b) Test section

2.2 Instrumentation and Experimental Procedure

In the present experiments, the pressure drop across the test section, the temperature along the axial direction as well as at the two exits of the test section and the velocity through the test section were measured. A differential

pressure transducer (Validyne DP15) was connected to the two taps along the test section. K type thermocouples of 45 μm diameter were flushed on the copper plate to measure the surface temperature along the axial direction. The inlet and outlet temperatures were measured by fixing the thermocouples between the test section and the unheated sections. The velocity was measured by a hot-wire sensor with an anemometer (TSI IFA 100 and TSI 1210-20w). The velocity was measured in a velocity measurement section which was installed in the loop. All the signals were connected to a data acquisition system consisting of a 12 bit A/D card (Keithley Das 1402), a computer and a software (TestPoint).

The oscillating flow facility is also capable of performing steady flow experiments. By leaving one end of the test section open to the atmosphere, steady flow and heat transfer experiments can be conducted with the same test section configuration and sensors. In the steady flow experiments, the main compressed air line was connected to the facility. A valve and a regulator were installed to adjust the flow velocity through the test section. After passing the test section, the coolant air was discharged to the environment. The experiments were performed by increasing the power input while keeping the flow velocity constant. By looping the test section to the oscillating flow regenerator, heat transfer experiments for oscillating flow can be conducted. Cooling water was passed through the four coolers installed at the two ends of the test section to remove the dissipated heat. The frequency of oscillating flow was adjusted by changing the motor speed. A fixed oscillation amplitude was tested in the present experiments. The experiments were proceeded by increasing the power input while keeping the oscillating frequency unchanged. To obtain a cyclic steady state, the oscillating velocity, pressure drop, and surface temperature were monitored. Over 80 cycles of data for each case were recorded.

3. RESULTS AND DISCUSSIONS

3.1 Heat Transfer Of Steady Flow Through A Porous Channel

In micro-electronics, devices can be damaged by excessively high local temperatures instead of the averaged one. Therefore, the temperature distribution along the flow direction of the test section is of practical interest in design. Fig. 2 presents the local surface temperature distribution along the flow direction and the bulk inlet and outlet temperature with the effect of Reynolds number for q = 0.8, 1.6, 2.4 and 3.2 W/cm^2.

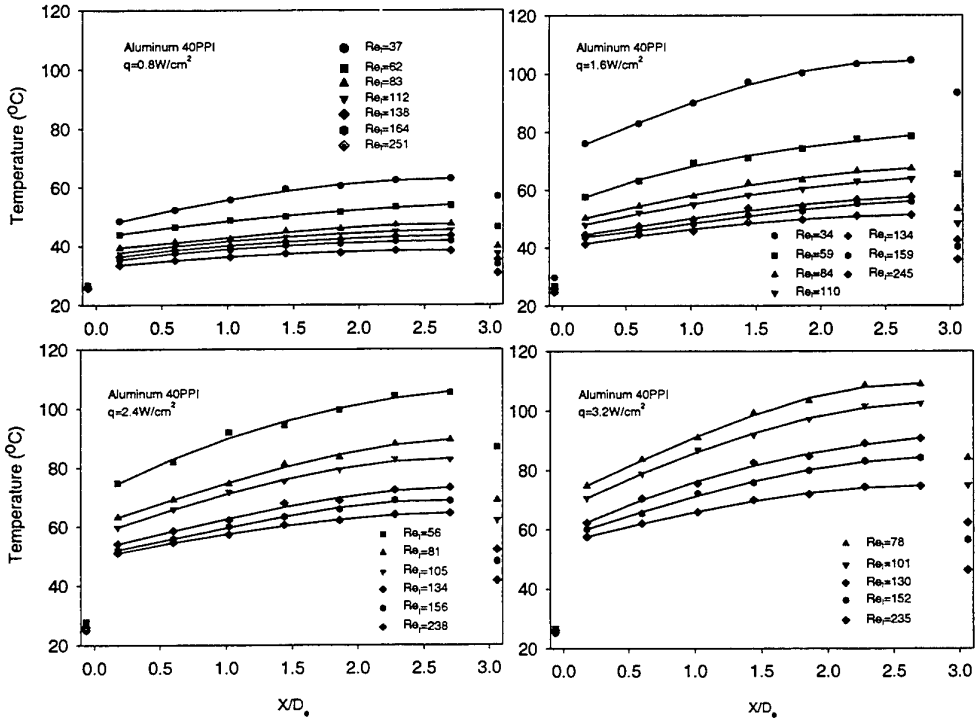


Figure 2. Surface temperature distribution along the flow direction (steady flow)

The Reynolds number here is defined based on the ligament diameter of the porous foam as

$$\mathrm{Re}_l = \frac{Ud_l}{\nu_f} \tag{1}$$

where U is the Darcy velocity through the test section, d_l is the ligament diameter of the porous foam and ν_f is the kinematic viscosity of the fluid.

It is obvious that the temperature level increases with the increase of axial position X/D_e, the decrease in Reynolds number, or the increase in power input. The inlet bulk temperature stays between 25~30 °C. The outlet bulk temperature increases with the increase of heat flux but decreases with the increase of Reynolds number. From Fig.2, it is seen that the surface temperature approaches a constant value when the flow approaches the thermally fully developed region. It is shown that higher Reynolds number will produce a more uniform surface temperature distribution.

Fig. 3 shows the local Nusselt number versus dimensionless axial position for power inputs q = 0.8 to 3.2W/cm^2 and the 40 PPI aluminum foam. The local Nusselt number was calculated by:

$$h_x = q/(T_w - T_i) \tag{2}$$

$$Nu_x = h_x D_e / k_f \tag{3}$$

where h_x is the local heat transfer coefficient, $D_e = 5H/3$ is the hydraulic diameter of the flow channel, H is the height of the channel, and T_w and T_i are local surface temperature and the inlet bulk temperature, respectively.

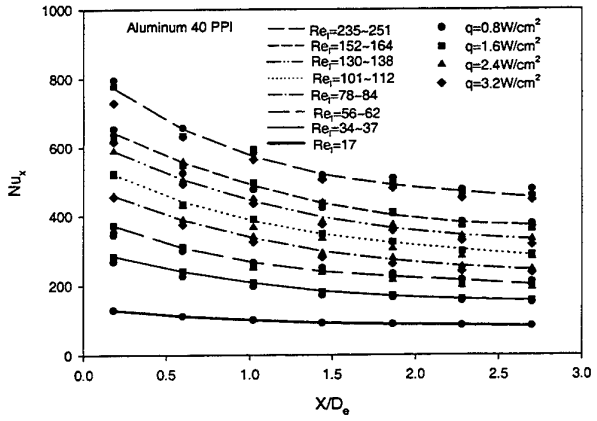


Figure 3. Effects of Reynolds number on local Nusselt number at different axial locations (steady flow)

In Fig. 3, it is seen that the local Nusselt number increases with the increase of the Reynolds number. In the thermal entrance region, the local Nusselt number is higher. With the increase of the axial distance, the Nusselt number for a fixed Reynolds number approaches the value for thermally fully developed flow (minimum constant value). For lower Reynolds number, the variation of local Nusselt number along the axial direction is much smaller than that of larger Reynolds number. This means that the thermal entrance length is shorter for a small Reynolds number than that of a large Reynolds number. The input heat flux has no effect on the local Nusselt number.

3.2 Heat Transfer Of Oscillating Flow Through A Porous Channel

Fig. 4 shows the cycle-averaged local surface temperature distribution of the test section with the effect of the ligament Reynolds number for power input q = 0.8, 1.6, 2.4 and 3.2 W/cm^2. In the present experiments, the

experimental data for oscillating flow was reduced by time-averaging over 50 completed cycles. To differentiate this average from an arbitrary time-averaging process, we call this kind of time-averaging process *cycle-averaging*. Once again, we observe that the cycle-averaged local temperature decreases with the increase of Reynolds number but increases with the increase of the input heat flux. Due to the reversing flow direction, there are two thermal entrance regions in the test section. The local temperatures near the both entrances are lower than that at the centre of the test section. The maximum temperature point appears at the centre of the test section. The distribution curves of the local surface temperature are convex with the centre of the test section as symmetric point.

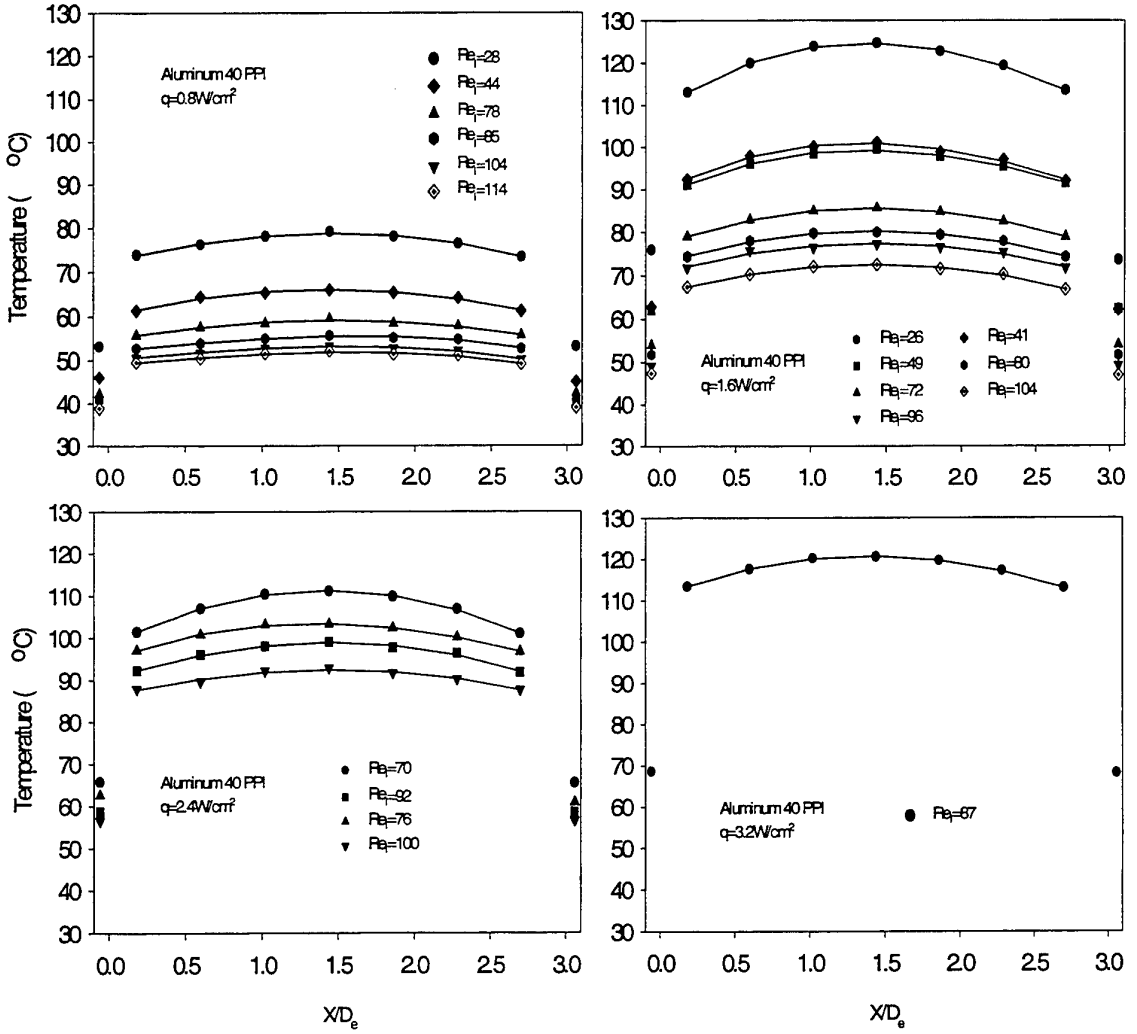


Figure 4. Cycle-averaged surface temperature distribution along axial direction (oscillating flow)

Fig. 5 shows the cycle-averaged local Nusselt number versus the dimensionless axial distance with the effect of Reynolds number based on ligament diameter of porous foam for oscillating flow. The definition of the Nusselt number is given in Eq. (3). In the calculation, T_w is the cycle-averaged surface temperature while T_i is the cycle-averaged air temperature at left (or right) exit. More than 50 cycles of experimental data were used in the cycle-averaging process. From the figure, it is seen that the cycle-averaged local Nusselt number increases with the increase of Reynolds number. It is obvious to see that there are two thermal entrance regions in the test section. In the thermal entrance region, the cycle-averaged local Nusselt number is higher. The cycle-averaged Nusselt number decreases as X/D_e approaches the centre of the test section. As a consequence, the distribution curves of the cycle-averaged local Nusselt number are concave with the centre of the test section as symmetric point.

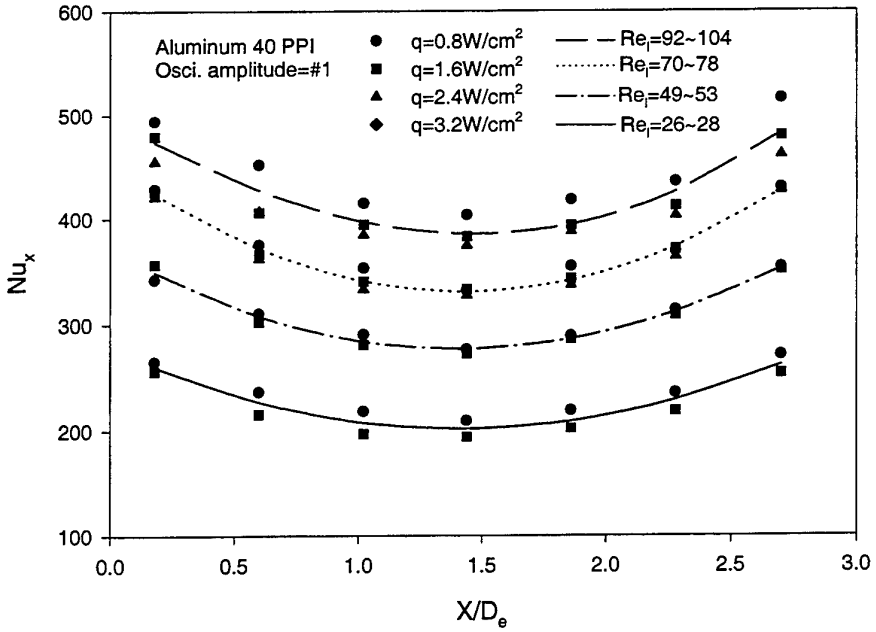


Figure 5. Effects of Reynolds number on local Nusselt number at different axial locations (oscillating flow)

3.3 Comparison Of Heat Transfer Of Steady And Oscillating Flow Through A Porous Channel

The local temperature distribution depends on the Reynolds number and power input. For steady flow, the surface temperature increases along the flow direction as seen in Fig. 2. The surface temperature approaches a constant value when the flow approaches the thermally fully developed region. However, for oscillating flow, there are two thermal entrance regions. The surface temperature distribution curves are of convex shape curve as seen in Fig. 4. In electronic cooling, the micro-electronic devices may fail due to a local excess high surface temperature instead of the averaged one. Therefore, it is important to compare the surface temperature lift for steady and oscillating flows. From the figures, it is observed that the temperature lift for steady flow is 1.5~3.5 times higher than that for oscillating flow. For example, for the case of q = 2.4 W/cm^2, Re_l = 76, the surface temperature lift for oscillating flow is about 8 °C, but for the case of q = 2.4 W/cm^2, Re_l = 81, the surface temperature lift for steady flow is about 30 °C. This indicates that the surface temperature distribution for oscillating flow is more uniform than that for steady flow.

As seen in Fig. 3, the local Nusselt number decreases along the flow direction for steady flow. As the dimensionless axial increases, the local Nusselt number approaches a minimum constant value (the thermally fully developed region). For oscillating flow, as shown in Fig. 5, the local Nusselt number does not decrease monotonically. The local Nusselt number decreases first and then increases after the centre point of the test section.

To evaluate the total heat dissipation rate from the electronic devices by the porous channel heat sink subjected to steady or oscillating flow, it is necessary to calculate the averaging Nusselt number for the whole length of the test section. A Length-averaged Nusselt number is used. It is defined as the averaged value of local Nusselt number along the axial direction. Fig. 6 shows the length-averaged Nusselt number for steady and oscillating flows with Reynolds number based on ligament diameter of the porous foam. It is clear that the length-averaged Nusselt number for oscillating flow is much higher than that for steady flow. The larger the Reynolds number, the larger the difference between the length-averaged Nusselt number of oscillating flow and steady flow. In the present experiments, for example, the length-averaged Nusselt number for oscillating flow is 1.4 times that of steady flow for $Re_l \approx 114$. The higher length-averaged Nusselt number is due to the higher local Nusselt number in the thermal entrance region. There are two thermal entrance regions for oscillating flow. This leads to the higher length-averaged Nusselt number for oscillating flow.

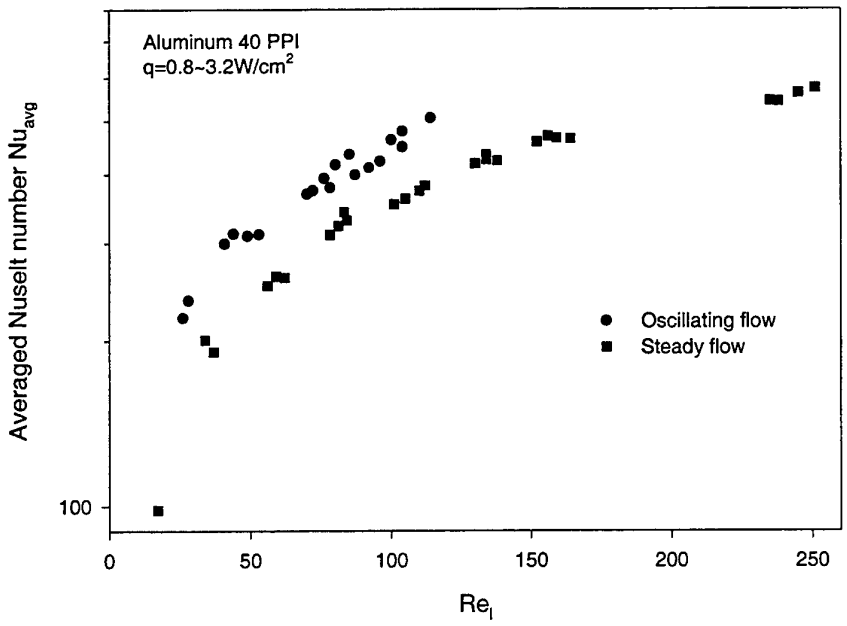


Figure 6. Comparison of averaged Nusselt number of steady and oscillating flow

4. CONCLUSIONS

In this study, experiments were conducted to study the heat transfer of a porous channel subjected both steady and oscillating flows. The velocity through the porous channel, the pressure-drop across the test section and the temperatures along the hot surface were measured. Based on the experimental results, the following conclusions can be drawn:

1. For steady flow, the local surface temperature increases monotonically as the dimensionless axial direction increases. The local surface temperature distribution for oscillating flow is a convex shape with a maximum point at the centre of the test section. The surface temperature distribution for oscillating flow is more uniform than that for steady flow.

2. For steady flow, the local Nusselt number decreases along the flow direction and approaches the thermally fully developed value. The cycle-averaged local Nusselt number for oscillating flow, however, decreases first and then increases after the centre point of the test section. There are two thermal entrance regions for oscillating flow through a porous channel. Both the local and length-averaged Nusselt numbers increase with an increase in ligament Reynolds number for steady and oscillating flow.

3. The length-averaged Nusselt number for oscillating flow is much higher than that for steady flow. The higher length-averaged Nusselt number indicates that the porous channel heat sink subjected to oscillating flow has a higher heat dissipation rate compared to steady flow.

4. The results obtained in the present experiments and the analysis demonstrate that a channel filled with high conductivity porous material subjected to oscillating flow is a new and effective method for cooling electronic devices.

ACKNOWLEDGEMENTS

The authors gratefully acknowledge the financial support provided under the National Science and Technology Board, Singapore Grant No. JT/ARC5/96 for the development of the experimental facility described in this paper.

REFERENCES

1. M. Mahalingam and H. Berg, International Journal of Hybrid Microelectronics, Vol.7, pp.1-9 (1984).
2. T. Burd, "CPU information and system performance summary," Internet site, Http://infopad.eecs.berkeley.edu/CIC/summary, (1995).
3. R. Simon, Solid State Technology, Vol.26, pp.131-137 (1983).
4. P. Cheng, C.T. Hsu, and A. Choudhury, Journal of Heat Transfer, Vol. 110, pp.946-954 (1988).
5. M. Kaviany, Int. J. of Heat and Mass Transfer, Vol.28, pp.815-858 (1985).
6. M.L. Hunt and C.L. Tien, Int. J. Heat Mass Transfer, Vol. 31, pp.301-309 (1988).
7. T.W. Tong, M.C. Sharatchandra and Z. Gdoura, Int. Comm. in Heat and Mass Transfer, Vol. 20, No. 6, pp.761-770 (1993).
8. P.C. Huang and K. Vafai, Journal of Thermophysics &Heat Transfer, Vol. 8, No.3, pp.563-573 (1994).
9. H.A. Hadim, and A. Bethancourt, Journal of Electronic Packaging, Vol.117, No.1, pp.46-51 (1995).
10. M. Sozen, "Use of porous inserts in heat transfer enhancement in cooling channels," *Proc. ASME Int. Mech. Eng. Congr. & Exhibition*, Atlanta, GA, USA, pp.1117-1122 (1996).
11. A.G. Fedorov, and R. Viskanta, Journal of Electronic Packaging, Vol.119, No.1, pp.8-16 (1997).
12. G. Hwang and C. Chao, Journal of Heat Transfer, Vol.116, pp.456-464 (1994).

EFFECTIVE THERMAL CONDUCTIVITY OF Bi-DISPERSED POROUS MEDIA

Z. Q. Chen, P. Cheng and C. T. Hsu
Department of Mechanical Engineering
The Hong Kong University of Science and Technology
Email: mepcheng@ust.hk; Fax: (852)-2358-1543

Keywords: thermal conductivity, bi-dispersed porous media, lumped-parameter method

ABSTRACT. A unit cell model was used to determine the effective thermal conductivity of bi-dispersed porous media based on the lumped-parameter method. Based on this model, the effective thermal conductivities of these media in the range of solid/fluid conductivity ratio between 0.01 to 10^5 with different micro- and macro- porosities were predicted. Measurements of effective thermal conductivities of two samples of bi-dispersed porous media (with micro-pore diameter of 80 μm and macro-pore diameters of 200 μm and 400 μm) saturated with three different fluids (air, FC-72 and water) respectively were conducted. For comparison, the effective thermal conductivity of a mono-dispersed medium with pore diameter of 800 μm saturated with the same fluid was measured. The measured data are shown to be in agreement with those based on theoretical predictions. The results indicated that the effective thermal conductivity of a bi-dispersed porous medium is smaller than that of the mono-dispersed porous medium saturated with the same fluid because of the contact resistance at micro-scale and higher porosity for bi-dispersed porous media in comparison with the mono-dispersed porous media.

1. INTRODUCTION

Recently, Hsu et al [1,2] obtained algebraic expressions for effective thermal conductivities of a number of porous media by applying the so-called lumped parameter method which is based on an electric resistance analog. This method consists of choosing a unit cell, dividing the geometry under consideration into solid, fluid, or composite layers (consisting of both fluid and solid), and assuming one-dimensional conduction in the direction of temperature gradient in the unit cell. The thermal resistance of the medium was obtained by assuming these layers were in parallel with one another while the thermal resistance of the composite layers was obtained by assuming the layers were in series. For the case of a porous medium consisting of packed spheres, Hsu et al [1,2] used a 2-dimensional model of touching square cylinders and a 3-dimensional model of touching cubes for the prediction of its effective thermal conductivity. They found that the results based on the 3-dimensional model are in better agreement with the experimental data of Nozad, et al.[3] than that of a 2-dimensional one. In many applications, such as bi-dispersed adsorbent, bi-dispersed capillary wicks in the heat pipe, there are micro- as well as macro- pores. The bi-dispersed porous structure, as shown in Fig. 1, is composed of clusters of large particles, which are agglomerated by small particles. There are micro pores and macro pores within and between the clusters of large particles respectively. Since the bi-dispersed wick structure significantly increases the area available for liquid film evaporation, so it has been proposed to be used in the evaporators of heat pipes.



(a) Sketch of a bi-dispersed porous medium (b) X-Ray photograph of sintered bi-dispersed powders

Fig. 1 Schematic of the porous media with bi-dispersed structure

In a most recent paper, Cheng and Hsu [4] applied the lumped parameter method to determine the effective stagnant thermal conductivity of a 2-dimensional bi-dispersed porous medium. In this paper, we will use a 3-dimensional model of touching cubes for predicting the effective stagnant thermal conductivity of bi-dispersed porous media. Thermal conductivity measurements on sintered bi-dispersed porous materials, saturated with air, FC-72 and water respectively, were also carried out. The experimental data is compared with theoretical predictions.

2. MODEL ANALYSIS

2.1 Effective Thermal Conductivity of Bi-dispersed Porous Media

We shall approximate the bi-dispersed medium made of small spheres by touching cubes as illustrated in Fig.2, where c_1, $a_1$and l_1 are the contact length, the length of the cubes and the length of the unit cell at the micro-scale, while c_2, a_2 and l_2 are the corresponding lengths at the macro-scale.

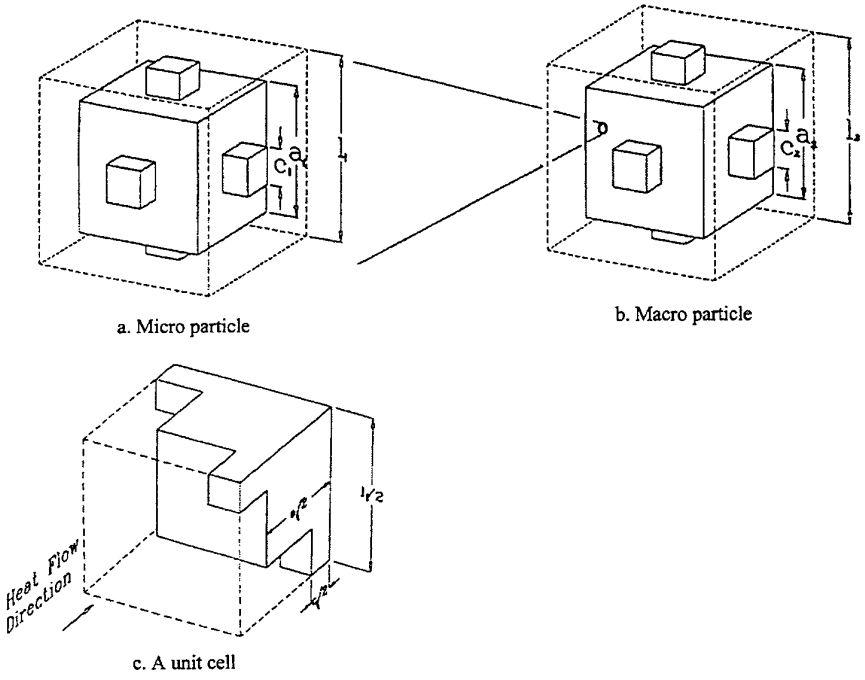


Fig. 2 In-line touching cubes and their unit cell of bi-dispersed porous medium

It is assumed that the structure of the sintered metal porous material that forms the porous cubes is geometrically similar to the periodic structure of the cubes forming the media. Therefore, the sintered materials are denoted at the micro-scale and the porous cubes are at meso-scale. To apply the lumped parameter method [2], we first consider the micro- structure of the solid materials at the left-hand side of Fig.2. According to Hsu, et al [2], the effective stagnant thermal conductivity of the porous cubes in the micro-scale is given by

$$\frac{k_{e1}}{k_f} = (1-\gamma_{a1}{}^2 - 2\gamma_{c1}\gamma_{a1} + 2\gamma_{c1}\gamma_{a1}{}^2) + \frac{\gamma_{c1}{}^2\gamma_{a1}{}^2}{\lambda_1} + \frac{\gamma_{a1}{}^2 - \gamma_{a1}{}^2\gamma_{c1}{}^2}{1-\gamma_{a1}+\gamma_{a1}\lambda_1} + \frac{2(\gamma_{c1}\gamma_{a1} - \gamma_{c1}\gamma_{a1}{}^2)}{1-\gamma_{c1}\gamma_{a1}+\gamma_{c1}\gamma_{a1}\lambda_1} \qquad (1)$$

where $\lambda_1 = k_f/k_s$ is the fluid/solid thermal conductivity ratio, $\gamma_{a1} = a_1/l_1$ and $\gamma_{c1} = c_1/a_1$ represent the geometric length scale ratio and contact length scale ratio at the micro-scale, respectively. The porosity within the micro porous cubes can be obtained by

$$\phi_1 = 1-(1-3\gamma_{c1}^{\ 2})\gamma_{a1}^{\ 3}-3\gamma_{c1}^{\ 2}\gamma_{a1}^{\ 2} \tag{2}$$

The effective stagnant thermal conductivity of the porous media consisting of spatially periods porous cubes at meso-scale is obtained by applying the lumped parameter method [2] once again to yield

$$\frac{k_e}{k_f} = (1-\gamma_a^{\ 2}-2\gamma_c\gamma_a+2\gamma_c\gamma_a^{\ 2})+\frac{\gamma_c^{\ 2}\gamma_a^{\ 2}}{\lambda}+\frac{\gamma_a^{\ 2}-\gamma_a^{\ 2}\gamma_c^{\ 2}}{1-\gamma_a+\gamma_a\lambda}+\frac{2(\gamma_c\gamma_a-\gamma_c\gamma_a^{\ 2})}{1-\gamma_c\gamma_a+\gamma_c\gamma_a\lambda} \tag{3}$$

where, $\lambda = k_f/k_{c1}$ is conductivity ratio, $\gamma_a = a_2/l_2$ and $\gamma_c = c_2/a_2$ are the geometric length scale ratio and contact length scale ratio at the meso-scale, respectively. Under these conditions, the total porosity of the bi-dispersed porous media is then given by

$$\phi = 1-[(1-3\gamma_c^{\ 2})\gamma_a^{\ 3}+3\gamma_c^{\ 2}\gamma_a^{\ 2}](1-\phi_1) \tag{4}$$

2.2 Effect of Contact Resistance and Porosity

The value of the effective thermal conductivity of a porous medium depends not only on the porosity, the thermal conductivity of the solid and the fluid phases, but also on whether the particles are in good contact, point contact or no contact. The effective thermal conductivity for bi-dispersed porous media can be computed using the 3-dimensional model given by Eq.(1)-(4). Fig. 3 shows the calculated results for $\phi = 0.4$, $\gamma_{a1} = \gamma_a$, $\gamma_c = 0.2$ and γ_{c1} from 0.1 to 0.5.

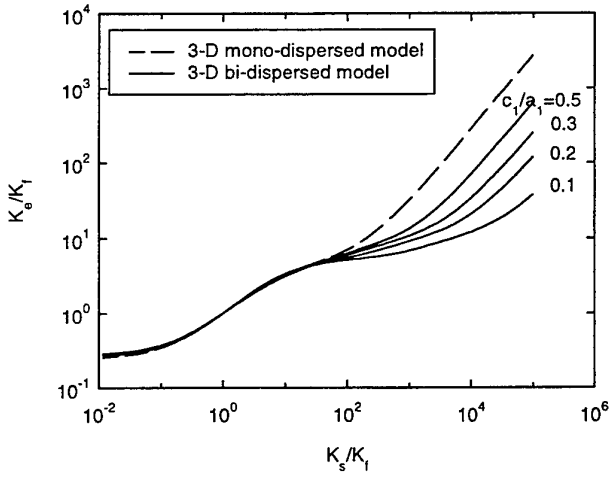


Fig. 3 Effect of touching parameter on the effective thermal conductivity of present model with the contact parameter fixed at $c_2/a_2 = 0.2$ and $\phi = 0.4$

Fig. 3 shows that the effective thermal conductivity increases with the increasing of micro-scale contact parameter γ_{c1}, especially when the difference of thermal conductivity of solid/fluid is large. For comparison, the results of mono-dispersed media with the same porosity and contact area are calculated from Eqs. (1)-(2). The comparison shows that the effective thermal conductivity of the media of the bi-dispersed porous structure is almost the same as that of mono-dispersed structure in the range when the solid/fluid conductivity ratio is between 1 to 100. This indicates that the effective stagnant thermal conductivity in this conductivity ratio is dominated by the total porosity and the effects of the contact resistance in the bi-dispersed porous medium are small. When the solid/fluid thermal conductivity ratio is higher than 100, the effects of the contact resistance in the bi-dispersed porous medium become very large.

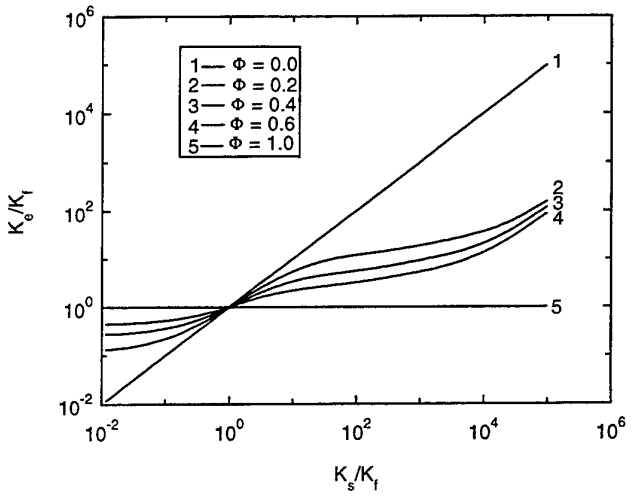


Fig. 4 Effect of porosity on the effective thermal conductivity of present model when $\gamma_{a1} = \gamma_a$, $\gamma_{c1} = \gamma_c = 0.2$

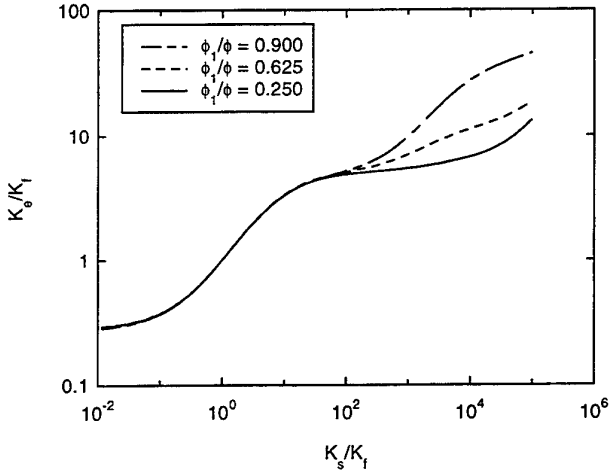


Fig. 5 Comparison of the effective thermal conductivity in different ratio of porosity within the porous cubes and the overall porosity when $\phi = 0.4, \gamma_{c1} = \gamma_c = 0.2$

Effect of porosity on the effective thermal conductivity of bi-dispersed porous medium is showed in Fig. 4. To a fixed contact area, $\gamma_{c1} = \gamma_c = 0.2$ and the same structure of micro-/macro- particles, $\gamma_{a1} = \gamma_a$, the effective thermal conductivity is affected seriously by the porosity. Fig. 5 shows the effective thermal conductivity of bi-dispersed porous material with the contact area $\gamma_{c1} = \gamma_c = 0.2$ and porosity $\phi = 0.4$ when the porosity ratio within the porous cubes and the overall porosity ϕ_1/ϕ of the bi-dispersed porous media ranging from 0.25 to 0.9. The effective thermal conductivity is not affected by porosity ratio ϕ_1/ϕ when the ratio of solid/fluid thermal conductivity is less than 100. But when the ratio of solid/fluid thermal conductivity is more than 100, the difference of effective thermal conductivity affected by porosity ratio is large. The reason is that the structures and shapes of micro- and macro- particles changed to different porosity ratio, so the contact resistance is also changed. In summary, the effective thermal conductivity of a porous medium is affected by

the microstructure of solid, porosity and the conductivity of the two constituents. This is the same as the mono-dispersed porous media analyzed by Hsu, et al [2].

3. EXPERIMENTAL INVESTIGATION

3.1 Experimental Apparatus

The steady-state method was employed to measure the effective thermal conductivity of sintered bi-dispersed porous media in this study. The experimental apparatus used in this investigation is shown in Fig. 6. The top and bottom faces of the test section were bounded by two copper plates. In order to eliminate the effects of natural convection, the heating plate was placed on the top while the cooling plate at the bottom. On the up side of the top, there were two stainless steel thermofoil heaters of about 6 Ω which were cemented to provide the heat input to the system and compensate heat loss respectively. A thick insulation polystyrene was applied to the test apparatus all around for insulation. The bottom cooling copper plate was attached to a thick plexiglass plate with channels slotted into it for cooling water flow. The chiller was used to supply cooling water at a constant temperature to obtain an isothermal cold surface. Three and five thermocouples were implanted at different position in the cold plate and heat plate respectively to measure the temperature variation on the heated and cooled surfaces. Several thermocouples were also mounted on both sides of top thick copper plate. By measuring the mean temperature difference of the both sides of the top thick copper plate, we can estimate the heat loss.

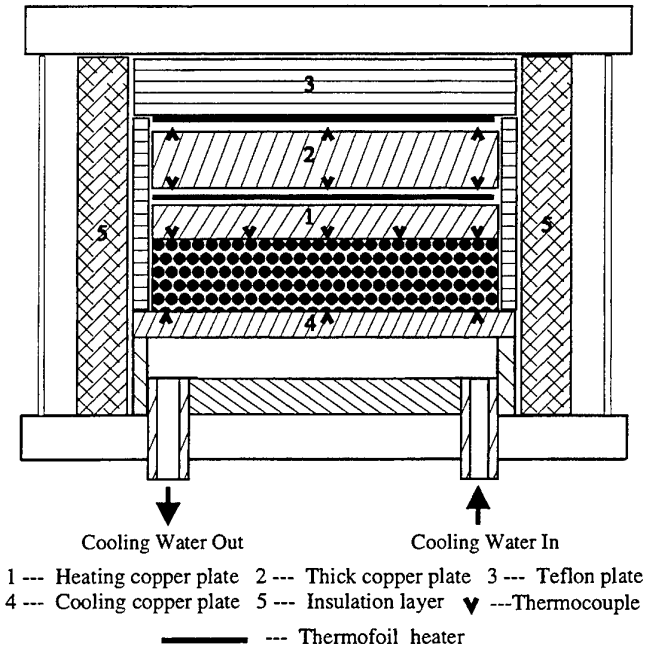


Fig. 6 Schematic of the experimental apparatus

3.2 Experimental Procedure

Thermal conductivity measurements were performed for various combination of sintered copper powders and saturated fluids. The porosity of sample was measured using the density method [5]. The results of these porosity measurements along with the other important parameters for each of the test specimens are listed in Table 1. In order to eliminate the effects of any deposits that might remain after the saturated tests, the samples were washed by distilled water. For the test with air, the porous sample was dried out in the drying box. While for the test with FC-72 and water, the sample was soaked in FC-72 and water respectively to ensure that it was fully wetted. Test to determine the effective thermal conductivity of porous sample in 3 readings of the temperature difference between heat plate and cold plate, varying from 10 °C to 30°C. The

mean temperature range of heat plate and cold plate was from 15°C to 60 °C. To ensure that a steady-state condition had been achieved, data were taken when the temperature did not vary for more than 0.3 °C over a 45-min interval. This steady-state procedure took approximately 6~8 hours for each measurement. All data of the temperature and heat flux were acquired by a high precision Solartron Data acquisition system.

Table 1 Wick samples, fluids and their properties

Wick material or Fluid	Solid/ fluid thermal conductivity (20°C) (W/m^2 K)	Micro-pore diameter (μm)	Macro- pore diameter (μm)	Porosity
Cu (sample 1)	391 *	80	200	52%
Cu (sample 2)	391 *	80	400	54%
Cu (sample 3)	391 *	(mono-dispersed)	800	49%
Water	0.59900			
FC-72	0.05643			
Air	0.02590			

*Data provided by Thermacore Inc.

3.3 Experiment Data and Comparison with the Model

Experiments were conducted with each of the test specimens to determine effective thermal conductivity. The three samples for tests were one sintered mono-dispersed copper powder porous media with pore diameter of 800 μm and two bi-dispersed copper powder with the micro- /macro- pore diameters of 80 μm/200 μm, and 80 μm /400 μm. Fig. 7 shows the results of these tests for one sintered copper mono-dispersed porous sample and the two sintered copper bi-dispersed porous samples, respectively. It can be seen that the effective thermal conductivity for three types of material increases slightly with a corresponding increase in the average specimen temperature. This is due to the increase of thermal conductivity of water and air with the increase of temperature. When the ratio of solid/fluid thermal conductivity is more than 100, the effective thermal conductivity of a mono-dispersed porous medium is much larger than of bi-dispersed porous medium due to the contact resistance at micro-scale because of the presence of the fluid in the bi-dispersed porous medium. So the effective thermal conductivity of bi-dispersed porous medium saturated with water and air is smaller than that of mono-dispersed porous medium saturated with the same fluid.

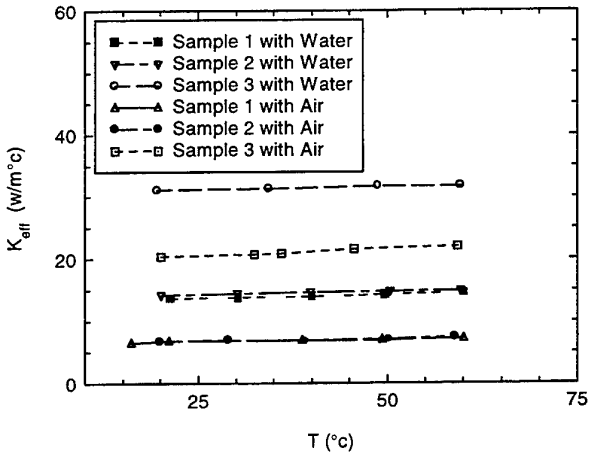


Fig. 7 Effect of temperature on the effective thermal conductivity

For sintered porous materials, the particles are in good contact, so contact areas of particles are very large, especially for micro- particles. This can be seen from Fig. 1. A comparison of experimental results of two bi-dispersed samples saturated by air, FC-72 and water, with several of the model predicted are shown in Fig.8. With the best fit, the experimental data are close to the present 3-dimensional model predicted with γ_{cl} =0.53,

γ_c =0.37 and ϕ_1/ϕ =0.342. To 2-dimensional cylinders model [4], the magnitude of effective stagnant thermal conductivity of cylinders for touching parameter γ_c is almost the same as the effective stagnant thermal conductivity of cubes with a touching parameter of γ_c^2. This is because the touching area ratio for cubes is equal to γ_c^2 while that for the square cylinders is equal to γ_c [2]. So the experimental data are also close to 2-dimensional model [4] predicted when the contact ratios of micro-, mecro- contact areas γ_{c1}, γ_c and porosity ratio ϕ_1/ϕ are 0.281,0.137 and 0.342 respectively. But results of the 3-dimensional model are closer to the experimental data. So the 3-dimensional model for bi-dispersed porous media can be used to estimate the effective thermal conductivity of sintered porous materials.

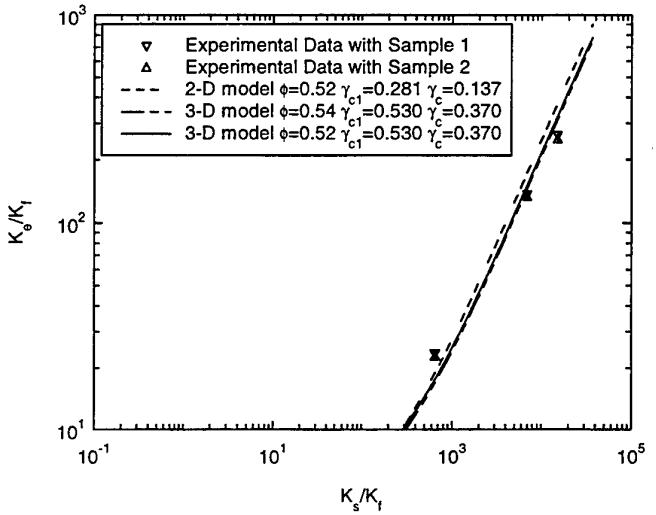


Fig. 8 Comparison of effective thermal conductivity of model (ϕ_1/ϕ =0.342) with experimental date

4. CONCLUSION

A unit cell model was used to determine effective thermal conductivity of bi-dispersed porous media based on the lumped parameter method [2]. Based on the presented model, algebraic expressions for the thermal conductivity of touching porous cubes were obtained. The steady-state method was used to determine the effective thermal conductivity of sintered bi-dispersed porous materials saturated with different fluids. The results of the experimental program were compared with the existing model and present model. It was found that the stagnant thermal conductivity based on present model with micro- and mecro- contact area ratio of 0.53 and 0.367 is close to the experimental data of sintered bi-dispersed copper porous materials. When the ratio of solid/fluid thermal conductivity is more than 100, the effective thermal conductivity of a mono-dispersed porous medium is larger than of bi-dispersed porous medium because of the contact resistance at micro-scale and higher porosity for bi-dispersed porous medium.

Acknowledgement This work was supported by RGC Grant HKUST6044/97E.

REFERENCES

1. C. T. Hsu, P. Cheng and K. W. Wong, Int. J. Heat and Mass Transfer v.37, pp.2751-2759 (1994).
2. C. T. Hsu, P. Cheng and K. W. Wong, ASME J. Heat Transfer v. 117, pp.264-269 (1995).
3. R. G.Norzad, Carbonell and S.Whitaker, Chemical Engineering Science v.40, pp.843-855 (1985).
4. P. Cheng and C.T. Hsu, Journal of Porous Media v.2, pp.19-38 (1999)
5. A. E. Scheidegger, "The physics of flow through porous media", *University of Toronto Press,* Toronto, Ontario, pp.10-12 (1963).

REWETTING PHENOMENA AND THERMAL STABILITY AT STEAM GENERATION ON SURFACES WITH POROUS COATINGS

Vassili I. Borzenko
Institute for High Temperatures of RAS (IVTAN)
Fax: (7-095)362 07 84, E-mail: litp@dataforce.net

Stanislav P. Malyshenko
Institute for High Temperatures of RAS (IVTAN)
Fax: (7-095)362 07 84, E-mail: litp@dataforce.net

Keywords: heat transfer enhancement, thermal stability, porous coatings

ABSTRACT. Application of porous coatings on the steam generating surfaces is one of the most reliable way of heat transfer and thermal stability enhancement of steam generation process. Based on the latest progress of the experimental investigations of the problem by Laboratory for Intensification of Thermal Processes IVTAN, the method dealing with the use of optimized porous coatings is proposed, for example for horizontal steam generating tubes of parabolic trough collectors of solar thermal plants working at direct steam generation mode. The basic phenomena produced by the porous coating for pool boiling and steam generation in horizontal tubes are presented and discussed. The results of applied investigations of power thyristors and composed superconductors thermal stabilization with the help of optimized porous coatings are given as an example of the perspectiveness of the use of porous coatings.

1.INTRODUCTION

The boiling surfaces activation technique with porous coatings is of considerable current use in refrigeration and chemical industries to heat transfer intensification at pool boiling [1-3]. In [4-7] some pecularities of physics of boiling on porous surface were established experimentally. These pecularities are determined by two-phase filtrarion process in porous space of the coating. First of all, it is the presence of two instead of one regimes of nucleate pool boiling for relatively thick and non-conductive coating. presence of maximums in the dependence of the critical heat flux q_{cl} on the thickness of the coating, sharp increase of relaxation periods of wall temperature T_w approaching to the transition points from one regime to the other, higher values of q_{cl}, compared to smooth surfaces. Heat transfer and hydraulic resistance at two-phase flow in vertical channels with inside porous coatings were the subject of experimental investigations [8,9], which also showed increase of critical heat flux and the possibility to reduce or avoid dry-out. The task of investigations of rewetting phenomena in horizontal channels with porous coatings originated from the problems of solar power plants with parabolic trough collectors working according to Direct Steam Generation principle [10]. The most important peculiarities of steam generation processes in Direct Steam Generation-DSG technology are:

- big length (L > 10 m) and diameters (40-120 mm) of horizontal or slightly inclined steam generating tubes;
- non-uniform through perimeter and in time heating of the tubes (20-100 kW/m^2);
- low mass flow rates ($\leq$ 500 kg/m^2 s);
- the necessity to reach high steam fractions on the outlet of the steam generating channels at pressures up to 10-16 MPa (x ~ 1).

Under these conditions the stratified and intermittent regimes of two-phase flows are possible, which inevitably lead to substantial non-uniformity of wall temperature over perimeter and length of the steam generating channels and probably to dry-out phenomena [10,11]. The possible way of solving these problems is the use of inside porous coatings of steam generation tubes [12,13]. This possibility and the expected new effects are investigated at pool boiling modelling experiments, described below. The interest to experimental investigations of stabilization of electric equipment, such as power thyristors, is explained by the necessity to reach high heat load removal in a wide range of ambient temperatures. Another important task in the electric device field is cryostabilization of superconductors at boiling of liquid helium. The results of these experiments together with the results of basic investigations of peculiarities of liquid helium pool boiling on the surfaces with porous coatings are also presented below.

2.REWETTING PHENOMENA AT STEAM GENERATION IN HORIZONTAL CHANNELS

The stratified and intermittent flows in horizontal and inclined pipes occur at low mass velocities of two-phase flows in horizontal channels. The porous coatings produce new effects, which can lead to decreasing the wall temperature non-uniformity in horizontal steam generating tubes.

Coating Friction Effect.

In homogenous model of the flow the critical velocity W_c below which the stratified and intermittent flows modes occur is in inverse proportion to 1/2 degree of friction factor ξ . In Teitel/Duckler/Barnea model [12] the mentioned velocities of gas and liquid phases that correspond to the stratified and intermittent modes start are determined by the law of conservation of momentum and decrease substantially with the growth of friction factor for liquid and gas phases ξ_L and ξ_G. As the results of our measurements in vertical tubes with inside porous coating show, ξ_L , ξ_G and ξ increase 3.5÷4 times compared to smooth tubes and that leads to 1.5÷2 times decrease of W_c according to homogenous model [14]. Within the Teitel/Duckler/Barnea model with increase of ξ_L and ξ_G the area of stratified and stratified wave modes pattern existence shifts to lower superficial liquid and gas velocities. Thus, it is possible to expect that at porous coatings presence the danger of stratified and intermittent flows can be substantially reduced.

Asimutal Heat-Pipe Effect

All cappillary effects at boiling on the surfaces with porous coatings are defined by percolation radius r_p which corresponds to the appearance of the connectedness of pores occupied by steam [5]. The percolation radius of the vapour-filled pores can be predicted, given the size distribution of pores and the pore lattice geometry, by methods of percolation theory. At partial dry-out of channel walls with porous coatings the cappillary pressure difference $\Delta p \approx \frac{2\sigma}{r_p}$ which makes liquids to run over from the full wetted area to the area of partial dry-out along the perimeter in asimutal direction. This process is a full analogue to that observed in heat-pipes and makes the device completely isothermic. In our case the opportunity for wetting the coatings due to asimutal heat-pipe effect is limitted by cappillary pressure and maximal way length from the lower generatrix to the upper is equal to the pipe diameter d . Assuming the pressure in gas phase over the cross section of the pipe equal we can receive the following estimation for the limiting perimeter-mean heat flux

$$\langle q \rangle_{max} \approx \frac{2}{\pi^2 d^2} \frac{k}{\mu} \rho H \cdot h \left(\frac{2\sigma}{r_p} - \rho g d \right) \qquad (1)$$

here h and k - thickness and permeability of the coating, ρ , μ , H, σ - density, viscosity, evaporation heat and surface tension of water, r_p - percolation radius. Taking for estimations $r_p \sim 10^{-5}$, $h \sim 10^{-4}$ m, $k \sim 10^{-11}$ m , $d \sim 10^{-1}$ m it is possible to receive for water at p = 10 MPa and t = 300°C the estimation: $\langle q \rangle_{max} \sim (10^4 \div 10^5)$ W/m^2 . Thus, at not big thicknesses of porous coatings $h \sim 10^{-4}$ m with permeability $k \sim (10^{-11} \div 10^{-10})$ m^2 and $r_p \sim 10^{-5}$ m asimutal heat-pipe effect can provide thermal stabilization of walls of steam generating channels at heat loads corresponding with DSG processes. Actually taking into account heat transfer due to thermal conductivity of the skeleton and convection the thermal stabilization due to porous coating is even more efficient.

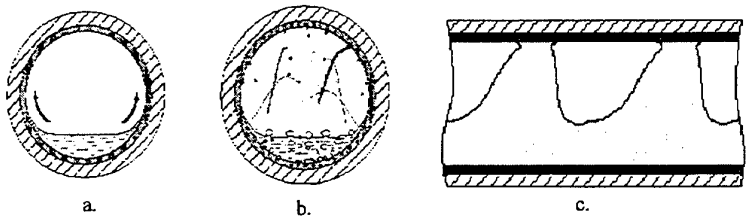


Figure 1. Mechanisms of rewetting in horizontal channel: a) asimutal heat pipe effect; b) drops wetting effect; c) wave rewetting

Drops-Wetting Effect.

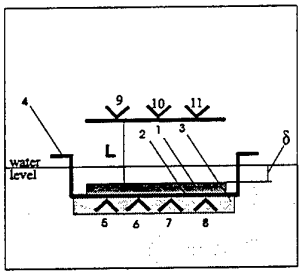
One of the most important results of our experiments in vertical tubes with inside porous coatings is the increase of thermal stability of steam generating channels near the flow parameters that correspond to high steam fractions and thin liquid films of the channel walls, and also in post dry-out area due to increase of rewetting effects [9].. Also, there a new hypothesis was offered about the changes in distributions of drops generated on the heated surface at the presence of porous coatings (the flow of high speed drops with dimensions $a \sim r_p$). The estimations of "shooting through"drops velocities give the values of up to 10 m/s order. It is clear that these drops will reach the opposite points on perimeter of the channel on the short distances from the generating points along the axle. It means that efficient wetting of the whole perimeter by drops will occur. In the area of high pressures the role of drops wetting effect, certainly decreases because the steam density increase and liquid density decrease. However, in this area the wall temperature non-uniformity in horizontal channels decrease substantially and the role of coating friction effect in the ensuring the channel perimeter wetting grows. Thus, even if the stratified and intemittent modes occur this effect provides additional wetting of the channel perimeter and decrease of temperature non-uniformity. The considerable influence of the drops wetting effect is indirectly confirmed by our experimental results in the area of pressure up to 16 MPa. However, the detailed experimental investigation and confirmation are needed.

Wave Rewetting Effect.

This wetting mechanism is essential for intermittent flow (Fig.1.). The main peculiarity of the process is proximate to the process of rewetting at pool boiling in second crisis of boiling. Due to this fact it is possible to investigate this mechanism in a modelling experiment at pool boiling.

Experimental Investigations of Rewetting.

For the experimental investigations of boiling on porous coatings a high pressure stainless steel chamber with optical windows was used [6]. Experimental technique combined direct visual observation of elementary processes with integral estimation of drops wetting effect by means of thermogram method. The task of modelling the processes in horizontal steam generating channel led to the construction of test part shown on Fig.2. Flat 30×8 mm NiCr test sample with thermocouples along the axle is heated by direct current transmission. The water level is regulated as well as the height of NiCr heat wire put in the gas area and also heated by electric current. The bubbles generated by porous coating knock out the secondary drops which partly



1-porous coating
2-NiCr plate
3- thermal insulation layer
4-contacts
5-11 - thermocouples

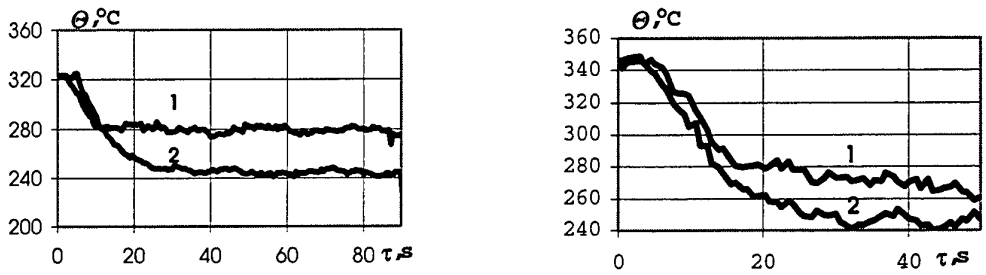
Figure 2. Test section scheme

reach the wire and create additional cooling of the wire. The temperature difference between the states of the wire with and without cooling by drops is the criterion of drops wetting efficiency. The experiment provides the data sufficient for calculating the heat flux evacuated from the wire by drops. Wave rewetting experiments were held on liquid nitrogen, which demands substantially lower critical heat fluxes do not leading to burn out of the test piece. The parameters of the porous test pieces were the same as in the water experiments.

Experimental Results on Drops Generation and Capturing.

The photograph analysis of the secondary drops did not show any evident correlation between the sample heat load and size and velocity of a drop. The collection of the observed types of drops (fast and small, bigger and more slow drops) seemed to be constant except the growth of the fast drops part with the heat load increase. The trace of the drop gives information on the velocity and size of each drop. The highest drop velocity value

observed in the tests at 0.3 MPa was about 6 m/s , the most of the drops had velocity about 1 m/s and size 0,14 mm.



a) b)

Figure 3. Comparative thermograms of drops rewetting effect for smooth 1) and porous 2) test pieces: a) L=15mm, q= 374 kW/m, δ = 3 mm; b) L=30 mm, q= 880 kW/m, δ = 6 mm

Thermogram method as applied to investigations of drops rewetting phenomena gives representative picture of the effect of the porous coating presence on intensification of rewetting. On Fig.3. two comparative thermograms are given demonstating the difference of the final temperature (after drops generation start) in cases of smooth and porous coated heaters. The wire in both cases is preheated up to the same temperature and cooling occurs only due to the drops generated by the sample. Fig.4. shows the experimental dependence of temperature difference θ_1-θ_2 on the sample heat flux. q. The calculation method for the heat flux evacuated by drops is based on the assumption that convective heat transfer coefficient is constant during the process. In this case it is possible to figure out the part q_d of the heat flux for which the drops wetting is responsible . The dependence of q_d on the sample heat flux is shown on Fig.5.

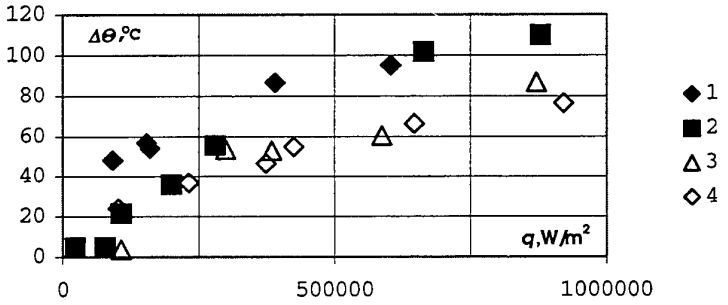


Figure 4. Difference between starting and final wire temperature as a function of sample heat flux. 1) porous sample L=15mm, δ=3mm; 2) porous sample L=15, δ=6mm; 3) smooth sample L=15 mm , δ=6 mm;4) smooth sample L=15, δ=3 mm

Comparison of porous and smooth surfaces concerning the phenomena that can reduce the unfavorable effect of stratification in horizontal steam generating channels showed the advantages of porous coatings. First of all, it is true for drops wetting effect that is at least up to 1,5 times more efficient at presence of the porous coating on the heater than for the case of the smooth wall heater.The influence of this effect can be more considerable in case of drops inpact on the surface that is also porous. The interaction of a secondary drop and porous surface was a subject of separate investigations. Vertical tube experiments together with the data on dry out in annular channel display the importance of the presence of porous coating on the wetted surface for stabilization of the heated wall temperature. That is the case when the highest increase of critical heat flux can be obtained. In order to test the influence of the porous coating presence on the wetted surface the following qualitative experiment was conducted. The receiver wire in drops generation test was removed by NiCr plate 30×8 mm also heated up to a initial temperature and power was kept constant during the test. Due to negligible temperature

coefficient of resistance of NiCr in the conditions of constant voltage the heat load on the plate was also fixed. The more efficient drops capturing at porous coating presence (Fig.6.). follows from higher decrease of temperature at equal heat loads on drops generating test sample.

The wave rewetting can be of great importance for intermittent flow mode due to the percolation mechanism of wetting coming into force with increase of temperature relaxation periods

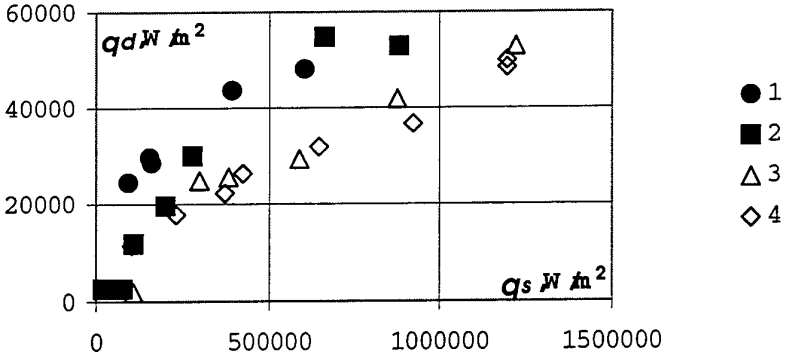


Figure 5. Dependence of the wire heat flux evacuated by drops on the sample heat flux L= 15 mm

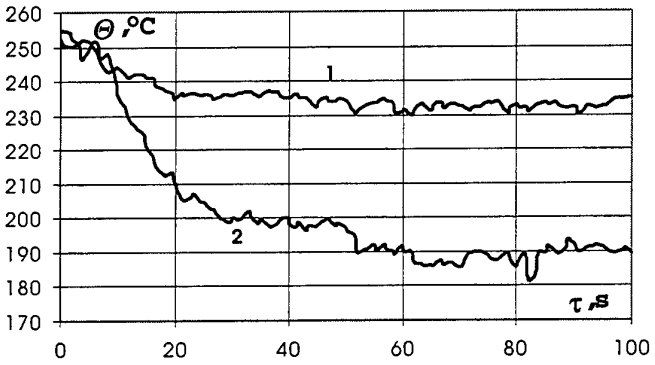


Figure 6. Comparative thermogram of drops wetting for smooth 1) and porous 2) wetted test samples; heat flux on drops generating surface q=1500 kW/m^2

3.NEW TYPE COOLER USING POROUS COATING FOR POWER THYRISTORS

Power semiconductor devices are of great use at present in power generation and in electric transport systems. Constant increase of their unit power demand new approach to the problems of thermal stability of such kind of equipment. Based on the experience in using porous coatings for heat transfer enhancement and thermal stabilization at boiling, a new type of cooler for power thyristors for use in electric transport was developed and tested recently by LITP IVTAN. The design of the cooler allowed to dissipate by natural air convection up to 1.6 kW of heat load. The cooler is designed according to thermal syphon principle. The heat removal from the heater surface is carried out by boiling of refrigerant on the evaporator with further condensation in air cooled condenser. For keeping the level of cooling agent in the pressure range 1-10 bar, a compensation volume is provided. Finned heated surface is covered with optimized porous coating. The device was tested on a specially constructed test bench together with the similar cooler without porous coating on the finned heater surface. NiCr heater was used for simulation of heating and water cooled condenser was used for cooling.

At experimental investigations of the cooler performance the value of 88 °C was taken as the limitting temperature of the thyristor body. Fig.7. gives comparison of test results of the both types of coolers, with and without porous coatings.

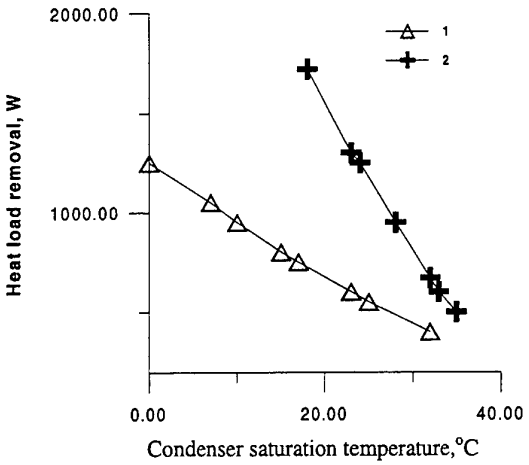


Figure 7. The results of tests on heat load removal by cooler (1- without porous coating, 2- porous coated) depending on the condenser saturation (ambient) temperature

Resulting from the experimental data a resume was made on the advisability of using porous coatings for the thermaql stabilization of power semiconductor devices. The new type cooler showed good performance in a wide range of ambient temperatures (-35...+45)°C, considerably exceeding the performance of the similar non-coated cooler.

4.COMPOSED SUPERCONDUCTORS WITH POROUS COATINGS

In most cases for cooling cryostatically stabilized composite superconductors liquid helium boilng on superconductor surface is used. Intensification of heat transfer rises the level of cryostatic stability of the superconductor. As the result, the design current density can be increaesed both by reducing the percentage of normal stabilizing material or by decrease of the area required for cooling. In order to investigate the peculiarities of heat transfer to helium at pool boiling on surfaces with porous coatings a detailed experiment was conducted [7]. Zinc was used as a material for porous coating, which was applied by electrochemical plating method. Porosity of the coating was less than 20%, while equivalent diameter of pores ranged from 3 to 30μm. Coatings were applied on the end face of copper rod. Coating thickness of the test sample was 10μm, 25μm and 50μm. A regular procedure was followed in heat transfer investigations. Copper cylinder insulated by vacuum jacket with one free end surface was used as a test zone. Heat flux was generated by a heater on the opposite side of the rod. Temperature calculation of the base underlying the porous coating was done on the basis of readings taken by three copper/iron -copper thermocouples embedded in the rod body. Heat load was changed stepwise. After each change of q the surface superheat $\theta=T_w - T_b$ was measured as a value corresponding to stedy-state conditions. Experiments were carried out both for rising and lowering of q, using porous coated samples and controls without coatings. Curves of pool boiling on horizontal surfaces facing upwards, both uncoated and with porous coatings, obtained in the experiments at increase and decrease of heat load are presented in Fig.8. As in the case of water [4,5], for helium pool boiling a bubble mechanism of vapour evacuation is associated with two modes of heat transfer. Transition from one mode to the other occurs at threshold values of heat flux $q=q^*$ characteristic of each coating. The heat transfer law $q\sim\theta^n$ at nucleate boiling mode I is characterized by n=1.95-2, which is close to pool boiling characteristics of uncoated surfaces. Near $q=q^*$ an abrupt decline to n=0.7÷1 is seen. The nucleate boiling with stabilized vapour film inside the coating (mode II) is characterized by n which is close to film boiling regime at smooth surface, but it corresponds to much lower values of superheat θ , i.e. higher heat transfer coefficient. Crisis of boiling occurs at heat loads far exceeding critical heat loads on smooth surfaces and at θ_{c1} exceeding the temperature difference at smooth surfaces by more than an order of magnitude (Fig.8). These findings show that application of porous coatings

leads to significant intensification in heat transfer during helium boiling over the entire superheat range of heating surface up to $\theta=T_c-T_b$ (T_c – the critical temperature of the superconductor). Whenever such coatings are adopted for increasing cryostatic stability of superconductors the maximum effect can be reached by choosing the most suitable properties of the coatings, such as porosity, permeability, thickness, partcles package pattern, particle size,etc.

Fig.9,10. give simple theoretical approach to understanding the new effects brought by the porous coating for the superconductor stability improvement. The normal zone evolution [7], as it follows from heat balance , depends on the relation between heat generation and heat transfer. Curves $q(T)$ and $W(T)$ can have several crossing points (equilibrium states), where $W(I,T)=q(I,T)$.

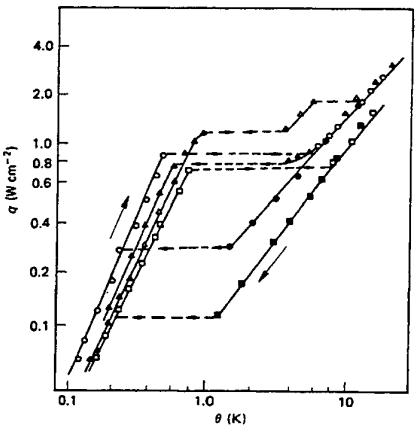


Figure 8. $q(\theta)$ **in the conditions of rising and dropping heat flux for various surfaces: smooth surface; with porous coating** h**=25μm; coating is stripped off; - q decreasing; - q increasing.**

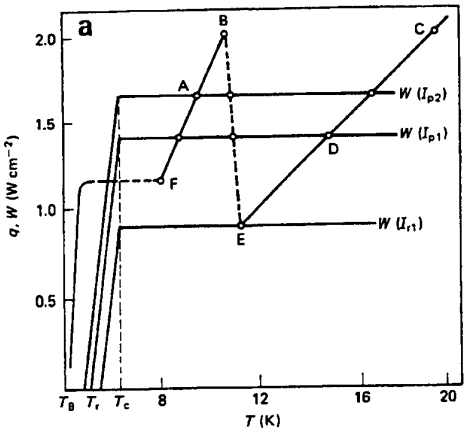


Figure 10. View of functions $q(T)$ **and** $W(I,T)$ **for porous coated conductor:** q**, —** W**.**

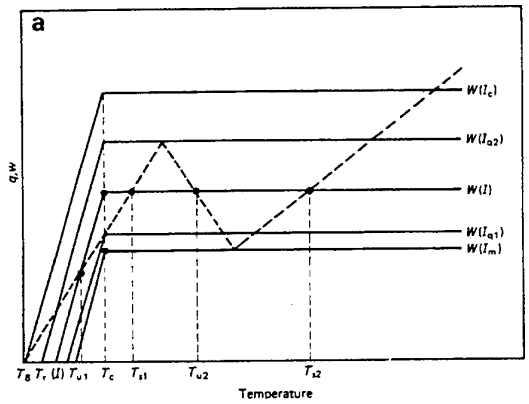


Figure 9. General view of functions q**(T) and** W**(I,T): - -** q**, —** W**.**

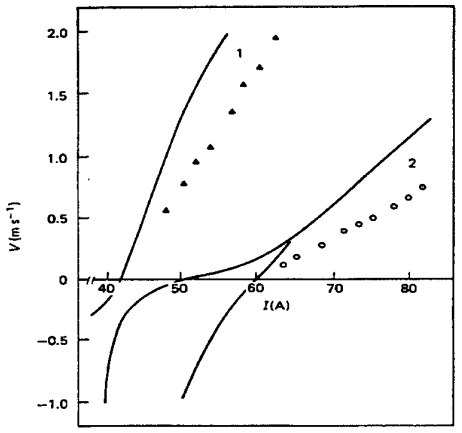


Figure 11. Porous coating effect on the velocity of normal zone: B=4T; 1,h**=0; 2,**h**=50μm; — calculations.**

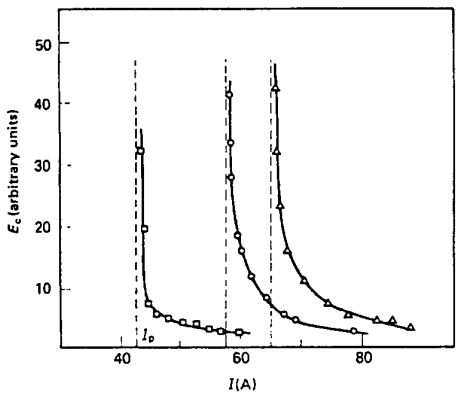


Figure 12. Porous coating effect on the magnitude of thermal pulse energy required for transfer of the conductor to the normal state. B=4T; h=0μm; h=30μm; h=100μm.

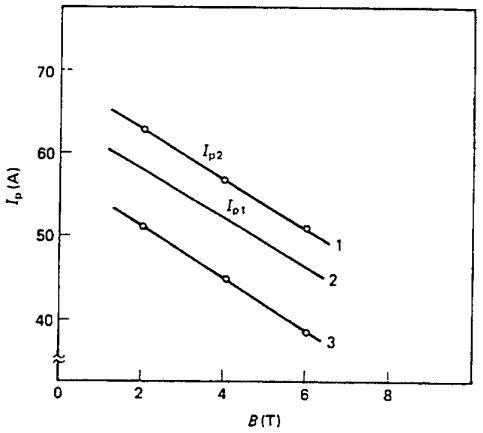


Figure 13. Comparison of experimental and calculated data of $I_p(B)$: ——— , calculated by the theorem of equal areas; 1, h = 30 μm, experiment; 2, h = 30 μm, calculation; 3, h = 0 μm, experiment.

If the conductor is in a homogeneous state with a constant temeperature over its length, the equilibrium will be stable at

$$\frac{\partial}{\partial T}(q - W) > 0 \qquad (2)$$

and unstable when the inequality sign changes. As it is shown in Fig.9. the number of stable states of a conductor depends on the current. At I I_m (I_m – full recovery current) q(T) W(I,T), and the only stable state will be the state of superconductivity. It means that at any initial temperature of the conductor, its final temperature will be equal to T_b. At I_m< I I_{q1} and I_{q2} I I_c (I_c – the critical current) the superconducting and normal states will be stable. At $I_{q1}<I<I_{q2}$ there are three stable states. Superconductors with porous coatings have substantially different characteristics of boiling curves (Fig.10.). It means that the conditions of the thermal equilibrium can be met at different boiling modes occuring on the same conductor surface. For current I_{p1} the state of thermal equilibrium is realized at the film boiling (point D), and for current I_{p2} at the nucleate boiling mode II (point A), where vapour film is stabilized in its thickness. Fig.11. shows the normal zone propagation velocity versus the current I. In the region of currents $I_{q1}<I<I_{q2}$ v(I) is not of a singled valued nature due to availability of two equilibrium temperatures T_{s1} and T_{s2}. Based on the experimental study of heat transfer to pool boiling helium and promising theoretical results on superconductor stability at use of porous coatings, experimental tests of Nb-Ti semiconductors with porous coatings were carried out [7]. The conductors were provided with the coatings similar to those which were used in the test pieces involved in heat transfer experiments. The coating thickness varied within the range of 20 ÷ 300 μm. Test conductors were 1.5m long and were positioned in homogeneous magnetic field normal to the sample central line. Experimental setup provided the possibility of thermal disturbance initiation in pulse and steady state regimes. The experiments were determining minimum propagating current I_p, full recovery current I_r, normal zone propagation velocity and minimum thermal pulse energy required for a stable normal zone E_m. The influence of the porous coating presence and thickness on the value of thermal pulse energy required for transfer of the superconductor to the normal state, received experimentally is given on Fig.12. as an example of the expected higher efficiency of the porous coated superconductor, compared to smooth. Fig.13. gives propagation current dependencies upon the magnetic field induction. Resulting from the experimental investigations it is possible to conclude that porous coatings ensure intensification of heat transfer and posses high effective specific heat. Their application promotes a better stability level of composed superconductors. It has been proved that the use of porous coatings makes it possible to increase significantly the minimum thermal disturbance energy required for transferring the superconductor to

the normal state, to rise the minimum propagation current and full recovery current, and to reduce the normal zone propagation velocity as compared to superconductors with smooth surface.

4.CONCLUSION

The task of heat transfer enhancement and thermal stabilization can be successfully solved with the help of porous coatings. This resume was proved for pool boiling of refrigerant in power thyristor cooling system and for thermal stabilization of composed superconductors at boiling of liquid helium. This is possible due to substantially higher q_{cl} and higher heat transfer coefficient on some regimes of pool boiling. In case of forced convection in channels, porous coatings produce some new effects, where drops generation and drops capturing are the main, creating new moisture exchange pattern, especially in case of horizontal channels. Modelling experiments showed more than 2 times higher efficiency of these effects compared to smooth surfaces.

ACKNOWLEDGEMENTS

We are grateful to Federal German Ministry of Science, Education, Research and Technology, DLR for support of this research (project 6-036-0041) as well as to Russian Foundation for Basic Research (grant 96-02-17546). Also, we would like to thank the entire working group of LITP IVTAN, especially, R.G.Muchnik, A.B. Andrianov, A.V.Zuev, I.A.Orlova, V.P.Baev and M.N.Makeev.

REFERENCES

1. A. Bergles, Heat Transfer Enhancement-the Encouragement and Accomodation of High Fluxes. Proc. ExHFT-4. V.4, pp. 1907-1919 (1997).
2. R.L.Webb, 1981. The Evolution of Enhanced Surface Geometries for Nucleate boiling. Heat Transfer Engineering. V. 2, No 3-4, pp. 46-69. (1981).
3. A.M. Czikk., P.S. O'Neill & C.F. Gottzmann, 1981 Nucleate Boiling from Porous Metal Films: Effect of Primary Variables. *Advances in Enhanced Heat Transfer.* HTD 18, 109-122 (1981).
4. S.P. Malyshenko,. The Peculiarities of Heat Transfer Crisis at Two-phase Flows in Steam Generating Channels with Inside Porous Coatings. *Proceedings of the Second International Symposium on Two-Phase Flow Modelling and Experimentation.* Vol.1,pp.321-328 (1999).
5. S.P. Malyshenko, Physics of Boiling on Porous Coated Surfaces and Enhancing of Thermal Stability of Equipment. *Proc. ExHFT-4.* V. 2, pp. 579-592 (1997).
6. V.I. Borzenko, S.P. Malyshenko, Investigations of Rewetting Phenomena at Steam Generation on Surfaces with Porous Coatings. *Journal de Physique,* vol.9, pp.531-536 (1999).
7. V.V. Andrianov, V.P. Baev, S.P. Malyshenko S.P., R.G. Muchnik & M.B. Parizh, Composed Superconductors with Porous Coating. *Cryogenics,* vol 29, • 3, 168-178
8. A.B. Andrianov, A.V. Zuev, L.L. Levitan, S.P. Malyshenko, I.A. Orlova, Hydraulic Resistance of Two-phase Flows in Pipes with Porous Coatings. *Teplofiz. Vys. Temp.* 32, No 1, 94-100 (Engl. transl. *High Temperature*, v.32, No 1) (1994).
9. S.P. Malyshenko, A.V. Zuev, L.L. Levitan, A.B. Andrianov, I.A. Orlova, Pecularities of dry-out development in pipes with inside porous coatings. *Teplofiz. Vys. Temp.* 35, No 3, pp. 424-431 (Engl. transl. *High Temperature*, v.35, No3 (1997).
10. M. Muller 1994. Direct Solar Steam in Parabolic Trough Collectors (DISS). PSA, CIEMAT, DLR (1994).
11. E. Dagan, M. Muller, F. Lippke, 1992. Direct Solar Steam Generation in Parabolic Trough Collector. P.S.A. (1994).
12. S.P. Malyshenko, A.V. Zuev, A.B. Andrianov, 1994. Heat transfer intensification and thermal stability enhancement for direct steam generators solar receivers using porous coatings. *Proc. 7th Internat. Symp. on Solar Thermal Concentrating Technologies.* IVTAN Publ. Moscow. v.4, 934-942 (1994).
13. S.P. Malyshenko, Boiling Phenomena in Direct Steam Generators with Porous Coatings. IVTAN-DLR. *Interim Report I on Contract No 6-036-0041* (1996).
14. Y. Taitel, Flow pattern transitions in two-phase flow. KN-14. *Proc. IHTC. Jerusalem.*pp.. 237-254. (1990).

NUMERICAL ANALYSIS OF TWO-PHASE FLOW IN POROUS MEDIA WITH FINITE ELEMENT METHOD

Qiang Bai
Department of Mechanical Science and Engineering
Kyushu University, Japan
Email: qiang@mech.kyushu-u.ac.jp; Fax: (+81) 92-641-9744

Takeshi Hyuga
Toshiba Company, Japan

Yasunobu Fujita
Department of Mechanical Science and Engineering
Kyushu University, Japan
Email: fujita@mech.kyushu-u.ac.jp; Fax: (+81) 92-641-9744

Keywords: boiling, porous media, two-phase mixture model, finite element method

ABSTRACT. A numerical procedure for analyzing two-phase flow and heat transfer in porous media was presented. Formulation was based on the two-phase mixture model, originally developed by Wang and Beckermann, in conjunction with a finite element method (FEM). An extended Forchheimer - Darcy law was employed to accommodate the procedure to a wide range of Reynolds number. The conservation equations were discretized by FEM on quadrilateral elements using an equal-order interpolation. To validate the proposed algorithm, boiling in a square, two-dimensional porous enclosure heated from below was simulated. Numerical results agreed well with those by Wang and Beckermann and experimental data by Sondergeld and Turcotte. Then free convection boiling from a horizontal cylinder embedded in porous medium and heated at uniform heat flux was analyzed. Numerical results include the variations in isotherm and iso-liquid saturation, and the flow fields as a function of heat flux and temperature of top surface. The present algorithm is adaptable to a variety of geometric configurations, thermal and hydrodynamic boundary conditions, and a wide range of flow velocity, thus applicable in tackling any types of problems of practical importance.

1. INTRODUCTION

Heat transfer and fluid flow associated with phase change from liquid to vapor in porous media are very important in a wide range of engineering applications; for example, nuclear reactor safety analysis, oil reservoir engineering, thermal energy storage and recovery, and porous heat pipe. Many experimental and numerical studies have been devoted to the two-phase flow in porous media in the last two decades [1]-[6]. Most numerical analyses are based on the separate flow model and using a finite difference method (FDM), and usually neglecting the capillary force term to simplify the numerical implementation, which limits their possibility of general use. Tung and Dhir[3] presented a scheme based on a hydrodynamic model in which pressure and void fraction are selected as independent variables instead of velocities in the governing equations. Their scheme can easily handle the problem with an arbitrary porous domain and allow for variable permeability and boundary conditions because a finite element method (FEM) is employed. In the calculation, however, void fraction must be calculated ahead and the capillary force term is neglected, which restrain wider applications of the scheme.

Recently, Wang et al. [7][8] presented a two-phase mixture model in which two phases of liquid-gas or liquid-vapor are regarded as constituents for a two-component binary mixture. Considering the two-phase mixture as a single fluid, they formulated conservation equations for mass, momentum and energy. Thus the conservation equations are reduced by a half when compared to the conventional separate flow model. Unfortunately, the numerical procedure in conjunction with FDM is based on the Darcy law which is valid only at low velocity for $Re < 0.2$ where Re is Reynolds number defined using the square root of permeability as a characteristic length. Practical problems of porous media are wide-ranging in permeability, porous material and fluid filling it, system geometry, and thermal and hydrodynamic boundary conditions. To accommodate in a more unified form to wide-ranging problems, a robust numerical algorithm with FEM is presented in this paper. Formulation is based on the two-phase mixture model of Wang and Beckermann [7] and an extended Forchheimer-Darcy law is used.

As the result the algorithm is adaptable to a wide range of Reynolds number, geometry, and thermal and hydrodynamic boundary conditions. Numerical results are presented for two-phase flow and heat transfer around a heated horizontal tube embedded in a porous rectangular enclosure.

2.GOVERNING EQUATIONS AND SUPPLEMENTAL RELATIONS

Governing Equations

The present numerical formulation is based on the two-phase mixture model of Wang and Beckermann [7]. Darcy law is used in their original formulation, while an extended Forchheimer-Darcy law is employed here to expand the developed algorithm to a wide range of flow velocity. Only the final form of the governing equations, mixture properties, supplemental and constitutive relations are listed in Table 1. Refer to Ref [7] for a rigorous derivation of these equations and the underlying assumptions.

When the Ergun constant C is set to zero, the formulation in Table 1 is consistent with that of Wang and Beckermann [8] because an extended Forchheimer-Darcy law comes to the Darcy law they employed. Note that the variables for two-phase mixture appearing in the equations in Table 1 have no subscript, while the subscripts l and v denote the intrinsic properties or variables in liquid and vapor phase, respectively. The conservation equations are usable irrespective of the single- and two-phase zones, while thermodynamic variables vary in three zones as shown in Table 2.

Numerical Procedure

Substitution of the momentum equation in Table 1 into the mass conservation equation gives the following Poisson-type pressure equation. After solving the pressure equation, flow field is calculated from the momentum equation.

$$\nabla\cdot\left(\frac{K}{\nu+\sqrt{K}C|\vec{u}|}\nabla p\right)=\varepsilon\frac{\partial\rho}{\partial t}+\nabla\cdot\left(\frac{K}{\nu+\sqrt{K}C|\vec{u}|}\right)\rho_k\vec{g} \tag{1}$$

Equations in Table 1, derived on the basis of the two-phase mixture model and an extended Fochheimer-Darcy law, compose a set of quasi-transient equations because of no unsteady term included in the momentum equation. Their solutions are found in following the steps shown in Fig. 1. When the relative errors in the mixture enthalpy and velocity fields are less than 10^{-5} between two consecutive iterations, convergence is considered to be achieved. The results obtained from the quasi-transient calculation are regarded as the solutions under the steady state conditions.

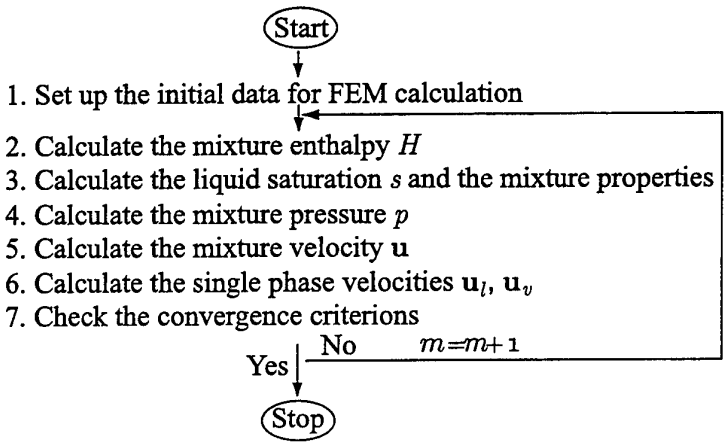


Fig. 1. Flow chart of the present algorithm

Table 1. Governing Equations and Supplemental Relations

Governing equation:	
Mass	$\varepsilon\frac{\partial\rho}{\partial t}+\nabla\cdot(\rho\vec{u})=0$
Momentum (Forchheimeer-Darcy Law)	$\rho\vec{u}=-\frac{K}{\nu+\sqrt{KC}\lvert\vec{u}\rvert}(\nabla p-\rho_k\vec{g})$
Energy	$\Omega_h\frac{\partial H}{\partial t}+\nabla\cdot(\gamma_h\vec{u}H)=\nabla\cdot(\Gamma_h\nabla H)+\nabla\cdot\left[f(s)\frac{K\Delta\rho}{\nu_v}h_{fg}\vec{g}\right]$
Mixture properties:	
Density	$\rho\equiv s\rho_l+(1-s)\rho_v$
Velocity	$\vec{u}\equiv(\rho_l\vec{u}_l+\rho_v\vec{u}_v)/\rho$
Enthalpy	$H\equiv\rho(h-h_{vsat})$ where $\rho h\equiv s\rho_l h_l+(1-s)\rho_v h_v$
Pressure	$p\equiv\lambda_l p_l+\lambda_v p_v$
Kinematic viscosity	$\nu\equiv\frac{1}{(k_{rl}/\nu_l)+(k_{rv}/\nu_v)}$
Kinetic density	$\rho_k\equiv\lambda_l\rho_l+\lambda_v\rho_v$
Effective heat capacitance ratio	$\Omega_h\equiv\varepsilon+\rho_s c_s(1-\varepsilon)\frac{dT}{dH}$
Effective diffusion coefficient	$\Gamma_h\equiv\frac{D(s)}{\rho_l}+k_e\frac{dT}{dH}$
Advection correction coefficient	$\gamma_h\equiv\frac{\lambda_l}{\lambda_l+\lambda_v}\cdot\frac{\rho}{\rho_l s}$
Capillary diffusion coefficient	$D(s)\equiv\frac{K}{\nu+\sqrt{KC}\lvert\vec{u}\rvert}\cdot\frac{\lambda_l\lambda_v}{\lambda_l+\lambda_v}\left(-\frac{dp_c}{ds}\right)$
Hidrance function	$f(s)\equiv\frac{\lambda_l\lambda_v}{\lambda_l+\lambda_v}\cdot\frac{\nu_v}{\nu+\sqrt{KC}\lvert\vec{u}\rvert}$
Relative mobilities	$\lambda_l\equiv k_{rl}\frac{\nu+\sqrt{KC}\lvert\vec{u}\rvert}{\nu_l+\sqrt{Kk_{rl}C}\lvert\vec{u}_l\rvert}$, $\lambda_v\equiv k_{rv}\frac{\nu+\sqrt{KC}\lvert\vec{u}\rvert}{\nu_v+\sqrt{Kk_{rv}C}\lvert\vec{u}_v\rvert}$
Supplemental relations:	
Diffusive mass flux	$\vec{j}\equiv-D(s)\cdot\nabla s+f(s)\frac{K}{\nu_v}(\rho_l-\rho_v)\vec{g}$
Phase velocities	$\rho_l\vec{u}_l=\frac{\lambda_l}{\lambda_l+\lambda_v}\rho\vec{u}+\vec{j}$, $\rho_v\vec{u}_v=\frac{\lambda_v}{\lambda_l+\lambda_v}\rho\vec{u}-\vec{j}$
Constitutive relations:	
Relative permeabilities	$k_{rl}=s^n$, $k_{rv}=(1-s)^n$ where $n=1$
Capillary pressure	$p_c\equiv p_v-p_l=\left(\frac{\varepsilon}{K}\right)^{1/2}\sigma J(s)$ where $J(s)=1.417(1-s)-2.120(1-s)^2+1.263(1-s)^3$
Effective thermal conductivity	$k_e\equiv(1-\varepsilon)k_s+\varepsilon s k_l+\varepsilon(1-s)k_v$

3. FINITE ELEMENT FORMULATION

The conservation equations in Table 1 are spatially discretized by a standard Galerkin method. An equal-order approximation is used for the mixture enthalpy, pressure, velocity, and the single-phase velocities.

Table 2. Variables in Different Phases

	liquid phase ($H \le -\rho_l h_{fg}$)	two-phase ($-\rho_l h_{fg} \le H \le 0$)	vapor phase ($H \ge 0$)
T	$(H + \rho_l h_{vsat})/(\rho_l c_l)$	T_{sat}	$T_{sat} + H/(\rho_v c_v)$
s	1	$-H/(\rho_l h_{fg})$	0
Ω_h	$\varepsilon + (1-\varepsilon)\rho_s c_s/(\rho_l c_l)$	ε	$\varepsilon + (1-\varepsilon)\rho_s c_s/(\rho_v c_v)$
Γ_h	$k_e/(\rho_l c_l)$	$D(s)/\rho_l$	$k_e/(\rho_l c_l)$
γ_h	1	$\rho\lambda_l/[s\rho_l(\lambda_l+\lambda_v)]$	$\rho_v\nu_v/(\rho_l\nu_l)$

With consideration of the boundary conditions as described later, the finite element formulations are expressed in the non-dimensional form as follows.

$$\int_\Omega H^*\Omega_h^m\overline{H}^{m+1}d\Omega = \int_{\Omega_h} H^*\left(\Omega_h\overline{H}\right)^m d\Omega - \Delta t\int_\Omega[H^*\nabla\left(\gamma_h\overline{\vec{u}}\overline{H}\right)^m + \nabla H^*\left(\Gamma_h\nabla\overline{H}\right)^m]d\Omega$$
$$+ \Delta t(1-\overline{\rho}_v)\overline{\nu}_l Ra_{2p}\int_\Omega \nabla H^* f(s)^m\vec{e}_y d\Omega \qquad (2)$$
$$+\Delta t\int_{\Gamma_q} H^*\left(\Gamma_h\frac{\partial\overline{H}}{\partial n} - (1-\overline{\rho}_v)\overline{\nu}_l Ra_{2p} f(s)^m\vec{e}_y\right)^m d\Gamma$$

$$\int_\Omega \nabla p^*\left(\frac{1}{\overline{\nu}}\nabla\overline{p}^{m+1}\right)d\Omega = -\frac{\varepsilon}{\Delta t}\int_\Omega p^*(\overline{\rho}^{m+1}-\overline{\rho}^m)d\Omega - \int_\Omega \nabla p^*\frac{(Ra_{2p}\lambda_l - Ra\lambda_l\theta^{m+1} + \overline{\rho}_v Ra_{2p}\lambda_v)\vec{e}_y}{\overline{\nu}}d\Omega$$
$$+\int_{\Gamma_s}\frac{p^*}{\nu}\left[\frac{\partial\overline{p}^{m+1}}{\partial n} + (Ra_{2p}\lambda_l - Ra\lambda_l\theta^{m+1} + \overline{\rho}_v Ra_{2p}\lambda_v)\vec{e}_y)\right]d\Gamma \qquad (3)$$

$$\int_\Omega u^*\overline{\vec{u}}^{m+1}d\Omega = -\int_\Omega\frac{u^*}{\overline{\rho}\overline{\nu}}\left(\nabla\overline{p}^{m+1} + Ra_{2p}\lambda_l - Ra\lambda_l\theta^{m+1} + \overline{\rho}_v Ra_{2p}\lambda_v\right)d\Omega \qquad (4)$$

$$\int_\Omega u_l^*\overline{\vec{u}}_l^{m+1}d\Omega = \int_\Omega\left\{\frac{\lambda_l}{\lambda_l+\lambda_v}\overline{\rho}\overline{\vec{u}}^{m+1} - \frac{1}{\overline{\nu}}\cdot\frac{\lambda_l\lambda_v}{\lambda_l+\lambda_v}\left[-\frac{d\overline{p}_c}{ds}\nabla s + (1-\overline{\rho}_v)Ra_{2p}\right]\right\}d\Omega \qquad (5)$$

$$\int_\Omega u_v^*\overline{\vec{u}}_v^{m+1}d\Omega = \int_\Omega\frac{1}{\overline{\rho}_v}\left\{\frac{\lambda_l}{\lambda_l+\lambda_v}\overline{\rho}\overline{\vec{u}}^{m+1} + \frac{1}{\overline{\nu}}\cdot\frac{\lambda_l\lambda_v}{\lambda_l+\lambda_v}\left[-\frac{d\overline{p}_c}{ds}\nabla s + (1-\overline{\rho}_v)Ra_{2p}\right]\right\}d\Omega \qquad (6)$$

Here variables with a superscript "-"are dimensionless. Their definitions are omitted here for lack of space. H^*, p^*, u^*, u_l^*, *and* u_v^* *are the weight functions for the mixture enthalpy, pressure, velocity, and the single-phase* velocities, respectively. The superscripts, m and m+1, denote the previous and present iteration levels. The last term of Eq. (2) accounts for the boundary condition in terms of dimensionless heat flux and the last term of Eq. (3) accounts for the boundary conditions expressed by dimensionless velocity. The direction of partial derivative of *n* in these two boundary condition terms is the outward normal on the boundaries.

4. CODE VALIDATION

To ensure the validation of the present numerical algorithm, numerical calculations were performed for the similar system as Wang et al. [8] numerically simulated and Sondergeld and Turcotte [1] experimented. Figure 2 shows the geometry and boundary conditions of this system in which subcooled water fills the porous media at atmospheric pressure and is heated below. In the present calculation the initial and boundary conditions and other parameters related to porous structures were set identical to those by Wang et al. [8]. Porous enclosure size is $L_y = L_x = 0.1984$ [m] and absolute permeability is $K=7*10^{-11}$ [m^2]. The total square domain is divided into a

mesh of 961 nodes and 900 elements. For various heat fluxes, the calculated temperature and liquid saturation distributions and fluid flow patterns are in accordance with the numerical results by Wang et al. [8] who employed Darcy law. For the Ergun constant set as 0.0 and 0.68, differences in all variables are very slight even at a highest heat flux of Q_w = 10 in the present calculation. This is because convection velocity is too low under the given conditions.

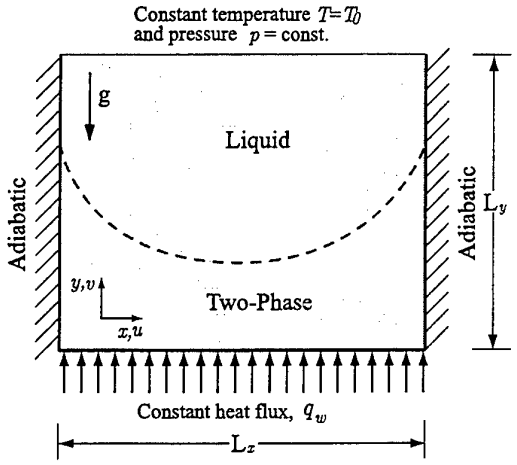


Fig.2. Schematic of the geometry and boundary conditions

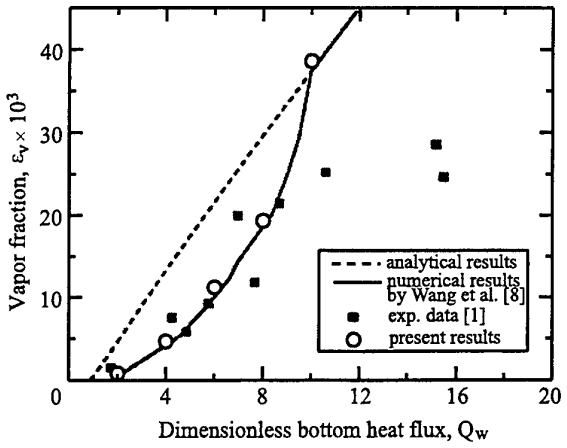


Fig.3. Comparison of the predicted and measured vapor fractions

Sondergeld and Turcotte [1] defined the volumetric fraction of vapor in the entire porous enclosure as a measure of the extent of two-phase zone and a measurable quantity in experiments. It runs

$$\varepsilon_v = \frac{1}{L_x L_y} \int_0^{L_x} \int_0^{L_y} (1 - s) dx dy$$

Figure 3 compares the calculated vapor fractions using the present numerical method with those of Wang et al. [8] and the measured data by Sondergeld and Turcotte [1]. Very good agreement between two predictions and measurements can be confirmed until a certain level of heat flux.

5. A HEATED TUBE IN POROUS MEDIA

Problems of flow and heat transfer around a heated pipeline buried in the ground are widely found in petroleum or gas transport engineering. Although some experimental and numerical researches on this type of problems have been carried out for cases of single phase fluid, published works involving phase change are very few because of complexity of related phenomena or irregularity of the domains of interest. In this section, flow and heat transfer with phase change around a heated tube embedded in porous media is numerically simulated using the algorithm developed in the forgoing sections, and the effects of heat flux and top surface temperature on the temperature and liquid saturation distributions, flow fields and the extent of two-phase zone will be discussed.

Figure 4 shows the geometry and boundary conditions of the system treated in the present analysis. A tube of D = 40 [mm] is embedded in a rectangular porous enclosure of uniform porosity and permeability and heated at uniform heat flux. The porous enclosure is filled with water at atmospheric pressure. Top surface is isothermal, maintained at a constant temperature of T_0. The other surfaces of the enclosure are adiabatic and subject to the no-slip boundary condition. Thus the initial and boundary conditions are written as follows.

Initial Conditions:

at t = 0: $\quad \overline{H} = \overline{H}_0 = \rho_l (c_l T_0 - h_{vsat}) / (\rho_l h_{fg})$ and $\overline{u} = 0$

Boundary Conditions:

at the top surface: $\overline{H} = \overline{H}_0 = \rho_l(c_l T_0 - h_{vsat})/(\rho_l h_{fg})$, $\overline{p} = 0$ and $\partial\overline{v}/\partial\overline{y} = 0$

at the tube surface: $q_w Dc_l/(k_e h_{fg}) = -\Gamma_h \partial\overline{H}/\partial\overline{y} + f(s)(1-\overline{\rho}_v)\overline{v}_v Ra_{2p}$ and $\overline{u} = 0$

at other boundaries: $\partial\overline{H}/\partial\overline{x} = 0$ and $\overline{u} = 0$

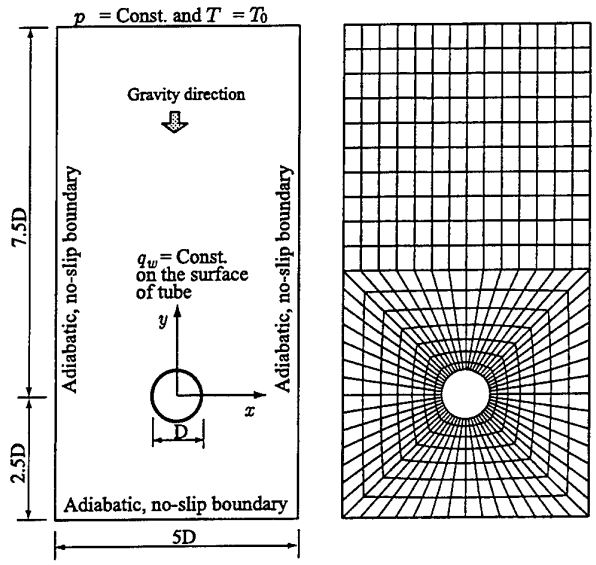


Fig.4. Schematic of the geometry, boundary conditions and mesh distribution in the present analysis

The parameters of the porous media are fixed as the porosity of ε =0.35 and the absolute permeability of K= 1.0 $*10^{-10}$ [m^2]. The other parameters are the same as used in the foregoing code validation section. The parameters of interest in the present analysis are the tube heat flux q_w and the top surface temperature T_0. The numerical results for three different combinations of these two parameters are shown in Fig.5 (a), (b) and (c), where the dimensionless stream functions ψ are on the left figure and the dimensionless isotherms θ and the iso-saturation lines s are on the right figure. An increment between two adjoin contour lines is $\Delta\psi$ = 0.5 or 0.05, $\Delta\theta$ = 0.2, and Δs = 0.01. In a non-dimensionalizing process of the governing equations the next three dimensionless parameters are formally obtained.

$$Q_w = q_w D/[k_e(T_{sat} - T_0)]$$
$$Ra = KDg\rho_l\beta_l(T_{sat} - T_0)/(\nu_l k_e)$$
$$Ra_{2p} = KDg\rho_l c_l/(\nu_l k_e)$$

The values of these parameters are given for reference in each figure. The two-phase Rayleigh number is common at Ra_{2p} = 395 in three cases, while the dimensionless heat flux Q_w and the liquid Rayleigh number Ra are different in each figure. When T_0 is changed for a fixed heat flux q_w, then Q_w and Ra vary simultaneously. If q_w is changed in proportion to (T_{sat}-T_0), then Q_w is unchanged while Ra varies. Thus the independent variations in q_w and T_0 result in simultaneous variations of Q_w and Ra. Note that these two dimensionless parameters are unable to change independently. In consideration of such a state of things the values of q_w and T_0 are given in Fig.5 along with values of Q_w and Ra.

The dotted line in Fig. 5 corresponds to the liquid saturation of s=1 and the dimensionless temperature of θ = 1. This line divides the domain into the subcooled liquid zone and the two-phase liquid and vapor zone. Two

symmetrical convection cells with an opposite rotating direction are seen in the figures of stream function. Isotherms in the subcooled liquid zone are elongated in the vertical direction due to the cell motion as seen in Fig.5 (a) and (b). In a comparison of Fig.5 (a) and (b) where the top surface temperature is kept constant and only the heat flux is changed, an increase in heat flux enforces the rotation of the cells and extends the fluid circulation area. It also makes the two-phase zone expand in the vertical direction. In Fig.5 (b) and (c) the heat

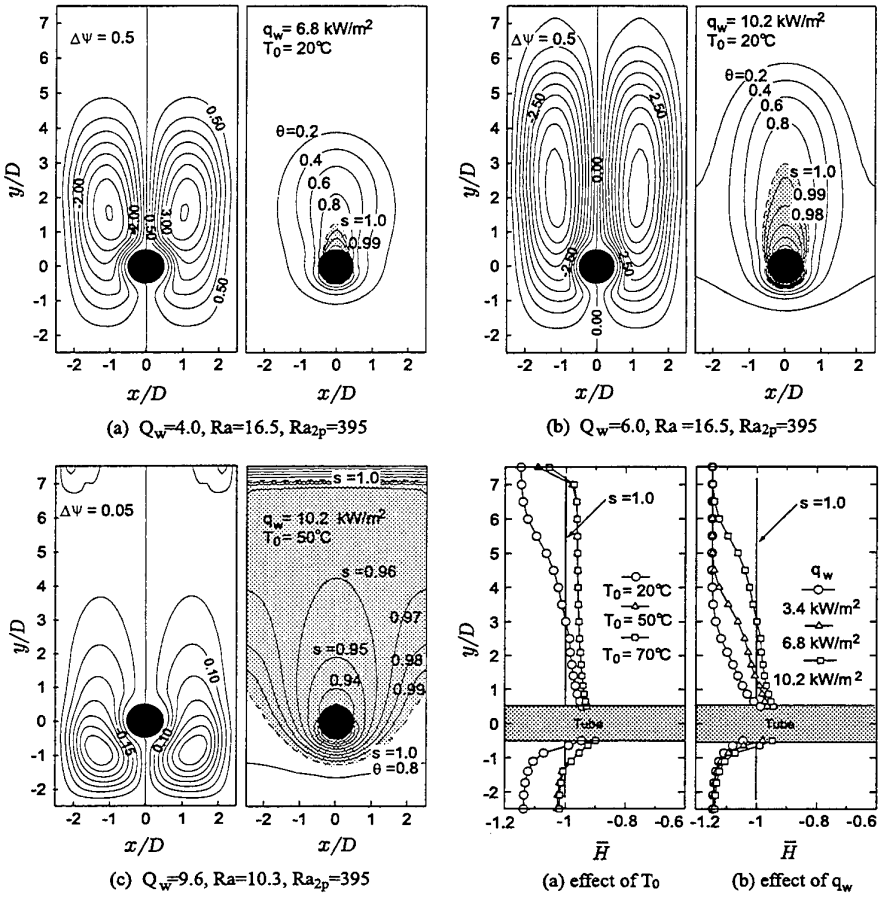


Fig.5. Contours of stream function, temperature and saturation

Fig.6. Effects of T_0 and q_w on dimensionless enthalpy $\bar{H} = H/(\rho_l h_{fg})$

flux is identical while the top surface temperature is different. A reduction of liquid subcooling at the top surface from 80 K in Fig.5 (b) to 50 K in Fig.5 (c) causes a drastic change in flow and temperature fields, thus in the separation of liquid and two-phase zones. In Fig.5 (c) the two-phase zone extends to reach the side walls, resulting in the separation of the liquid zone into the upper and lower two regions. As the temperature gradient in the vertical direction is reduced in the lower liquid zone, the cell motion is retarded and its centers are shifted to a lower position under a heated tube. In the upper liquid zone the isotherms run horizontally, thus heat is dissipated to the top surface by conduction. The liquid zone lies above the two-phase zone but no instability occurs in the numerical analysis. Figure 6 plots the dimensionless enthalpy $\bar{H}$ along the vertical centerline to discriminate the two-phase zone at $\bar{H} \geq -1$ and the liquid zone at $\bar{H} \leq -1$ The effects of T_0 and q_w on the vertical extent of the two-phase zone are seen in the figure.

In the case of Fig.5 (b), the volumetric vapor fraction is calculated as $\varepsilon_v = 4.7648 * 10^{-3}$ for the Ergun constant of C=0, and $\varepsilon_v = 4.8063 * 10^{-3}$ for C=0.68. This difference is so small that the Darcy model may be enough in use for numerical simulations of free convection in porous medium if the values of absolute permeability are moderate.

6. CONCLUSIONS

A numerical algorithm with finite element method to analyze two-phase flow and heat transfer in porous media was presented on the base of the two-phase mixture model coupled with an extended Forchheimer-Darcy law. The present numerical results were compared with those by Wang et al. and experimental data by Sondergeld and Turcotte, and confirmed the accuracy of the new algorithm. The effectiveness of the algorithm was shown for boiling on a heated tube in porous media. The new algorithm is a robust tool for two-phase flow in porous media with the following advantages: (1) Variety of permeabilities and other physical properties in each element of the calculated domain is allowable for FEM method. (2) Any configuration of the domain can be easily accommodated along with the different combinations of boundary conditions. (3) Problems with a relatively wide range of velocity can be applied for.

NOMENCLATURE

c	specific heat
C	Ergun constant
$D(s)$	capillary diffusion coefficient
$\vec{e}_y$	1 in y-direction and 0 in x-direction
$f(s)$	hindrance function
g	gravitational acceleration
h	enthalpy
h_{fg}	latent heat of heat
H	volumetric mixture enthalpy
j	diffusive mass flux
$J(s)$	capillary pressure function
k_e	effective thermal conductivity
K	absolute permeability
L	characteristic length, L_y or D
p	pressure
p_c	capillary pressure
q_w	heat flux on the wall
Q_w	dimensionless heat flux; $=\dfrac{q_w L}{k_e(T_{sat}-T_0)}$
Ra	Rayleigh number in the liquid region; $= KLg\rho_l\beta_l(T_{sat}-T_0)c_l/(\nu_l k_e)$
Ra_{2p}	Rayleigh number in the two-phase region $= KLg\rho_l c_l/(\nu_l k_e)$
s	liquid saturation
t	time
T	temperature
$\vec{u}$	superficial velocity vector
$\bar{\vec{u}}$	dimensionless velocity; $\vec{u}\rho_l c_l L/k_e$
$\bar{p}$	dimensionless pressure; $pc_l K/(k_e\nu)$
β	thermal expansion coefficient
ε	porosity or volumetric vapor fraction
θ	dimensionless temperature $(T-T_0)/(T_{sat}-T_0)$
γ_h	advection correction coefficient
Γ_h	effective diffusion coefficient
λ	relative mobility
ν	kinetic viscosity
$\bar{\nu}$	dimensionless kinetic viscosity; $=(\nu+\sqrt{K}C\lvert\vec{u}\rvert)/\nu_l$
ρ	density
$\bar{\rho}$	dimensionless density; $=\rho/\rho_l$
σ	surface tension
Ω_h	effective heat capacitance ratio

Subscripts

0	initial condition
l	liquid phase
v	vapor phase
k	"kinetic" property

REFERENCES

1. C. H. Sondergeld and D. L. Turcotte, Journal of Geophysical Research, v. 82, pp. 2045-2053(1977).
2. C. H. Sondergeld and D.L. Turcotte, Pure Appl.Geophys., v. 117, pp. 321-330(1978).
3. V.X. Tung and V. K. Dhir, Int. J.Multiphase Flow, v.16, pp. 985-1002 (1990).
4. H. H. Bau, and K. E. Torrance, Int. J. Heat Mass Transfer, v. 25, pp.45-55(1982).
5. K. E. Torrance, ``Boiling in Porous Media", *Proc. of ASME-JSME Therm. Eng. Joi. Conf.*, v.2, pp.593 - 606(1983).
6. P. S. Ramesh and K.E. Torrance, Int. J. Heat Mass Transfer, v. 33, pp. 1895-1908(1990).
7. C. Y. Wang and C. Beckermann, Int. J. Heat Mass Transfer, v. 36, pp. 2747-2758(1992).
8. C. Y. Wang, C. Beckermann and C. Fan, Numerical Heat Transfer, Part A, v. 26, pp. 357-398(1994).

FORCED CONVECTION AND FLOW BOILING IN MONO- AND BI- DISPERSED POROUS CHANNELS

Z. Q. Chen, P. Cheng and T. S. Zhao
Department of Mechanical Engineering
The Hong Kong University of Science & Technology
Email: mepcheng@ust.hk; Fax: (852)-2358-1543

Keywords: forced convection, boiling heat transfer, mono- and bi- dispersed porous media

ABSTRACT. Forced convection and flow boiling in channels packed with sintered copper bi-dispersed porous media (with micro-pores diameter of 80 μm and macro-pore diameters of 200/400/800 μm) were investigated in this paper. For comparison, the same channels were packed with sintered copper mono-dispersed porous media with pore diameters of 80/800 μm. The experiments were conducted using distilled water as the working fluid. The absolute permeabilities of the porous channels packed by the sintered copper mono- and bi-dispersed media were first determined by measuring pressure drops at different inlet velocities of the isothermal flow of subcooled water. Experiments were then performed for forced convection in the porous channels heated from below with constant heat flux. It was found that the convection heat transfer coefficients of fluid flow through bi-dispersed porous media are smaller than those of the same fluid flow through mono-dispersed porous media (with the same pore diameter as the micro-pore of the bi-dispersed media) at the same inlet fluid velocity. As the heat flux is increased further and boiling begins to occur, the pressure drop of the two-phase flow and characteristic curve of boiling were determined. It is found that the boiling phenomena inside the mono- and bi-dispersed porous media begins at very low wall superheats because of the increase of the specific heat transfer surface area and nucleation sites. The results indicated that the porous material is a highly effective two-phase heat sink, especially for bi-dispersed porous materials which have a lower flow resistance than that of the mono-dispersed porous materials having the same pore diameter as the micro-pore diameter of the bi-dispersed porous material.

1. INTRODUCTION

It is anticipated that the chip heat flux levels will be as high as 100 W/cm^2 or more in mainframe computers by the year 2000 [1]. Thus, conventional heat transfer techniques utilizing natural or forced convection will not be adequate to meet the future heat dissipation requirements of these chips. For this reason, considerable research on new cooling technologies for electronic equipment is currently underway [2]. For example, Koh et al [3,4] studied the problem of forced convection in a porous channel based on Darcy law model. Because of thermal dispersion effects, it has been found that the use of channels packed with high-conductivity porous material is an effective alternative method for enhancing single-phase forced convective cooling systems [5-7]. Typically, wall temperature would increase with the increase of heat loads for single-phase forced convective cooling systems. However, more uniform wall temperature distribution can be achieved through boiling and evaporation resulting in surfaces temperatures only a few degrees higher than the fluid saturation temperature. In addition, the latent heat exchange provides the capability of high heat flux removal at a low velocity.

Few experimental studies on flow boiling in porous media have been carried out despite their practical interest. Most previous studies focused primarily on boiling in a porous medium saturated with a stagnant liquid. In 1982, Naik and Dhir [8] investigated the temperature and pressure evolutions of a coolant that evaporates as it flows through a bed of steel spheres volumically heated by induction. A theoretical model was then developed for the temperature profile in the two-phase liquid zone. Recently, a mixture model for single-component multiphase flow in porous media was developed by Wang and Beckermann [9] and was later extended to multi-component multiphase flow by Wang and Cheng [10]. An experimental study on convective boiling in a porous media was recently conducted by Topin, et al [11], who analyzed the temperature field of three-phase zones, i.e. liquid, liquid-vapor and superheat vapor zones. Misceic, et al [12] studied the heat transfer of n-pentane flowing through a rigid, mono-dispersed fiber' porous media with and without phase change. The experimental study of two-phase heat dissipation in high-conductivity sintered porous channel heat sinks was investigated by Peterson et al [13], and their experimental results were verified by a numerical model. All of the existing literatures are for convection and boiling heat transfer in mono-dispersed porous media. Very few studies have

been carried out for boiling heat transfer in bi-dispersed porous media which are used for heat pipes applications.

The aim of this paper is to study the flow and heat transfer characteristics in sintered copper bi-dispersed porous media. For comparison, experiments were conducted for mono-dispersed porous media with the same pore diameters as the micro-pores of the bi-dispersed media at the same flow conditions. The experimental work was first conducted to obtain the pressure drop of water at isothermal temperature in both the mono-dispersed and bi-dispersed porous media. A study was also carried out for forced convection and flow boiling of fluid through mono- and bi- dispersed porous channels with heating from below. The data of heat flux versus wall superheats for mono- and bi- dispersed porous media were plotted to produce the characteristic-boiling curve.

2. EXPERIMENTAL APPARATUS AND PROCEDURE

2.1 Experimental Apparatus

The experimental apparatus for measuring the fluid flow and heat transfer characteristics in channels packed with small sintered copper spheres is shown in Fig. 1. The experimental apparatus was composed of a testing section, a cooling system, a heating system, a liquid vessel, a pump, two flow rate meters and an adjusting valve, etc. Distilled water was pumped from the liquid vessel and through the filter, flow rate meter, and was heated to the desired temperature at the inlet of the test section by an electrical resistance heater which was controlled by a HP PID controller. Exiting from the test section, the fluid passed through the condenser and into a liquid vessel which was used not only to mix the liquid, but also to control and stabilize the liquid pressure at the outlet of test section.

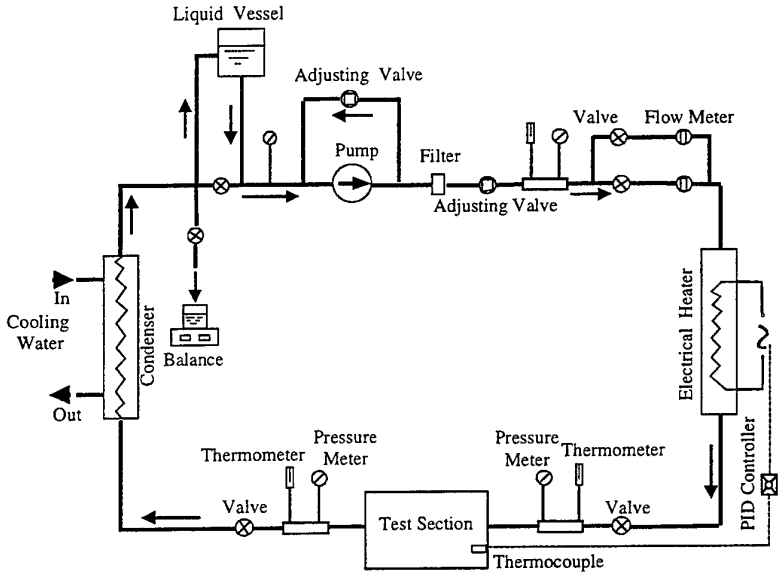


Fig. 1 Schematic of experimental system

The test section, as shown in Fig. 2, consisted of a porous channel, an inlet flow channel and an outlet flow channel. The channel was 30 mm in width, 10 mm in height, and was 50 mm in length packed with mono- and bi-dispersed porous media. The inlet and outlet flow channels were each 45-mm long and were made of Teflon, with the same inside cross sectional area as that of the test section. The test section was covered by polystyrene for insulation. In order to measure the absolute pressure in the inlet and outlet of the test section, two absolute transducers were installed in the inlet and outlet of the test section respectively. As shown in Fig. 2, a differential pressure meter was installed in the test section with five connected holes to the porous channel to test the relative pressure along the porous channel. Seven T-type thermocouples were inserted in the bottom of the porous channel to measure the heated wall temperature distribution. To enhance the thermal contact between the heated wall and the heater, a layer of epoxy adhesive of high thermal conductivity was used to

bond the heated wall and the heater. The output signals of the pressure transducers, temperature readings of the thermocouples, flow meter, the AC voltage across the film heater and the current through it were transmitted to a Solartron Data acquisition system. The electrical power to the electric heater was adjusted to the desired level using a transformer, while the flow rate, inlet temperature, and outlet pressure of water were simultaneously maintained at the desired conditions.

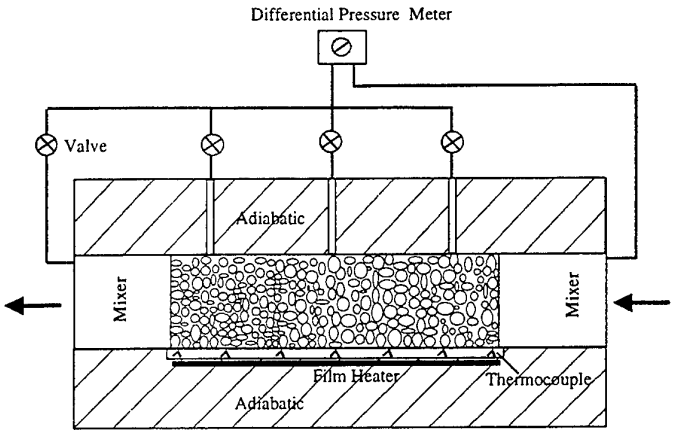


Fig. 2 Schematic of test section

2.2 Porous Samples

In these experiments, two types of mono-dispersed copper porous samples with pore diameters of 80 μm and 800 μm, and three types of bi-dispersed porous samples with micro-/macro- pore diameters of 80 μm/200 μm, 80μm/400μm and80μm/800μm were used. Table 1 lists the physical parameters and dimensions of test samples. The porosity of the five samples was measured using the density method [14] and is also listed in Table 1.

Table 1 Physical parameters of porous channels

Test Samples	Mean Pore Diameters d (μm)	Porosity ε (%)	Permeability $K\times10^{10}$ (m^2)
1	80	46	0.267
2	800	49	6.035
3	80/200	52	2.235
4	80/400	54	3.078
5	80/800	57	5.642

3. FORCED CONVECTION

3.1 Permeability

The pressure drop of the subcooled water along the porous channel was measured by the differential pressure transducers in the porous channels at different flow rates. The relationship between the pressure drop along the porous channel and inlet velocity is shown in Fig. 3. In the velocity range from 0 to 2.5 cm/s, the inlet velocity is nearly linearly proportional to the pressure gradient along the porous channel. The permeability can then be calculated according to the Darcy law. The permeabilities of five types of porous samples are also listed in Table 1. It is found that the permeability of the bi-dispersed porous medium is much larger than that of the mono- porous medium when the micro- pore diameters of bi-dispersed porous medium is the same as the pore diameters of mono-dispersed porous medium. Furthermore, the permeability of the bi-dispersed porous medium is found to be very close to the mono-dispersed porous medium when the macro- pore diameter of the bi-dispersed porous medium is the same as the pore diameter of the mono-dispersed porous medium. Therefore, the permeability of a bi-dispersed porous medium can be estimated as the permeability of the mono-

dispersed porous medium having the pore diameter the same as macro-pore diameter of the bi-dispersed porous medium.

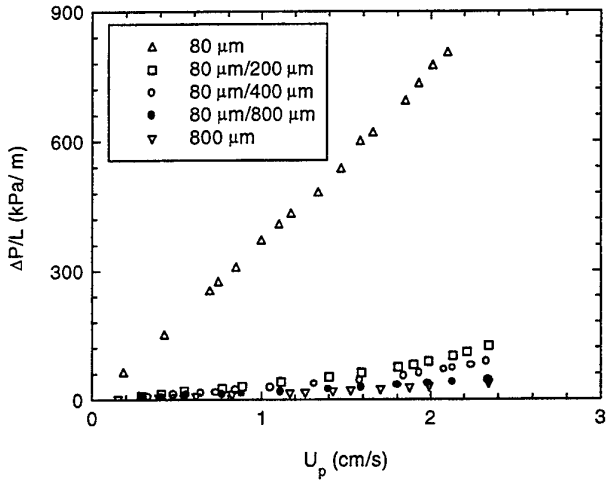


Fig. 3 Pressure drop vs. inlet velocity of fluid

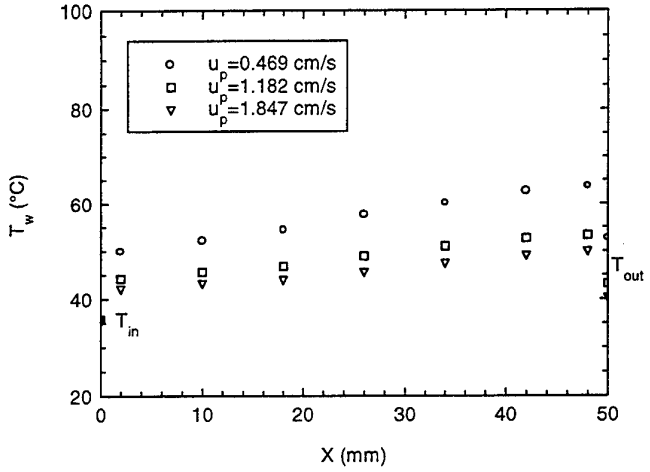


Fig. 4 Wall temperature in mono-dispersed porous channel of pore diameter 800 μm with single-phase flow (q=10 w/cm^2)

3.2 Temperature Distribution

For a porous channel heated from below with a constant heat flux, the wall temperature distributions along the flow direction in the channels packed with mono- and bi-dispersed porous samples are showed in Fig. 4 and Fig. 5 respectively. The bulk mean temperature of the fluid at the inlet and outlet of the channels are also marked as T_{in} and T_{out} in these figures. It is shown that the wall.temperature is decreased with the increase of the inlet velocity. In comparison of Fig. 4 and Fig. 5, it is shown that the wall temperature in the bi-dispersed porous channel is higher than that in the mono-dispersed porous channel at the same inlet water temperature (36°C), heat flux (10 W/cm^2) and inlet velocity (0.469 cm/s for mono-dispersed channel and 0.476 cm/s for bi-dispersed porous channel). It can be concluded that the forced convection heat transfer in the bi-dispersed porous channel is lower than that in the mono-dispersed porous channel (with the same pore diameter as the micro-pore diameter of the bi-dispersed media) when they are at the same boundary conditions.

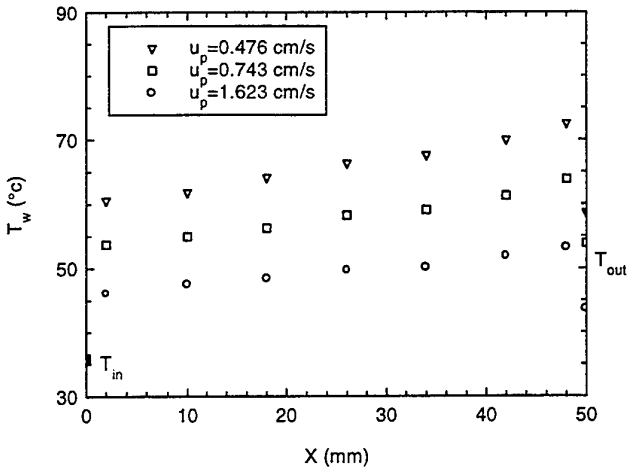


Fig. 5 Wall temperature in bi-dispersed porous channel of micro-/macro-pore diameters 80 μm/200 μm with single-phase flow (q=10 w/cm^2)

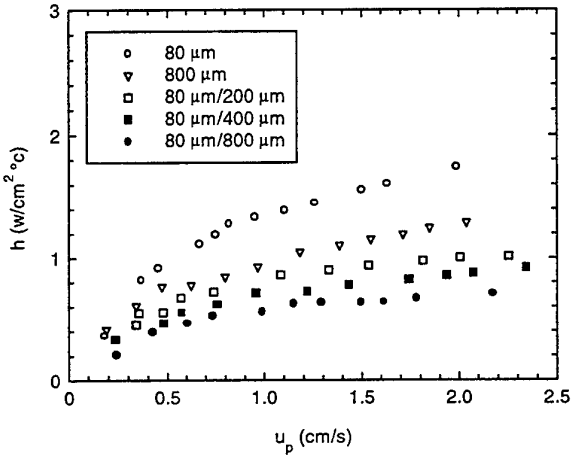


Fig. 6 Mean heat transfer coefficients vs. inlet velocity U_P in forced convection

3.3 Mean Heat Transfer Coefficients

The mean heat transfer coefficient for single-phase convection in the porous channel is defined as [12]

$$\overline{h} = q/(\overline{T}_w - \overline{T}_f) \tag{1}$$

where q is heat flux density, $\overline{T}_f$ is the mean fluid temperature , and $\overline{T}_w$ is the mean wall temperature calculated from the formula $(\sum_{i=1}^{7} T_{wi}\Delta x_i)/L$ with L being the length of porous channel. The mean heat transfer coefficients in mono- and bi-disperse porous channel computed according to Eq.(1) are illustrated in the Fig. 6. It is shown that the convection heat transfer coefficients in porous channel is very high because the porous medium has a high effective thermal conductivity and also because of the thermal dispersion effects. The heat transfer coefficients in bi-dispersed porous channel are smaller than in mono-dispersed porous channel. For a mono-dispersed porous medium, because its effective thermal conductivity and specific surface area are higher than the bi-dispersed porous medium when the pore diameter of mono-dispersed porous medium is the same as the micro- pore diameter of bi-dispersed porous medium. So the heat transfer coefficient in this mono-dispersed porous channel is higher than in the bi-dispersed porous channel subject to the same hydrodynamic and thermal boundary conditions.

When the pore diameter of a mono-dispersed porous medium is the same as the macro- pore diameter of bi-dispersed porous medium, the specific surface of mono-dispersed porous medium is smaller than that of the bi-dispersed porous medium. But the effective thermal conductivity of this mono-dispersed porous medium is higher than that of bi-dispersed porous medium. Meanwhile, the fluid through micro- pore of bi-dispersed porous channel is very slow because of its large flow resistance compared to macro- pore at the low inlet velocity, so the effect of convection heat transfer in micro- pores is very small. In addition, the heat conduction predominant at low inlet velocity. So the convection heat transfer coefficients in mono-dispersed porous channel is higher than in bi-dispersed channel subjected to the same boundary conditions when the pore diameter of mono-dispersed porous medium is the same as the macro- pore diameter of bi-dispersed porous medium.

4. TWO-PHASE FLOW AND BOILING Heat Transfer

4.1 Temperature Distribution

When boiling happens, the wall temperature distributions along the flow direction in the channel packed with

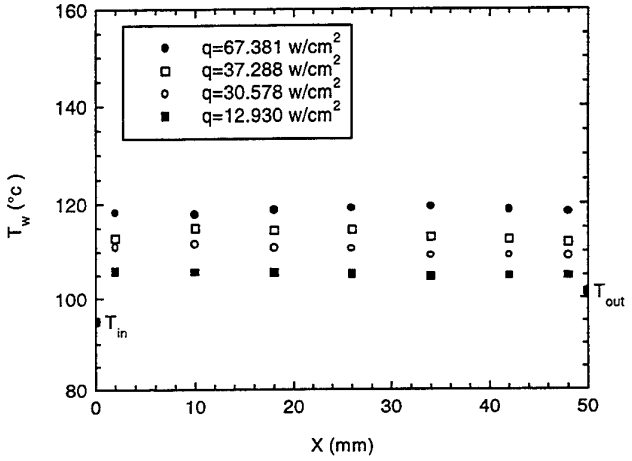


Fig. 7 Wall temperature in bi-dispersed porous channel with micro-/macro-pore diameters of 80 μm/200 μm (inlet velocity at 0.5 cm/s)

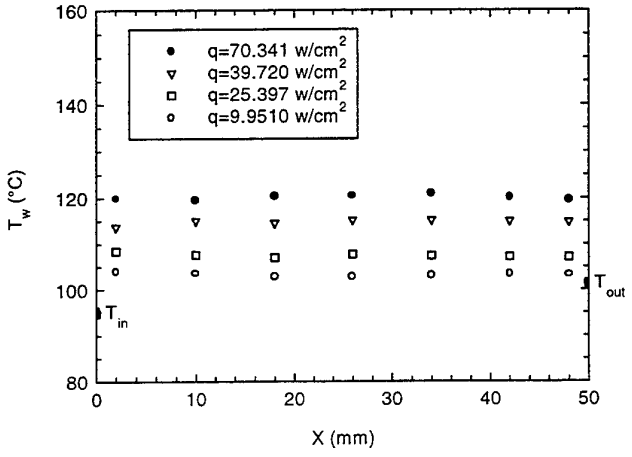


Fig. 8 Wall temperature in mono-dispersed porous channel with pore Diameter of 800 μm (inlet velocity at 0.5 cm/s)

bi- and mono-dispersed porous samples are showed in Fig. 7 and Fig. 8 respectively. The bulk mean temperature of the fluids at the inlet and outlet of the channels are also marked as T_{in} and T_{out} in these figures.

As shown, the wall temperature gradients along the porous channel are very small compared with single-phase flow because heat is removed from the wall by latent heat of vaporization. The influence of the heat fluxes on the wall temperature distributions for porous channel is also shown in Fig. 7 and Fig. 8 respectively. As shown, the wall temperature increases with increasing heat flux. The fluid outlet temperature corresponds closely to the saturation temperature at the outlet pressure of the porous channel at each run.

4.2 Pressure Drop

Fig. 9 shows the pressure variations along the channel packed with bi-dispersed porous media with micro-/macro-diameters of 80 μm/200 μm at inlet velocity of 0.5 cm/s when the boiling happens. As shown, the pressure drop increases with increasing heat flux. This is because boiling is enhanced with the increase of heat flux, and the vapor saturation increases in the porous channel, so the flow resistance increases with the increase of heat flux.

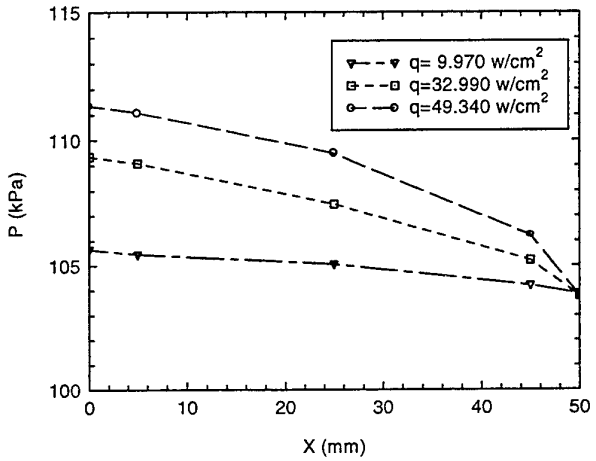


Fig. 9 Pressure variation in bi-dispersed porous channel of micro-/macro-diameters 80 μm/200 μm (inlet velocity 0.5 cm/s)

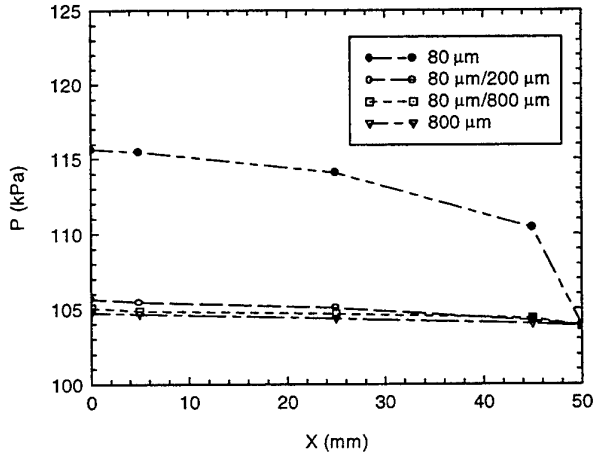


Fig. 10 Pressure variation in different porous channels with the heat flux of 10 w/cm^2 and inlet velocity 0.5 cm/s

When boiling occurs, the pressure drop along the mono- and bi- dispersed porous channel with the heat flux of 10 w/cm^2 and inlet velocity of 0.5 cm/s is shown in Fig. 10. As shown, when fluid flow through mono-dispersed porous channel with pore diameter of 80 μm, the pressure drop is very high because of its low permeability. The pressure drop along the bi-dispersed porous channel is much lower than in the mono-dispersed porous channel when the micro-pore diameter (80 μm) of bi-dispersed porous sample is the same as the pore diameter of mono-dispersed porous sample.

4.3 Boiling Curve

When boiling occurred in the porous channel, a characteristic boiling curve can be presented in terms of the wall superheats ($\Delta T_{sat}= \overline{T}_w - \overline{T}_{sat}$) versus the heat flux at the wall. Fig. 11 shows the characteristic boiling curve [$q = f(\Delta T_{sat})$] obtained experimentally for sintered porous channels.

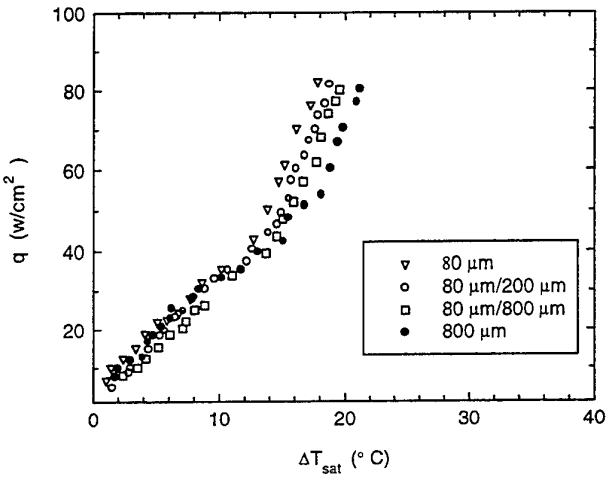


Fig. 11 Characteristic boiling curve for inlet velocity of 0.5 cm/s

The samples were two mono-dispersed porous media with pore diameters of 80 μm and 800 μm, and two bi-dispersed porous media with micro-/macro- pore diameters of 80 μm/200 μm and 80 μm/800 μm. The inlet velocity of fluid was 0.5 cm/s. As shown, boiling occurs with low superheats at the wall. This is due to the increase in the heat transfer specific surface and the larger nucleation site. For the subcooled flow boiling in porous channel, the mean heat transfer coefficient is very large for each channel tested at the same inlet temperature and velocity.

For a mono-dispersed porous sample, the heat transfer coefficient in porous channel with small pore diameter is higher than that in porous channel with large pore diameter. This is because the heat transfer specific area and nucleation sites in small pore diameter porous sample are higher than in large diameter porous sample. Fig. 11 shows the boiling curve for mono- dispersed porous samples with pore diameters of 80 μm and 800 μm. As shown, the heat transfer coefficient in porous channel with pore diameter of 80 μm is higher than that in porous channel with pore diameter of 800 μm.

When the fluid temperature exceeded the saturation temperature of fluid, boiling occurred in the pores if it satisfied the nucleating conditions. With the increase of heat flux, boiling enhanced and two-phase zone extended. When the boiling happened at the micro- pore at high heat flux, the vapor pressure in micro-pore will increase quickly, forcing the vapor immigrated to the macro- pores and the liquid entered the micro- pore in the mean time, the liquid-vapor exchange happened between macro- and micro- pore paths. Boiling in the micro-pores can enhance the heat transfer of bi-dispersed porous media, not only because of the increase in heat transfer specific area, but also the increase of nucleation sites. So, boiling heat transfer coefficients in bi-dispersed porous medium is higher than in the mono-dispersed porous medium having the same pore diameter as the macro-pore diameters of bi-dispersed porous media. As shown in Fig. 11, at the high superheat ΔT_{sat},

heat flux in bi-dispersed porous channels with micro-/macro-pore diameter of 80 μm/200 μm and 80 μm/800 μm are higher than in mono-dispersed porous channel with pore diameter of 800 μm.

When the pore diameter in the mono-dispersed porous channel is the same as the micro-pore diameter of bi-dispersed porous channel, the boiling heat transfer coefficient in the mono-dispersed porous channel is higher than in the bi-dispersed porous channel. This is because the heat transfer specific surface area in mono-dispersed porous channel is higher than in bi-dispersed porous channel. As shown in Fig. 11, the heat transfer coefficients in bi-dispersed porous channels with micro-/macro-pore diameter of 80 μm/200 μm and 80 μm/800 μm is smaller than in mono-dispersed porous channel with pore diameter of 80μm. But as the ratio of macro-/micro- pore diameters is not large, the heat transfer coefficients in bi-dispersed porous channels are close to those in mono-dispersed porous channel with the same size of pore diameter in mono-dispersed porous channels and micro- pore diameters in bi-dispersed porous channel.

5. CONCLUSIONS

The permeability of the bi-dispersed porous medium is much larger than that of the mono- porous medium when the micro- pore diameter of bi-dispersed porous medium is the same as the pore diameter of mono-dispersed porous medium. The permeability of the bi-dispersed porous medium is almost the same as the mono-dispersed porous medium when the macro- pore diameter of the bi-dispersed porous medium is the same as the pore diameter of the mono-dispersed porous medium. So the permeability of a bi-dispersed porous medium can be estimated as the permeability of the mono-dispersed porous medium having its pore diameter the same as macro-pore diameter of the bi-dispersed porous medium. The mean convection heat transfer coefficients of bi-dispersed porous channels are smaller than of mono-dispersed channels at the same inlet water temperature, heat flux and inlet velocity.

Boiling in porous media appears with low superheats at the wall because of the increase of the heat transfer surface area and the number of nucleation sites. The heat transfer coefficients in mono-dispersed and bi-dispersed porous channels are very high when boiling happened. The boiling heat transfer coefficients of bi-dispersed porous media are smaller than and close to those of mono-dispersed porous media when the pore diameter of mono-dispersed is the same as the micro-pore diameter of bi-dispersed media. In the mean time, the boiling heat transfer coefficients of bi-dispersed porous media are higher than of mono-dispersed porous media at high heat flux when the pore diameter of mono-dispersed is the same as the macro-pore diameter of bi-dispersed. So the bi-dispersed porous material is very useful for flow boiling at high heat flux with low flow resistance compared with the mono-dispersed porous material when the pore diameter is the same as micro-pore diameter of bi-dispersed porous material.

Acknowledgement This work was supported by RGC Grant HKUST6044/97E.

REFERENCES

1. H. R. Jacobs and J. P. Hartnett, "Thermal Engineering: Engineering Technologies and Critical Phenomena", *Workshop Report, NSF Grant No. CTS-90-04006*, pp.139-330 (1991).
2. G. P. Peterson and A. Ortega, Advances in Heat Transfer v.20, pp.181-314 (1990).
3. J. C. Y. Koh and R. Colony, Journal of Heat Transfer v.96, pp.324-330 (1974).
4. J. C. R. Koh and Steven, Journal of Heat Transfer v.97, pp.324-330 (1975).
5. M. L. Hunt and C. L. Tien, Int. J. Heat Mass Transfer v.31, pp.301-309 (1988).
6. V. X. Tung and V. K. Dhir, V. K., Journal of Heat Transfer v.115, pp.503-506 (1993).
7. G. J. Hwang and C. H. Chao, Journal of Heat Transfer v.116, pp.456-464 (1994).
8. A. S. Naik and V. K. Dhir, Int. Journal Heat Mass Transfer v.25, pp.541-552 (1982).
9. C Y. Wang and C. Beckerman, Int. Journal of Heat Mass Transfer v.36, pp.2747-2758 (1993).
10. C. Y. Wang and P. Cheng, Int. J. Heat Mass Transfer v.39, pp.3607-3618 (1996).
11. F. Topin, O. Rahli, L. Tadrist and J. Pantaloni, Journal of Heat Transfer, v.118, pp230-233A (1996)
12. M. Miscevic, L. Tadist, J. Pantaloni and R. Yu, R., Journal of Porous Media v.1, pp133-146 (1998).
13. G. P. Peterson and C. S. Chang, Journal of Heat Transfer, v.120, pp243-252 (1998).
14. E. Scheidegger, "The physics of flow through porous media", *University of Toronto Press*, Toronto, Ontario, pp.10-12 (1963).

G. Heat Pipes and Thermosyphons

THERMAL CONTROL OF ELECTRONIC COMPONENTS BY TWO-PHASE THERMOSYPHONS AND PULSATING HEAT PIPES

Nicolò Gavotti
ELBOMEC Thermalloy
Via del Tipografo 4
40138 Bologna (Italy)
Phone: +39051- 6030311, Fax: +39051-538717
E-mail: gavotti.n@elbomec.it

František Polášek
THERMAL MANAGEMENT
Dygrýnova 899
19800 Praha 9 (Czech Republic)
E-mail: suchanek@svuss.cz, Phone/fax: +4202-81915345

Keywords: two-phase coolers, tubular thermosyphon, thermosyphon loop, pulsating heat pipe, immersion thermosyphon, electronic equipment, thermal resistance

ABSTRACT. Passive closed two-phase heat transfer elements as wicked heat pipes, wickless two-phase closed tubular and looped thermosyphons and wickless pulsating heat pipes represents a promising solution for dissipating and spreading heat from electronic equipment to an external coolant. The paper presents results and practical experience from the research of various designs of thermosyphons and pulsating heat pipes for thermal control of electronic equipment.

1. INTRODUCTION

Cooling systems based on the principle of two-phase change (evaporation/boiling ↔ condensation) of a heat transfer medium in a closed space are progressively eroding the use of standard air and liquid (one-phase) coolers in the thermal control of electronic equipment. These two-phase heat transfer elements fall into two families:

Pumped Liquid Coolers
Where a pump supplies an evaporator with the liquid. They usually feature either forced liquid evaporation or boiling in their evaporator part. Such coolers can be further designed as:

1. indirect coolers, when the electronic equipment is attached to the outer surface of the evaporator part (usually called *cold plates*).
2. immersion coolers, when the electronic equipment is directly submerged in the liquid in the evaporator part.

Passive Coolers (without any forced pumping action)
With film evaporation or pool boiling of the liquid in the evaporator part. These passive two-phase heat transfer sealed elements are divided into three groups according to the return of the liquid from the cooled part (condenser) to the evaporator [18]:

1. wicked heat pipes, where a wick on the inner wall of the cooler serves as a capillary pump (Fig. 1).
2. wickless pulsating (oscillating) heat pipes (Fig. 2 - schema), in which the working fluid does not circulate between the evaporator and the condenser in the form of counter current liquid-vapor flow, but rather axially oscillates in the bundle of turns of capillary tubes. This oscillation movement of the working fluid is created by the bubble-boiling phenomenon in the evaporator zone [18].
3. wickless two-phase closed thermosyphons (in the further text just "thermosyphons"), in which gravity is used for returning the liquid from the condenser to the evaporator.

Thermosyphon coolers can be designed as:

- *tubular thermosyphon coolers* (Fig.3), or *rectangular vapor chamber heat spreaders* (Fig. 4), both with counter-current flow of the liquid and the vapor, or as

- thermosyphon loops, where the evaporator is connected to the condenser by a couple of individual channels, one for the liquid flow and the other for the vapor flow.

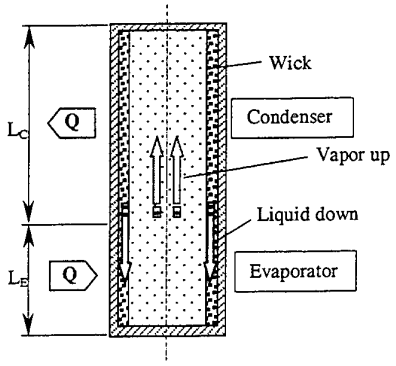


Fig.1 – Schema of a Wicked Tubular Heat Pipe

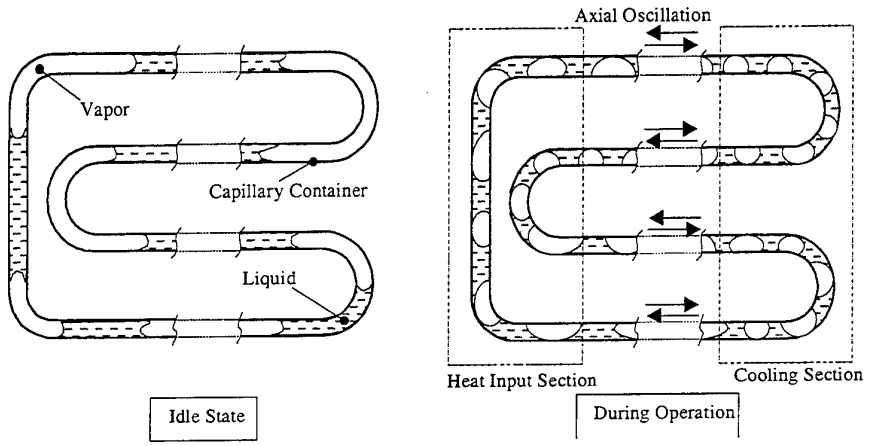


Fig. 2 – Schema of a Wickless Pulsating Heat Pipe

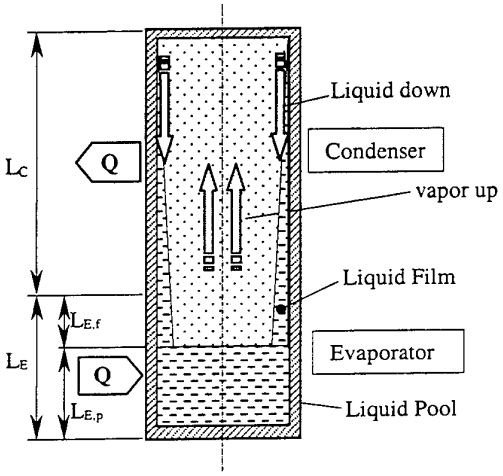


Fig. 3. Schema of a Wickless Tubular Thermosyphon

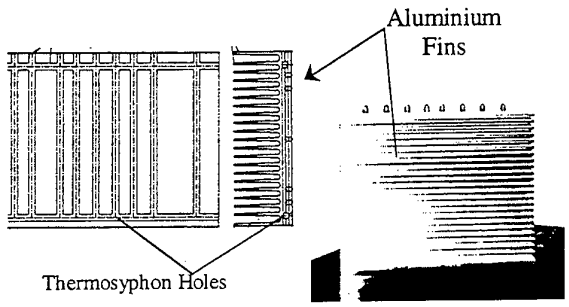


Fig. 4 – Vapor Chamber Thermosyphon used as a Heat Spreader.

Thermosyphon loops, but in general all passive coolers (heat pipes and thermosyphons), can be constructed as:

- *indirect coolers*, when the electronic equipment is attached to the outer surface of the evaporator part (Fig.5) or as
- *immersion coolers*, where the electronic equipment is submerged directly in the liquid in the evaporator part (Fig.6).

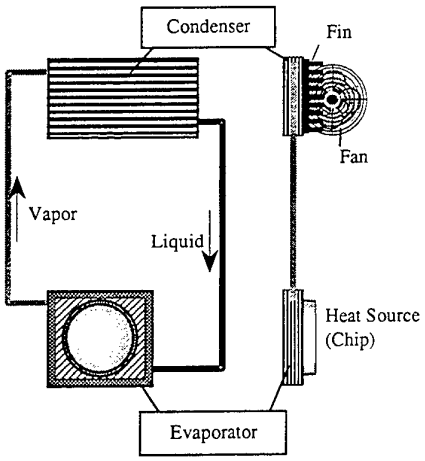


Fig. 5. Schema of an Indirect Thermosyphon Loop

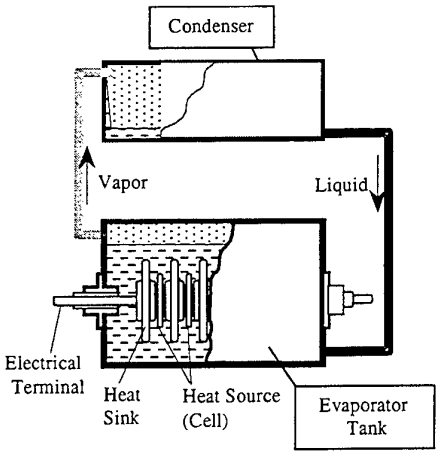


Fig. 6. Schema of an Immersion Thermosyphon Loop

This paper presents the results of our research program on:

- indirect tubular thermosyphon coolers,
- rectangular vapor chamber heat spreaders,
- indirect thermosyphon loops,
- immersion thermosyphon loops
- with regards to thermal control of electronic equipment.

2. BASIC DESIGN OF THERMOSYPHON COOLERS

We have designed, manufactured and tested a number of prototypes of the following thermosyphon coolers, some of which have been now serially manufactured and applied in the thermal control of electronic equipment [7][17][18][19][23].

Indirect Tubular Thermosyphon Coolers

A typical indirect thermosyphon cooler for power semiconductor elements is shown in Fig. 7. It is composed of several parallel tubular thermosyphons in one or two rows, whose evaporator parts are pressed into a copper or aluminium *input pad* (block). A series of lamellar fins is attached to the condenser parts.

The heat transferred from the outer surface of the input pad through one thermosyphon to the cooling air is defined as

$$Q_t = \frac{t_{IP} - t_{B,1}}{R_t} \tag{1}$$

where t_{IP} is the surface input pad temperature, in electronics usually about 80°C

$t_{B,1}$ is the inlet cooling air temperature (up to 40°C)

R_t is the total thermal resistance of one thermosyphon

The total thermal resistance of a thermosyphon is calculated as a series resistance network (Fig.8).

$$R_t = (R_{IP})_t + R_{W,E} + R_E + R_C + R_{W,C} + R_F \tag{2}$$

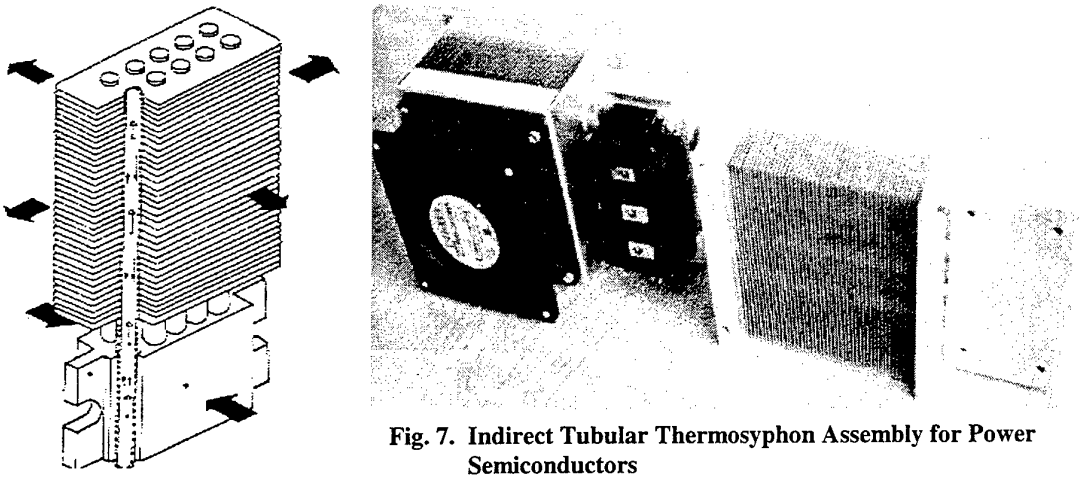


Fig. 7. Indirect Tubular Thermosyphon Assembly for Power Semiconductors

The dissipated heat is transferred by conduction from the input pad outer surface to the evaporator outer surface (thermal resistance R_{IP}), further by conduction through the evaporator wall to the inner evaporator surface (thermal resistance $R_{W,E}$). The thermal resistance due to falling film evaporation or bubble boiling at the pool is marked as R_E. Similar phase change transport phenomena at condensation of the vapor on the inner wall of the condenser part is marked as R_C. From the inner wall the heat is transferred by conduction through the condenser wall (thermal resistance $R_{W,C}$) and finally by natural or forced air convection from fins to the cooling air (thermal resistance R_F). The thermal resistance of vapor flow from the evaporator to the condenser part is neglectable.

While the thermal resistances $R_{W,E}$ and $R_{W,C}$ are usually small, the thermal resistances R_{IP}, R_E, R_C and R_F influence basically the total thermal resistance R_t and therefore it is necessary to determinate them correctly. Determination of the thermal resistance of fins R_F is a standard procedure for the free and forced air convection through fins.

The inner thermal resistance of a thermosyphon is therefore simplified to

$$R_i = R_E + R_C \tag{2a}$$

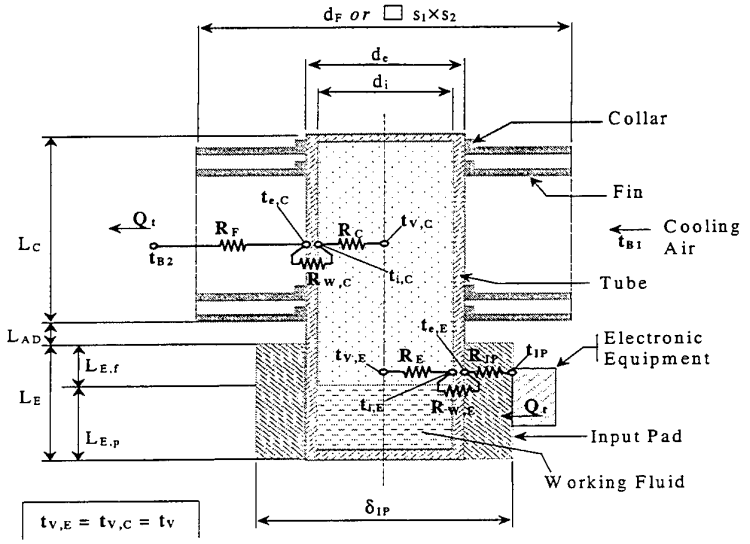


Fig. 8. Thermal resistance network of a tubular thermosyphon for electronics applications

Basic individual thermal resistances of a thermosyphon

a) Thermal resistance of an input pad, R_{IP}

The exact calculation of the heat transfer through an input pad requires the solution of three dimensional heat conduction equations. We have verified that the following simplified method is accurate enough for most electronics applications. In the case of a *uniform heat flux*, the outer surface temperature of the input pad t_{IP} is uniform and the thermal resistance R'_{IP} is determined by the thermal conductivity and by the dimensions of the input pad, which are induced in the so called conduction shape factor F_{IP} [21]. Equations for calculation of the thermal resistance of an input pad are given in the Table 1. In the case of a *non-uniform heat flux*, the outer surface temperature of the input pad t_{IP} is not uniform and the total thermal resistance of the input pad R_{IP} is:

$$R_{IP} = R'_{IP} + R''_{IP}$$

where

R'_{IP} is the same as in the case of uniform heat flux (Table I - eq. 4)

R''_{IP} is the spreading thermal resistance calculated according to the equation by S. Lee [8] (Table I – eq. 6)

Table 1. Heat Transfer in an Input Pad

$$R_{IP} = R'_{IP} + R''_{IP}$$ total thermal resistance of an input pad (3)

a) $$R'_{IP} = \frac{1}{\ddot{e}_{IP} F_{IP}}$$ uniform heating of input pad (4)

$$F_{IP} = \frac{2\pi L_E}{\ln\left\{\frac{2 s_t}{\eth d_e} sinh\left(\frac{\eth \ddot{a}_{IP}}{s_t}\right)\right\}}$$ single side heating of input pad (5a)

$$F_{IP} = \frac{2\pi L_E}{\ln\left\{\frac{2 s_t}{\eth d_e} sinh\left(\frac{\eth \ddot{a}_{IP}}{2 s_t}\right)\right\}}$$ double side heating of input pad (5b)

b) $$R''_{IP} = C\left[\frac{\sqrt{S_{IP}} - \sqrt{S_S}}{\lambda_{IP}\sqrt{\pi S_{IP} S_S}}\right]\left[\frac{a\ \lambda_{IP} S_{IP} R'_{IP} + \tanh\left(a\frac{\delta_{IP}}{2}\right)}{1 + a\ \lambda_{IP} S_{IP} R'_{IP} \tanh\left(a\frac{\delta_{IP}}{2}\right)}\right]$$ non-uniform heating of input pad (6)

where C = 0 uniform heating

C = 1 non-uniform heating; electronics in the center of the input pad

C = 1.41 non-uniform heating; electronics along the edge of the input pad

C = 2 non-uniform heating; electronics at a corner of the input pad

$$a = \frac{\pi^{3/2}}{\sqrt{S_{IP}}} + \frac{1}{\sqrt{S_S}}$$

b) Thermal resistance due to the phase change of the working fluid inside the evaporator part, R_E

R_E is the most important thermal resistance for the majority of electronic applications. It is determined by the heat transfer coefficient in the falling liquid film $h_{E,f}$ and by the heat transfer coefficient in the liquid pool $h_{E,p}$ according to the equation

$$R_E = \frac{L_{E,p}\, h_{E,f} + L_{E,f}\, h_{E,p}}{\pi d_i L^2_E h_{E,f}\, h_{E,p}} \quad (7)$$

where $L_E = L_{E,p} + L_{E,f}$ (8)

Owing to the small diameter of the pools in the thermosyphons (usually <30mm), to bubbles nucleation and sliding of vapor bubbles along the inside wall as well as to the vigorous agitation and mixing in the pool due to rising large bubbles and vapor slugs, boiling heat transfer is greatly enhanced. As a result, nucleate boiling heat transfer coefficients in the liquid pool of thermosyphons is significantly higher than the one predicted by nucleate boiling correlations for conventional boiling in large, open pools [2]. Similarly, nucleate boiling heat transfer coefficients in the liquid film in thermosyphons are higher than those for conventional boiling, partially due to the dispersion of liquid mist in the vapor flow by bursting bubbles at the liquid-vapor interface, and also to the mixing induced in the liquid film by sliding bubbles. For these reasons standard heat transfer coefficient correlations for pool boiling and inverse Nusselt correlation for falling film evaporation lead to quite inaccurate results [3]. Table 2 shows correlations by EL-GENK [2][3] for the evaporation and bubble boiling in a falling liquid film and for free liquid convection and bubble boiling in a liquid pool of the evaporator part.

Table 2. Heat Transfer in the Evaporator Part of a Tubular Thermosyphon

a) Evaporation and Bubble Boiling in a Falling Liquid Film

$$h_{E,f} = \left(h_N^3 + h_{f,NB}^3\right)^{1/3} \quad (9)$$

$$h_N = \frac{1.1\, f\acute{E}_L}{l_f\ Re_{L,f}^{1/3}} \quad (10)$$

$$l_f = \left[\frac{\mu_L^2}{g\,\rho_L(\rho_L - \rho_V)}\right]^{1/3} \quad (11)$$

$$Re_{L,f} = \frac{4\ q_{t,E}\ L_{E,f}}{\mu_L\ \ r} \quad (12)$$

$$q_{tE} = \frac{Q_t}{\pi\, d_i L_E} \quad (13)$$

$$h_{f,NB} = \frac{1.155\times10^{-3}\lambda_L}{l_f} N^{0.33}\, Pr_L^{0.35}\left(\frac{q_{t,E}\, l_b}{\rho_V\, r\, \nu_L}\frac{p_V\, l_b}{\sigma}\right)^{0.7} \quad (14)$$

$$N = \frac{\mu_L}{\left[\sigma\,\rho_L\sqrt{\dfrac{\sigma}{g(\rho_L - \rho_V)}}\right]^{1/2}} \quad (15)$$

$$l_b = \sqrt{\frac{\sigma}{g(\rho_L - \rho_V)}}$$

b) Free Convection and Bubble Boiling in the Liquid Pool

$$h_{E,p} = \left(h_{NC}^4 + h_{p,NB}^4\right)^{1/4} \quad (17)$$

$$h_{NC} = 0.475\left(\frac{\lambda_l}{d_i}\right) Ra_L^{0.35}\left(\frac{l_b}{d_i}\right)^{0.58} \quad (18)$$

$$Ra_L = \frac{\beta_L\, g\, d_i^4\, q_{t,E}\, \rho_L\, c_{p,L}}{\lambda_L^2\, \nu_L} \quad (19)$$

$$h_{p,NB} = \left(1.0 + 4.95w\right) h_{KU} \quad (20)$$

$$w = \left(\frac{\rho_V}{\rho_L}\right)^{0.4}\left[\frac{p_V\, \nu_L}{\sigma}\left(\frac{\rho_L^2}{\sigma\, g(\rho_L - \rho_V)}\right)^{1/4}\right]^{1/4} \quad (21)$$

$$h_{KU} = 6.95\times10^{-4}\left(\frac{\lambda_L}{l_b}\right) Pr_L^{0.35}\left(\frac{q_{t,E}\, l_b}{\rho_V\, r\, \nu_L}\frac{p_V\, l_b}{\sigma}\right)^{0.7} \quad (22)$$

c) Thermal resistance due to the phase change of the working fluid inside the condenser part, R_C

The thermal resistance due to the phase change of working fluids inside the condenser part depends on the inner surface of the thermosyphon $S_{i,C}$ and on the heat transfer coefficient h_C.

The calculation of heat transfer coefficient h_C is much easier than it was in the case of h_E because practically only two regimes of heat transfer exist at the condensation of vapor on the falling film. These regimes can be

described by means of the standard Nusselt's correlation for laminar falling film [15] and Uehara's correlation for turbulent falling film [22], and both correlations must be modified with regard to the shear stress effects due to vapor flow at high heat flows and to the effect of tube inclination [6] as it is shown in Table 3.

For most electronic applications the falling liquid film is laminar, the vapor pressure is $p_V^x < 0.3$ and the shear stress is low. Therefore, the equations (24) and (25) can be substituted by the simpler equation (32).

Table 3. Heat Transfer in the Condenser Part of a Tubular Thermosyphon

$$R_C = \frac{1}{h_C \, S_{i,C}} \tag{23}$$

$$h_C = \frac{Nu_C \, \lambda_L}{l_f} \tag{24}$$

$$Nu_C = \left(1 + 4 \, \tau_{LV}^{x\,2}\right)^{-1/4} \left[\left(f_p \, Nu_{lam}\right)^2 + Nu_{turb}^2\right]^{1/2} \tag{25}$$

$$Nu_{lam} = \frac{h_C \, l_f}{\lambda_L} = 0.925 \mathrm{Re}_{L,\theta}^{-1/3} \tag{26}$$

$$Nu_{turb} = \frac{h_C \, l_f}{\lambda_L} = 0.044 \, \mathrm{Pr}_L^{2/5} \, \mathrm{Re}_{L,\theta}^{1/6} \tag{27}$$

$$f_p = 1 \qquad \text{for } p_V^x < 0.3, \qquad p_V^x = \frac{p_V}{p_{cr}} \tag{28a}$$

$$f_p = \frac{1}{1 - 0.63 p_V^{x\,3.3}} \qquad \text{for } p_V^x \geq 0.3 \tag{28b}$$

The dimensionless shear stress τ_{LV}^x is given in [6].

$$\mathrm{Re}_L = \frac{Q_t}{\pi \, d_i \, \mu_L \, r} \tag{29}$$

$$\mathrm{Re}_{L,\theta} = f_\theta \; \mathrm{Re}_L \tag{30}$$

$$f_\theta = 1 \qquad \text{for } 0 \leq \theta < 10° \text{ (vertical or quasi-vertical position)} \tag{31a}$$

$$f_\theta = \frac{2.87 \, d_i}{L_C \sin\theta} \qquad \text{for } \theta > 10° \text{ (inclined position)} \tag{31b}$$

$$Nu_C = \frac{h_C \, l_f}{\lambda_L} = \frac{0.925}{\mathrm{Re}_{L,\theta}^{1/3}} \qquad \text{(simplified correlation suitable for most electronics applications)} \tag{32}$$

d) Thermal resistances due to the selected manufacturing procedures

Besides these basic thermal resitances, which can be estimated by means of equations as they originate from physical phenomena, two further thermal resistances must be taken into account for any tubular thermosyphon cooler. They are connected with:

the contact between the inner surface of the holes in the input pad and the external surface of the evaporator tube (the so-called *hole thermal resistance*);

the contact between the fin collar and the external surface of the condenser tube (the so-called *collar thermal resistance*).

Both these thermal resistances depend on the manufacturing procedures that single manufacturers adopt for the construction, and must be determined by manufacturers themselves through actual measurements. They are usually presented as constants for a given manufacturing procedure.

Limits to the thermal performance of a tubular thermosyphon

Thermosyphons generally operate in a wide range of temperatures, and the heat transfer regimes they are sometimes subjected to can reach up to their thermal performance limits. Among the known limits - sonic, boiling, interaction and vapor flow – mainly the *interaction limit* and the *boiling limit* (Table 4) must be considered in the calculation of any tubular thermosyphon cooler for electronic applications.

Table 4. Thermal performance limits of a tubular thermosyphon

a) Boiling Limit

Kutateladze equation for pool boiling

$$q_{b,E} = 0.16 \rho_V r \sqrt[4]{\frac{\sigma\, g(\rho_L - \rho_V)}{{\rho_V}^2}} \qquad (33)$$

$q_{b,E}$ (W/cm^2)	Working Fluid (t_V = 60°C)		
	Water	Methanol	Fluorinert® FC72
Calculated – eqn (33) d_i=14.88 mm; L_E=150 mm	69.55	57.99	17.84
Exper. – Sintered fibres	128.6	85.8	68.4
Exper. – Parallel grooves	88.7	65.4	37.4
Exper. – Cross grooves	106.8	79.4	55.7

b) Interaction Limit

$$Q_{t,I} = \frac{r A_V \left[\sigma\, g(\rho_L - \rho_V)\right]^{1/4}}{\left({\rho_L}^{-1/4} + {\rho_V}^{-1/4}\right)^2} \left(\frac{\rho_L}{\rho_V}\right)^{0.14} \tanh^2 Bo^{1/4} \qquad (34)$$

where $$Bo = d_i \left[\frac{\sigma}{g(\rho_L - \rho_V)}\right]^{-1/2} \qquad (35)$$

$Q_{t,I}$ (W) Calculated – eqn (34)	Working Fluid (t_V = 60°C)		
	Water	Methanol	Fluorinert® FC72
d_i = 14.88 mm	1772	977	206
d_i = 4 mm	67	===	===
d_i = 3 mm	52	===	===
d_i = 2 mm	20	===	===

The *boiling limit* (also *dry-out limit*, *burn-out limit*) of a thermosyphon relates to a certain critical radial heat flux at which individual vapor bubbles in the liquid pool of the evaporator part aggregate to each other to form a vapor film at the wall. This vapor film is insulating the inner evaporator surface from the evaporating liquid and, owing to the poor thermal conductivity of the vapor, only part of the heat input to the wall can be transferred and

a sudden increase in the evaporator wall temperature occurs. The boiling limit is calculated by means of the modified Kutateladze's correlation [10].

The *interaction limit* (also *flooding limit, entrainment limit*) of a thermosyphon occurs at high axial heat flows which cause relatively high velocities between the counter-flowing vapor and liquid, and consequently increase the shear stresses at the vapor/liquid interface. This can lead to an entrainment of liquid, which in its turn causes an insufficient liquid supply to the evaporator with consequent local dry-outs of the evaporator. The correlation by Faghri [5] can be used for calculating the entrainment limit.

Equations of the boiling and interaction limits are given in Table IV together with some calculated values of both limits in a tubular thermosyphon (inner diameter 14.88mm; evaporator length 150mm) for water, methanol, ethanol and FC72 as working fluids.

Straight Rectangular Thermosyphon Coolers - Heat Spreaders

Standard aluminium finned heat sinks are effective when the heat source to heat sink contact area is similar to the total baseplate area of the heat sink – that is, with uniform heat flux. However, power concentration and small footprint areas are typical features in today electronic devices, so that local overheating areas and hot spots are always possible. For the calculation of such non-uniform heat flux cases, the spreading resistance of the heat sink base must be taken into account - see equation (6). Sometimes, despite thick heat sink bases, the spreading effect is still unable to feed the peripheral fins with adequate thermal energy.

To enhance the spreading effect of the heat sink base, we drilled cross-holes to create a two-phase thermosyphon in the form of a vapor chamber inside the heat sink base (Fig. 4). Such finned heat sinks with thermosyphons in the base are applied for cooling IGBT modules in traction drives. Non-uniform heat dissipation from IGBT modules is effectively spread to heat sink fins, as thermosyphon bases serve as heat spreaders. The working fluid inside the thermosyphon wall in contact with the electronic equipment vaporizes and the vapor flows to fill the inner space of the thermosyphon. Given that the vapor temperature in the inner space of the thermosyphon is practically the same, the thermal resistance associated with vapor spreading is negligible and the thermosyphon acts as an effective heat spreader from a concentrate heat source to a larger surface.

Thermosyphon Loops

In a two-phase thermosyphon loop, the evaporator and the condenser parts are connected by small diameter tubing for vapor flow up and liquid flow down. From the point of view of the thermal control of electronic elements, this enables positioning the evaporator part directly in contact with the electronic equipment and the condenser part elsewhere (e.g. chassis of the system), but always at a higher level than the evaporator part. This is the basic advantage as compared to the tubular thermosyphon cooler, as well as the elimination of the entrainment thermal performance limit. The driving force in a thermosyphon loop is the pressure due to the difference in liquid height in the two tubings of the thermosyphon loop. This driving force must be greater than the sum of the pressure losses due to the wall friction that both vapor and liquid meet in the loop and to other local losses in tube curves, fittings etc.

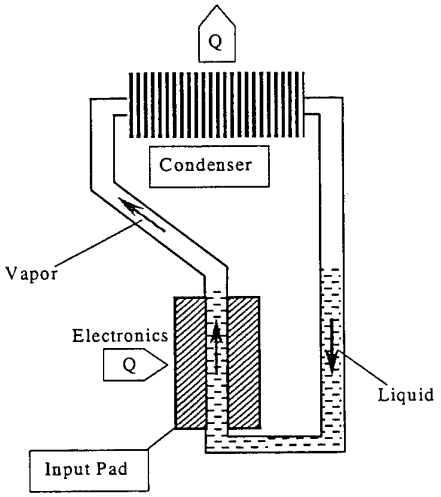


Fig. 9 - Thermosyphon Loop with Indirect Evaporator (Input Pad)

A higher demand in thermal performance increases the vapor flow rate and therefore the pressure drop. When the total pressure loss equals the maximum available driving force, the so-called *pressure loss limit* is reached [16] and a further increase in thermal performance will lead to dry-out of the evaporator surface.

Another limit to the thermal performance of a thermosyphon loop is the boiling limit, which is defined in the same way as for tubular thermosyphons. There are three basic possibilities as how to design the evaporator part of the thermosyphon loop:

1. *indirect evaporator*, consisting of a smooth tube fixed into a metal input pad (Fig. 8). The electronic equipment is attached to the outer surface of the input pad and the thermal resistance of the indirect thermosyphon loop has two parts. The first part is due to the heat conduction from the surface through the input pad to the evaporator tube, and its calculation depends on uniform or non-uniform heat flux from the electronic equipment to the input pad. This calculation is similar as in the case of the tubular thermosyphon. The second part is related to the boiling of the working fluid in the evaporator part and it depends on the operational regime of the thermosyphon loop. At low thermal performances we can use correlations for free convection and bubble boiling in a liquid pool (Table II) while at higher thermal performance levels we should use correlations for flow boiling.

2. *indirect evaporator as a rectangular chamber - cold plate* (Fig. 9), which has very low inner thermal resistance at the phase change liquid-vapor due to the special arrangement of the inner surface in the form of fine parallel channels or grooves, porous inserts etc. The electronic equipment is attached to the outer surface of the cold plate. The thermal resistance of a thin cold plate wall is very low and practically the total thermal resistance of the evaporator part is generated by the boiling thermal resistance in the liquid pool from the extended or enhanced inner surface of the evaporator part.

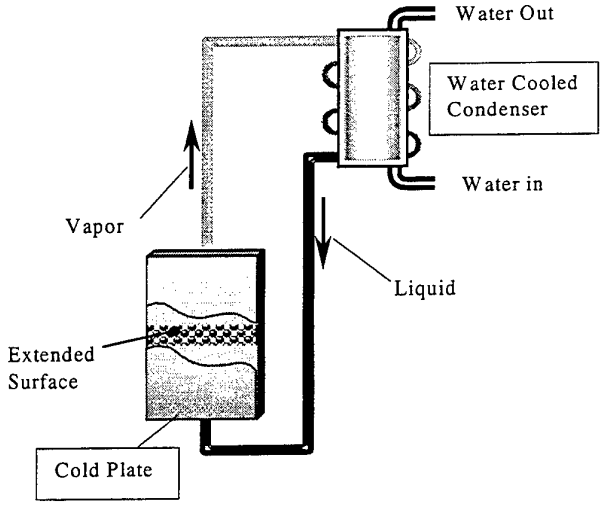


Fig. 9. Thermosyphon Loop with Indirect Evaporator (Cold Plate)

3. *immersion evaporator* (Fig. 6), when the electronic equipment is submerged directly into the liquid pool in the evaporator part. The advantage of immersion thermosyphon loops is the elimination of the contact thermal resistance between the electronic package and the evaporator part. But there are several disadvantages, as:
   - the necessity to use only dielectric liquids that usually show poor thermal properties, low critical heat flux at pool boiling and large temperature overshoot at boiling incipience,
   - higher production costs with regards to large pressure-proof containers with electric feed-through and lid.
   - maintenance problems.

3. CHOICE OF WORKING FLUIDS AND OPTIMUM FILLING

To cool present micro- and power electronic equipment, the surface temperature of the electronic package in contact with an indirect thermosyphon cooler usually ranges around 80°C, and the vapor temperature inside a thermosyphon is usually between 50°C and 70°C depending on geometrical parameters and other factors. In the temperature range from 50°C to 70°C water is the most convenient working fluid. Liquids like the FC family (FC72 or FC87) are most suitable for immersion coolers and for indirect electrically insulated coolers where an electrically insulated ceramic part in located between the metallic evaporator and the metallic condenser parts. In cold regions, where working temperatures lower than 0°C can occur, indirect thermosyphon coolers must use methanol, ethanol or water-ethylenglycol mixtures instead of pure water. From the point of view a compatibility

between the working fluid and the containing materials, water, methanol, ethanol and water-ethylenglycol mixtures may be used only with copper.

The optimum initial filling ratio of the working fluid in the evaporator part of a tubular thermosyphon influences the maximum thermal performance. The initial filling ratio should have an appropriate value to avoid any dry-out of the liquid film. The optimum initial filling ratio depends mainly on thermosyphon dimensions, on the type and vapor temperature of the working fluid and on the required thermal performance. EL-GENK [4] developed a calculation procedure to determine the optimum filling ratio. However, the thermal control of electronics often demands the vapor temperature and the thermal performance to change rapidly and frequently, and therefore some compromise on initial filling ratio should be considered. The initial filling ratio has basic influence on heat transfer in the evaporator part and little influence on heat transfer in the condenser part.

Table 5 shows a comparison of the experimental values of the inner thermal resistances of a tubular copper thermosyphon having inner diameter d_i = 14.88 mm, length of the evaporator part L_E = 150 mm, length of the condenser part L_C = 300 mm. The working fluids considered are water, methanol, ethanol and FC 72, the vapor temperature t_V is 60°C and the managed thermal power Q amounts to 280 W. The comparison is made for two initial filling ratios: $V_L/V_E = 0.25$ and $V_L/V_E = 0.75$.

Table 5. Comparison between calculated and experimental values of the inner thermal resistance of a tubular thermosyphon

Inner Thermal Resistance $R_i = R_E + R_C$ (K/kW)	Working Fluid (t_V = 60°C)			
	Water	Methanol	Ethanol	Fluorinert® FC 72
Q = 280W; d_i = 14.88 mm; L_E = 150 mm; L_C = 300 mm				
1) Calculated				
a) Filling 0.25	14.24	38.0	55.5	Q = 280W is above the interaction limit ($Q_{t,l}$ = 206 W)
b) Filling 0.75	24.05	51.4	73.8	
2) Experimental				
a) Filling 0.25	18.02	43.5	58.3	
Q = 140W; d_i = 14.88 mm; L_E = 150 mm; L_C = 300 mm				
1) Calculated				
a) Filling 0.25				327.0
b) Filling 0.75				554.2
2) Experimental				
a) Filling 0.25				338.2

The comparison clearly shows that the inner thermal resistance of the tubular thermosyphon is more than 50% higher in the case of larger initial filling ratio. For electronic applications, an initial filling ratio of 25% of the volume of the evaporator part is usually adopted.

For electronic applications of indirect thermosyphon loops the total inner volume of the evaporator part should be filled up by the liquid while in the case of immersed thermosyphon loops the total surface of electronic equipment should be submerged by the liquid.

4. ENHANCEMENT OF HEAT TRANSFER IN THE EVAPORATOR PART OF THERMOSYPHONS

The critical point in most applications of thermosyphons in electronics is the evaporator part, due to increasing heat fluxes – which are usually non-uniform and unsteady - from electronic equipment to the cooler. In the evaporator part, three main characteristics of heat transfer can be pointed out:

a) heat transfer coefficient at evaporation or boiling,
b) critical heat flux,
c) temperature overshoot at boiling incipience of highly wetting liquids, mainly FC type.

While the heat transfer coefficient at evaporation and boiling in the falling liquid films is high enough, it is usually important to enhance the heat transfer coefficient at free liquid convection and bubble boiling in a liquid pool. This is especially true for methanol, ethanol and FC liquids. Several enhanced and extended surfaces in the form of grooves, screen mesh, sintered powders or fibres, porous layer of alumina particles, porous studs etc have been successfully tested [1][7][11][13][14][20]. The calculated critical heat fluxes at pool boiling in the evaporator part of the tubular thermosyphon (see Table IV) go from 17.84 W/cm^2 for FC 72 to about 70 W/cm^2 for pure water. Some present and most future electronic equipment have heat fluxes in the range from 20 up to 200 W/cm^2, so that only certain liquids are able to meet their demanding requirements. Upgrading the critical heat flux by means of the above mentioned enhanced and extended surfaces is the today main task for many R & D engineers: for example, the critical heat flux at pool boiling of FC liquids is only from 10 to 20 W/cm^2. We tested two extended surfaces:

a) Parallel and cross rectangular capillary grooves (width of the grooves 0.4mm: depth of the grooves 0.5mm) directly cut into the inner copper wall of the evaporator part (Fig. 10);

b) Porous surfaces made from sintered copper fibres (diameter of fibres 30 ~ 50 μm, length of fibres 3 ~ 4 mm; thickness of sintered fibre layer 1.5 mm; porosity 0.7 ~ 0.8). Copper fibres were sintered directly onto the inner wall of the evaporator part (Fig. 11).

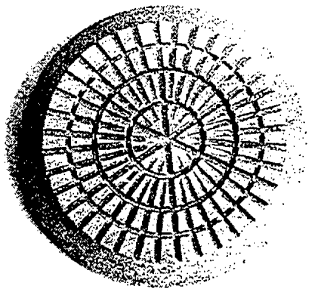


Fig. 10. Crossed Grooves Surface

Experimental results for water, methanol and FC72 as working fluids are presented in Table IV. From the comparison of the calculated results for critical heat fluxes on smooth surfaces (equation 33) and the experimental results from the two extended surfaces it is clear that sintered copper fibres increase the critical heat fluxes more than three times in the case of FC 72.

However, the Kutateladze correlation in its usual form might originate inaccurate results if straightforwardly applied to the study of pool boiling in strictly confined spaces, like the inside of an evaporator. A modified, tuned up version of the above mentioned correlation is currently being developed.

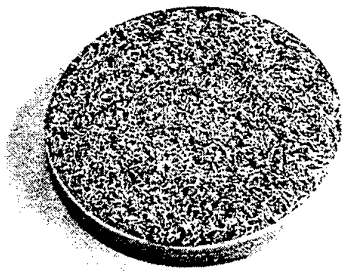


Fig. 11 – Sintered Copper Fibres

5. PULSATING HEAT PIPES

Operational Principle of a Pulsating Heat Pipe (PHP)

Contrary to the conventional heat pipe, where the working fluid inside a tube circulates continuously between the heat source and the heat sink in the form of counter current two phase flow, the working fluid in a PHP oscillates in its axial direction periodically (see Figure 2 at page 2). For a successful operation of a PHP, liquid plugs and vapor bubbles must coexist inside the capillary tube along its length. This can be achieved by vacuuming the tube and then partially filling it with a working fluid. Liquid plugs and vapor bubbles can coexist only when the inner diameter of the capillary tube is small enough (from 0.5 to 3 mm). Another very important condition for a successful operation of a PHP is the connection in series of a bundle of parallel capillary tubes into a single undulating turned tube (Figure 12). When one end of the bundle of turns of the undulating capillary tube is subjected to high temperature, the working fluid inside evaporates and increases the vapor pressure, which causes the bubbles in the evaporator zone to grow. This pushes the liquid column toward the low temperature end (condenser). The condensation at the low temperature end will further increase the pressure difference between the two ends. Because of the interconnection of the tube, the motion of liquid slugs and vapor bubbles at one section of the tube toward the condenser also leads to the motion of slugs and bubbles in the next section toward the high temperature end (evaporator). This works as the restoring force. The inter-play between the driving force and the restoring force leads to the oscillation of vapor bubbles and liquid slugs in the axial direction. The frequency and the amplitude of the oscillation are expected to be dependent on heat flow and mass fraction of the liquid in the tube. Through these oscillations, heat is supplied by the heat source at the evaporator end and is then carried to the condenser the heat is removed by a heat exchanger. Because many capillary tubes are connected to the evaporator part and because the size and location of vapor bubbles and liquid slugs are quite random, both pressure waves and bubble oscillations are generated randomly with different phases. During oscillation, bubbles can also coagulate.

Basic Design of Pulsating Heat Pipe Coolers for Electronics

The company Actronics has been manufacturing the following basic designs of pulsating heat pipe coolers:

A. Kenzan Fin

The PHP is practically a bundle of turns of capillary smooth tubes. This bundle is usually created by bending a long continuous capillary tube, as it is shown in fig. 12, where one part of tube turns (evaporator) is soldered to an input pad and another part (condenser) of tube turns serves as heat sinking pins (fins). Electronic components are attached to the input pad surface, while the heat sinking fins are cooled by either natural or forced air convection. This design is called *Kenzan Fin* [9][12].

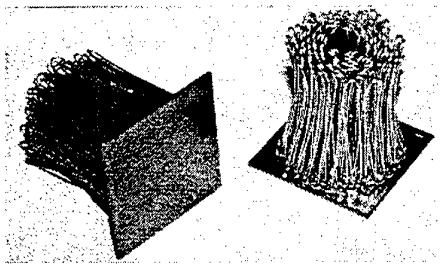


Fig. 12. Kenzan Fin PHP

Two Kenzan Fin PHP coolers for IGBT modules were developed and tested. One for natural air convection was composed by 1,500 turns of a copper capillary tube (external diameter 2.8 mm, internal diameter 2.2 mm). The length of the radiating (condenser) turns is 250 mm. the dimensions of the input pad are 500 (L) x 200 (W) x 50 (H) mm. The thermal resistance of this cooler is R = 0.0089 K/W at Q = 4,500 W. The cooler for forced convection was composed by 424 turns of the same copper capillary tube. Length and width of the

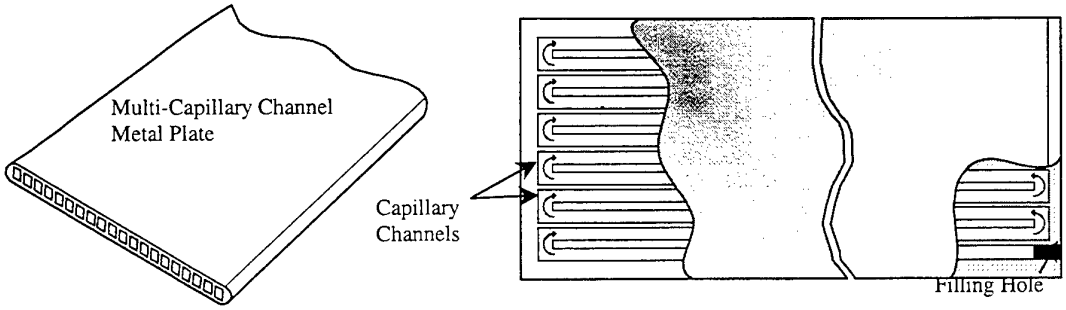


Figure 13. Schema of a flat plate pulsating heat pipe

radiating turns are 200 x 150 mm respectively, and the inpu pad is 110 x 190 mm. The thermal resistance of this cooler is R = 0.022 K/W at Q = 1800W and with a face air velocity v = 3 m/s. The performances of both coolers are practically independent from the inclination of the device.

B. Heat Lane

A new design of PHP, named Heat Lane [24], has been now developed. In this design, the bending of a long continuous extruded metallic flat plate with capillary channels inside (fig. 13) creates a bundle of turns. At both ends of the extruded plate the capillary channels are repeatedly turned in a way to form a serpentine tunnel. Both ends of the plate are then pressed and hermetically sealed by welding. Like in the Kenzan Fin design, one part of the bundle plate turns (evaporator) is soldered to an input pad and another part (condenser) of the bundle plate serves as radiation fins. Very effective louvered fins can also be soldered between two plates (Fig. 14) to generate a compact, light and high efficiency heat exchanger.

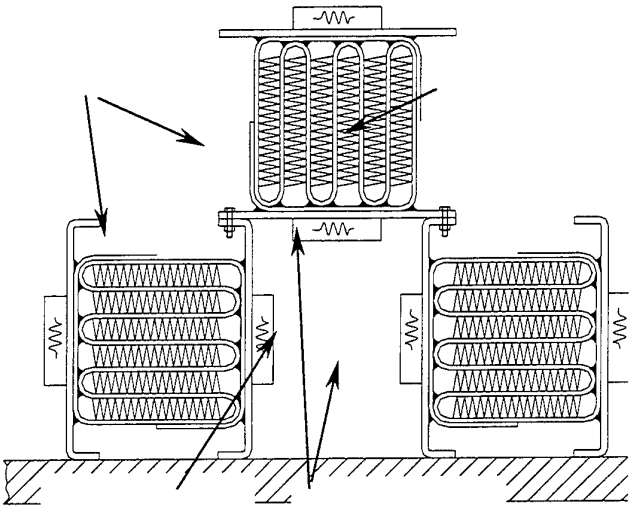


Figure 14. Pulsating heat pipe "heat lane" [12]

Applications of Heat Pipes in Computers

Heat pipes are used in notebooks, desktops and industrial PCs to transfer the dissipated heat from heat sources (usually CPUs only) to a location where cooling conditions are more favourable. For these reasons, such cooling systems are often called Remote Heat Exchangers (RHE). Their configuration is different according to application, power to be dissipated, ambient conditions (Fig. 15).

Both passive cooling (natural convection) and forced air cooling systems are available on the market.

Notebook applications of heat pipes

There are two basic designs to dissipate the heat generated by notebook CPUs by means of heat pipes:

a) Passive Cooling Design by Standard Wicked Heat Pipes

These designs use heat pipes to enhance the heat transfer from the CPU to the notebook case. At their side opposite to the CPU, heat pipes are usually attached to an aluminium plate that transfers the heat to the chassis or dissipates it under the keyboard. Many current notebooks are actually equipped with this kind of heat removing system: however, this design is limited to a thermal performance in the range of 8 W, mainly because the surface temperature of a notebook case cannot exceed 15°C over ambient for ergonomic reasons. To a certain extent, the thermal performance of such designs can be increased by using the so called Heat Pipe Hinge Systems, by means of which the heat is moved away from CPU, passes through an articulated joint and is then transferred to an aluminium plate located on the back of the display. Heat pipes for passive cooling of notebooks are usually miniature size, with outer diameter from 2 to 4 mm (circular shape) or thickness from 2 to 4 mm (flat sub-

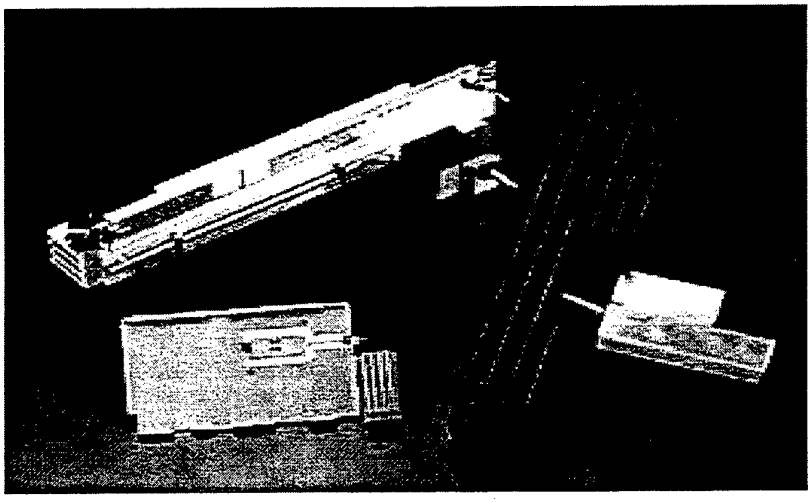


Figure 15. Remote heat exchangers (RHEs) for computer applications

rectangular shape). Copper tube and water filling is the best material combination as far as both compatibility and thermophysical properties. Heat pipes must also have an effective internal capillary structure, in the form of axial grooves, screen, sintered copper powder or bundle of fine wires. The thermal performance of these miniature heat pipes ranges from 5 to 20 W, depending on their diameter, vapor temperature and – mainly – wick type.

b). Passive Cooling by Pulsating Heat Pipes (PHPs)

New generations of microprocessors are continuously developed at faster and faster pace, and CPUs dissipating 25 to 35 W will soon equip every kind of PCs, including notebooks. Hence, none of the above mentioned completely passive cooling designs will be applicable any longer, as they would result in skin temperatures exceeding ergonomic limits. However, a passive cooling design is still acceptable at 35 W dissipated and 90°C maximum CPU temperature providing the heat is transferred from the CPU to a finned heat sink via a flat pulsating heat pipe. The heat sink temperature will rise up to around 60°C, but all the other parts of the notebook case will be kept within the temperature ergonomic limits. For the heat transfer from the CPU to a finned heat sink a U shaped, flat PHP has been developed by the company Actronics. The PHP body consists of a flat aluminium extrusion whose external rectangular shape incorporates many parallel capillary channels inside (fig. 14). A 2 mm thick, 50 mm wide and 250 mm long flat PHP with a very compact finned surface soldered to its cooled (condenser) part can transport up to 50 W with very small temperature drop.

c) Forced Air Convection with Heat Pipes

This kind of RHE (fig. 16) is widely employed in notebooks for its extreme compactness, light weight and design flexibility. It features a miniature heat exchanger cooled by a micro fan at the cooled end of the heat pipe. This carries the heat away from the CPU through the usual input pad. Sometimes a wider aluminium sheet is used instead of the input pad to gather the heat dissipated by other electronic devices, like video chipsets, memories and the like. The obvious choice for locating the micro fan (size 20 to 30 mm square) is the back panel of the notebook. Usual dimensions for the miniature heat exchanger are: 20-30 mm width, 10-20 mm height, 40-60 mm length. The highest thermal performance that can be expected by such cooling systems is around 12 W.

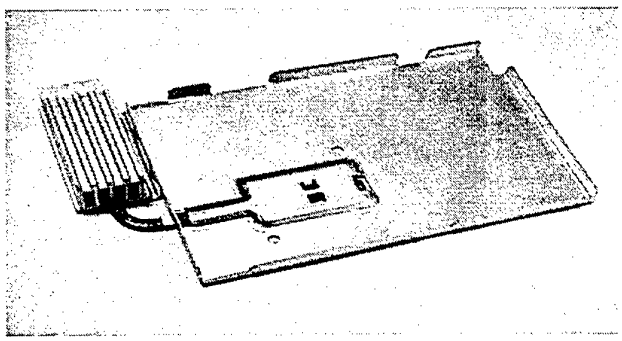


Figure 16. Forced Air Cooling System for Notebooks (Micro Fan is not shown)

Desktop applications of heat pipes

The typical cooling system adopted for today desktop computers features an electrically driven fan and a finned heat sink directly attached onto the processor. Almost all latest Pentium® processors are cooled this way. The finned heat sink can be machined from a standard aluminium extrusion or a die casted unit. Nevertheless, at present desktop computer manufacturers are actively studying the possibility of switching over a fully passive, fan-less solution, to increase reliability, reduce costs and eliminate the noise. This means that the CPU and other smaller heat sources must be put in condition to dissipate together from 30 to 50 W only by natural convection and radiation. A possible way to solve the problem is to use a heat pipe to remove the heat from the electronic components and carry it very effectively (with a minimum temperature drop) to a location close to the computer case, or, if possible, to the chassis itself or part of it acting as an external heat exchanger. Solutions of this kind are already in production for top-end PCs, industrial PCs and servers (Fig. 17). Particularly suitable for this job, systems using a flat pulsating heat pipe as the medium to thermally connect the input pad attached to the electronics with the remote dissipating unit are now under investigation as potential highest performers, like it was described for notebook cooling.

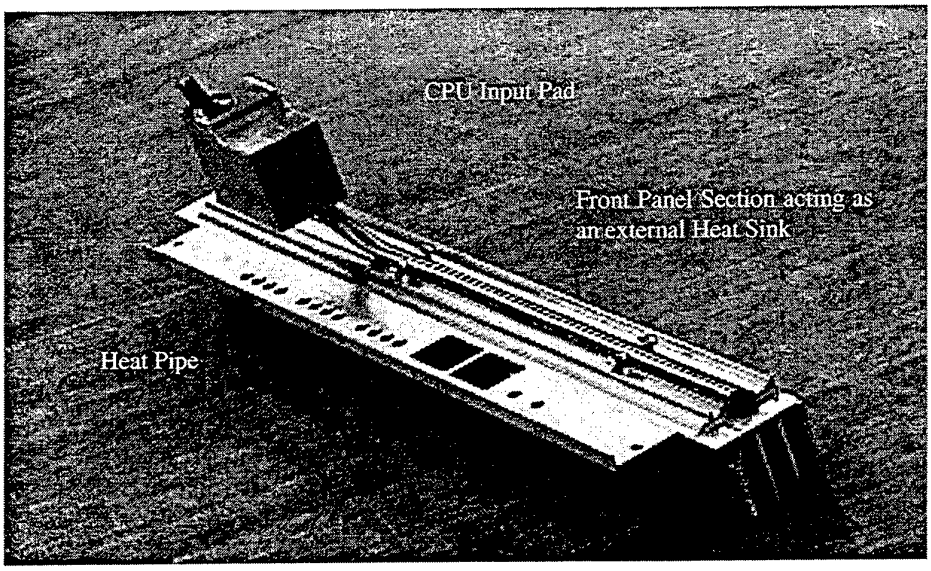


Figure 17. Telecom computer heat pipe passive cooling system

6. CONCLUSIONS

Results and practical experience from the R & D of various designs of two-phase thermosyphons and pulsating heat pipes for thermal control of electronic equipment were presented. These passive two-phase heat transfer elements are promising for dissipating and spreading heat from electronic equipment to an external coolant. Present thermosyphon designs are able to dissipated heat fluxes from electronic equipment up to a maximum value of 70 W/cm^2, depending mainly on the choice of the working fluid. Future electronic applications will require dissipating heat fluxes up to 200 W/cm^2 and suitable extended and enhanced inner surfaces for the evaporator part will have to be developed.

Passive cooling of high power notebook and desktop in the range of 30 to 50W dissipated can be realised by means of a flat pulsating heat pipe cooling system connecting the CPU and the other electronic components that need cooling to a finned heat sink, or to some metallic part of the computer case acting as an integrated radiating unit.

7. NOMENCLATURE

Latin

A	cross-sectional area	[m^2]
c_p	specific heat at contant pressure	[J/kg K]
d	diameter	[m]
D	diameter	[m]
f_p	pressure factor	
f_θ	inclination factor	
F	conduction shape factor	[m]
g	gravitational acceleration	[m/s^2]
h	heat transfer coefficient	[W/m^2 K]
H	spreading resistance factor	
l	characteristic length	[m]
l_b	bubble length scale	[m]
l_f	film thickness scale	[m]
L	length	[m]
N	velocity number	
$p^\times = p/p_{cr}$	pressure ratio	
P	pressure	[Pa]
q	heat flux	[W/m^2]
Q	heat flow	[W]
r	latent heat of evaporation	[J/kg]
R	thermal resistance	[K/W]
s	pitch	[m]
t	temperature	[°C]
v	velocity	[m/s]
$V^\times = V_L/V_E$	volume ratio of working fluid	

Dimensionless numbers

$Bo = l\left[\frac{\sigma}{(\rho_L - \rho_V)\, g}\right]^{-1/2}$	Bond number
$Nu = \frac{h\, l}{\lambda}$	Nusselt number
$\mathrm{Pr} = \frac{\mu\, c_p}{\lambda}$	Prandtl number
$Ra = \frac{\beta\, g\, \Delta t\, l^3 \rho^2 c_p}{\mu\, \lambda}$	Rayleigh number
$\mathrm{Re} = \frac{\rho\, v\, l}{\mu}$	Reynolds number

Greek

β	thermal expansion coefficient	[K^{-1}]
δ	thickness	[m]
Δ	difference	
λ	thermal conductivity	[W/m K]
μ	dynamic viscosity	[Ns/m^2]
ν	kinematic viscosity	[m^2/s]
ρ	density	[kg/m^3]
σ	surface tension	[N/m]
τ_{LV}	shear stress	[N/m^2]
$\tau_{LV}^\times$	dimensionless shear stress	
ω	parameter	
θ	inclination angle from vertical	[°]

Subscripts

AD	adiabatic
b	bubble
B	air
cr	critical state
C	condenser, condensation
e	external
E	evaporator, evaporation
f	film
F	fin
i	inner
I	interaction
IP	input pad
KU	Kutateladze number
lam	laminar
L	liquid
N	evaporation from film
NB	nucleous boiling
NC	natural convection
p	pool
t	tube
turb	turbulent
V	vapor
W	wall
θ	inclination
1	inlet
2	outlet

8. REFERENCES

1. J.Y. Chang, S.M. You, Boiling Heat Transfer Phenomena from Microporous and Porous Surfaces in Saturated FC-72. Int. J. Heat Mass Transfer Vol. 40, No. 38,pp. 4437-4447 (1997).
2. M.S. El-Genk, H.H. Saber, Heat Transfer Correlations for Small, Uniformly Heated Liquid Pools. Int. J. Heat Mass Transfer, Vol. 41, No. 2, pp. 261-274 (1998).
3. M.S. El-Genk, H.H. Saber, Heat Transfer Correlations for Liquid Film in the Evaporator of Enclosed, Gravity-Assisted Thermosyphons. J. Heat Transfer, Vol. 120, No. 2, pp. 477-484 (1998).
4. M.S. El-Genk, H.H. Saber, Determination of Operation Envelopes for Closed, Two-Phase Thermosyphons. Int. J. Heat Mass Transfer, Vol. 42, No. 4, pp. 889-903 (1999).
5. A. Faghri, Heat Pipe Science and Technology. Taylor and Francis, Washington D.C. (1995).
6. U. Gross, Reflux Condensation Heat Transfer Inside a Closed Thermosyphon. Int. J. Heat Mass Transfer Vol. 35, No. 2, pp. 279-294 (1992).
7. V. Hlavacka, F. Polášek, P. Štulc, V. Zboril, Heat Pipes for Electrical Engineering. SNTL. Publ., House, Prague (1990).
8. S. Lee, Calculating Spreading Resistance in Heat Sinks. Electronic Cooling, Volume 4, Number 1, January (1998).
9. G. Kobayashi, Y. Shikano, Boiling and Condensing Heat Transfer for Cooling of High-Power Semiconductor Rectification Equipment. Mitsubishi Electric Engineer, Vol. 48, No. 2, pp. 24-33 (1974).
10. S.S. Kutateladze, Heat Transfer in Condensation and Boiling, Report AEC No.3770 (1959).
11. M. Misale, G. Guglielmini, A.E. Bergles, FC-72 Pool Boiling From Finned Surface Placed in a Narrow Channel : Preliminary Results. Proc. 2nd European Thermal Sciences Conf. Rome (1996).
12. K. Mou, H. Chang, Study on Percentage of Liquid Filling of Separate Type Heat Pipe. Proc. 3rd Int. Heat Pipe Symposium, Tsukuba (1988).
13. I. Mudaiwar, Direct-Immersion Cooling for High Power Electronic Chips. Proc. Int. Electronic Packaging Conf. San Diego (1993).
14. W. Nakayama, Porous Surface Boiling and Its Application to Cooling of Microelectronic Chips. Proc. Symposium on Convective Heat and Mass Transfer in Porous Media,Ankara (1991).
15. W. Nusselt, Die Oberflächenkondensation des Waserdamptes. Z.Ver. D. Ing.,Vol. 60, pp. 541-575 (1916).
16. B. Palm, N. Tengblad, Cooling of Electronics by Heat Pipes and Thermosyphons - a Review of Methods and Possibilities. Proc. ASME Nat. Heat Transfer Conf. Houston (1996).
17. F. Polášek, P. Štulc, Cooling of Electronic Elements by Miniature and Medium-Sized Heat Pipes. Proc. European Thermal-Sciences Conf., Roma (1996).
18. F. Polášek, M. Zelko, Thermal Control of Electronic Components by Heat Pipes and Thermosyphons. Proc. Int. Heat Pipe Conf., Stuttgart (1997).
19. F. Polášek, Calculation of Heat Pipe Coolers for Power Electronic Applications. Research Report TM No.1, Prague (1998).
20. C. Ramaswamy, Y. Joshi, W. Nakayama, W.I. Johnson, Performance of a Compact Two-Chamber Two-Phase Thermosyphon: Effect of Evaporator Inclination, Liquid Fill Volume and Contact Resistance. Proc. 11th Int. Heat Transfer Conf. Kyongju (1998).
21. W.M. Rohsenow, J.P. Hartnett, E.N. Ganic, Handbook of Heat Transfer Fundamentals. McGraw-Hill Book Comp., New York (1985).
22. H. Uehara, H. Kusuda, T. Nakaoka, M. Yamada, Filmwise Condensation for Turbulent Flow on a Vertical Plate. Heat Transfer Japanese Research Vol. 12, No. 2, pp. 85-96 (1983).
23. -: Heat Pipe Coolers of Power Electronics. ELBOMEC Thermalloy Prospectus, Bologna (1996).
24. H. Akachi, F. Polášek, Thermal Control of IGBT Modules in Traction Drives by Pulsating Heat Pipes. Proc. Int. Heat Pipe Conf., Stuttgart (1997).
25. -: Remote Heat Pipe Heat Exchangers. Brochure by Thermalloy, Inc., Dallas Texas (1998).

A STUDY ON THE THERMAL-HYDRAULIC PHENOMENA OF DECAY HEAT REMOVAL SYSTEM USING THE CLOSED TWO-PHASE THERMOSIPHON LOOP

Yehchan Ahn
Department of Mechanical Engineering
Pohang University of Science and Technology
San31, Hyoja-Dong, Namgu, Pohang, 790-784, Korea
Email : ayc@postech.ac.kr ; Fax : +82-562-279-3199

Gooncherl Park
Department of Nuclear Engineering
Seoul National University
San56-1, Shinlim-Dong, Gwanakgu, Seoul, 151-742, Korea
Email : gcpark@plaza.snu.ac.kr ; Fax : +82-2-889-2688

Moohwan Kim
Department of Mechanical Engineering
Pohang University of Science and Technology
San31, Hyoja-Dong, Namgu, Pohang, 790-784, Korea
Email : mhkim@postech.ac.kr ; Fax : +82-562-279-3199

Keywords: thermosiphon, flow instability, two-phase

ABSTRACT. The purpose of this work is to understand the thermal-hydraulic characteristics of the closed two-phase thermosiphon loop. To do this, the experimental apparatus has been designed and constructed. It consists of evaporator part, condenser part, gas line, liquid line and recirculation line, and each part is made of copper tube with 17 mm ID and 19.05 mm OD. The length of Evaporator and condenser is 200 cm. Especially, the evaporator and the condenser parts are annular tubes whose inner tubes are heated or cooled by water flowing through annular passages. In this experiment, water is used as the working fluid in thermosiphon loop. We have observed the typical temperature and heat flux data. And we have also observed flow instabilities. Flow instabilities are presented by transient temperature, pressure, main flow rate data. There have been two kinds of instability – density wave oscillation and flow excursion. Local heat fluxes and wall temperatures along the evaporator and the condenser have been measured using the RdF micro foil heat flux sensors.

1. INTRODUCTION

In spite of the good safety record achieved by the nuclear power industry, several major accidents have added to the public's skepticism of nuclear power as an acceptable opinion for electrical generation. In particular two serious accidents – at Three Mile Island and Chernobyl – were crucial in this respect. Both showed that safety devices were vulnerable to human error, especially if the system is of a complicated character.

Consequently, new design options are currently being pursued to improve the safety of the new generation of nuclear power plants. One emphasis is on simpler or easier to operate units with passive or intrinsic characteristics which would provide not only inherent stability of the chain reaction but also ensure continual cooling of fuel and its containment system under major accidents. These features enable the plant to survive under severe potential accidents without human intervention.

As a result of such efforts, several concepts for passive safety devices have been developed [1-3]. Main purpose of these devices is to provide assured removal of decay heat to an ultimate heat sink. In this paper, a closed two-phase thermosiphon loop as a passive safety device is concerned and especially its thermal-hydraulic phenomena are investigated, using the experimental apparatus constructed. Closed two-phase thermosiphon loop is a separate type heat pipe whose evaporator and condenser are not in contact with each other. It is suitable for large-scale heat transfer between the distant cooling and heating mediums. Therefore it can be applied in nuclear power plants as a safety device. But it may produce flow instabilities. Previous researchers have studied flow instabilities [4-7] and they have classified flow instabilities into two groups – static and dynamic instabilities.

2. WORKING PRINCIPLE

A closed two-phase thermosiphon loop is shown in Fig. 1. When the evaporator and the condenser are exposed to two different temperature fields, the working fluid reaches a boiling temperature in the evaporator which is higher than the condensing temperature in the condenser. Since a liquid-vapor interface exists always in these two regions, the saturation pressure difference is produced and causes the working fluid to flow from the evaporator to the condenser. On the other hand, the liquid collecting at the condenser bottom or vertical section of the liquid line sets up a corresponding hydrostatic head difference which results in a net flow of the liquid from the condenser to the evaporator.

Under steady loop operation, the working fluid enters the base of the evaporator as a subcooled liquid, where heat is added by means of single-phase forced convection. This causes the bulk fluid temperature to rise with decreasing the pressure of bulk fluid and then makes subcooled boiling. After that, a marked improvement in heat transfer coefficient – bulk boiling -is observed and more and more vapor is generated. Vapor bubbles reduce the flow area with increasing the buoyant effect. As a result the pressure drop term will now include an additional loss due to momentum change. Under some condition, it is possible that all the liquid change to the vapor phase before it exits the evaporator.

If the perfect vaporization is not occurred at the end of evaporator, liquid is returned to the bottom of the evaporator and vapor flows along the gas line by the separator. The vapor reached the condenser inlet exchanges its latent heat with cooling water and the fluid flows in the annular pattern with vapor core. Hence the pressure drop will be very small. However if all vapor condense in the condenser or if liquid and vapor are stratified in vertical section of liquid line, the pressure will change significantly especially because of the hydrostatic head gain. Under the influence of gravity the condensate then flows through the liquid line to the bottom of the evaporator.

From the above description it is apparent that the fluid does not require any pumping. There are only two

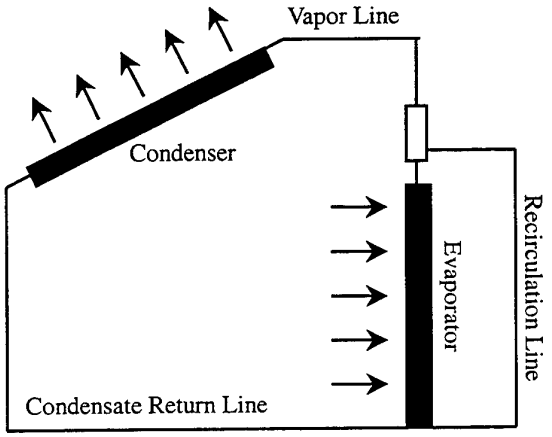


Fig.1 A closed two-phase thermosiphon loop

driving force, saturation pressure difference and gravity force, without any active force by pump.

3. EXPERIMENTAL APPARATUS

The schematic diagram of the experimental apparatus is shown in Fig. 2. The loop was made of copper tube with 17 mm ID and 19.05 mm OD except vertical part of liquid line and recirculation line, which were made of polypropylene tube to measure liquid level. Evaporator and condenser are annular tubes whose length is 200 cm, outer tube diameter is 10 cm. Their cutting plane is shown in Fig. 3. Evaporator was installed vertically and condenser was inclined at 30 degree from the horizontal plane. Heating and cooling water flow through their outer space and working fluid (water) flows through their inner tubes. Micro foil heat flux sensors are attached at outer wall of inner tube. They can measure heat flux and wall temperature. Eleven heat flux sensors were

installed along evaporator and ten (5 at upper wall, 5 at lower wall) along condenser. The arrangement of thermocouples is shown in Fig. 2. At inlet and outlet of evaporator and condenser, the temperatures of working fluid and heating or cooling water were measured. Pressures were also measured at inlet and outlet of evaporator and condenser. Main flow and recirculation flow rates were measured by corner tap orifice flow meters, which were symmetric for measuring bi-directional flow. All the tubes were insulated to prevent heat loss to atmosphere. Vacuum pump was installed at gas line.

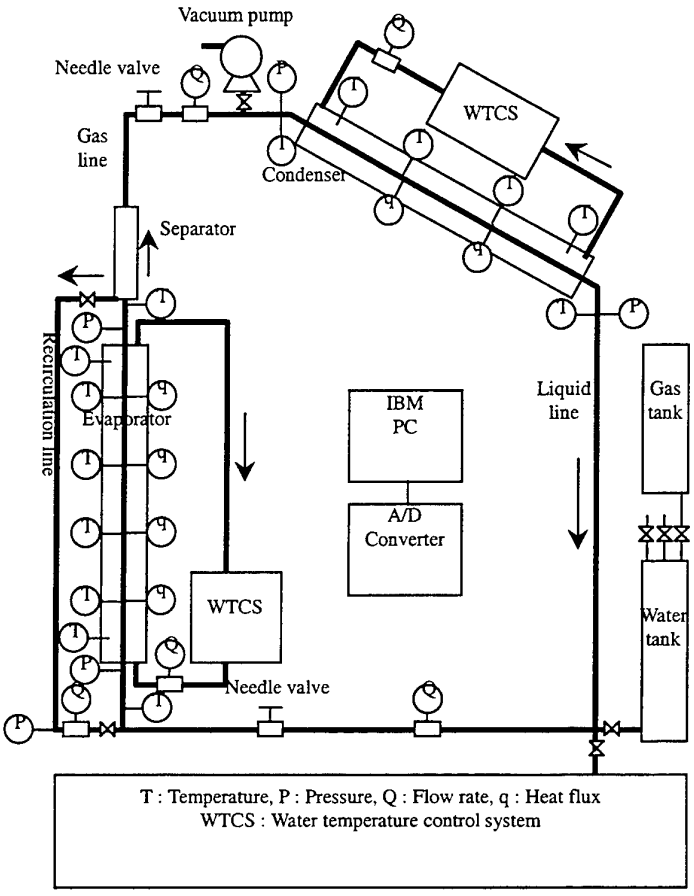


Fig. 2 The schematic diagram of the experimental apparatus

4. EXPERIMENTAL RESULTS

The working fluid was poured into the tank and loop, and then the loop was evacuated by vacuum pump. After that, heat was supplied to evaporator by heating water and eliminated at condenser by cooling water. When the temperature and pressure at all points achieved a steady state, the data were taken. Examples of temperature are shown in Fig. 3 and 4 and heat flux in Fig. 5 and 6. For all the cases, all values were averaged and static charge, which was defined by flooded evaporator length over total evaporator length was 40 %. Fig. 3 and 5 shows that single-phase forced convection region ranged from 0 to 50 cm of evaporator length and nucleate boiling region started around 50 cm position and change into two-phase forced convection region and dry-out occurred about 130 cm position. Fig. 4 and 6 shows that flow pattern in condenser is stratified flow and all the vapor were totally condensed before 100 cm position.

Transient behaviors of thermal-hydraulic values are shown from Fig. 7 to Fig. 9. For all the cases, static charge was 10 %. Around 10 % of static charge, flow instabilities occurred strongly. Fig. 7 shows temperature variation at each position. Temperature fluctuations are apparent at evaporator inlet and outlet, but not at condenser inlet

and outlet. Pressure or pressure drop variations are shown at Fig. 8. Violent flow instabilities were observed. There are two kinds of fluctuation. One is high frequency oscillation and the other is low frequency oscillation. Fig. 9 shows flow rate that was measured by turbine flow meter at gas line. It also shows two kinds of instability. It is supposed that high frequency oscillation may be density wave oscillation and low frequency oscillation may be flow excursion.

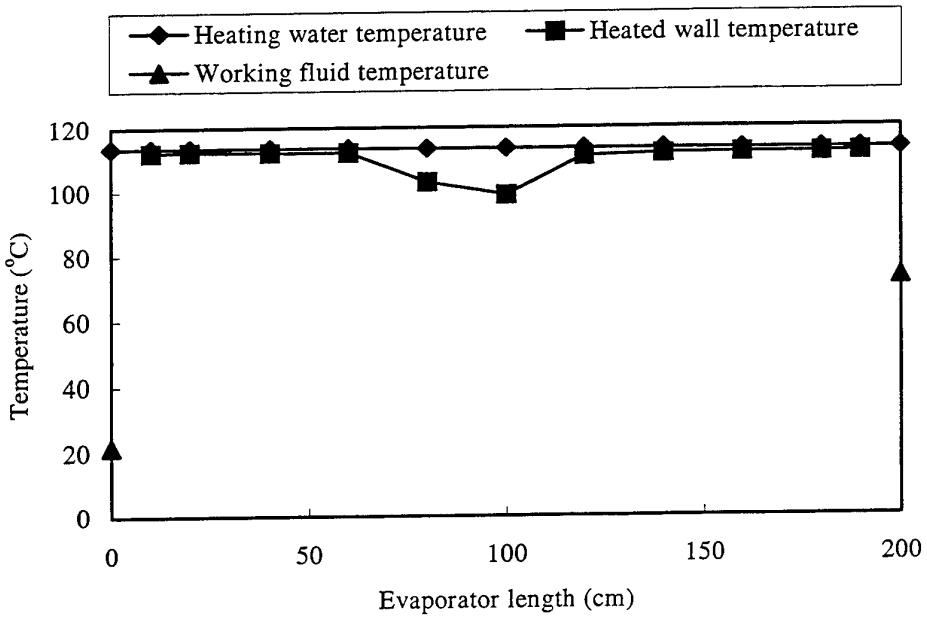


Fig. 3 Temperature distribution along evaporator

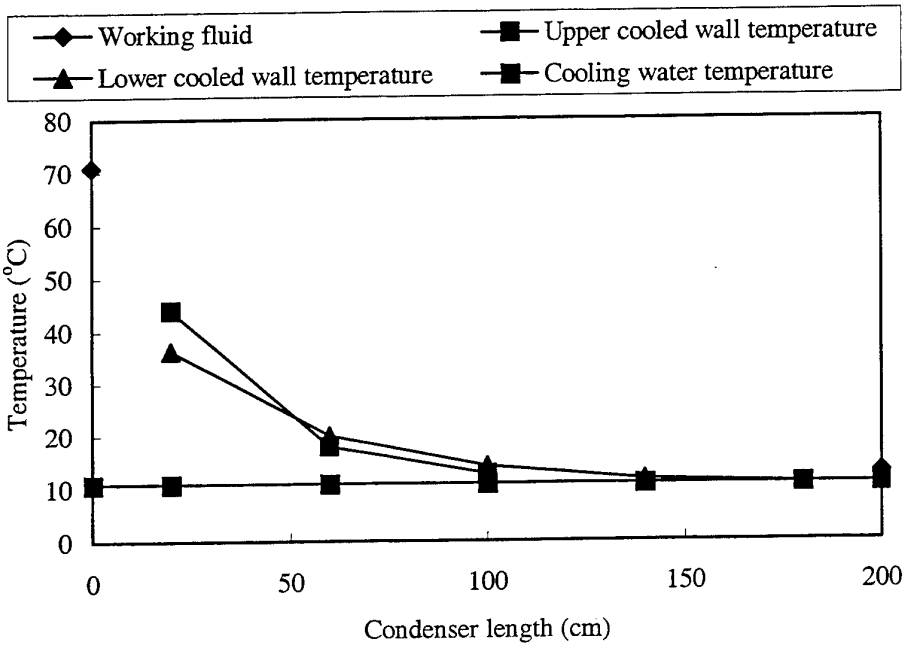


Fig. 4 Temperature distribution along condenser

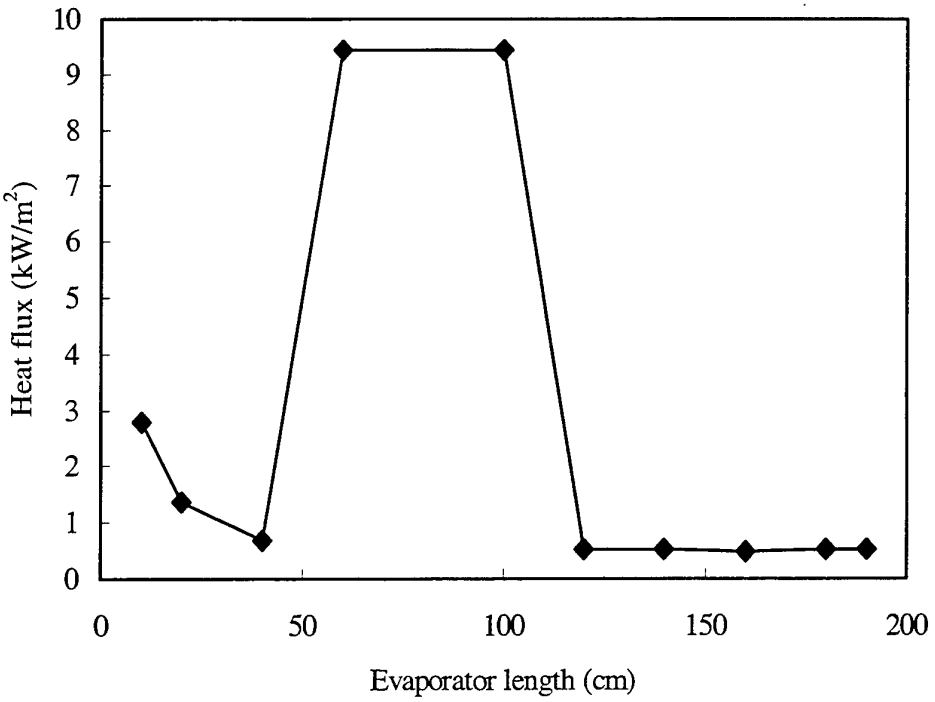


Fig. 5 Heat flux distribution along evaporator

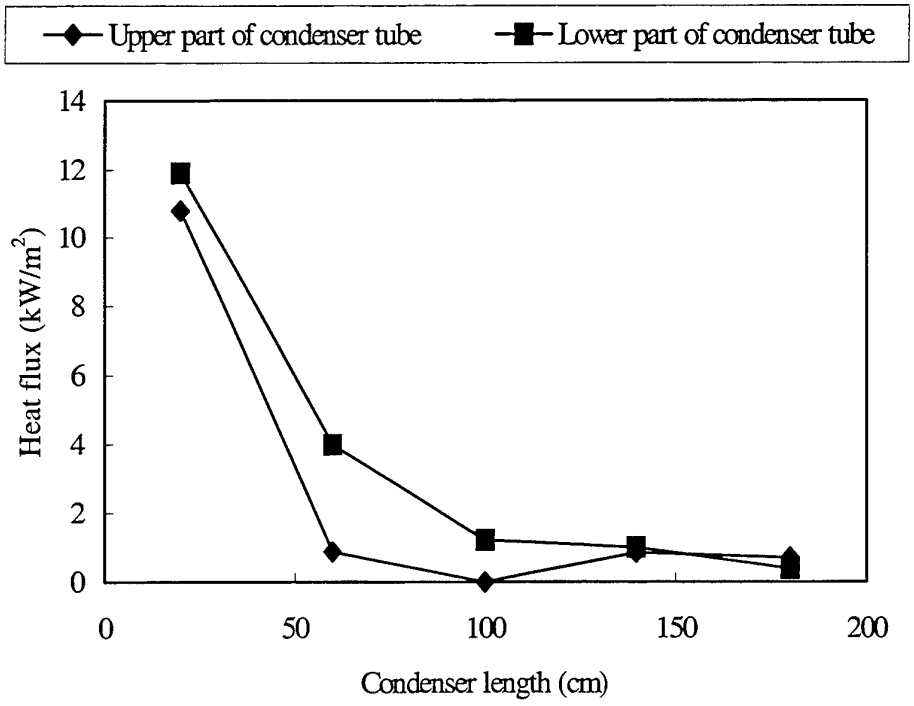


Fig. 6 Heat flux distribution along condenser

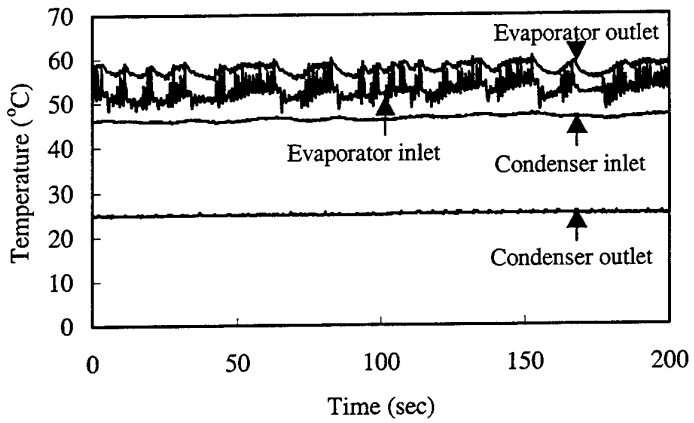


Fig. 7 Transient behavior of temperatures

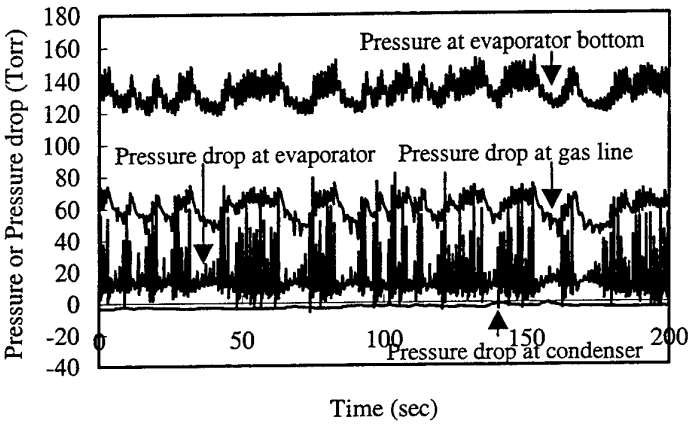


Fig. 8 Transient behavior of pressures

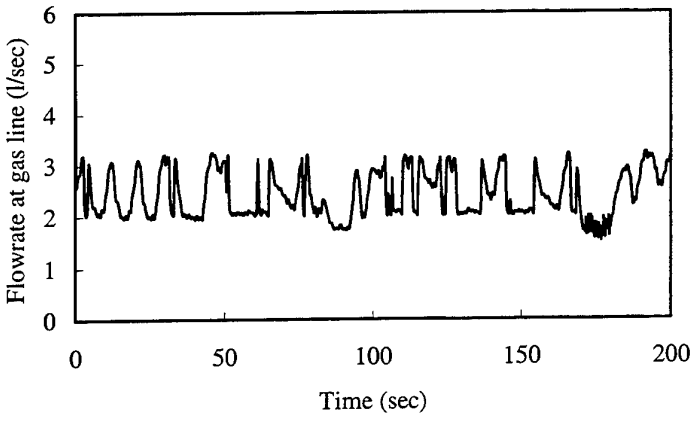


Fig. 9 Transient behavior main flow rate

5. CONCLUSIONS

The purpose of this work is to understand the thermal-hydraulic characteristics of the closed two-phase thermosiphon loop. To do this, experimental apparatus was constructed. From this study, typical temperature and heat flux data were presented and transient temperature, pressure and flow rate data were shown. By transient data, two kinds of instability were observed. It is supposed that high frequency oscillation may be density wave oscillation and low frequency oscillation may be flow excursion.

REFERENCES

1. R. J. Slember, From the Bottom up : Nuclear Technology Evolves for the Future, Part 1 - The Advanced Passive Reactor, Trans. Am. Nucl. Soc. v.61, pp.253 (1990).
2. R. J. Mc Candless, Simplicity : The Key to Improved Safety Performance And Economics, Nucl. Engrg. Int. v.34, pp.423 (1989).
3. K. Hannerz, The PIUS Principle And the Secure Reactor Concepts, Advances in Nuclear Science and Technology v.19, pp.41 (1987).
4. J. A. Boure, A. E. Bergles and L. S. Tong, Review of Two-Phase Flow Instability, Nucl. Eng. Des. v.25, pp.165-192 (1973).
5. M. Ishii, Study of Flow Instabilities in Two-Phase Mixtures, ANL-76-23 (1976)
6. G. Yadigaroglu, Two-Phase Flow Instabilities and Propagation Phenomena, in Thermohydraulics of Two-Phase Systems for Industrial Design and Nuclear Engineering, chap.17, Hemisphere, Washington, DC (1981)
7. R. T. Lahey, Jr. and M. Z. Podowski, On the Analysis of Various Instabilities in Two-Phase Flows, in Multiphase Science and Technology, v.4, chap.3, Hemisphere, Washington, DC (1989)

HEAT TRANSFER PERFORMANCE OF A CORRUGATE TUBE THERMOSYPHON

Masaso Hirashima
Department of Environmental Energy System, Oriental Kiden CO., LTD
4-12-8,Minami-Sennba,chyuo-Kku,Osaka,542-0081,JAPAN
Fax : (06)- 6872 - 1188

Emeritus. Kanji Negishi
Tokyo Metropolitan Institute of Technology
6-6,Asahigaoka,Hino-Shi,Tokyo,191-0065
Fax : (0721)-28- 4919

Keywords: heat pipe, thermosyphon, corrugate tube, heat transfer, evaporator, condenser

ABSTRACT. The two phase closed thermosyphon are highly efficient heat transfer element. At present,however,actual applications are mostly limited for thermosyphon using smooth tube as its container. In the present work, a corrugate tube was used as its container and distilled was used as the working fluid. The corrugated container is flexible and it has several features to allow the thermosyphon to be used in a wide range of application. In the first step of our study , the influence of inclination angle and fluid charge ratio on the heat transfer performance were studied. A useful formula to calcurate the heat transfer coefficient in the evaporator accounting for the effect of the liquid charge and inclination angle has been derived. In the second step, the condensation heat transfer coefficient is proposed as a function of the modified Nusselt theory by three parameters: the Lockhart-Martinelli parameter, inclination angle of the thermosyphon and fill ratio of the working fluid.

1. INTRODUCTION

A two phase closed thermosyphon is refereed to as an "gwickless heat pipe" which utilizes gravitation as a driving force for returning the fluid to the evaporator. Similar to a heat pipe equipped with a wick, the thermosyphon utilize the heat-transfer based on the latent heat of the working fluid from its evaporator to condenser. Therefor a thermosyphon can transport a large quantity of heat at a small temperature difference between its high and low temperature zones. In addition to this, the tbermosyphon compared to a wick-type heat pipe is featured by its simple structure, ease of manufacture, low cost and small thermal resistance. As presented in detail in [1], the two- phase closed thermosyphon has found wide possible application, which extends from a simple heat transporting element to a large waste heat recovery equipment in the industrial factories. Therefore, its further research and development are of current interest.

The research on the two-phase closed thermosyphon dates back to when Cohen and Bayley [2] conducted a basic study for its use in the cooling gas turbine blades and followed by many scholar in the world. In Japan, Imura et al. [3] studied a two phase closed thermosyphon and established an empirical formulas for the heat-transfer coefficients in the evaporation and condensation sections, although the formulas can only be applied to the case where it is smooth tube and installed vertically. The present research covers a study of a tow-phase closed thermosyphon using a corrugated tube. Generally the heat-transfer characteristics of a thermosyphon are closely related to the flow behavior of the working fluid in its container. This means that the use of a corrugated tube will affects the heat-transfer characteristics. Therefore the heat transfer coefficient formula developed for smooth tube thermosyphon can not be applied to that of the corrugated tube thermosyphon in its present form. This paper describes the characteristics of its heat transfer-performance.

2. EXPERIMENTAL APPARATUS AND METHOD

A schematic of the experimental apparatus used in this investigation is shown in Fig 1. The thermosyphon ① is made of a copper corrugated tube of 1310 mm long(average diameter,24.4mm, wave height,1.8mm, pitch, 5.6mm, wall thickness, 0.5mm). The lower half of the thermosyphon, 510mm in long, constitutes the evaporator, while its upper half of 510mrn long, constitutes a condenser.

The evaporator is made up of three sections, each consisting of a 170mm sheathed heater ②, which are connected in parallel to the electric source through regulators .

Condenser has a water jacket ③ to which cooling water , ④ controlled at a given temperature by a chiller, is fed (for its cooling) in three separate parts to make the temperature distribution of the condenser as uniform as possible. Therefore, the heat-transfer rate of the thermosyphone can be calculated on the basis of the water temperature differences between the water jacket outlet and inlet and the water flow is measured by the flow-meter ⑤. The present sturdy was conducted on a thermosyphon system with distilled water used as its working fluid ⑥. The temperature distribution of the syphon was measured by eleven T-type thermocouple ⑦ brazed on the outer surface of the container along its axial direction. The thermosyphon was provided with windows at both ends ⑧ and ⑨

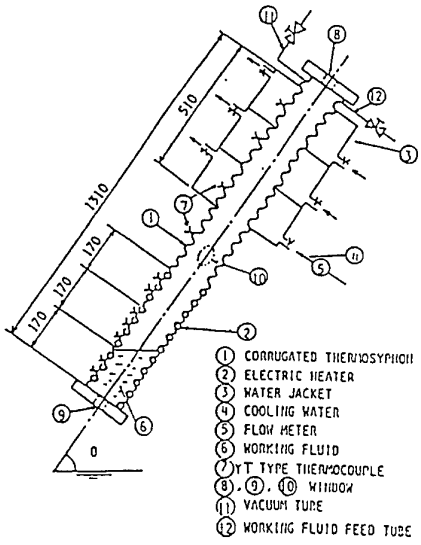


Fig. 1 Experimental apparatus of thermosyphon

3. HEAT TRANSFER RATE

3.1 Influence of Inclination Angle

An example of the change in the heat-transfer rate Q of the closed thermosyphon with regard to its inclination angle is given in Fig. 2, which shows the relationship between the magnitude of Q and the difference between the average temperature of the evaporator $\overline{Te}$ and the average temperature of the condenser $\overline{Tc}$; $(\overline{Te}-\overline{Tc})$. Fig 2 shows the results obtained with the fluid charge ratio (the ratio of the charge of working fluid into thermosyphon to the volume of its evaporator) V^+=40%. The heat-transfer rate of the thermosyphons largest at its inclination angle θ=30deg compared to that at θ= 60deg and 90deg (corresponding to the vertical state)when the comparison is made for the same temperature dfifference.

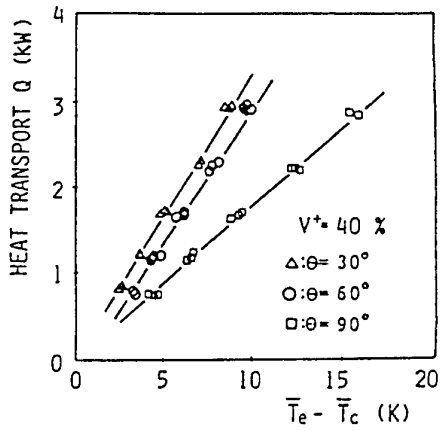


Fig.2 Evaporator-condenser temperature difference and heat transport (V^+ = 40%)

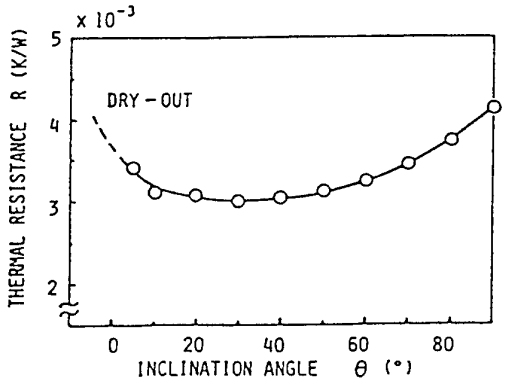


Fig. 3 Thermal registans (V^+ = 40%, Q=2kW)

The fact that the thermosyphon provides the largest heat transfer rate near an inclination angle of 30deg is closely related to the flow pattern of the working fluid stirred by its boiling. Specifically when a fluid pool is boiling ,which results in a sharp expansion of the boiling bubbles produced in the pool, the liquid above the

bubbles is blown up into the condenser and the liquid can reach the deepest portion of the condenser if the thermosyphon is inclined at an angle of approximately 30deg. The phenomena mentioned above can be represented by one of the characteristic values of a heat pipe, the thermal resistance [1] R=(Te-Tc)/Q, which is illustrated in Fig.3. This graph shows that the thermal resistance becomes lowest at an inclination angle of about 30deg suggesting that this inclination angle provides the highest heat-transport performance.

3.2 Influence of Fluid Charge

In a corrugated tube thermosyphon , compared to a smooth tube, a large amount of fluid collect in the concave portions of the tube walls in the condensing and adiabatic sections. This results in a shortage of fluid in the evaporator, as confirmed by the observation through the windows ⑧ and ⑨. The observation of fluid behavior in the thermosyphon reveals that the cyclic washing out of the condenser by the fluid blown up due to boiling is effective in activating the condensation, but its constant stagnancy in the condenser wall has an adverse effect on the heat transfer performance. Fig.4 shows the thermal resistance as a function of the fluid charge at the optimum inclination angle θ=30deg. It indicates the existence of the minimum thermal-resistance, namely, the optimum fluid charge in the vicinity of V^+ = 40 percent.

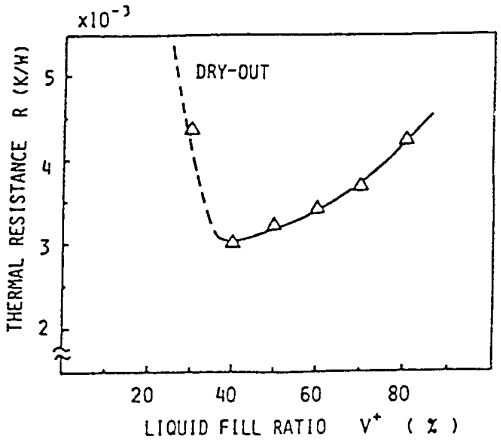


Fig. 4 Thermal registans (θ=30°, Q=2kW)

4. EVAPORATION HEAT TRANSFER COEFFICIENT

The heat transport of a corrugated tube thermosyphon studied in the present investigation, can be expressed by the following.

$$Q = h_e A_e (T_e \sim T_v) \tag{1}$$

where h_e is heat transfer coefficient at the evaporator, A_e is heat transfer area of the evaporator (larger than the area of the inner surface of a cylinder, having the same diameter by 37 percent due to the wavy shape of the inner surface), T_e is the average temperature of the evaporator and T_v is vapor temperature. The major purpose of the present study was to obtain a correction for the evaporation heat-transfer coefficient he defined by Eq.(1). To achieve this, the results of the present experiment are first compared with the results obtained by Imura et al [3] for a smooth-tube thermosyphon installed in a vertical position. They presented the following relation for the evaporation heat -transfer coefficient

$$h_e = 0.32 \frac{\rho_l^{0.65} \lambda_l^{0.3} C_{pl}^{0.7} g^{0.2} q_h^{0.4}}{\rho_g^{0.25} L^{0.4} \mu_l^{0.1}} \left(\frac{P_{in}}{P_a} \right)^{0.3} \tag{2}$$

Fig.5 shows a comparison between the results of the present measurements and Eq.(2) established by Imura et al. It shows that, if the thermosyphon is installed in a vertical position (θ=90deg) and is used at a large fluid charge ratio of V^+=80 percent the evaporation heat-transfer coefficient lies close to the Eq (2).

However, it is difficult to apply the measurements inclined to the case at the optimum inclination angle of 30deg or at the optimum fluid charge ratio of V^+=40percent. Fig 5 also reveals that, in the left-side zone of the figure where the heat flux is small, the heat-transfer coefficient of a corrugated-tube thermosyphon is larger than that of smooth-tube thermosyphon. In the present study, a new correlation was derived for the heat-transfer coefficient, accounting for the effects of the inclination angle and fluid charge ratio, as described below.

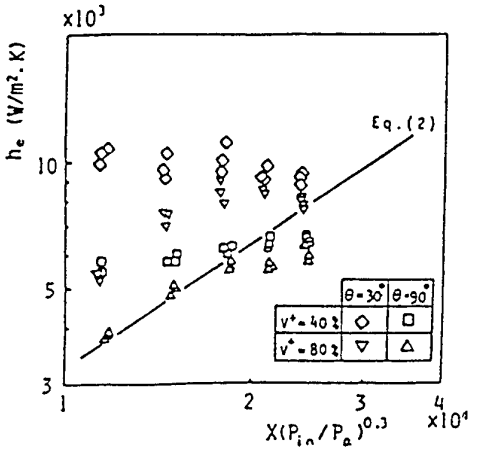


Fig. 5 Heat-transfer coefficient

First, dimensional analysis suggests that the Nusselt number Nu can be represented by the following expression:

$$N_u \propto Re^{*n1}\left(\frac{\rho_v}{\rho_l}\right)^{n2} Pr^{n3}\, Fr^{*n4}\left(\frac{1}{V^+}\right)^{n5} We^{*n6} \tag{3}$$

where the dimensionless numbers are respectively represented by the following.

$$Nu \equiv \frac{h_e \alpha}{\lambda_l}, Re^* \equiv \frac{q_h \rho_l \alpha}{L \rho_u \mu_l}, Pr \equiv \frac{\mu_l C_{pl}}{\lambda_l}$$

$$Fr^* \equiv \frac{q_h}{L\rho_u \sqrt{g\alpha}}, We^* \equiv \frac{q_h}{L\rho_u}\sqrt{\frac{\rho_u \alpha}{\sigma}}$$

The dimensionless numbers marked by * are dimensionless numbers defined with an equivalent vapor velocity [4] (q h /L ρ v). The values of indexes nl to n6 in Eq. (3) were obtained by applying the least squares method to the experimental data. Then, the Nusselt number was finally expressed as Eq.(4).

$$Nu \propto Re^{*1.1}\left(\frac{\rho_u}{\rho_l}\right)^{0.7} Pr^{1.5}\, Fr^{*-0.4}\left(\frac{1}{V^+}\right)^{0.5} We^{*-0.6} \tag{4}$$

for $3 \times 10^3 < Re^* < 4 \times 10^4$, $0.1 < Fr^* < 1$, $10^{-2} < We^* < 10^{-1}$

Rewriting this with respect to heat transfer coefficient he yields the following expression:

$$h_e = \psi X' \tag{5}$$

where

$$\psi = 6.40 \times 10^{-2} (\sin\theta)^{-0.52} \tag{6}$$

$$X' = \frac{q_h^{0.1} \rho_l^{0.4} \rho_v^{0.3} \mu_l^{0.4} C_{pl}^{1.5} \sigma^{0.3} g^{0.2}}{V^{+0.5} L^{0.1} \lambda_l^{0.5}} \tag{7}$$

for $4 \times 10^4 < X' < 2 \times 10^5$

In Fig. 6, the heat-transfer coefficient he is plotted against the parameter X defined by Eq. (7). It is observed in the figure that the experimental data lies close to each parallel line as shown in Fig.6 which correspond to those for different inclination angle θ.

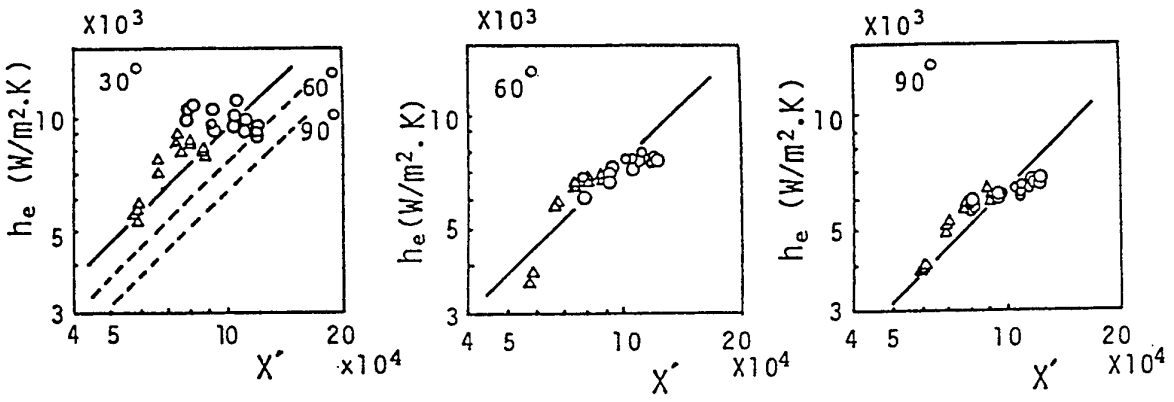


Fig. 6 Heat-transfer coefficient (O: V^+=40%; Δ:V^+=80%)

It should be noted that the inclination angle θ is included in the coefficient ψ as a function of (sin θ)given by Eq (6). This is shown in Fig.7.

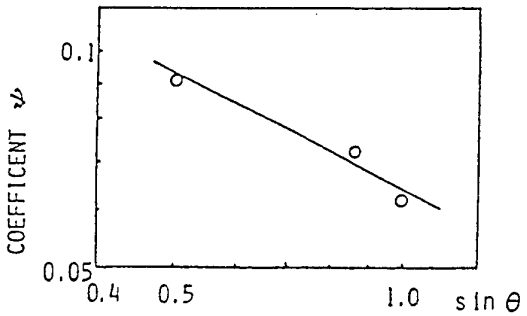


Fig. 7 Coefficient ψ

5. HEAT TRANSFER RATE IN THE CONDENSER

5.1 Comparison With Nusselt Theory

The results of the present experiment, in which the condensation heat-transfer coefficients obtained were compared to that of Nusselt theory. It should be noted that the condensation heat-transfer coefficient is defined as Eq (8)

$$h_c = \frac{Q}{A_c(T_v - \overline{T}_c} \tag{8}$$

where, the heat-transfer surface of the condenser is approximately 37 percent increased compare with that of the straight cylinder as in the case of evapoirator . The vapor temperature is represented by the adiabatic section temperature, as it is often done in the analysis of heat pipe [5,6].

Then the condensation heat-transfer coefficient defined as described above is compared with Nusselts film condensation heat-transfer coefficient expressed by the following equation with the influence of the thermosyphon inclination taken into consideration:

$$h_c = 0.925\left(\frac{\lambda_l^3 \rho l^2 Lg \sin\theta}{q_c \mu_l l_c}\right)^{1/3} \tag{9}$$

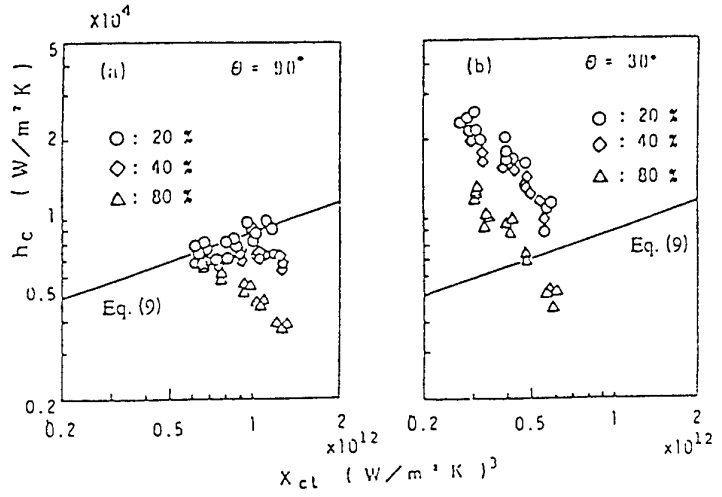


Fig. 8 Comparison of condensation heat-transfer coefficient to Nusselt Theory

Fig.8 (a)-(b)shows the comparisons between the result of the present experiment and Eq.(9). Fig.8 (a) shows the comparison for the vertical state-thermosyphon with the fluid charge ratio at different levels, while Fig.8 (b)shows the case at an angle of 30deg. The experimental values include those well represented by Eq.(9) and those showing a tendency quite opposite to the equation. These affect are discussed in following Sect 5.2.

5.2 Derivation of a Practical Formula for Condensation Heat-Transfer Coefficient

The fact in Sect 5.1 suggest that the condensation heat- transfer coefficient in the thermosyphon is influenced by the following three factors which is not included in the Nusselt film condensation.

(1) Vapor-liquid two phase flow [Lockhart -Martinelli Parameter]
(2) Inclination angle
(3) Working fluid charge ratio

In the present research, therefore, we studied the condensation heat-transfer coefficient from a new perspective by incorporating the effect of the above three points as described below.

5.2.1 Coefficient of vapor flow The effect of the vapor flow is available through the Lockhart-Martinelli parameter [7], which is used in discussing shear stress produced at the interface of vapor-liquid two phase flow in the high quality region, and is represented by the following equation:

$$X_u = \left(\frac{1-x}{x}\right)^{0.9}\left(\frac{\rho_v}{\rho_l}\right)^{0.5}\left(\frac{\mu_l}{\mu_v}\right)^{0.1} \tag{10}$$

The flow pattern in the condenser is an annular two-phase flow, which justifies the incorporation of the above parameter into the heat-transfer coefficient. The quality is considered to be x=0.5, because the thermosyphon condenser maintains an equilibrium between its vapor and liquid mass flows over its cross section at any point. Accordingly the Lockhart-Martinneli parameter for the present research can be represented by the following expression.

$$X_u = \left(\frac{\rho_v}{\rho_l}\right)^{0.5}\left(\frac{\mu_l}{\mu_v}\right)^{0.1} \tag{11}$$

5.2.2 Effect of the inclination angle The influence of the inclination angle on the condensation heat-transfer coefficient can be typically represented by Fig. 9 which assumes a maximum value in the vicinity of inclination angl θ=30deg-i.e sin θ=0.5. Accordingly, the experimental data were represented by a quadratic least-squares curves as indicated by the solid line in Fig 9. Thus, specifying the inclination angle which gives maximum condensation heat-transfer coefficient as θ_{opt},the inclination angle effect can be represented by the following Eq (12).

$$A_{eff}(\theta) = -1.46(\sin\theta = \sin\theta_{opt})^2 + 1.0 \qquad (12)$$

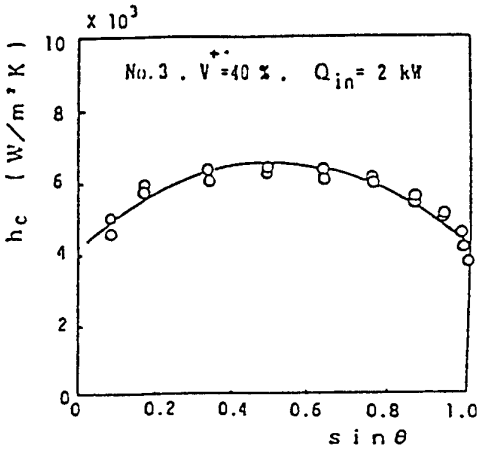


Fig. 9 Change in condensation heat-transfer coefficient by fluid charge ratio

5.2.3 Effect of the working fluid charge ratio The influence of the working-fluid charge ratio on the heat-transfer coefficient can be typically represented by Fig 10,which indicates that the heat transfer coefficient tend to decreases in the region where fluid charge ratio is larger than a certain value (approx. 0.3), and stays at a constant level when it is below this value. Accordingly, the experimental data were processed by making the portions of linear and quadratic equations continuous at their maximum values. Thus, specifying the fluid charge ratio at the point,where the quadratic equation and the linear line are joined as V^+_{opt} (V^+_{opt} obtained in the pre present research is 0.322). Then the effect of the fluid charge ratio can be represented as follows.

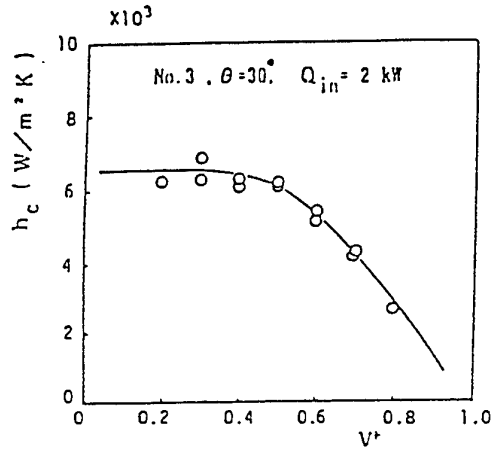


Fig. 10 Change in condensation heat-transfer coefficient by inclination angle

$$V_{eff}(V^+) = -2.38(V^+ - V^+_{opt})^2 + 1.0 \qquad (V^+ \geq V^+_{opt}) \qquad (13)$$

$$V_{eff}(V^+) = 1.0 \qquad (V^+ < V^+_{opt})$$

5.2.4. Correlation with Lockhart-Martinelli parameter According to the above proceeding, dimensionless number of the condensation heat-transfer coefficient which incorporate these two coefficients Aeff, Veff: can be represented as follows.

$$\left.\begin{aligned} &\frac{h_e}{X_e^{1/3} A_{eff} V_{eff}} \\ &X_e = \frac{\lambda_l^3 \rho_l^2 Lg}{q_e \mu_l l_c} \end{aligned}\right\} \qquad (14)$$

Thus, the relationship between this dimensionless number and the Lockhart-Martinelli parameter X_{tt} was determined and shown in Fig. 11.

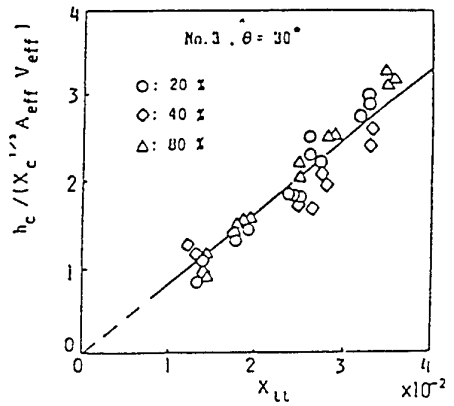


Fig.11 Correlation between condensation heat-transfer coefficient and Lockhart-Martinelli Parameter

5.2.5 Final equation for the condensation heat-transfer coefficient The results of the present research allow the condensation heat transfer coefficinet of a conrrugated tube thermosyphon to be processed into the following expression:

$$h_e = 82.4 X_c' \tag{15}$$

where

$$X_c' = \left(\frac{\lambda_l^3 \rho_l^2 Lg}{q_c \mu_l l_c}\right)^{1/3} \left(-1.46(\sin\theta - \sin\theta_{opt})2 + 1.0\right) \times \left(-2.38(V^+ - V^+_{opt})^2 + 1.0\right) \left(\frac{\rho_v}{\rho_l}\right)^{0.5} \left(\frac{\mu_l}{\mu_v}\right)^{0.1} \qquad (V^+ \geq V^+_{opt})$$

$$X_c' = \left(\frac{\lambda_l^3 \lambda_l^2 Lg}{q_c \mu_l l_c}\right)^{1/3} \left(-1.46(\sin\theta - \sin\theta_{opt})^2 + 1.0\right) \times \left(\frac{\rho_v}{\rho_l}\right)^{0.5} \left(\frac{\mu_l}{\mu_v}\right)^{0.1} \qquad (V^+ < V^+_{opt})$$

Then,a comparison between experimental values for the condensation heat-transfer coefficient and the value given by Eq.(15) is shown in Fig. 12 (a) to (c). The figures shows that the Eq.(15) provides for proper processing of the experimental values.

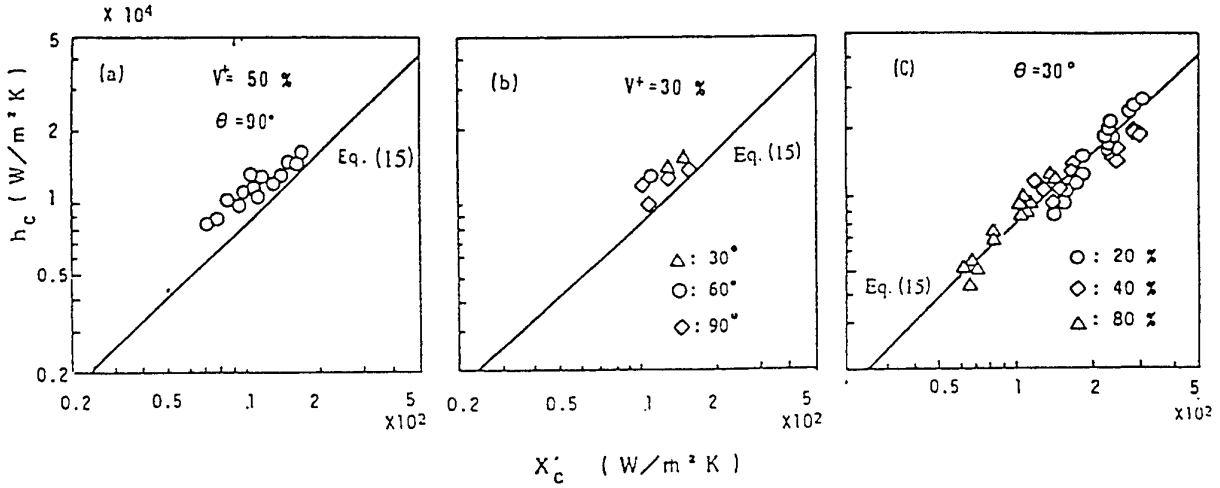


Fig. 12 Arrangement of condensation heat-transfer coefficient by Eq. (15)

6. CONCLUSION

The results obtained in the present study ,using a corrugated-tube as its container and distilled water as its working fluid, can be summerized as follows.

1. The highest heat-transfer performans can be attained when the fluid charge ratio is 40percent (of evaporator volume) and 30 deg of inclination angle(of thermosyphon)
2. A corrugated tube thermosyphon container, compared to its smooth tube ,provide a much higher evaporation heat transfer coefficient when operated at a low heat flux.
3. The evaporator heat transfer coefficient accounting for the effects of the liquid charge ratio and inclination angle is expressed by Eq (5).
4. The condensation heat transfer coefficient of the thermosyphon were successfully represented by Eq.(15). This equation was derived by modifying the Nusselt theory of condensation by the Lockhart-Martinnelli parameter in order to take into account the influence of the vapor flow on the condensing surface.
5. The coefficient on the inclination angle and the fluid charge ratio were successfully determined by processing the experimental data by the method of least square to represent them in terms of a quadratic equation and a coconbination of linear and quadratic equation,respectively.

NOMENCLATURE

A : heating area [m2]
Aeff: Coefficient on inclination angle
a : characteristic value of corrugated tube [m]
Cp : specific heat [J/(kg-K)]
Fr : Froude number
g : acceleration by gravity [m/s^2]
h : heat transfer coefficient [$W/(m^2-K)$]
L : latent heat [kJ/kg]
l : length [m]
Nu : NusseIt Number
n : index[Eq.(3)]
Pa : atmospheric pressure[Pa]
Pr : Prandtl number
Q : Heat transfer[W]
q_h : Fheat flux [W/m^2]
R : Thermal resistance [K/W]
Re : ReynoIds number
T : Temperature [K]
V^+ : Fluid charge ratio [%]
V_{eff} : coefficient on fluid charge ratio
We : Weber number
X' : parameter formula [Eq.(15)] [(W/m^2-K)]
Xc : parameter [Eq.(14)][$(W/m^2-K)]^3$
Xtt : Lockhart Martinelli parameter
x : quality
θ : inclination angle
λ : thermal conductivity [W/(m.K)]
μ : viscosity [Pa-s]
ρ : Density [kg/m^3]
σ : Surface tension [N/m]
ψ : coefficient[Formula(5)]

SUBSCRIPTS
E : Evaporator
l : liquid
v, g : vapor
a : adiabatic section
c : condensing section
opt : optimum value

REFERENCES

1. K.Negishi, K.Oshima ,and T,Ito,Practical Heat Pipe,Japan Association of Heat Pipes,Published by Nikkann Kogyo Shinbnsya ,(1985).
2. H.Cohen,and F. J.Bayley,Proc. Inst. Mech Eng, 169 (1955).
3. Imura,Kusuda,Ogata, Miyazaki, Sakamoto,Trans, JSME(in Japanese), 45 (393) ,B ,712,(1979).
4. Katto, Introduction to Heat Transfer, 315, published by Yookendo(1980).
5. Oshima, measurement and Control (in Japanese), 14(9),22(1975).
6. Yamamoto and Tanaka, Trans, JSME(in Japanese),53(490), B, 1840-1845 (1987).
7. Ueda,Gas-Liquid two phase flow, Published by Yookendo,260,(1981).

MINIATURE HIGH HEAT FLUX HEAT PIPES FOR COOLING OF ELECTRONICS

Z. J. Zuo and M. T. North
Thermacore, Inc.
780 Eden Road
Lancaster, PA 17601, USA
Email: zjz@thermacore.com; Fax: (717) 569-4797

Keywords: miniature heat pipe, high heat flux cooling, pulsating heat pipe, graded wick structure

ABSTRACT. This paper discusses two advanced heat pipe mechanisms that have the potential of achieving heat flux capabilities over 300W/cm^2. The mechanisms include Combined Pulsating and Capillary Transport (CPCT) and Graded Wick Transport (GWT) mechanisms. Theoretical models were developed to predict the performance of the advanced heat pipe mechanisms. Prototype heat pipes were tested to verify the heat flux capability of the mechanisms and the accuracy of the theoretical models. The advanced heat pipe mechanisms are feasible approaches to removing increasing heat dissipation densities in electronic equipment.

INTRODUCTION

Computer, telecommunications, and consumer and military electronics industries are reporting board-level heat dissipation that a couple years ago was seen only at the system level [1]. This problem is further compounded by the miniaturization of electronics. The result is increasing heat fluxes in electronics. New generation microprocessors such as Intel Pentium II and Digital Alpha AV6 generate heat fluxes from 15 to 20W/cm^2. Hewlett Packard chip packages generate heat fluxes of 80W/cm^2. Intel projects a heat flux level of 100W/cm^2 for its next generation chips [2]. Metal oxide semiconductor-controlled thyristors generate heat fluxes from 100 to 200W/cm^2 [3]. High voltage power electronics may generate heat fluxes of 300W/cm^2 [4]. Some laser diode applications require removal of 500W/cm^2 [5]. Metal extrusion heat sinks rely on heat conduction to spread heat and become inadequate at these high heat fluxes. Accordingly, more effective cooling approaches are needed.

Heat pipe cooling of electronics is becoming increasingly popular because of its advantages over extrusion heat sinks. Compared to extrusion heat sinks that rely on heat conduction to extend heat dissipation surfaces, a heat pipe cooler uses highly effective evaporation and condensation cycles to extend surface areas. In addition, heat pipes provide more packaging flexibility than extrusion heat sinks. Compared to other cooling techniques, such as forced single and two-phase flow cooling and direct immersion cooling, heat pipe cooling does not require mechanical pumps, valves or consume any power and consequently is quieter and more reliable.

The heat flux capability of a heat pipe is determined by what is normally called the boiling limit in the heat pipe evaporator. Axial grooves, mesh screens and sintered powder wicks are commonly used wicking structures, providing capillary pumping to return liquid to the evaporator. The evaporator wick also serves as extended surfaces for evaporation or boiling heat transfer enhancement. Previous studies reported that flat miniature heat pipes with axial grooves were capable of sustaining heat fluxes on the order of 40W/cm^2 [6, 7]. Heat pipes with sintered powder wicks can tolerate concentrated heat fluxes of up to 80W/cm^2 [8] without any sign of evaporator dry out. A common feature of these wicks is that they serve two functions: liquid return channels and heat transfer surfaces. At high heat fluxes, boiling occurs inside the wick and the resulting intensive liquid-vapor interactions could impede the returning liquid flow, leading to evaporator dry-out.

An alternative wick design, the inverted meniscus scheme, has been proposed and studied by many researchers [7, 9, 10, 11, 12]. The inverted meniscus design reduces the disruption to the returning liquid flow caused by boiling inside the wick. By doing so, the heat pipe's heat flux capability can be improved to 200W/cm^2 [13]. However, inverted meniscus heat pipes exhibit thermal resistances that are several times higher than those of conventional heat pipes, due to the poor thermal contact between the grooves and the porous plate. At high heat fluxes, a vapor blanket appears inside the wick adjacent to the heated groove surface, which not only causes large vapor pressure drop but also large ΔT across the vapor blanket. Khrustalev and Faghri [13] tested a flat miniature heat pipe with inverted meniscus wicks and found the evaporator thermal resistance to be 1°C-cm^2/W at 200W/cm^2.

Another evaporator enhancement technique is using internal solid posts (covered by porous wick layers) to extend

evaporating surfaces. Rosenfeld et al. [14] demonstrated 200W/cm^2 heat flux capability with a copper/water heat pipe with internal copper posts in the evaporator (each post was fed with liquid through a cable artery). The evaporator thermal resistance was measured at approximately 0.1°C-cm^2/W at 200W/cm^2.

Above discussions indicate that the best performing high heat flux evaporator design is the wick-covered internal post design. This is still far below the 300 to 500W/cm^2 heat dissipation characteristics of high power electronics and laser diodes. Therefore, more advanced fluid transport and heat transfer mechanisms will be required to meet the electronics industry's continuous demands for higher heat flux capability and lower junction temperature.

CPCT MECHANISM – THEORETICAL MODELING AND PROTOTYPE TESTING

Operating Principles of CPCT Mechanism

Figure 1 illustrates a thermally driven pulsating flow in an interconnected flow channel that forms a closed, serpentine loop. The channel is filled with a saturated liquid-vapor mixture. The channel's cross-sectional diameter is sufficiently small to allow the formation of liquid and vapor slugs by surface tension. As heating and cooling are applied to the two ends, vapor is generated in the heating section and condenses into liquid in the cooling section. The volume expansion due to the vaporization and contraction due to the condensation cause an oscillating motion of the fluid that sends vapor to the condenser and returns liquid to the evaporator. The oscillatory motion of the liquid and vapor slugs is self sustaining as long as the heating and cooling conditions are maintained.

Akachi [15] first used the thermally driven pulsating flow mechanism in heat pipes. The main advantages of a pulsating heat pipe include simple construction and low manufacturing cost. However, there are two shortcomings according to Akachi and Polasek [16]:

(1) Low heat flux capability. The heat flux capability of a pulsating heat pipe made of 2mm diameter copper tubes was 4W/cm^2. This is due to the limited surfaces available for boiling in tubes with smooth walls.
(2) Limited capability of working against gravity. The small flow channel can cause large pressure drop to the pulsating flow and thus limits the heat pipe's heat transport distance.

Figure 2 illustrates a CPCT mechanism that utilizes pulsating fluid motion and capillary pumping effect to supply liquid to high heat flux regions. This design may look similar to an inverted meniscus design but has a different operating principle: The grooves in a CPCT heat pipe serve as channels for the pulsating two-phase flow whereas the grooves in an inverted meniscus heat pipe are pure vapor passages. The sintered powder wicks provide capillary

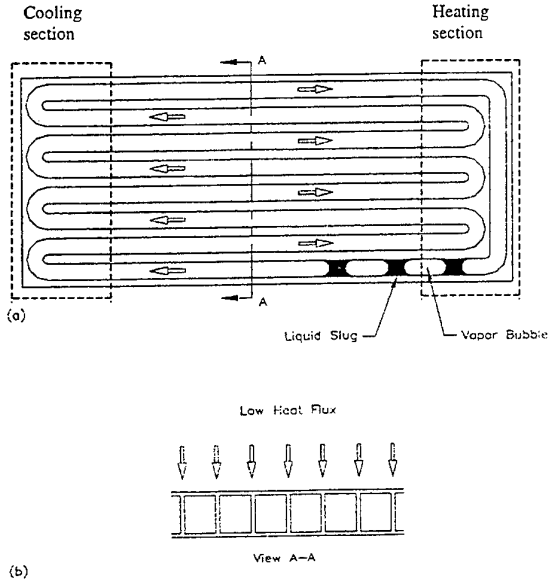


Figure 1. Thermally driven pulsating flow

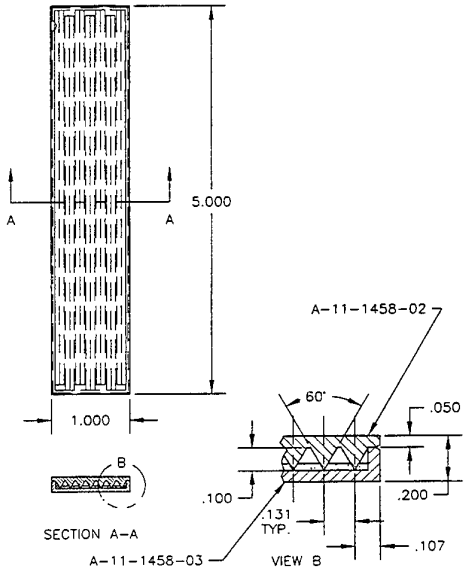


Figure 2. CPCT mechanism

pumping against gravity during startup and uniformly distribute liquid to eliminate hot spots. More importantly, the wicks provide extended surfaces and extra nucleation sites for boiling. The interconnected channel formed by the grooves accommodates the pulsating motion of the fluid that supplies bulk liquid to wet high heat flux regions.

Theoretical Model of CPCT Heat Pipe

The CPCT model consists of two portions: a capillary wick model and a pulsating flow model. The capillary wick model is described by the well-known Laplace-Young equation. The pulsating flow model determines the flow channel dimensions and the pulsating flow dynamics.

The flow channel cross-section hydraulic diameter must satisfy: $d_{groove} \leq 2\sqrt{\sigma/\rho_l g}$, which was established by Akachi and Polasek [16]. This equation provides an upper limit for the channel diameter. The channel design should also consider the dynamics of the pulsating flow. The governing equation of the pulsating flow has been derived as:

$$\frac{d^2x}{dt^2}+\left(\frac{8\mu_l P\phi_0}{\rho_l DA}\right)\frac{dx}{dt}+\frac{2A^2RT_{sat}}{(LA\rho_l\phi_0)[(L/2)A\rho_l(1-\phi_0)/\rho_v]^2}\left[(L/2)A\rho_l(1-\phi_0)+\frac{Q_e}{h_{fg}}t\right]x=0 \qquad (1)$$

where x, P, D, A, L, ϕ_0, R, T_{sat}, and Q_e are the working fluid displacement, the flow channel cross-sectional perimeter, diameter and area, the axial channel length, the gas constant of the vapor, and the heat pipe operating temperature and heat transfer rate, respectively.

Equation (1) is quite similar to the governing equation for mechanical vibrations with viscous damping, except for the last term that is not only a function of x but also a function of t. There is no closed-form analytical solution to Equation (2). Figure 3 shows the working fluid oscillation that was numerically solved using *MathCAD* based on the following conditions:

- Operating temperature $T_{sat} = 100°C$.
- Heat input $Q_e = 30$ W.
- Channel length $L = 5.25''$.
- Channel diameter $D = 2$ mm.
- Fluid fill ratio $\phi_0 = 0.73, 0.75, 0.80$.

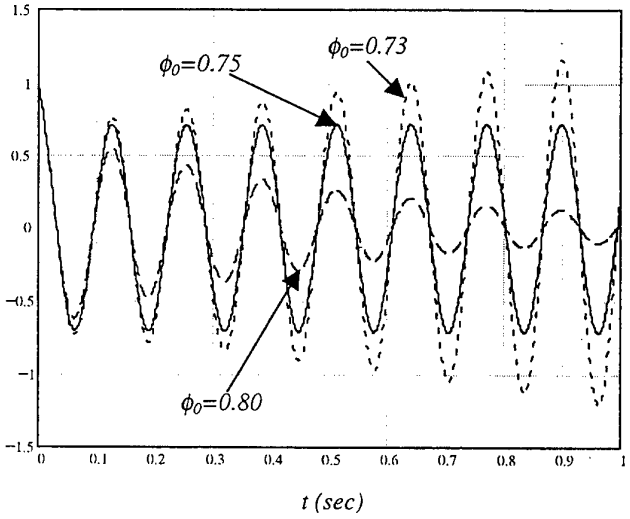


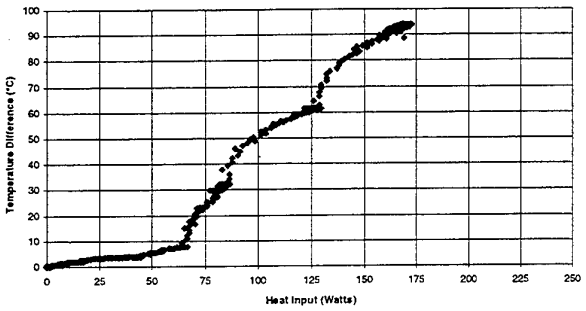
Figure 3. Fluid oscillation in a pulsating heat pipe

The x_{max} in Figure 3 is the fluid displacement due to initial disturbances (which can come from unstable boiling or heat input fluctuations). It was found that, with the given geometric and thermal conditions, the amplitude-to-displacement ratio (x_0/x_{max}) is always around 0.75, regardless of the magnitude of the initial disturbance (x_{max}).

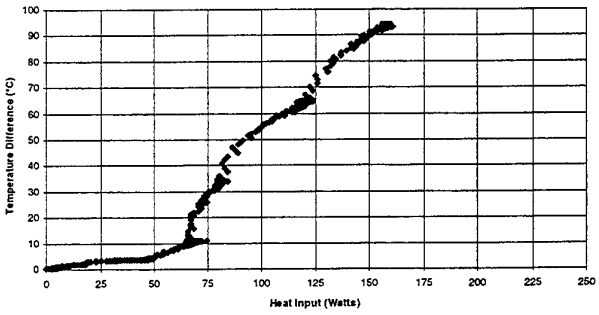
As shown in Figure 3, the fluid oscillation is sensitive to the fluid fill ratio. The oscillation gets amplified if the heat pipe is under-charged. This is due to the smaller damping effect resulting from the less liquid content. If the heat pipe is over-charged, the damping effect will dominate and the working fluid oscillation will die down. With the right amount of working fluid ($\phi_0 = 0.75$ in this case), steady state oscillation and consequently steady state performance is achieved.

CPCT Heat Pipe Test Results

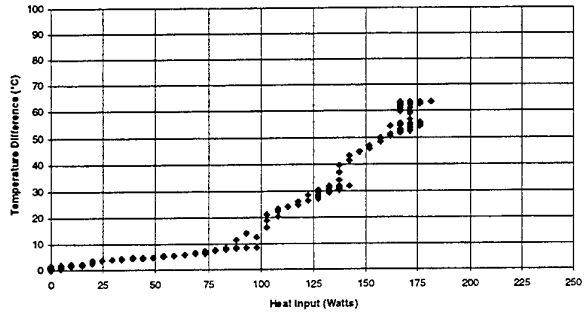
Figure 4 shows the measured thermal performance of CPCT heat pipes with different fill ratios. The heat pipe performance was measured in terms of the wall-to-wall temperature difference of the heat pipe. According to the model (Figure 3), the proper fill ratio is 75%. This is closely matched by the test results as shown in Figure 4.



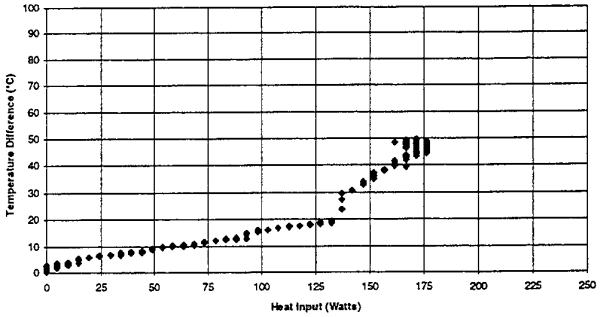
(a) 40% fill ratio



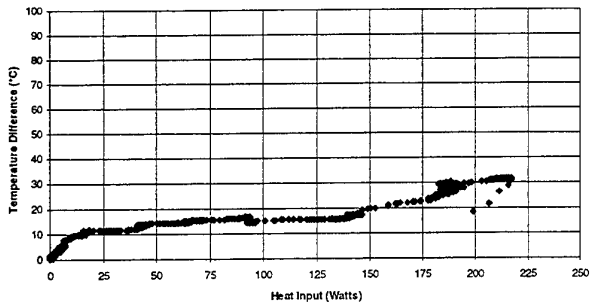
(b) 50% fill ratio



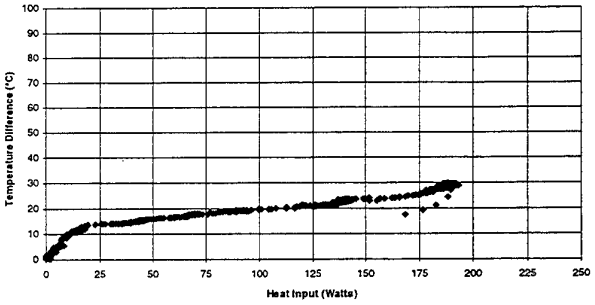
(c) 55% fill ratio



(d) 60% fill ratio



(e) 70% fill ratio



(f) 80% fill ratio

Figure 4. Measured thermal performance of CPCT heat pipes with various fill ratios

GWT MECHANISM – THEORETICAL MODELING AND PROTOTYPE TESTING

Operating Principles of GWT Mechanism

Figure 5 illustrates the GWT mechanism that utilizes fine powder wicks for capillary pumping and coarse powder wicks for liquid transport. Figure 5(a) illustrates that fine powder wicks are used in high heat flux regions and coarse powder wicks cover the rest of the surface. The small pore radius of the fine powder provides large capillary pumping, while the high permeability of the coarse powder reduces liquid flow resistance.

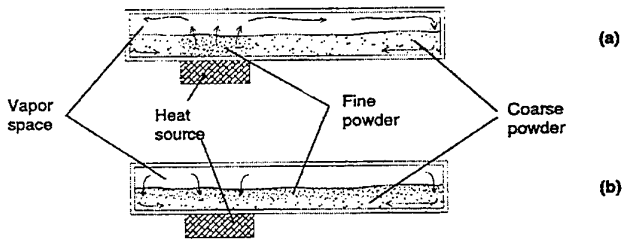


Figure 5. GWT mechanism

Figure 5(b) illustrates a variation of the GWT

mechanism where two wick layers with different pore radius and permeability are used. Fine powders are used in the outer layer and coarse powders are used in the inner layer. The advantage of this design, compared to the design shown in Figure 5(a) is that the heat flux locations are not restricted and fabrication of this type of heat pipes is likely to be easier. But large vapor bubbles growing inside the coarse wick layer may not be able to pass easily into the vapor space through the fine outer layer. Therefore, size combination of the outer and inner wick layers becomes critical for this type of design.

Theoretical Model of GWT Mechanism

In a flat heat pipe, the liquid flow in the graded wick structure is two-dimensional. The two-dimensional GWT model calculates the liquid flow pressure distribution inside the wick structure that is critical to determining the capillary limit. The model is based on two assumptions: (1) the liquid is incompressible; and (2) the liquid is saturated and its properties can be determined based on the vapor temperature. Figure 6 illustrates the coordinates that are used to describe the model.

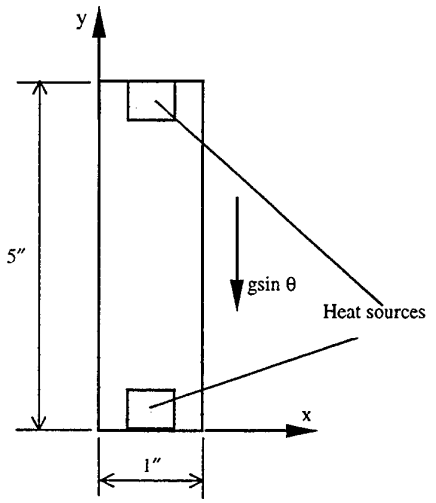


Figure 6. Coordinates of 2D GWT model

The 2D liquid flow in the wick structure can be described by Darcy's law:

$$\frac{\partial u}{\partial x}+\frac{\partial v}{\partial y}=\frac{1}{\rho_l h_{fg}\delta_{wick}}(-q'') \qquad (2)$$

$$-\frac{\partial p}{\partial x}-\frac{\mu_l}{K_{wick}}u=0 \qquad (3)$$

$$-\frac{\partial p}{\partial y}-\frac{\mu_l}{K_{wick}}v+\rho_l g\sin\theta=0 \qquad (4)$$

where q'' is the input heat flux distribution on the flat heat pipe surface. It is positive at the heat input regions, negative at the heat output (cooling) regions, and zero at the insulated regions.

Equations (2) – (4) can be combined into:

$$\frac{\partial^2 p}{\partial x^2}+\frac{\partial^2 p}{\partial y^2}=\frac{\mu_l}{K_{wick}}\frac{1}{\rho_l h_{fg}\delta_{wick}}\left(q''-\frac{Q}{L_x L_y}\right) \qquad (5)$$

where K_{wick} is the wick permeability that changes with location for a graded wick structure. Equation (6) can be solved for the liquid flow pressure distribution in the wick structure. The boundary conditions are: $\left.\frac{\partial p}{\partial y}\right|_{x=0,L_x}=\rho_l g\sin\theta$, $p|_{y=0}=p_v$ and $\left.\frac{\partial p}{\partial x}\right|_{y=L_y}=0$.

Once the liquid pressure (p) is determined, it is compared with the vapor pressure (p_v) to determine whether the capillary limit is reached, using the following criterion:

$$p_v-p \le \frac{2\sigma}{r_{c,wick}} \qquad (6)$$

If Equation (6) is not satisfied, the wick will not be able to provide sufficient capillary pumping force to overcome the liquid flow resistance. Both the liquid flow pressure (p) and the wick properties (K_{wick} and r_{wick}) are two-dimensional functions of locations (x and y). For sintered powder wicks, the permeability (K_{wick}) and the pore radius (r_{wick}) can be related as: $K_{wick} = 0.125 r_c^{2.207}$.

There is no closed-form analytical solution to Equation (5). Numerical methods are required to solve for the liquid pressure distribution. Figure 8 shows the dimensionless liquid pressure distribution within a graded wick structure. The calculations in Figure 8 were based on the following conditions:

- Heat pipe dimensions: 1″×5″×0.2″ (thick).
- Two, 200W/cm^2 heat sources attached to the heat pipe (as shown in Figure 7).
- Fine wicks (pore radius: 2.4×10^{-5} m) in heating regions. Coarse wicks (pore radius: 6.1×10^{-5} m) in non-heating regions.
- Horizontal orientation.

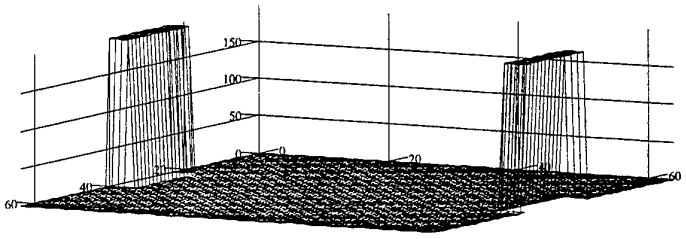


Figure 7. Heat flux distribution

In Figure 8, the dimensionless liquid pressure is defined as:

$$P_0 = \frac{p - p_v}{\frac{2\sigma}{r_{c,wick}}} \qquad (7)$$

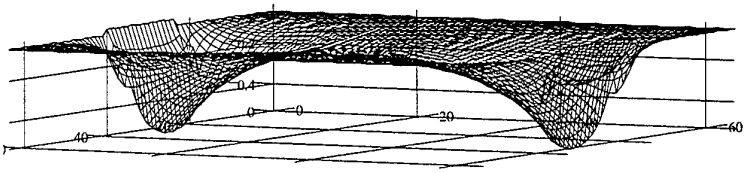
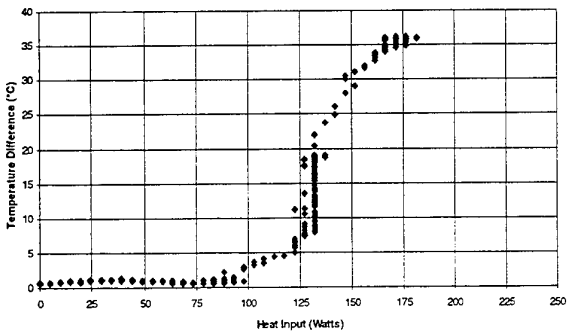


Figure 8. Dimensionless liquid pressure in a graded wick

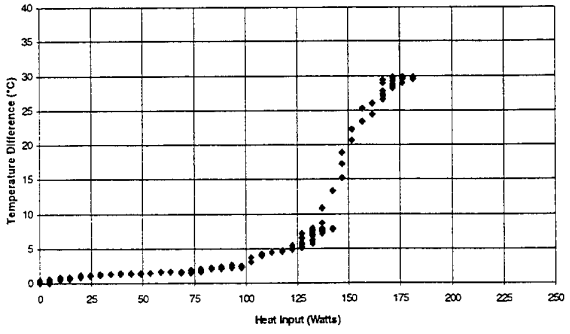
where p, p_v, and $r_{c,wick}$ are the liquid pressure, vapor pressure and wick pore radius, respectively. The wick capillary limit is reached when P_0 is below −1. According to Figure 8, the smallest P_0 is −0.53, indicating that this specific graded wick structure is capable of dissipating the specified heat fluxes without reaching the capillary limitation.

GWT Heat Pipe Test Results

Figure 9 shows the comparison of thermal performance of a conventional and a GWT heat pipe. The conventional heat pipe has a 0.050″ thick uniform powder wick. As shown, this heat pipe has a thermal resistance less than 0.05°C/W/cm^2 for heat fluxes less than 100W/cm^2. At higher heat fluxes, the heat pipe evaporator started to dry out. At around 125W/cm^2, the evaporator was significantly dried out and the temperature difference dramatically increased. At 175W/cm^2, the heat pipe thermal resistance reached 0.2°C/W/cm^2. The GWT heat pipe has a 0.030″ thick coarse powder wick covered by a 0.020″ thick fine powder wick. By using a graded wick structure, the sharp increase in temperature difference as seen in the conventional heat pipe is smoothened. The maximum thermal resistance is also reduced from 0.2°C/W to 0.17°C/W.



(a) Conventional heat pipe



(b) GWT heat pipe

Figure 9. Comparison of conventional and GWT heat pipe performance

CONCLUSIONS

CPCT heat pipes can dissipate 200W/cm^2 without showing signs of evaporator dry-out. Their performance is sensitive to the fluid fill ratio. The theoretical model is capable of accurately predicting the proper fill ratio. GWT heat pipes showed slight improvements over conventional heat pipes with uniform wicks. However, it is believed that with optimization of pore size and wick thickness, GWT heat pipes are capable of dissipating higher heat fluxes.

REFERENCES

1. B. M. Guenin, "Packaging: Designing for Thermal Performance", *Electronics Cooling*, Vol.3, No.2 (1997)
2. "Thermacore Market Survey: Electronics Cooling", Thermacore, Inc. (1998)
3. R. Ponnapan, J. E. Leland, J. E., Beam, G. Fronista, and J. A. Weimer, "Effective Cooling of MCT and IGBT Using Venturi Flow", *Intersociety Energy Conversion Engineering Conference Paper AP-97* (1995)
4. Y. Cao, J. E. Beam, and B. Donovan, "Air-Cooling System for Metal Oxide Semiconductor Controlled Thyristors Employing Miniature Heat Pipes", *J. Thermophysics and Heat Transfer*, Vol.10, No.3 (1996)
5. M. T. North and J. H. Rosenfeld, "Liquid Film Evaporation Cooled Laser Diode Array", *BMDO SBIR Phase II Final Report DASG60-92-C-0093* (1995)
6. D. Plesch, W. Bier, D. Siedel and K. Schubert, "Miniature Heat Pipes for Heat Removal from Microelectronic Circuits", *Micromechanical Sensors, Actuators and Systems*, ASME, New York, DCS-Vol.32 (1991)
7. D. Khrustalev and A. Faghri, "Thermal Characteristics of Conventional and Flat Miniature Axially-Grooved Heat Pipes", *Journal of Heat Transfer*, Vol.117, No.4 (1995)
8. "Therma-Base™ Heat Sink Application Notes", Thermacore, Inc. (1999)
9. R. J. Raiff and P. C. Wayner, "Evaporation from a Porous Flow Control Element on a Porous Heat Source", *International Journal of Heat and Mass Transfer*, Vol.16 (1973)
10. K. T. Feldman and D. L. Noreen, "Design of Heat Pipe Cooled Laser Mirrors with an Inverted Meniscus Evaporator Wick", *Proc. of the AIAA 18th Aerospace Sciences Meeting*, Pasadena, CA, AIAA-80-0148 (1980)
11. S. L. Solovev and S. A. Kovalev, "Heat Transfer and Hydrodynamics in the Inverted Meniscus Evaporator of a Heat Pipe", *Proceedings of the 6th International Heat Pipe Conference*, Grenoble, France, Vol.1 (1987)
12. H. Wulz and E. Embacher, "Capillary Pumped Loops for Space Applications: Experimental and Theoretical Studies on the Performance of Capillary Evaporator Designs", *Proceedings of the AIAA/ASME 5th Joint Thermophysics and Heat Transfer Conference*, Seattle, WA, AIAA-90-1739 (1990)
13. D. Khrustalev and A. Faghri, "Estimation of the Maximum Heat Flux in the Inverted Meniscus Type Evaporator of a Flat Miniature Heat Pipe", *Int. J. Heat and Mass Transfer*, Vol.39, No.9 (1996)
14. J. H. Rosenfeld, N. J. Gernert and M. T. North, "Internally Extended Surface Heat Pipe Evaporators for Micro-electronics Cooling", *Fundamentals of Phase Change: Boiling and Condensation*, ASME HTD-Vol.273, (1994)
15. H. Akachi, "Structure of a Heat Pipe", *U.S. Patent #4,921,041* (1990)
16. H. Akachi and F. Polasek, "Pulsating Heat Pipe: Review of the Present State of the Art", *Technical Report to Industrial Technology Research Institute Energy and Resources Laboratory, Chutung, Taiwan* (1995)

H. Conduction and Radiation

OPTIMIZATION OF THE ANNULAR FIN WITH BASE WALL THERMAL RESISTANCE

B.T.F. Chung
Department of Mechanical Engineering
The University of Akron, Akron, Ohio 44325-3903
Email: bchung@uakron.edu Fax: (330) 972-6027

Zhiwen Ma
Department of Mechanical Engineering
Georgia Institute of Technology, Atlanta, GA
Email: gt3032b@prism.gatech.edu Fax: (404) 685-3053

Keywords: optimal dimensions, annular fin, wall resistance

ABSTRACT. The paper deals with the optimization of the convective annular fins with consideration of the base wall thermal resistance. In practice, the surface temperature at the fin base is usually unknown. The general solution for annular fins of arbitrary profiles with the thermal resistance boundary is obtained analytically in terms of Bessel function. Consequently, the optimum heat transfer rate from the fin and the optimum fin dimensions are computed. The numerical results of the optimum design charts are presented in terms of fin characteristic number, profile number, and overall wall thermal resistance.

1. INTRODUCTION

The design technique of enhancing the performance of a heat conducting body by attaching fins as extended surfaces is well known in industry. Annular or circular fins are one of such heat exchanging devices that are used extensively to increase heat transfer rates, e.g., in compact heat exchangers for the aerospace industry. Since the weight and cost of the fin is an important consideration in the design, the optimum annular fin design has received considerable attention in the past. Brown [1] first investigated the optimum dimensions of annular fins of a rectangular profile. Mikk [2] considered convective circular fin of a triangular profile. Razelos and Imre [3] studied the optimization of annular fins with three profiles. Ullman and Kalman [4] performed optimal analysis for circular fins with four profiles, namely rectangular, triangular, hyperbolic, and parabolic shapes of the circular fins. Recently, Zubair et al. [5] studied the optimum circular fin with a variable profile and a temperature-dependent thermal conductivity. The aforementioned analyses for the optimization of convective fins were based on the assumption of known fin base temperature. However, in practice, the base temperature is not known a priori. It depends on the temperature inside the tube, the heat transfer coefficient between the inner surface of the tube and the flowing fluid, and the contact resistance at the base of the annular fin. The effect of these thermal resistances was taken into account by Aziz [6]. However, his analysis was retricted to the longitudinal fin of two specific profiles. His work was recently extended by Chung et al. [7] to include an arbitrary profile of longitudinal fins. To the best knowledge of the present authors, the wall thermal resistance effect has not been previously considered for the annular or circular fins, which are widely used in compact heat exchangers and nuclear reactors. The purpose of this work is to present a comprehensive study on the optimum dimensions and heat transfer characteristics of convective annular fins by considering convective heat transfer resistance at the inner surface of the pipe, the tube wall resistance and the contact resistance between the primary and extended surfaces. In this work, the temperature distributions and heat transfer from the annular fins of an arbitrary profile are solved analytically. The optimum dimensions and the associated maximum heat transfer are determined numerically using the Golden Search method. The optimum dimensions for both rectangular and hyperbolic optimal annular fins are presented graphically in terms of fin characteristic number and overall thermal resistance.

2. MATHEMATICAL ANALYSIS

The following assumptions are used in the heat transfer analysis:
1. The heat conduction in the fin is steady and one-dimensional.
2. The fin material is homogeneous and isotropic.
3. There is no heat generation inside the fin.

4. The heat transfer coefficient is constant over the surface of the fin, and the heat flow through the fin tip is negligible small.
5. The temperature of the ambient fluid is uniform, and fluid temperature at the tube side of the base wall is constant.
6. Curvature effect of the fin is neglected.
7. No radiation effect is considered.

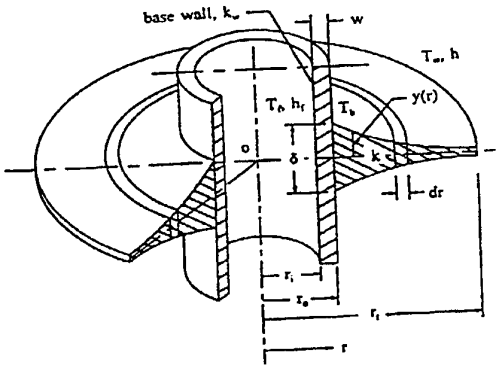


Figure 1. Schematic of annualar fin with an arbitrary

Temperature Profile

Considering an annular fin shown in Fig. 1, the profile function of radius, *y(r),* is expressed as

$$y(r)=\frac{\delta}{2}\left(\frac{r_o}{r}\right)^n \qquad (1)$$

where n is given and is referred to as profile number. The cases n=0 and n=1 represent the popular annular rectangular fin and annular hyperbolic fin respectively. The inside of the tube is supplied with a fluid at constant temperature T_f and convective heat transfer coefficient between the fluid and fin base, h_f is given. From the heat balance, at the steady state the energy equation for an annular fin is

$$\frac{d}{dr}\left[2\pi r\cdot 2y(r)k\frac{dT}{dr}\right]=2\cdot 2\pi r h(T-T_\infty) \qquad r_o\le r<r_t \qquad (2)$$

The boundary condition at the base wall including the wall thermal resistance is

$$k\frac{dT}{dr}=\frac{T_b-T_f}{\frac{1}{h_f r_i}+\frac{\ln(r_o/r_i)}{k_w}+R_{tc}} \qquad @\ r=r_o \qquad (3)$$

where R_{tc} is contact resistance between the primary and extended surfaces and T_b is the base temperature which remains to be determined. The fin tip is assumed to be insulated, i.e.,

$$\frac{dT}{dr}=0 \qquad @\ r=r_t \qquad (4)$$

Substituting the following non-dimensional variable and parameters

$$\gamma=\frac{r}{r_o},\ N_a^2=\frac{2hr_o^2}{k\delta},\ \rho=\frac{r_t}{r_o} \qquad (5)$$

into Eqs. (2)-(4), a non-dimensional differential equation is obtained

$$\frac{d}{d\gamma}\left[\gamma^{1-n}\frac{d\theta}{d\gamma}\right]=N_a^2\gamma\theta \qquad 1<\gamma<\rho \qquad (6)$$

The associated dimensionless boundary conditions are:

$$\frac{d\theta}{d\gamma}=\frac{\theta_b-1}{\frac{k}{h_f r_i}+\frac{k\ln(r_o/r_i)}{k_w}+\frac{R_{tc}k}{r_o}} \qquad @\ \gamma=1 \qquad (7)$$

$$\frac{d\theta}{d\gamma}=0 \qquad @\ \gamma=\rho \tag{8}$$

Solving Eqs. (6)-(8) yields the following temperature distribution in terms of the modified Bessel functions and profile number.

$$\theta = A_1\gamma^{\frac{n}{2}} I_{\frac{n}{2+n}}\left(\frac{2N_a}{2+n}\gamma^{\frac{2+n}{2}}\right) + A_2\gamma^{\frac{n}{2}} K_{\frac{n}{2+n}}\left(\frac{2N_a}{2+n}\gamma^{\frac{2+n}{2}}\right) \tag{9}$$

where I and K are the modified Bessel functions of the first and the second kind, respectively. After substitution of the above boundary conditions into Eq. (9), we arrive at the following expressions for coefficients A_1 and A_2

$$A_1=\frac{K_{-\frac{2}{2+n}}\left(\frac{2N_a}{2+n}\rho^{\frac{2+n}{2}}\right)}{D(\rho)},\quad A_2=\frac{I_{-\frac{2}{2+n}}\left(\frac{2N_a}{2+n}\rho^{\frac{2+n}{2}}\right)}{D(\rho)} \tag{10}$$

where

$$\begin{aligned} D(\rho) = {} & K_{-\frac{2}{2+n}}\left(\frac{2N_a}{2+n}\rho^{\frac{2+n}{2}}\right) I_{\frac{n}{2+n}}\left(\frac{2N_a}{2+n}\right) \\ & + K_{\frac{n}{2+n}}\left(\frac{2N_a}{2+n}\right) I_{-\frac{2}{2+n}}\left(\frac{2N_a}{2+n}\rho^{\frac{2+n}{2}}\right) - N_a\left(\frac{k}{h_f r_i}+\frac{k\ln(r_o/r_i)}{k_w}+\frac{kR_{tc}}{r_o}\right) \\ & -\left[K_{-\frac{2}{2+n}}\left(\frac{2N_a}{2+n}\rho^{\frac{2+n}{2}}\right) I_{-\frac{2}{2+n}}\left(\frac{2N_a}{2+n}\right) - I_{-\frac{2}{2+n}}\left(\frac{2N_a}{2+n}\rho^{\frac{2+n}{2}}\right) K_{-\frac{2}{2+n}}\left(\frac{2N_a}{2+n}\right)\right] \end{aligned} \tag{11}$$

Therefore the temperature profile given by Eq. (9) is expressed analytically in terms of fin radial ratio, profile number, fin characteristic number, and overall wall thermal resistance.

Heat Dissipation and the Optimum Condition

To determine the optimal dimensions of the annular fin, we maximize the heat dissipation for a given amount of annular fin volume which is given by

$$V = \int_{r_o}^{r_i} 2\pi r \cdot y(r)\,dr \tag{12}$$

With y(r) defined by Eq. (1), the dimensionless annular fin volume can be in terms of n and ρ

$$\frac{r_o^2\delta}{V}=\frac{(2-n)}{2\pi\left(\rho^{2-n}-1\right)} \tag{13}$$

From the definition given in Eq. (5), N_a^2 can be rewritten as

$$N_a^2=\frac{4\pi\, h\, r_o^4\left(\rho^{2-n}-1\right)}{kV(2-n)}=4Z_a\frac{\left(\rho^{2-n}-1\right)}{(2-n)} \tag{14}$$

where Z_a is the fin characteristic number which is similar to Biot number of a longitudinal fin

$$Z_a=\frac{\pi h r_o^4}{kV} \tag{15}$$

The thermal resistance term in Eq.(11) is rewritten into

$$\left(\frac{k}{h_f r_i}+\frac{k\ln(r_o/r_i)}{k_w}+\frac{kR_{tc}}{r_o}\right)N_a = 2R_a\sqrt{\frac{\rho^{2-n}-1}{2-n}} \tag{16}$$

where

$$R_a=\left(\frac{k}{h_f r_i}+\frac{k\ln(r_o/r_i)}{k_w}+\frac{kR_{tc}}{r_o}\right)\sqrt{Z_a} \tag{17}$$

We now define the non-dimensional rate of heat transfer from the fin in the form of

$$Q_a=\frac{q_b}{\sqrt{\pi khV}\,(T_f-T_\infty)} \tag{18}$$

where q_b is the dimensional heat transfer from the base. After substitution of $d\theta/d\gamma$ (γ=1) into Eq. (18) for q_b with the aid of Eqs. (7) and (9), the dimensionless heat dissipation can be expressed by:

$$Q_a=2\sqrt{\frac{2-n}{\rho^{2-n}-1}}\left[A_1 I_{-\frac{2}{2+n}}\left(\frac{2N_a}{2+n}\right)-A_2 K_{-\frac{2}{2+n}}\left(\frac{2N_a}{2+n}\right)\right] \tag{19}$$

where N_a is defined by Eq. (14) and A_1 and A_2 are given by Eq. (10). Note that using L'Hopital's rule, the expression $(\rho^{2-n}-1)/(2-n)$ in Eqs. (13)-(14), (16), and (19) approaches $\ln\rho$ for n=2. It is seen that the heat transfer is a function of radius ratio, ρ, profile number, fin characteristic number, and thermal resistance. Note that from Eqs. (10)-(12), both A_1 and A_2 are complicated functions of ρ because of the involvement of the denominator $D(\rho)$ shown in Eq. (11). The derivative under the optimum condition, $dQ_a/d\rho=0$, is extremely tedious to be evaluated analytically although it is not impossible. Therefore, in this work a numerical scheme with the aid of the Golden Search method is used to determine the maximum heat transfer and the optimum radius ratio for specified profile numbers annular fin character numbers and thermal resistances. Once the optimal radius ratio, ρ^*, is known, the optimum fin width, δ^*, can be obtained from Eq. (13).

3. RESULTS AND DISCUSSIONS

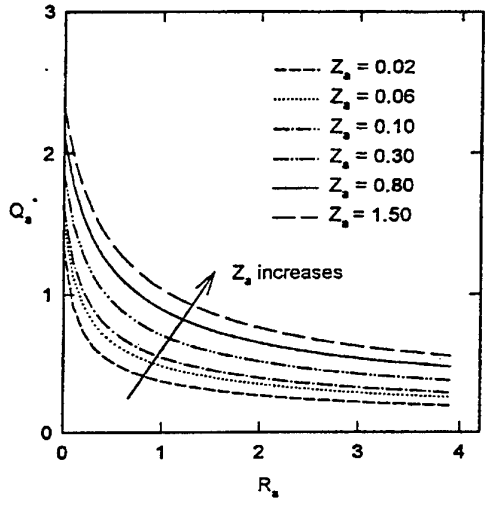


Figure 2. Maximum heat dissipation vs. wall resistance for annular rectangular fin with various Z_a

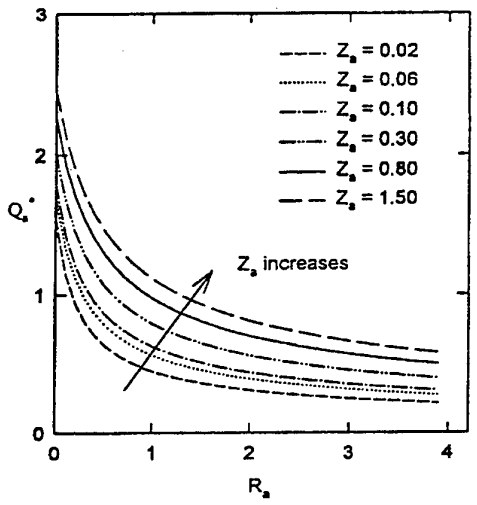


Figure 3. Maximum heat dissipation vs. wall resistance for annular hyperbolic fin with various Z_a

Figs. 2 and 3 present the variation of the optimum heat transfer with the overall thermal resistance for two types of annular fins commonly used. Fig. 2 is for the rectangular profile while Fig. 3 represents the hyperbolic profile with the same parameters. Similar to the longitudinal fins presented by Chung et al. [7], the optimum heat transfer decreases sharply with the increase of overall thermal resistance. From these two figures, it can be seen that for both types of annular fins, at R_a =0.75, the non-dimensional heat dissipation reduces to about one half of the value at R_a =0, regardless the value of Z_a. When R_a is larger than 3, the curves of optimum heat transfer practically become flat and its value is just 25% of that at zero wall resistance. This implies that the influence of wall resistance on optimal heat transfer reaches saturation. It is seen that the wall thermal resistance causes a significant decrease in the heat flow through the fin. The previous analyses by neglecting the wall thermal resistance could lead to a significant error in prediction of maximum heat transfer rate from the annular fin.

The influence of thermal resistance to the optimum radius ratio can be seen from Figs. 4 and 5. The optimum dimensionless fin height decreases with the increase of the wall resistance. When the fin characteristic number increases, the optimum fin becomes shorter and fatter. When the wall resistance is greater than 3, the optimum fin height becomes insensitive to the wall resistance for both profiles.

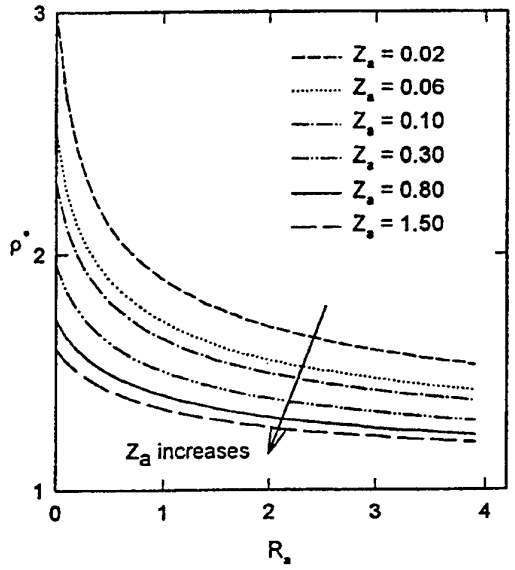


Figure 4. Optimum radius ratio vs wall resistance for annular rectangular fin with various Z_a

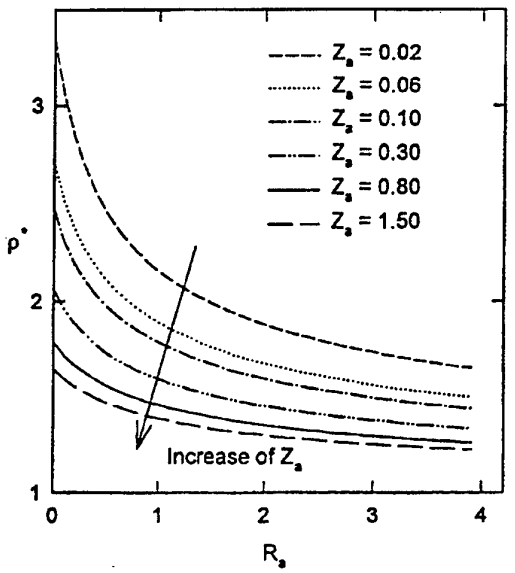


Figure 5. Optimum radius ratio vs wall resistance for annular hyperbola fin with various Z_a

Fig. 6 shows the variation of the non-dimensional heat dissipation with the profile number for zero thermal resistance (i.e., T_b=T_f). This figure reveals that for a lower fin characteristic number, (e.g., Z_a=0.05 or 0.10), optimum heat transfer increases with n first, after reaching a maximum value, then starts to decrease. For example, at Z_a=0.05 and Z_a=0.1, the maximum value of Q_a^* occurs at n=3.0 and n= 3.2 respectively. When Z_a>0.3, the maximum heat transfer occurs at a very large value of n beyond this figure. The optimum profile number increases with the increase of fin characteristic number. Therefore with the increase of Z_a, the optimum annular fin profile becomes more curved and sharper. This suggests that with a large Z_a, a fin with a more curved profile will enhance the heat dissipation.

The relation between the maximum non-dimensional heat dissipation and fin characteristic number for different annular fin profiles with zero wall resistance is illustrated in Fig. 7. In this figure, the curve with n=2 intersects with that of n=3 at Z_a=0.0138. This implies that at Z_a=0.0138, there exists an optimum profile number between 2 and 3. Fig. 8 depicts the variation of optimum annular fin height with Z_a at zero wall thermal resistance. The optimum fin height decreases rapidly with the increase of fin characteristic number. For given values of k, h and r_o, the increase of Z_a means a reduction of the fin volume, and the decrease of ρ^* leads to a smaller r_t.

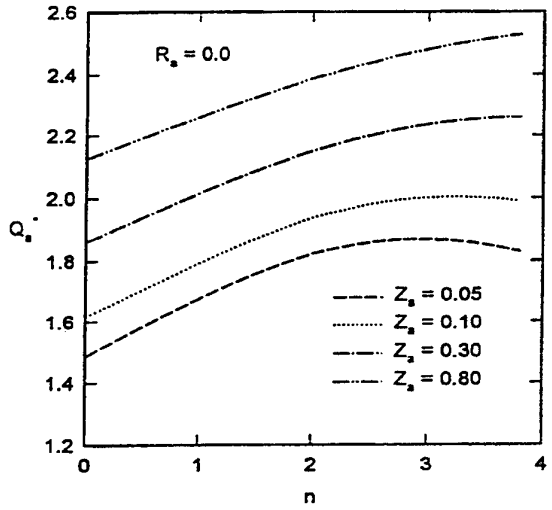


Figure 6. Variation of maximum heat dissipation vs. profile number with fin characteristic number as a parameter

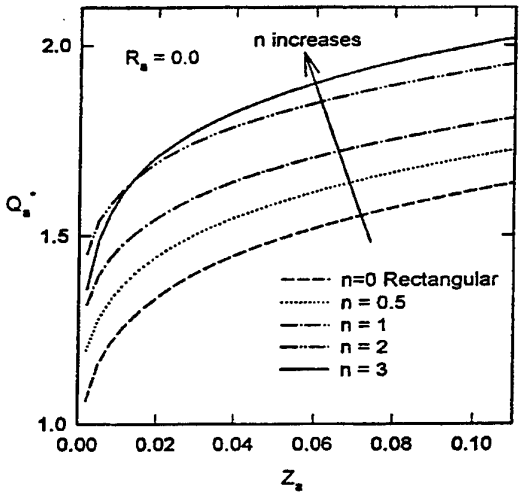


Figure 7. Relationship between the maximum heat dissipation and fin characteristic number for different profiles of annular fin

Note that Figs. 7 and 8 represent the same problem treated by Ullmann and Kalman [4], where the wall thermal resistance was neglected and the solution was given in a parametric form. The numerical results of two studies are in good agreement. However, for a known fin volume, the method proposed by Ullmann and Kalman [4] requires a trial and error procedure to obtain the optimum dimensions and the corresponding maximum heat dissipation. In the present work, the dimensionless parameters are derived rigorously from the governing equations and optimum dimensions can be obtained directly from Fig. 8 without any iteration. In practice, Figs. 7 and 8 appear to be more useful and convenient for the thermal designers to obtain the optimal fin design.

It should be pointed out that the results presented in the above figures can be used in the entire range of practical applications for the design purposes, since they cover the realistic ranges of parameters, $0.003 \leq Z_a \leq 0.12$ and $0 \leq R_a \leq 4$.

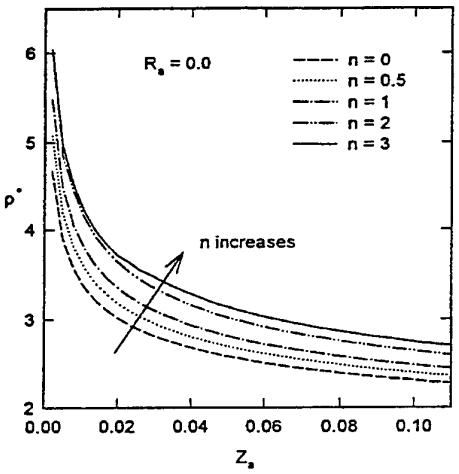


Figure 8. Relationship between the optimum radius ratio and fin characteristic number for different profiles of annular fin

4. CONCLUSIONS

In this work, the generalized heat transfer equation for an arbitrary annular fin profile is solved analytically in terms of the modified Bessel functions. The optimum radius ratio and its corresponding maximum heat dissipation are determined by the Golden Search Method. Design charts including the thermal resistance effect are presented for both the rectangular and hyperbolic annular fins in terms of two important parameters, the annular fin character number and overall wall thermal resistance. It is found that with the increase of the thermal resistance, both the maximum heat dissipation from the fin and the optimum annular fin height decrease rapidly. For given base pipe, fin and ambient conditions, the inclusion of thermal resistance leads to a shorter and fatter annular fin, in order to achieve the maximum heat transfer. It is further noticed that for a fixed R_a the optimum

fin profile number is a function of Z_a only, and it increases with the increase of Z_a. When Z_a increases, the optimum annular fin profile yields a more curved and sharper shape.

ACKNOWLEDGEMENTS

This study was supported by the Computational Mechanics Research Challenge grant sponsored by the Ohio Board of Regents.

REFERENCES

1. A. Brown, "Optimum Dimensions of Uniform Annular Fins", *Int. J. Heat Mass Transfer*, Vol. 8, pp 655-662, (1965).
2. I. Mikk, "Convective Fin of Minimum Mass", *Int. J. Heat Mass Transfer, Vol. 23*, pp. 707-711, (1980).
3. P. Razelos and K. Imre, "The Optimum Dimensions of Circular Fins with Variable Thermal Parameters", *J. Heat Transfer*, Vol. 102, pp. 420-425, (1980).
4. Ullman and H. Kalman, "Efficiency and optimized dimensions of annular fins of different cross- section shapes", *Int. J. Heat Mass Transfer*, Vol.32, pp.1105-1110, (1989).
5. S. M. Zubair, A. Z. Al-Garni, and J. S. Nizami, "The Optimal Dimensions of Circular Fins with Variable Profile and Temperature- Dependent Thermal Conductivity", *Int. J. Heat Mass Transfer*, 39, pp.3431-3439, (1996).
6. A. Aziz, "Optimization of Rectangular and Triangular Fins with Convective Boundary Conditions", *Int. Commun. Heat Mass Transfer*, Vol. 12, pp. 479-482, (1985).
7. B.T.F. Chung, Z. Ma, and F. Liu, "General Solutions for Optimum Dimensions of Convective Longitudinal Fins with Base Wall Resistances," *Proceedings of the 11th International Heat Transfer Conference*, Korea, Vol. 3, pp. 27-32, edited by J.S. Lee, Kyongju, Korea (1998).

NOMENCLATURE

h	heat transfer coefficient of ambient fluid surrounding the fin, $W/m^2 \cdot K$
h_f	heat transfer coefficient of source fluid at the tube side of the wall, $W/m^2 \cdot K$
k	conductivity of fin, $W/m \cdot K$
k_w	conductivity of pipe wall, $W/m \cdot K$
n	fin profile number, dimensionless
N_a	$= 2hr_o^2/k\delta$, annular fin parameter, dimensionless
q_b	local heat transfer rate of the annular fin, W
Q_a	$= q_b/\sqrt{\pi khV}(T_f - T_\infty)$, non-dimensional heat transfer, dimensionless
r	radial coordinate for annular fin, m
r_i	the inner radius of the annular fin base pipe, m
r_o	the outer radius of the annular fin base pipe, m
r_t	the radius of the annular fin tip, m
R_a	$= [k/h_f r_i + k\ln(r_o/r_i)/k_w + kR_{tc}/r_o]\sqrt{Z_a}$, overall thermal resistance for annular fin, dimensionless
R_{tc}	thermal contact resistance between primary and extended surfaces, $m^2 \cdot K/w$
T	local temperature of fin, K
V	fin volume, m^3
w	base wall thickness, m
Z_a	$= \pi h r_o^4/kV$, character number for annular fin, dimensionless

Greek Symbol

δ	fin thickness, m
ρ	$= r_t/r_o$, the radius ratio of annular fin, dimensionless
θ	$= (T - T_\infty)/(T_f - T_\infty)$, dimensionless temperature
γ	$= r/r_o$, dimensionless radial distance

Subscript

b	fin base
f	source fluid at the rear of the wall
∞	ambient fluid at the fin side

Superscript

*	optimum value

MODELING OF VISCOSITY AND THERMAL CONDUCTIVITY OF HYDROCARBONS BASED ON EQUATION OF STATE

X.Q. Guo, C.Y. Sun, S.X. Rong, G.J. Chen and T.M. Guo
High Pressure Fluid Phase Behavior & Property Research Laboratory,
University of Petroleum, P.O. Box 902, Beijing 100083, P.R. China

Keywords: viscosity, thermal conductivity, equation of state, hydrocarbons, mixtures

ABSTRACT. Based on the geometric similarity of P-V-T, T-μ-P and T-λ-P diagrams, viscosity (μ) and thermal conductivity (λ) models can be derived from an equation of state (EOS). The advantages of an EOS-based viscosity / thermal conductivity model are simple in form, applicable to both gas / liquid, high-pressure / low-pressure, and smooth phase transition of μ / λ in the near-critical region could be achieved. In this work, a modified version of the viscosity model based on Peng-Robinson (PR) EOS, and a newly established thermal conductivity model based on PR EOS were developed. Simple mixing rules were used for extension to mixtures. Extensive tests have been performed on pure hydrocarbons, carbon dioxide and nitrogen, hydrocarbon mixtures containing defined components as well as complex reservoir fluids. The comparison with those typical viscosity / thermal conductivity correlations currently adapted in the petroleum industry shows the superiority of the proposed models.

1. INTRODUCTION

Hydrocarbon viscosity (μ) and thermal conductivity (λ) are important transport properties in the petroleum / natural gas production and processing. Although numerous empirical / semi-empirical fluid viscosity / thermal conductivity correlations are available in the literature, however, separate correlations are generally required for gas / liquid, high-pressure / low-pressure systems and poor results are usually obtained for the complex reservoir fluid mixtures. In addition, fluid density is often involved in the viscosity / thermal conductivity correlations, hence, the selection of density correlation will affect the calculation results.

The attracting features of an EOS-based viscosity / thermal conductivity model are simple in form, applicable to both gas / liquid, high-pressure / low-pressure systems, density calculation is not involved, and smooth transition of gas / liquid properties in the near-critical region could be achieved. Furthermore, as a single EOS can be used in a chemical process / reservoir simulator for performing PVT, VLE (vapor-liquid equilibrium) and transport property calculations, the theoretical consistency is improved. In an earlier paper [1] we have proposed two viscosity models based on PR-EOS [2] and PT-EOS [3], respectively. The proposed models are capable of describing the viscosity of pure hydrocarbons and defined hydrocarbon mixtures satisfactorily, but rather poor results were obtained for the complex reservoir fluids. In this work, the original PR-viscosity model has been modified aiming at improving the viscosity prediction accuracy for reservoir fluid mixtures, including the highly asymmetric CO_2-injected enhanced oil recovery systems. In the second part of this work, following the similar approach, a new fluid thermal conductivity model was developed based on PR-EOS. No previous work in this direction was reported in literature.

2. VISCOSITY SECTION

The Modified PR-Viscosity Model

The technique of developing a viscosity (μ) model from an EOS based on the geometric similarity of P-V-T and T-μ-P relationships and the previous work done in this area have been discussed in detail in an earlier article by Guo et al. [1]. The modified PR (MPR) viscosity model proposed in this work is straightly given below:

$$T = \frac{rP}{\mu - b'} - \frac{a}{\mu(\mu + b) + b(\mu - b)} \tag{1}$$

where

$$a = 0.45724\frac{r_c^2 P_c^2}{T_c} \tag{2}$$

$$b = 0.07780\frac{r_c P_c}{T_c} \tag{3}$$

$$r = r_c \tau(T_r, P_r) \tag{4}$$

$$r_c = \frac{\mu_c T_c}{P_c Z_c} \tag{5}$$

$$\mu_c = 7.7 T_c^{-1/6} M^{1/2} P_c^{2/3} \tag{6}$$

$$\tau(T_r, P_r) = [1 + Q_1((P_r T_r)^{0.5} - 1)]^{-2} \tag{7}$$

$$b' = b\phi(T_r, P_r) \tag{8}$$

$$\phi(T_r, P_r) = \exp[Q_2(\sqrt{T_r} - 1)] + Q_3(\sqrt{P_r} - 1)^2 \tag{9}$$

where subscripts c and r denote the critical property and the reduced property, respectively. For hydrocarbons, carbon dioxide and nitrogen, the three parameters, Q_1, Q_2 and Q_3, were generalized in terms of acentric factor ω as follows.

When $\omega < 0.3$:

$$Q_1 = 0.829599 + 0.350857\omega - 0.747680\omega^2 \tag{10}$$

$$Q_2 = 1.94546 - 3.19777\omega + 2.80193\omega^2 \tag{11}$$

$$Q_3 = 0.299757 + 2.20855\omega - 6.64959\omega^2 \tag{12}$$

When $\omega \geq 0.3$:

$$Q_1 = 0.956763 + 0.192829\omega - 0.303189\omega^2 \tag{13}$$

$$Q_2 = -0.258789 - 37.1071\omega + 20.5510\omega^2 \tag{14}$$

$$Q_3 = 5.16307 - 12.8207\omega + 11.0109\omega^2 \tag{15}$$

It is to be noted that the functional forms of $\phi(T_r, P_r)$, Q_1, Q_2 and Q_3 are modified as compared with the original PR viscosity model.

Extension to Mixtures

For a mixture, Eq. (1) is rewritten as:

$$T = \frac{r_m P}{\mu_m - b'_m} - \frac{a_m}{\mu_m(\mu_m + b_m) + b_m(\mu_m - b_m)} \tag{1a}$$

where subscript m denotes mixture, and the mixing rules adapted for parameters a_m, b_m, b'_m and r_m are as follows:

$$a_m = \sum_i x_i a_i \tag{16}$$

$$b_m = \sum_i x_i b_i \tag{17}$$

$$b'_m = \sum_i \sum_j x_i x_j \sqrt{b'_i\, b'_j}\,(1 - k_{ij}) \tag{18}$$

$$r_m = \sum_i x_i r_i \tag{19}$$

Again, it is to be noted that the binary interaction coefficient, k_{ij}, is introduced to parameter b'_m in the MPR model, instead of a_m.

Selection of Correct Viscosity Root

Equation (1) is cubic in μ, standard subroutine can be used to solve the viscosity root. For a pure substance, if three viscosity roots were obtained at the specified temperature and pressure, the correct viscosity root is chosen as follows:

(1) In the liquid region (when the pressure is greater than the saturated vapor pressure at prevailing temperature), choose the maximum real root.
(2) In the sub-critical gas region (when the pressure is lower than the saturated vapor pressure at prevailing temperature), choose the smallest real root greater than b', as b' represents the asymptotic value of ideal gas viscosity at infinite temperature.
(3) In the supercritical region ($T > T_c$), choose the maximum real root.

The saturated vapor pressures (P^s) of pure substances were calculated using the Antoine equation for $P^s < 1500$ mm Hg, and the Lee-Kesler equation [4] for $P^s \geq 1500$ mm Hg. For a mixture, if the phase status is not known, it should be determined by using an equation of state.

Characterization of the C_7^+-Fraction in Reservoir Fluids

In performing the PVT and VLE calculations of reservoir fluids, for improving the calculation accuracy, the undefined C_7^+-fraction is, in general, divided into a number of pseudo-components. However, in viscosity calculations it was found that the calculation results are not sensitive to the subdivision of C_7^+-fraction, hence a single pseudo-component was used to represent the C_7^+-fraction in this work.

On the other hand, the selection of empirical correlation for evaluating the critical temperature (T_c), critical pressure (P_c) and acentric factor (ω) of pseudo-components has significant influence on the viscosity calculation results. In this work, the T_c-, P_c- correlations proposed by Twu [5] and the ω-correlation developed by Kesler and Lee [6] were chosen.

Test Results on the MPR Viscosity Model for Reservoir Fluid Mixtures

As mentioned in the Introduction, the MPR viscosity model is targeted at reservoir fluids, the comparisons of the calculation results with original PR viscosity model for pure substances and binary mixtures are omitted in this paper. In the following tables, the absolute average deviation (AAD) is defined as:

$$\mathrm{AAD}(\%) = \frac{1}{N_p} \sum_j \left| \frac{\mu_{cal} - \mu_{exp}}{\mu_{exp}} \right|_j \times 100 \tag{20}$$

Natural gas mixtures. Due to the lack of experimental viscosity data for the binary pairs involved in a natural gas mixture, all k_{ij}s were set to zero. Since no adjustable parameter was involved in the viscosity calculations for

reservoir fluid mixtures, hence the calculation results reported in the following sections are entirely predictive in nature.

The comparison of the viscosity prediction results for nine natural gas mixtures (the C_7^+-fraction content ranges from 0.4 to 7.9 mol%) based on six viscosity models (MPR, PR, Lohrenz [7], Lawal [8], Little [9] and PT [1]) are presented in Table 1. The superiority of MPR model for natural gas mixtures is clearly indicated.

Table 1. Comparison of Viscosity Prediction Results of Nine Natural Gas Mixtures based onVarious Models*

Gas sample	T (K)	P (MPa)	MPR AAD (%)	PR AAD (%)	Lohrenz AAD (%)	Little AAD (%)	Lawal AAD (%)	PT# AAD (%)
1	390.93	36.98	12.43	4.28	102	166	16	22.3
2	365.93	31.43	10.39	8.61	96.1	285	28.9	0.28
3	373.71	31.42	3.34	2.67	209	485	19	9.7
4	325.93	24.93	11.91	21.67	409	650	6.7	691
5	400.93	33.98	1.47	11.96	453	288	23.9	35.6
6	335.37	17.96	2.62	5.56	555	522	0.83	18
7	316.48	13.78	24.22	31.63	13032	294	28.2	24.3
8	398.71	39.62	20.45	33.91	448	645	6.9	18.7
9	375.93	30.42	1.45	--	339	146	3.8	12
Overall AAD (%)			9.8	15	1738	386.8	14.91	17.61**

* Data source: Lawal [8].
** Sample 4 excluded.
# Viscosity model based on PT EOS developed by Guo et al. [1].

Reservoir oil systems without CO_2-injection. Table 2 shows the comparison of the viscosity prediction results of twenty two reservoir oils (a total of 126 data points) based on six viscosity models (MPR, Pedersen and Fredenslund [10], Lohrenz [7], Lawal [8], Little [9] and PT [1]). The original PR model failed to describe most of the data tested, however, the MPR model proposed in this work produced the best results. The calculation accuracy could be further improved if suitable k_{ij} values were introduced.

CO_2-injected systems. Miscible flooding achieved by CO_2-injection is one of the major enhanced oil recovery (EOR) techniques, and the reduction of oil phase viscosity plays a critical role in such processes. Due to the highly asymmetric nature of the CO_2-injected reservoir oil systems, the accurate prediction of their viscosity is a challenging task and little has been reported in the open literature.

The proposed MPR model was firstly tested on an asymmetric binary system (CO_2-n-decane), containing CO_2 up to 85mol%. The overall AAD of the 70 data points tested is 7.2 % (with $k_{ij} = 0$), which is quite encouraging.

The MPR model has been applied to predict the viscosity of two CO_2–injected reservoir oil systems, the viscosity data (a total of 123 data points) were measured in this laboratory. The overall AAD is 12.6 %, which is reasonable for such highly asymmetric complex mixtures.

For illustration, the comparison of the performance of four viscosity-models [MPR, Pedersen [10], Lohrenz [7], and Du and Guo [11] on the prediction of the viscosity of an CO_2-injected reservoir oil system under saturation pressures corresponding to various CO_2-concentrations is given in Table 3. The overall AAD of MPR model is 7.98 %, far better than the other three models tested.

The MPR viscosity model presented in this paper has been successfully implemented into UTCOM4—a reservoir simulation software developed by the University of Texas at Austin, and applied to Chinese oil fields.

Table 2. Comparison of the Predicted Results of the Viscosity of Reservoir Oils based on Various Models

				AAD (%)					
Oil No.	N_p	T (K)	P-range (MPa)	MPR	Pedersen	Lohrenz	Little	Lawal	PT
1	13	338.2	17.37-34.58	7.84	11.69				5.89
1	9	348.2	17.99-38.71	8.21	11.50				4.60
1	13	360.2	11.82-41.47	7.41	11.40				4.38
1	10	377.2	20.03-44.23	6.80	11.84				3.40
2	11	359.2	5.24-38.02	21.41					
2	10	373.2	5.48-38.02	7.60					
3	1	336.5	8.01	5.16	94.54	57.05	24.29		
4	1	307.6	4.80	12.49	24.30	254.33	24.43	29.45	2.19
5	1	303.2	8.79	22.14	27.00	149.51	2.65	17.94	15.39
6	1	342.0	11.38	5.48		92.48	27.94	28.77	
7	1	412.0	59.23	46.02	98.55	216.27	114.64	40.91	67.79
8	1	376.5	27.85	2.31	6.32	208.49	21.79	5.94	9.47
9	1	394.3	0.55	20.52	15.89	102.35	55.11	15476.3	10.24
10	1	317.6	2.31	10.44	12.62	139.75	67.80	1.71	3.67
11	1	295.4	2.41	5.61		89.61	99.98	7.72	
12	1	380.9	4.27	39.22			36.49	3583.5	82.93
13	1	316.5	6.20	17.37	13.57	183.57	72.58	21.10	9.05
14	1	346.5	6.52	13.14	15.76	103.31	43.29	3.32	5.08
15	1	363.2	7.52	43.58	38.10	86.12	60.17	85.52	30.12
16	1	407.6	15.03	18.29	5.36	118.61	50.25	44.18	3.5
17	1	379.3	25.27	8.58	78.31	544.73	63.13	28.38	58.61
18	1	335.9	8.94	2.93	3.44	94.48	33.44	19.38	
19	5	335.9	15.89-34.57	5.31					
20	7	371.0	20.35-40.19	5.45					
21	6	366.5	27.45-38.98	2.84					
22	7	303.2	4.87-44.02	10.98					
22	6	323.2	5.32-44.02	12.20					
22	7	353.2	6.93-44.02	14.52					
22	6	374.8	8.00-44.02	22.87					
Overall AAD (%)				13.99	25.48	191.55	50.03	28.04	23.32

* Data sources: Oil No.: 1-2:Du [11], 3-18:Lawal [8], 19-21:Pedersen et al. [12, 13], 22:–Ahrabi et al. [14].

Table 3. Comparison of Viscosity Prediction Results of CO_2-injected Reservoir Oil Systems at Saturation Pressures based on Various Models*

CO2/Oil(mol/mol)	T(K)	ps(MPa)	μexp(cp)	MPR AAD(%)	Du AAD(%)	Pedersen AAD(%)	Lohrenz AAD(%)
0.0000	359.15	5.238	2.2974	8.76	2.33	33.88	633.83
0.0000	373.15	5.479	1.5916	10.47	22.67	40.95	720.88
0.3158	359.15	9.099	1.5833	12.03	30.17	26.94	688.40
0.3158	373.15	10.099	1.2597	5.65	33.30	27.07	682.36
0.7065	359.15	12.684	1.2298	21.06	25.28	27.00	619.43
0.7065	373.15	13.891	0.8938	6.00	29.18	48.67	712.81
0.8585	359.15	14.408	0.9494	8.36	17.38	52.28	711.72
0.8585	373.15	16.097	0.7554	0.35	20.10	63.17	720.55
1.0535	359.15	17.200	0.7246	6.43	16.27	83.33	789.58
1.0535	373.15	18.786	0.6804	0.74	17.15	69.33	669.12
Overall AAD (%)				7.98	21.38	47.26	694.87

* Data source: Du and Guo [15].

3. THERMAL CONDUCTIVITY SECTION

The Development of Thermal Conductivity Models Based on PR-EOS

A typical T-λ-P diagram for propane is shown in Fig. 1. From Fig. 1, it can be noted that geometric similarity is also observed between the P-V-T and T-λ-P diagrams. By reasoning, the technique adapted for establishing a viscosity model from an EOS should be also applicable to fluid thermal conductivity. The selection of EOS is rather arbitrary, for in consistency with the viscosity modeling, the popular PR and PT cubic EOS were chosen in this work (for saving space the mathematical description of PT-model is omitted in this paper).

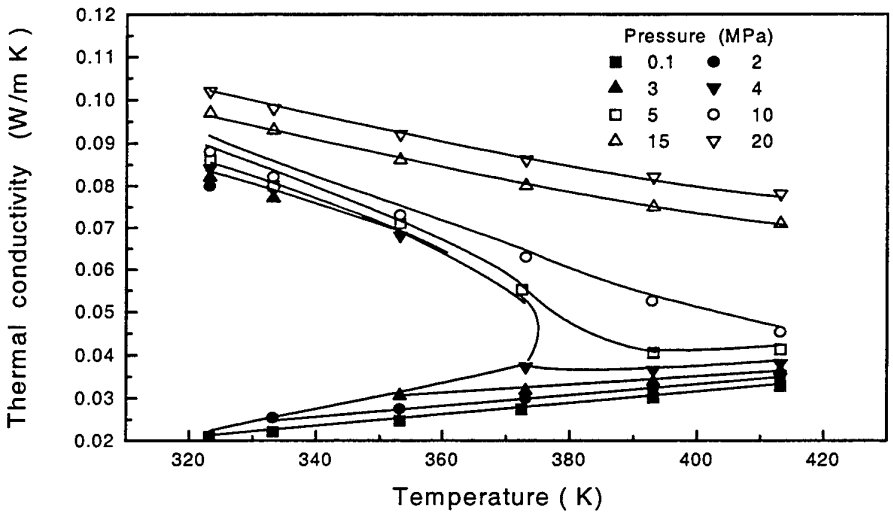


Figure 1. Typical T-λ-P diagram of propane

The thermal conductivity model developed from PR-EOS is as follows:

$$P = \frac{RT}{v-b} - \frac{a(T)}{v(v+b)+b(v-b)} \tag{21}$$

By substituting T for P, λ for v, and r for R, the following PR-thermal conductivity equation is obtained:

$$T = \frac{rP}{\lambda - b'} - \frac{a}{\lambda(\lambda+b)+b(\lambda-b)} \tag{22}$$

The corresponding parameters are evaluated as follows:

$$a = 0.45724\frac{r_c^{\,2}P_c^{\,2}}{T_c} \tag{23}$$

$$b = 0.07780\frac{r_c p_c}{T_c} \tag{24}$$

$$r = r_c\tau(P_r) \tag{25}$$

$$r_c = \frac{\lambda_c T_c}{P_c Z_c} \tag{26}$$

$$\lambda_c = T_c^{-1/6} M^{-1/2} P_c^{2/3} / 21 \tag{27}$$

$$b' = b\phi(T_r, P_r) \tag{28}$$

$$\tau(P_r) = [1 - Q_1 \times (1 - P_r^{0.5})]^{-2} \tag{29}$$

$$\phi(T_r, P_r) = 1 + Q_2 |1 - T_r|^{0.0125} + Q_3 |1 - T_r|^{1.75} + Q_4 [P_r^{0.25} - 1]^2 \tag{30}$$

The regressed Q_j values for 22 pure substances are listed in Table 4.

Table 4. Coefficients Q_1–Q_4 in Eq. (29) and Eq. (30)

Substance	Q_1	Q_2	Q_3	Q_4
Methane	0.970190	0.776883	0.347756	-0.138073
Ethane	0.958134	0.642968	0.960562	-0.002961
Propane	0.927366	1.915883	1.879568	0.025987
n-Butane	0.922081	2.108735	-1.608329	0.239525
n-Pentane	0.881556	2.284456	-10.540047	1.600419
n-Hexane	0.819612	2.184340	-1.156281	2.615769
n-Heptane	0.922903	4.652677	33.646595	2.977537
n-Octane	0.752467	0.675726	2.671826	5.743277
n-Nonane	0.999120	4.636064	2.465917	10.371459
n-Decane	0.845231	-1.284717	21.458351	5.962502
n-Undecane	1.000995	3.408888	6.331457	14.841777
n-Dodecane	0.999195	4.580865	7.825347	18.978289
n-Tridecane	1.008009	5.599662	6.216670	21.776913
n-Tetradecane	1.007128	4.212692	14.642992	22.331921
n-Pentadecane	0.988286	4.203979	14.540983	24.893528
n-Hexadecane	0.990758	4.609309	18.952227	28.157578
n-Heptadecane	1.271984	5.307981	32.092571	35.029812
n-Octadecane	0.991402	4.556245	24.449326	36.619545
i-Butane	0.994041	2.538210	3.873491	0.864157
i-Octane	0.974758	-6.349264	12.524574	3.054645
Nitrogen	0.923247	0.648666	0.125623	-0.138456
Carbon dioxide	0.929163	0.012330	0.433261	-0.054170

Rules for Choosing Correct λ-Root

The PR- thermal conductivity equation, Eq. (22), is cubic in λ. The rules for selecting correct λ-root for vapor, liquid and supercritical gas, are similar to the rules adapted for viscosity calculations described in the previous section.

Extension to Mixtures

The PR-thermal conductivity model for mixtures is expressed as follows:

$$T = \frac{r_m P}{\lambda_m - b'_m} - \frac{a_m}{\lambda_m(\lambda_m + b_m) + b_m(\lambda_m - b_m)} \tag{31}$$

The mixing rules adapted for the EOS parameters in Eq. (42) and Eq. (43), a_m, b_m, c_m, b'_m and r_m , are as follows:

$$a_m = \sum_i x_i a_i \tag{32}$$

$$b_m = \sum_i x_i b_i \tag{33}$$

$$b'_m = b_m \phi_m \tag{34}$$

$$\phi_m = \sum_i \sum_j x_i x_j \sqrt{\phi_i \phi_j}(1 - k_{ij}) \tag{35}$$

$$r_m = \sum_i x_i r_i \tag{36}$$

where x_i is the mole fraction of component i, and k_{ij} denotes the binary interaction parameter to be determined from experimental thermal conductivity data.

Test Results for Pure Substances

The thermal conductivity of twenty two pure substances including hydrocarbons, carbon dioxide and nitrogen have been calculated based on the proposed PR-model and PT-model over wide temperature and pressure ranges. The calculation results are shown in Table 5. The overall absolute average deviations (a total of 3273 data points) are 8.28% (PR-model) and 8.24% (PT-model), respectively. For comparison with existing thermal conductivity models, the calculated results based on the corresponding states theory (Pedersen et al. [12,13], the API method [16], and Stiel and Thodos [17] correlation are also listed in Table 5.

Test Results for Defined Mixtures

The thermal conductivity prediction results for eleven binary mixtures (a total of 277 data points) are presented in Table 6. The overall absolute average deviations are 14.39% (PR-model) and 13.29% (PT-model), respectively. For comparison, the calculated results based on the corresponding states theory (Pedersen et al. [12,13]) are also given in Table 6, the overall absolute average deviation of 21.25% is significantly higher than PR / PT model.

Test Results for Reservoir Oils

The thermal conductivity data of reservoir fluids are extremely scarce in the literature. Using the characterization method for C_7^+-fraction proposed by Twu [5], the developed thermal conductivity models have been applied to predict the thermal conductivity data of three reservoir oils reported by Baltatu et al. [18]. The prediction results are listed in Table 7. From Table 7 it can be seen that both PR and PT models are capable of giving reasonable thermal conductivity predictions for the complex reservoir oils tested.

Table 5. Comparison of the Calculated Results on the Thermal Conductivity of Pure Substances based on Various Models

Substance*	T(K)	P(MPa)	Status	N_P	PR AAD(%)	PT AAD(%)	API AAD(%)	Pedersen# AAD(%)	Stiel$^{\Delta}$ AAD(%)	Data source
Methane	277-478	0.1-34.5	g	98	2.89	3.57	8.21	3.45	6.39	[19,20]
Ethane	277-445	0.1-34.5	g	70	6.48	8.08	20.89	13.88	7.3	[21]
Propane	323-413	0.1-30.0	g, l	78	8.96	8.19	15.11	11.2		[22]
Butane	277-478	0.1-34.5	g, l	104	9.78	9.67	16.3	14.58		[23]
Pentane	298-473	0.1-220.5	g, l	79	3.47	3.38	12.28	9.56		[24]
Hexane	273-633	0.1-50.0	g, l	162	12.24	12.26	11.64	13.56		[22]
Heptane	273-633	0.1-50.0	g, l	162	15.81	15.44	11.29	12		[22]
Octane	273-633	0.1-50.0	g, l	162	13.67	13.71	13.78	9.53		[22]
Nonane	233-573	0.1-49.0	l	63	1.58	1.91	10.56	14.18		[24]
Decane	277-478	0.1-34.0	g, l	97	9.37	9.38	14.06	13.94		[22]
Undecane	253-453	0.1-350.0	l	20	1.01	0.95	11.79	14.77		[24]
Dodecane	273-453	0.1-196.0	l	62	0.98	0.95	7.73	23.54		[24]
Tridecane	273-677	0.1-49.0	l	96	1.63	3.08	8.76	15.99		[24]
Tetradecane	293-463	0.1-49.0	l	41	2.04	1.99	8.33	19.57		[24]

Pentadecane	303-463	0.1-49.0	l	30	0.95	0.91	15.24	22.53		[24]
Hexadecane	303-463	0.1-49.0	l	30	0.92	0.87	19.67	28.86		[24]
Heptadecane	308-458	0.1-49.0	l	48	0.45	0.42	30.23	36.66		[24]
Octadecane	326-460	9.8-49.0	l	49	0.48	0.39	33.96	43.15		[24]
i-Butane	193-384	0.1-50.0	g, l	44	1.31	1.32	13.9	17.07		[22]
i-Octane	290-580	0.1-4.0	g, l	220	9.48	9.83	26.45	40.87		[22]
N2	80-1400	0.1-60.0	g, l	610	9.13	8.06			4.73	[24]
CO2	220-1400	0.1-60.0	g, l	948	8.92	9.19			10.05	[24]
Overall				3273	8.28	8.24	15.5	18.45	7.85	

* Hydrocarbons are normal alkanes if not otherwise specified.

Corresponding states method (Pedersen et al. [12,13]).

Δ Stiel and Thodos [17].

Table 6. Comparison of Thermal Conductivity Prediction Results of Mixtures based on Various Models

Mixture	T (K)	P (MPa)	X_2 (mole frac.)	N_P	PR AAD(%)	PT AAD(%)	Pedersen AAD(%)	Data source
CH4(1)-C3H8(2)	366-371	0.1	0.0-1.0	26	14.04	13.97	12.67	[25]
CH4(1)-n-C4H10(2)	278-444	0.1-34.48	0.606	53	7.58	7.5	34	[26]
CH4(1)-CO2(2)	371	17.48	0.245	1	12.87	12.67	4.09	[25]
CO2(1)-C3H8(2)	369	0.1	0.0-1.0	21	20.08	14.8	24.34	[27]
N2(1)-CO2(2)	273-1047	0.1	0.0-1.0	70	27.83	23.94	23.32*	[25]
n-C7H16(1)-i-C8H18(2)	308-337	1.5-44.0	0.26-0.51	16	11.19	11.3	22.79	[28]
n-C7H16(1)-n-C11H24(2)	288-345	0.1	0.18-0.66	18	6.94	7.44	5.63	[29]
n-C7H16(1)-n-C16H34(2)	290-344	0.1	0.13-0.57	18	7.52	10.41	13.47	[29]
i-C8H18(1)-n-C14H30(2)	303-370	0.1	0.0-1.0	18	15.65	14.49	26.18	[30]
n-C11H24(1)-n-C16H34(2)	295-343	0.1	0.19-0.67	18	1.52	2.08	21.24	[29]
n-C7H16(1)-n-C11H24(2)-n-C16H34(3)	294-344	0.1		18	4.95	6.73	8.22	[29]
Overall				277	14.39	13.29	21.25	

Table 7. Comparison of Thermal Conductivity Prediction Results of Three Reservoir Oils based on PR- and PT-models*

Oil No.	T-range (K)	P-range (MPa)	N_P	PR AAD (%)	PT AAD (%)
1	303-494	3.45-13.8	12	7.51	7.23
2	334-494	1.38-10.3	8	9.42	9.48
3	298.81	1.52-5.07	2	11.3	11.49

* Data source: Baltatu et al. [18].

4. CONCLUSIONS

1. The original PR-viscosity model has been modified and successfully extended its application to reservoir fluid systems with / without CO_2-injection through re-correlation of the function $\phi(T_r, P_r)$ and Q_j - coefficients.
2. Extensive test results indicate the superiority of MPR-viscosity model over those empirical / semi-empirical viscosity correlations currently used in the petroleum industry. For mixtures, the calculation accuracy could be further improved if suitable values of binary interaction parameter k_{ij} were introduced.
3. EOS-based fluid thermal conductivity models have been developed, which were not reported previously. The proposed PR- and PT-thermal conductivity models are simple in form and capable of representing the thermal conductivity data satisfactorily for pure non-polar substances (hydrocarbons, CO_2 and N_2), hydrocarbon mixtures containing defined components, and complex reservoir fluids with / without CO_2-injection.

ACKNOWLEDGEMENTS

The financial support received from the China National Petroleum & Natural Gas Corporation and Natural Science Foundation of China are gratefully acknowledged.

REFERENCES

1. X.Q. Guo, L.S. Wang, S.X. Rong and T.-M. Guo, Fluid Phase Equilibria, v. 139, pp. 405 (1997).
2. D.Y. Peng and D. B. Robinson, Ind. Eng. Chem. Fundam, v. 15, pp. 59 (1976).
3. N. C. Patel and A. S. Teja, Chem. Eng. Sci., v. 37, pp. 463 (1982).
4. B. I. Lee and M. G. Kesler, AIChE J., v. 21, pp. 510 (1975).
5. C. H. Twu, Fluid Phase Equilibria 1984, v. 16, pp. 137 (1984).
6. N. G. Kesler and B. I. Lee, Hydrocarbon Processing, v. 55, pp. 153 (1976).
7. J. B. Lohrenz and C. R. Clark, J. Pet. Technol. *Oct.*, pp. 1171 (1964).
8. A. S. Lawal, *SPE/DOE Paper* 14926, presented at the *5th Symposium on Enhanced Oil Recovery*, Tulsa, April 20-23, 1986.
9. J. E. Little and H. T. Kennedy, SPE J. *June,* pp. 157 (1968).
10. K. S. Pedersen and Aa. Fredenslund, Chem. Eng. Sci., v. 42, pp. 182 (1987).
11. L.G. Du, Ph.D. Dissertation, University of Petroleum (Beijing), 1991.
12. K. S. Pedersen, Aa. Fredenslund and P. Thomassen, *Properties of Oils and Natural Gases,* Gulf Publishing Company, Houston (1989).
13. K. S. Pedersen, Aa. Fredenslund and P. Thomassen, *Contributions in Petroleum Geology and Engineering Properties of Oils and Natural Gases*. Gulf Publishing Company (1989).
14. F. Ahrabi, S. J. Ashcroft and R. B. Shearn, Chem. Eng. Res. Des., v. 65, pp. 63-67 (1987).
15. L.G. Du and T.M. Guo, The Chem. Eng. J., v. 47, pp. 163 (1991).
16. API, *Technical Data Book: Petroleum refining*, American Petroleum Institute, New York (1980).
17. L. I. Stiel and G. Thodos, *AIChE J.*, v. 10, pp. 26 (1964).
18. M. E. Baltatu, J. F. Ely, H. J. M. Hanley, M. S. Graboski, R. A. Perkins and C. D. Sloan, Ind. Eng. Chem. Proc. Des. & Dev., v. 24, pp. 325 (1985).
19. L. T. Carmichael, H. H. Reamer and B. H. Sage, J. Chem. & Eng. Data, v. 11, pp. 59 (1966).
20. H. L. Johnston and E. R. Grilly, J. Chem. Phys. 1946, v. 14, pp. 233 (1946).
21. L. T. Carmichael, V. Berry and B. H. Sage, J. Chem. & Eng. Data, v. 8, pp. 281 (1963).
22. N. B. Vargaftik, *Tables on the Thermophysical Properties of Liquids and Gases*, Washington D.C., Hemisphere Publishing Corporation (1975).
23. L. T. Carmichael and B. H. Sage, J. Chem. & Eng. Data, v. 9, pp. 511 (1964).
24. D. F. Jamieson, *Thermal Conductivity of Gases and Liquids*, Massachusetts: MIT Press (1965).
25. S. Bretsznajder, *Transport Properties of Fluids*, Washington D.C., Hemisphere Publishing Corporation (1975).
26. L. T. Carmichael, J. Jacobs and B. H. Sage, J. Chem. & Eng. Data, v. 13, pp. 489 (1968).
27. Y. S. Touloukian and P. E. Liley, *Thermal Conductivity: Nonmetallic Liquids and Gases,* New York, IFI/Plenum (1970).
28. I. M. N. A. Fareleira, S. F. Y. Li and W. A. Wakeham, International Journal of Thermophysics, v. 10, pp. 1041 (1981).
29. Y. Wada, Y. Nagasaka and A. Nagashima, International Journal of Thermophysics, v. 6, pp. 251 (1985).
30. D. F. Jamieson, J. B. Irving and J. S. Tudhope, *Liquid Thermal Conductivity: A. Data Survey to 1973*, H. M. Stationary Office, Edinburgh (1975).

DETERMINATION OF THE THERMAL DIFFUSIVITY OF AQUEOUS SOLUTIONS OF SALTS BY A LASER-INDUCED THERMAL GRATING TECHNIQUE

Jun Wang and Zhi-Hang Chen
College of Power Engineering, University of Shanghai for Science and Technology
516 Jun Gong Road, Shanghai 200093, China

Martin Fiebig
Institut für Thermo- und Fluiddynamik, Ruhr-Universität Bochum
Universitätsstraβe 150, D-44801 Bochum, Germany

Keywords: aqueous solutions of salts, laser-induced thermal grating, thermal conductivity, thermal diffusivity

ABSTRACT. The laser-induced thermal grating technique (LTG) has proved to be suitable for the accurate measurement of the thermal diffusivity of pure liquids, liquid mixtures and aqueous solutions of inorganic substances in a wide range of temperatures. Compared with conventional measurement methods, this optical technique has the advantage that no sensors need to be inserted in the sample, especially when measurements have to be made on electrically conducting and corrosive liquids such as aqueous solutions of salts. Due to the tiny temperature rise in the sample during measurements, the short measuring time, and the very small sample volume, the influence of free convection in the sample on the measurement is negligible. In this paper, the laser-induced thermal grating technique (LTG) and the experimental facility are described. Experimental results for aqueous solutions of inorganic salts, e.g. sodium chloride and magnesium chloride etc., are presented which are of importance for understanding a variety of chemical processes in engineering, including desalination processes and corrosion in heat exchangers.

1. INTRODUCTION

Transport properties of liquids are of high importance for engineering and scientific research. Experimental investigations of transport properties such as the thermal conductivity and thermal diffusivity of liquids involve a number of difficulties not encountered in experimental thermostatics. For instance, the conventional measurement techniques determine the thermal conductivity and thermal diffusivity under thermal non-equilibrium conditions with macroscopic temperature gradients in the sample. In order to obtain the thermal conductivity and thermal diffusivity with the highest accuracy, the temperature gradients have to be large enough to be measured with sufficient accuracy. This usually leads to errors in measurement, e.g. by free convection and radiation in the sample. In addition, the conventional measurement techniques cannot be used to determine the thermal conductivity and thermal diffusivity of electrically conducting and corrosive liquids including polar liquids and electrolyte solutions etc. unless specially designed sensors are applied for the desired electrical insulation and corrosion protection.

The laser-induced thermal grating technique (LTG) has proved to be suitable for the accurate measurement of the thermal diffusivity of pure liquids, liquid mixtures and aqueous solutions of inorganic substances in a wide range of temperatures. Two pulsed laser beams of identical intensity intersect each other in a slightly absorbing liquid sample and produce a spatially periodic intensity distribution, which results in a corresponding temperature distribution, i.e. the thermal grating in the interference region. By investigating the relaxation behaviour of the light diffraction at the grating, the thermal diffusivity of the sample is determined. Compared with conventional measurement methods, this optical technique has the advantage that no sensors need to be inserted in the sample, especially when measurements have to be made on electrically conducting and corrosive liquids such as aqueous solutions of salt. Due to the tiny temperature rise in the sample during measurements (less than 0.1 K), the short measuring time (a few milliseconds), and the very small sample volume (less than 0.1 millilitre), the influence of free convection in the sample on the measurement is negligible.

In this paper, the laser-induced thermal grating technique (LTG) and the experimental facility are described. Experimental results for aqueous solutions of inorganic salts, e.g. sodium chloride and magnesium chloride etc., are presented which are of importance for understanding a variety of chemical processes in engineering, including desalination processes and corrosion in heat exchangers.

2. MEASUREMENT TECHNIQUE

In the laser-induced thermal grating technique (LTG), the thermal diffusivity of a liquid sample is determined by measuring the decay time of a diffracted laser beam from a periodically heated region (thermal grating) which is produced by the interference of two high-intensity laser beams. Figure 1 shows schematically the principle of this measurement technique. Two pulsed laser beams of equal wavelength ($\lambda_h = 488\,nm$) and intensity from an Ar^+ laser intersect each other in an absorbing liquid sample at an angle θ. As a result of interference, a spatially periodic intensity distribution (optical interference fringe pattern) is produced during a light pulse ($0 < t < t_h$). By absorbing the light intensity, a spatially periodic, time-dependent temperature distribution (i.e., a transient thermal grating) corresponding to the interference fringe pattern is induced in the x-direction of the sample.

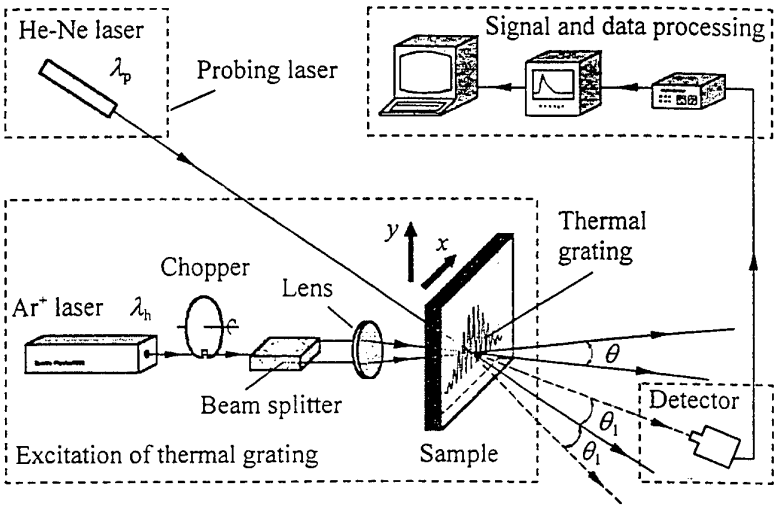


Fig. 1. Schematic of the laser-induced thermal grating technique

If the assumption of one-dimensional heat conduction in the modulation direction of temperature x is permissible, the thermal grating decays as

$$\delta T(x,t) = \Delta T(t)\cos qx = \Delta T(t_h)\exp[-(t-t_h)/\tau]\cos qx \qquad (1)$$

after the heating light pulse ($t > t_h$) due to heat conduction in the heated region. Here, $\delta T(x,t)$ represents the temperature fluctuation, $\Delta T(t)$ the maximum amplitude of the transient periodic temperature distribution, $\Delta T(t_h)$ the value of $\Delta T(t)$ at $t = t_h$, τ the relaxation time of $\Delta T(t)$, and q the modulus of the grating vector

$$q = 2\pi/\Lambda \qquad (2)$$

The grating constant Λ can be determined by the equation

$$\Lambda = \frac{\lambda_h}{2\sin(\theta/2)} = \frac{\lambda_h}{\theta} \quad (\theta \sim 0) \qquad (3)$$

Λ is typically around 50 μm, which corresponds to an intersection angle θ of about 0.55°. The time constant τ characterising the relaxation of the thermal grating is

$$\tau = 1/a q^2 \qquad (4)$$

where a is the thermal diffusivity of the liquid sample.

Due to the volume thermal expansion of the sample, the spatially periodic temperature distribution produces a corresponding modulation of refractive index $\Delta n(t) = (\partial n/\partial T)\Delta T(t)$, which acts as an optical grating. A He-Ne laser (λ_p=632.8 nm) serves as the probing laser for detecting the grating. According to diffraction theory [1-3], the intensity of the first-order diffracted beam at a sufficiently thin sample of thickness d is proportional to the square of the maximum phase variation of the grating, $\phi_m(t)$, which is written as

$$\phi_m(t) = \frac{2\pi d \Delta n(t)}{\lambda_p} = \frac{2\pi d}{\lambda_p}\left(\frac{\partial n}{\partial T}\right)\Delta T(t) \tag{5}$$

The time dependence of the diffracted intensity $I_1(t)$ after the heating pulse is therefore

$$I_1(t) \propto \phi_m(t)^2 \propto \left[\frac{2\pi d}{\lambda_p}\left(\frac{\partial n}{\partial T}\right)\Delta T(t)\right]^2 \propto e^{-2t/\tau} \qquad t > t_h \tag{6}$$

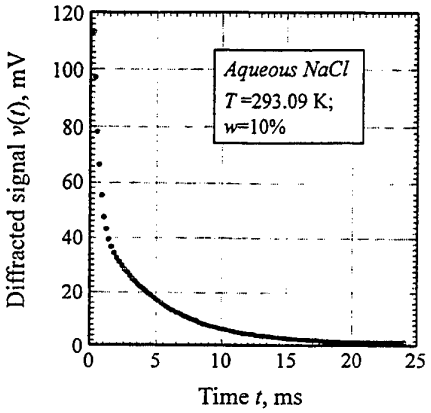


Fig. 2 Decay data for the diffracted signal for an aqueous solution of sodium chloride with a weight fraction of 10% NaCl at 293.09 K (only 133 of the 4000 registered data points are plotted here for clarity)

The time constant $\tau/2$ can subsequently be evaluated with which the diffracted intensity decays exponentially. The thermal diffusivity a of the sample is then determined as

$$a = 1/\tau q^2 \tag{7}$$

In the present measurement, the modulus q of the grating vector is determined by measuring the diffraction angle θ_1 instead of the intersection angle θ of the two heating laser beams

$$q = \frac{2\pi}{\lambda_p}\sin\theta_1 \tag{8}$$

The accuracy of the determination of θ_1 and q is estimated to be better than $\pm 0.55\%$ [4].

The intensity of the first-order diffracted beam is measured in the homodyne scheme with a photomultiplier tube (PMT) exactly at the measured diffraction angle θ_1. The output signal v(t) from the PMT is then amplified and recorded by a transient recorder. The relaxation time τ can thus be determined by fitting the acquired data for v(t) to Eq. (6) with the least-squares method.

In the measurements of aqueous salt solutions, the time dependence $v(t)$ of the diffracted signal seems to decay exponentially as in the case of pure liquids (see Fig. 2); however, it cannot be analysed with Eq. (6) to determine the relaxation time τ. Due to the Soret effect, the laser-induced periodic distribution of temperature leads to the

phenomenon of phase separation, i.e. a concentration grating, which is superposed upon the thermal grating and decays far more slowly compared with the thermal grating. In this case, the maximum phase variation $\phi_m(t)$ of the optical grating in Eq. (6) has to be modified as the sum of two terms [5]

$$\phi_m(t) = \phi_{\text{thermal}}(t) + \phi_{\text{concen.}}(t) \tag{9}$$

Here, $\phi_{\text{thermal}}(t)$ denotes the phase variation of the thermal grating and decays exponentially with the relaxation time τ. $\phi_{\text{concen.}}(t)$ is the phase variation of the concentration grating and has a life time of one to two orders of magnitude longer than the thermal grating. The diffracted signal can thus be modified and reduced to

$$v(t) \propto I_1(t) \propto \phi_m^2(t) = \left[\phi_{\text{thermal}}(t) + \phi_{\text{concen.}}(t)\right]^2 = \left(A e^{-t/\tau} + B t + C\right)^2 \tag{10}$$

To determine the relaxation time τ, we first take the square root of the measured data for $v(t)$ and fit the acquired data to

$$\sqrt{v(t)} \propto \sqrt{I_1(t)} \propto A e^{-t/\tau} + B t + C \tag{11}$$

with the standard non-linear least-squares method of Marquardt and Levenberg [5, 6]. The accuracy of the relaxation-time evaluation is estimated to be 3% [5].

3. MEASUREMENT RESULTS AND DISCUSSION

Using the laser-induced thermal grating technique, the thermal diffusivity of aqueous solutions of inorganic salts, such as sodium chloride and magnesium chloride, has been measured at atmospheric pressure and in an extended range of temperature, 293 – 373 K. The aqueous solutions had weight fractions of 5, 10, 15, and 20% salts.

Note that the intensity $I_1(t)$ of the first-order diffraction is inversely proportional to the square of the thermal conductivity λ of the liquid sample [1]. In consequence, it is usually difficult to obtain an adequate signal-to-noise ratio for the determination of the relaxation time τ, when measurements are taken on a liquid sample of relatively high thermal conductivity, e.g., water or aqueous solutions of salts. To intensify the diffracted signal, it is necessary to increase the heating pulse duration time t_h properly, e.g., to around 1000 μs in this work. However, an excessive increase in t_h will lead to a high initial temperature amplitude $\Delta T(t_h)$ of the thermal grating, which will in turn cause a large value of the maximum phase variation $\phi_m(t)$ of the optical grating [1]. Consequently, the basic theory of the thermal grating is no longer valid, and a distortion of the ideal experiment will arise and thereby lead to an error. Therefore, the heating pulse duration time must be controlled in experiments to obtain a small $\phi_m(t)$ and in the meantime a sufficiently strong diffracted signal.

The experimental results for the thermal diffusivity of aqueous solutions of sodium chloride and magnesium chloride are presented in Figures 3 and 4, respectively. The values for the thermal diffusivity a in Figures 3 and 4 are averages obtained from 10 independent measurements, the reproducibility of which is better than 3%. A comparison between the experimental results in this work and the thermal-diffusivity values found in [7] is also shown in the two figures. The thermal-diffusivity values for aqueous NaCl at 293 K and aqueous $MgCl_2$ at 294 K reported in [7] agree with the corresponding experimental results in this work within 3%.

As there have been few experimental data on the thermal diffusivity of aqueous NaCl and $MgCl_2$ reported up to now, we found the density ρ and the specific heat capacity c_p data for both aqueous solutions available in [8, 9] and derived the thermal conductivity of aqueous NaCl and $MgCl_2$ using the measured thermal diffusivity values in this work

$$\lambda = a \rho c_p \tag{12}$$

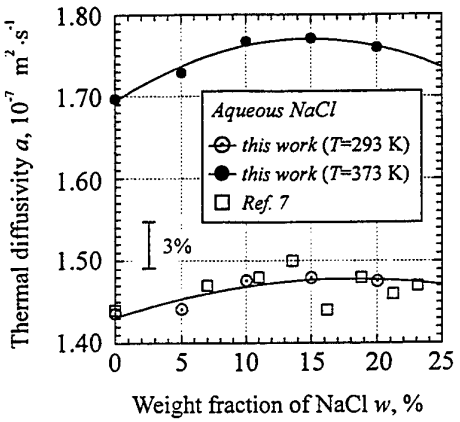


Fig. 3. Thermal diffusivity a of aqueous solutions of NaCl at 293 K and 373 K as a function of weight fraction w of the solute.

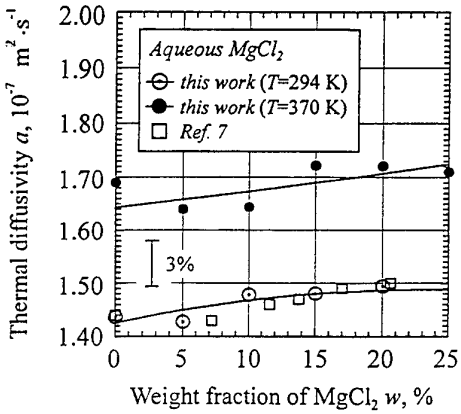


Fig. 4. Thermal diffusivity a of aqueous solutions of $MgCl_2$ at 294 K and 370 K as a function of weight fraction w of the solute.

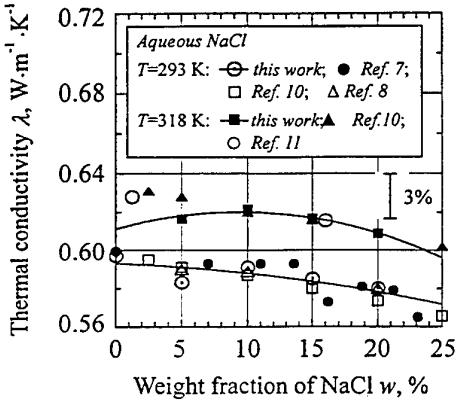


Fig. 5. Thermal conductivity λ of aqueous solutions of NaCl at 293 K and 318 K as a function of weight fraction w of the solute.

Figures 5 and 6 depict the thermal conductivity λ of other investigators for aqueous solutions of sodium chloride and Magnesium chloride and the calculated thermal-conductivity values. As shown in Figures 5 and 6, the thermal-conductivity data from Refs. [7, 8, 10 and 11] agree with the calculated values within 3%.

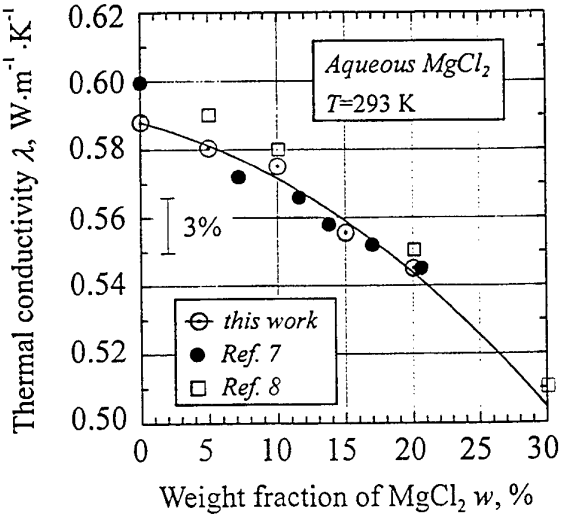


Fig. 6. Thermal conductivity λ of aqueous solutions of $MgCl_2$ at 293 K as a function of weight fraction w of the solute.

ACKNOWLEDGMENTS

The authors gratefully acknowledge the financial support of the work by the Deutsche Forschungsgemeinschaft (DFG) under Grant Fi. 139/41-4.

REFERENCES

1. Y. Nagasaka, T. Hatakeyama, M. Okuda, and A. Nagashima, Rev. Sci. Instrum. **59**(7), pp. 1156-1168 (1988).
2. G. Wu, M. Fiebig, and J. Wang, Fluid Phase Equil. v. 88, pp. 239-249 (1993).
3. H. J. Eichler, P. Günter, and D. W. Pohl, *Laser-Induced Dynamic Gratings*, Springer-Verlag (1986).
4. J. Wang, *Messung der Temperaturleitfähigkeit von Flüssigkeiten mittels laserinduzierter thermischer Gitter*, VDI-Verlag (1995).
5. J. Wang and M. Fiebig, Int. J. Thermophys. **19**(1), pp. 15-25 (1998).
6. W. H. Press et al., *Numerical recipes in Fortran*, Cambridge University Press (1992).
7. Verein Deutscher Ingenieure, *VDI-Wärmeatlas*, VDI-Verlag (1994).
8. W. Blanke, *Thermophysikalische Stoffgrößen*, Springer-Verlag (1989).
9. R. H. Perry and D. Green, *Perry's Chemical Engineer's Handbook*, McGraw-Hill (1984).
10. I. M. Abdulagatov and U. B. Magomedov, Int. J. Thermophys. **15**(3), pp. 401-412 (1994).
11. Maria L. V. Ramires et al., J. Chem. Eng. Data v. 39, pp. 186-190 (1994).

EXPERIMENTAL EVALUATION OF RADIATION REFLECTION CHARACTERISTICS OF REAL SURFACES FOR HEAT TRANSFER COMPUTATION

Toshiro Makino, Hidenobu Wakabayashi and Shin-ya Okada
Department of Engineering Physics and Mechanics Kyoto University
Email: a50141@sakura.kudpc.kyoto-u.ac.jp; Fax.:81-75-771-7286

Keywords: radiation energy exchange, bidirectional reflectance, measure of specular reflection, reflection characteristics modelling, surface roughness

ABSTRACT. This paper aims to clarify thermal radiation reflection characteristics of rough surfaces and to establish a technique for determining the parameters for heat transfer computation of radiation energy exchange among surfaces. Directional distribution of bidirectional reflectance ρ of metallic surfaces of root-mean-square roughness Σ=0.1~1 to the irradiation of a visible laser of wavelength λ=0.6328 μm and to that of an infrared laser of λ=3.39 μm is investigated experimentally. The optical roughness (Σ/λ) ranges from 0.028 to 1.27. A measure of specular reflection is presented. A model for describing the ρ -distribution is presented, and the experimental results of the ρ -distribution are analyzed to drive the values of input parameters for heat transfer computation quantitatively and systematically.

1. INTRODUCTION

Figure 1 explains a subject of thermal engineering for dealing with radiation energy exchange among surfaces. There are a number of surfaces, each of which emits radiation and reflects or absorbs radiation incident on the surface. Radiation emitted or reflected on a surface turns to incident radiation onto other surfaces. Knowledge of directional characteristics of reflection of surfaces is important for such a problem. Real surfaces in industrial and natural environments reflect the incident radiation more or less diffusely. The reflected energy distributes directionally as shown by a ⊸ curve in Figure 1. In the traditional heat transfer computation such reflection had been dealt most crudely with an assumption of perfect-diffuse reflection, which is illustrated by a dash line circle in Figure 1, to manage the reflection with configuration factors. With a backup of recent advance in computer technology, directional characteristics of reflection have become to be considered in a minimum size [2] by the summation of the specular reflection component R_S and the prefect-diffuse reflection component R_d which are represented by an arrow and by a solid line circle, respectively, in Figure 1. However, a good technique had not been presented for evaluating the values of R_s and R_d of individual real surfaces. Recently the authors [3] investigated directional distribution of bidirectional reflectance ρ of rough metallic surfaces experimentally and presented a technique for evaluating R_s and R_d on the basis of the experimental results of ρ -distribution. The authors [4] also presented a technique for analyzing the results of a simplified ρ -measurement to determine the values of R_s and R_d within an allowable order of inaccuracy. But, the rough surfaces in the previous works [3,4] were not strongly specular ones. It means first that the specimen surfaces were rough geometrically compared with slightly rough surfaces which appear in current in thermal engineering applications. It means second that the wavelength of incident radiation in the previous study was a visible one

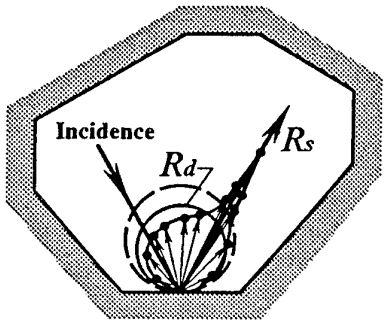


Figure 1. Radiation energy exchange among surfaces

while the rough surface with the same geometrical roughness behaves more specularly to the radiation of a longer wavelength in the infrared region, which is more important in thermal engineering.

In the present paper we extend the previous study to more specular-reflecting surface wards. First, directional distribution of bidirectional reflectance ρ is investigated experimentally to clarify the reflection characteristics. Second, a modelling technique is established to interpret the characteristics to a form of input parameters R_s and R_d of heat transfer computation of radiation energy exchange among the surfaces. Since real surfaces are more or less diffuse and more or less specular, we adopt, in this paper, adjective terms of 'perfect-specular' and 'perfect-diffuse' for ideally specular and ideally diffuse characteristics, respectively.

2. EXPERIMENTAL PROCEDURE

2.1 Rough Surface

Rough surface specimens are prepared of JIS-SUS304 austenite stainless steel plates. The plates are ground and polished to realize optically smooth surfaces of a maximum roughness less than 30 nm. The smooth surfaces are hand-ground by a wet-grinding technique with grinding powders of JIS-meshes 240, 400, 800, 1500 and 3000 so that the surfaces can have isotropic microgeometry. Microprofiles of the rough surfaces are measured by a stylus technique to know the root-mean-square roughness Σ and the self-correlation length τ_0 of the rough surface. Figure 2 shows the results of the measurement. A strong 1st-order correlation of Σ and τ_0 is noticed in this figure. The correlation coefficient is 0.96. Such strong correlation has been emphasized in the previous study [3]. It suggests us a direction for choosing representative specimens of rough surfaces for radiation characteristics investigation. We can put rough surfaces in order by considering either Σ or τ_0. In the present experiment for radiation characteristics, we choose three specimens of the rough surfaces in Figure 2. The three surfaces are those ground with grinding powders of JIS-meshes 240, 400 and 3000. Aluminum of 99.99 % in purity is vacuum-deposited thickly on the surfaces so that the film can trace the microgeometry of the substrate. Table 1 shows the values of parameters Σ and τ_0 for microgeometry of the three rough surface specimens.

2.2 Energy Distribution of Reflected Radiation

In the radiation reflection experiment we measure the directional distribution of reflected energy for incidence of a helium-neon laser whose wavelength λ of radiation in vacuum is 0.6328 μm in the visible (vis) region, and that for incidence of another helium-neon laser whose wavelength is 3.39 μm in the infrared (ir) region. The visible laser emits linearly polarized radiation and the output instability is less than ±0.5 %. On the other hand, the infrared laser emits randomly polarized radiation and the output instability is of an order of ±5 %. Therefore, in the visible measurement, reflection for s-polarized radiation incidence and that for p-polarized radiation incidence are measured to be averaged. In the infrared measurement, the output of the laser is monitored throughout the radiation measurement course to correct the measured data. Structure of the experimental set-up is the same in principle as that for the previous study [3]. The zenithal angle θ_I of incidence is set at 0, 20, 40 and 60°. The azimuthal angle θ_i of incidence is defined as $\theta_i = 0°$, since the specimens are isotropic in the surface microgeometry. The reflection measurement, except for the case of $\theta_i = 0°$, is made at 77~85 directions of reflection on each specimen and each θ_I.

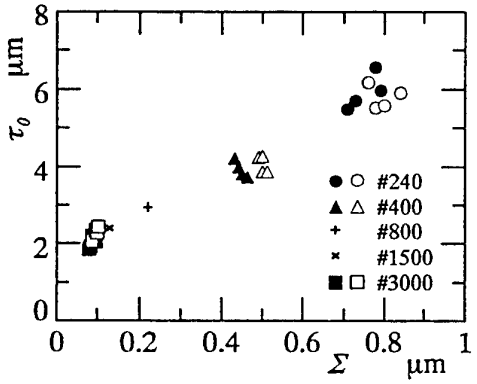


Figure 2. Parameters Σ and τ_0 for microgeome - try of rough surfaces

Table 1. Parameters for Microgeometry of Rough Surfaces

specimen No.	Σ μm	τ_0 μm	Σ/λ
1(vis)	0.802	5.80	1.27
2(vis)	0.513	4.05	0.811
3(vis)	0.0954	2.15	0.151
1(ir)	0.802	5.80	0.237
2(ir)	0.513	4.05	0.151
3(ir)	0.0954	2.15	0.0281

The directions are designated by the zenithal angle θ_R and azimuthal angle ϕ_R of reflection. The measurement points (directions) are distributed densely in the vicinity of the specular reflection direction. The measurement is abbreviated in the symmetrically equivalent directions for the present surfaces with isotropical microgeometry. In the case of $\theta_I = 0°$the number of measurement points is 9 on the incidence plane of $\theta_I = 0°$. Reflection for $\theta_I = \theta_R = 0°$ can not be measured by the present experimental set-up, and that for $\theta_I = \theta_R = 5°$ is measured to substitute the datum to that for $\theta_I = \theta_R = 0°$.

Radiation scattering on rough surfaces is characterized by the surface microgeometry and the wavelength λ of radiation which is interfered by the surface microgeometry. The microgeometry is represented by the roughness Σ as mentioned in section 2.1. Accordingly, the optical length (Σ/λ) can be a measure for the radiation characteristics of rough surfaces [5,6]. Table 1 shows the values of (Σ/λ) and names the specimens such as Specimen 1(vis) and Specimen 2(ir). In the present experiment we investigate the radiation characteristics of substantially six specimens in Table 1. It is natural to consider that the measure (Σ/λ) remains to be only a measure since the optical constant of the surface material depends on the wavelength of radiation.

3. EXPERIMENTAL RESULTS AND DISCUSSION

3.1 Bidirectional Reflectance

Figure 3 shows the experimental results of directional distribution of bidirectional reflectance ρ. In this figure ρ is plotted above a plane of $\sin\theta_R$ for the zenithal angle θ_R and the azimuthal angle ϕ_R of reflection respectively in the radial and circumfential directions. The incident radiation is incident from a direction of $\sin\theta_R$ and $\phi_R = \pi$. The partial volume between the curved surface of ρ and the $(\sin\theta_R - \phi_R)$ plane is proportional to the energy reflected in a partial solid angle in the direction of (θ_R, ϕ_R). In the case of perfect-diffuse perfect reflector (hemispherical reflectance $R_H = 1$ and ρ =const.), the ρ -distribution results in a cylinder of height $(1/\pi)$ in this plot. In the case of perfect-specular perfect reflector ($R_H = R_s = 1$ and ρ =const.), the ρ -distribution results in a needle of volume 1 and thickness 0. Numbers put near the peaks of the curved surfaces in the figure indicate the

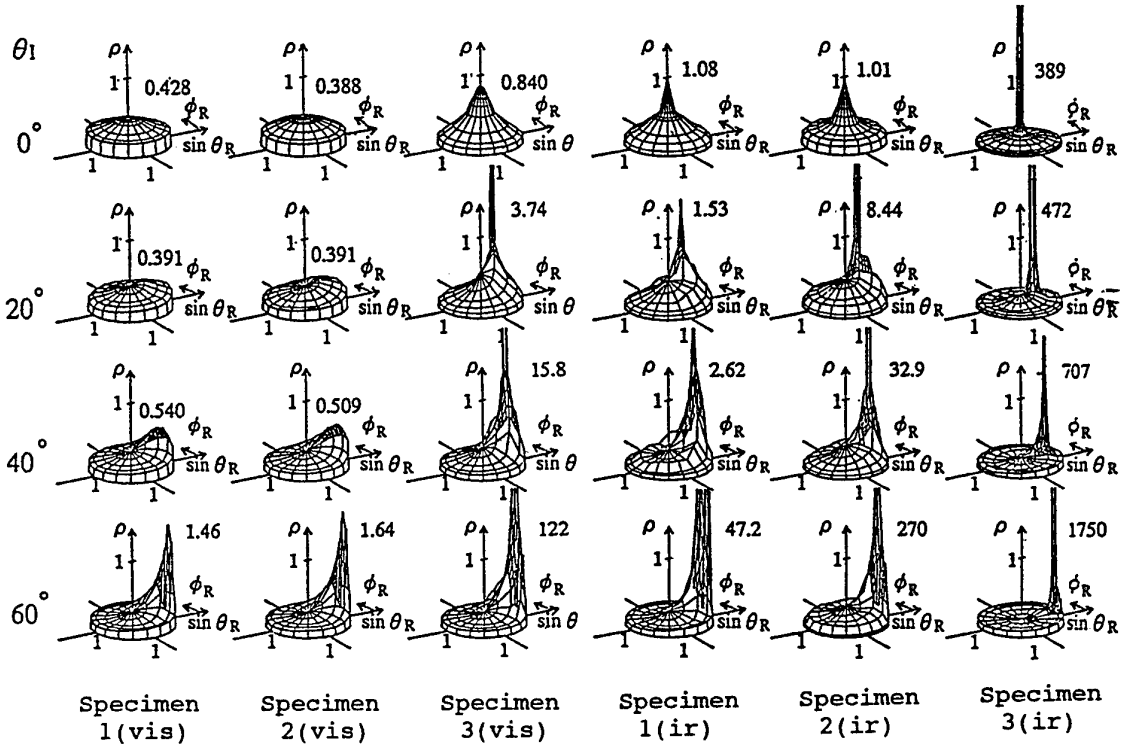


Figure 3. Directional distribution of bidirectional reflectance ρ

maximum values of ρ. Measurement points for (θ_R , ϕ_R) correspond to the crosspoints of the longitude and latitude lines on the curved surfaces. The optical roughness (Σ/λ) is larger in order of Specimens 1(vis), 2(vis), 1(ir), 3(ir), 2(ir) and 3(ir).

Roughly speaking, the peak of specular reflection grows sharper with a decrease of optical roughness (Σ/λ). The peak is sharper in the case of oblique incidence. Particularly in the cases of Specimen 3(ir) and Specimens 3(vis) and 2(ir) for θ_I =60° the peaks are extremely sharp, and the number of measurement points does not seem to be enough to trace the profile of the curved surface of ρ. As was pointed out in the previous study [3], the direction of maximum reflection energy is the specular direction of the zenithal angle $\theta_R = \theta_{Rmax} = \theta_I$ and the azimuthal angle θ_R =0°, in which ($\rho \cos\theta_R$) is maximum. The zenithal angle of maximum ρ is located at other angle than θ_{Rmax}.

3.2 Measure of Specular Reflection

In order to describe the specular reflection profile quantitatively, we carry out an additional series of experiment on each specimen and on each incident angle. Figure 4 explains the experiment. In this experiment, ($\rho \cos\theta_R$) which is proportional to reflection energy is measured in the plane of ϕ_R =0° and in the vicinity of the specular direction to find two angles of θ_R at which $\rho \cos\theta_R = (\rho \cos\theta_R)_{max}/2$. Difference of the two angles is denoted by α_h. Here we define a measure of specular reflection by,

$$K = (\rho \cos\theta_R)_{max}/\alpha_h \qquad (1)$$

This measure represents the gradient of the sharp peak of specular reflection. Figure 5 shows measured results of K. It should be noticed that both of the measure K and the optical roughness (Σ/λ) are plotted in a logarithmic scale system. The figure suggests that directional distribution of reflection can be classified roughly into three regions. Namely, in Region 1 of small (Σ/λ), K is high irrespective of the incident angle θ_I, and reflection is most specular. On the other hand, in Region 3 of large (Σ/λ), K is low irrespective of θ_I. In Region 2 of the intermediate (Σ/λ), K depends strongly on θ_I.

3.3 Models for Directional Distribution of Reflection

We show two models for the description of directional distribution of bidirectional reflectance ρ, in which reflectance ρ consists of two components: specular reflection component ρ_S and perfect-diffuse reflection component ρ_d. Reflectance ρ is written by $\rho = \rho_s + \rho_d$.

3.3.1 AND model. We have presented a model [3] for describing the ρ-distributions of rough surfaces which are in the intermediate region of specular-reflecting and perfect-diffuse-reflecting. On the specular component ρ_s, the model approximates the distribution of ($\rho_S \cos\theta_R$) above the ($\sin\theta_R$-ϕ_R) plane by an anisotropic body of rotation of the normal distribution function. On the perfect-diffuse component ρ_d, the model approximates the distribution of ρ_d above the ($\sin\theta_R$-ϕ_R) plane simply by a circular column of constant

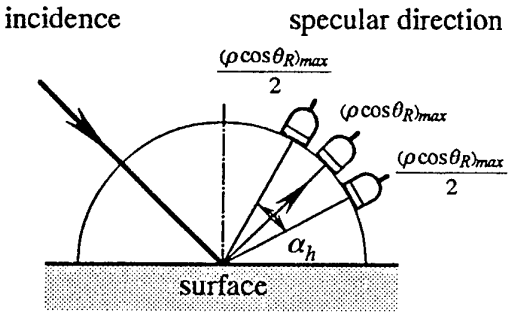


Figure 4. Measure K of specular reflection

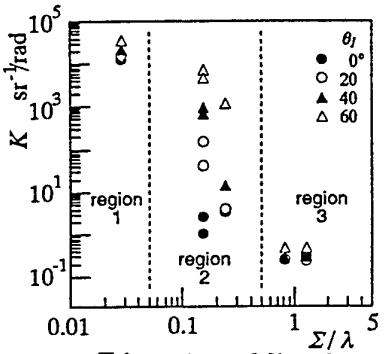


Figure 5. (Σ/λ) regions of directional distribution of reflection

ρ_d Provided the surface, the wavelength λ and incident angle θ_I of incident radiation are specified, the ρ-distribution is described as a function of θ_R and ϕ_R and with four kinds of parameters A, σ, ρ_d, and θ_{Rmax}. The equations are as follows:

$$\rho = \rho(\theta_R, \phi_R; A, \sigma, \rho_d, \theta_{Rmax}) \tag{2}$$

$$= \rho_s + \rho_d \tag{3}$$

$$\rho_s \cos\theta_R = A \exp\{-f^2/(2\sigma^2)\} \cos\{(\pi/2)(f/g)^2\} \tag{4}$$
at $(\theta_R, \phi_R) = (\theta_{Rmax}, 0)$,

$$f = 0, \quad g = (\text{real number}) \neq 0 \tag{5}$$
at $(\theta_R, \phi_R) \neq (\theta_{Rmax}, 0)$,

$$f = (p^2 + q^2)^{1/2} \tag{6}$$

$$g = \{-kp + (f^2 - k^2q^2)^{1/2}\}/f \tag{7}$$

$$p = \sin\theta_R \cos\phi_R - \sin\theta_{Rmax} \tag{8}$$

$$q = \sin\theta_R \sin\phi_R \tag{9}$$

$$k = \sin\theta_{Rmax} \tag{10}$$

where ρ_s is a function of θ_s and ϕ_R, and ρ_d is a constant independent of θ_R nor ϕ_R. By using this model the specular reflection component R_s and the perfect-diffuse component R_d of the directional-incidence hemispherical reflectance R_H are readily calculated. This model, which we call 'AND model' (anisotropic body of rotation of normal distribution function model) in the following, seems to be applicable to the description of the ρ -distributions of surfaces in Regions 2 and 3 in Figure 5.

3.3.2 Circular cone model. For the ρ -distribution of surfaces in Region 1, a new model should be presented to describe the sharp specular peaks. The model can be a crude one, because fine description of the sharp profiles of the peaks is meaningless in thermal engineering applications. We present a model for strongly specular surface in Region 1 in Figure 5. The new model approximates the specular reflection peak of $(\rho \cos\theta_R)$ curved surface above the $(\sin\theta_R\text{-}\phi_R)$ plane to a circular cone of height $(\rho \cos\theta_R)_{max}$ and bottom radius α_h, Provided the surface, the wavelength λ and incident angle θ_I of incident radiation are specified, the ρ-distribution is described as a function of θ_R and ϕ_R and with three kinds of parameters $(\rho \cos\theta_R)_{max}$, α_h and ρ_d. The equations are as follows:

$$\rho = \rho(\theta_R, \phi_R; (\rho \cos\theta_R)_{max}, \alpha_h, \rho_d) \tag{11}$$

$$= \rho_s + \rho_d \tag{12}$$

$$\rho_s \cos\theta_R = (\rho \cos\theta_R)_{max}(1 - \alpha/\alpha_h) \quad (0 \le \alpha \le \alpha_h) \tag{13}$$

$$\rho_s \cos\theta_R = 0 \quad (\alpha > \alpha_h) \tag{14}$$

where ρ_s is a function of θ_R and ϕ_R, and ρ_d is a constant independent of θ_R and ϕ_R. Quantity α is a valuable corresponding to the open zenithal angle around the specular reflection direction. The specular reflection component R_s and the perfect-diffuse component R_d of the hemispherical reflectance R_H are easily calculated also by this model. This model, which we call 'circular cone model' in the following, seems to be applicable to the direction of the ρ -distribution of surfaces in Region 1 in Figure 5.

3.4 Analysis of Directional Distribution of Reflection

We analyze the experimental results of ρ -distribution in Figure 3 on bases of the above two models. A best-fit technique is applied to determine the parameters for the models.

3.4.1 Not-strongly specular surfaces. For the not-strongly specular surfaces in Regions 2 and 3 in Figure 5, we examine the AND model. In this case, the zenithal angle θ_{Rmax} where ($\rho \cos\theta_R$) is maximum was known in the previous work [3] to agree with the zenithal angle θ_I of incidence. So that, we presume the value of θ_{Rmax} to be known and analyze the experimental results of ρ -distribution to determine the three parameters in the equation,

$$\rho = \rho\,(A, \sigma, \rho_d) \tag{15}$$

The objective function for the best-fit analysis is set as,

$$F = \sum_j w_j \{(\rho\cos\theta_R)_j^{calc} - (\rho\cos\theta_R)_j^{exp}\}^2 \tag{16}$$

$$w_j = \Delta\Omega_j / \sum_j \Delta\Omega_j \tag{17}$$

where j corresponds to each measurement point, and superscripts *exp* and *calc* denote the experimental and calculated values, respectively. The coefficient w_j is the weight for each measurement point, which is given so that it is proportional to the solid angle $\Delta\Omega_j$ represented by the point. The value of objective function F defined in Equations (16) and (17) corresponds to the mean deviation between experimental and calculational values of ($\rho \cos\theta_R$). In this analysis we apply a condition that the value of hemispherical reflectance R_H calculated by the model equations should agree with the value calculated by the integration of the experimental values of ρ. Mathematically speaking, a two-dimensional best-fit analysis is carried out substantially. Table 2 shows the results of the analysis for the parameters A, σ and ρ_d. The table also shows the values of F. These values are shown on lines without the indication $\downarrow$ in the table. By using the determined parameters of A, σ and ρ_d, reflection components R_s and R_d are calculated by,

$$R_S = \int_{-\pi}^{\pi} \int_0^{\pi/2} \rho_S \cos\theta_R \sin\theta_R \, d\theta_R \, d\phi_R \tag{18}$$

$$R_d = \pi\rho_d \tag{19}$$

Hemispherical reflectance R_H satisfies the equation,

$$R_H = R_s + R_d \tag{20}$$

Table 2 includes values of R_s, R_d, R_H and (R_s/R_H).

3.4.2 Strongly specular surfaces. For strongly specular surfaces in Region 1 in Figure 5, we examine the circular cone model. In this model since the direction where is no specular reflection is specified explicitly in Equation (14), ρ_d is determined by a one-dimensional analysis so that the reflected energy over the directions can agree between experimental and calculated values. We adopt an equation,

$$\sum_j (\rho\cos\theta_R)_j^{calc} \Delta\Omega_j = \sum_j (\rho\cos\theta_R)_j^{exp} \Delta\Omega_j \tag{21}$$

This equation includes only an unknown quantity of the parameter ρ_d. It is solved numerically on ρ_d. The solid angle $\Delta\Omega_j$ is given in a same manner as in the case of the analysis by the AND model. The reflectance R_s is described by,

$$R_S = \int_{-\pi}^{\pi} \int_0^{\pi/2} \rho_S \cos\theta_R \sin\theta_R d\theta_R d\phi_R$$
$$= \int_0^{\alpha} (\rho_S \cos\theta_R)_{max} (1 - \alpha/\alpha_h) \cdot 2\pi \sin\alpha \cdot d\alpha \quad (22)$$

In the case of strongly specular surface, α_h is small and sin α=α. Specular reflection component R_s is approximately written by,

$$R_S = \frac{\pi}{3} (\cos\theta_R)_{max} \alpha h^2 \quad (23)$$

The value of R_s is calculated directly by this equation using experimentally determined values of $(\rho \cos\theta_R)_{max}$ and α_h. Diffuse reflection component R_d is calculated by Equation (19) using the value of rd determined above. Hemispherical reflectance R_H is calculated by Equation (20). The value of R_H is not an experimental value as was the case in the analysis in section 3.4.1 for the AND model. Values of the determined parameters $(\rho \cos\theta_R)_{max}$, α_h and r_d are shown in Table 2. The values in lines with indication ↓ correspond to the results of the analysis by the circular cone model. This table includes the values of F which is a measure of fitting for Equation (21) and those of R_s, R_d, R_H and (R_s/R_H).

Table 2. Parameters for Radiation Heat Transfer Computation

specimen No.	θ_I↓ °	A sr^{-1}	σ	ρ_d sr^{-1}	F sr^{-1}	R_S	R_d	R_H	R_S/R_H
1(vis)	0	0.19	0.41	0.22	0.004	0.21	0.71	0.91	0.23
	20	0.17	0.44	0.19	0.009	0.20	0.60	0.80	0.25
	40	0.24	0.45	0.17	0.010	0.25	0.54	0.80	0.32
	60	0.36	0.38	0.14	0.023	0.28	0.46	0.74	0.38
2(vis)	0	0.21	0.62	0.17	0.002	0.36	0.54	0.91	0.40
	20	0.21	0.57	0.15	0.006	0.33	0.47	0.80	0.41
	40	0.27	0.49	0.14	0.010	0.35	0.45	0.80	0.44
	60	0.42	0.36	0.14	0.021	0.30	0.45	0.75	0.40
3(vis)	0	0.60	0.28	0.16	0.022	0.36	0.53	0.89	0.41
	20	0.60	0.26	0.17	0.065	0.31	0.55	0.86	0.36
	40	0.60	0.30	0.16	0.46	0.38	0.53	0.91	0.41
	60	*0.94*	*0.19*	*0.27*	*3.9*	*0.30*	*0.88*	*1.18*	*0.26*
	↓	*61.0*	*0.013*	*0.25*	*0.16*	*0.01*	*0.79*	*0.80*	*0.01*
1(ir)	0	0.50	0.26	0.17	0.031	0.27	0.56	0.82	0.33
	20	0.48	0.33	0.13	0.032	0.37	0.41	0.78	0.47
	40	0.77	0.20	0.17	0.049	0.26	0.53	0.80	0.33
	60	1.67	0.13	0.14	0.37	0.31	0.46	0.76	0.40
2(ir)	0	0.64	0.17	0.21	0.015	0.15	0.68	0.83	0.18
	20	0.43	0.30	0.17	0.071	0.28	0.54	0.83	0.34
	40	0.69	0.17	0.18	0.39	0.18	0.57	0.75	0.24
	60	*0.94*	*0.15*	*0.21*	*1.33*	*0.22*	*0.68*	*0.90*	*0.24*
	↓	*135*	*0.018*	*0.25*	*0.14*	*0.05*	*0.78*	*0.82*	*0.06*
3(ir)	0	↓ 389	0.031	0.098	0.036	0.38	0.31	0.69	0.55
	20	↓ 444	0.027	0.10	0.053	0.34	0.32	0.66	0.52
	40	↓ 542	0.025	0.094	0.054	0.35	0.30	0.65	0.54
	60	↓ 875	0.024	0.090	0.041	0.55	0.28	0.83	0.66

specimen No.	θ_I °	$(\rho\cos\theta_R)_{max}$ sr^{-1}	α_h rad	ρ_d sr^{-1}	F sr^{-1}	R_S	R_d	R_H	R_S/R_H

As seen in Table 2, the ρ -distributions of two cases shown by italic letters, in which considerably specular specimens are obliquely irradiated, are analyzed by the above two models. It is found that the results of analyses by both models failed. The AND model could not describe the profiles of the sharp peaks of specular reflection and the F values result in large ones. On the other hand, by the circular cone model the thick foot skirts of the peaks, which should have been attributed to the specular component R_s, have been absorbed by the perfect-diffuse component R_d, and too small R_s values have been resulted in.

3.4.3 Parameters for radiation transfer computation. Experimental results of ρ-distributions in Figure 3 impress us the difference in the sharpness of the specular reflection peaks. The measure K defined in section 3.2 can calibrate the sharpness. On the other hand, above two models deal the volumes of ρ -structures in Figure 3. And the reflectance components R_s and R_d are separated by a criterion whether the reflection is isotropic or not, which fits the thermal engineering policy. The R_s values in Table 2 are lower and scattered than our impression of Figure 3.

Through the above discussion in this section 3, performances of the AND model described by Equations (3)~(10) and the circular cone model described by Equations (12)~(14) have been demonstrated. It may be concluded that in most cases we can determine the parameters R_S and R_d for radiation heat transfer computation which considers the directional characteristics of reflection of rough surfaces in a minimum size. The exceptional cases which combination of the two model can not cover up are those of considerably specular surfaces of (Σ/λ)~0.1 with oblique irradiation. Further development of new models is desirable to deal with the exceptional cases, but two points should be pointed out relating to actual heat transfer computations in the present stage. The first point is that the incident radiation onto the surface is also more or less diffuse as well as the reflected radiation is. The second point is that round values of R_s and R_d are adopted for each θ_I band and each wavelength band in the heat transfer computation. From an engineering point of view, crude techniques are more suitable than sophisticated and accurate ones.

4. CONCLUSIONS

We have investigated an experimental technique for evaluating radiation characteristics of real surfaces of metals for heat transfer computation. Concluding remarks are as follows:

1) Root-mean-square-roughness Σ and self-correlation length τ_0 of rough metallic surfaces have a strong correlationship. The surface microgeometry is represented by Σ in this case.
2) A quantity K defined by Equation (1) can be a good measure of specular reflection.
3) Performance of the AND model (in section 3.3.1) is demonstrated in the description of directional distribution of reflection of not-strongly specular surfaces of an order of optical roughness $(\Sigma/\lambda)>0.1$.
4) For the description of directional distribution of reflection of strongly specular surfaces of an order of $(\Sigma/\lambda)<0.1$, the newly presented circular cone model is preferable.
5) By using the model techniques of 3) and 4) we can determine parameters R_S and R_d for radiation heat transfer computation in most cases of rough surfaces in a wide range of (Σ/λ).

ACKNOWLEDGMENT

The authors acknowledge Mr. K. Yuasa, an undergraduate student of Kyoto University for his collaboration in the course of this work. This work was/is partially supported by Grant-in-Aid for Scientific Research of The Ministy of Education, Science, Sports and Culture, Japan (No.(B)(2)10555068), and by Special Coordination Funds for Promoting Science and Technology, Japan (Research on Measurement Technology and Reference Materials for Thermophysical Properties of Solids).

REFERENCES

1. R. Siegel and J. R. Howell, *Thermal Radiation Heat Transfer*, 3rd ed., Chaps.6-8, Taylor & Francis Pub., Bristol, (1992).
2. S. Maruyama, "Radiation Heat Transfer between Arbitrary Three-Dimensional Bodies with Specular and Diffuse Surfaces", *Numerical Heat Transfer*, part A, vol.24, pp.181-196, (1993).

3. T. Makino, A. Nakamura and H. Wakabayashi, "Directional Characteristics of Radiation Reflection on Rough Metal Surfaces with Evaluation of Radiation Heat Transfer Parameters", *Proceedings of the 5th Asian Thermophysical Properties Conference*, Seoul, vol.2, pp.471-474, (1998).
4. S. Okada, H. Wakabayashi and T. Makino, "Directional Characteristics of Radiation Reflection on Rough Metal Surfaces with Description of Heat Transfer Parameters (Second Report)", *Proceedings of the 19th Japan Symposium on Thermophysical Properties*, Fukuoka, pp.83-86, (1998).
5. T. Makino and K. Kaga, "Scattering of Radiation on Rough Surface Modelled by Three-Dimensional Super-Imposition Technique", *JSME International Journal*, ser.B, vol.37, no.4, pp.904-911, (1994).
6. T. Yoshida, S. Tanaka and T. Makino, "A New Ellipsoidal Mirror-Type Reflectometer for Measuring Normal-Incident Hemispherical Reflectance Spectrum", *JSME International Journal*, ser.B, vol.36, no.1, pp.166-171, (1993).

THERMAL CONDUCTIVITY OF FIBER-FILLED AEROGELS

G. R. Cunnington and S. C. Lee
Applied Sciences Laboratory, Inc.
Hacienda Heights, California 91745
Email: sclee@appliedsciences.com; Fax: (626) 855-2524

Keywords: thermal conductivity, radiative properties, fiber-filled aerogel

ABSTRACT. A theoretical model is presented for computing the thermal conductivity of fiber-filled aerogels in terms of fiber and aerogel radiative properties, fiber and aerogels bulk densities, temperature and ambient gas pressure. Numerical results are compared with experimental radiative properties and heat wander data to demonstrate the validity of the model. Experimental data are for silica and silicon carbide fibers at several volume fractions in silica aerogel. Heat transfer data were measured in air at ambient pressure over a temperature range from 400 to 1,200 K. Excellent agreement between theory and experiment is seen in all cases.

1. INTRODUCTION

Aerogels, developed nearly 70 years ago by Kistler [1], have the desirable thermal insulating property of nearly eliminating heat transfer by gas conduction for the case of a non-evacuated, low bulk density thermal insulations. The chemical preparation process used to produce aerogels results in a very porous material in which the majority of the aerogel volume consists of very small pores. ne solid structure of the aerogel is composed of interlocking long chains of macromolecules having diameters on the order of a few nanometers. Nearly ninety percent of the pore volume formed by these tortuous macromolecular chains consists of micro-pores having characteristic diameters on the order of 5 to 50 nanometers, depending on the aerogel bulk density. This micropore structure eliminates convection and strongly suppresses gaseous conduction as the Knudsen number for air and common gases at atmospheric pressure is greater than unity for temperatures above 200 K. The macromolecular skeletal structure also significantly reduces conduction through the solid phase. However, because of their weakly bonded structure, aerogels are typically very fragile, and unless opacified, many are very transparent to thermal radiation [2-5]. This transparency seriously compromises their thermal insulation effectiveness at temperatures above ambient unless radiation attenuating additives are incorporated into the aerogel. The addition of fibers which are strongly absorbing and scattering in the infrared greatly improves the thermal performance [6] and significantly increases the structural properties of the aerogels.

Opaciftied aerogels materials are attractive candidates for use as high performance, light-weight thermal insulations in energy efficient applications such as propulsion and power systems, manufacturing and process industries and transportation. This paper summarizes the theoretical models used to compute the radiative properties of the fibers in an aerogel matrix and the total heat transfer as a function of pressure, temperature and bulk density for the purpose of developing and optimizing advanced light-weight thermal insulations for non-evacuated applications. Experimental validation of the modeling approach is demonstrated by comparison of experimental data with theoretical calculations of heat transfer for several fiber-filled aerogel systems. Finally, numerical results are presented demonstrating the optimization of two fiber-reinforced thermal insulations for use in air at temperatures over the range of 300 to 1,500 K The rigorous models of Lee [7-10] form the basis for the analysis of the radiative properties of fibers dispersed in the aerogel. The model also accounts for the interaction of fiber and aerogel optical properties. Radiation properties calculated for the composite medium are the absorption and scattering coefficients and the scattering phase function, all evaluated spectrally. Opacified aerogels are optically thick, and the computation of radiative heat transfer is based on a Rosseland type of mean coefficient in the diffusion approximation to. The coefficient is modified to correctly account for scattering and phase function as the product of the scattering coefficient and phase function. Total heat transfer is computed as the sum of the individual conductivities for gas, solid and radiation mechanisms. A coupled model is also presented for computation of heat transfer for intermediate values of optical thickness in terms of boundary emittances and temperatures. Agreement between this theoretical approach and experimental data for both radiative properties and heat transfer is very good [11,12].

2. THEORY

Radiative Properties

The fibers are modeled as infinitely long circular cylinders as fibers in thermal insulations are typically millimeters in length and a few micrometers in diameter. Because fibers are two-dimensional scatterers, the radiative properties of an isolated fiber and hence those of fibrous medium are strongly influenced by fiber orientation as shown by Lee [7-10]. In the case of fibers oriented randomly in space, the spectral extinction and scattering coefficients per unit length for a polydispersion of fiber sizes are given by

$$\{K_{\lambda r}, \sigma_{s\lambda r}\} = \frac{2f_v}{\pi} \sum_{i=1}^{N} \frac{x_i}{r_i} \int_0^{\pi/2} \{Q_{e\lambda}(\phi), Q_{s\lambda}(\phi)\} \cos\phi d\phi \tag{1}$$

Since the scattering cross section of fibers varies with incident angle, the product of the scattering coefficient $(\sigma_{s\lambda})$ and phase function $(p\lambda)$, must be considered together as a group. This group is given by

$$\langle \sigma_s p\lambda_r \rangle(\eta) = \frac{4f_v\lambda}{\pi^3} \sum_{i=1}^{N} \frac{x_i}{r_i^2} \int_0^1 \frac{i_\lambda(\eta,\phi)}{\sqrt{(1-\cos\eta)(1+\cos\eta-2\sin^2\phi)}} d(\sin\phi) \tag{2}$$

where i_λ is the theoretical single fiber scattering intensity function. The expressions for $Q_{e\lambda}, Q_{s\lambda}$ and i_λ are well summarized in texts such as Kerker and van de Hulst [14, 15]. Angle η is the scattering angle between the incident (μ, ω) and scattered (μ', ω') directions:

$$\cos\eta = \mu\mu' + [(1-\mu^2)(1-\mu'^2)]^{1/2} \cos(\omega-\omega') \tag{3}$$

For fibers randomly oriented in the azimuth ω_f while inclined at a specific polar angle ξfo from the normal to the boundaries, the radiative coefficients are given by

$$\{K_\lambda(\xi fo,\mu), \sigma_{s\lambda}(\xi fo,\mu)\} = \frac{2f_v}{\pi^2} \sum_{i=1}^{N} \frac{x_i}{r_i} \int_0^{\pi} \{Q_{e\lambda}(\phi), Q_{s\lambda}(\phi)\} \delta(\xi f - \xi fo) d\omega_f \tag{4}$$

where δ is the delta function. The angle of incidence ϕ is related to the incident direction and fiber orientation as

$$\sin\phi = \mu\mu f + [(1-\mu^2)(1-\mu_f^2)]^{1/2} \cos(\omega-\omega f) \tag{5}$$

The product of the scattering coefficient and phase function is given by

$$\langle \sigma_s p\lambda \rangle(\xi fo,\mu,\eta) = \frac{4f_v\lambda}{\pi^4} \sum_{i=1}^{N} \frac{x_i}{r_i^2} \int_{\sin\phi_-}^{\sin\phi_+} \int_0^{\pi/2} F d\xi_f d(\sin\phi) \tag{6}$$

where

$$\sin\phi_\pm = \mu\mu f \pm [(1-\mu^2)(1-\mu_f^2)]^{1/2} \tag{7}$$

$$F = \frac{i_\lambda(\eta,\phi)\delta(\xi f - \xi fo)/\sqrt{(1-\cos\eta)(1+\cos\eta-2\sin^2\phi)}}{\sqrt{(\sin\phi_+ - \sin\phi)(\sin\phi - \sin\phi_-)}} \tag{8}$$

It is evident from Eqs. (5) and (7) that the radiative properties of media containing aligned fibers are a function of the incident direction. In particular, the dependence of $\langle \sigma_s p\lambda \rangle$ on η is distinct for each incident direction. This is the critical distinction between the scattering characteristics of spatially random fiber orientation and preferentially oriented fibers.

The scattering coefficient-phase function product for a parrallel slab geometry is obtained by integrating over the azimuthal angle ω. In the case of fibers randomly oriented in space, we obtain

$$\langle \sigma_s P\lambda r \rangle(\mu,\mu') = \frac{1}{2\pi}\int_0^{2\pi} \langle \sigma_2 p\lambda \rangle(\eta)\,d\omega \tag{9}$$

For fibers randomly oriented in the azimuth but aligned in a given polar direction, we get

$$\langle \sigma_s P\lambda \rangle(\xi fo,\mu,\mu') = \frac{1}{2\pi}\int_0^{2\pi} \langle \sigma_s p\lambda \rangle(\xi fo,\mu,\eta)\,d\omega \tag{10}$$

The important difference between Eqs. (9) and (10) is that the former applies to fibers randomly oriented in space, and $\langle \sigma_s P\lambda \rangle$ on the RHS is independent of incident direction. On the other hand, $\langle \sigma_s P\lambda \rangle$ on the RHS of Eq. (10) varies with μ because the fibers are aligned in a specific polar direction. For a medium containing fibers oriented in multiple polar directions, radiative properties are computed as a weighted sum of all the directions.

Radiation Heat Transfer

Fibers are very effective in the absorption and scattering of radiation. As the spectral extinction coefficient of a fiber-filled aerogel is typically on the order of 50 to 100 cm^{-1}, insulation a few millimeters thick may be treated as an optically thick medium for radiation heat transfer analysis. The present radiation model involves the formulation of a radiative conductivity based on the fiber radiative properties in conjunction with the diffusion approximation [16]. Within the context of the diffusion approximation, radiation heat transfer through the fibrous aerogel is expressed similar to heat conduction as

$$qr = -k_r \frac{dT}{dy} \tag{11}$$

where the radiative conductivity k_r is defined as

$$k_r = \frac{16n^2\sigma T^3}{3}\int_0^{\infty} \frac{1}{\Gamma_\lambda}\frac{dI_{b\lambda}(T)}{dI_b(T)}d\lambda \tag{12}$$

The highly porous aerogel structure results in $n > 1.00 < 1.05$ [17]. In the above equation Γ_λ is defined as

$$\Gamma_\lambda = K_\lambda(\mu = 1)(1 - G_\lambda) + \sigma_{a\lambda} \tag{13}$$

where the first term accounts for fiber absorption and scattering and $\sigma_{a\lambda}$ is the aerogel absorption coefficient. Note that the fiber extinction coefficient is evaluated along the heat flow direction of μ =1. The scattering factor G_λ, which corresponds to the fraction of scattered radiation resulting from radiation traversing in the forward direction, is defined as

$$G_\lambda = \frac{1}{K_\lambda(\mu = 1)}\int_0^1 \int_{-1}^1 \langle \sigma_s p\lambda \rangle(\mu,\mu')\mu'\,d\mu'\,d\mu \tag{14}$$

Conduction Heat Transfer

The highly porous aerogel structure minimizes gas convection under atmospheric conditions. Solid conduction due to fiber-to-fiber contact is negligible because the fibers are unbonded. An exact theoretical model for the solid lattice conductivity is not possible due to the extremely complex geometric array of the macromolecules and the uncertainties in bonding strengths and phonon transport within and across bond and contact regions at a nanoscale level. Attempts to model the transport process in terms of packing arrangements of spheres [18,19] and with measurements of sound velocity [5] have met with little success. The approach taken in this study was to empirically derive an expression for the effective lattice conductivity in terms of aerogel material and bulk density with a geometric factor derived from experimental data for opacified aerogels in vacuum at low temperatures [20].

Conductivity of the aerogel. is assumed to be proportional to that of the solid material k_s, which for this study is silica, and the density of the aerogel. The density term is a proportionality factor empirically accounting for the change in the number of series/parallel conduction paths with the amount of solid material per unit volume of aerogel. Using experimental data, conductivity varies with bulk density to the 1.25 power for densities between 50 to 220 kg/m [3,19,20]. The relationship used to calculate the solid phase thermal conductivity in units of W/m-K, for denity in kg/m^3, is

$$k_p = 1.67 \times 10^{-5} k_s(T) \rho a^{1.25} \tag{15}$$

The temperature and pressure dependent thermal conductivity of the contained gas phase is a function of the thermal conductivity of the gas at atmospheric pressure, $k_{go}(T)$, pore diameter P, the temperature and pressure dependent mean free path of the gas, lm(TP), and the solid fraction of aerogel δ_s. The effective conductivity of the gas phase in the aerogel may be expressed as [21]

$$kg\,(T,P) = k_{go}(T)\, P\, (1-\delta s) / [\, P + l_m(T,P)] \tag{16}$$

The characteristic pore diameter for a structure composed of an array of randomly oriented rods made up of the chains of macromolecule sized spherical particles in terms of macromolecule diameter and solid fraction is [22] $P = 0.78\, d_p/\delta_s$. The conduction portion of the overall thermal conductivity is the sum of k_p and k_g.

Total Heat Transfer

Utilizing the radiative, solid and gas thermal conductivities derived in the preceding sections, the steady-state energy equation for combined radiation and conduction may be written as

$$\frac{d}{dy}\left[\left(k_r + k_p + k_g\right)\frac{dT}{dy}\right] = 0 \tag{17}$$

Assuming radiative equilibrium, the total heat transfer through a fiber matrix of thickness L between two gray boundaries with emittance ε_1 and ε_2 at temperatures T_1 and T_2 is

$$q_t = \frac{1}{C_o}\left\{\sigma\left(T_1^4 - T_2^4\right) + \frac{3k_c\tau_o}{4L}\left(T_1 - T_2\right)\right\} \tag{18}$$

where

$$C_o = \frac{3\tau_o}{4} + \left(\frac{1}{\varepsilon_1} - \frac{1}{2}\right)\left[\frac{1}{1+k_c/k_r(T_1)}\right] + \left(\frac{1}{\varepsilon_2} - \frac{1}{2}\right)\left[\frac{1}{1+k_c/k_r(T_2)}\right] \tag{19}$$

An effective total thermal conductivity for large optical thickness is defined as the ratio of the total heat flux given by Eq. (18) and the temperature difference across the thickness of the material:

$$ke = q_t L / (T_1 - T_2) \tag{20}$$

3. EXPERIMENTAL VERIFICATION OF MODELING

The accuracy of the theoretical modeling for the radiative properties of fibers in the aerogel was determined by comparison of calculated and experimentally determined spectral transmittances and reflectances of several fiberfilled silica aerogels. The spectral scattering and extinction coefficients and phase function are calculated, and these properties are then input into the Radiative Transfer Equation (RTE) to solve for the spectral normal transmittance and spectral hemispherical reflectance of finite slabs of fiber-filled silica aerogel with variables of fiber material, fiber size and orientation, fiber volume fraction, aerogel density and slab thickness. Specimens having identical compositional properties with those of the computational cases were fabricated and then measured for spectral transmittance and reflectance. The typical agreement between theory and experimental is illustrated by the comparison of calculated and measured spectral normal transmittance and spectral hemispherical reflectance data shown in Figs. 1and 2. The transmittance results of Fig. 1 are for a slab 0.32cm

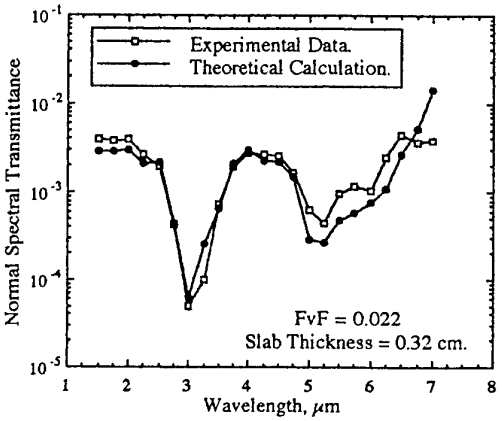


Fig. 1. Normal spectral transmittance, silica fiber-filled silica aerogel

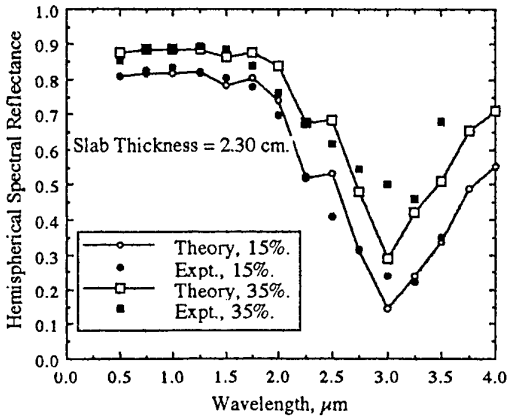


Fig. 2. Hemispherical spectral reflectance for 15 and 35 Wt. % alumina fibers in silica aerogel

thick with a silica fiber volume fraction of 0.022 and a silica aerogel bulk density of 80kg/m^3. Fiber diameter is 2.3 micrometers and the fibers are randomly oriented in space. Maximum uncertainties in measured transmittance data are 0.0005 for transmittance and 0.01 micrometers for wavelength [23]. The decrease in transmittance at wavelengths of 3.0 and 5.5 micrometers is due to strong absorption bands in the silica aerogel [6]. Increasing transmittance at 7 micrometer wavelength is the result of decreased fiber scattering as the real part of the silica refractive index approaches unity. Comparison of calculated and measured spectral hemispherical reflectance results for two volume fractions of alumina fibers in silica aerogel is illustrated by Fig. 2. Mean fiber diameter is 3.2 micrometers, fibers are randomly oriented in space, and fiber volume fractions are 0.0056 and 0.0149. Aerogel bulk density is 110 kg/m^3 and slab thickness is 2.30cm in both cases. Experimental uncertainties are 0.01 for both reflectance amplitude and wavelength. Again, aerogel absorption is the cause for the decrease in reflectance from 2.5 to 4.0 micrometers.

Validity of the heat transfer model is tested by comparison of data for effective thermal conductivity measured in air at atmospheric pressure with predicted thermal conductivity. Measurements were made using a guarded heat flow meter apparatus [11]. The agreement between theory and measurement is shown in Fig. 3 for three silica fiber-filled silica aerogel composites. In all cases the fibers are randomly oriented in space and the fiber diameter is a mean value of 2.3 micrometers with a standard deviation of 1.2 micrometers. Fiber volume fractions are 0.017, 0.030 and 0.027 for Specimens 1, 2 and 3, respectively. Overall bulk densities are 128, 146 and 198 kg/m3 for the specimens in the preceding order, and the corresponding aerogel bulk densities are 89, 77 and 136 kg/m3. The temperature dependences of measured effective thermal conductivities are in good agreement with the numerical results. Also, the comparison between absolute values of conductivity is very good. This agreement confirms the validity of the overall modeling approach. Calculated thermal conductivity values are generally within 10 percent of the measured data which is on the order of the experimental uncertainty. The uncertainty for these experimental thermal conductivity data is 11 percent at 400 K to 13 percent at 1,300 K [11]. Comparison between theoretical predictions and measured data for the thermal

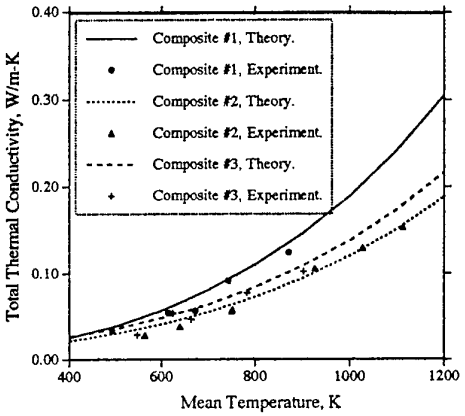


Fig. 3. Thermal conductivity of three silica fiber-filled function of SiC fiber diameter

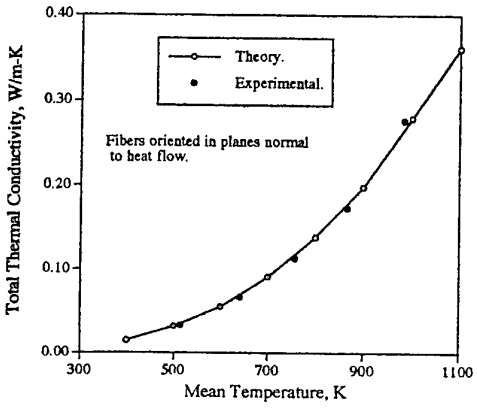


Fig. 4. Thermal conductivity of SiC and SiO2 fibers in silica aerogel

conductivity of an oriented fiberfilled silica aerogel composite is shown in Fig. 4. In this case the SiC fibers, mean diameter of 15 micrometers, are randomly oriented in planes which are parallel to the slab boundaries. The agreement between theory and experiment is excellent. It must be emphasized that the theoretical predictions in all cases are based on fundamental considerations and deterministic physical properties of the materials. A point to note regarding fiber orientation is that radiative heat transfer is a minimum for fibers randomly oriented in planes which are perpendicular to the direction of heat flow and a maximum when the planes are parallel to the heat flow direction.

4. NUMERICAL RESULTS

Influence of fiber properties of complex index of refraction, size and size distribution; fiber orientation; fiber volume fraction and aerogel density on heat transfer are discussed to illustrate their effect on heat transfer of a fiber-filled aerogel thermal insulation. These numerical results are illustrative of the optimization procedure for developing an advanced insulation for specific thermal requirements. The change in radiative thermal conductivity with fiber size for fibers randomly oriented is space in an aerogel matrix is seen in Figs. 5 and 6.

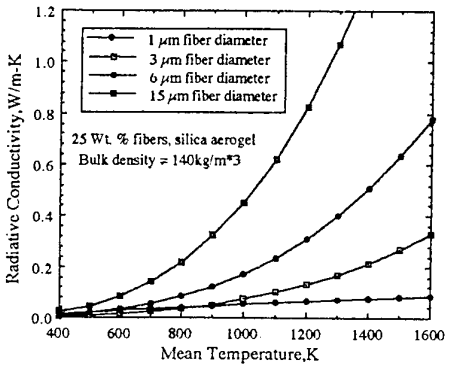


Fig. 5. Radiative thermal conductivity as a function of SiC fiber diameter

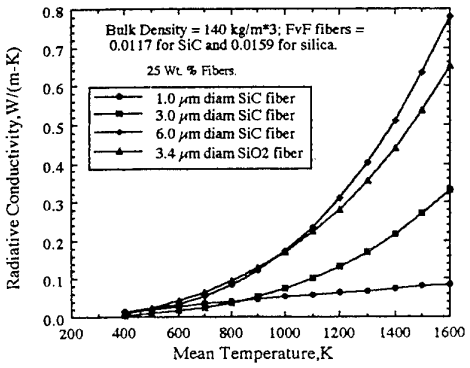


Fig. 6. Radiative thermal conductivities for SiC and SiO2 fibers in silica aerogel

The fiber volume fraction for SiC fibers is 0.0117, and it is 0.0159 for the silica fibers. Aerogel bulk density is 100kg/m^3. Some of the decrease in thermal conductivity with decreasing fiber diameter for both fiber types is the result of changes in scattering efficiencies with diameter for the wavelengths associated with the highetemperatures, but primarily, it is due to the increase in fiber number density which behaves inversely with fi* ber diameter. There are 2.5 times the number of 6μm diameter SiC fibers as there are of the 15μm. diameter fibers. At a temperature of 1,300 K the ratio of radiative thermal conductivities is 2.65. The number density ratio of 3 to 6 jum diameter fibers is 2.0, but the conductivity ratio is on the order of 2.5 for both SiC and silica fibers.

This small increase over the diameter ratio is again because of the larger scattering efficiency due to the more optimum size parameter for the smaller fibers at the wavelengths corresponding to the Planck energy distribution function for 1,300K. A greater increase is seen for a temperature of 1,600 K as the size parameter, modified by the complex refractive index, in the region of the peak wavelength of the Planck distribution approaches a value corresponding to the maximum scattering efficiency. A comparison of silica and SiC fiber effectiveness is seen from Fig. 6. The SiC fiber is more efficient because its refractive index approaches that of a metallic behavior in extinction and phase function parameters.

The effect of complex refractive index, ie, material composition, on radiative thermal conductivity is seen in Figs. 7 and 8. These results are for fibers randomly oriented in space but without an acrogel matrix. In all cases, carbon and SiC fibers are more efficient than alumina or silica fibers. Comparing on an equal fiber volume fraction basis, Fig. 7, silica fiber is the least effective for reducing radiative transport. However, on an equal insulation bulk density basis, Fig. 8, alumina and silica show equivalent radiative thermal conductivities. The thermal conductivity x bulk density parameter for SiC fibers is one-half that of silica or alumina fibers, and for carbon fibers it is one-quarter of the silica or alumina value.

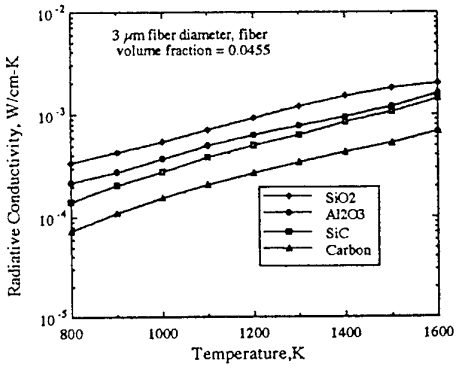


Fig. 7. Radiative conductivity of four fiber materials for constant fiber volume fraction

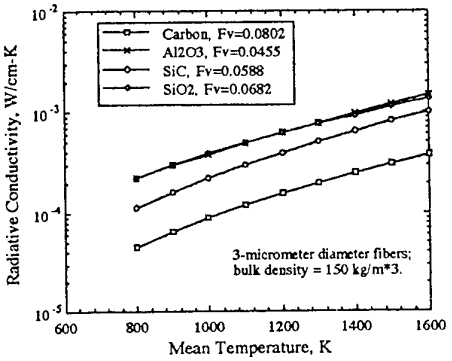


Fig. 8. Radiative thermal conductivity as a function of fiber material

6. CONCLUSION

A theoretical model for the prediction of heat transfer through high porosity composites containing fibers in a radiatively participating matrix is presented in this paper. The model utilizes Lee's theory for radiative properties of fibrous media that exactly account for the morphology of the fibers in the medium. The theoretical predictions for radiative preperties and total heat transfer are compared with radiative properties and heat transfer measurements made on silica aerogels filled with various fibers. The excellent agreement observed between experiment and theory validates the fidelity of the models for fibrous media containing randomly and preferentially oriented fibers. These model are used to demonstrate the effect of fiber properties on thermal conductivity to lead to optimization of advanced thermal insulations for energy conservation.

7. NUMENCLATURE

f_v = fiber volume fraction
G_λ = scattering parameter, Eq. 14
i_λ = fiber scattering intensity distribution
I_b = Blackbody radiation
$I_{b\lambda}$ = Planck function
k_r = radiative conductivity
K_e = extinction coefficient
M = number of fiber polar orientation
n = real part of complex refractive index
N = number of fiber sizes
P = size of equivalent pore spaces inside aerogel
Q = cross section
r = radius of fiber
T = temperature
x_i = fractional volume of fibers of radius r_i

Greek

α = size parameter, $2\pi r/\lambda$
δ_s = solid fraction of silica aerogel
$\Gamma\lambda$ = modified extinction coefficient, Eq. (18)
λ = wavelength
η = scattering angle

μ = direction cosine of angle ξ
ξ = polar angle
ϕ = angle of incidence
ω = azimuthal angle

Subscripts
e = extinction
f = fiber
r = random
s = scattering
λ = wavelength

REFERENCES

1. S.S. Kistler, Nature, v.127, pp.741 (1931).
2. R. Caps and J. Fricke, Solar Energy, v.36, pp.361-365 (1986).
3. J. Fricke, X. Lu, P. Wang, D. Buttner, and U. Heinemann, Int. Heat Mass Transfer, v.35, pp.2305-2309 (1992).
4. F. Schwertfeger, J. Kuhn, V.Bock, M. C. Arduini-Schuster, E. Seyfried, U. Schubert, and J. Fricke, *Thermal Conductivity 22*, pp. 589-598, edited by T. W. Tong, Technomic Publishing Company, Inc. (1993).
5. L. W. Hrubesh and R. W. Pekala, Report No. UCRL-JC-111333, Lawrence Livermore National Laboratory, Livermore, California (1993).
6. G. R. Cunnington, S. C. Lee, and S. White, J. Thermophysics Heat Transfer, v.12, pp.17-22 (1998).
7. S. C. Lee, J. Quant. Spectro Radiative Transfer, v.36, pp.253-263 (1986).
8. S. C. Lee, J. Thermophysics Heat Transfer, v.2, pp.303-308 (1988).
9. S. C. Lee, Int. Heat Mass Transfer, v.32, pp.311-319 (1989).
10. S. C. Lee, Int. Heat Mass Transfer, v.33, pp.2183-2190 (1990).
11. G. R. Cunnington, S. C. Lee, and S. M. White, Paper AIAA-97-3884, National Heat Transfer Conference, Balimore, Maryland (1997).
12. S. C. Lee and G. R. Cunnington, Paper AIAA-98-2840, 7th AIAA/ASME Joint Thermophysics and Heat Transfer Conference, Albuquerque, New Mexico (1998).
13. S. C. Lee and G. R. Cunnington, J. Thermophysics Heat Transfer, v.12, pp.297-303 (1998).
14. M. Kerker, *The Scattering of Light and Other Electromagnetic Radiation*, Academic Press (1969).
15. H. C. van de Hulst, *Light Scattering by Small Particles*, John Wiley & Sons, (1992).
16. M. Q. Brewster, *Thermal Radiative Transfer and Properties*, John Wiley & Sons, (1992).
17. R. P. Caren, J. Heat Transfer, v.93, pp.154-156 (1969).
18. S. Q. Zeng, A. J. Hunt and R. Greif, J. Heat Transfer, v.117, pp.1055-1058 (1995).
19. O. Neilsson, V. Bock, R. Caps, and J. Fricke, *Thermal Conductivity 22*, pp. 878-887, edited by T. W. Tong, Technomic Publishing Company, Inc. (1994).
20. S. Q. Zeng, P. C. Stevens, A. J. hunt, R. Grief, and D. Lee, Int. Heat Mass Transfer, v.39, pp.2311-2317 (1996).
21. U. Heinemann, R. Caps, and J. Fricke, Int. Heat Mass Transfer, v.39, pp.2115-2130 (1996).
22. C. L. Tien and G. R. Cunnington, *Ad. Heat Transfer*, v.9, Academic Press (1973).
23. G. R. Cunnington and S. C. Lee, J. Thermophysics Heat Transfer, v.10, pp.460-466 (1996).

SELF-SIMILAR GROWTH OF A COMPOUND LAYER IN THIN-FILM BINARY DIFFUSION COUPLES

Huifang Zhang & Harris Wong*
Mechanical Engineering Department, Louisiana State University
Baton Rouge, LA 70803-6413, USA
*Email: hwong@me.lsu.edu; FAX: (225)-388-5924

Keywords: thin films, binary diffusion couples, bulk diffusion, phase transformations

ABSTRACT. The diffusion controlled growth of a compound phase A_nB between two thin films of material A and B is studied with the nonlinear Kirkendall effect included. This growth process is important in electronic materials processing and in synthesis of high-temperature materials using multilayer films. Previous models of the growth rate do not solve the diffusion equation, and thus do not fully utilize the predictive capability. This paper describes a self-similar transformation that reduces the nonlinear, time-dependent diffusion equation with two free boundaries into a nonlinear ordinary differential equation, which is solved numerically by a shooting method. It is found that the intrinsic diffusion coefficients of A and B in A_nB can be determined from the positions of the interfaces without using the concentration profile. This provides a simpler method for measuring intrinsic diffusion coefficients. An asymptotic solution valid for small concentration gradients is derived and agrees with the numerical results.

1. INTRODUCTION

Solid-state diffusion between thin films occurs in many industrial applications. For example, during processing of electronic materials, the assembly is often heated to high temperatures, and atoms in a thin film will diffuse into adjacent films. This interdiffusion can destroy the function of the thin film device and can be prevented by diffusion barriers [1, 2]. A diffusion barrier separates materials A and B physically by interposing a barrier layer of material X chosen so that the undesirable intermixing of A and B is suppressed. Therefore, predicting the transport rate of A across X and of B across X, as well as the loss rate of X into A and B, are important for properly choosing a diffusion barrier.

Solid-state diffusion also plays a critical role in the synthesis of materials from multilayer thin films of alternating compounds A and B. Multilayer films provide a large interfacial area to facilitate interfacial reactions, which are different from the reactions in bulk diffusion couples [3]. For example, typically only one reaction phase (A_nB) appears rather than a series (... A_2B, AB, AB_2 ...). Further, interfacial reactions in multilayer films can form products that are metastable [4]. Thus, multilayer films have been used to form the amorphous phase of many different materials [5-9]. Multilayer films have also been used in synthesizing high temperature materials by solid-state reactions [10, 11]; atoms in the thin films diffuse and react at moderate temperatures to form a compound that can withstand high temperatures. In both applications, interdiffusion of atoms between thin films determines the synthesis rate and needs to be analyzed.

This work studies the growth rate of a compound layer A_nB between a film of A and a film of B (Fig. 1). At time $t = 0$, the A and B films are in direct contact. At $t > 0$, a compound A_nB is formed by interdiffusion between A and B. The width W of the compound layer grows with time as atoms of A and B diffuse through the interfaces into A_nB. It is assumed that equilibrium conditions hold at the interfaces so that the concentrations are constant. Kidson [12] studied this problem and arrived at an expression for the layer width:

$$W = p\, t^{1/2} , \tag{1}$$

where the proportionality constant p is expressed in terms of the interdiffusion coefficients, concentrations, and concentration gradients at the interfaces. However, Kidson did not present a solution to the nonlinear diffusion equation and did not evaluate the concentration profile within the product phase. Wagner [13] developed a model that relates the parabolic growth constant ($= p^2/2$) to integrals of the interdiffusion coefficient over concentration. Shatynski et al. [14] obtained a similar relation, assuming that the concentration gradients are constant in the product layer. This model is shown by Williams et al. [15] to be mathematically equivalent to

Wagner's model. Similar to Kidson's analysis, both models do not solve the diffusion equation and thus do not yield a value for the parabolic growth constant. In this work, by reducing the diffusion equation into a self-similar form, p is determined for the complete range of the stoichiometric factor n and the diffusivity ratio R = D_A/D_B, where D_A and D_B are, respectively, the intrinsic diffusion coefficients of A and B in A_nB [2]. It is observed that the parabolic growth constant for each moving interface varies linearly with D_A and D_B.

Based on this observation, a new method is suggested for determination of D_A and D_B by measuring the interfacial positions relative to a fixed maker point. Current techniques for calculation of D_A and D_B require measurement of the concentration profile in the compound layer [2, 12-16]. This is owing partly to a lack of a complete solution to the nonlinear diffusion equation. The self-similar solution shows that the concentration profile is insensitive to D_A and D_B. Hence, use of the profile to infer D_A and D_B is bound to be inaccurate. The new method, however, does not need the concentration profile; it is therefore simpler and likely to be more accurate.

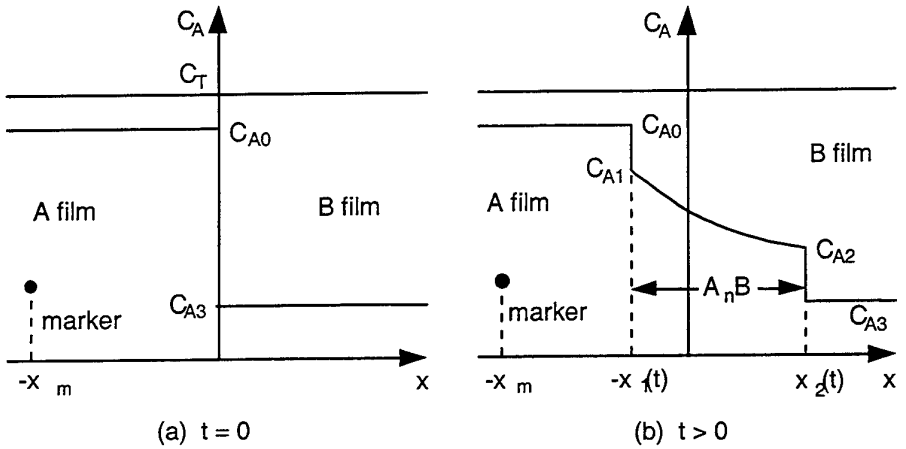


Fig. 1. Concentration of A versus position at time t = 0 (a) and t > 0 (b). The total concentration $C_T = C_A + C_B$ is assumed constant everywhere. Initially, the A film at concentration C_{A0} is saturated with B, and the B film is saturated with A at concentration C_{A3}. At t > 0, the compound layer is bounded by two interfaces at $x = -x_1$ and x_2, and at concentrations C_{A1} and C_{A2}, respectively. A marker point is planted at $x = -x_m$.

2. FORMULATION

Consider a film of material A in contact with another film of material B at a planar interface at time t = 0 (Fig. 1(a)). The A film at concentration C_{A0} is saturated with B and the B film is saturated with A at concentration C_{A3}. The materials can undergo interdiffusion as a result of thermally induced atomic diffusion. At t > 0, a single compound A_nB is formed between the films of A and B, as shown in Fig. 1(b). As atoms of A and B diffuse into the compound layer A_nB, the layer grows at the expense of the two unreacted films. The alloy layer does not contain exclusively the reacted atoms in stoichiometric ratio; there is an excess of unreacted A atoms near the A film, and an excess of unreacted B atoms near the B film. If $D_A >> D_B$ in A_nB, then the Fickian flux of A in the direction of A to B is larger than that of B in the reverse direction. Therefore, there is a net Fickian mass flux of A and B in the direction of A to B. However, the condition of constant total concentration $C_T = C_A + C_B$ in A_nB precludes this net mass shift. To preserve a constant total concentration, a bulk (Kirkendall) mass flux is generated that gives zero net total mass flux at every point in the compound layer [2, 17]. This leads to a nonlinear diffusion equation for the concentration C_A of A in A_nB:

$$\frac{\partial C_A}{\partial t} = \frac{\partial}{\partial x}\left(\tilde{D}\frac{\partial C_A}{\partial x}\right) \tag{2}$$

$$\tilde{D} = \frac{C_B}{C_T} D_A + \frac{C_A}{C_T} D_B \tag{3}$$

where C_B is the concentration of B in A_nB. Substitution of $C_B = C_T - C_A$ into (2) and (3) yields an equation that contains only C_A:

$$\frac{\partial C_A}{\partial t} = \frac{\partial}{\partial x}\left\{\left[\frac{C_A}{C_T}(D_B - D_A)\right]\frac{\partial C_A}{\partial x}\right\} \tag{4}$$

The origin of the coordinate x is located at the A-B interface at t = 0 (Fig. 1). If $D_A = D_B$, then the above equation reduces to the usual linear diffusion equation.

At a later time t, the compound layer is bounded by two interfaces: one between A and A_nB at $x = -x_1(t)$ and one between A_nB and B at $x = x_2(t)$, as shown in Fig. 1(b). Local equilibrium is assumed to hold at each interface so that C_A is known at the interfaces. Thus, at $x = -x_1(t)$,

$$C_A = C_{A1} \tag{5a}$$

$$(C_{AO} - C_{A1})\frac{\partial x_1}{\partial t} = -\left[\frac{C_{A1}}{C_O}(D_B - D_A) + D_A\right]\frac{\partial C_A}{\partial x} \tag{5b}$$

where C_{A0} is the concentration of A in the A film which is different from C_T due to finite solubility of B in the A film. At $x = x_2(t)$,

$$C_A = C_{A2} \tag{6a}$$

$$(C_{A2} - C_{A3})\frac{\partial x_2}{\partial t} = -\left[\frac{C_{A2}}{C_T}(D_B - D_A) + D_A\right]\frac{\partial C_A}{\partial x} \tag{6b}$$

where C_{A3} is the concentration of A in the B film. Here, C_{A0}, C_{A1}, C_{A2}, and C_{A3} are known constants. Equations (5b) and (6b) describe local mass conservation at the interfaces; the left side of each equation is the mass flux generated by sweeping an interface through a concentration jump, whereas the right side is the sum of the Fickian and bulk (Kirkendall) fluxes.

3. SELF-SIMILAR TRANSFORMATION

Since equations (4) - (6) contain neither a length nor a time scale, a self-similar solution is sought. A set of self-similar variables is defined:

$$y = \frac{x}{x_1(t)}, \quad C(y) = \frac{C_A(t, x)}{C_T} \tag{7}$$

The governing equation becomes

$$-yD\frac{dC}{dy} = \frac{d}{dy}\left\{[C(1-R)+R]\frac{dC}{dy}\right\}, \tag{8a}$$

$$R = \frac{D_A}{D_B}, \qquad D = \frac{x_1}{D_B}\frac{dx_1}{dt}, \tag{8b,c}$$

where R is the diffusivity ratio, and D is the dimensionless parabolic rate constant for the interface between A and A_nB. This rate constant can be viewed as a nondimensionalized effective diffusivity for the interface; it is an unknown constant that needs to be determined as part of the solution.

The boundary conditions (5) and (6) are also transformed. At the interface between A and A_nB, $y = -1$,

$$C = C_1 \tag{9a}$$

$$D(C_0 - C_1) = [C_1(1-R)+R]\frac{dC}{dy} \tag{9b}$$

At the interface between A_nB and B,

$$y = y_2\ , \qquad C = C_2 \tag{10a, b}$$

$$y_2 D(C_2 - C_3) = -[C_2(1-R)+R]\frac{dC}{dy} \tag{10c}$$

Here, $C_i = C_{Ai}/C_T$, i = 0 ... 3, are prescribed constants, and $y_2 = x_2(t)/x_1(t)$ is an unknown constant to be determined.

Equation (8) is an ordinary differential equation of second order and needs two boundary conditions for a solution. In addition, the locations of the interfaces are unknown functions of time which are reduced to two unknown constants D and y_2 by the self-similar transformation. Thus, totally four boundary conditions are needed to solve (8).

4. NUMERICAL METHOD AND RESULTS

A fourth order Runge-Kutta method is used to solve (8) - (10). Since D and y_2 are unknown, an iteration procedure is adopted and outlined below. A value for D is assumed first. This allows (8) to be integrated from y = -1 using the boundary conditions (9) for C and dC/dy. The integration proceeds until $C = C_2$ at which point the integration is stopped and the position corresponds to $y = y_2$. This value is substituted into (10b) to yield a new value for D, and the procedure is repeated until D converges [18]. A step size of 0.01 is used in the integration, and the results presented below are accurate to at least four significant figures.

Results of a particular case with $C_0 = 0.9$, $C_1 = 0.8$, $C_2 = 0.5$, and $C_3 = 0.15$ are presented first to illustrate the general characteristics of the solutions. It is found that the concentration profiles are insensitive to R, and y_2 varies nonlinearly with R. Solutions of D are plotted as a function of R in Fig. 2(a). It shows that D varies linearly with R. It is not obvious mathematically, from the governing equation and boundary conditions, that D should depend linearly on R. However, since D represents an effective diffusivity of the interface at $x = -x_1$, it can only be a linear combination of D_A and D_B. Thus, physical intuition projects D to be a linear function of R. Following the definition of D in (8c), a similar nondimensionalized effective diffusivity for the interface at $x = x_2$ can be defined:

$$K = \frac{x_2}{D_B}\frac{dx_2}{dt} \tag{11}$$

This effective diffusivity can be expressed in terms of D and y_2:

$$K = y_2^2 D \tag{12}$$

Values of K are plotted as a function of R in Fig. 2(b). Despite that y_2 is a nonlinear function of R, $y_2{}^2D$ varies linearly with R. This again confirms the physical intuition that the effective diffusivity for the interfaces should depend linearly on R.

The linear dependence of D and K on R simplifies presentation of numerical results. Let

$$D = d_1 R + d_0 \tag{13}$$

$$K = k_1 R + k_0 \ . \tag{14}$$

Thus, instead of $D = D(C_0, C_1, C_2, C_3, R)$ and $y_2 = y_2(C_0, C_1, C_2, C_3, R)$, the R dependence is determined explicitly, and d_0, d_1, k_0, and k_1 are only functions of C_0, C_1, C_2 and C_3.

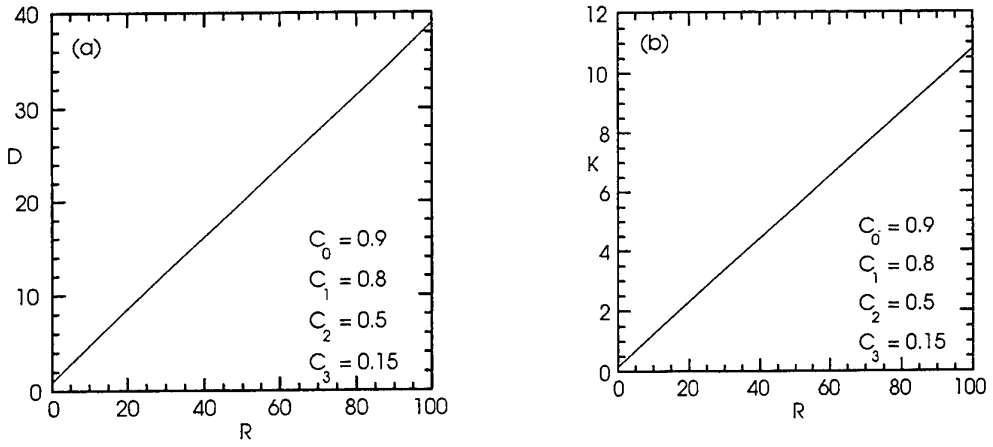


Figure 2. Effective diffusivities of the A-A_nB interface (a) and A_nB-B interface (b) versus diffusivity ratio. The dependence is linear with positive intercept at R = 0.

5. DISCUSSION

The self-similar solution can be applied to the measurement of the intrinsic diffusion coefficients D_A and D_B. From the self-similar solution, the interfacial positions $x_1(t)$ and $x_2(t)$ can be solved from (8c) and (11) with the initial conditions that $x_1 = x_2 = 0$ at $t = 0$:

$$x_1 = \sqrt{2DD_B t} \tag{15}$$

$$x_2 = \sqrt{2KD_B t} \ . \tag{16}$$

Thus, the width of the compound layer is

$$W = x_1 + x_2 = \left(\sqrt{D} + \sqrt{K}\right)\sqrt{2D_B t} \tag{17}$$

In most experiments, the layer width W is measured as a function of t, and plotted against $t^{1/2}$. The data form a straight line if the growth is controlled by diffusion:

$$W = p\, t^{1/2} \quad . \tag{18}$$

The slope p is found from the data, and comparison of (17) with (18) yields

$$p = \sqrt{2D_B}\left(\sqrt{d_1 R + d_0} + \sqrt{k_1 R + k_0}\right) \quad , \tag{19}$$

where D and K have been replaced using (13) and (14) to show explicitly their dependence on R. In (19), d_0, d_1, k_0, and k_1 are functions of only C_0, C_1, C_2, and C_3. Thus, they are determined once a thin film binary diffusion couple is chosen. Hence, only two unknowns are left in (19): R and D_B. If either one is given, then the other can be found from (19), and D_A follows immediately from $D_A = RD_B$.

One way of completing the solution is by measuring the concentration profile. A value for R can then be obtained by fitting the computed concentration profile to the experimental data. Once R is determined, D_B (and hence D_A) follows from (19). However, because the concentration profile is insensitive to R, this way of completing the solution is bound to be inaccurate.

If the interfacial positions can be measured relative to a fixed laboratory frame, then D_A and D_B can be found without using the concentration profile. Only a point of the laboratory frame is needed as a reference. This could be a marker point in either the A or B film away from the compound layer. For illustrative purposes, let a marker point be planted in the A film at $x = -x_m$, as shown in Fig. 1. If z_1 is the distance between the marker point and the left interface, and z_2 that the right interface, then

$$z_1 = -x_1 + x_m \tag{20}$$

$$z_2 = x_2 + x_m \quad . \tag{21}$$

The distances z_1 and z_2 are measured as a function of t. Plotting z_1 and z_2 versus $t^{1/2}$ yields two straight lines. The z-intercept at $t = 0$ is x_m. The slopes for z_1 and z_2 are, respectively,

$$p_1 = -\sqrt{2D_B(d_1 R + d_0)} \tag{22}$$

$$p_2 = \sqrt{2D_B(k_1 R + k_0)} \tag{23}$$

which are the slopes of $-x_1$ and x_2 versus $t^{1/2}$. These equations determine R and D_B, and therefore D_A. Thus, both D_A and D_B are found. Note that the parabolic growth constants ($p_1^2/2$ and $p_2^2/2$) for the interfaces vary linearly with R, whereas the parabolic growth constant ($p^2/2$) for the compound layer varies nonlinearly with R, as indicated by (19).

As an example, the self-similar solution is used to calculate the intrinsic diffusion coefficients of Ag and Zn in the -phase of Ag-Zn alloys. Williams et al. [15] conducted a detailed experimental study of Ag-Zn alloys. A Ag-Zn binary diffusion couple can form five equilibrium phases. Williams et al. fabricated alloy ingots with different compositions and used them as the terminal phases of diffusion couples. By combining two terminal phases with properly chosen compositions, they were able to study the growth rate of any one of the five phases. The data for the -phase are the most extensive, and are selected for comparison. Williams et al. measured the thickness of the -phase layer as a function of time at 400°C (Table III in their paper). When the thickness is plotted against $t^{1/2}$, a straight line is obtained, the slope of which is calculated as $p = 4.54 \times 10^{-6}$ m/s$^{1/2}$. The equilibrium concentrations at the interfaces are taken from their Table II for the -phase as $C_0 = 0.46$, $C_1 = 0.39$,

$C_2 = 0.327$, and $C_3 = 0.279$, assuming that A is Zn and B is Ag. For these equilibrium concentrations, the self-similar solution yields $d_0 = 0.1298$, $d_1 = 0.2256$, $k_0 = 0.2097$, and $k_1 = 0.3853$. Thus, everything is known in (19) except R (= D_{Zn}/D_{Ag}) and D_B (= D_{Ag}). However, since Williams et al. presented neither the concentration profile nor the location of the individual interface, there is insufficient information for finding R or D_B. Heumann and Lohmann [16] measured both the layer thickness and the concentration profile for the -phase at different temperatures, from which they calculated D_{Ag} and D_{Zn} using a method similar to Kidson's [12]. From their Fig. 15, at 400°C, $D_{Ag} = 2\text{x}10^{-12}$ m^2/s and $D_{Zn} = 1\text{x}10^{-11}$ m^2/s. This means $R = D_{Zn}/D_{Ag} = 5$. With this value of R, the self-similar solution can be completed; equation (19) yields $D_{Ag} = 1.54\text{x}10^{-12}$ m^2/s, which differs from the original value by 23%. Given the large uncertainty of the original data, this difference is acceptable. Hence, the self-similar solution gives at least consistent results.

6. CONCLUSIONS

This work studies the diffusion-controlled growth rate of a compound layer in thin-film binary diffusion couples. The Kirkendall effect is included which makes the diffusion equation nonlinear. A self-similar transformation reduces the nonlinear partial differential equation with two free boundaries to a nonlinear ordinary differential equation, which is solved numerically by a fourth-order Runge-Kutta method. An iteration scheme is developed for calculation of the unknown boundary locations. It is observed that the parabolic growth constants for the moving interfaces depend linearly on the intrinsic diffusion coefficients D_A and D_B. Based on this observation, a new method is suggested for determination of D_A and D_B by measuring the interfacial positions relative to a fixed marker point. Since the concentration profile is not needed in this method, it is simpler than the methods currently in use. An asymptotic solution valid for small composition variation is derived and agrees with the numerical results in the appropriate limit [18].

ACKNOWLEDGMENTS

We are grateful to Professors Even Ma, Efstathios Meletis, and Aravamudhan Raman for many helpful discussions. In addition, we thank Professor Ma for initiating our interest in this work, and Professors Raman and Kurt Schulz for their comments on the manuscript. Acknowledgment is made to the Donors of The Petroleum Research Fund, administered by the American Chemical society (PRF#34049-G5 to HW), and to the Louisiana Board of Regents (Research Competitiveness Subprogram, LEQSF1999-02-RD-A-21 to HW) for support of this research.

REFERENCES

1. J.W. Mayer, and S.S. Lau, *Electronic Materials Science: for integrated circuits in Si and GaAs*, Macmillan, New York (1990).
2. K.N. Tu, J.W. Mayer, and Feldman, L. C., *Electronic Thin Film Science*, Macmillan, New York (1992).
3. A.L. Greer, Applied Surface Sci. v.86, 329 (1995).
4. A.L. Greer, Materials Sci. Engineering v.A134, 1268 (1991).
5. J.Y. Cheng, and Chen, L. J., J. Appl. Phys. V69, 2161 (1991).
6. C. Michaelsen, Z.H.Yan, and Bormann, R., J. Appl. Phys. v.73, 2249 (1993).
7. J.H. Lin, and L.J. Chen, J. Appl. Phys. v.77, 4425 (1995).
8. J.Y. Shim, J.S. Kwak, E.J. Chi, H.K. Baik, and S.M.Lee, Thin Solid Films v.269, 102 (1995).
9. J.Y. Shim, J.S. Kwak, and H.K. Baik, Thin Solid Films v.288, 309 (1996).
10. Z.A. Munir, High Temperature Sci. v.27, 279 (1990).
11. Z.A. Munir, Metallurgical Transactions A v.23A, 7 (1992).
12. G.V. Kidson, J. Nuclear Materials. v.3, 21 (1961).
13. C. Wagner, Acta Metallurgica v.17, 99 (1969).
14. S.R. Shatynski, J.P. Hirth, and R.A. Rapp, Acta Metallurgica v.24, 1071 (1976).
15. D.S. Williams, R.A. Rapp, and J.P. Hirth, Metallurgical Transactions A v.12A, 639 (1981).
16. T. Heumann, and P. Lohmann, Z. Elektrochem. v.59, 849 (1955).
17. P.G. Shewmon, *Diffusion in Solids*, McGraw-Hill, New York (1963).
18. H. Zhang, Master thesis, Louisiana State University (2000).

HEAT TRANSFER PROPERTIES AND STRUCTURE OF $CaCl_2$ REACTOR BEDS USED FOR CHEMICAL HEAT PUMPS

Keiko Fujioka, Kiyomichi Oido and Yushi Hirata
Department of Chemical Science and Engineering
Graduate School of Engineering Science
Osaka University
Email: kfujioka@mxw.mesh.ne.jp

Keywords: heat transfer, effective thermal conductivity, porous pellet, gas-solid reaction

ABSTRACT. In order to develop a method to estimate the effective thermal conductivity of reactor beds for gas-solid chemical heat pumps, experiments on heat transfer and structure in the bed have been performed for the reaction of $CaCl_2$ with CH_3OH or CH_3NH_2 vapor. From the measurements with mercury porosimetry, it has been found that the void fraction inside the porous $CaCl_2$ particles was influenced considerably by the gas substance reacted with the particles. SEM observation revealed that the shape and aggregated state of fine grains of $CaCl_2$ also changed by reaction. Heat transfer experiments of the $CaCl_2$ bed have been carried out at the gas-phase pressure in the packed bed from 5 Pa to 0.1 MPa. The effective thermal conductivity of the bed, which had been subjected to the absorption and desorption reaction several times, was reduced to less than one half of that of the unreacted $CaCl_2$ bed. A model is proposed to predict the effective thermal conductivity of the reactor bed as well as that of the reactive pellets packed in the bed by taking account of their structural change due to reaction. From a comparison with the experimental results it has been proved that the predictions based on the model well express the effects of gas pressure and the structural change in reactive pellets on the effective thermal conductivity.

1. INTRODUCTION

The reaction of calcium chloride with methylamine or methanol vapor is applicable to driving chemical heat pumps for refrigeration or air conditioning by utilizing the waste heat at a low temperature below 363K that is usually difficult to reuse. In this gas-solid reaction system the packed bed is used as the standard reactor. Since the heat transfer is poor in the packed bed and the reaction in it is apt to be controlled by heat transfer, evaluation of heat transfer properties in the bed subjected to the reaction is important for designing high efficient gas-solid chemical heat pumps.

The solid particles involved in the reaction are usually porous pellets aggregated with small grains of $CaCl_2$ salt. Their thermophysical properties, such as density, heat capacity and thermal conductivity, vary with the progress of reaction [1,2]. Further, the pellets and grains may change in structure and morphology by reaction. Therefore, heat transfer properties in the reactor bed should be evaluated by taking into account of the geometrical structure of the reactive solids packed in the reactor as well as their variations of thermophysical properties. In this study the heat transfer mechanism is investigated based on the structural analysis for the packed bed reactor in the following $CaCl_2$ reaction systems.

Methylamine system

$$CaCl_2 + 2CH_3NH_2 = CaCl_2 \cdot 2CH_3NH_2 \quad (1)$$

$$CaCl_2 \cdot 2CH_3NH_2 + 2CH_3NH_2 = CaCl_2 \cdot 4CH_3NH_2 \quad (2)$$

$$CaCl_2 \cdot 4CH_3NH_2 + 2CH_3NH_2 = CaCl_2 \cdot 6CH_3NH_2 \quad (3)$$

Methanol system

$$CaCl_2 + 2CH_3OH = CaCl_2 \cdot 2CH_3OH \quad (4)$$

2. EXPERIMENTAL

The reactive solids in the above equations (1) to (4) are expressed in the general form of $CaCl_2 \cdot nCH_3NH_2$ and

$CaCl_2 \cdot nCH_3OH$ by using n which represents the moles of gas substance reacted with one mole of $CaCl_2$. In measuring thermophysical properties of the reactive solids involved in reversible gas-solid reactions, a particular attention must be paid so that the reaction does not proceed or the heat of reaction does not disturb the measurement. Further, the void fraction of the packed bed must be measured in each measurement, since it changes with reaction and appreciably affects heat transfer in the bed. We have developed a method satisfying these requirements [2].

Using this method the effective thermal conductivities were measured for the porous reactive solid that was maintained in one of the state described by the above equations. The reactions of Eqs. (2) and (3) are reversible in themselves, but the state of the reactive solid is kept unchanged or n is maintained constant as long as the pressure in gas phase is set at an appropriate value; for n=4 the pressure must be kept between the equilibrium pressures of the reaction (2) and (3) and for n=6 it must be above that of Eq(3). On the other hand, the reactions with n n<2, Eqs.(1) and (4), can be regarded as irreversible under the range from 273K to 293K for the measurement of effective thermal conductivity and the composition of the reactive solid with n<2 is kept unchanged at a very low pressure or even in the atmosphere of inert gas. Consequently measurements for the reactive solid with n<2 as well as porous and nonporous pellets of $CaCl_2$ anhydride were carried out in the atmosphere of Ar, N_2 or He gas in the pressure range of 5 Pa to 2 x 105 Pa. Nonporous $CaCl_2$ pellets were prepared by crushing solid $CaCl_2$ which was made by cooling a molten salt of $CaCl_2$.

The pore volumes and pore size distributions of $CaCl_2$ and $CaCl_2 \cdot nCH_3OH$ were measured by means of mercury porosimeter. SEM photographs of $CaCl_2$ and $CaCl_2 \cdot nCH_3OH$ were taken at each state where the absorption or desorption reaction is completed.

3. STRUCTURE

The bed investigated in this study is composed of porous pellets aggregated with small grains. In such a bed there are vacant spaces both inside and outside pellets, which are supposed to have different contributions to heat transfer. The effective thermal conductivity λ_{eff} of the bed may be expressed in terms of the bed void fraction ε_b of the vacant space outside the pellets and the pellet thermal conductivity λ_p. The latter is also regarded as a kind of effective thermal conductivity since it depends on the void fraction ε_p inside the pellets and the thermal conductivity of solid λ_s. Consequently, two kinds of effective thermal conductivities, λ_p and λ_s, and two kinds of void fractions, ε_b and ε_p, are necessary for the estimation of λ_{eff} in a porous particle bed.

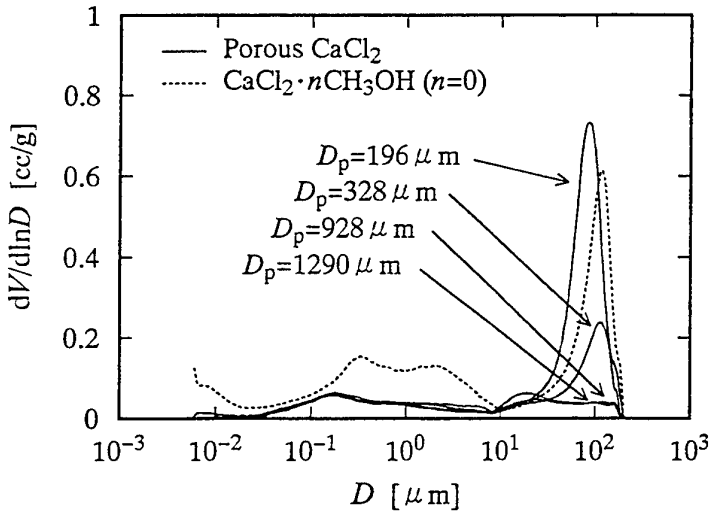


Fig.1 Pore size distributions of porous $CaCl_2$ and $CaCl_2 \cdot nCH_3OH$

3.1 Void Fractions

By means of mercury porosimetry ε_p of porous $CaCl_2$ pellets was determined first. Pore size distributions of $CaCl_2$ pellets in various sizes are shown by solid lines in Fig.1. Depending on the pellet size, all curves of dV/dlnD versus D are different in the region of pore diameter D>8 μm, while they coincide with each other in the region of D<8 μm. Therefore pores smaller than 8 μm may be considered to belong to those inside pellets, and the pellet void fraction ε_p inside the porous $CaCl_2$ was obtained as 0.332. The overall void fraction ε of the bed is given by the ratio of the total vacant volumes inside and outside the pellets to the bed volume. By denoting the bed void fraction outside the pellets by ε_b the three kinds of void fractions are related to each other as

$$\varepsilon_b = (\varepsilon - \varepsilon_p)/(1 - \varepsilon_p) \tag{5}$$

Using the pellet void fraction ε_p=0.332 and the average overall void fraction, ε=0.650, the bed void fraction ε_b was estimated to be 0.476 by Eq. (5).

3.2 Variations of Pellet Void Fraction

Porosimetry measurements of $CaCl_2 \cdot nCH_3OH$ pellets showed that the pore size distributions in the pellets varied largely with absorption or desorption of methanol. For example the dotted line in Fig.1 represents the pore size distribution for $CaCl_2 \cdot nCH_3OH$ (n=0) obtained after repeating reaction cycle three times, whose pellet void fraction ε_p based on the pore volume was twice as large as that of unreacted $CaCl_2$ pellets. With increasing n, the pellet void fraction of $CaCl_2 \cdot nCH_3OH$ decreased from n=0.6 to 0. On the other hand, the bed void fraction ε_b of $CaCl_2 \cdot nCH_3OH$ calculated from Eq.(5) was kept almost constant, i.e., ε_b=0.48. This may be due to that the measurements of overall void fraction were carried out under the condition where the bed was allowed to expand or contract freely during reaction.

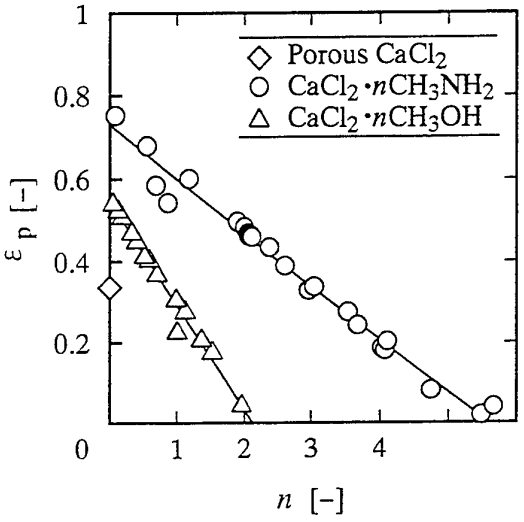


Fig.2 Variations of estimated pellet void fractions with *n*

It was impossible to perform porosimetry measurement of $CaCl_2 \cdot nCH_3NH_2$ pellets, because highly erosive vapor of CH_3NH_2, which gives serious damages to the instrument, is decomposed from the reacted pellets in a vacuum operation required before penetrating mercury into the sample. On the basis of nearly constant ε_b in $CaCl_2 \cdot nCH_3OH$ bed, it was assumed that the constant value of ε_b=0.48 was valid for $CaCl_2 \cdot nCH_3NH_2$ bed under free expansion or contraction. Then the pellet void fraction ε_p was obtained from the overall void fraction ε and the pellet void faction of ε_b=0.48. Figure 2 shows that the pellet void fraction decreases linearly with increasing n for both $CaCl_2 \cdot nCH_3OH$ and $CaCl_2 \cdot nCH_3NH_2$ pellets.

3.3 Deformation of Fine Structure of Pellet

Figure 3 shows SEM micrographs for a pellet of unreacted porous $CaCl_2$ (a), that of $CaCl_2 \cdot nCH_3OH$ after complete desorption in the first cycle (b) and that after the fourth cycle (c). A drastic transformation of pellet structure can be seen in these photographs. The unreacted $CaCl_2$ pellet consists of grains partially fused with each other. On the other hand, grains of the $CaCl_2 \cdot nCH_3OH$ (n=0) pellet subjected to four reaction cycles look like an aggregate of slender sticks which are not consolidated with each other, as shown in Fig.3 (c).



(a) $CaCl_2$ (b) $CaCl_2 \cdot nCH_3OH$ (n=0) after first desorption (c) $CaCl_2 \cdot nCH_3OH$ (n=0) after fourth desorption

Fig.3 SEM photographs of porous $CaCl_2$ and $CaCl_2 \cdot nCH_3OH$

4. HEAT TRANSFER

4.1 Pressure Dependence of Effective Thermal Conductivity

The operating pressure in a gas-solid chemical heat pump is determined based on the relation between equilibrium pressure and temperature for the reaction. In general, the pressure in heat pumping mode with absorption reaction is different from that in regeneration mode with desorption reaction. Therefore it is necessary to investigate the effective thermal conductivity of a reactor bed in a wide range of the gas pressure. In order to vary the pressure without making the reaction to proceed, an inert gas of Ar, N_2 or He was introduced into the vessel in which the effective thermal conductivity was measured. Thus the gas pressure was varied from 5 Pa to 0.1 MPa. Figures 4 and 5 show the variations of effective thermal conductivities with pressure for the beds of nonporous $CaCl_2$, porous $CaCl_2$ and porous $CaCl_2 \cdot nCH_3OH$ (n=0.048) pellets.

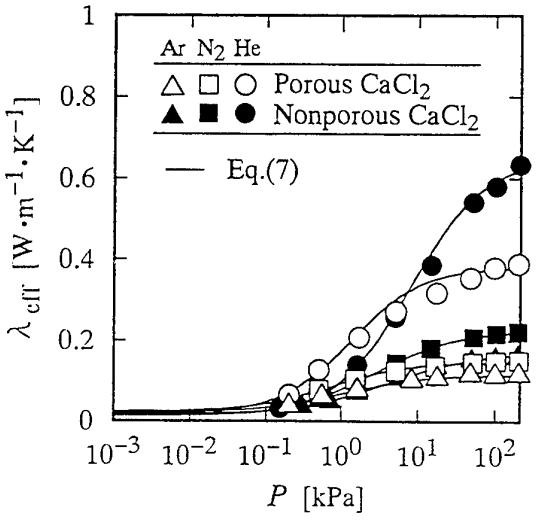


Fig.4 Variations of effective thermal conductivities of unreacted $CaCl_2$ bed with pressure (Porous; D_p=675 μm, Nonporous; D_p=178 μm)

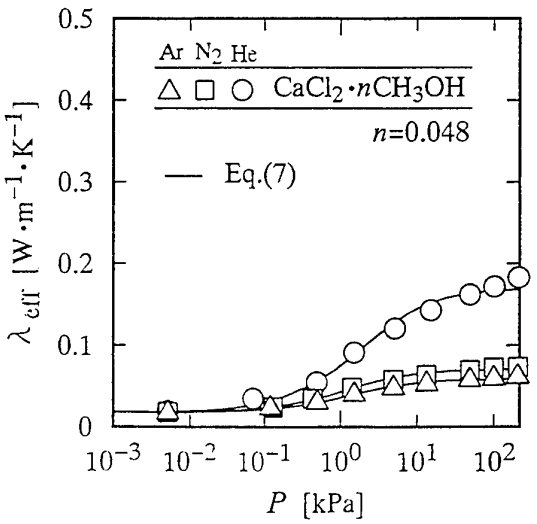


Fig.5 Variations of effective thermal conductivities of $CaCl_2 \cdot nCH_3OH$ bed with pressure (n=0.048; D_p=308 μm)

At the atmospheric pressure λ_{eff} depends on the substance in gas phase. This means that heat flows partially through the gas phase in the packed bed. With decreasing the gas pressure the mean free path of gas molecules increases to be comparable with the thickness of the gas film adjacent to the contact points between pellets and the heat transfer through the film becomes to be affected by the free molecular conduction. Therefore the effective thermal conductivity decreases with decreasing pressure. This effect appears more appreciable as the pressure becomes lower, yielding a sharp decrease in λ_{eff} around 1 kPa. At low pressures below 10 Pa, λ_{eff} is very small and almost independent of the gas substance, since heat transfer in the bed takes place mainly through the contact points of the pellets.

The data in Fig.4 indicate that the effective thermal conductivity of the bed of porous $CaCl_2$ pellets is smaller than that of nonporous $CaCl_2$. When once porous $CaCl_2$ has absorbed CH_3OH, its effective thermal conductivity is reduced to about one half of that of unreacted $CaCl_2$ as is shown by comparing Fig.4 with Fig.5. Such a decrease in the effective thermal conductivity due to reaction was also observed in the methylamine system.

4.2 Model for Effective Thermal Conductivity of Porous Bed

The thermal conductivity of a reactor bed packed with porous pellets probably depends on the thermal conductivities of gas and solid, λ_g and λ_s, and pellet void fraction ε_p and bed void fraction ε_b inside and outside the pellets. If one introduces an effective thermal conductivity λ_p to express heat transfer through a pellet, which may be expressed in terms of ε_p, λ_g and λ_s, one can simplify the analysis for heat transfer in the porous bed by assuming that the bed is composed of particles with thermal conductivity λ_p and gas with thermal conductivity λ_g and void fraction ε_b. With the purpose to further take account of the pressure dependence of effective thermal conductivity and the heat transfer through the contact points between pellets, a model equation is derived by extending the models proposed by Kunii and Smith [3] and Okazaki et a. [4].

Consider an elementary cell in the form shown in Fig.6. The cell consists of two adjoining spheres whose contact surface is specified by angle ψ. When the gas in the void is stagnant and the radiative heat transfer can be neglected, heat transfer in the vertical direction in Fig.6 is assumed to take place by the following mechanism: (1) conduction only through the fluid in the macro void space, (2) conduction through the solid and gas phases near the contact surface in series, (3) conduction through the contact surface of the solid pellets.

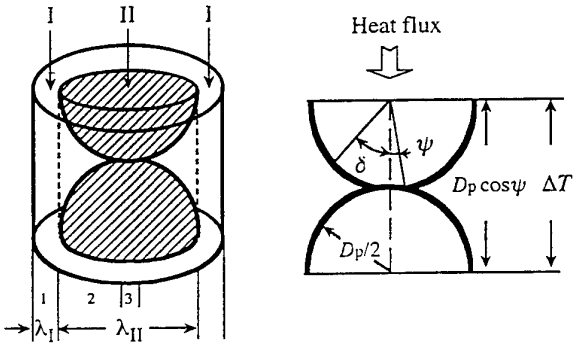


Fig.6 Heat transfer model in a packed bed

Denote the part associated with mechanism (1) by I and that with mechanism (2) and (3) by II, and the fractional areas corresponding to these parts are E and 1-E, respectively. Assuming that the volume of II is equal to that of a cylinder with diameter D_p and height $D_p\cos\psi$, its fractional area is given by

$$1-E=(3/2)(1-\varepsilon_b)\cos\Psi \tag{6}$$

Since the heat flux through the cell is the sum of the flux through the macro void part and that through the solid part, the effective thermal conductivity λ_{eff} is expressed by the following equation

$$\lambda_{eff}=E\lambda_I+(1-E)\lambda_{II} \tag{7}$$

where II is the thermal conductivity of the gas, whose pressure dependence can be calculated by the Kennard equation [5] from the thermal conductivity at the normal pressure in vast space, λ_g°, using the temperature jump distance β and the mean free path of gas molecules L.

$$\lambda_I = \frac{\lambda_g^0}{1 + 2\beta L / D_p \cos\psi} \tag{8}$$

On the basis of the model proposed by Kunii and Smith [6] the apparent thermal conductivity of part II, λ_{II}, has been derived by taking account of the dependence of gas conductivity on pressure by Kennard equation as follows;

$$\lambda_{II} = n_c \sin^2\psi . \lambda_p + 2n_c . \lambda_g^o \left[\frac{K}{K-1}(\cos\delta_O - \cos\psi) + \left(\frac{K}{K-1}\right)^2 (\cos\psi + 2\beta L/D_p) \ln \frac{K(\cos\psi + 2\beta L/D_p) - (K-1)\cos\delta_O}{K(\cos\psi + 2\beta L/D_p) - (K-1)\cos\psi} \right] \tag{9}$$

where $\kappa = \lambda_g^\circ / \lambda_p$, $\cos\delta_0 = (1 - 1/n_c)$ and L denotes the mean free path of gas molecules. n_c represents the effective number of contact points per hemisphere introduced by Okazaki et al. [4] to express conductive heat transfer in beds. Contact numbers are estimated by the correlation equation [6], and $\cos\psi$ can be obtained from the extrapolation of the measured effective thermal conductivity to zero pressure.

The validity of the above equations has been exa mined for beds of glass beads and nonporous $CaCl_2$ whose pellet thermal conductivity were determined experimentally. The effective thermal conductivities were calculated by Eqs.(6) - (9) using the thermal conductivity of glass, 1.0 W/mK, and that of solid $CaCl_2$, 2.36 W/mK, respectively. The calculations express well the pressure dependence of effective thermal conductivities, as shown by solid lines in Fig.4.

Then the pellet thermal conductivities of porous anhydride and reactive solids of $CaCl_2$, λ_p, and the unknown parameter, β, in the above equations have been determined so as to minimize the variance between calculated and measured λ_{eff}. Calculated variations of λ_{eff} with pressure are given by solid lines in Figs. 4 and 5. The values of λ_p, which have been obtained by changing the substance of gas phase, i.e., Ar, N_2 and He, show little dependence on the gas substance in the pellet.

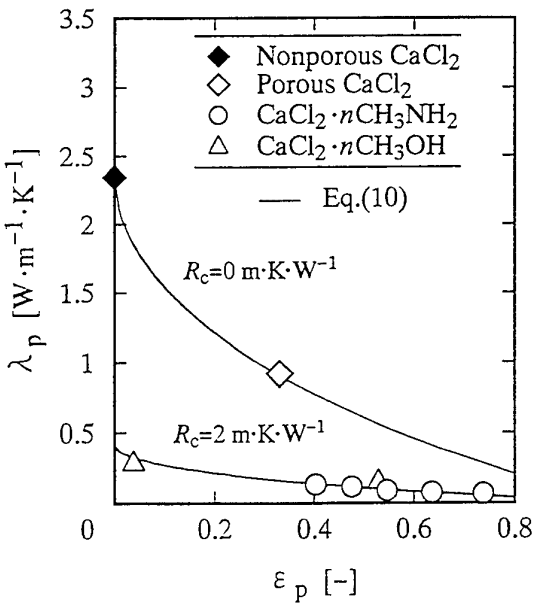


Fig.7 Relation between thermal conductivities and void fractions of pellet

4.3 Model for Pellet Thermal Conductivity

Absorption and desorption of reactive gas cause simultaneous changes in solid composition and void fraction of pellets, as mentioned in 3.2. Further, transformation of fine structure of the pellets takes place during reaction. In order to investigate these effects on heat transfer, pellet thermal conductivity λ_p of $CaCl_2 \cdot nCH_3NH_2$ are plotted against pellet void fraction ε_p in Fig.7. A significant difference can be seen between λ_p for the unreacted porous $CaCl_2$ anhydride and λ_p for the

reacted pellets. The thermal conductivity of $CaCl_2 \cdot nCH_3NH_2$ pellet is about one fourth as small as that of $CaCl_2$, when compared at the same void fraction.

An expression to evaluate the change in pellet thermal conductivity is derived below. It has been described that the pellet thermal conductivity is less dependent on the gas phase, while the effective thermal conductivity is significantly dependent on it. This may suggest that the heat conduction through the gas phase in the pellet is so small that the heat flows mainly through the solid phase. The pellet structure shown in Fig.8 may be represented by the unit cell model proposed by Luikov et al. [7]. In order to take account of the change in contacting state due to reaction, Luikov's model has been modified by adding contact resistance R_c on the upper and the lower surfaces of the cell, as shown in Fig.8. The modified expression is given by

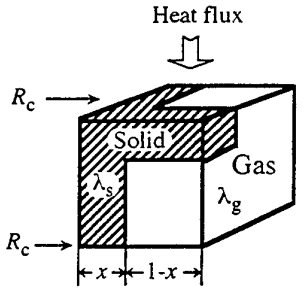


Fig.8 Unit cell for a porous pellet

$$\lambda_p = \frac{x^2}{R_c + 1/\lambda_s} + (1-x)^2\lambda_g + x(1-x)\left[\frac{\lambda_s\lambda_g}{(1-x)\lambda_s + x\lambda_g + R_c\lambda_s\lambda_g}\right] \tag{10}$$

where x is the thickness of solid phase obtained from the pellet void fraction.

4.4 Estimation of Pellet Thermal Conductivity

In the estimation λ_p by Eq.(10), the thermal conductivity of reactive solid, λ_s, must be given in advance. But there have been no reference on λ_s of solid products reacted with gas. Hence we could not do other than assume that λ_s is equal to that of the unreacted $CaCl_2$, λ_s=2.36 W/mK. One of the possible reasons supporting this assumption is that the gas substance reacted with $CaCl_2$ must be treated as condensed phase or solid in estimating thermophysical properties of volume and heat capacity [1], but it is impossible to know the absolute value of λ_s. The thermal conductivity of gas phase, λ_g, in Eq.(10) was calculated from Eq.(8) by replacing $D_p\cos\psi$ with the distance between grains, which was taken to be the mean diameter of pores inside the pellet measured by porosimeter, 0.5 μm.

Estimated pellet thermal conductivities are shown in Fig.7 by solid lines together with those determined from the measured effective thermal conductivity. Close agreement has been obtained between estimated and experimentally determined pellet thermal conductivities, λ_p, by taking R_c=0 mK/W for CaCl or R_c=2 mK/W for $CaCl_2 \cdot nCH_3NH_2$. This implies that the contact resistance on the surface of reactive grain is larger than that of unreacted CaCl, which is in accord with the difference in grain structure demonstrated by SEM observations. In unreacted $CaCl_2$ pellets the contact resistance between grains seems to be negligible since the grains are tightly fused or consolidated. On the contrary, in reactive pellets there is no fusion between grains but they are just in contact with each other. Contact resistance due to the micro roughness of contacting surface of the grains may yield a significant decrease in the thermal conductivity of reactive pellets.

4.5 Estimation of Effective Thermal Conductivity

The above investigation has been performed for unreacted $CaCl_2$ and reactive solids with $n \leq 2$, since only these pellets could be used for the measurements of pressure dependence of effective thermal conductivity, from which the pellet thermal conductivity was obtained. By using Eqs.(6) - (9) for λ_{eff} and Eq.(10) of λ_p, the effective thermal conductivity can now be estimated for any condition of the reactive solids with $n>2$. The estimation has been performed by two steps; first λ_p was calculated by Eq.(10) using β and R_c determined for $n \leq 2$ and ε_p obtained from the measured overall void fraction. Then λ_{eff} was estimated by Eqs.(6) - (9). Figure 9 shows a comparison of measured and estimated effective thermal conductivities, λ_{eff}, of beds of $CaCl_2 \cdot nCH_3NH_2$. In this figure the gas phase for $CaCl_2 \cdot nCH_3NH_2$ with $n \leq 2$ is nitrogen at 101.3 kPa and that of $CaCl_2 \cdot nCH_3NH_2$ with $n \geq 2$ is methylamine at a pressure appropriate to maintaining the reactive solid in one of

the equilibrium states, that is, between 12 kPa and 20 kPa for n=4 and about 35 kPa for n=6. The effective thermal conductivity for n≤2 is larger than that for n>2 because the thermal conductivity λ_g under the normal condition and the pressure of nitrogen were larger than those of methylamine. Thus, the formulas derived from the model in this study can satisfactorily describe the variations of effective thermal conductivity of porous reactive solid beds under an arbitrary condition of the solid phase composition, pellet void fraction, gas substance and pressure.

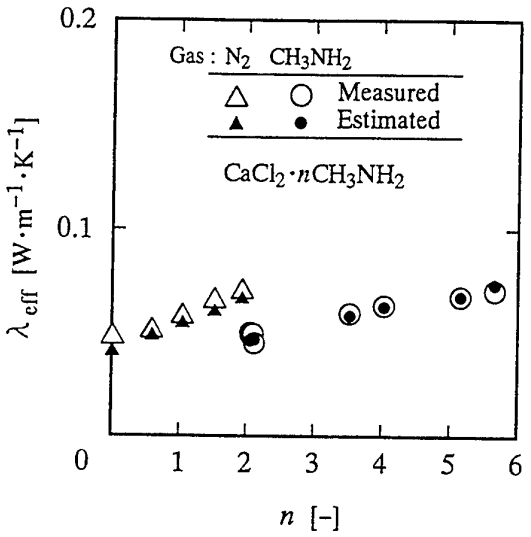


Fig.9 Measured and estimated effective thermal conductivity of $CaCl_2 \cdot nCH_3OH_2$ bed

5. CONCLUSION

Experimental study on the effective thermal conductivity and structure of $CaCl_2$ reactive solid beds have been performed to examine their changes due to reaction. Two kinds of void fractions, which are essential to the study of heat transfer in a bed packed with porous pellets, have been obtained from the porosimetry measurements. In the bed which was allowed to expand or contract freely, the bed void fraction, ε_b, could be assumed to be unchanged, while the pellet void fraction, ε_p, varied with reaction. SEM observations made it clear that transformation of fine structure of pellets was caused by reaction. The effective thermal conductivity of the bed of reactive solid was reduced to less than one half of that of unreacted $CaCl_2$, which was caused by the change in pellet void fraction and aggregation state of grains of reactive solid. Model equations have been developed to estimate the effective thermal conductivities of bed and pellet, λ_{eff} and λ_p, the basic idea of which will be of help for understanding the mechanism of heat transfer in a reactor bed of porous pellets.

REFERENCES

1. K. Fujioka, S.Kato, S.Fujiki and Y.Hirata; "Variation of Molar Volume and Heat Capacity of Reactive Solids of $CaCl_2$ Used for Chemical Heat Pumps", Journal of Chemical Engineering of Japan, v29, 858-864 (1996).
2. K. Fujioka, S.Kato and Y.Hirata; "Measurements of Effective Thermal conductivity of $CaCl_2$ Reactor Beds Used for Driving Chemical Heat Pumps", Journal of Chemical Engineering of Japan, v31, 266-272 (1998).
3. D. Kunii, and J.M.Smith, "Heat Transfer Characteristics of Porous Rocks",A.I.Ch.E.J, v6, 71-78 (1960)
4. M. Okazaki, I.Ito and R.Toei; "Effective Thermal Conductivities of Wet Granular Materials", AIChE Symposium Series, v163, 164-176 (1977).
5. E.H. Kennard, *Kinetic Theory of Gases*, Mac-Graw-Hill,New York and London (1938).
6. K. Ridgway, and K.J.Tarbuck; "The Random Packing of Spheres", Brit.Chem.Eng., v12, 384 (1967).
7. A.V. Luikov, A.G.Shshkov, L.L.Vasiliev and Yu.E.Fraiman; "Thermal Conductivity of Porous Systems", Int.L.Heat Mass Transfer, v11, 117 (1966).

ON THE USE OF DIAMOND-COATED JUNCTIONS TO ENHANCE THERMAL CONTACT CONDUCTANCE

Kee-Chiang Chung
Professor, Department of Mechanical Engineering
National Yunlin University of Science and Technology
Touliu City, Yunlin 640, TAIWAN
Email:chungkc@pine.yuntech.edu.tw; Fax:(886)5531-2022

Chien-Ting Chen
Undergraduate research assistance, Department of Mechanical Engineering
National Yunlin University of Science and Technology
Touliu City, Yunlin 640, TAIWAN

Keywords:diamond coatings, thermal conductance, thermal enhance

ABSTRACT. An experimental investigation was conducted to determine the degree to which the overall thermal contact conductance at the interface of contacting tungsten carbide (WC) surfaces could be enhanced through the use of vapor deposited diamond coatings. Effect of coating thickness on the thermal contact conductance was studied using three different diamond coating thicknesses. It was apparent that the thermal contact conductance enhancement effect was greatest at low contact pressures and decreased significantly with respect to increases in the contact pressure.

1. INTRODUCTION

When two surfaces are brought together, they contact in only a relatively few discrete points, due to the individual surface roughnesses and microscopic asperities. Yovanovich [1] have demonstrated that the actual contact area is between two and five percent of the apparent contact area by experimental investigations. Because of this significant area reduction, a thermal resistance occurs at the interface, resulting in a temperature discontinuity [2]. Heat can be transferred across the interface by conduction through the actual contacts, conduction through the substance in the gaps around the contacts, and radiation across the gap, or a combination of all three called overall thermal contact conductance as shown in Fig. 1. The most common method of

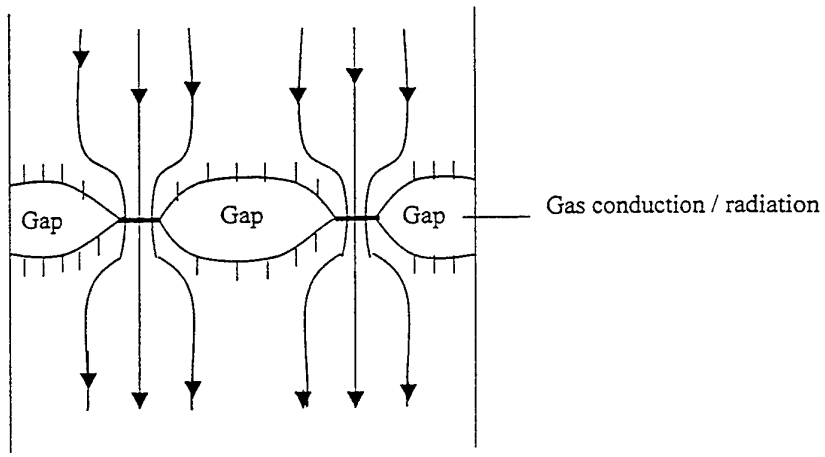


Fig. 1. Heat flow through contacting surfaces

enhancing the thermal contact conductance is to increase the apparent contact pressure at the interface. Unfortunately, this is not always possible due to design or load restrictions. One of the more promising methods

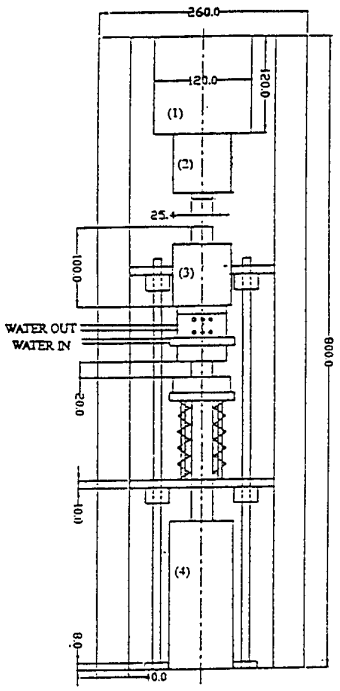
for improving the thermal performance of electronic systems involves the use of special surface treatments and/or thermal control materials inserted or added to the interface between subcomponents or components [3]. In such situations, the thermal contact conductance can be enhanced through the use of thermal greases, thin metal foils, or a thin metal coating deposited on one or both of the surfaces. The advantages and disadvantages of these techniques, thermal grease, thin metal foils and coating deposition, have been presented and discussed by Peterson and Ortega [4]. However, thermal grease cannot be employed in many critical electronic assemblies because of the possibility of the grease evaporating and contaminating nearby sensitive components. Foils are attractive from a theoretical point of view but in practice they are not used very often. This is because soft foils tend to wrinkle, which can result in an increase rather than a decrease in the contact resistance. Furthermore, soft foils are flimsy, often deflecting under their own weight, which makes them difficult to handle and apply effectively. Surface treatments include surface preparation as well as the addition of vapor-deposited materials on the contacting surface. Metallic coatings are free of the contamination problems associated with thermal greases and the handling problems associated with soft foils. In addition, many investigators [5-10] have reported as much as an order of magnitude improvement in the thermal contact conductance when one of the contacting surfaces of a joint is coated.

Due to its excellent thermal and electrical properties, diamond appears to be the most promising material for meeting the thermal and electrical requirements for future advanced industrial application. The most wide used material in cutting tool inserts for machining operations is tungsten carbide (WC). Thus, this paper studied the using chemical vapor deposition technique coated diamond films on WC substrate to increase the thermal contact conductance. Besides being the hardest known material, diamond also has other unique properties which makes it ideal for many engineering applications. For example, diamond film is one of the most potential material for thermal control purpose because of its excellent thermal and electrical properties. However, there has been limited work with diamond film for thermal enhancement applications. An experimental study will conduct in this paper including diamond film coated on WC substrates, test facilities setup, and the effect of surface characteristics on thermal contact conductance. It is believed that the using of diamond film should be able to decrease the interface thermal resistance and to increase the thermal performance of most thermal systems.

2. EXPERIMENTAL APPARATUS

An experimental investigation was conducted to determine the thermal contact conductance between WC samples coated by diamond. A series of static heat transfer tests were conducted to determine the effects of contact pressure on various surface coatings. A schematic diagram of the test apparatus is shown in Fig. 2. The test specimens, which were 2.54 cm long and 2.54 cm in diameter, were made of WC. The test samples were placed in a vertical alignment with two heat flowmeters. Each heat flowmeter, which was made of 304 stainless steel, was approximately 10.16 cm long and 2.54 cm in diameter. The length of the heat flowmeters and the heavy insulation ensured that the heat flux through each heat flowmeter was one-dimensional. Four holes, 1.27 cm deep, were radially drilled in each heat flowmeter to accommodate the thermocouples. The holes in the heat flowmeters for thermocouples were 1.6 mm in diameter and drilled perpendicular to the axes of the heat flowmeters. Bare thermocouples, made from 28-gauge copper/constantan wire, were placed in each hole for sensing the temperatures along the centerline of the heat flowmeters. Upon installation of these bare thermocouples, a silver grease having high thermal conductivity was used to fill the holes containing the thermocouples. These thermocouples were used to measure the axial temperature gradient of the test stacks, whereby the interface temperature can be calculated for the secondary and primary surfaces.

In performing the experiments, heating and cooling systems were employed to create a one-dimensional, steady-state heat flow across the heat test interface. A heat source was supplied to the top of the test stack by an electrical resistance heater. The heat flow was prevented from conducting out the top of the heater unit by inserting an insulating spacer between the heater and the upper support plate. The temperature at the test interface was kept constant with the use of a temperature controller which regulated the power to the heater. The heat sink or cooling unit was placed at the bottom of the test stack. Tap water was used as the cooling medium. The use of a three-way gate valve and volumetric flowmeter provided a method of controlling the cooling water mass flow to the cooling system. A thermal grease was applied to all interfaces except for the test interface in order to enhance the heat transfer across the contacting interface.



(1) Heater

(2)Insulation with heat flowmeter

(3)Cooling system

(4)Air cylinder

All dimensions are mm

Fig. 2. Experimental apparatus

The effect of the applied contact pressure on the test interface was studied. These pressures were achieved by a push-rod attached to a pneumatic pressure cylinder that activated a bellows. The entire system, which included the heater, heat flowmeters, test samples and heat sink, was placed on top of this bellows, forming a stack. The force present in the sink was measured by a calibrated device consisting of a load cell, pressure transducer, air cylinder and the base plate. This cylinder was raised and lowered gradually to avoid impact forces that might alter the contacting surface characteristics. .

Experimental Procedure

Tests were conducted to determine the thermal contact conductance for both uncoated/coated and coated/coated junctions. Uncoated interfaces were tested first to establish a baseline thermal contact conductance value for each sample. Three different coating thicknesses of test samples were employed to investigated the effect of coating thickness.

The same experimental procedure was followed for all the tests. First, the cooling system was turned on. Then, the three-way gate valve on the cooling fluid control panel was set to the flow position. The test samples were stored in a vacuum environment prior to testing. Each test specimen was removed from the vacuum container when needed. Next, the sample was carefully placed between the heat flowmeters. In conducting such an experiment of this kind, it was imperative that the test column be in perfect alignment. If it was not, then there would be a variance in the tolerance between the test stack members which in turn would cause undesirable thermal resistance at the contact interfaces other than the test interfaces. These resistances could produce nonuniform temperature distribution on local cross sections of the stack near the interfaces, and hence the temperature measurements of the heat flowmeter would not represent the appropriate value. The test sample should be tested with machined directions aligned approximately parallel. The test column was aligned visually and a slight load was applied to the test column to prevent the specimen from shifting during the evacuation of the test chamber. The average heat flux for a test was calculated by using a finite difference approximation for the temperature gradient. The overall thermal contact conductance was then calculated using the average heat flux of the heated and cooled specimens divided by the temperature drop across the test interface.

3. UNCERTAINLY ANALYSIS

An experimental investigation is not complete without estimation of the uncertainties associated with the

measured values. An estimate of measured quantities and the resulting calculated values of uncertainty will be made based on the procedure described by Schenck [11].

The experimental thermal contact conductance was determined from the temperature drop and the heat flow rate across the interface. The heat flux through the interface was considered to be the mean of the thermal fluxes through the heat flowmeters. The heat flux of the upper heat flowmeter was estimated to be 18% higher than that of the lower heat flowmeter. The uncertainty in the overall thermal contact conductance of the diamond-coating interface is calculated to be 11.5%, approximately.

4. RESULTS AND DISCUSSION

The ideal of this experimental setup was to provide a means to determine the effect on thermal contact conductance of the diamond coating interface under various contact pressures. The data obtained from the thermocouples were used to calculate the temperature jump across the test interface and the corresponding thermal contact conductance.

The uncoated WC substrate sample is tested first. Based on these baseline thermal performance characteristics, it is possible to experimentally determine potential improvements in the thermal performance with coated surfaces. This investigation involves the experimental determination of the thermal contact conductance of WC substrate jointed to the surface coated with diamond. The calculated overall thermal contact conductance data for bare surface sample is compared with those of coated surface pairs in order to obtain the dimensionless overall thermal contact conductance, defined as the ratio of the overall thermal contact conductance for the same pressure.

The results of bare specimen and three different thicknesses of diamond coatings samples are presented in Fig. 3. Under the constant interface temperature, contact pressures were varied from 1.37 MPa to 3.73 MPa. The three diamond coating thicknesses are 6, 14 and 31 μm, respectively. Basically, the overall thermal joint conductance

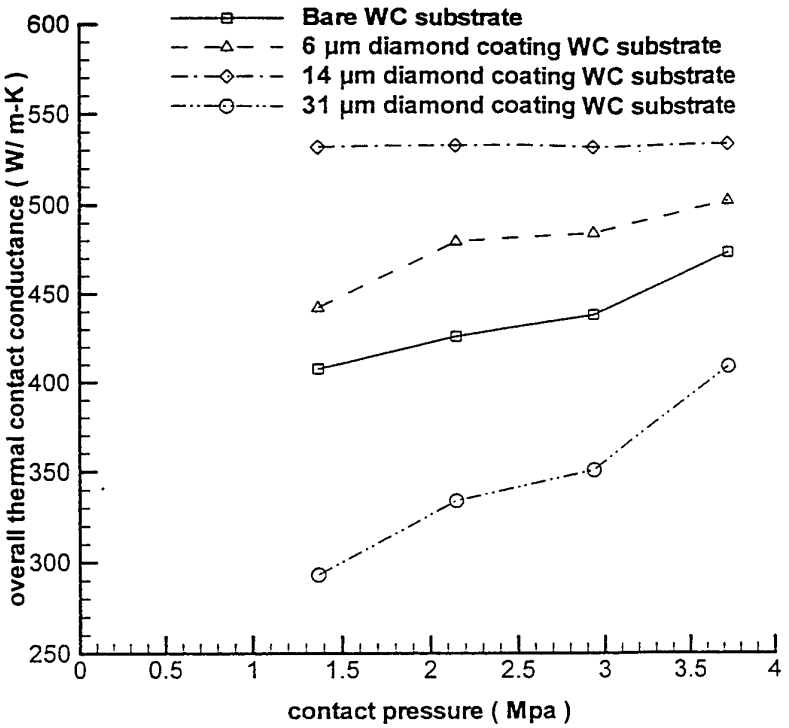


Fig. 3. Overall joint conductance as a function of pressure

increased with increasing interfacial load. As expect, the measured results for each sample are different due to minor variations in the surface characteristics of the contacting surfaces. The greatest enhancement of the thermal contact conductance was obtained for 14 μ m diamond coatings, as shown in Fig. 3. The thicker coating sample (31 μm) presented a lower overall thermal contact conductance at the interface. In order to obtain the optimum thicknesses of the layer for different interface pressures, both the uncoated and coated junction results were curefit using a linear regression technique, the dimensionless overall thermal contact conductance defined as the ratio of thermal contact conductance for the coated joint and the thermal contact conductance for the uncoated joint at the same pressure, were computed.

The dimensionless overall thermal contact conductance data for diamond coatings are presented in Figure 4. The ratios of the coated overall thermal contact conductance to the overall uncoated thermal contact conductance at four different pressures are plotted as a function of the coating thickness, t. As illustrated in Fig. 4, three different coating thicknesses were tested and the ratio of the coated thermal contact conductance to the uncoated thermal contact conductance at four different pressures were plotted as a function of the coating thickness. The results indicate that the dimensionless overall thermal contact conductance increases as the coating thickness increases, up to thickness of 14 μm. At this point, the dimensionless overall thermal contact conductance decreases with increasing coating thickness. The reason might be due to that when the coating thickness is increased at constant pressure, the enhancement of the thermal contact conductance results from the increase of contact area. If the coating thickness is increased further, the enhancement due to the increase in area is overshadowed by the increase of the bulk thermal resistance of the coating material. An optimum thickness is reached when the combination of these two effects results in the minimum resistance. It is believed that an optimum coating thickness exists in such coated junctions. Basically, moderate coating thickness can enhance thermal conductance due to the coating material displacing the interstitial gas and increasing the contact area. However, excessive coating thickness will increase the bulk thermal resistance of the coating material and decrease the thermal conductance at the interface.

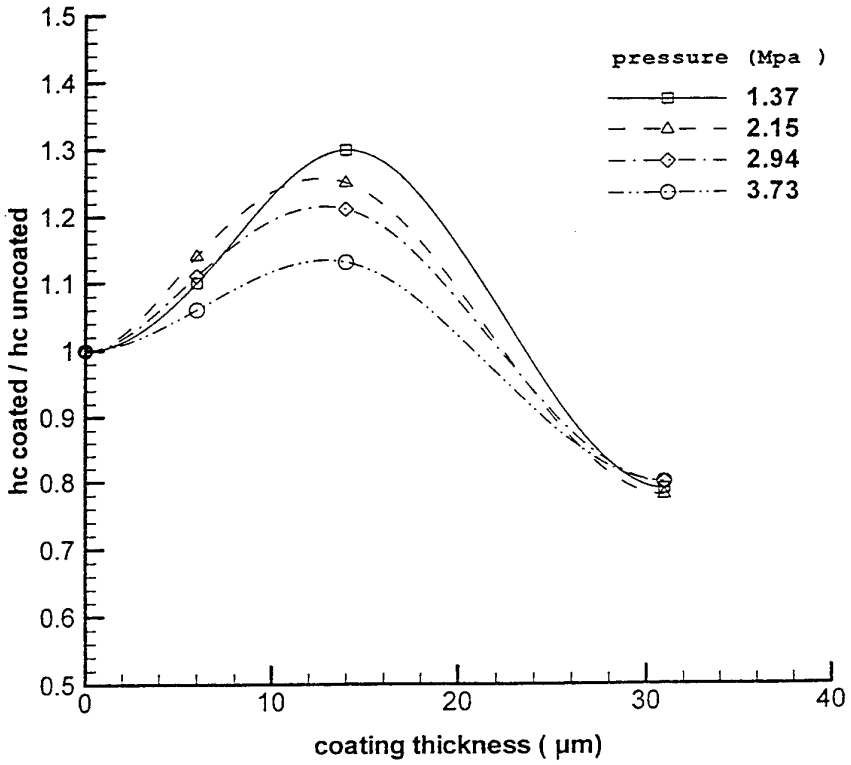


Fig. 4. Dimensionless Overall joint conductance as a function of coating thickness

It is also apparent from Fig. 4, that at a constant coating thickness, the enhancement of the overall thermal contact conductance decreases as the pressure increases. When the pressure is initially increased, the contact area of the coated joints increases much faster than for the uncoated joints. As the pressure continues to increase, the rapid increase in contact area is decreased by the surface asperities which have penetrated the coatings and are in contact with the WC substrate. However, for the 6 μm coating thickness sample, a deviation was found at 1.37 Mpa pressure. This is probably in large part due to differences in the surface profile of the specimens. The surface of this specimen exhibited significant crowing. This would prohibit contact over the annulus surrounding the raised portion of the surface, causing decreased thermal conductance.

5. CONCLUSIONS

The theoretical models of the heat transfer at the junctions can provide excellent opportunities for parametric investigations. Such studies are extremely useful in analyzing new machine tools designs. However, in most instances, the geometries of real design systems are sufficiently complex that analytical techniques are difficult to use and experimental investigations have been conducted to provide data for analysis. The use of diamond coatings to enhance thermal contact conductance has been studied experimentally. To study the effect of coating thickness, a steady-state conductive heat transfer experiments were conducted. The phenomena of optimum coating thickness was observed in this investigation. Basically, moderate coating thickness can enhance thermal conductance due to the coating material displacing the interstitial gas and increasing the contact area. However, excessive coating thickness will increase the bulk thermal resistance of the coating material and decrease the thermal conductance at the interface. When the coating thickness is too thick, exceeding the optimum coating thickness which produces the high thermal contact conductance, a negative effect on the enhancement thermal contact conductance can result.

The experimental results also show a common tendency for the enhancement of the dimensionless thermal contact conductance to increase as the contact pressure decreases. The discrepancy of some measured data is probably in large part due to differences in surface profile of the specimens caused by the manufacturing process. The overall thermal contact conductance can be enhanced by coating 6 and 14 μm diamond but opposite effect cab be observed in 31 μm diamond coatings. It should be noted that these values may only be valid for contacting surfaces which have surface characteristic values similar to those tested in the experimental investigation.

REFERENCES

1. M. Yovanovich, "Theory and Applications of Constrictions of Constriction and Spreading Resistance Concepts for Microelectronic Thermal Control," Keynote Address, *Proceedings of the International Symposium on Cooling technology for Electronic Equipment,* Honolulu, Hawaii, (1987).
2. M. A. Lambert and L.S. Fletcher, AIAA Journal of Thermophysics and Heat Transfer v.8, pp.341-348, (1994).
3. E. G. Marotta, M. A. Lambert and L.S. Fletcher, AIAA Journal of Thermophysics and Heat Transfer v.8, pp.349-357, (1994).
4. G. P. Peterson, and A. Ortega, *Thermal Control of Electronic Equipment and Devices, Adv. Heat Transfer,* V 30, p. 181, (1990).
5. B. B. Mikic, and G. Carnasciali, "The Effect of Thermal Conductivity of Plating Material on Thermal Contact Conductance", *ASME Paper No. 69-WA/HT-9,* (1969).
6. V. W. Antonetti, and M. M. Yovanovich, ASME J. Heat Transfer v. 107, p. 513 (1985).
7. K. C. Chung, AIAA Journal of Thermophysics and Heat Transfer v.9, pp.681-685, (1995)
8. T.K. Kang, G. P. Peterson, and L. S. Fletcher, "Enhancing the Thermal Contact Conductance Through the Use of Thin Metallic Coating", *ASME Paper No. 89-HT-23*, (1989).
9. K. C. Chung and J. W. Sheffield, AIAA Journal of Thermophysics and Heat Transfer v.9, pp.329-334, (1995)
10. K. C. Chung, H. K. Benson and J. W. Sheffield, ASME Journal of Heat Transfer v.117, pp.508-610, (1995)
11 H. Schen, *Theories of Engineering Experimentation*, 3rd Ed., Hemisphere Publishing Corporation, Washington, (1979).

I. Microscale Heat Transfer

TWO-PHASE FLOW PATTERNS IN AN ULTRA-SMALL-SCALE FLOWING PASSAGE

Ziping Feng and Akimi Serizawa
Department of Nuclear Engineering
Kyoto University, Yoshida, Sakyo-ku, Kyoto 606-8501, Japan
Email: serizawa@kuiae.kyoto-u.ac.jp; Fax: 0081-75-753-5829;

Keywords: ultra-small tube, two-phase flow, flow pattern, visualization

ABSTRACT. The air-water two-phase flow patterns are visualized in a 25μm ultra-small flowing passage through a microscope. The superficial velocities of both two phases are covering a broad range of J_L=0.003-17.52m/s and J_G=0.0012-295.3m/s. Four distinctive flow patterns, namely, dispersed bubbly flow, gas slug flow, liquid ring flow and liquid lump flow, are observed and their special features are described. Among the four flow patterns, the liquid ring flow is a newly observed one that is characterized with a series of symmetrically distributed liquid rings surrounding the gas core.

1. INTRODUCTION

Advances in the modern engineering sciences, including electronic packaging, chemical processing, aircraft heat dissipating and various thermal-controlling systems have resulted to an urgent demand on the technology of removing dramatic high heat flux from a very small area and to provide the desired temperature uniformity. To meet these requirements, a series of small sized (generally in the order of 1mm or less) heat transfer devices has been designed recently. These devices involve micro-heat pipes, mini heat exchangers, micro-scale thermosyphon, oscillating capillary heat pipe, and porous heat exchanger, etc. In order to improve the performance of such a heat dissipation device, the information of the two-phase flow and its mechanisms in the small (of 1mm order) or ultra-small (of 1μm order) flow passage is required. The fundamental knowledge, such as the flow pattern, void fraction, pressure drop, liquid film thickness etc., are critical for the engineering design and practical performance, however, are quite limited so far. A comprehensive investigation of the two-phase flow characteristics in this kind of flow passage is very urgent both for the heat transfer, two-phase flow science and some other engineering practices. Understanding of this knowledge will be greatly beneficial to the modern and future electronic, space aviation, semiconductor, chemical process, bioengineering and even military equipment. Unfortunately, all the published works are conducted with capillaries of diameter larger than 500μm [1-4], while that of the diameter less than 500μm is still untouched and has been an central unresolved problem in the two-phase science. Based on these backgrounds, we visualized the air-water two-phase flow patterns in a 25μm round tube. From the experimental observation it is evident that the two-phase flow patterns in ultra-small tubes are quite different from that of the ordinary tubes as well as 1mm order micro-tubes. These differences are represented by the occurrence of a kind of liquid ring flow pattern that has a symmetrical liquid ring structure surrounding the gas core. Also, we obtained a liquid lump flow pattern that is decorated with the discrete liquid lumps. Besides, the dispersed bubbly flow and slug flow patterns are also observed and their special features are described.

2. EXPERIMENTAL APPARATUS

A schematic diagram of the test facility and the visualization system is shown in Fig.1 and Fig.2, respectively. The test section consists of a kind of transparent silica capillary tube with circular cross section and positioned horizontally. The tube inner diameter is 25μm and the outer diameter is 150μm. The whole length of the tube is 10000μm in which 8000μm is visible. Air phase is supplied by a high pressure gas bottle that also provides the pressure head for the water tank. As water is driven with high pressure air, no pump is used in the experiment. The two-phase flow is obtained through a mixer with diameter of 300μm (as shown in Fig.1). Air is injected into the mixer axially while the water is introduced peripherally. The inlet pressure of the test section is measured with a precise pressure gauge connected to the mixer, while the outlet pressure is roughly equal to atmospheric pressure.

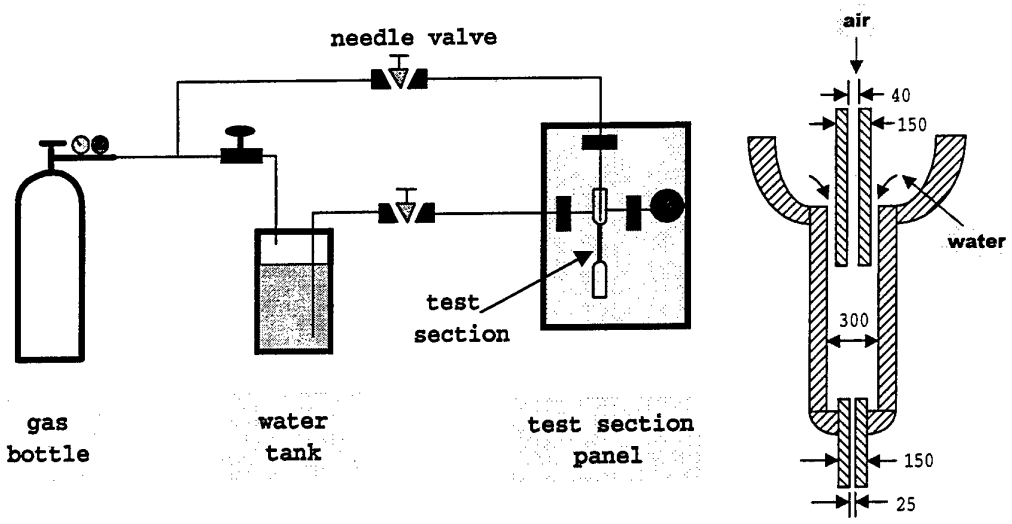


Figure 1. Schematic diagram of the experimental facility

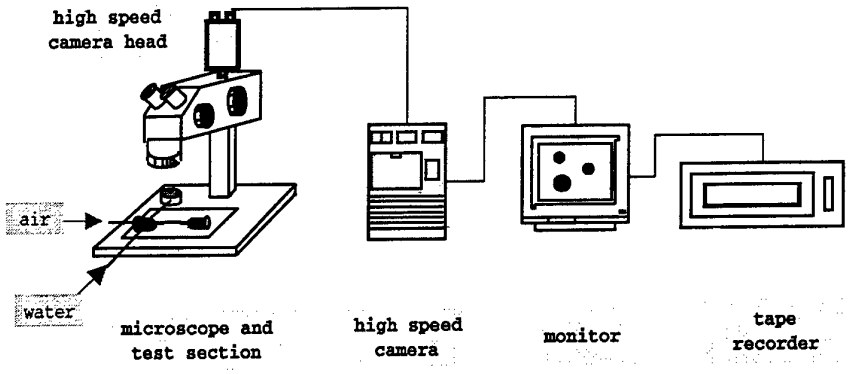


Figure 2. Assembling of the visualization system and the arrangement of test section

In order to measure the two-phase flow rate, a series of precise injection syringes are installed at the outlet of the test section through an injector head. These syringes can collect the two-phase flow coming from the test section and accurately read out the volumetric flow rates of both air and water phases. Because of the volumetric flow rate is extremely small in the cases such as dispersed bubbly flow, more than 24 hours are waited to get enough fluid volume. The visualization of the flow pattern was realized through a precise microscope (NIKON, SMZ-U type) which can magnify the image up to 150 times as that of the original size. A high-speed camera system (FASTCAM-Rabbit, CANON) with recording speed of 30 to 600 frames per second and shutting speed of 1/30 to 1/10000 second was mounted together with microscope. The light beam used for the visualization is provided through a adjustable light source under the test section. Two-phase flow patterns were visualized at the 7000μm (D/d=280) to 9000μm (D/d=360) part from the inlet of the test section. It is valuable to note that due to the effect of beam refraction, tube diameter is a little enlarged and it's not proportional to tube length in these obtained images.

3. VISUALIZATION RESULTS AND DISUSSION

Dispersed Bubbly Flow

Dispersed bubbles are observed when the gas flow rate is very small such as J_G=0.0083m/s. There are two kinds of bubbles in the present test. The one is finely dispersed bubbles with size smaller than the tube diameter.

Another kind of bubble has a size of near to or a little larger than the tube diameter, but the distance between two consecutive bubbles is much long, for example, more than ten times of the tube diameter. This flow pattern is also considered as a dispersed bubbly flow. It is very often that two kinds of bubbles appear together as a pair of bubble in which the small-sized bubble follow the larger one. It seems that the motion of small bubble is strongly influenced by the larger bubble. If the distance between two bubbles is within a certain range, they will move together in the same speed. If this distance is over a certain range, the small bubble will loose its inertia force and stick on the wall. A very interesting phenomenon was frequently happened. That is, the separation-closing-separation motion of bubbles within a bubble group, as shown in Fig.3. Where the distance between two bubbles is larger at t=2.6867s, while they become closer when t=2.7183s. The period of this distance oscillation is approximately equal to 0.6s under this condition. The mechanism for this relative movement has not been clarified. We think that it is probably due to the Bjerknes force between two nearby bubbles [5]. That is, one bubble is exposed to the pressure field generated by the self-sustained vibration of another bubble. This force can be an attractive or separating one, depends on the phase difference between two vibration bubbles. This, however, needs further research.

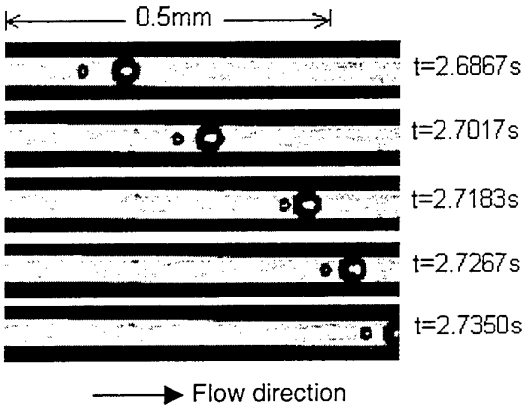


Figure 3. Relative movement and interaction between two bubbles (inlet pressure is *P*=0.24*MPa*; gas phase superficial velocity is *JG*=0.0083*m/s*; liquid phase superficial velocity is *JL*=0.0012*m/s*)

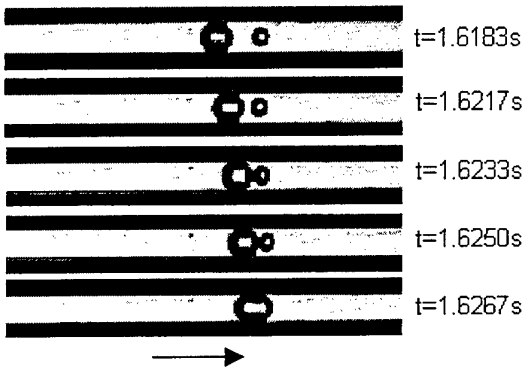


Figure 4. Emerging process of a still bubble with a moving large bubble (inlet pressure is *P*=0.24*MPa*; gas phase superficial velocity is *JG*=0.0083*m/s*; liquid phase superficial velocity is *JL*=0.0012*m/s*)

The dispersed bubbles observed in the present experiments are always maintaining a spherical shape, except those of the size equals to or a little larger than the tube diameter. This is mainly due to the high interfacial pressure difference and the strong rigidity of micro-sized bubble, which can be estimated by the well-known Laplace-Young equation

$$P_G - P_L = \frac{2\sigma}{R} \tag{1}$$

Applying this equation to a 5μm bubble we can find that the pressure difference on the bubble interface is almost reaches to 0.3bar. This pressure difference is sufficient to maintain a bubble with high spherical shape and to prevent the bubble shape from being distorted. Thus, the coalescence between two moving bubbles is hardly to be observed in such a small tube. In the present test, the observation is mainly conducted at the region of *L/D*=320-360. A whole length observation was also conducted, however, no coalescence between two moving bubbles was observed. The only condition under which the bubble coalescence occurs is when a large bubble is moving to a still one, as shown in Fig.4.

Of course, this does not mean that the bubble coalescence is impossible in ultra-small channels. In the present test, the shortcoming of the mixer prevents us from getting a large amount of bubbles inside the test channel.

Suppose that a more precise mixer has been adopted, we can expect that bubble coalescence may occur at very high void fraction conditions. But, this void fraction should be much higher than that of the ordinary tubes.

Gas Slug Flow

In ordinary sized tubes, the transition from the dispersed bubbly flow to slug flow requires the process of agglomeration or coalescence. The deformation of the bubble shape results in a zig-zig motion and therefore provides a chance for bubbles to be coalescent into a larger, Taylor-type bubbles. With increase in gas flow rate the bubble density increases and a point is reached where the dispersed bubbles become so closely packed that many collisions occur and the rate of the agglomeration to large bubbles increases sharply. This results in a transition to slug flow [6].

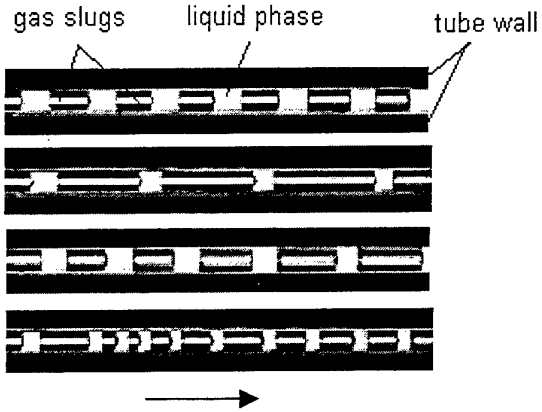


Figure 5. Typical gas slug flow pattern (the bright line in the center of the gas slug is the refractive light)

In ultra-small tubes, as mentioned above, the rigidity of bubble is high and bubbles are always keeping a spherical shape so that the coalescence loses its base. This induces a totally different mechanism for the dispersed bubbly flow transiting into the slug flow. From the experimental observation it is quite clear that the occurrence of the slug flow is rather an entrance phenomenon than inducing from the tube inside. Slug flow occurs only if the gas volume flow rate is higher at the tube entrance and the speed of long gas bubble is not high enough to overcome the strong surface tension force of the liquid bridge between them.

The distinctive difference between the slug flow and the dispersed large bubbly flow (of the bubble diameter is near to or a little larger than the tube diameter) in ultra-small tube is that the length of liquid slug between two consecutive gas volumes is more smaller than that of the gas slug itself. A typical slug flow pattern is given by Fig.5. It can be seen that the length of the gas slug is more than one tube diameter. The gas slug in the ultra-small tube is featured with a spherical head and a flat rear, which is similar as that of in larger scale pipes. However, the small bubbles following the gas slug is hardly to be observed.

During the experiment it is found that the pressure drop induced by the slug flow is awfully high. This means the sliding between gas slug and tube wall is suppressed and a dry zone has been developed under the gas slug. It is considered that the surface tension force plays an important role to this suppression. The surface tension force keeps liquid phase to a slug structure and prevents it from being dispersed as film. On the other hand, the ultra-small size of the gas slug will result a high pressure difference on the gas-liquid interface. This pressure difference pushes the gas slug to occupy the whole space of the tube cross-section and therefore it is difficult for the liquid film to be existed underneath the gas slug. Because of the same reason, slug coalescence is also seldom observed in the present experiment.

Liquid Ring Flow

The liquid ring flow can be developed from a slug flow pattern when the gas flow rate increases to such an extent that the liquid slug is too short to support a stable liquid bridge between two consecutive gas slugs. In other words, when the gas flow rate is sufficiently high, the length of the gas slug is increased while that of the

liquid slug is decreased. In a certain gas flow rate value, liquid slug will be penetrated by the gas slug and therefore a liquid ring is constructed. The liquid ring flow has never been observed by the conventional tubes, however, is quite often with the present tube size.

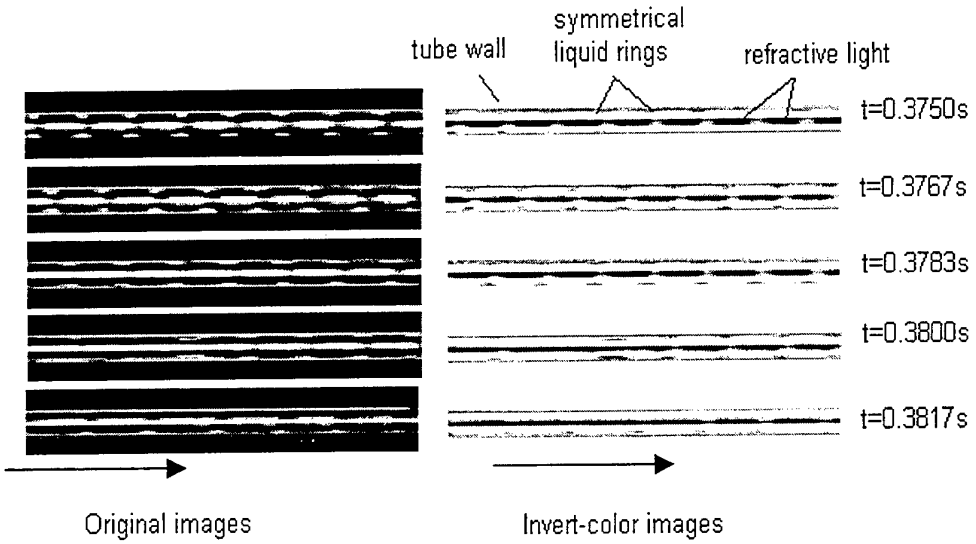


Figure 6. Typical liquid ring flow pattern, where the bright line in the original images (blank line in the invert-color images) is the refractive light (inlet pressure is P=0.30MPa, gas phase superficial velocity is JG=7.02m/s; liquid phase superficial velocity is JL=0.34m/s)

Fig.6 is the typical liquid ring flow structure where the liquid film on the wall is symmetrically distributed. From the experimental observation it is evident that the liquid ring flow transited from the gas slug flow when the gas velocity is high. In low gas velocity conditions, the liquid ring firstly appears in the middle of a long gas slug. It seems that this liquid ring is originally from a liquid bridge separating two consecutive gas slugs. When the gas velocity is high, many symmetrical liquid rings will appear on the tube wall with almost equal distance. The transition from the slug flow to the liquid ring flow in present ultra-small tube has some similarity with that of the slug-churn-annular flow transitions in conventional tubes. For example, two processes are all due to the breaking of the liquid slug. However, in ultra-small tube the liquid slug is broken into the discrete liquid rings rather than a uniformly distributed liquid film surrounding the gas core in the large sized tubes. This is considered as the results of the strong surface tension force. The surface tension force prevents the liquid ring from being dispersed as the film. On the other hand, even if there is liquid film under the gas core, the high pressure difference on the gas-liquid interface will push the liquid to the ring region.

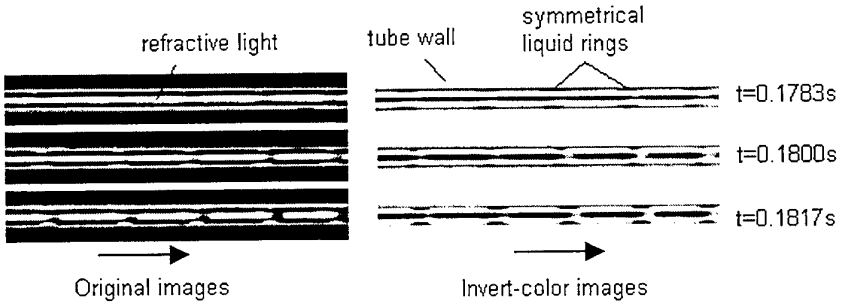


Figure 7. Growing process of still liquid rings, obtained when inlet pressure is P=0.31 Mpa; gas phase superficial velocity is JG=6.4m/s; liquid phase superficial velocity is JL=0.38m/s

Because of its special shape, the motion of liquid ring is determined by the force balance between the viscosity force from the wall and the drag force from the gas core. When the former one is dominant, liquid ring will stick on the wall and grow up, as shown in Fig.7. This growth is a result of the accumulation of the liquid film coming from the upstream. In this case we can sure that there is a liquid film in the upstream of the growing liquid ring. When the height of the liquid ring approaches to a certain value, the drag force from the gas core becomes dominant and the liquid ring moves to the downstream.

Liquid Lump Flow

In liquid ring flow, if we further increase the gas flow rate, a liquid lump flow, of which the liquid phase is entrained by the high-speed gas core and liquid lumps are sliding on the wall, will be developed, as shown in Fig.8. The shape of liquid lump is very similar as that of the wavy flow in a horizontal large tube. Similar as that of in liquid ring flow, the viscose force between tube wall and liquid lump and the drag force on the gas-liquid interface will dominate the motion of liquid lumps. When the former one is not strong enough, liquid lump will be still and shrink gradually. Because this shrinking is taking place within tens of milliseconds, the liquid lump should have been dispersed to the downstream with the status of liquid film.

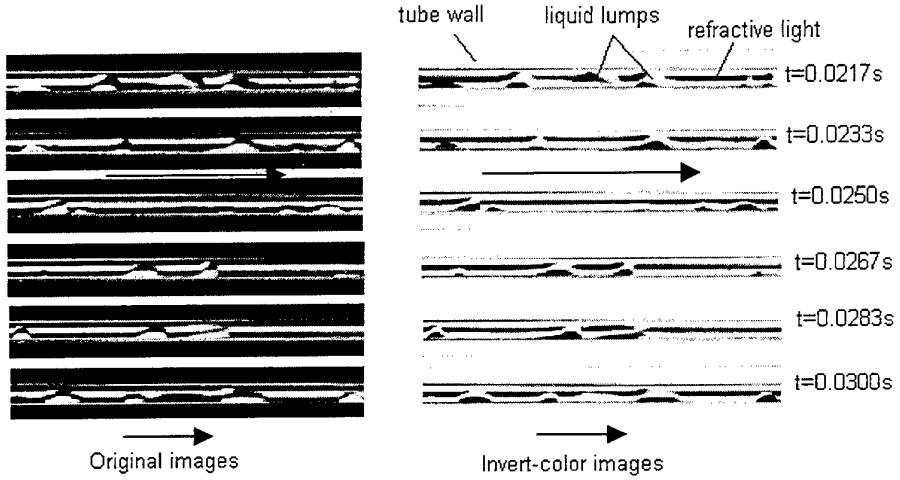


Figure 8. Typical liquid lump flow pattern, obtained when inlet pressure is P=0.29MPa, gas phase superficial velocity is JG=59.5m/s; liquid phase superficial velocity is JL=0.19m/s

It is valuable to indicate that there are distinctive differences between the conventional wavy flow and the present flow pattern. First, the effect of the gravity force is negligible in the ultra-small tubes. During the experiments it is found that the liquid lump is shifting from side to side. The appearing position of the liquid lump is dependent to its entry position and will keep on the certain side through the whole passage. Of course, the liquid lump position can also be influenced by a little distortion of the tube. Second, a dry zone may be developed between two consecutive liquid lumps being the effect of the surface tension force. When a liquid lump contacts with tube wall, the strong surface tension force will prevent it from spreading into the liquid film. Thus a dry zone may be developed. This dry zone, however, is not stable. It will be wetted by liquid film when the liquid flow rate is increased, as shown in Fig.9. Where a thick liquid film is developed on the wall and results to a high liquid lump. When the height of the liquid lump is sufficient, it will touch the other side of the wall so that bridge the gas core into gas slugs.

4. CONCLUSION

Air-water two-phase flow patterns are visualized in a $25\mu m$ ultra-small tube through a microscope. Four different flow patterns are observed and their detailed features are described. Among the four flow patterns, the liquid ring flow is a newly observed one which is represented by a symmetrically distributed liquid ring surrounding the continuous gas core. It is considered that this flow pattern is developed from the gas slug flow when the gas velocity is high. Liquid rings are uniformly distributed along the tube axis and a dry zone may be developed between two consecutive liquid rings. This dry zone can also appear in the gas slug flow and the

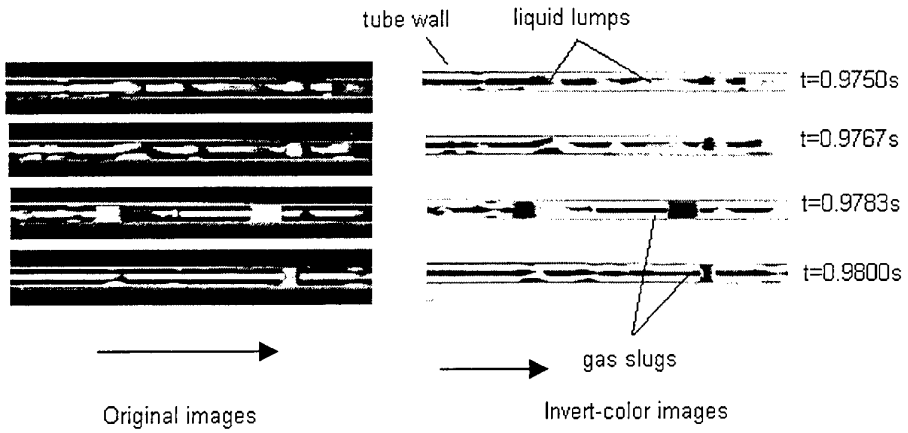


Figure 9. When the liquid flow rate is higher, liquid lumps will touch the other side of the wall and a gas slug will be constructed (obtained when inlet pressure is P=0.29MPa, gas phase superficial velocity is JG=27.6m/s; liquid phase superficial velocity is JL=0.51m/s)

liquid lump flow, however, we are not sure about the existence of this dry zone because sometimes the distinctive liquid film can also be observed on the wall. Therefore, more precise instruments are required to measure the detailed liquid film distribution on the wall.

The present study is just the first step to a comprehensive understanding of the two-phase flow in ultra-small flowing passage. A further detailed research is undertaking by the present authors. The flow pattern map and detailed liquid film thickness distribution will be the main topic of the following reports.

ACKNOWLEDGMENTS

The present research is financially supported by The Monbusho's Grant-in Aid for JSPS (Japan Society for the Promotion of Science) Fellows. One of the authors, Mr. Ziping Feng, his studying is also supported by the JSPS.

REFERENCES

1. J. Biswas and P. F. Greenfield, Two-phase flow through vertical capillaries-existence of a stratified flow pattern, *Int. J. Multiphase Flow*, Vol.11, pp553-563, (1985).
2. A. M. Barajas and R. L. Panton, The effects of contact angle on two-phase flow in capillary tubes, *Int. J. Multiphase Flow*, Vol.19, pp.337-346, (1993).
3. T. Fukano and A. Kariyasaki, Characteristics of gas-liquid two-phase flow in a capillary tube, *Nuclear Engineering and Design*, Vol.141, pp59-68, (1993).
4. H. Ide, H. Matsumura, Y. Tanaka and T. Fukano, Flow patterns and frictional pressure drop in gas-liquid two-phase flow in vertical capillary channels with rectangular cross section, *Trans. JSME*, 63(606B), pp452-460, (1997).
5. L. A. Crum, Bjerknes forces on bubbles in a stationary sound field, *JASA*, Vol.75, part 1, pp1363-1370, (1975).
6. Y. Taitel, D. Barnea and A. E. Dukler, Modeling flow pattern transitions for steady-upward gas-liquid flow in vertical tubes, *AIChE J.*, Vol.26, pp345-354, (1980).

MEASUREMENT OF FRICTION FACTORS FOR R134A&R12 THROUGH * MICROCHANNELS

L.S. Ding, H. Sun, X.L. Sheng, B.D.Lee
Institute of Environmental & Energy Source Engineering
Beijing Polytechnic University
Beijing 100022, P.R.China
Email: lsding@solaris.bjpu.edu.cn; Fax: (0086)-10-6739-5281

Keywords: microchannels, friction factors, liquid refrigerants, R12, R134a

ABSTRACT. An experimental work was conducted to investigate the pressure drops & friction factors for liquid of R134a and R12 through the micro-channels with triangular and rectangular cross sections. The equivalent diameters were 0.6mm and 0.4mm. The test section was different from the one before. The friction factors for liquid flow of refrigerant R-134a and R-12 were measured. Results show the correlation of the friction factors can be expressed as a formula $f=c/Re^m$. But the influence of roughness can't be neglected in the comparison. The third series of specimen were designed and manufactured in accordance with the experience before.

1. INTRODUCTION

Refrigerants, to be an important working fluid, not only be used for the refrigerating cycle in industry, but also be used for the integrated cooling of electronic circurls through the miniature heat exchanger using the microchannels. It can be able to cause the lower temperature of surface while the high intensity heat was brought out. Since the research of microchannels started by Tuckermann[1], hundreds of papers concerned appeared in the past twenty years. Pfahler[2] investigated the behavior of liquid in extremely small flow channels having 0.5-4.65μm deep, 95-115 μm wide , 10.5-10.9μm long with n-propanol and silicon oil. the material of microchannels were silicon wafer. Xin[3] research liquid water in microchannels having the 900μm-2.7mm deep with 150-300μm deep, the transition Reynolds Number Re_c and formula of f were given. Peng[4,5,6] did the research for microchannels having De=133—367μm with cross section of rectangular & triangular. The transition Reynolds number and formula of f Re equation were given. Adams[7] did the research for microchannels using water. It is found the different results be given from different researchers--different friction factor f, different transition Reynolds number Re_c, different formula of the friction factor f which were compared with the theory formula obeying the N-S equation. After our initial research of microchannels for refrigerants[8], we continue to do the systematically research [9-13]. Our schedule about the research of fluid flow and heat transfer of refrigerants in microchannels includes three parts: (1)Single phase liquid refrigerants, (2)Flow boiling of the refrigerants, (3)Super-saturatured gas refrigerants. Here is one of the first part in this paper.

2. EXPERIMENTAL APPARATUS

Test Loop

Fig.1 shows the test loop of refrigerants. Fulling the liquid refrigerants, tank No.1 were the source of the system. Passing through the dryer, liquid refrigerants had been supercooled through the first supercooler, then passed through the mass flowrate meter and second supercooler, arrived the test section. The mass flowrate of refrigerant was regulated by a valve before the test section. The refrigerants then entered the second tank, the pressure of which was controlled by both recovery machine and another regulation valve on the tank. All the liquid refrigerants was entered in the recovery tank No.3 through the recovery machine until its fulling enough. The position of Tank No.3 would be changed with the source tank No.1 if it was almost empty. An air conditioned test room having temperature and humidity auto-control had been built up for the test. Environmental temperature for test was set on 25°C±0.5°C. Test loop had already positioned in it for minimizing the heat loss/gain during the test. Sensors of pressure and pressure-difference with its transmitters were used for the measurement of pressure P and pressure drops ΔP of refrigerants during it passed through the microchannels. They were positioned in the headers of inlet and outlet respectively. Sensors of temperature were made in Copper/Contant Copper and were positioned in the center of inlet/outlet headers, the outside walls of

*The project is supported by NNSFC

microchannels along the flow direction, inlet/outlet of pressure difference sensor and outlet of the supercoolers respectively. HP-3852A Data Acquisition System were used to get all the electric data from sensors of pressure, temperature and mass-flowrate of refrigerants.

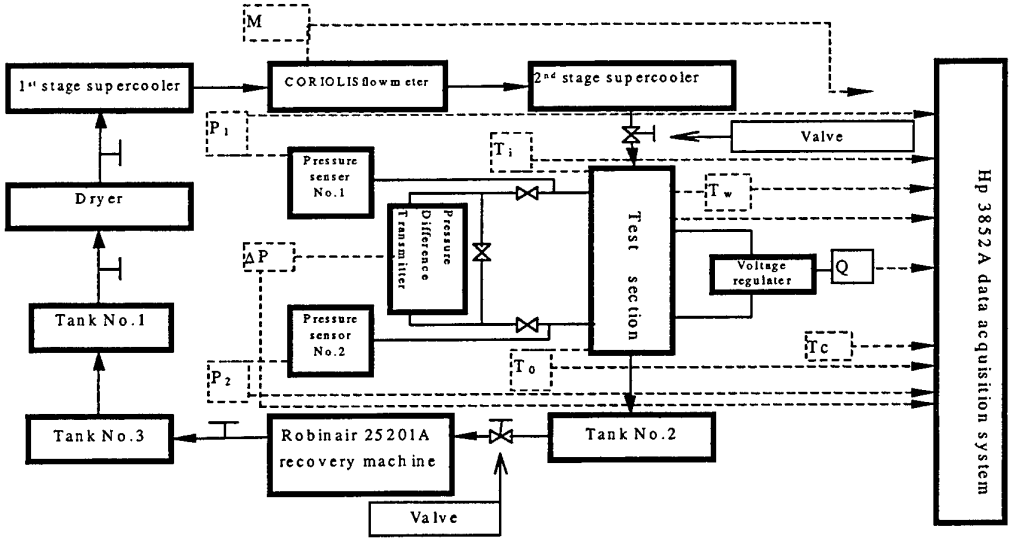
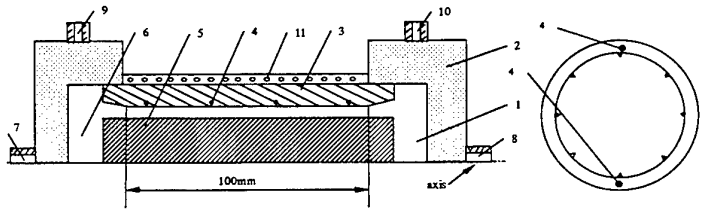


Fig. 1. Experimental loop of the refrigerants and measurement system for the testing of microchannels

Test Section

A new series of test section were manufactured specially for the improvement of refrigerant measurement, see Fig.2. It consists of inner core made of stainless steel and outside cylinder made of brass. The microchannels were manufacturing using Spark-Erosion Wire Cutting technique. The shape of cross section was square and 60° triangular. The materials of test section see Table 1. The size of microchannels see Table 2. Comparatively the new test section can be able to delete the phenomena of 'local collusion' between adjacent channels. Also, the inlet losses of the fluid flow can be able to decrese. Surface Roughness had been measured by Instrument Talysurf 5P-120. The roughness was around 2-3μm for the stainless steel surface using WEDM technique. The relative roughness for the microchannels under test was around 0.3-0.75%. The physical properties of the liquid refrigerants see Table 3.



1, 6-header
2-cover
3-brass case
4-thermocouples
5-stainless steel core
7, 8-inlet/outlet
9, 10-to sensors
11-electric heater

Fig. 2 Profile of the test section

Table 1. Properties for the Materials of Test Section

	Brass	Stainless steel (1Cr18Ni9Ti)
Density (kg/m^3)	8500	7800
Coefficient of expansion (10^{-4}cm/°C)	16.4	11.5
Thermal conductivity (W/m.K)	111	61
Specific heat (kJ/kg. °C)	0.385	0.46

Table 2. Dimensions of the Microchannels

Test section	Shape	Cross section		Distance between channels (mm)	Length of channel (mm)	Number of channels	Roughness	
		De(μm)	Length of side(μm)				Absolute (μm)	Relative (%)
1		400	400	7.5	100	12	≈2-3	0.5-0.75
2	∇	400	690	7.2	100	12		0.5-0.75
3		600	600	11.2	100	8		0.33-0.5
4	∇	600	1040	10.7	100	8		0.33-0.5

Table 3. Physical Properties of the Liquid Refrigerants

	Testing liquid		Comparable liquid
	R-134a [16]	R-12	Water
Molecular formula	CH_2F-CF_3	CCl_2F_2	H_2O
Molecular weight	102.03	120.91	18.02
Boiling point(101kpa) °C	-26.22	-29.79	100
Density of saturated liquid (25°C) (Kg/m^3)	1207	1313	1000
Conductivity (W/m.K)	0.088 (10°C,0.5Mpa)	0.072 (25°C)	0.586 (25°C)
Surface tension (mN/m)	7.71(26.7°C)	8.9 (26.7°C)	71.97 (25°C)
Polarity	Yes	No	Yes
Moment dipole	2.058d [14]	0	6.23×10^{-30} (c.m) [15]
Nonabsorbable gas (%)	1.05-1.5	1.05-1.5	≥0.3-0.4
Lubrication oil	No	yes	No
Specific heat of the saturated liquid (25°C) (KJ/Kg.)	1.3895(0.5Mpa, 15°C)	0.975	4.18
Viscosity of the saturated liquid (mpa.s)	0.198	0.257	1.006

3. EXPERIMENTAL RESULTS

After the leakage testing, vacuuming and feeding the refrigerants, start to the test. The temperature, pressure and mass flow rate were reaching a steady state. Notice the time difference between the two records were taken 9 second. Uncertainty is shown in Table 4.

Table 4. Uncertainty

Equivalent diameter De	Length of channel L	Pressure difference ΔP	Mass flow rate M	Friction factor f	Re
2.5%	0.1%	2.0%	1.0%	12.6%	3.0%

The correlation between friction factor f and Re Number for fully developed fluid flow is:

$$f=C/Re \quad (1)$$

where the constant C was related to the shape of cross section and type of fluid flow:

$$f=53.33/Re, \text{ for triangular, laminar } (Re<2200) \quad (2)$$

$$f=56.91/Re, \text{ for square, laminar } (Re<2200) \quad (3)$$

$$f=64/Re, \text{ for circular, laminar } (Re<2200) \quad (4)$$

$$f=0.3164/Re^{0.25}, \text{ for turbulent } (3000<Re<2*10^4) \quad (5)$$

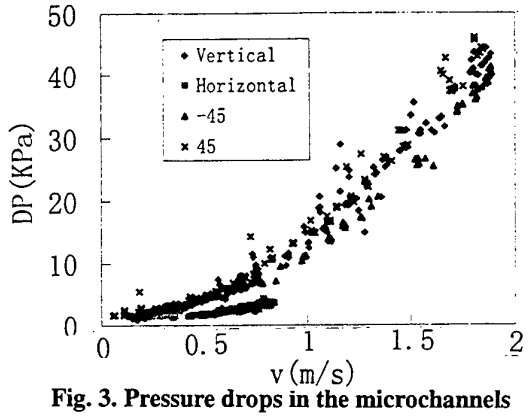


Fig. 3. Pressure drops in the microchannels having different position angles with R12 passing through

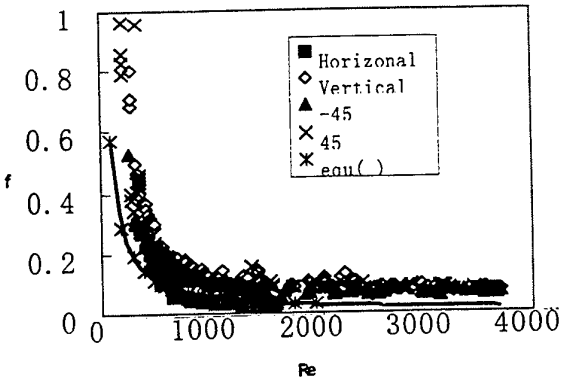


Fig. 4. Friction factors in microchannels having different position angles with R12 passing through

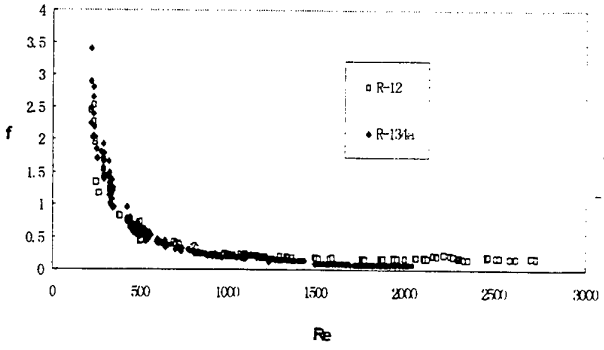


Fig. 5. Friction factors in microchannels with vertical position & R12 & R134a

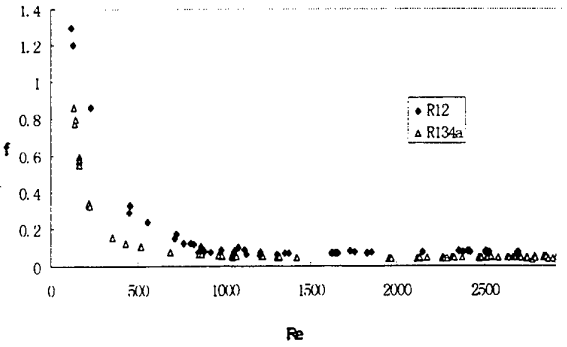


Fig. 6. Friction factors in microchannels with horizontal position & R12 & R134a

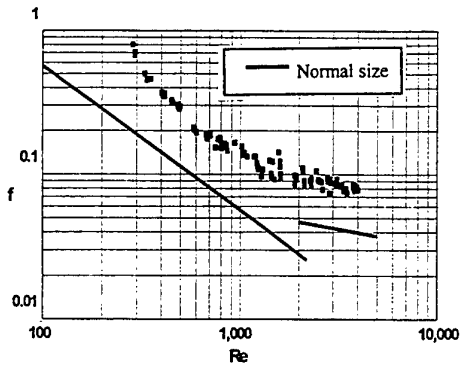


Fig. 7. Friction factor and De=0.4mm of microchannels having square cross section with liquid refrigerant passing through

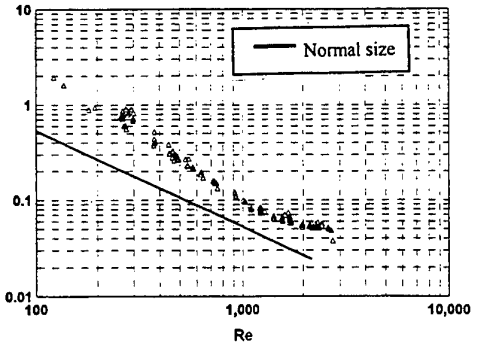


Fig. 8. Friction factor and De=0.4mm of microchannels having triangular cross section with liquid refrigerant passing through

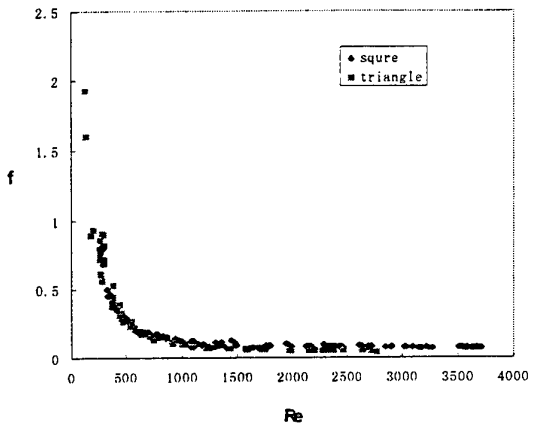


Fig. 9. Friction factors in microchannels having the different shape of cross section and the same equivalent diameter (de=0.4) with the liquid of refrigerant R12 passing through

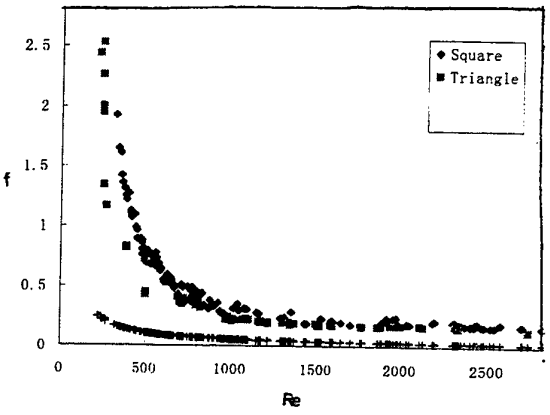


Fig. 10. Friction factors in microchannels having the different shape of cross section and the same equivalent diameter (de=0.6) with the liquid of refrigerant R12 passing through

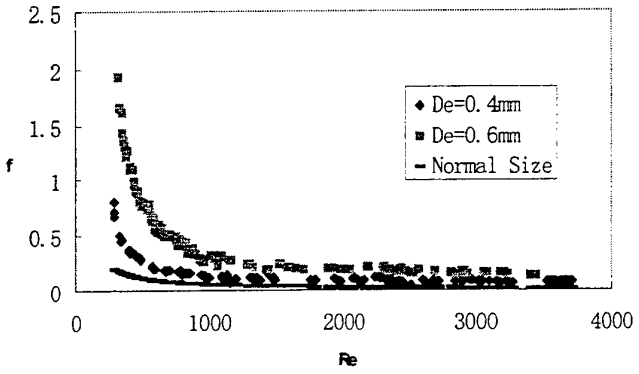


Fig. 11. Friction factors in microchannels having the different equivalent diameters with same square shape of cross-section with the refrigerant R12 passing through

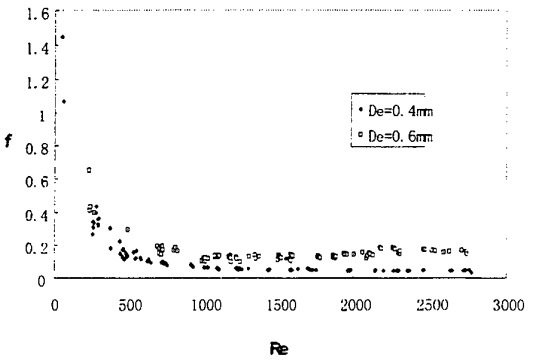


Fig. 12. Friction factors in microchannels having the different equivalent diameters and same triangular shape of cross-section with the refrigerant R12 passing through

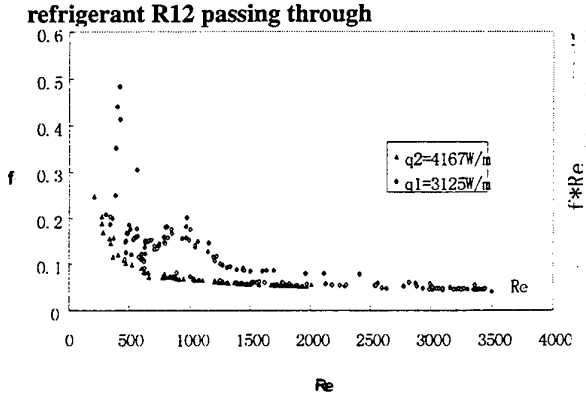


Fig. 13. Friction factors in microchannels having the different liquid temperature with the refrigerant R12 passing through

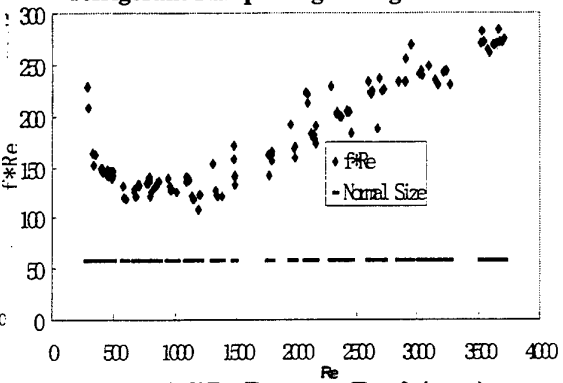


Fig. 14. f*Re-Re curve (De=0.4mm,)

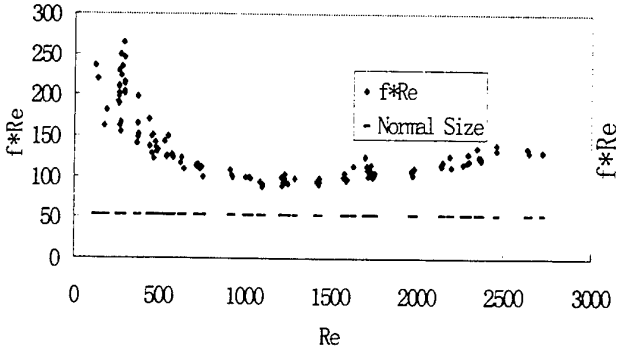


Fig. 15. f*Re-Re curve (De=0.4mm, Triangle)

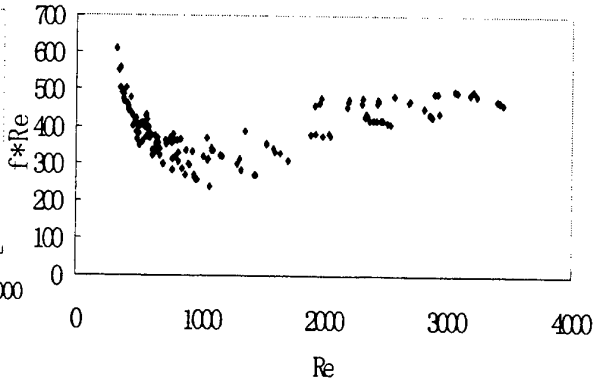


Fig. 16. f*Re-Re curve (De=0.6mm, Square)

Results

1. The friction factors of microchannels having the different position angles as a function of Reynolds number are shown in Fig.3,4. and Fig.5,6. It should be notice that the ΔP and f having the horizontal position be smaller than that of the vertical position for refrigerant R-12 and R134a. Also, the temperature of the microchannel at the upper position was a little bit larger than that of the lower position. Both of them are in the case of supercooling.

2. The friction factors of microchannels having the different shape of cross section with the same equivalent diameter as a function of Reynolds number are shown in Figs.7-10. The friction factors f of microchannels having cross section of square shape were larger than that of triangular shape.

3. The friction factors of microchannels having the different equivalent diameter with the same shape of cross section as a function of Reynolds number are shown in figure 11,12. The friction factors f of microchannels having the larger equivalent diameter were smaller than that of the smaller equivalent diameter.

4. The friction factors of microchannels having the different heat flux as a function of Reynolds number are shown in Fig.13. The friction factors f of microchannels having the larger heat flux is smaller than that of the smaller heat flux.

5. The friction factors of microchannels passing through the different refrigerant R134a and R12 with the same position angle as a function of Reynolds number are shown in Fig.5,6. The friction factor f of microchannels for R134a were smaller than that of the R12 in turbulent zone.

6. The f.Re values of microchannels having the different shape and size of cross section as a function of Reynolds number are shown in Fig. 14, 15, 16. The correlation of the f-Re is expressed as:

$$f=C/Re^{m} \qquad (6)$$

where C and m are related to the shape and size of cross section, the type of fluid flow. See table 5.

$f=(\Delta p.De)/(0.5\rho u^2 L)$, $Re=u.De/v$, De: equivalent diameter(m), ΔP: pressure difference(Pa),

ρ: density(kg/m^3), u: velocity(m/s), v: viscosity(Pa·s), L: length(m).

Table 5. Test Results

Shape of micro-channels	Equivalent diameter (μm)	Range of Re	Transition Re_c	Laminar		Fully developed turbulent	
				m	C	m	C
	600	400-3500	(1400,1500)	1.3717	3191.1	0.276	1.345
	400	400-3500	(1500,1800)	1.1269	6887.2	0.2888	0.7991
Δ	600	200-2500	(1100,1500)	1.4543	6887.2	0.5823	16.759
Δ	400	200-2500	(1100,1500)	1.5129	3387.8	0.5784	3.1494

Analysis

The influence of relative roughness. The larger the equivalent diameter is, the less the relative roughness is. Then the friction factor become smaller. Different range of roughness can be able to get by different machining technique. Roughness measured of stainless steel machined by milling machine and WEDM were around 0.2μm and 2-3μm respectively. Smaller roughness exists for some smooth surface, for instance, glass, pyrex and silicon wafer polished. The friction factor of theory is under the condition of absolute smooth surface and obeying the N-S equation. The results from our test show the friction factors f is larger than that of theory. But it is hard to compare for the roughness is larger than the smooth surface. Since another specimen of microchannel having smaller roughness (about 0.2μm)that we had tested, results show that the friction factors were smaller than that of the theory[12]. So the comparisons between the experimental data and theory data are true only under the case of similar roughness, then the analysis can be able to decide whether or not the N-S Equation is correct for microchannels. Also the transition Reynolds number is influenced by roughness.

The influence of mocular properties of liquid. Surface tension, polarity and contact angle between the liquid and solid surface of the liquid are important influence factors. Refrigerants 134a are polarity liquid having smaller surface tension. See Table 3. It is assumed the wetting between the R134a and metal were some better than the R12 and the same metal, since the R12 are unpolarity. The relation between the high energy potential surface-metal and polaity organic refrigerant R134a will be important. Advanced research should be continued. Also, the higher the temperature is, the smaller the surface tension and the viscosity both for R134a and R12 are. Then the friction factor must be smaller in accordance with the temperature.

The influence of non-absorbable gas and gavity. During our experiment,, friction factors of microchannels having vertical position were larger than that of horizontal position. One of the possible reason will be the influence of non-absorbable gas in the liquid. The percent in volume at least 0.5-1.5% except the gas left over by the vacuuming. Those gas left over the upper part of the system and test section during the horizotal position. At the vertical position, all the non-absorbable gas should be passed through the whole cross section of microchannels. Two phase flow were formulated, and the press drop will be larger. Another reason will be the influence of Gravity. The capillarity of refrigerants will be decrease by the Gravity. The pressure drop will be increasing. But in the horizontal position of test section, capillarity will not influenced by the gravity. And the center of layer is more cooled, the thin layers is lower than 1mm(≈0.6mm). The driven potential from Marangoni-Benard convection is possible.

The influence of test section. The material having smooth surface and small size will be needed for the comparison between the experiment and theory obeying the N-S equation. The material having some roughness surface with larger size will be needed also for the possible usage in Engineering. The comparisons between the test sections having the same roughness is useful.

The influence of the possible phenomena of collusion of liquid between the adjacent channels. Experiments showed as the reference [11], The phenomena of local collusion of liquid between the adjacent channels had been already caused the local decrease of pressure drop. This phenomena will be occurred specially for the refrigerant having higher pressure.

4. CONCLUSIONS

1. The influence of surface roughness is an important factor. For comparisons between the data of experimental and theory, the factor of relative roughness should be considered.
2. Under the same conditions, comparatively the friction factors of microchannels having different shape and

size of cross-section with different type of flow as a function of Reynolds Number as:

$$f=C_f/Re^m$$

3. where : m>1 for laminar, m<1 for turbulent C_f is a factor influenced by the shape of cross section of microchannels and the flow type. Also, the transition Reynolds Number from laminar to turbulent are smaller than that of the normal size.
4. The friction factors of microchannels were influenced by the refrigerants.The friction factors of R134a were less than that of R12 in the turbulent zone while they were similar in the laminar zone.
5. Comparisons between the test sections of new series and old series .The new series test section can be able to measure the pressure drops more precisely and repeatedly.
6. For the advanced fundamental research the third series of test section using silicon wafer is necessary. It has been designed and manufactured.

REFERENCES

1. D.B. Tuckerman, and R.F.W. Pease, "High Performance Heat Sinking For VLSI", IEEE Electron Device Letters, ED22, pp. 126~129 (1984).
2. J. Pfahler, J. Harley, and H.H. Bau, "*Liquid And Gas Transport In Small Channels*", Microstructures, Sensors and Actuators, DSC-Vol. 19 (1990)
3. M.D. Xin, "Experimental Research of Forced Convective Heat Transfer in Rectangular Microchannels", *Proceedings on the heat and mass transfer,* Institute of Thermophysics of China, (1992).
4. X.F. Peng, and G.P. Peterson, "*The Effect of Thermofluid and Geometrical Parameters on Convection of Liquids through Rectangular Microchannels*", Int.J.Heat Mass Transfer, Vol. 38, No. 4, pp. 755~758 (1995)
5. X.F. Peng, and G.P. Peterson, "*Convective Heat Transfer and Flow Friction for Water Flow in Microchannel Structures*", Int.J.Heat Mass Transfer, Vol. 39, No. 12, pp. 2599~2608 (1996).
6. X.F. Peng, and B.X. Wang, "Liquid Flow and Heat Transfer in Microchannels with/without Phase Change", *A special keynote lecture in the Tenth International Heat Transfer Conference* (1995)
7. T.M. Adams, S.I. Abdel-khalik, S.M. Jeter, and Z.H. Qureshi, "*An Experimental Investigation of Single-phase Forced Convection in Microchannels*", Int. Heat Mass Transfer, V. 41, Nos. 6-7, pp. 851-857 (1998).
8. L.S. Ding, M.J. Jiang, and H. Sun, "Measurement of Heat Transfer Characteristics and Friction Factors for the Refrigeration Evaporators", Heat Transfer and Technology, ed. by B.X. Wang, Higher Education Press, pp. 315~326 (1996).
9. H. Sun, "The research on flow boiling of CfC-12 in microchannels", *Proceedings on the heat science facing the 21st century* (1997).
10. W.L. Liu, "Experimental Research and Mechanism Analysis on Heat Transfer and Liquid Flow in Microscale Channels", Master's Thesis (1997).
11. F. Huang, "CFC12 Flow in Microchannels: Single–phase flow and boiling heat transfer" ,Master's Thesis (1998).
12. H. Guo, F. Huang, L.S. Ding, "*The research on the friction factor for microchannel heat exchanger*", Refrigeration, No. 4, pp. 8-13 (1998). (in Chinese)
13. X.L. Sheng, "Flow Characteristics of Refrigerant R12 and R134a in Microchannels", Master's Thesis, Beijing Polytechnic University (1999).
14. M. Barao, "Mocular Properties of Alternative Refrigerants", Int. J. Of Thermophysics, V. 18, No. 2, pp. 419-439 (1997).
15. *Inorganic Chemistry,* p276, Tianjing University (1983).
16. M.S. Zhu, "Properties of thermophysics for HFC-134a"

CHARACTERISTICS OF FRICTIONAL RESISTANCE FOR GAS FLOW IN MICROTUBES

Zhixin Li, Dongxing Du, Zengyuan Guo
Department of Engineering Mechanics, Tsinghua University
Email: lizhx@tsinghua.edu.cn; Fax:(86-10)-62781610

Keywords: microtubes, gas flow, characteristics of frictional resistance

ABSTRACT. A new tube-cutting method that was proven feasible by experimental results is adapted to measure the pressure and Mach number distribution along a microtube. Experiments and computation were also performed concerning the average Fanning friction factor of five microtubes with diameter ranging from 80.0 to 166.6 μm. It is found that the pressure distribution in a microtube became nonlinear at higher Mach number and the product of measured average Fanning friction factor C_{fa} and the Reynolds number Re is higher than 16 predicted by Moody chart for laminar flow. Numerical results show that the gas compressibility leads to a variation of the velocity profile, which results in a larger velocity gradient at the tube inner wall surface and consequently a larger friction coefficient. The transition from laminar to turbulence in microtubes occurs at $Re \approx 2300$, which is consistent with the results in macro tubes.

1. INTRODUCTION

Micro channels with diameter ranging from 100 to 0.1 micrometer have found applications in such areas as integrated cooling of the electronic components, micro heat exchangers, biochemical applications, and microelectromechanical systems (MEMS), etc.. It is more than likely that new applications will be found in the near future. Therefore, the study of microscale heat and momentum transfer is becoming an important subject of recent investigation. However, the experimental data reported by different authors are not in accord with each other. Wu and Little [1] measured the friction factor for both laminar and turbulent gas flow in very fine channels used for micro miniature Joule-Thomson refrigerators. The equivalent diameter of the channel is 45.46~83.08 μm. The results showed higher friction factor than that expected from classical Moody-Chart. Phafler et. al. [2,3] conducted experimental measurements of the friction coefficients for gas flow in microchannels with equivalent diameter ranging from 0.96 to 39.7 μm. They observed that the friction coefficients were 15% lower than those predicted by conventional theory. Choi [4] reported that the product of measured friction factor f and Reynolds number Re for gas flow in microtubes, of which the inside diameter ranges from 3.0 to 81.2 μm is 50.2-53.3, is lower than 64 for incompressible laminar flow. Harley et al. [5] conducted experimental and theoretical investigation of low Reynolds number, high subsonic number and compressible gas flow in trapezoid microchannel with equivalent diameter of 15.77 μm. The measured friction factor was in good agreement with the theoretical prediction of isothermal, locally fully developed gas flow.

Compressibility is an important influential factor to the of gas flow and heat transfer in microtubes. Prud'homme et al. [6] and van den Berg et al. [7] neglected the transverse velocity and used a perturbation expansion to solve the isothermal , compressible Navier-Stokes equations for laminar flow in a circular tube. For low Reynolds and Mach number flow, they obtained a 'locally self-similar' velocity profile and $f \cdot Re$ remains approximately 64. The heat transfer group of Tsinghua University conducted some theoretical and experimental investigations on the effect of compressibility for gas flow and heat transfer in microtubes. The analytical results and numerical simulation presented by Guo et al. [8,9] showed that the gas compressibility affects the velocity profile not only in amount, but also in shape. The variation of velocity profile is a function of local Mach number. Li et al. [10] performed experiments concerning the characteristics of gas flow resistance in microtubes with diameter of 84.7 and 144.4 μm. The measured frictional coefficients were higher than the classical value for incompressible, fully developed laminar flow in macro tubes.

Since no instruments with fine spatial resolution were available, most experimental study on micro flow were limited to the measurement of global quantities such as the mass flow rate, the inlet and outlet pressures of the

microchannel etc. Few researchers got the pressure distribution although it is important for the study on the characteristics of fluid flow in microchannels. Liu et al. [11] proposed and fabricated an integrated micro-channel/pressure sensor system using combined surface and bulk micromachining. Pong et al. [12] measured the pressure distribution along a micro-sized channel which is 3000 μm in length, 1.2 μm in height and 40 μm in width. They observed that the pressure distribution is not a linear function of the streamwise distance and the effect of Knudson Number is obvious.

In this paper, a new 'tube-cutting' method is adapted to measure the pressure distribution along a microtube and the resistance of gas flow in microtubes are also experimentally studied. Numerical simulation was also performed to analyze the experimental results.

2. EXPERIMENTAL PRINCIPLE

The basic principle of the tube-cutting method is based on the following fact. For steady adiabatic subsonic gas flow in microtubes, the mass flow rate, G, is one-to-one correspondence to the back pressure, p_b, when the stagnation pressure p_0 and the stagnation temperature T_0 are kept constant. In another word, the characteristics of fluid flow in a certain microtube can be determined by p_0, T_0, p_2 or by p_0, T_0, G.

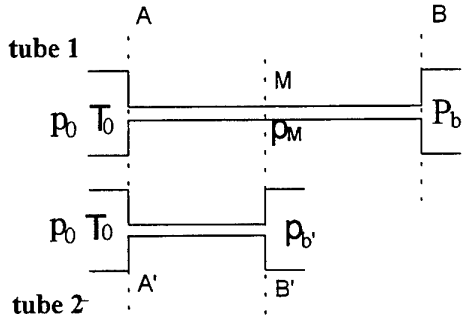


Fig. 1. Schematic of experimental principle

The experimental principle is schemed by Fig 1, in which tube 1 and tube 2 are microtubes with same diameter and material. During the experiments, make the inlet parameters, p_0, T_0, constant and adjust the back pressure of tube 2 to equate the mass flow rate of tube 2 to that of tube 1. From the above analysis, the fluid flow in the part, AM, of tube 1 is the same with tube 2, and the outlet pressure of tube 2, $p_{b'}$, will equal to the static pressure p_M of the tube 1. In fact, the essential of the tube-cutting method is to reappear the flow condition in section AM of tube 1 using the shorter tube 2. The pressure distribution along the microtube 1 then can be obtained indirectly by employing several microtubes with different length by this way.

3. EXPERIMENTAL APPARATUS

The experimental apparatus is depicted schematically in Fig 2. Nitrogen gas flows from a regulated high-pressure cylinder into a buffer chamber, goes through the test tube into the back pressure chamber, then flows past the pressure regulating valve and stationary flow valve, finally passes through a flow rate measurement unit into atmosphere. The test microtubes were prepared using glass-drawing technology and were treated as smooth tubes. The pressure regulation valve and stationary flow valve make it possible to regulate the back pressure of microtubes continually and steadily. In the flow measurement unit, the volumetric flow rate of the gas flow is determined by timing the exit gas replacing the water in a vessel whose volume was precisely measured beforehand.

Table 1 Dimension of the Microtube for Pressure Distribution Measurement

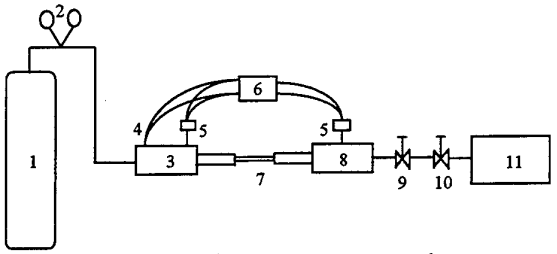
d_i (μm)	length L (mm)							
108.3	21.9	31.2	39.0	47.7	55.7	65.3	73.5	81.0

Precise knowledge of the microtube dimension is extremely important for the accurate evaluation of experimental results. The diameter of the microtube was measured with calibrated optical and scanning electron microscope, and the results agree within 2.5% of each other. The diameter and length of the microtube

or pressure distribution measurement are listed in Table 1, while the dimensions of microtube used for the measurement of average characteristics of frictional resistance are shown in Table 2.

Table 2. Diameter and Length of Microtubes Used for the Measurement of the Average Characteristics of Frictional Resistance

No	d_i (μm)	L (mm)
1	80.0	31.2
2	108.3	42.90
3	132.1	48.0
4	149.3	66.2
5	166.3	61.3
6	449.0	285.2
7	536.0	171.6



1. High-pressure nitrogen cylinder
2. pressure regulator
3. buffer chamber
4. thermocouple
5. pressure transmitter
6. precise millivoltmenter
7. test microtube
8. back pressure chamber
9. pressure regulation valve
10. stationary flow valve
11. flow rate measurement unit

Fig. 2. Experimental apparatus

4. RESULTS AND DISCUSSIONS

4.1 Calibration Experiment

To verify the reliability and veracity of the experimental apparatus, calibration experiments were performed. Due to the comparative larger inner diameter and lower Mach number, the gas flow in microtube No.6 and No.7 listed in Table 2 can be regarded as incompressible laminar flow. It can be clearly seen from Fig.3. that the measured C_f Re agrees well with that of incompressible, fully developed laminar flow in tubes, which indicates that the experimental apparatus and data processing system are reliable.

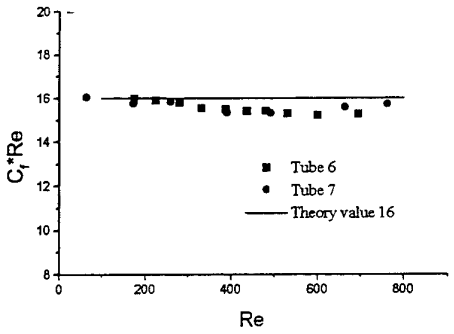


Fig. 3 Results of calibration experiments

Table 3. Experimemtal Conditions for the Pressure Distribution Measurement

No.	Stagnation pressure p_0 (Pa)	Stagnation temperature T_0 (K)	Inlet Mach number M_{in}
1	284130	299.50	0.087
2	383491	299.10	0.12
3	477861	299.10	0.14

4.2 Pressure Distribution Along the Microtube

The tube-cutting method was used to measure the axial pressure distribution in the microtube whose dimensions are listed in table 1. Table 3 lists three different experimental conditions and Fig.4 and Fig.5 show the experimental results. It is noted from Fig.4 and Fig.5 that at the forepart of the microtube, the Mach number is small and the pressure distribution is approximately linear, while at the rear part, the Mach number increases rapidly and the pressure distribution manifests different trend under different experimental conditions. The outlet Mach number of experimental condition No.1 is 0.243, so the pressure drop still remains approximately linear due to lower compressibility. Under the experimental condition of No. 2, the Mach number at the tube exit is higher (0.439) and the pressure drop deviates from linear distribution. In

experimental condition of No.3, the outlet Mach number is the highest (0.643) and the effect of compressibility is the largest, which leads to the largest pressure gradient at the exit of the microtube.

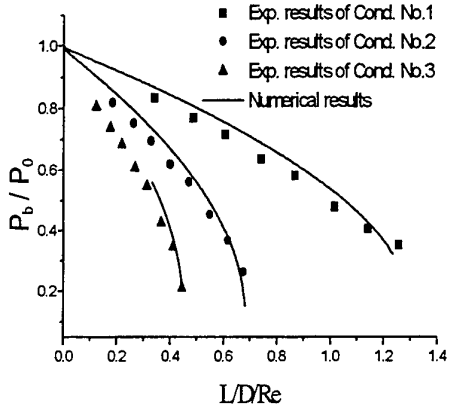


Fig. 4 Pressure distribution along the microtube

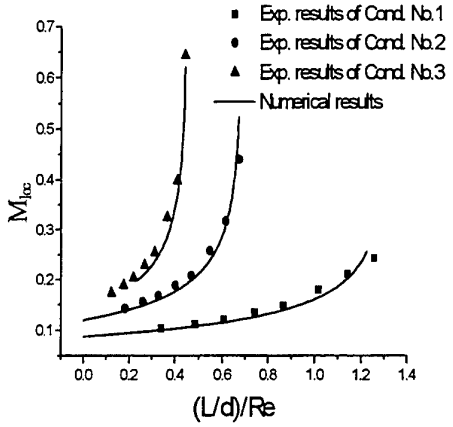


Fig. 5 Local Mach number variation along the microtube

To meet the demand of simulating compressible gas flow in microtubes, a revised SIMPLER algorithm was developed based on the characteristic of nearly invariable radial pressure for internal tube flow. Corresponding to three experimental conditions, numerical results were represented by solid lines in Fig.4 and Fig.5. It is obvious that the calculation results agree well with experimental ones and then it can be concluded that the tube-cutting method is feasible.

4.3 Average Characteristics of Frictional Resistance in Microtubes

Fig.6 shows the product of measured average Fanning friction factor C_{fa} and Reynolds number Re versus average Mach number M_{ave} in microtubes. It is noted that at lower average Mach number ($M_{ave} < 0.3$), which corresponds to lower gas compressibility, $C_{fa} \cdot Re$ in microtubes differs little from that of incompressible and fully developed laminar tube flow and still remains approximately 16; while at higher M_{ave} region ($M_{ave} > 0.3$), the measured $C_{fa} \cdot Re$ are consistently higher than the classical value and increases with the increasing average Mach number. For example, the value of $C_{fa} \cdot Re$ is up to 18 at $M_{ave} = 0.5$, which is 12% higher than 16. It can be concluded that the compressibility will lead to a higher frictional resistance for gas flow in microtubes.

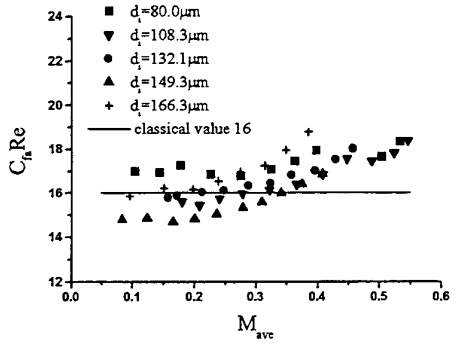


Fig. 6 Frictional resistance for gas flow in microtubes

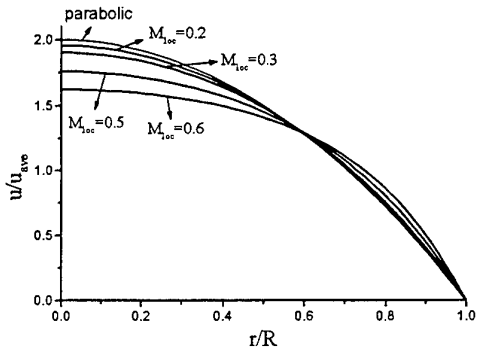


Fig. 7 Velocity profile at different local Mach number

The frictional resistance of internal flow is dominated by the velocity gradient at the wall surface of the tube, but the velocity gradient can not be determined until the velocity profile is known clearly. Therefore, two dimension model for compressible gas flow in a smooth circular tube was employed to analyze the experimental results. Fig.7 shows the dimensionless velocity profile at different local Mach number, from which it can be seen that the velocity profile in microtube is no longer parabolic, but a function of local Mach number. The higher the local Mach number, the more the velocity profile deviates from the parabolic one. Fig.7 shows that the gas compressibility in microtubes brings about a increase of velocity gradient at wall surface and therefore leads to higher frictional resistance. The experimental results of gas flow resistance in microtubes are clearly interpreted by numerical simulation.

4.4 Flow Transition in Microtubes

Transition from laminar to turbulent flow in tubes is accompanied by a noticeable change in the law of resistance. For internal micro flow systems, different researchers got different even conflicting results. Wu et al.[1] and Peng et al. [13] reported the early transition form laminar to turbulent flow in microchannels, but Choi et al. [4] didn't find the early transition phenomenon. To determine the critical Reynolds number of transition from laminar to turbulent for gas flow in microtubes, the experimental results of Fanning friction factors versus Reynolds number are plotted in Fig.8. It can be clearly seen that at $Re \approx 2300$, the relation between C_f and Re changes remarkably which indicates that the internal microflow undergo a transition from laminar to turbulent regime. The numerical value of the Reynolds number at which transition occurs is in substantial agreement with the results in macro tubes.

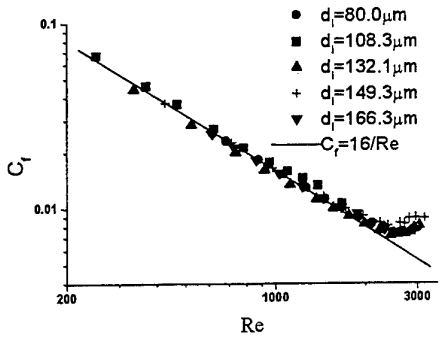


Fig. 8 Fanning friction factor vs Reynolds number

4.5 Uncertainty Analysis

An approximate analysis of uncertainty was carried out, using Darcy equation for incompressible pipe flow:

$$\Delta p = 4C_f \mathrm{Re}\frac{1}{\mathrm{Re}}\frac{1}{d}\frac{\rho v^2}{2} \tag{1}$$

Eqn.1 can be arranged as,

$$C_f \mathrm{Re} = \frac{\pi\rho}{8\mu}\frac{\Delta p}{G}\frac{d^4}{1} \tag{2}$$

The independent variables in the experiments are mass flow rate, G, pressure drop, Δp, tube diameter, d, and tube length, 1. The experimental uncertainty of $C_f \mathrm{Re}$ can be derived using Eqn.2,

$$\frac{\delta(C_f \mathrm{Re})}{(C_f \mathrm{Re})} = \left\{\left(\frac{\delta(\Delta p)}{\Delta p}\right)^2 + \left(4\frac{\delta d}{d}\right)^2 + \left(-\frac{\delta 1}{1}\right)^2 + \left(-\frac{\delta G}{G}\right)^2\right\}^{1/2} \tag{3}$$

Take the experiment for microtube No.1 listed in Table 2 as an example, the relative error of G, Δp, d, 1 are 1.5%, 2%, 0.1% and 2% respectively and the relative error of measured $C_f \mathrm{Re}$ predicted by Eqn.3 is 8.4%.

To verify the veracity of the above approximate method, the experimental uncertainty of tube No.1 was also analyzed numerically by means of the method provided in reference[14]. It can be calculated that the

uncertainties of the experimental value of C_f Re are 8.6%~9.5%, which agrees well with the results of approximate analysis. The exactness of the approximate method was proven positively by numerical results.

The experimental uncertainties of C_f Re for microtubes of No.1~No.5 estimated using Eqn.3 are 8.4%, 6.5%, 5.6%, 5.8% and 5.7% respectively. It can also be deduced from Eqn.3 that the error of diameter measurement is the primary influential factor to the precision of experimental results and the experimental uncertainties are controlled below 10%.

5. CONCLUSIONS

1. A tube-cutting experimental method can be used to measure the pressure and Mach number distribution in a microtube. The experimental results for the microtube with diameter of 108.3 μm indicate that at the forepart of the microtube, the pressure drop remains approximately linear due to its lower Mach number; at the rear part, the pressure drop increases and deviates from linear distribution results from higher compressibility effect.
2. The product of the measured average Fanning friction factor C_{fa} and the Reynolds number Re in microtubes differs little from those predicted by Moody chart when the average Mach number is less than 0.3, whereas it became larger and increases with increasing average Mach number.
3. The numerical analysis indicates that the higher frictional resistance for gas flow in microtubes was attributed to the gas compressibility, which leads to a shape variation of the velocity profile from parabolic, results in increasing velocity gradient at the wall surface of the tube and therefore results in a increase of the Fanning friction factor.
4. It is deduced from the present experimental results that the transition from laminar to turbulence in microtubes occurs at $Re \approx 2300$, which is consistent with the result in macro tubes. The phenomenon of early transition in microtubes reported by some researchers was not observed in the experiments.
5. Uncertainty analysis shows that the inaccuracy of diameter measurement of microtubes dominates the overall error of the experimental results. Extreme care must be taken on the measurement of the diameter of microtubes.

REFERENCES

1. P. Y. Wu and W. A. Little, Measurement of Friction Factors for the Flow of Gases in Very Fine Channels Used for Microminiature Joule-Thomson Refrigerators, Cryogenics, May, pp.273-277 (1983).
2. J. Pfahler, J. Harley and H.Bau, Liquid and Gas Transport in Small Channels, ASME DSC-vol.19, pp.149-157 (1990).
3. J. Pfahler, J. Harley and H.Bau, Gas and Liquid Flow in Small Channels, ASME DSC-vol.32, pp.49-60 (1991).
4. S. B. Choi, R. F. Barron and R. Q. Warrington, Fluid Flow and Heat Transfer in Microtubes, ASME DSC-vol.32, pp.123-133 (1991).
5. J. C. Harley,. Y. F. Huang, H. H. Bau and J. N. Zemel, Gas Flow in Micro-Channels. J. Fluid Mech., v.284, pp.257-274 (1995).
6. R. K. Prud'homme, T. W. Chapman and J. R. Brown, Laminar Compressible Flow in a Tube, Appl. Sci. Res. v.43, pp. 67-74 (1986).
7. H. R. van den Berg et al, Compressible Laminar Flow in a Capillary. J. Fluid Mech., v.246, pp.1-20 (1993).
8. Z. Y. Guo and X. B. Wu, Compressibility Effect on the Gas Flow and Heat Transfer in a Microtube, Int. J. Heat Mass Transfer, 40(13), pp.3251-3254 (1997).
9. Z. Y. Guo and X. B. Wu, Further Study on Compressibility Effects on the Gas Flow and Heat Transfer in a Microtube, Microscale Thermophysical Engineering, v.2, pp.111-120 (1998).
10. Zh. X. Li, D. X. Du and Z. Y. Guo, Experimental Study on the Characteristics of Resistance for Gas Flow in Microtubes, J. of Thermophysics, v.19 (4), pp.459-463 (1998)(in Chinese).

11. J. Q. Liu, Y. C. Tai, K. J. Pong and C. M. Ho, Micromachined Channel/Cressure Sensor Systems for Microflow Studies, the 7th International Conference on Solid State Sensors and Actuators, Transducers'93, pp.995-998 (1993).
12. K. J. Pong, C. M. Ho, J. Q. Liu and Y. C. Tai, Non-Linear Pressure Distribution in Uniform Microchannels, ASME FED-vol.197, pp.51-56 (1994).
13. X. F. Peng, G. P. Peterson, B. X. Wang, Friction Flow Characteristics of Water Flowing Through Rectangular Microtubes, Experimental Heat Transfer, vol.7, pp.249-264 (1994).
14. R. J. Moffat, Contributions to the Theory of Single-Sample Uncertainty Analysis, J. Fluid Engng., vol.104, pp.250-258 (1982).

STUDY ON HEAT TRANSFER FOR FLOW FILM CONDENSATION IN VERTICAL MINI TUBE WITH INTERFACIAL WAVES

Xiao-Ze Du
Thermal Engineering Department
Tsinghua University, Beijing, 100084
Tel. 86-010-62782987
E-mail: duxiaoze@mail.cic.tsinghua.edu.cn

Bu-Xuan Wang
Thermal Engineering Department
Tsinghua University, Beijing, 100084
Tel. 86-010-62784530
E-mail: bxwang@mail.tsinghua.edu.cn

Keywords: flow film condensation, mini tube, interfacial waves

ABSTRACT. The Kelvin-Helmholtz instability of phase-change interface during flow film condensation in vertical mini tube has been studied by means of work or energy analysis. According to the interfacial boundary conditions acquired, the film thinning effect and the phase change area enlarging effect by interfacial waves on heat transfer enhancement are analyzed in different diameter tubes. It is indicated that in mini diameter tube, more obvious heat transfer enhancement due to interfacial waves can be expected than in normal-sized tube, and the interfacial waves enhance the heat transfer mainly by film thinning effect.

The revised Nusselt models, which take care the factors neglected by Nusselt, such as variable wall surface temperature and interfacial transport phenomena, are remarkably successful to predict the relevant parameters in traditional industrial fields [1]. It is well-known that, the heat transfer enhancement of condensation affected by phase change interfacial waves is not more than 20% if the shear stress between liquid and vapor phase can be neglected, and the interfacial waves take effect only as Re_l>20~30 [2]. However, in many heat transfer conditions, the tube diameter of heat exchangers is reduced to less than 3~5mm, named as mini tube, such as generally appeared in two-phase flow micro system or for conditions of high heat flux. Analysis on flow condensation indicated that, in such mini tubes, the bend effect of condensate film can't be neglected, which void the "plate" approximations in Nusselt theory [3], so the surface tension can take obvious effect on condensation. Also in mini tube, the shear stress on liquid-vapor interface has more important effect than gravity. Surely, the increasing effect of shear stress and surface tension will disturb the condensate film and enhance the instability of the film. It is therefore logical to deduce that the interfacial waves may have more obvious effect on heat transfer in mini tube than in normal scale tube. It is the purpose of the present paper to investigate the effect of interfacial waves on heat transfer during flow film condensation in mini tube.

According to literature [4], the present paper assumes the amplitudes of the waves growing due to the Kelvin-Helmholtz instability. Occurence of finite amplitude capillary waves is responsible for such an appearance. The interface waving and the interfacial boundary conditions are treated by work or energy analysis, based on which, the effect of interfacial capillary waves on heat transfer characteristics of flow film condensation in mini tube are analyzed.

1. ANALYSIS ON INTERFACIAL WAVING

The saturated vapor flow at temperature of T_s condensed on the cooled inside wall surface of a vertical mini tube, formed the liquid film as shown in Fig.1. The film was affected jointly by gravity, shear stress on surface and surface tension due to the film bending. The interfacial waves between liquid and vapor phases were initiated because of external effects. According to Kelvin-Helmholtz instability theory, the amplitude of the waves can be promoted by the suction force at the wave crest, developed as a result the Bernoulli effect. In addition, the capillary force caused by film bending in axial direction can also enhance the waving. The capillary force caused by film bending in radial direction will restrain the interface waving. When the waves spread to the tube wall, the enhancement of condensed film instability will be restricted also by capillary adhesion force between the wall and the fluid. Thus, the waving rules should be established by the equilibrium

of these forces.

Assumed: a) The interfacial waves grow from the state of zero amplitude such that the cross sectional area parallel to the axis of the liquid under the wave profile, A_{wave}, remains constant during the growth of the waves. b) The pressure drop from the base to the top of the liquid lump can be neglected. c) The wave profile is expressed as cosine function, $y(z)=\delta+\zeta\cos\left(\frac{2\pi}{\lambda}z\right)$, where ζ and λ are the amplitude and wavelength. d) The initial film thickness δ is thought to be constant in range of the wavelength.

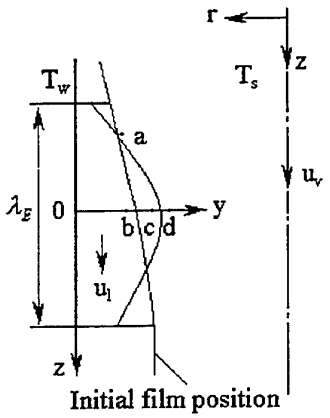


Fig.1 Physical model

The work generated or energy evolved, E(y) by the forces, F, to increase the amplitude of waves, can be obtained as

$$E(y)=\int_0^{y-\delta}[F_B(\zeta)-F_s(\zeta)]d\zeta,\ \text{for}\ \delta\le y\le 2\delta \tag{1-a}$$

$$E(y)=\int_0^{y-\delta}[F_B(\zeta)-F_S(\zeta)]d\zeta-2\int_{\delta}^{y-\delta}F_w(\zeta)dz_0,\ \text{for}\ 2\delta\le y\le R \tag{1-b}$$

where z_0 is the intersecting position of interfacial waves and tube wall. $E(y)>0$ indicates that the system has enough energy to make the waves grow. $E(y)<0$, the system doesn't acquire the ability to maintain interface waving increasingly. So $E(y)=0$ means the most impossible state of the waving interface. The parameters in Equation (1-a) and (1-b) are calculated as follows:

From $y(z)=\delta+\zeta\cos\left(\frac{2\pi}{\lambda}z\right)$, z_0 is given by

$$z_0=\frac{\lambda}{2\pi}\cos^{-1}\left(-\frac{\delta}{\zeta}\right) \tag{2}$$

where $\lambda=\lambda_E$, $A_{wave}=\delta\lambda_E$ if $\zeta\le\delta$; and also $A_{wave}=\int_{-z_0}^{z_0}y(z)dz$ for $\zeta>\delta$, then,

$$\lambda=A_{wave}/\left\{\frac{\delta}{\pi}\cos^{-1}\left(-\frac{\delta}{\zeta}\right)+\frac{\zeta}{\pi}\sin\left[\cos^{-1}\left(-\frac{\delta}{\zeta}\right)\right]\right\} \tag{3}$$

Because the wavelength λ is much smaller than the tube length, the pressure drop within the respect of order of wavelength can be neglected, i.e. $p_a=p_b$ for example in Fig. 1. Again, according to assumption b), $p_b=p_c$, so we can induce from Bernoulli Equation:

$$F_B(\zeta)=p_c-p_d=\frac{\rho_v}{2}\left(\bar{u}_v-\bar{u}_l\right)^2\left[\left(\frac{R-\delta}{R-\delta-\zeta}\right)^4-1\right] \tag{4}$$

where, $\bar{u}_v$ and $\bar{u}_l$ are the average velocity of liquid and vapor phases respectively.

By the well-known Young-Laplace Equation, we have the interfacial force on condensate film surface as

$$F_s(\zeta) = -\sigma_{lv}\left(\frac{1}{r_{lv,1}} + \frac{1}{r_{lv,2}}\right) \tag{5}$$

with, $\frac{1}{r_{lv,1}} = \frac{1}{R-\delta-\zeta}$; $\frac{1}{r_{lv,2}} = \frac{y''}{\left(1+y'^2\right)^{3/2}}\Big|_{z=0} = -\zeta\frac{4\pi^2}{\lambda^2}$, and the force on the wall surface as

$$F_w(\zeta) = -\sigma_{lv}\cos\beta\left(\frac{1}{r_{lw,1}} + \frac{1}{r_{lw,2}}\right) \tag{6}$$

where β is the angle between wavy interface and tube wall, i.e. $tg\beta = y'\big|_{z=z_0}$; $\frac{1}{r_{lw,1}} = \frac{1}{R}$; $\frac{1}{r_{lw,2}} = \frac{y''}{\left(1+y'^2\right)^{3/2}}\Big|_{z=z_0}$; y is the position of waving interface as shown in Fig.1.

Differentiating z_0 with respect to ζ, we obtain

$$dz_0 = \left[\frac{1}{2\pi}\frac{d\lambda}{d\zeta}\cos\left(-\frac{\delta}{\zeta}\right) + \frac{\lambda}{2\pi}\frac{-1}{\sqrt{1-\delta^2/\zeta^2}}\left(\frac{\delta}{\zeta^2}\right)\right]d\zeta \tag{7}$$

in which $\frac{d\lambda}{d\zeta}$ can be determined from differentiating Eq. (3).

The disturbing wavelength λ_E is related to tube diameter and flow conditions. Refer to [4], we obtain

$$\frac{\left(\bar{u}_v - \bar{u}_l\right)^2}{I_0'(2\pi r_I/\lambda_E)} I_0(2\pi r_I/\lambda_E)\rho_G = \sigma \tag{8}$$

where, I_0 is the Bessel function, $r_I = R - \delta$ is the initial position of phase change interface.

The condensate liquid film thickness, δ, and average velocity of liquid and vapor phases, $\bar{u}_v, \bar{u}_l$ are predicted by the following model of flow condensation with smooth vapor-liquid interface.

2. MODEL OF FLOW CONDENSATION IN VERTICAL MINI TUBE

2.1 Mathematical Model

Neglecting the waves on liquid-vapor interface, inertia term in momentum equation and convective term in energy equation of liquid phase, one can express the mathematical model of flow condensation in mini vertical tube as:

Momentum equation of condensate film.

$$\frac{1}{r}\frac{\partial}{\partial r}\left(r\mu\frac{\partial u_l}{\partial r}\right) - \frac{dP_l}{dz} + \rho_l g = 0 \tag{9}$$

with boundary conditions: $r = R$, $u_l = 0$;

$$r = R - \delta, \quad -\mu \frac{\partial u_l}{\partial r} = \tau_\delta \tag{10}$$

τ_δ denotes the shear stress on vapor-liquid interface.

Energy equation of condensed film.

$$\frac{2\pi\lambda(T_s - T_w)}{\ln(R/(R-\delta))} = \frac{d\dot{m}_{zl}}{dz} \cdot h_{lv} \tag{11}$$

Were m_{zl} is the liquid flux at z, h_{lv} is the latent heat of vapor.

Continuity equation.

$$\dot{m}_{zl} + \dot{m}_{zv} = \dot{m}_{vo} \tag{12}$$

2.2 Solution Of The Model

Velocity field in liquid film.

Combined Eq. (9) and the boundary conditions, Eq. (10) yields:

$$u_l = \frac{1}{2\mu}\left(\frac{dp_l}{dz} - \rho_l g\right)\left[\frac{r^2 - R^2}{2} - (R-\delta)^2 \ln\frac{r}{R}\right] - \frac{\tau_\delta (R-\delta)}{\mu} \ln\frac{r}{R} \tag{13}$$

Mass flux of liquid film.

$$\dot{m}_{zl} = \int_{R-\delta}^{R} 2\pi r \rho_l u_l dr \tag{14}$$

From energy equation of condensate film, we can obtain another expression of mass flux:

$$\dot{m}_{zl} = \frac{1}{h_{lv}} \int_0^z \frac{2\pi\lambda(T_s - T_w)}{Ln(R/R-\delta)} \cdot dz \tag{15}$$

Average velocity of vapor flow.

$$\bar{u}_v = (\pi R^2 \rho_v u_{vo} - \dot{m}_{zl}) / [\pi(R-\delta)\rho_v] = \frac{R^2}{(R-\delta)^2} u_{vo} - \frac{\dot{m}_{zl}}{\pi(R-\delta)^2 \rho_v} \tag{16}$$

Pressure drop.

$$\frac{dp_v}{dz} = \rho_v g - \frac{2\tau_\delta}{R-\delta} \tag{17}$$

In small diameter tube, the bend of liquid film along axial direction can not be neglected [3]. A force balance for the curved vapor-liquid interface gives,

$$p_v - p_l = \frac{\sigma}{R-\delta} \tag{18}$$

Differentiating with Eq. (18) respect to z yields the pressure drop of liquid film

$$\frac{dp_l}{dz}=\rho_v g-\frac{2\tau_\delta}{(R-\delta)}+\frac{\sigma}{(R-\delta)^2}\frac{d(R-\delta)}{dz} \tag{19}$$

Shear stress on vapor-liquid interface τ_δ

$$\tau_\delta=\pm\frac{c_f}{2}\rho_v(\overline{u_{zv}}-u_{lv})^2+\frac{1}{2\pi(R-\delta)}\cdot\frac{d\dot{m}_{zl}}{dz}(\overline{u_{zv}}-u_{lv}) \tag{20}$$

where the calculation of friction factor c_f can be refered to [5].

The equations (13)~(20) are solved numerically. At a certain axial location, z, the film thickness δ is calculated, and in turn the values of system quality, x, liquid Reynolds number, Re_l, and average velocity of condensate film, $\bar{u}_l$, are calculated as: $x=\frac{\dot{m}_{v0}-\dot{m}_{zl}}{\dot{m}_{v0}}$, $Re_l=\frac{4\dot{m}_{zl}}{\mu_l\pi D}$, $\bar{u}_l=\frac{\dot{m}_{zl}}{\rho_l\pi\left[R^2-(R-\delta)^2\right]}$. With smooth vapor-liquid interface, the Nusselt number of condensation heat transfer at every step is obtained by

$$Nu=\frac{2}{\ln[R/(R-\delta)]} \tag{21}$$

3. INFLUENCE OF INTERFACIAL WAVES ON HEAT TRANSFER

Generally speaking, the interfacial wave enhances the heat transfer by three kinds of effects [6,7]: the film thinning effect, the convection effect and the phase change area enlarging effect. For low Prandtl number of liquid film, Pr<10, and low Reynolds number, the convection effect can be neglected [6]. Therefore, we focus here on the other two kinds of effects, as follows:

For every step Δz, following the hypothesis of smooth interface, at first, we determine the in-situ film thickness $\delta_l(z)$ and the average velocity of liquid and vapor phases. The disturbing wavelength λ_E can hence be calculated form Eq. (8). Utilizing the work analysis introduced in Part 1, the in-situ interfacial boundary conditions can be acquired. The interfacial waves make the film thickness varying in range of the wavelength. At the same time, the waves enlarge the phase-change area. Therefore, the condensation heat transfer coefficient is yielded from:

$$\alpha_{wave}=\frac{1}{\lambda_E}\int_0^{\lambda_E}\frac{k}{R\ln\frac{R}{R-y(z)}}ds \tag{22}$$

where k is the thermal conductivity of condensate film, $ds=\sqrt{1+y'^2}dz$ is the elementary area of waving interface. At different time, the condensate film thickness varies between $\delta_l(z)\pm\zeta$ as, $y(z)=\delta_l(z)+\zeta\cos\left(\frac{2\pi}{\lambda_E}z\right)$. Hence, the Nusselt number with interfacial waves will be

$$Nu_{wave}=\frac{2\alpha_{wave}R}{k} \tag{23}$$

4. RESULT AND DISCUSSION

Typical analysis were made for illustrating the saturated vapor flow in vertical tube of i.d. 3mm and 6mm with Re_{v0}=2200 and the temperature drop between the vapor and wall is taken as ΔT=5°C.

Figure 2 shows the energy involved to increase the amplitude varies for different vapor qualities, x. With smooth phase-change interface, the two-phase flow system should be in its unsteady equilibrium and correspondingly, the ability to produce wave and to increase the amplitude will be equal to zero. Once the interface begins to wave, the suction forces increase at first, due to the narrowing of vapor flow passage, which promotes the waving. Subsequently, the surface tension that restrains the interfacial waves increases gradually. The common effect of the forces tends to make the system realizing a somewhat new equilibrium.

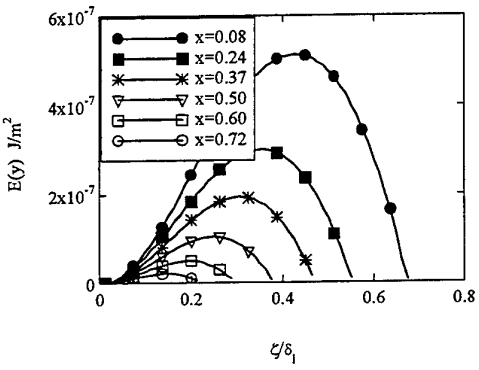


Fig.2 Energy involved in displacing the wave crest (d=3mm)

It is also seen from Figure 2 that, during the process of flow condensation, the interfacial waves become increasingly enhanced as the vapor quality, x, decreases, namely the increase of liquid Reynolds number Re_l. As the condensation going on, the liquid film becoming thicker leads to the augment of liquid-vapor interface bending along axial direction, so that the influence of capillary force $F_S(\zeta)$ on the interface promotes the interface waving obviously. Besides, from Equation (4), a thicker liquid film means that the interfacial waves are sensitive to the Bernoulli effect. Both of these reasons increase the film instability.

Figure 3 shows that the influence on Nusselt number of flow condensation heat transfer with or without the consideration of interfacial waves in vertical tube of 3mm i.d.. Even as the liquid Reynolds number Re_l is lower to 30, the enhancement of heat transfer due to interfacial waves is still to be feasible. To the present example, in spite of the small liquid Reynolds number, the maximum heat transfer enhancement may be up to 20%. The result shows that in mini tube, for specified inlet Reynolds number, Re_l, the decrease of tube diameter increases the vapor velocity and exacerbates the bend of condensed film, with also lead to the increasing instability of liquid film, which makes the influence of interface waving being obvious.

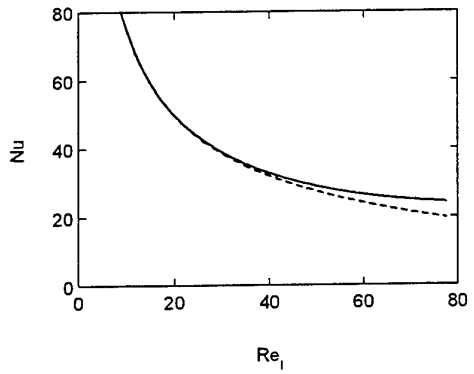


Fig. 3 Influence of interfacial waves (d=3mm)

— with and ---without consideration of interfacial waves

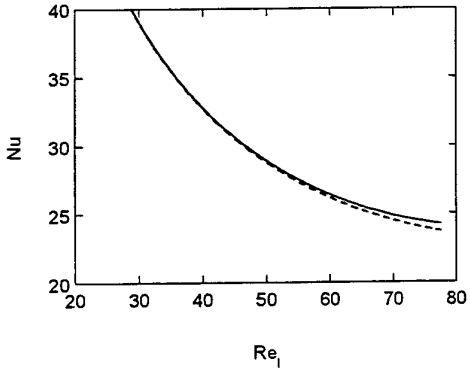


Fig. 4 Influence of area enlarging effect. (d=3mm)

— with and --- without consideration of interfacial area enlarging effect

Figure 4 shows that, neglecting the phase change area enlarging effect due to the interfacial waves hardly has any effect on heat transfer. The results indicate that at least in range of low liquid film Reynolds number, the dominating reason of the enhancement of heat transfer is the film thinning effect due to the interfacial waves.

The Nusselt number for flow film condensation in vertical 6mm i.d. tube is shown in Figure 5. With same inlet vapor Reynolds number, Re_{v0}=2200, as in 3mm i.d. tube, the vapor velocity decreases and hence, weakens the Bernoulli effect. Also, the larger diameter weakens the bend of liquid film and reduces the effect of the capillary forces on interfacial waves. Therefore, comparing with the flow condensation process in tube of 3mm in

diameter, the influence of interfacial waves on heat transfer is weakened obviously.

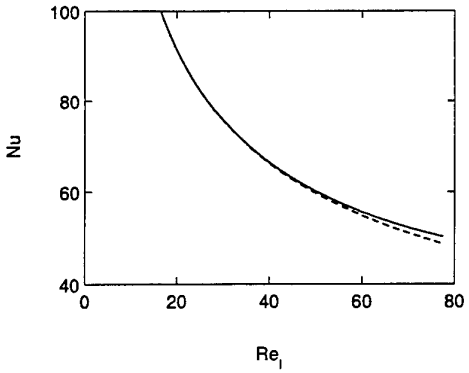


Fig.5 Influence of interfacial waves (d=6mm)
— with and --- without consideration of interfacial waves

5 CONCLUSIONS

A work or energy analysis has been adopted to determine the effect of interface waving on heat transfer for flow film condensation in a vertical mini tube. The results could be concluded as:

(1) With the same inlet vapor Reynolds number Re_{v0}, as tube diameter decreased, interfacial waves can appear even in very low film Reynolds number of less than 30, and hence more obvious heat transfer enhancement effect can be obtained than in normal tube.
(2) During the process of flow condensation, the interfacial waves become increasingly enhanced as the vapor quality x decreases.
(3) In mini tube, the interfacial waves enhance the heat transfer mainly by film thinning effect, the heat transfer enhancement due to the enlargement of interfacial area because of waves doesn't play very important role.

ACKNOWLEDGEMENT

The research project is financially supported by National Natural Science Foundation of China.

REFERENCES

1. J. W. Rose, Trans. IChemE, v.76, pp.143-152 (1998).
2. F. P. Incropera and D. P. Dewitt, *Fundamentals of Heat and Mass Transfer*, John Wiley & Sons Inc. (1985).
3. W M Rohsenow, Applied Mechanics Reviews, v.23, pp. 487-496 (1970).
4. Ramkrishna Das and S. Pattanayak, The Canadian J Chem. Eng., v.74, pp. 49-57 (1996).
5. W. H.Henstock and T. J.Hodgson, AIChE J., v.22, pp.990-1000 (1976).
6. Akio Miyara, "Numerical analysis on heat transfer of falling liquid films with interfacial waves", *Heat Transfer 1998-Proceedings of 11th IHTC*, v.2, pp.57-62, edited by J. S. Lee, Kyongju, Korea(1998).
7. S. Jayanti and G. F. Hewitt, Int. J. Heat Mass transfer, v.47, pp.179-190 (1997).

NON-EQUILIBRIUM MASS TRANSFER AT LIQUID-VAPOR INTERFACE

Takaharu Tsuruta
Department of Mechanical Engineering, Kyushu Institute of Technology
1-1, Sensui-cho, Tobata-ku, Kitakyushu 804-8550, JAPAN
E-mail: tsuruta@mech.kyutech.ac.jp; Fax: +81-93-884-3140

Gyoko Nagayama
Department of Mechanical Engineering, Kyushu Institute of Technology
1-1, Sensui-cho, Tobata-ku, Kitakyushu 804-8550, JAPAN
E-mail: v96223sg@tobata.isc.kyutech.ac.jp; Fax: +81-93-884-3140

Keywords: non-equilibrium system, evaporation, condensation, reflection, molecular dynamics

ABSTRACT. Purpose of the present study is to understand the mechanism of interphase mass transfer between liquid and vapor under non-equilibrium conditions. The molecular dynamics (MD) simulation is used to examine details of condensation and evaporation from a viewpoint of microscopic description. The simulations are made for a monatomic-molecule system consisting of 6912 argon molecules expressed by the Lennard-Jones intermolecular potential. Velocity distributions of the leaving molecules from the liquid surface are obtained and the effects of non-equilibrium conditions are discussed. We found that the reflection on the condensing surface show differences from equilibrium results since the incident molecules have mean velocity due to the net mass transfer rate. On the other hand, the condensation coefficient and the velocity distribution functions for the evaporated molecules show no dependence on the non-equilibrium conditions. Furthermore, the energy accommodation coefficients of the reflecting molecules are examined and compared with each other.

1. INTRODUCTION

In the expression of an interphase mass transfer rate between liquid and vapor, the condensation/evaporation coefficient plays an important role but it has been an unknown factor. In theoretical studies, the condensation/evaporation coefficient has been considered to have a uniform value irrespective of kinetic motion of molecules. As depicted in Fig.1, net evaporation or condensation rate can be obtained from the difference of fluxes of molecules moving outward from and toward the liquid surface, provided that the velocity distribution functions at the surface can be given correctly. In general, the distribution function of molecules moving from the interface has been assumed to be the well-known Maxwellian:

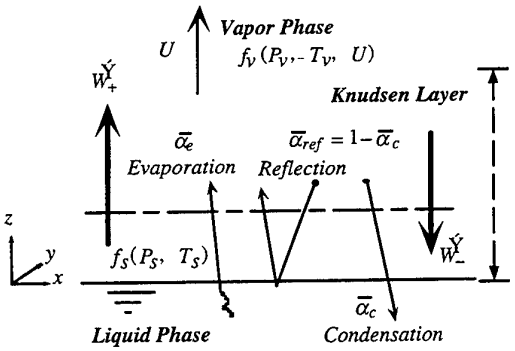


Fig. 1. Macroscopic description of interphase mass transfer by Kinetic theory of gases

$$f_s = n_s\left(\frac{m}{2\pi kT_s}\right)^{3/2}\exp\left[-\frac{m}{2kT_s}\left(V_x^2+V_y^2+V_z^2\right)\right] \tag{1}$$

where m is the mass of molecule, k the Boltzmann constant, V the velocity and n_s is the number density of molecules being equal to the saturated vapor density at the surface temperature T_s. Also, a following local equilibrium distribution function in the bulk-vapor phase is applied:

$$f_v = n_v\left(\frac{m}{2\pi kT_v}\right)^{3/2}\exp\left[-\frac{m}{2kT_v}\left\{V_x^2+V_y^2+(V_z-U)^2\right\}\right] \tag{2}$$

and Schrage[1] derived a formulation for the interphase mass transfer rate for near-equilibrium condition as

$$\dot{m} = \zeta \frac{1}{\sqrt{2\pi R}} \left(\frac{P_s}{\sqrt{T_s}} - \frac{P_v}{\sqrt{T_v}} \right), \text{ where } \zeta = \frac{2\overline{\alpha}_c}{2-\overline{\alpha}_c} \quad (3), (4)$$

The condensation coefficient is $\overline{\alpha}_c$ defined as an averaged condensation probability, that is, a fraction of incident molecules upon a liquid surface, which remain in the liquid phase. The remaining fraction of impinging molecules are reflected. Since the two coefficients, the condensation and evaporation coefficients, should coincide with each other under the thermal equilibrium condition, the same value has been generally used even in the near-equilibrium state and represented by the term of condensation coefficient.

$$\overline{\alpha}_e = \overline{\alpha}_c \quad (5)$$

Later, Labuntsov [2,3] revised Schrage's expression by considering the non-equilibrium effects in the Knudsen layer adjacent to the liquid surface (Fig. 1), and proposed a modified expression instead of eq. (4):

$$\zeta = \frac{2\overline{\alpha}_c}{2-0.798\overline{\alpha}_c} \quad (6)$$

Labuntsov's equation has been used for many practical situations in the evaporation and the condensation where the surface phenomena are dominant compared with the internal thermal resistance. However, the condensation coefficient remains unknown. Then, some experimental efforts to obtain the reliable value are being continued. For liquid-metals such as mercury (Niknejad & Rose[4]) and potassium (Ishiguro & Sugiyama[5]), values close to unity have been obtained in the experiments of the film condensation heat transfer. On the other hand, for polyatomic vapors such as water, methanol, carbontetrachloride and glycerol vapor, values less than unity have been reported in the experimental studies using a dropwise condensation method by Tanaka Hatamiya[6] and by Tsuruta et al.[7] and a shock-tube technique by Fujikawa et al.[8] and Maerefat et al.[9]. These experimental works, however, were based on the Labuntsov's or similar-type equations developed for the near-equilibrium condition. For the practical non-equilibrium situations where the net mass transfer rate is not zero, there is no material supporting the same values between the condensation coefficient and the evaporation coefficient.

2. BACKGROUND ON THIS STUDY

To consider the interaction between the vapor molecules and the liquid surface molecules, we have investigated the condensation/evaporation coefficient from the molecular dynamics viewpoint. Our previous studies [10-12] indicate that the condensation/evaporation coefficient of monatomic molecules depends on the translational energy of vapor molecules and the liquid surface temperature. The results are shown in Fig.2 and a following formulation has been presented for the condensation coefficient:

$$\alpha_c = \alpha \left\{ 1 - \beta \exp\left(-\frac{E_z}{kT_s} \right) \right\}, \text{ where } E_z = (1/2) m V_z^2 \quad (7)$$

where two parameters α and β in Fig.2 depend on the surface temperature T_S. Eq. (5) indicates that the vapor molecules with the large normal component of translational energy can be easily condensed. Also, it is found that an increase of the surface temperature raises the reflection probability.

We examined the molecules leaving from the surface and the distribution densities for the evaporating, reflecting and all leaving molecules were compared with the Maxwellian. The results for the normal component of velocity V_z are shown in Fig.3, where we can find some systematic differences from the Maxwellian. That is, although the velocity distribution density of all leaving molecules is consistent with the Maxwellian very well, yet the evaporating and reflecting molecules show different distributions. The distribution density for the evaporating molecules is larger than the Maxwellian in the higher velocity region but smaller in the lower velocity region. On the other hand, the reflecting molecules show the larger distribution density in the lower

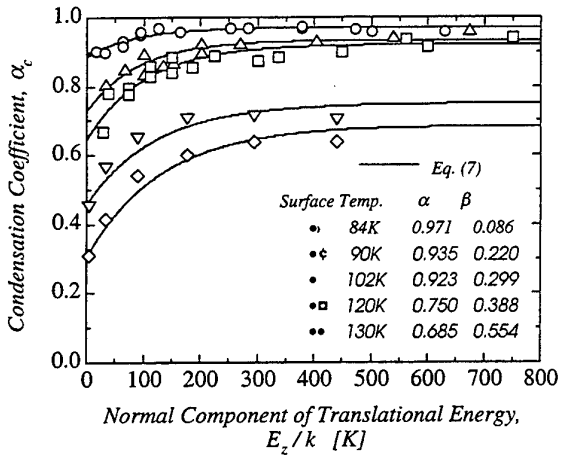


Fig. 2. Condensation coefficient of argon

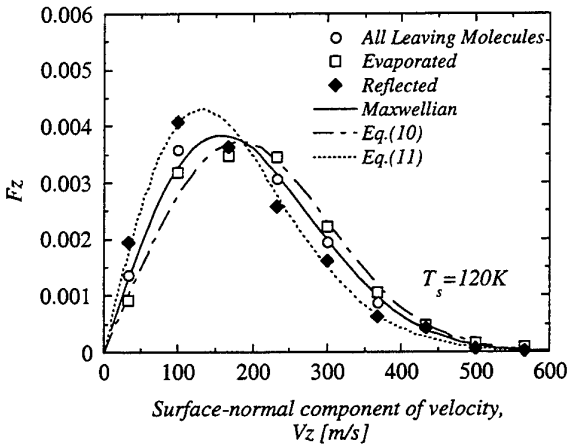


Fig. 3. Velocity distribution density for 120K surface in equilibrium system

velocity region and the smaller density in the higher velocity region. It is easily understood from a viewpoint of equilibrium that the large density of evaporating molecules in the higher velocity region corresponds to the larger condensation probability of incident molecules. Since the Maxwellian distribution for all leaving molecules is composed of both the distribution functions for the evaporating and reflecting molecules, they are expressed using the evaporation coefficient and the condensation coefficient as follows:

$$f_e = \alpha\left\{1-\beta\exp\left(-\frac{mV_z^2}{2kT_s}\right)\right\}n_s\left(\frac{m}{2\pi kT_s}\right)^{3/2}\exp\left(-\frac{mV^2}{2kT_s}\right) \tag{8}$$

$$f_r = \left[1-\alpha\left\{1-\beta\exp\left(-\frac{mV_z^2}{2kT_s}\right)\right\}\right]n_s\left(\frac{m}{2\pi kT_s}\right)^{3/2}\exp\left(-\frac{mV^2}{2kT_s}\right) \tag{9}$$

where $V^2 = V_x^2 + V_y^2 + V_z^2$. The density functions of velocity distribution for the evaporating and the reflecting molecules, F_e and F_r, are obtained by normalizing their velocity distribution functions. The densities for the surface-normal (z-) component are written as

$$F_{e,z} = \frac{1-\beta\exp\left\{-mV_z^2/(2kT_s)\right\}}{1-\beta/2}\left(\frac{m}{kT_s}\right)V_z\exp\left(-\frac{mV^2}{2kT_s}\right) \tag{10}$$

$$F_{r,z} = \frac{1-\alpha+\alpha\beta\exp\left\{-mV_z^2/(2kT_s)\right\}}{1-\alpha(1-\beta/2)}\left(\frac{m}{kT_s}\right)V_z\exp\left(-\frac{mV^2}{2kT_s}\right) \tag{11}$$

Figure 3 indicates these distribution densities are in good agreements with the simulation data.

3. MOLECULAR DYNAMICS SIMULATION

Non-Equilibrium Simulation Method

By following the molecular dynamics simulations for the equilibrium liquid-vapor system, a basic cell of 54.8Å x 64.8Å x 389 Å is used for the non-equilibrium system. Fig.4 shows a snapshot containing 6912 argon

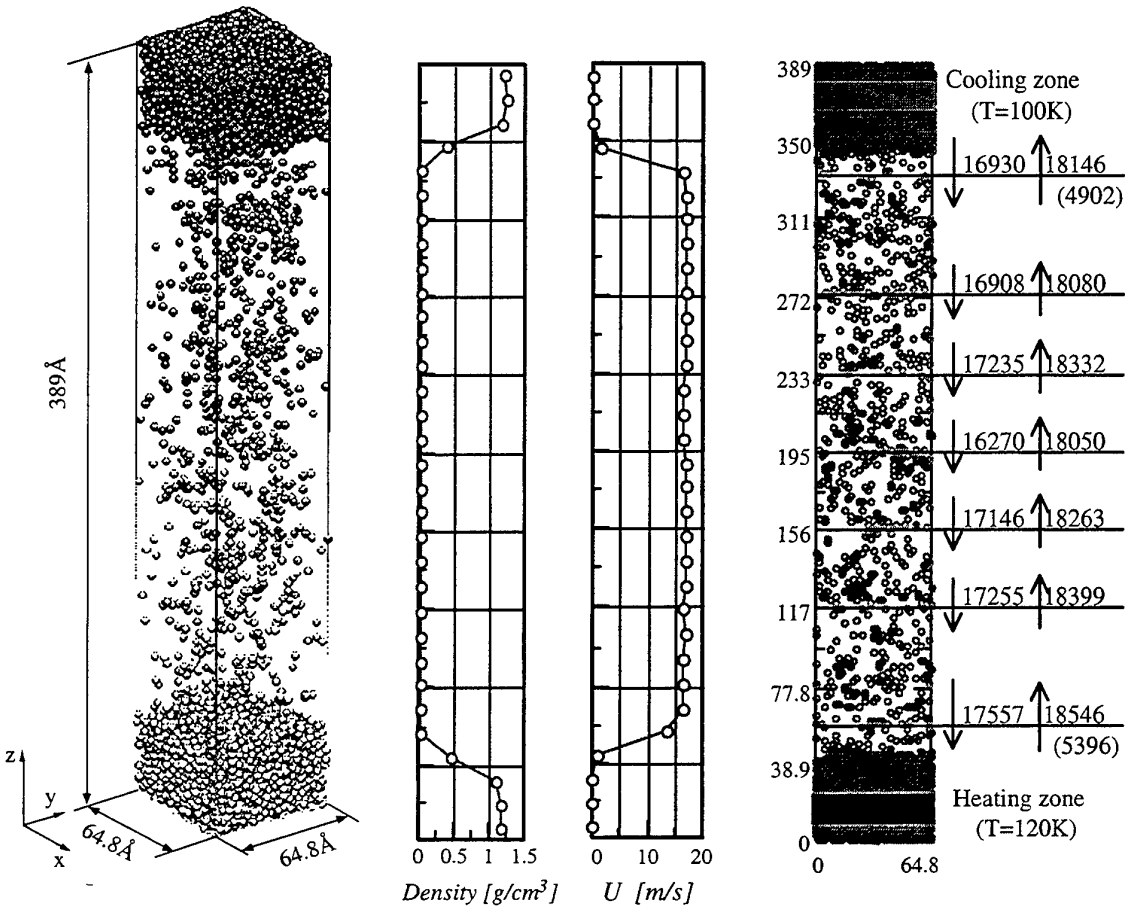


Fig. 4. Non-equilibrium system of molecular dynamics

molecules. The Lennnard-Jones model is used for the intermolecular potential and the periodic boundary conditions are applied for all boundaries. To formulate the non-equilibrium system, a high-temperature control zone of 120K and a low-temperature control zone of 100K are located in the bulk liquid phase. The molecules in these zones are controlled at different temperatures. The upper zone is for cooling and the lower zone is for heating. The steady state under the non-equilibrium condition is maintained for a duration of 5,000ps (1,000,000steps) and the time-averaged temperature of the evaporating surface is evaluated as 113K and the condensing surface is 108K. The vertical density profile and the averaged velocity profile in the z-direction U are shown in Fig.4, where the mean flow rate of vapor from the evaporating to the condensing surface is evaluated to be about 17m/s. Also, the numbers of molecules crossing several horizontal planes during 2,500ps are indicated at the right side in Fig.4. The lowest plane is defined in this study as the evaporating surface, which has net evaporation rate out from the surface. And the highest plane is defined as the condensing surface, which has net condensation rate towards the surface. The numbers of reflected molecules are shown in the parentheses ( ).

Velocity Distributions

The velocity distributions at the evaporating and condensing surfaces are examined and compared with eqs. (10) and (11) which are established under the equilibrium conditions. For the tangential component V_x and V_y, there are no marked differences from the Maxwellian velocity distributions. For the normal component V_z, the velocity distribution functions of all leaving, evaporated and reflected molecules at both surfaces are shown in Fig.5. The evaporated molecules are found to agree well with the eq. (10) and all leaving molecules seem to have no marked difference from the Maxwellian velocity distribution functions. On the other hand, the reflected

molecules are found to be different from the eq. (11) for the equilibrium condition. The reflected molecules on the condensing surface shift from the eq. (11) towards the higher velocity region and those on the evaporating surface shift towards the lower velocity region. Since the incident molecules on the condensing surface have mean velocity due to the net mass transfer rate under the non-equilibrium conditions, it is considered that the reflected molecules can not accommodate to

the surface molecules. In a similar way, the reflected molecules on the evaporating surface have lower velocity than those in the equilibrium conditions. These indicate that the informations on the non-equilibrium conditions are expressed by the reflected molecules and the characteristics on condensation and evaporation are independent on the non-equilibrium condition. In other words, the velocity distribution functions for evaporating molecules shown by eq. (10) can be used to non-equilibrium systems and the reflecting results shown by eq. (11) should be modified for the non-equilibrium system. The reflecting behavior will need further examination.

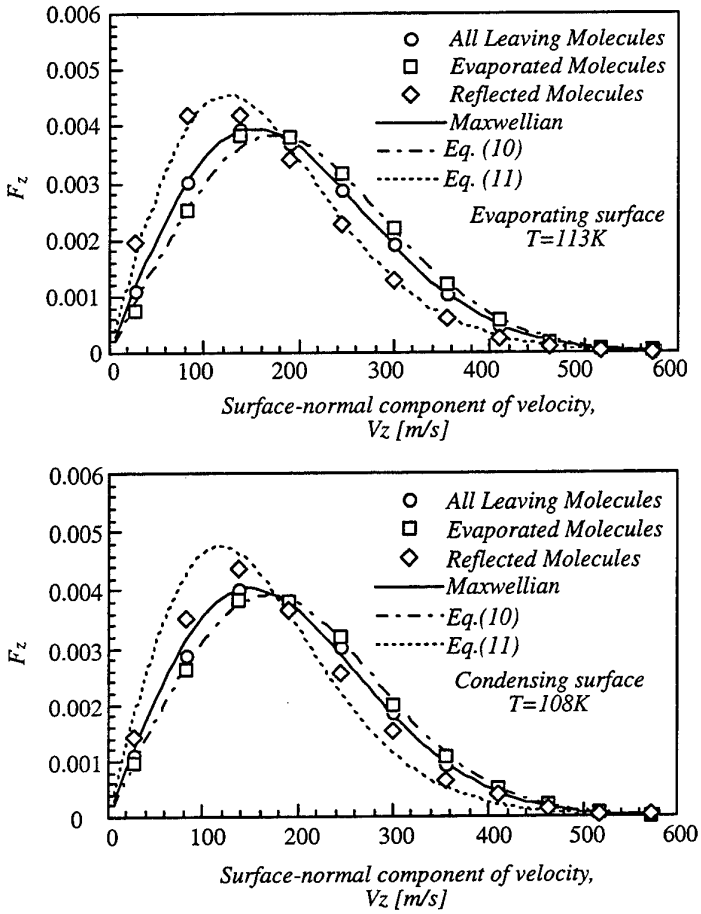


Fig. 5. Velocity distribution functions for evaporating and condensing surface of non-equilibrium system

Condensation/Evaporation Coefficient

The condensation coefficients at both surfaces are obtained as a fraction of condensing molecules to all incident molecules. In the similar way, the evaporation coefficients are obtained as a fraction of evaporating molecules to all molecules departing from the liquid surface. The results for the evaporating surface are presented in Fig.6 as a function of the normal component of translation energy and compared with eq. (7) obtained in the equilibrium system. The condensation coefficient agrees well with eq. (7) but the evaporation coefficient is found larger than eq. (7). The reason is considered due to the decrease of the incident molecules on the evaporating surface. This results in the decreases of reflected and leaving molecules. Fig.7 shows the results of the condensation and evaporation coefficient on the condensing surface. As same as the evaporating surface, the condensation coefficient is in good agreement with the eq. (7). On the other hand, the evaporation coefficient is below the curve of eq. (7). This is because of the increase of the reflected molecules on the condensation surface. These results indicate that the condensation coefficient defined as the condensation probability is independent of the non-equilibrium condition and can be characterized by the dynamics on the interaction between the surface molecules and the condensing molecules given by eq. (7). Also, the evaporation coefficient should be defined as the evaporation probability based on the Maxwellian of the liquid molecules. The velocity distribution of evaporating molecules in the non-equilibrium system is expressed by eq. (10) obtained in the equilibrium system.

Although the velocity distribution of all leaving molecules are seemed to show no marked difference from the

Maxwellian in Fig.5, it shifts, however, towards high velocity region on condensing surface and towards low velocity region on evaporating surface. That is, by considering that all leaving molecules consist of evaporated and reflected molecules, the ratio of reflected molecules will affect the velocity distribution of all leaving molecules on liquid-vapor surface. Since there is small deviation from the results of equilibrium at the evaporating surface, the decrease of reflected molecules caused very small difference for all leaving molecules.

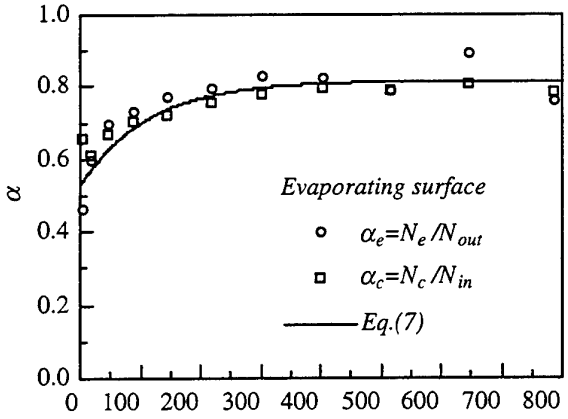


Fig. 6. Condensation and evaporation coefficients for evaporating surface

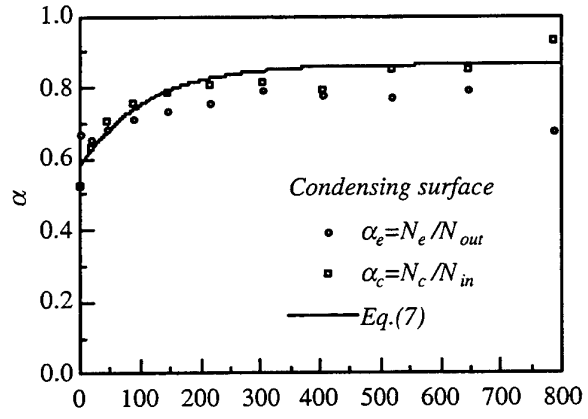


Fig. 7. Condensation and evaporation coefficients for condensing surface

Energy Accommodation Coefficient of Reflected Molecules

To understand the behaviors of reflected molecules, the energy accommodation coefficients at the evaporating and condensing surfaces are obtained for each directions, i=x,y,z.

$$\alpha_i=(E_{in,i}-E_{out,i})/(E_{in,i}-E_{s,i}) \tag{12}$$

where $E_{in,i}$ is the averaged incident energy of one reflected molecule, $E_{out,i}$ is the averaged energy of one reflected molecule after the reflection, and $E_{s,i}$ is the averaged energy of the surface molecule depending on the surface temperature. Here, we can found from Fig.8 and Fig.9 that the tangential components (i=x,y) of

accommodation coefficients on both surfaces are closed to 1 for each incident energy level, but the normal components shows a dependency on the incident energy. The curve of the normal components of the accommodation coefficient indicates that the large incident energy results in the larger accommodation coefficient. Also, the results of evaporating surface show larger values than the condensing surface. It is not possible in this study to clarify the reflection behaviors, but we are considering that the collision number during the surface interaction in the interface zone plays an important role in the reflection.

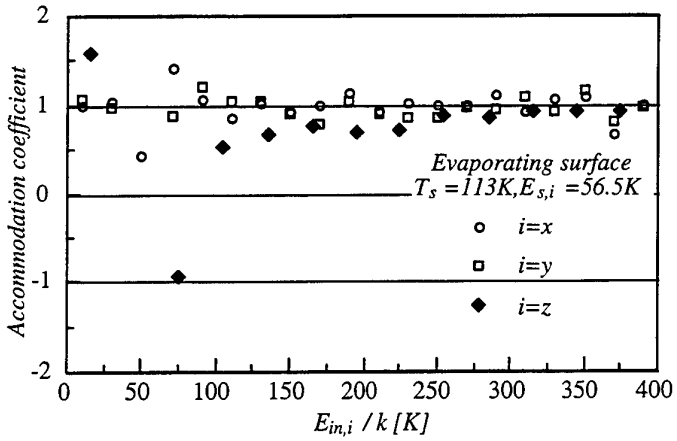


Fig. 8. Accommodation coefficient for reflecting molecules on evaporating surface

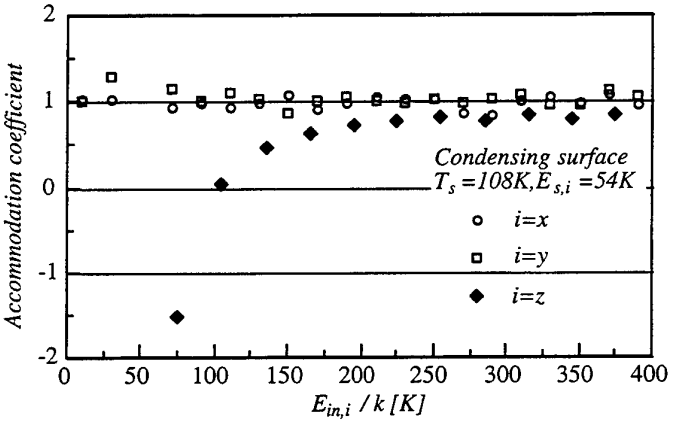


Fig. 9. Accommodation coefficients for reflecting molecules on condensing surface

CONCLUSIONS

1. The condensation coefficient of monatomic molecule depends on its normal component of translational energy and the liquid-surface temperature. It does not depend on the non-equilibrium conditions and can be applied for the non-equilibrium system. The evaporation coefficient, which defined as the evaporating probability of the liquid molecules, can be also expressed in a similar expression.
2. Velocity distributions of evaporating molecules in the non-equilibrium system can be expressed by eq. (10) obtained in the equilibrium system. And the results of reflecting molecules seem to shift from eq. (11) according to the effect of the non-equilibrium conditions.
3. The reflections at the evaporating and condensing surfaces are diffusive reflection for the surface tangential direction, while the energy change of the surface normal component shows different behavior depending on the incident energy.

NOMENCLATURE

E = energy of molecule
F = distribution density of velocity
f = velocity distribution function
k = Boltzmann constant
m = mass of molecule
$\dot{m}$ = mass flux
n = number density
P = pressure
R = gas constant
S = pressure ratio of vapor to surface
T = temperature
U = macroscopic velocity
V = velocity
x,y,z = coordinates
α_c = condensation coefficient
α_e = evaporation coefficient
α, β = parameters of evaporation / condensation coefficients

REFERENCES

1. R.W. Schrage, A Theoretical Study of Interphase Mass Transfer, pp. 32-43,Columbia Univ. Press, New York (1953).
2. D. A. Labuntsov, An Analysis of Intensive Evaporation and Condensation, *High Temperature (Engl. Transl.)*, vol. 5, pp. 579-647 (1967).
3. D. A. Labuntsov & A. P. Kryukov, *Int. J. Heat Mass Transfer*, vol. 22, pp. 989-1002 (1979).
4. J. Niknejad & J. W. Rose, *Proc. of the Royal Society of London,* A 378, pp. 305-327 (1981).
5. R. Ishiguro & K. Sugiyama, An experimental study on intensive condensation of potassium, *Proc. 8th Int. Heat Transfer Conf.,* San Francisco, vol. 4, pp. 1635-1640 (1986).
6. H. Tanaka & S. Hatamiya, Drop Size Distributions and Heat Transfer in Dropwise Condensation - Condensation Coefficient of Water at Low Pressures, *Proc. 8th Int. Heat Transfer Conf.,* San Francisco, vol. 4, pp. 1671-1676 (1986).
7. T. Tsuruta, T. Masuoka & Y. Kato, *Therm. Sci. and Eng.,* vol. 2, No. 1, pp. 98-103 (1994).
8. S. Fujikawa, M. Okuda, T. Akamatsu & T. Goto, *J. Fluid Mech.*, vol. 183, pp.293-324 (1987).
9. M. Maerefat, S. Fujikawa, T. Akamatsu & T. Mizutani, *Exp. Fluids,* vol. 7, No. 8, pp. 513-520 (1989).
10. T. Tsuruta, N. Sakamoto & T. Masuoka, *Therm. Sci. and Eng.,* vol. 3, No. 3, pp. 85-90 (1995).
11. T. Tsuruta, H. Tanaka, K. Tamashima & T. Masuoka, Molecular Dynamics Study on Interphase Mass Transfer Between Liquid and Vapor Phases - Effects of Translational Energy on Condensation and Evaporation Coefficients, *Trans. of JSME.* , vol. 63, No. 612, pp. 2776-2783 (1997).
12. T. Tsuruta, H. Tanaka & T. Masuoka, Molecular Dynamics Study on Non-Equilibrium Interphase Mass Transfer Between Liquid and Vapor, *Proc. 11th Int. Heat Transfer Conf.,* Kyonju (1998).

MICROSCALE HEAT TRANSFER AT FAST TIME STUDIED BY NOVEL LASER-BASED MEASUREMENT TECHIQUES

K. X. He, J. C. Wang
Department of Physics, Alabama A & M University, Normal AL 35762
Email: kxhe@helium.physics.aamu.edu; Fax: (256) 851-5622

Alan Chow
National Aeronautics and Space Administration, George C. Marshall Space Flight Center,
Marshall Space Flight Center, AL 35812

Jiada Mo
Department of Mechanical Engineering, Memphis State University,
322 Engineering Science, Memphis, TN 38152

Carl Holden
National Aeronautics and Space Administration, Langley Research center,
Hampton, VA 23681

Keywords: chinese tea, microscale heat transfer, nonlinear optics, ultrafast laser, fluorescence

ABSTRACT. In present paper we report on the first study of transient microscale heat transfer in liquid which contained the nature organic material of chinese tea solution. Heat transport by phonons has been studied by single picosecond pulse degenerate four wave mixing (DFWM) technique. The sound velocity in chinese tea solution was measured as 1133.6 m/s which is compared with the sound velocity in methanol. The molecules of chinese tea can absorb a photon and then relax non-radiatively or radiatively back to the electronics ground state. Ultrafast laser induced fluorescence (ULIF) at 674.1nm was recorded and radiative transition for the chinese tea molecules was very strong. Convection in chinese tea solution has also been studied by self action with both horizontal- and vertical laser propagation through the chinese tea cell. The dependence of the location of the red ULIF on the intensity of the laser beams clearly show that the real behavior of chinese tea molecules in transient heat transport.

1. INTRODUCTION

Transient microscale heat transport in laser - liquid heating is fundamental of chemical analysis and biomedical diagnostics including destroy tissue by thermal surgery [1,2,3]. To understand the absorption and heating mechanisms at nanoseconds and shorter the nonlinear optics techniques have been developed as novel laser-based measurement techniques. In present paper we report on the first study of transient microscale heat transfer in liquid which contained the nature organic material of chinese tea solution. The chinese green tea solution was used as nonlinear medium as well as the liquid for studding microscale heat transfer at fast time.

Heat transport by phonons was studied by single picosecond pulse degenerate four wave mixing (DFWM). The sound velocity in chinese tea solution was measured as 1133.6 m/s which is compared with the sound velocity in methanol. The physical picture of this process is that two of the input beams interfere to create an interference pattern and associated index of refraction grating. The third input beam is diffracted from this index grating to become the fourth or signal beam. Non-intrusively measured liquid quantities by DFWM can be including total density, individual species density, temperature, velocity, and the speed of sound.

Ultrafast laser induced red fluorescence associated with the study of laser induced convection by nonlinear optics effects directly provides the real behavior of chinese tea molecule in transient heat transport. The molecule can absorb a photon and then relax non-radiatively or radiatively back to the electronics ground state. Ultrafast laser

induced fluorescence (ULIF) at 674.1nm was observed and radiative transition for the chinese tea molecules was very strong. The molecule of chinese tea absorbed a single photon should relax radiatively or non-radiatively bake its original state very rapidly. The very interesting result in this paper is that the dependence of the location of the red ULIF on the intensity of the laser beams. From one side we could see red color along the path of a relatively narrow column located the middle of bottom half of the cell while the intensity of the laser beam above a certain value.

Convection in chinese tea solution has been studied by self-action. We only consider third order nonlinear effects here and the refractive index n follows a kerr law dependence on intensity. It is [4]

$$n=n_0+n_2|\mathbf{E}|^2.$$

The nonlinear refraction coefficient n_2 is related to the third order susceptibility, and $|\mathbf{E}|^2$ is the intensity of the incident laser beam, n_0 is the linear refractive index of the nonlinear optical material. If the intensity $|\mathbf{E}|^2$ exhibits spatial and temporal variations, the refractive index will also be space- and time- dependent. This leads to such phenomena as self-focusing, self- defocusing, self-phase modulation and multiple rings patterns of laser diffraction. The development of temperature gradients in liquids results in convective flows that can significantly influence heat transport in the liquids and therefore the propagation of the light beam.

2. HEAT TRANSPORT BY PHONONS

Heat transport by phonons has been studied by single picosecond pulse degenerate four wave mixing (DFWM) technique. The laser source is an active and positive mode-locking laser (YG-401C, International Corporation). The laser pulse repetition rate was 10Hz. The pulse duration of infrared wave at 1.06 μm was 42 picosecond (ps) and second harmonic wave at 532 nm from this laser was 30 ps. The crossed laser pulses make an optical interference pattern inside the sample. The sudden rise in sample temperature followed by impulsive thermal expansion generates counterpropagating coherent phonon. The frequency of coherent phonons is tunable. The propagating direction of coherent phonons is determined by the geometry of the excitation laser beams. The first step in the experiment was measuring single picosecond pulse transient-grating. The strong phase conjugate (PC) signal was observed. The intensity full width at the half maximum (FWHM) of the time delayed PC signal was 15 ps. The second step considered here was measurement of population grating decay. In fig. 1, stronger beam 1 (0.44mJ) and beam 3(0.68mJ) act as pump beams. The beam 2 which is much weaker (0.12mJ) with a variable delay acts as a probe beam. At the beginning the delay time between the beam 1 and beam 3 was scanned and fix the micro-stage position at the maximum of PC signal. The time delay between beam 1 and beam 2 is performed by moving the position of M4 to change the distance between the M4 and the chinese tea cell. After moving the M4, the direction of beam 2 and interaction area of beam 1, beam 2 and beam 3 must check for each time to keep same accuracy of each measurement. The results of PC signal as a function of delay time between beam 1 and beam 2 is shown in Fig. 2. The decay signal superimposed on an ultrasonic modulation, which results from density excursion due to local heating. The time between maximum and minimum of PC signal was 1.9 ns.

In our experiment the decay signal superimposed on a ultrasonic modulation which results from density excursion due to local heating was observed. The main contribution to this modulation is an enhanced ultrasonic wave. There is a strong absorption in chinese tea solution on wavelength region of pump laser. The crossed pump laser pulses E_1 and E_3 make an optical interference pattern inside the chinese tea solution. The absorbed energy converts to heat by fast radiationless relaxation, and a temperature grating is created. This sudden rise in temperature followed by impulsive thermal expansion generates ultrasonic wave. The grating
pitch is given by [5]:

$$L=\lambda/\sin(\theta/2).$$

Where λ is the wavelength of the pump laser pulse and θ is the crossing angle of the pump laser beam. In our experiment, λ is 532 nm and θ is 7°, the L ~ 4.36μm. From the Fig.4, it is ease to find out the counter propagating coherent phonons with frequency $f = 2.6\times 10^8$ Hz. This result indicated that the sound velocity in chinese tea

solution is (v = fL) 1133.6 m/s which is compared with the sound velocity in methanol [5]. The density of chinese tea does not change instantaneously just after the excitation. As ultrasonic waves move in the excitation region, the density oscillates in the excitation region. The phase conjugate signal should be modulated. After the ultrasonic waves go out of the excitation region, a thermal grating remains and usually decays at a slow rate by thermal diffusion. By solving the wave equation for the density ρ and the thermal diffusion equation, we can obtain the change of the density $\Delta\rho$ and the temperature rise ΔT.

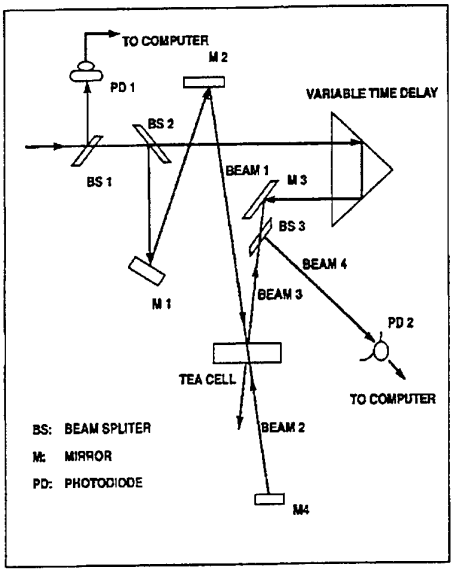


Fig.1 The geometry of single picosecond pulse degenerate four wave mixing and a schematic diagram of the setup for the measurement of the population grating.

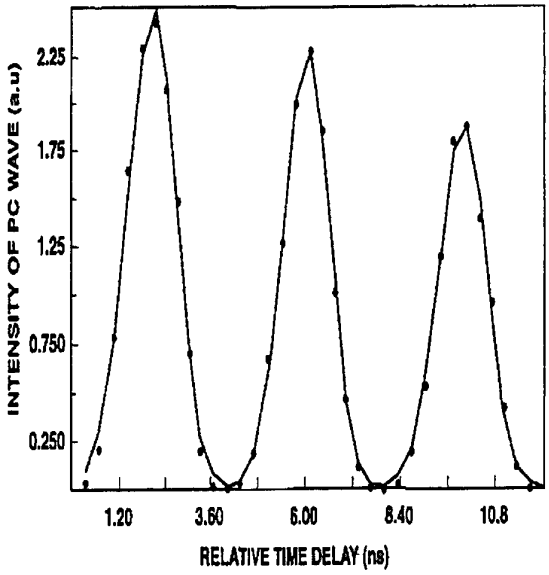


Fig.2 The results of PC signal as a function of delay time between beam1 and beam2 .

3. THE ABSORPTION AND EMISSION SPECTRUM

Fig. 3 shows that the dependence of intensity of transmitted beam on the intensity of incident beam was linear and the absorption coefficient at 532nm was constant ~ 0.717/cm. The intensity of red fluorescence emitted from chinese tea solution was also very strong. Fig. 4 shows that red fluorescence has a peak at 674.1 nm with a base width =20nm . The fluorescence decay time was recorded to be less than or equal to a few nanoseconds (2 to 3ns) and it was shown to be pump beam polarization dependent, i.e., the emitted red fluorescence is seen only in the direction perpendicular to the polarization direction of the exciting laser beam. The red fluorescence was recorded by a 0.85 meter double monochrometer (SPEX model 1404). The absorption spectroscopy for chinese tea solution in methanol was recorded and it is shown in Fig. 5. It showed a broad absorption band ranging from UV to IR. There is a strong absorption in chinese tea solution on wavelength region of pump laser which was second harmonic of Nd:YAG laser (532nm).

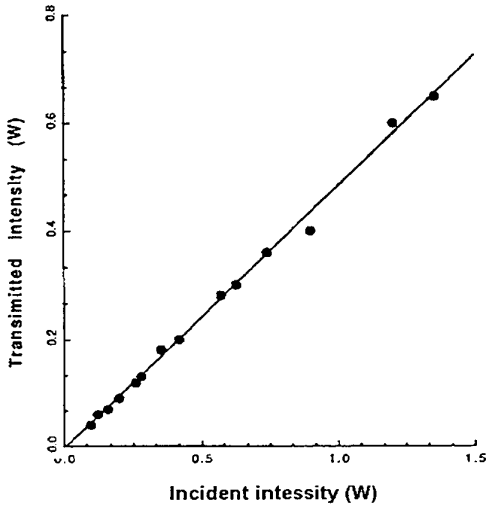


Fig.3 The dependence of intensity of transmitted beam on the intensity of incident laser beam.

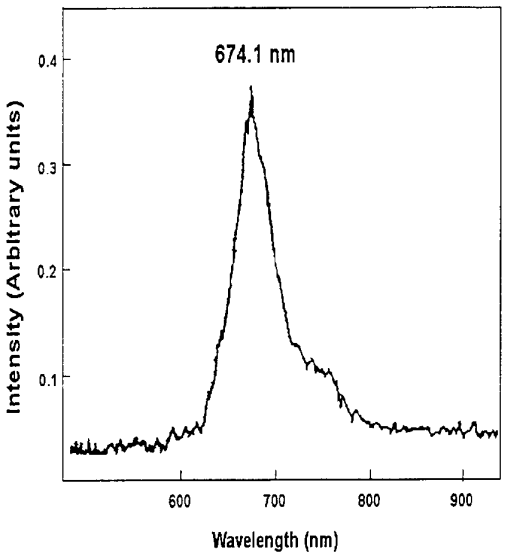


Fig.4 The red fluorescence emitted from chinese tea solution with a peak at 674.1 nm.

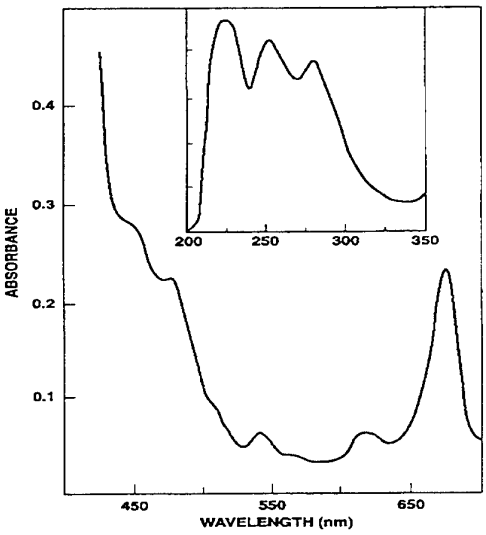


Fig.5 The absorption spectroscopy for chinese tea solution in methanal .



Fig.6 Typical transient multiple diffraction ring tern pattern associated with self-defocusing during the time of laser "turn on ".

4. CONVECTION AND SELF ACTION

Convection in chinese tea solution has also been studied by self action with both horizontal- and vertical laser propagation through the chinese tea cell. A second harmonic (532nm) from a cw modelocked Nd: YAG laser (Antars 76-s) with 70 ps pulse duration was used as the light source in this experiment. A laser beam of 2.0mm diameter and 0.5mrad divergence was made normally incident on a 1cm tea cell without focus. The intensities of 532nm laser

beams with TEM_{00} were 40 W/cm^2. Ethanol was used as the solvent for chinese tea. The used concentrations by weight of the chinese tea solution in ethanol were from 9.78 x 10^{-3}, and the best concentration was found to be 5.92×10^{-3}. When the intensity of the laser beam was above a certain threshold value, I_{th} = 3 W/cm^2, the transmitted light could form rings on a screen at a distance of 3 m from tea cell.

Horizontal Laser Propagation

A typical view of the concentric rings is shown in Fig. 6. This photograph was synchronously taken during the time of the laser "turn on" (open the laser shutter) with an exposure rate of 0.01 s. The concentration of chinese tea solution was 5.92×10^{-3}. Beyond this time the rings changed themselves from circular symmetry to half-circular symmetry very quickly. Fig. 7 shows this change from circular symmetry to half-circular symmetry about 0.01 s after laser "turn on". For the case of horizontal radiation propagation, motion of the medium is transverse to the optical beam axis. In the bottom- half of cell, the liquid always remains at rest. In top-half of cell, heave cold liquid is situated above light hot liquid. If former moves downward and the latter upwards, there is a release of potential energy which can provide kinetic energy for the motion. There is thus a possibility that the equilibrium will be unstable. A free convection flow is one produced by buoyancy forces. Temperature differences are introduced through absorption and the consequent density differences induce the motion; hot liquid tends to rise, cold to fall. The chinese tea solution establishes hot rising region and cold falling regions with horizontal motion at top and bottom maintain continuity.

Vertical Laser Propagation

In the case of vertical radiation propagation heat transport runs largely along the light beam axis. Since there was no motion of the liquid across the beam, the vertical propagation was closed to the conditions expected for the chinese tea solution at rest. We observed that the transient multiple diffraction rings from chinese tea solution can keep good circular symmetry for all time of investigation. The number of rings could be as many as sixty to one handed. The result is shown in Fig. 8.

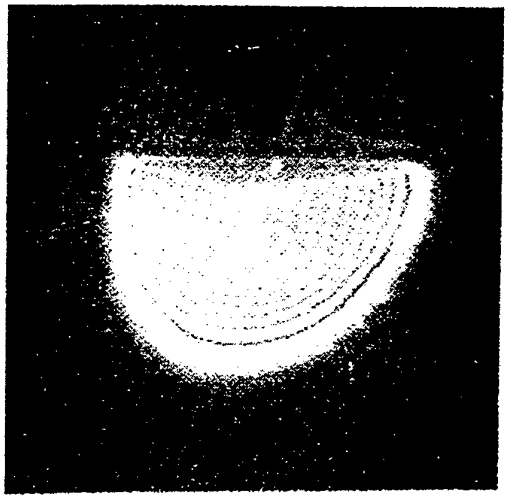


Fig.7 Typical transient multiple diffraction ring pattern with half-circular symmetry obse-rved after a few seconds of laser "turn on"

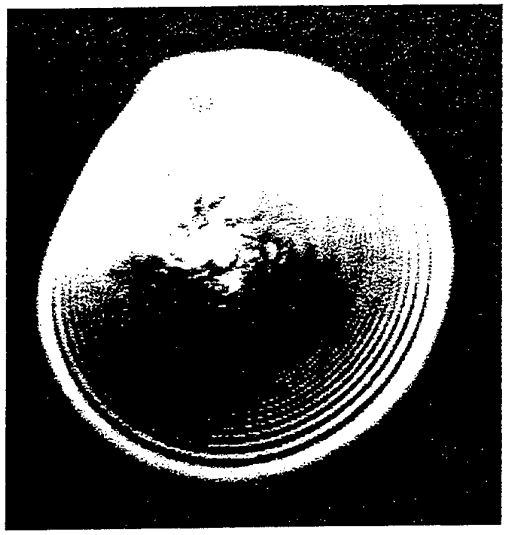


Fig.8 The transient multiple diffraction rings from chinese tea solution can keep good circular symmetry for all time of investigation when laser vertically through the chinese tea cell

5. MOLECULAR DYNAMICS

Chinese tea, a well known of natural organic material, has been reported as one of the types of new media to prevent cancer from happening. It is also known that chinese tea has extremely large third-order nonlinearity. Tea as the national beverage in China was first known to be used 4000 years ago as a herbal medicine. The main component parts are basic element of tea which can stimulate blood vessel, accumulated blood circulation, stimulate kidney and help drain toxin. Another organic molecules include citric acid, Vitamin, aromatic oil and chlorophyll, inorganic component include Manganese (Mn), Fluoride (F) and same salts. The one of the main contributions to the third-order nonlinearity in chinese tea solution could be from the chlorophyll molecular. In the theoretical model used for investigation, it has been assumed that the tea molecules first absorb light and then convert the absorbed energy to heat. After laser pulse arrives heating by proximity effect will occur. The thermalization of a liquid molecule with its surrounding occurs quickly, typically less then 10ps. The diffraction-limited spot size at optical wavelength is on the order of several microns. Most liquids are poor conductors of heat, and the thermal energy does not diffuse far from the heated region during the short interval of the laser pulse and the relaxation time.

The molecule can absorb a photon and then relax non-radiatively or radiatively back to the electronics ground state. Non-radiative transitions convert the absorbed photon into thermal energy, resulting in heating of the liquid. Radiative transitions result in a photon emission instead of heating the molecule. Radiative transition in many liquids, including water, always are negligible, and are not considered in their analysis. Consider radiative transition for the chinese tea molecules was very strong, the molecule of chinese tea absorbed a single photon should relax radiatively or non-radiatively bake its original state very rapidly.

Ultrafast laser induced fluorescence (ULIF) at 674.1nm was observed in the 1cm tea cell. The important thing is the dependence of the location of the red ULIF on the intensity of the laser beams. From one side we could see red color along the path of a relatively narrow column located the middle of bottom half of the cell. Fig. 9 shows this very interesting result. At lower intensity of the laser beam the tea cell was observed as full of uniform red color which is shown in Fig. 10. Combine the convection studied by self-action, these results provided the real behavior of the chinese tea molecules in laser-liquid heating. Temperature differences are introduced through absorption and the consequent density differences induce the motion; hot liquid tends to rise, cold to fall. The investigation of the tracing of the molecules in more detail is to be down.

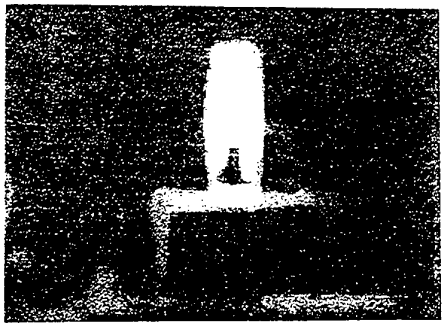


Fig. 9 Red color of ULIF along the path of a narrow column located the middle of bottom half of the cell.



Fig.10 At lower intensity of the laser beam the tea cell was observed as full of uniform red color.

In chinese tea solution, two main different processes can give rise to orientation gratings: alignment of the molecules along the field direction and distortion of the molecule's electron cloud by the field, both of which lead to a transient refractive-index grating in the material. In general, the effect of molecular of orientation Kerr effect is considerably bigger in magnitude then other effects. Additionally, all other effects contributed to Kerr effect essentially instantaneous, with a time constant of $\sim 10^{-15}$ second. In our experiment the duration of laser pulse is 30 picosecond.

The main contribution to transient grating in chinese tea solution is reorientation of chinese tea molecules. The reorientation should occur in chinese tea solution due to anisotropic molecules whose optical polarizability along different axes are unequal. In the absence of a field, the molecules of the liquid are randomly oriented, and its refractive index is isotropic. The periodic polarization field induces dipole moments that exert torque causing the molecule to be rotated into alignment with the field.

6. CONCLUSIONS

Transient microscale heat transfer in liquid which contained the nature organic material of chinese tea solution has been studied. The chinese green tea solution was used in this work as nonlinear medium as well as the liquid for heat transfer. Heat transport by phonons has been studied by single picosecond pulse degenerate four wave mixing (DFWM) technique. Ultrafast laser induced fluorescence (ULIF) at 674.1nm was recorded and radiative transition for the chinese tea molecules was very strong. Convection in chinese tea solution has also been studied by self action with both horizontal- and vertical laser propagation through the chinese tea cell. The dependence of the location of the red ULIF on the intensity of the laser beams related to the real behavior of chinese tea molecules in transient heat transport were discussed.

Acknowledgements- This work is supported by NASA grant NAG8-1335. The authors would like to thank Dr. Wang Jing for her excellent job preparing our camera-ready manuscript.

REFERENCES

1. Jon P. Longtin, C. L. Tien, Int. Heat Mass Transfer V. 40, pp 951-959 (1997).
2. C. A. Sacchi, J. Opt. Soc.Am.B V.8, pp. 337-345 (1991).
3. G. Chen, C. L. Tien, Journal Of Heat Tranfer V. 116, pp325-331 (1994).
4. Y. R. Shen, *The Principle of nonlinear optics,* Wiley, New York (1984).
5. K. Ishikawa, Y. Takahashi, U. Tanaka, Y. Fukuda, T. Hashi, Opt.Commun V. 76, pp 81-85 (1990).

J. Heat Transfer Enhancement

TURBULENT AUGMENTED HEAT TRANSFER FROM THE SURFACE OF AN IMMERSED TUBE IN A MAGNETOFLUIDIZED BED

Satish C. Saxena
Multiphase Reactor Research Laboratory
The University of Illinois at Chicago
Email: saxena@uic.edu; Fax: (312) 996-0808

Vitaly L. Ganzha
Luikov Institute of Heat and Mass Transfer of Belarussion Academy of Sciences,
15 P. Brovka Street, Minsk 220072, Belarus

Keywords: heat transfer, magnetofluidized bed, turbulent regime

ABSTRACT. Heat transfer from horizontal heater heat-transfer probes submerged in a fluidized bed of iron particles exposed to a uniform magnetic field collinear with air flow is investigated experimentally at ambient conditions. Two heater heat-transfer probes have been designed, one for the measurement of total heat-transfer rates and the other for the measurement of local heat-transfer rates at different angular positions on the horizontal cylindrical heat-transfer surface. Measured total heat transfer rates have high values, and differences in the values for fixed and stabilized regimes from those in the fluidized regime are small. This is interpreted as implying that major heat transfer occurs by gas convection and it is shown that turbulence augments the gas convective heat transfer. This is also confirmed by direct measurements with a strip heater cylindrical heat-transfer probe at different angular positions. The mechanistic theory of heat transfer based on the concept of turbulent boundary layer on the heat transfer surface developed by the authors is found to successfully predict the measured heat-transfer rates from surfaces immersed in magnetofluidized beds.

1. INTRODUCTION

Magnetofluidized-bed reactors are of great practical significance as pointed out in the reviews of Liu et al. [1] , and Saxena et al. [2]. It is therefore of great importance to understand the hydrodynamic and heat-transfer characteristics of magnetically stabilized fluidized bed reactors, Rosenweig et al. [3, 4]. A magnetically stabilized fluidized bed (MSFB) is simply a fluidized bed of magnetic particles exposed to an external uniform time-invariant magnetic field (H) collinear with the gas-flow. As the gas velocity, U_g , is increased, the bed pressure drop (ΔP_b) increases linearly with increase in U_g until a velocity U_{mf} is reached, and the bed exhibits a behavior similar to a fixed-bed which is adequately described by Carman-Kozeny formulation. At $U_g = U_{mf}$, the effective bed weight is balanced by the gas drag force on the particles, and $\Delta P_b = W/A$. Here W is the bed weight and A is the bed cross-sectional area. As U_g is further increased beyond U_{mf} , the magnetic particles start to align and arrange themselves along the magnetic lines of force. Here H plays an important role, and conventional incipient fluidization behavior relating to the onset of bubbling observed for H = 0, is not encountered. Instead the particle rearrangement occurs and causes the bed to expand and the interstitial gas velocity decreases keeping the bed in a packed configuration. More particle ordering is accomplished as U_g is increased and depending on the value of H, the bed arrangement ceases at a characteristic gas velocity U_{mb} . For $U_g \geq U_{mb}$, the bed exhibits bubbling phenomenon. The bed for U_g values bounded between U_{mf} and U_{mb} is referred to as the magnetically stabilized bed (MSB). The bed regime for $Ug > U_{mb}$ is designated as MSFB or partially stabilized fluidized bed. A MSB is a very promising state for technological applications as it enables to combine the advantages of greater gas throughput and favorable transport, hydrodynamical and rheological properties without gas bypassing. The thrust of this work is to investigate the heat-transfer properties of a MSB.

Two cylindrical heater heat-transfer probes have been employed to investigate the total and angular heat-transfer rates from the surface of an immersed horizontal cylindrical tube in a bed of iron particles fluidized by air and exposed to an uniform constant magnetic field collinear with the gas flow. The experiments are conducted at ambient conditions of temperature and pressure. The experimental facility and procedure for making a run is described in the next section.

2. EXPERIMENTAL FACILITY

The design details and dimensions of the various components constituting the experimental facility are described in detail in earlier publications [5 - 7] from this laboratory and hence here only major details in brief are given. A 45kW single-stage, positive displacement, air - cooled and flood-lubricated rotary screw type air compressor in conjunction with two filters, a regenerative desiccant drier, and a vertical tank suitably manifolded with several gauges and control valves supplies compressed, filtered and dried air at a maximum rate of 8.5 m^3/ min at 700 kPa and 311 K, and is metered through a combination of three rotameters. The water-cooled Helmholtz coils housed in a Delrin casing having an inner and outer diameters of 0.358 and 0.568 m respectively and separated by a gap of 0.171 m and rated for operation at 60V and 15 A can produce a uniform and time-invariant magnetic-field intensity up to 27, 137 A/m. The field is measured by a self calibration gaussmeter connected to a transverse-type Hall probe, 15.24 mm in diameter and 58 mm in length.

The fluidization column is constructed from a 12.5 mm thick transparent Plexiglas pipe with an internal diameter of 0.102 m. The calming section is 0.21 m long and has a 6.35 mm thick air distributor plate with nineteen holes of 9.53 mm diameter arranged in concentric circles. The combined height of test bed and freeboard sections is 3.5 m and air enters in these sections through a combination gas distributor plate comprising of a 12.4 mm thick Plexiglas plate having sixty - one holes of 4.26 mm diameter, and a 0.57 mm thick interchangeable brass orifice plate having sixty-one holes of 2.00 mm diameter. The pressure drop across this plate, ΔP_d , is found to vary with the superficial air velocity, U_g , by the following power-law type expression:

$$\Delta P_d \text{ (kPa)} = 3.03\ U_g^{1.92} \text{ (m/s)} . \qquad (1)$$

The exponent value suggests that the flow through the distributor plate resembles to that through an orifice.

A heater heat-transfer probe to measure the total heat-transfer coefficient, h_w, is designed by Ganzha and Saxena [8] and is employed in the present work. It is made by winding 80 μm copper wire over a 22 mm diameter Bakelite rod. It is held in position by glue and is machined to a depth of one wire radius, and finally finished with a coat of an electric -resistant varnish. The average diameter and overall length of the finished heater probe are 22.9 mm and 97.4 mm respectively. The probe comprises of three independent sections of 24 mm length. The probe is horizontally installed in the bed with its axis at a distance of 47 mm above the distributor plate.

The probe constitutes an arm of a Wheatstone bridge whose ratio arms comprise of 250 and 2500 ohm resistors. The probe is calibrated at 323.2 K by adjusting the resistance of the fourth arm to get the bridge balance. While measuring h_w , the power supplied to the bridge is varied to get the bridge balance. The current through the probe is also measured and hence h_w is computed rather easily as detailed by Ganzha and Saxena [8].

A second heater heat-transfer probe is specially designed by Ganzha and Saxena [9] to measure the angular dependece of h_w on the cylindrical surface and is used in this work. The probe consists of a cylindrical Bakelite rod of 24.9 mm outer diameter and is 96.9 mm long. A slot of 5.7 mm width and 1.5 mm depth is machined on its surface along the cylinder length. A strip heater, prepared by winding 80 μm insulated

copper wire on a Bakelite strip, is installed in the surface slot of the Bakelite rod. The other measurement details are similar to that as for the probe designed for the measurement of total heat-trasfer rates from the cylindrical surface [8].

The experimental program involves to measure h_w as a function of U_g when it is horizontally mounted close to the distributor plate (L = 47 mm), and then far up in the freeboard of the fluidization column, L = 2.7 m. In each case, measurements are taken as a function of U_g for three angular positions of the strip heater obtained by rotation around its axis. These are: (a) the strip heater is located at the stagnation point (0° position) , equatorial region (90° position) , and downstream region (180° position) . Next, the probe is mounted in a bed of iron particles and h_w measurements are repeated as for the case with no particles. For the probe of Fig. 2A, h_w measurements are taken as a function of U_g and H. The specific results and their implications are discussed in the next section.

3. RESULTS AND DISCUSSION

The measured h_w values as a function of U_g for the iron particle bed and for six values of H are shown in Fig. 1. At H = 0, the conventional fluidized-bed behavior is observed, viz., h_w increases linearly with U_g until U_{mf} is reached when a sudden increase in its value occurs due to bed fluid-

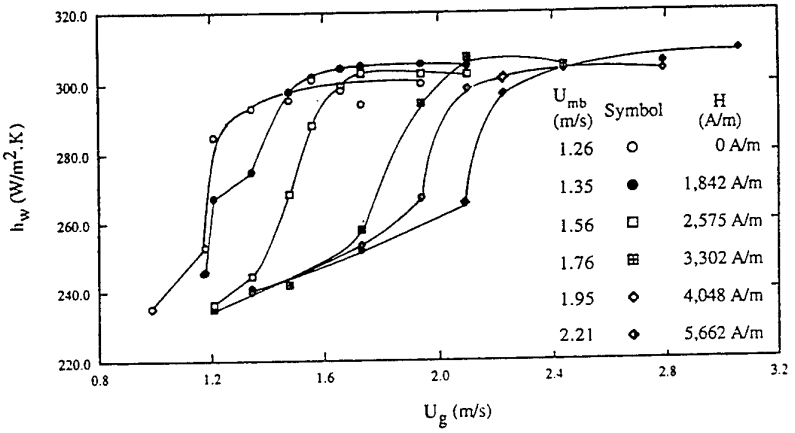


Fig. 1. Variations of h_w with increasing U_g and H for the iron bed.

ization, and h_w approaches to an approximately constant value for larger U_g values, Botterill [10] . For all H values, the h_w variation can be understood in terms of three regimes, Saxena et al. [2]. For $U_g < U_{mf}$, the fixed - bed regime prevails and h_w increases slowly with increase in U_g . For $U_{mf} \leq U_g < U_{mb}$, h_w values increase with increase in U_g of about the same magnitude as in the fixed-bed regime. For $U_g \geq U_{mb}$, the bubbling regime characterized by extensive particle movement brings about a rapid increase in h_w values with increase in U_g and h_w approaches towards a maximum value as U_g is further increased; similar to a conventional bubbing fluidized bed [10].

To understand the mechanistic detailes of the heat-transfer process, one very important feature to note in the results of Fig. 1 is that the differences in the h_w values in the fixed- and stabilized-bed regimes from that in the fluidized-bed regime are not very significant, (about 20%). This implies that the gas convection component responsible for the heat transfer process is a major contributor to the heat-transfer process, and particle convection component is relatively insignificant under these conditions, Saxena [11]. Further, the large h_w values would suggest that the gas flow at the heat-transfer surface is highly turbulent. On the other hand,

calculations of Reynolds number based on probe diameter (22.9 mm) for velocities of Fig. 1 reveal its variation in the range about 2,000 - 3,500 only. This would imply that the presence of particles and the gas dispersion system (gas-distributor plate) adopted in these experiments is augmenting turbulence in the gas flow. To establish this conclusively the second probe is employed to conduct special experiments which are detailed below.

This second probe is capable of measuring h_w at different angular positions on the surface, Saxena et al. [9]. Three positions have ben examined in this work. Position 0°, refering to the upstream region around the stagnation point; position 90°, refering to the equatorial region; and position 180°, refering to the downstream region. In Fig. 2 are reported the h_w measurement results for the three positions (0°, 90° and 180°). In Fig. 2A, h_w values refer to bed of iron particles with probe axis at a

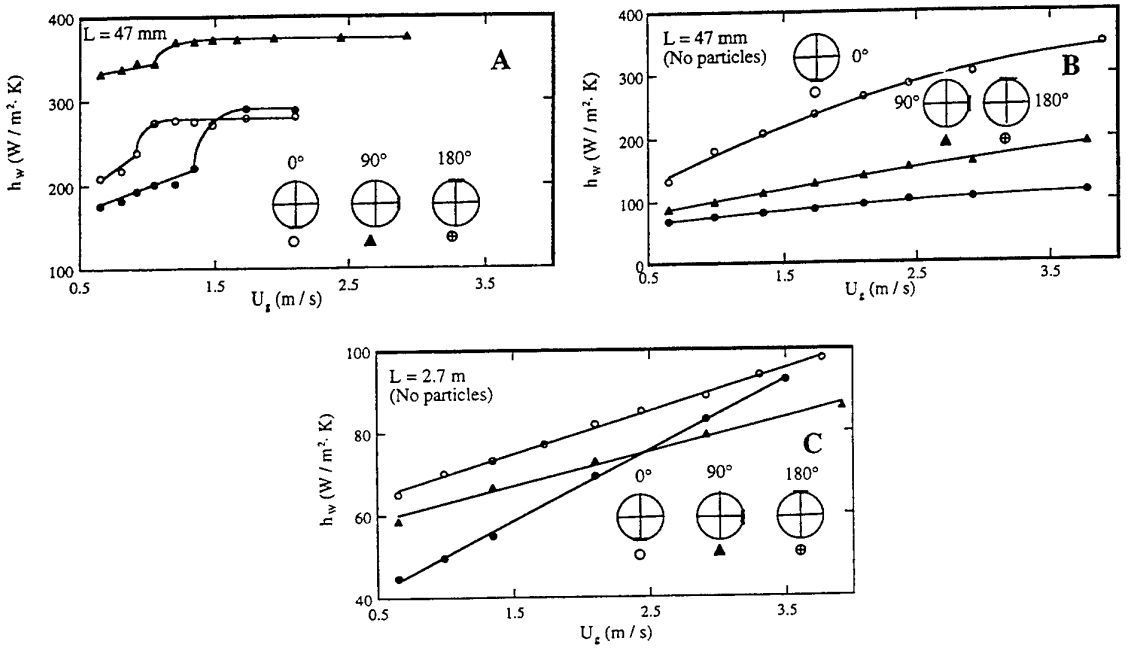


Fig. 2. Variation of h_w with U_a at different angular positions.

distance of 47 mm above the distributor plate. Figure 2B refers to an empty column (no particles) with probe at the same location as in data of Fig. 2A, and Fig. 2C also refers to an empty column but the probe is located at a distance of 2.7 m above the distributor plate.

The heat-transfer rates are largest for the equatorial position in the presence of bed (Fig. 2A). The significant point to note here is that h_w values are insignificantly different in the fixed and fluidized states. For the fixed and the initial fluidized state, h_w in the upstream region around the stagnation point are larger than the corresponding values in the downstream region. The two sets of values are almost the same in the fluidized state at higher U_g values. The cap of defluidized solids at the 180° position keeps the heat-transfer rates smaller than those at 0° and 90° positions; Saxena et al. [12]. However, the rates increase as the solids are fluidized. h_w values are higher for the fluidized state than for the fixed-bed state. The air pocket at 0° position keeps the h_w values smaller than that at 90° position but these h_w values are greater than at 180° position, highlighting the significance of turbulence in the air pocket and in the upstream region , in general [12, 13].

To disentangle the role of bed particles as a source of turbulence and to evaluate the contribution of gas convection to the heat-transfer rate, experiments have been conducted in an empty column with no particles and the probe located at the same distance from the distributor plate with the results presented in Fig. 4B. The h_w values at all the three positions increase with increase in U_g , the rate of increase being largest for the region around the stagnation point. Further, h_w values for the 0°position are also the largest, and the values at the 90° position are larger than at the 180° position. These results are in agreement with those reported in the literature for relatively larger Reynolds number [14]. The relatively larger values of h_w around the stagnation point are attributed to enhanced local turbulence than at 90° and 180° positions. A comparison of h_w values of Figs. 2A and 2B is interesting from the viewpoint of discriminating the contribution of gas convection and particle convection. However, in this comparison it is necessary to note that in Fig. 2A, the probe surface is exposed to interstitial gas velocity while in the case of Fig. 2B to the superificial gas velocity. For rough comparison the bed voidage may be taken as 0.5 so that U_g values in Fig. 2A must be reduced by 50% while comparing with the values in Fig. 2B.

A comparison of this nature reveals that at 0° position, the two cases of Figs. 2A and 2B are almost the same. This is because at the stagnation point, a gas pocket engulfs the probe and particles play only an insignificant role. In the equatorial region, a similar comparison reveals that paritcles play a very important role as a source of turbulence and thereby almost augmenting the heat-transfer rate by a factor of 2 to 3. The downstream wake region h_w values also indicate the significant role of particles as a source of turbulence in as much as the heat-tranfer rates for the fixed- and stabilized- bed regimes are about twice as large as in the case without particles.

The h_w data of Fig. 2C are taken primarily with the goal to disentangle the role of distributor plate as a source of turbulence in the air stream flowing past the heat-transfer probe. It is expected that any turbulence created by the distributor plate in the gas stream will almost subside by the time it reaches the probe located at L = 2.7 m. At all the three positions, h_w values are much smaller at L = 2.7 m than at L = 47 mm. This clearly established the important role of the distributor plate as a significant source of turbulence for the gas stream. This is not difficult to visualize as each orifice shoots a gas jet with a velocity more than 40 times the superficial gas velocity. These jets will interact with each other to create a turbulent flow.

The heat-transfer coefficient at the stagnation point under the assumption that the flow is almost laminar is correlated by the following relation [15]:

$$h_w = 0.806 k_g \left(2U_g / vD\right)^{1/2} Pr^{0.4}, \qquad (2)$$

for $0.1 \leq Pr \leq 10$. Pr for the experimental conditions of this work is 0.71. The experimental and computed h_w values are compared in Table 1. The experimental values are always greater than

Table 1. Experimental and Calculated h_w (W/m^2. K) Values at the Stagnation point for L = 2.7 m

U_g (m/s) 0.65	1.0	2.0	3.0	3.8	
h_w (cal.) 36.7	47.5	64.5	79.0	88.9	
h_w (exp.)	65.0	70.1	79.0	90.0	97.6

the theoretical values and the agreement improves as U_g increases. The maximum disagreement of about 40 % reduces to less than 10 % at the highest gas velocity. Part of the disagreement may be attributed to the turbulences in the incoming gas stream while flowing through the column.

4. CONCLUDING REMARKS

The analysis and interpretation of total and angular measured heat-transfer coefficients have shown that the gas convection component of the heat-transfer coefficient in the experimental data reported here have played a major role as compared to the particle convective component. This is because of the turbulence created in the gas flow by the presence of particles and the design of the gas distributor plate. Ganzha et al. [16] developed a heat-transfer model for large particle fluidized beds in which the gas convective component is computed under the assumption of a turbulent boundary layer at the heat-transfer surface. The results of their mechanistic theory have been simplified by Ganzha and Saxena [8] to apply for the present case in the following form:

$$h_w = \left(k_g / d_p\right)\left(0.116 Re^{0.8} + 5.67\right). \tag{3}$$

Computed values of h_w form the above relation are compared with the experimental values as a function of U_g in Fig. 3. The agreement is considered good and a confirmation to the concept of

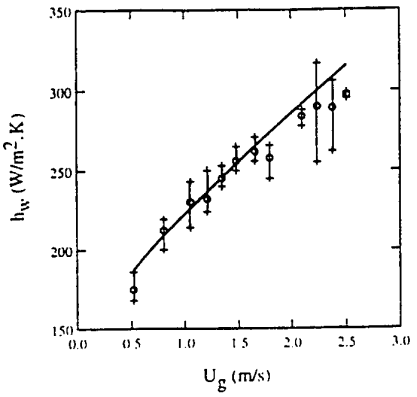


Fig. 3. Comparison of experimental and calculated h_w values.

turbulent augmented gas convection heat-transfer in magnetofluidized beds as the major contributor to the total heat-transfer rate.

The applicability of the above h_w expression is for the fixed- and magnetically stabilized- bed regimes for U_g values bounded by U_{mb} . It is proposed to estimate U_{mb} by the semi-theoretical expression proposed by Ganzha and Saxena [17].

The experimental U_{mb} values determined from the measurements of bed pressure drop, ΔP_b, as a function of decreasing U_g by adopting the procedure of Saxena and Shrivastava [5] are listed in Table 2 as a function of H. Also indicated in this table are the calculated U_{mb} values from the

Table 2. Comparison of experimental and calculated U_{mb} (m/s) values

H, A/m 0	1,842	2,575	3.302	4,048	5,662	
U_{mb} (exp.)	1.26	1.35	1.56	1.76	1.95	2.21
U_{mb} (cal.)	---	1.33	1.51	1.66	1.83	2.06

expressions of Ganzha and Saxena [17]. The agreement between computed and experiemtnal values is good and the accuracy of the Ganzha and Saxena [17] correlation is estimated as better than 10%.

NOMENCLATURE

A, bed cross-sectional area, m^2
d_p, average particle diameter, m
D, probe diameter, m
h_w, heat-transfer coefficient, W/m^2. K
H, magnetic-field intensity, A/m
k_g, gas thermal conductivity, W/m. K
L, length of either a bed section or total bed, m
Pr, Prandtl number, dimensionless
Re, Reynolds number, dimensionless
U_g, superficial gas velocity, m/s
U_{mb}, superficial minimum bubbling gas velocity, m/s
U_{mf}, superficial minimum fluidization gas velocity, m/s
W, weight of the bed, N

Greek Symbols
ΔP_b, bed pressure drop, N/m^2
ΔP_d, distributor pressure drop, N/m^2
ν, kinetic gas viscosity, m^2/s

Acronyms
MSB, magnetically stabilized bed
MSFB, magnetically stabilized fluidized bed

REFERENCES

1. Y. A. Liu, R. K. Hamby and R. D. Colberg, Powder Technology v. 8, pp. 3-41 (1991).
2. S. C. Saxena, V. L. Ganzha, S. H. Rahman and A. F. Dolidovich, Advances in Heat Transfer v. 25, pp. 151 - 249 (1994).
3. R. E. Rosensweig, Science v. 204, pp. 57 - 60 (1979).
4. R. E. Rosensweig, J. H. Siegell, W. K. Lee and T. Mikus, *AIChE Symp. Ser.*, v. 207, No. 205, pp. 8-16 (1981).
5. S. C. Saxena and S. Shrivastava, Powder Technology v. 64, pp. 57 - 67, (1991).
6. W. Y. Wu, A. Navada and S. C. Saxena, Powder Technology v. 90, pp. 39-46 (1997).
7. W. Y. Wu, K. L. Smith and S. C. Saxena, Powder Technology v. 91, pp. 181-187 (1997).
8. V. L. Ganzha and S. C. Saxena, Int. J. Heat & Mass Transfer v. 41, pp. 209- 218 (1998).
9. V. L. Ganzha and S. C. Saxena, Int. J. Heat & Mass Transfer v. 41, pp. 203-208 (1998).
10. J. S. M. Botterill, *Fluid-Bed Heat Transfer,* Academic Press, New York, (1975).
11. S. C. Saxena, Advances in Heat Transfer v. 19, pp. 97 - 190, (1989).
12. S. C. Saxena, N. S. Grewal, J. D. Gabor, S. S. Zabrodsky and D. M. Galershtein, Advances in Heat Transfer v. 14, pp. 149 - 247, (1978).
13. I. Goel and S. C. Saxena, 7th *Int. Conf. Fluidized Bed Combustion*, v. 2, pp. 804 - 818 (1983).
14. J. H. Lienhard, *A Heat Transfer Textbook*, Prentice-Hall, Inc., New Jersey, (1981).
15. F. M. White, *Heat Transfer*, Addison-Wesley Publishing Co., Reading, Massachusetts, (1984).
16. V. L. Ganzha, S. N. Upadhyay and S. C. Saxena, Int. J. Heat Mass Transfer v. 25, pp. 1531 - 1540 (1982).
17. V. L. Ganzha and S. C. Saxena, A Model for the Calculation of Minimum Bubbling Velocity of a Magnetically Stabilized Admixture Bed, Powder Technology, in press.

DRAG REDUCTION AND HEAT TRANSFER ENHANCEMENT OF WATER FLOW IN A PIPE USING NEW SURFACTANTS FOR ENVIRONMENTALLY ACCEPTABLE DRAG REDUCING ADDITIVES

Kazuo Nobuchika, Toru Nakata, Kenji Sato
Fumihisa Yamagishi, Sumiko Tomiyama
Technical Research Laboratories Div.
Toho Chemical Industry Co., LTD.
E-mail: JDU04655@niftyserve.or.jp; Fax: 0468-66-5731

Hideo Inaba, Akihiko Horibe, Naoto Haruki
Dept. of Mechanical Engg.
Faculty of Engng., Okayama University
E-mail: Inaba@mech.okayama-u.ac.jp; Fax: +81-86-251-8266

Keywords: flow-drag reduction, convection heat transfer, surfactant, circular tube

ABSTRACT. The drag reduction of a water flow with new drag reducing surfactants (mixture of amine oxide nonionic type surfactants and imidazolium betaine amphoteric type surfactants) which were selected as environmentally acceptable drag reducing additives was investigated experimentally. The flow resistances of the water flow with two kinds of surfactants were markedly reduced as compared with that of a water flow with only amine oxide under the conditions of cold water and hot water supplies, respectively. The heat transfer enhancement experiments were carried out using spring coil which was inserted in the test circular tube as a turbulence promoter. As a result, it was observed that heat transfer coefficient of the water flow with N-stearyl-NN-dimethylamine oxide using the spring coil increased up by about four times as compared with that without the spring coil. Useful non-dimensional correlative equations for flow resistance and heat transfer were derived by various non-dimensional parameters.

1. INTRODUCTION

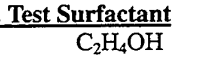
Recently, a flow drag reduction effect by the addition of polymers or surfactants into a water flow in a pipe has been used for an effective thermal energy transport system. This flow drag reduction effect is generally called "Toms effect". The Toms effect is caused by addition of a small quantity of polymers or surfactants to a water whose flow condition is turbulent in a pipe. It is expected that a flow rate is increased and a pumping power is reduced in a water transportation system by using these additives. It is said that the drag reduction in a turbulent flow is caused by suppressing the occurrence and development of turbulent vortexes by means of a deformation of polymer thread in a water flow [1].

On the other hand, some kinds of the surfactants make a rod-like micelle with the connection of spherical micelles in water [2]. For example, these are Cetyltrimethylammonium Bromide, Dodecyltrimethylammonium Chloride, mixture of N-oleyl-NN-dihydroxyethylamine oxide (OHAO) and 2-lauryl-N-carboxymethyl-N-hydroxyethyl imidazolium betaine (MOHAOLB), mixture of N-behenyl-NN-dimethylamine oxide (BMAO) and 2-lauryl-N-carboxymethyl-N-hydroxyethyl imidazolium betaine (MBMAOLB) or N-stearyl-NN-dimethylamine oxide (SMAO). As a result, the rod-like micelle has the same function as the polymer thread. If MOHAOLB, MBMAOLB or SMAO is added to water, it is more suitable for domestic hot and cold water transportation systems as compared with the polymer solution. It is the reason that the rod-like micell of surfactants in a water is broken easier than the polymer thread by a stronger mechanical shearing force, it is easy for the broken micelle structure to recover in a weak shearing force flow. The use of a water solution with surfactants is limited by temperature of water solution, since there is the optimum temperature range of making the rod-like micelle structure.

The purpose of this study is to investigate the drag reduction of a water flow with MOHAOLB, MBMAOLB, and also the heat transfer enhancement experiments of a water flow with SMAO were carried out using spring coil which was inserted in the test circular tube as a turbulence promoter.

2. DESCRIPTION OF TEST SURFACTANTS AND EXPERIMENTAL METHOD

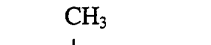
2.1. Test Surfactant



N-oleyl-NN-dihydroxyethylamine oxide

R : $CH_3(CH_2)_7CH{=}CH\text{-}(CH_2)_8$-

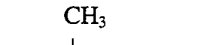
MW : 371



N-behenyl-NN-dimethylamine oxide

R : $CH_3(CH_2)_{21}$-

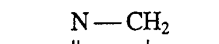
MW : 369



N-stearyl-NN-dimethylamine oxide

R : $CH_3(CH_2)_{17}$-

MW : 313



2-lauryl-N-carboxymethyl-N-hydroxyethyl imidazolium betaine

R : $CH_3(CH_2)_{10}$—

MW : 326

Fig. 1. Molecular formulas of surfactant

3. EXPERIMENTAL APPARATUS AND PROCEDURE

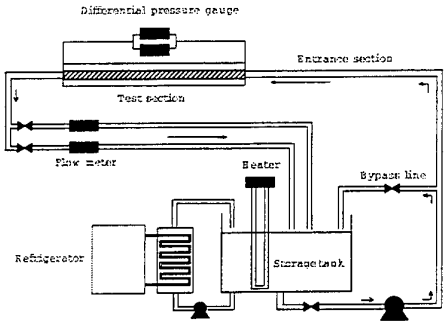


Fig. 2. Schematic diagram of experimental apparatus

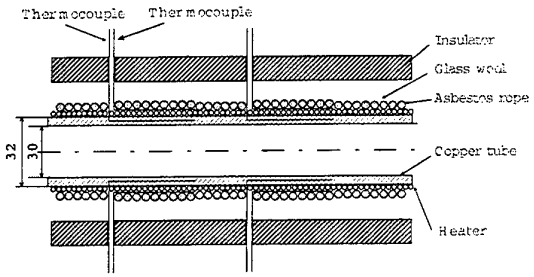


Fig. 3. Cut view of test section for heat transfer experiment

Schematic diagram of experimental apparatus [3] for drag reduction and heat transfer measurements is presented in Fig. 2. The present experimental apparatus consisted of three parts, that is a test section for flow and heat transfer measurement, a centrifugal pump as fluid circulation power source, and a test fluid circulation pipe line. Test fluid temperature in a storage tank was controlled by circulating brine cooled with a refrigerator, and its temperatures were measured with T type thermocouples at the inlet and outlet of the test section pipe. Six pieces of stainless steel and polyvinyl chloride circular tubes (inside diameter d = 16 mm, length L = 2 m) were used as the test section for flow resistance experiment of MOHAOLB water solution and MBMAOLB water solution. An entrance section was equipped at the inlet of each test section tube in order to obtain a full-developed flow

velocity in a pipe. The pressure-losses in the axial direction of test tube were automatically recorded with a differential pressure transmitter that connects two pressure taps mounted on the inlet and outlet of test section tube. The measuring accuracy of pressure measuring system was estimated within ± 3 % in consideration of measuring accuracy of the differential pressure transmitter.

The cut view of the test section tube for heat transfer experiment of SMAO water solution is shown in Fig. 1. The copper tube (inside diameter d = 30 mm, outside diameter d_0 = 32 mm, length L = 2 m) was used for the heat transfer experiment. The heating part on the copper tube was divided into 12 sections in the flow direction. The manganese wire electric heater insulated with glass fiber was used at each heating section. A constant wall temperature condition on heating surface was obtained by controlling an electric input power of each heater. The heating surface temperature T_w in each section was measured by T type thermocouple buried in a groove (depth 0.5 mm, diameter 0.5 mm) at the middle of each heating section. For the purpose of reducing the heat-loss and protecting the test section, a heatproof asbest rope with glass fiber and urethane foam thermal insulating material was covered on each electric heater. As a result, the heat-loss from the heater to the environment could be reduced within a maximum of 4.6 % against total transmitted heat. The average heat transfer coefficient α of each heating surface on the circular tube was calculated from Eq. (1).

$$\alpha = \frac{1}{n} \cdot \sum_{i=1}^{n} \left[\frac{Q_i}{\Delta T_i \cdot S_i} \right] \tag{1}$$

In this equation, the Q_i is the net heat transmitted to the test fluid at each heater section (each electric input power Q_{hi} - heat-loss Q_{li}). The ΔT_i is the temperature difference between each heating surface temperature T_w, and bulk temperature of the test fluid. The S_i means each heating surface. Subscript i refers to each heating surface element. The n is a number of heating section (n = 10).

The flow drag measurement of MOHAOLB water solution was carried at the tube inlet test fluid temperature of 5 °C and 15 °C for various MOHAOLB concentrations and mean velocities. The flow drag measurement of MBMAOLB water solution was carried at the tube inlet test fluid temperature of 80 °C for various MBMAOLB concentrations and mean velocities. The heat transfer coefficient measurement of SMAO water solution was performed at a constant inlet test fluid temperature of 60 °C and constant tube wall temperature of 62 °C and at a constant inlet test fluid temperature of 80 °C and constant tube wall temperature of 82 °C for various SMAO concentrations and mean velocities.

4. EXPERIMENTAL RESULTS AND DISCUSSIONS

Drag Reduction Behavior in Pipe

MOHAOLB water solution. The relationships between pipe friction coefficient λ and the modified Reynolds number Re' of water, OHAO water solution and MOHAOLB water solution in the test section (inside diameter d = 16 mm) are shown in Fig. 4 and Fig. 5 for various MOHAOLB concentrations (C_c) at the inlet test fluid temperature of 15 °C and 5 °C. In Fig. 4 and Fig. 5, the modified Reynolds number Re' was calculated from Equation. (2) that meant a Non-Newtonian behavior of OHAO water solution and MOHAOLB water solution .

$$Re' = 8^{1-n} \cdot \left\{ \frac{3n+1}{4n} \right\}^{-n} \cdot \left\{ \frac{\rho \cdot V^{2-n} \cdot d^n}{K} \right\} \tag{2}$$

In the case of Newtonian fluid where n = 1, Eq. (2) is reduced to the ordinary Reynolds number Re. As in a Newtonian fluid, the friction factor of a laminar pipe flow and in a turbulent pipe flow are:

$$\lambda = \frac{64}{Re'} \tag{3}$$

$$\lambda = 0.3164 \cdot Re'^{-\frac{1}{4}} \tag{4}$$

which are presented as solid lines in Fig. 4.

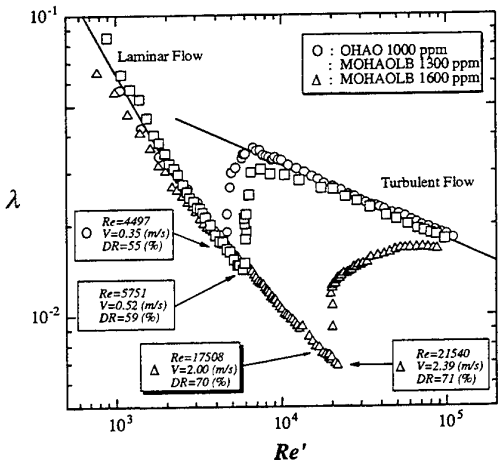


Fig. 4. Relationship between λ and Re' of MOHAOLB water solution (t = 15 °C, d = 16 mm)

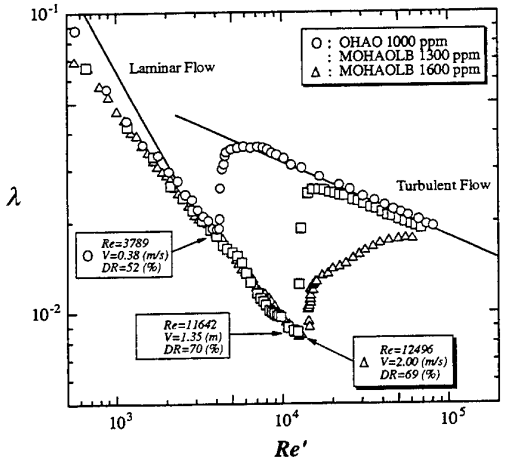


Fig. 5. Relationship between λ and Re' of MOHAOLB water solution (t = 5 °C, d = 16 mm)

The results in Fig. 4 reveal that the pipe friction coefficients λ of both OHAO water solution and MOHAOLB water solution show a good agreement with the theoretical prediction in Eq. (3) in a laminar flow in the range of Re' < 1800. On the other hand, the data of λ of OHAO water solution in the range of Re' > 3789 are in good agreement with the Blasius resistance formula (Eq. (4)) in a turbulent flow. While, the data of λ of MOHAOLB water solution coincide with the theoretical prediction (Eq. (3)) in a laminar flow.

On the other hand, the data of λ of MOHAOLB water solution in the range of Re' > 12496 are in good agreement with the Blasius resistance formula (Eq. (4)) in a turbulent flow. This behavior of MOHAOLB water solution could be explained by the fact that the pipe flow was laminarized by the suppression of an occurrence and a development of turbulent vortexes by means of deformation of a rod-like micelle structure of MOHAOLB in a water solution. A decreasing rate of λ_c to Re' becomes smaller with an increase in Re'. Moreover, the value of λ_c approaches to the minimum one as the Re' increases.

Consequently, the data of λ_c increase suddenly with increasing of Re' over the minimum one. Finally, the data of λ_c approach to the Blasius resistance formula (Eq. (4)) in a turbulent flow. This behavior of λ_c could explained by the fact that disappearance of Toms effect was caused by destroying a rod-like micelle structure of MOHAOLB in a water solution by a strong mechanical shear force in the large Re' numbers.

The friction drag for MOHAOLB in which the amine oxide was mixed with amphoteric surfactant, was reduced further than the only amine oxide. From Fig. 4, in case of 15 °C, OHAO 1000ppm showed the drag reduction by the maximum of 55%. However, it was improved up to 71% by adding the amphoteric surfactant of 600ppm. It is seen from the data in Fig. 5 that the drag reduction for OHAO at 1000ppm increased by maximum of 52%. However, it was improved up to 70% by adding the amphoteric surfactant of 600ppm.

MBMAOLB water solution. The relationships between λ and Re' of BMAO water solution and MBMAOLB water solution in the test section (inside diameter d = 16 mm) are shown in Fig. 6 for BMAO 2000ppm and MBMAOLB 3200ppm at the inlet test fluid temperature of 80 °C. Two solid lines in Fig. 6 refer to the theoretical prediction in Eq. (3) and the Blasuis resistance formula in Eq. (4) for a turbulent flow, respectively.

In this figure, it is found that the friction pipe coefficients λ of both BMAO water solution and MBMAOLB water solution show good agreement with the theoretical prediction in Eq. (3) in a laminar flow in the range of Re'<800. The data of λ of BMAO water solution agree with the Blasius resistance formula of Eq. (4) in the range of Re' > 1800. While, the data of λ of MBMAOLB water solution are in good accordance with the theoretical

prediction of Eq. (3) in a laminar flow.

On the other hand, the data of λ of MBMAOLB water solution in the range of Re' > 212100 are in good agreement with the Blasius resistance formula of Eq. (4) in a turbulent flow. The value of λ approaches to the minimum one as the Re' increase. Consequently, the data of λ increase suddenly with increasing of Re' over the minimum one. Finally, the data of λ approach to the Blasius resistance formula of Eq. (4) in a turbulent flow. This behavior of MBMAOLB water solution is explained by the same reason of MOHAOLB water solution above-mentioned.

The friction drag for the only amine oxide could be reduced by mixing the amphoteric surfactant. From Fig. 6, it is seen that the flow drag reduction for BMAO 2000ppm reached the maximum of 10%. However, it was improved up to 83% by adding the amphoteric surfactant of 1200ppm.

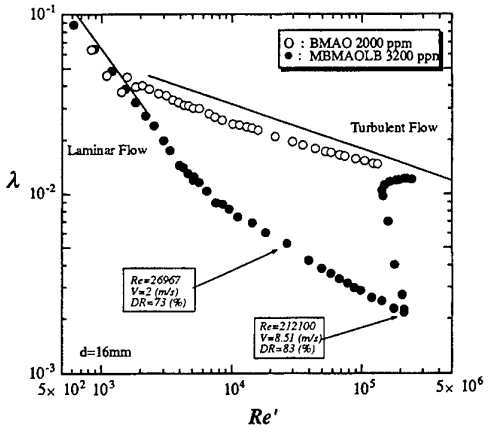
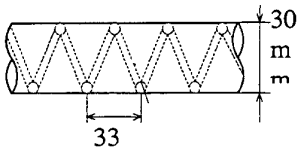


Fig. 6. Relationship between λ and Re' of the MBMAOLB water solution (t = 80 °C, d =16 mm)

Heat Transfer Characteristics in a Pipe Flow

SMAO water solution. Referring to heat transfer coefficient measurement of SMAO water solution, the relationship between $Nu/Pr'^{1/3}$ and Re' in a tube diameter of d = 30 mm is shown in Fig. 8.



Diameter (e)=3.3mm
Pitch (P)=33mm, P/e=10

Fig. 7. Spring coil for heat- transfer enhancement

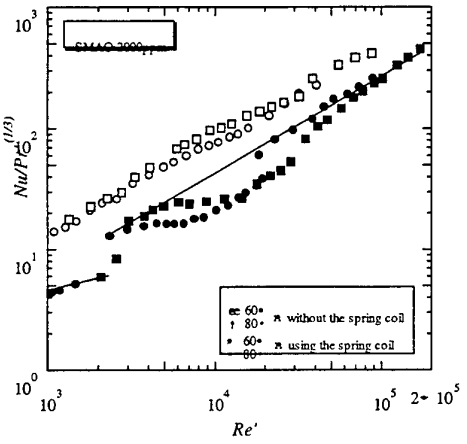


Fig. 8. Relationship between $Nu/Pr'^{1/3}$ and Re' of SMAO water solution (d = 30 mm)

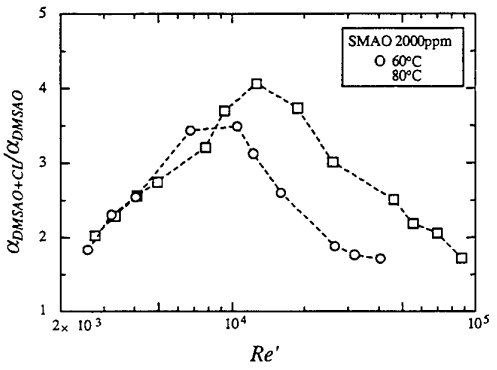


Fig. 9. Rate of increase of heat transfer coefficient in inserting the spring coil

From the data in Figs. 8 and 9, the heat transfer coefficient for the case in which the spring coil (Fig. 7) was inserted in the tube as a turbulence promoter increase by four times as compared with one without the spring coil. From Fig. 10 and Fig. 11, it is elucidated that the friction drag for the insertion of spring coil increase markedly.

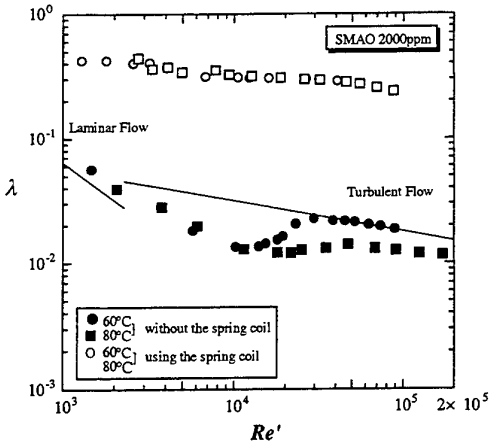


Fig. 10. Relationship between λ and Re of SMAO water solution (d = 30 mm)

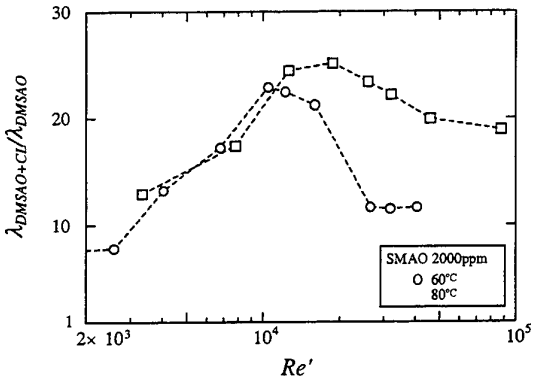


Fig. 11. Rate of increase of frictional drag coefficient in inserting the spring coil

5. CONCLUSIONS

From measuring results of the drag reduction and heat transfer characteristics of water solution with four kinds of surfactants OHAO, MOHAOLB, BMAO and MBMAOLB the following conclusions are obtained.

(1) Flow drag reductions of MOHAOLB and MBMAOLB water solutions were measured for pipe inside diameter *d* ranging from 16 mm. The coefficient of pipe frictions λ for both water solutions showed a good agreement with the theoretical prediction in a laminar pipe flow, while they were reduced as compared with those of water in a turbulent flow.

(2) In the case of cold water (5~15°C), the use of OHAO was effective. In the case of hot water (60~80°C), the use of surfactant of BMAO was effective. When those amine oxides were mixed with the amphoteric surfactant, the friction drag for mixture of amine oxide and amphoteric surfactant was reduced to a great extent as compared with that for the only amine oxide.

(3) The heat transfer coefficient for the SMAO surfactant by using the spring coil in the tube increased by four times as compared with that without the spring coil.

NOMENCLATURE

d : inside diameter of pipe, K : pseudoplastic viscosity, n : index number or number of heating section, Nu : Nusselt number, Pr' : modified Prandtl number, Q : heat, Re' : modified Reynolds number, S : heating surface, T : temperature, V : average flow velocity in pipe, α : heat transfer coefficient, ρ : density, λ : coefficient of pipe friction.

ACKNOWLEDGEMENT

This project is involved in the New Sunshine Project promoted by MITI. The NEDO is the implementing organization of this project.

REFERENCES

1. T. Shihou and H. Hirata, Proc. 37th Rheology Symposium, p. 109, (1989).
2. P.S. Virk, E.W. Merrill, H.S. Mickley and K.A. Smith, The Toms Phenomenon: turbulent pipe flow of dilute polymer solutions, J. Fluid Mech., Vol. 30, Part 2, p. 305, (1967).
3. H. Inaba, K. Ozaki and H. Asano, Flow Resistance Reduction and Heat Transfer in a Tube by Surfactants, 1st National Heat Transfer Symposium of Japan, E343, p. 1063 (1994).

AN EXPERIMENTAL STUDY ON THE COMPOUND ENHANCEMENT OF TUBESIDE HEAT TRANSFER WITH AIR FLOW

Zhou Qiang-Tai, Wang Ze-Ning, Zhang Hua and Xiong Fei
Department of Power Engineering, Southeast University, Nanjing 210018, China
Tel.(86)-25-3792573 Fax:(86)-25-7712719

Cheng Lin
Shangdong University of Technology, Jinan 250061, China
Tel.(86)-25-2944917

Keywords: tubeside heat transfer, compound enhancement, spirally corrugated tube, twisted type insert

ABSTRACT. The techniques of enhancing tubeside heat transfer have been studied extensively. However, the reports of research concerned with the combination of two different techniques, termed compound enhancement are very limited in the literature. In this paper, the experimental results of compound enhancement of tubeside heat transfer with combination of spirally corrugated tubes and twisted-tape inserts are presented. The test facility for the experiments and the experimental method are described. The experiments are conducted for the spirally corrugated tubes and the twisted-tape inserts respectively, and for the combination of spirally corrugated tubes with the twisted-tape inserts. Experiments are performed with air in the fully developmental turbulent region ($Re=10^4$-10^5). Large volumes of experimental data are presented in the paper. Empirical correlations are developed in the form of convenient use for heat exchanger application. Performance evaluation are given for spirally corrugated tubes and twisted-tape inserts, and for the combination of spirally corrugated tubes with twisted-tape inserts.

1. INTRODUCTION

In the process and energy source industries the configuration usually thought of when heat exchanger is considered is the venerable shell-and-tube type with one working fluid flowing inside the tube and another flowing outside usually with cross-flow. Tubeside heat transfer has a lower coefficient compared with the cross-flow, and, therefore, tubeside heat transfer enhancement is usually required for improvement of the performance of heat exchanger.

A great deal of experimental studies have been devoted to the enhancement of tubeside heat transfer. And many types of tubeside heat transfer enhancement technique have been developed. Two types of tubeside heat transfer enhancement device, i.e. spirally corrugated tubes and twisted tape inserts, being utilized extensively in the process and energy source industries have been reported in the literature. Spirally corrugated tubes have been shown to have several advantages over other rough surfaces such as: (1) easy fabrication, (2) limited fouling, and (3) higher enhancement in heat transfer rate compared with the same increase in friction factor. Twisted tapes are one of the simplest among the various enhancement devices and can be fabricated in any moderately equipped workshop.

Tubeside heat transfer coefficient can reach at most 2.0-2.3 times the bare tube value by using any single devices of tubeside enhancement. In many cases higher tubeside heat transfer coefficient is required for the balance of the thermal resistances on both tube and shell sides, or for the compactness of heat exchangers, or for there safe operation. As mentioned by Bergles[1] and Balaras[2], two or more of the enhancement techniques may be utilized simultaneously to produce an enhancement larger than that produced by only one technique. The simultaneous use is termed compound enhancement.

The reports of the studies on the compound enhancement of tubeside heat transfer are very limited in the literature. Therefore, the compound enhancement of tubeside heat transfer by simultaneous use of spirally corrugated tubes and twisted tape inserts in turbulent air flow is investigated in the present study to examine if there exists a product or overlapping effect of each technique.

2. EXPERIMENTAL APPARATUS

The schematic drawing of the experimental circuit assembly is shown in Fig.1. The apparatus is an air-to-water heat exchanger of double tube type, as mentioned in [3]. Heated air by an electrical heating device 5 flows through the test section, i.e. the tube side of the heat exchanger 8, from an air compressor 1, which is followed by an air tank 2 to obtain stable flow conditions. The flow rate is controlled by valve 3 and measured by two turbine meters 4 in parallel. The test section follows an stabilized section 7 and a mixing chamber 6 and is followed by another mixing chamber. Heated air is cooled in the test section by cooling water which is supplied to the annulus side of the heat exchanger by a centrifugal pump 11. The water flow rate is measured with a turbine flow meter which follows the pump. Passing through the heat exchanger water is directed to the cooling tower 9 and water tank 10 and then circulated in the loop.

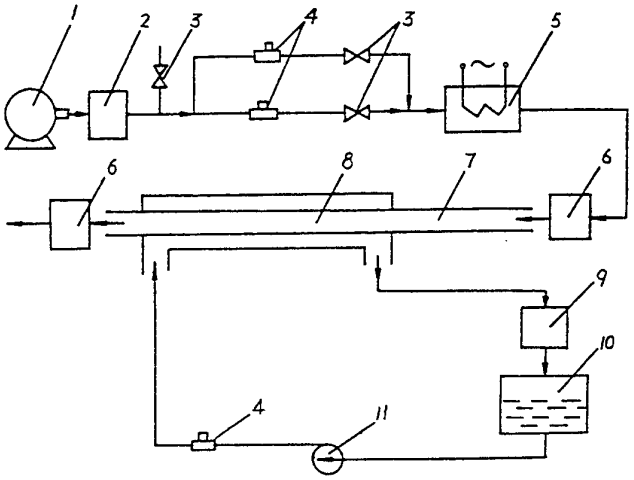


Fig.1. Experimental apparatus

Air temperature is measured with calibrated Chromel-Constantan thermocouples of 0.5^{mm} diameter installed at the inlet and the exit of the test section and with precision mercury thermometer having 0.1°C minimum graduation installed at the mixing chambers. Water temperature is measured by mercury thermometers with 0.1°C minimum graduation located at the inlet and outlet of the annulus side of the heat exchanger. Pressure taps are located at either ends of the test section and at the air flow rate meter nearby, and connected to the U-tube or inclined manometer for measurement of the pressure drop and static pressure.

The estimated uncertainties in the present study are 8.4 percent for the measurement of friction factor and 8.7 percent for the measurement of heat transfer coefficient, respectively.

The spirally corrugated tubes for the investigation all have single-start corrugation. Six tubes have about 1810^{mm} length with 37^{mm} ID, whose dimensions are listed in Table 1. The dimensionless corrugation height h/Di, varies from 0.0317 to 0.0539, and the corrugation pitch to height ratio, p/h, ranges from 9.41 to 16.89. That is in the usual use region. A smooth tube is experimented also in the tests for comparision.

Three twisted tapes with 1850^{mm} length, 1.0^{mm} thickness and twisted ratio Y of 2.46, 3.54 and 5.16, respectively, are investigated in this study.

In order to establish the flow pattern, a steady-flow entrance section of 1200^{mm} length having the same internal configuration as test section is provided upstream of the test section (See Fig.1).

Table 1. Tube Dimensions for Present Tests

Tube No.	D_o mm	D_i mm	h mm	p mm	H/D_i	p/h
1	39.92	36.95	1.22	20.6	0.0330	16.89
2	39.97	37.01	1.60	20.9	0.0432	13.06
3	40.05	37.13	2.00	21.1	0.0539	10.55
4	40.12	36.97	1.53	16.0	0.0414	10.45
5	40.22	37.09	1.71	16.1	0.0461	9.41
6	39.87	36.92	1.17	16.0	0.0317	13.68
S	39.95	37.12	0	0	0	0

3. EXPERIMENTAL PROCEDURE AND DATA REDUCTION

Experimental procedures were described in [3] in detail. Smooth tube tests for heat transfer and pressure drop were conducted initially. The results were compared with the existing equations, which were used to examine the experimental apparatus. And then, the experiments for spirally corrugated tubes, or/and twisted tape inserted were performed.

Heat transfer studies were carried out with the heated air flowing inside the tubes being the heating medium of the heat exchanger in the range of Reynolds number from 10^4 to 10^5. The inlet temperature of the air into the test section was maintained at the value of about 150°C. Data acquisition was conducted under steady-state condition. Heat transfer rates Q were determined by the enthalpy drops of the air in the test section which generally agreed with the values calculated from the enthalpy rises of the cooling water.

The overall heat transfer coefficient K_i, based on the internal heat transfer area A_i ,was calculated by equation

$$K_i = Q/(A_i \Delta T) \tag{1}$$

On the other hand K_i could be expressed as

$$1/K_i = 1/\alpha_i + (R_w + R_f + 1/\alpha_o)(A_i / A_o) \tag{2}$$

Under the assumption of constant physical properties and maintaining the constant mass flow rate of water in annulus side of the heat exchanger, the annulus-side heat transfer coefficient α_o could be considered to be constant. Therefore, the tubeside heat transfer coefficient α_i was obtained from seperating α_i and α_o from K_i using iterative method with constant value of (R_w+R_f).

The isothermal pressure drop experiments were conducted at ambient temperature. The tubeside pressure drop data of the test section were presented in terms of friction factor, f, versus tubeside Reynolds number Re, defined as

$$f = (\Delta p / 4)(L / D_i)(\rho u^2 / 2) \tag{3}$$

4. RESULTS AND DISCUSSIONS

Experimental results of friction factor and heat transfer for the twisted tapes inserted in smooth tube are shown in Fig.2. For smooth tube Blasius formula for friction factor

$$f_S = 0.079\,Re^{-0.25} \tag{4}$$

and Kays and Crawford formula[4] for heat transfer coefficient

$$Nu_S = 0.022\,Re^{0.8}\,Pr^{0.5} \tag{5}$$

fit our data quite reasonably as seen in Fig.2. The experimental results show that the twisted tape insert with twisted ratio of Y=2.5 has a value of heat transfer coefficient 1.9-2.0 times that of smooth tube (Nu/Nu_S=1.9-2.0) and a value of friction factor 4.4-5.5 times that for smooth tube (f/f_S=4.4-5.5).

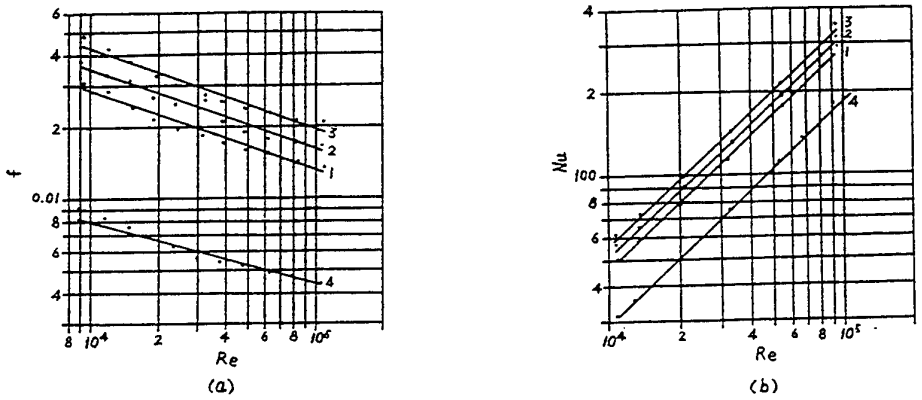


Fig.2. Data and correlations of friction factor (a) and Nusselt number (b) for twisted tapes inserted in smooth tube. 1-Y=5.16; 2-Y=3.54; 3-Y=2.46; 4-smooth tube

The result of friction factor and heat transfer for the twisted tapes inserted in smooth tube had been correlated with convenient Equs.

$$f = 1.61 Re^{-0.34} (H/D_i)^{-0.55} \quad (6)$$

$$Nu = 0.06 Re^{0.79} Pr^{0.4} (H/D_i)^{-0.26} \quad (7)$$

with deviation not exceeding $\pm$ 10 and $\pm$ 7 percent, respectively[5].

The experimental results of spirally corrugated tubes are shown in Fig.3 for friction factor and heat transfer. Spirally corrugated tubes have higher value of heat transfer coefficient and of friction factor than that of smooth tube, depending on the values of h/D_i , p/h and Reynolds number. In the test ranged of h/D_i , p/h and Re in the

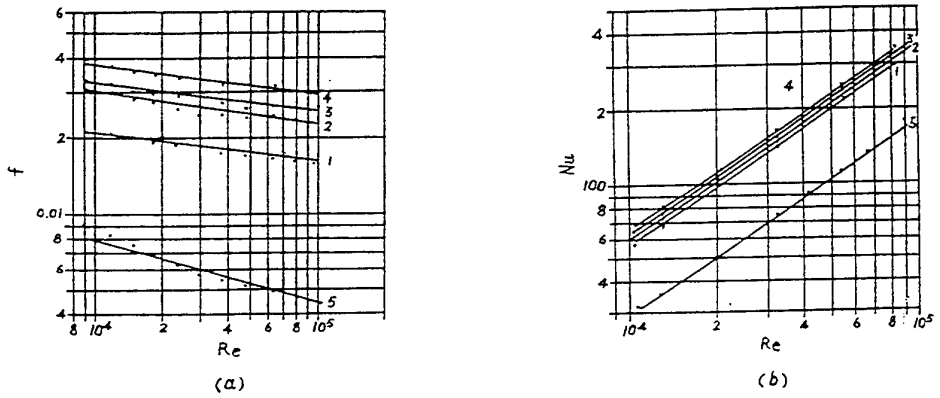


Fig. 3. Data and correlations of friction factor (a) and Nusselt number (b) for spirally corrugated tube. Curves represent Tube No. In Table 1: 1-No.6; 2-No.2; 3-No.4; 4-No.5; 5-No.S

present study, Nu/Nu_S and f/f_S vary from 1.8 to 2.3 and from 2.8 to 7.1, respectively. Experimental data for spirally corrugated tubes had been correlated with Equs. (8) and (9) for friction factor and heat transfer[5] with deviation not exceeding $\pm$ 10 and $\pm$ 6 percent, respectively.

$$f = 5.28 Re^{-0.11} (h/D_i)^{0.92} (p/h)^{-0.53} \tag{8}$$

$$Nu = 0.15 Re^{0.78} (h/D_i)^{0.17} (p/h)^{-0.20} \tag{9}$$

Performance evaluation had been conducted using the method similar to Webb[6] and mentioned by Zhou[7] to calculate the increase ratio in heat transfer rate, Q/Q_S , for equal pumping power and heat transfer area (P/P_S=1 and A/A_S=1), and the reduction ratio of heat transfer area, A/A_S , for equal heat transfer rate and pumping power (Q/Q_S =1 and P/P_S =1), and the decrease ratio in pumping power , P/P_S , for equal heat transfer rate and heat transfer area (Q/Q_S =1 and A/A_S=1) compared with smooth tube[3]. But one criterion of the Q/Q_S for A/A_S=1 and P/P_S =1 will be given in the present paper.

It was found out that for the twisted tapes inserted in smooth tube the performance evaluation criterion Q/Q_S showed little difference for the twisted ratios Y=2.5 and Y=3.5, and had a value varying from 1.25 to 1.15 in the range of Reynolds number from 10^4 to 10^5. And the twisted tape insert with Y=5.2 had a value of Q/Q_S around 1.15-1.1. Spirally corrugated tubes had a higher value of criterion Q/Q_S . For the range of h/D_i=0.03-0.04 and p/h=10.5-17, spirally corrugated tubes gave a value of Q/Q_S varying between 1.45and 1.3 in the range of Re from 10^4 to 10^5.

The experiments had been performed for compound enhancement of spirally corrugated tubes with twisted tape inserts[3]. Some of the experimental results for friction factor f, Nusselt number Nu and criterion Q/Q_S are shown in Fig.4. It was found out that the compound enhancement gave higher performance in lower Reynolds number region, Re=10^4-3×10^4, than that in higher Reynolds number range, e.g. Re=8×10^4-10^5. In lower Re region compound enhancement offered a value to tubeside heat transfer coefficient 3.2-3.7 times that of smooth tube, i.e. Nu/Nu_S=3.2-3.7, and a value about 1.6-1.8 to the performance criterion of Q/Q_S , 20-30 percent higher than that of the spirally corrugated tube. But the ratio of Nu/Nu_S reduced to 2.9-3.2 for Reynolds number from 8×10^4 to 10^5 and Q/Q_S fell to the level similar to the spirally corrugated tube value.

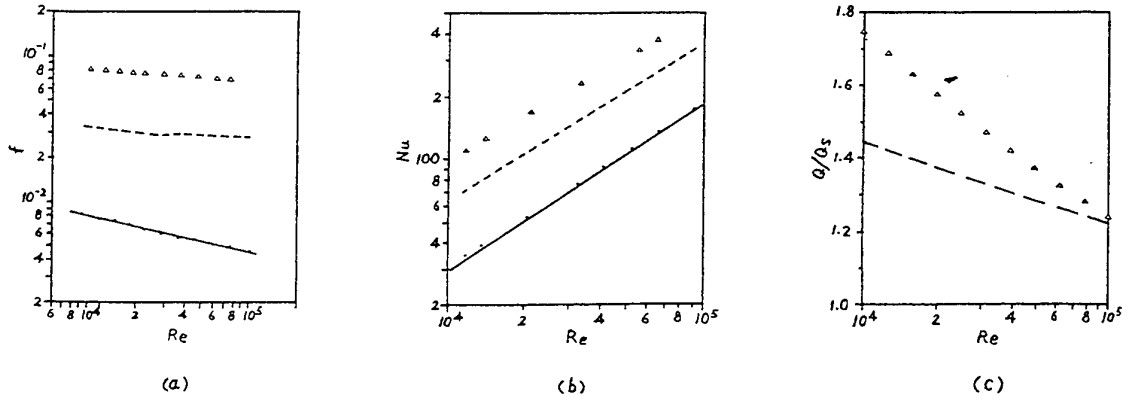


Fig. 4. Friction factor f , Nusselt number Nu and criterion Q/Q_S vs Re
– – Smooth tube; ------ Spirally corrugated tube No.2; ΔΔΔΔ Twisted tape (Y=3.54) inserted in the spirally corrugated tube No.2

The influence of geometric parameters of spirally corrugated tube in the test range on the performance criterion Q/Q_S for the compound enhancement seemed not significant, especially for the lower Reynolds number, e.g. Re=10^4-3×10^4. But the twisted direction of the twisted tape, along or counter to the ridge direction of the spirally

corrugated tube, gave more significant effect on the values of f/f_S , Nu/Nu_S and Q/Q_S in the whole region of Reynolds number from $Re=10^4$ to $Re=10^5$, as seen in Fig. 5.

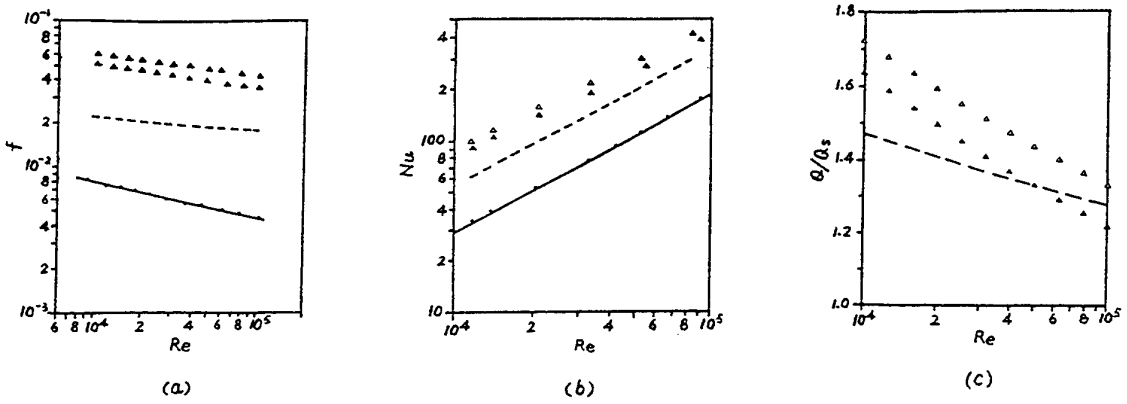


Fig. 5. Friction factor f , Nusselt number Nu and criterion Q/Q_S vs Re
– – Smooth tube; ------ Spirally corrugated tube No.6; ΔΔΔΔ and ▲▲▲▲ Twisted tape (Y=3.54) inserted in the spirally corrugated tube No.6 with counter to and along the ridge direction, respectively

The results of friction factor and heat transfer for compound enhancement of spirally corrugated tubes combined with twisted tapes had been correlated with the expressions in the form of

$$f = 1.47\,Re^{-0.051} f_{t.t} f_{s.c.t} / f_s \tag{10}$$

and

$$Nu = [0.986 + 0.276(Re/10^5) - 0.345(Re/10^5)^2]Y^{-0.037} Nu_{t.t} Nu_{s.c.t} / Nu_s \tag{11}$$

with deviation not exceeding ±11 and ±7.0 percent, respectively[3].

5. CONCLUSIONS

Experiments of the friction factor and heat transfer characteristics for twisted tapes, spirally corrugated tubes and simultaneous use of both twisted tapes and spirally corrugated tubes have been conducted in turbulent air flow. The conclusion remarks are summarized as follows:

(1) The twisted tape inserted in smooth tube with twisted ratio Y=2.5 shows higher value of heat transfer than that for twisted ratio Y greater than 2.5, and has a value of heat transfer coefficient 1.9-2.0 times that of smooth tube. But the performance criterion value of Q/Q_S shows little difference in the twisted ratio range from 2.5 to 3.5, and varies from 1.25 to 1.15 in the Reynolds number region $Re=10^4$-10^5.

(2) The heat transfer coefficient ratio of spirally corrugated tubes to smooth tube, Nu/Nu_S , is in the range of 1.8-2.3 for the geometric parameters of spirally corrugated tubes, h/D_i and p/h, being within the test limits in the present study. And the spirally corrugated tubes with geometric parameters in the range of h/D_i=0.03-0.04 and p/h=10.5-17 give the performance criterion Q/Q_S around 1.3 to 1.45, depending on the values of Reynolds number.

(3) Compound enhancement shows more effective than any single enhancement techniques, especially in the lower Reynolds number region ($Re=10^4$-3×10^4). In this region tubeside heat transfer reaches the value of 3.2-3.7 times that of smooth tube and performance criterion Q/Q_S attains the value of 1.6-1.8 for spirally corrugated tubes combined with the twisted tape having counter twisted ratio Y=3.5. But in high Reynolds

number, equal to or greater than 10^5, although the tubeside heat transfer for compound enhancement still has a higher value than any single enhancement devices, the performance criterion Q/Q_S has fallen to the level around spirally corrugated tube value.

(4) Equs. (6)-(11) fit with the experimental data in the present study reasonably well.

NOMENCLATURE

A	heat transfer area
D	tube diameter
f	friction factor
h	corrugation height
H	twisted pitch defined for 180 degree rotation of twisted tape
K	overall heat transfer coefficient
L	axial length
p	corrugation pitch
P	pumping power
Q	heat transfer rate
R	thermal resistance
u	axial mean velocity
Y	twisted ratio for twisted tape $Y=H/D_i$
Nu	Nusselt number
Pr	Prandlt number
Re	Reynolds number
$\triangle p$	pressure drop
$\triangle T$	log-mean temperature
α	heat transfer coefficient
ρ	fluid density

Subscripts

f	pertains to fouling
i	based on tube inside
o	based on tube outside
s	pertains to smooth tube
w	pertains to tube wall
t.t	pertains to twisted tape
s.c.t	pertains to spirally corrugated tube

REFERENCES

1. A.E. Bergles, "The Current Status of Heat Transfer Enhancement", *Heat Transfer Enhancement and Energy Conservation*, Editor in Chief: S.J.Deng, Hemisphere Publishing Corporation, New York, pp.11-48(1990).
2. C.A. Balaras, "A Review of Augmentation Techniques for Heat Transfer Surface in Single-Phase Heat Exchangers", Energy, Vol. 15, pp. 899-906(1990).
3. Z.N. Wang, "A Study of Compound Enhancement of Single-Phase Tubeside Heat Transfer", *Ph. D. Dissertation*, Southeast University, China (in Chinese) (1995).
4. W.M. Kays and M.E. Crawford, *Convective Heat and Mass Transfer (2nd Ed.)*, McGraw Hill Book Company, New York (1980).
5. H. Zhang, "A Study of Tubeside Heat Transfer Enhancement", *M.Sc. D. Dissertation*, Southeast University, China (in Chinese) (1995).
6. R.L. Webb and E.R.G. Eckert, "Application of Rough Surfaces to Heat Exchanger Design", Int. J. Heat Mass Transfer, Vol. 15, pp. 1647-1658(1972).
7. Q.T. Zhou and S.Y. Huang, *Heat Transfer Enhancement for Boilers and Heat Exchangers*, China Water Resources and Electric Power Press, Beijing (in Chinese) (1991).

EXPERIMENTAL INVESTIGATIONS OF ENHANCED EVAPORATION SURFACES FOR COOLING SYSTEMS IN MOTOR VEHICLES

Bettina Schmidt, Rainer Mertz, Manfred Groll
Institute for Nuclear Technology and Energy Systems (IKE)
University of Stuttgart, Germany
Email: b.schmidt@ike.universität-stuttgart.de; Fax: +49-711-689-2010

Keywords: evaporation cooling, heat exchanger surface, heat transfer coefficient, capillary structure

ABSTRACT. Experimental investigations are carried out to obtain more information about the heat and especially the mass transfer phenomena concerning evaporation of water from a prototype evaporation surface for low consumption and electric motor vehicles. One prototype evaporator with various structured surface coverings of different materials is tested. The basic test section consists of an industrial prototype evaporator with fine longitudinal re-entrant grooves. The test conditions of the air temperature and the air humidity vary between 20 °C and 40 °C and 20 % and 40 % respectively. The heat fluxes range from 430 W/m^2 to 1175 W/m^2. Water is used as working fluid. Results of the prototype evaporator and three different structures of different material properties, covering the surface of the prototype, are presented in this paper. First results show a good heat transfer from the evaporation surface to the air flow above the surface.

1. INTRODUCTION

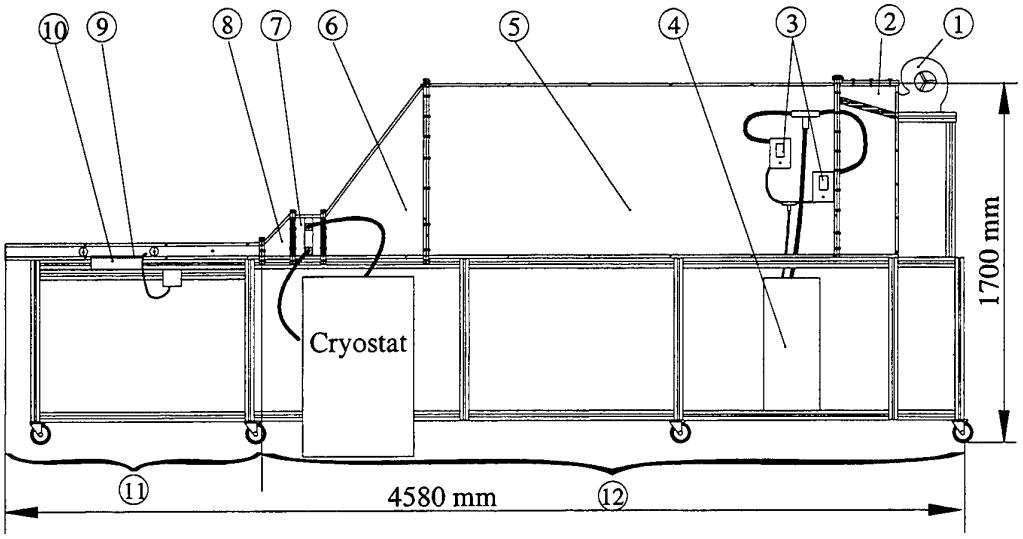
In Europe, the use of air-conditioning systems in motor vehicles became more and more important during the last years. Not only the automobiles of the luxury class are equipped with air-conditioning systems, but also middle class vehicles. The development and investigation of a new air-conditioning system is discussed in the paper which can be used especially for low consumption and electric cars, either as an independent system or as an additional system for conventionally air-conditioned cars, to reduce energy consumption and costs. The air-conditioning and cooling systems used today in cars are in general based on the cold steam compression process. This technique is limited by the convective heat transfer coefficient on the airflow side and the pressure drop inside the heat exchanger [1, 2]. The interest in light-weight, but not less powerful air-conditioning systems results from the effort to save raw materials, energy and costs during manufacturing and operation. Another aspect is the increasing pollution of the environment, which should be minimised. A light-weight air-conditioning system, based on the evaporation of water, can contribute to achieve such goals.

The evaporation effect of water is known for quite a long time, but there is still information needed to determine the heat and especially the mass transfer from an evaporator surface to an air stream. In the last 20 years investigations were mostly carried out for the air-conditioning technology for buildings. These stationary facilities are very large and their technology cannot be easily scaled down to small movable systems, like motor cars, where size and water consumption have to be reduced to a minimum. Moreover, the discussed prototype evaporation surface has also the function of a heat exchanger, i.e. not the air stream shall be cooled but the prototype evaporation surface itself. The evaporation of water from a suitable surface, i.e. the superimposition of heat and mass transfer allows a high cooling effect. For the technical realisation, suitable surfaces and distribution systems have to be developed and investigated. They shall possess good wettability, resistance to fouling and corrosion, and of course shall be economic to manufacture [7]. Available knowledge on heat exchangers with evaporation surfaces [3 - 6] does not allow to design evaporative heat exchanger systems for cars with satisfactory precision. To remedy this lack of information, fundamental system-related experimental studies are necessary, which take into account the complicated geometrical and operational boundary conditions of air-conditioning systems for cars.

To obtain experimental information about the heat and mass transfer phenomena from a prototype evaporation surface, a test rig was developed and built. A prototype evaporation surface and three cover-materials were tested at air temperatures between 20 °C and 40 °C and relative air humidities between 13 % and 46 %, at constant air velocity of 6 m/s. The employed heat fluxes range between 430 W/m² and 1175 W/m². The cover material layers consist of a fleece structure, containing cellulose, a synthetic fabric and a metal felt.

2. EXPERIMENTAL SET-UP

The experimental set-up consists of two sections, the air-conditioning-unit and the test-section-unit (Fig. 1). These two units consist of several components.



① Ventilator
② Drying Module
③ Steam Lances
④ Steam-Air-Moisturizer-Unit
⑤ Evaporation-Module
⑥ Geo I
⑦ Heat-Exchanger-Module
⑧ Geo II
⑨ Prototype
⑩ Cu-Block
⑪ Test-Section-Unit
⑫ Air-Conditioning-Unit

Fig. 1. Experimental Set-up

2.1 Air-Conditioning-Unit

The air-conditioning-unit includes a ventilator (0.65 kW, 5100 m;/h), a drying-, an evaporation- and a heat-exchanger-module and Geo I and Geo II. After the ventilator, the drying-module follows, which contains the drying pearls (in case that they are needed) to dehumidify the air. Then follows the evaporation-module, including two steam lances which are connected to the steam-moisturiser-unit. The steam produced in the moisturiser-unit is led through two tubes to the steam lances and moistens the air in the channel. The two staggered steam lances are placed at the beginning of the cross-section of the evaporation-module. After the evaporation-module, the heat-exchanger-module is located. Here the air temperature is adjusted via a sheet metal radiator, which is connected to a cryostat. Between the evaporation- and the heat-exchanger-module, unit Geo I is placed, a module to change the cross-section. Another module of this kind, Geo II, is located after the heat-exchanger-module and in front of the test-section-unit. All modules as well as the test-section-unit are manufactured of high-impact-resistant, transparent plates of Makrolon and are detachably fixed onto a frame made of aluminium.

2.2 Test-Section-Unit

The test-section-unit consists mainly of the prototype evaporation surface. The sensors for measuring the air velocity, the air temperature and the relative air humidity are placed in front of and behind the prototype evaporator, the air pressure in the channel is measured in front of the prototype evaporator. A glass water tank is connected over a flow meter to the prototype evaporation surface. The water in this tank is temperature-controlled by a second cryostat. Beneath the prototype evaporator surface, a copper block, thermally insulated to the environment, is employed. The copper block is heated with eight heater cartridges (200 W per cartridge), and provided with 33 thermocouples (type K, NiCr-Ni) (Fig 2).

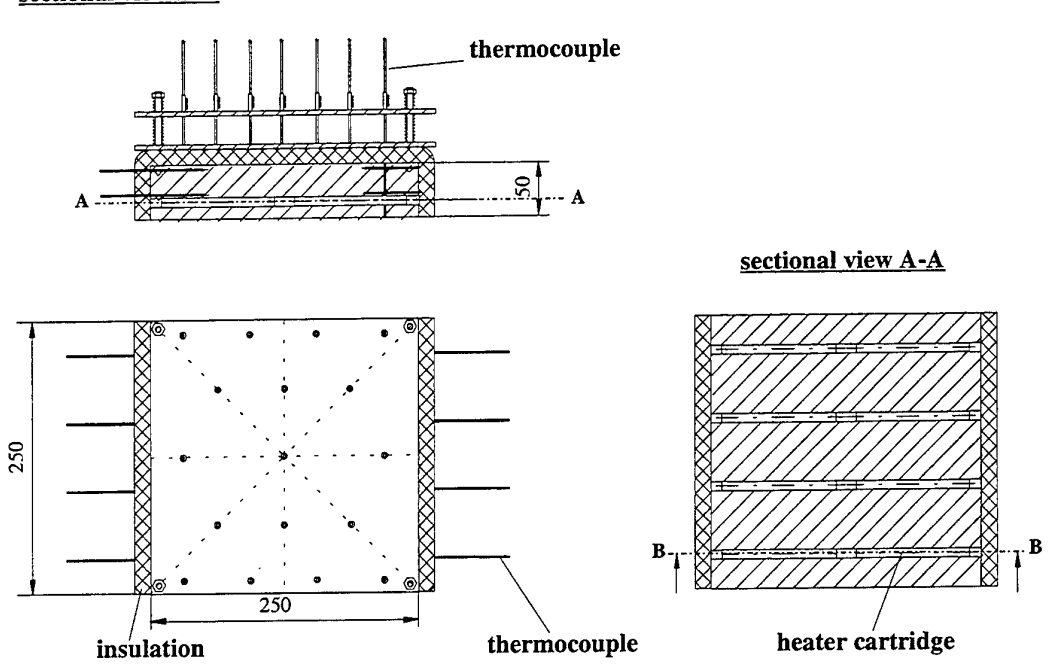


Fig. 2. Copper Block with Electric Heater Cartridges and Thermocouples

Above the heater cartridges, 16 thermocouples are installed, 8 of them in two planes, to determine the average heat flux. Another 17 thermocouples are placed close to the bottom side of the prototype evaporator for measuring the average temperature of the prototype surface. The signals of the calibrated thermocouples and sensors are conducted to a PC-based data acquisition system which is used for recording the measurement data. An A/D-converter changes the analog values to digital data, which are stored in files and can be used later for the evaluation of the experiments.

2.3 Prototype Evaporator Surface

The prototype evaporator surface consists of an aluminium ground-plate which is 350 mm long, 320 mm wide and 15 mm high and a capillary structure soldered onto the plate. In the manufacturing process, the capillary structure is first folded to a meander shaped aluminium foil and then compressed to form fine longitudinal re-entrant capillary grooves (Fig. 3). The about 250 capillary grooves cover an area of 250 mm x 250 mm and the grooves have a height of 2 mm and a width of 1 mm.

To supply the capillaries with water from the water tank, a circumferential channel is milled into the ground-plate (Fig. 4). The water enters the capillary grooves from two sides and is transported by capillary forces to the free evaporation surface (Figs. 3 and 5).

For various experiments, the prototype evaporation surface was covered with different materials, to enhance the evaporation rate. First a fleece structure, containing cellulose was used, then a synthetic fabric structure and thirdly a metal felt. The double-plied fleece structure has a nepped surface. The synthetic fabric is woven of a synthetic yarn with hydrophilic properties. The metal felt has a fibre thickness of 15µm.

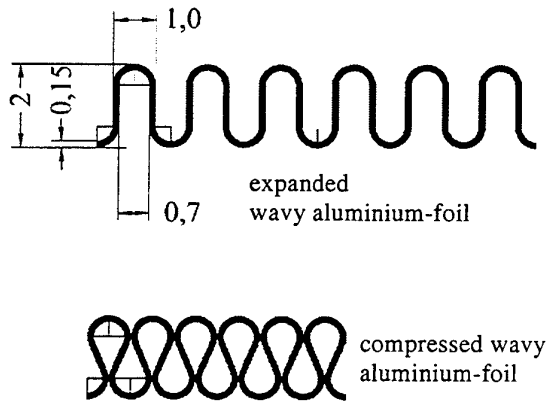


Fig. 3. Cross Section of the Capillary Structure

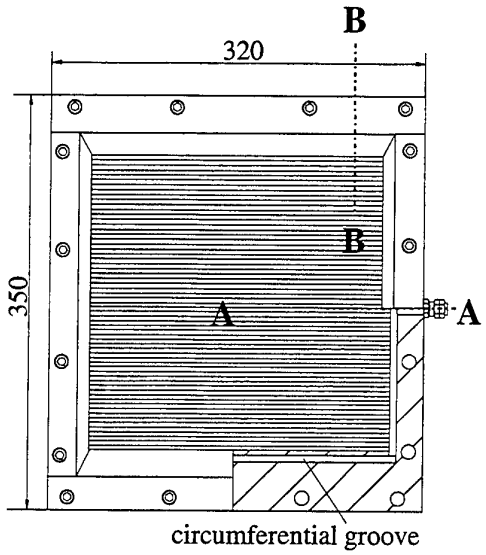


Fig. 4. Prototype Evaporation Surface with Circumferential Groove

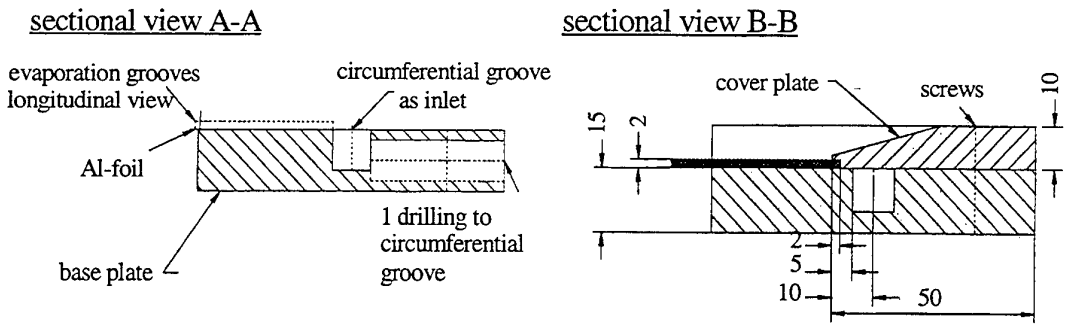


Fig. 5. Details of the Prototype Evaporation Surface

3. EXPERIMENTAL INVESTIGATIONS

3.1 Experimental Conditions

Before the experiments are carried out, steady test conditions have to be set. First the ventilator is adjusted to an air velocity of 6 m/s, that means a turbulent mass flow of about 100 l/s with a Reynolds number of Re .35,000 (Re = (w * d_h)/ <, with air velocity: w, hydraulic diameter: d_h, cinematic viscosity: <). The air of the laboratory environment is sucked in the ventilator and is blown through the test channel. In the modules of the test channel, the air is conditioned. With the drying unit or the steam-moisturiser-unit the needed air humidity is adjusted (in a range of 13 % to 46 % relative humidity). Then, with the sheet metal radiator and a cryostat (working fluid water) the air temperature is set to a value in the range between 22 °C and 40 °C. The air temperature profile over the cross section of the channel is sufficiently constant. The second cryostat (working fluid water) adjusts the water temperature of the water tank (between 22 °C and 40 °C) and the eight heater cartridges heat up the copper block

(0 to 200 W per cartridge). Approximately 1 h is needed till steady state conditions are reached, and a test-run lasts for about 2 h.

One of each two sensors for the air velocity, air humidity and air temperature (thermocouples) is placed before and behind the prototype evaporation surface. Only one pressure sensor measures the air pressure in the channel before the test section, because the pressure drop over the evaporation surface is very low and cannot be determined with customary pressure gauges. The pressure in the channel is slightly higher than the air pressure in the laboratory (< 10 Pa). 33 thermocouples are used to measure the temperature distribution in the copper block and the temperature of the evaporation surface. In the water tank, another thermocouple is situated. All thermocouples are of type K, (NiCr-Ni) and were calibrated in a water bath. There reference temperature was measured with a platinum resistance thermometer PT-100 with a precision of +/- 0.025 K and a resolution of +/- 0.01 K.

3.2 Experimental Results

The start temperature of the prototype evaporator surface is in the range between T_{sur} = 20 °C and 35 °C. Until steady state conditions are reached, about 1 h after the start, the surface temperature of the prototype evaporator decreases for constant air temperature T_{air}. This is the characteristic of an isothermal heat transfer; only the temperature of the working fluid water is reduced.

For the prototype evaporation surface and the three different cover materials, the heat transfer coefficient has been approximately determined and the results are shown in Tables 1, 2 and Fig. 6. For the fleece and the fabric structures, the experiments show a decrease of the heat transfer coefficient a with increasing air temperature T_{air}.

Table 1. Heat Transfer Coefficient α for the Prototype Evaporation Surface and Two Cover Materials

α [W/(m²K)]	φ [%]	20		25
	T_{air} [°C]	25	27	22
Aluminium-Plate with Capillary Grooves only		69	-	-
Grooves Coated with fabric		74	68	82
Grooves coated with Fleece		110	87	146

Table 2. Heat Transfer Coefficient α for the Metal Felt

Temperature T_{air} [°C]	22.8	25.0	28.4	40.0
Relative Humidity φ [%]	α [W/(m² K)]			
13	-	-	-	13
30	-	102	120	-
40	180	-	-	-
46	-	113	-	-

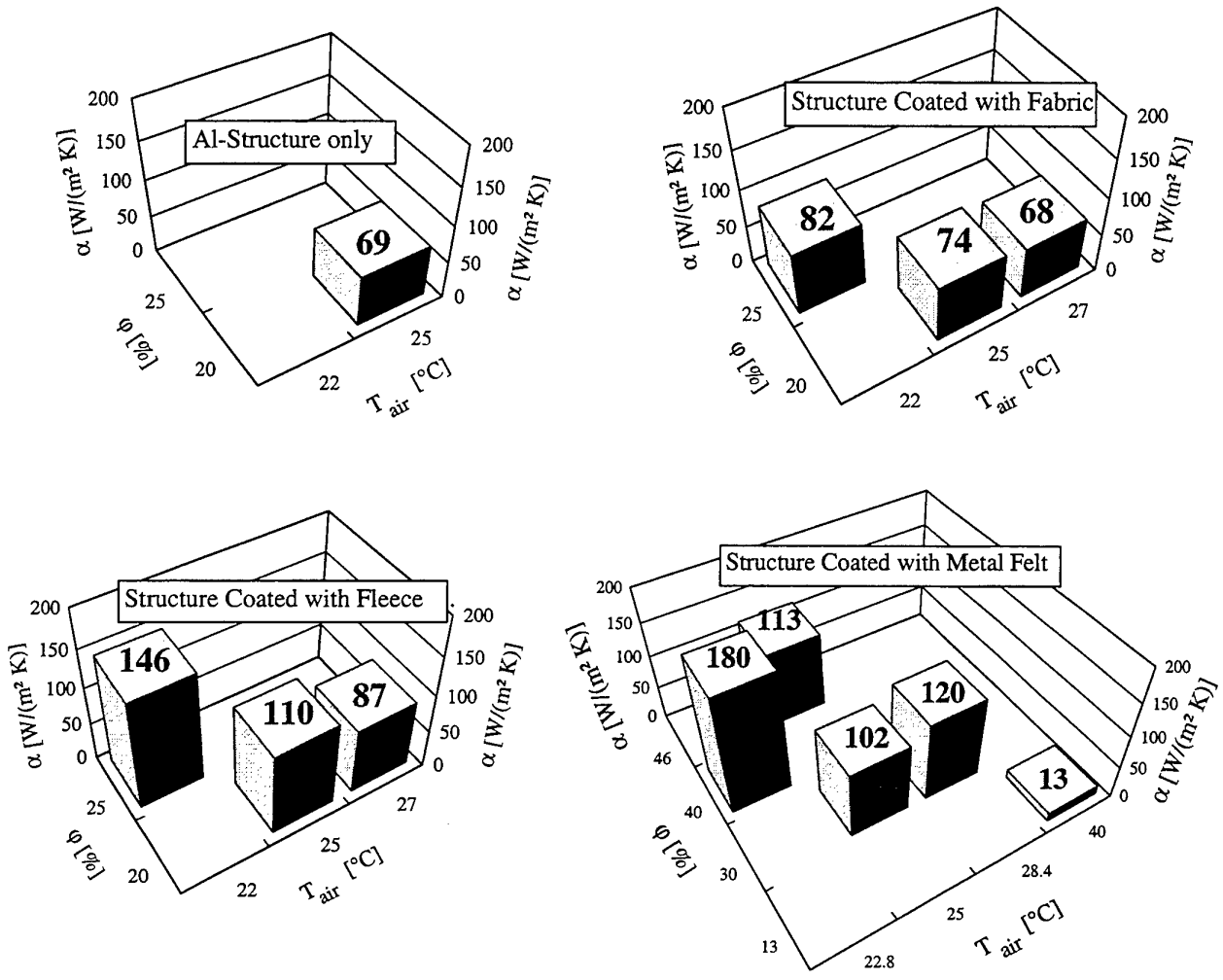


Fig. 6. Heat Transfer Coefficient a for All Tested Structures

For the metal felt, the heat transfer coefficients are increasing with increasing air temperature. This structure shows the highest heat transfer coefficient of 180 W/(m² K) for T_{air} = 22.8 °C and n = 40 % . The first experiments do not allow to exactly find out the influence of the relative air humidity on the heat transfer coefficient but they show, that the influence of the air temperature is dominant. The most important parameter is the surface structure. The suction properties, the wettability, the thermal conduction and evaporation properties should be as high as possible.

In Fig. 7. the obtained surface temperature reductions are shown for the prototype evaporator (wavy aluminium structure only), the synthetic fabric and the fleece coating the wavy evaporator surface. For the bare wavy aluminium structure, the temperature reduction was only 0.7 K, but for the wavy structure covered with fabric or fleece, a temperature reduction of 2.1 K and 3.1 K, respectively, is obtained under the same test conditions with air temperature of 25 °C and relative air humidity of 20 %. For the metal felt, the achieved temperature reduction was between 1.7 K and 4.2 K for air temperatures between 22.8 °C and 28.4 °C and relative air humidities between 31.5 % and 46 %. The respectively obtained highest heat fluxes are shown in Fig. 8.

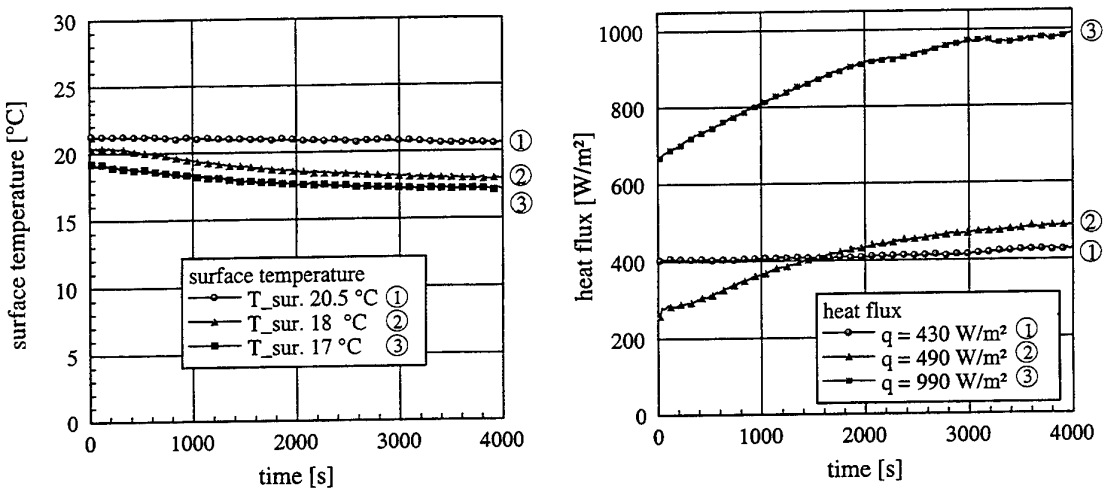


Fig. 7. Transient Behaviour of Average Surface Temperature and Corresponding Evaporation Cooling Heat Flux. Relative Humidity: 20 %, Channel Air Temperature: 25 °C.
①: Prototype Evaporator (Aluminium-Plate with Capillary Grooves only), ②: Fabric-Covered Grooves, ③: Fleece-Covered Grooves.

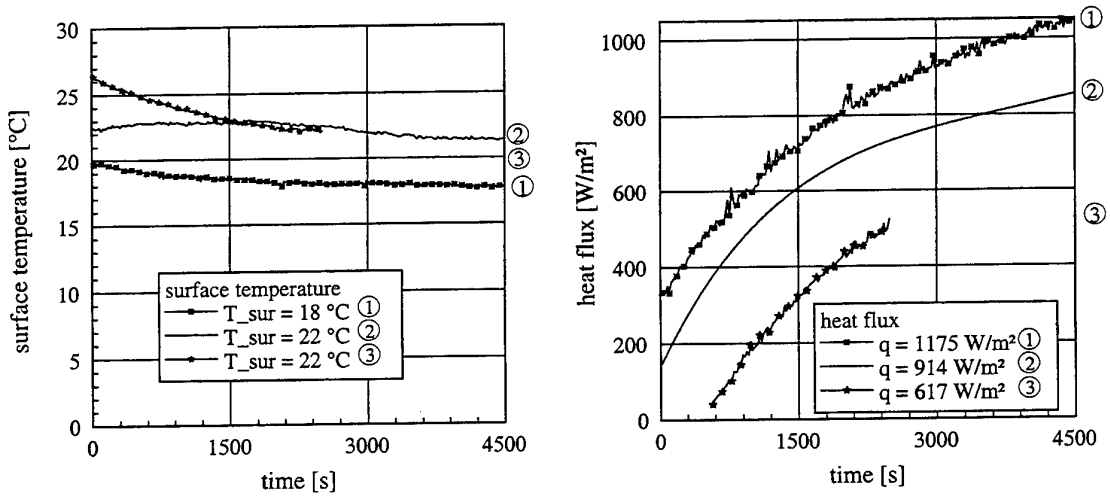


Fig. 8. Transient Behaviour of Average Surface Temperature and Corresponding Evaporation Cooling Heat Flux for Metal-Felt Covered Grooves.
Air Temperatures and Air Humidities of: ①: 25.5 °C and 46 %, ②: 28.4 °C and 31.5 % and ③: 22.8 °C and 39.3 % (Test was Aborted at 2500 s).

The active evaporation area of the capillaries of the prototype evaporator is smaller than that of the fabric-, the fleece- and the metal felt-structure. By increasing the active heat transfer surface by the cover materials, more water is evaporated. Heat fluxes of 430 W/m² for the wavy aluminium structure only, 490 W/m² with the fabric, 990 W/m² with the fleece structure and up to 1175 W/m² for the metal felt are reached. The fabric-, fleece and metal felt coated structure also provides a better water distribution on the evaporation surface. A comparison between the individual structures shows that the fleece and the metal cover have better suction properties than the fabric. Another advantage of the metal felt is its higher thermal conductivity, therefore the heat is more effectively transported to the active evaporation surface and so the prototype is cooled down more efficiently.

4. CONCLUSIONS

To investigate the heat and mass transfer from an evaporation surface, intended for an air-conditioning-system in a low consumption vehicle or as support for a conventional air-conditioning-system, four different surface structures are tested. The first test structure consists of re-entrant capillary grooves. The three further tested surfaces, a fleece structure, a synthetic fabric and a metal felt cover this capillary base structure. Various experiments are carried out under different test conditions: air and water (evaporation working fluid) temperatures in the range from 22 °C to 40 °C, relative air humidities between 13 % and 46 % and constant air velocity of 6 m/s. All heat transfer coefficients obtained with covered surface structures are higher than those of the capillary structure only. The obtained cooling effect can be expressed by heat fluxes between 430 W/m² and 1175 W/m² and heat transfer coefficients in the range from 68 W/(m²K) to 180 W/(m²K) with the metal felt cover material showing best results.

It was found that the prototype evaporator surface covered with either fabric, fleece or metal felt has an acceptable heat and mass transfer performance. But more experimental data are needed, e.g. the influence of the air velocity, and also other materials shall be tested, before a final judgement can be made.

ACKNOWLEDGEMENT

This research is supported by Stiftung Energieforschung Baden-Württemberg, D-76131 Karlsruhe.

REFERENCES

1. W. Leidenfrost and B. Korenic, "Experimentelle Überprüfung einer Berechnungsmethode für die Leistungsvoraussage verdunstungsgekühlter Kondensatoren", Brennstoff Wärme Kraft v.34(1), pp.9-14 (1982).
2. O. Fischer and A. Sommer, "Experimental investigation of spray-enhanced tube and plate-fin heat exchangers", *6th Lahr Cooling Tower Workshop, Pisa, Italy (1988)*.
3. W. Lakenbrink, "Gekoppelter Wärme- und Stoffübergang bei Verdunstungskühlung", Brennstoff Wärme Kraft v.37(12), pp.493-495 (1985).
4. R.L. Webb and A. Villacres "Performance simulation of evaporative heat exchangers", Heat Transfer Engineering v.6(2), pp.493-495 (1985).
5. H.-M. Hellmann "Berechnung des Betriebsverhaltens von Verdunstungskühlern und -kondensatoren", Wärme- und Stoffübertragung v.28, pp.299-311 (1993).
6. W. Leidenfrost and B. Korenic, "Evaporative cooling and heat transfer augmentation related to reduced condenser temperatures", Heat Transfer Engineering v.3, pp.38-59 (1982).
7. H. Gentner "Vergleichende Untersuchung von mechanisch, elektrisch und thermisch angetriebenen Kälteanlagen zur Fahrzeugklimatisierung", *VDI Forschungsberichte, Reihe 19: Wärmetechnik/ Kältetechnik,* Nr. 82 ISBN 3-18-308219-5 (1995).

FEASIBILITY STUDY OF NEW HEAT TRANSPORTATION SYSTEM WITH DRAG-REDUCING SURFACTANT ADDITIVES

Peiwen Li
Mechanical Engineering Laboratory, AIST, MITI, Japan, Energy Conservation Center
Email: energy18@mmail.mel.go.jp ; Fax: +81-298-58-7275

Yasuo Kawaguchi and Akira Yabe
Mechanical Engineering Laboratory, AIST, MITI, Japan
Email: m4050@mel.go.jp ; Fax: +81-298-58-7275
Email: yabe@mel.go.jp ; Fax: +81-298-58-7033

Keywords: thermal energy transportation, drag reducing, surfactant additives, feasibility

ABSTRACT. Utilizing drag-reducing fluid -water added with surfactant, the pumping power in thermal energy transportation can be reduced significantly. When surfactant is added to a installed system that uses water, the increased flow rate and deterioration of heat transfer can result in a drop in the temperature level and total heat to users. At the same time, the pump system must be modified due to the lowered pumping power. A simulation was conducted to predict the exergy and energy transportation efficiency. The minimum heat transfer reduction in order to maintain high exergy efficiency was discussed through the prediction.

1. INTRODUCTION

Since the discovery of Tom's effect [1,2], the reduction of turbulent friction between a solid surface and fluid by adding drag-reducing additives has received increasing attention for saving the pumping power in fluid transportation. Polymers were initially used as drag-reducing additives for turbulent water flow to reduce 80% of the drag. However, polymer solutions are strongly affected by mechanical forces, which may result in the loss of the property of low friction drag. Surfactants were found in the last decade also to reduce 70% to 80% of the friction drag but to be less affected by mechanical forces [3,4]. Therefore, surfactants are now being considered as practical drag-reducing additives.

One successful application of drag reduction by adding polymers was in the Trans-Alaska-Pipeline, where the desired discharge of one million barrels per day was obtained without having to construct additional pumping stations [5]. A more recent application of the drag-reducing effect is to reduce the pumping power in district heating and cooling systems where surfactants are used as additives in closed circuits [6 - 8]. Although the environmental contamination arising from the minor toxic effect of surfactants may restrict their practical application in industry, for a closed circuit the effect on the environment can be minimized to an acceptable level.

By adding a surfactant to a district heating and cooling system, a dramatic decrease in the pressure drop of the system will occur because of the reduction of friction drag. At the same time, the heat transfer capability of the drag-reducing flow will also decrease significantly because of the drastic suppression of turbulence in the flow by additives. Due to the installed pumps and heat exchangers, the performance of the whole system will be modulated to a new state and so the new conditions need to be predicted by simulation.

The deteriorated performance of the heat exchangers will adversely affect the overall performance of the district heating and cooling system, and so heat transfer enhancement is crucial. To adopt the available heat transfer enhancing methods, the heat transfer coefficients can be improved at the expense of larger pressure loss in the heat exchangers [9 - 11]. The energy transportation efficiency and the total exergy of the district heating and cooling system with enhanced heat transfer are simulated in this work.

The surfactant concentration and temperature of the solution affects the drag-reducing property. However, once the surfactant concentration and temperature have been selected properly, the district heating and cooling system can run under rather stable conditions, therefore drag reduction and heat transfer reduction are considered not affected by the temperature variation in the system. The effect of temperature and concentration on the drag-reducing capability were well addressed elsewhere [12 - 14].

2. ANALYSIS

Drag Reduction and Heat Transfer Reduction

The addition of surfactant to water decreases the turbulent friction drag dramatically with only 10-30% of the former friction drag of water left. One of our typical experimental results is shown in Fig. 1 using surfactant of CTAC at 30°C. However, various types of surfactant can meet the need of the temperature being interested, for example, Dobon at 40-130 °C [15,16]. The drag reduction (DR) and heat transfer reduction (HTR) are defined by the following equations:

$$DR = \frac{f_0 - f}{f_0} \tag{1}$$

$$HTR = \frac{Nu_0 - Nu}{Nu_0} \tag{2}$$

where, Nu_o and f_o represent the values by water flow under otherwise same conditions.

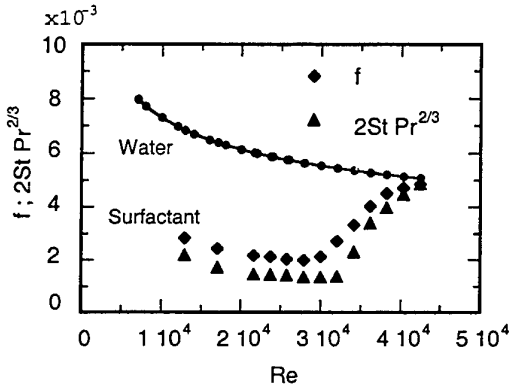


Fig. 1 Typical drag reduction and heat transfer reduction of surfactant solution
[---in two-dimensional channel with flow section of 40x500mm, the Reynolds number at the minimum friction factor is called "critical Reynolds number"]

Thermal Energy Transportation System using Drag-Reducing Additives

An energy transportation system is arranged including two heat exchangers and a closed circulation transportation pipeline added with surfactant, one of the heat exchangers transmits heat from the energy source to the circulating surfactant solution and the other transmits heat from the circulating drag-reducing flow to the user-side at low temperature. Figure 2 shows the schematic diagram of such a system.

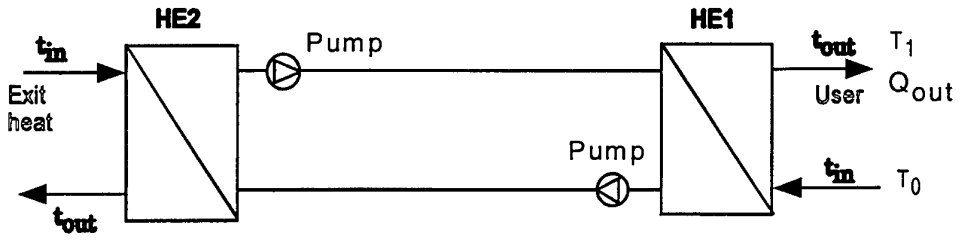


Fig. 2. The diagram of thermal energy transportation system using drag-reducing fluid

Definition of Energy Transportation and Exergy Efficiency

The energy transportation system uses pumping power to make use of wasted thermal energy. Therefore, the energy utilization coefficient or energy transportation efficiency may be defined as the ratio of the output

thermal energy over the input pumping power, given by:

$$\eta_I = \frac{Q_{out}}{Q_p} \tag{3}$$

Q_{out} is the useful heat. The pumping power is related to the flow rate of the fluid, the pipeline distance and pipe diameters as well as the components in the circulation system like heat exchangers, valves, strainers and bends. Generally speaking, the reduction of pumping power caused by the reduction of drag will increase the energy transportation efficiency. However, due to the installed pumps and heat exchangers, the flow rate of the drag-reducing flow will increase to a new level automatically according to the pump characteristics in the normal situation. More importantly, total heat and temperature level available to the user-side will also change because of the heat transfer reduction and the new running conditions. Therefore, the exergy efficiency is defined as the output exergy over the pumping power, given by:

$$\eta_{II} = \frac{\frac{T_1 - T_0}{T_1} Q_{out}}{Q_p} \tag{4}$$

From the equation, a reduction of pumping power helps to increase exergy efficiency and decrease of temperature T_1 or totally transported thermal energy Q_{out} will reduce the exergy efficiency.

Pumping Power Cost

A centrifugal pump has a property curve of volumetric flow rate against pressure drop at a fixed rotating speed. Once the surfactant solution is added to the district heating or cooling system with installed pumps, the flow rate will increase dramatically because of the significant reduction of pressure drop. Limited by the pipeline's flow rate or velocity, it may be necessary to shut down the series- or parallel- connected pumps or otherwise, a new pump or lower rotating speed may be needed in case only one pump was originally installed. This case is described in the later sections.

Heat Exchangers

In case of using surfactant solution as a medium to transport thermal energy, plate type heat exchanger is suitable. As regular running condition, the flow in transportation pipes is better to run at a Reynolds number of around the "critical Reynolds number". Therefore, in heat exchangers, the Reynolds number is different from the critical Reynolds number of the transportation pipe. This enables the heat exchanger to avoid the worst condition of heat transfer reduction. For this reason, the heat transfer reduction for the plate type heat exchanger is selected at around 40%. Our recent investigation on the diameter effect of drag-reducing flow also showed the possibility that the drag-reducing flow in the heat exchanger degrades into turbulent flow if it passes through a constricted channel [17,18]. For the simulation, one kind of plate heat exchanger was chosen with its heat transfer coefficient and pressure loss given by the following equations:

$$Nu = 0.1815\,Re^{0.65}\,Pr^{0.43}\left(\frac{Pr}{Pr_w}\right)^{0.25} \tag{5}$$

$$\Delta p = \frac{4.0 f G^2 L}{2.0 \rho 2.0 \delta} \quad (Pa) \tag{6}$$

$$f = \frac{1}{4[1.82\log_{10}(Re) - 1.64]^2} \tag{7}$$

where δ is the distance between two plates, G is mass flux in plate channels and 2δ is used as equivalent diameter in Nu and Re.

At a certain penalty of pressure loss in the heat exchanger, heat transfer can be enhanced by using a vortex generator, inserting a micelle-destroying device, modifying the heat transfer surfaces etc. [19,20]. However, the penalty of pressure loss must be at very low level.

Pipe Line Pressure Drop and Heat Loss During Transportation

The diameter of the transportation pipe is regulated by industrial standard to ensure a certain range of flow velocity and pressure loss based on pump capacity. For simulation of the industrial condition, the pump characteristics were based on an actual commercial product J511. The pipe frictional pressure drop was calculated by the following equations:

$$\Delta p = \frac{4 f_t G_t^2 L}{2 \rho D_i} \left(\frac{\mu}{\mu_w}\right)^{-0.14} \quad \text{(Pa)} \tag{8}$$

$$f_t = 0.0035 + \frac{0.264}{(D_i G_t / \mu)^{0.42}} \tag{9}$$

where G_t is mass flux of the pipe flow. Strainer and valve pressure drop was assumed to be around 6 mH_2O in total in the transportation circuit. Local pressure loss was assumed to be 50% of that for straight section. When using surfactant solutions, the drag reduction of local pressure loss is less than that of straight pipe, therefore a devalued drag reduction of 0.6DR was assumed for local pressure loss. Here, DR stands for the drag reduction of straight pipe. For the pressure drop in heat exchangers, a similar devalued drag reduction of 0.5DR was assumed. These assumptions are summarized in Table 1.

Table 1 Pressure Loss Estimation of Components in the System

Components	Straight pipe	Local pressure loss	Strainer	Valve	Heat exchanger
Pressure drop	Δp (calculation)	0.5 Δp	3 mH_2O	3 mH_2O	(calculation)
Drag reduction	DR	0.6DR	0	0	0.5DR

Because of the use of a surfactant solution, the thermal resistance inside the transportation pipe can be increased due to the heat transfer reduction of the flow. However, compared to the thermal resistance of the thermal insulation layer, the increase is too small to contribute to the improvement of the total thermal resistance. Estimation in this study of thermal resistance showed an improvement of no more than 0.3%, which was thus ignored.

Even if the pipe system is well thermally insulated, the heat loss can not be ignored in the energy transportation efficiency analysis. The heat loss was calculated assuming that the forward and return pipes were 0.125m in inner diameter set in one tunnel underground at a depth of 1.2m.

3. RESULTS AND DISCUSSIONS

Example Conditions of a District Heating System

The example is assumed to transport thermal energy at 110 °C to a user 10 km away from the energy source. Heat at lower than 40°C to the user can not be used and thus the temperature of T_0 in Fig. 2 is limited to no lower than 40 °C. The above two temperatures are the restrictions of the simulation. The temperature and the total heat to the user are open parameters to be calculated. As listed in Table 2, when surfactant solution is used, with the energy source and user-side inlet temperature keeping no change, the pumping system adjusts to a new flow rate which thus results in a changing of heat received by the user.

The pumping characteristics of the cases listed in Table 1 are plotted in Fig. 3. Case 1 is for the original water and case 2 for the one with surfactant added to the system. In case 2, because of drag reduction, the flow rate increased too much to demonstrate any benefit by using surfactant and both η_I, η_{II} are even lower than that of water case as seen in Table 2. However, in case 3, using only one original pump, a significant reduction of pumping power was obtained and also, both η_I and η_{II} increase significantly. In case 2 and 3 the heat transfer reduction was assumed as 40%. At the expense of increased pressure drop in heat exchangers, the heat transfer

can be enhanced [9], which thus enable to improve both the temperature level and the total heat output to the user as shown in case 4.

Table 2 The Parameters of Heat Exchangers

User side (t_{in} =40 °C)	Pumping power	Heat Source (t_{in}=110 °C)
t_{out} W Q A	HE1-Δp HE2-Δp DR HTR W H	A W Q η_I η_{II} No.
°C m^3/h MW m^2	mH_2O mH_2O % % m^3/h mH_2O	m^2 m^3/h MW -- -- --
80.0 29.52 1.35 30.97	1.1 1.1 0 0 29.52 59.8 x 2	24.75 29.52 1.59 142 16 1
77.4 29.52 1.26 30.97	1.33 1.33 80 40 45.29 43.3 x 2	24.75 29.52 1.50 118 13 2
77.1 29.52 1.25 30.97	0.82 0.82 80 40 34.27 28.0 x 2	24.75 29.52 1.49 240 25 3
78.6 29.52 1.30 30.97	2.87 2.87 80 10 32.93 26.3 x 2	24.75 29.52 1.55 257 28 4

Note : The difference of Q from heat source and user-side is caused by the heat loss in transportation

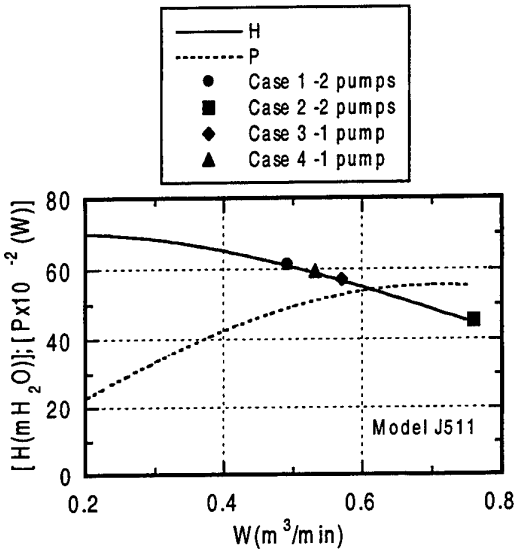


Fig. 3 The variation of pumping parameters

Effect of Heat Transfer Reduction on the Total Thermal Energy Transportation Efficiency

It is known through the above discussions that the flow rate and pressure drop of the system using surfactant are determined based on the pump characteristics as well as the drag reduction DR. DR is usually at rather stable values for surfactant solutions. Therefore, the most important parameters affecting the overall performance of the thermal energy system will be the heat transfer reduction in heat exchangers.

If the heat transfer deteriorate in heat exchangers, the total output heat and its temperature level will decrease. With the temperature at energy source fixed to be 110 °C and the inlet temperature at user side be 40 °C, a simulation was conducted to predict the magnitude of the deterioration of overall performance. The flow rate and pressure drop was based on the case 3 listed in Table 2 assuming that no measures were taken to enhance the heat transfer. When the heat transfer reduction HTR varies from 10% to 80%, the output heat and its temperature as well as energy transportation efficiency η_I, η_{II} are plotted in Fig.4. With the increasing HTR, both the output heat and its temperature decrease, which thus resulted in the decreas of exergy efficiency. η_I denotes the ratio of obtained heat to the cost of pumping power and η_{II} denotes the ratio of the exergy of benefit to cost. When the HTR is over 60%, the exergy difference between original water case and the surfactant case becomes quite small. When HTR reaches 80%, no benefit is obtainable by using surfactant in stand of water.

If the HTR is not larger that 50%, the exergy efficiency can be satisfied. Therefore heat transfer reduction of 20% to 45% may be acceptable when using surfactant additives in district heating and cooling system, and the

increment of exergy over that of water case is at a magnitude of 50% to 70%. Nevertheless, heat transfer deterioration is the key obstacle in using surfactant additives in district heating and cooling system because, the heat transfer reduction is at least at the level of 40% in heat exchangers as a common practice. In order to have only 10% to 30% reduction of heat transfer coefficient, enhancing measures must be taken.

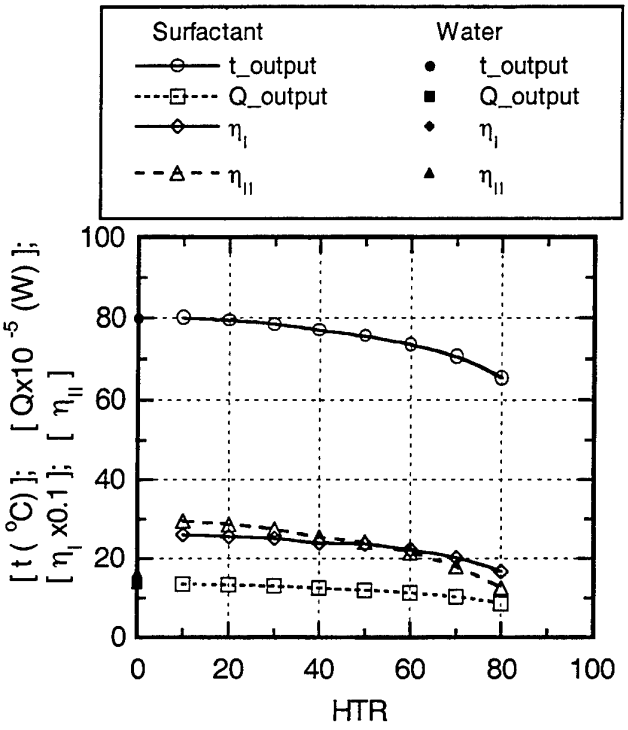


Fig. 4 The effect of HTR to η_I, η_{II} and output total heat and temperature
[-----use only one original pump]

4. CONCLUDING REMARKS

The potential of using surfactant additives in district heating system for energy conservation is discussed in the work. To evaluate the energy conservation ability, the energy transportation efficiency and exergy efficiency were proposed for system using waste heat. Because of the dramatic reduction of pressure drop by adding surfactant in installed system using water, there is possibility that flow rate rises too much to get the benefit by using drag-reducing fluid. Therefore, it is necessary to rearrange pumps.

Although pumping power can be reduced significantly by using drag-reducing fluid, the thereby resulted heat transfer reduction will influence the exergy of the system. The system simulation showed that when the heat reduction is over 60%, it is impracticable to replace water by drag-reducing fluid. However, heat transfer reduction of 20% to 45% may be acceptable with an improvement of exergy efficiency to 70% to 50%. Nevertheless, low level of heat transfer reduction is important in order to achieve high exergy efficiency in the system using drag-reducing fluid. The system exergy was simulated also for the case that heat transfer reduction is only 10% by introducing the method proposed by the authors in enhancing heat transfer at larger pressure drop in heat exchangers. And the exergy has 70% improvement over that of original system using water.

REFERENCES

1. B.A. Toms, 1948, Proc. 1st Intern. Congr. on Rheology, Vol. II, pp135-141, North Holland, Amsterdam 1948.

2. K.J. Mysels, 1949, "Flow of Thickened Fluids", U.S. Patent 2,492,173,December 27, 1949.
3. D. Ohlendorf, Interthal, W., and Hoffmann, H., 1986, , Rheol Acta Vol.25, pp468-486 (1986).
4. H. W. Bewersdorff, and D. Ohlendorf, 1988, Journal of Colloid and Polymer Science, Vol. 266, No. 10 (1988), pp941-953.
5. A.Gyr, H.-W.Bewersdorff, "Drag Reduction of Turbulent Flows by Additives", Fluwer Academic Publishers (1995), The Netherlands.
6. Y. Kawaguchi, Y. Tawaraya, A. Yabe, K. Hishida, and M. Maeda, 1996, ASME 1996 Fluid Engineering Division Conference, Vol.2, pp47-52.
7. Y. Kawaguchi, Y. Tawaraya, A. Yabe, K. Hishida, and M. Maeda, 1996, Proc. 8th International Symposium on Application of Laser Techniques to Fluid Mechanics, Lisbon, July, 8-11, 1996.
8. Y. Kawaguchi, H. Daisaka, A. Yabe, K. Hishida, and M. Maeda, 1997, Proc. 2th International Symposium on turbulence Heat and Mass Transfer, June,1997, Delft.
9. P.W. Li, H. Daisaka, Y. Kawaguchi, A. Yabe, K. Hishida, M. Maeda, 1998, 2nd Engineering Foundation Conference on Turbulent Heat Transfer, Manchester, UK,1998, Vol.2, P21-P29.
10. K. Gasljevic, E.F. Matthys, ASME Journal of Heat Transfer, Vol.119, pp80-88.
11. J. Pollert, J.L. Zakin, J. Myska, and P. Kratochivil, 1994, Czech Republic, Proc. Int. District Heating and Cooling 1994 conference, pp.141-156.
12. A.V. Shenoy, 1984, Colloid & Polymer Science, Vol. 262, pp.319-337.
13. H.W. Bewersdorff, Structure of turbulence and drag reduction, Edited by A.Gyr, IUTAM Symposium, Zurich, Switzerland, 1989, pp293-312.
14. Y. Kawaguchi, Y. Tawaraya, M. Tanaka, Journal of Mechanical Engineering Laboratory, Vol.49 (1995), No.4. (in Japanese), pp12-21.
15. A. Steiff, K. Klopper, Fluid Division Conference, Summer Meeting, 1996 ASME, FED-Vol.237. pp235-242.
16. A. Steiff, K. Klopper, P.M. Weinspach, Heat Transfer 1998, proceedings of 11th IHTC, Kyongju, Korea, Vol.6,317-322.
17. P.W. Li, Y. Kawaguchi, A. Yabe, 35th National Heat Transfer Symposium, Vol.2, 1999.
18. H. Usui, T. Itoh, T. Saeki, 1998, Rheologica Acta, Vol. 37, No.2, pp122-128.
19. Hideo Inaba and Naoto Haruki, 1996, Proceedings of the 3rd KSME-JSME Thermal Engineering Conference, Oct. 20-23, ,Kyongju, Korea, pp iii215-220.
20. Sato Kimitoshi, Mimatsu Junji & Kumada Masaya, 1998, Proceedings of the National Heat Transfer Symposium of Japan, May 27-29, Nagoya, Japan, pp693-694.

FLOW AND HEAT TRANSFER CHARACTERISTICS OF WATER SOLUTION WITH FLOW DRAG REDUCTION ADDITIVE IN CURVED TUBES

Hideo Inaba
The Graduate School of Natural Science and Technology, Okayama University
Email:inaba@mech.okayama-u.ac.jp; Fax: (086)-251-8266

Naoto Haruki
Department of Mechanical Engineering, Okayama University
Email:haruki@mech.okayama-u.ac.jp; Fax: (086)-251-8266

Akihiko Horibe
The Graduate School of Natural Science and Technology, Okayama University
Email:horibe@mech.okayama-u.ac.jp; Fax: (086)-251-8266

Keywords: flow drag reduction, curved pipe, convection heat transfer, surfactant

ABSTRACT. This paper has focused to investigate the flow drag reduction and heat transfer characteristics of surfactant solution in curved pipes. In this study, Dodecyltrimethyl Ammonium Chloride ($C_{12}H_{25}N(CH_3)_3$ = 263.89) was used as a surfactant, and Sodium Salicylate ($C_7H_5NaO_3$ = 160.10) was added to the surfactant solution for the enhancement of making rod-like micell surfactant structure. From the experimental results of flow drag resistance of the surfactant solution and water in curved tubes, it was found that the friction factor of the surfactant solution flow decreased markedly in comparison with that of water flow in a turbulent flow. Therefore, the flow drag reduction effect was examined in detail in some curved pipes. It was seen that 4 local flow resistances of the position of upside, downside, inside and outside of the curved tube were different one another. The angle and radius of curved test tubes exerted the influence on the friction factor of the surfactant solution flow. The heat transfer of the surfactant solution and water flows was measured in the same curved tubes under the constant heat flux heating condition. The heat transfer in the laminar flow measured in curved tubes increased as compared with that in a straight tube. This increase of the heat transfer was caused by the secondary flow in the curved tubes. However in the turbulent flow of the surfactant solution, it was seen that the heat transfer reduction effect was confirmed in the same measuring range as the flow drag reduction one. As a result, the secondary flow in the curved tube provided the decreasing tendency of both the flow drag and heat transfer reduction effect.

1. INTRODUCTION

Recently, the flow drag reduction effect obtained the addition of some kinds of the flow drag reduction's materials into a water pipe flow has been used for an effective thermal energy transport system. This flow drag reduction effect is called Toms effect. The Toms effect is caused by addition of a small quantity of polymers, surfactants or fibrous materials to the turbulent water flow. It is said that the flow drag reduction in a turbulent flow is caused by suppressing the occurrence and development of turbulent vortexes by means of a deformation of polymer thread in a water flow [1]. On the other hand, some kinds of the surfactants make a rod-like micell with the connection of spherical micells in water [2], and this rod-like micell has the same function as the polymer thread. As compared with the water flow, it could be expected that a flow rate is increased, that is, a pumping power is reduced, and the heat loss from a pipe wall is decreased in the thermal energy transport system by using the Toms effect. Many investigations have been conducted on the flow drag reduction and heat transfer characteristics of water solution with surfactants and polymers (inaba et al [3], USUI et al.[4], KAWAGUCHI et al.[5], etc.). These investigations have been performed in a straight test section, but very little consideration appears to be given to the flow with flow drag reduction additives through curved pipes.

In the present study, the flow drag and heat transfer reduction characteristics of the surfactant solution flow in the several curved pipes have been studied experimentally. From these experimental results, useful nondimensional correlative equations for flow resistance and heat transfer were derived by various parameters (curved angle from a curve inlet θ, radius of curvature of the pipe R, flow velocity and concentration of surfactant in water solution.).

2.VISCOSITY MEASUREMENT OF THE SURFACTANT SOLUTION

The flow drag additive used in this study was the surfactant of Dodecytrimethyl Ammonium Chloride, DTAC. The water solution with DTAC as a working fluid was made by mixing both DTAC and Sodium Salicylate (counter-ion of DTAC). The concentration of sodium salicylate added into the water solution was the same as that of DTAC, due to the rod-like micell structure formation of DTAC. The viscosity of the DTAC solution was measured with both a capillary viscometer and a rotating cylinder viscometer. The measuring accuracy of both the capillary and rotating cylinder viscometer was examined by using distilled water as a reference fluid. The obtained results of distilled water with the rotating cylinder viscometer agreed with the water within a standard deviation of ±1.9 %. On the other hand, the obtained results of distilled water by the capillary viscometer agreed with the reference data of water within a standard deviation of ±3.1 %. The Pseudoplastic viscosity K and index number n in equation (1) of the DTAC solution were estimated by the obtained results of the DTAC solution with these viscometers. The relationship between K and DTAC concentration C_d is shown in Fig. 1 for various DTAC solution temperatures T_d. And the relationship between n and C_d is presented in Fig. 2. It was understood that the data of pseudoplastic viscosity K of the DTAC solution were almost equal to those of water in the range of $C_d \leq 1000$ ppm. However, the data of K of the DTAC solution in the range of $C_d \geq 1000$ ppm increased with increasing of C_d. While, the data of n for the DTAC solution are almost equal to $n = 0.95$.

The index number n of the DTAC solution was expressed by the following equation (2) within a maximum deviation of ±4.01 %. The pseudoplastic viscosity K of the DTAC solution was expressed by the following equation (3) within a maximum deviation of ±17.8 %.

$$\tau = K \cdot \gamma^n \tag{1}$$

$$n = 0.95 \tag{2}$$

$$K = \mu_w + A \cdot \exp\{B/T_d\} \tag{3}$$

$$\begin{cases} A = \left(-2.043\times10^{-5}\times C_d + 5.233\times10^{-7}\times {C_d}^2\right)\times10^{-10} \\ B = 4654 \end{cases}$$

Applicable range: $T_d = 10 \sim 25^\circ C$, $\gamma = 1.18 \sim 72.41\ {}^1/_s$

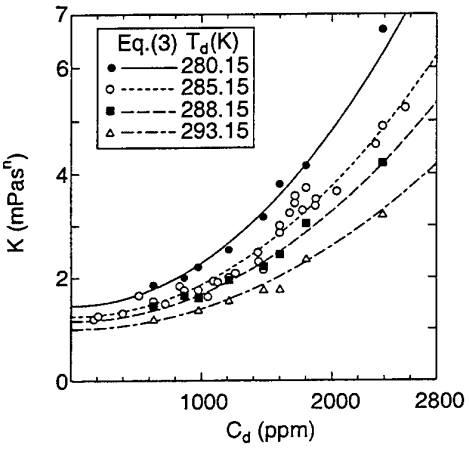


Fig. 1. Relationship between K and C_d of the DTAC solution

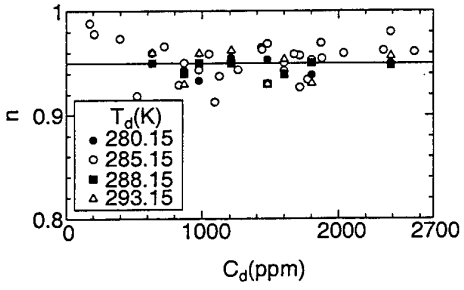


Fig. 2. Relationship between n and C_d of the DTAC solution

3. EXPERIMENTAL APPARATUS AND PROCEDURE

The Schematic diagram of experimental apparatus for drag reduction and heat transfer measurements is presented in Fig. 3. The present experimental apparatus consisted of a curved test section for flow drag and heat transfer measurement, a centrifugal pump as fluid circulation power source, temperature control devices, and a test fluid circulation pipe line. Test fluid temperature in a storage tank was controlled by circulating brine cooled with a refrigerator, and its temperature was measured with T type thermocouples at the inlet and outlet of the test section. The curved test sections were made of stainless steel with the diameter d of 0.0177m. An entrance section was equipped at the inlet of each curved test section pipe in order to obtain a full-developed flow velocity in a pipe. The experiments for the flow resistance and heat transfer were carried out by using several curved pipes with various angle from the inlet of curved pipe, θ= 45°, 90° , 180° and 270° , and the curvature ratio of R (curvature radius of the pipe) to r (radius of the pipe) R/r of 10, 17, 25 and 50.

The pressure-loss (ΔP) in the axial direction of the curved pipe was automatically recorded with digital signals from a differential pressure gauge connected by pressure taps mounted on the inlet and outlet of curved test section pipe. The outlet pressure taps consisted of four small holes that were drilled on the upside, downside, inside and outside walls of the curved pipe. In this experiment, the average pressure-loss of four pressure-loss measured in four measuring position was used. The measuring accuracy of pressure measurement system was estimated within ± 3.0 % in consideration of measuring accuracy of the differential pressure gauge. The pipe friction coefficient λ of the curved test pipe was calculated from the following equation (ℓ : axial length of the curved pipe).

$$\Delta P = \lambda \frac{\ell}{d} \frac{1}{2} \rho U_m^2 \tag{4}$$

The heat transfer experiment was carried out under the thermal boundary condition of a uniform heat flux. The uniform heat flux condition was performed by the curved stainless steel pipe charged directly with electricity. The inlet heat flux from the stainless pipe to the water solution was calculated from an electric input power Q. The wall temperature of the curved pipe was measured at 40 positions in the axial as well as in the circumferential direction of the curved pipe. The stainless steel pipe was thermally insulated by a glass wool insulates material. The average heat transfer coefficient α was calculated from

$$\alpha = \frac{Q}{A \cdot \Delta T} \tag{5}$$

Where, ΔT is the temperature difference between the average heating surface T_w and the bulk mean temperature of the test fluid T_m. A means total heating surface. The accuracy o the average heat transfer was estimated within 10~15 %.

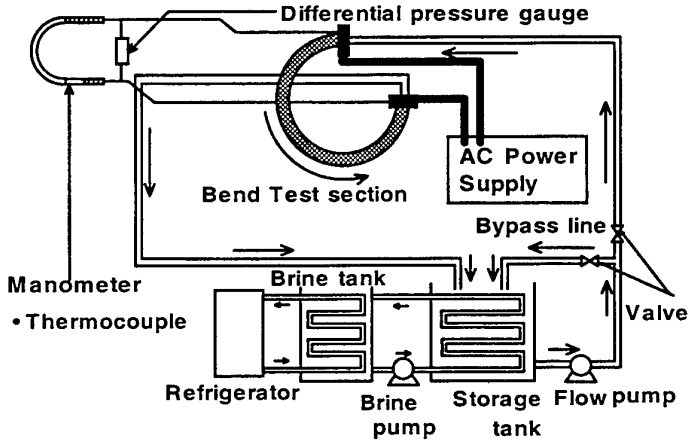


Fig. 3. Schematic diagram of experimental apparatus

4. EXPERIMENTAL RESULTS OF FLOW DRAG REDUCTION EFFECT

Flow Drag Reduction Effect

The relationship between a pipe friction coefficient λ and the modified Reynolds number *Re'* of water and the DTAC solution in the curved test section ($R/r = 20$, $\theta=180°$) are shown in Fig. 4 for various DTAC concentrations C_d at the inlet test fluid temperature of 12 °C. In Fig. 4, The modified Reynolds number *Re'* was calculated from equation (6) by using equation (1) that meant a Non-Newtonian behavior of the DTAC solution.

$$Re' = 8^{1-n} \cdot \left\{\frac{3n+1}{4n}\right\}^{-n} \left\{\frac{\rho \cdot U_m{}^{2-n} \cdot d^n}{K}\right\} \tag{6}$$

In Fig. 4, equations (7) and (8) shown by solid lines indicate previous correlation of friction factor in the curved pipe for fully developed laminar and turbulent flow of Newtonian fluid, respectively. The dash lines in Fig. 4 show the flow resistance in the straight circular pipe for the laminar and turbulent flow.

$$\frac{\lambda}{\lambda_s} = \frac{21.5K}{(1.56+\log K)^{5.73}}, 13.5 < K < 2000 \quad \left[\lambda_s : \text{pipe friction coefficient in the straight pipe, } K = Re(r/R)^{0.5}\right] \tag{7}$$

$$\lambda\sqrt{R/r} = 0.029 + 0.304\left\{Re(r/R)^2\right\}^{-0.25} \qquad \left[0.034 < Re(r/R)^2 < 300\right] \tag{8}$$

The result from this figure revealed that the pipe friction coefficients λ of the DTAC solution and water showed good agreement with the previous correlation in equation (7) in a laminar flow in the range of $Re' < 10^4$. On the other hand, the data of λ of water in the range of $Re' > 10^4$ were in good agreement with the equation (8) in a turbulent flow. While, the λ of the DTAC solution of $Re' > 10^4$ was below that of the curved pipe water flow in equation (8). Therefore, it was found that the flow drag reduction effect of the DTAC solution appeared in the case of the curved pipe flow. This effect of the DTAC solution was explained by the fact that the pipe flow was laminarized by suppression of an occurrence and a development of turbulent vortexes by means of deformation of a rod-like micell structure of DTAC in the solution. However, the λ of DTAC solution for $C_d = 561$ ppm were equal to equation (8). Under the condition of this concentration, the rod-like micell structures could not be formed in the DTAC solution because its concentration of C_d was below the critical micell concentration (*cmc*) of making a rod-like micell structure. Consequently, the data of λ increased suddenly with increasing of *Re'* over the value of *cmc*. Finally, the data of λ approached to the curve of equation (8) in a turbulent flow. This behavior of λ was explained by the fact that the disappearance of Toms effect was caused by destroying a rod-like micell structure of DTAC by a strong mechanical shear force in the range of large *Re'* numbers.

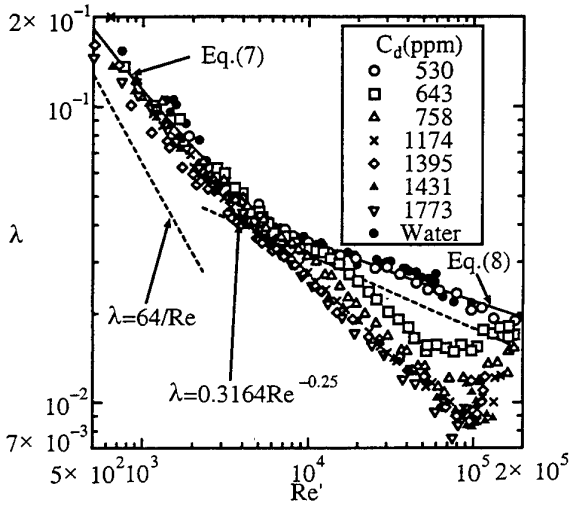


Fig. 4. Relationship between λ and *Re'* (R/r =34, θ= 270°)

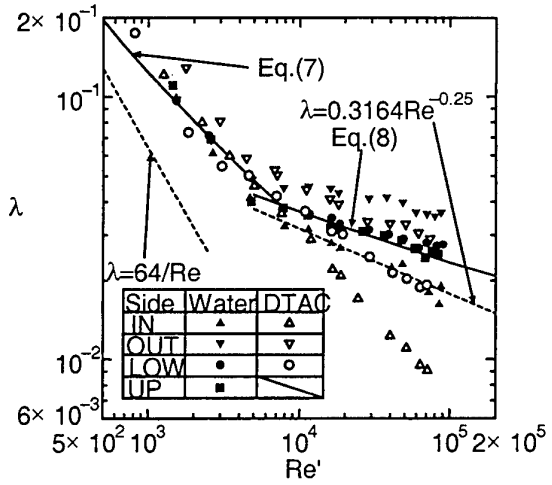


Fig. 5. The difference of flow resistance in the circumferential position

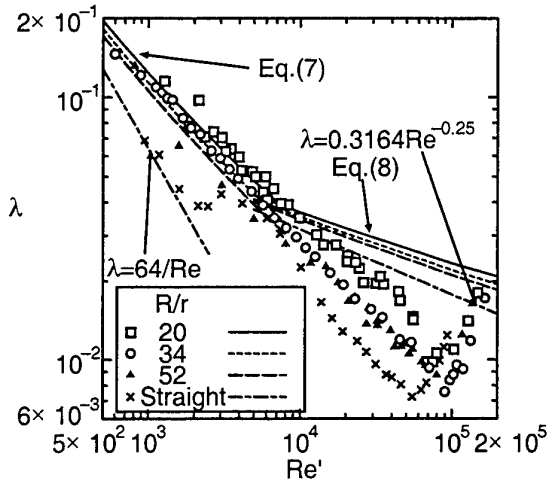


Fig. 6. Relationship between *Re'* and λ for various *R/r* (θ = 270°, C_d = 1500 ppm)

Flow resistance distribution on the curved pipe in the circumferential direction. Figure 5 shows the flow resistance distribution of water and the DTAC solution on the curved pipe in the circumferential direction. As shown in Fig. 5, the λ of water and the DTAC solution at the inside was the largest one, and λ at outside was the smallest one as compared with the data of other three side positions. The value of λ at low and upside were equal to each other, and were between those at the inside and outside position.

Flow drag reduction characteristics for various curvature ratios. Figure 6 indicates the relationship between *Re'* and λ of the DTAC solution for three curvature radius ratios. Other parameters of the curved test section were fixed at θ = 270° and C_d = 1500 ppm. From the data of Fig. 6, it is seen that the Toms effect in the curved pipe was to a lesser extent effective as compared with that in the straight pipe since the value of λ in the curved pipe was greater than that of straight pipe in the turbulent flow. This phenomenon was caused by the fact that the secondary flow by the centrifugal force predominated over the flow condition in the straight pipe. However, the value of λ in the curved pipe approached to that in the straight pipe with increasing *R/r*, since the centrifugal force was inversely proportional to curvature radius *R* and the flow pattern in the curved pipe shifted gradually to that in the straight pipe as *R/r* increased.

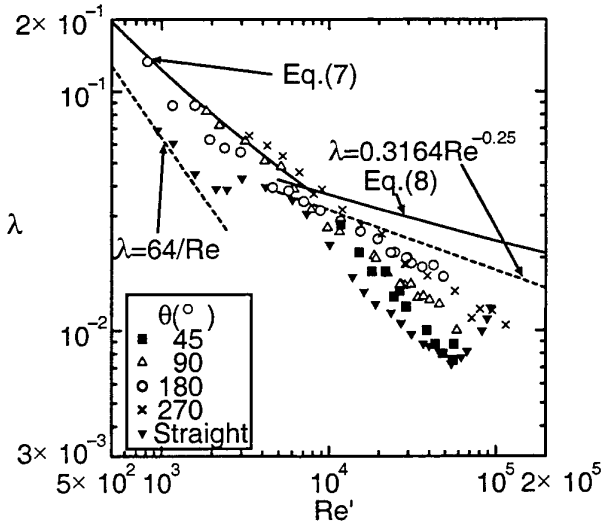


Fig. 7. Relationship between *Re'* and λ for various θ (*R/r* = 20, C_d = 1300 ppm)

Flow drag reduction characteristics for various curved angle θ. The relationships between *Re'* and λ for four curved angles of θ= 45°, 90°, 180° and 270° are mentioned in Fig. 7. Under the experimental condition of C_d = 1300 ppm and *R/r* = 20. As could be seen from Fig. 6, it was found that the Toms effect in the curved pipe were clearly influenced by curvature angle θ. That is, as the θ is decreased, the friction factor in the curved pipe decreased and approached to the that in the straight pipe. Therefore, it could be concluded that there was the same Toms effect as the straight pipe in the case of small curvature angle.

From the experimental data of λ for the DTAC solution in the curved pipe, the correlation of the DTAC solution in the flow drag reduction range was expressed by the following equation (9) within a standard deviation of 7.17 %. Where, *De* is the Dean number ($=Re'\times(r/R)^{0.5}$), and θ is the curvature angle from the inlet part.

$$\lambda = 6.75\times\left(\frac{R}{r}\right)^{-0.560}\cdot\theta^{0.146}\cdot De^{-0.500} \tag{9}$$

Application range : *R/r* = 20~50, θ=π/4~3/2×π, C_d > 1000 ppm

5. EXPERIMENTAL RESULTS OF HEAT TRANSFER REDUCTION EFFECT

Heat Transfer Reduction Effect

Referring to heat transfer coefficient measurement of the DTAC solution, the relationship between $Nu/Pr'^{1/3}$ and *Re'* for *R/r* = 34 and θ = 270° is shown in Fig. 8. The modified Prandtl number *Pr'* was calculated from following equation (10) by using equation (1), which means a Non-Newtonian behavior of the DTAC solution in the same calculation method of *Re'* in equation (6). The thermal conductivity λ' and specific heat *Cp* of the DTAC solution in equation (10) were selected with those of water because they were almost equal to those of water at a given same temperature.

$$Pr' = \frac{Cp\cdot\left\{\frac{3n+1}{4n}\right\}^{n}\cdot K\cdot\left\{\frac{8U_m}{d}\right\}^{n-1}}{\lambda'} \tag{10}$$

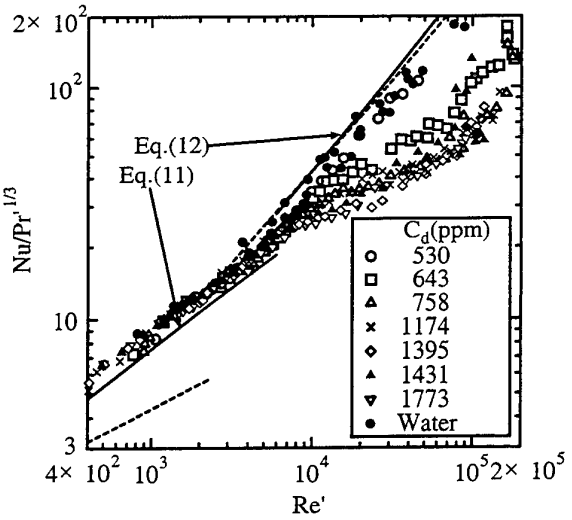


Fig. 8. Relationship between *Re'* and $Nu/Pr'^{1/3}$ (*R/r* = 34, θ=270°)

Two solid lines in Fig. 8 refer to the heat transfer equations in the curved pipe for a laminar water flow (Equation. (11) and for a turbulent water flow (Equation. (12)), respectively. And the straight lines indicated by the dash line in Fig. 7 show the heat transfer in the straight circular pipe for the laminar and turbulent flow obtained

for a straight pipe in the laminar flow range. This heat transfer enhancement was caused by the secondary flow in the curved pipe, which caused by of the centrifugal force. However, the value of $Nu/Pr'^{1/3}$ for the DTAC solution was below that of water flow equation (12) in the turbulent flow range of $Re' > 10^4$. Therefore, the heat transfer reduction effect of the DTAC solution in the curved pipe appeared in the same range of the flow drag reduction effect as shown in Fig. 4.

$$Nu = \left[\frac{0.32+3\frac{r}{R}}{0.86-0.8\frac{r}{R}}\right] \times Re^{0.5}\, Pr^{1/3}\left(\frac{d}{\ell}\right)^{0.14+0.84\frac{r}{R}} \tag{11}$$

$$Nu = 0.021 Re^{0.85}\, Pr^{0.4}\left(\frac{r}{R}\right)^{0.1} \tag{12}$$

Heat transfer reduction characteristics for various curvature radius ratios. The experimental results of the effect of R/r on the heat transfer reduction for the DTAC solution are shown in Fig. 9. This heat transfer measurement was carried out by using the same curved pipe as shown in Fig. 6. The present experimental results showed that the values of $Nu/Pr'^{1/3}$ in the curved pipe were greater than that in the straight pipe in the range of heat transfer reduction effect. As compared with the flow drag reduction effect (Fig.6), the influence of R/r on $Nu/Pr'^{1/3}$ was similar to that on the pipe friction coefficient λ.

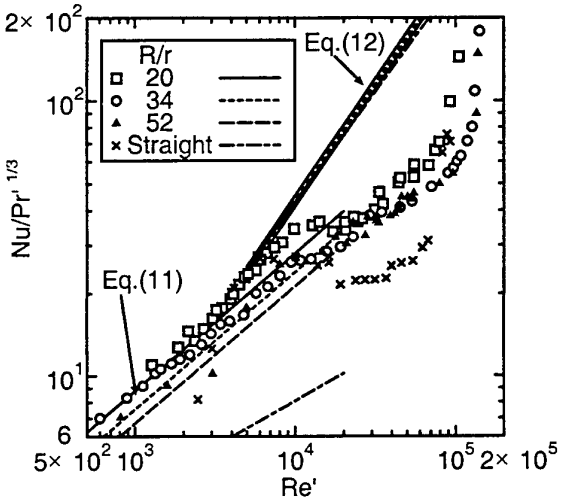


Fig. 9. Relationship between $Nu/Pr'^{1/3}$ and Re' (θ=270°, C_d = 1500 ppm)

Heat transfer reduction characteristics for various curvature angle. In Fig.10, the present heat transfer measurement for the DTAC solution were carried out with the several curvature angle θ under the fixed condition of R/r and C_d. According to Fig. 10, the heat transfer coefficient of the DTAC solution in the curved pipe showed the tendency to approach to that in the straight pipe with decreasing of θ.

The obtained data of heat transfer coefficient for the DTAC solution were non-dimensionalized in terms of R/r, θ and De by the following equation (13) within a standard deviation of ± 7.76 %.

$$\frac{Nu}{Pr'^{1/3}} = 5.269 \times \left(\frac{R}{r}\right)^{-0.388} \cdot \theta^{0.125} \cdot De^{0.383} \tag{13}$$

Application range : R/r = 20~50, θ=π/4~3/2×π, C_d > 1000 ppm

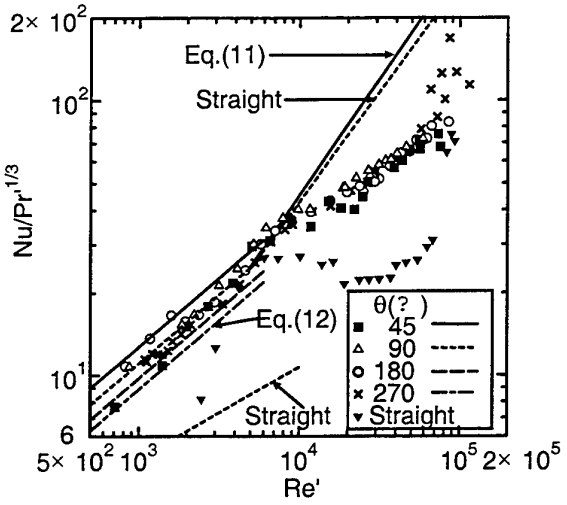


Fig. 10. Relationship between $Nu/Pr'^{1/3}$ and Re' (R/r =20, C_d = 1300 ppm)

6. CONCLUSIONS

From measurement results of the viscosity, drag reduction and heat transfer coefficient of the water solution with a surfactant (Dodecyltrimethyl ammonium Chloride and Sodium Salicylate as a counter-ion), the following conclusions were obtained.

1. From experimental results of viscosity for the DTAC solution, its viscosity showed a Non-Newtonian behavior. A useful correlative equation for viscosity of the DTAC solution was proposed.
2. Flow drag reduction of the DTAC solutions was measured for curvature radius ratio ranging from 20 to 50, and θ ranging from 45° to 270°. The pipe friction coefficient λ for the DTAC solution showed good agreement with the previous correlation in a laminar curved pipe flow, while λ of the DTAC solution was smaller than that of water in a turbulent curved pipe flow. This flow drag reduction effect of the DTAC solution in the curved pipe was to a lesser extend ineffective as compared with that in the straight pipe.
3. From heat transfer experiments for the DTAC solutions in several curved pipes, it was noticed that the heat transfer coefficient in the turbulent curved pipe flow for the DTAC solution decreased by suppressing turbulent vortexes, as compared with that of water. The value of $Nu/Pr'^{1/3}$ for the curved pipe was over that in the straight pipe flow due to the secondary flow
4. Useful correlative equations for flow drag resistance and heat transfer of the DTAC solution were proposed in terms of some non-dimensional parameters.

REFERENCES

1. T. Shihou and H. Hirata, "Viscoelastic Properties of Aqueous Detergent System V", *Proceedings of the 37th Rheology Symposium, pp. 109 – 112*, Japan (1989)
2. P. S. Virk, E. W. Merrill, H. S. Mickley and K. A. Smith, "The Toms Phenomenon : turbulent pipe flow of dilute polymer solutions", J. Fluid Mech., v. 30, Part 2, pp. 305 – 328 (1967)
3. H. Inaba and N. Haruki, "Drag Reduction and Heat Transfer Characteristics of Water Solutions with Surfactants in a Straight Pipe", Heat Transfer Japanese Research, v. 27, No. 1, pp. 1 – 15, Japan (1998)
4. H. Usui, T. Itoh and T. Saeki, "Drag Reduction Pipe Flow of Surfactant Solutions", *Proceedings of the Fluids Engineering Division Conference, v. • , pp. 159 – 163*, Japan (1996)
5. Y. Kawaguchi, Y. Tawaraya, A. Yabe, K. Hishida and M. Maede, "Turbulent Transport Mechanism in a Drag Reducing Flow with Surfactant Additive Investigated by Two Component LDV", *Proceedings of the 8th International Symposium on Application of Laser Techniques to Fluid mechanics, pp. 29. 4.1 – 29.4.7*, Lisbon (1996)

TRANSIENT DEVELOPMENT OF HEAT TRANSFER ENHANCED BY OSCILLATING FLOWS PAST A CIRCULAR CYLINDER

Chin-Tsau Hsu and Man-Kim Kwan
Department of Mechanical Engineering
The Hong Kong University of Science and Technology, Hong Kong
Email: mecthsu@ust.hk, memkkwan@ust.hk

Keywords: oscillating flows, circular cylinder, DNS, streaming, heat transfer enhancement

ABSTRACT. The enhanced heat transfer by oscillating flows past a hot circular cylinder is studied numerically under the conditions of a constant and uniform heat flux on the cylinder surface and a constant temperature at far-away. The stagnant ambient fluid is initially heated by the cylinder to a steady temperature distribution, and is then set forth with a sinusoidal oscillation to cool the cylinder. The velocity field is first computed with a two-dimensional DNS method, and then used to calculate the temperature distribution at the same instant. The transient development of temperature deviation from the initial temperature represents the enhanced cooling due to the oscillating flow. This temperature deviation is presented graphically to demonstrate the existence of two heated regions near the left and right stagnation points on the cylinder against fluid oscillation. The development of the temperature pattern due to the enhanced cooling is found to be highly correlated to the secondary streaming patterns associated with the oscillating flow.

1. INTRODUCTION

Oscillating flows past a circular cylinder is one of the challenging fluid mechanics problems. Typical phenomena include streaming, Honji instability, vortex shedding and turbulence generation [1, 2]. There are two dynamic parameters to characterize the problem: the Keulegan Carpenter number KC and Reynolds number Re_D, which are defined respectively by:

$$KC = \frac{U_\infty * T*}{D*} = \frac{2\pi A_\infty *}{D*} \text{ and } Re_D = \frac{U_\infty * D*}{\nu *},$$

where U_∞ * is the amplitude of the far-field fluid velocity oscillation, T* the period of oscillation, D* the cylinder diameter, A_∞ * the far-field displacement amplitude and ν* the fluid kinematic viscosity (Hereafter, a variable with an asterisk denotes a dimensional quantity).

When a hot cylinder is placed in a cold stagnant ambience, the heat generated from the cylinder is transferred mainly through conduction to the ambient fluid that eventually reaches a steady state, if the buoyant free convection is neglected. If the fluid is set forth with an oscillation, additional heat is transferred away from the cylinder by flow motion. This increase in the rate of heat transfer subsequently leads to the cooling of the heated cylinder. This type of heat transfer is usually termed as the enhanced heat transfer because the transfer involves no net mass flow, in difference to the conventional convective heat transfer where the forced flow is steady. Applications of enhanced heat transfer include those in a hot wire anemometer and a pulse-tube heat exchanger, to name a few. To our knowledge, there exists little works on the enhanced heat transfer due to oscillating flows, even though considerable efforts were devoted to the convective heat transfer in a steady flow past a stationary circular cylinder [3]. Heat transfer enhanced by the vibrations of cylinder in steady mean flows was computed recently by Karanth *et al.* [4] and Cheng *et al.* [5], who focused on the influences of vortex shedding and lock-on phenomena, respectively. Experimental works on the same topic include those by Saxena & Laird [6] and Cheng *et al.* [7]. In both experiments, they observed considerable increase in heat transfer, maximum 60% and 34% respectively.

In the present study, a Direct Numerical Simulation (DNS) method was implemented to delineate the transient development of velocity and temperature fields of an oscillating flow past a heated circular cylinder. We limit this study to the regime of low Reynolds number so that the flow is laminar and two-dimensional in nature; hence, DNS can be described simply with a two-dimensional formulation. Steady flows of air past a stationary circular cylinder are computed first for code validation. Then, a case study for airflow of Re_D = 200 and KC = 1 is performed to demonstrate the unique flow and heat transfer characteristics when the external flow is oscillatory.

2. MATHEMATICAL FORMULATIONS

Consider the stagnant air surrounding a circular cylinder under the environment of no gravity is initially heated by the cylinder to a steady temperature distribution Θ_{st}*, and is then set into an inviscid flow oscillation according to U_∞*cos(2πt*/T*) at infinity. The governing equations for air flows and heat transfer are the two-dimensional continuity, Navier-Stokes and energy equations. We use the far-field velocity amplitude U_∞* as the velocity scale and the cylinder radius R* as the length scale. The convection time scale and the pressure scale are then given by R*/U_∞* and ρ*(U_∞*)^2 respectively, where ρ* is the fluid density. Finally, the dimensionless temperature is defined by $\frac{\Theta^*-\Theta_\infty^*}{Q^*/k^*}$, where Θ_∞* is the initial far-field temperature at $r^* = r_\infty^*$, Q* the total heat output per unit length from the cylinder and k* the thermal conductivity of air. The dimensionless governing equations in cylindrical coordinates become:

$$\frac{\partial u_r}{\partial r} + \frac{u_r}{r} + \frac{1}{r}\frac{\partial u_\theta}{\partial \theta} = 0 \tag{1}$$

$$\frac{\partial u_r}{\partial t} + u_r\frac{\partial u_r}{\partial r} + \frac{u_\theta}{r}\frac{\partial u_r}{\partial \theta} - \frac{u_\theta^2}{r} = -\frac{\partial p}{\partial r} + \frac{2}{Re_D}\left(\nabla^2 u_r - \frac{2}{r^2}\frac{\partial u_\theta}{\partial \theta} - \frac{u_r}{r^2}\right) \tag{2}$$

$$\frac{\partial u_\theta}{\partial t} + u_r\frac{\partial u_\theta}{\partial r} + \frac{u_\theta}{r}\frac{\partial u_\theta}{\partial \theta} + \frac{u_r u_\theta}{r} = -\frac{1}{r}\frac{\partial p}{\partial \theta} + \frac{2}{Re_D}\left(\nabla^2 u_\theta - \frac{2}{r^2}\frac{\partial u_r}{\partial \theta} - \frac{u_\theta}{r^2}\right) \tag{3}$$

$$\frac{\partial \Theta}{\partial t} + \frac{1}{r}\frac{\partial (r u_r \Theta)}{\partial r} + \frac{1}{r}\frac{\partial (u_\theta \Theta)}{\partial \theta} = \frac{2}{Re_D\,Pr}\left[\frac{1}{r}\frac{\partial}{\partial r}\left(r\frac{\partial \Theta}{\partial r}\right) + \frac{1}{r^2}\frac{\partial^2 \Theta}{\partial \theta^2}\right] \tag{4}$$

where p = dimensionless pressure,
u_r = dimensionless velocity in the radial direction,
u_θ = dimensionless velocity in the circumferential direction,
Θ = dimensionless temperature,

and $\nabla^2 = \frac{\partial^2}{\partial r^2} + \frac{1}{r}\frac{\partial}{\partial r} + \frac{1}{r^2}\frac{\partial^2}{\partial \theta^2}$. Here, θ = 0° is aligned with the direction of flow oscillation.

Initial Conditions: Fluid is stagnant and the temperature field is described by the steady state conduction.

Thus, for t < 0, $u_r = u_\theta = 0$ everywhere (5a, b)

$$\Theta = \Theta_{st} = \frac{\ln(r_\infty / r)}{2\pi} \tag{6}$$

Boundary Conditions: For the velocity field, impermeable and no slip conditions are imposed on the cylinder surface, and a sinusoidal potential flow along the x-axis is applied at far field. For the temperature field, constant temperature gradient condition is applied on the cylinder surface and constant temperature condition to the far-away boundary, respectively.

At $r = 1$, $u_r = u_\theta = 0$ (7a, b)

$$\frac{\partial \Theta}{\partial r} = -\frac{1}{2\pi} \tag{8}$$

At $r = r_\infty$, $u_r = -(1 + 1/r_\infty^2)\cos\theta\cos(\pi t / KC)$ (9a)

$$u_\theta = -(1 + 1/r_\infty^2)\sin\theta\cos(\pi t / KC) \tag{9b}$$

$$\Theta = 0 \qquad (10)$$

These boundary conditions were imposed for $t \geq 0$. Note that from equation (9) the dimensionless oscillation period is given by $T = 2KC$.

3. NUMERICAL PROCEDURES

The numerical code adopted a staggered grid such that velocities and scalar variables (p and Θ) were located at the mesh face and center respectively. In the code, fractional time step used by Kim and Moin [8] was implemented to solve equations (1-3). Time was advanced by Adams-Bashforth scheme, whereas the convective and viscous terms were discretized using the 4^{th} order and 2^{nd} order central difference schemes respectively. After the velocities were obtained, the temperature distribution at that time step was calculated by solving equation (4) with the power-law scheme [9]. The grids were uniformly spaced in the θ direction and exponentially stretched in the r direction. For the present study, the time interval $\Delta t/T$ was 1×10^{-3}. The number of grids in the r and θ directions were 256 and 180 respectively. Lastly, r_∞ was set to be 100.

4. CODE VALIDATION

To validate the numerical code, it is first exercised to calculate the forced convection for steady flow past a heated circular cylinder, under the condition of a constant temperature at the cylinder surface. This case represents the limit case of $KC \rightarrow \infty$ in the formulation given in section 2, except the difference in the surface boundary condition on temperature. Figure 1 shows the variation of mean Nusselt number Nu_D with the Reynolds number Re_D. Here, the Nusselt number is defined as $Nu_D = h^*D^*/k^*$, where h^* is the angular-averaged heat transfer coefficient. From fig. 1, it appears that the present results agree excellently with the numerical results [10-12] and the experimental data [13-16] by others.

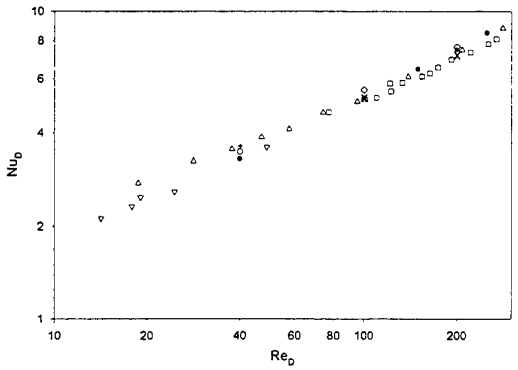


Fig. 1. Nu_D vs. Re_D for a steady and uniform flow past a circular cylinder. ●, Present data; +, Chen and Weng [10]; ○, Dennis *et al.* [11]; ◇, Jian and Goel [12]; □, Hilpert [13]; △, Krall and Eckert [14]; ×, McAdams [15]; ▽, Tsubouchi and Masuda [16].

5. NUMERICAL RESULTS

With the confidence in code validation, the code is then used to compute the enhanced cooling of a heated circular cylinder subjected to the oscillating flows, for different values of Re_D and KC at fixed Pr = 0.7. Due to the limit of text, here we present only the results of Re_D = 200 and KC = 1. Before showing the results, the definition of period-averaged quantity $\bar{q}$ and angular-averaged quantity <q> are provided first.

The period-averaged mean $\bar{q}$ is defined by:

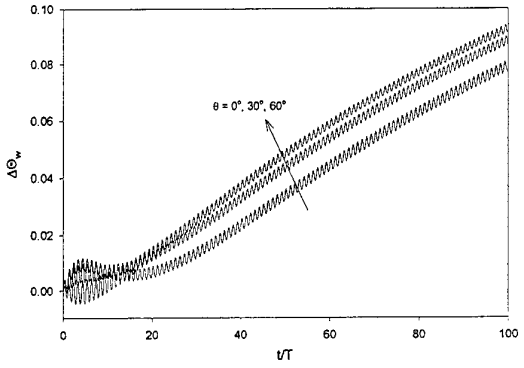
$$\bar{q}(r,\theta,\tau) = \frac{1}{T}\int_{-T/2}^{T/2} q(r,\theta,t+\tau)dt\,.$$

The period-averaged result at the n^{th} cycle implies that at $\tau = (n-1/2)T$. On the other hand, the angular-averaged quantity <q> is given by:

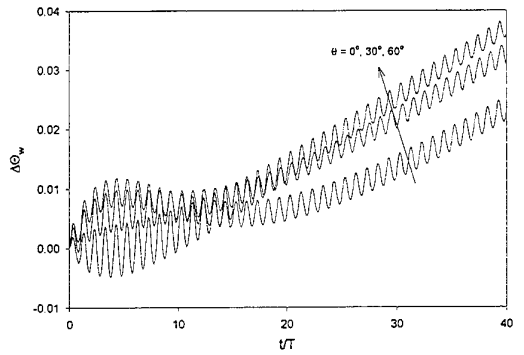
$$< q > (r,t) = \frac{1}{2\pi}\int_0^{2\pi} q(r,\theta,t)d\theta .$$

Figure 2(a) shows the transient development of the enhanced cooling of surface temperature on the cylinder wall during the first 100 cycles. Here, $\Delta\Theta$ is defined as $\Delta\Theta = \Theta_{st} - \Theta$ to represent the enhanced temperature change due to flow oscillations, and the subscript w donates the value on the cylinder wall. It should be reminded that a positive value of $\Delta\Theta$ implies an enhanced cooling.

From fig. 2(a), it appears that the mean values of $\Delta\Theta_w$ at θ = 0°, 30° and 60° all increase monotonically after the first 20 cycles. To demonstrate the initial thermal response to the flow oscillation, the first 40 cycles are enlarged and shown in fig. 2(b). It can be seen that during the first 20 cycles, the oscillation amplitude are still changing. In addition, the mean values of the curves at different θ switch their trends and even cross each other. Explanation will be given later.



(a) first 100 cycles.

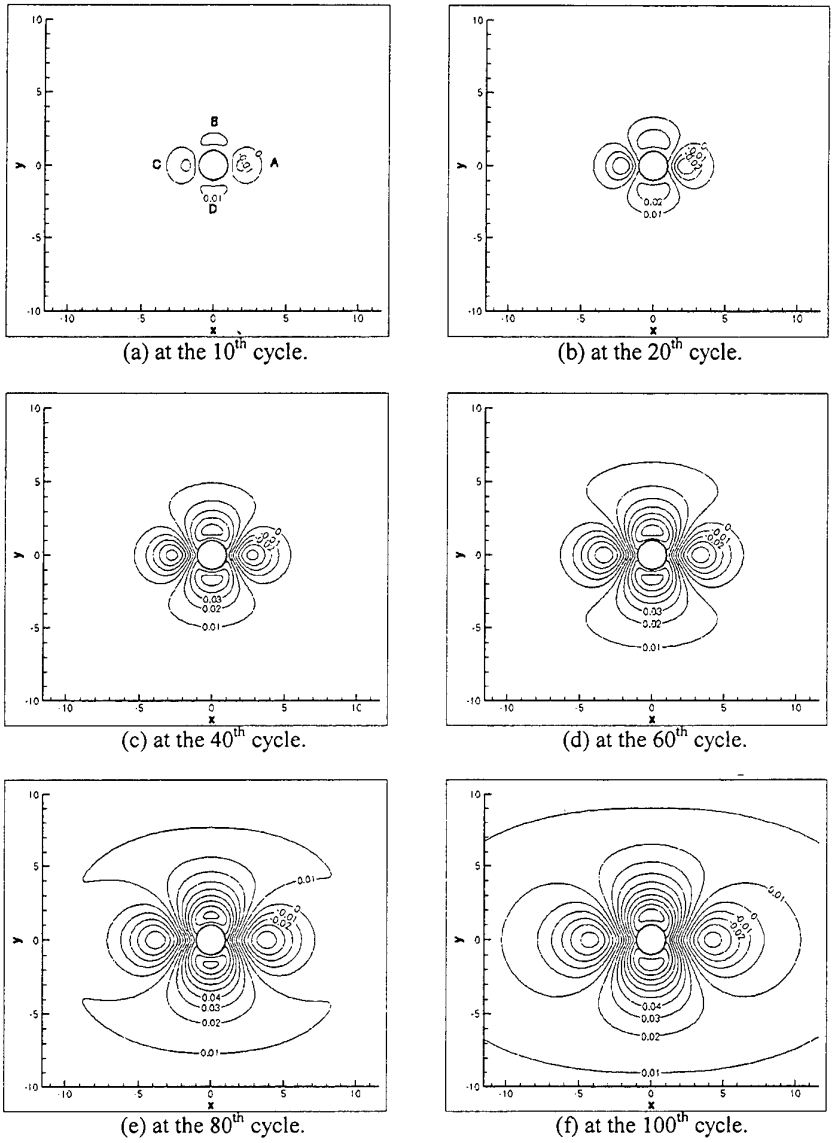


(b) first 40 cycles..

Fig. 2. Transient development of $\Delta\Theta$ on the wall at various θ.

To demonstrate how the mean temperature field responses to the convective cooling due to oscillating flow, the contours of the period-averaged $\Delta\overline{\Theta}$ at different oscillation cycles are plotted in fig. 3. Note that each closed contour represents the location where the local temperature change caused by flow oscillation is the same. In each figure, four regions are found, two on the x- and two on the y-axis. These regions are symmetrical with respect to the two axes. For convenience, these four regions are denoted as A, B, C and D respectively, as labeled in fig. 4(a) as an example. The values of $\Delta\Theta$ in regions B and D at different the cycles are all positive, whereas those in regions A and C are negative

(i.e. temperature is higher than that of stagnant conduction). This redistribution of the temperature is associated with the secondary mean flow named streaming, of which the transient streaming patterns are given next in fig. 4.



(a) at the 10th cycle. (b) at the 20th cycle.

(c) at the 40th cycle. (d) at the 60th cycle.

(e) at the 80th cycle. (f) at the 100th cycle.

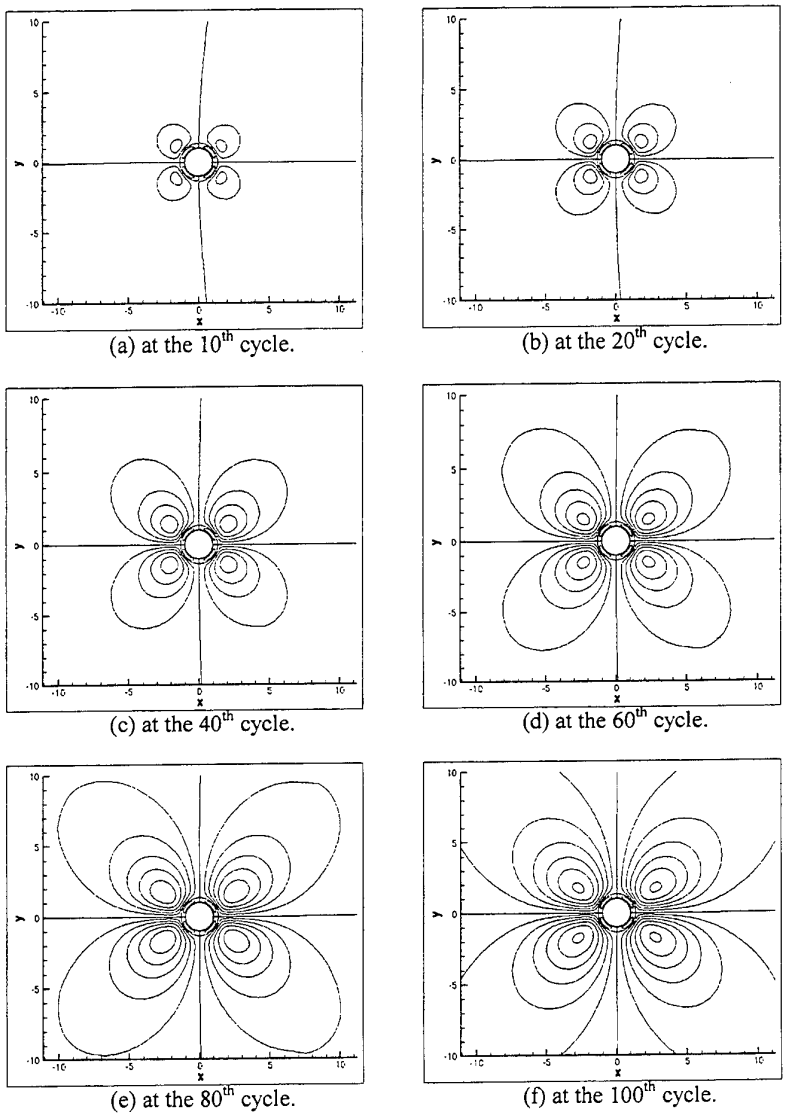
Fig. 3. Transient development of heat transfer enhancement. The labels on the closed contours are $\Delta\overline{\Theta}$.

In fig. 4, the streamlines of the secondary mean flow as computed from the period-averaged velocities are plotted. Here, the stream function ψ is defined as:

$$\frac{\partial \psi}{\partial \theta} = r u_r, \quad \frac{\partial \psi}{\partial r} = -u_\theta .$$

In the figures, it can be seen that there are eight recirculation cells (four inner and four outer) at all times, in agreement with the observation by Tatsuno [17]. The pattern becomes symmetrical with respect to both x and y axes at the 100th cycle. In the first quadrant, the inner cell re-circulates in the clockwise direction, while the outer cell in the counter-clockwise direction. The direction of this mean circulation reverses in the fourth quadrant. Therefore, along the positive x-axis, the circulation of the inner cells carries the cold fluid towards the cylinder surface, whereas that of the outer cells carries the hot fluid toward the outer boundary. As a result, the local temperature deviation in region A as

shown in fig. 3 increases. In fact the temperature redistribution is attributed to the convection effect from both the first order oscillation and the secondary streaming. The contribution due to first order oscillation is the consequence of the correlation between the oscillations in velocity and temperature, and is confined in the inner region near the cylinder. On the other hand, the contribution due to secondary streaming is the convection of the secondary mean circulating flow against the mean temperature gradient, and is dominant in the outer region of the cylinder. As a result, as the inner domain is cooled by the oscillation correction, it is expected that the temperatures in regions A and C will eventually move to the outer region as shown in fig. 3(e)-(f).



(a) at the 10^{th} cycle. (b) at the 20^{th} cycle.

(c) at the 40^{th} cycle. (d) at the 60^{th} cycle.

(e) at the 80^{th} cycle. (f) at the 100^{th} cycle.

Fig. 4. Transient streaming patterns. Two nearby contours represent the difference in $\overline{\psi}$ being 0.008.

The transient development of $\Delta\overline{\Theta}_w$ distribution over on the upper-half of the cylinder is shown in fig. 5. Due to heating effect in regions A and C, the value of $\Delta\overline{\Theta}_w$ in all the curves is lowest (hottest) at $\theta = 0^\circ$ and 180° (except the one at the 10^{th} cycle), and becomes leveled in $45^\circ < \theta < 135^\circ$. At the 10^{th} cycle (see fig. 4), the outer recirculation cells are still weak but the inner cells have been fully developed. The inner cells transport the cold fluid towards the two (left and right) stagnation points of the cylinder and bring the hot fluid away from the top and bottom ends of the cylinder. As a result, the lowest value of $\Delta\overline{\Theta}_w$ occurs at $\theta = 90^\circ$. This phenomenon also explains the initial transient behavior of $\Delta\Theta_w$ in fig. 2.

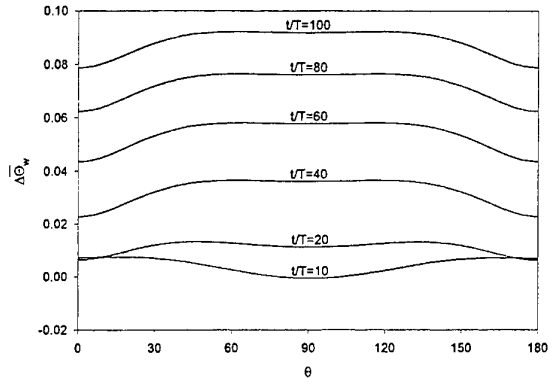


Fig. 5. The distribution of mean temperature drop $\Delta\overline{\Theta}_w$ over the cylinder surface at different cycles of oscillation.

Figure 6 shows the results of $\Delta < \overline{\Theta} >_w$ in the first 100 cycles, which is the angular-averaged values of $\Delta\overline{\Theta}_w$. It also represents the averaged mean temperature drop on the cylinder surface as cooled by the oscillating flow. This averaged value is always positive, i.e., the cooling of the cylinder increases monotonically during the entire computation. Apparently, the cooling of the cylinder does not reach the steady state at the end of 100 cycles of flow oscillation.

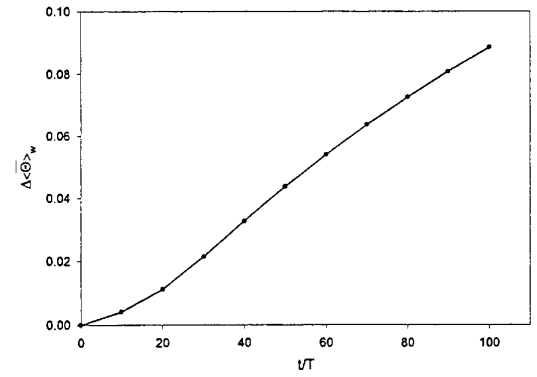


Fig. 6. The averaged surface temperature drop $\Delta < \overline{\Theta} >_w$ during the first 100 cycles of oscillation.

6. CONCLUSING REMARKS

Enhanced heat transfer in oscillating flows past a circular cylinder has been studied for the first 100 cycles, and the transient temperature change was illustrated graphically. The results of the present study show that, due to the flow direction of secondary streaming, redistribution of heated fluid generated two heated regions near the left and right stagnation points of cylinder. Despite the existence of these heated regions, it is also found that the value of $\Delta < \overline{\Theta} >_w$ is always positive (i.e. cooling) and increases with time. The results of fig. 6 shows that the surface cooling of the circular cylinder continues even after 100 cycles of oscillations, while the oscillating flow is basically stationary. The slow development of the mean temperature then becomes a challenging task in numerical computation, because of its long time scale as compared with the short time scale of flow oscillation. The details on tackling this long time scale problem will be presented in the next paper.

ACKNOWLEDGEMENT

This work was supported by the grants RI95/96.EG15, HKUST815/96E and HKUST6165/98E of Hong Kong SAR Government.

REFERENCES

1. T. Sarpkaya, 1986, "Force on a Circular Cylinder in Viscous Oscillatory Flow at Low Keulegan-Carpenter numbers," *Journal of Fluid Mechanics*, vol. 165, pp. 61-71.
2. M. Tatsuno and P. W. Bearman, 1990, "A visual study of the flow around an oscillating circular cylinder at low Keulegan-Carpenter numbers and low Stokes numbers," *Journal of Fluid Mechanics*, vol. 211, pp. 157-182.
3. S. W. Churchill and B. Bernstein, 1977, "A correlating equation for forced convection from gases and liquids to a circular cylinder in crossflow", *Journal of Heat Transfer*, vol. 99, pp. 300-306.
4. D. Karanth, G. W. Rankin and K. Sridhar, 1994, "A finite difference calculation of forced convective heat transfer from an oscillating cylinder," *International Journal of Heat and Mass Transfer*, vol. 37, no. 11, pp. 1619-1630.
5. C.-H. Cheng, J.-L. Hong, and W. Aung, 1997, "Numerical prediction of lock-on effect on convective heat transfer from a transversely oscillating circular cylinder," *International Journal of Heat and Mass Transfer*, vol. 40, no. 8, pp. 1825-1834.
6. U. C. Saxena and A. D. K. Laird, 1978, "Heat transfer from a cylinder oscillating in a cross-flow," *Journal of Heat Transfer*, vol. 100, pp. 684-689.
7. C.-H. Cheng, H.-N. Chen and W. Aung, 1997, "Experimental study of the effect of transverse oscillation on convection heat transfer from a circular cylinder," *Journal of Heat Transfer*, vol. 119, pp. 474-482.
8. J. Kim and P. Moin, 1985, "Application of a fractional-step method to incompressible Navier-Stokes equations," *Journal of Computational Physics*, vol. 59, pp. 308-323.
9. S. V. Patankar, 1980, *Numerical Heat Transfer and Fluid Flow*, Hemisphere, Washington, DC.
10. C. H. Chen and F. B. Weng, 1990, "Heat Transfer for incompressible and compressible fluid flows over a heated cylinder," *Numerical Heat Transfer*, part a, vol. 18, pp. 325-342.
11. S. C. R. Dennis, J. D. Hudson and N. Smith, 1968, "Steady laminar forced convection from a circular cylinder at low Reynolds number," *Physics of Fluids*, vol. 11, pp. 933-940.
12. P. C. Jian and B. S. Goel, 1976, "A numerical study of unsteady laminar forced convection from a circular cylinder," *Journal of Heat Transfer*, vol. 98, pp. 303-307.
13. R. Hilpert, 1933, "Wärmeagabe von geheizten Drähten and Rohren im Luftstrom," *Forschungsarbeiten auf dem Gebiete des Ingenieurwesens*, vol. 4, pp. 215-224.
14. K. M. Krall and E. R. G. Eckert, 1973, "Local heat transfer around a cylinder at low Reynolds number," *Journal of Heat Transfer*, vol. 95, pp. 273-275.
15. W. H. McAdams, 1954, *Heat Transmission*, McGraw Hill, New York.
16. T. Tsubouchi and H. Masuda, 1967-68, "On the experimental formulae of heat transfer from single cylinders by forced convection," *Reports of the Institute of High Speed Mechanics*, vol. 19, pp. 221-239.
17. M. Tatsuno, 1973, "Circulatory streaming around an oscillating circular cylinder at low Reynolds numbers," *Journal of the Physical Society of Japan*, vol. 35, no. 3, pp. 915-920.

K. Solar Energy and Nuclear Energy

NUMERICAL INVESTIGATION OF THE FLUID FLOW AND HEAT TRANSFER IN A SOLAR DOMESTIC HOT WATER STORE WITH A MANTLE HEAT EXCHANGER FOR THE SOLAR LOOP

E. Hahne, H. Mandel, H. Drück
Institut für Thermodynamik und Wärmetechnik (ITW)
Universität Stuttgart, Germany
Pfaffenwaldring 6; 70550 Stuttgart
Email: mandel@itw.uni-stuttgart.de; Fax: +49(0)711 685 3503

Keywords: solar heating, thermal store, TRNSYS simulation, CFD-analysis

ABSTRACT. In order to obtain a high solar fraction *f* with a thermal solar system for domestic hot water supply, it is desirable to build up and maintain as long as possible a thermal stratification in the hot water store. For this purpose, special precautions must be taken while charging the store with hot fluid from the collector loop. One concept to charge the store in a stratified way is to use a store with a mantle heat exchanger. A TRNSYS [1] simulation study with idealized assumptions shows, that this store concept could improve the efficiency of solar domestic hot water systems considerably. In order to investigate in greater detail the possibilities of charging a store in a stratified way by using a mantle heat exchanger, numerical simulations of the fluid flow and heat transfer phenomena inside the annular gap have been carried out. The commercial Computational Fluid Dynamics (CFD)-software FLUENT has been used for this purpose.Two-dimensional as well as three-dimensional models were used. Because of the transient process of charging a long calculation time is required. Hence only the fluid flow and the heat transfer in an annular gap are examined. Thermal stratification inside the gap was assumed as initial condition. Both the area around the inlet pipe as well as the entire geometry are investigated in detail. The results show that charging in a stratified way works well if the incoming fluid is hotter than the fluid at the top of the annular gap. In the case of charging the annular gap with a relatively cold fluid, the stratification is partly destroyed in the upper part of the gap. In the bottom part on the other hand, where the temperatures are lower than that of the charging fluid, the stratification is widely preserved. Concluding it can be said that stores with a mantle heat exchanger can be considered a very interesting alternative to existing store concepts, that make great efforts to obtain and maintain thermal stratification.

1. INTRODUCTION

In many Central European countries and particularly in Germany there is an increasing market for thermal solar systems for domestic hot water supply and space heating. They usually consist of a collector, a hot water store, an auxiliary heat exchanger and a controller. In recent years they have more and more been developed into high-tech systems, see Fig. 1. The hot water store is charged on sunny days via a solar loop. It generally contains a water-glycol mixture as heat transfer fluid. The store is discharged via the domestic hot water loop. A conventional boiler (auxiliary heater) is used to maintain the temperature level (e.g. 60°C) in the top of the store (e.g. during bad weather periods). Finally the controller ensures the correct operation of the entire system. One of the central components determining the solar fraction *f* is the hot water store. Hence this component will now be considered in detail.

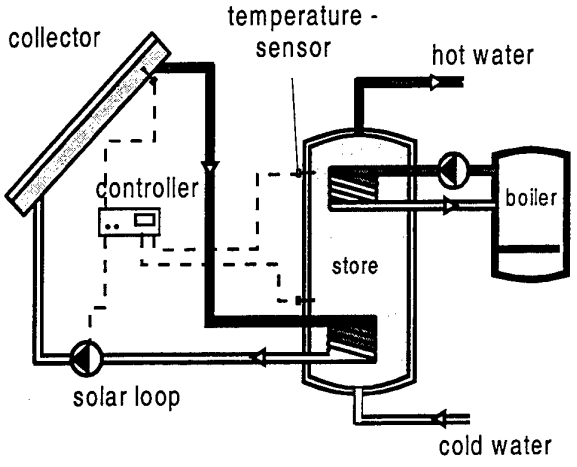


Fig. 1. Schematic construction of a conventional solar system for domestic hot water preparation

As mentioned before the hot water store is discharged via the domestic hot water loop. Hot

water is taken from the upper part of the store while cold water is supplied to the the bottom of the store, see Fig. 1. Because of its higher density, the cold water remains in the lower part of the store and a temperature stratification will develop. If necessary, the water in the upper part of the store is maintained at a preset temperature with an auxiliary heater. Therefore, this part will be called "auxiliary volume" V_{aux}. The size of this volume is a criterion for the comfort of the solar system for domestic hot water supply and must be adapted to the user's behaviour. In conventional stores, the fluid from the solar loop enters the heat exchanger in the lower part of the store and is cooled down. Hence this part of the store will be called solar volume V_{Sol}. The aim is to maintain a thermal stratification inside the store, so that the preset temperature is better kept and auxiliary heat is saved. In addition, the temperature of the heat transfer fluid leaving the heat exchanger towards the collector will be lower than within a fully mixed store. This decreases the "reduced temperature difference" $T^*_m = (\vartheta_{fl,m} - \vartheta_{am}) / E_{glob,C}$ of the collector and leads in turn to a higher collector efficiency η. In this equation $\vartheta_{fl,m}$ is the mean collector temperature, $E_{glob,C}$ the irradiation in the collector plane and ϑ_{am} the ambient temperature.

Finally, a comparison of two stores having the same internal energy but one is stratified, the other fully mixed, shows that the availability $E_{x,S}$ of the stratified store is larger than that of the fully mixed one, according to equation (1), see [2]:

$$E_{x,s} = m_s \cdot c_s \left[(T_s - T_{am}) - T_{am} \cdot \ln \frac{T_s}{T_{am}} \right] \qquad (1)$$

with m_s being the mass, c_s the specific heat, T_s the Kelvin temperature of the store and T_{am} the ambient Kelvin temperature.

The inevitable heat transport by conduction in the water and in the walls of the store will gradually destroy any stratification. Since this kind of heat transport is relatively slow, the temperature stratification nevertheless can be considered as quasi –stationary. This is shown by a simple theoretical example in which heat is transported by conduction in a water column of the height $H_S = 1.5$ m (conduction in the wall of the store and heat losses to the surroundings are neglected). A temperature step profile is chosen as initial condition with a temperature of 60°C in the top half, and 20°C in the bottom part of the store. Since the temperature profile is stable, no convection occurs. The results show, that the step profile changes very slowly. It takes 10 hours until a gradient zone occurs in 1/3 of the entire store height, see Fig.2. This time interval is approximately the maximum time period between two discharges by the user. With an immersed heat exchanger in the lower part of the store the temperature there rises very quickly. When around noon, the highest collector temperatures are reached, the natural convection from the solar heat exchanger will destroy any temperature stratification and a more or less uniform temperature is obtained within the store. Compared to the stratified situation the temperature will be lower in the top part and higher in the bottom part. With an increased temperature around the solar heat exchanger it might well be that the decreasing irradiation in the afternoon cannot be used or only to a small extent. For such a case the mantle heat exchanger is assumed to be useful. It is formed by a mantle around the actual store, with the fluid flowing in the annulus around the storage vessel, Fig. 3.

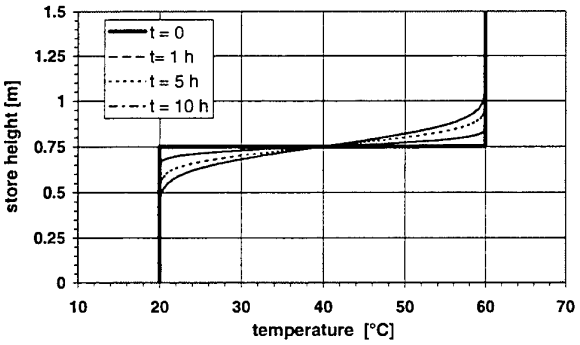


Fig. 2. Dismantling of stratification due to conduction

In order to minimize heat losses to the surroundings, the water for domestic use is stored in the inner tank. The inlet of the solar loop is connected to the top of the outer tank. The oulet is connected to the bottom of the outer tank, opposite to the inlet. Thus the fluid of the solar loop flows from top to the bottom of the annular gap and with a low flow rate it can be expected, thermal stratification develops in the gap and stratification will be preserved in the entire store.

If the fluid entering the gap is colder than the water in the auxiliary part of the store, it can be expected, that, it will quickly sink down to a level, where its temperature roughly matches its surroundings. If on the other hand, the fluid is hotter than the auxiliary part, heat transfer occurs immediately. Whether this really happens will be checked in the following chapters with a detailed numeric simulation of the flow field in the annulus.

2. THERMAL SOLAR SYSTEM WITH A STORE USING A MANTLE HEAT EXCHANGER

A TRNSYS-simulation study was carried out. For reference two systems were used: one with a flat plate collector (FPC) and the other with an evacuated tube collector (ETC) [3]. Each system was investigated with both, a conventional heat exchanger and a mantle heat exchanger. The solar fraction f of either configuration is compared to that of the reference system. Two modes of charging the mantle heat exchanger are assumed: stratified and not stratified. The solar fraction is a measure for the savings of fossil fuel. Meteorological data for simulating one year of operation are those of the test reference year of Würzburg. Hot water demand was modelled for a typical Central European four person's household (Q_{load} = 2937 kWh/a corresponding to a total consumption of 200 l/d of hot water at a temperature of ϑ = 45°C. The required temperature is adjusted by mixing the hot water from the auxiliary part of the store (60°C < ϑ <95°C) with cold water of a temperature ϑ = 10°C. Hot water is drawn from the store at three different times of the day (80 l at 7 p.m. and 7 a.m. and 40 l at noon). The mass flow rate of the respective hot water discharges is $\dot{m}_{load}$ = 396 kg/h. The remaining data of the individual components of the reference systems (e.g. collector efficiency, control strategy, ...) were taken from well designed systems investigated in a comparison test, performed at the ITW for a German consumer magazine [4]. For charging the store ($\dot{m}_{sol}$ = 50 kg/(h m^2 collector area)) with the mantle heat exchanger two cases were examined: In the first the fluid from the solar loop enters the store at the top, in the second case the fluid enters the gap below the auxiliary volume of the store (in this example the auxiliary volume occupies the upper half of the store), see Fig. 3. Here, heat transfer occurs only in the solar part and not in the auxiliary part. The results of the simulations are summarized in Table 1.

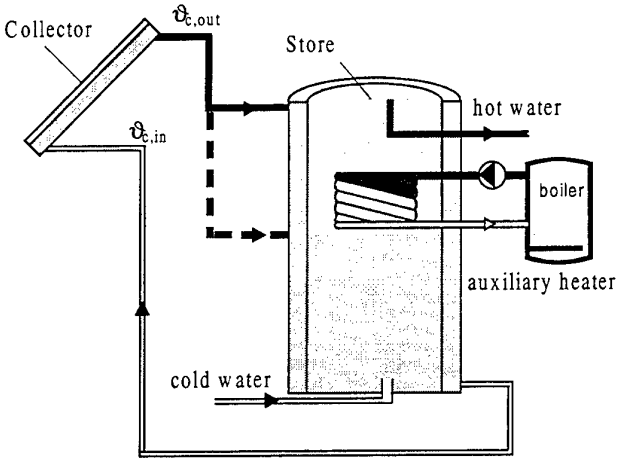


Fig. 3. Scheme of a solar system using a mantle heat exchanger

Table 1. Comparison of the Solar Fraction of Different Solar Systems

	reference system	system with mantle heat exchanger (collector hot leg at half height)				system with mantle heat exchanger (collector hot leg at top)			
		with stratified charging		without stratified charging		with stratified charging		without stratified charging	
	f [%]	f [%]	Δf [%]	f [%]	Δf [%]	f [%]	Δf [%]	f [%]	Δf [%]
system with FPC	46,76	47,06	0,3	45,50	-1,26	47,51	0,75	16,5	-30.26
system with ETC	49,85	50,64	0,79	48,40	-1,45	50,87	1,02	27,7	-22,15

The results show, that the solar fraction f increases only when stratification is maintained during charging. If this is not the case, the solar fraction is reduced drastically. The cause for this is, that under operating situations with collector hot leg temperatures being below those of the heated part of the store, heat is removed from the top to the lower part of the store.

That means, that the auxiliary part has to be heated in turn by the auxiliary heater and the back flow to the collector is raised, due to the higher temperature in the solar part of the store. It is possible to avoid this effect by decreasing the mass flow rate in the solar loop. With these so-called "low flow systems" the temperature at the collector outlet increases quickly. Moreover, the impulse of the incoming fluid is small, so that the thermal stratification is not penetrated. Fünfgeld [5] determined improvements of the solar fraction up to 10% (relative) for low flow systems ($\dot{m}_{sol}$ = 10 ÷ 20 kg/(h m^2 collector area)) with charging stratified. But such improvements are only possible for solar fractions f below 40%. They will become smaller for systems with f more than 50%. Since the preservation of the thermal stratification during charging appears to be crucial for the improvement, a CFD- analysis of fluid flow and heat transfer in the annular gap is performed.

3. CFD-ANALYSIS OF FLUID FLOW AND HEAT TRANSFER IN THE ANNULAR GAP OF A STORE WITH A MANTLE HEAT EXCHANGER

The results, presented in the section above, show, that solar systems for domestic hot water supply using a low flow concept combined with a mantle heat exchanger only have advantages over conventional systems, if the assumption was made, that thermal stratification is preserved. Whether this assumption is justified will be shown by a numerical simulation of the transient charging process. The commercial CFD-package FLUENT/UNS [6] is used for this purpose. It solves the Navier-Stokes equations with a finite volume method.

The superposition of forced convection and free convection, makes it relatively difficult to solve the problem numerically. The buoyancy forces due to density differences are normally described by means of the Bousssinesq- approximation. Gray and Giorgini [7] have derived a number of criteria for the validity of the Bousssinesq- approximation. Three of these criteria are:

$$\left|\frac{\beta \bar{g} L}{c_P}\right| \mathrm{Pr} \le 0.1 \qquad \left|\frac{1}{\beta}\frac{d\beta_\infty}{dT}\Theta\right| \le 0.1, \qquad \left|\frac{\beta \bar{g} L}{c_P}\frac{T_\infty}{\Theta}\right| \le 0.1, \qquad (2)$$

with $\Theta = (T_H - T_C)$, denoting the maximal temperature difference, β the volumetric thermal expansion coefficient, $\bar{g}$ the gravitational acceleration and L the characteristic length.

When combined, the three relationships enclose the gray colored domain in Fig. 4 in which the Boussinesq-approximation is valid results for water of ϑ = 15°C. For the store considered here, the operation conditions seem to fall outside the area of validity. Merker [8] points out however, that these restrictions are too severe and the Boussinesq-approximation has a greater range of validity. Therefore, further considerations should be made. In Fig. 5 and Fig. 6 the density differences $\Delta\rho = \rho(\vartheta)$ $\rho(40°C)$ for water and for a water-glycol- mixture are presented. Tabulated values are used for the density of water and water- glycol, respectively, see [9]. The density difference was also determined with the Boussinesq approximation. The deviations are very small for the water glycol mixture. The deviations are comparatively large for water and low temperatures. Whether the Boussinesq approximation can be applied or not, and whether a turbulence model has to be employed for the numerical simulation of the fluid flow in the annulus will be checked with a simplified two-dimensional example.

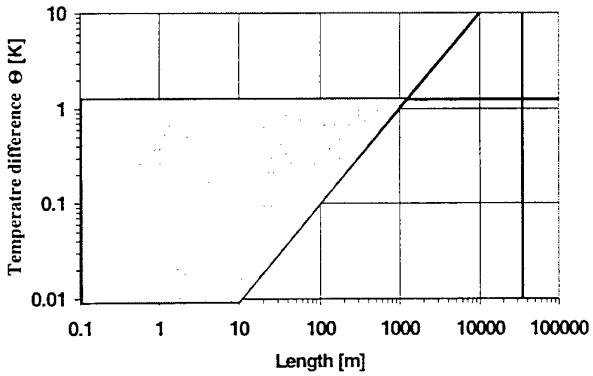


Fig. 4. Range of validity of the Bousinesq-approximation for water (ϑ_∞ = 15°C and p_∞=1,013 bar)

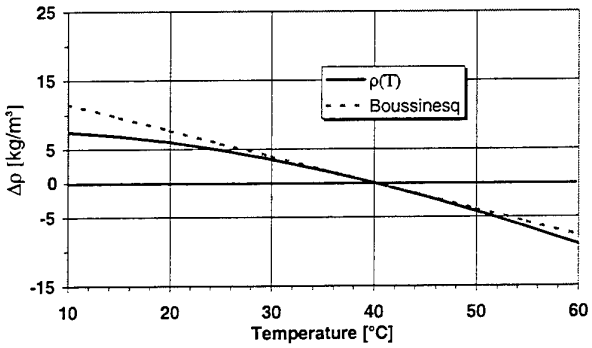


Fig. 5. Temperature dependency of the density difference for water

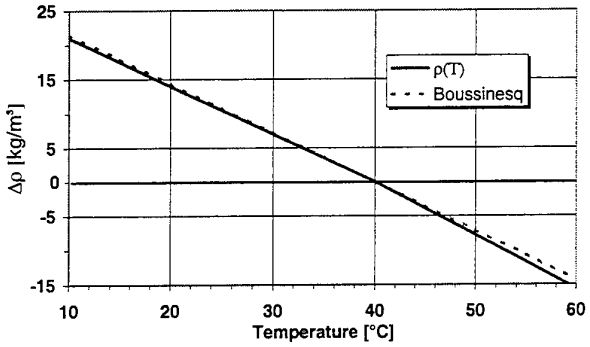


Fig. 6. Temperature dependency of the density difference for water-glycol

3.1 Two-Dimensional Calculations

Because of the large requirement on "Central Processing Unit" CPU-resources the preliminary investigations are carried out for a two-dimensional model which corresponds to a section of the annulus, Fig. 7. The section extends over half the store- height and 1/3 of the mantle circumference in length. Although not all physical processes are considered with this two-dimensional model, this investigation offers the possibility, to gain an impression of the effect of different simulation conditions. Starting again from a reference case, see Table 2, further calculations with different simulation parameters are carried out (e.g., the use of a turbulence model, or temperature-dependent density, ...).

Table 2. Data of the Reference Model

Geometry		**Initial- and boundary condition**	
Height	H_S = 1,2 m	Inlet	parabolic velocity profile, with w_m= 0,084 m/s ϑ_{in} = 50 °C resp. 70°C
Length	L = 0,78 m		
Inner ∅ d_i	D_i = 0,48 m		
Pipe ∅	d_{Rohr}=0,016	Outlet	const. pressure
Length	s_1 = 0,1 m	Wall	outer surface: adiabat, inner surface: temperature profile
Distance	s_2 = 0,02 m	Initial temperature	ϑ_0=60

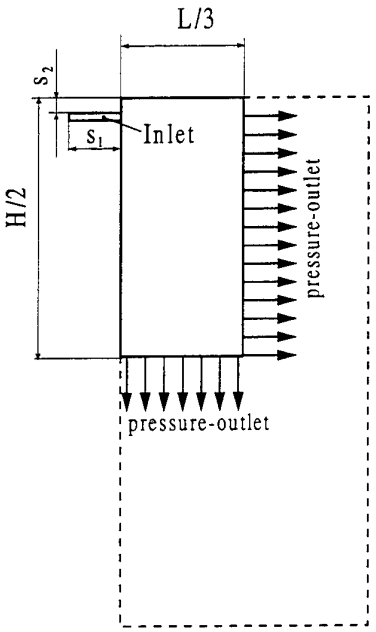


Fig. 7. Geometry of the two- dimensional investigations

The inlet velocity of the water-glycol-mixture (30 % glycol) corresponds to that of a low flow system. Therefore, a laminar fluid flow in the annular gap is assumed for the reference case. For the coupling of pressure and the velocity a SIMPLE-method is used. The buoyancy forces in the momentum equation are described by the Bousssinesq approximation. The time increment for the simulation is Δt =0,01 s. The grid of the calculated section has 9636 volume elements. The velocity field in the annular gap was initialized with that of a stationary isothermal fluid flow.

Two cases are examined: The fluid entering the annular gap is either colder (ϑ_{in} = 50°C) than that in the auxiliary heating part (ϑ_{in} = 60°C) or hotter (ϑ_{in} = 70°C). The thermophysical properties for the fluid correspond to a water-glycol mixture (30 % glycol) with 40°C [9].

The temperature fields, resulting from different simulations conditions for the first case an after 42 seconds, are shown in Fig. 8. Due to the density difference, the colder fluid entering the gab, always sinks down. Consequently the stratification can be maintained in principle. The results determined with the RNG-k-ε turbulence –model ($k = 7 \cdot 10^{-5}$ m^2/s^2, $\varepsilon = 9 \cdot 10^{-5}$ m^2/s^3) are almost identical to those of the reference case. The difference between the two results of a simulation, which were computed with a and this one, calculated with the, are already more visible. Switching from the Boussinesq approximation to the use of a temperature dependent density lead to more visible differences.

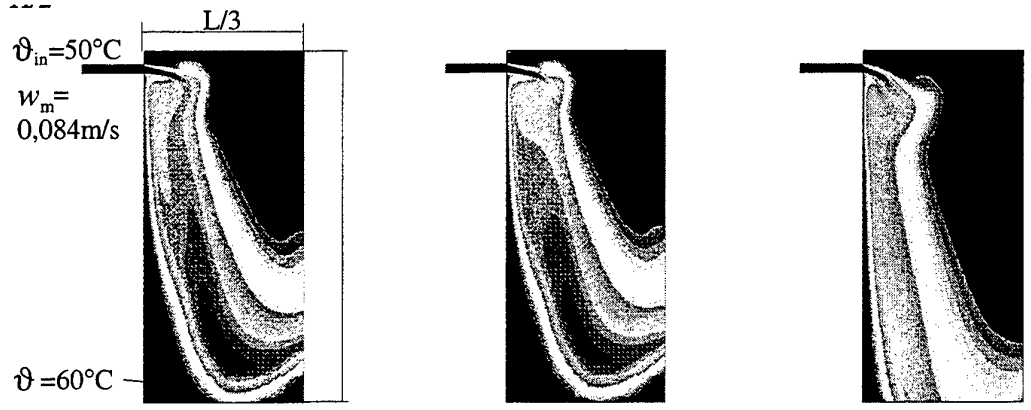


Fig. 8. Temperature fields after 42 seconds of charging the hot water store with 50°C warm water

Qualitatively, the results of all three calculations agree well. But in the calculation with the temperature dependent density, the incoming colder fluid stretches further downwards than in the reference. The boundary layer grows less quickly. This indicates that the buoyancy forces are underpredicted by the Boussinesq Approximation. The conclusion of the first simulations is, that the use of a turbulence model is unnecessary. Despite the differences between the results with and without the Boussinesq approximation, the approximation will be further retained, because of the comparability to the reference case. Charging the store with a relatively hot fluid (ϑ_{in} = 70°C) is shown in Fig. 9. Here the hot fluid is stratified in the upper part of the store, see Fig. 9. All results obtained so far, agree with Furbo and Shah's [10] results. The authors examined a store with a "mantle tank" experimentally and concluded that a thermal stratification could be developed and maintained.

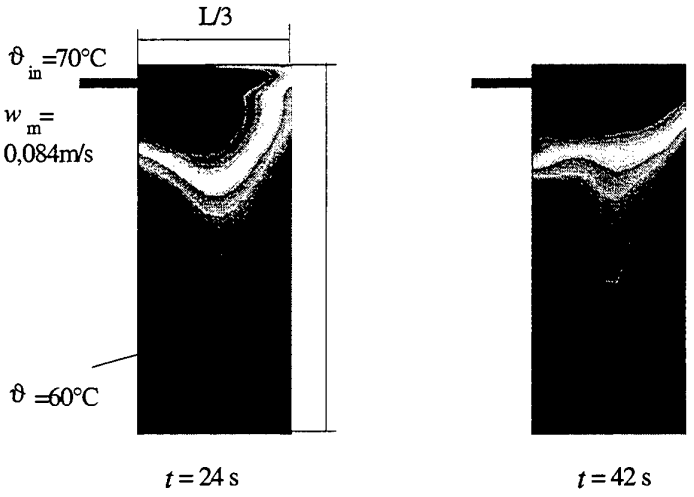


Fig. 9. Temperature fields after 42 seconds of charging the hot water store with 70°C hot water

Finally the results will be confirmed by means of a three-dimensional calculation, presented in the following.

3.2 Three Dimensional Calculations

The examined geometry is shown in Fig. 10. Table 3 lists some of the data necessary for the simulation. In order to limit the CPU time, the water in the inner tank was not modelled. Due to symmetry only half of the annulus is

modelled. The starting temperature of the fluid in the upper half of the annulus ($H_S > 0{,}6$ m) is $\vartheta_0 = 60°C$. This initial condition is obtained when the upper half of the hot water store is kept at this temperature by the auxiliary heater. In the lower part of the store, up to a height of $H_S = 0.2$ m, the initial temperature is 20°C. This condition is the result of discharging, when cold water flows into the lower part of the store. In the section between these temperatures ($0{,}2 < H_S < 0{,}6$), a linear temperature profile from 20°C to 60°C is assumed. A time step of $\Delta t = 0{,}001$ s is used for the simulations.

Table 3. Data for the Calculation of the Entire Geometry

Geometry		**Initial- and boundary condition**	
Height	$H_S = 1{,}2$ m	Inlet	parabolic velocity profile with $w_m = 0{,}084$ m/s $\vartheta_{in} = 50$ °C resp.. 70°C
Outer ∅	$D_a = 0{,}52$ m		
Inner ∅	$D_i = 0{,}48$ m		
Pipe∅	d_{pipe}=0,016	Outlet	const. pressure
Length	$s_1 = 0{,}1$ m	wall	outer surface: adiabatic, inner surface: temperature profile
Distance	$s_1 = 0{,}02$ m	Initial temperature	ϑ_0=20°C for H_S<0.2 m 20°C<ϑ_0<60 for 0.2m <H_S <H_S< 0.6 m ϑ_0=60°C for H_S>0.6 m
Number of elements	90606		

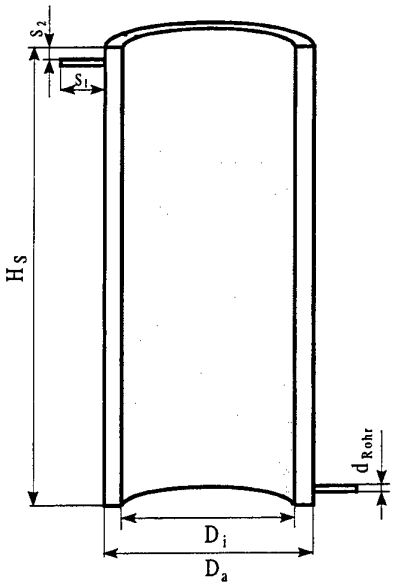


Fig. 10. 3D-Geometry

The temperature distributions in the annular gap at different times of charging with warm fluid of $\vartheta_{in} = 50°C$ are presented in Fig. 11. It can be seen, that the incoming fluid sinks down directly after the inlet, because of the effect of gravity. In the course of its flow, the sinking fluid meets colder fluid levels and the temperature gradient (responsible for the sinking) decreases. Consequently, the sinking cold front broadens. As soon as the sinking fluid meets a fluid colder than itself, the flow direction reverses. This phenomenon can be explained as the result of a sort of impact. The same flow pattern can be observed in experimental investigations [11]. In the bottom part, where the temperatures are lower than those of the charging fluid, the stratification is preserved. Summarizing it can be said, that in this case, the thermal stratification is preserved during charging the store. The heat will be stored in a stratified way.

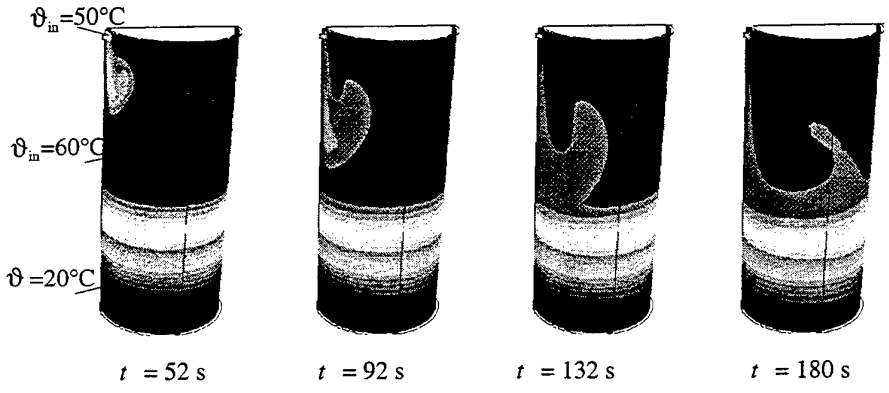


Fig. 11. Temperature field in the annular gap for different times during charging with warm fluid of 50°C (temperature scale from 20°C to 60°C)

Finally charging is examined with fluid ($\vartheta_{in} = 70°C$) hotter than the water in the store ($\vartheta = 60°C$). The temperature field in the annular gap after 116 seconds is shown in Fig. 12. Except for the inlet temperature no other data were modified compared to the above calculation. Although a steady mass flow exists in the gap and hot fluid enters at the top while cold fluid leaves at the bottom, the temperature stratification is not disturbed. On the contrary, an additional layer of hot fluid forms at the top of the store. This is possible, because of the low flow rate. The results confirm, that charging the store at the top with hot water is uncritical.

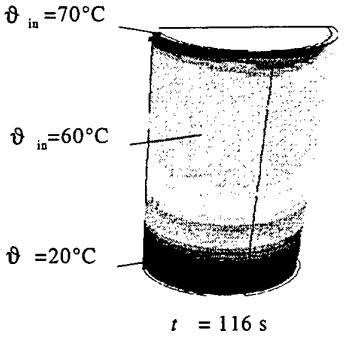


Fig. 12. Temperature field in the annular gap after 116 s, charging with hot fluid of 70°C (temperature scale from 20°C to 70°C)

4. SUMMERY

Solar stores can be improved applying low flow and a mantle heat exchanger. A TRNSYS simulation performed with the assumption that a thermal stratification is maintained, shows how much the solar fraction can be increased, when a store with a mantle heat exchanger is used in combination with a low- flow system. In order to verify that thermal stratification is preserved in the store, the fluid flow and the heat transfer in the annular gap are examined by means of a CFD analysis. The results show, that charging the store with fluid hotter than that in the store, is uncritical. In this case, the stratification survives very well. If on the other hand, the incoming fluid is colder than the auxiliary heating part of the store, a slight mixing of levels with different temperatures will occur and the stratification is partly destroyed. The stratification is still maintained in that part of the store, which is colder than the incoming fluid. The numerically determined results agree qualitatively with the results obtained by Furbo, Shah [10]. Their experiments with a low flow system combined with a store with a mantle heat exchanger also show, that the stratification is maintained.

5. REFERENCES

1. S.A. Klein, et al.: *TRNSYS, A Transient Simulation Program Version 14.1*, University of Wisconsin, Madison, USA (1994).
2. E. Hahne, *Technische Thermodynamik*, Addison-Wesley, Bonn, (1994).
3. M. Schwab, *Energetische Potentiale innovativer Speicherkonzepte bei solaren Brauchwasser-Erwärmungsanlagen*, Studienarbeit am ITW, (1996).
4. Stiftung Warentest, test spezial „Energie & Umwelt, März (1995).
5. C. Fünfgeld, M. Mack, K. Vanoli, *Low Flow, ein neues Konzept auf dem Prüfstand*, Institut für Solarenergieforschung GmbH Hameln-Emmerthal, Tagungsband zum 8. Internationalen Sonnenforum, Berlin (1992).
6. FLUENT/UNS USER'S GUIDE, Fluent Incorporeted, (1996).
7. D. Gray, A. Giorgini, *The validity of the Boussinesq approximation for liquids and gases,* International Journal of Heat and Mass Transfer, 19, 545-551, (1976).
8. G. Merker, *Konvektive Wärmeübertragung, Berlin, Heidelberg*, Springer Verlag (1987).
9. J. Straub, Stoffwerte Wasser, VDI- Wärmeatlas 7. Auflage, Abschnitt Db, VDI- Verlag Düsseldorf, (1997).
10. S. Furbo, L.J. Shah, *Correlation of experimental and theoretical Data for Mantle Tanks used in Low Flow Systems*, ISES '97, Proceedings, (1997).
11. M. Hohenstein, Doppelmantelspeicher in thermischen Solaranlagen: Systemverhalten solarer Brauchwasseranlagen, Philipps-Universität Marburg, (1994).

CHARACTERISTIC OF SOLAR COLLECTOR UTILIZING ELECTRO-HYDRO-DYNAMICAL EFFECT

Masaki Sato
Department of Electrical and Electronic Engineering
The Hachinohe Institute of Technology
Email:masaki @ hi-tech.ac.jp; Fax:81-0178-25-1430

Hidetoshi Aoki
Department of Energy Engineering
The Hachinohe Institute of Technology

Yutaka Wako
Food Technology
The Hachinohe Institute of Technology

Keywords: electro-hydro-dynamics(EHD), EHD solar collector, corona wind, heat transfer enhancement

ABSTRACT. In this paper, a solar collector utilizing electro–hydro-dynamical(EHD) effect is proposed for improvement of the collector efficiency. The EHD solar collector is cylindrical and a double structure made of glass. Between the outer cylinder and the inner cylinder, there are black round stones for thermal storage and R123 as heat transporting medium is supplied in the inner cylinder. Two line electrodes are arranged at upside of the surface of R123 and the top of the outer cylinder is covered by a disk electrode made of copper. On the disk electrode, a heat exchanger is put. By applying direct high voltage between the electrode, corona wind occurs in the vapour of R123. In result, we are able to expect heat transfer enhancement from the collector toward the heat exchanger and improvement of collector efficiency.

1. INTRODUCTION

Generally speaking, any heat transfer mechanism is complicated when an electric field is applied. Complex interactions between electric, flow and temperature fields, require, in some cases, that the governing equations be solved simultaneously. However, in the case of forced convection heat transfer with negligible natural convection, the temperature fields are determined theoretically by the flow fields. In cases of condensation heat transfer, the flow of condensate determines the heat transfer rate. Therefore, the heat transfer enhancement techniques utilizing electric fields are frequently called electro-hydro-dynamical augmentation methods of heat transfer. Earlier[1,2], one of the authors attempted to apply corona wind to improve the solar collector efficiency. In this case, a source of electricity on the market was used to cause corona wind in the vapour of R123.This paper meals with the EHD solar collector using an outdoor source with the solar cells. In this paper, it is experimentally clarified that the heat transfer is enhanced by EHD effect, that of, corona wind in the solar collector.

2. EXPERIMENTAL APPARATUS

The EHD solar collector is cylindrical and a double structure made of glass shown in Fig.1. Between the outer cylinder and the inner cylinder, there are black round stones for thermal storage and R123 as the heat transporting medium was supplied in the inner cylinder. Two line electrodes are arranged at upside of the surface of R123 and the top of the outer cylinder is covered by a disk electrode made of copper. On the disk electrode, a heat storage is put .By applying direct high voltage between the electrodes, corona wind occurs in the vapour of R123.As results, the heat transfer is enhanced from the heat collector toward the heat storage. A system of the EHD solar collector is shown in Fig.2. The outdoor source is composed of solar cell, invertor, transformer and rectifier. The output of solar cell is converted to direct high voltage by using the inverter, transformer, and the rectifier.

3. RESULTS AND DISCUSSION

The temperatures of the heat storage was compared in case of applying voltage between electrodes of the EHD

solar collector and not applying voltage. The temperatures of the heat storage are shown in Fig.3. These experiment were carried out in the month of December. It is seen that the temperature of the heat storage in case of applying voltage is higher than that of not applying voltage. The maximum difference of the temperature in two case is 4(°C). The effect of corona wind is recognized. Because the heat storage was enhanced by applying the direct high voltage between two line electrodes and the disk electrode.

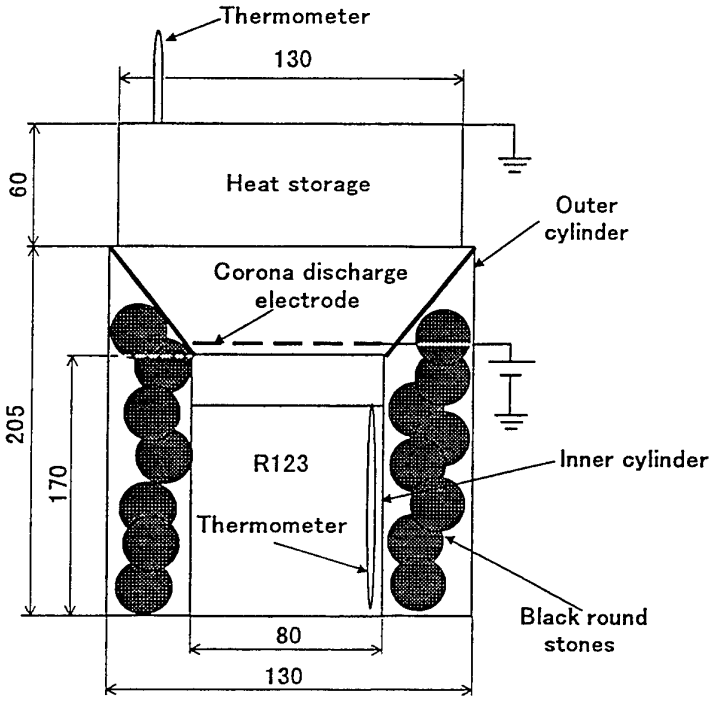


Fig.1 A schematic of the EHD solar collector

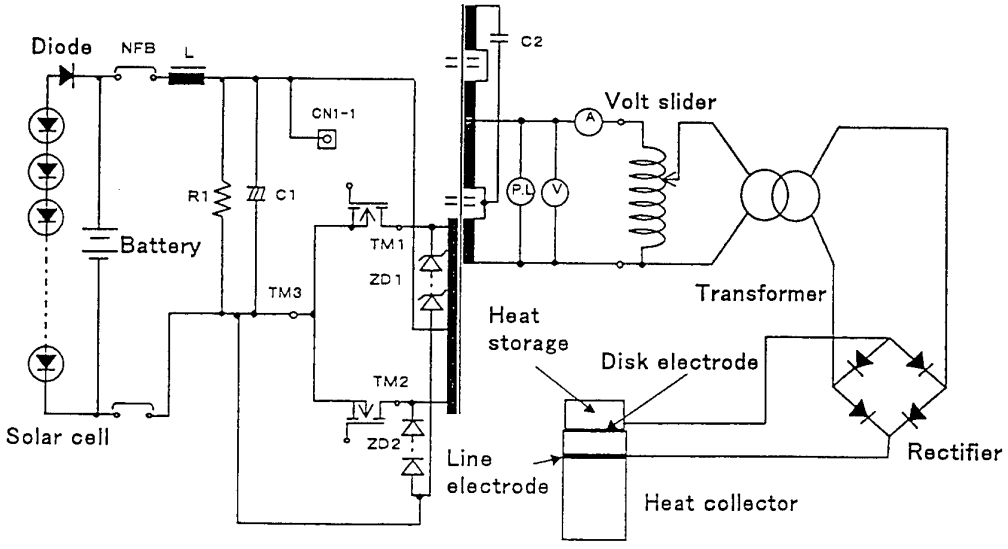


Fig.2 A system of the EHD solar collector

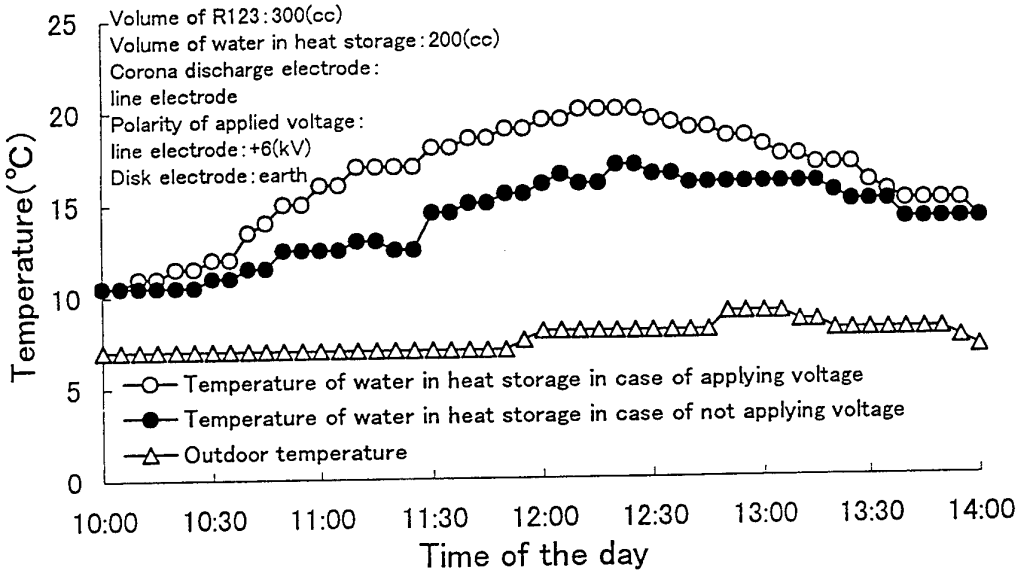


Fig.3 Water temperature in the heat storage

4.CONCLUSIONS

A system of the EHD solar heat collector was tested by utilizing the outdoor source of electricity with the solar cells. It was experimentally clarified that the temperature of the heat storage in case of applying voltage between electrode of the EHD solar collector was higher than that of not applying voltage. Namely, the effect of corona wind was recognized.

REFERENCES

1. M.Sato, H.Aoki and Y.Wako, Proceedings of JSES/JWEA Joint Conference pp.269-272(1997)
2. M.Sato, H.Aoki and Y.Wako, Proceedings of JSES/JWEA Joint Conference pp.433-435(1998)

DETERMINATION OF THE OPTIMUM CONDITIONS FOR MAXIMUM SOLAR ENERGY COLLECTION OF PLANE REFLECTOR-TILTED SOLAR COLLECTOR SYSTEMS

H.M.S. Hussein, G.E. Ahmad, and M.A. Mohamad
Solar Energy Department
National Research Centre
Email: hmshussein@hotmail.com; Fax: 00 202 3370931

Keywords: theoretical analysis, flat-plate collector, plane reflector, design parameters, operational parameters

ABSTRACT. The present paper presents theoretical analysis of the instantaneous, daily, and yearly enhancement in solar energy collection of tilted flat-plate solar collector augmented by a plane reflector. The shadow effect due to the reflector on the collector is considered in the analysis. A FORTRAN computer program has been constructed based on the analysis to optimize different operational and design parameters of plane reflector-tilted flat-plate solar collector systems. These parameters include reflector-collector system orientation and tilt angles, collector elongation ratio, and reflector overhang ratio.

1. INTRODUCTION

Fixed flat-plate solar energy devices suffer from drawbacks such as relatively high initial cost and low solar energy collection and energy output, specially, in winter when energy demand is high. The use of inexpensive plane reflectors to enhance the solar energy collection of tilted flat-plate solar collectors can provide acceptable efficiencies at higher operating temperatures with minimal tracking.

The geometrical arrangement of plane reflector-collector systems with the reflector located below the collector was investigated by McDaniels et al.[1], Baker et al.[2], and Larson [3]. They determined optimal tilts of the reflector and collector for winter space-heating applications. Other investigators analyzed the performance of a flat-plate solar collector with a single plane reflector located either south or north facing [4-7]. Their results showed that the single reflector-collector system is suitable for providing selective performance enhancement in winter or in summer. Garg and Hrishikesan [8], and Narasimha Rao et al. [9] optimized the reflectors tilt angles of a two plane reflectors-collector system with the reflectors located north/south and east/west facing, respectively. The enhancement achieved in solar collection of a horizontal flat-plate collector by four plane reflectors located south, north, east, and west facing was analyzed by Kumar et al. [10].

The present paper aims to optimize the different operational and design parameters of plane reflector-tilted flat plate solar collector systems for achieving maximum daily and yearly solar energy collection.

2. ANALYSIS

The schematic diagram of the plane reflector-tilted collector under consideration is shown in Fig.1. The plane area ABCD represents the reflector, while the tilted flat-plate solar collector is represented by EFGH. The area EFgh represents the horizontal position of the collector. To generalize the analysis for any orientation of the plane reflector-tilted flat plate solar collector system, an off-south angle (ζ) is considered. The analysis is based on the following assumptions:

1. The global solar radiation is considered in the present analysis.
2. The plane reflector is specular with a constant reflectivity ($\rho_r = 0.88$), irrespective of the radiation incidence angle.
3. The transmittance-absorptance products of the collector are functions of the incidence angles of both the incident and reflected radiation.
4. Shading of the reflector on the collector is taken in consideration.

For a unit vector (I_b) along the solar beams incident on the plane reflector corner C shown in Fig.1, the components of I_b in the coordinate system (x1, y1, z1) can be represented as follows:

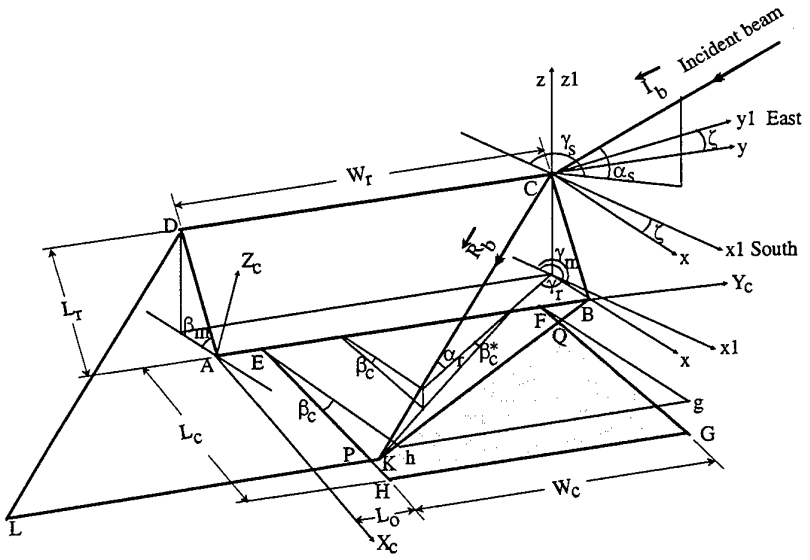


Fig. 1. Schematic diagram of the plane reflector-tilted collector system.

$$I_{b_{x1}} = \cos(\alpha_s)\cos(\gamma_s) \qquad \text{for} \quad 0 \le \gamma_s \le 360° \qquad (1)$$

$$I_{b_{y1}} = -\cos(\alpha_s)\sin(\gamma_s) \qquad \text{for} \quad 0 \le \gamma_s \le 360° \qquad (2)$$

$$I_{b_{z1}} = -\sin(\alpha_s) \qquad (3)$$

A rotation ζ about the z1-axis results in another coordinate system (x, y, z) as shown in Fig.1. Then, a rotation β_m about y-axis results in the coordinate system (x2, y2, z2) as shown in Fig.2. As a result, the components of I_b in the coordinate system (x2, y2, z2) can be expressed as follows:

$$I_{b_{x2}} = I_{b_{x1}}\cos(\beta_m)\cos(\zeta) - I_{b_{y1}}\cos(\beta_m)\sin(\zeta) - I_{b_{z1}}\sin(\beta_m) \qquad \text{for} \quad -90° \le \beta_m \le 90°, \; -180° \le \zeta \le 180° \qquad (4)$$

$$I_{b_{y2}} = I_{b_{x1}}\sin(\zeta) + I_{b_{y1}}\cos(\zeta) \qquad \text{for} \quad -180° \le \zeta \le 180° \qquad (5)$$

$$I_{b_{z2}} = I_{b_{x1}}\sin(\beta_m)\cos(\zeta) - I_{b_{y1}}\sin(\beta_m)\sin(\zeta) + I_{b_{z1}}\cos(\beta_m) \qquad \text{for} \quad -90° \le \beta_m \le 90°, \; -180° \le \zeta \le 180° \qquad (6)$$

Applying the lows of planar reflection, the components of the unit vector (R_b) along the reflected ray in (x2, y2, z2) coordinate system can be expressed as follows:

$$R_{b_{x2}} = I_{b_{x2}} \qquad \text{for} \quad -90° \le \beta_m \le 90° \qquad (7)$$

$$R_{b_{y2}} = I_{b_{y2}} \qquad (8)$$

$$R_{b_{z2}} = -I_{b_{z2}} \qquad \text{for} \quad -90° \le \beta_m \le 90° \qquad (9)$$

The components of the unit vector R_b at point C in the coordinate system (x1, y1, z1) can be expressed as follows:

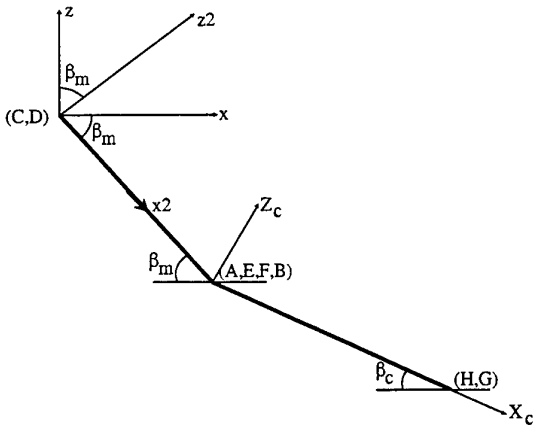


Fig. 2. Side view of the reflector-collector system showing the different coordinate systems.

$$R_{b_{x1}} = R_{b_{x2}} \cos(\beta_m)\cos(\varsigma) + R_{b_{y2}} \sin(\varsigma) + R_{bz2} \sin(\beta_m)\cos(\varsigma) \quad \text{for} \quad -90° \le \beta_m \le 90°, \; -180° \le \zeta \le 180° \tag{10}$$

$$R_{b_{y1}} = -R_{b_{x2}} \cos(\beta_m)\sin(\varsigma) + R_{b_{y2}} \cos(\varsigma) - R_{b_{z2}} \sin(\beta_m)\sin(\varsigma) \quad \text{for} \quad -90° \le \beta_m \le 90°, \; -180° \le \zeta \le 180° \tag{11}$$

$$R_{b_{z1}} = -R_{b_{x2}} \sin(\beta_m) + R_{b_{z2}} \cos(\beta_m) \quad \text{for} \quad -90° \le \beta_m \le 90° \tag{12}$$

As a result of the above analysis, the azimuth, altitude and incidence angles of the reflected beam incident on the tilted surface of the collector can be obtained as follows:

$$\gamma_r = -\tan^{-1}\left[R_{b_{y1}} / R_{b_{x1}}\right] \quad \text{for} \quad R_{b_{x1}} < 0 \;, R_{b_{y1}} \ge 0 \tag{13a}$$

$$\gamma_r = 90° \quad \text{for} \quad R_{b_{x1}} = 0 \;, R_{b_{y1}} > 0 \tag{13b}$$

$$\gamma_r = 180° - \tan^{-1}\left[R_{b_{y1}} / R_{b_{x1}}\right] \quad \text{for} \quad R_{b_{x1}} > 0 \;, R_{b_{y1}} \ge 0 \;\; \text{or} \;\; R_{b_{x1}} > 0 \;, R_{b_{y1}} < 0 \tag{13c}$$

$$\gamma_r = 270° \quad \text{for} \quad R_{b_{x1}} = 0 \;, R_{b_{y1}} < 0 \tag{13d}$$

$$\gamma_r = 360° - \tan^{-1}\left[R_{b_{y1}} / R_{b_{x1}}\right] \quad \text{for} \quad R_{b_{x1}} < 0 \;, R_{b_{y1}} < 0 \tag{13e}$$

$$\alpha_r = -\tan^{-1}\left[R_{b_{z1}} / \left|\left[R_{b_{x1}}^2 + R_{b_{y1}}^2\right]^{1/2}\right|\right] \tag{14a}$$

$$\alpha_r = 90° \quad \text{for} \quad R_{b_{x1}} = R_{b_{y1}} = 0, \; R_{b_{z1}} < 0 \tag{14b}$$

$$\alpha_r = -90° \quad \text{for} \quad R_{b_{x1}} = R_{b_{y1}} = 0, \; R_{b_{z1}} > 0 \tag{14c}$$

$$\theta_r = \left|90°-\left(\alpha_r - \beta_c^*\right)\right| \tag{15}$$

where β_c^* is a modified-tilt angle of the collector as shown in Fig.1. This angle depends on the position of point K, at which the reflected beam from the reflector corner C is incident on the tilted plane of the collector, and can be calculated as follows:

$$\beta_c^* = \tan^{-1}\left[\cos(\gamma_r - \gamma_m)\tan(\beta_c)\right] \tag{16}$$

3. COLLECTOR AREA ILLUMINATED BY THE REFLECTOR

The area of the tilted collector illuminated by reflected beams from the reflector depends on the reflector-collector system geometry and Sun position (α_s and γ_s). It is represented in Fig.1 by the plane area EFQKP. This area can be computed from a knowledge of the position of point K Based on the knowledge of the system geometry and reflected beam angles (α_r and γ_r), the position of point K can be easily determined in the coordinate system (X_c, Y_c, Z_c) at point A as illustrated in Fig.1.

4. COLLECTOR AREA SHADOWED BY THE REFLECTOR

As a result of fixing the reflector-collector system in position, the reflector may cast a shadow on the collector surface at certain times. For any orientation of the reflector-collector system, the conditions responsible for causing this shadow can be summarized as follows:

1. If $\beta_m > 0$, and $\alpha_s < \beta_m$, and $90° < |(\gamma_m - \gamma_s)| < 270°$
2. If $\beta_m < 0$, and $\alpha_s > |\beta_m|$, and $270° < |(\gamma_m - \gamma_s)| < 90°$
3. If $\beta_m < 0$, and $90° < |(\gamma_m - \gamma_s)| < 270°$

In these cases, the solar beam incident on the reflector corner C continues on to the shadow point K as shown in Fig.3 (i.e. $\alpha_{sh} = \alpha_s$ and $\gamma_{sh} = \gamma_s + 180°$). Based on the knowledge of the system geometry and shadow angles (α_{sh} and γ_{sh}), the coordinates of point K, shown in Fig.3, can be determined. Consequently, the collector shadow area EFQKP, shown in Fig.3, can be computed in a similar way to that used for computing the illuminated area.

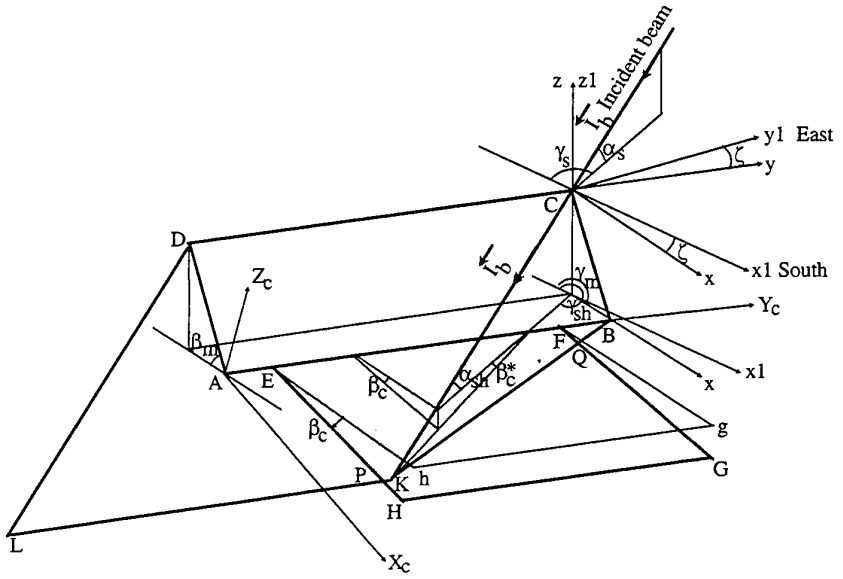


Fig. 3. Schematic diagram of the plane reflector-tilted collector system in case of shadow.

5. SOLAR ENERGY COLLECTION CALCULATION

The rate of total energy absorbed by the solar collector with no reflector can be calculated as follows:

$$Q_a = \left[(\tau\alpha)_{bc} G_{bc} + (\tau\alpha)_{dc}(G_{dc} + G_{rc})\right] A_c \quad (17)$$

The components of the global solar radiation incident on the collector tilt surface are estimated theoretically by ASHRAE model [11], While the transmittance-absorptance products of these components are evaluated from correlation given in Duffie and Beckman [12].

The rate of energy reflected from the plane reflector and absorbed by the collector can be evaluated as follows:

$$Q_r = \left[(\tau\alpha)_{brc} \rho_r G_{br} \cos\theta_r\right] A_{ill} \quad (18)$$

where G_{br} is estimated at the reflector tilt angle (β_m), while $(\tau\alpha)_{brc}$ is evaluated at the reflected beam incident angle on the collector surface (θ_r).

For shadow caused by the reflector on the collector, the loss of energy rate absorbed by the collector can be calculated as follows:

$$Q_{sh} = \left[(\tau\alpha)_{bc} G_{bc}\right] A_{sh} \quad (19)$$

The instantaneous enhancement (boost) factor in solar energy collection of tilted collector by plane reflector can be expressed as follows:

$$IBF = 1 + (Q_r - Q_{sh}) / Q_a \quad (20)$$

Based on the analysis discussed in the previous sections, a FORTRAN 77 computer program has been constructed to compute the instantaneous, daily, and yearly enhancement (boost) factors in solar energy collection of the collector for different operational and design parameters of the reflector-collector system. The program contains a subroutine for predicting the global solar radiation intensities G_{bc}, G_{dc}, G_{rc}, and G_{br}. The program contains also several subroutines for computing day length, solar angles, reflected beam angles, illuminated and/or shadowed area of the collector, and collector transmittance-absorptance products ($(\tau\alpha)_{bc}$, $(\tau\alpha)_{dc}$, and $(\tau\alpha)_{brc}$).

6. RESULTS AND DISCUSSIONS

The numerical calculations of the present analysis have been carried out for a plane reflector-tilted collector at Cairo, Egypt (i.e. $\phi_{loc} = \phi_{st} = 30°$). The main characteristics of the input data to the computer program are as follows:

1. The reflector height (L_r) is equal to the collector length (L_c).
2. The reflector tilt angle is the noon optimum angle, i.e. the angle at which the illuminated point K, shown in Fig.1, coincides on the collector corner G at noon.

For selected days represent winter and summer solstices and spring equinox, the effect of the tilt angle of a south facing reflector (i.e. $\zeta = 0.0$) on the daily boost factor in the integrated daily solar energy collection of the collector is represented in Fig.4. For all the selected days, Fig.4 shows that the daily boost factor reaches its maximum value at a reflector tilt angle equal to the reflector noon optimum tilt angle of each day. For a plane reflector-tilted collector system with the reflector oriented south facing or north facing (i.e. $\zeta = 0.0°$ or $180.0°$), the effect of the collector tilt angle on its yearly solar energy collection at different latitudes is shown in Fig.5.

Figure 5 shows that the optimum tilt angle of the collector is about (ϕ - 10.0°) for the south facing reflector, while it is about (ϕ + 10.0°) for the north facing one. For a collector tilted at its optimum tilt angle, Fig.5 shows that the south facing reflector gives higher yearly solar energy collection than the north facing one. For a south facing reflector-collector system with the collector at its optimum tilt angle corresponding to the local latitude (i.e. β_c=20.0°), Fig.6 shows the collector yearly boost factor for five different categories of tilting the reflector. These categories are tilting the reflector once a day at its noon optimum angle, once a month at the noon optimum angle of the 15 th day of each month, once a season at the noon optimum angle of winter and summer solstices and spring and autumnal equinox, twice a year at the noon optimum angle of winter and summer solstices, and once a year at the noon optimum angle of spring and/or autumnal equinox.

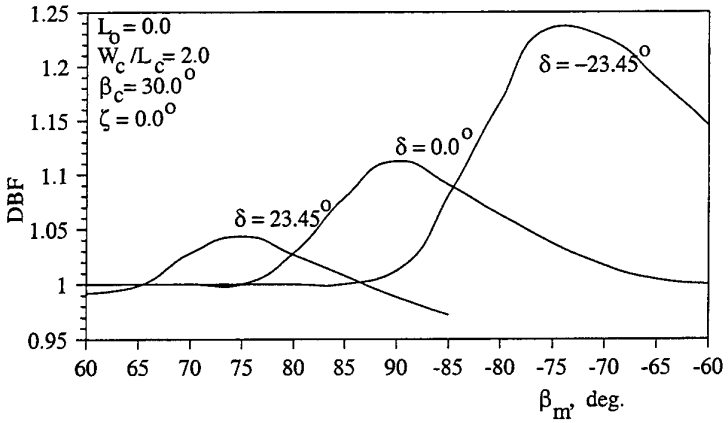


Fig. 4. Effect of the tilt angle of the south facing reflector on the collector daily boost factor.

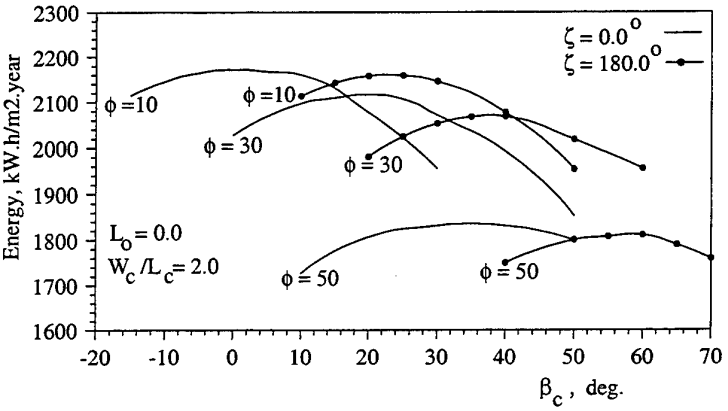


Fig. 5. Effect of the collector tilt angle on its yearly solar energy collection.

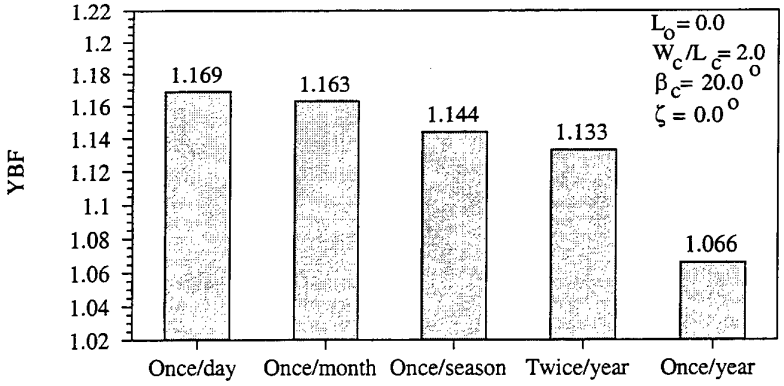


Fig.6. Effect of the south facing reflector tilt angle categories on the collector yearly boost factor.

Figure 6 shows that changing the reflector tilt angle once a day, once a month, once a season, twice a year, and once a year provides yearly enhancement in the solar energy collection of 16.9%, 16.3%, 14.4%, 13.3%, and 6.6% respectively. Figure 7 shows the effect of the collector elongation ratio W_c/L_c on the collector daily and yearly boost factors with the reflector tilted once a day at its noon optimum angle. This figure shows that the collector daily boost factor increases with the increase of W_c/L_c ratio in winter, spring and autumnal seasons. In contrast, the increase of W_c/L_c ratio over 2.0 causes a slight decrease in the collector daily boost factor in summer season. This is a result of the shadow cast on the collector by the reflector at the beginning and end of the summer days. Besides, Fig.7 shows that the optimum elongation ratio for maximum yearly boost factor is about 4.0. Similar results are also noticed for the effect of the reflector overhang ratio L_o/L_c on the daily boost factor as shown in Fig.8.

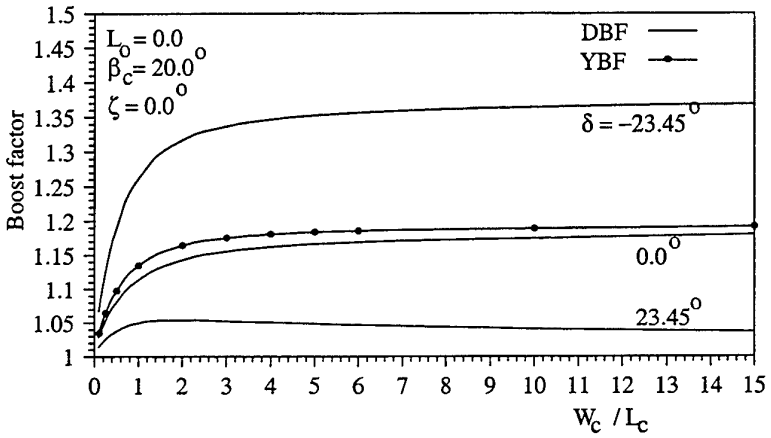


Fig. 7. Effect of collector elongation ratio on its daily boost factor.

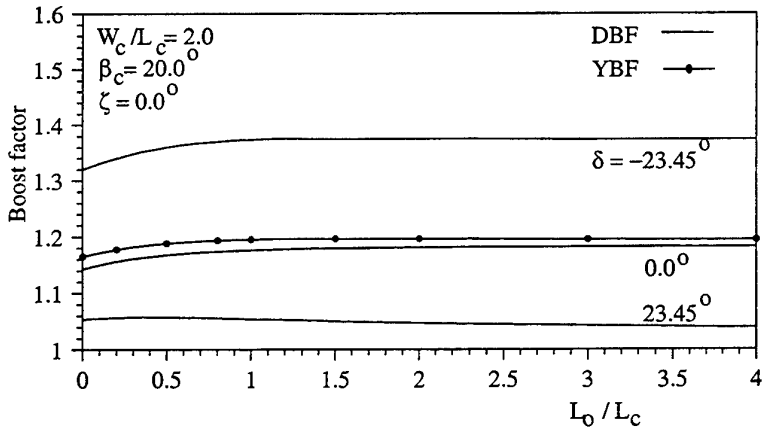


Fig. 8. Effect of the reflector overhang ratio on the collector daily boost factor.

7. CONCLUSIONS

From the theoretical analysis of tilted flat-plate solar collectors augmented by plane reflectors, it is concluded that:

1. Tilting the reflector at its noon optimum tilt angle provides maximum daily boost factor.
2. For a reflector height (L_r) equal to the collector length (L_c), the optimum tilt angle of the collector is about (ϕ -10.0°) and (ϕ +10.0°) for a south and a north facing reflector, respectively.
3. Changing the tilt angle of the south facing reflector at its noon optimum angle up to twice a year provides more than 10.0% yearly enhancement in the collector solar energy collection.

4. The south facing reflector provides higher yearly solar energy collection than the north facing one.
5. For maximum yearly solar energy collector, the optimum elongation ratio of the collector W_c/L_c is about 4.0, while that of the reflector overhang ratio L_o/L_c is about 1.0.
6. The present analysis is an efficient tool to optimize the plane reflector-tilted flat-plate solar collector systems.

REFERENCES

1. D.K. McDaniels, D.H. Lowndes, H. Mathew, J. Reynolds, and R. Gray, Solar Energy, v.17, pp.277-283 (1975).
2. S. Baker, D.K. McDaniels, H.D. Kaehn, and D.H. Lowndes, Solar Energy, v.20, pp.415-417 (1978).
3. D.C. Larson, Solar Energy, v.24, P.203 (1980).
4. S.L. Grassie and N.R. Sheridan, Solar Energy, v.19, P.663 (1977).
5. I.S. Taha and S.M. Eldighidy, Solar Energy, v.25, pp.373-379 (1980).
6. H.F. Chiam, Solar Energy, v.26, pp.503-509 (1981).
7. A.V. Narasimha Rao, R.V. Chalam, S. Subramanyam, and T.L. Sitharama Rao, Energy Conversion and Mangement, v.34, pp.309-326 (1993).
8. H.P. Garg and D.S. Hrishikesan, Solar Energy, v.40, P.295 (1988).
9. A.V. Narasimha Rao, S. Subramanyam, and T.L. Sitharama Rao, Energy Conversion and Management, v.35, pp.309-554 (1994).
10. R. Kumar, S.C. Kaushik, and H.P. Garg, Energy - The International Journal, v.20, pp.511-522 (1995).
11. *ASHRAE Handbook of Fundamentals*, P.27:1 (1985).
12. J.A. Duffie and W.A. Beckman, *Solar Engineering of Thermal Processes*, John Wiley & Sons Inc., New York (1980).

NOMENCLATURE

A = Area, m^2.
DBF = Daily boost factor.
G = Global solar radiation intensity, W/m^2.
IBF = Instantaneous boost factor.
L = Length, m.
Q = Rate of energy, W.
W = Width, m.
YBF = Yearly boost factor.

Greek letters

α = Beam altitude angle, deg. (0° to 90°).
β = Surface inclination angle, deg. (0° to ±90° ; towards x-direction is +ive).
δ = Declination angle, deg. (0° to ±23.45°).
γ = Azimuth angle, deg. (0° to ±360° ; clockwise from north is +ive).
θ = Incidence angle, deg.
ρ = Reflectivity of reflector.
$(\tau\alpha)$ = Transmittance-absorptance product.
ϕ = Latitude, deg. (0° to ±90°; north is +ive).
ζ = Off-south angle, deg. (0° to ±180°). $= (\gamma_m - 180°)$ deg.

Subscripts

a = Absorbed.
bc = Beam radiation incident on the collector.
br = Beam radiation incident on the reflector.
brc = Reflected beam radiation from the reflector.
c = Collector.
dc = Diffuse radiation incident on the collector.
ill = Illuminated.
loc = Local.
m = Reflector.
o = Reflector overhang.
r = Reflected.
rc = Reflected radiation from the surroundings.
s = Solar beams.
sh = Shadow.
st = Standard.

DEVELOPMENTS AND DESIGNS OF SOLAR ENGINEERING FRESNEL LENSES

Ralf Leutz, Atsushi Akisawa and Takao Kashiwagi
Tokyo University of Agriculture and Technology,
Department of Mechanical Systems Engineering
2-24-16 Naka-cho, Koganei-shi, Tokyo 184-8588, Japan
email ralf@star.cad.mech.tuat.ac.jp, phone/fax +81-42-388-7076

Akio Suzuki
UNESCO
Bouvin 3.26 SC/EST, 1, rue Miollis, 75732 Paris Cedex 15, France

Keywords: Fresnel lens, imaging, nonimaging, solar collector, solar concentrator

ABSTRACT. This paper deals with the suitability of Fresnel lenses of imaging and nonimaging designs for solar energy concentration. The paper's scope is the review of long known, and recently developed Fresnel lenses, and the analyes of their characteristics for utilization as solar concentrators, putting an emphasis on a lens designed by the authors. Nonimaging optics are presented as offering the possibilities needed for a breakthrough of Fresnel lenses in commercial solar energy concentration, both in photovoltaic and thermal power conversion.

1. INTRODUCTION

Fresnel lenses are used as solar concentrators since they offer high optical efficiency along with minimal weight and low cost. Applications that demand medium and high concentration ratios (>20), such as monocrystalline photovoltaic generation of electricity, are often equipped with imaging Fresnel lenses. Accurate tracking has to be employed to keep the focus of the lens in place on the receiver. Fresnel lenses are to find a much wider field of utilization, if their optics are adjusted to the requirements of a seemingly moving sun.

Nonimaging optics (Welford, Winston 1989) offer the possiblity to design Fresnel lenses as stationary concentrators with low concentration ratios. For medium flux applications, nonimaging Fresnel lenses are forgiving errors due to installation, low precision tracking, and the finite size of the sun. Not photographic imaging counts, but the homogeneous illumination of a receiver. Two pairs if acceptance half angles are defined, θ in the cross-sectional plane, and ψ perpendicularly to it. They are spanning a part of the hemisphere, thus opening a window through which the concentrator 'sees' the sun. Fresnel lenses of nonimaging design are usually (but not necessarily) of convex shape, while their imaging counterparts are most often flat.

2. FRESNEL LENS DESIGNS FOR THE COLLECTION OF SOLAR ENERGY

Initially, most Fresnel lenses propositioned for solar energy use had not been designed for collection of solar rays. These lenses were imaging devices subject to strong focal forshortening, once the solar rays were no longer entering at an angle normal to the collectors surface. Imaging lenses are designed starting with their focal length. The design principle is trying to eliminate aberrations in order to accomplish a most exact focus. While a neat focal point is characteristic to very high concentration ratios (defined as ratio of aperture, or lens area, to receiver area), imaging is not necessary for collecting solar energy. If not for some cases where high concentration is needed, why should one trouble oneself with accurate tracking of the sun due to the use of imaging lenses under the appearently moving sun?

Table 1 gives an overview of recently achieved developments in the design of Fresnel lenses suitable for solar energy collection. The designs listed are not evaluated but can be described by certain characteristics. Fresnel lenses can be designed according to principles and assumptions which are listed below. The number of designs in Table 1 is not exhaustive but common trends are emerging.

Design Principles
Nonimaging optics: The lens in question is designed according to the principles of nonimaging optics, which were discovered in the 1970's, and found well suited for solar energy applications.

Table 1: Major Developments in Fresnel Lenses Suitable for Solar Energy Applications.

Year	Researcher(s)	Application	Nonimaging optics	Solution numerical only	Cross-sectional angle θ	Perpendicular angle ψ	Minimum deviation prisms	Edge ray principle	Fashionable design	Thin lens, $f >> d$	Prism size, $\Delta x \rightarrow 0$	Flat lens
1822	Fresnel[1]	Lighthouse	–	–	–	–	–	–	–	–	–	O
1951	Miller *et al.*	Condensers	–	–	–	–	–	–	–	–	O	O
1973	Szulmayer	Solar	–	–	–	–	–	–	–	–	O	O
1975	Nelson *et al.*	Solar	–	–	–	–	–	–	–	–	O	O
1977	Collares-Pereira *et al.*[2]	Solar	–	–	–	–	–	–	–	O	O	–
1978	O'Neill	Solar	–	–	O	–	O	–	–	–	O	–
1979	Collares-Pereira	Solar	O	O	O	–	–	O	–	O	O	–
1979	Kritchman *et al.*	Solar	O	O	O	–	–	O	–	O	O	–
1981	Lorenzo, Luque	Solar	O	O	O	–	–	O	–	O	O	–
1984	Tver'yanovich	Solar	–	O	–	–	–	–	–	–	O	O
1997	Erismann[3]	Infrared	–	O	–	–	–	–	O	–	O	–
1999	Leutz *et al.*	Solar	O	O	O	O	O	O	–	–	O	–

[1]First aspherical lens, refer to Ancin *et al.*, 1989
[2]Refractive index $n \rightarrow \infty$, idea W. T. Welford
[3]Aspherical lens in spherical shape

Solution numerical only: The nature of the mathematics used in Fresnel lens design sometimes does not allow an analytical solution. If the number and extent of assumptions are to be reduced, numerical solutions may be called for. As this generally requires a large numer of iterations, computer based simulations are needed.

Cross-sectional angle θ: Any lens, whether of rotational symmetry (3D), or line focusing (2D) is designed with the help of a cross-sectional acceptance half angle which determines the part of the sky the lens may 'see'. Imaging lenses are generally designed focusing paraxial rays only, $\theta = 0$. However, the absorber, first, is larger than the focal *point*, and second, can be moved out of focus, in a way that some rays incident at an angle θ are collected.

Perpendicular angle ψ: The focal areas of line focusing, 2D-lenses (imaging or nonimaging) are sensitive to changes of the incidence angle not only in the cross-sectional, but also in perpendicular plane. The significance of this has often been overlooked when designing Fresnel lenses for solar applications, where 2D characteristics are desired.

Minimum deviation prism: Optical losses during refraction at a prism are least at the minimum deviation prism, where the angles of incident and exiting rays to the respective prism surface are equal.

Edge ray principle: This principle goes along with nonimaging design of Fresnel lenses. Light incident at maximum combinations of acceptance half angles is directed towards one end of the absorber. Fresnel lenses as a rule refract light incident from left of the optical axis of each prism towards the right side of the absorber, and vice versa.

Fashionable design: Solar energy applications, as well as manufacturing technologies usually require the outer side of the lens to be flat. Given this and the principle of minimum deviation prisms, an optimum convex shape of the Fresnel lens emerges from the simulation. Relaxing either principle, the design of lenses of other shapes is possible. 'Fashionable' could mean circular, for example.

Assumptions

Thin lens, $f >> d$: When the thickness of the lens d becomes small in comparison to its focal length f, the sine theorem can be applied during the simplified simulation of the lens. Furthermore the lens is often assumed to have no thickness at all at the thinnest point, $d = 0$. With this assumption, it becomes possible to set up an equation describing the refracted (but not relocated) rays emerging from a prism, in relation to prism center and absorber.

Prism size, $\Delta x \rightarrow 0$: The size of prisms in comparison to the absorber width is assumed to be small in all designs. Each prism is designed only once, but with some $\Delta x > 0$ extending from the design point, ideally in both directions. If that Δx becomes too large, the direction of the ray emerging from one of the extremes of the prism may not point to the absorber. In combination with the edge ray principle of nonimaging designs, extreme rays from extreme ends of the prism will miss the absorber. For imaging designs, any prism width greater than zero is influencing imaging quality, since the width of the ray emerging from the prism is always larger than the focal point, with width zero. In some imaging designs with very high optical quality requirements, one of the active prism surfaces if curved to account for this potential error, as was Fresnel's original center prism. Prisms cannot be made smaller than a multitude of wavelengths, if the rules of geometrical optics should hold accurate.

Flat lens: Fresnel lenses, in particular imaging Fresnel lenses are often assumed to be flat. This does not have to be the case, imaging lenses can be shaped, as nonimaging Fresnel lenses can be designed as flat lenses. Optimized nonimaging lenses with smooth outer surface must be shaped to allow for concentration of light incident from both the left and the right extremum given by the acceptance half angle(s).

Nonimaging Optics

Nonimaging optics were discovered for their use in solar energy with the discovery of the (reflective, not refractive) Compond Parabolic Concentrator (CPC) by Winston (1974), refined by Rabl (1976). A book named 'The Optics of Nonimaging Concentrators' by Welford and Winston (1978), later enlarged as 'High Collection Nonimaging Optics' (Welford and Winston, 1989), became the standard text for nonimaging applications in solar energy, and other fields. The linear CPC is designed starting with a cross-sectional acceptance half angle spanning part of the hemisphere, thus accepting a fraction of the sun's energy, collecting solar rays whenever the collector, enabled and restrained by the acceptance half angle, is able to 'see' the sun. The higher the concentration ratio, the smaller the acceptance half angle. The CPC's mirror walls are of parabolical shape. A nonimaging concentrator is called ideal when all light within the limits of the edge rays is refracted onto the absorber. Nonimaging Fresnel lenses approach, but do not reach the ideal due to blocking and unused tip losses inherent in the prisms' design, and the effects of refraction in the perpendicular plane.

It did not take long until the concept of nonimaging optics was applied to (refracting) Fresnel lenses. In the 1970's, both Kritchman *et al.* (1979a, 1979b, 1981, 1984), and Collares-Pereira *et al.* (1977, 1979) designed bifocal Fresnel lenses, which are essentially nonimaging devices. Both groups of designers intended to construct nonimaging lenses to enhance the ability of the lens to collect rays from a appearantly moving sun within a cross-sectional pair of acceptance half angles. O'Neil (1978) designed a focusing lens, but realized that his lens could compensate for tracking errors within narrow limits. Lorenzo and Luque followed 1981, and are followed by the work of Leutz *et al.*, which is probably the first nonimaging design of a Fresnel lens offering finite size prisms and a lens thick enough for manufacturing, taking into account the perpendicular acceptance half angle. These milestones of development have been listed in Tab.1, to compare design principles and assumptions made.

3. IMAGING FRESNEL LENSES

Typical imaging (flat) Fresnel lenses are designed as focusing devices, i.e. the main parameter is the focal length of the lens. Flat nonimaging Fresnel lenses have not yet been published, although this would not be impossible (only if one surface has to remain smooth). As long as certain assumptions are made, focusing lenses can be solved analytically. Such assumptions include the (reasonable) definition of the lens as thin, meaning that its focal length f must be much greater than its thickness d, $f >> d$. Two papers were published in 1951 (Miller *et al.*, and Boettner, Barnett). The former group had designed and constructed Fresnel lenses for technical applications beginning in 1948, taking advantage of the new plastic materials. Their lens designs are of imaging type, and the losses at a Fresnel lens as well as the spectral behaviour of the prisms (Oshida, 1961) are already

well understood.

Research has focused on the development of evaluation techniques for Fresnel lenses under solar radiation. Ray tracing has been applied to find whether an incident ray hits an absorber, or misses it (Nelson et al., 1975). The forshortening of the lens' focus has destroyed many hopes to successfully use imaging Fresnel lenses as solar collectors. Tracking is an expensive option, and has only recently been developed to a stage of maturity. Harmon (1977), who evaluates mass-produced focusing Fresnel lenses for their applicability in photovoltaics, probably captures what most results of simple lens analyses indicate, when he describes the lens as being

> "...an inefficient concentrator with losses that begin at 20 per cent and rise to about 80 per cent as the focal distance decreases. However, the lens is capable and adequate for low concentration purposes with photovoltaic systems. The most attractive aspects of using this lens as a solar concentrator are its availability and its potential low cost."

Designs can become more complicated than the typical focusing lens outlined, when a cover, or a coating is involved, or when the lens sports grooves on both sides. In these cases, analytical solutions can no longer be offered, and numerical calculations are introduced. One reason why research has in the past often treated only the feasibility of existing focusing devices for solar energy applications might be the lack of computing power solving numerical problems for lenses with hundreds of prisms, which, done by hand, should be a mighty task indeed.

The design of some simple Fresnel lenses shall be conducted to enable evaluation of focusing lenses for use as solar collectors. The focal length of a plano-convex Fresnel lens condenser can be written with the lens formula

$$1/f = 1/i + 1/o \tag{1}$$

where the conjugates, i.e. the distances of image and object points from the refracting surface of the thin lens, are denoted i, and o, respectively. In case of the plano-convex collector lens, $o = \infty$, and $1/f = 1/i$.

The f/number is a measure for the aperture of the lens. It describes the ratio of effective focal length to diameter of the lens. The f/number is a measure for the flux concentration of the imaging lens; while the geometrical concentration ratio C approaches the theoretical maximum, the heat flux in the focal point is related to the amount of radiation concentrated.

$$\text{f/number} = f/2R \tag{2}$$

with R denoting the distance of the extreme paraxial ray from the optical axis of the system. Smaller f/numbers mean larger apertures, and vice versa. Fresnel lenses are free from spherical aberration since every step is designed separately for focusing. Due to their thinness both absorption losses within the material, and the change of those losses over the lens profile are small. Fresnel lenses can be designed as very 'fast' lenses, having a small f/number. Only Fresnel lenses 'faster' than f/0.5, i.e. with a diameter twice their focal length are called "impractical" by Fresnel Technologies (1995).

A typical imaging Fresnel lens with grooves facing inwards shall be presented here. The design has an analytical solution, and follows Tver'yanovich (1984). In accordance with Fig.1, three equations can be set up to describe the lens. The prism angle α is the goal of a simulation written.

$$n \sin \alpha = \sin \beta \tag{3a}$$

$$\tan \omega = R/f \tag{3b}$$

$$\beta = \alpha + \omega \tag{3c}$$

Some iterations yield an expression for $\tan \alpha$

$$\tan \alpha = (R/f)\,(\cos \omega / n - \cos \omega) \tag{4}$$

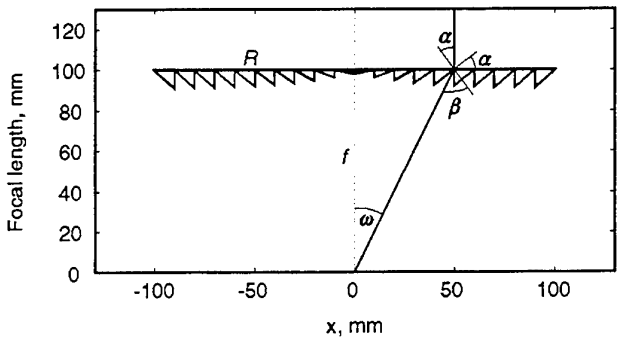


Figure 1: Simple Fresnel lens with grooves facing inward. Analytical solution.

Substutiting cos ω with the expression $f/(R^2 + f^2)^{1/2}$ gives a final expression for the prism angle α in terms of focal length f, and aperture R.

$$\tan \alpha = R / (n (R^2 + f^2)^{1/2} - f) \qquad (5)$$

The result of a simulation based on this Eqn.5 is shown in Fig.1. From the figure, it becomes obvious that the lens has at its thinnest points no thickness at all. The focal lenght is taken as f = 100 mm, and the aperture runs for $0 \le R \le R_{max}$, by steps of R / 10 where R_{max} = f to reach an f/number of 0.5 for this lens. Similar procedures can be applied to generate lenses with grooves facing outward (Tver'yanovich, 1984), or a 'dome' shaped lens, where f = const.

4. NONIMAGING FRESNEL LENSES

Shaped Fresnel lenses of bifocal, or nonimaging type are more recently developed lenses for collection of solar rays. Of course, imaging lenses can be designed with curvature, too, but the curvature is most advantagous for solar energy applications with linear nonimaging designs, since light incident from both sides of the optical axis can be concentrated without violating the smooth surface requirement. Most probably, the late W. T. Welford deserves the honour to be credited with the initial idea for the design of curved lenses, based on his experiences with nonimaging optics that led to his and R. Winston's book (Welford, Winston 1978). Collares-Pereira *et al.* acknowledge a private communication with Welford in their first paper on the subject, which in turn is referred to in the first paper of Kritchman's group.

Contrary to imaging devices, nonimaging Fresnel lenses are designed starting not with the focal length of the lens, but with a pair of design angles, termed 'acceptance half angles'. These acceptance half angles are opening the collector's aperture which is explicitly designed to accept rays incident from directions within a certain angle. As opposed to reflective mirrors, the behaviour of lenses depends both on the incidence in the cross-sectional plane, and on the one in the perpendicular plane. When designing collectors with line focus (2D), this makes a difference, as is seen from the prism's optics. Although Collares-Pereira (1979) realizes the importance of the perpendicular fraction of the incoming ray when tracing rays through his lens, he did not include the perpendicular ray into its design. Neither did any of the other authors listed before 1999, even though most lenses for solar energy applications are expected be used as linear 2D-concentrators, with N-S orientation and daily tracking.

An example for a nonimaging linear lens for daily tracking and seasonal tilt is given in Fig.2. The lens 'sees' a fraction of the sky defined by its acceptance half angles θ and ψ. Light incident within these angles is refracted upon the absorber. The system being nonimaging, there is a rather diluted linear image of the sun on the absorber, reducing the 'hot spot' problem of imaging concentrators.

Collectors with rotational symmetry (3D) offer the possibility of higher concentration, and flux ratios, but are usable only with accurate two-axis tracking. Line focusing lenses are suitable for one-axis tracking, as the perpendicular design angle is causing less severe focal forshortening than the cross-sectional acceptance half angle. Linear nonimaging Fresnel lenses can be used as stationary concentrator with small concentration ratios, thus overcoming the focal shortcomings of imaging devices.

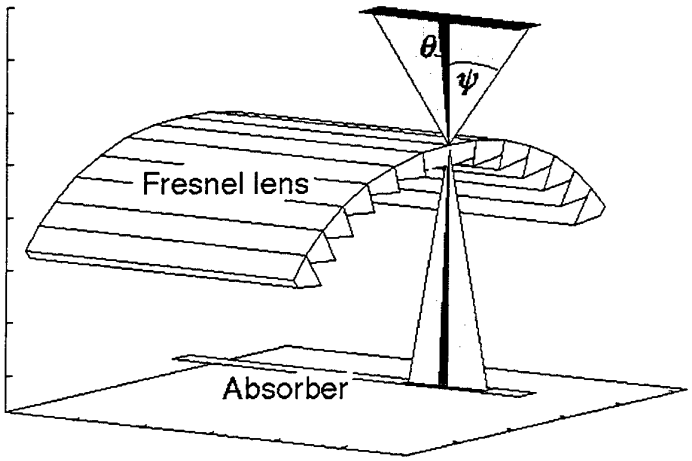


Figure 2: Nonimaging linear Fresnel lens numerically designed by Leutz et al., 1999. Schematic of acceptance half angles: cross-sectional θ and perpendicular ψ. Oversized prisms.

5. CONCLUSIONS AND COST CONSIDERATIONS

This paper lists some design principles used and assumptions made by the designers of various Fresnel lenses that have been developed in the last 250 years. Interest in Fresnel lenses for solar energy applications rose in the latter half of the 20th century due to the availability of plastics, especially Polymethylmetacrylate (PMMA) which has a good transmissivity and resistance for sunlight. The design of more and more sophisticated Fresnel lenses goes along the lines of two related developments. Manufacturing technology has improved from moulding, grinding, and polishing glass by hand to diamond turning machines operating at accuracies of less than 1/1000 mm. For many design problems in optics there are no analytical solutions. Only with the help of numerical simulations by computer, available since the 1970's, modern Fresnel lenses can be calculated. Two design trends can be observed:

1. Imaging, often flat lenses focusing paraxial rays with concentration ratios ideally approaching infinity; these systems need accurate two-axis tracking. Their suitability for most solar applications is questionable due to their sensitivity of tracking, or manufacturing errors. Even the size of the solar disk could pose a problem. Judged from our own experiments with shaped imaging lenses, it can be said that focal aberrations with imaging Fresnel lenses are impractically large for their use as solar concentrators, unless high precision tracking is to be employed. Even if the absorber should be designed larger, and positioned closer to the back of the lens, the moving focus would soon exceed the scope of the receiver. Additionally, imaging lenses create a more or less defined focal area, which leads to 'hot spots' on oversized absorbers. Thus, the only way to successfully utilize imaging Fresnel lenses in solar energy concentration is to employ accurate tracking.

2. Nonimaging, most often convex shaped lenses for low and medium concentration, one-axis tracking, or stationary collectors. Nonimaging Fresnel lens concentrators are thought to be very competitive solar collectors. Their optical qualities approach those of the CPC collector family (Lorenzo, Luque 1982). Fresnel lenses are lightweight, and cost effective. If tracking requirements are kept to a minimum, savings in crystalline photovoltaic surface area due to concentration will off set the cost of the Fresnel lens. O'Neill (1994) expects a levelized electricity price for large photovoltaic systems incorporating Fresnel lenses, and produced at a rate of 30 MW/a, of US 7-15 cents/kWh.

Of the more sophisticated lenses mentioned, some have never left the computer of the designer, some prototypes have been built, and only the imaging lens of O'Neill (1978, 1992, 1994) has found its way to mass-production. A company has been set up in 1983, found support with the United States Department of Energy, and supplies photovoltaic modules incorporating the lens. The largest projects using the two-axis tracking systems are two plants of 100 kW each, in Texas, U.S.A. Although convex shaped, nonimaging lenses can be manufactured as

flat lenses and bent into shape, significantly lowering manufacturing complexity. As the solar market grows, Fresnel lenses, in particular nonimaging devices, are expected to increase their share.

REFERENCES

1. B. A. Anicin, V. M. Babovic, D. M. Davidovic (1989) Fresnel Lenses; *American Journal of Physics* v57, 4, 312-316
2. E. A. Boettner, N. E. Barnett (1951) Design and Construction of Fresnel Optics for Photoelectric Receivers; *Journal of the Optical Society of America* v41, 11, 849-857
3. M. Collares-Pereira (1979) High Temperature Solar Collector with Optimal Concentration: Non-Focusing Fresnel Lens With Secondary Concentrator; *Solar Energy* v23, 409-420
4. M. Collares-Pereira, A. Rabl, R. Winston (1977) Lens-Mirror Combinations with Maximal Concentration; *Applied Optics* v16, 10, 2677-2683
5. F. Erismann (1997) Design of Plastic Aspheric Fresnel Lens with a Spherical Shape; *Optical Engineering*, April; also available from *http://www.wavelengthoptics.com/ techpap1.htm*
6. Fresnel Technologies, Inc. (1995) Fresnel Lenses; brochure available at *http://www.fresneltech.com/html/ products.html*}, or Fresnel Technologies, Inc., 101 West Morningside Drive, Fort Worth, Texas 76110, USA
7. S. Harmon (1977) Solar-Optical Analyses of Mass-Produced Plastic Circular Fresnel Lens; Technical note, *Solar Energy* v19, 105-108
8. E. M. Kritchman, A. A. Friesem, G. Yekutieli (1979a) Efficient Fresnel Lens for Solar Concentration; *Solar Energy* **22**, 119-123
9. E. M. Kritchman, A. A. Friesem, G. Yekutieli (1979b) Highly Concentrating Fresnel Lenses; *Applied Optics* v18, 15, 2688-2695
10. E. M. Kritchman, A. A. Friesem, G. Yekutieli (1981) A Fixed Fresnel Lens with Tracking Collector; *Solar Energy* v27, 13-17
11. E. M. Kritchman (1984) Two Stage Linear Fresnel Lenses; *Solar Energy* v33, 1, 35-39
12. R. Leutz, A. Suzuki, A. Akisawa, T. Kashiwagi (1999) Design of a Nonimaging Fresnel Lens for Solar Concentrators; *Solar Energy* v65, 6
13. E. Lorenzo, A. Luque (1981) Fresnel Lens Analysis for Solar Energy Applications; *Applied Optics* v20, 17, 2941-2945
14. E. Lorenzo, A. Luque (1982) Comparison of Fresnel Lenses and Parabolic Mirrors as Solar Energy Concentrators; *Applied Optics* v21, 10, 1851-1853
15. O. E. Miller, J. H. McLeod, W. T. Sherwood (1951) Thin Sheet Plastic Fresnel Lenses of High Aperture; *Journal of the Optical Society of America* v41, 11, 807-815
16. D. T. Nelson, D. L. Evans, R. K. Bansal (1975) Linear Fresnel Lens Concentrators; *Solar Energy* v17}, 285-289
17. M. J. O'Neill (1978) Solar Concentrator and Energy Collection System; United States Patent 4069812
18. M. J. O'Neill (1992) Fourth-Generation, Line-Focus, Fresnel Lens Photovoltaic Concentrator; *Proceedings of the Fourth Sunshine Workshop on Crystalline Silicon Solar Cells*, 153-160, 25-26 November, Chiba (near Tokyo), Japan
19. M. J. O'Neill, A. J. McDanal (1994) Fourth-Generation Concentrator System: From the Lab to the Factory to the Field; *1994 IEEE First World Conference on Photovoltaic Energy Conversion, Conference Record of the Twenty Fourth IEEE Photovoltaic Specialists Conference*, Vol. 1, 816-819, 5-9 December, Waikoloa, Hawaii, United States of America
20. Oshida (1961) Step Lenses and Step Prisms for Utilization of Solar Energy; *New Sources of Energy, Proceedings of the Conference, United Nations*, Vol. 4, S/22, 598-603, 21-31 August, Rome
21. Rabl (1976) Optical and Thermal Properties of Compound Parabolic Concentrators; *Solar Energy* v18, 497-511
22. W. Szulmayer (1973) A Solar Strip Concentrator; *Solar Energy* 14, 327-335
23. E. V. Tver'yanovich (1984) Profiles of Solar-Engineering Fresnel Lenses; *Geliotekhnika* 19, 6, 31-34; translated into English in *Applied Solar Energy* 19, 6, 36-39
24. W. T. Welford, R. Winston (1978) The Optics of Nonimaging Concentrators, New York
25. W. T. Welford, R. Winston (1989) High Collection Nonimaging Optics, San Diego
26. R. Winston (1974) Principles of Solar Concentrators of a Novel Design; *Solar Energy* 16, 89-95

EXPERIMENTAL STUDY OF A COMPACT SOLAR COLLECTOR

Eman-Bellah S. Mettawee
Department of Solar Energy
National Research Center of Egypt
E-mail: mettawee@hotmail.com; Fax: +20 2 4306888

Ghazy M. R. Assassa
Department of Mechanical engineering
Faculty of Engineering at Shoubra, Zagazig University

Keywords: solar energy, storage, latent heat

ABSTRACT. The performance of a compact solar collector based on latent heat storage is investigated experimentally. In this collector the absorber plate-container unit performs the function of absorbing the solar energy and storing phase change material (PCM). The solar energy is stored in paraffin wax that is used as a PCM and is discharged to cold water flowing in pipes located inside the wax. The collector's effective area is assumed $1m^2$ and its total volume is divided into 5 sectors. The experimental apparatus is designed to simulate one of the collector's sectors, with apparatus-absorber effective area of $0.2m^2$. Outdoor experiments are carried out to demonstrate the applicability of using a compact solar collector for water heating. A total of 20 thermocouples are used to record the temperature variation of PCM. The time wise temperatures of the PCM are recorded during the processes of charging and discharging together with the solar intensity. Experiments are conducted for different water flow rates of 0.0083 to 0.0217kg/h m^2 and the useful heat gain (Qu) is calculated. The effect of the water flow rate on (Qu) is studied. The heat transfer coefficients are calculated for the charging process. The propagation of the melting and freezing front are studied during the charging and the discharging processes.

Experimental results show that in the charging process average heat transfer coefficient increases sharply after increasing the melt layer thickness as the natural convection grows strong. The local heat transfer coefficient is a strong function of distance from the top of the wax container as well as the time. In the discharge process the useful heat gained increases as the water mass flow rate increases.

1. INTRODUCTION

An efficient energy management program must invariably involve energy storage to be able to cater to fluctuating demands and at the same time to obtain a higher performance from the primary power plant. Energy storage systems also assume greater significance in the context of waste heat utilization and in situations dealing with intermittent supplies of input energy like solar energy. In view of this the use of latent heat storage systems has attracted much attention in the past few years considering their amenability for higher energy densities.

Many studies concerning the thermal characteristics of heat exchangers based on PCMs have been devoted to the thermophysical properties and to the problems associated with the physicochemical behavior of PCM (Lane [1], Abhat [2]). Successful utilization of PCM as a heat storage media mainly depends on developing efficient and low cost means of containment. For passive or air-cooled active solar system, several methods of encapsulating PCMs have been developed [3] and [4]. Ilken and Toksoy [5] reviewed the energy storage systems using heat exchangers with different geometry and the solution methods for related phase change problems. Rabin et al. [6] proposed a new type of integrated collector storage system for low-temperature heat supply.

In the present work an experimental investigation of the proposed apparatus is represented. The charging and discharging processes are carried out for paraffin wax as a PCM. A parametric study is carried out to study the effects of the water flow rate and the variation of solar energy on the discharging and the charging characteristics. The heat transfer characteristics is also discussed.

2. EXPERIMENTAL SETUP

An experimental model of one sector of the compact solar collector is designed and built to investigate the charging and the discharging processes. The volume and the construction of each sector are decided according to the input solar energy during the charging process. A schematic cross-section of the components of the experimental model is shown in Fig. 1. The experimental apparatus consists of a steel absorber-container unit of 1.3 m in length and cross-section's dimensions are as shown in figure. The absorber plate is inclined by an angle equals 45°. The sides of the container are thermally isolated with 50-mm thick layer of polyurethane and outside wooden layer of 20mm in thickness. A copper pipe of 12mm inner diameter and 1.35 m long is embedded inside the PCM to carry the heat transfer fluid inside the collector. A 3mm thick transparent glass cover is placed 25mm apart from the absorber plate. A 50mm thick polyurethane layer is placed over the cover to provide thermal insulation in the discharging process.

Table 1. Physical Properties of Paraffin Wax

Volumetric latent heat of fusion $\lambda\rho$	165 kJ/dm^3
Melting temperature T_m	53.5 °C
Solid phase density	0.81 kg/dm^3
Liquid phase density	0.78 kg/dm^3
Thermal conductivity	0.21 W/mK
Specific heat	2.5 kJ/kg.K

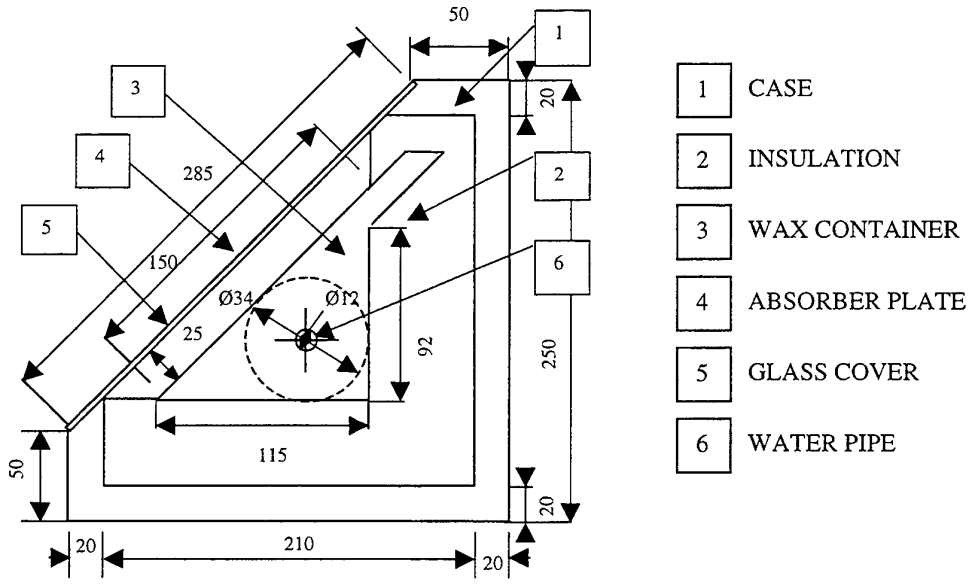
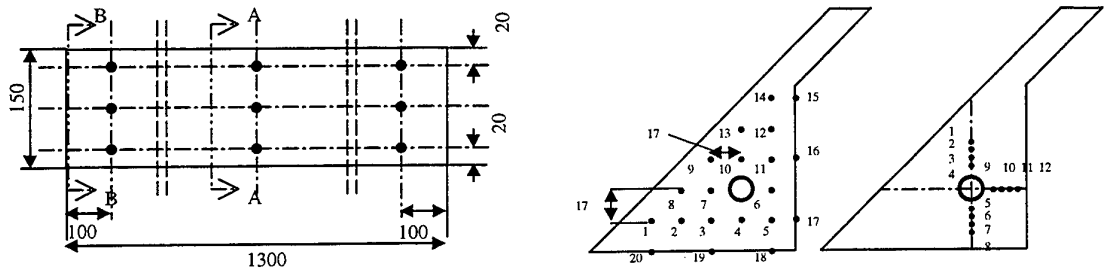


Fig. 1. Schematic of the experimental apparatus cross section

In the charging process water inlet and outlet valves are closed. The charging process starts when the absorber plate is exposed to the solar ray. The temperature distribution along the surface of the absorber plate is measured at three sections as shown in Fig. 2.a. Increasing its temperature by solar radiation leads to increase the temperature of the PCM contained in the test section. The PCM melts when its temperature reaches the melting point. The temperature in the radial distribution of the PCM is measured with 20 Cu-Co thermocouples after each a period of 30 minutes. Figure 2.b shows the positions of the thermocuples located in the cross section of the test section. Solar intensity is measured in the same inclination of the absorber plate. The ambient air temperature is also measured. The charging process ends when the PCM melts completely.



(a) on the absorber plate **(b) inside the PCM** **(c) around heat flow pipe**

Fig. 2. A position of thermocouples

In the discharge process water inlet and outlet valves are opened. The water inlet and outlet temperatures are measured with two thermocuples inserted inside the heat flow pipe at its inlet and its outlet. The temperature distribution inside the PCM around the heat flow pipe is measured with twelve thermocuples as shown in Fig. 2.c. The inlet temperature is approximately constant (Ti =33 ±2°C). The mass flow rate is ranged from 0.0083 to 0.0217kg/m^2 h (from 0.1 to 0.26 lit/min for an absorber area of 0.2 m^2).

3. RESULTS

Charging Process

Temperature distribution. Experimental results for the charging process where the PCM, is initially in the solid state, is heated by solar energy radiation and then is melted are shown in Fig. 3. The figure represents the relations between the time and the temperature of the PCM at some selected points located in Fig. 3. The figure shows that the temperature of the thermocouples increases gradually in the solid state with low temperature gradient due to the low thermal conductivity of the solid PCM. The temperature of the upper position located thermocouple reaches the melting point first, and then the temperature difference between the upper position thermocouples and the lower position ones increases. After complete melting the difference in temperature between the top and the bottom decreases due to the enhancement of natural convection. Similar characteristics of heating curves are observed at the other positions along the PCM.

Heating curves show that the tope positions are higher in temperature than the lower ones. This behavior may be attributed to the used geometry of the test section. In addition after melting of the top portion the enhancement of the free convection in the liquid phase of the PCM decreases the difference between the temperature of liquid PCM and that of absorber plate. However, at the bottom the low thermal conductivity and the thickness of the solid PCM increase the thermal resistance.

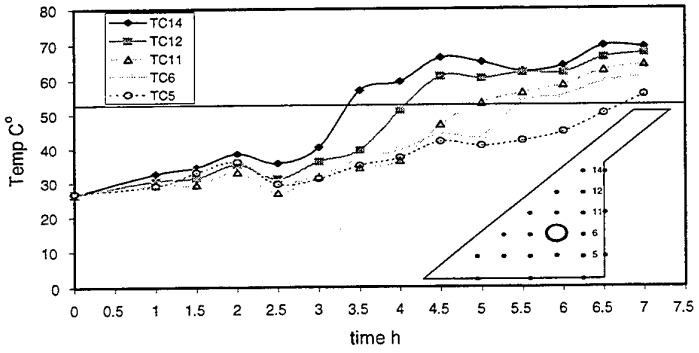


Fig. 3. Temperature distribution inside the PCM (charging process)

Solid-liquid interface. Figure 4 shows the solid-liquid interface contours as a function of time using average input solar intensity of 750 W/m^2. The figure shows that, the PCM starts to melt at a layer adjacent to the absorber plate. As the layer thickness increases and the natural convection grows strongly, heat is no longer transported directly across the melt layer, but is carried along the back face of the absorber plate to the interface by the recirculating flow. For each advanced time the melt layer thickness at the upper portion is greater than the lower one. This indicates that significant natural convection motions are confined to the uppermost portion of the melt region.

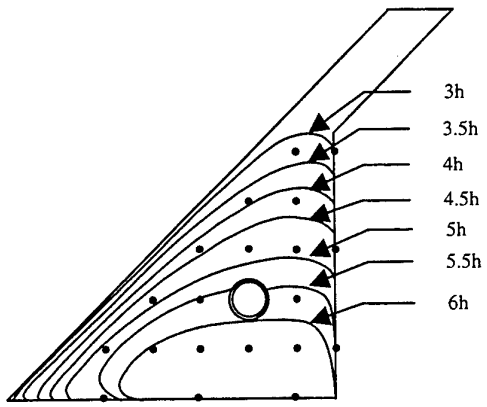


Fig. 4. Sequential melting contour (charging process)

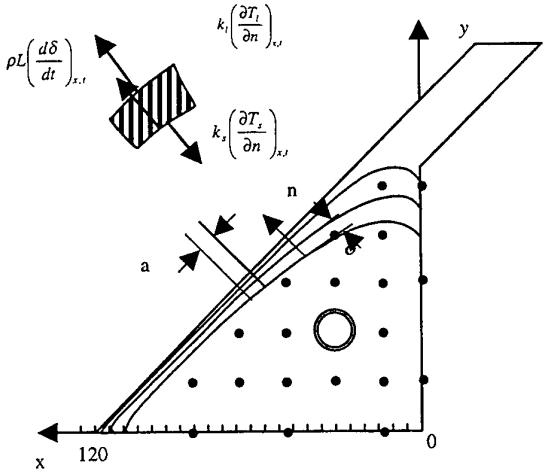


Fig. 5. Model of melting front in charging process

Heat transfer characteristics. During the charging process the local heat transfer coefficient may be evaluated from the local thermal energy balance at the melting surface as shown in Fig. 5. An instantaneous energy balance at the interface may be written as:

$$k_s\left(\frac{\partial T_s}{\partial n}\right)_{x,t} - k_l\left(\frac{\partial T_l}{\partial n}\right)_{x,t} = \rho L\left(\frac{d\delta}{dt}\right)_{x,t} \tag{1}$$

This energy balance is used to determine the local heat transfer coefficient $h_{x,t}$, which is defined by:

$$-k_l\left(\frac{\partial T_l}{\partial n}\right)_{x,t} = h_{x,t}(T_W - T_m) \tag{2}$$

Then from equations (1) and (2) local heat transfer coefficient $h_{x,t}$ at any location x and at any time t is determined from:

$$h_{x,t} = \left(\rho L\left(\frac{d\delta}{dt}\right)_{x,t} + k_s\left(\frac{\partial T_s}{\partial n}\right)_{x,t}\right) \Big/ (T_W - T_m) \tag{3}$$

Where $\left(d\delta/dt\right)_{x,t}$ is measured from the experimental data as shown in Fig. 5 and $\left(\partial T_s/\partial n\right)_{x,t}$ is calculated as:

$$\left(\frac{\partial T_s}{\partial n}\right)_{x,t} = \left[\left(\frac{\partial T_x}{\partial x}/y\right)_{x,t} + \left(\frac{\partial T_y}{\partial y}/x\right)_{x,t}\right] \Big/ 2 \tag{4}$$

The surface area $A_{x,t}$ is calculated by multiplying the surface width (a) by the length of the wax container. Then average heat transfer coefficient $h_{m,t}$ at any time may be obtained as:

$$h_{m,t} = \left(\sum h_{x,t} * A_{x,t}\right) / \sum A_{x,t} \quad (5)$$

The variation of the local heat transfer coefficients with the width of the absorber-container unit for solar intensity of 750 W/m^2 is presented in Fig. 6. The presence of the heat flow pipe affects the region around it. The heat transfer coefficient calculations are performed outside that region but within that region the results are interpolated as shown in the figure. Examination of the figure reveals that the local heat transfer coefficient terminates to be almost nearly equal to zero then increase with the time. The local heat-transfer coefficient decreases monotonically with increasing the distance from the back wall of unit (with x). However, it slightly increases near the bottom of the unit due to the bottom wall temperature effect. The conduction in the welded bottom wall from the absorber plate increases the bottom wall temperature.

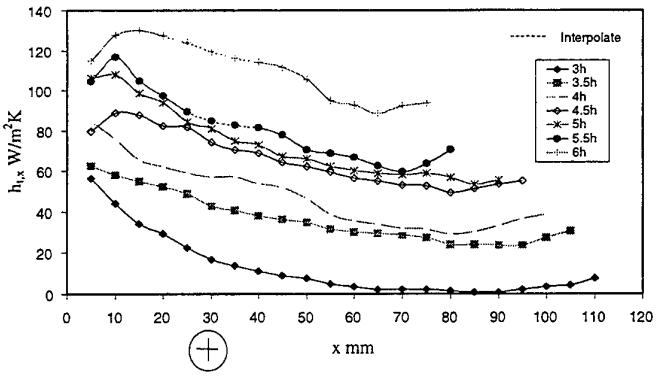


Fig. 6. Local heat transfer coefficient (charging process)

The average heat transfer coefficient along the interface and the solar intensity as a function of time are shown in Fig. 7. At the starting of melting the average heat transfer coefficient has small values that indicates the heat is transferred by conduction. After a while the average heat transfer coefficient increases sharply due to the increase of the thickness of the liquid PCM see Fig. 4, that leads to a great increase in the natural convection.

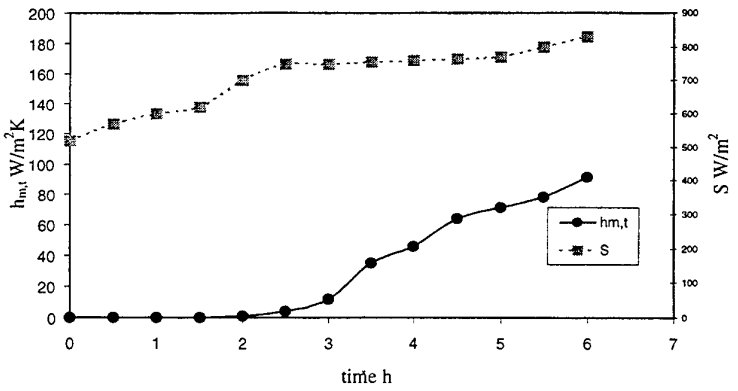


Fig. 7. Average heat transfer coefficient (charging process)

Discharge Process

Temperature distribution. During the discharge process, the temperature distribution of the PCM at 12 thermocouples around the heat flow pipe (shown in Fig. 2.c) versus time is displayed in Fig. 8.a, b, c for water

flow rate of 0.0217 kg/m^2 h. Inspection of each figure shows that the curves may be divided into three stages I, II, III. In the first stage I, PCM temperature decreases gradually around its freezing point then, in the second stage it remains approximately constant. The primarily decrease in temperature is due to the release of sensible heat at the liquid PCM. In the second stage the PCM starts to solidify, the approximately horizontal lines, stage II, correspond to latent heat releasing. The decrease in temperature at the end of stage II represents sensible heat releasing stage III of the solid state PCM. The temperature of the thermocouples located in the closest positions to the heat flow pipe decreases gradually with no apparent latent heat releasing period. This due to the self-blocking of the solid PCM around the heat flow pipe.

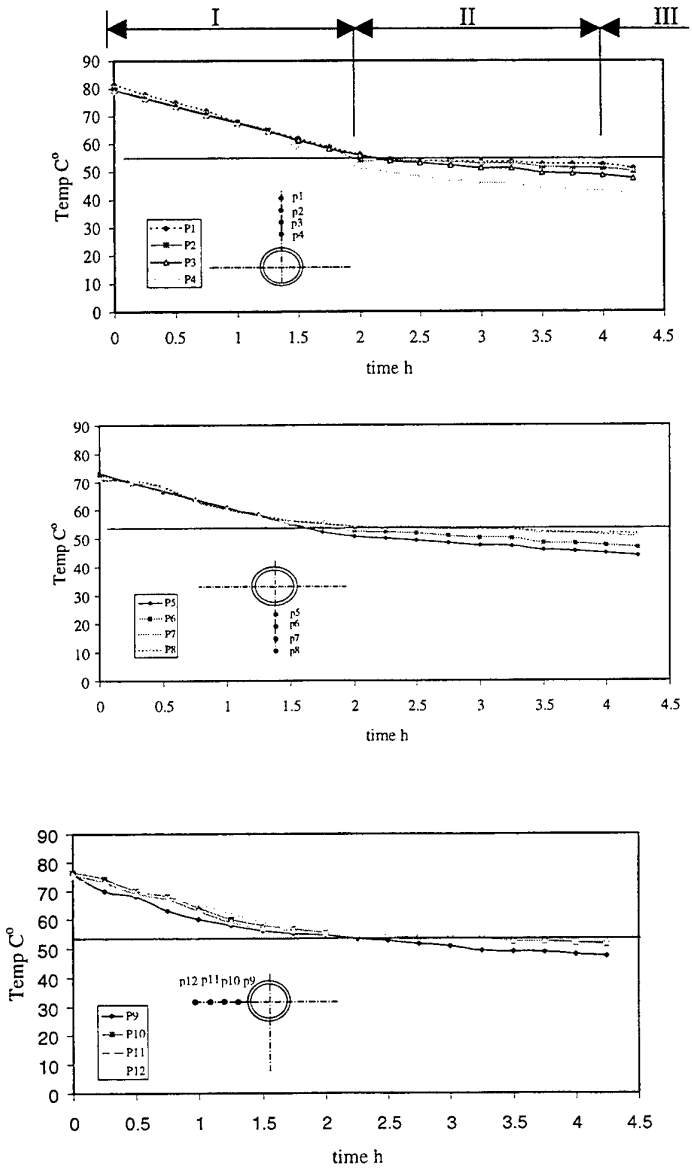


Fig. 8. Temperature distribution around the pipe (discharging process)

Solid-liquid interface. During the discharge process, solid-liquid interface could be found using the readings of the thermocouples around the heat flow pipe. Figure 9.a and b show the solid-liquid interface contours as a function of time using two different water mass flow rates. Examination of the two figures shows that

propagation of the melt contour is similar for the use mass flow rates. Freezing takes place primarily below the heat flow pipe, with little occurring at the top and the sides. This is due to the natural convection-taking place in the liquid PCM. In the melting zone the relatively cold PCM moves downward due to the gravity effect along with a decrease in temperature in the lower portion. After a primarily period of time, during which solid PCM layer thickness increases, then natural convection effect decreases. The elliptic shape of the frozen PCM gradually changes by time to approximately circular shape. This may be attributed to indicate that the heat transfer is dominated by conduction.

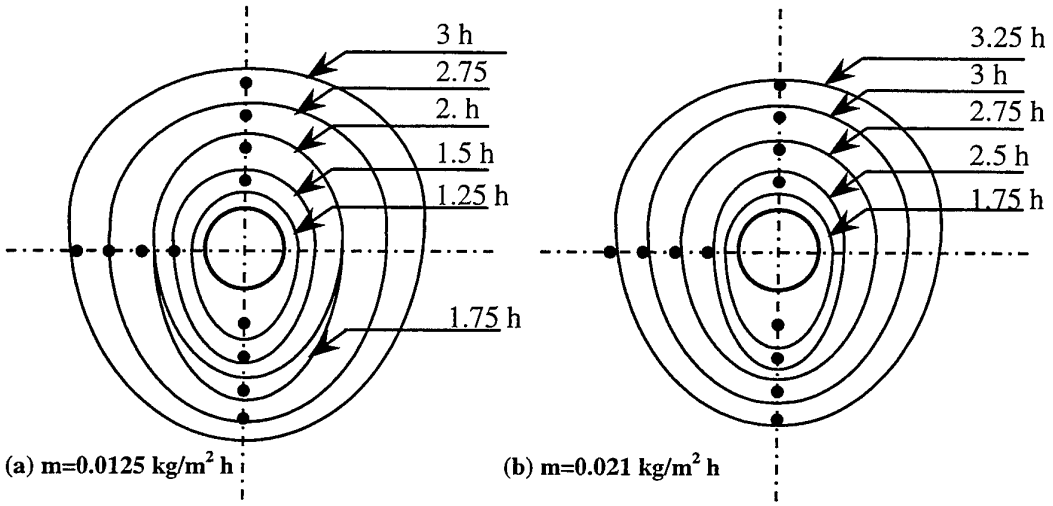


Fig. 9. Sequential frozen contour (discharging process)

Useful heat gained. During the discharge process the useful heat gained is given by the following equation:

$$Q_u = m.C_p.(T_{out} - T_{in}) \tag{6}$$

Figure 10 shows the pattern of variation in the useful heat gained (Q_u) in relation to time at two different water flow rates. As shown in the figure the useful heat gained increases as flow rate increases.

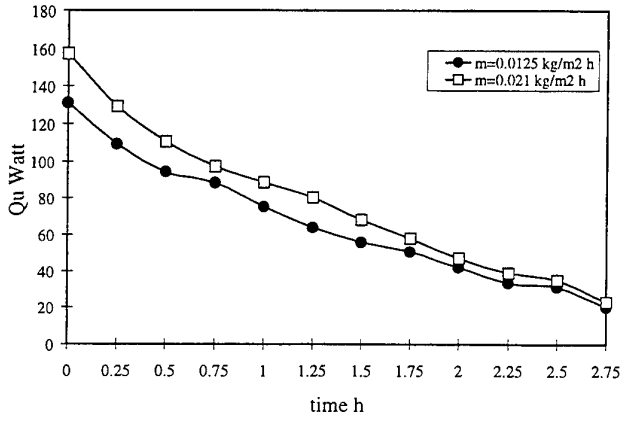


Fig. 10. Useful heat gained (discharging processe)

4. CONCLUSIONS

Experiments are carried out to investigate the heat transfer characteristics of a compact solar collector during the charging and discharging processes. The following conclusion may be drawn within the parameters covered in the present study.

1. During the charging process the solid-liquid profiles being formed through melting are approximately similar irrespective to the time.
2. In the discharging process the solid-liquid interface takes an elliptic shape at the sensible heat releasing stage due to natural convection. However, the shape tends to be more circular at the latent heat releasing stage.
3. The useful heat gained increases as the water mass flow rate increases.
4. The sharp decrease of the heat gained during the latent heat releasing stage is due to the low thermal conductivity of the solid paraffin wax.
5. In the charging process the local heat transfer coefficient decreases monotonically with increasing the distance from the top of the wax container. In the case of increasing solar intensity by using reflector the local heat transfer coefficient shows different trends due to the natural convection.
6. During the charging process the average heat transfer coefficient is very small at the starting of melting indicating that the heat is transferred by conduction. It increases with the time, as the natural convection grows stronger with the increase of the melt layer thickness.

NOMENCLATURE

A	surface area of each melt sector, m^2	k_s	Thermal conductivity of solid PCM, W/m.K
a	width of each melt sector, m	T_l	Temperature of liquid PCM, °C
c_p	Specific heat of cooling water, J/kg°C	T_m	Melting temperature of PCM, °C
$h_{m,t}$	average heat transfer coefficient, W/m^2	T_s	Temperature of solid PCM, °C
$h_{x,t}$	Local heat transfer coefficient, W/m^2	T_W	Absorber wall temperature of, °C
L	Latent heat of fusion, J/kg	t	time, sec
m	Mass flow rate, kg/hm^2	Q_u	Useful heat gained, W
n	normal direction of the melt surface	δ	Thickness of PCM, m
k_l	Thermal conductivity of liquid PCM, W/m.K		

REFERENCES

1. G. A. Lane, Solar heat storage: *latent heat material*, V. I, CRC. Press (1983).
2. A. Abhat, Solar Energy v.30, pp. 313-332 (1983).
3. Mac Cracken, "Phase change materials for thermal storage", *Proceeding of Solar Energy Storage Options, San Antonion*, TX, 44, (1979).
4. Lane and Rossow, "Encapsulated of heat of fusion storage materials", *Proceeding of the second southeastern Conference on Application of Solar Energy*, Baton Ronge, La, 442 (1976).
5. B. Z. Ilken and M. Toksoy, "The solution methods used in the heat transfer problems with phase change. Research paper", Dokuz Eylul University, Izmir, Turky, No. FBE/MAK-89-AR-131 (1989).
6. Y. Rabin, I. Bar-Niv, E. Korin, and B. Mikic, Solar Energy v.55, pp. 435-444 (1995).

PERFORMANCE IMPROVEMENT OF A NON-CONVENTIONAL SOLAR WATER PUMP

K.Sumathy
Department of Mechanical Engineering
The University of Hong Kong, Hong Kong.
Email: ksumathy@hkucc.hku.hk; Fax: 852-2858-5415

Keywords: Flat-plate collector, displacement tanks, solar water pump

ABSTRACT. Details of a solar thermal water pump, which operates using a low boiling liquid is briefly described. The values of efficiencies of such a pump reported by the earlier researchers [1,2] are very low - being of the order of about 0.1 percent. In this paper an attempt is made to find out the reasons for such low efficiencies. A few changes to be made in the experimental set up to improve the performance of the pump re discussed. Also suggested are the modifications required in the analysis to reduce the large difference reported by the researchers between the measured and predicted performances.

1. INTRODUCTION

A perusal of the literature, on the subject of solar water pump, reveals that a pump can be operated mainly on any of the following three principles: (1) Pump driven by turbine operating with steam or an organic vapour generated using solar flat plate collectors or concentrators; (2) Pump driven by electricity obtained from solar cells; (3) An unconventional pump in which the vapour of a low boiling point liquid generated through flat plate collectors provides the motive power for lifting water, while the condensation of the vapour and the subsequent decrease in pressure provides for suction.

In the first method not only that the capital cost of the system is high, but also the operation and maintenance problems are many because of the number of stages involved in conversion of solar energy to hydraulic work. In the second method, the present cost of the solar cells makes the system uneconomical. The third method appears to be an attractive proposition. Researchers [1-3] have worked on a pump, operating on this principle, with n-pentane as the working substance. Not only are the values of the efficiencies reported by these investigators are low, but also the difference between the predicted and observed efficiencies is large. This paper is intended to discuss these aspects.

2. SYSTEM DESCRIPTION

The pump consists of an array of flat plate solar collectors and a set of tanks to displace the water. n-Pentane is heated in the flat plate collectors by thermosiphon flow. When the pressure in the separation tank reaches the pressure corresponding to the discharge head of the pump, valves 1 & 2 are opened slowly. Pentane vapour separating in tank S enters vessel A containing water. Water in vessel A, in turn, is gradually transferred to vessel B which initially contains air at atmospheric pressure. Air in vessel B gets compressed. When the pressure of air in vessel B reaches the pressure corresponding to the discharge head of the pump, the compressed air will displace water in vessel C to the overhead tank D to effect the required pumping.

When water in vessel C is completely pumped out, valves 1 & 2 are closed. At this instant vessel A contains pentane vapour and vessel B contains water and compressed air. Valve 3 is now opened to the required extent to allow the water from overhead tank D to flow through the cooling coils in vessel A. As pentane vapour starts condensing the pressure in vessel A decreases and eventually reaches the value that corresponds to the saturation pressure of pentane at the condensing temperature. During this period water in vessel B returns to vessel A. This reduces the pressure of air in vessel B, which in turn permits the well water to be sucked into vessel C through the one way valve 4. The system is now ready to perform the next cycle of events.

In the p - v diagram shown in Fig.2, 1-2-3-4-1 shows the processes undergone by pentane in the first cycle of events. The time lag between the first cycle of pumping the water and the second cycle equals the time required to generate pentane vapour and the condensation of the vapour in the first cycle. During the period of condensation, pentane in the collectors is being continually heated by solar energy. Hence, at the start of the

second cycle of pumping the water, the temperature and hence the pressure of pentane will be higher than those at the beginning of the first cycle. This pressure is shown as the one that corresponds to states 5 and 6 in Fig.2. Valves 1 & 2 are opened slightly at this instant. Pentane vapour at state 6 in the separation tank S expands to state 7 to reach the pressure corresponding to the discharge head.

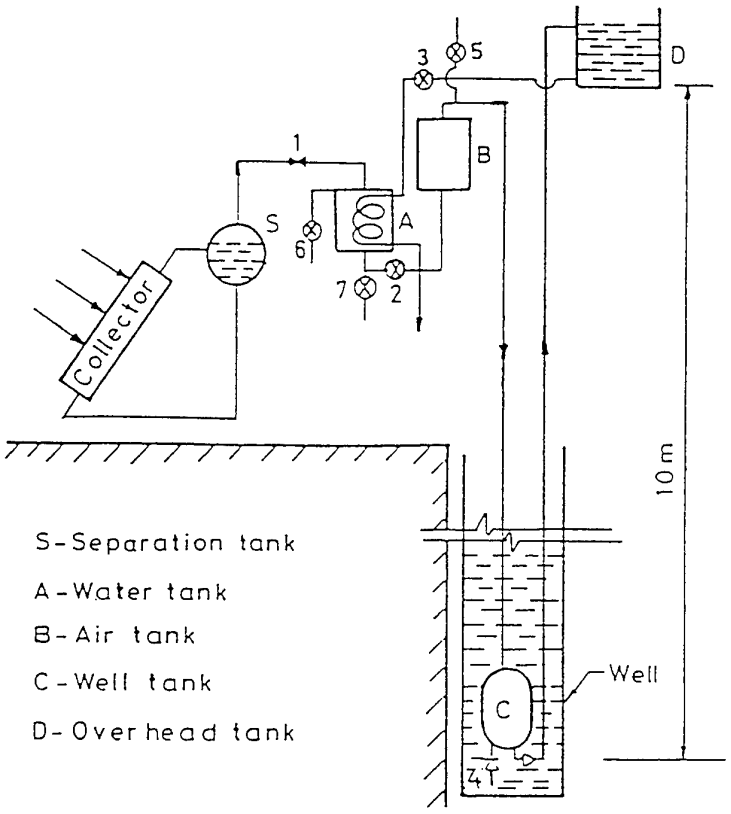


Fig.1. Schematic of a solar thermal water pump.

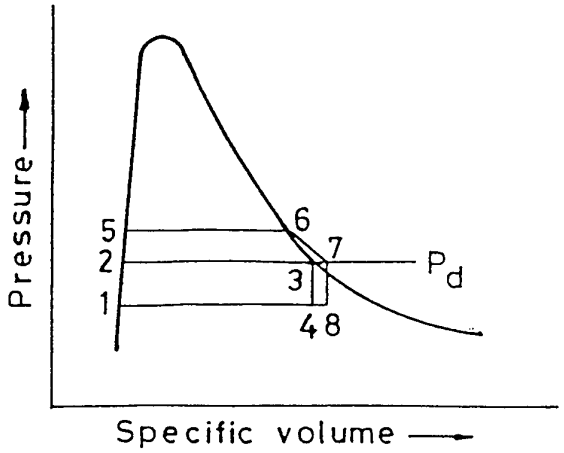


Fig.2. p - v Diagram

The process of lifting water and the subsequent condensation of pentane in tank A follows the same pattern as before. The processes undergone by pentane during this cycle is shown in Fig.2, by 2-5-6-7-8-1. Similar sets of events occur in the subsequent cycles and the pump continues to operate as long as the pentane in the collectors can get heated up.

3. REASONS FOR THE LOW EFFICIENCY OF THE PUMP

Low efficiencies of devices operating on flat plate collectors are too well known. However, in this case, the efficiency is rather very low, which is clearly shown in Fig.3. These values are taken from reference 1 & 2. This necessitates a careful investigation.

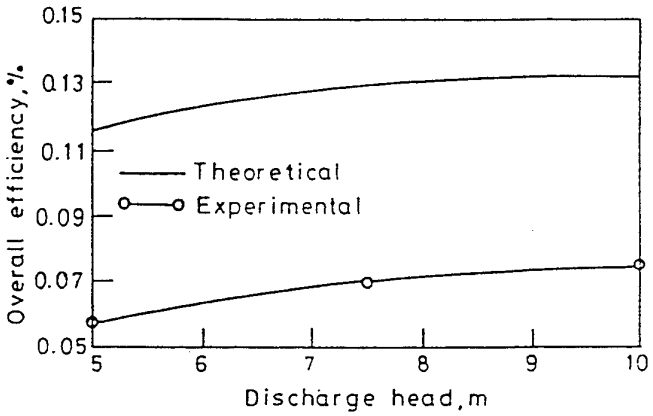


Fig.3 Overall efficiency vs discharge head

(1) The manner in which the pentane vapour displaces water in vessel A, requires a careful review. Since the rate of vapour generation through flat plate collectors is low due to obvious reasons, the water can only be displaced slowly by this vapour. Slow displacement causes condensation of some amount of vapour during the pumping process. This requires more pentane to do the job than the estimated quantity. To improve the performance, it is essential that the pentane vapour displaces water as quickly as possible.

(2) In the experimental work of the other researchers [1,2], the flat plate collectors are operating at unnecessarily very high temperatures beyond 10.30 hours. This reduces the collection efficiency and thus the overall efficiency of the pump.

(3) The exposed area of the collector is not optimized in the work of the other researchers.

(4) Volumes of vessels A, B and C are not also optimised.

(5) Heat loss in vessel B is not considered.

4. MODIFICATIONS SUGGESTED TO INCREASE THE EFFICIENCY OF THE PUMP

(1) The disadvantage associated with the slow displacement of water by vapour can only be eliminated by resorting to instantaneous filling. This could be achieved by having a storage tank, where the vapour could be collected at the required pressure to be used as and when required. This avoids the condensation of vapour in vessel A during the process of pumping the water.

(2) When the collector reaches the minimum pressure required to operate the pump there is no need to further heat the pentane in the collectors. From this instant onwards as and when the pentane vapour is used for pumping water the collector must be able to replenish this vapour by making use of solar

energy to just supply the required enthalpy of vaporisation. However, the amount of pentane vapour used by the pump in each cycle is much less than the generating capacity of the collectors. This causes the pentane in the collectors to be unneccssarily heated to very high temperatures at the cost of efficiency. This problem can only be eliminated by proper optimisation of the volumes of vessels A, B & C and the collector just supplies only that mass of pentane vapour which the vessels A, B & C can handle in each cycle. If this is not possible one or more parallel pumping can be done using the vapour generated by the collectors.

(3) Vessel B has to be insulated very well. It is also advisable to have a insulating float in vessel B. This reduces the problem of condensation of pentane vapour during the period of pumping.

5. DIFFERENCE BETWEEN PREDICTED AND MEASURED PERFORMANCES

In the work of the cited Researchers there has been large difference in the two efficiencies. The marked difference between the observed and predicted performance can be attributed to several reasons. The major factor is that the practical number of cycles per day is very much less than the predicted number of cycles as shown in Fig 4.

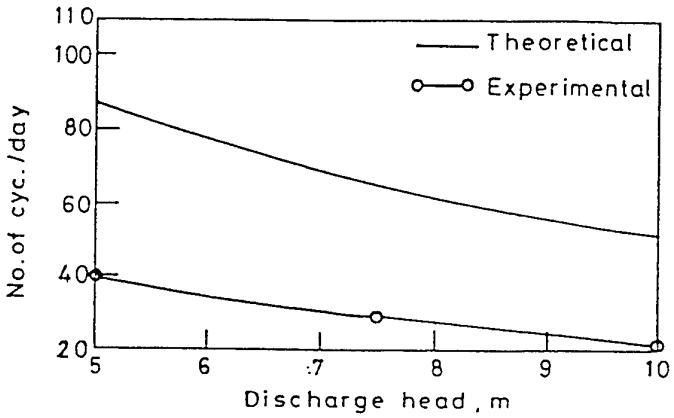


Fig.4. Number of cycles per day vs discharge head

This is because (i) The pump requires, at the beginning, a higher pressure than the discharge pressure for it to operate. (ii) The actual condensation time is high compared to the predicted one. (iii) Quite often the pump has to be stopped from working to remove the liquid pentane floating on water in vessel A. (iv) There is also a heat loss from the pentane vapour to the surroundings and also water in vessel A. When these factors are considered in theory this predicted efficiency reduces there by decreasing the difference between the two.

6. CONCLUSION

The above analysis shows that considerable modifications can be made in the experimental set up to improve its efficiency. The assumption made in the theory should suit the practical conditions to have a clear picture of what is happening in the pump. This work, both experimental and theoretical is in progress.

REFERENCES

1. D.P. Rao and K.S. Rao, "Solar Water Pump for Lift Irrigation", Solar Energy, Vol.18, pp.405-411, 1976.
2. K.W.Kwant, D.P. Rao and A.K. Srivastava, "R. Hariprakesh Rao, "Experimental Studies of a Solar Water Pump", Proc. of the International Solar Energy Society Congress, New Delhi, India, pp. 1917-1921, 1978.
3. A.Venkatesh, "Solar Thermal Water Pump", Proc. of the International Solar Energy Society Congress, Denver, Colorado, USA, pp. 2135-2140, 1991.

NEUTRONIC PERFORMANCES OF THE (D,T) DRIVEN HYBRID BLANKETS, FUELED WITH U_3O_8 AND UF_4 FOR VARIOUS COOLANTS TO BREED FISSILE FUEL FOR LWRS

O. Ipek
Mechanical Engineering Department
Suleyman Demirel University (SDU), 32260 ISPARTA TURKEY
Email: oipek@mmf.sdu.edu.tr Fax: (00 90) 246 708 59

Keywords: CFFE, fissile breeding, hybrid blanket, fusil breeding

ABSTRACT. In the present work, the possibility of spent nuclear fuel rejuvenation in fusion reactors is investigated for different fuels and coolants. Cumulative Fission Fuel Enrichment (CFFE) and neutronic performances of the (D,T) driven hybrid blankets, fueled with U_3O_8 and UF_4, are investigated under first wall load of 5 MW/m^2. Fissile fuel zone is considered to be cooled with three coolants, flibe (Li_2BeF_4), Natural Lithium (Li) and Eutectic Lithium ($Li_{17}Pb_{83}$) respectively. In the fuel zone is considered to be cooled with the different coolants mentioned above with volume fraction of 45.5%, ε = 1:1, for each coolants. Again, the behavior of the fuels mentioned above are observed during 48 month for discrete time intervals of Δt =15 days and by a plant factor of 75%. At the end of the operation time, calculations have shows that (CFFE) values have varied between 4.51% and 8.49% depending on the fuel and coolant type. The best enrichment performance is obtained in Li_2BeF_4 coolant blankets for each fuels. CFFE reach maximum value (8.49%) in UF_4 fueled blanket (in Row# 1) after 48 months. The lowest CFFE value (4.51%) is in U_3O_8 fueled blanket (in Row# 8) and Natural Lithium coolant at the end of the operation period. So, the enrichment would be sufficient for LWR reactor. The best Tritium Breeding Ratio (TBR), 1.5054, is obtained in U_3O_8 fueled blanket with Eutectic Lithium (Li) coolant. At the beginning of the operation, TBR values were 1.2942 in U_3O_8 fueled blanket 1.2175 in UF_4 fueled blanket. At the end of the operation, TBR reach 1.5034 in U_3O_8 fueled blanket and 1.4510 in UF_4 fueled blanket.

1. INTRODUCTION

Energy requirements are supplied in increasing proportion by nuclear reactors. The maximum capability of fossil fuel and hydraulic energy has almost been reached. Renewable energy sources lack any advantage due to irregular energy production. Therefor, the 21st century's energy requirement is nearly impossible to meet by the classic methods of present-day energy production[1]. Logistical problems, such a fuel transport and distribution, and environmental problems, such as particulate pollution and excessive CO_2 in the atmosphere, could limit the usage of fossil fuel for energy production. So, nuclear energy has important role in future energy projection of developing country. Nuclear energy production ratio in all king of energy production vary between 30 and 50% in Hungry, Switzerland, Sweden and some other countries. This ratio is higher than 60-70%[1].

High energy fusion neutron having a 14.1 MeV energy will be release in a (D,T) fusion reactor. 75% of the fusion energy is carried by these neutrons in the form of kinetic energy. The important criteria is, either the neutron energy is absorbed by the fuel to breed useful nuclear materials or converted to thermal energy by collision with moderator or coolant. All these processes can occur in the blanket of the hybrid reactor [2]. The possibility of rejuvenation of nuclear fuel in a hybrid blanket is an attraction field for early generation fusion reactors. Present-generation nuclear power plants are producing nuclear waste materials in substantial quantities, resulting in a concern from the standpoint of safety and proliferation of nuclear materials. Hence, methods to reduce the amount of radioactive waste inventory, as well as to reduce the amount of fissionable material are required to operate nuclear plants will be beneficial. On the other hand, nuclear reactors become more attractive when earth's tritium, uranium and deuterium resources are considered.

Today, a great number of LWRs are operational to meet the increasing demand on nuclear energy production. They require substantial quantities of slightly enriched (3-4%) nuclear fuel and use essentially the natural uranium as fuel. It is estimated that natural uranium source will be used up around the middle of the 21st century. In these reactors the ^{235}U isotope of the natural uranium is the reactive material and has an abundance of only 0.7%. As the LWRs have modest conversion ratio (0.6-0.7). plutonium production is also relatively slow. Hence, LWRs can exploit only about 1% of natural uranium fuel, and still 99% of the fissionable natural

uranium resource not being used for energy production. These reactors produce great amount of actinides as nuclear waste material which are one of the nuisances of present day. Previous work has demonstrated in extensive studies that the nuclear waste actinide material can be used with great efficiency as the fissile fuel component of a so called fusion-fission (hybrid) reactor . In a hybrid reactor, the actinides can be converted into new type of fissile materials with very high thermal fission cross sections which may turn out to become very precious nuclear fuel for special applications[3-5].Burn-up of the actinides that the basic nuclear fuel material uranium is subject to diverse nuclear transmutation in the course of the energy production process in a nuclear power plant, such as, (n,γ),(n,2n),(n,p) ,(,α), ect. in fusion fission reactor blankets and the rejuvenation of nuclear fuel for multiple recycling in critical nuclear reactor were subjects of investigation[6-9].

In the present work, a hybrid blanket system has been investigated for U_3O_8 and UF_4 fuels with coolant flibe, natural lithium and eutectic lithium respectively. The main objective is to study the rejuvenation behavior in a hybrid blanket coupled with a substantial electricity production in situ. In order to allow comparison of the evaluated neutronic parameters with previous studies on the hybrid reactors, an experimental hybrid blanket geometry is chosen, which was evaluated and presented to the international scientific community on different occasions[10,11,4].

2. BLANKET GEOMETRY

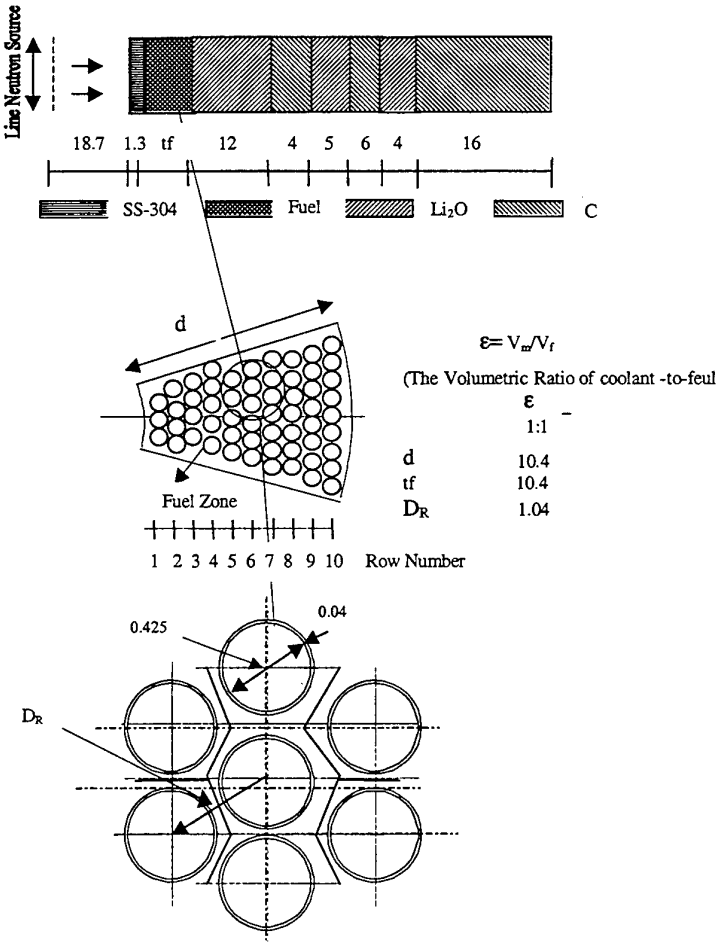


Fig. 1. Cross - Sectional view of the investigated blanket (Dimensions are given in cm)

The main emphasis is concentrated on a detailed neutronic treatment of rejuvenation procedure in a fusion-fission hybrid reactor fueled with U_3O_8 and UF_4 respectively. Fissile fuel zone is considered to be cooled with three coolants , flibe (Li_2BeF_4), Natural Lithium (Li) and Eutectic Lithium ($Li_{17}Pb_{83}$) with volume fraction, a

volumetric ratio of coolant-to-fuel (ε), of 45.5% for each coolant, respectively. The fissile fuel zone is composed of fuel rods which contain fuels mentioned above in 10 row in radial direction. The radial reflector is made of Li_2O and C(graphite) in a sandwich structure. This measure reduces the neutron leakage drastically, leads to better neutron economy[11] and supply more tritium production. The calculation is performed on an experimental hybrid blanket geometry which was presented to the international scientific community on different occasions[8-15]. Fig. 1. shows the basic structure of the investigated hybrid blanket in this study. The atomic densities and material composition of the investigated hybrid blanket in this work are given in Table 1.

In this concept, a line neutron source in a cylindrical cavity simulates the fusion plasma chamber. The latter is surrounded by a first wall made of 304-stainless steel. Recent work has shown that in fusion reactors, a first wall made of SS-304 without Mo and Nb components would give a C- class nuclear waste material after a life time of 30 years which will be suitable for shallow burial after the decommissioning of the fusion reactor[16,17]. The neutronic performance of fuel zone is investigated in 6 different modes.

1. U_3O_8 fuel with Flibe coolant in the hybrid blanket (Mode 1)
2. U_3O_8 fuel with Natural Lithium. coolant the in hybrid blanket (Mode 2)
3. U_3O_8 fuel with Eutectic Lithium coolant in the hybrid blanket (Mode 3)
4. UF_4 C fuel with Flibe coolant in the hybrid blanket(Mode 4)
5. UF_4 fuel with Natural Lithium. coolant in the hybrid blanket(Mode 5)
6. UF_4 fuel with Eutectic Lithium coolant in the hybrid blanket (Mode 6)

3. NUMERICAL CALCULATION

3.1 Calculation Methods

Neutronic analysis of fusion-fission (hybrid) blankets have been realized by using ANISN-ORNL[18] computer code that solves Boltzmann Transport Equation and neutron transport and activity cross section data libraries TRANSX-2[19] and CLAW-IV [20] in S_{16}-P_3 approximation, by using Gaussian quadrate sets to obtain a high accuracy for the deep neutron penetration problems[21] during different stages of this study. The letter represents an extended version of Los Alamos National Laboratory(LANL) cross section data library CLAW[22].

Temporal variations of the fissile fuel in the blanket are evaluated for neutron energy flux ($\Phi_w = 2.22*10^{14}$ (14.1 MeW) (n/cm^2 sec)) of 5 MW/m^2 on the first wall. The plant factor (PF) is taken as 75%. For neutronic calculations, the fuel zone is divided into 10 equidistant sub-zone, as shown in Fig.1. This corresponds to the ten fuel rows in the fissile zone in order to follow the space and time dependent nuclide density variations more accurately. Line neutron source on the first wall is preferred to a line neutron source including fusion plasma conditions because effects on the neutronic performance of the hybrid blanket of plasma density up to 10^{21} (D,T)/cm^3 were ignored.

The nuclear quality of the fuel has been followed in each fuel rod individually while considering variations in the neutron spectrum and in the atomic densities of all fissile and fissionable isotopes over the radial coordinate within the fissile zone for discrete time intervals Δt=15 days for (D,T) fusion modes. The change of the fuel composition during hybrid reactor plant operation is evaluated for discrete time interval Δt, as follows:
For Breeding reactions (indices b)

$$+\Delta N2 = PF.\Delta t.N1.\int_E \sigma_{b1}(E).dE.\Phi(E).dE + \Delta t\lambda_{b1}.N1 \qquad (1)$$

Indices 1 and 2 denote mother and daughter isotopes, respectively.

For Depletion reactions (indices dep)

$$+\Delta N = PF.\Delta t.N.\int_E \sigma_{dep}(E).dE.\Phi(E).dE + \Delta t\lambda.N \qquad (2)$$

Equations (1) and (2) consider the variations of the atomic densities of the fissionable isotope through both nuclear transmutations and as well as radioactive decay.

Table 1. Number Densities of Nuclides the Blankets zone at Start-up

Zone	Dimension [cm]	Material	Species	Atomic Densities ($10^{24}cm^{-3}$)
Cavity	0-18.7	Air		
First Wall	18.7-20.0	SS-304	^{12}C	7.873-4 [(a)]
			Si	6.734-4
			Cr	1.728-2
			Fe	5.926-2
			Ni	8.055-3
Fuel Zone	Fuel	U_3O_8	U^{235}	5.674-5
			U^{238}	8.048-3
			O	2.162-2
		UF_4	U^{235}	4.175-5
			U^{238}	5.805-3
			F	2.339-2
	Clad	SS-316	Si	1.540-4
			Cr	1.496-4
			^{55}Mn	1.579-4
			Fe	5.189-4
			Ni	7.368-4
			Mo	9.020-5
	Coolants	Flibe (Li_2BeF_4)	^{6}Li	8.255-4
			^{7}Li	1.015-2
			^{9}Be	5.489-3
			F	2.196-2
		Natural Lithium (Li)	^{6}Li	1.586-3
			^{7}Li	1.950-2
		Eutectic Lithium ($Li_{17}Pb_{83}$)	^{6}Li	1.902-4
			^{7}Li	2.340-3
			Pb	1.235-2
Tritium Breeding Zone	30.4-42.4	Li_2O	^{6}Li	4.638-3
	46.4-51.4		^{7}Li	5.704-2
	57.4-61.4		O	3.084-2
Reflector Zone	42.4-46.4		Al	3.014-3
	51.4-57.4	Graphit	C	1.128-1
	61.4-77.4			

a- Read as 7.873×10^{-4}

3.2 Temporal Change of the General Neutronic Data

Table 2 shows general integral data for all investigated cases for the (D,T) fusion driver at the beginning and at the end of a plant operation period of 48 months. The Tritium Breeding Rate (TBR) has the highest value for natural lithium coolant, followed by eutectic lithium coolant, and flibe. The excess tritium produced in blanket is to be used by external satellites (D,T) fusion reactors. On the other hand, (D,T), reactor must be designed self-sustaining with respect to tritium supply. TBR varies between 1.2921 and 1.5034 depending on the type of fuel, coolant and volume fraction at the end of the operation. The highest and lowest values are 1.5034 and 1.2921 in mode 3 and mode 4 respectively.

In all type, The TBR become higher than unity. Therefore, the blankets with (D,T) mode is self-sufficient with respect to tritium breeding and can provide enough tritium for their own fusion driver. Tritium production in ^{6}Li isotope increases almost linearly, caused by an increase of the neutron population due to the accumulation of fissile fuel in the blanket. Total energy generation in the blanket namely energy multiplication factor can be denoted by M. M has increased linearly over a 4 years of plant operation because of fissile fuel accumulation in the blanket. M varies between 2.7362 and 4.6344 depending on the type of the fuel, coolant during the operation

period. The highest and lowest values are 4.6344 and 2.7362 in mode 1and mode 6 with volume fraction of 45.5%, ε = 1:1, respectively. So, M increases only by about 48% in the mode 1 at the end of the opera. The increase of M can be considered relatively low for a hybrid reactor. Note that a quasi-invariable energy production over the operation period is essential to exploit the installed non-nuclear island of the plant (turbines, generators, heat exchangers etc.) at an optimal level.

The spatial nonuniformity of the fission energy density, defined with the help of peak-to average fission power density ratio " Γ " . This has a favourable effect with regard to a uniform exploitation of the fissile zone in the blanket. At the beginning of the operation peiod, the hihgest and lowest values, Γ , are 1.4752 and 1.2550 in mode 1 and in mode 5 respectively. At the end of operation period, the highest and lowest values are 1.6146 and 1.2779 in mode 1 and mode 5 respectively. As there is an increase of the neutron multiplication in the blanket, the neutron leakage " L" in radial direction out of the blanket increases slightly.

Table 2. Neutronic Data per (D,T) Fusion Neutron in Investigated Blankets

Time		Flibe		Nat. Lithium		Eutec. Lithium	
(Month)		U_3O_8	UF_4	U_3O_8	UF_4	U_3O_8	UF_4
0	T6	1.0714	1.0319	1.2293	1.1585	1.2942	1.2175
	T7	0.1270	0.1290	0.1904	0.1932	0.0943	0.0961
	TBR	1.2010	1.1654	1.4196	1.3540	1.3885	1.3156
	Σ_f	0.1280	0.0916	0.1357	0.0970	0.1317	0.0943
	$\nu\Sigma_f$	0.5938	0.4664	0.6235	0.4917	0.5990	0.4707
	M	3.1404	2.6992	3.3110	2.8328	3.1969	2.7362
	Γ	1.4752	1.2490	1.3786	1.2550	1.4745	1.3494
	L	0.0727	0.0687	0.0928	0.0861	0.0912	0.0824
48	T6	1.1794	1.1556	1.3005	1.2388	1.4066	1.3506
	T7	0.1303	0.1318	0.1941	0.1963	0.0968	0.0953
	TBR	1.3122	1.2921	1.4946	1.4374	1.5034	1.4510
	Σ_f	0.2393	0.1845	0.2020	0.1501	0.2384	0.1897
	$\nu\Sigma_f$	0.8619	0.7362	0.7930	0.6574	0.8566	0.7453
	M	4.6344	3.9639	4.2046	3.5598	4.6294	3.0329
	Γ	1.6146	1.4480	1.4193	1.2779	1.5416	1.4069
	L	0.0796	0.0755	0.0982	0.0913	0.0995	0.0907

T6, $^6Li(n,\alpha)T$ reaction ;T7, $^7Li(n,\alpha)T$ reaction ; TBR , Tritium Breeding Ratio; Σ_f , Fission Reaction ; $\nu\Sigma_f$, Fission Neutron Breeding; M . Energy Multiplication; Γ , Average Power Density in Fuel Zone; L Radial Neutron Leakage

3.3 Fissile Fuel Breeding

Fig.2. shows the temporal variations of the Cumulative Fissile Fuel Enrichment (CFFE) (^{235}U, ^{239}Pu, ^{241}Pu) over a total operation period of t=48 months for selected fuel rods (row#1, row#3 and , row#5, row#8, row#10 for ten-row fuel zone) in (D,T) driven hybrid reactor modes for flibe, natural lithium and , eutectic lithium cooled blankets, respectively. One can observe that the fuels become usable in LWR after a time of about 24-36 months depending on the coolant, fuel and, the position of the fuel rods in the fissile zone. One can notice that UF_4 fuel has a slightly higher enrichment ability than U_3O_8 fuel. CFFE.value change between 4.5 and 8.49 % depending on the position of the fuel rods in fissile zone and mode.

The highest and lowest CFFE value is in (row# 1) mode 4 and (row# 6,7) mode 2 respectively, at the end of the 48 months. During all stages of the rejuvenation process, all fissionable isotopes in fuel will contributed to nuclear heat generation and consequently to the electricity production of the hybrid reactor.

3.4 Fuel Burn-up Grade

For a reactor engineer, it would be most interesting to estimate the grade of fissile fuel utilization in the course

the rejuvenation process in the hybrid blanket in situ. This ban be measured easily with the help of fissile fuel burn-up(BU). It can be calculated as follows:

$$BU = (PF.\Delta t.E_f\ 2.22x10^{14}.F_w.C_f.\iint \Sigma_f(E)\Phi(E).dE.dV)/m_{FU} \quad (3)$$

Where E_f = energy per fission, 200 MeV, C_f =conversion factor, $1.6021x10^{-19}$ MW s/1MeV, F_w = are of the first wall, m_{FU} = nuclear fuel charge, Φ : Neutron Flux. Fig.3 (A) shows the average fuel burn-up in the hybrid blanket as a function of plant operation period. Burn-up levels become comparable over 4 years to those LWRs. Burn-up value is the lower in UF_4 fueled modes than other mode. The lowest burn-up level is in UF_4 fueled blanket and flibe coolant during operation period.

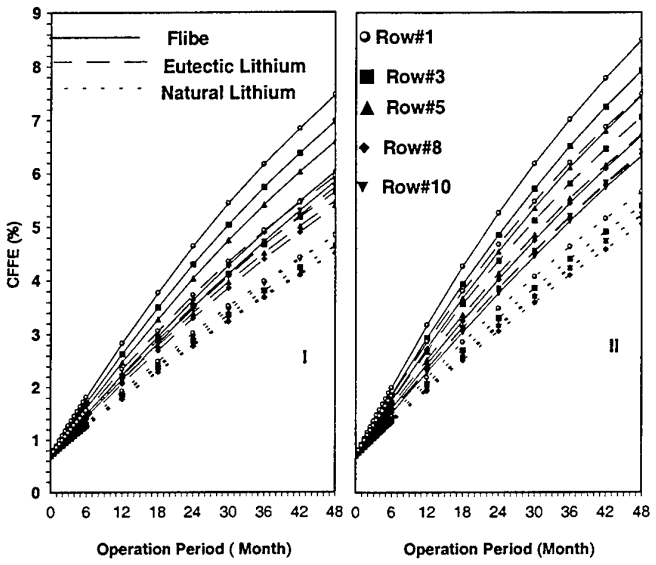


Fig. 2. Temporal increase of fissile fuel quality in the blanket with different coolant and volume fraction of 45.5(ε=1:1), I, fuled with U_3O_8 fuel, II, fuled with UF_4 fuel

3.5 Figure -of-Merit

It would be interesting to evaluate the fuel regeneration ability of hybrid reactors in form of a Figure-Of-Merit (FOM) which can be defined as ratio of the amount of net ^{239}Pu mass generated to the fission power output of the hybrid blanket. Mathematical formulation of FOM in net ^{239}Pu [gr/(MW_{th} year)] or [kg/(GW_{th} year)] can be described as follows[23].

$$m_{Pu} = PF.\Delta t 2.22x10^{14}.F_w.C_{Pu}.\iint \left[\Sigma_{r,}{}^{238}{}_U(E) - \Sigma_{dep,}{}^{239}{}_{Pu}(E)\right]\Phi(E).dE.dV \quad (4)$$

$$C_{Pu} = 3.968x10^{-22}\,gr/P^{239}Pu$$

$$FOM = m_{Pu/P_{th}} \quad (5)$$

P_{th} is thermal power production in the blanket. Fig.3 (B). depicts the FOM values for all modes. At startup, the FOM values are high in all modes. A rapid accumulation of the fissile fuel component ^{239}Pu causes a increase of fission power production in the hybrid blanket with the all modes. FOM values of UF_4 fuel are higher than U_3O_8 fuel. Flibe cooled blanket breeds the fissile fuel more efficiently than other coolants. In all modes, FOM values decrease during the operation period while M increase as can be seen Table 2. The FOM-values in Fig.3 (B). are comparable to those reported in other fission-fission (hybrid) reactor design studies[24].

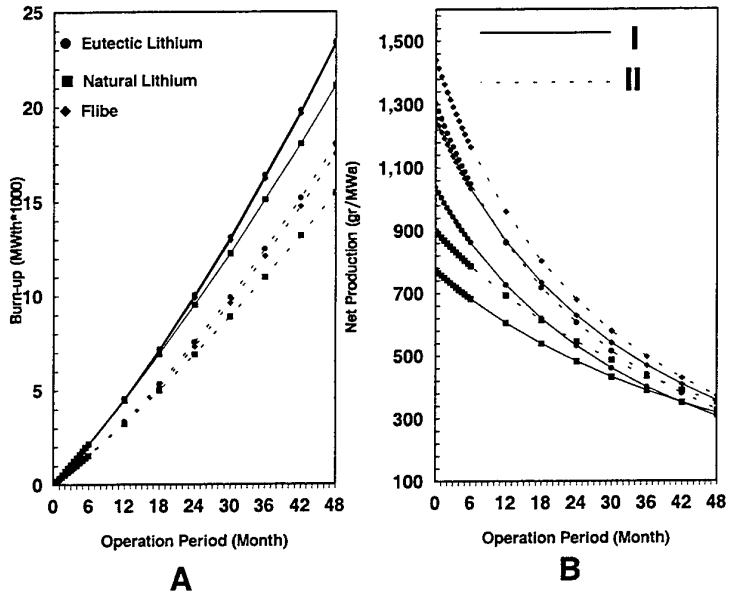


Fig. 3 (A). Temporal increase of fissile bur-up(BU) in the investigated blankets, (B) Temporal variation of the FOM,I: fuled with U_3O_8 fuel, II fuled with UF_4 fuel

3.6 Safeguard Aspect of The Plutonium Component

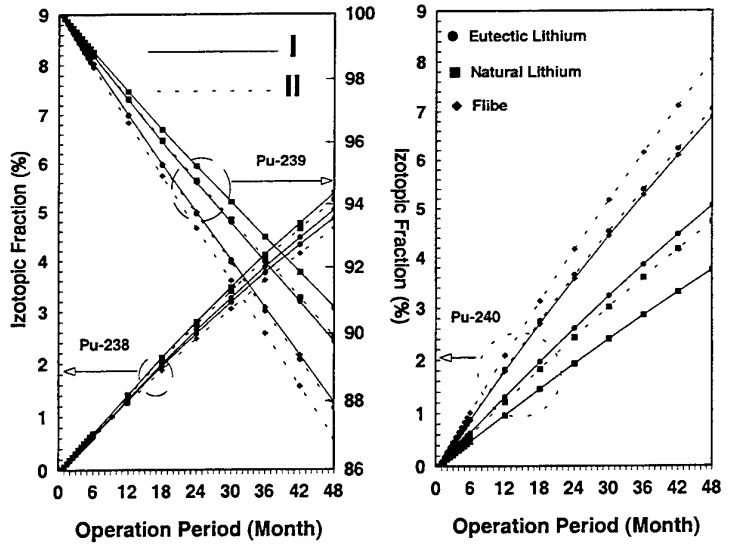


Fig. 4. Temporal variation of the percentages of the isotopes during rejuvenation with (D,T) fusion driver, I: fuled with U_3O_8 fuel, II fuled with UF_4 fuel

Fig 4 shows isotopic percentage of ^{238}Pu and ^{239}Pu in the bred plutonium for all modes. Isotopic percentage of ^{238}Pu is lower than ^{240}Pu in flibe coolant, but higher in other coolants. It would be of primary interest to follow the non-prolific level of the plutonium fuel during rejuvenation. The intensity of spontaneous fission neutrons in ^{240}Pu is about 50000 times higher than in ^{239}Pu so that only a few percent of ^{240}Pu would already denaturate the generated plutonium to a non-prolific level[25]. Previous analyses has indicated that the ^{240}Pu content must be <5% in weapon grades plutonium fuel[26,27]. Therefore, ^{240}Pu in excess of 10% can be considered as sufficient

to denaturate the plutonium safely. The isotopic percentage of ^{240}Pu at the end of the operation period has higher value in modes with flibe coolant, this value is lower than 5% as can be seen from Fig.4.

4. CONCLUSIONS

In this study, possibility of fuel rejuvenation .for various coolants has analyzed in hybrid blankets. The main conclusions are as follows:

1. The breeding periods vary between 24 and 36 months to reach a CFFE = 3 - 7.01%, depending on the type of fuel and coolant and after 4 years operation period, CFFE values can reach between 4.50 and 8.49% , depending on the type of fuel and coolant. This can help to construct compact LWRs with moderate power levels 300 MW_{el}. The best rejuvenation performance is obtained with flibe coolant and . UF_4 fueled hybrid blanket is superior compared to the U_3O_8 fuels for rejuvenation purposes.

2. A fusion breeder fueled with (UF_4 or U_3O_8) produce weapon grade ^{239}Pu. It must be denatured for commercial utilization. Fusion driven fuel rod containing (UF_4 or U_3O_8) breed higher quality nuclear fuel compared to fission reactor.

3. The isotopic percentage of ^{240}Pu in the plutonium has a higher value (8.032%) in mode 4 at the end of the operation period. In all modes with flibe and eutectic lithium coolant, the isotopic percentages of ^{240}Pu is higher than 5% at the end of the operation period, but it is lower than 5% in all modes with natural lithium coolant. So, Fuel can be considered sufficient to denature the plutonium safety in the blankets with flibe and eutectic lithium coolant. During operation period, it is possible to breed a high quality, but denatured plutonium for LRWs. This is an important factor with regard to international safeguarding. The proposed system offers an extremely high level of safeguarding.

4. Thus, the calculations have shown that the same fuel rods after irradiation in any of the investigated modes can be used directly in LWRs. The fusion driven hybrid blankets can breed nuclear fuel with safeguarding.

5. REFERENCES

1. J.A. Maniscalo,..et al., 'Recent Progress in Fusion-Fission (Hybrid) Reactor Design Studies', Nuclear Technology /Fusion, 1 (4), p. 419,(1981).
2. H.Yapici, I. Cürtüttü, V. Özceyhan, et al, ' Potential of a fusion-fission hybrid reactor using for various coolants to breed fissile fule for LWRs' ,Annals of Nuc. Ener , Elsevier Pergamon, Received 23 July, accepted 27 October (1998), U.K
3. S. Sahin, M. Al-Eshaik, ' Fission Power Flatting in Hybrid Blankets Using Mixed Fuel', Fus.Tech., Vol.12, p.295, (1987).
4. S. Sahin, A. Erisen, A, and Y. Çebi., 'A Fast Hybrid Blanket with Flat Fusion Power over a long Operation Period', Trans. Am., Nucl., Soc, 54, 134, (1987).
5. S. Sahin, A. Erisen, and Y. Çebi, 'Realization of a Flat Fission Power Density in a Hybrid Blanket over long Operation Periods', Fusion Technology, Vol.15, p.37,(1989).
6. S. Sahin, and H. Yapici, 'Rejuvenation of CANDU Spent Fuel in a Hybrid Blanket', Trans. Am. Nucl. Soc. 59,105, (1989).
7. S. Sahin, and H. Yapici, 'Investigation of the neutronic potential of moderated and fast (D,T) hybrid blankets for rejuvenation of CANDU spent fuel', Fusion Tech., 16,331, (1989).
8. S. Sahin, E. Baltacioglu, and, H.Yapici,, ' Potential of a catalyzed fusion driven hybrid reactor for the regeneration of CANDU spent fuel' , Fusion Tech. , 20,26, (1991).
9. S. Sahin, H. Yapici, and E. Baltacioglu, 'Rejuvenation of LWR Spent Fuel in a Catalyzed fusion-Fission Hybrid Blanket', Kerntechnik, 59(6), 270, (1994).
10. S. Sahin, M.Abdul Raoof. M, ' Neutronic Parameters of a Clindrical Hybrid Blanker Driver By a Simulated Line Source', Fusion Technol. ,Vol.10, p.1315, (1986).
11. S. Sahin, T.A. Al-Kusayer et al, 'Preliminary Design Studies of a Cylindrical Expperimental Hybrid Blanket with Deuterium-Tritium Driver' , Fusion Technology , Vol.10, p. 84, (1986).
12. S. Sahin, H.Yapici, and ,E. Baltacioglu,' Heavy water reactor spent fuel regeneration with fusion neutrons', Trans. Am. Nucl. Soc. 1989. 60,176, (1989).
13. S.Sahin., S.Unalan, and H.Yapici, 'Decrease of the CANDU Spent Nuclear Waste Inventories in Fusion-Fission (Hybrid) Reactors, International Journal of Energy Environment Evonomics', 4(1) , pp. 67-97, (1996).

14. S. Sahin,.H. Yapici.,' Rejuvenation of CANDU Spent Fuel in a Hybrid Blanket', Trans. Am. Nucl. Soc., 59, p.105, (1989).
15. S. Sahin, and H.Yapici, 'Investigation of Neutronic Potential of Moderated and Fast (D,T) Hybrid Blankets for Rejuvenation of CANDU Spent Fuel', Fusion Technology , 16, p.331, (1989).
16. J. D. Lee, 'Waste Disposal Assessment of HYLIEE-II Structure' , Fus. Tech., Vol.26, No. 4, p.174, (1994).
17. S. Sahin, R. Moir, and S. Ünalan, 'Neutronic Investigation of a Power Plant Using Peaceful Nuclear Explosive', Fusion Technology, Vol.26 No. 4, pp.1311-1325, (1994).
18. Jr. Engle, , 'A One- Dimensional Discrete Ordinates Transport Code with Anisotropic Scattering', K-1693, Oak Ridge National Laboratory, Oak Ridge, TN, W.W,1970,). ANISN, update (1996).
19. R.E. MacFarlane,.'TRANSX-2, A code for Interfacing MATXS Cross - Section Libraries to Nuclear Transport Codes', LANL, (1993).
20. T.A. Al-Kusayer, S. Sahin., and A. Drira.,' Coupled 30 Neutrons 12 Gamma Ray Cross - Section with Retrieval Programs for Radiation Transport Calculations. Radiation Shielding Information center', RSIC Newsletter, Oak Ridge National Laboratory, CLAW-IV, May (1988).
21. Bondarenko, 'Group Constant for Nuclear Reactor Calculations, Consultant Bureau, New York,1964.
22. R.J. Barett, R.E. MacFarlane, 'CLAW couple 30 neutrons, 12 gamma-ray group cros section for neutron trsnsport calculations',. LA-7808-MS, Los Almos Scientific Laboratory, Los Alamos, Nm.,1979.
23. H.Yapici, O. Ipek, V.Özceyhan, A. Eri• en, ' Analysis of the Rejuvenation Performance By Using Uranium Fuels(UN,UC,UO_2,U_3Si_2) And Different Coolants For Various Volume Fraction In The Hybrid Blanket', Annals of Nuclear Energy, Elsevier Pergamon, accepted 04 June, 1999, U.K.
24. E. Greenspan, 'Fusion-Fission Hybrid Reactor, Advances in Nuclear Science and Technology', Vol.16, Plenum Press, New York,(1984).
25. W. Mayer, S.S. Loyalka, et al., 'The Homemade Nuclear Bomb Syndrome, Nuclear Safety', Vol.18, p.427.,(1977).
26. S. Sahin, J. Ligou, 'The Effect of the Spontaneous Fission of Plutonium-240 on the Energy Release in a nuclear Explosive', Nuclear Technology, Vol. 50, No. 1, p. 88,(1980).
27. S. Sahin, 'Reply to the Remarks on the Pluntonium-240 Induced Preignition Problem in a Nuclear Device', Nuclear Technology, Vol. 54. No. 3, p. 431, (1980).

L. Thermal Storage

GENERAL MODEL OF ANALYZING THE THERMAL PERFORMANCE OF LATENT HEAT THERMAL ENERGY STORAGE SYSTEMS WITH VARIOUS PCM CAPSULES

Yanbing Kang*, Yinping Zhang, Yi Jiang, Yingxin Zhu**
Department of Thermal Engineering,
Tsinghua University, Beijing, 100084, P.R.China
E-mail*: ybkang@environment.thtf.com.cn
E-mail**: zhangyp@mail.tsinghua.edu.cn

Keywords: thermal energy storage, phase change material, heat transfer

ABSTRACT. The present study describes and classifies latent heat thermal energy storage (LHTES) systems according to their structural characteristics. A general model is developed for analyzing the thermal characteristics of the various typical LHTES systems to simulate thermal characteristics such as instantaneous heat transfer rate, instantaneous thermal storage capacity, etc. of the various typical LHTES systems. The model is verified using experimental data in the literature. An illustrative example is undertaken to analyze the thermal performance of various LHTES systems. The general model can be used to select and optimize the system structure and to simulate the thermal behavior of various typical LHTES systems.

1. INTRODUCTION

Efficiency and environmental concerns have increased the importance of thermal energy storage (TES) systems in such fields as solar energy systems, greenhouses and power plants. Among the available technologies for thermal storage systems, latent heat thermal energy storage (LHTES) systems can store a great amount of thermal energy in a small volume with a relatively small temperature variation. Recently, for the purpose of effective load leveling of electric power system, much attention has been given to cool storage air-conditioning systems.

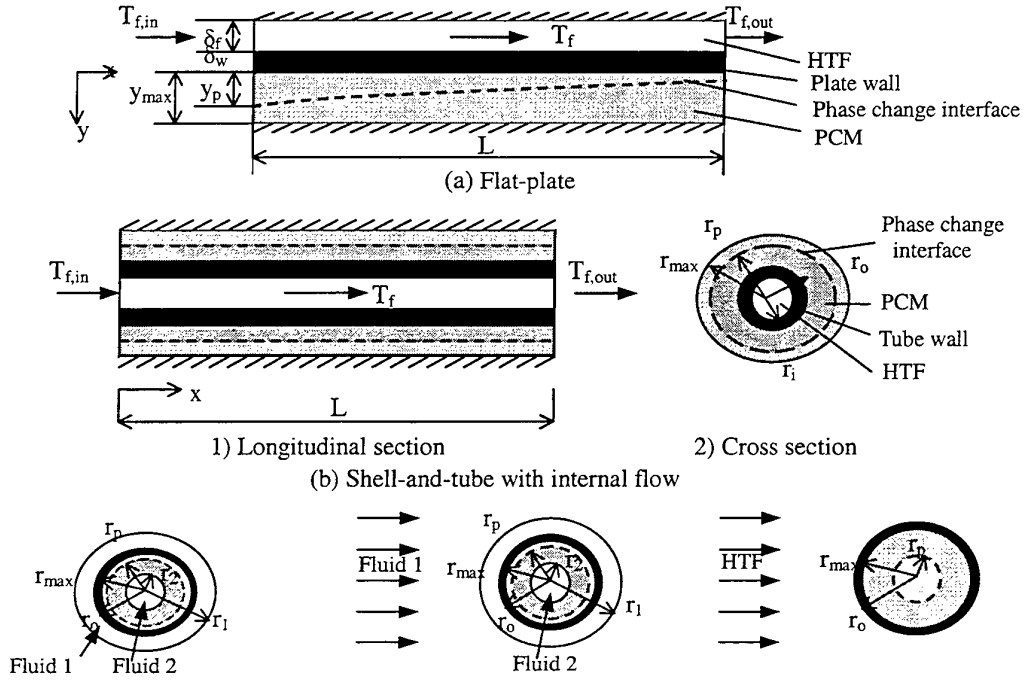


Fig.1 Schematics of typical LHTES systems

Many theoretical studies concerning the thermal characteristics of LHTES systems have been undertaken. Multi-layer[1], shell-and-tube[2-5] and spherical[6-8] systems based on PCM (phase change material) were studied. Since those researchers all focused on the thermal performance of a specific type of LHTES, the applicable range of their models is quite limited. In fact, many LHTES systems used in practical applications which at first seem to be different, share common features from the heat transfer point of view. The present work will (1) identify the common features of various LHTES systems often used in practical applications and (2) build a general model capable of analyzing the thermal characteristics of various LHTES systems.

2. CLASSIFICATION AND THE COMMON FEATURES OF TYPICAL LHTES SYSTEMS

Typical LHTES systems used in engineering applications can be classified based on their structural characteristics as packed bed systems and shell-and-tube systems. For packed bed systems, the PCM container can be spherical, rectangular, cylindrical, etc. The systems can also be divided according to the flow type as internal flow or external flow (including parallel flow and cross flow). Flat-plate structures and shell-and-tube structures with internal flow are outward phase change systems, while shell-and-tube structures with parallel flow or cross flow and spherical packed bed are inward phase change systems. Some typical LHTES systems often used in engineering applications are shown in Fig.1. The systems all have PCM or uniform PCM capsules distributed uniformly in the system. The heat transfer in each system is two-dimensional conduction with solid-liquid phase change and an unknown fluid temperature variation along the axial direction. The PCM thermal resistance and the effective heat transfer area both vary with time and space. The analysis of the different type of LHTES differs in the value of some characteristic parameters, such as characteristic dimension, thermal resistance, etc. All systems share common feature as summarized shown in Fig.2. The parameters for the various systems in the figure are listed in Table 1.

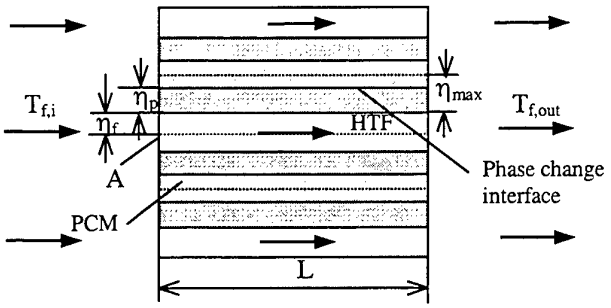


Fig.2 Schematic of general LHTES system

3. GENERAL MODEL OF SOLID-LIQUID LHTES SYSTEMS

The analysis is simplified by assuming

(1) Axial conduction in PCM and natural convective heat transfer in liquid PCM are negligible.
(2) Ste<<1 and the HTF capacitance can be ignored which means that the sensible thermal storage capacity can be neglected compared with latent thermal storage capacity.
(3) For inward phase change structures, $L>>r_o$.

General Heat Transfer Model of Solid-Liquid LHTES Systems

The energy equation for the PCM:
$$H_m \cdot \rho_p \cdot \frac{\partial A_{c,p}(t,x)}{\partial t} = U \cdot P \cdot \left| T_f(t,x) - T_m \right| \quad (1)$$

The energy equation for the HTF:
$$\dot{m}_f \cdot c_{p,f} \cdot \frac{\partial T_f(t,x)}{\partial x} = -U \cdot P \cdot (T_f(t,x) - T_m) \quad (2)$$

where
$$U = h_f \cdot R_r \quad (3)$$

and
$$R_r = \frac{R_f}{R_f + R_w + R_p}, \quad (4)$$

subject to the initial conditions $A_{c,p}(t=0, x)=A_{c,p,0}(x)$, $T_f(t=0, x)=T_{f,0}$
and the boundary condition $T_f(t, x=0)=T_{f,in}(t)$.
The analysis can be simplified using the following dimensionless parameters

$$\theta_f = \frac{T_f - T_m}{T_{f,in} - T_m},\ \overline{A}_{c,p} = \frac{A_{c,p}}{A_{c,max}},\ Fo = \frac{a_p t}{A_{c,max}},\ X = \frac{x}{L},\ Ste = \frac{c_{p,p}|T_m - T_{in}|}{H_m},$$

$$NTU = \frac{h_f A}{\dot{m}_f c_{p,f}},\ Bi = \frac{h_f P}{k_p},\ \Phi = \frac{R_w + R_p}{R_f \cdot Bi}$$

where $a_p = \frac{k_p}{\rho_p c_{p,p}}$, $R_r = \frac{R_f}{R_f + R_w + R_p} = f\left(Bi, \overline{A}_{c,p}\right) = \frac{1}{1 + Bi \cdot \Phi}$

The dimensionless parameters can be used to transform equations (1)-(4) into dimensionless equations

$$\frac{\partial \overline{A}_{c,p}(Fo,X)}{\partial Fo} = Ste \cdot Bi \cdot R_r(Fo,X) \cdot |\theta_f(Fo,X)| \tag{5}$$

$$\frac{\partial \theta_f(Fo,X)}{\partial X} = -NTU \cdot R_r(Fo,X) \cdot \theta_f(Fo,X) \tag{6}$$

Subject to the initial conditions $\overline{A}_{c,p}(Fo = 0,X) = \overline{A}_{c,p,0}(X)$, $\theta_f(Fo = 0,X) = \frac{T_{f,0} - T_p}{T_{f,in} - T_p}$

and the boundary condition $\theta_f(Fo, X = 0) = 1$

Numerical Algorithm

Integrating equations (5)-(6) give

$$\overline{A}_{c,p}(Fo,X) = \overline{A}_{c,p,0}(X) + \int_0^{Fo} Ste \cdot Bi \cdot R_r(Fo,X) \cdot |\theta_f(Fo,X)| \cdot dFo \tag{7}$$

$$\theta_f(Fo,X) = \exp\left(-\int_0^X NTU \cdot R_r(Fo,X) \cdot dX\right) \tag{8}$$

$\theta_f(Fo,X)$ and $\overline{A}_{c,p}(Fo,X)$ can be obtained by integrating numerically over space and time. The integration required iteration at each step since R_r is implicitly a function of $\overline{A}_{c,p}$. From the initial condition, $\overline{A}_{c,p}(Fo=0,X) = \overline{A}_{c,p}(0,X)$. $\overline{A}_{c,p}$ increases with time for both charging and discharging processes. As $\overline{A}_{c,p}(Fo,X)$ approaches 1, the phase change front has crossed the entire PCM region and can no longer move radically. Therefore, the actual heat transfer area will begin to decrease (Fig.3). The axial position where the PCM is completely solidified/melted is designated as $X_{in}(Fo)$. For Ste<<1, the thermal storage capability of that region can be neglected. So the actual heat transfer area can be written as

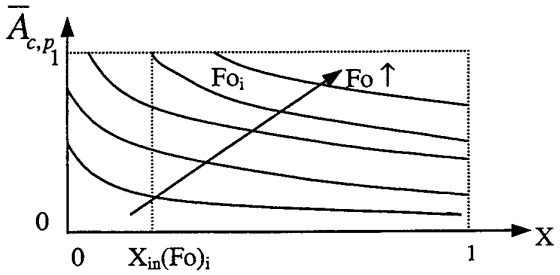


Fig. 3 Typical phase change interface variation

$$A_{act}(Fo) = A \cdot (1 - X_{in}(Fo)) \tag{9}$$

The lower limit for the integration in equation (8) can then be replaced by $X_{in}(Fo)$.
The dimensionless overall heat transfer coefficient based on the overall heat transfer area is

$$U^*(Fo) = \int_{X_{in}}^{1} \frac{U(X,Fo)}{h_f(X,Fo)} = \int_{X_{in}}^{1} R_r(Fo,X)\cdot dX \tag{10}$$

For a given LHTES system, $\overline{A}_{c,p}(Fo,X)$ and $\theta_f(Fo,X)$ are calculated first and then the transient heat transfer rate, thermal storage capacity and molten mass fraction for a thermal discharging process or frozen mass fraction for a thermal charging process are computed using

$$q(Fo) = \dot{m}_f \cdot c_{p,f} \cdot \left|\theta_f(Fo,X=1) - \theta_f(Fo,X=0)\right| \cdot (T_m - T_{f,in}(Fo)) \tag{11}$$

$$Q(Fo) = \int_0^{Fo} q(Fo)dFo \tag{12}$$

$$F_r(Fo) = \frac{\int_0^{Fo} q(Fo)dFo}{A_c \cdot (1-\varepsilon) \cdot \rho_p \cdot H_m} = \int_0^1 \overline{A}_{c,p}(Fo,X)\cdot dX \tag{13}$$

Model Parameters for Each System

The key point in applying the general model for each system is to determine suitable parameters for each system. The parameters used in the model are listed for each type of LHTES system in Table 1. Of the parameters, the equations for Φ were determined using the thermal resistance and those for the other parameters were obtained according to the geometric characteristics of various systems.

ApplicAbility of the General Model

The model can be used to analyze two dimensional solid-liquid latent heat transfer problems with an unknown fluid temperature distribution along the axial direction for all the LHTES systems listed in Table 1. The general model can calculate the instantaneous HTF temperature distribution, the instantaneous phase change interface along the axial direction, the heat transfer rate, the thermal storage capacity, the overall heat transfer coefficient, the effective heat transfer area and the molten/frozen PCM mass fraction. Some of these parameters are important but difficult to measure for monitoring the charging or discharging processes. The model can also be used when the mass flow rate and/or the HTF inlet temperature vary with time and when the convective heat transfer coefficient varies with time or space and it is also valid for simultaneous charging and discharging processes and for when the PCM is initially partially solidified.

4. MODEL VALIDATION

The general model was used to simulate the thermal behavior of several types of LHTES systems such as flat-plate system, shell-and-tube designs with parallel flow and packed beds with spherical capsules.

The simulated results are compared with the results of a quasi-steady-state analysis for one-dimensional conditions and experimental data respectively.

Comparison with Quasi-Steady Solution

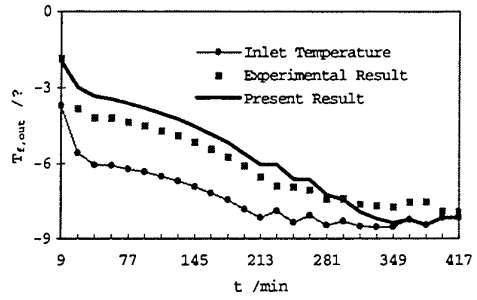
Ref. [9] studied the phase change process for a single infinite flat-plate, a single cylinder and a single sphere full of PCM with constant wall temperature. The results of the present model are compared with the quasi-steady solution for these one-dimensional phase change problems. The present model was used with the extreme condition that the fluid mass flow rate is large enough so that the temperature difference between the inlet and outlet can be neglected. The relative deviations between the two sets of results range from 0.5-4.5 %.

Comparison with Experimental Data

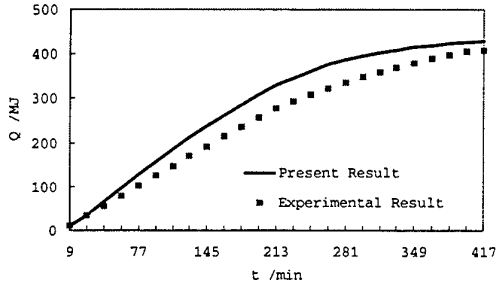
The model predictions were compared with the experimental data[10] for a spherical packed bed LHTES system. The experimental system had an ice-storage unit packed with ice spheres. The experimental conditions were: r_o=0.0485m, r_{max}=0.0475m, A_c=0.785m^2, ε=0.24, L=2.5m, k_w=12.4W m^{-1}·K^{-1}, T_m=0°C and H_m=334kJ/kg. Ice was used as the PCM and glycol solution (33wt.% glycol) was used as the HTF. The computational result and the experimental data are compared for both cool charging and discharging processes in Figs. 4 and 5. The reasonable agreement between them shows that the model can be used to predict the thermal performance of various systems.

Table 1. Characteristic parameters for each system used in the general model

General model	Fig. 3	η_p	$\overline{A}_{c,p} = \frac{A_{c,p}}{A_{c,max}}$	$A_{c,max}$	P	Φ	$\eta_{p,max}$ (δ_w=0, r_2=0)	η_f (δ_w=0, r_2=0)	Cell number (δ_w=0, r_2=0)
Flat-plate	Fig. 1 (a)	y_p	$\frac{y_p}{y_{max}}$	$W \cdot y_{max}$	W	$\frac{k_p \cdot \delta_w}{k_w \cdot W} + \frac{y_{max}}{W}\overline{A}_{c,p}$	$\frac{V}{A}$	$\frac{\varepsilon}{1-\varepsilon}\cdot\frac{V}{A}$	$\frac{H}{y_{max}+\delta_f}$
Shell-and-tube with Internal flow	Fig. 1 (b)	r_p	$\frac{r_p^2 - r_o^2}{r_{max}^2 - r_o^2}$	$\pi(r_{max}^2 - r_o^2)$	$2\pi \cdot r_i$	$\frac{k_p \cdot \delta_w}{k_w \cdot W} + \frac{y_{max}}{W}\overline{A}_{c,p}$	$\frac{2\frac{V}{A}}{(\frac{1}{\sqrt{\varepsilon}}-\sqrt{\varepsilon})}$	$\sqrt{\varepsilon}\cdot\frac{2\frac{V}{A}}{(\frac{1}{\sqrt{\varepsilon}}-\sqrt{\varepsilon})}$	$\frac{A_c}{\pi r_{max}^2}$
Shell-and-tube with parallel flow	Fig. 1 (c)	r_p	$\frac{r_{max}^2 - r_p^2}{r_{max}^2 - r_2^2}$	$\pi(r_{max}^2 - r_2^2)$	$2\pi \cdot r_o$	$\frac{1}{2\pi}(\frac{k_p}{k_w}\ln\frac{r_o}{r_{max}} - \frac{1}{2}\ln(1-\overline{A}_{c,p}\cdot(1-(\frac{r_2}{r_{max}})^2)))$	$2\frac{V}{A}$	$\frac{1}{\sqrt{(1-\varepsilon)}}\cdot 2\frac{V}{A}$	$\frac{A_c}{\pi r_1^2}$
Shell-and-tube with cross flow	Fig. 1 (d)	r_p	$\frac{r_{max}^2 - r_p^2}{r_{max}^2 - r_2^2}$	$\frac{(1-\varepsilon)\cdot A_c}{\frac{1}{r_o^2}(r_{max}^2 - r_2^2)}$	$(1-\varepsilon)\cdot A_c \cdot \frac{2}{r_o}$	$\frac{r_o^2}{2(1-\varepsilon)\cdot A_c}(\frac{k_p}{k_w}\ln\frac{r_o}{r_{max}} - \frac{1}{2}\ln(1-\overline{A}_{c,p}\cdot(1-(\frac{r_2}{r_{max}})^2)))$	$2\frac{V}{A}$	$2\frac{V}{A}$	1
Sphere packed bed	Fig. 1 (e)	r_p	$1-\left(\frac{r_p}{r_{max}}\right)^3$	$(1-\varepsilon)\cdot A_c$	$(1-\varepsilon)\cdot A_c \cdot \frac{3}{r_o}$	$\frac{r_o^3}{3(1-\varepsilon)\cdot A_c \cdot r_{max}}(\frac{k_p}{k_w}(1-\frac{r_{max}}{r_o}) + (1-\overline{A}_{c,p})^{\frac{1}{3}} - 1)$	$3\frac{V}{A}$	$3\frac{V}{A}$	1

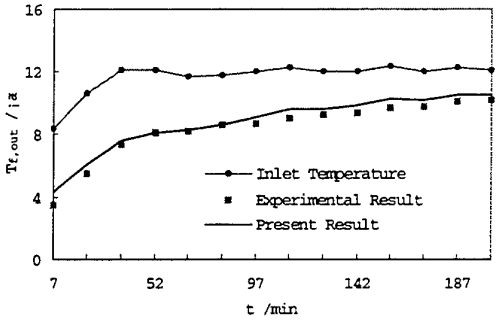


(a) Comparison of the outlet HTF temperature

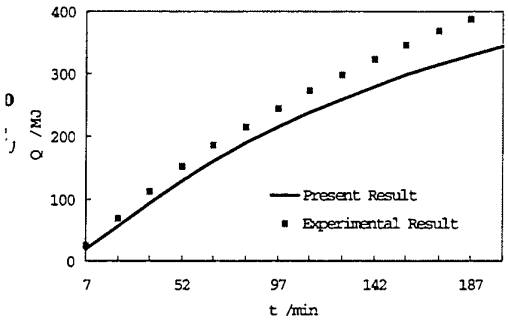


(b) Comparison of the thermal storage capacity

Fig. 4 Model validation with experimental data
(Cool charging process, $\dot{m}_f$ =3.913kgs^{-1}, h_f=83.2 Wm^{-2}K^{-1} [12])



(a) Comparison of the outlet HTF temperature



(b) Comparison of the thermal storage capacity

Fig. 5 Model validation with experimental data
(Cool discharging process, m_f=2.613kgs^{-1}, h_f=76.2Wm^{-2}K^{-1}[12])

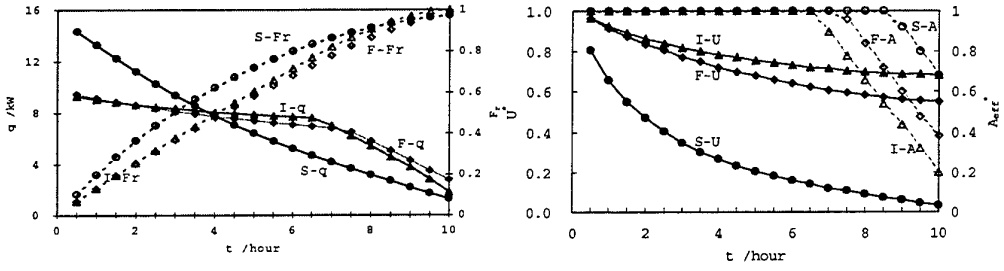
5. ILLUSTRATIVE EXAMPLE

For a given LHTES system in Fig. 3, relating known parameters are: T_m=20 °C, H_m=200kJkg^{-1},$c_{p,p}$=2.0kJkg^{-1}K^{-1}, ρ_p=1000kgm^{-3}, A_c=1m^2, L=2m, ε=0.35 and HTF is air, $T_{f,in}$=10°C.

The instantaneous thermal behavior including the timewise variation of the heat transfer rate, the frozen mass fraction, the dimensionless heat transfer coefficient and effective heat transfer area of flat-plate system (F), shell-and-tube system with internal flow (I) and sphere packed bed (S) are presented in Fig. 6. The values of the overall performance for each system are listed in Table2 and the convective heat transfer coefficients for the various structures were obtained from the formula in Refs. [11-14]. The shell-and-tube system with internal flow has the best performance for these conditions. In addition, the results indicate that the decrease trend of heat transfer area is approximately linear. The PCM solidifies faster near the entrance than near the exit, which reduces the effective heat transfer area.

Table.2 The Value of Relative Parameters of Each Structure

	Flat-plate (F)	Shell-and-tube with Internal flow (I)	Sphere packed bed (S)
$\eta_{p,max}$	0.02	0.0364	0.06
η_f	0.0108	0.0215	0.06
Cell number	33	240	1



(a) Variation of heat transfer rate and frozen mass fraction

(b) Variation of dimensionless overall heat transfer coefficient and effective heat transfer area

Fig. 6 Thermal behavior of different LHTES systems (k_p=0.5Wm^{-1}K^{-1}, V/A=0.02, v_f=4ms^{-1}, solid lines refer to the left coordinate and dash lines refer to the right coordinate)

6. CONCLUSIONS

The common features of various LHTES systems often used in practical applications were used to develop a general heat transfer model which is valid for variable flow rates and variable inlet HTF temperatures, and for finned structures. The general model can be used to simulate the thermal behavior under various operating conditions. The model was verified by experimental results in the literature. In addition, an illustrative example is undertaken to analyze the thermal performance of different LHTES systems with the model. The general model provides guidance for system selection and optimization and performance simulation of solid-liquid LHTES systems.

REFERENCES

1. P. Brousseau and M. Lacroix, Study of the thermal performance of a multi-layer PCM storage unit, *Energy Convers. Mgmt* Vol.37, No.5, pp.599-609 (1996).
2. Y. Cao and A. Faghri, Performance characteristics of a thermal energy storage module: a transient PCM/forced convection conjugate analyses, Int. J. Heat Mass Transfer, Vol.34, No.1, pp.93-101 (1991).
3. Y. Cao and A. Faghri, A numerical analysis of Stefan problems for generalized multi-dimensional phase-change structures using the enthalpy transforming model, Int. J. Heat Mass Transfer, Vol.32, No.7, pp.1289-1298 (1989).
4. Y. Cao and A. Faghri, A study of thermal energy storage systems with conjugate turbulent forced convection, Journal of Heat Transfer, Vol.114, November, pp.1019-1027 (1992).
5. M. Esen and A. Durmus, Geometric design of solar-aided latent heat storage depending on various parameters and PCMs, Solar Energy, Vol.62, No.1, pp.19-28 (1998).
6. T. Homma et al., Heat characteristics of spherical latent heat storage capsules, Proc. of 7th International Conference on Thermal Energy Storage, Sapporo, Japan, pp.313-318 (1997).
7. D. Arnold, Dynamic simulation of encapsulated ice stores: ASHRAE Trans., Vol.96 (1): 1103-1110 (1991).
8. D. Arnold, Laboratory performance of an encapsulated ice stores: ASHRAE Trans., Vol.97 (2): 1170-1177 (1991).
9. Y. P. Zhang, H. P. Hu, X. D. Kong and Y. H. Su, Thermal Energy Storage-Theory and Application, China Science and Technology Book Company (in Chinese), (1996).
10. H. Li, The experimental research on the ice storage equipment's utility of heat transfer, Thesis of Master Degree of Tsinghua University in China (in Chinese), (May 1997).
11. W. M. Rohsenow, Handbook of heat transfer fundamentals, pp.108, McGraw-Hill, (1985).
12. W. M. Rohsenow, Handbook of heat transfer applications, pp.445, McGraw-Hill, (1985).
13. W. M. Kays, Convective heat and mass transfer, pp.248-252, McGraw-Hill, (1980).
14. F. P. Incropera and D. P. Dewitt, Fundamentals of Heat and Mass Transfer (Fourth Edition), pp.378-380, John Wiley & Sons, (1996).

NOMENCLATURE

A = overall heat transfer area, m^2
$A_{c,p}$ = cross sectional area over which phase change has occurred, m^2
A_c = cross sectional area of LHTES system, m^2
c_p = specific heat, $J\ kg^{-1}K^{-1}$
F_r = molten/frozen PCM mass fraction
h_f = convective heat transfer coefficient, $W\ m^{-2}K^{-1}$
H_m = heat of fusion, Jkg^{-1}
k = thermal conductivity, $W\ m^{-1}K^{-1}$
L = length, m
m_f = heat transfer fluid mass flow rate, kgs^{-1}
P = wetted perimeter of fluid duct, heat transfer area unit length, m
q = heat transfer rate, W
Q = thermal storage capacity, J
r = radius, m
R = thermal resistance, KW^{-1}
Ste = Stefan number
t = time, s
T_f = heat transfer fluid temperature, K
T_m = PCM melting temperature, K
U = overall heat transfer coefficient, $W\ m^{-2}K^{-1}$
v_f = heat transfer fluid velocity, $m\ s^{-1}$
V = volume, m^3
W = width, m
x = axial coordinate, m

Greek symbols

ρ = density, $kg\ m^{-3}$
δ = thickness, m
ε = LHTES system porosity
Φ = structural thermal resistance coefficient
η = coordinate of phase change interface or fluid duct , see Fig.3, m

Subscripts

ave = average
eff = effective
f = fluid, fin
i = inside
in = inlet
max = maximum
o = outside
out = outlet
p = PCM
w =wall

HIGH TEMPERATURE LATENT HEAT THERMAL ENERGY STORAGE SYSTEM FOR SOLAR RANKINE ENGINES

Takeo S. Saitoh
Professor of Dept. of Aeronautics and Space Engineering
Tohoku University, Sendai 980-8579, Japan
Phone : +81-22-217-6974; Fax : +81-22-217-6975
E-mail: saitoh@cc.mech.tohoku.ac.jp

Akira Hoshi
Research Associate
Phone : +81-22-217-6977; Fax : +81-22-217-6977
E-mail: hoshi@cc.mech.tohoku.ac.jp

Keywords: high temperature, latent heat, thermal energy storage, solar Rankine

ABSTRACT. Thermal energy storage is of importance in effective use of thermal energy for many application to utilize such as renewable energies including solar, geothermal, sky radiation, and load leveling to reduce peak electricity demand. Among several thermal energy storage technologies, the latent heat thermal energy storage (LHTES) system using phase change material (PCM) is useful in charging and discharging a large amount of heat during melting and solidification. The LHTES systems are also considered to be very promising to reduce carbon dioxide (CO_2) emissions and to mitigate global warming. Man's activities have exceeded a critical level at which their effects give an impact to earth's environment.

A lot of investigations concerning the LHTES systems have been reported in recent years. However, almost all of the past investigations have been well classified into category of a low temperature range. In the future, the high-density heat storage system for industrial applications, space crafts and automobiles will be of importance.The high-temperature LHTES systems are capable of having the high-density TES and permit heat extraction at a constant high-temperature condition. But some investigations are necessary for the heat transfer enhancement since thermal conductivity of the PCM is relatively low. In the present paper, the charging characteristics of the high-temperature LHTES system are discussed numerically. As an application, the present LHTES system is applied to solar Rankine engine will be introduced and the possible thermal performance and validity of this engine will be also discussed.

1. INTRODUCTION

Melting and solidification of phase change material (PCM) is of practical importance in latent heat thermal energy storage (LHTES) systems which are considered to be very promising to use thermal energy for many applications such as solar energy utilization system and load leveling at power plants. Further, the LHTES systems are considered to be very promising to reduce carbon dioxide (CO_2) emissions. Among several thermal energy storage technologies, the LHTES system using PCM is useful in charging and discharging a large amount of heat during melting and solidification.

A pioneering analysis of the melting of an unfixed solid PCM in a horizontal cylinder was done by Bareiss and Beer[1]. They presented a theoretical model for close-contact melting between the PCM solid and the cylinder wall, when the Stefan number is relatively small. The proposed equation is quite useful to obtain the melting rates for the case where the flow effect in a melt layer is presumed to be minor. Using assumptions similar to the lubrication theory, Bahrami and Wang[2] investigated melting in a spherical capsule and presented a closed form solution for the melting process. Moallemi and Viskanta[3] analyzed the problem of melting around a moving cylindrical heat source and also performed experiments with paraffin as PCM.

Two melting modes are involved in melting in enclosures. One is close-contact melting between the solid bulk and the capsule wall, and another is natural convection melting in the liquid (melt) region. Close-contact melting processes for a single enclosure have been solved using several numerical methods (e.g. Saitoh and Kato[4]). In addition close-contact melting heat transfer characteristics including melt flow in the liquid film under inner wall

temperature distribution were analyzed and simple approximate equations were already presented by Saitoh and Hoshi[5].

Investigations concerning the thermal energy storage (TES) for solar energy utilization system have been reported in recent years. LHTES unit using form-stable high-density polyethylene (HDPE) was developed by Abe et al.[6]. An experiment was performed for both charging and discharging modes. Esen et al.[7] optimized the thermal performance of the cylindrical latent heat storage tanks theoretically. Numerical works pertaining to cyclic phase change and energy storage in solar heat receivers have been done by Hall et al.[8].

In the present paper, we will propose high-temperature LHTES system (accumulator). Most of the conventional LHTES systems utilize PCM with relatively low melting point. The principal purpose of the past LHTES system was applications to space heating / cooling. However, since fossil fuel like petroleum, coal, and natural gases will sooner or later run out in the next century, natural energy like solar, wind, and biomass will rise as one of alternative energy sources.

One of the most promising means to produce power from these natural energies is the solar Rankine engine which operates under low temperature range below 200°C. Among other possibilities is of course photo voltaic (PV) cell. Solar heat is collected and stored as pressured hot water in the LHTES tank (accumulator) in day time, and the steam turbine or other expander will be operated whenever energy demand exists. Dynamic power generation system other than PV system will be the key technology in the near future.

This paper describes the theoretical design of the high-temperature LHTES tank including contact melting process in the vertical cylindrical capsule, and clarifies the charging characteristics. And it is shown that evaporated steam mass is approximately doubled compared to the conventional one if the latent heat TES system were adopted.

2. THEORETICAL FORMULATION

Heat Conduction Melting

The vertical cylindrical capsule seems to be more practical than horizontal one for high-temperature LHTES system in consideration of capsule material, manufacturing and cost. A schematic model and coordinate system used in the numerical solution are shown in Fig.1. The primary assumptions made in the present study are following:

(1) The properties are constant,
(2) Volumetric expansion during melting is negligible,
(3) Natural convection is negligible.

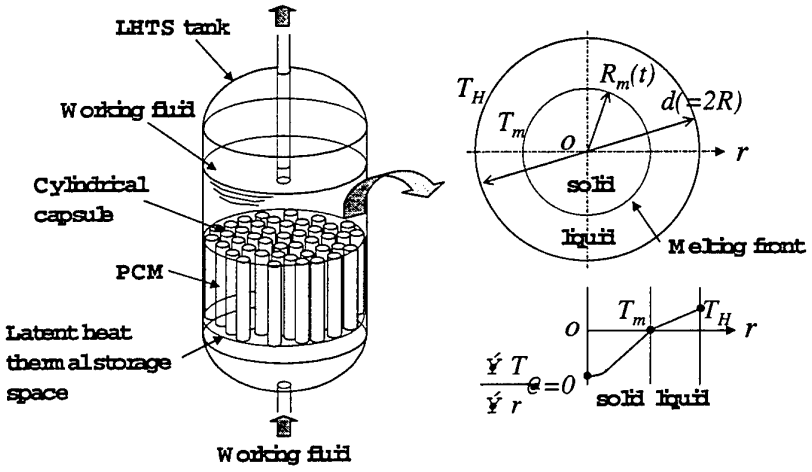


Fig.1 Schematic model for high-temperature LHTES accumulator

The governing energy equations for the liquid and the solid region can be described as below, considering the above assumptions. Symbols are listed at end of paper.

Liquid:

$$\frac{\partial T_l}{\partial t} = a_l\left(\frac{\partial^2 T_l}{\partial r^2} + \frac{1}{r}\frac{\partial T_l}{\partial r}\right) \qquad R_m(t) < r < R \tag{1}$$

Solid:

$$\frac{\partial T_s}{\partial t} = a_s\left(\frac{\partial^2 T_s}{\partial r^2} + \frac{1}{r}\frac{\partial T_s}{\partial r}\right) \qquad 0 < r < R_m(t)_l \tag{2}$$

The initial condition and the boundary condition are

Initial condition:

$$T_s(r,0) = T_c \qquad 0 < r < R \tag{3}$$

Boundary conditions:

$$T_l(R,t) = T_W \qquad t > 0 \tag{4}$$

$$\frac{\partial T_s(0,t)}{\partial r} = 0 \qquad t > 0\,. \tag{5}$$

A heat balance equation at the solid-liquid interface is given by

$$\begin{aligned} \rho L\frac{dR_m(t)}{dt} &= \rho L\dot{R}_m(t) \\ &= k_s\frac{\partial T_s(R_m(t),t)}{\partial r} - k_l\frac{\partial T_l(R_m(t),t)}{\partial r} \qquad t > 0\,. \end{aligned} \tag{6}$$

Here, we will adopt the SOR (Successive Over-Relaxation) method for numerical integration of governing equations.

Close Contact Melting

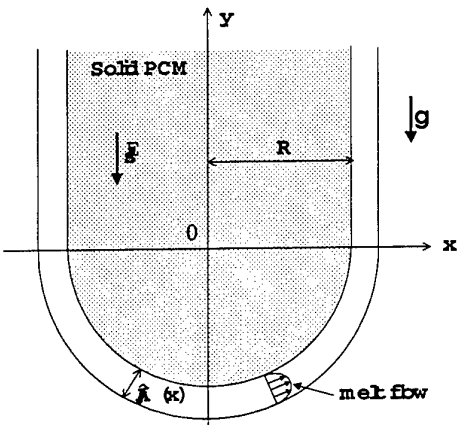


Fig.2 Analytical model for close-contact melting

Formulation will be shown for the close-contact melting in bottom of a vertical cylindrical capsule initially packed with the solid PCM. A model and coordinate system used in the present analysis are shown in Fig.2. It is assumed that the liquid film between the solid PCM and capsule wall is very thin.

The momentum equation can be simplified to

$$\frac{dp}{dx} = \mu \frac{\partial^2 u}{\partial y^2} \tag{7}$$

The boundary conditions on the capsule inner wall ($y=0$) and at the solid-liquid interface ($y=\delta$) are

$$\begin{aligned} &y = 0: \quad u = v = 0, \quad T = T_w \\ &y = \delta: \quad u = 0, \quad v = -\dot{s}, \quad T = T_m \end{aligned} \tag{8}$$

A mass balance in a small element surrounded by dx and δ is given by

$$\rho_l \cdot 2\pi x \int_0^{\delta} u dy = 2\pi \int_0^x \rho_s \dot{s} x dx \quad . \tag{9}$$

The energy balance equation for the liquid film is described as below

$$\frac{d}{dx} \int_0^{\delta} u(T - T_m) dy = a \left[\left. \frac{\partial T}{\partial y} \right|_{y=\delta} - \left. \frac{\partial T}{\partial y} \right|_{y=0} \right] \quad . \tag{10}$$

The following approximate solution yields for molten gap width δ^*.

$$\delta^* = \frac{\rho^* f(\mathrm{Ste})}{2\dot{s}^*} \tag{11}$$

where,

$$f(\mathrm{Ste}) = \sqrt{25 + 10\mathrm{Ste}} - 5 \tag{12}$$

The melting velocity of the solid PCM can be determined from the following force balance equation.

$$2\pi \int_0^r px dx = \Delta \rho g V_s \tag{13}$$

The melting velocity of solid PCM is as follows:

$$\dot{s}^* = \left[\frac{1}{24} \rho^{*3} \mathrm{Ar}\, \mathrm{Pr}\, f^3(\mathrm{Ste}) \frac{V_s}{\pi R^3} \right]^{1/4} \tag{14}$$

3. NUMERICAL RESULTS AND DISCUSSION

Figure 3 shows the complete melting time when the volume of a vertical cylindrical capsule is kept constant. A shell and tube type heat exchanger system is practical for high-temperature LHTES system in consideration of manufacturing. The vertical cylindrical capsule with large aspect ratio give better thermal performance than the horizontal one in charging and discharging processes.

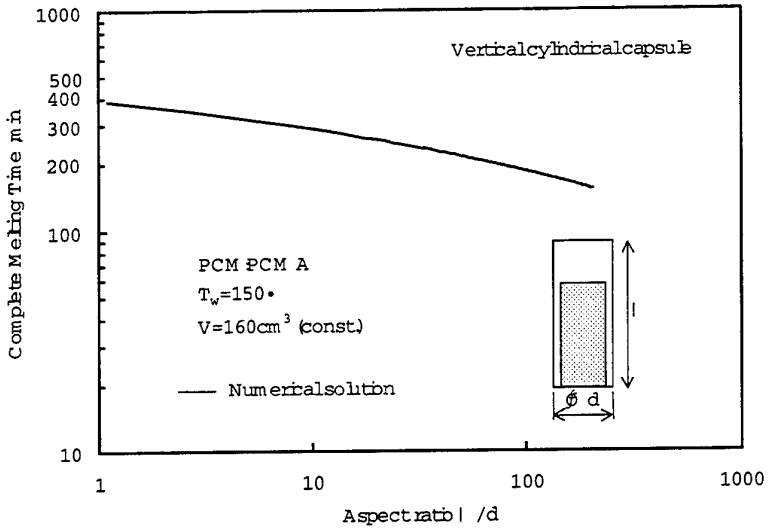


Fig.3 Complete melting time

Molten mass fraction versus real time under the same cylinder length is shown in Fig.4. Complete melting time decreases with decreasing cylinder diameter. About 15-20% of the total mass melts due to close-contact melting at the bottom of the cylinder.

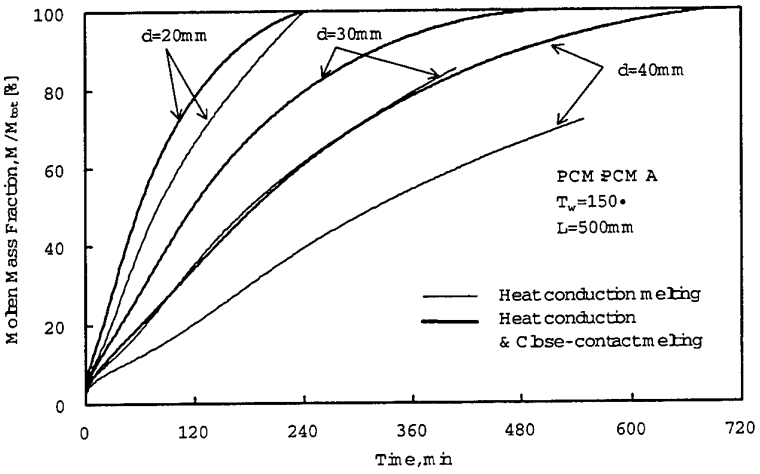


Fig.4 Time variation of molten mass fraction with cylinder diameter

4. APPLICATION TO SOLAR RANKINE ENGINES

As an application, a kind of solar Rankine engine will be constructed and the possible thermal performance and validity of this engine will be discussed. Solar Rankine engines are composed of solar collector, thermal energy storage tank, and steam expander. High-temperature water produced by the solar collector is stored in the LHTES tank. Steam from this tank operates the steam expander. Figure 5 shows outline of this solar Rankine cycle system. The volume and pressure of LHTES tank are indicated as V_0[m^3] and P[kg/cm^2]. The steam consumption rate in the expander is Gs[kg/s]. Another parameters are shown in the figure.

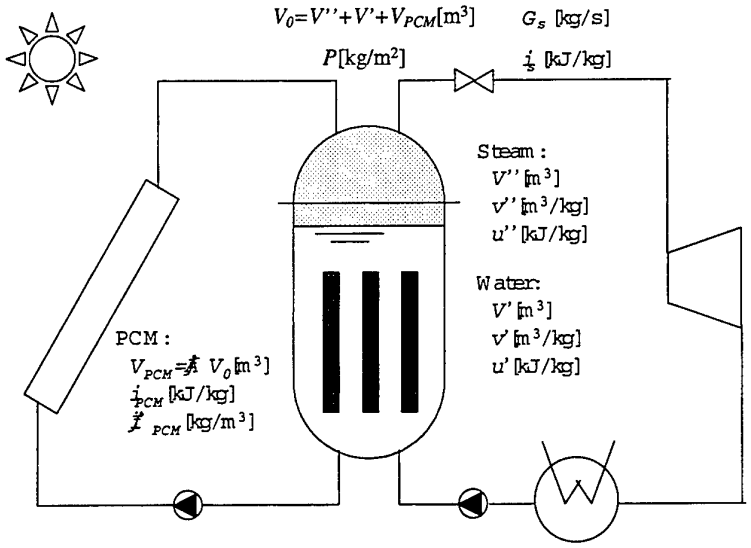


Fig.5. Solar Rankine system

The quantity of evaporation is given by

$$\frac{dG}{dP}=\frac{1-\eta}{X}\frac{d}{dP}\left(\frac{u''-u'}{v''-v'}\right)+\frac{G}{X}\frac{d(i''-X)}{dP}+\frac{1}{X}\frac{d(\rho_{PCM}V_{PCM}i_{PCM})}{dP}. \tag{15}$$

where

$$X=\frac{v''r_s}{v''-v'} \tag{16}$$

Figure 6 shows a comparison of pressure variation between the LHTES system and the conventional steam accumulator for the evaporation time. It is clearly seen that the present LHTES system is superior to the conventional steam accumulator.

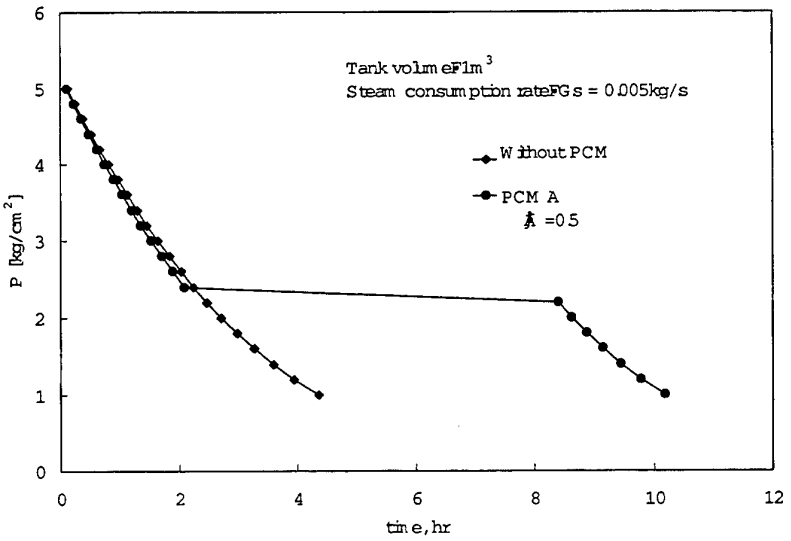


Fig.6 Pressure variation and evaporation time

Figure 7 shows the effect of melting point of the PCMs on pressure variation. The PCM with higher melting point gives a higher pressure plateau and can elongate the complete evaporation time.

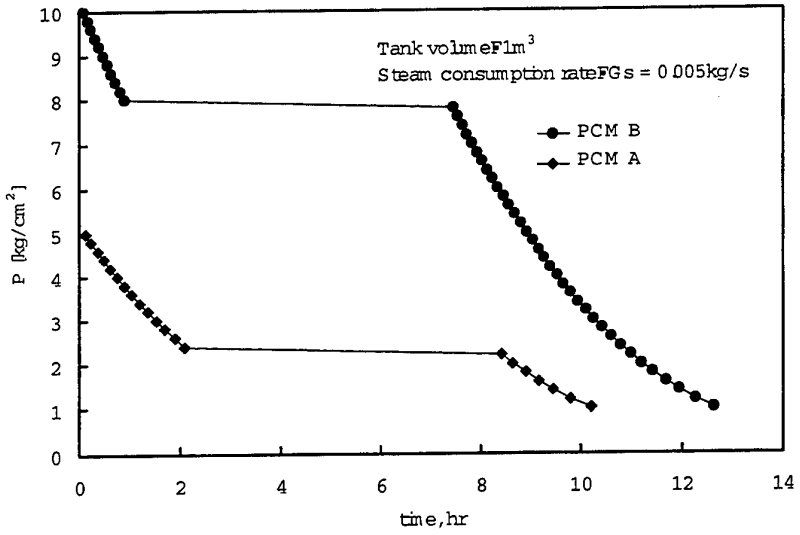


Fig.7 Comparison of PCMs

Figure 8 shows the evaporated steam mass with varying the packing factor η and charging pressure. The evaporated steam mass by the present LHTES system is twice as much as that by the conventional steam accumulator.

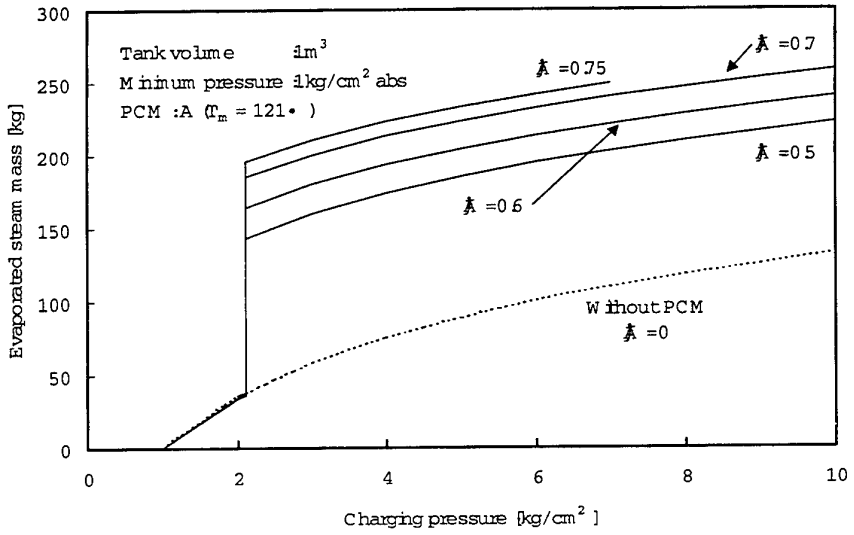


Fig.8 Evaporated steam mass

5. CONCLUDING REMARKS

The high-temperature latent heat thermal energy storage system with applications to solar Rankine power systems and other energy storage systems was proposed in this paper. The following conclusions may be drawn from the present study.

1. Mathematical formulation for the LHTES tank with vertical PCM cylinder was done and the melting characteristics were clarified in detail.
2. The principal performance including the evaporated steam mass was estimated if this system were applied to solar Rankine cycle engine.
3. The evaporated steam mass by the present system is twice as much as that by the conventional steam accumulator.

NOMENCLATURE

Ar	: Archimedes number	R	: capsule radius
a	: thermal diffusivity	T	: temperature
c_p	: specific heat at constant pressure	T_c	: initial temperature
d	: diameter	T_m	: melting point
G	: quantity of evaporation	T_w	: wall temperature
Gs	: steam consumption	t	: time
g	: gravitational acceleration	u, v	: velocity
i', i''	: enthalpy	u', u''	: internal energy
k	: thermal conductivity	v', v''	: specific volume
L	: latent heat	Greek symbols	
l	: length of cylinder	δ	: width of molten gap
P, p	: pressure	η	: packing factor of PCM
Pr	: Prandtl number	ρ	: density
R_m	: melting front	Subscripts and Superscripts	
r, x, y	: coordinates	l	: liquid
r_s	: latent heat of evaporation	s	: solid
Ste	: Stefan number	*	:dimensionless quantity
$\dot{s}$	: shift velocity of solid bulk		

REFERENCES

1. M.Bareiss and H.Beer, "An Analytical Solution of the Heat Transfer Process during Melting of an Unifixed Solid Phase Change Material inside a Horizontal Enclosure", *Int. J. of Heat Mass Transfer*,27,739(1984).
2. P.T.Bahrami and T.G.Wang, "Analysis of Gravity and Conduction-Driven Melting in a Sphere", *Trans. ASME, J. Heat Transfer*, 109,806(1987)
3. M.K.Moallemi and R.Viskanta, "Melting Around a Migrating Heat Source", *Trans. ASME, J. Heat Transfer*, 107,451(1985)
4. T.S.Saitoh and H.Kato, "Numerical Analysis for Combined Natural Convection and Close-Contact Melting in a Cylindrical Capsule", *Trans. JSME(B)*,60-569,223(1994).
5. T.S.Saitoh and A.Hoshi, "Analytical Solution for Close-Contact Melting in Cylindrical and Spherical Capsules with Arbitrary Wall Temperature Profile", *Trans. of the JSRAE*,14-3,285(1997).
6. Y.Abe et al.,"Charge and Discharge Characteristics of a Direct Contact Latent Thermal Energy Storage Unit Using Form-Stable High-Density Polyethylene", *Trans. Of the ASME*, J. of Solar Energy Engineering,106,466(1984).
7. M.Esen,A.Durmus and A.Durmus, "GEOMETRIC DESIGN OF SOLAR-AIDED LATENT HEAT STORE DEPENDING ON VARIOUS PARAMETERS AND PHASE CHANGE MATERIALS", *Solar Energy*, 62-1, 19(1998).
8. C.A.Hall III,E.K.Glakpe and J.N.Cannon, "Modeling Cyclic Phase Change and Energy Storage in Solar Heat Receivers", *J. of Thermophysics and Heat Transfer*, 12-3,406(1998).

THERMAL STORAGE AND HEAT TRANSFER IN PHASE CHANGE MATERIAL INSIDE THE SPHERICAL CAPSULES OF A PACKED BED THERMAL STORAGE SYSTEM

Yingqiu Zhu Yanbing Kang Yinping Zhang Yi Jiang
Department of Thermal Engineering Tsinghua University, Beijing, 100084
Email: zhuyq@mailserver.cic.tsinghua.edu.dn

Keywords: phase change heat transfer, spherical capsules, thermal storage, dimensionless formulae

ABSTRACT. A theoretical model is developed to analyze the characteristics of the thermal storage and heat transfer processes in the packed bed system. Dimensionless formulae are developed using theoretical and numerical analysis. Dimensionless radius of the phase change interface in the spherical capsules, dimensionless axial temperature variation in the heat transfer fluid and the thermal storage in the packed bed system can be obtained through a numerical method, with alternative iteration between temperature and thermal resistance. Simulation results are carefully compared with experimental results. Dimensionless correlations are developed for air and liquid respectively. These simple formulae provide guidelines for the design and optimization of the packed bed thermal system.

Nomenclature

A — sectional area of the tube, m^2
Bi — Biot number
c_p — specific heat, kJ/kg·°C
D — tube diameter, m
Fo —Fourier number
h_f —convective heat transfer coefficient, W/m^2··°C
H_m — heat of fusion of PCM, kJ/m^3
k — thermal conductivity of PCM, W/m·°C
L — tube length, m
$\dot{m}_f$ — mass flow rate of heat transfer fluid, kg/s
$\dot{m}_{fA}$ — total mass flow rate of heat transfer fluid, kg/s
NTU — number of transfer unit
q — energy stored in PCM, J
$\bar{q}$ — dimensionless q
Q — total energy stored in PCM, J
$\bar{Q}$ — dimensionless Q
r — radius, m
r_p — phase change interface radius, m
$\bar{r}_p$ — dimensionless r_p
R_c — convective resistance between fluid and PCM, m·°C/W
R—thermal conductive resistance, m·°C /W
Ste — Stefan number
t — time, s
T_f — fluid temperatur, ·°C
T_t — tube wall temperature, °C
T_m—PCM phase-change temperature, ·°C
x — axial coordinate, m
X — dimensionless x
ε — interspace radio
α_p — thermal diffusivity of PCM, m^2/s
ρ — density, kg/m^3
θ_f — dimensionless temperature of fluid

Subscripts

f — heat transfer fluid
i — inside wall of tube
o — outside wall of tube
in — inlet
out — outlet
t — tube
p — phase change material

1. INTRODUCTION

Since phase change materials (PCMs) have large latent heats and store thermal energy at approximately constant temperature, PCMs are widely used in solar energy systems, air-conditioning systems and space-based power plants [1,2]. Packed bed thermal storage system is a kind of latent heat thermal storage geometry widely used in practical systems, especially in ice storage for central air-conditioning systems. After cooling fluid flows through the packed bed thermal storage system causing the PCM inside the spherical capsules to solidify, the PCM can absorb a large amount of energy as latent heat. Detailed study of phase change storage units is needed to provide a basis for design and optimization of this kind of phase change heat exchanger.

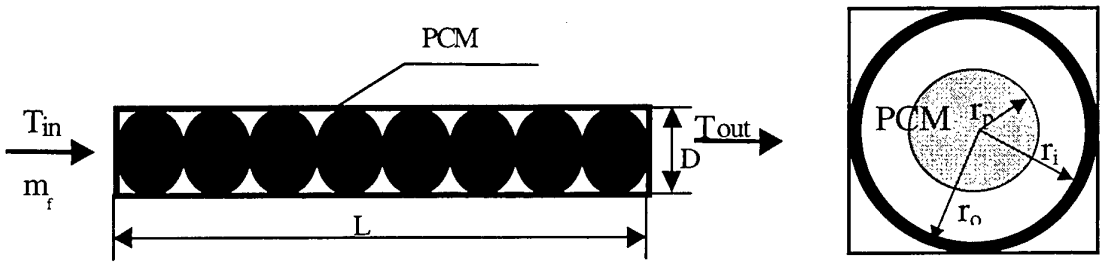
A typical PCM unit similar to that in Fig.1 was studied in this paper. The energy balance equations are simplified using an order of magnitude analysis. Then a theoretical model is developed to analyze the characteristics of the thermal storage and heat transfer processes in the packed bed system. Dimensionless formulae are developed using theoretical and numerical analysis to widen the applicability of the theoretical model. Dimensionless radius of the phase change interface in the spherical capsules, dimensionless axial temperature variation in the heat transfer fluid and the thermal storage in the packed bed system can be obtained through a numerical method, with alternative iteration between temperature and thermal resistance.

Although numerical method can obtain precise results for specific situations, the results can not be easily generalized to other situations. So it is necessary to present simple relationships of these parameters. Numerical results were obtained from the PCM energy storage module over a wide range of the governing parameters. Over 50000 data were used to determine the dimensionless correlations. Because the parameter ranges for liquid or gas heat transfer fluids are very different, the respective correlations were derived separately. The results of these correlations compare well with the previous numerical data. Correlations for the temperature distribution, the radius of the phase change interface and the amount of energy storage clearly illustrate the effects of the governing parameters. These simple formulae provide guidelines for the design and optimization of the packed bed thermal system.

2. MATHEMATICAL FORMULATION AND SOLUTION

Fig. 1 presents a typical module, which consists of a hollow tube with a heat transfer fluid flowing through the PCM spherical capsules. The following assumptions are made to simplify the analysis:

1) The physical properties of the phase change material in both the liquid and solid phases are constant



(a) cross section **(b) longitudinal section**

Fig.1 The schematic of latent heat storage module

2) Thermal conduction in the axial direction is neglected in both the phase change material and the heat transfer fluid.
3) The flow of the heat transfer fluid is fully developed and turbulent.
4) Thermal convection in the phase change material in the liquid phase is neglected.
5) The PCM is initially at its phase-change temperature.
6) The natural convection heat transfer coefficient between the heat transfer fluid and the tube is constant.
7) Ste<<1, which means that the sensible heat can be neglected compared with the latent heat in the PCM.

Assumption (1) is widely used in the literature because previous research has shown that it has little influence on the results. Since the tube length is very large compared to the diameter of spherical capsules, assumptions (2) and (3) are reasonable. In addition, the flow is usually turbulent to enhance the heat transfer. Assumption (4) gives conservative results that do not deviate much from experimental result because the cooling and heating processes tend to be near the phase change temperature. Assumption (6) is reasonable for the small temperature ranges usually used in PCM. Assumption (7) implies that $H_m >> c_{p,p}$, which is appropriate for many phase change materials.

The mathematical model is based on the following equations:

$$c_{p,f} \cdot \dot{m}_f(t) \frac{\partial T_f(x,t)}{\partial x} = h_f \cdot \frac{4\pi r_o^2}{2r_o} \cdot \left(T_t(x,t) - T_f(x,t)\right) \tag{1}$$

$$\frac{T_t(x,t) - T_f(x,t)}{T_m - T_f(x,t)} = \frac{R_c}{R_c + R_t + R_p(x,t)} \tag{2}$$

$$\rho_p \cdot H_m \cdot 4\pi \cdot r_p^2(x,t) \frac{\partial r_p(x,t)}{\partial t} = -h_f(x,t) \cdot 4\pi \cdot r_o^2 \cdot \left|T_t(x,t) - T_f(x,t)\right| \tag{3}$$

subject to the following boundary condition:

$$T_f(x = 0, t) = T_{in}(t),$$

and the initial conditions:

$$r_p(x, t = 0) = r_i$$
$$T_f(x, t = 0) = T_m$$

where $\dot{m}_f(t)$, R_c, R_t and R_p can be expressed as follows:

$$\dot{m}_f(t) = \frac{2\pi}{3(1-\varepsilon)} \cdot \frac{r_o^2}{A} \cdot \dot{m}_{fA}(t)$$

$$R_c = \frac{1}{4\pi \cdot r_o^2 \cdot h_f}, \quad R_t = \frac{1}{4\pi \cdot k_t}\left(\frac{1}{r_i} - \frac{1}{r_o}\right), \quad R_p(x,t) = \frac{1}{4\pi \cdot k_p}\left(\frac{1}{r_p} - \frac{1}{r_i}\right)$$

The following dimensionless parameters are used to analyze the characteristics of the PCM heat exchanger unit:
dimensionless fluid temperature: $\theta_f = (T_f - T_{in})/(T_m - T_{in})$

dimensionless length: $X = x/L$

dimensionless phase change interface radius: $\bar{r}_p = r_p / r_i$

dimensionless time: $Fo = \alpha_p t / r_i^2$

number of transfer units: $NTU = \dfrac{h_f \cdot 4\pi r_o^2 \cdot L / 2r_o}{\dot{m}_f \cdot c_{p,p}} = h_f \cdot 2\pi r_o \cdot \dfrac{L}{\dot{m}_f \cdot c_{p,p}}$

dimensionless thermal storage : $\bar{q} = q_t / (\frac{4}{3}\pi r_i^3 \cdot \rho \cdot H_m) = 1 - \bar{r}_p^3$

$$\bar{Q} = \int_0^1 \bar{q} dX = \int_0^1 (1 - \bar{r}_p^3) dX$$

Equations (1) and (3) can be rewritten in dimensionless forms as:

$$\frac{\partial \theta_f}{\partial X} = \mathrm{NTU} \cdot (1-\theta_f) \frac{R_c}{R_c + R_t + R_p} \tag{4}$$

$$\frac{\partial \overline{r^3}_p(x,t)}{\partial \mathrm{Fo}} = -9\mathrm{Ste} \cdot \mathrm{Bi} \cdot (1-\theta_f) \cdot \frac{R_c}{R_c + R_t + R_p} \tag{5}$$

subject to the following boundary condition:

$$\theta_f(\mathrm{X},\mathrm{Fo}) \equiv 0, \text{ for } X=0,\ Fo>0$$

and the initial conditions:

$$\bar{r}_p(\mathrm{X},\mathrm{Fo}) \equiv 1, \text{ for } 0 \le X \le 1,\ Fo=0$$

$$\theta_f(\mathrm{X},\mathrm{Fo}) \equiv 1, \text{ for } 0 \le X \le 1,\ Fo=0$$

where

$$\mathrm{Ste} = c_{p,p} \cdot |T_m - T_{in}| / H_m \ , \ \mathrm{Bi} = \frac{h_f \cdot r_o^2}{k_p \cdot 3r_i}$$

The solutions are:

$$\bar{r}_p \approx \sqrt[3]{1 - \int_0^{\mathrm{Fo}} 9\mathrm{Ste} \cdot \mathrm{Bi} \cdot (1-\theta_f) \cdot \frac{R_c}{R_c + R_t + R_p} d\mathrm{Fo}} \tag{6}$$

$$\theta_f(\mathrm{X},\mathrm{Fo}) = 1 - \exp\left(- \mathrm{NTU} \cdot R_c \cdot \int_0^X \frac{d\mathrm{X}}{R_c + R_t + R_p} \right) \tag{7}$$

Equations (1-3) and Eqs. (6) and (7) are also suitable for time-dependent inlet temperature and mass flow rate.

To solve the problem, the tube wall conductive resistance R_t is neglected because R_t is small relative to R_c and R_p, then equations (6) and (7) are rewritten as follows:

$$\begin{aligned} \bar{r}_p(X_i, \mathrm{Fo}_j) &\approx \sqrt{1 - \int_0^{\mathrm{Fo}} 9\mathrm{Ste} \cdot \mathrm{Bi} \cdot (1-\theta_f) \cdot \frac{R_c}{R_c + R_t + R_p} d\mathrm{Fo}} \\ &\approx \sqrt{1 - \sum_{k=1}^{j} 9\mathrm{Ste} \cdot \mathrm{Bi} \cdot (1-\theta_f(X_i, \mathrm{Fo}_k)) \cdot \frac{1}{1 + R_p(X_i, \mathrm{Fo}_j)/R_c} \Delta \mathrm{Fo}} \end{aligned} \tag{8}$$

$$\begin{aligned} \theta_f(X_i, \mathrm{Fo}_j) &= 1 - \exp\left(- \mathrm{NTU} \cdot R_c \cdot \int_0^X \frac{d\mathrm{X}}{R_c + R_t + R_p} \right) \\ &\approx 1 - \exp[-\mathrm{NTU} \cdot \Delta X \cdot \sum_{k=1}^{i} \frac{1}{1 + R_p(X_i, \mathrm{Fo}_j)/R_c}] \end{aligned} \tag{9}$$

$(X_i = i\Delta X;\ i=1,...M;\ \mathrm{Fo}_j = j\Delta \mathrm{Fo};\ j=1,...N)$

To obtain a solution, $\bar{r}_p(X_i,Fo_j)$ and $\theta_f(X_i,Fo_j)$ are alternatively computed until a convergence for each time step. Therefore, the method is called the alternative iteration between temperature and thermal resistance method. The converged results were assumed to be reached when the maximum relative change of $\bar{r}_p(X_i,Fo_j)$ and $\theta_f(X_i,Fo_j)$ between the consecutive iterations was less than 1×10^{-4}. Different grid sizes for the same problem were tested and it was demonstrated that the numerical solutions were essentially independent of the grid size used. The final grid size $\Delta X=0.05$, the time step $\Delta Fo=0.1$ in gas fluids cases and $\Delta X=0.05$, $\Delta Fo=0.05$ in liquid fluids cases.

2. COMPARISON OF RESULTS

Fig.2-Fig.7 compare the present numerical solutions with some experimental results of literature [3]. The dimensionless numerical solutions are rewritten in dimension form in order to compare with the experimental results. The difference between the two results is inevitable because the experiments are not exactly fit for the model (shown in Fig.1). The ice is not entirely filled in the spherical capsules and the interspace ratio is 8~9%. The heat transfer and the energy storage capacity decrease when capsule surface is dirty. As a result, all experimental results are less than theoretical results. By examining the results of Fig.2-Fig.7, we observe that the difference between the numerical and the experimental results is relatively great at the beginning of the energy storage. The reason is that the sensible heat is neglected in the theoretical model but it is an important factor at the beginning of the experiments. The error between the numerical and the experimental results can be neglected near the end and the trends of the two results are similar. This proves the theoretical model is correct.

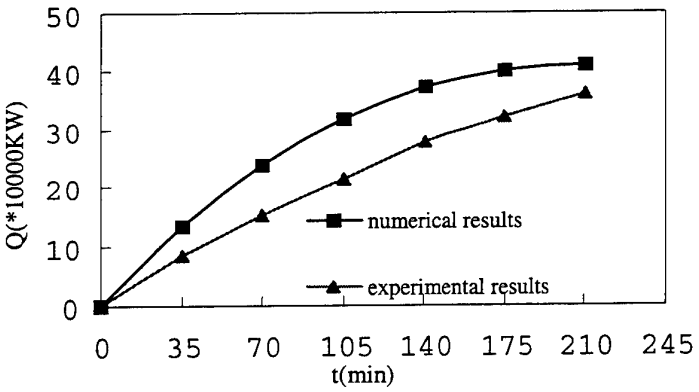


Fig.2 Comparison of thermal storage Q (T_{in}=10°C, $\dot{m}_f$ =7m³/h)

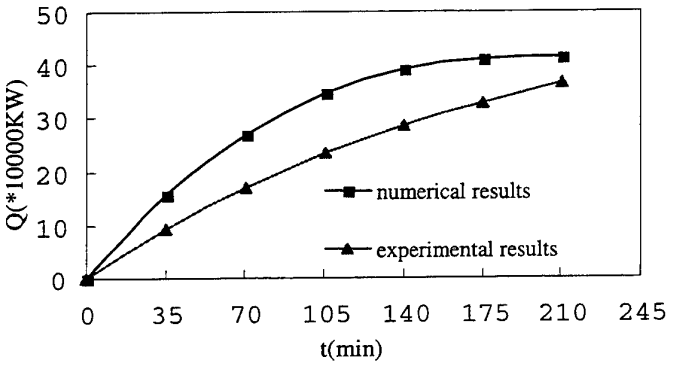


Fig.3 Comparison of thermal storage Q (T_{in}=10°C, $\dot{m}_f$ =9m³/h)

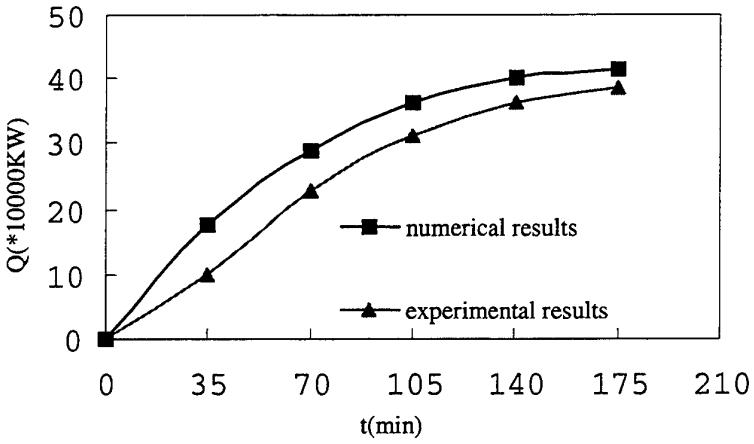


Fig.4 Comparison of thermal storage Q (T_{in}=10°C, $\dot{m}_f$ =11m^3/h)

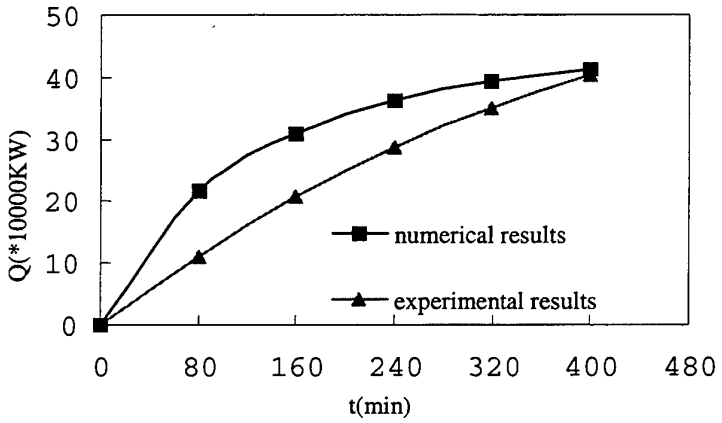


Fig.5 Comparison of thermal storage Q (T_{in}=-10°C, $\dot{m}_f$ =15m^3/h)

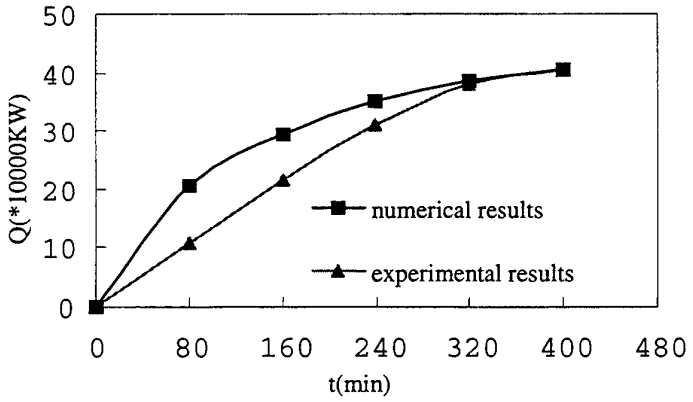


Fig.6 Comparison of thermal storage Q (T_{in}=-9°C, $\dot{m}_f$ =15m^3/h)

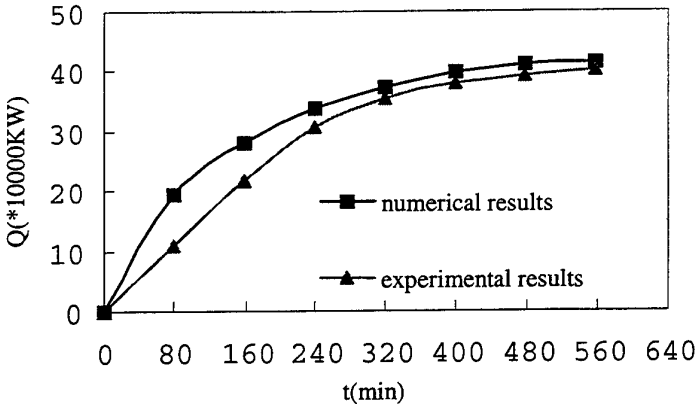


Fig.7 Comparison of thermal storage Q (T_{in}=-8°C, $\dot{m}_f$ =15m³/h)

4. DIMENSIONLESS CORRELATIONS AND DISCUSSION

From equations (8) and (9), the governing parameters are:

$$\bar{r}_p = f_1(Ste, Bi, NTU, Fo, X) \tag{10}$$

$$\theta_f = f_2(Ste, Bi, NTU, Fo, X) \tag{11}$$

Numerical results were obtained for the PCM energy storage module over a wide range of the governing parameters. Over 50000 data were used to determine the dimensionless correlations. Because the parameter ranges for liquid or gas heat transfer fluids are very different, the respective correlations were derived separately using the least square method.

a) Liquid Heat Transfer Fluid

The liquid mass flow rate is large in most cases, so NTU and the dimensionless temperature θ_f can be assumed to be zero on the condition that L/D is not large.

The dimensionless correlations are then:

$$\begin{aligned} \bar{r}_p &= 1 - 1.45 \times Bi^{0.133} \times Ste^{0.715} \times Fo^{0.711}, \quad \text{for } 0 \le \bar{r}_p \le 0.25 \\ \bar{r}_p &= 1 - 1.121 \times Bi^{0.266} \times Ste^{0.883} \times Fo^{0.875}, \text{for } 0.25 < \bar{r}_p \le 1 \end{aligned} \tag{12}$$

$$\theta_f(X, Fo) \approx 0 \tag{13}$$

$$\bar{Q} = \int_0^1 \bar{q} dX = \int_0^1 (1 - \bar{r}_p^3) dX = 1 - \bar{r}_p^3 \tag{14}$$

The parameter ranges for these correlations are: Bi=10~50 and Ste=0.05~0.30. Figs.8 and 9 compare the numerical data with the values of equations 12 and 14. The average errors between the correlations and the numerical data are 5.25% and 4.76%, respectively.

The expressions show that Ste and Fo primarily affect the results while the influence of Bi is small. Therefore the effect of the convective coefficient h_f on heat transfer rate is not large since the greatest heat transfer resistance is not on the fluid side but on the PCM side.

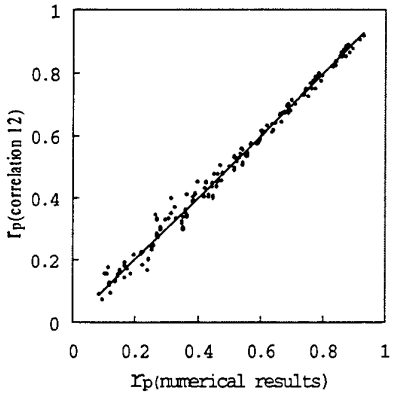


Fig.8 Comparison of $\bar{r}_p$ predicted by the numerical data and the correlation

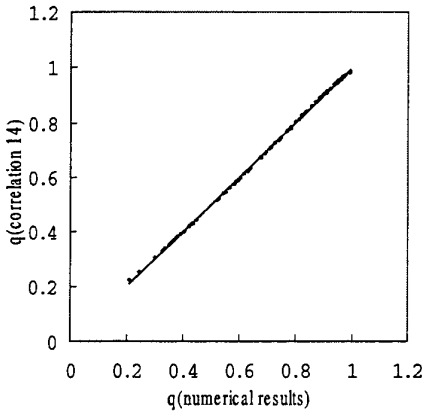


Fig.9 Comparison of $\bar{q}$ predicted by the numerical data and the correlation

b) Gaseous Transfer Fluid

Dimensionless correlations can be derived for a system using a gaseous heat transfer fluid using the same method:

$$\begin{aligned}\bar{r}_p &= 1-0.576\times Fo^{1.438}\times Ste^{1.445}\times Bi^{1.120}\times e^{(-0.807\times NTU\times X)},\ \text{for } 0\le \bar{r}_{p,s}\le 0.9\\ \bar{r}_p &= 1-0.476\times Fo^{1.241}\times Ste^{1.236}\times Bi^{1.394}\times e^{(-1.075\times NTU\times X)},\ \text{for } 0.8\le \bar{r}_{p,s}\le 1\end{aligned} \tag{15}$$

$$\begin{aligned}\theta &= 1-0.715\times Ste^{0.175}\times Bi^{0.310}\times Fo^{0.178}\times e^{(-0.561\times NTU\times X)},\ \text{for } 0\le\theta\le 0.45\\ \theta &= 1-0.881\times Ste^{0.179}\times Bi^{0.272}\times Fo^{0.182}\times e^{(-0.504\times NTU\times X)},\ \text{for } 0.4<\theta\le 1\end{aligned} \tag{16}$$

$$\bar{Q} = \int_0^1 \bar{q}\,dX = \int_0^1 (1-\bar{r}_p^3)\,dX \tag{17}$$

The parameter ranges are: Ste=0.05~0.30, Bi=1~5, NTU=5~30 and X=0.1~1.0. The comparisons between the numerical data and equations (15-16) are shown in Figs.10 and 11.

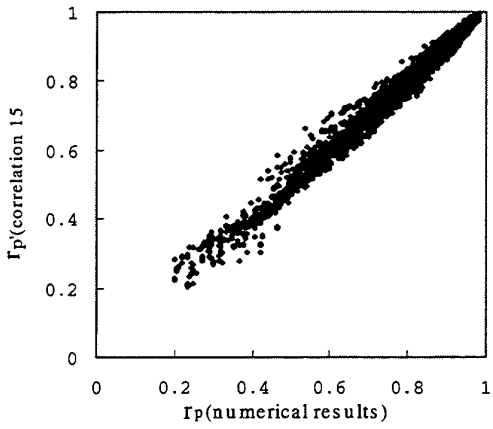


Fig.10 Comparison of $\bar{r}_p$ predicted by the numerical data and the correlation

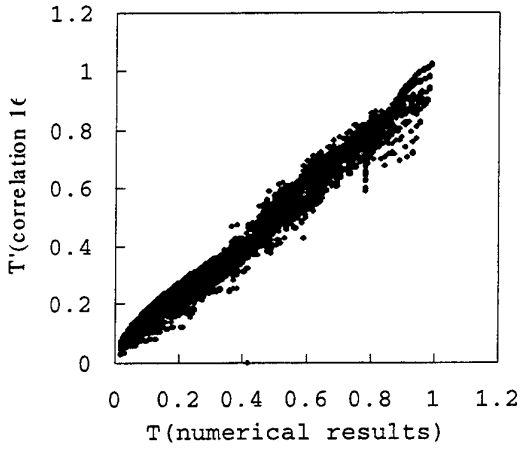


Fig.11 Comparison of θ predicted by the numerical data and the correlation

In contrast to the liquid heat transfer fluid, Bi is also an important parameter along with Ste and Fo affecting the heat transfer rate for gaseous heat transfer fluid. Therefore, increasing h_f causes $\bar{r}_p$ to increase very rapidly. NTU affects the slope of $\bar{r}_p$ -x curve: The bigger NTU is, the bigger the absolute value of the slope of $\bar{r}_p$ -x curve is. Thus, Fo, Ste and Bi strongly influence the dimensionless temperature θ. NTU is the primary factor affecting the axial variation of θ. Increasing NTU will increase the difference between the inlet and outlet temperatures.

5. CONCLUSIONS

1. The temperature distribution and the rate of solidification in a packed bed thermal storage system with spherical capsules are discussed considering the axial temperature variation of the heat transfer fluid in the system. The results compare well with previous experimental data.
2. Correlations for the temperature distribution, the rate of solidification and the heat flux in the phase change material are then developed for gaseous and liquid heat transfer fluids to clearly illustrate the effects of the governing parameters. These formulae provide guidelines for the design and optimization of tube PCM heat exchangers.

REFERENCE

1. Y.P. Zhang, H.P. Hu, X.D. Kong, Y.H. Su, Latent heat storage-Fundamentals and application, Hefei: Publishing Company of University of Science & Technology, 1996.10,pp.1-4, pp.289-335, in Chinese.
2. G.R. Ming, Technology of Thermal Control of Satellite, Beijing: Publishing Company of Yuhang, 1991.1, pp.205-216, in Chinese.
3. H. Li, Experimental research of thermal characteristic in ice cooling storage system, master's thesis, 1997.5, in Chinese.
4. Y.Q. Zhu, Y.J. Zhang, Y. Jiang, Thermal Storage and Heat Transfer in Phase Change Material outside a Circular Tube with Axial Variation of the Heat Transfer Fluid Temperature, Journal of Solar Energy Engineering, 1999.
5. D. Arnold, C. Eng, Dynamic simulation of encapsulated ice stores: Part I-The model, Ashare Transaction, 96(1), 1990.
6. D. Arnold, C. Eng, Dynamic simulation of encapsulated ice stores: Part II-Model development and validation, Ashare Transaction 100(1), 1994.

HEAT TRANSFER ENHANCEMENT OF DIRECT CONTACT MELTING PROCESS IN THERMAL STORAGE SYSTEM BY VIBRATION

Mineo Oka
PANDA Laboratory.
1642-406 Nagae, Hayama KANAGAWA, 240-0113 JAPAN
Phone & Fax: +81-468-76-2970
Email: HFB01261@Nifty.ne.jp

Keywords: phase change, melting, thermal storage, vibration

ABSTRACT. Direct contact melting takes place in many natural and technological processes. Important applications of this process are thermal storage systems. In these systems, phase change material (PCM) is stored in a small capsule that is melted by heating peripherally, In this melting process, melting rate is important factor for the efficiency of the system. In this paper, utilization of vibrating motion of heating wall is proposed to enhance the melting rate. Effect of vibrating motion of the heating wall is studied. Non-steady heat transfer phenomena of direct contact melting process is studied theoretically while only steady state is studied in recent analytical researches. In this paper, it is clarified that the vibrating motion of heating wall enhances the heat transfer and melting rate.

1. INTRODUCTION

Direct contact melting processes take place in lots of natural and technological processes. Recently, this process is investigated as a basic mechanism of a thermal energy storage system. In this system, Phase Change Material (abbreviated to PCM) is packed in a capsule. In melting process, capsules are heated peripherally. Solid PCM is pushed toward the heating wall by its weight. A thin liquid layer is formed between the contact surface of the heating wall and solid PCM. The melted liquid PCM flows out through this gap. Almost all melting occurs in this thin liquid layer.

Many basic research studies were made about this process not only experimentally, but also numerically and analytically. They are summarized by Bejan [1]. The melting rate is an important factor for the efficiency of the thermal storage system. Several researches were performed to enhance this melting rate. Oka and Hasegawa [2] and Taghavi [3] suggested utilization of the rotating motion. Saito, et al. proposed that of the heating wall with grooves [4]-[7]. In order to enhance the melting rate, it is important to reduce the pressure in the gap and to bring the melting surface close to the heating wall. Oka and Hasegawa advocated for the use of porous material as a heating wall [8]-[10].

In this paper, we demonstrate that vibrating motion is an effective method to enhance the melting rate and heat transfer between the solid and the heating wall. Our study will be a theoretical analysis of the vibrating problem.

2. FULL GOVERNING EQUATIONS

Since the main purpose of this paper is the investigation of the effect of vibration motion, it is best to use a simple geometry so that analytical methods can be employed. In this paper, two dimensional flat heating wall is considered (Fig.1). Cylindrical coordinates system, r, z are used. In the course of melting, the whole solid PCM is assumed to be at the melting temperature, T_m

There are several limiting conditions under which the melting process can be analyzed, .
(1) external force is given (2) melting Rate is given (3) gap height is given

In former researches, case (1) is used,because this condition is closely related to the practical cases. Oka, et al. investigated and compared these three conditions and found that from mathematical point of view these three cases are essentially the same [11]. In this paper, case (2) is studied to build up the governing equations, because of the simplicity of the reduction.

The horizontal heating wall is vertically vibrated with a harmonic excitation of given amplitude and frequency.

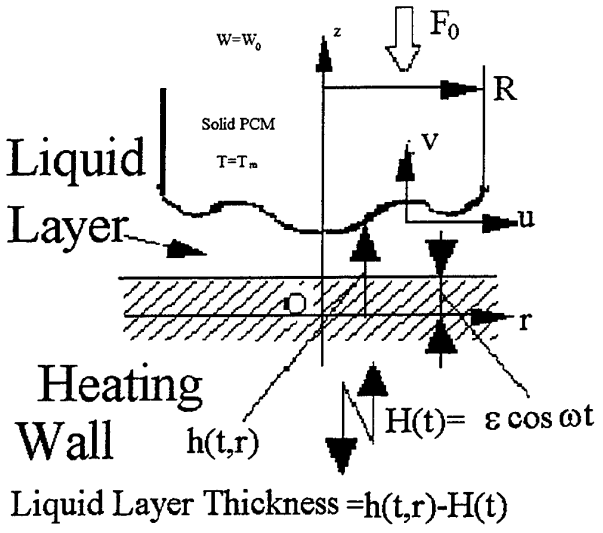


Fig. 1 Coordinate system

That is, the heating wall position is given by $H(t) = \varepsilon\cos\omega t$. When the PCM is melting close to the heating wall, a thin liquid layer is formed between the melting surface and the heating wall. Let the position of the melting surface be h(r, t), then the gap thickness is h(r, t) - H(t). The melted liquid flows through this layer with holizonal velocity component, u, and vertical one, v. Denote the temperature of the liquid by T, wall temperature by T_w which is given and constant.

The temperature difference between the heating wall and the melting temperature is relatively small. So, all physical quantities such as viscosity and conductivity are assumed constant. The governing equations in dimensional form are as follows;

$$\frac{1}{r}(ru)_r + V_z = 0 \tag{1}$$

$$u_t + uu_r + vu_z = \frac{1}{\rho}p_r + v\left(\left\{\frac{1}{r}(ru)_r\right\} + u_{zz}\right) \tag{2}$$

$$v_t + uv_r + vv_z = -\frac{1}{\rho}p_z + v\left(\frac{1}{r}(rT_r)_r + T_{zz}\right) \tag{3}$$

$$T_t + uT_r + vT_z = \chi\left(\frac{1}{r}(rT_r)_r + T_{zz}\right) \tag{4}$$

$$z = h(r,t) : u = 0, v = -W, T = T_{m,} - \rho c\chi T_z = \rho_s L \cdot W \tag{5}$$

$$z = H(t) = \varepsilon\cos\omega t : u = 0, v = H_t, T = T_w \tag{6}$$

Eq.(1) is the balance of mass, Eqs. (2) and (3) are the horizontal and vertical component of the balance of linear momentum and Eq. (4) is the energy balance, all for an incompressible Navier-Stokes-Fourier fluid in cylindrical co-ordinates. Eqs. (5) and (6) describe the non-slip and thermal boundary conditions at the moving

wall and moving PCM boundary (melting surface). The PCM is pushed to the heating wall by the force F. This force is a reaction force that is obtained by integrating the pressure between gap.

$$F = 2\pi \int_0^R p \cdot r dr \tag{7}$$

3. NON-DIMENSIONALIZED EQUATIONS

To non-dimensinoalize the above equations, typical scales will now be introduced; they in turn define dimensionless quantities which provide information about the significance of the viscous terms arising in the equations describing the problem. Let F_0, h_0, W_0 be scales for the external force, gap thickness and vertical velocity of the fluid at the melting wall. Considering the balance of the heat flux at the melting surface and the latent heat, $vSt=h_0W_0$ is obtained. That is, $St=h_0W_0/\chi$ is a measure for the ratio of vertical heat convection (due to melting) to conduction. Further more, balancing the horizontal pressure gradient with the corresponding viscous term, we obtain the estimate,

$$\frac{1}{\rho}\frac{1}{R}\frac{F_0}{\pi R^2} = v\frac{1}{h_0^2}\frac{RW_0}{h_0} \Rightarrow F_0 = \frac{\pi\rho v W_0 R^4}{h_0^3} \tag{8}$$

Where R is the radius of the cylindrical PCM. If W_0 is given, h_0, F_0 are,

$$h_0 = \frac{\chi St}{W_0}F_0 = \frac{\pi\rho v R^4}{\chi^3 St^3}W_0^4 \tag{9}$$

The other hand, there are several time scales in this problem. That is,

(a) Time Scale of Oscillation(non-steadiness): $1/\omega$
(b) Time Scale of Fluid Flow: h_0/W_0
(c) Heat Transfer (Fourier Number): h_0^2/χ
(d) Time Scale of Melting: (PCM Volume) / $\left(\pi W_0 R^2\right)$

Using relation eq. (9), the ratio of (c). to (b). is equal to St. The ratio (b). to (a). measures the importance of the non-steady-term to the convection terms in the Navier-Stokes equation defined here as $\gamma \equiv h_0\omega / W_0$. Then the ratio of (c). to (a). is expressed as γSt ,i.e., the ratio of the heat transfer to the non-steadiness. Negligibility of 4. is tantamount to the assumption that process can be regarded as periodic.

More over, the order of h_0 / R is $10^{-3} \sim 10^{-4}$. Typical value, $\Delta T \sim 1-10°C, R \sim 5-10cm$ and the external force ~10-100N are used which were used in the experiments done by Saito, et al. (1991a). This is small for the most ordinary conditions, so that we can neglect the terms that include h_0 / R. In this paper, we consider the region of small ΔT, say, $\Delta T \sim 1-10$, which gives the order of Stefan number $St = c\Delta T / L$, $10^{-2} \sim 10^{-3}$. In this case, the order of Reynolds' number, $Re = h_0 \cdot W_0 / v = St / Pr$, is $10^{-3} \sim 10^{-4}$. As for water, Prandtl number is $Pr \approx 13$. Reynolds' number is 10 times smaller than Stefan number. Terms that include Re can be neglect, while Prndtl number may be negligible in many practical cases.

Using these parameters, non-dimensionalized governing equations take the following form;

$$\frac{1}{r}(ru)_r + v_z = 0 \tag{10}$$

$$u_{zz} = p_r \tag{11}$$

$$p_z = 0 \tag{12}$$

$$T_{zz} = St(\gamma T_t + uT_r + vT_z) \tag{13}$$

$$z = h(r,t): u = 0,\ v = -1,\ T = 0,\ -T_z = 1 + \gamma h_t \tag{14}$$

$$z = \varepsilon \cos t: u = 0,\ v = \varepsilon\gamma \sin t,\ T = 1 \tag{15}$$

$$F = 2\pi \int_0^1 p \cdot r dr \tag{16}$$

4. SIMILAR SOLUTIONS FOR LIQUID PART

We can see that the system, eqs. (10)-(15) admits a similarity solution of the form,

$$u = r\phi_z(z,t), v = -2\phi(z,t), p = 3A(t)(1-r^2) \tag{17}$$

h: function of time only (independent form r)

Substituting this into the governing equations, (10)-(15), yields the single equation

$$\phi_{zz}(z,t) = -12A(t) \tag{18}$$

Integrating this twice, and invoking the boundary conditions, this equation can be solved remaining the gap h unknown;

$$\phi(z,t) = \frac{A}{2}\left[(h-z)^2\{2(z-\varepsilon\cos t) + h - \varepsilon\cos t\}\right] + \frac{1}{2} \tag{19}$$

where A is given as;

$$A = \frac{1+\varepsilon\gamma\sin t}{(h-\varepsilon\cos t)^3} \tag{20}$$

The gap h is determined by solving energy equation, eq. .(13). Force is given by integrating eq.(16), that is

$$F = 6\pi A(t) \int_0^1 (1-r^2) \cdot r dr = \frac{3}{2}\pi A(t) \tag{21}$$

5. TEMPERATURE FOR NON-CONVECTION CASE

As h is function of time only, the boundary condition for temperature in eqs. (14) and (15) are

$$z = h(t): T = 0,\ T_z = -(1+\gamma h_t) \tag{22}$$

$$z = \varepsilon \cos t: T = 1 \tag{23}$$

When convection terms in energy equation, (13) can be neglected, energy equation is reduced to heat conduction equation by putting St=0,

$$T_{zz} = 0 \tag{24}$$

that has a solution remaining the gap h unknown;

$$T = \frac{h - z}{h - \varepsilon \cos t} \tag{25}$$

Substituting this into the second boundary condition in eq.(22), we get the final equation that determines the gap h;

$$\gamma h_t = -1 + \frac{1}{h - \varepsilon \cos t} \tag{26}$$

As the first, let's assume the amplitude of the vibration, ε is small. The gap h can be expanded in power series of ε.

$$h = 1 + \varepsilon h_1 + \varepsilon^2 h_2 + \ldots \tag{27}$$

(0th order solution is obviously 1)

Substituting this into eq.(26), expanding the second term in right hand side using Taylor expansion and correcting equating coefficients of equal powers of ε, we obtain;

$$\gamma h_{1t} + h_1 = \cos t \tag{28}$$

$$\gamma h_{2t} + h_2 = h_1{}^2 + \cos^2 t - 2h_1 \cos t \tag{29}$$

$$\gamma h_{3t} + h_3 = 2h_1 h_2 - h_1{}^3 + \left(-2h_2 + 3h_1{}^2\right)\cos t - 3h_1 \cos^2 t + \cos^3 t \tag{30}$$

$$\gamma h_{4t} + h_4 = 2h_1 h_3 + h_2{}^2 - 3h_1{}^2 h_2 + h_1{}^4 + 2\left(-h_3 - 3h_1 h_2 + 2h_1{}^3\right)\cos t - 3\left(-h_2 + 2h_1{}^2\right)\cos^2 t - 4h_1 \cos^3 t + \cos^4 t \tag{31}$$

etc.

Now we are looking for the periodical solutions, homogeneous solutions that converge zero can be neglected. Periodical solutions are as follows;

$$h_1 = \frac{1}{1+\gamma^2}(\cos t + \gamma \sin t) \tag{32}$$

$$h_2 = \frac{\gamma^2}{2\left(1+\gamma^2\right)^2} - \frac{\gamma^2}{2\left(1+\gamma^2\right)^2\left(1+4\gamma^2\right)}\left[2\gamma\left(2-\gamma^2\right)\sin 2t + \left(1-5\gamma^2\right)\cos 2t\right] \tag{33}$$

$$h_3 = \frac{\gamma^3}{4\left(1+\gamma^2\right)^3\left(1+4\gamma^2\right)}\left[-2\gamma\left(5+2\gamma^2\right)\cos t + \left(3-7\gamma^2-4\gamma^4\right)\sin t\right] + \frac{\gamma^3}{4\left(1+\gamma^2\right)^3\left(1+4\gamma^2\right)\left(1+9\gamma^2\right)}\left[2\gamma\left(5-41\gamma^2+26\gamma^4\right)\cos 3t - \left(1-40\gamma^2+91\gamma^4-12\gamma^6\right)\sin 3t\right] \tag{34}$$

$$h_4 = \frac{\gamma^4\left(3-7\gamma^2-4\gamma^4\right)}{4\left(1+\gamma^2\right)^3\left(1+4\gamma^2\right)} + [\text{terms including } \cos 2t, \sin 2t, ...] \tag{35}$$

We are interested in the average gap height rather than the periodical motion, average gap height, $\bar{h}$ is calculated from constant terms in eqs. (33) and .(35). That is;

$$\bar{h} = \bar{h} + \varepsilon^2\overline{h_2} + \varepsilon^4\overline{h_4} = 1 + \frac{\gamma^2}{2\left(1+\gamma^2\right)^2}\varepsilon^2 + \frac{\gamma^4\left(3-7\gamma^2-4\gamma^4\right)}{4\left(1+\gamma^2\right)^3\left(1+4\gamma^2\right)}\varepsilon^4 + ... \tag{36}$$

(Odd order terms don't affect the average gap height)

Fig. 2 displays how $\overline{h_2}$ and $\overline{h_4}$ arising in eq. (36) vary as functions of the Strouhal numbers. Evidently, the first correcting term, $\left|\overline{h_2}\right|$ takes positive values. This means that the vibrating motion always enhances the gap height. In this paper, the melting rate is fixed; thus, as the gap height becomes larger, the total force is reduced. However, this result can also be interpreted for the solution when the total force is given and holds fixed: in this case, the vibrating motion should reduce the gap height. On the other hand, the second correcting term, $\left|\overline{h_4}\right|$ takes negative values, thus reducing the gap height again somewhat.This term should be small in comparison to $\left|\overline{h_2}\right|$ in order not to change the sign of the combination and indeed $\left|\overline{h_4}\right|$ is smaller than $\left|\overline{h_2}\right|$. From Fig. 2, it is seen that this is the case for $\gamma \in (0,10)$ which corresponds to $1/\omega \approx 10^3 - 10^4$, valid under many practical situations. Fig. 3 displays the gap height as a function of γ for various values of ε. It is seen that the gap height can be increased by approximately 10% by the vibrating motion of the heating wall.

6. EFFECT OF CONVECTION TERMS-STEFAN NUMBER

In many practical condition, Stefan number, St is small so that it can be neglected. However in some cases, it is becoming large. In these cases, convection effects are no longer negligible. Here, we consider the convection effect in the energy equation. If the Stefan number is small compared to unity, the first order perturbation can be considered. More specifically, let temperature be expanded in a power series of the Stefan number as follows,

$$T = T_0 + St \cdot T_1 + ... \tag{37}$$

The zeroth order term, T_0 is given by eq.(25). Letting h be unknown function again the first order term, T_1 is obtained by solving the equation,

$$T_{1zz} = St\left(\gamma T_{0t} + u_0 T_{0r} + v_0 T_{0z}\right) \tag{38}$$

$$T_0 = \frac{h-z}{h-\varepsilon\cos t}, u_0 = -3A(h-z)(z-\varepsilon\cos t)r \tag{39}$$

$$v_0 = A(h-z)(z-\varepsilon\cos t)[h-z-(z-\varepsilon\cos t)] - \frac{z-\varepsilon\cos t}{h-\varepsilon\cos t} + \varepsilon\gamma\sin t\frac{h-z}{h-\varepsilon\cos t} \tag{40}$$

$$z = h(t) : z = \varepsilon\cos t : T_1 = 0 \tag{41}$$

As eqs. (39)-(40) are polynominals of z, T_{1zz} is also given by a polynominal of z. Then it can be integrated by z with boundary conditions eq. (41). Calculation is straightforward but the result is too long to print out.

The other hand, the unknown function, h and its derivative, h_t are included in the expression of T_1 that are

determined by the boundary condition,

$$T_z(z=h) = -(1+\gamma h_t) \tag{42}$$

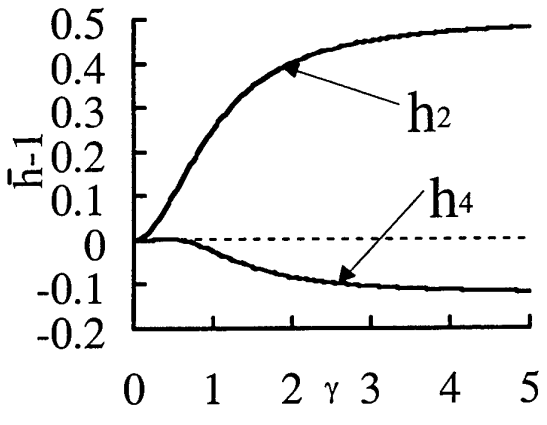


Fig. 2 Each order solutions for gap height

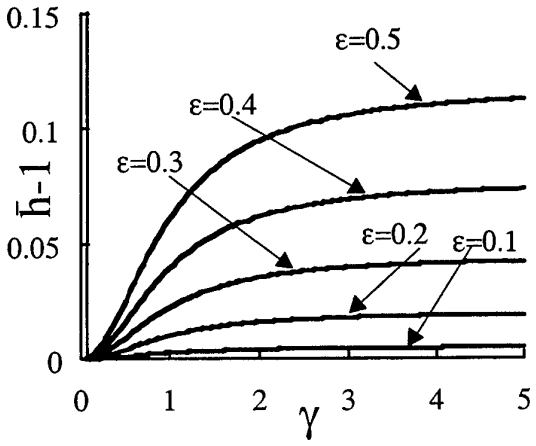


Fig. 3 Gap height change

To solve this equation, h and T are expanded in power series of ε and St. Here, solutions up to the first order are considered. That is,

$$h = h_{00} + h_{01} + \ldots + St(h_{10} + h_{11} +) + \ldots \tag{43}$$

$$T = T_{00} + T_{01} + \ldots + St(h_{10} + h_{11} +) + \ldots \tag{44}$$

T_{00z} , ..., are calculated from T_0 and T_1:

$$T_{00z} = 1 \tag{45}$$

$$T_{10z} = h_{10} + \frac{7}{20} \tag{46}$$

$$T_{01z} = h_{01} - \cos t \tag{47}$$

$$T_{11z} = \frac{1}{3}h_{01t} - 2h_{01}h_{10} + h_{11} + 2h_{10}\cos t - \frac{1}{6}\sin t + \frac{3}{20}\gamma \sin t \tag{48}$$

Substituting these into eq. (42), the equations that determine h are given by

$$h_{00} = 1 \tag{49}$$

$$\gamma h_{10t} + h_{10} = -\frac{7}{20} \rightarrow h_{10} = -\frac{7}{20} \tag{50}$$

$$\gamma h_{01t} + h_{01} = \cos t \rightarrow h_{01} = \frac{1}{1+\gamma^2}(\cos + \gamma \sin t) \tag{51}$$

$$\gamma h_{11t} + h_{11} = \frac{1}{3} h_{01t} - 2h_{01}h_{10} + 2h_{10}\cos t - \frac{1}{6}\sin t + \frac{3}{20}\gamma \sin t \tag{52}$$

h_{00} and h_{01} are given explicitly and h_{10} and h_{11} are given by ordinary differential equations that are solved successively. Substituting the solutions of h_{00} and h_{01} and h_{10}into eq.(52), the differential equation that determines h_{11} is

$$\gamma h_{11t} + h_{11}$$
$$= \frac{1}{60}\{42\cos t + (10 - 9\gamma)\sin t\} + \frac{1}{30(1+\gamma^2)}\{-21(\cos t + \gamma \sin t) + 10(\sin t - \gamma \cos t)\} \tag{53}$$

The zeroth order solution of ε becomes,

$$h_0 = 1 - St\frac{7}{20} \tag{54}$$

This means that the gap height h is getting smaller by the convective effect. This effect appears in non-vibration. As for the first order solution of ε, non-homogeneous terms of eqs. (51) and (53) are proportional to sin t and cos t so that $h_1 = h_{01} + St \cdot h_{11}$ does not effect the average gap height. The effect of convection will appear in higher order terms.

7. CONCLUSIONS

Direct contact melting process that takes place in a capsule for thermal storage system is investigated theoretically. Vibrating motion of heating wall is proposed to enhance melting rate and heat transfer. The process on a flat heating wall is investigated analytically using perturbation method. Axi-Symmetric Cylindrical coordinate system is used. Case under on-convective condition and constant melting rate is studied. By vibrating motion, the average gap height is getting large. This means heat transfer is enhanced. It is easily interpreted that the average gap height is reduced and melting rate is getting large when total force is given. This effect appears in 1000~10000Hz frequency in many practical condition. The gap height is enlarge 10% by vibrating motion.

REFERENCES

1. A. Bejan, Single Correlation for Theoretical Contact Melting Results in Various, Geometries, *Int. Comm. Heat & Mass Transfer,* Vol. 19 (1992), p.473.
2. M. Oka, and E. Hasegawa, Contact Melting of Rotating Phase-Change Material on a Heated Wall, *Trans. JSME B,* Vol. 56-524 (1990) p. 1131, (Japanese).
3. K. Taghavi, Analysis of Direct-Contact Melting Under Rotation *Trans. ASME, Jour. Heat Transfer*, Vol. 112 (1990), p. 137.
4. A. Saito, et al., Heat Transfer Enhancement in Direct Contact Melting Process, *Trans. 68th JSME Annual Meeting, Vol. B* (1991-3) p. 242 (Japanese).
5. A. Saito, et al., Analytical Study on Heat transfer Enhancement in Direct Contact Melting Process, *Trans. the 28th Japan Heat Transfer Symposium,* (1991-5), p.29 (Japanese).
6. A. Saito, et al., Analytical Study on Heat transfer Enhancement in Direct Contact Melting Process, *Trans. Japanese Assoc. of Refrigeration,* Vol. 8-2 (1991-7) p.141 (Japanese).
7. A. Saito, et al., Heat Transfer Enhancement in Direct Contact Melting Process, *Trans. JSME B* Vol. 57-541 (1991-9), p.3141 (Japanese)
8. M. Oka, and E. Hasegawa, Direct Contact Melting Process on a Porous Heating Wall, 1995 *IMECE HTD-*Vol. 321, p.733.
9. M. Oka, and E. Hasegawa, Direct Contact Melting Process on a Curved wall Coated with a Porous layer, *5th Int. Sym. Thermal Eng. & Sc. for Cold Regions,* (1996-5),p.207.
10. M. Oka, and E. Hasegawa, Contact Melting Process on an Arbitrary shape wall Coated by Porous layer, *31st IECEC,* (1996-8),p.2084.
11. M. Oka, and E. Hasegawa, On the Steady Melting of a Phase-Change Material Placed on a hot Wall, *Trans. .JSME Vol. B* Vol. 55 (1989), p.1653.

BEHAVIOR OF CHARGE AND DISCHARGE OF THERMAL ENERGY IN A STORAGE TYPE HEAT EXCHANGER

Hsiang-Hui Lin Guey-Tian Lin Bing-Chwen Yang* Shr-Hau Huang
Energy & Resources Laboratories
Industrial Technology Research Institute, Taiwan
*Email: f810565@erl.itri.org.tw

Keywords: thermal energy storage, phase change, heat exchanger

ABSTRACT. Heat exchanger with thermal energy storage is a good candidate that suited for the waste heat recovery. Phase change material is very suited for this kind of application for the use of latent heat. A heating chamber with enhancement coil was built to study the behavior of pentaerythritol ($C(CH_3O)_4$) subjected to heating and cooling process. The specific heat was measured and latent heat was calculated for the samples after different cycles of charge and discharge process. Then a numerical simulation was performed to understand the transient temperature distribution of pentaerythritol subjected the constant input heat flux. Finally, a shell and tube heat exchanger was modified to act as a storage type heat exchanger and pentaerythritol was chosen as the thermal energy storage medium and filled inside the tube. A hot air generator with heating capacity 36kW and flow rate 26 CMM was used as the hot air supplier. The maximum temperature of the supplied air is 350 °C. This full scale test facility was used to simulate the usage of storage type heat exchanger as a recupeator in a boiler.

1. INTRODUCTION

The crisis of global warming made the reduction of carbon dioxide (CO_2) from the burning of fossil fuel necessary for the sustainable of our world. A high efficiency of energy usage and reduction of the consumption of fossil fuel are the important ways to achieve this purpose. Waste heat recovery from a boiler or any other industrial furnace is an easy way to increase the efficiency of energy usage. There are several types of heat exchangers that can be used as a recuperator in the waste heat recovery system [1]. Heat exchanger with thermal energy storage is a good candidate that suited for the waste heat recovery. Traditional, the material with high heat capacity was used as the material to storage thermal energy. It is easy to fabricated and have been used extensively in the boiler as a recuperator to preheat the supplied air. The disadvantages of this kind of heat exchanger are (1) the large amount of energy storage material is needed to meet the heat duty and (2) the large thermal stress is induced due to the large temperature difference during the operation cycle. In order to solve these two problems, the phase change material was employed as the thermal energy storage medium. In this study, a shell and tube heat exchanger was modified to act as a storage type heat exchanger and pentaerythritol ($C(CH_3O)_4$) was chosen as the thermal energy storage medium and filled inside the tube. The experimental facility was set up to learn the behavior of the phase change material during the repeated charge and discharge of thermal energy at the different processes. In this study, some of the thermal and physical properties of pentaerythritol were examined experimentally in advance to understand its phenomena during phase change process. After that a series of experiments were performed to study the total amount of thermal energy that can be charged and discharged during each cycle. The variation of the thermal energy storage capacity with time was calculated in order to understand the speed of decay of the pentaerythritol.

2. PROPERTIES OF PENTAERYTHRITOL

Prior to the application of pentaerythritol in the storage type of heat exchanger, a small-scale experimental facility was set up to observe its physical phenomena during the phase change. This facility was also used to study the thermal properties of pentaerythritol and its heat transfer mechanism during the heating and cooling process.

Experimental Set-Up

One heating chamber was constructed for this series of experiments to study the behavior of pentaerythritol during the phase change can be shown in Fig. 1. The double shell chamber made by stainless steel with two observing windows on the outer shell and heating element inside the inner shell. A pressure gauge and release valve was installed on the top to prevent the overpressure due to the evaporation of the pentaerythritol. The

maximum output power of the heating element is 800W. The cooling water was circulated on the top and bottom cover to protect the O-ring and increase the cooling rate during the cooling process. Three K-type thermocouples (T.C-1 to 3 as shown in Fig.1) were inserted between the two shells to measure the temperature variation and distribution of the pentaerythritol. Another thermocouple (T.C-4) was put on the inner shell for the purpose of heating control to avoid the evaporation of pentaerythritol. The thermocouples were put in the half height of the heating element and immersed in the pentaerythritol. In order to increase the heat transfer rate from inner shell to the outer shell, the enhancement element made by copper with the start shape was also inserted.

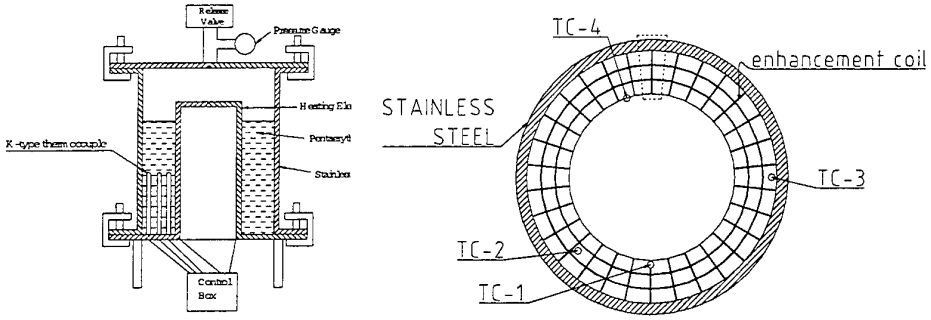


Fig.1. The heating chamber for study the behavior of pentaerythritol

Experimental Observation

The temperature variation for the pentaerythritol during heating and cooling process was studied with the heating chamber. In this series of experiments, 518 g of pentaerythritol was put in the chamber. The heating power was controlled at 400 W. When the temperature at T.C-1 was reached 249 °C, we turned off the heating power and cooling water. It is meant that the pentaerythritol was cooled by natural convection through outer shell only. The temperature variation during this process can be shown in Fig.2. It is found that there is a constant temperature region during the cooling process. That means a phase change was occurred at the temperature around 180 °C.

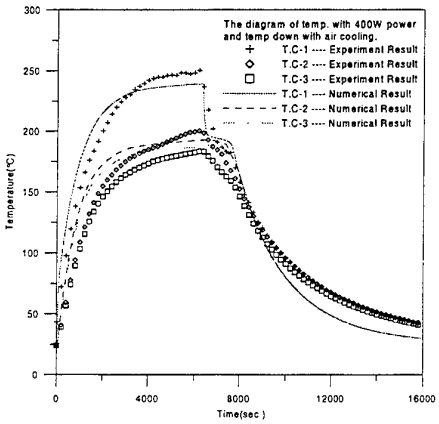
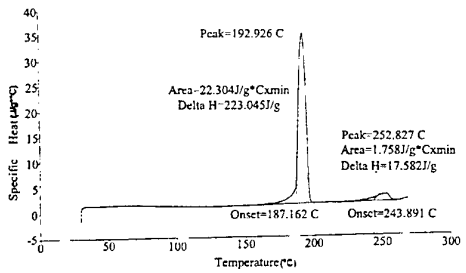


Fig.2. Temperature variation during the heating and cooling process

In order to understand the behavior of pentaerythritol during the phase change, another series of experiments with continue heating and cooling were performed. During these experiments, the sample of pentaerythritol was taken after several cycles of process. The specific heat for these samples was measured with Differential Scanning Calorimeter. The result was shown in Fig.3. It is found that there are two peak of specific heat. One is located at about 187 °C, the other at about 255 °C. From the experimental observation, it is found that there is not any visible phase change occurred at the first peak specific heat temperature. This is so-called form-stable phase change. The peak specific heat was resulted from the change of crystal structure of pentaerythritol. However, the quick change from solid to liquid and evaporated to the gas was occurred at the same temperature. The physical observation shown that the hole was existed near the inner wall if the temperature of pentaerythritol was higher than the temperature of second peak specific heat. The result was shown in Fig. 4. This is the result of second peak specific heat. The latent heat around the first peak and second peak specific heat were also calculated and shown in Table 1.



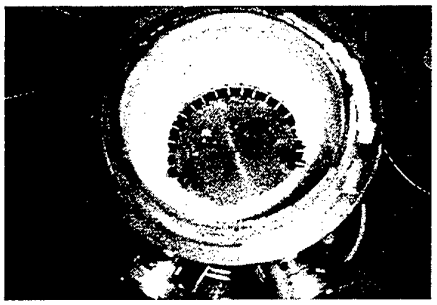


Fig. 3 The variation of specific heat

Fig. 4 Result shown the vaporization near wall

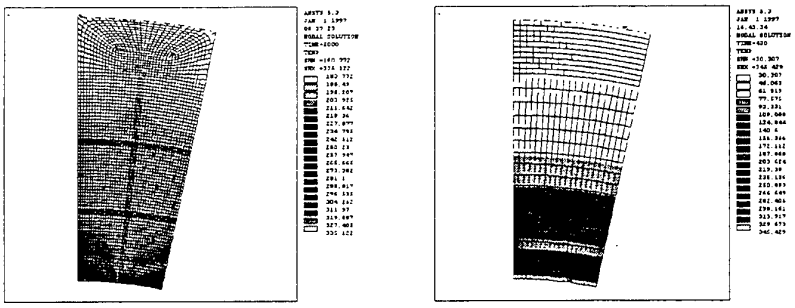
Table 1 Latent Heat of Pentaerythritol After Different Cycles

Sample	Cycles	Phase change temperature (°C)	Latent Heat (J/g)	Phase change temperature (°C)	Latent Heat (J/g)
1	1	187	239	258	24.8
2	5	187	209	254	16.0
3	10	187	235	257	20.7
4	15	187	230	257	16.2
5	20	187	217	252	14.9
6	25	187	218	249	13.2
7	30	187	223	253	17.6

3. NUMERICAL SIMULATION

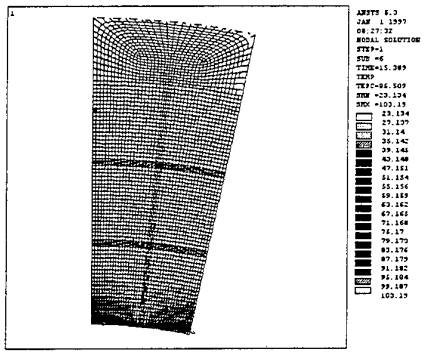
A numerical simulation was also performed to study the temperature variation of pentaerythritol during the phase change cycle. The ASYSY was used in this simulation. Due to the geometry symmetry of the g heating chamber, the control volume used in this simulation can be chosen the area surrounded by the dash line as shown in Fig.1. Several assumptions were applied: (1) the uniformed heat flux (400W for heating) was applied on the inner shell; (2) the natural convection was employed on the outer shell; (3) the thermal properties were constant except specific heat of pentaerythritol; (4) 2-D model was used.

The first simulation was performed for the heating chamber with and without the enhancement coil. The results for these two cases were shown in Fig.5. It was found that it took only about 430 seconds for the T.C-1 to reach the evaporation temperature for the heating chamber without enhancement coil and only the near wall region had reached the phase change temperature. However, it took about 5000 seconds for the T.C-1 to reach the evaporation temperature for the heating chamber with enhancement coil and almost all the pentaerythritol inside the chamber was subjected to phase change. This is due to the low thermal conductivity of pentaerythritol. This is why we inserted the enhancement coil made by copper inside the heating chamber [2,3]. The transient temperature distribution for the pentaerythritol during the heating and cooling process can be shown in Fig.6.

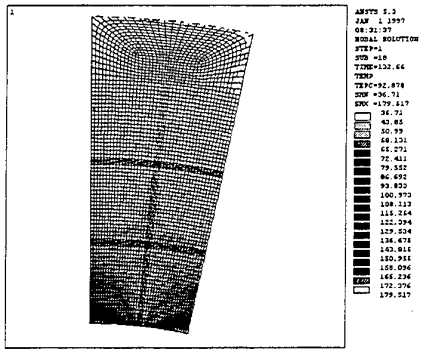


(a) with enhancement coil (b) without enhancement coil

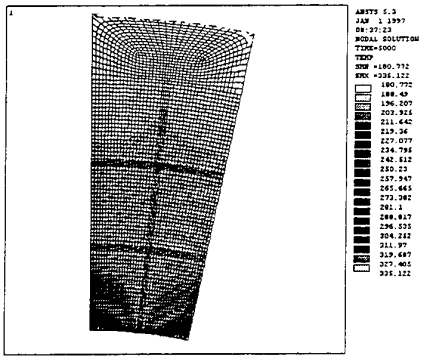
Fig. 5 The numerical results for the temperature distribution



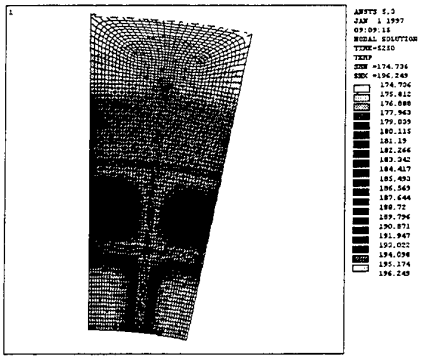
(a) 16 seconds (heating)



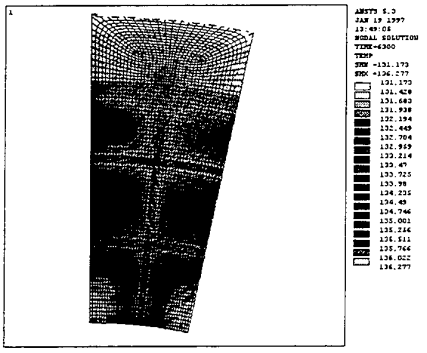
(b) 133 seconds (heating)



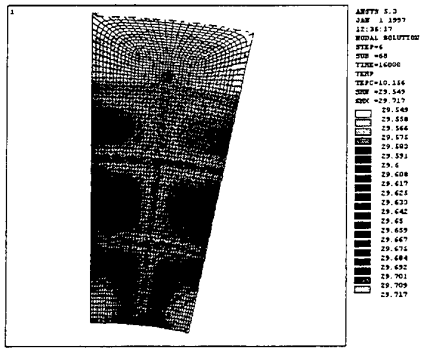
(c) 5000 second (T.C-1 > 249 °C) (end of heating)



(d) 5250 seconds (cooling)



(e) 6300 seconds (cooling)



(f) 16000 seconds (end of cooling)

Fig. 6 The transient temperature variation of pentaerythritol during one cycle

The comparison of numerical results and experimental for 5 cycles is shown in Fig. 7 [4].

4. FULL SCALE TEST FACILITY

In this study, a shell and tube heat exchanger was modified to act as a storage type heat exchanger and pentaerythritol was chosen as the thermal energy storage medium and filled inside the tube. A hot air generator with heating capacity 36kW and flow rate 26 CMM was used to simulate the hot exhaust gas from the boiler. The maximum temperature of the supplied air was 350 °C. Two identical heat exchangers were applied in this testing facility (Fig.8). During the experiments, hot air was forced through one heat exchanger and the cold air

passed the other heat exchanger. The flow passage of both hot and cold air was reversed when the amount of energy storage was full. This meant that the pentaerythritol inside the storage type heat exchanger during the heating process passed the phase change region, i.e., subject the crystal structure change. This experimental facility was set up to learn the behavior of the phase change material during the repeated charge and discharge of thermal energy processes.

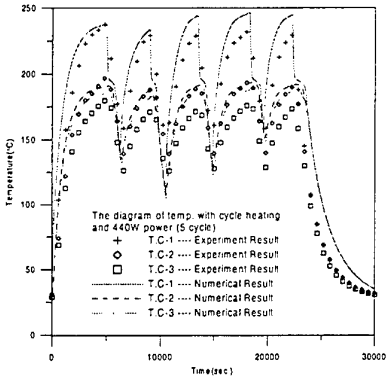


Fig. 7 Comparison of numerical and experimental data for 5 cycles

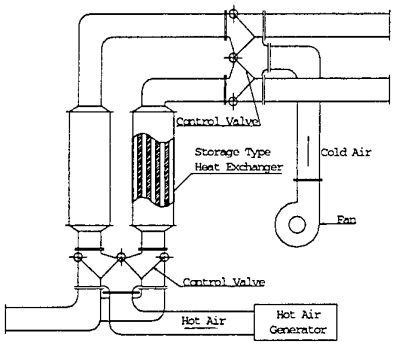


Fig. 8 Full scale test facility

5. RESULTS AND DISCUSSION

The results shown in Fig.4 indicated that the temperature for the second peak specific heat is the critical point for the usage of pentaerythritol. The phase change for the pentaerythritol that occurred at this temperature not only liquefied but also evaporated. After the vaporization occurred, the cooling process can not totally recovery them back to the solid state. This phenomena suggests that pentaerythritol should be maintained lower than this temperature to avoid vaporization. This also posts some limitation for the application of pentaerythritol. The capacity of thermal energy storage for a storage type heat exchanger with phase change material is dependent on the change of latent heat. It can be expressed as the variation of specific heat (as shown in Fig. 3). The results for the pentaerythritol after 30 cycles of testing show that the latent heat for the first phase change region is almost maintained at constant (as shown in Table 1). This means that the thermal properties are not affected significant by the cycles.

6. CONCLUSIONS

1. Most of the phase change material is low thermal conductivity, so the heat transfer enhancement is required inside the container in order to use all of the material in the container.
2. The agreement between numerical results and experimental data can support the correct design of container for the phase change material.
3. Pentaerythritol is a good candidate for the thermal energy storage material for the system operated at the temperature lower than 200 °C.
4. The economic and overall analysis for the waste heat recovery system with thermal energy storage that employed phase change material need more study in order to set up the criteria for the application of phase change material.

REFERENCE

1. J. Yagi and T. Akiyama, "Storage of Thermal Energy for Effective Use of Waste Heat from Industries," Journal of Material Processing Technology, v. 48, pp. 793-804, 1995
2. L.C. Chow, J.K. Zhong, and J.E. Beam, "Thermal Conductivity Enhancement for Phase Change Storage Media," Int. Comm. Heat and Mass Transfer, v. 23, pp. 91-100, 1996
3. Y. Zhang and A. Faghri, "Heat Transfer Enhancement in Latent Heat Thermal Energy Storage System by Using the Internally Finned Tube," Int. J. Heat and Mass Transfer, v. 39, pp. 3165-3173, 1996
4. H.H. Lin, G.T. Lin, and B.C. Yang, "The Technologies for Energy Recovery and Application," Final Report submitted to the Energy Commission, Taiwan, ROC.

SOLAR ENERGY STORAGE, UTILIZING PARAFFIN WAX AS A PHASE-CHANGE MATERIAL

N.El Chazly[**(1)], **N.Khattab**[**(2)], **S.El-Deeb**[**(3)] **and A.El-Sharkawy**[**(4)]
**(1), (3) Prof., **(4)Eng., Mech.Eng. Dept., National Research Centre, Dokki, Cairo
**(2) Assoc. Prof., Solar Energy Dept., National Research Centre, Dokki, Cairo
E-mail: aymr@intouch.com

M.El-Kotb
Prof., Mech.Power Eng.Dept., Faculty of Eng., Cairo University.

Keywords: phase-change material, latent heat, paraffin wax, energy storage.

ABSTRACT. A thermal energy storage medium must meet the requirements of a stable storage material with high heat capacity. Heat storage based on the sensible heating of media such as water, rock and earth represent the first generation of solar energy storage subsystems and technology for their utilization is well developed. However, recently the heat storage based on the latent heat associated with a change in phase of a material offers many advantages over sensible heat storage. The most important characteristic of such a subsystem is its sufficient storage capacity. The PCM (phase change material) behavior is visualized by constructing an idealized model thermal capacitor subjected to simulated solar system environmental conditions which include thermal cycling utilizing the latent heat of paraffin for heating and cooling. The proposed model of the capacitor is of flat plate geometry consisting of two panels compartments forming the body of the capacitor containing the paraffin, welded from their inner surfaces to a thin copper one allowing the passage of the water. The whole structure was assumed to be insulated to minimize heat loss. An analysis of the model is conducted using Goodman technique [1]. To generate data about the temperature distribution, the melt thickness, and the heat stored in the PCM under two types of conditions were generated; namely (i) constant mass flow rate tests for various water inlet temperatures and (ii) constant water inlet temperature for various mass flow rate. It was found that water outlet temperature increases with time until it becomes nearly equals to the inlet temperature.Increasing the mass flow rate for a given inlet temperature, decreases the time required for outlet temperature to reach a given value. Increasing inlet temperature for a given mass flow rate gives a very rapid decrease in the time required for the outlet water temperature to reach a given value. Instantaneous rate of heat storage was determined from the inlet-to- exit temperature differential and measured flow rate. This rate was then integrated numerically to determine the cumulative total energy stored as a function of time .It was found that the instantaneous rate of heat storage decreases till reaching a nearly constant value. The total or cumulative heat storage as a function of time, showed a nearly linear trend in the mid-range time, and it increased with increasing inlet temperature.

1. INTRODUCTION

Solar energy systems for heating and cooling are considerably more complex in practice than conventional systems because they usually evolve from the integration of several systems which include collector, a heat storage unit and heat exchanger to dissipate heat to the building. Perhaps, the great need and challenge exists in the area of the energy storage subsystems because solar energy is not a constant supply. The lack of viable system to store this energy is one of the major limitations encountered in many residential heating systems which utilize this unconventional energy source. One of the most widely used storage systems is sensible heat storage, which utilize very large volume of storage media. These systems are not, in general rapidly responsive and obviously offer little control of operating temperature. Systems which can lead to appreciable reduction in the volume of storage medium. Temperature control and give a rapid response, is one based upon a solid liquid phase transformation. Many investigations performed in the field of the phase change materials reveal that the most promising materials which posses the characteristics necessary for phase change material are certain classes of organic compound such as the paraffin hydrocarbon and fatty acids [2]. The thermal behaviour of paraffin wax is studied extensively by [3] Sharma, et al [4]. Storage systems using paraffin wax have been studied by Hajieva et al [5]and Morrison et al [6].

Although many investigations are performed in storage systems, yet, they still need appropriate relation which

can be used to design a heat storage subsystems (thermal capacitor) based on the utilization of the energy absorbed during a solid-liquid phase transformation of long chain paraffin hydrocarbons. So, the object of this work is to develop an appropriate model through careful analysis which may be used to describe the performance of thermal capacitor and to verify the validity of the model by comparing the theoretical predictions with the results of other theoretical techniques and carefully controlled earlier experiments.

2. ANALYTICAL WORK

The storage medium consisting of a phase change material combines sensible and latent heat storage while providing high heat capacity and high rate of heat transfer to the latent heat storage material. The development of an analytical model which would predict the performance of thermal energy storage units, must simulate solar system environmental conditions including thermal cycling. So, the analysis should be based on physical changes occurring during the operation of thermal capacitor.

The operations of the thermal capacitor could be divided into three regions during a heat storage cycle; namely, (i) a premelting region, (ii) a melting region, (iii) a postmelting region. In the premelting and postmelting regions, heat is absorbed by the phase change material as a sensible heat. In the melting region heat is absorbed as latent heat of fusion as the phase change material undergoes phase transformation (solid ↔ liquid). Similar regions can be identified for a heat dissipation cycle.

Numerical Simulation

Basic model and assumptions A simplified model was assumed to have a flat plate geometry consisting of two chambers filled with paraffin wax and joined together forming a narrow channel allowing the flow of the fluid, Fig. 1 .

Goodman technique [1] The mathematical model used in this analysis is based on some assumptions:

1. The initial temperature of the paraffin is the melting temperature.
2. The process under consideration consists of melting, then heating the resulting liquid.
3. Heat conduction in y- direction only.
4. The temperature gradient across the fluid passage wall is negligible.
5. Heat losses from the storage unit to the surroundings are negligible.

Governing equations A solution using the "Heat-Balance Integral" is utilized for solving the location of the melt line in heat – conduction problems involving a change of phase, and is summarized by the following equations:

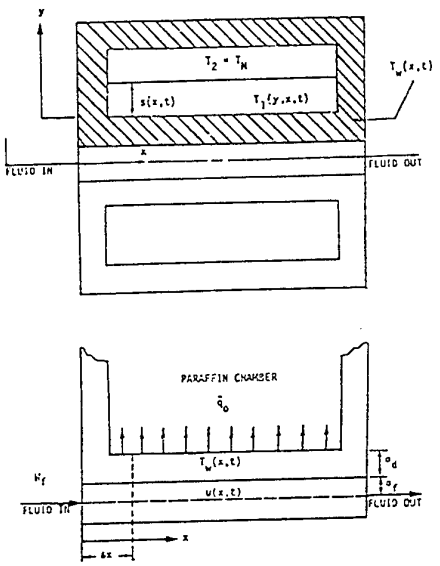


Fig. 1 Simplified Thermal Capacitor Model

$$\frac{\partial^2 w_1}{\partial y^2}(y,x,t) = \frac{1}{\alpha_1}\frac{\partial w_1}{\partial t}(y,t), \quad 0 < y < s(x,t) \tag{1}$$

$$k_{1y}\frac{\partial w_1}{\partial y}(0,t) = h(w_1(0,t) - \omega_\infty), \text{ at } y = 0 \tag{2}$$

$$\frac{\partial w_1}{\partial y}(y,x,t) = -\frac{\rho l}{k_{1y}}\frac{\partial s}{\partial t} \tag{3}$$

$$w_1 = 0 \qquad \text{at } y=s(x,t) \tag{4}$$

$$w_1 = 0 \text{ and } s = 0, \qquad \text{at } t=0 \tag{5}$$

where "w "and " ω " are the excess temperatures and are given by:

$$w_1 T_1 - T_M \quad ; \quad \omega = u - T_M \tag{6}$$

The excess energy φ in the liquid phase produced by phase transformation is given by:

$$\varphi = \int_0^{s(t)} w_1(y,x,t)dy \ , \qquad 0 < y < s(x,t) \tag{7}$$

The heat supplied to a region which has undergone a change of phase or ,
"heat balance integral" is given by:

$$\frac{d\varphi}{dt} = \frac{L}{c_p}\frac{ds}{dt} - \frac{k_{1y}}{\rho c_p}\frac{\partial w_1}{\partial y}(0,t) \tag{8}$$

The temperature distribution in the region that has undergone a phase change can be obtained by assuming a second degree polynomial for w_1 at any given time of the form:

$$w_1 = a + by + cy^2 \tag{9}$$

Three conditions are necessary in order to obtain the constants; mainly got from boundary conditions equations .
The resultant for the location of the phase boundary is given by:

$$\Gamma = \frac{1}{12P}\left[\begin{array}{l} [(1+2p)+(2+p)s]\,[1+ps(2+s)]^{1/2} - \dfrac{2(p-1)}{\sqrt{p}}\ln\dfrac{[1+ps(2+s)]^{1/2}}{1+\sqrt{p}} + \dfrac{[1+s)p]^{1/2}}{1+\sqrt{p}} \\ -4p(p-1)\ln\dfrac{-1+p(2+s)+[1+ps(2+s)]^{1/2}}{2p} + (p^2+5p)\dfrac{s^2}{2} + 2(p^2+4p-2)s \\ -(1+2p) \end{array}\right] \tag{10}$$

where the normalized variables are given by:

$$\Gamma = \frac{h^2\omega_\infty t}{k_{1y}L} \tag{11}$$

$$S = \frac{hs}{k_{1y}} \tag{12}$$

$$P = 1 + \frac{2\omega_\infty}{L/C_p} \tag{13}$$

The ratio of the wall temperature to the fluid temperature is given by:

$$\frac{w_1(0,t)}{\omega_\infty} = \frac{(p-1)s^2 + 2(p-2)s - 2 + 2[1+ps(2+s)]^{1/2}}{(p-1)(2+s)^2} \tag{14}$$

An energy balance on an elemental section of the thermal capacitor gives:

$$T_{N,n} - T_{0,n} = \frac{Q}{C_p w_f t} \tag{15}$$

where" Q" is the total heat absorbed (or rejected) by the fluid when the phase boundary moves a distance "s", and is given by:

$$Q = Q_1 + Q_2 \tag{16}$$

$$Q = sAL\rho + \frac{w_1(0,t)}{2} C_p \rho A s \tag{17}$$

where Q_1 is the energy absorbed because of a change in phase (melting) and Q_2 is the energy absorbed because of sensible heating.

The complete analysis of the thermal capacitor is carried out by dividing the capacitor into sixteen strips of equal size as illustrated in Fig. 2 and then applying the Goodman solution separately to each strip. For the first strip the free stream temperature initially is assumed to be equal to the inlet temperature to the capacitor and that the material in the capacitor undergoes a phase change over a thickness s, (s') calculated from equation (10) for a

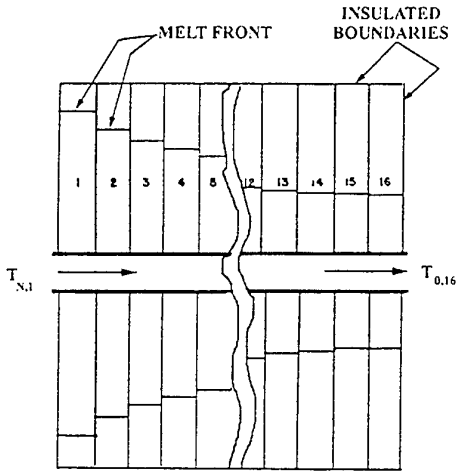


Fig. 2 Division of the Capacitor into 16 strips

given time t. The outlet temperature of the fluid in the first strip is calculated now from equations (15), (16) and (17) and a new (average) free stream temperature computed from:

$$\omega_{\infty,1} = \frac{T_{N,1} + T_{0,1}}{2} - T_M \tag{18}$$

The iterative procedure is repeated to give a second value for " $\omega^k{}_{\infty,1}$ ".

The aforementioned computational procedure is used for each strip. Finally, the outlet temperature of the last strip gives the emergent temperature of the fluid from the capacitor.

3. RESULTS AND DISCUSSIONS

A type of thermal capacitor capable of storing solar energy as latent heat of fusion through the use of pure paraffin hydrocarbon was analyzed using the "Goodman Technique" previously described. The present work predicts the behavior and performance of this type of phase change subsystem. A computer program has been constructed to analyze this system, aiming at computing the amount of heat or energy stored in such a phase-change material; paraffin wax, useful in energy systems storage, together with temperature distribution along fluid passage,and the rate of storing heat from fluid entrance to exit. Also the thickness of melted layer of the wax was computed for the strips which form the whole wax used in the capacitor.

Computer Program Validation

The validation of the computer program used to analyze the proposed model has been done by comparing the results obtained from this theoretical analysis based on Goodman technique, to those obtained from other techniques, [7], by using same paraffin wax properties and same boundary and initial conditions. The paraffin hydrocarbon (n. Eicosane) used, has the following properties:

1. Melting point, 96.5°F.
2. Latent heat of fusion, 107.5 Btu / lb
3. The initial inlet temperature supply 144°F.
4. The mass flow rate, 322 lb/hr.

Figure 1 shows the schematic diagram of the capacitor, together with initial and boundary conditions.
The verification of the present work has been based on the comparison of the different techniques from the points of view of:

1. Fluid outlet temperature.
2. Cumulative heat stored.

These parameters have been plotted as functions of time in Fig.3 and Fig.4. It is obvious that the Goodman technique modeled by the present computer program is in good agreement with the other ones.

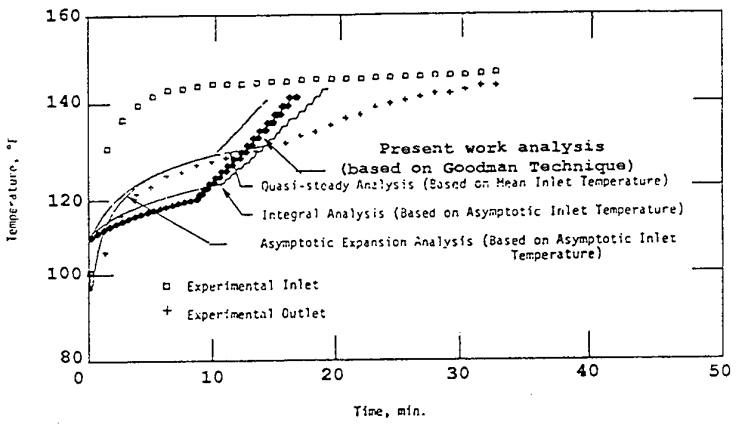


Fig. 3 Variation of experimental intlet and outlet temperature and analytical outlet temperature with time for & mean inlet temperature of 144°F and a collant flow rate of 322 1b/hr

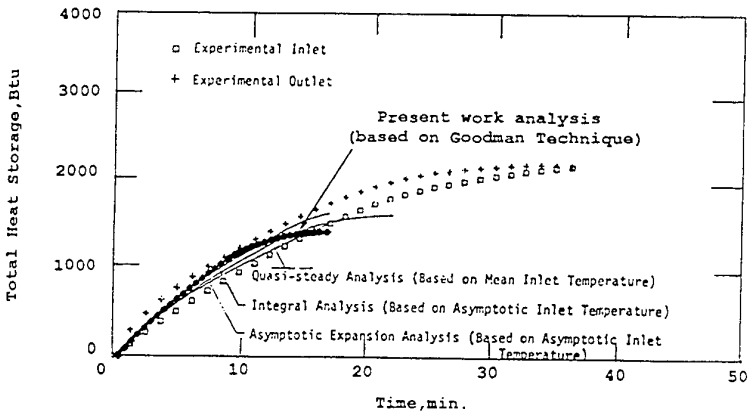


Fig. 4 Variation of total heat storage with time for a mean inlet temperature of 144 °F and a collant flow rate of 322 lb/hr

Analysis of paraffin wax (Pentacosane)

The phase change material used in this work is the "Pentacosane". Its physical properties are given in Table 1, [3].

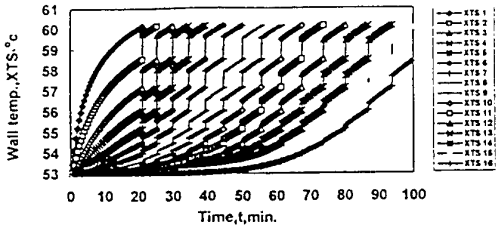
Table 1 Properties of Pentacosane

Material	No. of carbon atoms	Melting point,°C	Latent heat of fusion kJ/kg	Density kg/m^3 at 20°C	Specific heat, Solid (s),liquid (l)
Paraffin wax (Pentacosane)	25	53.56 °C	238	818 (s) 760 (l)	2.95 (s) 2.51 (l)

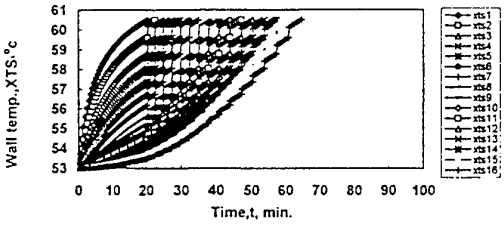
Effect of Fluid Mass Flow Rate on Temperature Distribution at Constant Fluid Inlet Temperature,T_{in} = 65°C

The variations of fluid channel wall temperature (XTS) with time along each strip for the whole sixteen strips, at different mass flow rates (m.f.r); 30 and 90 kg/hr, at constant inlet temperature, T_{in} = 65°C are given in Fig. 5(a,b). It is obvious that the temperature increases with time and the rate of increase in temperature decreases from first to last strip, that is because the first strip is adjacent to the inlet of the fluid and then will be hotter than those below.

Comparing the behaviour of the wax for two different fluid mass flow rates, it is clear that it behaves similarly, that is to say that wax temperature increases with time, but it is obvious that for all strips, the time decreases with increasing mass flow rate to reach a completely melted strip. This may be proved by comparing the melting time of one of the strips; strip 16, which is the outlet of the fluid, as shown in Fig. 6 .



(a) mass flow rate (m.f.r.)=30kg/hr



(b) mass flow rate (m.f.r.)=90kg/hr

Fig. 5 Temp. of fluid channel wall with time T_{in} 65°C

The outlet fluid channel wall temperature (XTS) from each strip,versus strip's number at specified times; at which one or more strips get melted, are shown in Fig.7 . Increasing time, tends to increase the number of

melted strips, and for the same time, the temperature in each strip decreases going from fluid inlet to fluid outlet Increasing fluid mass flow rate, the number of melted strips increases for the same time. This is verified by the relation given in Fig.8 , which represents the time of melting versus the number of melted strips.

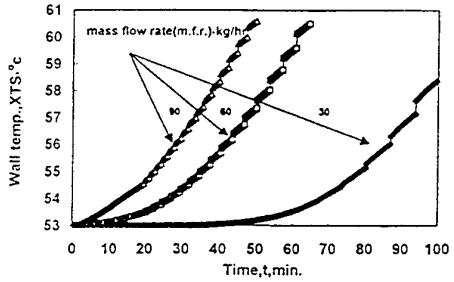
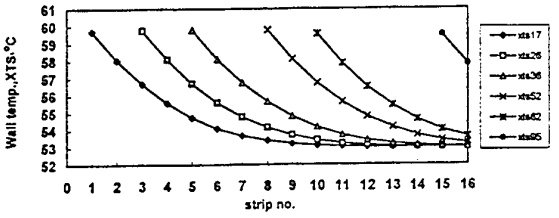


Fig. 6 Fluid Temp. of the channel wall with time, for different flow rates at strip 16, T_{in} =65°C



(a) mass flow rate (m.f.r.)=30kg/hr

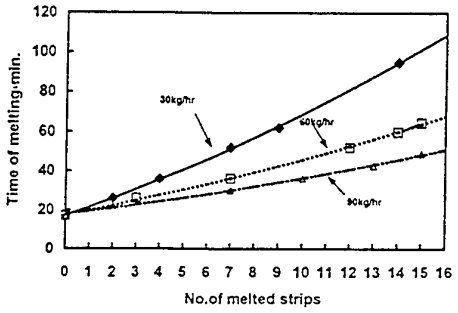
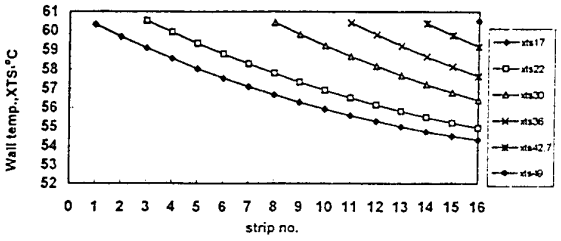


Fig. 8 Effect of mass flow rate on the no. of melted strips at T_{in} =65°C



(b) mass flow rate (m.f.r.)=90kg/hr

Fig. 7 Temp. of fluid channel wall at different time with strip no., T_{in}, 65°C

Effect of Fluid Inlet Temperature at Constant Fluid Mass Flow Rate on Temperature Distribution

The effect of fluid inlet temperature, at a specific fluid mass flow rate, on temperature distribution with time is presented in Fig.9. Increasing fluid inlet temperature, tends to increase the outlet temperature or the the temperature of the last strip, and to decrease time. This means that the charging process is more efficient with higher fluid inlet temperature.

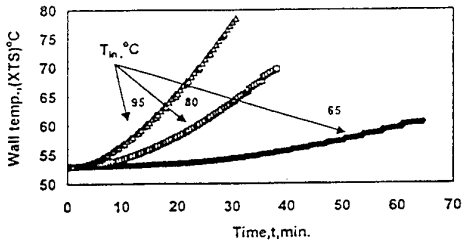
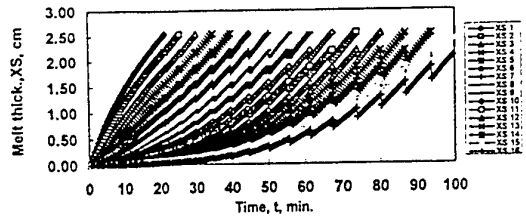


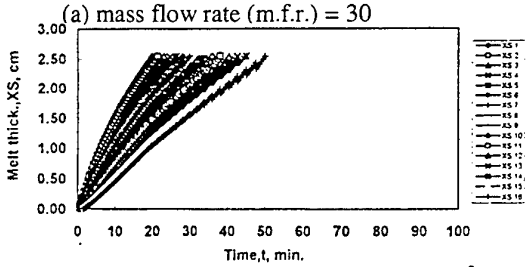
Fig. 9 Effect of fluid inlet temp. on temp. of fluid channel wall at a mass flow rate = 60kg/hr

Effect of mass flow rate (m.f.r.) on melt thickness (XS) at constant inlet temperature, T_{in} = 65°C

For different mass flow rates (30, 90 kg/hr) and constant inlet temperature 65°C, the melt thickness progress of wax, increases with time as shown in Fig. 10(a,b). From these figures, it is obvious that the rate of increasing of of wax melt thickness (XS), decreases going downstream from the first strip to the last one; that is because going from up to down, the strips are hotter as the hot fluid goes downwards, and the heat transfer is higher at the fluid inlet. For different fluid mass flow rates and constant inlet temperature, it is clear that for all strips, the time taken for melting a certain thickness of paraffin wax decreases with increasing mass flow rate. The previous results are verified by comparing the melt thickness of paraffin with time for strip 16, which is the outlet of the fluid, at three different mass flow rates, Fig.11.



(a) mass flow rate (m.f.r.) = 30



(b) was melted thick. With time, T_{in}=65 °C

Fig. 10 Wax melted thick vs time, T_{in} = 65°C

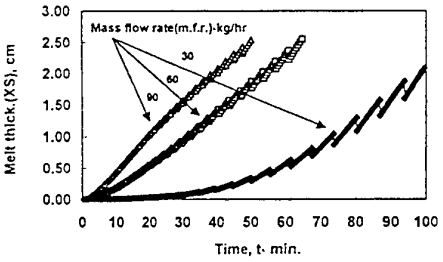


Fig. 11 Wax melted thick for different flow rates at strip 16, T_{in} = 65°C

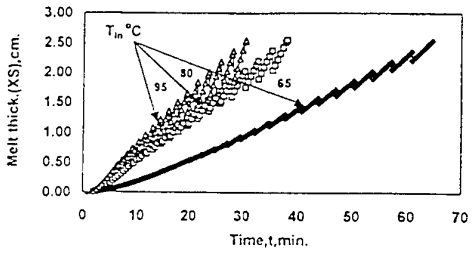
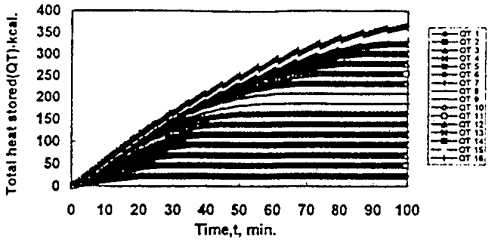
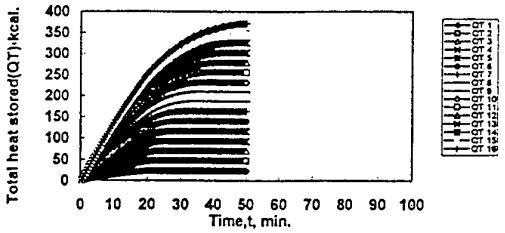


Fig. 12 Effect of fluid inlet temp. on wax melt thick at a mass flow rate = 60kg/hr



(a) mass flow rate (m.f.r) = 30kg/hr



(b) mass flow rate (m.f.r) = 30kg/hr

Fig. 13 Total heat stored vs time, T_{in} = 65°C

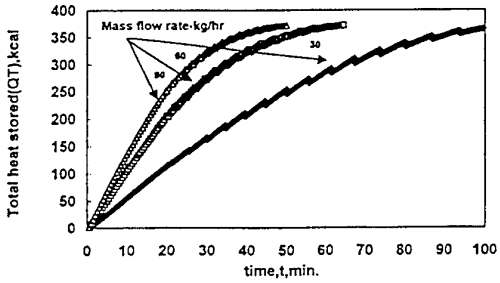


Fig. 14 Effect of mass flow rate on total heat stored wi, strip 16, T_{in} = 65°C

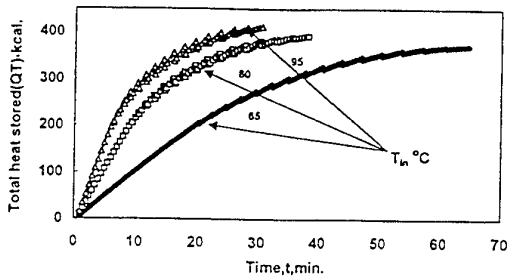


Fig. 15 Effect of fluid inlet temp T_{in} on total heat stored, at a mass flow rate, (m.f.r.)=60kg/hr

<u>Effect of fluid inlet temperature at constant fluid mass flow rate, on melt thickness (XS)</u>

The effect of fluid inlet temperature, at a specific fluid mass flow rate, on wax melt thickness with time is presented in Fig.12. Increasing fluid inlet temperature, tends to decrease melting time.

<u>Effect of mass flow rate on cumulative heat stored (QT) at constant inlet temperature,T_{in}=65°C</u>

The cumulative storage of heat with time in all the strips are shown in Fig 13. The heat stored is accumulated from the first to the last strip, so that the heat stored in strip number (2) for example is the summation of heat

stored in strip (1) and that of strip (2), that is to say, the stored heat corresponding to strip (16) is the total cumulative heat stored in the whole paraffin wax contained in the reservoir. By comparing the heat stored at three different mass flow rates with time, it is to be noticed that, increasing mass flow rate, increases total heat stored and decreases the time taken to store maximum possible heat. Fig. 14 confirms the fact that at a specified time for a specified strip namely the last one, the heat stored in paraffin wax is higher at higher mass flow rate.

Effect of fluid inlet temperature at constant fluid mass flow rate, on total heat stored (QT)

The variation of cumulative heat stored with time for three different inlet temperatures, mainly, 65, 80 and 95^{0}C at a specified mass flow rate is given in Fig. 15. It is obvious that increasing inlet temperature, increases the total heat stored, and decreases the time required to store maximum possible heat.

4. CONCLUSIONS

A latent heat storage unit I, simulated using an analytical model based on Goodman technique, has been developed. The model was handled assuming uniaxial heat conduction with change of phase and a absence of natural convection in the phase change material. The storage mode was only considered in this study. The outlet temperature rises rapidly to a plateau and remains relatively constant throughout the melting process. The plateau depends upon the inlet fluid temperature and fluid mass flow rate. The paraffin melt time depends also upon fluid flow rate and fluid inlet temperature, the melt time varied from 40 minutes at 90 kg/hr mass flow rate to 100 minutes at 30 kg/hr , and from 30 minutes at fluid inlet temperature of 95°C to 65 minutes at 65°C . High flow rate and high fluid inlet temperature, tends to increase storage rate as the melt time decreases.

NOMENCLATURE

c_p = specific heat of paraffin
h = heat transfer coefficient between the wall and the fluid
k_{ly} = effective thermal conductivity of paraffin for liquid phase in y- direction
L = latent heat of fusion of paraffin
s = melt thickness
t = time
T_1 = temperature of paraffin for liquid phase
T_2 = temperature of paraffin for solid phase
T_M = melting point temperature of paraffin
T_N = fluid inlet temperature
T_∞ = fluid outlet temperature
u = fluid temperature
ρ = density of paraffin
α = thermal diffusivity of liquid paraffin

REFERENCES

1. T.R.,Goodman, " The Heat –Balance Integral and Its Application to Problems Involving a Change of Phase, " ASME Trans.,vol. 80 , No. 2, pp 335-342, (1958).
2. A. Abhat, "Low Temperature Latent Heat Thermal Energy Storage", Thermal Energy Storage Proceedings of the lectures of a course, held Ispra, Italy, pp.1-5, June, (1981).
3. S. Hirman, A. Suwono, and G. A. Mansoori, "Characterization of Alkanes and Paraffin waxes for Application as Phase Change Energy Storage Medium" Energy Sources, vol. 16, No. 1, pp.117, 128 Jan-Mar, (1994).
4. S. K. Sharma, and S. Singh, "Paraffin Wax as Phase change Thermal Storage Material," Proceeding of the workshop on solar energy storage held Punjab University, Chandijarh, India, No. 16-18, Mar, pp. 77-87, (1979).
5. M. Hadjieva, S.T. Kaneu, and J. Argirou, "Thermo Physical Properties of some Paraffins Applicable to thermal Energy Storage" Solar Energy Materials and Solar Cells, vol. 27, No. 2, pp.181-187, (1992).
6. D. J. Marrison and S. I. Abdel Khalik, "Effect of Phase Change Energy and Liquid-Based Solar Heating Systems" Solar Energy, No. 20, pp. 57-67, (1978).
7. B. John A.,L.,Chang-Kwang,G.,Selcuki, and M.,James C., "A Solar Energy Storage Subsystem Utilyzing The Latent Heat of Fusion of Paraffin Hydrocarbons", A Progress Report, pp 75-83,(1975).

MECHANISM OF HEAT AND MASS TRANSFER DURING GAS HYDRATE COOL STORAGE PROCESS

Liquan Xiao, Shiping Wang
Institute of Chemical Engineering
South China University of Technology
Email: shawgon@163.net; Tel.: 8620-8711-2997

Keywords: gas hydrate, cool storage, heat and mass transfer

ABSTRACT. Gas hydrate cool storage systems have been developed since the end of 1980s. Compared with the prevalent ice-storage systems, gas hydrate cool storage systems are characterized by higher phase-change temperature and very large latent heat released during phase-change process. Higher phase-change temperature can avoid the decease of the COP of water-chiller unit and make the air-conditioning system more effective. This paper analyzed the complicated process of heat and mass transfer inside an indirect-contact gas hydrate cool-storage tank. It's indicated that condensation, evaporation and hydration are a combined and mutually-influenced process. A qualitative model is disgust to explain the behavior of hydrate cool storage.

1. INTRODUCTION

In 1990s, the use of air-conditioning equipment improves so rapidly in China's metropolis as to causes the urban consumption of electric power increases fiercely. The most electric consumption is always coincident with the peak of electric network so that it augments the difference between peak and valley therefore aggravates the working condition of power system. Under this circumstance, the technology of cool storage comes into being, the principle of which is to operate the chiller during valley periods and store cool energy to feed the peak demand during daytime. The popular saying for this is "cutting the mountain, leveling the valley". Cool storage can effectively mitigate the burden of electric network and plays a more and more important role in the economy of China.

Because it'll absorb a great quantity of heat during ice fusion, the thermal capacity of ice is very large. Using ice for cool storage medium is prevalent all over the world. The ice forming temperature is 0 °C that is much lower than the chilled water temperature of common air-conditioning unit. Thus when water chiller unit is working under ice-forming condition, the COP of the refrigeration system decreases which makes the electricity consumption increases. On the other hand, the phase-change temperature of some kind of gas hydrate is within the favorite scope of 5 °C-12 °C and at the same time, the heat of phase-change process is comparable with that of ice. The above characteristic makes gas hydrate a very promising candidate of cool-storage medium.

The idea of cool storage using gas hydrate was first mentioned by Tomlinson [1] of Oakridge National Laboratory in the year of 1982. Since then, U.S and Japan energetically paid their attention to the industrialization research of cool-storage using gas hydrate. Yutaka [2] is the foremost authority in using gas hydrate as indirect-contacting cool-storage equipment.

This paper aims at the analysis of heat and mass transfer process during gas-hydrate cool-storage process in the indirect-contact equipment. Combined with some of our experiment results on our small pilot-plant, a qualitative model is established to give some guidance to the practical design of gas-hydrate cool-storage system.

2. INTRODUCTION OF INSTALLATION

Our test plant is somewhat resembles of Yutaka's system in which it has involved the principle of heat pipe, activating the hydration process by the cycle of evaporation and condensation of refrigerant. The sketch of our test plant is indicated as Figure 1.

The cylindrical cool storage tank is made of stainless steel and can resist pressure of 1.6 MPa. There are two sets of heat exchangers inside it: the condenser in the upper part of the tank and the evaporator in the lower part of the tank. Cool storage medium is divided into three layers: the liquid layer in the bottom, the water layer in the

middle and the gas layer on the top of the tank, the thickness of each layer is indicated respectively by H_l, H_w, H_g. There are four viewing windows on the peripheral of the tank. The whole tank is kept adiabatic using polyurethane foam sheet. Our plant differs from that of Yutaka's in that our plant cancelled the returning tube of condensed liquid. It is confirmed from our result that this cancellation is beneficial to the hydration because:

1) the liquid droplet can re-evaporate when penetrating the water layer, absorbing the heat of hydration, making the temperature homogeneous;
2) a large amount of droplet can increase the contact area of two phase of refrigerant and water and thus accelerate hydration;
3) descending of droplet along with the rising of gas bulb reinforce the disturbance of water layer and help boost the mass transfer.

Experimental phenomena are reported elsewhere [3,4]. This paper will focus on the process of heat and mass transfer inside the cool-storage tank.

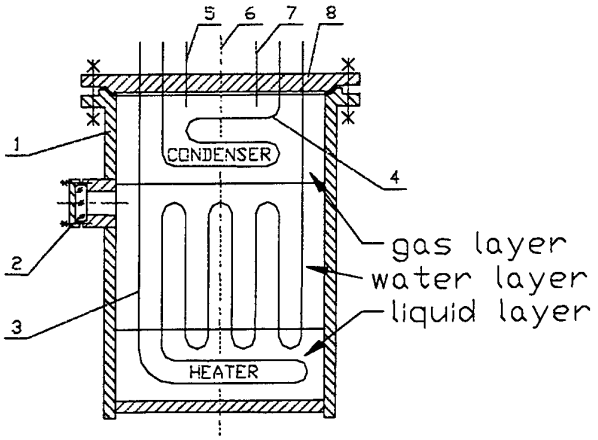


Fig. 1. Schematic structure of cool storage tank

3. ANALYSIS OF COOL STORAGE PROCESS

Actual cool-storage process includes the combination of condensation of vapor, hydration and the evaporation of liquid refrigerant which makes the process much complicated. During cool storage, the condenser makes the partial pressure of gaseous refrigerant drop, which brings on the evaporation of liquid and the decrease of water temperature. When the water temperature sinks to the hydrate-forming point generally higher than ice point, hydration occurs in the water layer. Heat released during hydration is absorbed by the evaporation of liquid refrigerant.

3.1 Variation of Pressure During Cool Storage

The condensation and evaporation of refrigerant constitutes a cycling process. There is a difference ΔP between the partial pressure above liquid layer and the corresponding saturated pressure of refrigerant because of condensation, which is a little similar to the capillary suction head of heat pipe. This pressure difference ΔP has great influence on the hydration rate and the property of formed hydrate.

Fig. 2 shows the variation of pressure using HFC-134a as hydration medium and n-butanol as additive. It's indicated in Fig. 2 that at the beginning of cool-storage, there's a sudden drop of the pressure inside the tank which is exactly the above mentioned pressure difference ΔP. The descent of pressure as a function of elapsed time exhibits a configuration of exponential decay.

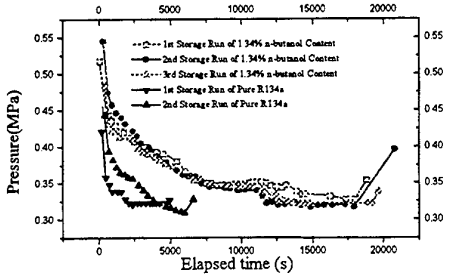


Fig. 2. Pressure variation during cool storage

The above mentioned pressure difference ΔP must be equalized with three forces as follows:

3.1.1 Gravity. The static pressure caused by the height of water layer H_w will prevent freon from evaporating therefore stagnate the hydration rate. It is naturally deduced from this conclusion that gas-hydrate cool-storage equipment should be designed horizontal.

3.1.2 Resistance to the bulb and droplet. The resistance of the hydrate bulk drifted in the water layer to the rising bulb and descending droplet is very difficult to give a quantitative analysis because of the co-existence of triple phase of gas, liquid and solid. Generally speaking, if the density of formed hydrate is smaller than that of water, it'll drift on the surface of water preventing bulbs and droplets from rising and descending. Our experiment [5] confirmed that the addition of some kind of additives can eliminate hydrate drift and accelerate hydration.

3.1.3 Surface tension at the interface of refrigerant and water. The evaporation of freon is similar to boiling except that the latter is regulated by the superheat of container's wall but the former is a process controlled by the difference of partial pressure. Freon bulb must overcome the bondage of surface tension to rise into upper space. It's known from bulb kinetics that the intensity of boiling heat transfer is decided by the frequency of bulb rising f the relation of which with the bulb diameter D_d can be described by following equation [6]:

$$fD_d = C \tag{1}$$

At the other hand, rising bulb diameter D_d can be determined by:

$$D_d = 0.0208\theta\sqrt{\frac{\sigma}{g(\rho_l - \rho_d)}} \tag{2}$$

In the above formula, θ is the contacting tangle, σ is the surface tension. It is clearly indicated the smaller the surface tension is, the higher the frequency of bulb rising is, and the more rapid evaporation is. Use of surfactant can notably decrease the surface tension of freon-water interface therefore accelerate hydration.

It is found by Miller and Smythe [7] that the pressure is exponentially decaying during formation of CO_2 hydrate which is qualitatively verified by the result showed in Fig. 2. Their expression is:

$$\ln\left[\frac{p_0 - p_\infty}{p - p_\infty}\right] = kt \tag{3}$$

in which, t is the elapsed time.

3.2 Heat Balance During Cool Storage

Heat balance of hydrate cool-storage plants has been investigated in literature [8] and the following equation has been deduced:

$$\dot{m}_f \cdot \Delta H = A \cdot \alpha \cdot (T_f - T_c) \tag{4}$$

The left is heat of hydration and the right is heat conveyed by the condenser, $\dot{m}_f$ is the hydration rate, ΔH the specific hydration heat which is determined as following:

$$\Delta H = a_2 \cdot R - a_3 \cdot R \cdot T \tag{5}$$

where, R is the gas constant, a_2 and a_3 is the constant coefficient in phase equilibrium equation of Kirchhoffs type as following:

$$\ln p = a_1 + a_2 / T + a_3 \cdot \ln T \tag{6}$$

whereas the hydration rate $\dot{m}_f$ is determined by [9]:

$$\dot{m}_f = C\exp(-\frac{\Delta E}{RT})\exp\left(-\frac{a}{\Delta T_s^{\,b}}\right)p^{\gamma} \tag{7}$$

where ΔE is the activation energy which is related with kind of refrigerant, ΔT_s is the degree of supercooling. It can be easily seen from above that as for one certain refrigerant, hydration rate will increase along with the augmentation of supercooling and pressure. Equation (7) can be simplified as:

$$\dot{m}_f = B \cdot \exp(-\frac{a}{\Delta T_s^{\,b}}) \tag{8}$$

The coefficient B is usually called rate constant which reflects the kinetic property at the interface of refrigerant and water, hanging on variety of factors such as area of interface, rate of mass diffusion, temperature, pressure as well as the kind of medium.

3.3 Temperature Variation During Cool Storage

Fig. 3 shows the temperature variation of two complete cycles of cool storage and release using HCFC-142b as hydration medium. It can be apparently seen that the temperature of gas layer is always lower than that of liquid layer and the difference between them is corresponding to the difference of partial pressure ΔP on the temperature-pressure diagram.

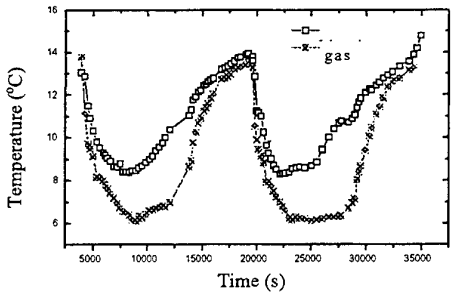


Fig. 3. Temperature variation in cool storage tank

Fig. 3 shows the saturation temperature is continually decreasing during cool storage process along with the

declining of pressure. Therefore it is necessary to lower the temperature of chilled water in order to maintain condensation which killed the hydrate's advantage of higher phase-change temperature. That is to say, too great supercooling is no benefit to cool storage.

It's known from Equation (7) that the hydration rate is in proportion to the power of pressure. Thus refrigerant having higher saturated vapor pressure such as HFC-134a and HFC-152a is more likely to form hydrate, whereas those of which the saturated vapor pressure is relatively low such as HCFC-141b is less active in hydrate forming and needs great supercooling [10]. It is contradictory to the practical use of hydrate cool storage.

The fact that additive can mitigate the pressure drop in hydrate forming process which is shown in fig.2 also help to reduce supercooling. At the other hand, the increase of medium charge seems have such effect due to the enhancement of medium's recycling amount [11]. But the increase of medium charge will result in the expansion of container's volume, there must be an optimal value of the amount of charge which is determined by the mass flow of cycling medium. This problem is not yet mentioned in literature.

3.4 Model of Heat & Mass Transfer During Hydration

Condensation, evaporation and hydration are combined and mutual-influenced process in cool storage container. Condensation is a very classical problem depicted by Nusselt model, whereas evaporation can be theoretically expressed as following [12]:

$$\dot{m}_e = \frac{1}{\sqrt{2\pi \cdot RT}} \Delta p \tag{9}$$

where $\dot{m}_e$ is the theoretical maximum evaporation rate, Δp is the partial pressure difference caused by condensation of vapor.

In order to research the heat and mass transfer during hydration, Y.H. Mori [13] investigated the behavior of one single freon bulb with some evaporating droplet in it rising through water layer and gives the heat balancing equation as:

$$Q_v = Q_c + Q_h \tag{10}$$

where Q_c is the heat transferred from ambient water to the bulb, Q_h is hydration heat gain, whereas Q_v is the heat absorbed by the evaporation of freon droplet, and:

$$Q_c = \pi D^2 \alpha_c (Tc - Td) \tag{11}$$

where D is the diameter of bulb, and α_c is the convection heat transfer coefficient calculated by:

$$Nu = 0.121 (Pe)^{1/2} \tag{12}$$

where, $Nu = \alpha_c D/\lambda_c$, $Pe = UD/K_c$, λ_c,K_c is the thermal conductivity and thermal diffusivity of water, U the velocity of bulb rising which can be estimated to be nearly 0.2m/s.

Hydration heat Q_h can be deduced from above formulas (4) through (7), and Q_v is easily calculated using basic thermodynamic theory.

The key of this model is the calculation of hydration rate $\dot{m}_f$ which boils down to the determination of the rate constant B in Equation (8). As far as the current state-of-the-art of hydrate kinetic is concerned, it is very difficult to quantitatively calculate it. On account of this, the above model is merely a qualitative one.

4. ANALYSIS OF COOL RELEASE PROCESS

Cool release is the process of hydrate decomposition which involving three phases of gas, liquid and solid which

is more complicated than the melting of ice. Attention to hydrate decomposition is originated from the purpose of exploiting large amount of seabed natural gas hydrate. Compared to its forming process, decomposition of gas hydrate is relatively simple. It was pointed out by Kamath *et al* [14]that different kind of gas hydrate comply with the same rule of decomposition as following:

$$\frac{1}{A_h}\frac{dm_d}{dt} = 2.327\times10^{-4}(\Delta T_d)^{2.05} \tag{13}$$

which indicates that the control criterion of decomposition is the temperature difference.

4.1 Pressure Variation During Cool Release

Fig. 4 shows that the regaining of pressure during hydrate decomposition seems to be a near-linear process as differs much from the exponential decay of pressure drop during hydrate forming. Additives have some effect on the slope of the line. Line of pressure variation of pure refrigerant is relatively flat which means that hydrate decomposition rate is low. Adding n-butanol of concentration of 1.34 % to water can effectively accelerate the decomposition process but more addition of n-butanol doesn't bring on evident effect.

Such phenomenon is originated by the drifting of hydrate. When there is no additive in solution, the formed hydrate is very porous and loose in structure and lighter than water. Heat conducted from external environment can reach hydrate only through natural convection of water. Therefore the decomposition of hydrate is evidently stagnated by the water layer. Certain concentration of additives will make the formed hydrate denser and heavier than water. Formed hydrate will deposite to the surface of the condenser and heat can be directly conducted to it. But superfluous additive is of no benefit to hydrate decomposition.

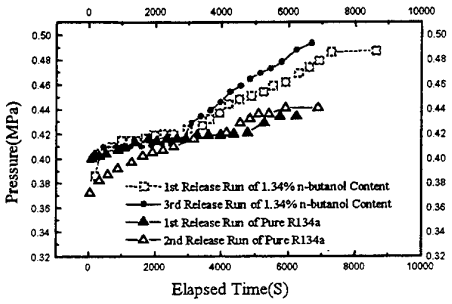


Fig. 4. Pressure variation during cool release

4.2 Temperature Variation During Cool Release

Fig. 5 shows that the temperature of water layer rises rapidly at the beginning of decomposition. This is because that hydrate decomposition rate is so low that it is not adequate to absorb the entering heat which result in the temperature rising of water. There is a temperature platform thereafter near 12.5°C which indicates the balancing of entering heat and the absorbed heat during hydrate decomposition which is a kind of near-isothermal process during this period of time. It is worthwhile to note that near mid-term of the whole process, there is a valley value of water temperature which indicates that the decomposition rate reaches its peak value at this time. The water temperature goes on rising gradually until the end of decomposition thereafter.

The above phenomenon can be explained by the variation of the coefficient of heat transfer diagrammed in Fig.6. It is clearly shown that the coefficient of heat transfer is relatively low at the start of decomposition and increases rapidly along with the decomposition of hydrate. Near mid-term of the process, there is a peak value of the coefficient of heat transfer and thereafter, decreases gradually until end of decomposition as is similar to the variation of water temperature. Although the media used in experiments of Fig. 5 and Fig. 6 are different, the relative peak time of coefficient of heat transfer in Fig. 6 coincide with the relative valley time of water temperature which verifies the above analysis of temperature variation.

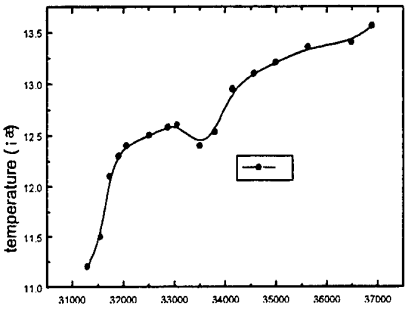


Fig. 5. Temperature variation during cool release (R142b)

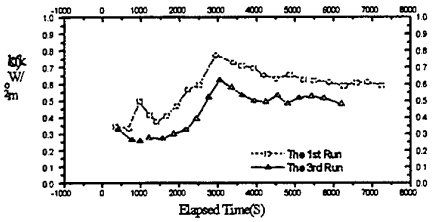


Fig. 6. Variation of coefficent of heat transfer (R134a)

The above variation can be explained from the mechanism of hydrate decomposition which is a conduction-controlled process differing much from hydrate forming. At the start of decomposition, released water accumulate around hydrate forming a film of water which increases heat resistance resulting in a low coefficient of heat transfer. When more and more hydrate becomes decompose, large amount of gas bulb will penetrate the water film and diffuse to the environment bringing on the reinforcement of the disturbance of water film and the increase of convective coefficient of heat transfer. Along with the gradually exhaustion thereafter, the amount of gas bulbs reduces drops off which result in the decrease of the coefficient of heat transfer.

5. CONCLUSIONS

It can be concluded from above analysis that:

1) condensation, evaporation and hydration are mutual-influenced process in which condensation is the most pivotal;
2) some kind of additive can evidently reduce surface tension at the freon-water interface and greatly improve the characterization of formed hydrate;
3) heat and mass transfer during hydrate forming and decomposition boils down to the kinetic of hydrate. Higher pressure will lead to higher hydration rate and coefficient of heat transfer. Under atmospheric pressure, a large degree of supercooling is needed.
4) pressure drop during cool storage is an exponentially decaying process, whereas the regaining of pressure during cool release is a linear increasing process;
5) cool release is a mainly conduction-controlled process. Different kind of hydrate exhibits similar behavior in hydrate decomposition.

From the standpoint of practical use, mediums of atmospheric saturation pressure are more likely to be used for industrialization. Therefore, the reinforcement of heat and mass transfer during hydration of such mediums is a problem needs more investigation in future.

REFERENCES

1. J.J.Tomlinson, Heat pump cool storage in a clathrate of freon, Proc. of 17th IECEC, Los Angeles, Aug. 1982.
2. Y. Yutaka, A. Saito, et al., A method of efficient ice cool energy storage using heat transfer of direct-contact phase change between working medium and PCM in an enclosure, Int.J. of JSME, Series B,Vol.32, No.3, 1989.
3. S.S. Lu., S. P. Wang and S. J. Deng, Experimental study on the characterization of refrigerant hydrate as a cool storage medium, Proc. of the 4th Int. Symp. on Heat Transfer,Beijing,1996.
4. S. S. Lu, Mechanism and application of gas hydrate cool storage, Doctoral dissertation of SCUT, 1997.
5. L. Lu and S.P. Wang, Effect of additives on the cool storage process of R-142b hydrate, J. of SCUT, Mar. 1999 (in Chinese).

6. R.T. Lin, Boiling heat transfer, Science Press, 1988 (in Chinese).
7. E.Dendy Sloan, Clathrate Hydrates of Natural Gases, Marcel Dekker Inc., 1990.
8. Kai-hua Guo, Bi-fen Shu and Yi Zhang, Transient behavior of energy charge and solid-liquid phase Change in mixed gas-hydrate formation, Proc. of the 4th Int. Symp. on Heat Transfer,Beijing,1996.
9. A. Visniauskas and P. R. Bishnoi, A kinetic study of methane hydrate formation, Chem.Eng. Sci., v. 38,1983.
10. Y.Cai, S.P.Wang and S. S.Lu, Experimental research on gas hydrate cool storage of alternative refrigerant R141b, J. of HVAC, May 1997 (in Chinese).
11. Y. Utaka,et al., Gas hydrate cool storage using direct-contact heat transfer of liquid-vapor phase-change and natural circulation of refrigerant in closed vessel, JSME Int. J., Series B, Vol.36, No.1,1993.
12. Q.F.Ma and C.F.Ma, Design manual of heat exchanger, Vol.2, Mechanical Industry Press, 1989 (translated from Germany).
13. Y. H.Mori and F. Isobe F., A model for gas hydrate formation accompanying direct-contact evaporation of refrigerant drops in water, Int. Comm. Heat &Mass Transfer,Vol. 18, 1991.
14. J.H. Qiu and T.M. Guo, Current situation of research on the kinetic of forming and decomposition of gas hydrate, J. of Chem. Eng., Vol.46, No.6, 1995.

DEVELOPMENT OF ICE THERMAL STORAGE TYPE AIR CONDITIONING AND HOT WATER SYSTEM FOR THE HOUSE

Shigeo Aoyama, Kazuhiko Machida, Kazuyuki Hamada
Refrigeration Research Laboratory, Matsushita Refrigeration Company
E-mail: aoyama@mrc.mei.co.jp ; Fax:+81-6-6782-1120

Masao Matsushita
Technical Development Laboratory, National House Industrial Corporation
E-mail: m-matusita@panahome.co.jp ; Fax:+81-6-6834-8983

Masao Kimura
Technical Research Center, The Kansai Electric Power Company
E-mail: K541802@kepco.co.jp ; Fax:+81-6-6494-9827

Keywords: ice thermal storage, air conditioning, hot water storage

ABSTRACT. The present paper has dealt with the examination about the ice thermal storage type air conditioning and hot water system for the house. So far, the achievement of the latent heat storage system such as ice thermal storage system was more difficult for the house than that of the sensible heat storage system because the sensible heat storage tank becomes complicated structure and high cost. However, we have achieved ice thermal storage type air conditioning and hot water system for the house for the first time, by setting small thermal storage tank including new thermal storage capsules and hot water storage tank under floor in the newly built house.

1. INTRODUCTION

Recently, importance of energy conservation has been appealed in the world scale to control CO_2 emissions, one of gases making global warming, for the prevention of global warming. Further, development of thermal energy storage technology using electric power at nighttime attracts big attention socially. The first reason is that using surplus electric power at nighttime effectively can contribute to making the electric power load uniform. The second reason is that the fossil fuels ratio of electric power generation at midnight (from 1:00 a.m. to 6:00 a.m.) is lower than the ratio at daytime (CO_2 emissions is lower about 20-25% in Japan). Especially, ice thermal storage type air conditioning system, which is set the thermal storage tanks, is commercialized for the building and the factory and that system is rapidly popularized for these several years in Japan. From such a background, the authors are now developing the air conditioning and hot water system using thermal energy storage technology for the house. Then, this paper reports the outline of the ice thermal storage type air conditioning and supplying hot water system, now developing, and a part of the result that we examined actual running characteristics of the development system in a general house.

2. OUTLINE OF THE DEVELOPING SYSTEM

2.1 Merit of the Developing System

This system can conserve space and time in constructing in addition to merit of low running cost that the conventional thermal storage system possesses so far. Those merits are enumerated as follows.

1) The system can operate the ice thermal storage mode and the hot water supplying mode at the same time both at daytime and at nighttime.
   The system has the refrigerant cycle control that can achieve using waste heat, produced in the mode of ice thermal storage or cooling, to supply hot water. Especially, The system can achieve not only using waste heat in the ice thermal storage mode at nighttime to supply hot water but also only using waste heat in the cooling mode at daytime to supply hot water.

2) The system can operate the air conditioning mode at the time of the thermal storage mode at nighttime.
   The cycle control of this system can achieve the air conditioning mode at the time of the thermal storage mode at nighttime (23:00-7:00) if necessary, though this system is thermal storage system using the

electric power at nighttime. However, the amount of thermal storage decreases at nighttime.

3) The system can produce hot water of high temperature (max: 85C).
The warm water of about 60-65C is saved in the hot water storage tank by heat pump unit using refrigerant HCFC-22 and when there is the demand of the high temperature hot water, it is possible to heat with a supplementary heater (4kW) afterwards, to burn up to about 85C. Moreover, because a supplementary heater is set up, supplying hot water with a supplementary heater is enabled as emergency treatment when the heat pump unit breaks down.

4) The system can operate the automatic reheating and the manual reheating in daytime.
Whether the warm water of about 55C (correspond to the amount of the hot water of about 2/3 at the hot water setting temperature: 65C) is always kept by " Automatic reheating switch " on the system controller or the warm water of about 55C is kept by " Manual reheating switch " can be selected for corresponding also in case of hot water shortage at daytime.

5) The ice thermal storage tank and the hot water storage tank can be set up in the house below the floor level.
Because the ice thermal storage tank and the hot water storage tank of this system are set up after foundation construction of the newly built house, the space below the floor level that is dead-space so far can be effectively used.

6) Adopting pipes made from plastic can be up the efficiency in the connection between each unit.
Replacing the past copper pipes to the polybutene plastic tube with the heat insulation material becomes some merit. The first merit is that the polybutene plastic has both heat-resistance (the highest use temperature: 90C) and flexibility. The second merit is making construction efficiency up, because there is no need to connect pipes between each unit on the way, and melting and connecting the polybutene joints only in each unit entrance can connect between each unit.

2.2 System Configurations

This system is composed by heat pump unit, tank unit and indoor unit. The heat pump unit is constituted from heat source unit and pump unit and has two functions of air conditioning and supplying hot water. And the system is separated to 3 circuit, heat source circuit, thermal storage and air conditioning circuit, supplying hot water storage circuit as showed Fig.1. In this system cooling and heating is done indirectly, and heat medium inside heat source circuit is refrigerant HCFC-22, heat medium inside the thermal storage and air conditioning circuit is brine (ethylene glycol solution 30wt%) and heat medium inside the hot water storage is water. And heat transfers from HCFC-22 to brine and from HCFC-22 to water through double tube heat exchanger for thermal storage and air conditioning and hot water storage. This system can operate the hot water storage mode at nighttime to store thermal energy to use for supplying hot water at daytime and operate the thermal storage mode at nighttime to store thermal energy to use for air conditioning at daytime. So that this system can shift a part of load at daytime to load at nighttime.

2.3 Heat Pump Unit

The heat pump unit used for this system is composed by the heat source unit (air heat source type heat pump, standard cooling capacity 4.2kW, refrigerant HCFC-22) and the pump unit which provides with the hot water pump, brine pump, switching valves, etc.

First, the heat source unit provides with three heat exchangers. One is heat exchanger between refrigerant and air, adopted fin and tube (called air heat exchanger). One is heat exchanger between refrigerant and brine, adopted double for air conditioning tubes (called brine heat exchanger). The other one is heat exchanger between refrigerant and hot water adopted double tubes with the leakage detection tube for hot water storage (called hot water heat exchanger). Moreover, the heat source unit provides with 4-way reversing valves, 2-way reversing valves, and the temperature type expansion valves to switch the refrigerant circuit to each running mode.

On the other hand, the pump unit on the thermal storage and the air conditioning circuit side provides with the brine pump, the fixed flow quantity valve, and 3-way reversing valve for circulating brine, controlling flow quantity and switching the circuits. And the pump unit on hot water storage circuit side provides with the hot

water pump, the pressure type control valve, the flow control valve, and the supplementary heater (4kW) for circulating water, controlling flow quantity and heating to supplement. In this system, the fixed flowing quantity valve keeps constant flow quantity of brine to thermal storage tank in the thermal storage mode at nighttime using thermal storage and air conditioning circuit, not concerned with presence of air conditioning demand in indoor unit. And the pressure type control water valve mechanically controls flow quantity of water into heat exchanger between refrigerant and hot water by detecting condensing pressure in heat source unit to get hot water of about 60-65C.

2.4 Tank Unit

There are two types of tank, the tank for thermal storage and the tank for the hot water storage. They are both made from polybutene plastic and the content product is 380 liters per one. And they can be put the side on the foundation below the floor level of the newly built house, so the space below the floor level that is dead-space so far can be effectively used. About 7,000 thermal storage capsules, made from polyethylene of 40mm in the diameter, are enclosed in a thermal storage tank. Both water as thermal storage material and sub-cooling prevention material are enclosed internally in the thermal storage capsules.

In the ice thermal storage mode between the nights of summer, the low temperature brine obtained with the heat source unit is transported to the thermal storage tank. And the low temperature brine flows in the space surround the thermal storage capsules enclosed in the ice thermal storage tank and absorbs heat from water in the thermal storage capsules, so water is cooled. Finally, thermal energy of 85,500kJ for one in the thermal storage tank is saved by running the ice thermal storage mode until Ice Packing Factor (volume ratio of amount of ice in the thermal storage tank to the tank content product) becomes about 60 vol%. On the other hand, in the ice thermal storage mode between the nights of winter, the high temperature brine obtained with the heat source unit is transported to the thermal storage tank. Finally, thermal energy of 19,100kJ for one in the thermal storage tank is stored by running the thermal storage mode until temperature of brine in the thermal storage tank outlet becomes about 52C.

Moreover, to evade the mixture phenomenon of the temperature stratification in the hot water storage tank setting horizontally, exactly to control the thickness of the mixture layer the header for attenuating water velocity is set up at the water supply entrance to the hot water storage tank.

2.5 Indoor Unit

As the indoor unit, fan coil unit is adopted and 2 way reversing valve (ON-OFF control) is set up in each fan coil unit for the plural installation. The type of fan coil unit includes the ceiling built-in type for Japanese-style room and the floor putting type.

3. CYCLE CONTROL SPECIFICATION OF THE DEVELOPING SYSTEM

3.1 Running Mode

This system can operate the hot water storage mode at nighttime to store thermal energy to use for supplying hot water at daytime and operate the thermal storage mode at nighttime to store thermal energy to use for air conditioning at daytime. So this system has some running modes for the combination of the following items.

Running time zone ... nighttime (23:00-6:59) , daytime (7:00-22:59)
Running mode ... 1) Ice thermal storage & hot water storage mode
2) Ice thermal storage mode, 3) Cooling mode
4) Thermal Storage & hot water storage mode
5) Thermal Storage mode, 6) Heating mode, 7) Hot water storage mode

3.2 Control Specification

The outline of control specification of the system showed is shown below with cycle chart of each running mode.

1) Ice thermal storage & hot water storage mode at nighttime (Fig. 1)
In heat pump unit, hot water heat exchanger works as condenser and brine heat exchanger works as evaporator. Then brine cooled by brine heat exchanger is circulated by brine pump and water inside thermal storage capsules in thermal storage tank is frozen to ice by the cold brine to store ice thermal energy.

On the other hand, hot water (max: 65C) heated by hot water heat exchanger using waste heat is circulated by hot water pump and stored to hot water storage tank. (This running mode is completed at return temperature from the hot water storage tank S2 ≥ 40C)

2) Ice thermal storage mode at nighttime (Fig. 2)
In heat pump unit, air heat exchanger works as condenser and brine heat exchanger works as evaporator. Then brine cooled by brine heat exchanger is circulated by brine pump and the cold brine freezes water inside thermal storage capsules in thermal storage tank to store ice thermal energy. (This running mode is completed at return temperature from the thermal storage tank S1 ≤ -6C)

3) Cooling mode at daytime
*Cooling mode A at daytime (Fig. 3)
First, if there is certain thermal energy in thermal storage tank (return temperature from the thermal storage tank S1<7C), heat pump unit is not run and brine is circulated by brine pump to transport the cold brine in thermal storage tank to indoor units for cooling. (This running mode is completed at return temperature from the thermal storage tank S1 ≥ 7C)
*Cooling mode B at daytime (Fig. 4)
After that, if there is uncertain thermal energy in thermal storage tank (return temperature from the thermal storage tank S1 ≥ 7C), heat pump unit starts to run and brine cooled by brine heat exchanger is circulated by brine pump to transport the cooled brine to indoor units for cooling.
In heat pump unit, hot water heat exchanger works as condenser and brine heat exchanger works as evaporator. So the system can recover waste heat, namely the system can achieve using waste heat in the cooling mode at daytime to store hot water in hot water storage tank and can run the cooling mode in indoor units simultaneously.

4) Thermal storage & hot water storage mode at nighttime (Fig.5)
In heat pump unit, brine heat exchanger works as condenser and air heat exchanger works as evaporator. Then brine heated by brine heat exchanger is circulated by brine pump and the hot brine heats water inside thermal storage capsules in thermal storage tank to store thermal energy.
On the other hand, hot water (max: 85C) heated by a supplementary heater is circulated by hot water pump and stored to hot water storage tank. (This running mode is completed at return temperature from the hot water storage tank S2 ≥ 65C)

5) Thermal storage mode at nighttime (Fig. 5)
In heat pump unit, brine heat exchanger works as condenser and air heat exchanger works as evaporator. Then brine heated by brine heat exchanger is circulated by brine pump and the hot brine heats water inside thermal storage capsules in thermal storage tank to store thermal energy. (This running mode is completed at return temperature from the thermal storage tank S1 ≥ 52C)

6) Heating mode at daytime
*Heating mode A at daytime (Fig. 3)
First, if there is certain thermal energy in thermal storage tank (return temperature from the thermal storage tank S1>40C), heat pump unit is not run and brine is circulated by brine pump to transport the hot brine in thermal storage tank to indoor units for heating. (This running mode is completed at return temperature from the thermal storage tank S1 ≤ 40C)
*Heating mode B at daytime (Fig. 6)
After that, if there is uncertain thermal energy in thermal storage tank (return temperature from the thermal storage tank S1 ≤ 40C), heat pump unit starts to run and brine heated by brine heat exchanger is circulated by brine pump to transport the hot brine to indoor units for heating.

7) Hot water storage mode
* Hot water storage mode A at nighttime (Fig. 7)
In heat pump unit, hot water heat exchanger works as condenser and air heat exchanger works as evaporator. Then hot water heated by brine heat exchanger is circulated by hot water pump and hot water is poured into top of the hot water storage tank. And heat pump unit is run until return temperature from the hot water storage tank S2 becomes over 40C.

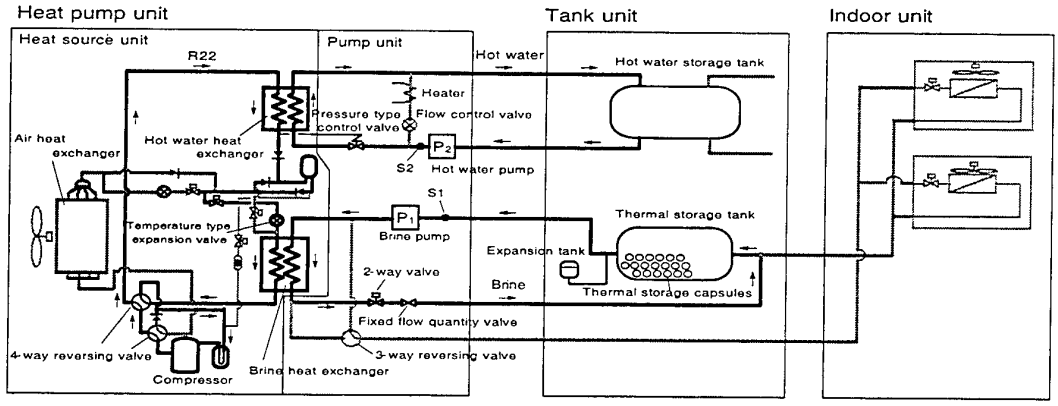


Fig.1. Chart of cycle of the ice thermal storage & hot water storage mode at nighttime

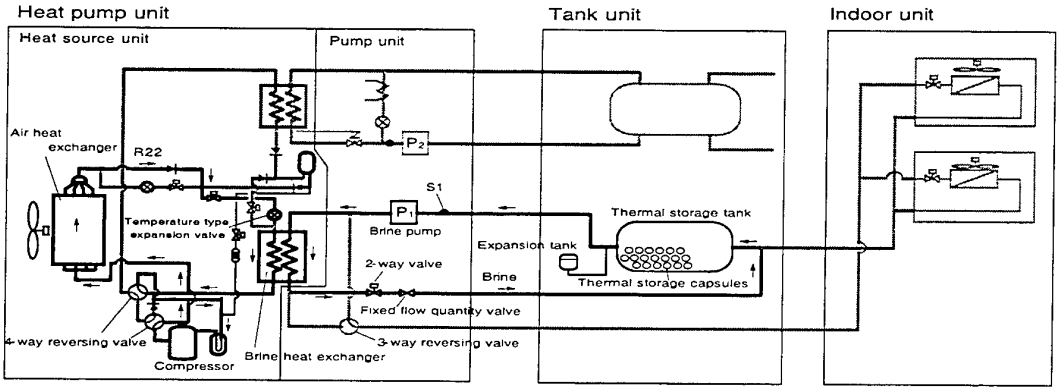


Fig.2. Chart of cycle of the ice thermal storage mode at nighttime

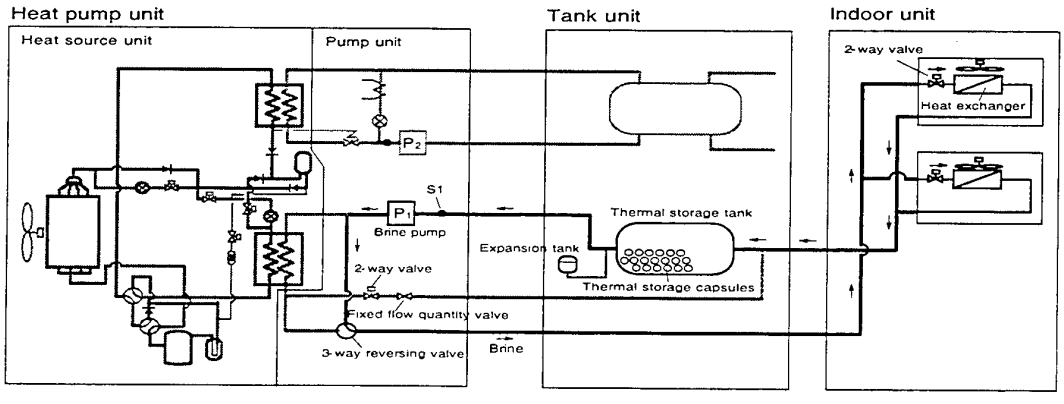


Fig.3. Chart of cycle of the cooling mode A at daytime and the heating mode A at daytime

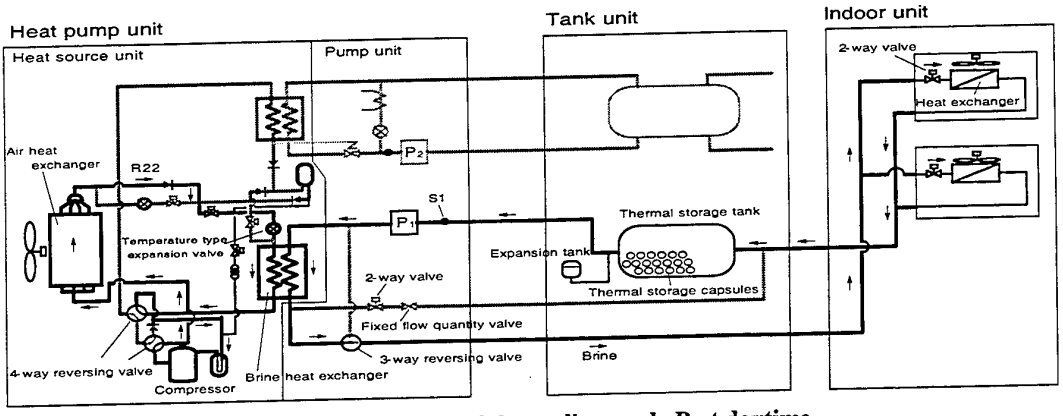


Fig.4. Chart of cycle of the cooling mode B at daytime

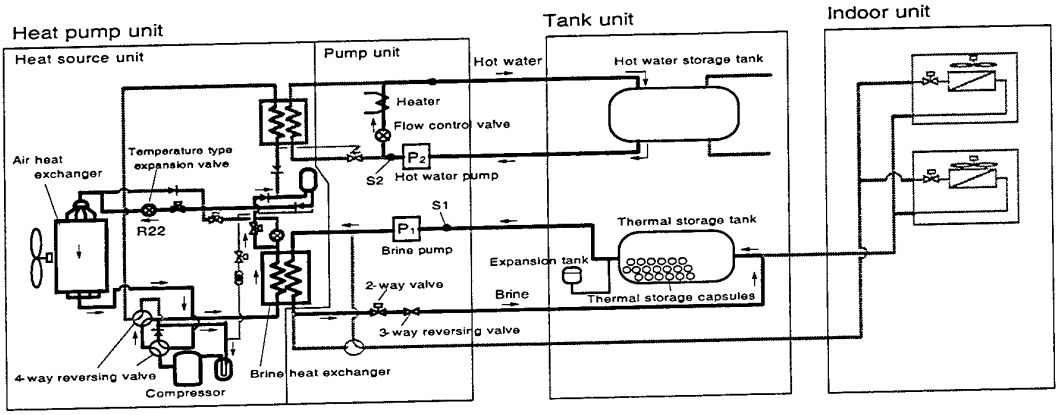


Fig.5. Chart of cycle of the thermal storage & hot water storage mode at nighttime

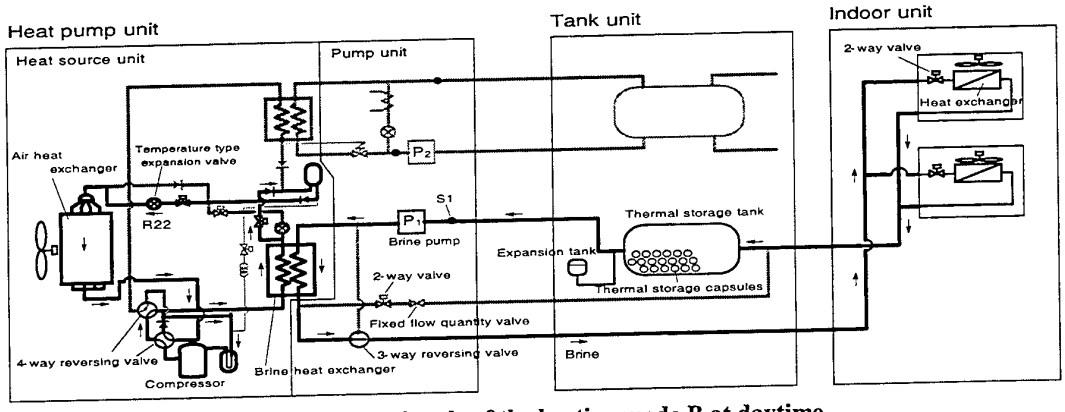


Fig.6. Chart of cycle of the heating mode B at daytime

* Hot water storage mode B at nighttime (hot water storage cycle of Fig.5)
If setting temperature of supplying hot water is equal to 85C, after heat pump unit stops running, using a supplementary heater creates hot water of about 85C and the hot water is stored to hot water storage tank, then this running mode is completed at return temperature from the hot water storage tank S2 ≥ 65C.

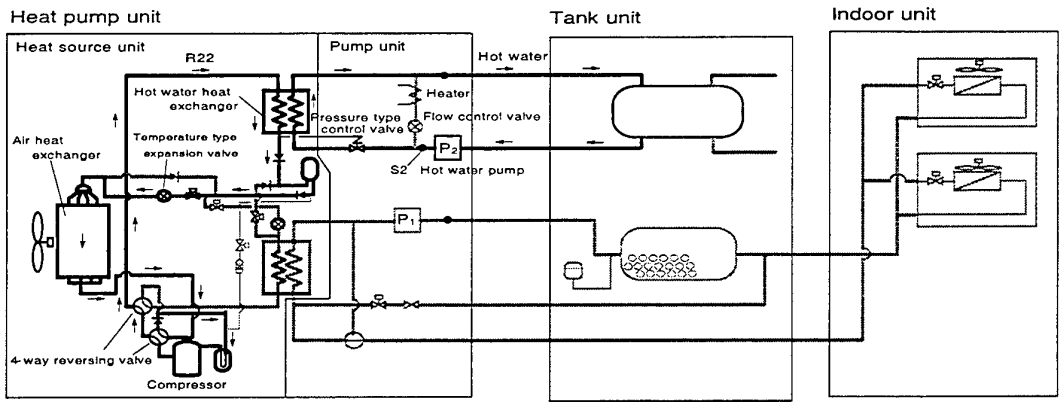


Fig.7. Chart of cycle of the hot water storage mode A at nighttime

4. RUNNING CHARACTERISTIC OF THE DEVELOPING SYSTEM

4.1 Characteristic of the Heating and Supplying Hot Water Mode

The authors set up this developing system in a general house at the end of 1998 and have run the system in winter (Shiga Pref. in Japan on February 23, 1999). Fig.8-10 shows one example of the result of operating the system in a general house.

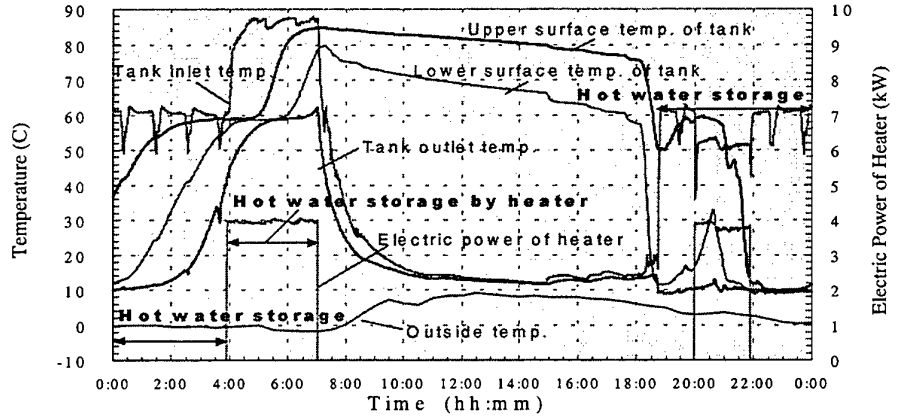


Fig.8. Time history of temperature and electric power consumption related to hot water storage cycle

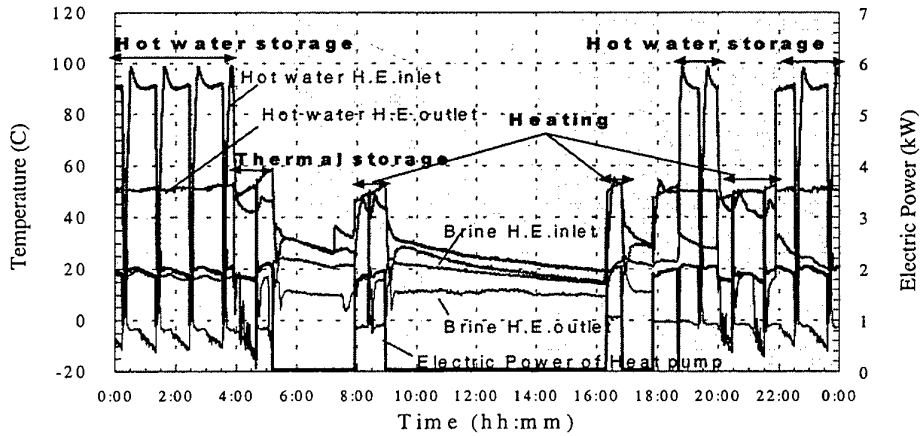


Fig.9. Time history of temperature and electric power consumption related to heat pump cycle

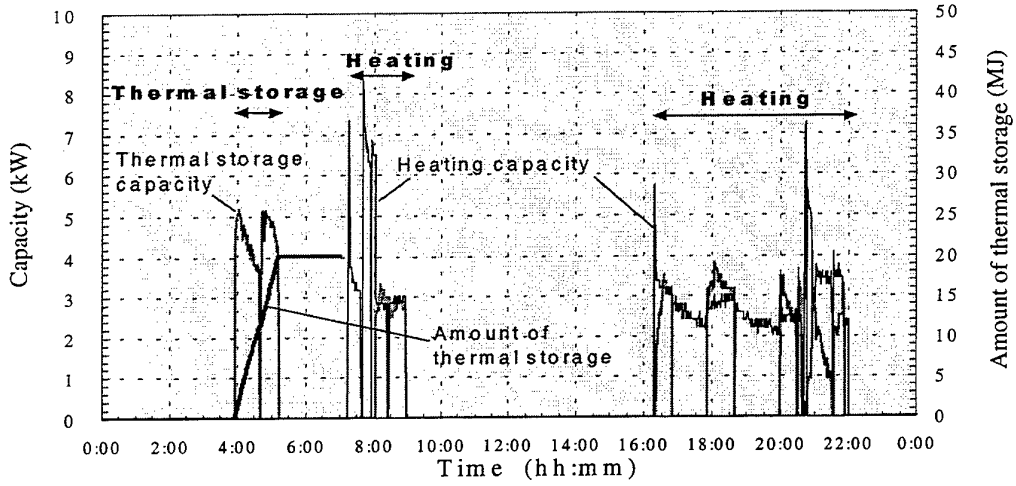


Fig.10. Time history of capacity and thermal storage quantity

In addition, the average of electric power consumption and the amount of electric power consumption at nighttime and daytime in winter (from February to March, 1999) are shown in Table 1 as the result of arranging each unit of the system.

Table 1. Results of amount of electric power consumption of heating and supplying hot water in winter (1999/2-3)

	Nighttime	Daytime	Sum. of day
Heat pump unit	6.93 (kWh)	10.14 (kWh)	17.07 (kWh)
	16.4%	24.0%	40.5%
Heater for supplying hot water	16.38 (kWh)	4.62 (kWh)	21.00 (kWh)
	38.8%	11.0%	49.8%
Pump unit	0.68 (kWh)	1.92 (kWh)	2.60 (kWh)
	1.6%	4.5%	6.2%
Indoor uint	0.08 (kWh)	1.43 (kWh)	1.51 (kWh)
	0.2%	3.4%	3.6%
Total of the system	24.07 (kWh)	18.11 (kWh)	42.18 (kWh)
	57.1%	**42.9%**	100.0%

The following were clarified from these.

1) The amount of electric power consumption at nighttime was 24.1 kWh/day, amount of electric power consumption at daytime was 18.1 kWh/day in the average of this period. Then load shifting ratio from daytime to nighttime becomes about 57%, so that we can say that the developing system is effective to make the electric power load uniform though operating period of the system is heating period in winter.

2) Because there is no problem on thermal environment of indoor in running heating, we think that the developing system obtains the prospect in heating capacity and indoor amenity.

3) The amount of electric power consumption of the heater for supplying hot water occupied by about 50% of the whole and it proved to be over the amount of electric power consumption of heat pump unit. It is a factor that reheating time of supplying hot water became long, because the number of the family became seven persons more than four persons of standard set number, then the amount of supplying hot water increased.

4) The supplementary heating function using an electric heater enables to supply the hot water of high temperature. However, the amount of electric power consumption increases because the time of using the electric heater becomes long when the amount of supplying hot water increases. Therefore, it was clarified that the use condition (region and number of persons of the family, etc.) for this system to improve merit exist.

5. CONCLUSION

This paper reported the outline of the ice thermal storage type air conditioning and supplying hot water system using thermal energy storage technology for the house, now developing, and a part of the result that we examined actual running characteristics of the development system in a general house. Though there are some problems in the practical use of the ice thermal storage system which has the function of air conditioning for the house and supplying hot water, we think that this system has the possibility of practical use from the heating examination result at this time.

FLOW AND HEAT TRANSFER OF ICE WATER SLURRY IN A STRAIGHT PIPE

Hideo Inaba, Akihiko Horibe, and Naoto Haruki
The graduate School of Natural Science and Technology, Okayama University
Email: inaba@mech.okayama-u.ac.jp; Fax: (086)-251-8266

Maki Yokota and Shigeo Aoyama
Matsushita Refrigeration CO.LTD

Keywords: ice water slurry, melting heat transfer, heat exchanger, ice thermal energy storage system

ABSTRACT. This paper has dealt with melting heat transfer characteristics of ice water slurry in an inside tube of horizontal double tube heat exchanger in which hot water circulated in an annular gap between the inside and outside tubes. In this study, two kinds of heat exchangers were used; one is made of acrylic resin tube for flow visualization and the other is made of stainless steel tube for melting heat transfer measurement. The result of flow visualization revealed that ice particles flowed along the top of inside tube in the ranges of small ice packing factor and small ice water slurry velocity, while ice particles diffused into the whole of tube and flowed like a plug built up by ice particles for large ice packing factor and high velocity. Moreover, it was found that the flowing ice plug was separated into numbers of small ice clusters by melting phenomenon. Experiments of melting heat transfer were carried out under some parameters of ice packing factor, ice water slurry velocity and hot water temperature. Consequently, the correlation equation of melting heat transfer was derived as a function of those experimental parameters.

1. INTRODUCTION

Recently, a thermal energy storage systems for air conditioning has been developed actively for the purpose of saving energy and reducing the peak electrical demand in the daytime during summer. In particular, a great deal of attention has been paid to the ice thermal energy storage system since it would be beneficial to be able to utilize the large latent heat of melting ice. A number of investigations of ice thermal energy storage systems [1] have been carried out, such as static ice storage system in which ice is formed on the cooling coil surface in a thermal energy storage vessel using excess electric power supply during the night time, and the storaged ice is utilized for air conditioning load during the day time. In this common ice thermal storage system, a cooled water is used as a transportation medium of cold thermal energy from the thermal storage vessel to heat exchanger of air conditioner. However, the freezing heat-transfer performance decreases as time elapses, because the ice layer developed on the cooling coil results in an increase in thermal resistance for ice formation. As a solution to this problem, a thermal energy storage/transport system with ice water slurry has been considered [2-4]. This system has some merits, in which the heat transfer performance is more efficient, and the transported thermal energy with latent heat from the heat storage vessel to the heat exchanger is larger than that of the common chilled water transport system. It is required to clarify fundamental heat transfer mechanism of ice water slurry under various conditions, for advanced thermal energy storage system in a district air cooling.

The objective of the present study is to investigate the heat transfer characteristics of flowing ice water slurry in a straight pipe, and thus to provide fundamental information for the new ice thermal energy storage system.

2. EXPERIMENTAL APPARATUS AND PROCEDURE

The schematic diagram of experimental apparatus is shown in Fig.1. The apparatus fundamentally consists of a test section, an ice water slurry tank, a hot water circulating loop, and associated measuring instruments. The test section is a horizontal double tube heat exchanger of 2,000 mm in length with an entrance section of 800 mm in length. Ice water slurry flows in an inside tube of the heat exchanger and hot water circulates in an annular gap between the inside and outside tubes. In this study, two kinds of heat exchangers are used; one is made of acrylic resin tube (inner diameter of inside tube: d_i=14 mm, inside tube thickness: t_i=2.0 mm, inner diameter of outside tube: d_o = 37 mm, outside tube thickness : t_o=3.0 mm) for flow visualization and the other is made of stainless steel tube (d_i=14 mm, t_i=1.65 mm, d_o = 37.1 mm, t_o=2.8 mm) for melting heat transfer measurement. The ice water slurry tank, which is covered with insulation material, is 500 mm in height and 500 X 500 mm in cross section with stainless steel plate of 2 mm in thickness. An agitator is set in the ice water

slurry tank to mix water and ice particles for getting prescribed ice water slurry which has uniform ice packing factor in the test section inlet.

In this study, ice packing factor (IPF = volume of ice / volume of ice water slurry) of ice water slurry is very important factor, so an IPF controller and an IPF measuring device are used. IPF controller, which is a double tube, is shown in Fig.2. Water flows out from ice water slurry in the inside tube of the IPF controller through small holes of 1 mm in diameter to an annular gap between the inside and outside tubes. IPF of ice water slurry in the inside tube is controlled with water out valve.

For measuring IPF of ice water slurry, the electric conductivity method is chosen in this experiment. It is a method using a principle that the electric conductivity of mixture depends on the packing rate of the components of the mixture. The electrical conductivity of ice (σ_i=10^{-7}~10^{-8} S/m) shows great difference from that of water (tap water, σ_w=5 X 10^{-3}~1.2 X 10^{-2} S/m) , therefore IPF can be accurately measured using this method. Figure 3 shows the detail of the IPF measuring device. It consists of an electrode for ice water slurry, an electrode for water, an electric power supply, and measuring instruments. The electrode for water is used to correct the difference of the electric conductivity of water itself. Considering the balance between the resistance rate of the ice water slurry and that of water, the theoretical IPF is obtained by solving

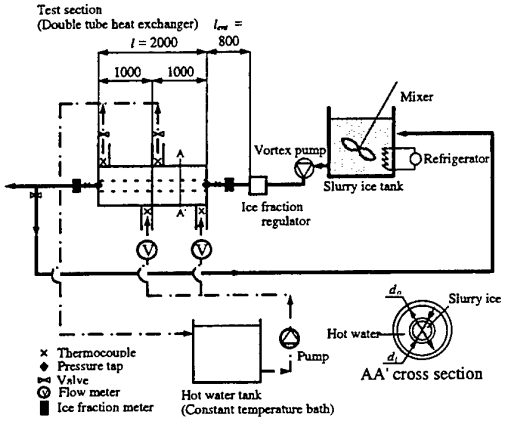


Fig. 1. Schematic diagram of experimental setup the following Maxwell's equation [5].

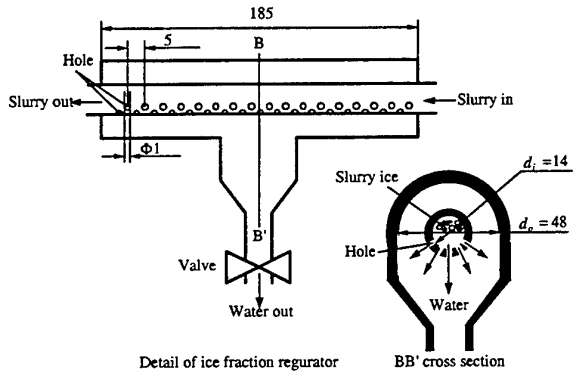


Fig. 2. Detail of IPF controller

$$IPF = \{ [(\gamma_{mix}/\gamma_w) -1] / [(\gamma_{mix}/\gamma_w) + 0.5] \} \times 100 \quad (1)$$

Where γ_w is resistance rate of water which is reciprocal of electrical conductivity σ_w, γ_{mix} is that of ice water slurry. However, the Maxwell's equation is the theoretical one based on that ice particle is spherical, so the relationship between γ_{mix}/γ_w and IPF is determined as shown in Fig.4. As a result, the following equation is used to determine IPF of the ice water slurry in this experiment.

$$IPF = \{ A + B\times [(\gamma_{mix}/\gamma_w) - 1] / [(\gamma_{mix}/\gamma_w) + 0.5] \} \times 100 \quad (2)$$
$$A= - 0.0016, B=1.1$$

The velocity of ice water slurry in the test section is controlled by a vortex pump with an inverter. Thermocouples (C.A.: 0.1 mm O.D.) are set in the test section to measure both the inlet and outlet temperature of the ice water slurry and the hot water. Mean diameter of ice particles, which are made by rotary ice slicer in this experiment, is 1.20 mm. Figure 5 shows the distribution of ice particle diameter.

The experiments are performed using the following procedure. Ice particles are mixed with water in the ice water slurry tank. After controlled IPF and velocity of ice water slurry, it is passed through the test section and heated by hot water. The amount of melting heat transferred from hot water to ice water slurry is calculated with the difference between the inlet and outlet temperature of hot water. In addition, the behavior of the ice particles passed through the test section is recorded by a video camera using the test section for flow visualization.

For the present experiment, the ice water slurry velocity, u_i, ranged from 0.15 to 0.6 m/s, the IPF of ice water slurry at the test section inlet, IPF_{in}, between 0 and 15%, the hot water temperature, T_{hin}, between 20 and 30 °C, and the hot water velocity, u_h=0.35 m/s.

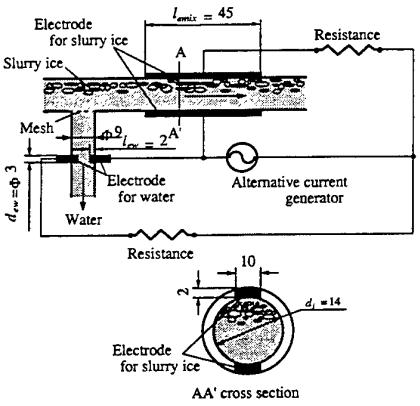


Fig. 3. Detail of IPF measuring device

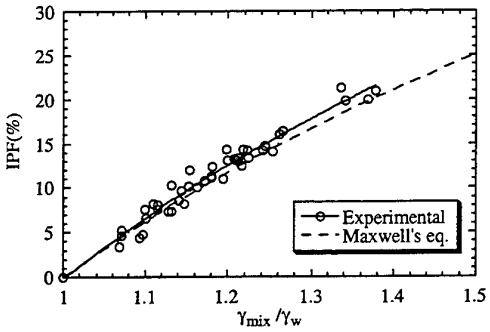


Fig. 4. Relationship between γ_{mix}/γ_w and IPF

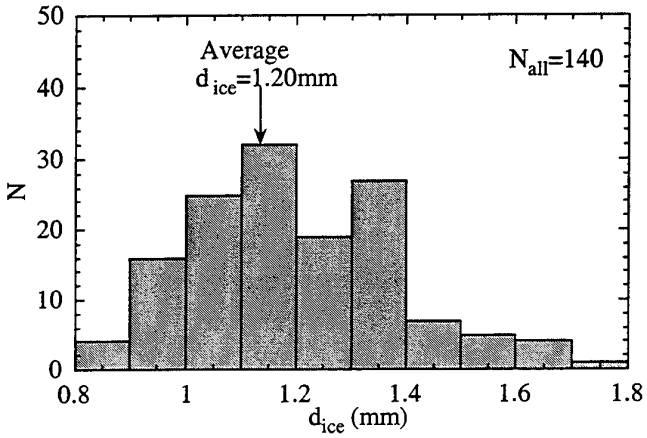


Fig. 5. Diameter of ice particle

3. RESULTS AND DISCUSSIONS

Flow and Melting Characteristics of Ice Particles

To investigate transport characteristics of the ice water slurry, it is particular interest to determine distribution of the ice particles in the pipe. Figure 6 presents typical flow pattern of the ice particles in the pipe for ice water slurry velocity u_i = 0.2 m/s. In the case of IPF = 5 %, the ice particles flow almost perfectly in the upper part of the pipe along the inner surface (floating ice flow) because of its buoyancy. As IPF increases, it is observed that ice particles diffuse into the whole of the pipe and flow like a plug built up by ice particles. In this experiment, for u_i = 0.15~0.6 m/s, approximately the same phenomenon is observed as compared with that for u_i = 0.2 m/s.

Figure 7 shows the melting characteristics of ice particles in the pipe under condition that IPF in the pipe inlet :IPF_{in} = 5 %, velocity of ice water slurry: u_i = 0.2 m/s, hot water temperature, T_{hin} = 20 °C. As shown in Fig.7, the flowing ice layer becomes thin and it is separated into numbers of small ice clusters by melting phenomenon. In addition, it is observed that the small clusters tend to rotate along the inner surface of the pipe as shown in Fig.7(d). The reasons for these phenomena may be considered that a drag force, which is based on the difference of the ice water slurry velocity distribution in the pipe, acts on the ice clusters.

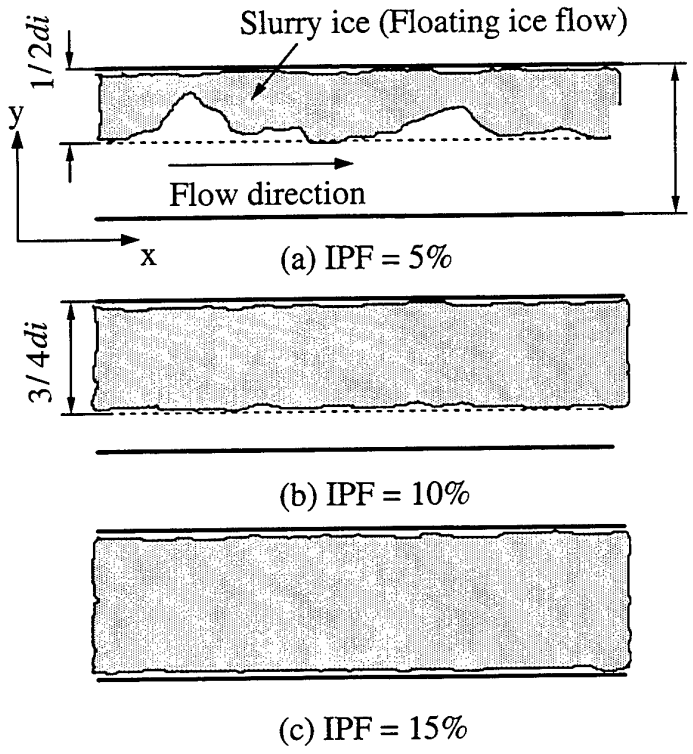


Fig. 6. Flow pattern of ice particles

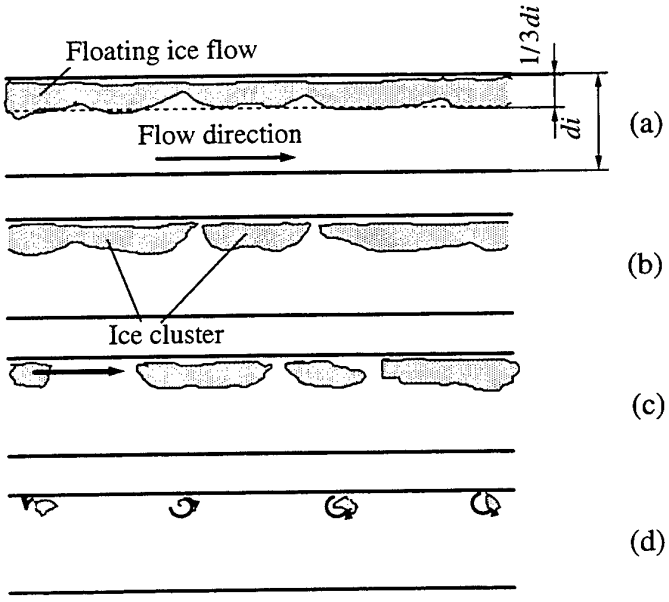


Fig. 7. Melting characteristics of ice water slurry

Effects of Ice Water Slurry Velocity on Exchanged Heat and Overall Heat Transfer Coefficients

Figure 8 presents the effects of ice water slurry velocity, u_i , on exchanged heat between ice water slurry and hot water, Q. The ordinate also denotes IPF of ice water slurry in the pipe outlet, IPF_{out}. In addition, Figure 9 shows relationship between overall heat transfer coefficients, K, and ice water slurry velocity,u_i. The overall heat transfer coefficients, K, is defined in the following equations.

$$K = Q / L\Delta \tag{3}$$

$$\Delta T = (\Delta T_{in} - \Delta T_{out}) / \ln(\Delta T_{in}/\Delta T_{out}) \tag{4}$$

$$\Delta T_{in} = T_{hin} - \tag{5}$$

$$\Delta T_{out} = T_{hin} - T_{iout} \tag{6}$$

where L: length of pipe, T_{hin}: temperature of hot water at inlet, T_{iin} and T_{iout}: temperature of ice water slurry at inlet and outlet. As shown in figures, Q and K increase with increasing in ice water slurry velocity, u_i. For small ice water slurry velocity (u_i <0.3 m/s), Q and K of ice water slurry show larger values than that of water (IPF_{in}=0%). This fact is explained by considering that turbulence in the thermal boundary layer due to ice particles and latent heat of ice melting effect heat transfer coefficients between the pipe and ice slurry water. On the other hand, for large ice water slurry velocity, the thermal boundary layer becomes thin. In addition, the heat transfer due to forced convection increases with increasing in velocity, therefore the effects of melting heat transfer decreases relatively. As a result, Q and K at IPF_{in} =5~10 % become almost same values of that water.

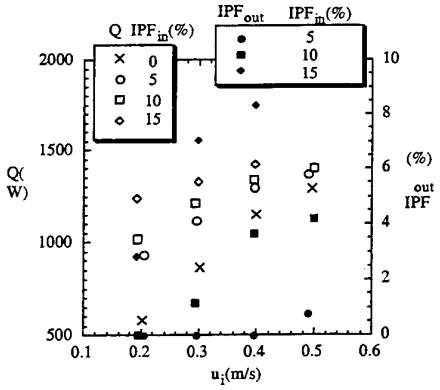


Fig. 8. Relationship between Q, IPF_{out} and u_I(T_{hin}=20°C)

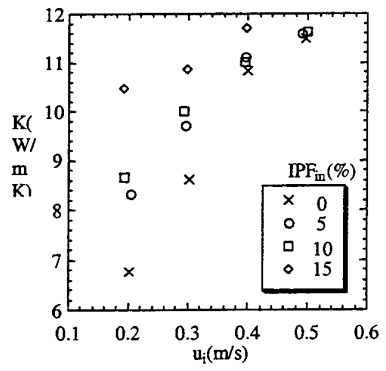
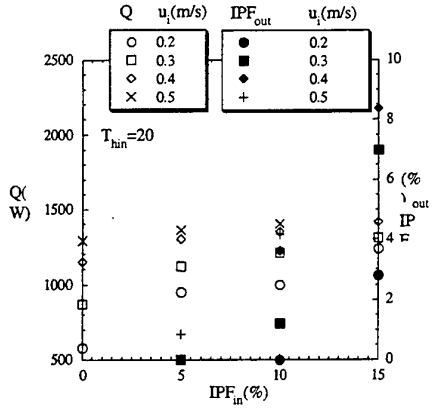


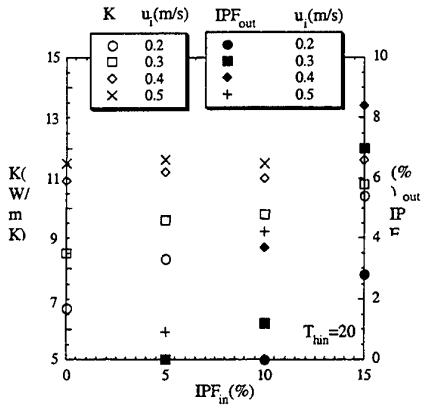
Fig. 9. Relationship between K and u_I (T_{hin}=20°C)

Effects of IPF on Exchanged Heat and Overall Heat Transfer Coefficients

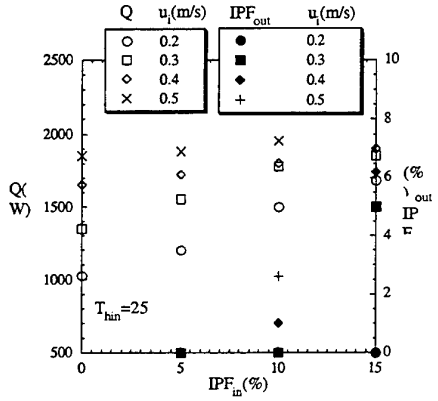
Figure 10 shows the relationship between exchanged heat, Q, IPF of ice water slurry at outlet of the pipe, IPF_{out}, and IPF of ice water slurry at inlet of the pipe, IPF_{in} for hot water temperature T_{hin} = 20, 25, 30 °C, respectively. Figure 11 represents overall heat transfer coefficient, K. It is seen in the figures, Q, and K increase with an increase in IPF_{in}. However the increasing rate of Q, and K are not same for each T_{hin}. In the case of T_{hin} = 20 °C , the increasing rate increases with increasing in IPF_{in}. This fact is explained by considering that the contact area between ice particles (ice cluster) and inner surface of the pipe increases in an increase in IPF_{in} as shown in Fig.6. The increasing rate for T_{hin} = 25 and 30 °C is smaller than that for T_{hin} = 20 °C at IPF_{in}=10~15 %. On the other hand, in the case of IPF_{in}=0~5 %, it increases with increasing in T_{hin}. These phenomena can be explained by the fact as follows. As hot water temperature rises, melting of ice particles becomes fast and contact area between ice particles and inner surface of the pipe decreases. Therefore, the tendency of increasing rate shows mentioned above at IPF_{in} =10~15 %. In the case of IPF_{in}=0~5 %, ice particles melt perfectly in the pipe for T_{hin} = 20~30 °C as shown in the figures, so the effects of ice particles become small. Q increases with increasing in the difference between hot water temperature and ice water slurry temperature, which depends on hot water temperature, T_{hin}.



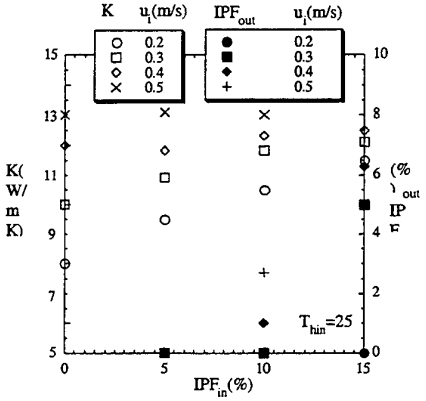
(a) T_{hin} = 20 °C



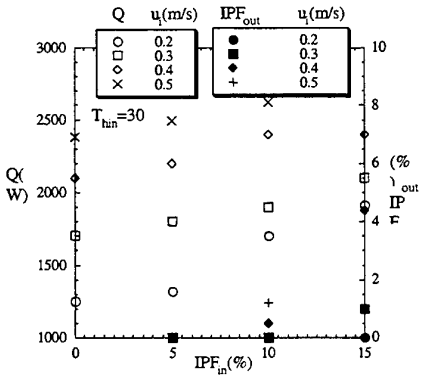
(a) T_{hin} = 20 °C



(b) T_{hin} = 25 °C

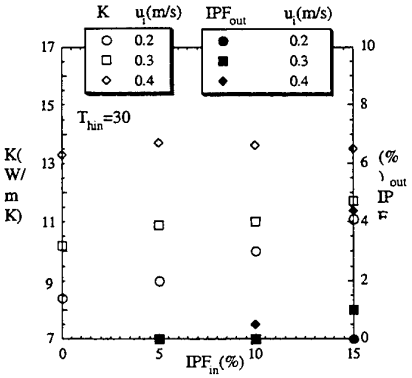


(b) T_{hin} = 25 °C



(c) T_{hin} = 30 °C

Fig. 10. Relationship between Q, IPF_{out} and IPF_{in}

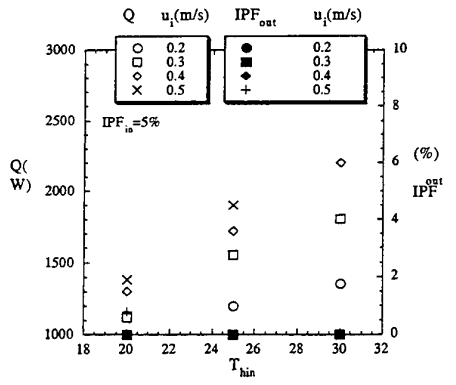


(c) T_{hin} = 30 °C

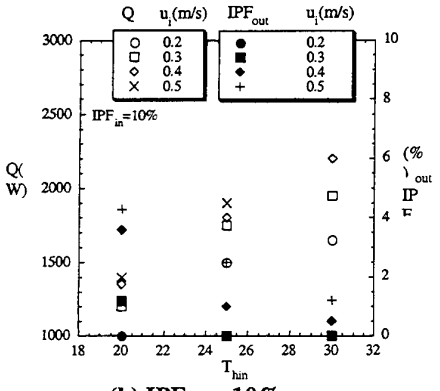
Fig. 11. Relationship between K, IPF_{out} and IPF_{in}

Effects of Hot Water Temperature on Exchanged Heat and Overall Heat Transfer Coefficients

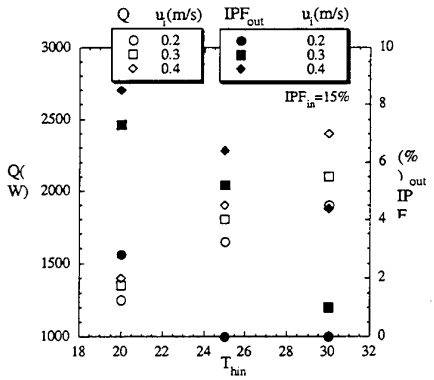
Figures 12 and 13 show the effects of hot water temperature, T_{hin}, for IPF of ice water slurry at inlet, IPF_{in} = 5, 10, 15 %, respectively. Q, and K increase with an increase in T_{hin} as shown in the figures. The tendency of that varies according to ice water slurry velocity, u_i. For small velocity (u_i < 0.3m/s) , the increasing rate of Q decreases with an increase in hot water temperature , T_{hin}. In the case of small velocity, ice particles tend to melt in the pipe. As hot water temperature rises, the distance from the pipe inlet to the point, where ice particles melt



(a) IPF_{in} = 5%

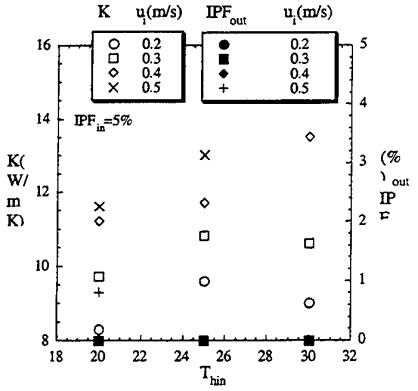


(b) IPF_{hin} = 10%

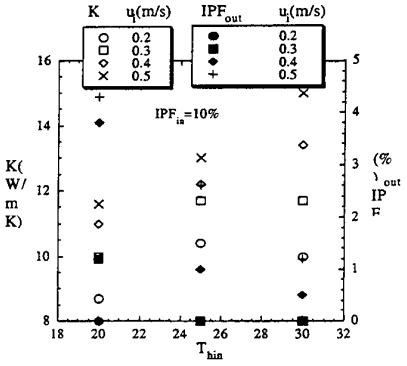


(c) IPF_{hin} = 15%

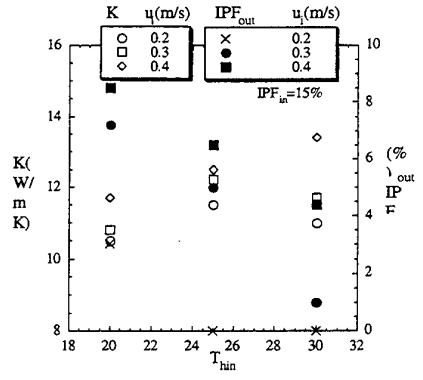
Fig. 12. Relationship between Q, IPF_{out} and T_{hin}



(a) IPF_{in} = 5%



(b) IPF_{hin} = 10%



(c) IPF_{hin} = 15%

Fig. 13. Relationship between K, IPF_{out} and T_{hin}

perfectly in the pipe, decreases. After the point, there is no effect of ice particles on heat transfer and the increasing rate of Q decreases. On the other hand, for large ice water slurry velocity, the increasing rate of Q shows almost constant value because of that is roughly the same as the tendency of water as shown in Figs. 8 and 9.

Non-Dimensional Correlation for Overall Heat Transfer Coefficients

By correlating overall heat transfer coefficients using some non-dimensional parameters, which are obtained with the experimental results mentioned above, the Nusselt number Nu* is expressed by the following equation within the deviation of ±8.1% as shown in Fig.14.

$$Nu^* = 1.91\times Re^{0.33} IPF_{in}^{0.085} Ste^{0.34} \quad (7)$$

$$[Re = 1.2\times10^3 \sim 4.7\times10^3,\ IPF_{in} = 5\sim15\%,\ Ste = 0.25\sim0.38]$$

where $Nu^* = K/\lambda_w$, (λ_w : thermal conductivity of water) , Re is the Reynolds number : $Re = u_i d_i/\nu_w$, (ν_w: kinematic viscosity of water), Ste is Stefan number: $Ste = Cp_w(T_h - T_i) / L_i$, ($Cp_w$: specific heat of water, $T_h=(T_{hin}+T_{hout})/2$, $T_i=(T_{iin}+T_{iout})/2$, L_i is latent heat of freezing).

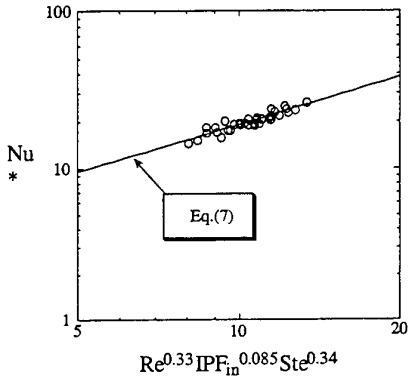


Fig. 14. Correlation of Nusselt number Nu*

4. CONCLUSIONS

Experiments have been carried out to investigate melting characteristics of ice water slurry in the pipe. The following conclusions may be drawn within the range of parameters covered in the present study. (1) The flow pattern of ice particles in a pipe varies depending on IPF_{in} within the ranged from u_i=0.15 to 0.6 m/s. The flowing ice layer becomes thin and it is separated into numbers of small ice clusters by melting phenomenon. (2) For small ice water slurry velocity (u_i <0.3 m/s), exchanged heat, Q, shows larger values than that of water, while for u_i >0.4 m/s and IPF_{in}<10%, Q is almost same as that of water. (3) The increasing rate of Q for T_{hin} = 25 and 30°C is smaller than that for T_{hin} = 20°C at IPF_{in}=10~15%. On the other hand, in the case of IPF_{in}=0~5%, it increases with increasing in T_{hin}. (4) Useful non-dimensional correlation for overall heat transfer coefficient is derived in terms of various non-dimensional parameters.

REFERENCES

1. T. Ibamoto, Refrigeration, 62, p. 1 (1987).
2. H. Inaba, Refrigeration, 71, p. 10 (1996).
3. T. Hamaoka, 9th Lecture series of Multiphase Flow, 9, p. 27 (1997).
4. T. Kitahara, et al., Settuhyou, 4, p. 259 (1990).
5. J.C. Maxwell, Atreatise on electricity and magnetism, 1, Do ver Publication Inc., p. 440 (1956).

EFFECTIVE ADDITIVES FOR PREVENTING RECRYSTALLIZATION IN ICE-SLURRY SYSTEMS

Shu-Shen Lu
Chemical Engineering Research Institute
South China University of Technology, China
Email: kyoku21@mmail.mel.go.jp; Fax: 81-298-58-7091

Takaaki Inada, Akira Yabe, Xu Zhang
Nanotechnology Division
Mechanical Engineering Laboratory, Japan
Email: inada@mel.go.jp; Fax: 81-298-58-7091

Svein Grandum
Energy Systems Department
Institute for Energy Technology, Norway
Email: svein.grandum@ife.no; Fax: 47-63812905

Keywords: crystal growth, recrystallization inhibition, ice slurry, antifreeze protein

ABSTRACT. In thermal-energy-storage systems that use ice slurry as the working fluid, the shape and size of the crystals must be optimized during the ice creation process. Therefore, methods for preventing ice from recrystallizing during long-term storage and long-distance transport should be developed. Here, for use in ice-slurry systems, we studied two potential additives in solution (concentration of 5mg/ml), Tween surfactants and Polyvinyl Alcohol (PVA), and compared their capability to inhibit recrystallization and to inhibit ice crystal growth with that of pure water and antifreeze proteins (AFPs). For Tween, we studied Tween 80, 81, and 85, and for PVA, we studied three different molecular weights (31000–50000, 89000-98000, and 124000-186000 separately). The inhibition of ice crystal growth was determined by optical microscopy, and the inhibition of recrystallization by the splat cooling method. The results showed that, among the additives studied here, PVA of molecular weight 31000-50000 was relatively more effective in inhibiting recrystallization and had better long-term solubility properties, thus making it a potential additive in ice-slurry cold-storage systems.

1. INTRODUCTION

Thermal energy storage and transport systems that use ice slurry as the working fluid have shown promising characteristics due to their flowability and large cooling capacity[1]. Compared with conventional systems that use sensible heat, ice slurry systems have a lower mass flow rate and are more compact in size. Obtaining good storage and transport characteristics of the ice slurry require optimizing the crystal shape and size during the ice creation process. Furthermore, methods for preventing ice from recrystallizing during long-term storage and long-distance transport are important.

Antifreeze proteins (AFPs), which are found in fish living in the Antarctic Ocean who can depress the freezing point of their blood in a non-colligative manner [2], have been proposed as effective additives for making ice slurry resistant to recrystallization[3,4]. Despite numerous studies on the phenomena and mechanism of AFPs produced in certain fish and insects [5], the mechanism remains unclear, including the role of hydrogen bonding, the interaction of the protein's structure with ice, and possible hydrophobic interaction between the protein and water[6]. However, the demand for inhibiting recrystallization and ice crystal growth is widespread, for example, for expanding the shelf life of blood platelets, for increasing the efficacy of cryosurgery in tumors, for producing freeze-resistant fish, and for stopping crystallization of frozen foods. AFPs solutions have not yet been used in commercially available ice-slurry cold-storage systems mainly because AFPs are relatively expensive and easily affected by bacterial degradation. Therefore, ice slurry systems need additives that are cost-effective and are not easily affected by bacteria.

In this study, we examined two groups of potential additives, Tween surfactants and Polyvinyl Alcohol (PVA). Firstly the ice crystal growth pattern has been determined by using optical microscopy. Secondary we compared the recrystallization inhibition of these additives with that of pure water and AFP solutions. The

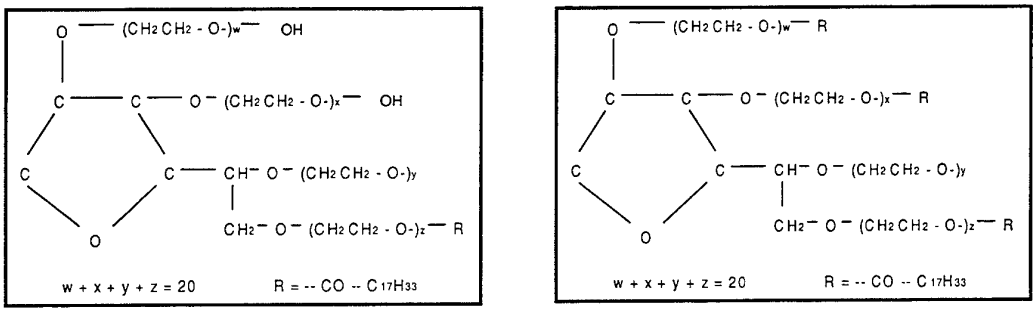
recrystallization inhibition ability was determined by using the splat cooling method borrowed from metallurgy[7,8], because splat cooling method can show the ice grains growth process in detail after annealed inside cold room with a low temperature. Recrystallization is driven by the need to lower the free energy within and between adjacent ice grains, and recrystallization inhibition capacity can be reflected by the ice grains growth ability or grains sizes after long time's annealing. If a system consists of particles of another substance within the boundaries without liquids, the particles will inhibit boundary migration to avoid increasing the grains' surface area, even though these particles can not inhibit recrystallization. Therefore, when recrystallization inhibition is used as evidence for the presence of antifreeze, sufficient salt or another small-molecule solute is needed to insure some liquid is present in the system [8]. Then, the effective additives present in the ice/liquid interface can be adsorbed onto the surface and thus inhibit crystal growth and inhibit variation in grain size. This is the reason why we added NaCl to the solutions in this study.

After capacities on inhibiting ice crystal recrystallization have been determined from various additives, other physical properties will be also very important to realize the industrial application. At one paragraph of this paper, long time solubility of different solutions has been discussed and considered to be one key factor to choose the potential additives in ice-slurry cold-storage systems.

2. EXPERIMENTAL MATERIALS

Pure Water and AFPs

We used pure water and AFP type I, type III at a 5mg/mL concentration as references to compare the effects of the Tween and PVA additives.

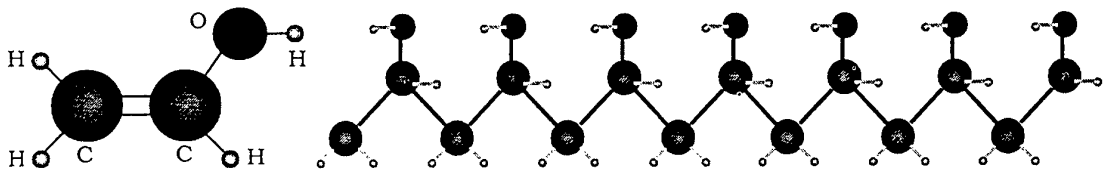


a. Tween 80 b. Tween 85

Fig. 1 Molecular structure of Tween surfactants

Tween Surfactants

Tween detergents are nonionic surfactants comprising a sorbitan ring, alkyl groups, and approximately 20 ethylene oxide units (Fig.1) [9]. For example, Tween 80 is widely used in biochemical applications, such as in the solubilization of proteins, isolation of nuclei from cells in culture, growth of tubercule bacilli, and emulsification and dispersion of substances in medicinal and food products. In this study, we used solutions of Tween 80, Tween 81, and Tween 85 at a 5mg/mL concentration containing 0.5 mg/mL of NaCl.



a. Vinyl Alcohol b. Polyvinyl Alcohol

Fig. 2 Molecular structure of vinyl alcohol and PVA

Polyvinyl Alcohol (PVA)

PVA is a polymer made from vinyl alcohol. When many vinyl alcohol monomers are linked together, a long polymer molecule is formed. Different lengths of the polymer molecule will induce different molecular weights. Here, we used solutions of PVA at three different molecular weights (31000–50000, 89000-98000, and 124000-186000 separately) at a 5mg/mL concentration containing 0.5 mg/mL of NaCl. Fig.2 shows a representative segment of the structure of a PVA polymer molecule. The PVA molecule consists of a long chain of carbon atoms to which hydrogen atoms and OH groups are attached. The OH groups are considered to be the latent ability to interact with ice surface by hydrogen bonding[10].

3. ICE CRYSTAL GROWTH OBSERVATION BY OPTICAL MICROSCOPY

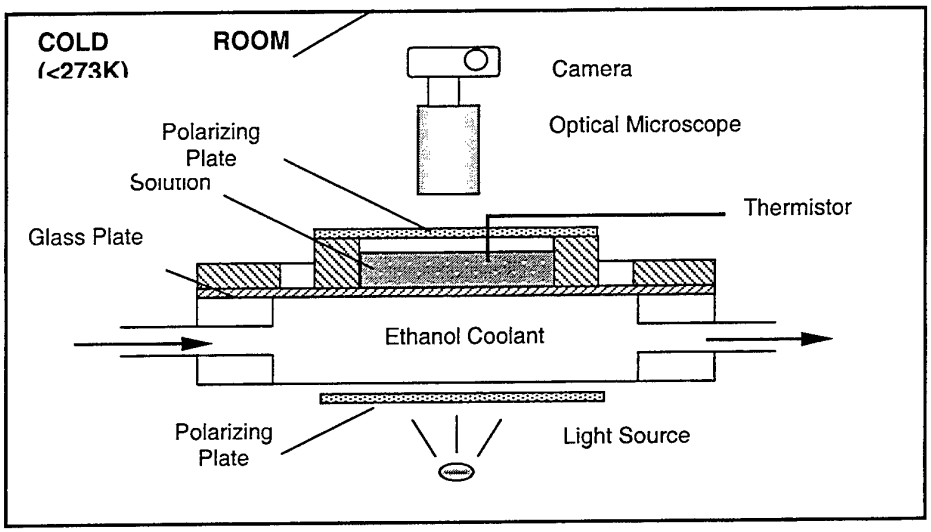
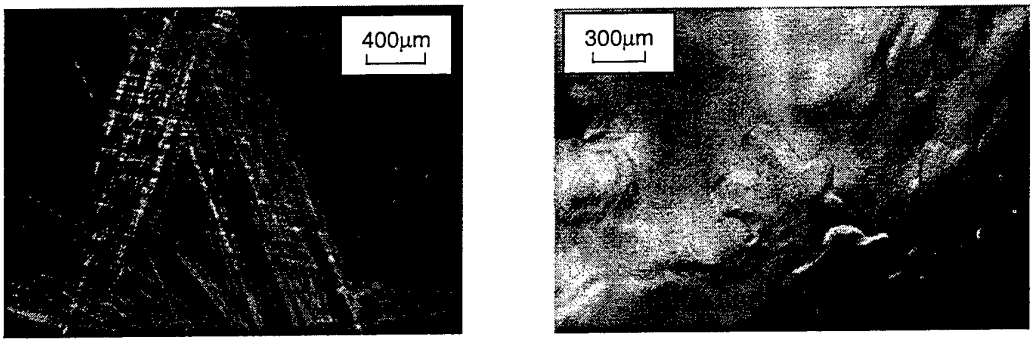


Fig. 3 Experimental apparatus for observing ice crystal growth

Imaging the growth pattern of ice crystals for the different solutions of additives was easily achieved by using optical microscopy (Fig.3). The temperature of the solution was controlled by an ethanol flow. To decrease the heat flux between the solution and atmosphere and to minimize the temperature gradient inside the solution, the experimental apparatus was set in a cold room at 273K or lower. The solution temperature was measured by using a thermistor. Crystal growth was initiated by inserting a seed ice crystal in a steady-state supercooled solution. Color images of the ice crystal patterns were obtained by using polarizing plates.



a. AFP type I solution (5mg/ml)

b. PVA solution (5mg/ml)

Fig. 4 Images of ice crystal growth

AFPs are effective in inhibiting crystal growth and in creating defined crystal structure, two characteristics that

are effective for resisting recrystallization. One possible mechanism for the strong interaction betwwen AFP molecule and ice crystal surface is that the amphiphilic structure of the α-helical AFP type I molecule dominates the hydrophilic amino acids on one side and hydrophobic amino acids on the opposite side [4]. Although several parameters affect the ice crystal growth pattern, for example the solution concentration and temperature, the ice crystal pattern for the AFP type I solution can be categorized into three groups; dendritic for low temperature(<272.2K), needle-type(272.2K<T<272.9K), and hexagonal bipyramids(272.9K<T<273.2K)[4]. Fig.4a shows needle-type crystals growing along the c-axis in AFP type I solution. These needle-type crystals crisscross each other in bundles but exist as individual crystals.

Numerous observations have been made of ice growth in supercooled pure water and aqueous solutions[11,12]. In this study, when either pure water or Tween surfactant soution was used as the working fluid, the crystals were always dendritic. When PVA was used (5mg/ml), crystal growth was inhibited, irrespective of molecular weight (Fig.4b); the ice crystal firstly grew as a hexagonal crystal along the a-axis, and then was inhibited and showed the clear boundary. This shows PVA was effective in inhibiting the ice crystal growth, but its' effect is not so strong as the AFP solutions.

4. SPLAT COOLING METHOD

Recrystallization by the Splat Cooling Method

In the method of splat cooling(Fig.5), a 10μL droplet of the additive solution was released 2m above a glass plate, which is cooled below 200K by liquid nitrogen, inside a cold room at a constant temperature of 266K. As the droplet hit the plate, it immediately froze as an ice wafer that was approximately 10mm in diameter and 20μm to 50μm thick and had grains of ice less than 1μm (below the resolution of the optical microscope at 60x magnification). The test plates with ice wafers were sealed in a chamber to retard evaporation of the thin ice discs and annealed for 14 hours inside the cold room at temperature of below melting point. The grain size will increase with annealing time if the solutions of additives have not capacity of inhibiting recrystallization. Many different solutions can be processed in the experiment at one time. Images of the ice wafers were then photographed at 50 x magnification by using a camera installed on the optical microscope.

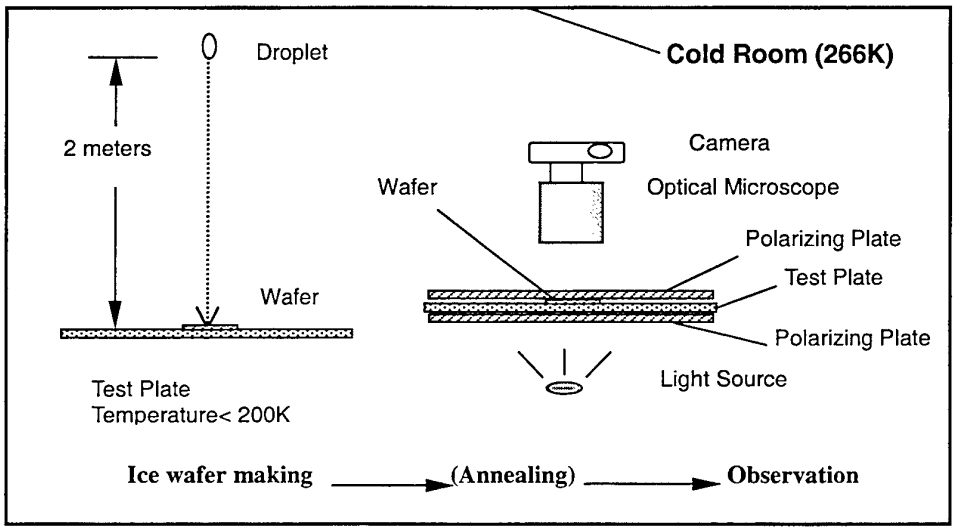
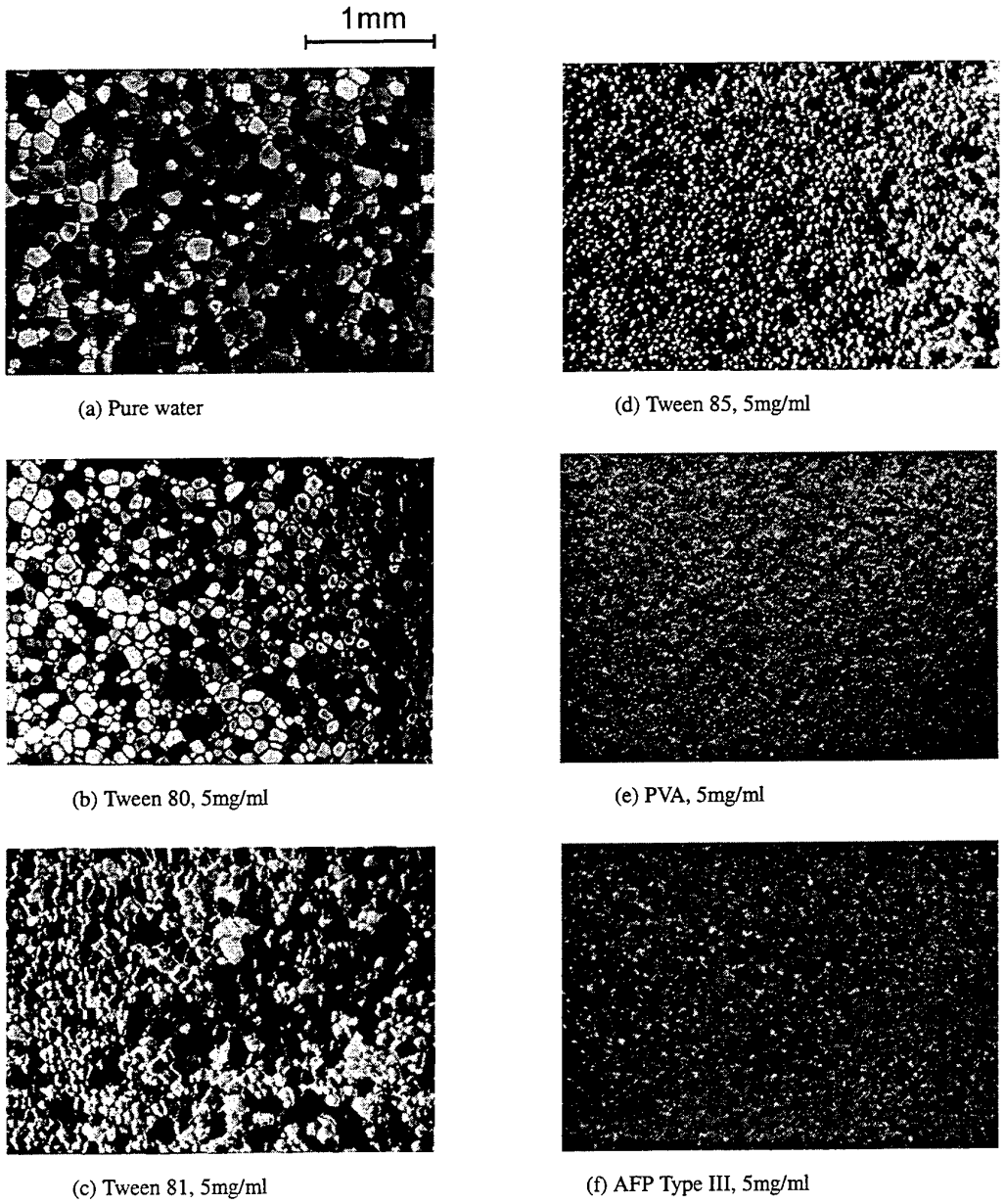


Fig. 5 Splat cooling method

Experimental Results

Although the rate of grain growth is a function of grain size and temperature and other factors (e.g., pressure and humidity), the splat cooling method is an effective method for determining the capability of additives to inhibit ice recrystallization. Our results show that such capability in increasing order was pure water (ineffective)< Tween surfactants < PVA < AFP (effective).

Fig.6 shows the ice wafers for different solutions formed by splat cooling. The results confirm that AFP type III effectively inhibits ice recrystallization, and that PVA is more effective than the Tween surfactants, irrespective of the PVA molecular weight. Among the Tween surfactants, Tween 85 was the most effective.



(a) Pure water

(d) Tween 85, 5mg/ml

(b) Tween 80, 5mg/ml

(e) PVA, 5mg/ml

(c) Tween 81, 5mg/ml

(f) AFP Type III, 5mg/ml

Fig.6 Ice wafers formed by the splat cooling method and annealed at 266K for 14 hours

5. SOLUBILITY OF SOLUTIONS

Solubility in water is another important property of additive solutions. Our results show that Tween surfactants showed sedimentation after being stored in the closed bottle at room temperature for three months. Similarly, the PVA solutions of medium and high molecular weights (89000-98000 and 124000-186000) showed sedimentation after being stored for three months. The PVA solution of low molecular weight (31000-50000),

which was 98-99% hydrolyzed, showed the best solubility in water even after being stored for three months, thus making it a potential ideal additive for ice slurry systems for long-term operation.

6. SUMMARY AND CONCLUSIONS

Due to the possible ability to inhibit recrystallization, Tween and PVA additive solutions were studied as potential working fluids in ice-slurry cold storage systems . Images (by using optical microscopy) revealed that the PVA solutions (concentration of 5mg/ml), irrespective of molecular weight, were effective in inhibiting the growth of ice crystals. Images also revealed that dendritic crystal patterns always occurred when either pure water or Tween surfactants were used as the working fluid in our experimental conditions. The results from the splat cooling method showed that PVA and Tween 85 were relatively more effective than Tween 80 and 81 in inhibiting recrystallization. The results also showed that, among the solutions studied here, the PVA solution of molecular weight 31000-50000, which was 98-99% hydrolyzed, had the best solubility in water after long-time storage (six months), thus making it be potential additive in ice-slurry systems.

To determine the relationship between the flow behavior of ice crystals and the concentration of the solution and to obtain the overall flow characteristics of the ice slurry during tube flow, the experiments at macro-loop are needed to simulate the real ice slurry operating conditions. On the other hand, we suggest and plan to use scanning tunneling microscope (STM) to identify the spatial localization and the adsorption-inhibition mechanism of polymers onto available adsorption sites of the ice crystal at the molecular level. Such information is also needed to reveal the antifreeze mechanism of AFPs.

REFERENCE

1. S. Fukusako, et al., "Research and Development Activities on Ice Slurries in Japan", *IIR Working Party, "Fine Crystalline Ice Slurries"*, Yverdon-Les-Bains, Switzerland(1999).
2. Y. Yeh and R. E. Feeney, Chemical Reviews, Vol.96, pp.601-617(1996).
3. S. Grandum, et al., J. Thermophys. HeatTransfer, Vol.11, pp.461-466(1997).
4. S. Grandum, et al., J. Crystal Growth, (in press) (1999).
5. P. L. Davies and B. D. Sykes, Current Opinion Structure Biology,Vol.7,pp.828-834(1997).
6. P. Smaglik, The Scientist, Vol.12. No.18, pp.4-5(1998).
7. C. A. Knight, J. Hallett and A. L. Devries, Cryobiology, Vol.25, pp.55-60(1988).
8. C. A. Knight, D. Y. Wen and R. A. Laursen, Cryobiology, Vol.32, pp.23-34(1995).
9. Aldrich Chemical Company. *Aldrich Catalog/Handbook of Fine Chemical.* Aldrich Chemical Co., Inc. Milwaukee, WI. (1986).
10. H. E. Assender and A. H. Windle, Polymer, Vol.39, pp.4295-4302(1998).
11. W. C. Macklin and B. F. Ryan, Phil. Mag., Vol.14, pp.847-860(1966).
12. Y. Furukawa, Appl. Phys. Japan, Vol.61, pp.776-789(1992).

HEAT RECOVERY FROM DOMESTIC WARM WATER APPLICATION FOR BIFILAR HEATING FLOORS

C. D. Lăzărescu; I. Olaru; C. Antohi; V. Ciocan
Department of Building Installations
"Gh. Asachi" Technical University, Iasi, Romania
Email: instal@tuiasi.ro ; Fax: ++40-32-233368

Keywords: heat pipe, heat storage and recovery, bifilar heating coil

ABSTRACT. The paper presents a system for heat recovery from the domestic waste warm water from buildings with application for heating floors with bifilar coil. Although at a low temperature level, the recovered heat can be used directly for floor heating of some areas situated on the ground floor of the buildings, eventually an extra electric heater being provided for the secondary warm water (i.e. from the coil). The paper also describes a variant of accomplishing heating floor that leads to increase of its life span, by using bifilar coil. On taking into account the method of laying down the two pipes, there results more constructive variants, but in order to simplify the problem only the case of full slab type radiating floor was analyzed.

1. HEAT PIPES HEAT RECOVERY SYSTEM FROM DOMESTIC WARM WATER

The idea of global solutions in the field of energy production and usage seems to have been abandoned lately, the rendering valuable of the local solutions for increasing the efficiency of the power usage, no matter of its form, being tried for the moment. Many interesting things have been accomplished in the field of using the household consumption warm water for heating, one of them being the recovery of the heat contained in the used household waters. The heat thus recovered has been used either for the production of the hot consumption water of the heating, in both cases a supplementary heating source being used due to the low temperature level of the recovered heat. Unlike the classic recovery diagrams, which contain accumulation heat exchangers (boilers), our solution employs heat pipes exchangers, the thermal energy thus recovered being used directly for floor heating some rooms of for pre – heating the hot consumption water. In fact, our solution can also be considered as a method for storing the thermal energy in the residual water combined with its extraction by means of the heat pipes. The diagram of the installation is presented in Figure 1, where the following symbols are used:

A_c - used household warm water
RSG - fat collector tank for collecting the used warm water
A_{uc} - drainage warm used water
R_g - discharge cock
FP - hair filter
R_s - tank for storing the filtered warm used water
R_p - tank for pre-heating the warm water used for heating
TT - heat pipes
t_v - temperature in the evaporation zone of the heat pipes
t_c - temperature in the condensation zone of the heat pipes
RTU - room clock thermostat
TEA, TEA_1 - magnet valve (thermoelectrical heads)
AT, AT_1 - contact thermostat
KK - plug box
FP5000 E - Laing- type pump electric heater assembly
HC - Heating Coil

Generally speaking, the consumers discharge in the sewage used water with temperatures ranging between 35 - 45°C; thus, temperatures t_v = 30 - 40°C in the evaporation zone of the heat pipes from the R_s tank can be easily obtained.

The system for heat recovery with heat pipes is combined in the presented variant with one of the Laing Qualitherm 2000 floor heating solutions; this solution, the most widely employed in Romania, can supply

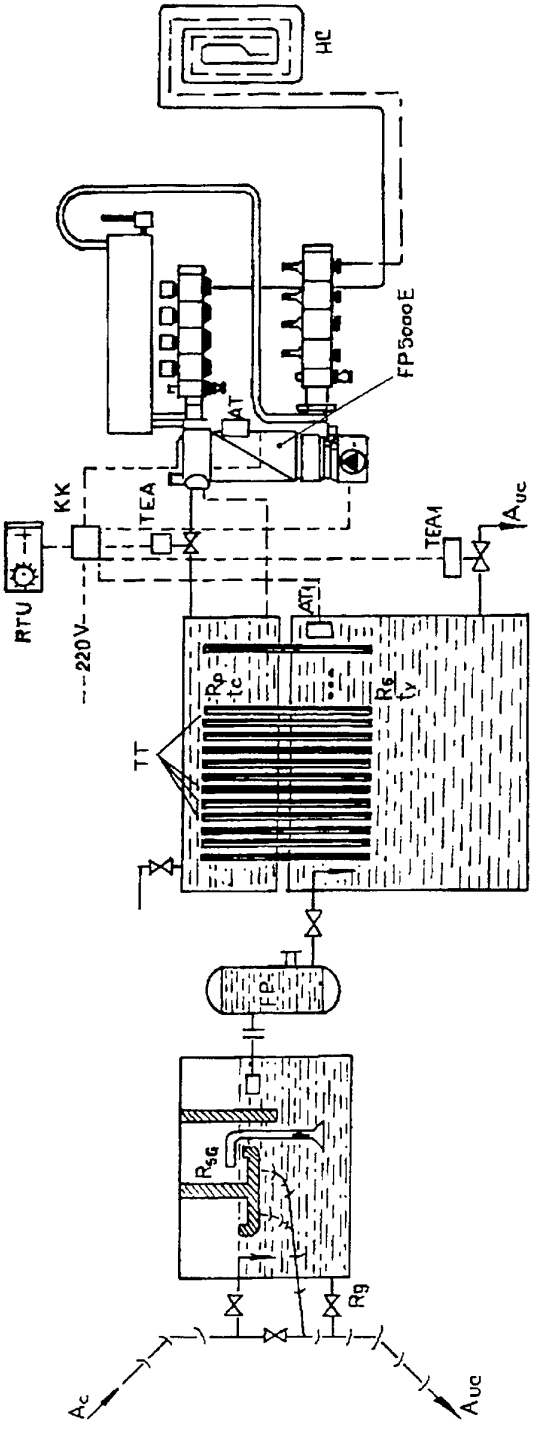

HC
FP5000E
AT
KK
TEA
TEAI
Auc
RTU
220V
ATI
Rp
tc
Rg
tv
TT
FP2
RSG
Rg
Ac
Auc

Figure 1

powers up to maximum 15 kW at temperatures $t_{departure} / t_{return} = 35/30\,^{\circ}C$ and at discharges of 2580 l/hour of the thermal agent in the heating coils. Generally speaking, the heat pipes recovery system can accomplish the pre-heating of the water from the circuit of the heating coil but when the temperature t_v decreases below 30°C, the TEA_1 magnet valve opens, thus allowing the admission of a higher temperature water from the RSG tank. The suggested system can be used for preparing the consumption warm water with minimum modifications in the period when the heating installation is not operating; at the same time, the heat pipes recuperator is employed as a pre-heating step of the cold water from the supply network system. The application domain of the suggested system is large enough, ranging from the blocks of flats up to 100 apartments, hotels with 200 – 250 places, generally speaking buildings with warm water consumption of maximum 20 – 25000 l/daily which allow the accumulation of used warm water in the basement.

Advantages

The suggested solution can accomplish important energy economies with minimum investments as the heat pipes recuperators are cheap, do not require pumps for operation, have a theoretically life durability in the suggested temperature domain while maintenance is simpler than that of the usual heat exchangers.

Disadvantages

The suggested system imposed the needs for collecting the used waters from the warm water consumption objects distinctly apart from the cold water consumption ones. Note: at lavatories, showers and bathtubs one accomplish automatically controlled drainage lines for water whose temperature is above or below a certain pre-established one. The system requires a careful maintenance by the periodical cleaning both of the collecting tank for the crude used water and of the hair filter.

2. HEATING FLOOR WITH BIFILAR COIL

The power conjuncture, the development of the plastic materials domain and the improvement of the thermal insulation of the buildings have contributed during the last years to the reintroduction in usage of the low temperature warm water radiating floors.

The research process of the heating floors is done nowadays with a view both to a thorough knowledge of their operation and to the solving of the unfavourable aspects, namely:

1. The permeability of the plastic pipes walls to oxygen, a fact leading to the corrosion of the installation metallic parts;
2. The fiability problem on a period comparable to that of the classic installations.

The first problem can be solved either by treating the water with inhibitors (an expensive solution) or by using plastic materials pipes, which have an aluminium foil embedded in the wall thickness, a foil constituting an antioxygen barrier.

Some important progresses have also been done in the solving of the second problem due to the spectacular development of the plastic materials domain. Thus, the materials used nowadays in the manufacturing of the radiating floors coils have an improved structure, containing special additives to steady the properties on a long term. The manufacturing companies indicate a life span of about fifty years, a considerable one but, anyway, smaller than that of the building.

The access to the coil in the case of its damage only by destroying the slab-finish in which it is included, led us to the idea of using a bifilar coil. One of the two pipes is a reserve one, thus increasing the system fiability. The bifilar coil can be accomplished either by mounting two distinct pipes tangent to the generator, or by including it in the protecting layer common for the two pipes. The reserve pipe considered to be filled with air.

On talking into account the method of laying down the two pipes, there result more constructive variants. To simplify the problem, the case of full slab type radiating floor was analyzed. The considerations can be also extended for the type- radiating floor often used today (pipes included in a slab-finish having a reduced thickness and being very well thermally insulated both from the resistance slab and the side walls).

Variant I

In this variant the bifilar coil is laid down in such a way so that the two pipes should be set one under the other, the "active" pipe (the one the water circulates through) being the top one (Figure 2).

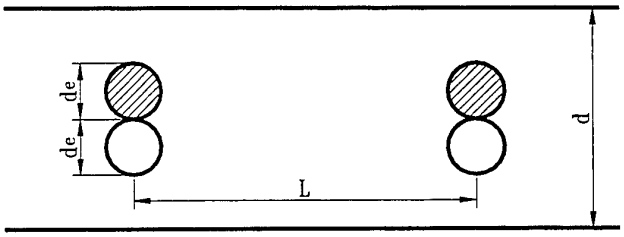


Figure 2

The moment when the active pipe is deteriorated, the water drains out and the reserve pipe becomes the "active" one by filling with water. The advantage of this variant consists in keeping constant the pitch of the coil.

Variant II

Two cases are distinguished in this variant; here they are.

A) The bifilar coil can be set as presented in Figure 3. In this case a constant pitch is kept for the "active" pipe, i.e. $L+d_e$, the reserve coil having a variable pitch ($L-2d_e$, $L+d_e$; Figure 3a).

If the "active" coil is deteriorated, the reserve pipe becomes the "active" and the new variant there will be obtained important non - uniformities of the temperatures on the upper and lower sides of the floor due not only to variable pitch ($L-d_e$, $L+3d_e$) but also the air "pockets" (reserve pipe) (Figure 2b).

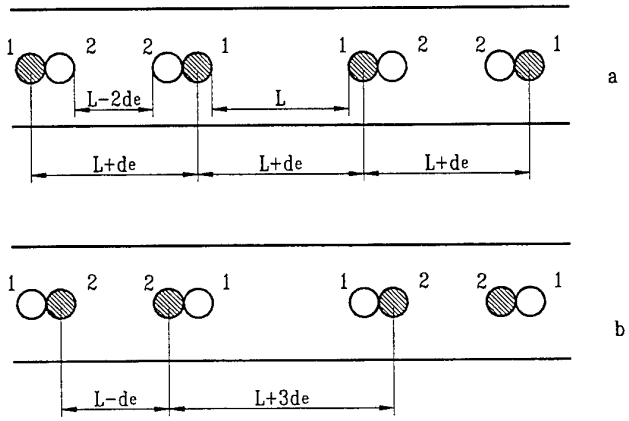


Figure 3

B) To diminish this shortcoming, the coil could be laid down in such a way so that the length of the floor between the two pipes should remain constant and equal with L (Figure 3).

In the variant (c), the pipe noted with 1 is "active" and has the variable pitch $L+3d_e$, $L+d_e$; in the variant (d) (Figure 4d), the pipe 1 is deteriorated and the pipe 2 becomes "active". One obtains the same situation, i.e. variable pitch but with the same variation. Thus, the case (c) is identical with (d) – while (a) is not identical with (b) – and, besides, the difference between the two pitch values is smaller in the case (c) and (d) as compared with (b):

(b): $(L+3d_e) - (L - d_e) = 4d_e$

(c) or (d): $(L+3d_e) - (L+d_e) = 2d_e$

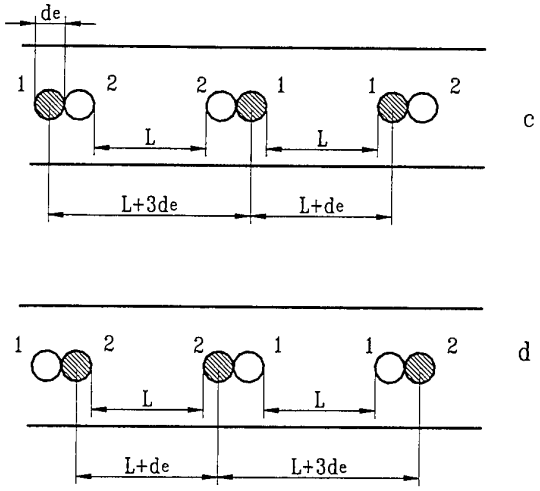


Figure 4

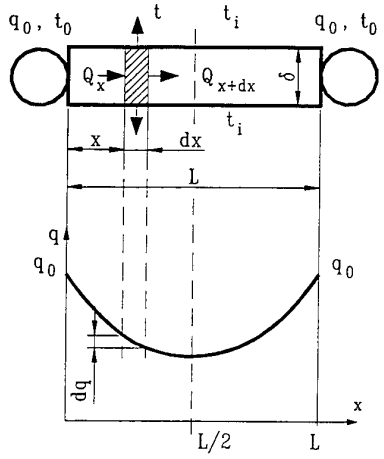
Variant III

This variant is derived from the variant I, considering that warm water with the same temperature circulates in the same direction in the two pipes.

Variant IV

This variant is derived from the variant II B, considering that warm water with the same temperature circulates in the same direction in the two pipes.

Specialised literature presents an analytical model for solving the heating floor. It is necessary that we should do a short reviewing of it because we have tried to solve our new variants with the help of this model: The heating floor is considered from a thermotechnical viewpoint as a plane wall with inner heat sources. The floor part between the consecutive pipes whose thickness is equal to the diameter of the pipe called "fin" is been analysed:



The notations from Fig. 5 are the following:
$\theta_0 = t_0 - t_i$ supertemperature at the fin base [°C];
t_0 temperature at the fin foot [°C];
t_i inner temperature of the room [°C];
$\theta = t - ti$ supertemperature of the fin at a distance x from the fin base [°C];

L distance between two consecutive heat sources [m];
δ fin thickness [m];
λ fin thermal conductivity coefficient [W/mK].

Figure 5

One considered as a fin length L and thickness δ a small infinite element of thickness dx through which passes a heat flow Q_x in the direction x and whose surface perpendicular to the direction of the heat flow is $A = \delta \times b$, where b is the fin width.

On starting from the writing down of the heat flow given by the small infinite element to the above and, respectively, below environment, a quadratic differential equation is obtained:

$$\frac{d^2\theta}{dx^2} - m^2 \cdot \theta = 0 \tag{1}$$

This equation represents the stationary heat exchange equation with an unidimensional temperature variation, where:

$$\frac{\chi_s + \chi_i}{\lambda \cdot \delta} = m^2 \tag{2}$$

and χ_s and χ_i are the global heat exchange coefficients from the fin towards the upper and, respectively, the lower area. The solution of the equation is of the following from:

$$\theta = \theta_0 \cdot \frac{ch \cdot \left[m \cdot \left(\frac{L}{2} - x \right) \right]}{ch \cdot \left(m \frac{L}{2} \right)} \tag{3}$$

The solution of the equation allows us to compute the average value of the temperature in the fin:

$$\theta_m = \frac{1}{L} \int_0^L \theta \cdot dx = \theta_0 \cdot \frac{ch\left(m \frac{L}{2} \right)}{m \frac{L}{2}} \tag{4}$$

then we can determine the unknown value of the problem, i.e. the values of the heat flows in an upward and downward direction, the values of the average temperature at the upper and lower surfaces of the floor.

3. CONCLUSIONS

The bifilar coil does not require other assembling and fastening technologies as compared with the classic variant. One invests only in a supplementary length, obtaining in exchange an increase in the floor fiability by the existence of the reserve pipe. The presence of the latter eliminates the necessity of destroying the floor in the case when the coil is degraded (with a view to its replacement), therefor, it eliminates one of the great disadvantages of the floor in the classic variant.

The variants III and I and the variants IV and II B can constitute a method of performing the quantitative adjustment. In this case, the bifilar coil would be used not only for increasing the floor fiability but also for accomplishing a "basic" heating (when the water circulates through only one pipe) completed with a "peak" one (when the water circulates through the two pipes).

REFERENCES

1. A. Abhat, "Application of Heat Pipes to Thermal Energy Storage Systems", AIAA, 15th Thermophysics Conference Snowmess, Colorado, 1980.
2. I. Olaru, C.D. Lăzărescu, "A method for Increasing the Life of the Warm Water Heating Floors", CIB W67 Symposium, 3rd International Congress on Human Ecology, Viena 1996.
3. I. Olaru, V. Pavel, C.D. Lăzărescu, M. Rotariu"Heating Floors – a solution for energy saving in buildings", Energex '96, 6th International Energy Conference, Beijing, 1996.

M. Melting and Solidification

MEASUREMENT OF TRANSIENT DOUBLE DIFFUSIVE CONVECTION AND CRYSTAL GROWTH USING REAL-TIME PHASE-SHIFTING INTERFEROMETER

Shigenao Maruyama, Kiyohiro Takahashi and Atsuki Komiya
Institute of Fluid Science, Tohoku University
E-mail: maruyama@ifs.tohoku.ac.jp; Fax: +81-22-217-5243

Masud Behnia
School of Mechanical and Manufacturing Engineering,
The University of New South Wales
E-mail: m.behnia@unsw.edu.au; Fax: +61-2-9663-1222

Keywords: crystal growth, double diffusive convection, phase-shifting interferometer

ABSTRACT. In the process of crystal growth in solutions, double diffusive convection due to thermal and solutal gradients occurs. A measurement system composed of a rapid heat-transfer control system and an accurate real-time phase-shifting interferometer has been developed to investigate the transient diffusive convection. The heat-transfer control system has a small test-cell in which the liquid temperature is controlled by non-equilibrium thermoelectric devices. In-situ measurement of the transient double diffusive convection and crystal growth rates of $NaClO_3$ are carried out by using this system. Transient double diffusive fields are observed clearly, and the crystal growth rates of the present experiments show similar tendencies to the data of microgravity experiments.

1. INTRODUCTION

Investigation of the crystal growth in solutions is closely related to the effective and high quality production of medicine, food and new materials. During the process of crystal growth in the solutions, double diffusive convection driven by buoyancy force due to thermal and solutal gradients occurs [1], which has an effect on the mechanism of crystal growth. Therefore, it is important to investigate the mechanism of double diffusive convection and its effect. Many works have been done on double diffusive convection. Maruyama et al. have simulated the double diffusive convection in a cell when the direction of thermal and mass convection are same or opposite, using thermal and solutal Rayleigh number as parameters [1]. Chang et al. [2] have made an analysis about the influence of the ratio between thermal and solutal buoyancy on the transient double diffusive convection, as well as investigated the mechanism of flow and behavior of unstable vibration.

In the present study, double diffusion fields and the crystal growth rates are examined under transient double diffusive convection. Transient concentration distribution and solutal gradient are delivered from the double diffusion fields. The relation between the super saturation on the crystal surfaces and crystal growth rate is investigated from some transient experiments. In order to make an accurate measurement of double diffusion field, a real-time phase-shifting interferometer is adopted in which phase dividing 3-CCD camera for polarized beam is used. The test cell is made of the active thermal control units developed by Maruyama [3] and solution around a seed crystal of $NaClO_3$ at a saturation temperature is cooled rapidly. The obtained result of the growth rate has been compared with the existing experimental data obtained in the microgravity conditions.

2. EXPERIMENTAL SYSTEM

2.1 Measurement System

The experimental apparatus is shown in Fig.1. A specially designed real-time phase-shifting Mach-Zehnder interferometer [4] is utilized to measure the thermal and mass diffusion fields. This interferometer can attain much higher accuracy compared with the conventional one by using phase-shifting technique [5]. By polarizing beam splitter, the semiconductor laser beam (wave length: 680nm) is separated into two beams, the reference beam and the measurement beam. The planes of vibration of these two beams are perpendicular to each other. After passing the test-cell and a compensator, the beams are mixed by another beam splitter. Since the polarized planes are perpendicular to each other, the beams will not interfere just after mixing. The magnification of objective lens can be changed as one, three, five, and ten times.

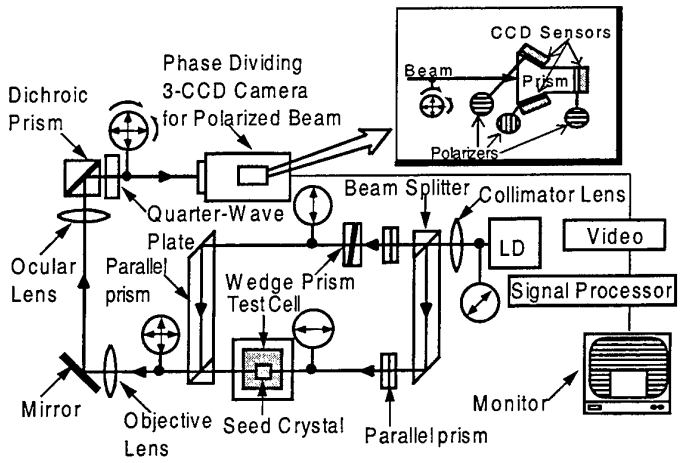


Fig. 1. System of experimental apparatus

A quarter-wave plate is placed at an angle $\pi/4$ to the two polarized beams. The two linearly polarized beams passed through the quarter-wave plate and become clockwise or counter clockwise polarized with respect to each other and interfere. The circularly polarized beams are delivered into a specially made phase dividing 3-CCD camera, which includes a 3-CCD prism, three CCD sensors and polarizers as shown in Fig.1. The difference in polarizing angles between any two polarizers is $\pi/4$. The original phase-shifting interferometer constructed by Onuma et al. [6] is composed of three independent TV cameras with polarizers, but it is difficult to adjust these cameras in the same optical condition. The present 3-CCD camera reduces this difficulty in optical arrangement, and reduces the size of the interferometer [4]. The interferogram obtained by the 3-CCD camera are processed by a signal processor as has been described by Onuma et al. [6] and Nakadate et al. [5]. The digital data of the interferogram are recorded in a video recorder in a gray scale.

2.2 Test Cell

Figure 2 shows a schematic diagram of the test-cell. The test-cell is specially designed for the transient measurement of the thermal and diffusion fields. Saturated solution and a seed crystal are contained in the cell. Active thermal control units [3] installed on the upper and lower sides of the walls control the temperature in the test-cell. The active thermal control unit includes an aluminum base plate, Peltier elements and a heat sink. The four Peltier elements are independently operated by a computer to control the temperature of the solution and crystal. The temperature in the cell can be controlled rapidly to within an accuracy of ± 0.1°C.

The size of the glass-cell is 12mm square and approximately 1.6mm in thickness. The seed crystal is attached on the lower base plate to observe the double diffusive convection and plume. $NaClO_3$ crystal and its aqueous solution are used in the present experiments. The shape of the seed crystal is rectangular solid. And the saturation temperature of the solution was approximately 26°C. Before the experiment of double diffusive convection, uniform temperature field in the cell is precisely maintained at the saturation temperature. As the experiment starts, rapid temperature control system is operated according to a programmed sequence. The operating time is 25[s]. When the experiment finishes, the temperature in the cell is automatically set to the saturation temperature. Temperature profiles on base plates are shown in Fig. 3. The temperatures are maintained at steady values accurately by adopting the active thermal control unit and a digital computer control system.

3. RESULT AND DISCUSSION

3.1 Relation between the Fringe Shift and the Temperature or Concentration

The experimental result of an interferogram is a superimposition of temperature and concentration difference. In order to determine the temperature and concentration fields, the relation between fringe shift of the interferogram and temperature or concentration should be determined in advance. Hence, preliminary experiments are carried out.

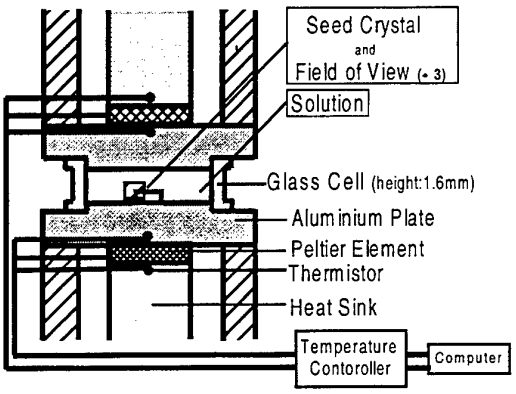


Fig. 2. Schematic diagram of the test-cell

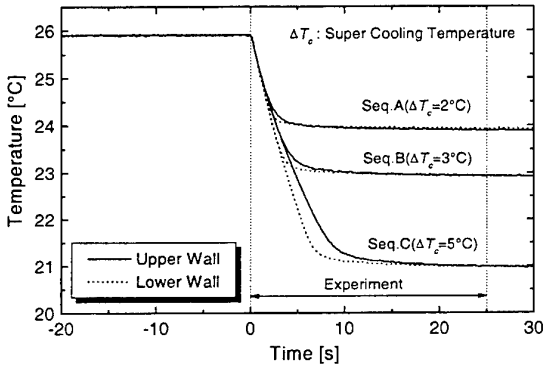


Fig. 3. Various temperature sequences on base plate

The relation between fringe shift and temperature can be obtained by using the test cell described above. At first, the temperature of the solution is maintained at the saturation value. Then, the solution is cooled to the super cooling temperature. Measuring fringe shift, which moves across the measuring point in the bulk, we can obtain the relation between the fringe shift and the temperature. The relation is summarized as follows:

$$\Delta T = (T - T_0) = 0.220 \times f_T \tag{1}$$

A specially designed test cell is set up to measure the relation between the fringe shift and the concentration [7]. The obtained fringe numbers, f_w of interferogram in the test cell against the difference of concentration is approximated as follows:

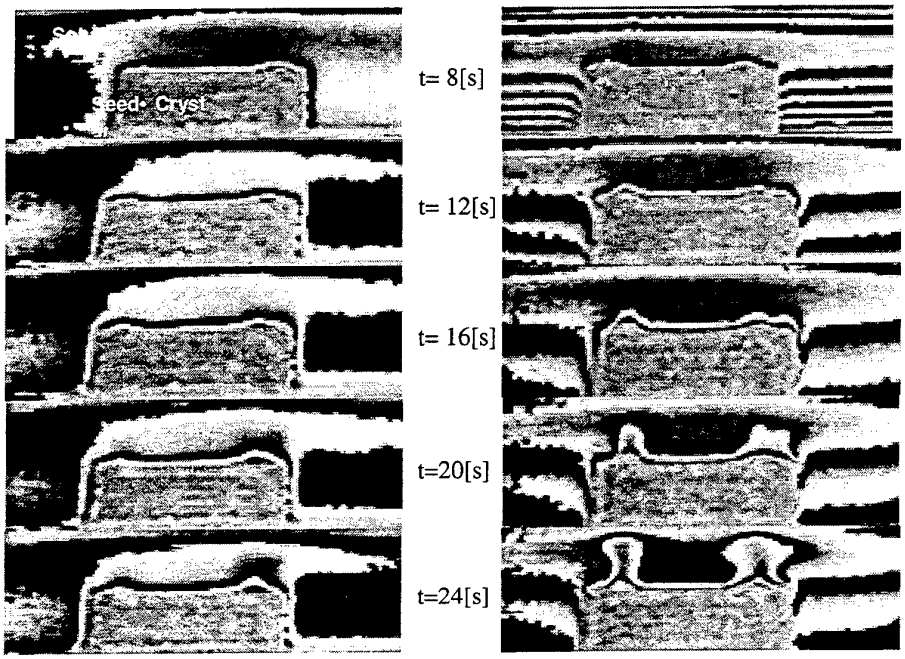
$$\Delta w = (w - w_0) = 0.0732 \times f_w \tag{2}$$

The relation in eq. (1) and (2) is the case when the optical path of the test cell is 10mm. This relation has to be corrected to match the length of the seed crystal.

3.2 Observation of Plume

Interferograms around the seed crystal are shown in Fig.4. To observe the transient double diffusive convection and plumes around the seed crystal widely, we used the one-time-magnification objective lens. The size of the seed crystal used in present experiments is 0.76mm of height, 2.31mm of width and 1.92mm of length. These photos are case (a) Seq. A in Fig.3 (ΔT_c = 2°C) and (b) Seq. C (ΔT_c = 5°C), respectively. The saturation temperature is 26.0°C.

When the uniform temperature distribution in the test cell is maintained at the saturation temperature (t=0s), natural convection does not occur in the small test cell. As soon as a rapid temperature control starts according to the programmed sequence in the computer, interferograms driven by temperature and concentration change are observed. In the case of ΔT_c = 5°C, plumes driven by buoyancy force occurred. Plumes become larger as the solution is cooled and the seed crystal grows. On the other hand, in the case of ΔT_c = 2°C, plumes are hardly observed. Therefore, in the case of ΔT_c = 2°C, the influence of plume is small compared with the case of ΔT_c = 5°C and it is nearly equal to the genuine diffusion field.



(a) ΔT_c=2°C (b) ΔT_c=5°C

Fig. 4. Interferograms around the seed crystal

To examine the condition plumes occur, solutal Rayleigh number Ra_D is evaluated. The solutal Rayleigh number is defined as follows:

$$Ra_D = g\beta_D \frac{(w - w_r)l^3}{D\nu} \tag{3}$$

where g is the gravitational acceleration [m^2/s], β_D is volume coefficient of expansion [1/K], w is concentration at measuring points [wt %], w_r is concentration at bulk solution, l is the height of the seed crystal [m], D is solute diffusivity [m^2/s], and ν is kinetic viscosity [m^2/s].

Volume coefficient of expansion β_D is delivered from the relation between concentration and density of $NaClO_3$ solution obtained by a preliminary experiment. β_D is defined as follows:

$$\beta_D = \frac{\rho - \rho_r}{\rho_r(w_r - w)} \tag{4}$$

where ρ is the density of solution at the measuring points [Kg/m^3], and ρ_r is density of the bulk solution.

To estimate viscosity η [Pas], the following approximation in the case of $NaClO_3$ saturated solution at 20°C obtained by Maruyama et al. [8] is used.

$$\eta = 2.67(T + 273.15)^{-7.26} \times 10^{16} \tag{5}$$

The solute diffusivity D is a function of temperature. In order to calculate the diffusivity, the equation of Stokes-Einstein [9] is adopted for estimating the value. From the measurement of viscosity of $NaClO_3$, D is approximated as a function of temperature by Maruyama et al. [8]:

$$D(T) = D_0 \left(\frac{T + 273.15}{T_0 + 273.15} \right)^{8.62} \tag{6}$$

where D_0 is the solute diffusivity at T_0. The solute diffusivity of $NaClO_3$ solution at saturation temperature T_s=25°C was measured by Maruyama et al. [10].

The Rayleigh numbers Ra_D are obtained by using these quantities. In the case of ΔT_c = 5°C, the Rayleigh number Ra_D is 2.67×10^4 at 24 [s] when the characteristic length l is height of the seed crystal, i.e. l=0.76 [mm] . Similarly in the case of ΔT_c = 2°C, Ra_D is 1.34×10^4 at 24 [s]. Ra_D in the case of ΔT_c = 5°C is about twice as large as that of ΔT_c = 2°C at 24 [s].

3.3 Transient Double Diffusive Field

Figure 5 shows the transient double diffusion field in the vicinity of the crystal surface. The case of (a) Seq. B (ΔT_c = 3°C) and (b) Seq. C (ΔT_c = 5°C) are compared in Fig.5. These photos are taken by using the three-time-magnification objective lens. Transient double diffusive fields can be observed clearly in Fig. 5. As soon as rapid temperature control starts, the horizontal interferogram of thermal diffusion can be seen in bulk solution region. At first, intervals between fringes are dense, but when the temperature in the test cell achieves super cooling temperature, the intervals become wide. On the other hand, in the vicinity of crystal surface, interferogram of mass diffusion develops with time. The interferograms are affected by the double diffusive convection.

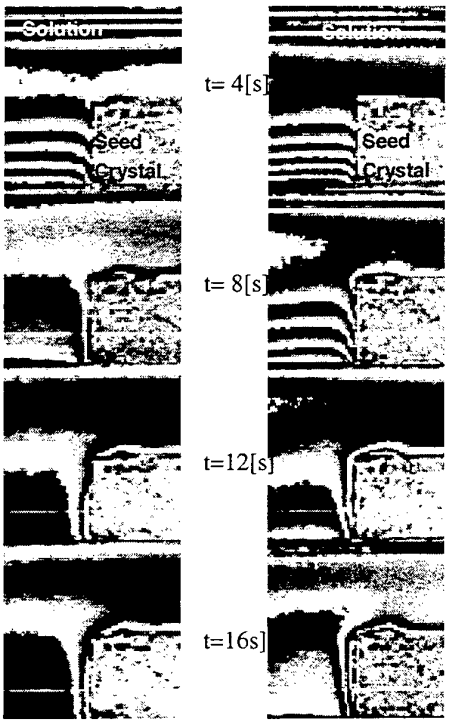


Fig. 5. Interferograms of diffusion field in the vicinity of crystal surface

3.4 Super Saturation of Bulk Solution and Crystal Surface

The measuring points for temperature and surface concentration are shown in Fig.6. Variations of temperature at measuring points are shown in Fig.7. These data are obtained from the relation between the fringe shift and

the temperature as shown in eq. (1). Sequences in Fig.7 correspond to those in Fig.3. The variations of temperature are different with temperature profiles on the base plate because of the influence of heat conduction and mass diffusion. It can be considered that the temperature at the vicinity of crystal surface is equal to that of at the bulk, because the thermal diffusivity is two orders of magnitude larger than the mass diffusion coefficient.

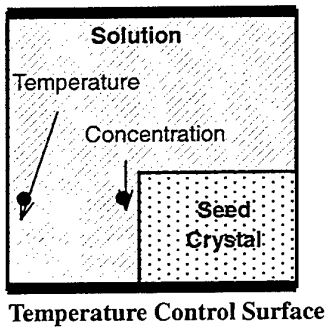


Fig. 6. Schematic drawing of measuring points

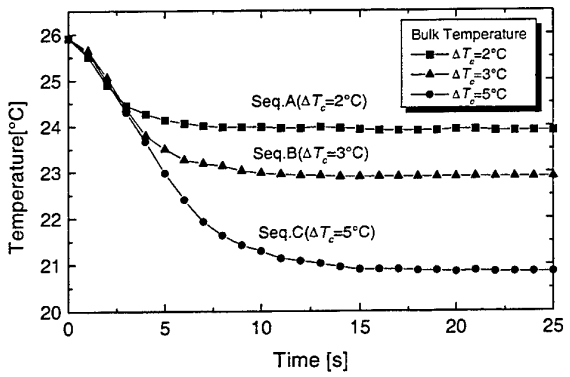


Fig. 7. Variation of temperature at the measuring point

Variations of supersaturation σ_s for some temperature conditions are shown in Fig.8. Supersaturation ratio is defined by the following equation:

$$\sigma_s = (w - w_{sat})/w_{sat} \tag{7}$$

where w [wt %] is the concentration at the measuring points and w_{sat} is saturation concentration at the cooling temperature. Solid marks are supersaturation of bulk solutions and unshaded marks are those at the surface of the seed crystal as shown in Fig.6. Because the measurement time is very short, 25 [s], concentration field in the cell is not affected by the rotation of plume. It is considered that the temperatures of bulk solution and surface of the seed crystal are almost the same. So, the higher super cooling temperature ΔT_c results larger difference in supersaturation between the bulk and the surface. Supersaturation at the bulk increases with time and settles in the constant value. Supersaturation at the vicinity of surface also increases just after the start of experiment, but it begins to decrease with time. This phenomena is noticeable in the case of ΔT_c=5°C. In the vicinity of crystal surface, concentration decreases as crystal grows. Therefore, as time passes, the decrease of supersaturation becomes more noticeable than the increase by the cooling of solution.

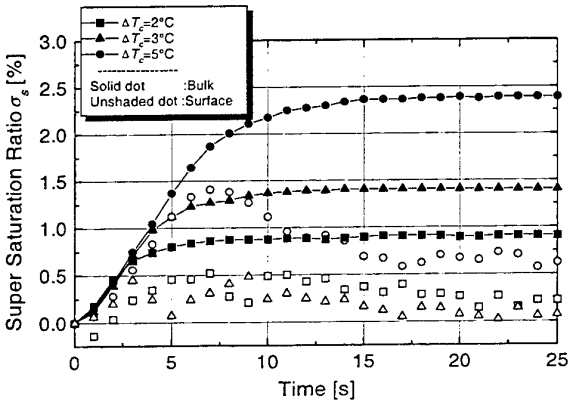


Fig. 8. Variation of supersaturation σ_s

3.5 Crystal Growth Rate Measured from Diffusion Field

Concentration distribution in the vicinity of the crystal surface obtained from fringe of inteferograms is plotted in Fig.9. This data is for the case of super cooling temperature ΔT_c=5°C. From these data, solute gradients at the crystal surface dw/dx can be obtained.

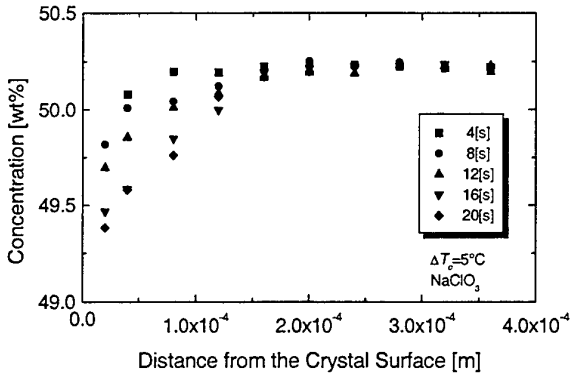


Fig. 9. Concentration distribution in the vicinity of the crystal surface

Crystal growth rate is estimated by the following equation:

$$R = \frac{\rho_{sol}}{\rho_{cry}} D(T) \frac{dw}{dx} \tag{8}$$

where ρ_{sol} is the density of solution, ρ_{cry} is the density of crystal, D is the solute diffusivity and dw/dx is solute gradient at crystal surface. Solute gradient is measured from concentration distribution in the vicinity of the crystal surface, e.g., Fig.9. The solute diffusivity $D=0.7\times10^{-9}$ (m^2/s) is used. This diffusivity of $NaClO_3$ solution at saturation temperature T_s=25°C was measured by Maruyama et al. [10].

Crystal growth rates of $NaClO_3$ under several super saturation ratios are shown in Fig.10. The data obtained by present experiments are summarized by time from the beginning of the experiment. Crystal growth rates obtained by microgravity experiments carried out by Maruyama et al. [11] and the growth rates for small σ_s [12] are also plotted as references. Microgravity experiments are carried out under the microgravity environment generated by parabolic flight of an airplane. The growth rates obtained by the present experiments have a similar tendency to that obtained in the microgravity experiments. The growth rate increases with σ_s at small σ_s, then the increase becomes small at a comparatively large σ_s. The scatter of crystal growth rates obtained by present experiments are stabilized compared to that of microgravity experiment. From these results, it is seen that the influence of the gravity is small under the condition of present experiments.

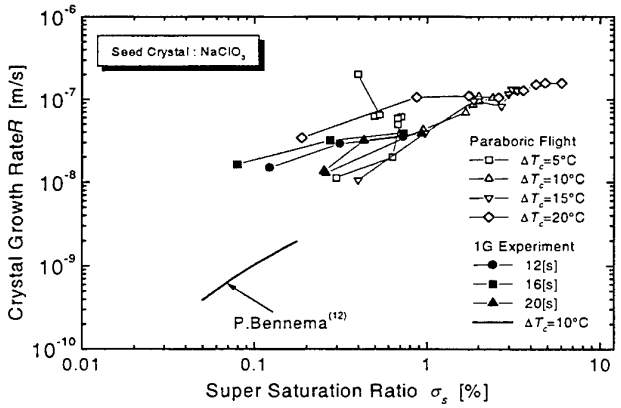


Fig. 10. Crystal growth rates of $NaClO_3$

Compared to the Bennnema's growth rates at small σ_s, the data obtained by present experiments show a different tendency and have almost ten times larger values. The difference is considered that the roughness of the crystal surface enhances the crystal growth. In the present experiments, seed crystal grows by rapid cooling, which makes the surface rough and as a result of this, the growth rates become larger. Further experiments and analyses should be done to give a detailed understanding of this phenomenon.

4. CONCLUSIONS

Transient double diffusive convection and crystal growth rate in the process of crystal growth in solutions are measured by using a real-time phase-shifting interferometer and a rapid temperature control system. Transient double diffusive convection can be observed clearly. Plumes can be observed transiently in the short experimental time of 25[s]. The plume occurs clearly when the super cooling temperature ΔT_c is 5°C. But in the case of ΔT_c=2°C, plumes can not be observed clearly. The relation between occurrence of transient plumes and super cooling temperature should be investigated by further experiments and analysis.

The relation between the supersaturation on the surface of the seed crystal and the crystal growth rate is measured. Crystal growth rates obtained by present experiments are compared with that of the microgravity experiments and of experiments at very small supersaturation. Present experimental data have similar tendency with the data of microgravity experiments made by Maruyama et al. And scatters are suppressed compared with microgravity experiments. But present experimental data are one order of magnitude larger than that of experiments at small supersaturation made by Bennnema. This may be due to the difference in the roughness of crystal surface in the two experiments. Further experiments are needed to give a detailed explanation of this phenomenon.

REFERENCES

1. S. Maruyama, Y. Miyagawa, K. Tsukamoto and T. Aihara, Transient simulation of double diffusive convection of crystal growth in microgravity, *Proceeding of the Sixth International Symposium on Transport Phenomena in Thermal Engineering*, Vol.2, Begel House, pp.1072-1077, (1993).
2. J. Chang and T.F. Lin, Unsteady Thermosolutal opposing convection of liquid-water mixture in a square cavity-2. Flow structure and fluctuation analysis, *Int. J. Heat Mass Transfer.* Vol.36, No.5, pp.1333-1345. (1993).
3. S. Maruyama, Active Heat Transfer Control by Non-equilibrium Thermoelectric Device, *Pro.33rd. National Heat Transfer Symposium of Japan*, pp.127-128, (1996).
4. S. Maruyama, T. Shibata and K. Tsukamoto, Measurement of Diffusion Fields of Solutions Using Real-time Phase-shift Interferometer and Rapid Heat-transfer Control System, *Experimental Thermal and Fluid Science*, (to be published)
5. S. Nakadate and M. Issiki, Real-time Fringe Pattern Proceedings and its Applications, *Proc. Photo Instrum. Eng.*, Vol.2544, pp.74, (1995).
6. K. Onuma, K. Tsukamoto and S. Nakadate, Application of real-time phase-shift interferometer to the measurement of concentration field, *Journal of Crystal growth*, Vol.129, pp.706, (1993).
7. S. Maruyama, A. Komiya, J. Yabana and M. Higano, Measurement of mass diffusion coefficient of solutions using real-time phase-shift interferometer, *Pro.18th.Japan Symposium on Thermophysical Properties*, pp.117-120, (1997).
8. S. Maruyama, T. Shibata, K. Tsukamoto, and K. Shimizu, Measurement of Solutal and Thermal Diffusion in Systems Subjected to Rapid Cooling Under Microgravity During Parabolic Flight, *Heat Transfer-Japanese Research 27 (2)*, pp.114-129, (1998).
9. R.C. Reid, J.M. Pravsnitz and T.K. Sherwood, The Properties of Gases and Liquids, *McGraw-Hill, Inc*, (1985).
10. S. Maruyama, A. Komiya, Z. Guo and T. Shimoyama, Accurate Measurement of Mass Diffusion Field and Diffusion Coefficient Using Real-time Phase-shift Interferometer, *Proceedings of PSFVIP-2*, PF074, (1999).
11. S. Maruyama, J. Yabana, N. Sumi, A. Komiya, K. Tsukamoto and K. Shimizu, Measurement of Diffusion Field and Crystal Growth Rate from Solution in Microgravity and Normal Gravity, *J. Jpn. Soc. Microgaravity Appl*, Vol. 15, pp.571-576, (1998).
12. P. Bennema, Interpretation of the Relation Between the Rate of Crystal Growth from Solution and the Relative Supersaturation at low Supersaturation, *Journal of Crystal Growth*, Vol. 1, p. 287, (1967).

ON CHARACTERISTICS OF A RECTANGULAR, ANNULAR NATURAL CIRCULATION LOOP WITH THE INNER TUBE FILLED WITH A PHASE CHANGE MATERIAL OR AIR UNDER CYCLIC PULSATING HEAT LOAD

C. J. Ho and G. H. Tan
Department of Mechanical Engineering
National Cheng Kung University, Tainan, Taiwan 70101
E-mail: cjho@mail.ncku.edu.tw; Fax: 886-6-2352973

Keywords: thermosyphon, melting/solidification, pulsating heat load.

ABSTRACT. An experimental investigation has been made of characteristics of a rectangular, annular single-phase natural circulation loop with the inner tube filled with a solid-liquid phase change material (PCM) or air under cyclic pulsating heat load. A rectangular, annular loop of 150 cm in height and 75 cm in width was constructed with an annular gap of 0.6 cm, within which water was filled. The inner tube of the annular loop was filled with a PCM (n-Eicosene) or air. Under the cyclic pulsating heat load, the temperature within the water-filled annular loop with PCM- or air-filled inner tube were all found to evolve into a steady periodic variation for the range of parameters considered. The water temperature and/or its fluctuating amplitude along the heater or cooler sections of the loop with the PCM-filled inner tube were found to be markedly lower than those measured in the loop with the air-filled inner tube under the identical conditions. On the other hands, along the insulated sections of the loop a somewhat minute difference in temporal variations of the water temperatures exists between the loops with PCM- and air-filled inner tube. In addition, at the outer wall along the cooler section, a time-periodic variation of temperature was detected in synchronizing with the pulsating heat load. Parametric effects of varying amplitude and period of the pulsating heat input, as well as of varying the inlet temperature of the water-cooled jacket were investigated.

1. INTRODUCTION

The single-phase natural circulation loops (thermosyphons), in which buoyancy-driven fluid flow is created by heat addition to and removal from the fluid in different parts of the system, arise in many engineering applications. Examples include the process industry, solar heating and cooling systems, geothermal power generation, internal combustion engine and computer cooling, emergency cooling of nuclear reactors, turbine blade cooling, and natural convection heat exchangers. Extensive reviews of the thermosyphon systems and their applications can be found in [1-4].

Extensive investigations of analyses and/or experiments have been conducted for the dynamic response of the natural circulation loop to changes in heat removal from or addition to the system and steady-state performance of the system, as exemplified in Refs. [5-9]. From the existing literature concerning the rectangular natural circulation closed loop, it can be noticed that the heating conditions considered were restricted to that of time-independent heat input at the heated section of the loop. In practice, however, the circulation loop could be subjected to a time-periodic heat load, and as a result a periodic thermal behavior arises. To our best knowledge, there is no previous effort to study performance of a rectangular natural circulation loop under a condition of time-dependent heat input. In the present study, an on-off pulsating heat load on the heated section of a rectangular circulation loop was therefore considered. The cyclic pulsating heat load simulates the boundary condition encountered in the surroundings of many thermal systems. Oscillatory responses of a circulation loop to a time-periodic heat load are of great concern in practical applications, as the fluctuations of temperature may be undesirable. The undesirable temperature oscillation in the circulation loop could be managed by incorporating the solid-liquid phase materials as passive thermal control medium. As demonstrated in [10-13], the absorption/release of latent heat associated with solid-liquid phase change process can be utilized as a thermal buffer for the temperature fluctuation of a thermal system subjected to a time-dependent heat load. Objective of the present study is, accordingly, to investigate experimentally heat transfer characteristics in a single-phase rectangular, annular loop with the inner tube filled with a solid-liquid phase change material (PCM) under cyclic pulsating heat load. To reveal the thermal damping efficacy of the PCM-filled inner tube on the response of the circulation loop to the cyclic heat load, an additional annular loop with empty inner tube (filled with air) was also investigated in the present study.

ON CHARACTERISTICS OF A RECTANGULAR, ANNULAR NATURAL CIRCULATION LOOP WITH THE INNER TUBE FILLED WITH A PHASE CHANGE MATERIAL OR AIR UNDER CYCLIC PULSATING HEAT LOAD

C. J. Ho and G. H. Tan
Department of Mechanical Engineering
National Cheng Kung University, Tainan, Taiwan 70101
E-mail: cjho@mail.ncku.edu.tw; Fax: 886-6-2352973

Keywords: thermosyphon, melting/solidification, pulsating heat load.

ABSTRACT. An experimental investigation has been made of characteristics of a rectangular, annular single-phase natural circulation loop with the inner tube filled with a solid-liquid phase change material (PCM) or air under cyclic pulsating heat load. A rectangular, annular loop of 150 cm in height and 75 cm in width was constructed with an annular gap of 0.6 cm, within which water was filled. The inner tube of the annular loop was filled with a PCM (n-Eicosene) or air. Under the cyclic pulsating heat load, the temperature within the water-filled annular loop with PCM- or air-filled inner tube were all found to evolve into a steady periodic variation for the range of parameters considered. The water temperature and/or its fluctuating amplitude along the heater or cooler sections of the loop with the PCM-filled inner tube were found to be markedly lower than those measured in the loop with the air-filled inner tube under the identical conditions. On the other hands, along the insulated sections of the loop a somewhat minute difference in temporal variations of the water temperatures exists between the loops with PCM- and air-filled inner tube. In addition, at the outer wall along the cooler section, a time-periodic variation of temperature was detected in synchronizing with the pulsating heat load. Parametric effects of varying amplitude and period of the pulsating heat input, as well as of varying the inlet temperature of the water-cooled jacket were investigated.

1. INTRODUCTION

The single-phase natural circulation loops (thermosyphons), in which buoyancy-driven fluid flow is created by heat addition to and removal from the fluid in different parts of the system, arise in many engineering applications. Examples include the process industry, solar heating and cooling systems, geothermal power generation, internal combustion engine and computer cooling, emergency cooling of nuclear reactors, turbine blade cooling, and natural convection heat exchangers. Extensive reviews of the thermosyphon systems and their applications can be found in [1-4].

Extensive investigations of analyses and/or experiments have been conducted for the dynamic response of the natural circulation loop to changes in heat removal from or addition to the system and steady-state performance of the system, as exemplified in Refs. [5-9]. From the existing literature concerning the rectangular natural circulation closed loop, it can be noticed that the heating conditions considered were restricted to that of time-independent heat input at the heated section of the loop. In practice, however, the circulation loop could be subjected to a time-periodic heat load, and as a result a periodic thermal behavior arises. To our best knowledge, there is no previous effort to study performance of a rectangular natural circulation loop under a condition of time-dependent heat input. In the present study, an on-off pulsating heat load on the heated section of a rectangular circulation loop was therefore considered. The cyclic pulsating heat load simulates the boundary condition encountered in the surroundings of many thermal systems. Oscillatory responses of a circulation loop to a time-periodic heat load are of great concern in practical applications, as the fluctuations of temperature may be undesirable. The undesirable temperature oscillation in the circulation loop could be managed by incorporating the solid-liquid phase materials as passive thermal control medium. As demonstrated in [10-13], the absorption/release of latent heat associated with solid-liquid phase change process can be utilized as a thermal buffer for the temperature fluctuation of a thermal system subjected to a time-dependent heat load. Objective of the present study is, accordingly, to investigate experimentally heat transfer characteristics in a single-phase rectangular, annular loop with the inner tube filled with a solid-liquid phase change material (PCM) under cyclic pulsating heat load. To reveal the thermal damping efficacy of the PCM-filled inner tube on the response of the circulation loop to the cyclic heat load, an additional annular loop with empty inner tube (filled with air) was also investigated in the present study.

2. EXPERIMENTS

The single-phase rectangular, annular natural circulation loop used in the experiments is illustrated schematically in Fig. 1. Stainless steel tubes of 2.7-cm outer diameter (2.3-cm inner diameter) and 4.3-cm outer diameter (3.7-cm inner diameter) were used, respectively, as the inner and outer tube of the annular loop. Inside the four legs of the inner tube, a research-grade paraffin, n-Eicosene (99% pure) with a fusion temperature of 37°C, was selected as the PCM. Prior to filling into the inner tube, the paraffin was carefully degassed. The four legs of the loop were connected with four steel 90° bends. The heated section of length 90 cm consists of an electrically insulated heating tape (Lauda, BIH101080) on the outside of the outer tube, which is heated electrically with a D.C. power supply (0 ~ 110 Volts, 0 ~ 10 Amperes). The power supply is equipped with a timer such that an on-off electric power input to the heating section with a variable pulsating time-period up to 30 minutes can be produced. Meanwhile, the cooled section of length 75 cm is a double pipe heat exchanger with a plastic outer pipe of 9.5-cm inner diameter, which is connected to a constant temperature bath with a mixture of water and ethanol as the heat transfer medium flowing through the cooler jacket. Within the annular circulation loop, water was used as the circulating fluid. The whole assembly was insulated with 5 cm of insulation tubing. To reflect directly the effect of the PCM-filled inner tube, an identical annular circulation loop was also constructed but with an empty (air-filled) inner tube.

The circulation loop is equipped with a total of 19 T-type thermocouples, as indicated in Fig. 2, to monitor temperature of water inside the annular loop as well as of the outer annular wall temperature in the heated and cooled sections. Each thermocouple measuring the water temperature was positioned approximately near the cross-sectional center of the annular loop. A data logger was used to record the temperature measurement. The uncertainty in the measuring the temperature with the T-type thermocouples and recording them with the data logger was estimated to be ±0.3°C. The experimental uncertainty associated with determining the heat input to the loop was estimated to be within 5%.

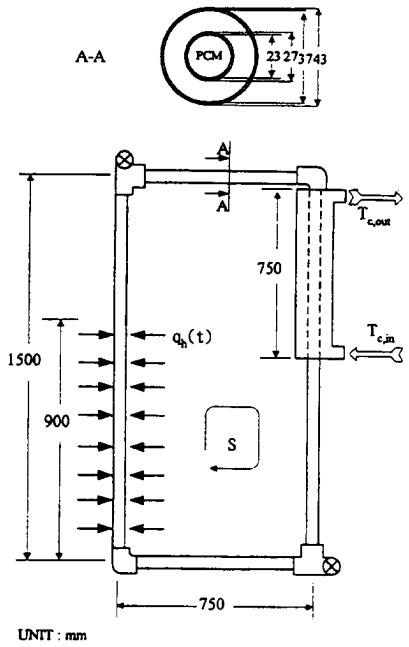


Fig. 1 . Schematic diagram of the experimental annular natural circulation loop.

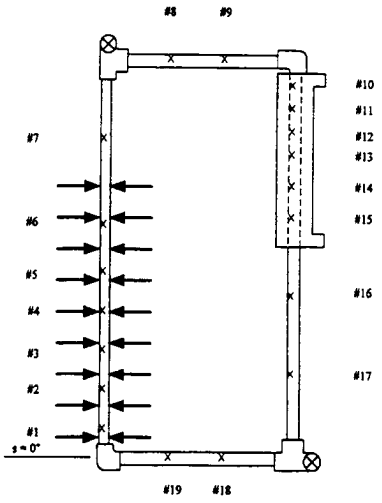


Fig. 2 Location of thermocouples in the loop.

The experimental procedure adopted in the present study is as follows. The annular loop was filled with distilled water. The constant temperature bath connected to the cooling jacket was first set to establish internally the temperature at a predetermined value. The heat exchange fluid of the constant temperature bath was then switched on to circulate through the cooler jacket of the loop. Meanwhile, the heating tape was turned on to supply the heated section a selected magnitude of the pulsating on-off heat flux A_q at a certain time

period p. Readings of the thermocouples were recorded until a steady periodic state was reached. The steady periodic variation was usually detected in the annular loop after approximately six to ten cycles of pulsating heat load into the heated section. To further ensure the steady periodic condition, the experiments in the present study were performed at least over a time interval of nineteen cyclic pulsating heat load.

3. RESULTS AND DISCUSSIONS

Two series of experimental tests have been conducted for the two annular loops with the PCM-filled and the air-filled inner tube, respectively. Pertinent parameters of the present experiment were varied for the two annular loops as follows: the pulsating heat flux through the heated section $A_q = 4000, 6000, 8000\ W/m^2$; the on-off heating period p = 10, 20 minutes; and the inlet temperature of the cooling jacket $T_{c,in}$ = 5, 9, 14°C. Their parametric influences on the behaviors of the annular loop as well as the thermal damping efficacy, if any, of the PCM filled in the inner tube shall be presented referring with the case of $A_q = 6000\ W/m^2$, p = 20 minutes, and $T_{c,in}$ = 9°C as the base condition.

For all the tests undertaken for the loop with PCM-filled or air-filled (empty) inner tube, following an initial transient oscillatory regime, a steady periodic regime was observed for variation of the water temperature with a time-period equal to that of the imposed pulsating heat load at the heated section. Figures 3-5 display, respectively, the steady periodic variations of temperature at various locations along the heated, cooled, and adiabatic sections of the loop under the condition of $A_q = 6000\ W/m^2$, p = 20 minutes, $T_{c,in}$ = 9°C. The fluid temperature fluctuations appear to be markedly intensified longitudinally along the heated section, as revealed in Fig. 3. Meanwhile, magnitudes of the steady temperature fluctuations for the loop with the PCM-filled inner

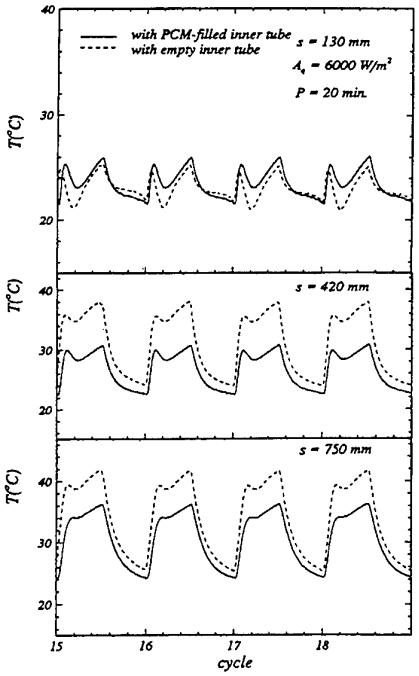


Fig. 3. Steady periodic variation of temperature at three locations along the heated section for $A_q = 6000\ W/m^2$, p = 20 minutes, $T_{c,in}$ = 9°C.

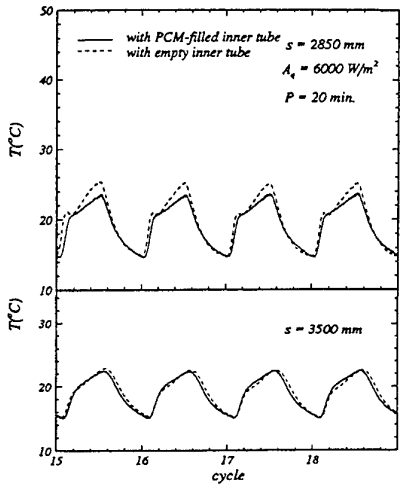


Fig. 4. Steady periodic variation of temperature at two locations along the cooled section for $A_q = 6000\ W/m^2$, p = 20 minutes, $T_{c,in}$ = 9°C.

tube can be seen substantially smaller than those for the loop with the empty inner tube, in particular in the region where the fluid temperature is substantially higher than the fusion temperature of the PCM. At the location s = 750 mm near the exit of the heated section, for instance, a fluctuation amplitude of approximately 4°C arises for the loop with PCM-filled inner tube, while an amplitude of 7°C for the loop with the empty inner tube. Such a nearly half reduction of the temperature fluctuation clearly reflects the thermal damping efficacy of the PCM filled in the inner tube to the cyclic heat load. Contrary to the heated section, as displayed in Fig. 4, the oscillatory behavior of the fluid temperature appears relatively moderate and becomes gradually subdued along the cooled section. Furthermore, it can be noticed that the fluid temperature through the cooled section remains below the fusion temperature of the PCM. No significant damping on the oscillatory fluid temperature by the PCM-filled inner tube can thus be expected along the cooled section, as depicted in Fig. 4. For the insulated sections of the annular loops, the steady temperature oscillations are typified in Fig. 5 at one location, respectively, along the upper and lower horizontal section. The temperature fluctuation at the upper insulated section is markedly higher than that at the lower section. Further from Fig. 5, it can be seen that significant thermal damping on the temperature fluctuation due to the PCM-filled inner tube occurs at the upper insulated section, where the fluid temperature oscillates around the melting point of the PCM. On the contrary, along the lower insulated section the fluid temperature remains well below the fusion point of the PCM so that the temperature fluctuation appears rather insensitive to whether the inner tube filled with PCM or not. Another fact worthy of mentioned here is that at the outer wall along the cooler section, regardless of the inner tube being filled with PCM or air, a time-periodic variation of temperature was detected in synchronizing with the pulsating heat load. As illustrated in Fig. 6, the periodic variation of the averaged wall temperature at the cooled section under the condition of $A_q = 6000\ W/m^2$, p = 20 minutes, $T_{c,in}$ = 9°C can be well approximated by a sinusoidal function.

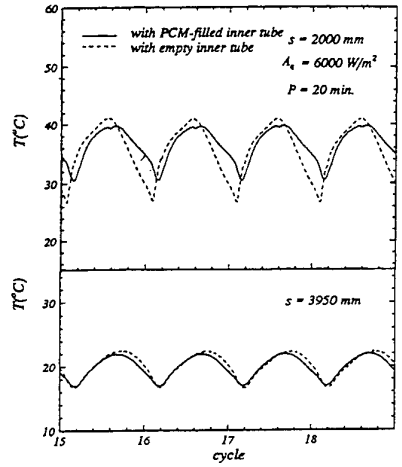


Fig. 5. Steady periodic variation of temperature at locations along the upper and lower adiabatic section for $A_q = 6000\ W/m^2$, p = 20 minutes, $T_{c,in}$ = 9°C.

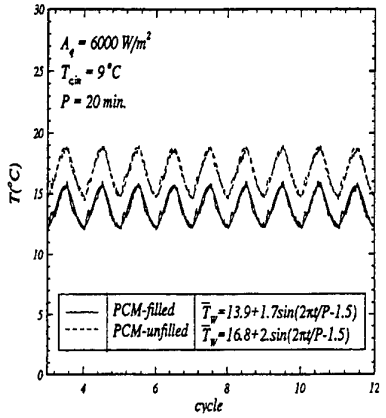


Fig. 6 Steady periodic variation of surface averaged temperature at the cooled section of the annular loop with the inner tube filled with PCM or air for $A_q = 6000\ W/m^2$, p = 20 minutes, $T_{c,in}$ = 9°C.

In Fig. 7, the periodically-averaged values of the fluid temperature $\overline{T}$ along the annular loops with the PCM-filled or empty inner tube are shown for the case of $A_q = 6000\ W/m^2$, p = 20 minutes, $T_{c,in}$ = 9°C. It should be noted that the amplitude of the temperature fluctuation is defined here as the average of the maximum and minimum fluid temperature deviation from the periodic mean value. An overview of the experimental data reveals that the periodic mean values along the heated section of the both annular loops exhibit somewhat linear increase trend but at different rate. A markedly lower increase rate and thus a lower value of the fluid temperature can be discerned for the loop with the PCM-filled inner tube, in particular along the second-half portion of the heated section. For the insulated and cooled sections of the loop, the PCM filled in the inner tube

appears exerting little influence on the periodic mean temperature profile of the fluid.

Also included in Fig. 7 is the corresponding distribution of fluctuation temperature amplitude A_T along the annular loops. In a similar manner to the periodic mean temperature, the temperature fluctuation amplitude exhibits a relatively sharp increase along the heated section of the annular loop with the empty inner tube. A maximum fluctuation amplitude of about 9°C is detected along the vertical insulated section following the heated section. A gradually decrease of the fluctuation amplitude appears then through the upper insulated section, reaching a local minimum amplitude of approximately 4.5°C. Entering the cooled section, a slight increase of the fluctuation amplitude arises before a more moderate decrease trend resumes through the following insulted section. For the annular loop with the PCM-filled inner tube, a similar observation of the temperature fluctuation amplitude can be made. Moreover, in conformity with the results shown in Figs. 3-5, the thermal damping effects of the PCM filled in the inner tube can be further inferred from the substantially lower fluctuation amplitude displayed in Fig. 7, in comparison with that for the loop with empty inner tube.

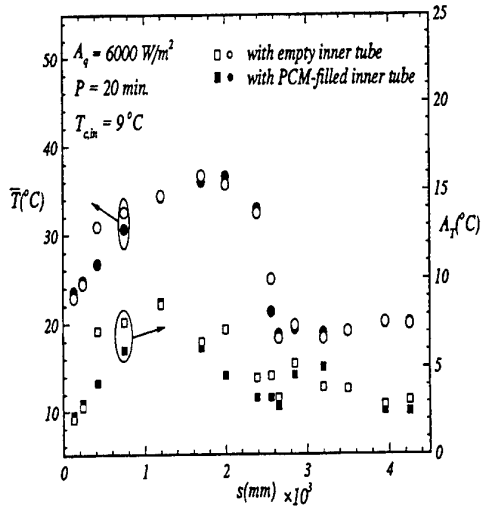


Fig. 7 Distributions of the periodic mean value and the fluctuation amplitude of the fluid temperature along the annular loops for A_q = 6000 W/m², p = 20 minutes, $T_{c,in}$ = 9°C.

Further increase/decrease of the magnitude of the pulsating heat load on the heated section induces, as can be expected, a marked increase/decrease of the periodic mean temperature throughout the annular loop with/without the PCM filled in the inner tube as depicted in Fig. 8. Moreover, it can be noticed that the periodic mean temperature along the annular loop shows little dependence on the PCM filled in the inner tube except for the second-half heated section, where a marked reduction of the fluid mean temperature can be detected. The reduction magnitude of the mean temperature in the heated section, due to the latent-heat damping, tends to be further augmented under a higher pulsating heat load. The above-described influences of varying the pulsating heat load on the mean fluid temperature can be generally observed for the fluctuation amplitude of fluid temperature along the loop as well. As can be seen in Fig. 8, the magnitude of temperature fluctuation as well as its reduction associated with PCM filled in the inner tube display a significant bearing with the imposed pulsating heat load. Under a higher the pulsating load, higher temperature amplitude arises through the annular loop. Meanwhile, the amount of amplitude reduction caused by the PCM in the inner tube becomes enlarged, in particular along the second-half heated section.

Next, in Fig. 9 the effects of varying the time-period of the pulsating heat load is presented. By inferring from Figs. 7 and 9, the increase of the on-off heating period can be seen to induce a marked higher fluctuation magnitude of the fluid in the loop. Little dependence of the periodic mean temperature on the period of the pulsating heat load can be readily discerned from the figures. Further scrutiny of Figs. 7 and 9 reveals that the thermal damping efficacy on the temperature fluctuation caused by the PCM-filled inner tube appears to be rather insensitive to variation of the period of the pulsating heat load.

Finally, the parametric effect of the inlet temperature of the cooling jacket at the cooled section on the fluid temperature field is illustrated in Fig. 10. In conjunction with Fig. 7, it can be seen that a cooler inlet coolant temperature through the cooling jacket gives rise to substantial decrease of the periodic mean temperature through the loop. Similar to that of varying the period of the pulsating heat load, the variation of the coolant inlet temperature tends to exert minute influence on the temperature amplitude or the thermal damping efficacy associated with filling PCM into the inner tube of the loop.

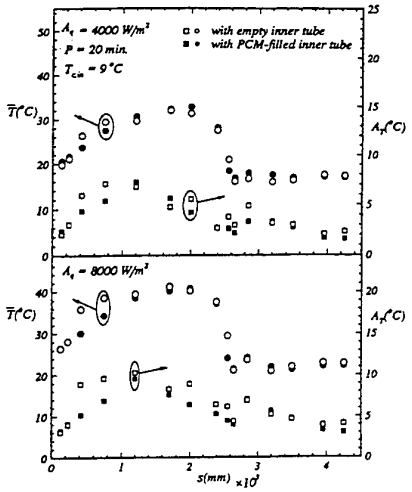


Fig. 8 Influence of the magnitude of pulsating heat load on the periodic mean value and the fluctuation amplitude of the fluid temperature along the annular loops for p = 20 minutes and $T_{c,in}$ = 9°C.

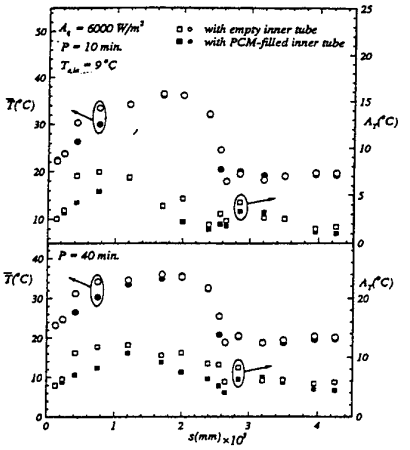


Fig. 9 Effect of the period of pulsating heat load on the periodic mean value and the fluctuation amplitude of the fluid temperature along the annular loops for $A_q = 6000\ W/m^2$ and $T_{c,in}$ = 9°C.

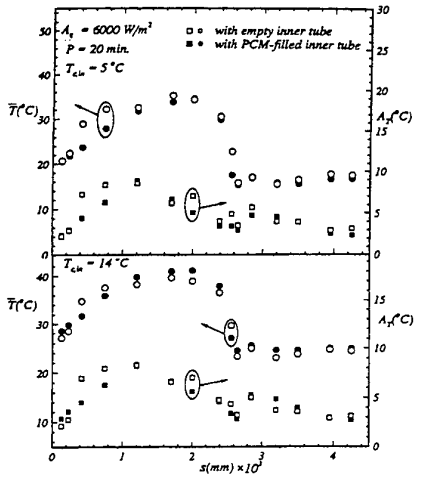


Fig. 10 Dependence of the periodic mean value and the fluctuation amplitude of the fluid temperature along the annular loops on the inlet temperature of the cooling jacket at the cooled section for $A_q = 6000\ W/m^2$ and p = 20 minutes.

4. CONCLUDING REMARKS

In the present experiment, the results of fluid temperature development in a rectangular annular single-phase natural circulation loop with inner tube filled with PCM or air under a cyclic pulsating head load have been presented. The fluid temperature variation inside the annular loop with the inner tube filled with PCM or air has been found to evolve into a steady time-periodic variation for the parameters under consideration. With the inner tube filled with PCM, the fluid temperature and/or its fluctuation amplitude along the heated or cooled sections of the annular loop can be substantially reduced. On the other hands, along the insulated sections of the loop a somewhat minute difference in temporal variations of the water temperature exists between the loops with PCM- and air-filled inner tube. In addition, at the outer wall along the cooled section, a time-periodic variation of temperature in synchronizing with the pulsating heat load was detected. Moreover, the thermal damping efficacy by the PCM-filled inner tube on the temperature fluctuation appears to be greatly enhanced

with the increase of amplitude, but rather insensitive to the variation of the time period of the imposed pulsating heat load. The influence of varying the coolant inlet temperature tends to exert an influence similar to that of varying the time period of the pulsating heat load.

ACKNOWLEDGMENTS

The authors are grateful for the support for this study from National Science Council under the Project Nos. NSC87-2212-E006-054 and NSC88-2212-E006-022.

REFERENCES

1. D. Japikse, *Advances in Heat Transfer*, v. 9, pp.1-111(1973).
2. Y. Zirin, Nuclear Engineering Designs, v. 67, pp. 203-225(1981).
3. B. Norton, and S. D. Probert, Applied Energy, v. 11, pp. 167-196(1982).
4. R. Greif, ASME Journal of Heat Transfer, v. 110, pp. 1243-1258(1988).
5. P. S. Damerell and R. J. Schoenhals, ASME Journal of Heat Transfer, v. 101, pp. 672-676(1979).
6. K. P. Hallinan and R. Viskanta, International Journal of Heat Fluid Flow, v. 6, pp.256-264(1985).
7. K. P. Hallinan and R. Viskanta, Heat Transfer Engineering, v. 7, pp. 43-52(1986).
8. B. J. Huang, and R. Zelaya, ASME Journal of Heat Transfer, v. 110, pp. 487-493(1988).
9. C. J. Ho, S. P. Chiou and C. S. Hu, International Journal of Heat and Mass Transfer, v. 40, pp. 3553-3558(1997).
10. C. J. Ho and C. H. Chu, International Journal of Heat and Mass Transfer, v. 36, pp. 725-733(1993).
11. D. Pal and Y. Joshi, Numerical Heat Transfer, Part A, v. 30, pp. 19-34(1996).
12. D. Pal and Y. Joshi, ASME Journal of Electronic Packaging, v. 119, pp. 40-50(1997).
13. C. J. Ho and Y. T. Cheng, Heat and Mass Transfer, v. 34, pp.509-515(1999) .

HEAT AND MASS TRANSPORT DURING DISSOLUTION IN A BINARY METALLIC SYSTEM

A. A. Boral and F. B. Cheung
Department of Mechanical and Nuclear Engineering
The Pennsylvania State University, University Park, PA 16802, USA
Email: fxc4@psu.edu; Fax: (814) 863 4261

S. W. Shiah
Department of Naval Architecture and Marine Engineering
Chung Cheng Institute of Technology, Taoyuan, Taiwan, ROC

Keywords: heat and mass transport, dissolution, binary metallic system

ABSTRACT. The process of combined natural convection heat and mass transport during dissolution of a vertical soluble metallic substrate in an otherwise quiescent molten metallic pool is studied theoretically. The problem is formulated using the Boussinesq approximation, taking full account of the density variation of the binary metallic solution due to concentration and temperature differences across the dissolution boundary layer. Also accounted for are the solubility of the metallic substrate on the species transport and the motion of the solid-liquid interface at the dissolution front. The governing system is solved using a combined analytical-numerical technique to determine the velocity, temperature, and concentration profiles in the dissolution boundary layer. Results are presented showing the dependence of the rate of dissolution on the key controlling parameters of the binary metallic system.

1. INTRODUCTION

Heat and mass transport during dissolution of a vertical metallic substrate in a molten metallic pool is of considerable practical importance in conjunction with the formation of alloys, casting of metals, corrosion of high-temperature containers, and safety analysis of advanced nuclear reactors. The latter arises in a postulated core-meltdown accident in a heavy water reactor in which a pool of molten aluminum would form in the lower head of the reactor vessel. The molten aluminum tends to dissolve the carbon steel structure that is submerged in the pool. In most cases, the solid substrate (i.e., the carbon steel structure) is at a temperature considerably below the molten pool temperature and has a density larger than the pool density. As a binary solution is formed near the dissolution front, significant density gradients induced by both the concentration and the thermal fields would develop in the solution layer. Under the influence of gravity, these density gradients give rise to a strong buoyancy force that causes the dissolved material (i.e., the binary solution) to move along the solid-liquid interface, thus resulting in the development of a dissolution boundary layer. Experimental measurements of dissolution in binary metallic systems performed by previous investigators have been emphasized either on the composition of the alloy resulting from the dissolution process [1, 2] or on the extent of dissolution under various flow conditions [3-5]. While these experimental studies provide some useful data on the material composition and the overall dissolution, they offer very little information on the characteristic features of the dissolution heat and mass transport processes. Theoretical studies of the subject matter have been limited to those of Cheung et al. [6, 7] and Shiah et al [8]. They found that the Sherwood number depends strongly on the saturated concentrations of the substrate at the dissolution front and the degree of saturation in the ambient metallic pool. Their studies, however, have been restricted to the case of an isothermal binary metallic system in which the buoyancy force arises entirely due to concentration differences. The assumption of an isothermal system severely limits the applicability of their results since in most cases, the solid substrate is likely to be at a temperature well below the ambient pool temperature. In such cases, the effects of thermal buoyancy need to be taken into account. In this study, the process of combined natural convection heat and mass transport during dissolution of a vertical soluble metallic substrate submerged in an otherwise quiescent molten metallic pool is studied theoretically. The substrate, having a density different from the ambient pool, is considered to be at a temperature well below the ambient pool temperature. Owing to the complexity of the problem, only the case for which the temperature-induced flow and the concentration-induced flow are aiding each other is considered in this study. The problem is formulated for a general binary metallic system but numerical results are obtained specifically for an iron-aluminum system.

2. MATHEMATICAL FORMULATION

A schematic of the physical system under consideration is shown in Figure 1. The vertical soluble substrate (i.e. iron plate) having a density higher than the ambient fluid is submerged in a pool of quiescent molten metal (i.e. molten aluminum) that is at a temperature above the substrate temperature. The dissolved material flows downward along the plate due to the combined thermal and concentration induced density gradients.

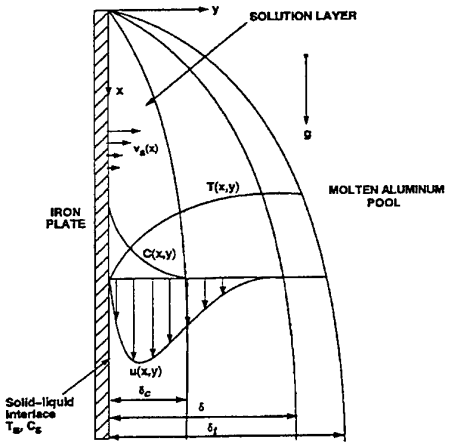


Figure 1. A schematic of the binary metallic system under consideration showing the configuration of the dissolution boundary layer.

To facilitate the mathematical formulation of the problem, the dissolution process is treated to be steady and the solid-liquid interface (i.e. the dissolution front) to remain vertical. These simplifications are appropriate since the dissolution process is usually slow owing to a small mass diffusivity for the aluminum alloy system. The extent of wall erosion is small compared to the length of the plate. A two-dimensional Cartesian coordinate system moving with the dissolution front is employed such that the interface is always located at y = 0. In the moving coordinate system, the transverse component of the velocity at the solid surface is no longer zero, but has a value equal to the local dissolution velocity, v_s. Assuming a steady, two-dimensional, laminar boundary-layer flow, the equations governing the momentum, heat and mass transport in the dissolution boundary layer can be written as:

$$\frac{\partial(\rho u)}{\partial x}+\frac{\partial(\rho v)}{\partial y}=0 \tag{1}$$

$$\rho u\frac{\partial u}{\partial x}+\rho v\frac{\partial u}{\partial y}=\mu\frac{\partial^2 u}{\partial y^2}+g(\rho-\rho_\infty) \tag{2}$$

$$\rho C_p u\frac{\partial T}{\partial x}+\rho C_p v\frac{\partial T}{\partial y}=k\frac{\partial^2 T}{\partial y^2} \tag{3}$$

$$\rho u\frac{\partial C}{\partial x}+\rho v\frac{\partial C}{\partial y}=D\frac{\partial}{\partial y}\left(\rho\frac{\partial C}{\partial y}\right) \tag{4}$$

Note that the local density ρ is a strong function of the local concentration and temperature. Hence the local density variation needs to be accounted for in the continuity equation. The boundary conditions for the above set of the governing equations are:

$$y=0:\quad u=0,\ C=C_s,\ T=T_s \tag{5}$$

$$v = v_s = -\frac{D}{1-C_s}\left.\frac{\partial C}{\partial y}\right|_{y=0} \tag{6}$$

$$x = 0 \text{ or } y \to \infty: \quad u = 0,\ C = C_\infty,\ T = T_\infty \tag{7}$$

where C_s is the saturated concentration at the solid-liquid interface. The term $(1-C_s)$ in the denominator of Equation (6) represents the induced flow correction for the transverse component of liquid velocity at the interface.

The value of C_s in Equation (5) is a function of the interface temperature, T_s, which is taken to be the same as the substrate temperature. Shiah et al. [8] used the experimental data for the solubility of metals in molten aluminum at high temperatures and obtained the following for the saturated concentration:

$$\ln C_s = \frac{A_1}{T_s} + B_1 \tag{8}$$

where C_s is in weight %, T_s is in degree Kelvin, and A_1, B_1 are constants. For the iron-aluminum system under consideration, these constants have values of $A_1 = -7.74 \times 10^3$ and $B_1 = 8.89$. For a given value of T_s, the above expression can be used to determine the saturated concentration.

To complete the mathematical formulation of the problem, various ambient pool concentrations are considered with C_∞ being bounded between zero and the saturated value at the interface C_s. It can simply be related to C_s by:

$$C_\infty = aC_s \tag{9}$$

Physically, the fraction *a* can be viewed as the degree of saturation of the ambient molten metallic pool.

For a binary metallic system, the local density of the fluid can be expressed as:

$$\rho = \rho_m\left[1-\left(1-\frac{\rho_m}{\rho_w}\right)C\right]^{-1} \tag{10}$$

where C is the local mass fraction, ρ_m is the density of the metallic solvent (i.e. molten aluminum), and ρ_w is the density of the substrate (i.e. iron). The ratio ρ_m/ρ_w can be written as:

$$\frac{\rho_m}{\rho_w} = \frac{\rho_{m,s} + \Lambda_m(T-T_S)}{\rho_{w,s} + \Lambda_w(T-T_S)} \approx \frac{\rho_{m,s}}{\rho_{w,s}} \equiv d \tag{11}$$

where the reference temperature has been chosen to be T_s. The error associated with the above approximation has been observed to be less than 1% for $(T_\infty - T_s) < 150K$.

Equation (10) can be rewritten as:

$$\frac{\rho}{\rho_s} = \left[\frac{\rho_{m,s}}{\rho_s} - \beta_m(T-T_s)\right][1-(1-d)C]^{-1} \tag{12}$$

where β_m $\{\equiv -\Lambda_m/\rho_s\}$ is the coefficient of thermal expansion of the metallic solvent (i.e. molten aluminum). The density at the interface in the above equation is given by:

$$\rho_s = \rho_{m,s}[1-(1-d)C_s]^{-1} \tag{13}$$

which depends on the values of d, C_s, and $\rho_{m,s}$. On the other hand, the ambient pool density is given by:

$$\rho_\infty = (\rho_{m,s} + \Lambda_m \Delta T)[1-(1-d)aC_s] \tag{14}$$

where $\Delta T = (T_\infty - T_s)$ is the overall temperature difference across the thermal boundary layer.

3. ANALYSIS

3.1 Similarity Transformation

By evaluating the thermophysical properties of the individual species at the saturated temperature, the governing equations can be reduced to a system of ordinary differential equations by a similarity transformation. Upon introducing a stream function ψ defined by:

$$u = \frac{\rho_s}{\rho}\frac{\partial \psi}{\partial y} \quad \text{and} \quad v = -\frac{\rho_s}{\rho}\frac{\partial \psi}{\partial x} \tag{15}$$

and the dimensionless temperature and species distributions defined by:

$$\theta = \frac{T_\infty - T}{T_\infty - T_s} \quad \text{and} \quad \phi = \frac{C_\infty - C}{C_\infty - C_s} \tag{16}$$

the similarity variables are given in the following forms:

$$\eta = c_1 x^{-1/4} Y \tag{17}$$

$$\psi = c_2 x^{3/4} f(\eta), \ \theta = \theta(\eta) \ \text{and} \ \phi = \phi(\eta) \tag{18}$$

where η is the Blasius similarity variable and Y is the Howarth-Dorodnitsyn variable given by:

$$Y = \int_0^y \frac{\rho}{\rho_s} dy \tag{19}$$

The coefficients c_1 and c_2 in Equations (17) and (18) are given respectively by:

$$c_1 = \left(\frac{g\rho_s^2}{4\mu_s^2}\right)^{1/4} \quad \text{and} \quad c_2 = \left(\frac{g\mu_s^2}{4\rho_s^2}\right)^{1/4} \tag{20}$$

where quantities with the subscript *s* represent values at the solid-liquid interface. In terms of the similarity variables, the governing system reduces to the following set of ordinary differential equations:

$$\left(\frac{\rho}{\rho_s} f''\right)' - 2(f')^2 + 3ff'' + 1 - \frac{\rho_\infty}{\rho} = 0 \tag{21}$$

$$\left(\frac{\rho}{\rho_s}\theta'\right)' + 3\,\mathrm{Pr}\, f\theta' = 0 \tag{22}$$

$$\left(\frac{\rho}{\rho_s}\phi'\right)' + 3Scf\phi' = 0 \tag{23}$$

where for a given binary system, the Prandtl number and Schmidt number have been assumed constant as a first approximation. The boundary conditions for the above set of equations are:

$$f'(0) = 0 \quad \text{and} \quad \theta(0) = \phi(0) = 1 \tag{24}$$

$$f(0) = \frac{1}{3Sc}\frac{C_s(a-1)}{1-C_s}[-\phi'(0)] \tag{25}$$

$$f'(\infty) = \theta(\infty) = \phi(\infty) = 0 \tag{26}$$

where Equation (25) represents the condition at the moving dissolution front and the superscript prime denotes total derivative with respect to η. Equations (21)-(23) can be integrated simultaneously with respect to η with the initial conditions given by Equation (24) and (25). However, the initial values for f''(0), θ'(0), and ϕ'(0) are unknown and need to be guessed to start the integration. An iterative technique, using the modified Newton-Raphson shooting scheme, was employed to correct the initial guesses for these values. Equations (21)-(23) were integrated numerically from $\eta = 0$ to $\eta = \eta_\infty$ (a finite approximation for $\eta = \infty$) using the IMSL Adams-Gear subroutine for stiff equations. This IMSL subroutine uses the fifth-order backward differentiation formula (BDF) method and variable stepsize. Some initial calculations were done by varying η_∞ to determine its effect on the solutions. It was found that for η_∞= 250 the solutions stabilized to 5 digits. The computations were started using a small value of η_∞ (say, 50 or smaller) and the value was successively increased until the boundary conditions given by Equation (26) were satisfied within a specified tolerance, ε (say, 10^{-4}). The values of f''(0), θ'(0), and ϕ'(0) so determined were used to calculate the transport quantities and the local dissolution rate.

3.2 Rate of Dissolution

An expression for the local dissolution rate can be derived from Equations (6), (9), (16) and (17) in terms of the dimensionless concentration gradient ϕ'(0) at the solid-liquid interface. This is:

$$v_s = \frac{[(1-a)C_s]^{3/4}}{\sqrt{2}(1-C_s)x}Gr_x^{1/4}[-\phi'(0)] \tag{27}$$

where Gr_x is the local Grashof number defined as:

$$Gr_x = \frac{g(1-a)C_s x^3}{\nu_s^2} \tag{28}$$

For a vertical substrate having a total length of L, the average dissolution rate is:

$$\bar{v}_s = \frac{1}{L}\int_0^L v_s dx \tag{29}$$

Substituting Equations (27) and (28) into Equation (29):

$$\bar{v}_s = \frac{2\sqrt{2}[(1-a)C_s]^{3/4}D}{3(1-C_s)L}Gr_L^{1/4}[-\phi'(0)] \tag{30}$$

where Gr_L is the overall Grashof number defined by:

$$Gr_L = \frac{g(1-a)C_s L^3}{\nu_s^2} \tag{31}$$

From Equations (27) and (30), a dissolution rate constant can be introduced as:

$$V_0 = \frac{[(1-a)C_s]^{3/4}}{1-C_s}[-\phi'(0)] \tag{32}$$

In terms of V_0, the local and the average dissolution rates can be expressed respectively in the following form:

$$\frac{v_s x}{\nu_s} = \frac{V_0 Gr_x^{1/4}}{\sqrt{2}Sc} \quad \text{and} \quad \frac{\bar{v}_s L}{\nu_s} = \frac{2\sqrt{2}V_0 Gr_L^{1/4}}{3Sc} \tag{33}$$

The problem thus boils down to determining the dissolution constant, V_0. Once the value of V_0 is obtained, the local and the average dissolution rates can be calculated.

For the special case under consideration, the ambient pool is a pure molten aluminum, i.e., $C_\infty = 0$ or $a = 0$. Equation (32) reduces to:

$$V_0 = \frac{C_s^{3/4}}{1-C_s}[-\phi'(0)] \tag{34}$$

From Equations (21)-(26), it can be shown that $\phi'(0)$ is a function of d, Sc, Pr, C_s, and $\beta_m \Delta T$. It follows that for a given binary system, the dissolution constant, V_0, is dependent only on the saturated concentration, C_s, and the thermal buoyancy force, $\beta_m 3\Delta T$.

4. RESULTS AND DISCUSSION

Numerical calculations have been performed for an iron-aluminum system over the interfacial temperature range of 1000K ≤ T_s ≤ 1200K for which the substrate-to-solvent density ratio varies from 0.31 to 0.30, the Schmidt number varies from 130 to 60, and the Prandtl number varies from 0.014 to 0.010. The calculated velocity, temperature, and concentration profiles for the case of T_s = 1100K are shown in Figures 2 to 4, respectively, with the thermal buoyancy force as a parameter. For all cases shown in Figure 2, the value of f' increases from zero at the solid-liquid interface (i.e., $\eta = 0$) to a maximum value at a location close to the edge of the concentration boundary layer (see Figure 4). It then decreases to zero toward the edge of the velocity boundary layer. The maximum value of f' increases as the thermal buoyancy force is increased. It should be noted that the maximum value of f' also increases with the saturated concentration of the substrate at the dissolution front. The latter quantity, in turn, increases with the saturated temperature. Due to space limitation, however, this is not shown in the figure.

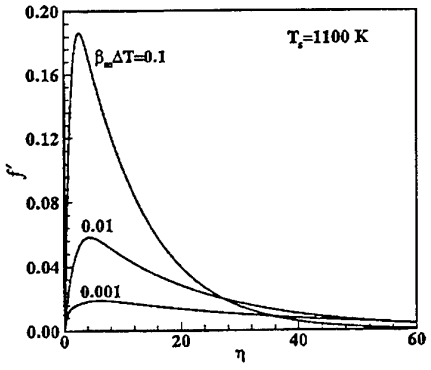


Figure 2. Modified axial velocity profiles for an aluminum-iron (Al-Fe) system at T_s=1100 K.

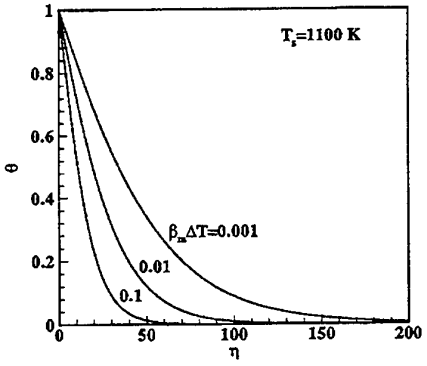


Figure 3. Distribution of modified temperature for an aluminum-iron (Al-Fe) system.

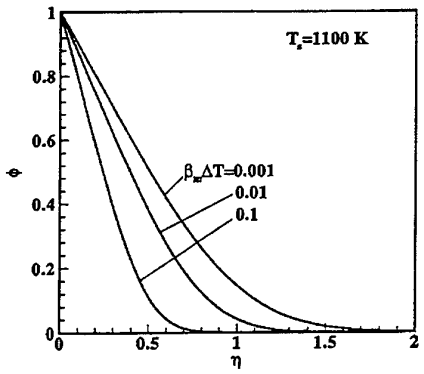


Figure 4. Distribution of modified mass fraction for an aluminum-iron (Al-Fe) system at T_s=1100 K.

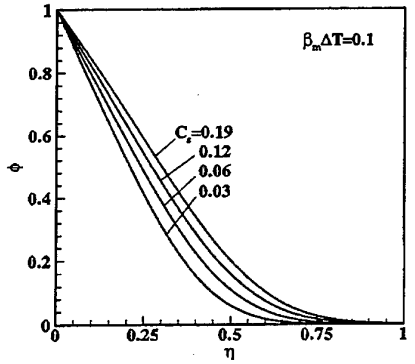


Figure 5. Distribution of modified mass fraction for an aluminum-iron (Al-Fe) system at $\beta_m\Delta T$=0.1.

For all cases shown in Figure 3, the dimensionless temperature decreases monotonically with η from unity at the solid-liquid interface (i.e., η = 0) to zero at the edge of the thermal boundary layer. The dimensionless temperature profile is a strong function of the thermal buoyancy force. As the latter quantity is increased, the thermal boundary layer thickness decreases, resulting in a larger temperature gradient and thus a higher heat transfer at the solid-liquid interface. Note from Figures 2 and 3 that the thermal boundary layer is thicker than the velocity boundary layer as expected for small-Prandtl-number fluids. The dimensionless concentration also decreases monotonically with η from unity at the solid-liquid interface to zero at the edge of the concentration boundary layer. As the thermal buoyancy force is increased, the concentration boundary layer thickness decreases, resulting in a larger concentration gradient and thus a higher mass transport at the solid-liquid interface. Note from Figures 2 and 4 that the concentration boundary layer is considerably thinner than the velocity boundary layer as expected for small-Schmidt-number fluids. Figure 5 depicts the concentration profiles with the saturated concentration as a parameter, which changes from 0.03 to 0.19, corresponding to a variation in the saturated temperature from 1000 K to 1300 K. In this figure, the thermal buoyancy force is fixed constant. For all cases considered, the concentration boundary layer is very thin. The dimensionless concentration decreases monotonically from unity at the solid-liquid interface to zero at the edge of the concentration boundary layer. As the saturated concentration is increased, the dimensionless concentration at a given location η increases, resulting in a smaller concentration gradient at the dissolution front. Physically, this is due to the blowing effect at the solid-liquid interface induced by the dissolution process. Note from Equation (34) that the rate of dissolution depends not only on the concentration gradient at the dissolution front but also on the saturated concentration itself. As the saturated concentration is increased, the rate of dissolution actually increases, although the concentration gradient at the wall decreases.

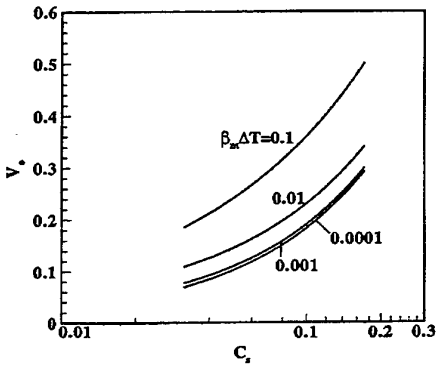


Figure 6. Numerical data for the dissolution constant for an aluminum-iron (Al- Fe) system.

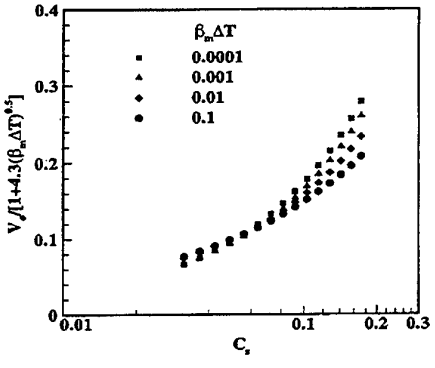


Figure 7. Normalized data for the dissolution constant for an aluminum-iron (Al-Fe) system.

Based on the numerical results obtained for the iron-aluminum system, the dependence of the dissolution constant on the saturated concentration and the thermal buoyancy force is shown in Figure 6, which is presented in a semi-log plot. The dissolution constant is a strong function of both parameters. For a given thermal buoyancy force, the dissolution constant increases considerably with an increase in the saturated concentration. On the other hand, at a given saturated concentration, the dissolution constant decreases with a decrease in the thermal buoyancy force. For values of $\beta_m \Delta T$ less than 0.001, the dissolution constant approaches to its lower limit, having the same value as that due to mass transport alone, similar to those reported by Cheung et al. [6,7]. Note that for all cases shown in the figure, the dissolution constant approaches asymptotically to zero as the saturated concentration becomes very small. An attempt has also been made to single out the effects of the thermal buoyancy force by merging the various curves for the dissolution constant. The results are presented in Figure 7 where the dissolution constant is being divided by the specified function of the thermal buoyancy force as shown. The various numerical data merge very nicely into a single curve for saturated concentration less than 0.1. At higher values of C_s, however, the numerical data appear to be quite scattered, indicating a different dependence of the dissolution rate on the thermal buoyancy force.

5. CONCLUSIONS

1. For a binary metallic system, the dissolution heat and mass transport processes are controlled by six key dimensionless parameters. These include the saturated concentration of the substrate at the dissolution front, the thermal buoyancy force, the degree of saturation, the Schmidt number, the Prandtl number, and the density ratio of the substrate and the solvent.
2. Both the local and the average rates of dissolution can be conveniently described in terms of the dissolution constant given by Equation (34). Once the value of the dissolution constant is known, the local and the average dissolution rates can be uniquely determined.
3. For a given binary metallic system with zero degree of saturation in the ambient pool, the dissolution constant depends only on the thermal buoyancy force and the saturated concentration of the substrate at the dissolution front.
4. During dissolution of a vertical iron plate in a pool of molten aluminum, the effects of the thermal buoyancy force on the rate of dissolution is as important as the effects of the saturated concentration of the substrate. To realistically predict the rate of dissolution, the temperature-induced flow needs to be considered in addition to the concentration-induced flow.

REFERENCES

1. M. Niinomi and Y. Ueda, Trans. Japan Institute of Metals, Vol. 23, pp. 709-717 (1982).
2. V. I. Dybkov, J. Material Science, Vol. 25, pp. 3615-3633 (1990).
3. P. k. Gairola, R. K. Tiwari and A. Ghosh, Metallurgical Trans., Vol. 2, pp. 2123-2126 (1971).
4. M. Niinomi, Y. Ueda and M. Sano, Trans. Japan Institute of Metals, Vol. 23, pp. 780-787 (1982).
5. M. Niinomi, Y. Suzuki and Y. Ueda, Trans. Japan Institute of Metals, Vol. 25, pp. 429-439 (1984).
6. F. B. Cheung, B. C. Yang, D. Li, D. H. Cho and M. J. Tan, AIChE Symposium Series, No. 295, Vol. 84, pp. 396-403 (1993).
7. F. B. Cheung, B. C. Yang, S. W. Shiah, D. H. Cho and M. J. Tan, ASME Proc., HTD Vol. 281, pp. 43-49 (1994).
8. S. W. Shiah, B. C. Yang, F. B. Cheung and Y. C. Shih, Int. J. Heat Mass Transfer, Vol. 41, pp. 3759-3769 (1998).

HEAT AND MASS TRANSFER IN FREE SURFACE FLOWS WITH SOLIDIFICATION

A.V. Kuznetsov
Dept. of Mechanical & Aerospace Engineering
North Carolina State University, Campus Box 7910, Raleigh, NC 27695-7910, USA
E-mail: avkuznet@eos.ncsu.edu; Fax: (919) 515-7968

Keywords: solidification, free surface flow, binary alloy, macrosegregation

ABSTRACT. The objective of this paper is to discuss the theory of free surface flows with solidification. This type of open-channel flows is relevant to a number of important manufacturing processes, such as the horizontal continuous casting of carbon steel. Since carbon steel is a binary alloy, in formulating a mathematical model in addition to accounting for fluid flow and heat transfer, it is also necessary to account for the solute transport and for the two-phase region (the mushy zone) effects. Difficulties of the theory are discussed.

1. INTRODUCTION

Classical free surface flows received considerable attention in the literature. A good overview on open-channel flows is given in [1]. Both analytical and numerical investigations of open-channel flows are presented in [2-4]. However, open channel flows with solidification have not received so far sufficient attention. This gap needs to be filled, because these flows are relevant to a number of important industrial applications, such as the strip casting of carbon steel.

In recent years, there has been a number of papers devoted to modeling of the heat transfer and fluid flow for different schemes of both vertical [5-9] and horizontal [10-14] strip casting processes. These papers present extensive investigations of both fluid flow and heat transfer in the solidifying strip. However, further insight into this process is needed, such as investigation of coupling flow and heat transfer with solute transport and accounting for the free surface behavior.

In recent publications a number of models for describing fluid flow of binary alloys during solidification have been proposed, mainly for the case when the flow is caused by natural convection. Derivation of the set of governing equations for the mushy zone based on the mixture theory approach was originally reported in [15, 16] and recently extended to account for microscopic phenomena in [17, 18]. The derivation of the set of governing equations based on a volume-averaging procedure is presented in [19-21]. An excellent review of different models with basic features of each model summarized is given in [22]. Very recently, a three-phase model (solid, liquid and gas phases) of the mushy zone has been proposed in [23, 24] and comparisons against the two-phase model have been carried out.

2. FORMULATION AND MATHEMATICAL MODEL

The schematic diagram of the problem is displayed in Fig. 1. We consider free surface flow of a binary alloy, for example, carbon steel, on a horizontal surface (casting table) which moves with a constant velocity, U. We assume that the binary alloy enters the moving surface with the fully developed relative velocity profile, where relative means relative to the surface. In the beginning of the computational domain the binary alloy is completely in the liquid state, that is its temperature is above the liquidus temperature. A constant heat flux is withdrawn from the surface, and this causes solidification of the alloy as it flows downstream. At the end of the computational domain the alloy is completely solidified, and the solid strip leaves the moving surface with the same constant velocity, U. This process is an example of a free surface flow with solidification. It also should be noted that in the beginning of the casting table, when $0 \le x \le X^*$, alloy at the free surface is in the liquid state while farther downstream, when $x > X^*$, alloy at the free surface is in the mushy state. In establishing the mathematical model for this process, it is assumed that the transport process is steady, two-dimensional and laminar; the properties of the solid and liquid phases are homogeneous and isotropic, the solid phase is stationary and rigid, no microporosity forms in the strip; the solid and liquid in the mushy zone are in local

thermal and phase equilibrium, the thermophysical properties are constant, but may be different for liquid and solid phases; heat transfer by radiation and convection from the free surface is negligible; and that the thin layer approximation can be invoked.

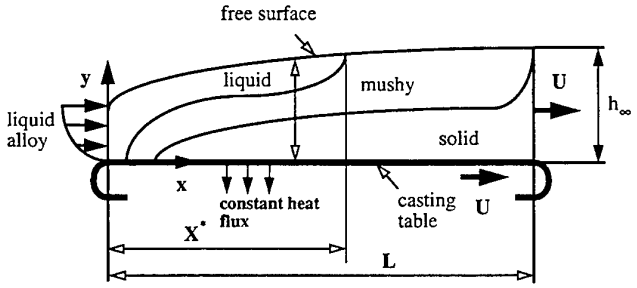


Fig. 1. Schematic diagram of free surface flow with solidification

Under the present set of assumptions, the governing equations presented in Ganesan and Poirier [19], Poirier et al. [20] and Beckermann and Viskanta [25] are parabolized and put into the following form:

2.1 Momentum Equation

$$\frac{\rho_L}{\varepsilon}U\frac{\partial u}{\partial x}+\frac{\rho_L}{\varepsilon^2}\left[u\frac{\partial u}{\partial x}+v\frac{\partial u}{\partial y}\right]=-\frac{\partial p}{\partial x}+\frac{\mu_L}{\varepsilon}\frac{\partial^2 u}{\partial y^2}-\left(\frac{\mu_L}{K}+\frac{\rho_L F}{K^{1/2}}|u|\right)u \tag{1}$$

where

$$K=K_0\frac{\varepsilon^3}{(1-\varepsilon)^2} \tag{2}$$

$$F=0.13\varepsilon^{-3/2} \tag{3}$$

2.2 Continuity Equation

$$U\frac{\partial}{\partial x}[\rho_L\varepsilon+\rho_S(1-\varepsilon)]+\rho_L\frac{\partial u}{\partial x}+\rho_L\frac{\partial v}{\partial y}=0 \tag{4}$$

2.3 Energy Equation

$$[\varepsilon\rho_L c_L+(1-\varepsilon)\rho_S c_S]U\frac{\partial T}{\partial x}+\rho_L c_L\left[u\frac{\partial T}{\partial x}+v\frac{\partial T}{\partial y}\right]=\frac{\partial}{\partial y}\left([\varepsilon k_L+(1-\varepsilon)k_S]\frac{\partial T}{\partial y}\right)-\rho_L\Delta h\,U\frac{\partial \varepsilon}{\partial x} \tag{5}$$

2.4 Solute Conservation Equation

The form of the solute conservation equation which is usually utilized in computations of the solidification of binary alloys includes both the average concentration of the solute and the concentration of the solute in the liquid phase [25]. For the case of the strong forced convection, however, this form of the solute conservation equation is found numerically unstable. Therefore in the present study we utilize the form of the solute conservation equation suggested in [20] which contains only the concentration of the solute in the liquid phase:

$$[\rho_L\varepsilon+\kappa\rho_S(1-\varepsilon)]U\frac{\partial C_L}{\partial x}+\rho_S C_L(1-\kappa)U\frac{\partial \varepsilon}{\partial x}+\rho_L\left[u\frac{\partial C_L}{\partial x}+v\frac{\partial C_L}{\partial y}\right]=\rho_L\frac{\partial}{\partial y}\left[\varepsilon D_L\frac{\partial C_L}{\partial y}\right] \tag{6}$$

To complete formulation of the mathematical model, a pertinent assumption for the pressure field is required. For this free surface flow, a hydrostatic pressure distribution is assumed over the layer thickness:

$$p = \rho_L g[h(x) - y] \tag{7}$$

After determining C_L from Equation (4), the mass of the solute per unit volume of the mixture can be found as:

$$\overline{\rho C} = \rho_S(1-\varepsilon)C_S + \rho_L \varepsilon C_L = [\rho_S(1-\varepsilon)\kappa + \rho_L \varepsilon]C_L \tag{8}$$

In the present study the solidus and liquidus curves are approximated by the linear relationships:

$$C_L = (T - T_p)/\Gamma \qquad \text{for} \qquad 0 < \varepsilon < 1 \tag{9}$$

$$C_S = \kappa C_L \qquad \text{for} \qquad 0 < \varepsilon < 1 \tag{10}$$

From Equations (8)-(10) it follows that the local liquid fraction, ε, can be determined from the equation:

$$\varepsilon(T, \overline{C}) = \frac{\overline{\rho C} - \rho_S \kappa (T - T_p)/\Gamma}{(\rho_L - \rho_S \kappa)(T - T_p)/\Gamma} \tag{11}$$

Boundary conditions for Equations (1), (4)-(6) can be summarized as:

$$T = T_{in},\ C_L = C_{in},\ u = u_{in},\ v = v_{in} \qquad \text{at x=0} \tag{12}$$

At the boundary y = 0:

$$[\varepsilon k_L + (1-\varepsilon)k_S]\frac{\partial T}{\partial y} = q'',\ \frac{\partial C_L}{\partial y} = 0,\ u = 0,\ v = 0 \qquad \text{at y = 0} \tag{13}$$

$$\frac{\partial T}{\partial y} = 0,\ \frac{\partial C_L}{\partial y} = 0,\ \frac{\partial u}{\partial y} = 0,\ \frac{dh}{dx}(u + U) = v \qquad \text{at y = h(x)} \tag{14}$$

In the numerical procedure, the last condition in Equation (14) is replaced by the equivalent condition of conservation of mass flow, i.e.:

$$\int_0^{h(x)} \{[\varepsilon \rho_L + (1-\varepsilon)\rho_S]U + \rho_L u\} dy = \rho_S U h_\infty \tag{15}$$

Equation (15) is obtained by integrating the continuity equation, Equation (4), from 0 to h with respect of the variable y and utilizing the last condition in Equation (14). In obtaining Equation (15) it is additionally assumed that the metal at the free surface is completely liquid. The case when the metal at the free surface becomes mushy is discussed later on.

3. DIFFICULTIES OF MODELING OF FREE SURFACE FLOWS WITH SOLIDIFICATION

3.1 Analysis Of Conservation Principals After Free Surface Starts To Solidify

As it is shown in Fig. 1, at a certain position on the casting table, namely, at $x = X^*$, metal at the free surface of solidifying strip changes form the completely liquid to the liquid-solid (mushy) state. From this point on, for $x > X^*$, there are only two zones in the strip: the solid zone and the mushy zone. In formulation of the

mathematical model given by Equations (1), (4)-(6) it is assumed that the solid phase, including the solid "matrix" in the mushy zone, is rigid.

The solute transport equation, Equation (6), requires a special analysis for the case when the metal at the free surface becomes mushy (the position at the casting table where is happens is denoted as X^*). Equation (6) can be recast as:

$$\frac{\partial}{\partial x}\left[U\overline{\rho C}\right]+\frac{\partial}{\partial x}\left[u\rho_L C_L\right]+\frac{\partial}{\partial y}\left[v\rho_L C_L\right]=\rho_L\frac{\partial}{\partial y}\left[\varepsilon D_L\frac{\partial C_L}{\partial y}\right] \tag{16}$$

From the physical point of view, Equation (16) means that the mass of the solute in a unit volume changes due to relative motion of the melt in the strip and due to solute diffusion in the melt.

Consider mass flow rate of the solute through a cross-section of the strip. For the obvious reasons, the amount of solute which passes a cross-section of the strip in x-direction per unit time must be the same at any cross-section of the strip. Integrating Equation (16) from 0 to h(x) and utilizing Equation (15) and boundary conditions given by Equations (13) and (14) result in the following equation:

$$\frac{\partial}{\partial x}\int_0^{h(x)}\left[U\overline{\rho C}+u\rho_L C_L\right]dy=-U\frac{dh}{dx}C_L\rho_L(1-\varepsilon)\left(1-\frac{\rho_S}{\rho_L}\kappa\right)_{y=h(x)} \tag{17}$$

The physical meaning of the integral on the left-hand side of Equation (17), $\int_0^{h(x)}\left[U\overline{\rho C}+u\rho_L C_L\right]dy$, is the mass flow rate of the solute through a cross section of the strip whose position is characterized by the coordinate x. This solute mass flow rate must be the same for any value of the coordinate x. This requirement is satisfied as long as $\varepsilon = 1$ at $y = h(x)$ because for $\varepsilon = 1$ the right-hand side of Equation (17) equals zero. This requirement fails for $\varepsilon < 1$, that is when the metal at the free surface becomes mushy. This happens because, according to our model, the motion of the free surface occurs due to the flow of liquid metal at the free surface. According to Equation (8), the equilibrium concentration of the solute in the liquid metal is higher than in the solid plus liquid mixture at the same temperature. When the metal at the free surface becomes mushy, the amount of solute transported by the moving free surface exceeds the amount of solute which can be transported according to the equilibrium relationship.

A similar problem appears in considering flow of mass through a cross-section of the strip. By integrating the continuity equation, Equation (4), from 0 to h(x) and utilizing the boundary condition given by the last of Equations (13) the following is obtained:

$$\frac{\partial}{\partial x}\int_0^{h(x)}\left\{\left[\varepsilon\rho_L+(1-\varepsilon)\rho_S\right]U+\rho_L u\right\}dy=-\frac{dh}{dx}U\rho_L(1-\varepsilon)\left(1-\frac{\rho_S}{\rho_L}\right) \tag{18}$$

The physical meaning of the integral on the left-hand side of Equation (18), $\int_0^{h(x)}\left\{\left[\varepsilon\rho_L+(1-\varepsilon)\rho_S\right]U+\rho_L u\right\}dy$, is the mass flow rate through a cross section of the strip. According to Equation (18), the conservation of mass flow through a cross section of the strip is satisfied as long as $\varepsilon = 1$ at the free surface. This condition fails when the metal at the free surface becomes mushy.

Though the conservation of mass flow through a cross-section of the strip can be saved by replacing the boundary condition given by the last Equation (14) with the following boundary condition at $y = h(x)$:

$$\frac{dh}{dx}\left\{\rho_L u+\left[\rho_L\varepsilon+\rho_S(1-\varepsilon)\right]U\right\}=\rho_L v \tag{19}$$

It is still impossible to fix the problem with conservation of the flow of the solute which appears for $x > X^*$. Therefore for $x > X^*$ the mathematical model given by Equations (1) and (4)-(6) becomes invalid and it is necessary to switch to another mathematical model.

For $x > X^*$ the flow relative to the solidifying matrix in x-direction is very small because of small permeability of the mushy zone. It is assumed that this flow can be neglected. Therefore the only motion in the strip is the motion caused by shrinkage of the metal in the mushy zone. It is assumed that this contraction motion causes deformation of the solid phase in the mushy zone and occurs by motion of both the solid and liquid phases. This results in the following forms of the x-momentum, continuity, energy, and solute conservation equations, respectively:

$$u = 0 \tag{20}$$

$$U\frac{\partial}{\partial x}[\rho_S(1-\varepsilon)+\rho_L\varepsilon] + \frac{\partial}{\partial y}\{[\rho_S(1-\varepsilon)+\rho_L\varepsilon]v\} = 0 \tag{21}$$

$$[\varepsilon\rho_L c_L + (1-\varepsilon)\rho_S c_S]U\frac{\partial T}{\partial x} + [\varepsilon\rho_L c_L + (1-\varepsilon)\rho_S c_S]v\frac{\partial T}{\partial y} = \frac{\partial}{\partial y}\left([\varepsilon k_L + (1-\varepsilon)k_S]\frac{\partial T}{\partial y}\right) - \rho_L \Delta h\, U\frac{\partial \varepsilon}{\partial x} \tag{22}$$

$$U\frac{\partial}{\partial x}(\overline{\rho C}) + \frac{\partial}{\partial y}(v\overline{\rho C}) = 0 \tag{23}$$

Equations (20)-(23) must be solved subject to the following boundary conditions:

At the boundary y = 0:

$$[\varepsilon k_L + (1-\varepsilon)k_S]\frac{\partial T}{\partial y} = q'',\ v = 0 \tag{24}$$

At the free surface y = h(x):

$$\frac{\partial T}{\partial y} = 0,\ \overline{C} = \text{const},\ \frac{dh}{dx}(u+U) = v \tag{25}$$

where

$$\overline{C} = \frac{\overline{\rho C}}{\rho_S(1-\varepsilon)+\rho_L\varepsilon} \tag{26}$$

is the average mass fraction of carbon in the solid-liquid mixture.

3.2 Diffusion Boundary Layer

According to the model utilized in this research, solute redistribution in the strip is governed by two processes: by convective transport and by diffusion of the solute in the liquid phase. As it is noted in Kuznetsov [27], among these two processes the dominating process is convection. It can be checked by comparison of the coefficients in the convective and diffusion terms in the dimensionless form of Equation (6). However, the diffusion of the solute in the liquid can result in an essential *local* redistribution of the solute in a *particular* part of the strip. To analyze this effect in the present investigation computations with accounting for the solute diffusion in the liquid phase are carried out.

Numerical simulations are performed using CRAY T90 supercomputer for carbon steel with carbon concentration $C_{in} = 0.6\%$, casting velocity $U = 0.15\,m/s$, heat flux at the casting table $q'' = 4.8\times10^{6}\ W/m^2$ and carbon diffusion coefficient in the liquid phase $D_L = 2\times10^{-9}\ m^2/s$. The physical domain is remapped to a rectangular computational domain by performing a pertinent transformation of the coordinates, as described in Kuznetsov [27, 28]. Governing equations are solved by starting from the inlet cross-section and marching in the x-direction. A very small step in the x-direction is utilized to insure the stability and accuracy of the results. The following thermophysical properties of the steel and geometrical and test data are utilized in the computations:

$$L=0.95\ m;\quad h_\infty = 0.007\ m;\quad T_{in} = 1813\,K;\quad T_p = 1799.3\,K;\quad C_{in} = 0.6\%;\quad C_E = 4.3\%;$$
$$\rho_L = 7200\,kg/m^3;\ \rho_S = 7600\,kg/m^3;\ k_L = 30\,W/(mK);\ k_S = 30\,W/(mK);\ c_L = 650\,J/(kgK);$$
$$c_S = 650\,J/(kgK);\quad \Delta h = 2.7\times10^{5}\,J/kg;\quad q'' = 4.8\times10^{6}\,W/m^2;\quad \nu_L = 10^{-6}\,m^2/s;$$
$$K_0 = 5.56\times10^{-11}\,m^2;\ \Gamma = -60.376\,K;\ \kappa = 0.3413 \qquad (27)$$

Figure 2 depicts distributions of the average concentration of carbon in the solidified strip near the casting table computed with different number of nodal points in y-direction for $C_{in} = 0.6\%$, U = 0.15 m/s, $q'' = 4.8\times10^{6}\ W/m^2$. Computations are carried out accounting for diffusion (solid curves: $D_L = 2\times10^{-9}\ m^2/s$) and neglecting diffusion (dotted curve: $D_L = 0\ m^2/s$). It can be seen that for all computed cases when diffusion was taken into account, near the casting table there is a narrow region, a kind of a boundary layer, which is considerably depleted of the solute.

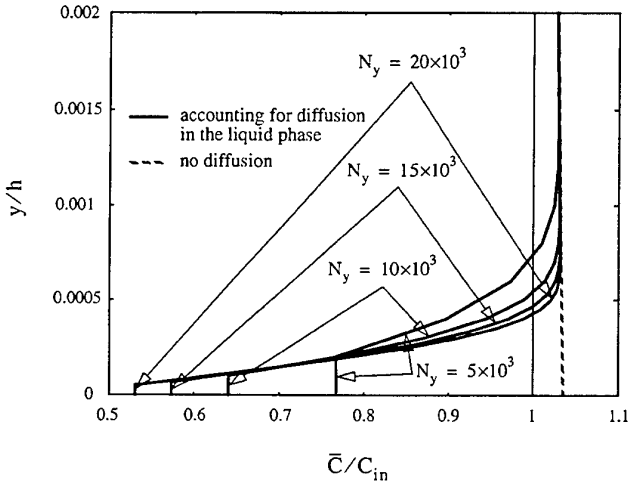


Fig. 2. Distributions of average concentration of carbon in the solidified strip near the casting table computed with different number of nodal points in the y-direction

This *diffusion* boundary layer has recently been numerically found by several authors [26], [28, 29]. According to [26], this diffusion boundary layer is a result of the solute diffusion in the liquid near an impermeable wall. Consider the situation when metal in contact with the casting table is in the mushy state. Intensive cooling from the casting table leads to a strong positive temperature gradient in the mushy region. Since temperature and liquid concentration in the mushy zone are coupled through Equation (9), and the value of Γ is negative, this positive temperature gradient causes negative concentration gradient in the interdendritic liquid. Thus carbon concentration in the liquid phase decreases from a maximum at the casting table to the inlet concentration outside the mushy zone. This concentration gradient in the liquid phase causes solute diffusion from the border with the casting table towards the inner part of the strip. The border between the casting table and the strip is

modeled as an impermeable wall. For this reason, the outflow of the solute from the border with the casting table can not be compensated and the interdendritic liquid near the casting table has a lower carbon concentration than if there was no solute diffusion. The solid phase which forms from this interdendritic liquid is also depleted of the solute. This results in a lower average carbon concentration in a thin layer near the casting table. The width of this diffusion boundary layer is small due to large value of the Lewis number, $Le = \alpha_L / D_L$.

As it can be seen in Fig. 2, the solute concentration at the surface is not grid independent. As it is shown in Thevik and Mo [29], when the control-volume size in y-direction tends towards zero ($N_y \to \infty$), the average solute concentration at the surface, $\overline{C}$, tends towards κC_{in}. Diffusion boundary layer is not a numerical effect, it is an effect produced by the governing equations plus boundary conditions. This is not just a specific effect which appears in modeling of strip casting, it was also found numerically in modeling a conventional casting process [26]. On the other hand, no experimental evidence of such a considerable concentration drop at the casting surface has ever been found. This makes us to conclude that the equilibrium assumption, which is usually used in modeling solidification processes, fails in a small tiny region near the cooled wall. This equilibrium assumption is given in our model by Equations (9) and (10), and it in fact utilizes the equilibrium diagram to relate temperature and solute concentration in the mushy zone. According to our analysis, utilizing equilibrium diagram results in an unphysical concentration drop near the wall. Therefore, if accounting for the solute diffusion in the liquid phase is desirable, equilibrium relations given by Equations (9) and (10) should be replaced by the equations of nonequilibrium theory of solidification.

ACKNOWLEDGMENTS

The support provided by the North Carolina Supercomputing Center (NCSC) under an Advanced Computing Resources Grant and by the AvHumboldt Foundation is greatly appreciated.

NOMENCLATURE

- c specific heat at constant pressure [$J\,kg^{-1}\,K^{-1}$]
- C_L mass fraction of the solute (carbon) in the liquid phase
- C_S mass fraction of the solute in the solid phase
- $\overline{C}$ average mass fraction of the solute in the solid-liquid mixture, $\overline{\rho C}/[\rho_S(1-\varepsilon)+\rho_L\varepsilon]$
- C_E mass fraction of the solute in the eutectic
- D_L diffusivity of the solute in the interdendritic liquid [$m^2\,s^{-1}$]
- h height of the free surface [m]
- h_∞ strip thickness at the end of the casting table [m]
- k thermal conductivity [$W\,m^{-1}K^{-1}$]
- K permeability [m^2]
- K_0 permeability coefficient [m^2]
- L length of the casting table [m]
- p pressure [Pa]
- q'' heat flux to the casting table [$W\,m^{-2}$]
- T temperature [K]
- T_p melting temperature of the pure iron [K]
- v vertical velocity component [$m\,s^{-1}$]
- u relative (to the solidified matrix) horizontal velocity component [$m\,s^{-1}$]
- U withdrawing velocity [$m\,s^{-1}$]
- x horizontal coordinate [m]

X^* position at the casting table starting from which metal at the free surface becomes mushy [m]
y vertical coordinate [m]

Greek Symbols

α thermal diffusivity, $k/(\rho c)$ [$m^2 s^{-1}$]

Δh latent heat of solidification [$J\ kg^{-1}$]

ε volume fraction of liquid

Γ slope of liquidus line [K]

κ segregation coefficient, C_S / C_L

μ_L dynamic viscosity of liquid metal [$kg\ m^{-1}s^{-1}$]

ν_L kinematic viscosity of liquid metal [$m^2\ s^{-1}$]

ρ density [$kg\ m^{-3}$]

$\overline{\rho C}$ mass of the solute per unit volume of the solid-liquid mixture, $\rho_S(1-\varepsilon)C_S + \rho_L \varepsilon C_L$ [$kg\ m^{-3}$]

REFERENCES

1. V.T. Chow, *Open-channel hydraulics*, McGraw-Hill, NY (1959).
2. P. Garcia-Navarro, F. Alcrudo and J.M. Savirón, *J. Hydraulic Eng.*, v. 118, pp. 1359-1371 (1992).
3. S. Thomas, W.L. Hankey, A. Faghri and T. Swanson, *J. Heat Transfer*, v. 112, pp. 728-735 (1990).
4. M.M. Rahman, W.L. Hankey and A. Faghri, *Int. J. Heat Mass Transfer*, v. 34, pp. 103-114 (1991).
5. M. Shiomi, K. Mori and K. Osakada, *Proceedings of the Seventh International Conference on Modeling of Casting, Welding, and Advanced Solidification Processes VII*, pp. 793-800 (1995).
6. C.-M. Raihle, H. Fredriksson and S. Östlund, *Proceedings of the Seventh International Conference on Modeling of Casting, Welding, and Advanced Solidification Processes VII*, pp. 817-824 (1995).
7. S.M. Hwang and Y.H. Kang, *ASME Journal of Heat Transfer*, v. 117, pp. 304-315 (1995).
8. T. Saitoh, H. Hojo, H. Yaguchi and C.G. Kang, *Metallurgical Transactions*, v. 20B, pp. 381-390 (1989).
9. J.D. Hwang, H.J. Lin, W.S. Hwang and C.T. Hu, *ISIJ International*, v. 35, pp. 170-177 (1995).
10. P.J. Bradbury and J.D. Hunt, *Proceedings of the Seventh International Conference on Modeling of Casting, Welding, and Advanced Solidification Processes VII*, pp. 739-746 (1995).
11. S. Caron, E. Essadiqi, F.G. Hamel and J. Masounave, *Light Metals*, pp. 967-973 (1990).
12. R.K. Mallik and S.P. Mehrotra, *ISIJ International*, v. 33, pp. 595-604 (1993).
13. I. Jimbo and A.W. Cramb, *ISS Transactions*, v. 15, pp. 145-150 (1994).
14. M. Digruber, S. Haas and W. Schneider, *Proceedings of the Eighth International Conference on Modeling of Casting, Welding, and Advanced Solidification Processes VIII*, pp. 663-670 (1998).
15. W.D. Bennon and F.P. Incropera, *Int. J. Heat Mass Transfer*, v. 30, pp. 2161-2170 (1987).
16. P.J. Prescott, F.P. Incropera and W.D. Bennon, *Int. J. Heat Mass Transfer*, v. 34, pp. 2351-2359 (1990).
17. J. Ni and F.P. Incropera, *Int. J. Heat Mass Transfer*, v. 38, pp. 1271-1284 (1995).
18. J. Ni and F.P. Incropera, *Int. J. Heat Mass Transfer*, v. 38, pp. 1285-1296 (1995).
19. S. Ganesan and D.R. Poirier, *Metallurgical Transactions*, v. 21B, pp. 173-181 (1990).
20. D.R. Poirier, P.J. Nandapurkar and S. Ganesan, *Metallurgical Transactions*, v. 22B, pp. 889-990 (1991).
21. J. Ni and C. Beckermann, *Metallurgical Transactions*, v. 22B, pp. 349-361 (1991).
22. R. Viskanta, *JSME Int. J., Series II 33*, pp. 409-423 (1990).
23. A.V. Kuznetsov and K. Vafai, *Int. J. Heat Mass Transfer*, v. 38, pp. 2557-2567 (1995).
24. A.V. Kuznetsov and K. Vafai, *Numerical Heat Transfer, Part A*, v. 29, pp. 859-867 (1996).
25. C. Beckermann and R. Viskanta, *PhysicoChemical Hydrodynamics*, v. 10, pp. 195-213 (1988).
26. Schneider, M.C. & Beckermann, C. 1995. Int. J. Heat Mass Transfer 38, 3455-3473.
27. A.V. Kuznetsov, *Int. J. Heat Mass Transfer*, v. 40, pp. 2949-2961 (1997).
28. A.V. Kuznetsov, *Numerical Heat Transfer, Part A*, v. 33, pp. 515-532 (1998).
29. H.J. Thevik and A. Mo, *Metallurgical Transactions*, v. 28B, pp. 665-669 (1997).

Ahmad, G.E. 751
Ahn, J. 212
Ahn, Y. 557
Akisawa, A. 759
Akisawa, A. 1145
Allcock, H.R. 1483
Altraide, A. 191
Amazouz, M. 917
Amazouz, M. 1084
An, E. 355
An, E. 367
Anderson, R. 1033
Ando, D. 1226
Antohi, C. 866
Aoki, H. 748
Aoyama, S. 843
Aoyama, S. 852
Arlabosse, P. 923
Asano, H. 1122
Asano, H. 1438
Assassa, G.M.R. 766
Baba, A. 1710
Bae, S.C. 1153
Bai, Q. 521
Bai, W.D. 1703
Bartoli, C. 247
Behnia, M. 873
Benali, M. 917
Benali, M. 1412
Benning, L. 1483
Bhattacharyya, S. 1353
Bi, Q.C. 393
Bi, Q.C. 438
Bingue, J.P. 1266
Bockhorn, H. 1573
Boral, A.A. 888
Borisov, I. 422
Borzenko, V.I. 512
Bossi, L. 239
Buchner, H. 1573
Bull, S.R. 18
Cai, J.Y. 416
Cai, S. 1651
Cannon, A.M. 1483
Cao, X.Y. 1281
Cao, X.Y. 1603
Cao, Z.H. 1651
Carrere-Gee, C. 923
Casey, R.T. 1524
Cen, K.F. 1281
Cen, K.F. 1333
Cen, K.F. 1566
Cen, K.F. 1586
Cen, K.F. 1603
Chai, L.H. 343
Chan, A.M.C. 408
Chan, C.K. 1508
Chan, C.K. 1515
Chandratilleke, T.T. 191
Chang, L.J. 1002
Chazly, N.E. 826
Chen, C.T. 636
Chen, D.Z. 1595
Chen, G.H. 910
Chen, G.H. 1048
Chen, G.J. 588
Chen, G.Y. 1553
Chen, H.P. 1496
Chen, J. 1397
Chen, M.J. 1581
Chen, Q.H. 379
Chen, T.K. 393
Chen, T.K. 416
Chen, X. 270
Chen, Y. 1427
Chen, Y. 1433
Chen, Y. 1632
Chen, Z.H. 355
Chen, Z.H. 367
Chen, Z.H. 598
Chen, Z.Q. 505
Chen, Z.Q. 529
Cheng, K. 1212
Cheng, P. 505
Cheng, P. 529
Cheng, P. 1192
Cheng, X.H. 1728
Cheng, Y.C. 1476
Cheung, C.S. 1397
Cheung, F.B. 888
Cheung, F.B. 1289
Chi, Y. 1333
Chi, Z.H. 1586
Chiu, H.H. 1640
Cho, H.K. 384
Choi, M. 1532
Chou, C.S. 474
Chou, T.C. 1257
Chow, A. 680
Chua, H.T. 1145
Chung, B.T.F. 581
Chung, J.D. 1532
Chung, K.C. 636
Chung, S.K. 229

Ciocan, V. 866
Cote, R. 1084
Cui, W.Z. 379
Cui, Y.B. 1662
Cunnington, G.R. 613
Da Veiga, V.R. 1114
Dai, X.W. 1632
Davis, S.B. 1686
Deeb, S.E. 826
Deng, P.G. 1217
Deng, X.H. 1217
Denner, H.D. 1212
Diaz, G. 940
Ding, L.S. 650
Dong, Y.X. 980
Druck, H. 740
Du, D.X. 658
Du, D.X. 665
Du, J.H. 490
Dubble, E.H. 1007
Duluc, M.C. 127
Eder, A. 1273
Eder, A. 1296
Eisen, S. 1366
El-Kotb, M. 826
Elphick, I.G. 408
Eschenbacher, J.F. 262
Fagguani, S. 247
Fan, M.X. 1566
Fan, W.C. 1340
Fedkin, M.V. 1483
Fei, Q. 1002
Feng, B. 1560
Feng, Y. 1208
Feng, Z. 643
Feng, Z.X. 1646
Fiebig, M. 598
Francois, M.X. 127
Francois, M.X. 1164
Fridman, A. A. 96
Fridman, A.A. 1266
Fu, H.L. 497
Fu, X.Y. 1033
Fudym, O. 923
Fujii, I. 1540
Fujii, T. 1122
Fujii, T. 1438
Fujioka, K. 628
Fujita, Y. 521
Fujiyoshi, M. 1404
Fushimi, J. 399
Gale, T.K. 1686
Ganzha, V.L. 688
Gao, X. 1566
Garner, S.D. 1007
Gavotti, N. 539
Gerlach, C. 1273
Gerlach, C. 1296
Goldstein, R.J. 206
Gong, L.H. 1198
Gopinath, A. 1170
Gori, F. 239
Grandum, S. 860
Groll, M. 708
Groll, M. 957
Groll, M. 1130
Gu, F. 1305
Gu, Z.Z. 1651
Guo, F.Z. 1203
Guo, F.Z. 1208
Guo, T.M. 588
Guo, X.F. 1433
Guo, X.Q. 588
Guo, X.S. 1566
Guo, Y.C. 1508
Guo, Y.C. 1515
Guo, Z. 658
Guo, Z.Y. 118
Guy, C. 1412
Hahne, E. 740
Hamada, K. 843
Han, B. 206
Han, P. 270
Han, X. 1603
Hara, T. 1178
Haruki, N. 695
Haruki, N. 723
Haruki, N. 852
Haruki, N. 1138
Hatabaka, M. 288
Hawlader, M.N.A. 451
He, K.X. 680
Hein, D. 1347
Hetsroni, G. 72
Hetsroni, G. 255
Hiller, G. 1677
Hirashima, M. 564
Hirata, M 57
Hirata, Y. 628
Hisazumi, Y. 1122
Ho, C.J. 881
Hoffmann, S. 1573
Hofmann, M.A. 1483
Holden, C. 680
Honda, T. 1546
Horibe, A. 695
Horibe, A. 723
Horibe, A. 852

Horibe, A. 1138
Hosatte, S. 1084
Hoshi, A. 796
Hsiau, S.S. 474
Hsieh, S.S. 1015
Hsu, C.T. 505
Hsu, C.T. 731
Hu, G. 1333
Hu, W. 279
Huang, J. 1002
Huang, S.H. 821
Huang, X. 355
Huang, X. 367
Huang, X.Y. 497
Hugron, I. 1412
Hui, C.K.P. 1090
Hussien, H.M.S. 751
Hwang, I.J. 295
Hwang, Y.W. 965
Hyuga, T. 521
Ichimiya, K. 184
Inaba, H. 695
Inaba, H. 723
Inaba, H. 852
Inaba, H. 1138
Inada, T. 860
Inatomi, Y. 302
Ipek, O. 778
Ishizuka, M. 321
Iwai, H. 161
Izumi, M 399
Jang, K.J. 1015
Jebali, F. 127
Jegla, Z. 1624
Jeong, U.C. 295
Jerbi, F.J. 1164
Jiang, X.J. 1586
Jiang, Y. 788
Jiang, Y. 804
Jiang, Y. 1059
Jiang, Y. 1066
Joko, M. 262
Jones, J.C. 1313
Jordan, M. 1273
Jung, I.S. 212
Kage, H. 932
Kakimoto, K. 302
Kalabin, E.V. 328
Kameda, K. 1138
Kaneda, M. 302
Kang, Y.B. 788
Kang, Y.B. 804
Kang, Y.M. 430
Kasagi, N. 972
Kashiwagi, T. 759
Kashiwagi, T. 1145
Kato, Y. 1546
Katsuta, M. 1153
Kaviany, M 32
Kawaguchi, Y. 716
Kellam, E.C. 1483
Kennedy, L.A. 96
Kennedy, L.A. 1266
Khalatov, A. 422
Khattab, N. 826
Kida, T. 1138
Kim, M. 557
Kim, M.O. 384
Kim, M.S. 965
Kim, Y.J. 295
Kimura, M. 843
Kimura, T. 1540
Klein, H.P. 1130
Komiya, A. 873
Koo, J.H. 1289
Koyama, S. 445
Kudra, T. 917
Kuge, K. 1546
Kumagai, S. 399
Kuo, J.T. 474
Kurosaki, Y 84
Kuwahara, K. 149
Kuwahara, K. 445
Kuznetsov, A.V. 896
Kwan, M.K. 731
Kwanka, K. 1347
Ladevie, B. 482
Ladevie, B. 923
Lam, W.C. 1404
Lazarescu, C.D. 866
Lecomte, D. 923
Lee, B.D. 650
Lee, J.S. 212
Lee, L. 1098
Lee, S.C. 613
Lee, T.H. 384
Lee, T.S. 1581
Lee, T.S. 1640
Leong, K.C. 497
Leung, D.Y.C. 1427
Leung, D.Y.C. 1553
Leutz, A. 759
Li, B.Q. 1433
Li, B.Q. 1722
Li, C.F. 255
Li, G.H. 1615
Li, H.B. 1433
Li, H.P. 270

Li, J. 335
Li, M. 1728
Li, P.W. 716
Li, Q. 1203
Li, Q. 1208
Li, Q.Y. 1615
Li, R. 355
Li, R.Y. 367
Li, X.Z. 1212
Li, Y.D. 1420
Li, Z. 658
Li, Z.W. 1388
Li, Z.Y. 177
Li, Z.Z. 1603
Li, Z.Z. 1646
Liang, J.T. 1184
Liao, G.X. 1340
Liao, H.Q. 1722
Lin, F. 1388
Lin, G.T. 821
Lin, H.H. 821
Lin, J.Y. 1041
Lin, R. 1360
Lin, W.Y. 1508
Linak, W.P. 1686
Ling, S.C. 1446
Liu, B.M. 451
Liu, C. 373
Liu, C.Y. 497
Liu, D.C. 1496
Liu, H. 1420
Liu, H.C. 1640
Liu, H.T. 1468
Liu, X.G. 1651
Liu, Y. 1305
Liu, Y. 1615
Liu, Y.F. 1591
Liu, Y.P. 1595
Liu, Y.W. 1212
Liu, Z.L. 1360
Liu, Z.T. 1397
Liu, Z.Y. 1054
Lloyd, A.C. 138
Lorenzine, M. 247
Lou, H. 1241
Lu, G.Q. 1192
Lu, S.S. 860
Lu, Y.Z. 1054
Lubiez, J.V. 1164
Luo, W.H. 1566
Luo, Y. 416
Luo, Y.H. 393
Luo, Z.Y. 1566
Lvov, S.N. 1483
Ma, W.M. 1305
Ma, Z. 581
Ma, Z.Y. 1333
Machida, K. 843
Madadnia, J. 349
Makino, T. 604
Malyshenko, S.P. 512
Mandel, H. 740
Martiny, M. 221
Maruyama, S. 873
Matsuno, Y. 932
Matsushita, M. 843
Mayinger, F. 1273
Mayinger, F. 1296
Mayinger, F. 1366
Mayinger, F. 1379
Mbarawa, M. 1524
McClain, R.L. 940
Mei, Y.G. 980
Meng, X.Z. 459
Meng, X.Z. 1159
Mertz, R. 708
Mertz, R. 957
Mettawee, E.S. 766
Meyer, J.P. 1076
Meyer, J.P. 1105
Meyer, J.P. 1114
Mi, J. 1609
Miller, A. 1033
Milton, B.E. 1524
Mo, J. 680
Mohamad, M.A. 751
Morford, R.V. 1483
Morin, M. 1412
Mosyak, A 72
Mosyak, A 255
Mujumdar, A.S. 910
Mujumdar, A.S. 932
Murayama, Y. 1546
Mutaf-Yardimci, O. 96
Nagayama, G. 672
Nakabe, K. 262
Nakamura, S. 1715
Nakata, T. 695
Nathan, G.J. 1609
Negishi, K. 564
Neo, E.C. 161
Ng, K.C. 1145
Ng, M.L. 1476
Nguyen, T.H. 349
Nguyen, T.V. 1453
Nie, J.H. 177
Nigmatulin, R 110
Nishio, S. 360

Nobuchika, K. 695
North, M.T. 573
Novellani, M. 466
Nursubyakto 191
Ofner, B. 1366
Ogura, H. 932
Oido, K. 628
Oka, M. 813
Okada, S.Y. 604
Olaru, I. 866
Oliveira, A.A.M. 32
Ooyatsu, N. 1710
Osa, N. 445
Ota, T. 199
Ozoe, H. 288
Ozoe, H. 302
Pacheco-Vega, A. 940
Paitoonsurikarn, S. 972
Pan, Y.K. 910
Pao, H.P. 1446
Park, G. 557
Park, G.C. 384
Park, G.C. 430
Park, K.S. 1532
Peng, X.F. 343
Petit, P.J. 1076
Polasek, F. 539
Poslushny, G. 1500
Prechtl, P. 1379
Qiu, J.R. 1560
Qiu, Y. 980
Que, X.C. 279
Quitard, M. 482
Raghavan, G.S.V. 1090
Ramsden, V. 349
Ren, B.Z. 1002
Ro, S.T. 965
Rong, S.X. 588
Rozenblit, R. 72
Sadhal, S.S. 229
Saenger, M. 1677
Saha, B.B. 1145
Saito, T. 84
Saitoh, T.S. 796
Saitoh, T.S. 1226
Saitoh, T.S. 1233
Sanchez, J.G. 1098
Santini, R. 466
Sato, K. 695
Sato, M. 748
Satoh, I. 84
Saveliev, A.V. 96
Saveliev, A.V. 1266
Saxena, S.C. 688
Schmidt, B. 708
Scholz, K.H. 1500
Schulz, A. 221
Seames, W.S. 1686
Sen, M. 940
Serizawa, A. 643
Shao, H. 279
Sharkawy, A.E. 826
Sheen, P.J. 949
Shen, B.X. 1496
Sheng, X.L. 650
Shevtsov, S. 422
Shi, M.H. 905
Shiah, S.W. 888
Shih, Y.C. 1289
Shimogori, M. 1710
Shoji, M. 335
Shu, Z.D. 1703
Smid, J. 474
So, R.M. 169
Soudarev, A. 1500
Stehlik, P. 1624
Stubington, J.F. 1662
Stubington, J.F. 1669
Sugimto, K. 1438
Sugiyama, T. 1024
Sumathy, K. 774
Sun, C.C. 1257
Sun, C.Y. 588
Sun, G.J. 1586
Sun, H. 650
Sun, J.Y. 1041
Sun, L.S. 1728
Sun, S.J. 1404
Sun, X.X. 1728
Suzuki, A. 759
Suzuki, H. 1024
Suzuki, K. 161
Suzuki, K. 262
Suzuki, Y. 972
Swanepoel, W. 1105
Swift, G.W. 2
Syred, N. 422
Tadrist, L. 466
Tagawa, T. 288
Tagawa, T. 302
Tagishi, A. 1715
Takahashi, K. 873
Takarayama, N. 1710
Takeguchi, S. 1153
Tan, G.H. 881
Tanaka, H. 360
Tao, W.Q. 177
Tian, F.J. 1433

Tomiyama, S. 695
Toriyama, K. 184
Trinh, E.H. 229
Tsai, H.H. 474
Tsai, Y.C. 1015
Tsuchimoto, N. 1438
Tsuruta, T. 672
Vanhorn, S.R. 1321
Vesely, S. 1500
Vigneault, C. 1090
Vinogradov, E. 1500
Vitali, J.A. 1321
Wakabayashi, H. 604
Wako, Y. 748
Wang, A.L.T. 1669
Wang, B.X. 343
Wang, B.X. 490
Wang, B.X. 665
Wang, C.Y. 1460
Wang, D.Q. 459
Wang, F. 1333
Wang, J. 598
Wang, J.C. 680
Wang, J.F. 1048
Wang, L.B. 980
Wang, N.N. 1250
Wang, Q.H. 1560
Wang, Q.W. 177
Wang, S. 118
Wang, S.P. 835
Wang, X. 905
Wang, X. 1122
Wang, X. 1489
Wang, X.S. 1340
Wang, Y. 1646
Wang, Z.G. 459
Wang, Z.G. 1159
Wang, Z.N. 701
Watanabe, C. 445
Watanabe, M. 335
Wei, C.Y. 1333
Wei, Q.D. 1651
Wei, X.J. 1483
Wendt, J.O.L. 1686
Weng, L.C. 1640
Werther, J. 1677
Whitaker, S. 482
Willers, E. 1130
Wittig, S. 221
Wong, H. 621
Wu, C.Z. 1427
Wu, C.Z. 1632
Wu, F. 1217
Wu, G.T. 1002
Wu, J. 1560
Wu, X.P. 1340
Wu, Y.Z. 1212
Wyczalek, F.A. 1327
Xiang, J. 1728
Xiao, L.Q. 835
Xin, M.D. 379
Xing, K.Q. 373
Xiong, F. 701
Xiong, Z.H. 1632
Xu, B.Y. 1427
Xu, S.S. 1657
Xu, X.D. 1198
Xu, X.F. 1566
Xu, X.Y. 1433
Xu, Y.Q. 1305
Yabe, A 716
Yabe, A 860
Yabe, T. 1153
Yamada, N. 1233
Yamagishi, F. 695
Yamanaka, T. 1024
Yamashita, T. 1438
Yan, J.H. 1333
Yan, W.M. 949
Yan, W.P. 1591
Yan, Z.D. 1397
Yang, B.C. 821
Yang, B.C. 1289
Yang, D. 1566
Yang, H. 1212
Yang, H.M. 1305
Yang, K. 199
Yang, K.T. 940
Yang, L.W. 1184
Yang, S.M. 310
Yang, X.L. 1433
Yao, B. 1340
Yao, Q. 1281
Ye, X.H. 270
Yeh, C.L. 1640
Yin, X.L. 1427
Yokota, K. 1546
Yokota, M. 852
Yokoya, S. 335
Yong, Y.P. 1651
Yoshikawa, H. 199
Yoshino, H. 1241
Yoshizawa, Y. 1546
You, L.X. 1468
Yu, B.F. 459
Yu, B.F. 1159
Yu, C.J. 1566
Yu, H.L. 355

Yu, H.L. 367
Yu, J. 445
Yu, S.M. 1250
Yu, W.P. 905
Yu, X.L. 1397
Yue, D.T. 1002
Yun, Y. 1703
Zakharov, Y. 1500
Zeng, D.L. 373
Zhang, G. 379
Zhang, H. 621
Zhang, H. 701
Zhang, H.S. 1595
Zhang, H.X. 1048
Zhang, J.W. 1603
Zhang, L. 1198
Zhang, L. Winston 989
Zhang, L.Z. 1066
Zhang, L.Z. 1560
Zhang, S.H. 1489
Zhang, S.Z. 1048
Zhang, W. 1203
Zhang, X. 860
Zhang, X.L. 355
Zhang, X.S. 997
Zhang, Y. 910
Zhang, Y. 1646
Zhang, Y.H. 980
Zhang, Y.P. 788
Zhang, Y.P. 804
Zhang, Y.P. 1059
Zhang, Y.P. 1066
Zhang, Z.J. 490
Zhao, C.Y. 169
Zhao, L.F. 1489
Zhao, L.J. 910
Zhao, T.S. 438
Zhao, T.S. 529
Zhao, Z.L. 1427
Zheng, J.X. 393
Zheng, L. 1360
Zheng, Q.G. 1703
Zhou, H. 1586
Zhou, J. 379
Zhou, J. 1694
Zhou, J.H. 1281
Zhou, J.M. 1615
Zhou, J.S. 1566
Zhou, L.P. 997
Zhou, Q.T. 701
Zhou, T.H. 1468
Zhou, X.Y. 1483
Zhou, Y. 1184
Zhou, Z.J. 1281
Zhu, N. 316
Zhu, W.X. 1184
Zhu, Y.Q. 804
Zhu, Y.X. 788
Zhu, Y.X. 1059
Zou, Z.Q. 1728
Zubkov, P.T. 328
Zuo, Z.J. 573
Zuo, Z.J. 1007